

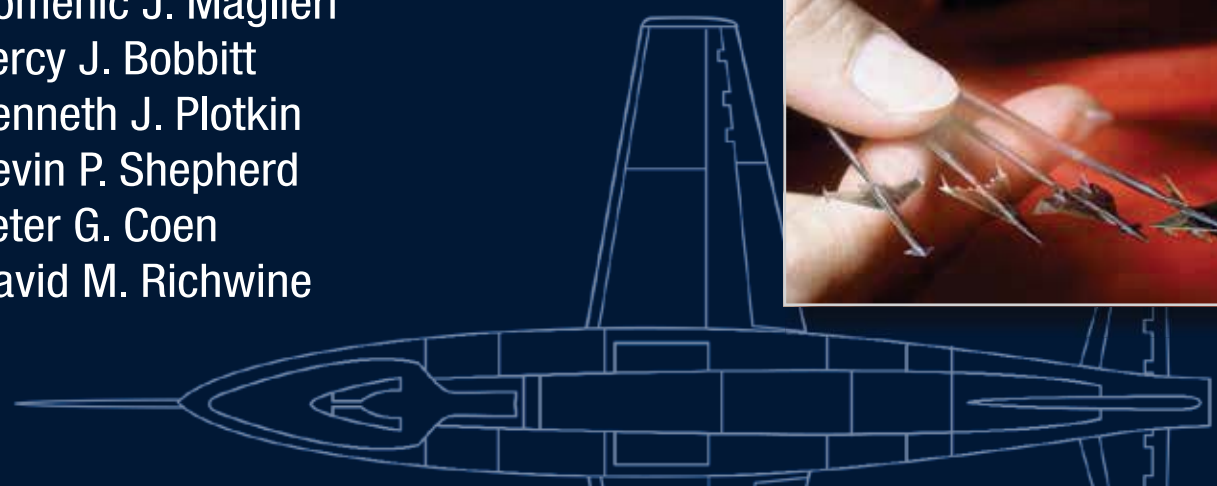


SONIC BOOM

Six Decades of Research



Domenic J. Maglieri
Percy J. Bobbitt
Kenneth J. Plotkin
Kevin P. Shepherd
Peter G. Coen
David M. Richwine





SONIC BOOM

Six Decades
of Research

By

Domenic J. Maglieri (Eagle Aeronautics, Inc.)

Percy J. Bobbitt (Eagle Aeronautics, Inc.)

Kenneth J. Plotkin (Wyle Laboratories, Inc.)

Kevin P. Shepherd (NASA Langley Research Center)

Peter G. Coen (NASA Langley Research Center)

David M. Richwine (NASA Langley Research Center)

NASA/SP-2014-622
Langley Research Center
Hampton, Va. 23681-2199

Notice: Trade names and trademarks are used in this report for identification only. Their usage does not constitute an official endorsement, either expressed or implied, by the National Aeronautics and Space Administration.

ABOUT THE AUTHORS

Domenic J. Maglieri graduated from the University of Pittsburgh in 1951 with a Bachelor of Science (BS) degree in Mechanical Engineering/Aeronautical Engineering (ME/AE) and began his professional career at the National Advisory Committee for Aeronautics (NACA) Langley Aeronautical Laboratory (LAL) (now NASA Langley Research Center [LaRC]). He has over 60 years of experience in noise control and measurements on subsonic and supersonic aircraft, rotorcraft, and vertical/short take-off and landing vehicles. He retired from the National Aeronautics and Space Administration (NASA) in 1986 and joined Eagle Aeronautics as Director for Projects. He is considered one of the leading national and international experts on sonic booms. His sonic boom flight-test involvement began in 1957 and has continued for over a half century. During his 35-year career with NACA/NASA and 28 years with Eagle Aeronautics, he has participated in every major sonic boom flight-test program and has authored or co-authored over 160 publications, 100 of which are on sonic boom. He is a Fellow of the Acoustical Society of America, a board certified member of the Institute of Noise Control Engineering, and an Associate Fellow of the American Institute of Aeronautics and Astronautics (AIAA).

Percy J. Bobbitt graduated from Catholic University in 1949 with a BS degree in AE and began his career at the NACA LAL in 1950. During his 40-year NACA/NASA career, he specialized in supersonic and transonic flow theory, aircraft aerodynamics, aeroelastic loads, aerothermodynamics, orbital entry vehicles, supersonic parachutes, shuttle thermal protection, wind-tunnel flow quality, and laminar flow control. He retired in 1990 as Chief of the Applied Aerodynamics Division, where he was responsible for the conduct of aeronautical research in fundamental fluid flows, configuration aerodynamics, test techniques, and propulsion system integration. He was a key member of the Shuttle Certification Committee for first flight, and he and his division were major contributors in bringing the National Transonic Facility to operational status. He joined Eagle Aeronautics, Inc. in 1990 as Chief Scientist and for the past 24 years has been active in applied CFD code research, particularly in the area of sonic boom generation, propagation, prediction and in the design of low-boom configurations. He has written over 100 published technical reports, received numerous awards from NASA, the AIAA, and the Society of Automotive Engineers (SAE, now SAE International), and is an AIAA Fellow.

Kenneth J. Plotkin received his BS degree from the Polytechnic Institute of Brooklyn in 1965 and his Master of Engineering (ME, 1966) and Doctorate of Philosophy (Ph.D., 1971) from Cornell University, where he first became acquainted with sonic boom. He has worked at Wyle Laboratories for over 40 years, rising to the position of Chief Scientist. His interests over that time period have included analytical and experimental aspects of aircraft and highway noise modeling, atmospheric sound propagation, community noise, rocket noise, high-speed fluctuating flow, truck tire noise, psychoacoustics, community noise, noise control, and sonic boom. He has been involved with sonic boom for nearly half a century and is internationally recognized for his contributions to understanding and alleviation of sonic booms. He is a Fellow of the Acoustical Society of America and has been a member of the AIAA for over 50 years.

Kevin P. Shepherd received MS (1972) and Ph.D. (1979) degrees from the Institute of Sound and Vibration Research, University of Southampton, U.K. He has been engaged in acoustics research at NASA LaRC for over 30 years. His research interests have ranged from wind turbine noise and sound propagation of aircraft noise, including helicopters, airport noise, and sonic boom. His sonic boom research interests have centered on their effects on people and structures and have spanned the past 20 years. He currently heads the Structural Acoustics Branch at NASA LaRC. The primary areas of research are prediction and reduction of aircraft interior noise, engine acoustic liner technology, flyover noise synthesis and simulation, and airport community noise and sonic boom. He has published extensively and is a Fellow of the Acoustical Society of America.

Continued next page

Peter G. Coen received his BS degree in Aerospace Engineering from Polytechnic Institute of New York in 1983 and his MS in Aeronautical Engineering from The George Washington University in 1991. He began his career at NASA's Langley Research Center in 1983 and has worked in the areas of systems analysis, technology integration and multi-disciplinary design, analysis and optimization (MDAO). Most of his career has been focused on supersonic cruise flight. During the NASA High Speed Research (HSR) Project he served on the Propulsion and Airframe Technology Integration Teams and led the Longitudinal Control Alternative Project (LCAP), an early MDAO effort. Post HSR, he continued to work in the area of supersonic aircraft design, with increasing emphasis on sonic boom reduction. He was the NASA technical monitor for the DARPA Quiet Supersonic Platform (QSP) Program and Shaped Sonic Boom Demonstration. Since 2003 he has been the NASA focal point for supersonic technology development and currently serves as Project Manager for the High Speed Project. He has been a member of AIAA since early in his career.

David M. Richwine received his Bachelor of Science/Mechanical Engineering (BS/ME) degree from the University of Virginia in 1983 and MEA from The George Washington University in 1986. He has worked in aeronautics research for over 30 years at NASA LaRC and NASA Dryden Flight Research Center (DFRC). During his 17 years at NASA DFRC, initial duties included aerodynamics, structures, flow visualization, and flight systems for the F-18 High Alpha Research Program and other research experiments on the X-29, B-52, SR-71, and various F-18 research aircraft. Later duties included technical and project management of the F-15B Flight Research Testbed and various flight-test fixtures for supersonic and subsonic flight research experiments. He also served as the Dryden Project Manager for DARPA's QSP Program and F-5E flight test. At NASA LaRC, he has primarily performed project management duties in support of NASA's Supersonics Project and is currently assigned as a Deputy Project Manager for NASA's High Speed Project. He has been a member of the AIAA for over 20 years.

ACKNOWLEDGEMENTS

The authors wish to express their appreciation to the many contributors for their assistance in the preparation of this comprehensive publication. Thanks to Betty P. Joyner of Eagle Aeronautics, Inc. for her untiring efforts in the preparation, compiling, and editing of the many draft versions of the text, equations, tables, and figures. Special appreciation is also extended to Susan H. Stewart of the NASA Langley Information Management Branch for her editorial efforts in guiding this document through publication as well as Susan K. Miller of the Technical Library in searching for, and providing copies of, the many references contained in this report.

Thanks and appreciation to Kenna K. Macauley of Analytical Mechanics Associates, Inc. for the preparation of the final figures and graphics; Mark A. Chambers of NCI Information Systems, Inc. for his untiring efforts as technical editor; and Michael Sean Walsh, also of NCI, for cover design and print preparation.

The authors would also like to thank the Peer Review Committee, comprised of James M. Luckring of NASA LaRC as the Committee Chairman and three former NASA LaRC employees with over 140 years of experience in the field of aeronautics research, for sharing their expertise, invaluable insight, and comments. These Committee members were Joseph R. Chambers, Christine M. Darden, and William L. Willshire.

CONTENTS

ABOUT THE AUTHORS	iii
ACKNOWLEDGEMENTS	iv
CONTENTS	v
INTRODUCTION	1

CHAPTER 1

THE SONIC BOOM PHENOMENON

Description of Shock Flow Field and Development of the Sonic Boom Footprint	5
Ray Paths	7
Sonic Boom Ground Footprint	8
Review of the U.S. Sonic Boom Flight Database	10
The Decade of the 1950s.....	10
The Decade of the 1960s.....	10
The Decades of the 1970s, 1980s, and 1990s	11
The First Decade of the 21st Century	11
Sonic Boom Flight Database – Aircraft Types.....	12
Range of Boom Overpressures Experienced	18
Chapter 1 Summary Remarks	19
Chapter 1 References	19

CHAPTER 2

INFLUENCE OF THE ATMOSPHERE

Primary Booms	23
Macro Atmospheric Effects	24
<i>Temperature and Wind Gradients</i>	24
<i>Effects on Boom Amplitudes</i>	26
<i>Effect on Lateral Spread</i>	27
<i>Lateral Spread Footprint</i>	28
<i>Focusing at Lateral Cutoff</i>	30
<i>Reflection Factor</i>	33
Micro Atmospheric Effects	35
<i>Signature Distortions</i>	35
<i>Effect of Aircraft Pitching Motion</i>	41
<i>Effect of Time of Day</i>	43

CHAPTER 2 continued

<i>Turbulence and Gust Structure</i>	44
<i>Effect of Microphone Orientation</i>	47
<i>Signature Deturbing</i>	51
<i>Off-Track Variability</i>	52
Statistical Variations	53
<i>Effect of Mach Number</i>	54
<i>Effect of Lateral Distance</i>	55
<i>Rise Time Variability</i>	56
<i>Joint Acoustic Propagation Experiment (JAPE) Sonic Boom Experiments</i>	57
Atmospheric Absorption	59
Secondary Booms	62
Chapter 2 Summary Remarks	65
Chapter 2 References	65

CHAPTER 3

INFLUENCE OF MANEUVERS

Nature of Focus Patterns.....	71
Military Operations.....	72
Dives	73
Climbout/Pushover	74
Turns	76
Transition Flight.....	78
On-Track	79
Lateral Locations	84
Modeling Focus Boom Footprint.....	84
Influence of Signature Shape	85
Design Cruise and Incoming Transition Signatures.....	88
Dedicated Flight Transition Experiments	91
Launch Vehicle Transition Focus Boom	92
Focus Boom Avoidance Charts	95
Sonic Booms at High Subsonic Mach Numbers.....	98
Booms from Low-Altitude Level Flight.....	98
Booms from Dive Pull-Up Maneuver	100
Chapter 3 Summary Remarks	101
Chapter 3 References	102

CHAPTER 4**IN-FLIGHT FLOW-FIELD SIGNATURE MEASUREMENTS**

Review of Available Methods	105
Brief Review of Existing Database	107
Early Flight Tests	108
Insight into Nature of Flow Field	108
Measurements of Near-Field Shocks from Passing Aircraft	110
Insight into Effects of Aircraft Lift	111
Validation of CFD Codes	115
SR-71 Aircraft	115
F-5E Inlet Spillage Shock Measurements (ISSM)	119
Shaped Sonic Boom Demonstrator (SSBD) Aircraft	120
F-15B Quiet Spike™ Aircraft	124
Flow-Field Database Utilization	127
Chapter 4 Summary Remarks	129
Chapter 4 References	129

CHAPTER 5**APPROACHES TO SONIC BOOM MINIMIZATION**

Boomless Flight	133
Schematic of Flight Situation	133
Boom Responses	134
Boom Minimization through Aircraft Operations	135
Influence of Altitude and Mach Number	135
Flight Path Angle	136
Mach Cut-Off Operations	138
Tailoring Flight Path	143
Active Control-Unsteady Flight Path	144
Boom Minimization through Aircraft Shaping	146
Configuration/Planform	146
Volume and Lift Distribution	148
<i>Vehicle Shaping – Wind-Tunnel Results</i>	149
<i>Vehicle Shaping – Flight Test Results</i>	150
<i>Exhaust/Aft Shock Interaction – Flight Test Results</i>	152
Wing Planform	154

CHAPTER 5 *continued*

Wing Dihedral	155
Low-Boom Concepts	159
<i>Supersonic Transports</i>	159
<i>Supersonic Business Jets</i>	163
Boom Minimization through Exotic Concepts	165
Heat or Mass Addition	166
<i>Airstream Alteration</i>	166
<i>Thermal Fins</i>	168
<i>Forward Swept Keel</i>	171
<i>Focused Microwave Energy</i>	172
Shock Refraction	173
Exhaust Jet Sheet Deflection	174
Other Unique Exotic Minimization Schemes	175
Overview of Exotic Concepts	177
Chapter 5 Summary Remarks	178
Chapter 5 References	179

CHAPTER 6**THEORETICAL CONSIDERATIONS AND APPLICATIONS**

Fundamental Boom Theory	185
Signature Evolution	190
Signature Aging and Shock Coalescence	196
Pressure Signature Propagation in a Real Atmosphere	197
Ray Tracing	197
Pressure Signature Propagation Codes	201
The Near-Field/Mid-Field Dilemma	204
Shock Smearing and Fitting	204
Mid-Field Pressure Propagation Methods	206
Lateral Variation and Extent of Sonic Boom Signatures	208
Hypersonic Sonic Boom Methodology	214
Boom Predictions and Correlations with Experiment	227
Correlation of Boom Predictions for Aircraft	228
Bodies of Revolution	229
Diamond Cross-Section, Body and Wing Body	232
Apollo Capsule	233

CHAPTER 6 *continued*

Saturn V Launch Vehicle	236
Space Shuttle	239
Peak Overpressure Predictions	250
Chapter 6 Summary Remarks	250
Chapter 6 References	251

CHAPTER 7**SONIC BOOM MINIMIZATION FOR VARIOUS AERODYNAMIC CONFIGURATIONS**

F-Function Boom Minimization	261
The Rapid Pressure Recovery/Expansion	268
Minimization of Sonic Boom Using Various Optimization Schemes	269
The Effect of Engine Nacelles on Sonic Booms	286
F-Function Methodology	286
The Effect of Engine Exhausts on Sonic Booms	304
Calculated Results for Initial Slope and Contours of Jet Plumes	308
Calculation of Exact $\eta(0)$	312
Configuration Design/Analyses Concepts	314
Large Supersonic Commercial Transport Jet Studies	314
Supersonic Commercial Jets	316
Supersonic Business Jet Studies	331
Recent Supersonic Business Jet Studies	332
Chapter 7 Summary Remarks	339
Chapter 7 References	339

CHAPTER 8**RESPONSE TO SONIC BOOMS**

Factors Involved in Sonic Boom Exposures	345
Loading on Buildings	345
Sonic Boom Stimuli	347
Structural Response	350
Damage Complaints	350
Induced Damage	350
Damage Studies	351
<i>Plaster Cracking</i>	351

CHAPTER 8 *continued*

<i>Window Breakage</i>	354
<i>Wall Damage</i>	358
<i>Damage to Historical Structures</i>	360
Building Response to Low Amplitude and Shaped Booms	361
Human Response	366
Loudness and Annoyance	367
<i>Startle</i>	369
<i>Rattle</i>	371
Sleep Interference	372
Acceptability	372
Effects on Human Health	375
Animal Responses	376
Other Responses	378
Seismic	378
Marine Life	380
Effect on Other Aircraft	383
Observations from Intense Boom Levels	385
Chapter 8 Summary Remarks	386
Chapter 8 References	387

CHAPTER 9

SONIC BOOM SIMULATION DEVICES AND TEST TECHNIQUES

Validation of Sonic Boom Design and Predictive Codes	393
Wind Tunnels	394
<i>Test Section Flow Quality</i>	395
<i>Models</i>	396
<i>Pressure Measurement Plate</i>	399
<i>Pressure Measurement Probes</i>	401
<i>Pressure Measurement Rails</i>	407
<i>Model Support</i>	409
Ballistic Range – Free Flight Models	412
Signature Distortions by Turbulence	415
Ballistic Range – Projectiles and Duct Flow Turbulence	416
Spark Discharge and Gas-Filled Bubble	421
Shock Tube Horn and Air Jet	423
Shock Tube and Grid Turbulence	425

CHAPTER 9 *continued*

Projectiles into Atmospheric Turbulence	427
Spark Discharge and Fan Duct Turbulence	429
Quantifying Focus Boom Intensities	434
Mach Cutoff Focus Using Ballistic Range-Mixed Gases	434
Transition Focus Utilizing a Rocket Sled Track	435
Maneuver Focus	437
<i>Spark Mirror Reflector</i>	437
<i>Shock Tube Reflector</i>	439
<i>Ballistic Range-Mixed Gases</i>	439
Underwater Studies	440
Blasting Caps/Flooded Quarry	441
Ballistic Range Water Tank	444
Diffraction and Refraction of Sonic Boom Due to Buildings and Topography	450
Spark Discharge – Parabolic Mirror	451
Ballistic Range – Projectiles	455
Indoor-Outdoor Subjective Response	460
Headphones	461
Loudspeaker Chambers	463
<i>BBN Chamber</i>	463
<i>Lockheed Chamber</i>	464
<i>University of Toronto Institute for Aerospace Studies (UTIAS) Chamber</i>	465
<i>NASA Langley Chamber</i>	468
<i>Lockheed Martin Chamber</i>	470
<i>Gulfstream Portable Chamber</i>	470
<i>Sound Restitution Cabin</i>	472
<i>In-Home Sonic Boom Simulation</i>	474
<i>Georgia Tech Simulator</i>	476
<i>NASA LaRC Indoor Sonic Boom Simulator</i>	477
Piston Systems	479
Explosive Charges	480
<i>Exercise Crackerjack</i>	480
<i>Exercise Westminster</i>	483
<i>U.S. Army/Construction Engineering Research Laboratories (USA/CERL)Tests</i>	486
Building Response Simulations	488
Linear Charges	488
Air Modulation Devices	496
<i>Royal Aircraft Establishment (RAE) Blunderbuss</i>	496

CHAPTER 9 *continued*

<i>LTV Twin Shock Tube</i>	497
<i>General Applied Science Laboratories (GASL)</i>	497
<i>Wyle Laboratories</i>	499
Piston-Driven Devices	499
Loudspeakers	500
<i>Wyle Laboratories Acoustic Drivers</i>	500
<i>Acta Simulator Experiment</i>	503
Chapter 9 Summary Remarks	505
Chapter 9 References	505

CHAPTER 10

OUTLOOK FOR CIVILIAN SUPERSONIC OVERLAND FLIGHT

Predicted Annoyance to Cruise Boom Levels	515
Transition Focus Boom	516
Atmospheric Distortion of Sonic Boom Signatures	517
Sonic Boom Induced Structural Damage, Vibration, and Rattle	518
Research Needs	519
Low-Boom Flight Demonstration	520
Chapter 10 Summary Remarks	520
Chapter 10 References	521

INTRODUCTION

When Chuck Yeager piloted the Bell X-1, an experimental aircraft designed specifically to penetrate the sound barrier, to a speed of Mach 1.07 in level flight at 42,000 ft. on October 14, 1947, it ushered in the era of manned supersonic flight. The introduction of the Century Series fighter aircraft in the 1950s, with their ability to fly at supersonic speeds in level flight due largely in part to the incorporation of Richard Whitcomb's area rule as an aircraft design feature, brought into prominence the sonic boom phenomenon. Since then, sonic booms from military aircraft are widely observed around the world and studies aimed at understanding and controlling sonic booms continue to play a role in the formation of environmental impact statements regarding the establishment of military operational training areas.

Shock waves are inherent to supersonic flight in the atmosphere, and the passage of these shock waves over people, animals, and structures on the ground cannot be completely eliminated. However, the real concern is for civil supersonic overland flight operations that will cause repeated sonic booms over very large areas. The feasibility of routine civil supersonic flight operations and particularly their acceptance by the general public for overland routes may be largely a function of the severity of the sonic boom but also encompasses a plethora of sociological as well as technological considerations.

Practical methods for shaping the boom signature and reducing the intensity to an acceptable level are possible. There was a concerted research effort beginning in the 1960s that produced a multitude of sonic boom flight tests, wind-tunnel experiments, and laboratory tests to establish a credible database, along with hundreds of theoretical investigations in conjunction with the proposed United States Supersonic Transport (SST) Program and the eventual entry of the British-French Concorde into commercial service in 1976. As a result of some of the earlier sonic boom studies, the Federal Aviation Administration (FAA) prohibited civil aircraft from exceeding Mach 1 (or the sonic boom from reaching the ground) over the United States in 1973 (ref. I.1). To comply with the above restriction, British and French commercial aviation regulatory authorities confined Concorde supersonic operations to overwater routes until its final flight in 2003.

Countless papers, journals, and conference proceedings have been published as a result of the SST, Concorde, and various military flight programs. The first Sonic Boom Symposium sponsored by the Acoustical Society of America (ASA) summed up the state of the art as of 1965 (ref. I.2) and recognized the complexity of sonic booms in that so many disciplines were involved in sonic boom research. Engineers and scientists from diverse disciplines including mathematics, aerodynamics, atmospheric physics, meteorology, physical acoustics, structural dynamics, architectural acoustics, geophysics, electronics, and physiological and psychological acoustics were represented. Each discipline had made contributions toward the understanding and minimization of sonic booms and their impact. The 1965 ASA Symposium was followed by ASA symposiums in 1970 (ref. I.3) and 2002 (ref. I.4). NASA also sponsored Sonic Boom Research conferences in 1967, 1968, and 1970 (refs. I.5, I.6, and I.7) dealing with boom generation, propagation, prediction, and minimization.

In 1988 (ref. I.8), 60 of the world's experts in sonic boom attended a 2-day NASA Sonic Boom Workshop to review the status of sonic boom methodology and understanding and to establish the research needs in theory, minimization, atmospheric effects during propagation, and human response. Three primary challenges were identified – (1) establish criteria for acceptable shaped sonic boom signatures, (2) design a viable aircraft with acceptable boom signatures, and (3) quantify atmospheric effects on shaped boom signatures. Soon after the 1988 gathering, significant efforts went into conducting further research on sonic boom and were then reported at annual NASA Sonic Boom Workshops that were held in 1992 (ref. I.9, Vol. 1, and ref. I.10), 1993 (ref. I.11 and ref. I.12), 1994 (ref. I.13 and ref. I.14), and in 1995 (ref. I.15 and ref. I.16). The First Annual High-Speed Research Workshop, held in 1992, also addressed sonic boom issues (ref. I.17, Part 3). Since then, additional flight, experimental and theoretical studies have been conducted resulting in a multitude of publications on the subject of sonic boom.

The numerous publications over the past six decades address the physics, measurement, and minimization of sonic booms and have been included in the reference materials of this publication. In 2010, NASA published Benson's historical review entitled "Softening the Sonic Boom: 50 Years of NASA Research" (ref. I.18), followed by the publication "Quieting the Boom: The Shaped Sonic Boom Demonstrator and the Quest for Quiet Supersonic Flight" (ref. I.19). The authors recommend these publications as additional historical resources for those interested in sonic boom research.

The goal of the authors is for this publication to serve as a comprehensive reference document. The chapters of this document have been structured so that the reader can obtain an overall understanding of sonic boom research conducted over the past six decades and so that a researcher can acquire details on a specific area of interest. The authors have attempted to present the most original data and terminology from the reference materials, but have adapted many of the figures in this document from these reference materials for improved clarity and standardization of nomenclature.

With a publication of such wide scope, some important information and references may be left out. Representative papers have been chosen for some subjects and in other cases there simply may have been an oversight or they may have been published after this report was completed.

Introduction References

- I.1 Code of Federal Regulations, Title 14, Vol. 2, Part 9 – General Operating and Flight Rules, Subpart 1 – Operating Noise Limits, Sec. 91.817, Civil Aircraft Sonic Boom, 1973.
- I.2 Proceedings of the Sonic Boom Symposium. J. Acoust. Soc. Am., Vol. 39, Issue 5B, May 1966.
- I.3 Proceedings of the Second Sonic Boom Symposium. J. Acoust. Soc. Am., Vol. 51, Issue 2C, Feb. 1972.
- I.4 Sonic Boom Symposium. Journal of Acoustical Society of America, Vol. 111, No. 1, Part 2 of 2, Jan. 2002.
- I.5 Sonic Boom Research. NASA SP-147, April 1967.
- I.6 Second Conference on Sonic Boom Research. NASA SP-180, May 1968.
- I.7 Third Conference on Sonic Boom Research. NASA SP-255, Oct. 1970.
- I.8 Status of Sonic Boom Methodology and Understanding. NASA CP-3027.
- I.9 High Speed Research: Sonic Boom, Vol. I. NASA CP-3172, Feb. 1992.
- I.10 High Speed Research: Sonic Boom, Vol. II. NASA CP-3173, Feb. 1992.
- I.11 High Speed Research: Sonic Boom, Vol. I. NASA CP-10132, May 1993.
- I.12 High Speed Research: Sonic Boom, Vol. II. NASA CP-10133, May 1993.
- I.13 High Speed Research: 1994 Sonic Boom Workshop, Atmospheric Propagation and Acceptability Studies. NASA CP-3279, June 1994.
- I.14 High Speed Research: 1994 Sonic Boom Workshop, Vol. II – Configuration Design, Analysis, and Testing. NASA CP-1999-209699, Dec. 1999.
- I.15 1995 NASA High Speed Research Program Sonic Boom Workshop, Vol. I. NASA CP-3335, Sept. 1995.
- I.16 1995 NASA High Speed Research Program Sonic Boom Workshop, Vol. II – Configuration Design, Analysis, and Testing. NASA CP-1999-209520, Dec. 1999.

- I.17 First Annual High-Speed Research Workshop. NASA CP-10087, Part 3, April 1992.
- I.18 Benson, Lawrence R.: Case 4, Softening the Sonic Boom: 50 Years of NASA Research. NASA's Contributions to Aeronautics, Vol. 1, edited by Richard P. Hallion, NASA/SP-2010-570-Vol 1, 2010, pp. 180–274.
- I.19 Benson, Lawrence R.: Quieting the Boom: The Shaped Sonic Boom Demonstrator and the Quest for Quiet Supersonic Flight. NASA SP-2013-601, 2013.

CHAPTER 1 THE SONIC BOOM PHENOMENON

This chapter is intended to provide a brief overview of the general nature of sonic booms beginning with a description of the flow field and shocks surrounding vehicles in supersonic flight together with the acoustic ray paths, along which the shocks propagate to the ground, and the role the atmosphere plays in establishing the sonic boom footprint on the ground. Both primary and secondary carpet booms are produced by supersonic aircraft and the differences in their character are described. Discussions are provided relative to the character of the boom signature measured under both stable and unstable atmospheric conditions within the primary carpet, during steady cruise flight, along the aircraft ground track, and laterally out to the cutoff where the ray paths become tangent to the ground and booms are no longer observed. In addition, the focus boom region that is produced during transition flight of the aircraft as it accelerates from subsonic to supersonic speed is also discussed.

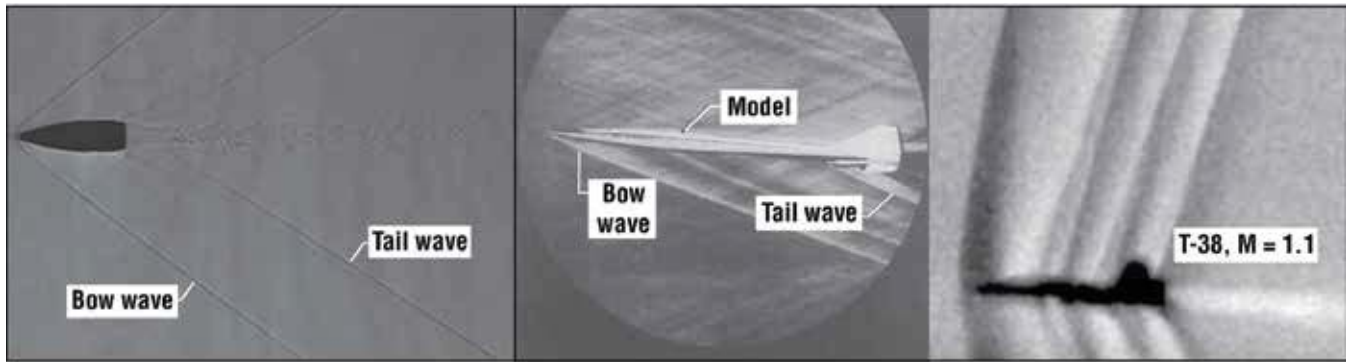
Complaints from members of communities exposed to sonic booms within the ground footprint have ranged from those members complaining about being startled and annoyed to those raising their concerns of interrupted sleep and worries of detrimental effects on their long-term health. In addition, concerns about structural damage and the effect of booms on wildlife and marine life, and the potential for triggering earthquakes and avalanches are also mentioned. Answers to, and alleviation of, all these concerns required a better understanding of the sonic boom in regard to its generation, propagation, and prediction. The research paths included analytical and experimental efforts involving wind-tunnel tests of supersonic vehicle models, laboratory simulation devices, and test techniques such as boom simulation chambers, ballistic ranges, and explosive charges as well as flight-test programs. For over 6 decades, the development and use of experimental simulation techniques have fulfilled a wide variety of boom research needs. Use of these devices has complemented and, in some cases, taken the place of complex, lengthy, and costly supersonic flight tests. All three of these research paths – analytical, experimental laboratory, and flight tests – contributed equally to providing the understanding of and solutions to the sonic boom problem. However, sonic boom flight tests are always the final requirement.

The chapter concludes with a review of the United States sonic boom flight-test programs that have been conducted over the past 6 decades. Each of these flight activities contributed to the understanding of sonic booms that in turn stimulated and guided analytical and laboratory efforts. Discussion of the thrust of these sonic boom flight-test programs along with an indication of concurrent analytical and laboratory efforts will be presented.

Description of Shock Flow Field and Development of the Sonic Boom Footprint

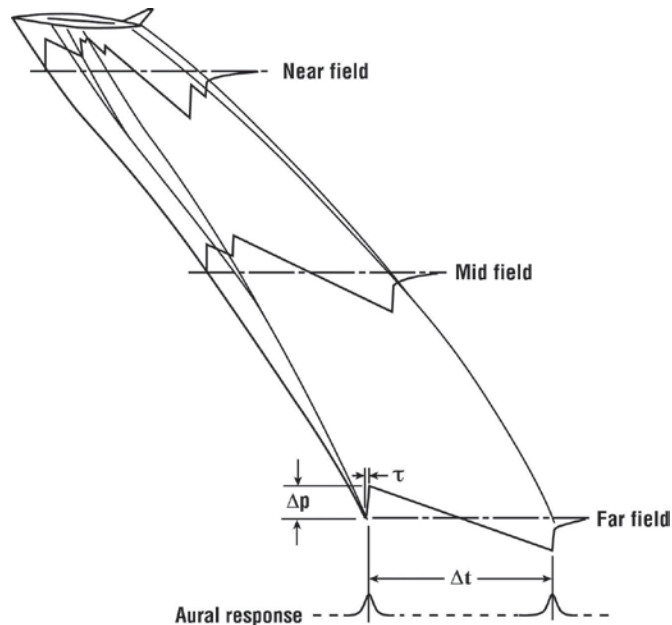
Any body that moves through the air at speeds exceeding the local speed of sound has an associated system of near-conical shock waves attached to the body, as shown in figure 1.1. A simple body of revolution (i.e., a projectile) generally has two shocks – one attached to the front called the bow shock and the other emanating from the rear called the tail shock (fig. 1.1(a)). More complicated configurations, such as the small aircraft model and the full-scale aircraft on the right (ref. 1.1) shown in figure 1.1(b), produce whole systems of shock waves. At very large distances from the body, the wave system tends to coalesce into bow and tail waves as in the case of the simple projectile.

Figure 1.1(c) shows a schematic diagram representing the shock flow field surrounding an aircraft in flight. In the near field, close to the aircraft, the pressure signature exhibits several shocks that emanate from the nose of the aircraft, the canopy, inlet, wing, and tail. As these shocks propagate away from the aircraft to the mid field, some of them have coalesced such that the pressure signature now consists of only three shocks. In the far field, only the bow and tail shocks remain to form the N-wave signature at the ground.



(a) Flow field from a projectile.

(b) Typical flow field for aircraft configurations.



(c) Near-, mid- and far-field boom signatures.

Figure 1.1. Shock flow field pressure.

At the ground, compression occurs at the bow shock in which the local pressure rises to a value above atmospheric pressure. Increments in pressure (both positive and negative) relative to the atmosphere are typically denoted by the symbol Δp . Following the bow shock, a slow expansion then occurs until a value below atmospheric pressure is reached, after which there is a sudden recompression at the tail shock. Generally, as the bow and tail shocks reach their maximum value they have a slight slope associated with these shocks known as rise time (τ), after which, in the case of the bow shock, the pressure decreases in a linear fashion to the tail shock. This nominal sonic boom N-wave signature moves with the aircraft and is associated with continuous supersonic flight, not just with breaking the sound barrier.

A full-range microphone placed on the ground would detect the N-wave pressure time history, as indicated in figure 1.1(c). Since the human ear is sensitive to higher frequencies, it responds to the rapidly changing part of the waveform and not to the portion that is changing slowly. If the time interval Δt between those two rapid compressions is small, as for a bullet, the ear is not able to distinguish between them and they seem to be as one explosive sound, or crack. If the time interval is on the order of 0.10 sec or greater, as is the case for an aircraft at high altitude, the ear detects two booms (or bangs) corresponding to the rapid pressure changes at the front and rear of the N-wave signature. It is of interest to note that the sonic boom overpressures normally observed from supersonic aircraft at nominal flight altitudes are on the order of only 1.0 lb/ft² to 3.0 lbs/ft² more than the uniform atmospheric pressure of ~ 2116 lbs/ft² experienced by the body at sea level.

Ray Paths

The atmosphere above and below the aircraft plays a significant role in establishing the character of the sonic boom signature as it propagates away from the aircraft to the ground and defines the extent of the boom footprint on the ground. Two types of effects are present. The first type is classified as macro effects that are comprised of atmospheric pressure, temperature, and wind profiles and gradients. These result in the bending or refraction of the ray paths along which the shocks propagate and thus define the intensity, location, and lateral extent of the sonic boom footprints. In contrast, turbulence, especially in the lower layers of the atmosphere near the ground, plus atmospheric absorption and molecular relaxation are classified as micro effects, yet can have a significant effect on altering the boom signature causing large variations in the shock strength and rise times.

The influence of macro effects of the atmosphere, temperature, and wind above and below an aircraft on the sonic boom ground footprint is presented in the ray diagram of figure 1.2. Rays describe the paths that the shocks travel along as they propagate away from the aircraft. On the right-hand side of figure 1.2 are examples of temperature and wind profiles for a representative atmosphere. Note that there is a portion of the higher atmosphere above the aircraft flight altitude, the thermosphere, in which the temperature increases with altitude as compared to the lower portions of the atmosphere below the aircraft. The rays that propagate above the aircraft are turned downward towards the ground as they reach the thermosphere. Below the aircraft (the tropopause), the downward propagating rays that are refracted continue until they reach the thermosphere and are then bent downward back towards the ground. The wind-speed gradient will also influence refraction and may reinforce or counteract the effects due to temperature gradient.

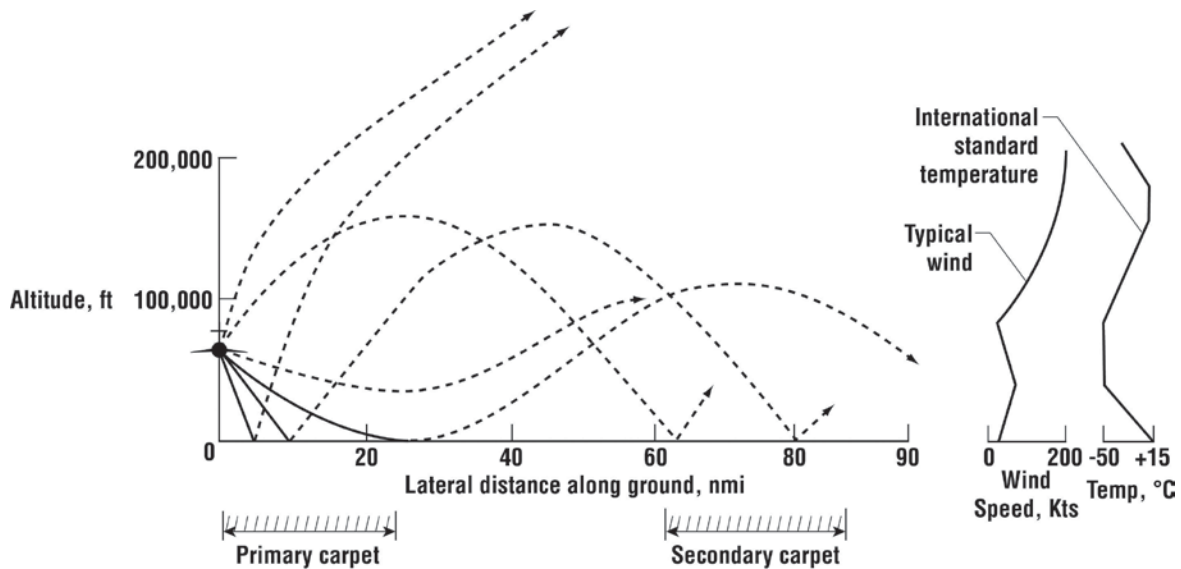


Figure 1.2. Ray path diagram in plane normal to that of flight.

On the left-hand side of figure 1.2 is a ray diagram showing a variety of ray paths that the shock waves travel for an aircraft in supersonic flight at an altitude of 60,000 feet, traveling toward the viewer. The downward propagating rays, shown by the solid lines, impact the ground to form the primary boom carpet, as indicated in the figure. At a lateral distance of about 25 nmi in the example shown, the rays refract away from the ground and thus define the lateral extent of the primary boom carpet.

Also indicated is a secondary carpet, at about 65 to 85 nmi from the flight track, in which the dashed-line rays impact. These dashed-line rays arrive in two different ways – they either travel directly to the secondary carpet as a result of bending in the upper atmosphere or they may first impinge in the primary carpet, reflect upward from the surface, and then bend downward after traveling through a portion of the upper atmosphere. The representation of the secondary carpet in this illustration is somewhat oversimplified, because there is reason to believe that it could consist of several well-defined impact areas (ref. 1.2). Variations in atmospheric wind and temperature profiles,

however, could cause these impact areas to be ill defined. Some of the steep-angle rays above the aircraft may travel in such a way that they are dissipated without ever approaching the ground.

Sonic Boom Ground Footprint

The nature of the sonic boom carpets for a representative civil supersonic transport during which the aircraft flies a large portion of the distance supersonically is shown in figure 1.3. Two ground exposure patterns in which booms can be experienced are shown. The primary boom carpet contains the normally observed sonic boom shortly after the passage of the aircraft and results from shocks that have propagated through the atmosphere below the aircraft. Secondary boom carpets involve the portion of the atmosphere above the aircraft as well as that below the aircraft. Between the primary and secondary carpets exists a region in which no sonic booms are observed. The secondary booms, which can arrive as much as 10 to 15 min after the passage of the aircraft, are more remote from the ground track with overpressure levels much smaller than those within the primary carpet.

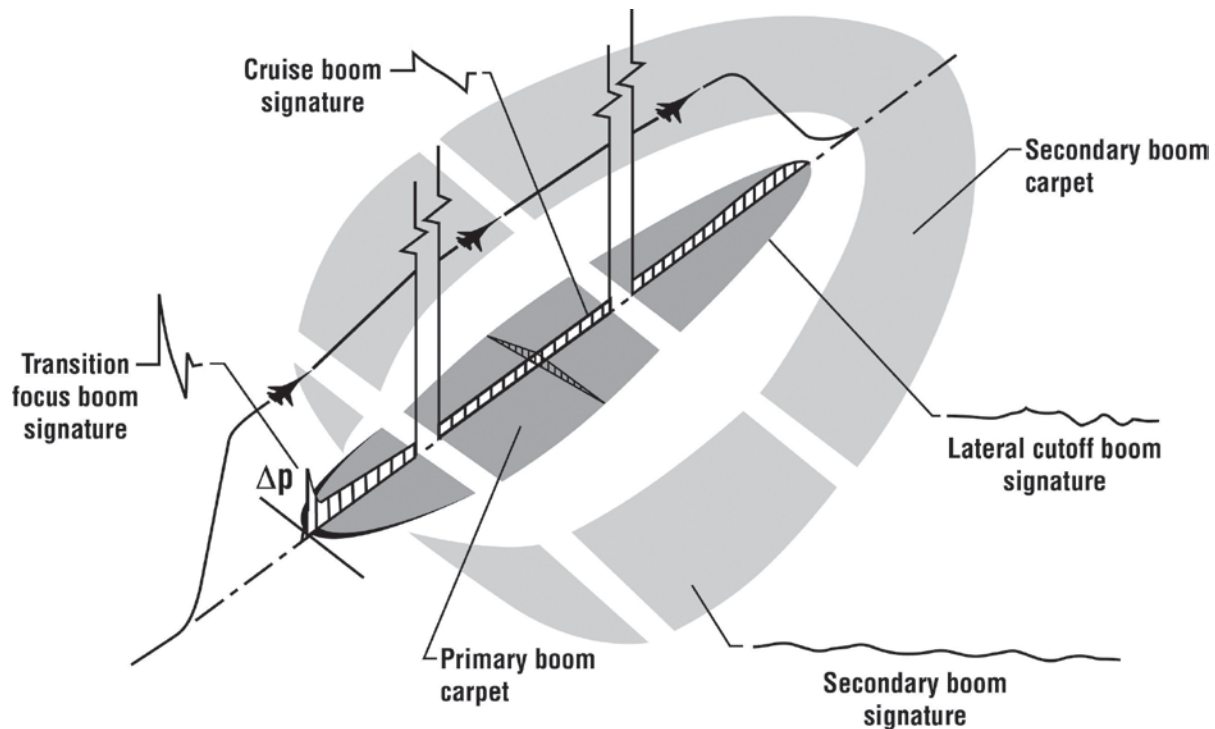


Figure 1.3. Schematic of sonic boom ground exposures.

The waveform characteristics of the boom signatures in the boom carpet can vary widely at different observation points as indicated in the figure. A focus boom having a signature as shown in the left side of figure 1.3 is the first boom to impact the ground. Focus booms will always result when any aircraft accelerates from subsonic to supersonic speeds. In addition, any rapid deviation of a vehicle from steady-level supersonic flight such as turns, dives, and pushover usually associated with military operations can also result in considerable modifications in the location, number, and intensity of the ground shock wave patterns, resulting in multiple booms and focused booms. For civil supersonic operations, all maneuvers that could result in a focus boom on the ground can be avoided except for the unavoidable transition focus boom. The transition focus booms, which occur along the crescent shaped black region shown in the lower left of figure 1.3, are followed by a region on the ground (shaded area) in which multiple booms are observed. Transition focus booms can be placed to within a few thousand feet of a designated location and can be minimized by proper scheduling of acceleration and altitude, and by favorable shaping of the aircraft and thus the boom signature. The focus booms associated with aircraft of the past 6 decades are similar in overall shape to the N-wave signatures generated in steady-level flight operations but with leading and trailing shocks that have been amplified. Focus booms are a one-time occurrence and are not dragged along with the aircraft as are the primary and secondary carpet booms.

In the region of the primary boom carpet, on or near the ground track, N-wave signatures are usually observed. For military aircraft at typical high-altitude cruise conditions, these booms have usually been on the order of 1 lb/ft² to 3 lbs/ft² in intensity and from 0.10 to 0.30 sec in duration. In addition to the macro atmospheric effects previously discussed, micro atmospheric effects can alter the boom signatures causing large variations in the shock strength and increased shock rise times as shown in figure 1.4 (ref. 1.3). The measured boom signatures shown in figure 1.4 were recorded by five microphones (100 feet apart) arranged in a cruciform array. The aircraft was flown at a slightly different Mach number and altitude on two different days, one day having low-wind conditions and the other with high winds and gusts.

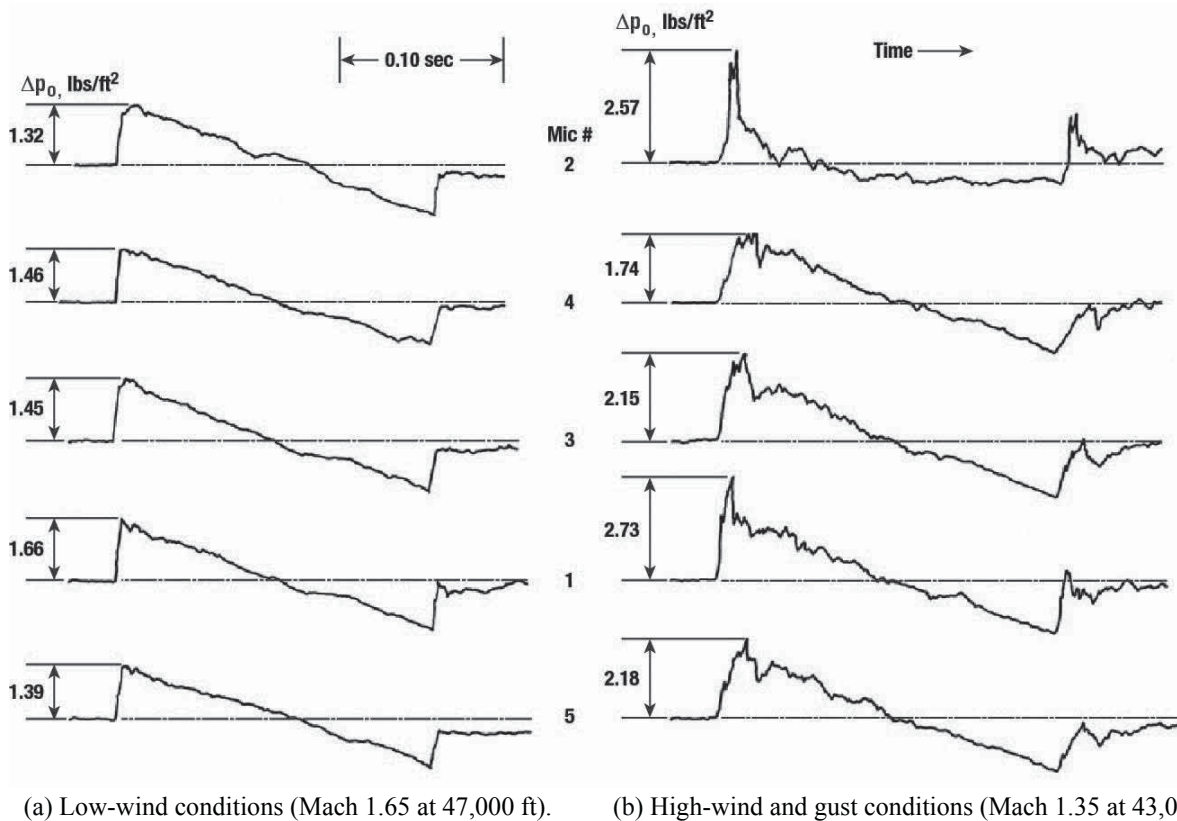


Figure 1.4. Variability in boom signatures resulting from the atmosphere (adapted from ref. 1.3).

Referring back to figure 1.3, at the fringes of the primary boom carpet near the lateral cutoff, the signatures degenerate into weak sound waves and they lose their N-wave characteristics. In the region of the secondary boom carpet, the disturbances tend to be very weak in intensity (on the order of 0.02 to 0.20 lb/ft²) and persist over longer periods of time (on the order of 5 to 10 sec).

Higher overpressure N-wave booms within the primary boom carpet have resulted in complaints from those within the communities overflowed that include being startled and annoyed, loss of sleep, and concern about the long-term effects on their health in general. Worries of booms causing structural damage, their effects on wildlife and marine life, and the potential for causing avalanches and even earthquakes have also been cited. On the other hand, the lateral cutoff booms and the secondary booms, which do not have an N-wave character and are much lower in intensity, tend to be more of a curiosity and are not apt to be the source of serious community response problems. Near the lateral cutoff, booms usually resemble low rumbles or rolling thunder. Secondary booms are generally not audible (0.1 to 1.0 Hz), but can cause building vibrations that can be detected.

lbs/ft² to 2.0 lbs/ft² SST booms would not be acceptable. Research on methods to reduce sonic booms became all important and provoked research in the areas of improvement of sonic boom prediction methods, methods to minimize booms by means of aircraft operations, and the shaping of the aircraft's volume and lift distribution. This research also included studies and wind-tunnel tests on several exotic schemes such as altering the flow field surrounding the aircraft to create a phantom body. These studies, along with several major efforts conducted in England and France, provided considerable insight as to the generation, propagation, prediction, and minimization of sonic booms and their effects on people, animals, and structures. A major portion of the findings from these flight tests are presented and discussed in Chapters 5–9.

The Decades of the 1970s, 1980s, and 1990s

Following the decision to terminate the U.S. SST effort and the shift by England and France to limit the supersonic segment of Concorde operations to overwater sonic boom studies continued at a much slower pace during the 1970s, 1980s, and early 1990s and focused primarily on developing a database for the formation of environmental impact statements regarding the establishment of military operations areas (MOAs) (ref. 1.5) and the Apollo and Space Shuttle programs (ref. 1.6). Substantial progress was made toward the understanding of atmospheric propagation. Molecular absorption was found to make a significant contribution in establishing the boom signature rise time and was identified as becoming more influential and beneficial as boom overpressure decreased. It was also validated that turbulence is the primary cause of boom signature distortions, as demonstrated in the early flight tests of the 1960s (discussed in Chapter 2). Psychoacoustic studies showed that boom signatures having large rise times were indeed quieter than conventional N-wave signatures. Limiting civil supersonic operations to overwater routes as an option to overland routes also posed a concern for marine life. This concern was addressed by the development of models for penetration of the sonic boom into the ocean, along with laboratory and flight experiments as discussed in Chapter 9.

NASA's High Speed Civil Transport (HSCT) and High Speed Research (HSR) Programs in the early and mid-1990s caused a major resurgence of sonic boom studies. The era of aircraft design by linear supersonic area rule was coming to a close and the era of Computational Fluid Dynamics (CFD) analysis began to transform modern aircraft design and analysis as discussed in Chapter 6. The activities of the 1960s directed towards sonic boom minimization approaches that focused on aircraft operations and exotic approaches, such as altering the airstream surrounding the aircraft, continued at a slower pace. The use of aircraft shaping to achieve sonic boom minimization continued at an accelerated pace (Chapters 5 and 7).

The First Decade of the 21st Century

In the early 2000s, the Defense Advanced Research Projects Agency (DARPA) funded the Quiet Supersonic Platform (QSP) (ref. 1.7) that was to be a long-range highly efficient low-boom supersonic airplane having an initial boom of 0.3 lb/ft². Included in the QSP effort was the Shaped Sonic Boom Demonstrator (SSBD) flight-test program (ref. 1.8) and its follow-on effort, the Shaped Sonic Boom Experiment (SSBE). Prior to the SSBD, all supersonic aircraft were classed as N-wave designs with minimal concern for sonic boom minimization. As a result, all of the sonic boom signatures from sonic boom flight tests prior to this program were saw-toothed or N-wave. Theory and wind-tunnel tests indicated that proper shaping of the aircraft's volume and lift distributions would alter and soften the boom signature. The SSBD flight test became the first flight demonstration in which a full-scale aircraft flying in a real atmosphere was designed to produce more desirable shaped signature at the ground. A picture of the F-5E baseline aircraft and its modified version, the SSBD, is shown in figure 1.5 (ref. 1.8). Also shown are the original and modified equivalent area distribution plots and resulting boom signatures measured at the ground.

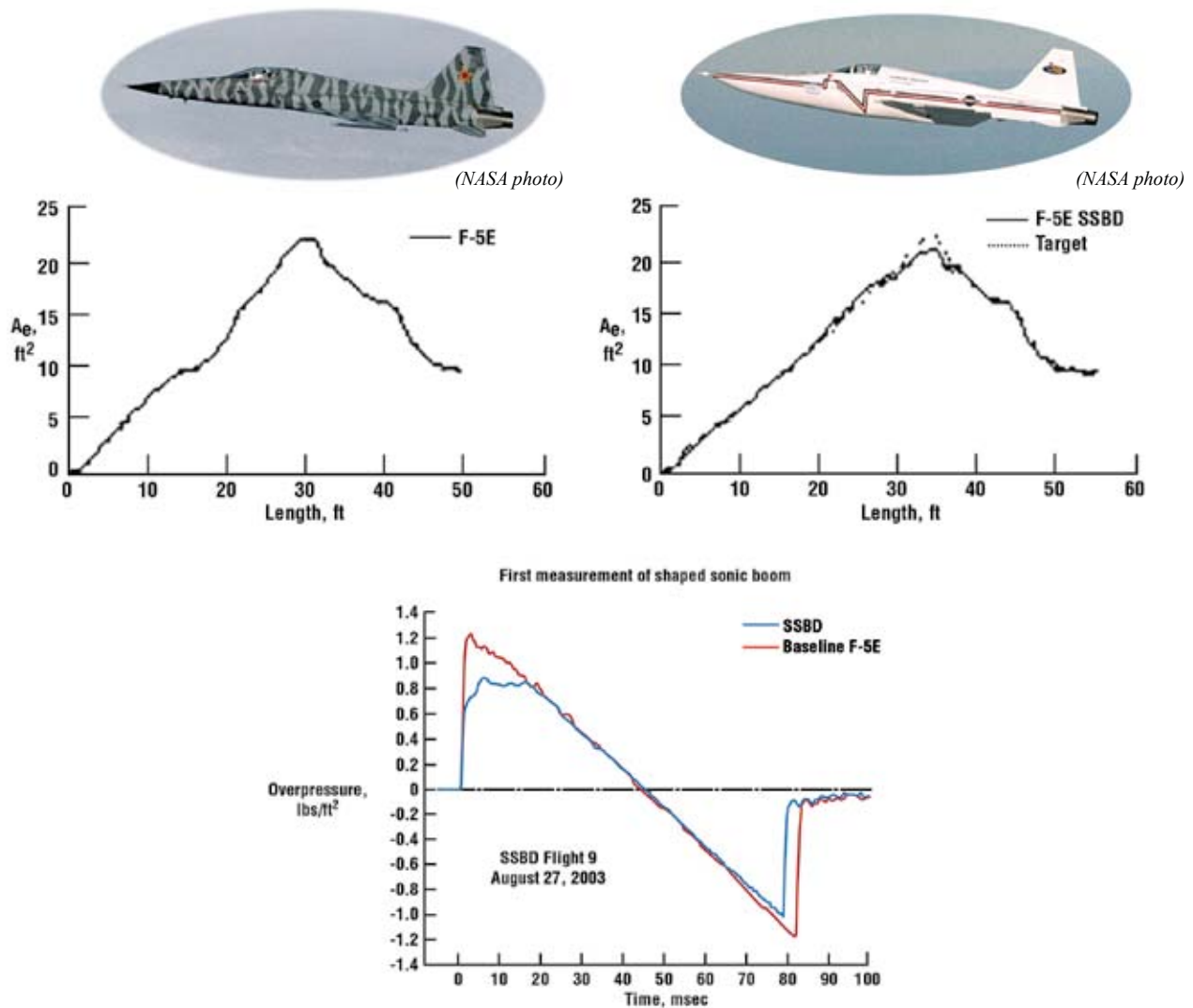


Figure 1.5. Modification of the F-5E into the SSBD (adapted from ref. 1.8).

This finding stimulated a renewed interest in designing low-boom aircraft capable of finding community acceptance to civil supersonic flight operations. The NASA Low-Boom tests conducted at EAFB in 2007–2008 (refs. 1.9, 1.10, and 1.11) along with the NASA Waveforms and Sonic boom Perception and Response (WSPR) (ref. 1.12) low-boom community response pilot program conducted at EAFB in 2011 – 2012 are expected to provide further information that could be used to define community acceptance metrics and levels discussed in Chapter 10.

Even as these efforts were proceeding, the requirement to find solutions that will minimize the transition focus boom did not go unchallenged. Several U.S. sonic boom flight-test programs that included transition flight maneuvers were conducted in 1961, 1965, 1970, and 1994. In 2011, NASA completed a series of transition focus boom flight tests identified as Superboom Caustic and Analysis Measured Program (SCAMP) that were specifically aimed at quantifying the focus boom footprint (see refs. 1.13, 1.14, and Chapter 3 of this publication).

Sonic Boom Flight Database – Aircraft Types

Some interesting points must be made regarding the large database for sonic booms from aircraft. Most of the database is from aircraft operating within the Mach number range 1.0 to 3.0 and altitudes from about 50 feet to 80,000 feet. In addition, Space Shuttle measurements have been made on flights spanning supersonic and hypersonic conditions from Mach 1.3 at an altitude of 58,000 feet to Mach 23 at an altitude of 250,000 feet during reentry flight. About half the database is essentially steady-level flight since the flights were aimed at the operational range of the proposed U.S. SST. The other half of the sonic boom database includes combat

maneuvering training operations that occur in Military Operating Areas that include various types of maneuvers and low and high Mach-altitude operations.

The sonic boom signatures, which were for the most part saw-tooth type or N-waves, had overpressures for steady-level flight that ranged from about 0.75 lb/ft² to 3.0 lbs/ft² (excluding flights at very low altitudes and focus booms due to maneuvering). Since the military inventory of supersonic aircraft was devoid of any vehicles that would generate very low overpressure levels along the ground track or signatures that are non-N-wave in shape, little information is available for low-boom shaped signatures. The previously mentioned NASA Low Boom flight test recorded booms down to a few tenths of a lb/ft² through the use of a special dive maneuver using an F-18 (ref. 1.9) and booms of less than 0.1 lb/ft² have been measured from a small reentry vehicle (refs. 1.15 and 1.16).

Table 1.2 lists the 19 supersonic aircraft for which sonic boom ground measurements have been obtained and also includes the Space Shuttle Orbiter on reentry. The vehicles ranged in size from about 46 feet in length for the F-5/T-38 to 185 feet for the XB-70. Wing spans of the vehicles ranged from 25 feet for the F-5/T-38 to 105 feet for the XB-70. Gross weights varied from 10,000 lbs for the X-15 to 450,000 pounds for the XB-70. Measurements have also been obtained on the Shuttle and Apollo ascent and reentry. Although not part of the U. S. sonic boom flight database, sonic boom ground measurements were obtained on the Concorde and TU-144 civil supersonic transports. Pictures of aircraft included in the U.S. sonic boom flight database, as well as the Concorde and the TU-144 civil supersonic transports are shown on the next few pages.

Table 1.2. Aircraft Types for which Data is Available in the United States Sonic Boom Flight Database

<i>Aircraft</i>	<i>Length, Feet</i>	<i>Span, Feet</i>	<i>Gross Weight, Pounds</i>
F-4	63	38	50,000
F-5 (T-38)	46	25	15,000
F8U-3	59	40	30,000
F-14	63	40	45,000
F-15	64	43	40,000
F-16	48	31	20,000
F-18	56	38	30,000
F-100	47	38	20,000
F-101	67	40	35,000
F-104	55	26	16,000
F-105	65	34	25,000
F-106	71	38	30,000
F-111	76	32	70,000
B-58	97	57	100,000
SR-71	107	56	130,000
XB-70	185	105	450,000
X-15	50	22	10,000
Tornado	55	28	40,000
STS Orbiter	122	78	200,000
SSBD	50	25	15,000

Aircraft Types for which Data is Available in the United States Sonic Boom Flight Database



(NASA photo, EC84-29772)

McDonnell Douglas F-4C Phantom II.



(NASA photo, EC03-0229-Fr-43)

Northrop F-5E Tiger II.



(NASA photo, ED06-0072-4)

Northrop T-38 Talon.



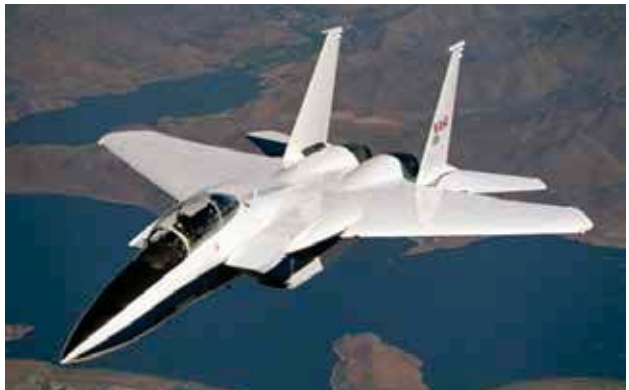
(Photo courtesy of Don Mallick)

Chance Vought F8U-3 Crusader.



(NASA photo, EC85-33116-04)

Grumman F-14 Tomcat.



(NASA photo, EC96-43546-01)

McDonnell Douglas F-15B Eagle.



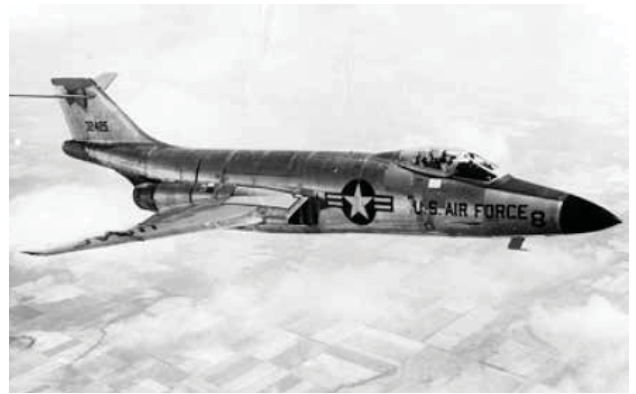
(NASA photo, EL-1996-00110)

General Dynamics F-16 Fighting Falcon.



(U.S. Air Force photo)

North American F-100D Super Sabre.



(U.S. Air Force photo)

McDonnell F-101A Voodoo.



(NASA photo, EC77-8023)

Lockheed F-104 Starfighter.



(U.S. Air Force photo)

Republic F-105D Thunderchief.



(NASA photo)

Convair F-106B Delta Dart.



(NASA photo, EC68-2085)

General Dynamics F-111A Aardvark.



(U.S. Air Force photo)

Convair B-58 Hustler:



(NASA photo, EC92-09241-1)

Lockheed SR-71 Blackbird.



(NASA photo, EC85-33116-04)

*North American XB-70A Valkyrie
(note the aircraft is in supersonic cruise configuration).*



(NASA photo, EC88-0180-1)

North American X-15.



(U.S. Air Force photo by Airman 1st Class Christopher Griffin)

Panavia Tornado.



(NASA photo, EC89-0100-011)

*Space Transportation System (STS) Orbiter
(Space Shuttle).*



(NASA photo, EC03-0210-1)

*Northrop Grumman F-5E Shaped
Sonic Boom Demonstrator (SSBD).*

Examples of Once Operational Supersonic Transports for which Sonic Boom Data Have Also Been Obtained



(NASA photo, EC76-5886)

*Aerospatiale-British Aerospace Concorde
Supersonic Transport (SST).*



(NASA photo, EC98-44749-23)

Tupolev TU-144 Supersonic Transport (SST).

Range of Boom Overpressures Experienced

The ranges of overpressures involved in community response, structural, and special studies under various flight-test programs are listed chronologically shown in table 1.3. B-58 training represents military operational booms to which various U.S. cities have been exposed to supersonic training flights of the USAF, with no relation to a sonic boom research purpose. Sonic boom levels were less than 5 lbs/ft² (refs. 1.3 and 1.17). Little Boom (ref. 1.18) refers to studies at Nellis AFB to evaluate the potential of using sonic booms from flying aircraft supersonically at very low altitudes as a combat weapon. Overpressures as high as 120 lbs/ft² were experienced. St. Louis was one of the B-58 training flight programs, with the community response observations (ref. 1.17) being conducted as a piggyback operation. Project Little Man (ref. 1.19) refers to a study to establish the influence of booms of up to about 14 lbs/ft² on light aircraft during takeoff, landing, and cruise flight. The Oklahoma City community response tests (refs. 1.20, 1.21, and 1.22) were conducted over a period of 6 months with about eight booms/day of overpressures from about 1.3 lbs/ft² to 1.7 lbs/ft². The White Sands (ref. 1.23) test was conducted to investigate building response and damage due to sonic booms of up to about 25 lbs/ft². Chicago, like St. Louis, was another of the B-58 training flight programs with the emphasis on examining the variability of sonic boom signatures due to the atmosphere, which differed from the desert area (ref. 1.3). A summary of boom complaints and damage were also documented. Joint Task Force II (ref. 1.24) was an effort similar to project Little Boom wherein boom levels of 144 lbs/ft² were measured.

Table 1.3. Range of Sonic Boom Overpressures Experienced in Various Studies

	Community	Structural	Special Studies	References
B-58 Training	1960-65			1.3 and 1.17
Little Boom	1960			1.18
St. Louis	1961-62			1.17
Little Man	1963			1.19
Oklahoma City	1964			1.20, 1.21 and 1.22
White Sands	1965			1.23
Chicago	1965			1.3
Joint Task Force II	1965			1.24
NSBEO-EAFB	1966-67			1.25
Nellis-EAFB	1992-95			1.27
NASA Low Boom	2006-07			1.9, 1.10 and 1.11
NASA WSPR	2011-12			1.26

0 10 20 30 100 150
Sonic boom overpressure, lbs/ft²

During the 1966–1967 time period, the U.S. National Sonic Boom Program conducted an extensive sonic boom study at EAFB and involved the USAF, Federal Aviation Administration (FAA), National Oceanic and Atmospheric Administration (NOAA), and National Aeronautics and Space Administration (NASA) (ref. 1.25). In 1987, the USAF conducted an extensive flight-test program to measure the sonic boom signatures from all existing military supersonic aircraft. This activity involved eight aircraft performing 43 steady-supersonic flights over a 6-day period. This measured database (called BOOMFILE) is presented in reference 1.26. It is not included in the table since it does not relate to response studies. Instead, the database is useful for verification of analytical codes for further studies of boom propagation through the atmosphere. From 1992 through 1995, the Western USA Sonic Boom survey (ref. 1.27) was conducted to acquire residents' reactions to long-term exposures to sonic booms in the Nellis AFB, Nevada and EAFB, California regions. In order to acquire a database regarding the response of humans outdoors and indoors to low-level sonic booms, along with building responses, NASA conducted the 2006–2007 Low Boom (refs. 1.9, 1.10, and 1.11) and 2011–2012 WSPR flight-test programs (ref. 1.12) at EAFB.

Chapter 1 Summary Remarks

Any body that moves through the air at speeds exceeding the local speed of sound has an associated system of shock waves that, when propagated to the ground, are observed as a sonic boom. The sonic boom ground signature is characterized by a bow shock with a local pressure rise followed by an expansion, other shocks and the tail shock which all typically coalesce into an N-wave.

The sonic boom ground footprint from the aircraft shock waves propagates through the atmosphere above and below the aircraft and is comprised of primary carpet booms that result from shock waves propagating through the atmosphere below the aircraft. The secondary carpet booms result from shock waves that propagate through the atmosphere above and below the aircraft. Atmospheric effects can play an important role in the character and magnitude of these primary and secondary carpet booms.

Primary booms have been intensely researched resulting in an extensive database on 19 aircraft. Apollo and Shuttle vehicles and boom signatures have been measured from flights at Mach numbers of 1.12 at a test altitude of 50 feet up to Mach 23 at an altitude of 250,000 feet. The normally observed sonic booms from military aircraft at flight altitudes are in the 1.0 lb/ft² to 3.0 lbs/ft² range. However, sonic boom overpressures from less than 0.1 lb/ft² to 144 lbs/ft² have been measured during specially designed flight tests. With the exception of the Shaped Sonic Boom Demonstrator (SSBD) signature, all 6 decades of measured primary boom carpet signatures have been sawtooth or N-wave in character.

Secondary boom signatures are shockless and an order of magnitude lower in overpressure and frequency than those of primary booms. As a result, they are difficult to sense outdoors but can be noticeable indoors as vibrations.

Chapter 1 References

- 1.1 Weinstein, Leonard: An Optical Technique for Examining Aircraft Shock Wave Structures in Flight. NASA CP-3279, June 1994, pp. 1–17.
- 1.2 Plotkin, K. J.; Page, J. A.; and Haering, E. A: Extension of PCBoom to Over-The-Top Booms, Ellipsoidal Earth, and Full 3-D Ray Tracing, AIAA 2007-3677, May 2007.
- 1.3 Hilton, David A.; Huckel, Vera; and Maglieri, Domenic J.: Sonic Boom Measurements during Bomber Training Operations in the Chicago Area. NASA TN D-3655, Oct. 1966.
- 1.4 Von Gierke, Henning E. and Nixon, Charles W.: Human Response to Sonic Boom in the Laboratory and the Community. *J. Acoust. Soc. Am.*, 51, 1972, pp. 766–782.

- 1.5 Draft Environmental Assessment: Reserve Military Operations Area New Mexico. USAF Tactical Air Command. Dec. 1989.
- 1.6 Environmental Impact Statement: Space Shuttle Program. April, 1978.
- 1.7 Wlezien, R. and Veitch, L.: Quiet Supersonic Platform. AIAA Paper 2002-0143, Jan. 2002.
- 1.8 Pawlowski, Joseph W.; Graham, David H.; Boccadoro, Charles H.; Coen, Peter G.; and Maglieri, Domenic J.: Origins and Overview of a Shaped Sonic Boom Demonstration Program. AIAA Paper 2005-0005, Jan. 2005.
- 1.9 Sullivan, Brenda M.; Klos, Jacob; Buehrie, Ralph D.; McCurdy, David A.; and Haering, Edward A., Jr.: Human Response to Low-Intensity Sonic Booms Heard Indoors and Outdoors. NASA TM 2010-216685, June 2010.
- 1.10 Klos, Jacob and Buerie, Ralph D.: Vibro-Acoustic Response of Buildings Due to Sonic Boom Exposure, June 2006, Field Test, NASA TM-2007-214900, Sept. 2007.
- 1.11 Klos, J.: Vibro-Acoustic Response of Buildings Due to Sonic Boom Exposure: July 2007 Field Test, NASA TM-2008-215349, Sept. 2008.
- 1.12 Page, J.; Hodgdon, K.; Hobbs, C.; Wilmer, C.; Kreker, P.; Koeing, C.; Holmes, T.; Cowart, R.; Gaugler, T.; Shumway, D.; Rosenberger, J.; and Phillips, D.: Waveforms and Sonic Boom Perception and Response (WRSP) Low Boom Community Response Program Pilot Test Design, Execution, and Analysis. Wyle Report WR 12-15, Dec. 2012.
- 1.13 Page, Juliet; Plotkin, Ken; Piacsek, Andrew; Sparrow, Vic; Salamone, Joe; Cowart, Robbie; Elmer, Kevin; Ladd, John; and Maglieri, Domenic: Superboom Caustic Analysis and Measurement Program (SCAMP) Comparison Report, Wyle Report WR 11-23, October 2011.
- 1.14 Plotkin, Ken; Page, Juliet; Salamone, Joe; Sparrow, Vic; Cowart, Robbie; Elmer, Kevin; Welge, Bob; and Piacsek, Andrew: Analysis of Acceleration Focus Booms from Four Low-Boom Configuration Designs. Wyle Report WR 11-26, Dec. 2011.
- 1.15 Plotkin, K. J.; Franz, R. J.; and Haering, E. A., Jr.: Prediction and Measurement of a Weak Sonic Boom From an Entry Vehicle. Paper 2aPA3, Fourth Joint Meeting of the Acoustical Society of America and the Acoustical Society of Japan, Nov. 2006.
- 1.16 Plotkin, K. J.; Haering, E. A., Jr.; and Murray, J. E.: Low-Amplitude Sonic Boom From a Descending Sounding Rocket. Proceedings of the 17th International Symposium on Nonlinear Acoustics, American Institute of Physics, Melville, New York, July 2005, pp. 615–618.
- 1.17 Nixon, Charles W. and Hubbard, H.: Results of the USAF-NASA-FAA Flight Program to Study Community Response to Sonic Booms in the Greater St. Louis Area. NASA TN-D 2705, 1965.
- 1.18 Maglieri, Domenic J.; Huckel, Vera; and Parrott, Tony L.: Ground Measurements of Shock Wave Pressure for Fighter Airplanes Flying at Very Low Altitudes and Comments on Associated Response Phenomena. NASA TN D-3443, 1966.
- 1.19 Maglieri, D. J. and Morris, Garland J.: Measurements of the Response of Two Light Aircraft to Sonic Booms, NASA TN D-1941, 1963.
- 1.20 Hilton, D. A.; Huckel, V.; Steiner, R.; and Maglieri, D. J.: Sonic Boom Exposures During FAA Community Response Studies Over a 6-Month Period in the Oklahoma City Area. NASA TN D-2539, Dec. 1964.

- 1.21 Maglieri, Domenic J. and Sothcott, Victor E.: Summary of Sonic Boom Rise Times Observed During FAA Community Response Studies Over a 6-Month Period in the Oklahoma City Area. NASA CR 4277, 1990.
- 1.22 Borsky, P. N.: Community Reactions to Sonic Booms in the Oklahoma City Area. National Opinion Research Center, AMRL Rept. TR 65-67, Repts. I and II, 1965.
- 1.23 Blume, John A. and Associates: Structural Reaction Program. National Sonic Boom Study Project. FAA Rept. SST-65-15, Vol. I, Apr. 1965.
- 1.24 Nixon, C. W.; Hille, H. K.; Sommer, H. D.; and Guild, Elizabeth: Sonic Booms Resulting From Extremely Low Altitude Supersonic Flight: Measurements and Observations on Houses, Livestock and People. AMRL-TR-68-52, USAF, Oct. 1968.
- 1.25 National Sonic Boom Evaluation Office: Sonic Boom Experiments at Edwards Air Force Base. NSBEO 1-67 (Contract AF 49(638)-1758) Stanford Research Institute, July 28, 1967.
- 1.26 Lee, R. A. and Downing, J. M.: Sonic Booms Produced by the United States Air Force and United States Navy Aircraft: Measured Data. AL-TR-1991-0099, 1991.
- 1.27 Fields, James M.: Reactions of Residents to Long-Term Sonic Boom Noise Environments. NASA CR 201704, June 1997.

CHAPTER 2 INFLUENCE OF THE ATMOSPHERE

In this chapter, the influence of the atmosphere on primary carpet sonic booms is examined in terms of the macro and micro effects; macro being associated with the so-called gross effects of pressure, temperature, and wind profiles and the micro being associated with turbulence, especially in the first few thousand feet of the earth's atmosphere. The role of atmospheric absorption on boom signatures is also addressed. The chapter concludes with a discussion of the influence of the atmosphere on the secondary over-the-top booms.

For more than half a century, it has been observed that when the atmosphere between the aircraft and the ground was quiescent, the sonic boom signatures acquired from supersonic overflights have always been undistorted N-wave shapes. This is illustrated in figure 2.1, which presents a set of measured sonic boom signatures from four different vehicles operating at a range of Mach numbers and altitudes. All of the signatures represent on-track measurements for steady level flight. Included are the Space Shuttle Orbiter, Concorde, SR-71, and F-104.

However, it has also been observed that the atmosphere, in particular the lower few thousand feet of the earth's boundary layer, exerts a significant influence on the final character of the ground-measured signature.

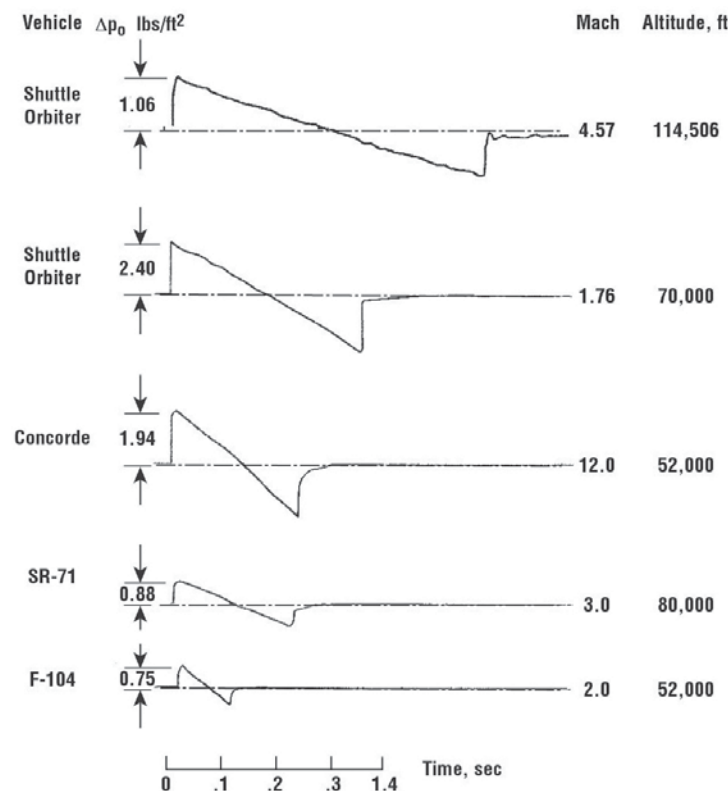


Figure 2.1. Measured sonic boom signatures in a quiescent atmosphere.

Primary Booms

Figure 2.2 is intended to indicate the atmospheric parameters that significantly influence the sonic boom signature as it propagates from the vehicle to the ground. These atmospheric influences are classified as macro and micro effects. Current sonic boom prediction capabilities can account for flights in non-standard atmospheres with winds and for the influence of atmospheric absorption. However, the prediction codes cannot account for the influence of local atmospheric instabilities (such as turbulence), especially those that occur within the earth's boundary layer.

Referring to figure 2.2, a few pertinent features should be noted. First, viscous losses, heat, conduction, and turbulence effects are known to be influential in the lower few thousand feet of the earth's surface. Atmospheric absorption or relaxation plays its role from the ground to tropopause. At greater altitudes, humidity is nearly non-existent. The effects of absorption and molecular relaxation and clouds on sonic boom signatures, especially in increasing shock rise times, will be discussed in later sections.

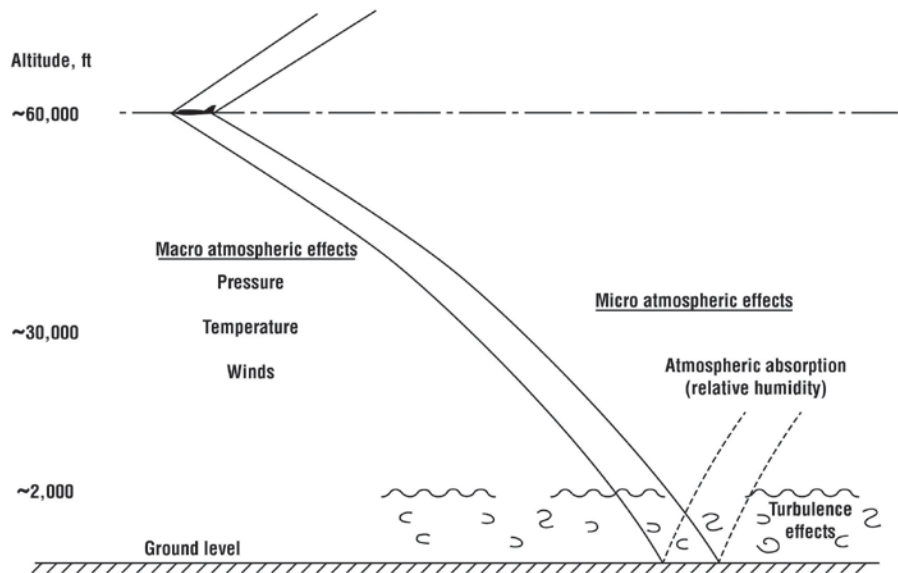


Figure 2.2. Atmospheric parameters influencing sonic boom signature characteristics.

Macro Atmospheric Effects

The next few figures relate to the macro influences of the atmosphere on sonic booms (i.e., the effects of temperature and winds on the on-track and lateral boom propagation). One of the most detailed studies of meteorological effects on sonic boom, based on analysis of NASA data prior to the summer of 1964, was given by Kane and Palmer (ref. 2.1). In general, subsequent investigations have confirmed many of their conclusions.

Temperature and Wind Gradients

It is known that atmospheric temperature variations between the airplane and the ground will cause the ray path, which describes the path of the shock wave through the atmosphere, to refract. In general, a negative temperature gradient (temperature decreases with increasing height above the ground) will cause the ray to bend upwards, while a positive temperature gradient will cause it to bend downwards. This distortion of the ray path leads to the formation of shadow zones beyond the edge of the primary boom carpet (negative temperature gradient) and secondary booms (positive temperature gradient). The effect of temperature variations on boom strength under the airplane has been studied for several model atmospheres. These models characterize meteorological conditions including tropopause heights and associated temperature gradients, temperature inversions near the ground caused by nocturnal radiation, snow cover, coastal clouds, multiple temperature inversions due to mixing and advection, frontal temperature inversions, and combinations of the above. As such, these temperature profiles contain many variations of lapse rate and inversions that cause the ray paths of sonic booms to curve. The models are summarized in figure 2.3 (ref. 2.1), which shows the standard atmosphere with no winds for reference.

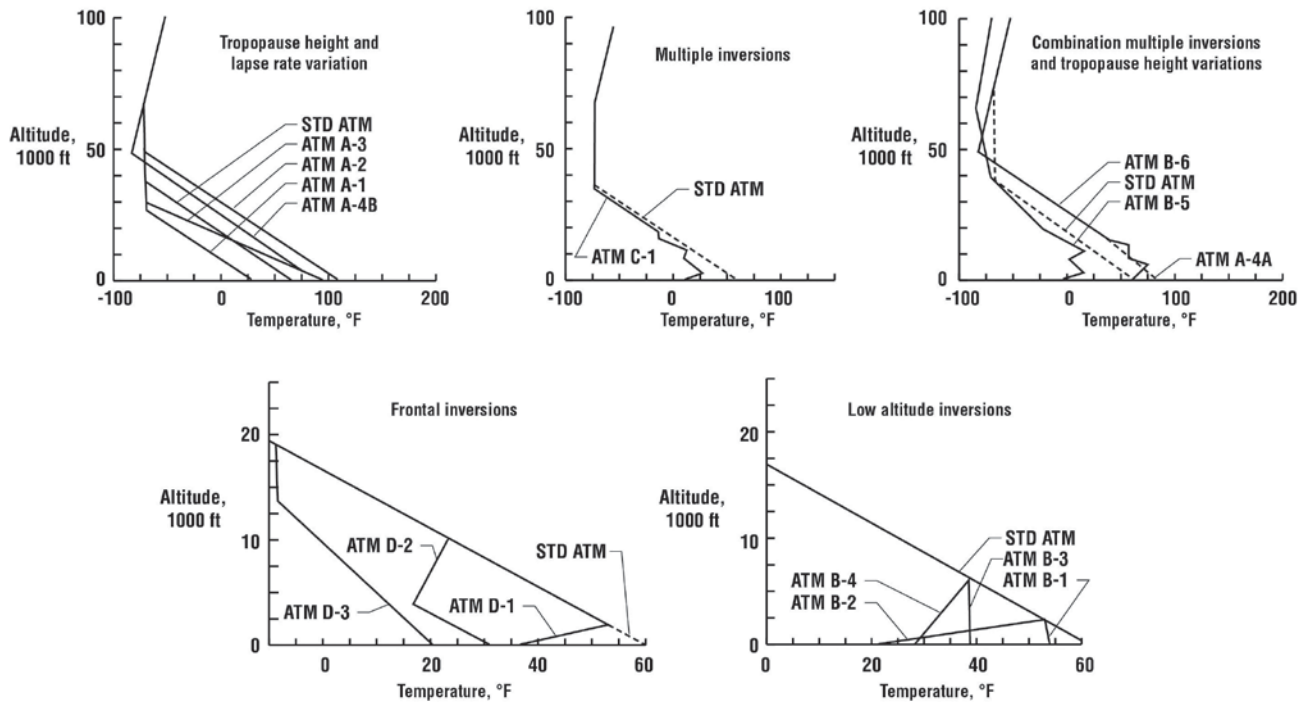


Figure 2.3. Summary of atmospheric models (ref. 2.1).

Variation in wind speed, wind shear, and direction between the airplane and the ground will tend to alter the ray path in much the same manner as variations in temperature. In general, headwinds cause the rays to bend up away from the ground, while tailwinds cause them to bend downwards. Distortion of the ray paths will cause some variation in sonic boom strength. This variation was investigated by constructing a set of model wind profiles and calculating the resulting ground overpressures. The wind models were selected to be characteristic of gradients in zonal and meridional wind components, high-speed jet streams near the tropopause, and low-level jet streams over the Great Plains. Each model was assumed to be omnidirectional (i.e., no lateral shear). The wind models were summarized in figure 2.4 (ref. 2.1) for each of the above categories.

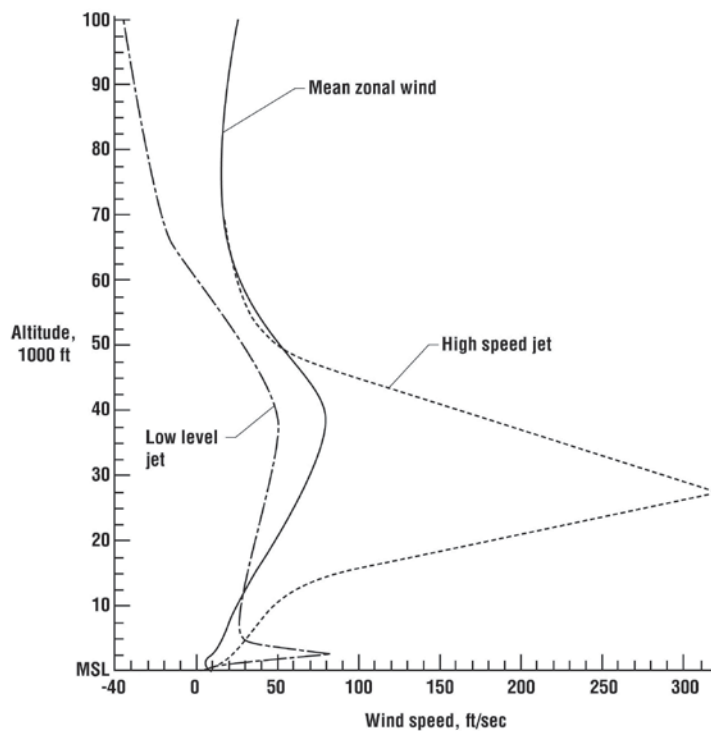


Figure 2.4. Summary of model wind profiles (ref. 2.1).

The effect of winds on the overpressures received at the ground was studied by assuming that the wind velocities were aligned parallel and perpendicular to the airplane flight path. In this manner, the influence of headwinds, tailwinds, and sidewinds was studied.

Effects on Boom Amplitudes

A summary of the macro influences of the atmosphere on sonic boom overpressures is given in figure 2.5 (ref. 2.1) for several horizontally stratified atmospheres. The effect of temperatures is shown at the top of the figure, while the lower portion shows the effects of winds. Calculations of on-track overpressure for steady level flights above the troposphere through various models of atmospheric temperature profiles (fig. 2.3) and wind profiles (fig. 2.4) were divided by the overpressures in a standard atmosphere with no winds for Mach numbers from Mach cutoff (Mach 1.16 for flight above the tropopause; 36,000 ft, in a standard atmosphere) to Mach 3.0.

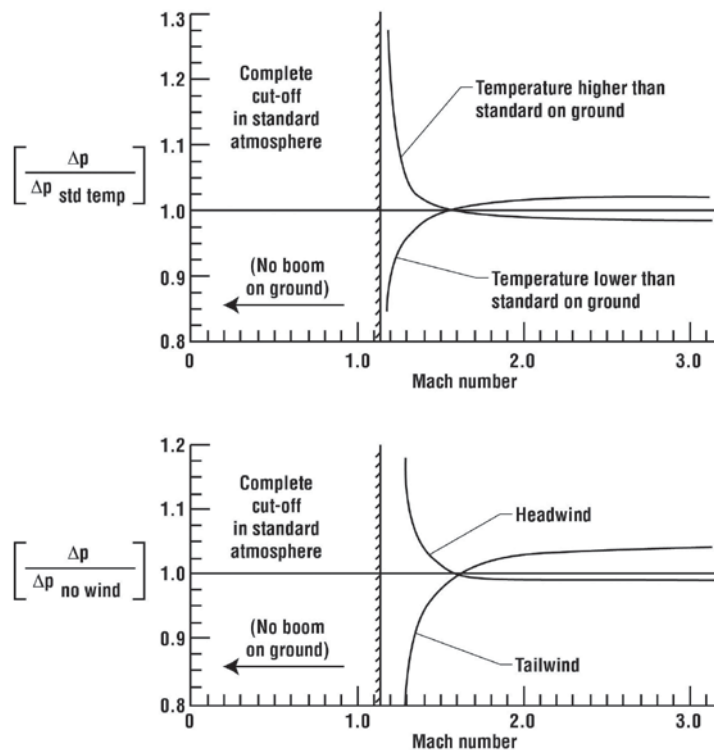


Figure 2.5. Effect of temperature and winds on sonic boom overpressures (ref. 2.1).

The results indicate that for flight at Mach > 1.5 , the largest influence of temperature and wind profiles on the sonic boom overpressure along the aircraft ground track is generally no more than about ± 5 percent from that generated in the still (no wind) standard atmosphere. One can observe that for Mach > 1.5 , temperatures lower than standard on the ground and tailwinds at altitude increase the boom levels. On the other hand, temperatures higher than standard on the ground and headwinds at altitude decrease the boom levels. This is a result of the decrease in the length of the ray paths for the former case and an increase in ray path lengths in the latter case.

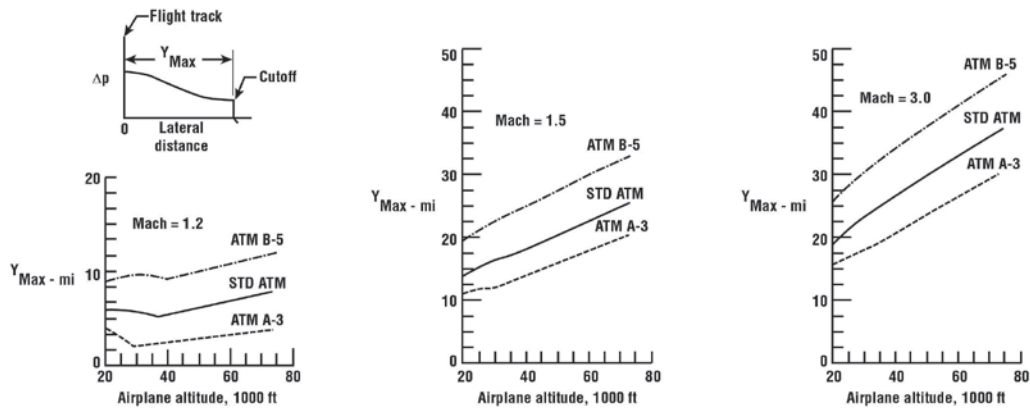
Signature shapes were assumed to be unaltered from the initially propagated N-wave. It is of interest to note that even with the extreme high-speed jet wind profile (270 ft/sec at 30,000 ft altitude) at Mach > 1.5 , the increase or decrease in overpressure (depending upon whether applied as a headwind or tailwind) is quite small, the order of 1 percent or 5 percent, respectively. A similar finding for essentially the same jet stream conditions was reported using the ZEPHYRUS computer program (ref. 2.2), which is capable of modeling signature propagation in a windy atmosphere. Reported results from analysis of Concorde flight experience (ref. 2.3) note that while boom variability turned out to be low for cruising-flight booms on the ground track, the variability is higher at distant lateral locations.

For flight at Mach numbers between 1.0 and 1.5 the meteorological conditions in the tropopause between the airplane and the ground result in more significant variations in the overpressure. For Mach < 1.5, temperatures lower than standard at the ground generally reduce the overpressure, while higher temperatures generally result in focusing and increase in the boom level. For physically realistic conditions, this variation may be as much as ± 15 percent at Mach 1.2. For Mach < 1.5, headwinds generally increase (focus) the boom while tailwinds decrease the boom. Winds may cause variation in the overpressure from that in a still atmosphere (no wind) of as much as ± 20 percent at Mach 1.3. However, later flight experiments relating to continuous flight at Mach cutoff (ref. 2.4), to be discussed in Chapter 5 of this publication, show that overpressure increases (focusing) of up to a factor of 3.0 are possible.

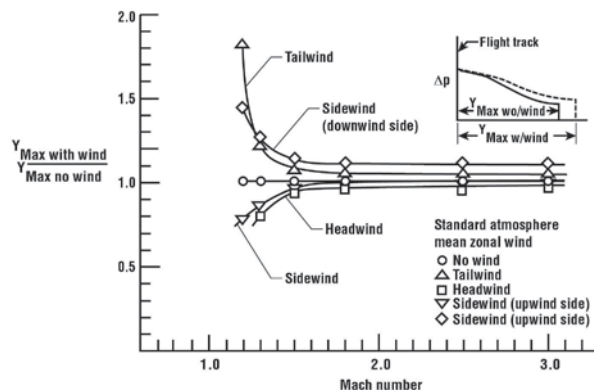
Effect on Lateral Spread

Variations in the temperature and wind profiles will cause variations in the location of the lateral cutoff as compared to a standard atmosphere without winds. The lateral cutoff is the point on the ground where the sonic boom ray path is refracted upward. As such, the shock pattern is not observed at ground level and only acoustic rumbles are observed beyond this point. Lateral cutoff is independent of the aircraft type and depends only upon the aircraft altitude, Mach number, and atmosphere. The extent of the lateral distribution of sonic boom strength was computed for each of the atmospheric models shown previously in figures 2.3 and 2.4.

The variation in lateral extent is shown in figure 2.6 (ref. 2.1) for the two models of temperature profiles that produced the widest deviations from the values in the standard atmosphere and for the mean zonal wind. The lateral extent in the standard atmosphere is shown for reference. Figure 2.6(a) shows that, in the extreme temperature profile cases, variations in the boom total lateral spread of from 5 to 10 miles may occur. In general, temperatures lower than standard on the ground will increase the lateral extent, Y_{max} , while ground temperatures higher than standard will decrease Y_{max} .



(a) Temperature variations.



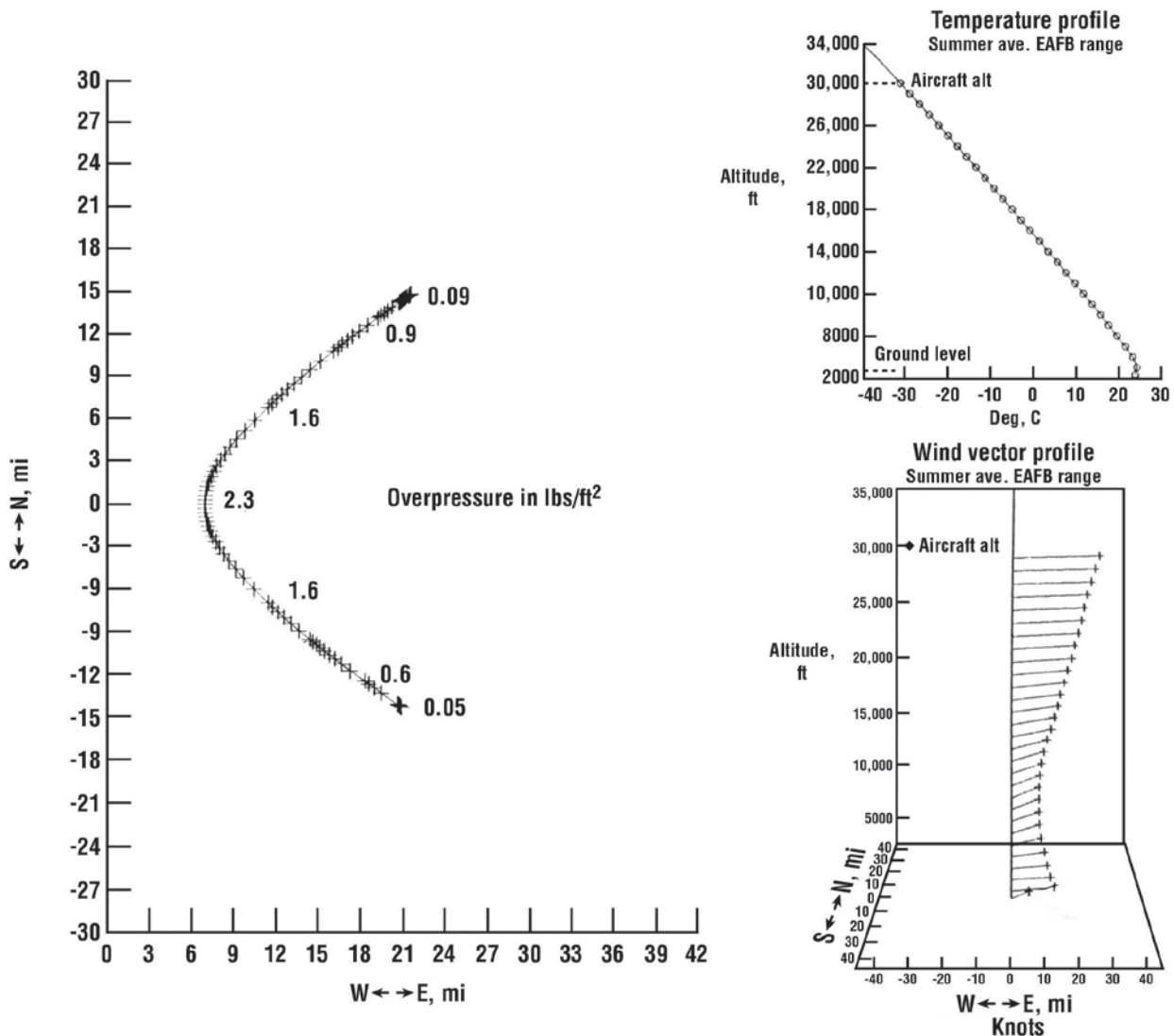
(b) Wind variations.

Figure 2.6. Influence of temperature and wind on lateral cutoff (adapted from ref. 2.1).

Wind shears will also affect the location of lateral cutoff as shown in figure 2.6(b). The magnitude of the variation caused by moderate winds was studied in the standard atmosphere with the mean zonal wind profile. The value of Y_{max} was computed for a headwind, tailwind, and sidewind. For purposes of comparison, these three Y_{max} values were divided by the value of Y_{max} with no wind for the same Mach number and altitude, and are shown plotted against airplane Mach number. Figure 2.6(b) shows that for moderate winds the maximum variation occurs at Mach numbers near 1.2. For Mach numbers greater than 1.5, the variation is of the order of ± 5 percent. In general, tailwinds and side winds (on the downwind side) increase the value of Y_{max} , while headwinds and sidewinds (on the upwind side) decrease Y_{max} . Strong winds, on the other hand, may substantially increase the magnitude of Y_{max} .

Lateral Spread Footprint

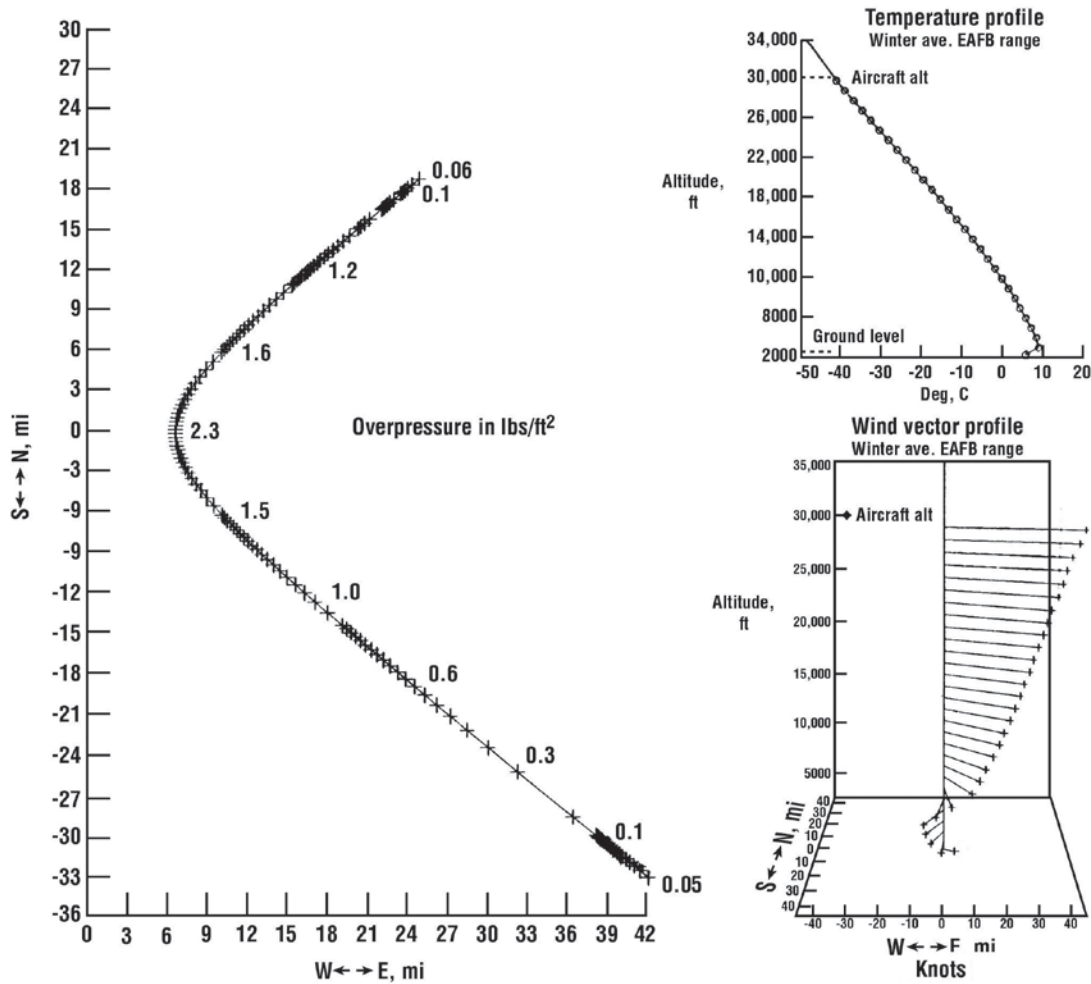
A relatively large amount of sonic boom information has been acquired at EAFB. In 1992, Lundberg (ref. 2.5) assessed the state-of-the-art methodologies for long-term sonic boom prediction in seasonally varying atmospheres in the EAFB supersonic flight corridor. Predictions of the sonic boom footprints for steady flight at altitudes of 10,000 feet and 30,000 feet were made for flights east- and west-bound for average atmospheres observed at EAFB during the four seasons of the year. Results for the average summer and winter atmosphere are given in figures 2.7 and 2.8, respectively.



(a) F-111, Mach 1.34 steady at 30,000 feet MSL east-bound.

(b) Average summer atmosphere at EAFB.

Figure 2.7. Summer atmospheric conditions and resulting sonic boom ground footprint for east-bound flight (adapted from ref. 2.5).



(a) F-111, Mach 1.34 steady at 30,000 feet MSL east-bound.

(b) Average winter atmosphere at EAFB.

Figure 2.8. Winter atmospheric conditions and resulting sonic boom ground footprint for east-bound flight (adapted from ref. 2.5).

The predicted sonic boom ground footprint for an east-bound flight of an F-111 aircraft flying steady-level at a Mach number of 1.34 and at an altitude of 30,000 feet MSL is shown on the left side of each figure. The summer and winter average temperature profiles and winds are presented on the right-hand side of the figures.

Note that there is about a 10°C increase in the temperature between winter and summer and almost a halving of the wind speed. Although these differences have a small influence of the sonic boom overpressure levels along the footprint ground track, a significant difference is quite evident regarding the lateral extent of the boom footprint to each side of the aircraft ground track – to more than a doubling of the cutoff distance to the south from 14.2 miles to 33 miles between summer and winter due to the wind speed gradient. Table 2.1 (from ref. 2.5) presents lateral cutoff distances associated with all four seasons’ annual atmospheric conditions and also includes the lateral cutoff for flight in a standard atmosphere with no wind.

Table 2.1. Predicted Lateral Spread of Sonic Boom for the EAFB Range Average Seasonal Atmospheres and Standard Atmosphere for an Eastbound Aircraft in Steady Level Flight at an Altitude of 30,000 Feet MSL (from ref. 2.5)

Description	Mach	On Track Peak Overpressure lbs/ft ²	Cut-off		
			Distance, miles North	South	Width miles
Eastbound windy					
Winter	1.34	2.3	18.9	33.0	51.9
Spring	1.32	2.2	17.8	23.3	41.1
Summer	1.34	2.3	14.9	14.2	29.1
Fall	1.33	2.2	19.0	30.7	49.7
Std. Atmosphere No Wind	1.41	2.4	>16.2	>16.2	>32.4

Focusing at Lateral Cutoff

In addition to examining the influence of temperature and winds on the extent of the sonic boom lateral cutoff, Palmer and Kane (ref. 2.1) showed that, as in the case of focusing under the flight track (see fig. 2.5), intensification of the boom to the side of the flight track may occur simultaneously with the lateral cutoff. Results of their studies are given in figure 2.9 (ref. 2.1) for flights above the tropopause for assumed wind conditions on standard cold and hot days. The figure indicates the wind components required to cause off-track focusing for a range of Mach numbers from 1.10 to 1.40.

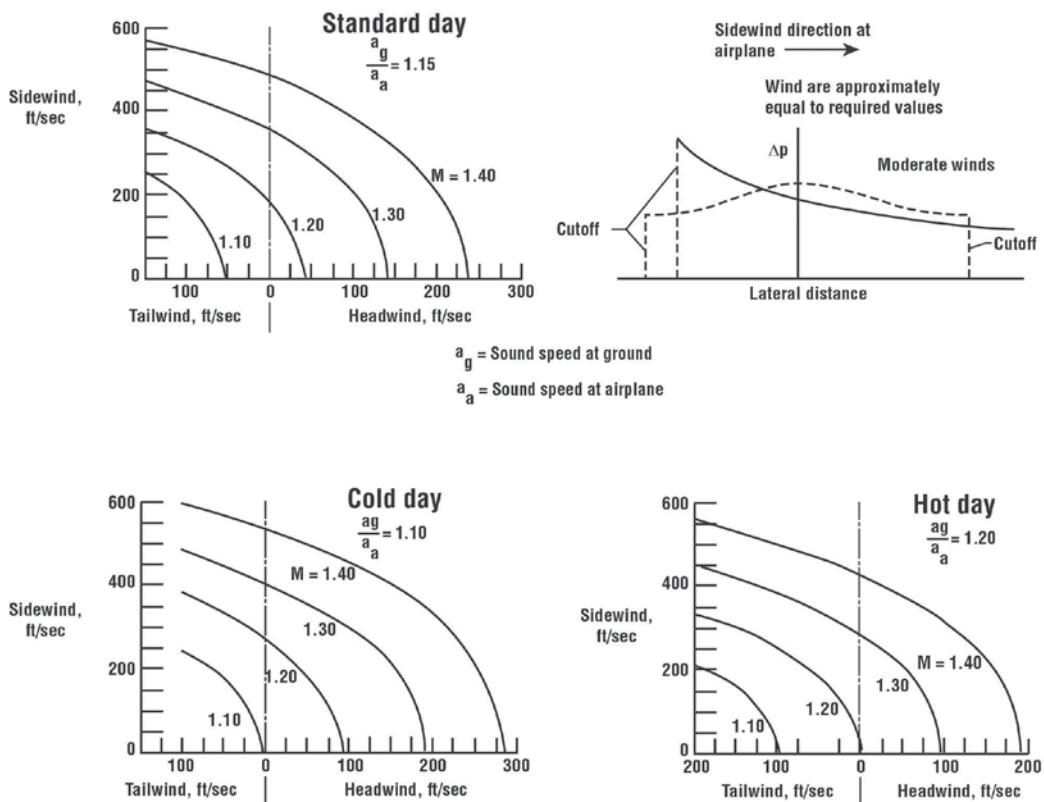


Figure 2.9. Wind speeds required to produce focusing off the flight track (adapted from ref. 2.1).

As stated in reference 2.1, it is evident that this off-track focusing situation is restricted to the very low Mach numbers because of the large magnitude of the wind speeds required at the higher Mach numbers.

Dressler and Fredholm (ref. 2.6) and Lundberg, Dressler, and Lagman (ref. 2.7) argued that the combination of sidewinds and turbulent scattering would cause a large increase in the sonic boom level near lateral cutoff and, as such, a continuous line of focused overpressure would exist on each side of the flight track throughout the cruise phase of flight of an SST. There was also a concern that even without large sidewinds there could be focusing at lateral cutoff during steady-level flight due to atmospheric refraction in that the linear theory shows that as the ray tube area goes to zero at grazing, the boom levels go to infinity (see fig. 69 of ref. 2.8). However, Haglund and Kane (ref. 2.8) point out that the linear theory incorrectly predicts an infinite intensity at cutoff due to ray focusing.

Flight test measurements during this time period did not indicate that sidewinds and turbulence scattering would cause large increases in the boom level near lateral cutoff or that boom levels would be infinite. Two cases are shown in figures 2.10 and 2.11 that illustrate the character of the sonic boom signatures for various distances from the ground track out to and beyond the lateral cutoff for an aircraft in steady-level flight. Figure 2.10 (ref. 2.9) displays signatures measured to each side of the ground track (station 5) at three lateral locations of 5, 17, and 26 miles. The predicted lateral cutoff in a standard atmosphere with no winds for flight at Mach 2 and an altitude of 52,200 feet is shown to be about 21 miles from the aircraft ground track.

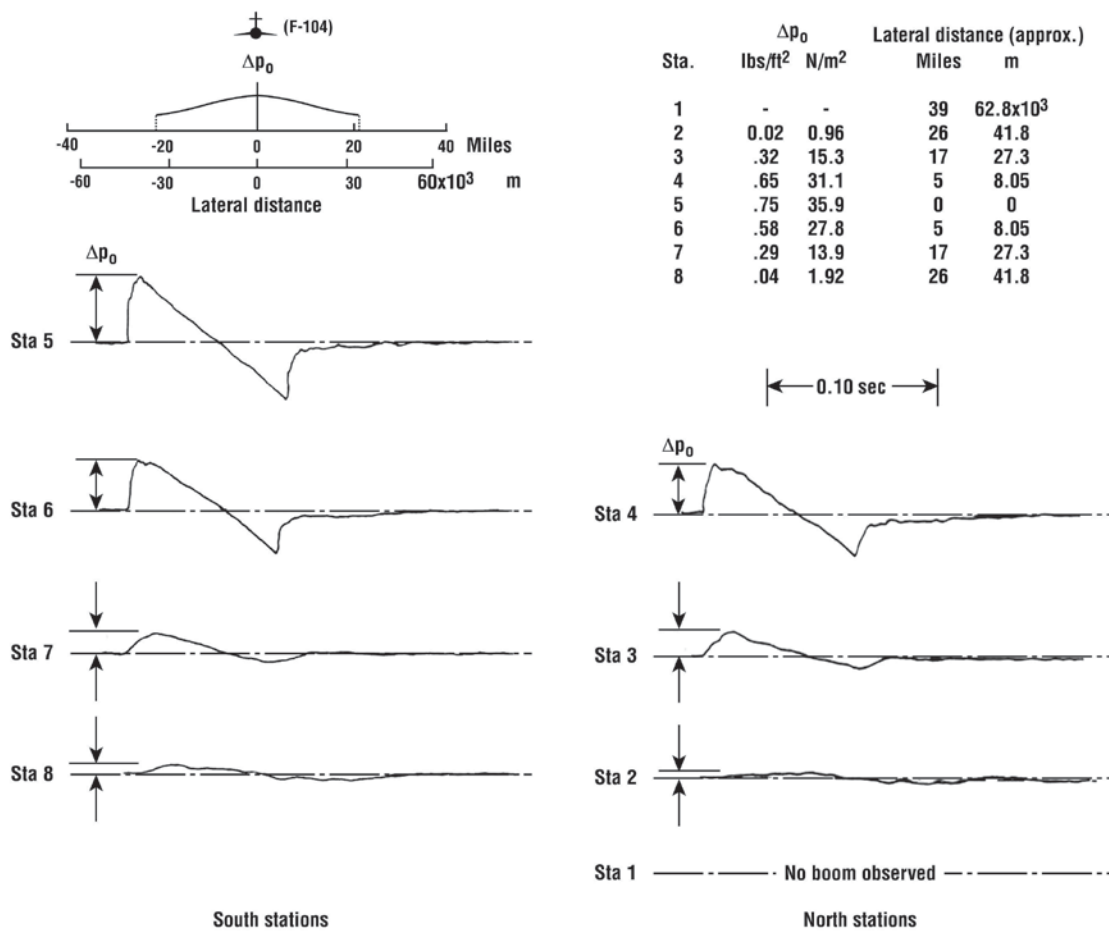


Figure 2.10. Measured sonic boom ground pressure signatures at several measuring stations at different distances to each side of the aircraft ground track. Airplane in steady-level flight at an altitude of 52,200 feet (15,911 m) and Mach 2: flight 3 (adapted from ref. 2.9).

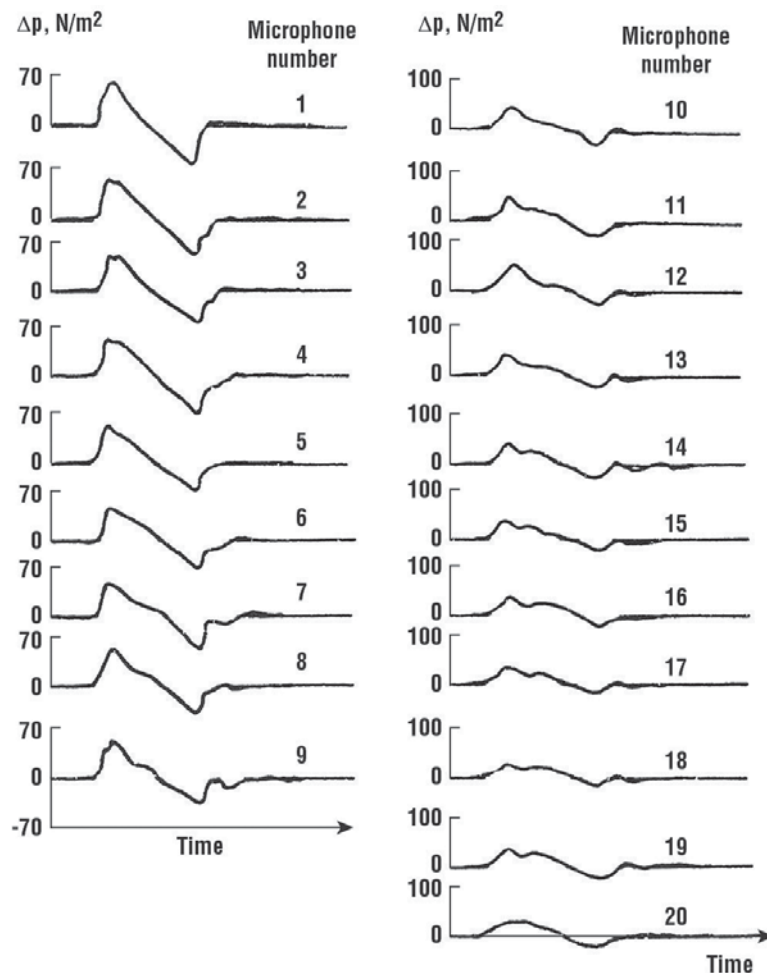
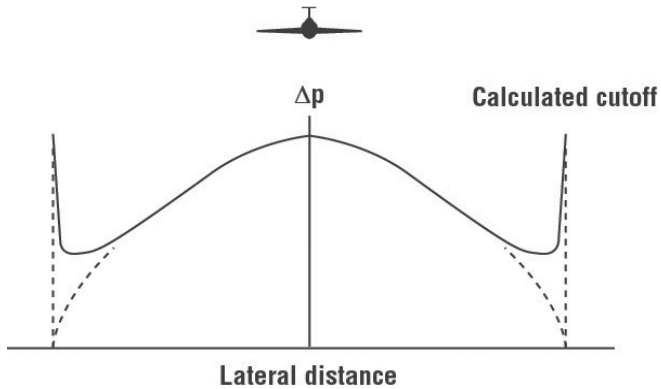


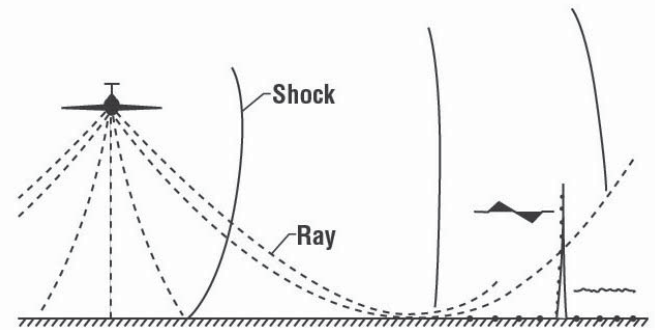
Figure 2.11. Measured signatures in French tests. Distance between transducers is 1000 m. Closest transducer to flight track is number 1 (adapted from ref. 2.10).

These data were obtained at mid-morning and under fairly quiescent atmospheric conditions. The signatures measured to each side of the track are similar in shape and display a progressive rounding and decay with increasing lateral distance. A similar set of measurements from steady-level flight obtained in France and cited by Onyeowu (ref. 2.10), describing the character of the boom signatures to one side of the aircraft ground track to beyond the lateral cutoff is shown in figure 2.11. The lateral cutoff for a standard atmosphere with no winds is estimated to occur between transducers 17 and 18. Once again, the signatures display a progressive rounding and decay with increasing lateral distance.

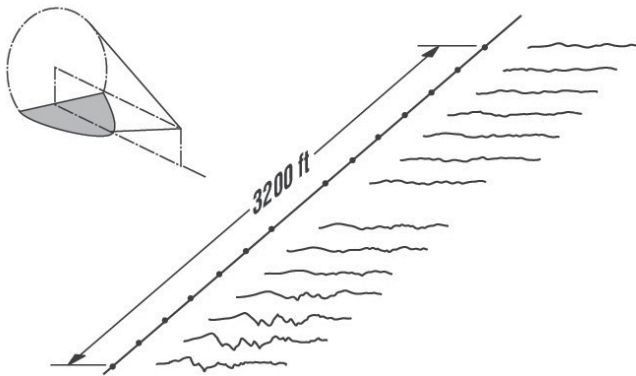
Dressler and Fredholm (ref. 2.6) stated that focusing at lateral cutoff was not being observed in the field measurements because of the extreme difficulty in positioning the recording instruments at or near where the peak magnification would occur. In 1970, during the 1500-foot high BREN tower tests (refs. 2.11 and 2.8), a concerted effort was made, through a special series of flight tests, to more quantitatively define the situation at lateral cutoff (specifically to observe if focusing does occur due to atmospheric refraction). A view of the test arrangement and resulting data are shown in figure 2.12 (ref. 2.11). Figure 2.12(a) schematically illustrates the lateral cutoff focus concern. The experimental flight-test setup is indicated schematically in figure 2.12(b). A 3200-foot horizontal-crosswise ground array near the lateral cutoff location with a 200-foot microphone spacing and a 1500-foot vertical microphone array with 100-foot spacing are indicated. The flights were accomplished so that the edge of the exposure pattern was placed in or near this array. The data shown in figure 2.12(c) are representative of those obtained from the 3200-foot array during one aircraft flight. A definite trend in signature shape variation is evident.



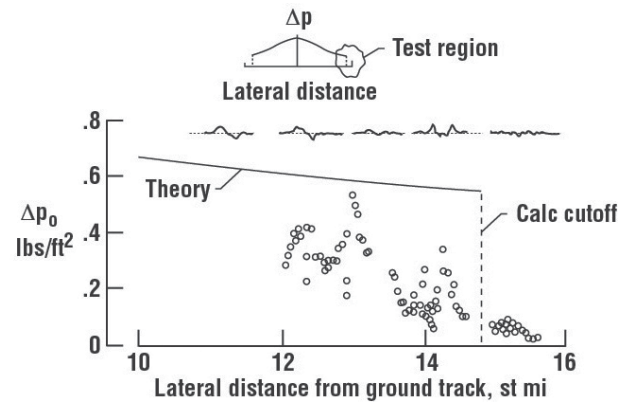
(a) Schematic of lateral cutoff focus concern.



(b) Sketch of experiment test setup.



(c) Signatures observed near lateral cutoff.



(d) Variation of overpressure near lateral cutoff.

Figure 2.12. Characteristics of sonic boom near lateral cutoff (adapted from ref. 2.11).

By means of repeated flights offset in lateral distance from the tower, numerous overpressure signatures were measured at the edge of the pattern. Some of these signatures, and the associated peak overpressure data, are presented in figure 2.12(d). It can be seen that there is a general decrease in overpressure as distance increases. There is also a corresponding trend away from N-shape signatures, which are observed as booms, to a U-shape signature and finally to signatures with no definite shape characteristics, which are observed as acoustic rumbles. There is no indication of large overpressure enhancement at the edge of the carpet. Other work of significance regarding sonic booms beyond the lateral cutoff (in the shadow zone) can be found in references 2.12 and 2.13.

Reflection Factor

Signature rounding and decay is influenced by increasing distance, ground impedance, shock incidence angle, shock reflection coefficient K_R (defined as the total pressure jump divided by the pressure jump in free air) and turbulence scattering. It should be noted that most of the flight-test measurements used in determining ground reflection coefficient have been acquired on hard clay desert, dry lake beds or outlying sandy areas, paved surfaces, or flat rooftops. Scant data exist on measurements over snow cover, grassy areas, gravel surfaces, and ocean waves.

Walker and Doak (ref. 2.14) looked at the effect of changes in ground impedance and shock incidence angle on an N-wave signature for on-track and lateral locations out to cutoff. Kane and Palmer (ref. 2.1) discuss the variation of the ground reflection factor and how it varies theoretically from a value of 2.0 for an oblique shock for locations near the ground track to 1.0 for a normal shock as would occur at lateral cutoff. Haglund and Kane (ref. 2.8) present measured values that varied from 2.18 to 0.86. Onyeowu (ref. 2.10) used the Haglund-Kane results to derive an empirical relation for a variable reflection factor. Figure 2.13, excerpted from his paper, shows the variation of the reflection factor near cutoff using his empirical formula.

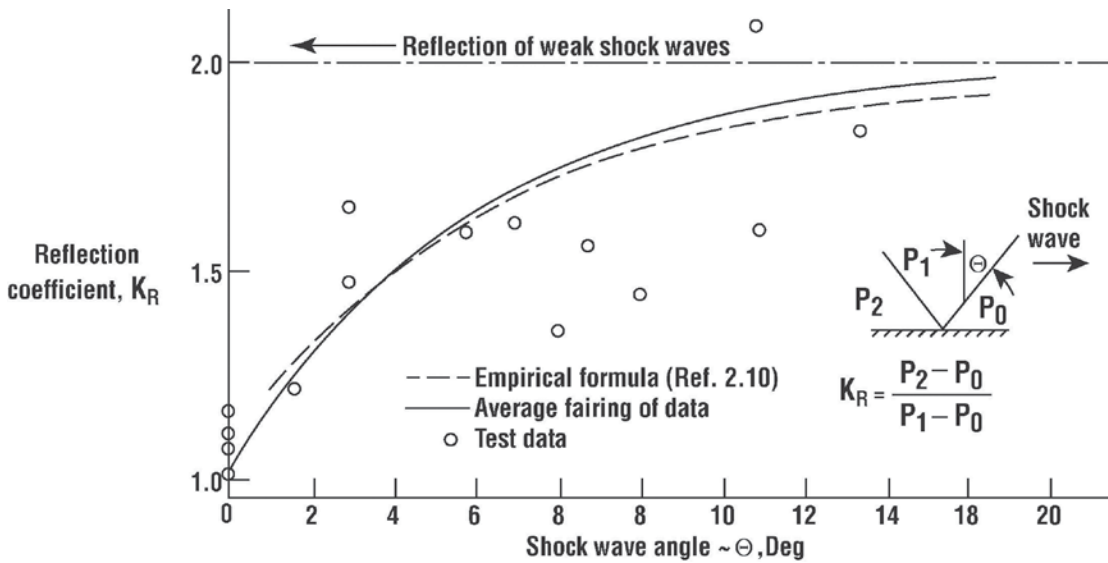


Figure 2.13. Variation of reflection factor near cutoff (ref. 2.10).

Onyeowu went on to show the effect of the variable reflection factor on the overpressure distribution with lateral distance from the aircraft ground track using the measured data of reference 2.9 and assuming a standard atmosphere. These results are given in figure 2.14 (ref. 2.10).

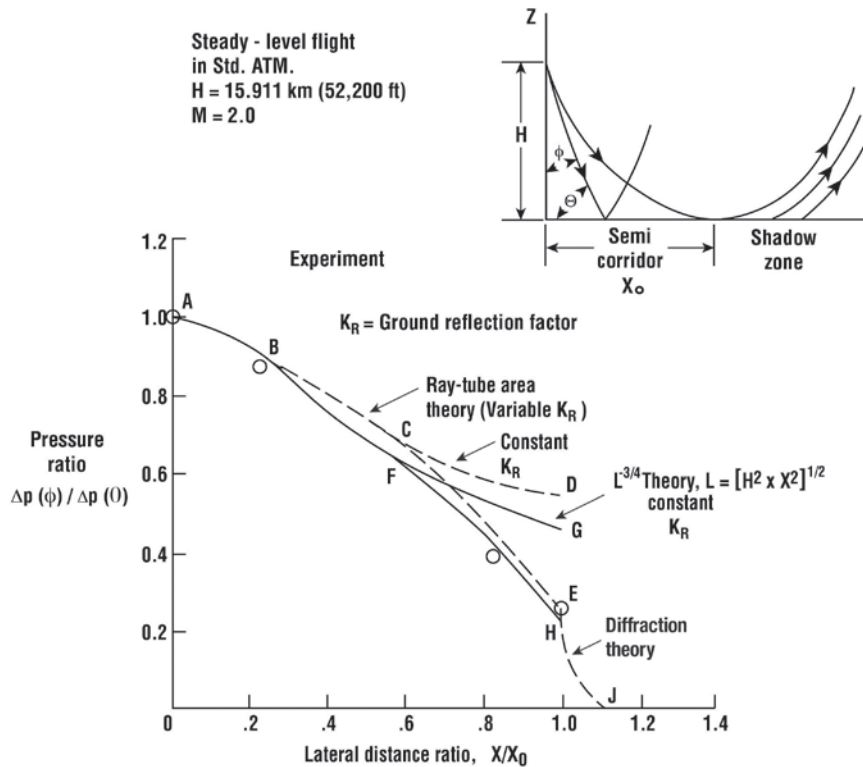


Figure 2.14. Lateral distribution of overpressure showing effects of reflection factor varying with angle of incidence and diffraction into shadow zone (ref. 2.10).

The three experimental points represent the flight data. The nominal curve with $K_R = 1.9$ is designated ABFG and the simple theory of Whitham using a variable K_R is designated ABFH. Curves ABCD and ABCE are from the Hayes ray-tube area theory with a constant and variable K_R , respectively. It can be seen that the simple theory of Whitham using a variable K_R is in better agreement with the measured data than the ray-tube area approach. Onyeowu also notes that the effects of variations in K_R only become noticeable beyond the last 40 percent of the distance to lateral cutoff.

Micro Atmospheric Effects

The previous discussion was limited to the study of the effect of a horizontally stratified atmosphere on the propagation of the sonic boom (so called macro effects). As noted by Kane and Palmer (ref. 2.1), the turbulent process in the atmosphere (micro effects) is the result of some form of instability. This may be either a result of mechanical instability, such as produced by wind shear, or flow over obstacles, or thermal instability such as produced by solar heating of the ground. These forms of instability produce random, turbulent fluctuations in wind and temperature that can only be studied and described in statistical terms.

Signature Distortions

One of the first flight experiments that pointed to the fact that disturbances in the lowest few thousand feet of the atmosphere may be most significant in affecting the shapes of the sonic boom signatures measured at the ground was obtained during a sonic boom flight test program at EAFB in 1961 (ref. 2.15). The results are illustrated by the data of figure 2.15 (ref. 2.15).

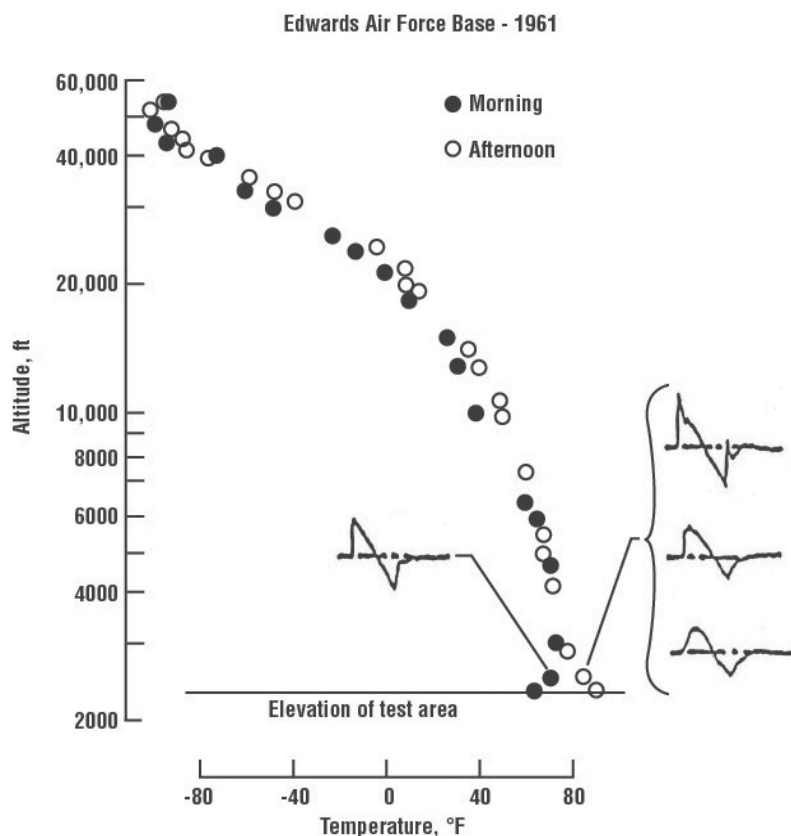


Figure 2.15. Effect of earth's boundary layer on temperature profile (adapted from ref. 2.15).

Temperature is plotted against altitude as determined from wiresonde and rawinsonde soundings taken during the flight times. The filled symbols represent the temperature profile existing for the morning flights whereas the open symbols apply to the afternoon flight. It may be seen that the temperature conditions of the upper atmosphere do not vary appreciably from the morning to the afternoon. On the other hand, in the first thousand or so feet of the lower atmosphere (within the earth's boundary layer), the temperature profile varies markedly. In the morning, a temperature inversion exists during which time the surface layer of the atmosphere is quiescent. Later in the day, as the surface temperature increases, the temperature profile may change to the extent that a super-adiabatic (i.e., temperature decreases with height at the rate greater than 10°C per kilometer and is referred to as absolute instability) lapse rate condition can exist as indicated. For such a temperature profile, the surface layer of the atmosphere is inherently unstable and severe thermal-induced turbulence may be generated. There is a strong correlation between the type of signature measured and the temperature profile in the lower atmosphere.

Consistent N-wave types of signatures were measured when the lower atmosphere was quiescent, whereas large variations in the shape of the signatures from peaked to rounded were measured when the lower atmosphere was considered to be unstable.

Past experience in the measurement of sonic booms during flight tests has indicated a substantial amount of variability in the signatures (see reference 2.16) compared to the expected N-wave signature. In order to establish that the signature variability that was being observed was not due to instrumentation, a special flight test was conducted (ref. 2.17). The objective of this test was to obtain comparable data from several channels of measuring instrumentation of the same type under conditions where weather effects would be essentially eliminated. In order to do this, seven of the microphones having a frequency response of 0.10 to 10,000 Hz were shock-mounted in a 3 by 3-foot reflection board within an area of less than 1 square foot. Data obtained from this instrument setup for a special flight test, are shown in figure 2.16 (from ref. 2.17).

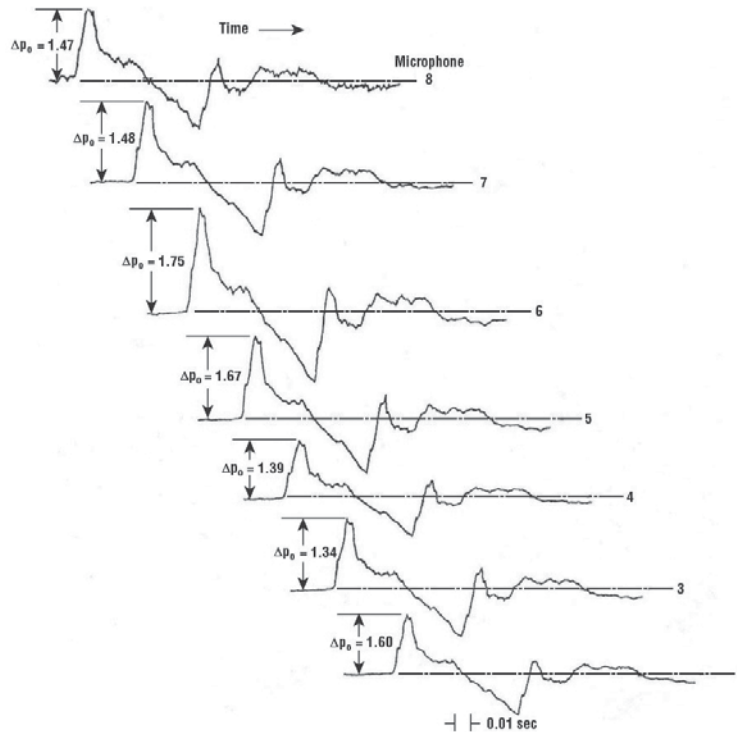


Figure 2.16. F-104 Sonic boom signatures from seven microphones grouped within a one-square foot area on ground, Mach 1.52 and altitude of 41,200 feet, Δp_o is in lbs/ft² (adapted from ref. 2.17).

Data were obtained from an F-104 in steady flight at an altitude of 41,200 feet and at a Mach number of 1.52. The test was accomplished at about 1400 hours when there was considerable atmospheric turbulence and thermal activity in the test area.

The most obvious result of figure 2.16 is that the measured boom signatures, which are peaked in character, show remarkable similarity. Peak amplitudes of the signatures presented in the figure are somewhat different because of variations in the sensitivity of the various channels of equipment. However, the measured peak values indicated in the figure are noted to be within a range of ± 15 percent or the equivalent of about ± 1 dB. It is concluded that the signature distortions are a result of atmospheric influences and that any variability resulting from instrumentation and measurement procedures are minimal.

The signature variability observed during flight experiments at EAFB, which appears to be associated with the changes in the lower layers of the atmosphere, was also noted to occur during the 6-month sonic boom over-flight program in Oklahoma City where the atmosphere, especially the lower layers, is not typical of the desert regions of EAFB, California. Some results are presented in figure 2.17 (ref. 2.18). The data shown were derived from an accurately calibrated and oriented array of matched microphones along the aircraft ground track. The variations in the wave shapes measured during one steady flight of an F-104 at a speed of Mach 1.7 and at an altitude of

28,000 feet are sketched for the appropriate measurement locations. A wide variation in wave shape occurs even over a distance on the ground of a few hundred feet. This variation in boom signature shape, which is associated with changes in atmospheric conditions, resulted in substantial variations in the peak ground overpressure (about a factor of 3.0), the larger values being associated with the sharply peaked waves and the lower values with the rounded-off waves.

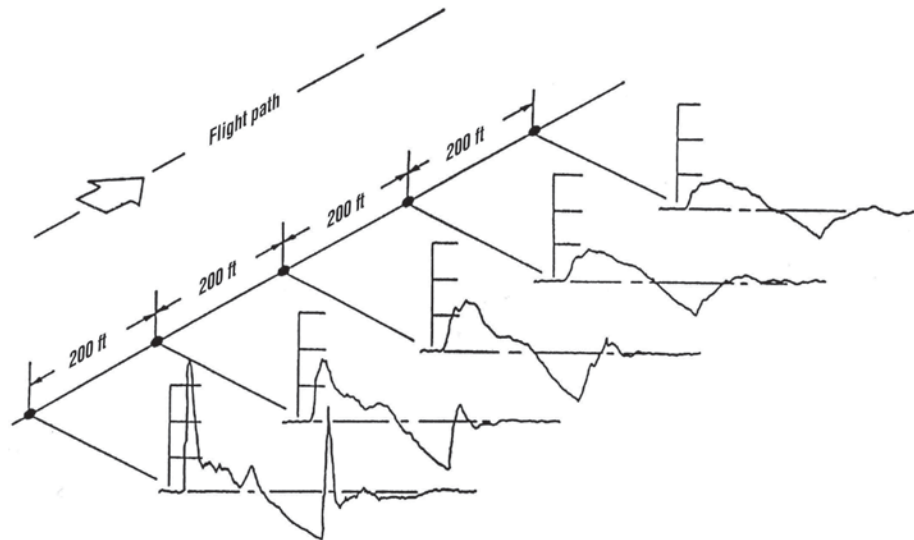


Figure 2.17. Variations in sonic boom signatures along ground track for steady-level flight (adapted from ref. 2.18).

Variations in sonic boom signature shape similar to those observed at EAFB and Oklahoma City were also measured during the USAF B-58 training mission over the Chicago area. The data are shown in figure 2.18 (ref. 2.19) and are measured signatures from the five microphones in a cruciform array spaced 100 feet apart under the aircraft flight track. The signatures on the left hand side of the figure were obtained for a different flight on a different date and for markedly different weather conditions than those on the right hand side of the figure. The surface weather conditions differed mainly in wind velocity and wind direction. The signatures on the right-hand side of the figure were obtained for wind velocities on the order of 28 knots with gusts, whereas the signatures on the left hand side were obtained for lower wind velocities. A much wider variation in the signature shapes exists for the condition of high winds. The main distortions of the signatures in each case are once again associated with the rapidly rising portions of the boom signatures, and these distortions are of the same general nature as has been previously observed for other airplanes and other atmospheric conditions in other geographical areas.

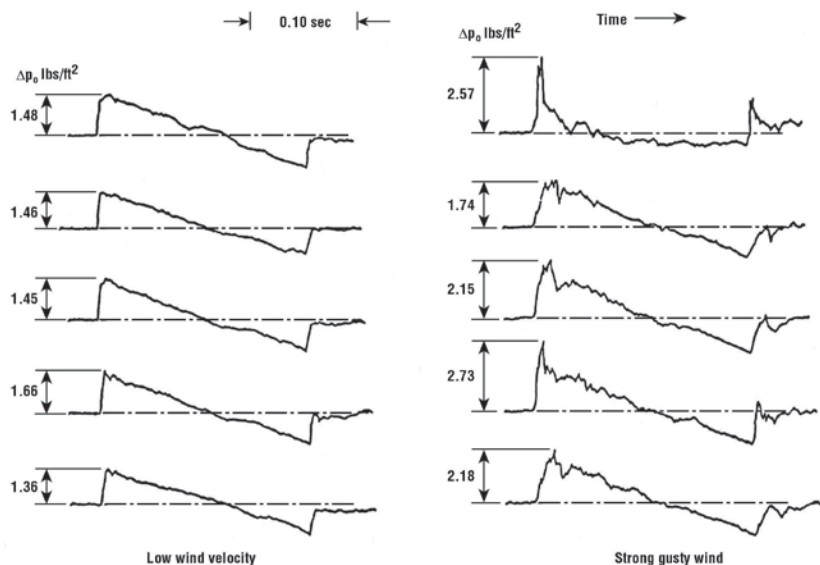


Figure 2.18. Sonic boom from two B-58 flights over the city of Chicago under different atmospheric conditions (adapted from ref. 2.19).

As a follow up to the EAFB, Oklahoma City, and Chicago experiments shown in the previous figures, another experiment at Wallops Island, Virginia was performed to investigate the effects of time with regard to atmospheric distortion effects. This experiment was performed using two airplanes of the same type that were flown at the same altitude of 40,000 feet and Mach number 1.5, on the same nominal flight track, and about 5 seconds apart, as illustrated in the upper portion of figure 2.19 (ref. 2.15). By means of the 1500-foot ground microphone array it was possible to measure sonic boom signatures that traveled along essentially the same ray path from high altitude to the ground for a distance of approximately 15 miles along the ray path, but at slightly different times.

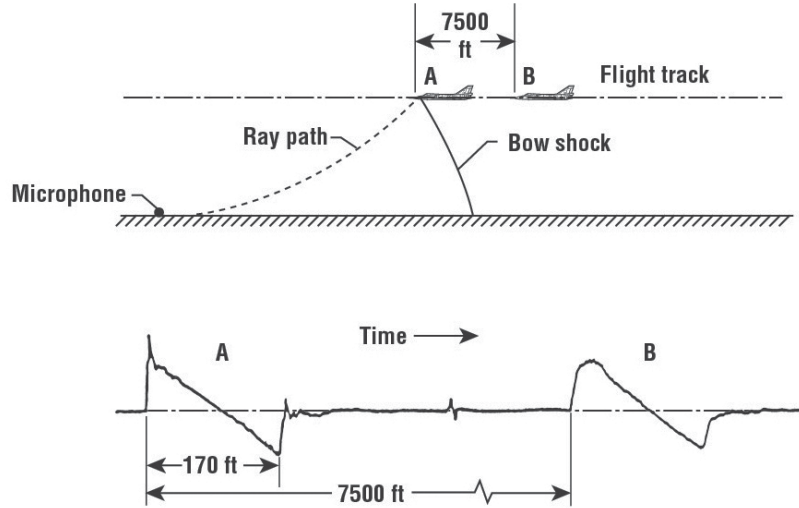


Figure 2.19. Measured sonic boom pressure signatures for two F-106 aircraft flying at Mach 1.5, an altitude of 40,000 feet, and 5-second time intervals over Wallops Island, Virginia (adapted from ref. 2.15).

The signature tracings at the bottom of figure 2.19 illustrate one of the results of the experiment. It can be seen that quite different shapes are associated with measurements at times a few seconds apart. Such a result suggests that the integrated effects of changes in the atmospheric conditions along a given ray path may be significant even for such a small difference in time.

Another demonstration that the boom signature may vary widely over short distances and time is illustrated in figure 2.20 (ref. 2.15). These results were obtained at Wallops Island, Virginia where the first few thousand feet of the atmosphere are not typical of the desert region of EAFB.

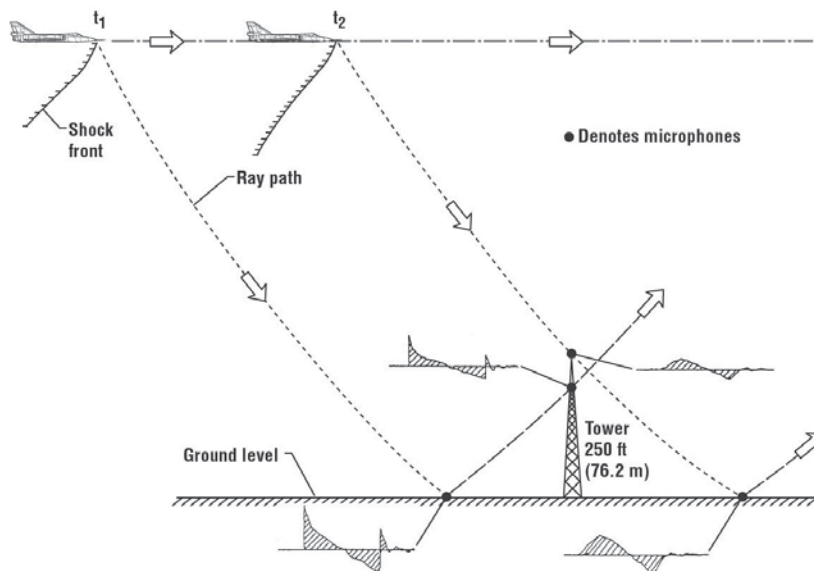


Figure 2.20. Effect of atmosphere on boom signatures measured on tower and ground for two F-106 flights over Wallops Island, Virginia; Mach 1.5, 40,000-ft altitude, and at 5-second time intervals (adapted from ref. 2.15).

Flights were made over an instrumented range consisting of a linear microphone array of 100-foot spacing on the ground and extending over about 1500 feet, in combination with a vertical array on an instrumented tower extending to about 250 feet at 50-foot intervals above the ground. An F-106 was flown at an altitude of 40,000 feet and at a Mach number of 1.5 for a variety of weather conditions. The objective of the studies was to correlate the sonic boom measurements with the extensive meteorological data obtained on the instrumented tower.

In situations where waveform distortion was noted to exist, it was found that similar wave shapes were measured both at the ground surface and on the instrumented tower. A particularly interesting and significant result of these studies is illustrated by the waveform tracings, which suggest that similar types of distortions exist at points along any given ray path and that waveforms on nearby paths may differ markedly.

Results indicate that, for these particular tests, the 250-foot layer of the atmosphere near the surface of the ground did not appreciably affect the signature shapes. It follows then that the portion of the atmosphere above 250 feet was important for the conditions of this experiment with regard to wave shape distortions.

In an attempt to gain more insight into the influence of the first few thousand feet of the atmosphere on boom signatures, a unique flight experiment was performed. The Goodyear blimp, *Mayflower*, was used to carry microphones to an altitude of 2000 feet above Rogers Dry Lake at EAFB, well above the level of the active lower layer and at a height where both the incident and reflected boom signatures would be captured. An F-106 aircraft was flown over the test site in steady level flight numerous times at Mach 1.5 and at an altitude of 40,000 ft MSL. The results are presented in figure 2.21 (ref. 2.15).

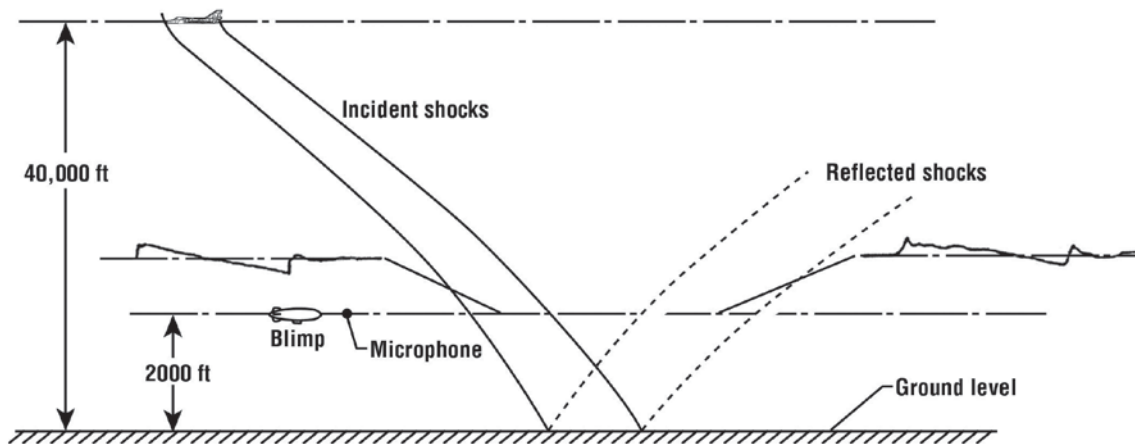


Figure 2.21. Influence of lower-layer atmosphere on sonic boom signatures for an F-106 aircraft flying over EAFB at Mach 1.5 and at an altitude of 40,000 feet (adapted from ref. 2.15).

It can be seen that the incident boom signature, which has not yet entered the active lower layer of the atmosphere, is a fairly clean undistorted N-wave. On the other hand, the reflected signature, which has traveled twice through the active lower layer, is distorted, with a bow and tail shocks showing peaked character. It is to be noted that the lakebed surface upon which the incident shocks reflected from is flat, smooth, and hard and expansive without any nearby structures, trees, bushes, or underbrush. Since the two waveforms were measured at different times, the experiment does not give direct information concerning the effects of the lowest 2000 feet. However, a larger proportion of incident waveforms (as contrasted to reflected waveform) was relatively undistorted. This would suggest that the 2000-foot surface layer was responsible for a major portion of the distortion, even though the distortion could not be proven to be solely attributed to the lowest 2000 feet.

A similar flight experiment to that shown in figure 2.21 was conducted during the 2004 NASA Shaped Sonic Boom Experiment (SSBE). The SSBE was a follow-up flight test program to the 2003 Shaped Sonic Boom Demonstration (SSBD) flight tests, which were aimed at proving the persistence of a shaped sonic boom signature to the ground. During SSBE, a sailplane with a wing-tip mounted microphone was used as the airborne measurement platform. The test setup and results of this particular flight test are shown in figure 2.22 (developed from refs. 2.20 and

2.21). An F-5E was flown at a steady Mach number of 1.4 and altitude of 32,000 feet and the glider was at about 6000 feet above the desert floor, well above any active lower layer of the atmosphere. At this height, both the incident and reflected boom signatures were captured.

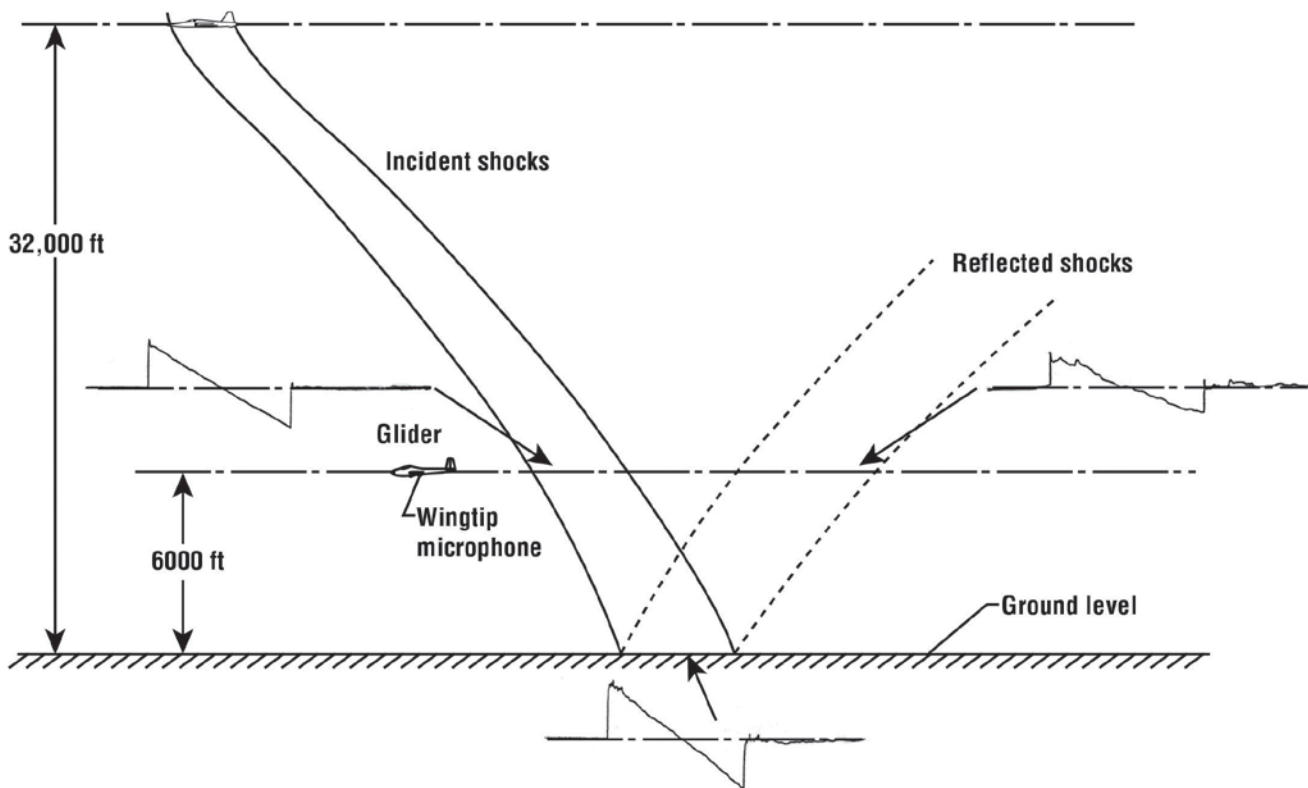


Figure 2.22. Influence of lower-layer atmosphere on sonic boom signatures for an F-5E aircraft flying over EAFB in 2004 at Mach 1.4 and at an altitude of 32,000 feet (ref. 2.20 and 2.21).

Once again, it can be seen that the incident boom signature, which has not yet entered the lower layer of the atmosphere, is a fairly clean undistorted N-wave. The signature at ground level shows little distortion resulting from its travel through the 6000 feet from the glider to the ground. On the other hand, the reflected signature that has traveled twice through the lower layer has experienced some distortion in the form of peaking of the bow and tail shocks. Here again, as was the case in figure 2.21, the experiment gives direct information concerning the effects of the lowest 6000 feet and suggests that for the EAFB desert environment below 6000 feet, surface layer is responsible for a major portion of the signature distortion.

The data presented in the last few charts produced evidence that suggests that there is a strong correlation between signature distortion and identifiable local disturbances in the atmosphere. A special flight experiment was performed in an attempt to produce evidence of direct correlation between signature distortion and identifiable local atmospheric disturbances. Figure 2.23 (ref. 2.22) illustrates the test setup and resulting boom measurements. Use was made of a large subsonic KC-135 aircraft to generate wing tip vortices (ref. 2.23) in the test area, which consisted of a 7000-foot array of microphones, in such a manner that the shock waves produced by an F-106 in steady level flight at Mach 1.5 and an altitude of 35,000 feet would pass through these vortex disturbances.

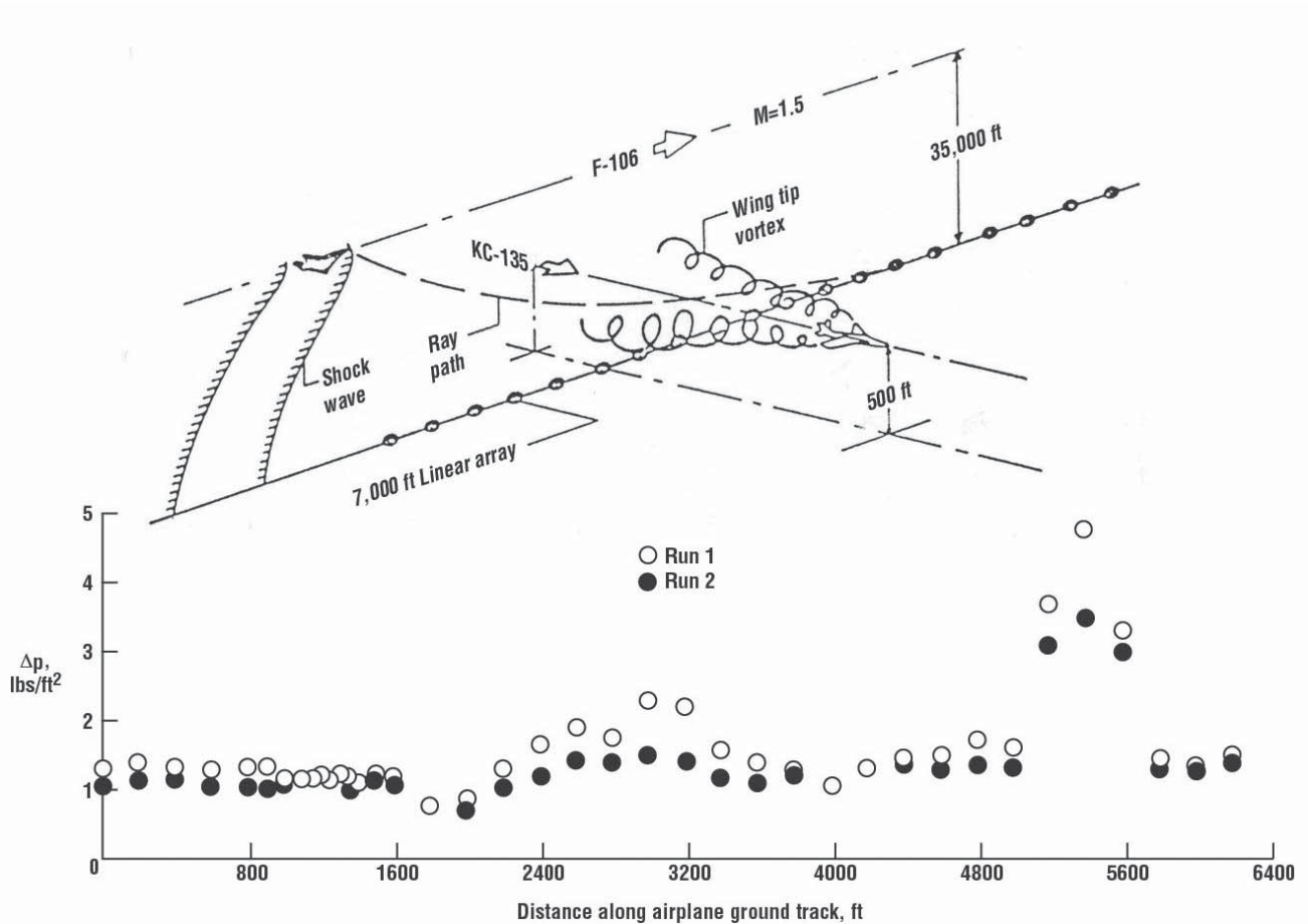


Figure 2.23. Test arrangements and results from aircraft shock wave-vortex interaction experiment (adapted from ref. 2.22).

The resulting measurements of peak overpressure values (two flights) from the microphones in the linear ground array are shown at the bottom of figure 2.23. Of particular interest are the six data points at distances from 5200 to 5600 feet along the ground track where markedly larger overpressure values were recorded. Although the peak overpressures increased a significant amount over those locations beyond the influence of the wing-tip vortex generated by the KC-135 aircraft, no significant changes were noted in the overall character of the signature shapes from those not affected by the KC-135 vortices. Such an observation suggests that the turbulence structure within the wing-tip vortices are different than that of the lower layer of the atmosphere.

Effect of Aircraft Pitching Motion

It was recognized that measurements of sonic boom signatures on the ground may be affected by variations in the aircraft pitching motion (lift variations) as well as by the atmosphere. An experiment was performed in an attempt to evaluate the effects on measured signatures of altitude perturbations of the aircraft about its nominal flight path. In order to accomplish this study, the same test setup, shown in figure 2.23, was employed. A schematic of the test setup and results are presented in figure 2.24 (ref. 2.15). The aircraft was flown at a fixed altitude and Mach number and on a given heading directly over and along a 6200-foot-long array of 40 microphones, as shown in figure 2.24(a). The aircraft, which was specially instrumented to record its motions, was flown both in steady level and pitching motion flight. All flights were made at a nominal altitude of 35,000 feet and a Mach number of 1.5 with an F-106 aircraft. For the pitching motion flight, the pilot caused the airplane to deviate from steady level flight conditions by cycling the controls to produce a $\pm 0.5g$ normal acceleration at the center of gravity of the aircraft. These induced motions have a period of about 1 second and thus, the wavelengths of the motion were about 1500 feet for the particular flight conditions.

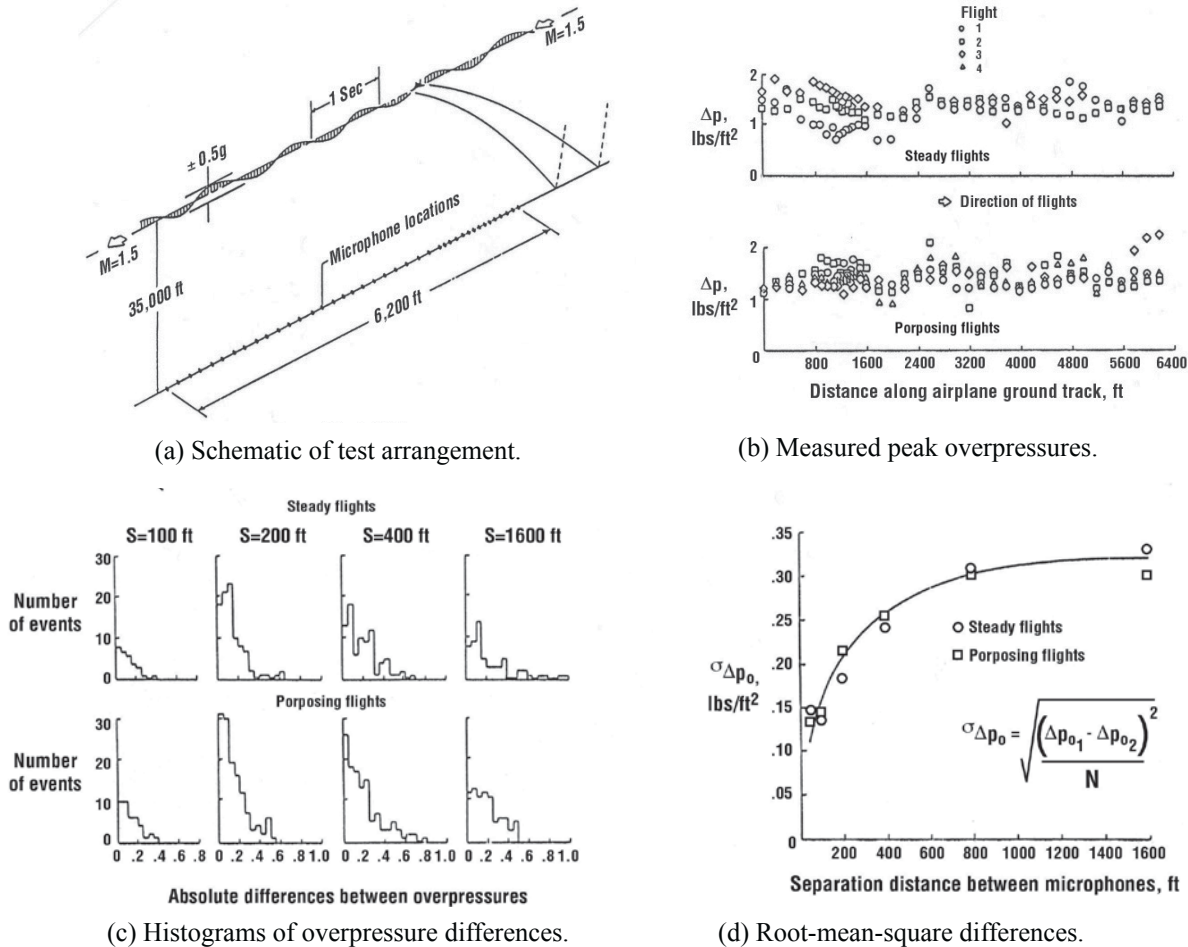


Figure 2.24. Influence of an F-106 aircraft's motion on sonic boom signatures at ground. The aircraft was flying over EAFB at Mach 1.5 and an altitude of 35,000 feet (adapted from ref. 2.15).

Ground overpressure measurements for the two types of flights are shown in figure 2.24(b). The data points for three steady flights and for four pitching motion flights were obtained from individual microphones located at various stations along the ground track as indicated in the schematic sketch of figure 2.24(a). Note that the same ranges of overpressure were measured for each of the flight conditions. Furthermore, an inspection of the data suggests the occurrence of cyclic variations of the overpressures for both the steady and pitching motion flight conditions. Since it is believed that the pitching motion flight condition might produce a cyclic variation of overpressure at a preferred wavelength on the ground, the data of several such flights were analyzed in such a manner as to accentuate this effect, if it existed. These results are shown by the individual histograms shown in figure 2.24(c) that indicate variations in the absolute values of the differences in the overpressures measured at pairs of points and are separated by the distances indicated. If the effects of the airplane motion were faithfully transmitted to the ground, it is reasonable to expect that smaller differences in overpressure values would be obtained at some separation distances than at others. The sample data from these histograms (fig. 2.24(c) represent separation distances varying from 100 feet to 1600 feet for comparison. In order to better define the trend of the variations, the data are presented in a more convenient form in figure 2.24(d).

The quantity Δp , which is the root mean square overpressure difference, is plotted as a function of separation distance for the distances for which data are available. A single curve seems to represent the variation of Δp as a function of distance for both the steady and pitching motion flight cases. Both sets of data are seen to increase monotonically as a function of separation distance. Such a result strongly suggests that perturbations about the flight track of the order resulting from the $\pm 0.5 g$ pitching motion flight do not propagate faithfully to the ground from high altitude. It is therefore believed that the observed variations in boom level along the ground track are due mainly to atmospheric effects rather than to effects of the aircraft's pitching motion. For lift dominated vehicles, such as the XB-70 or an SST, these findings may not be applicable.

Effect of Time of Day

During the 1966 time period, systematic measurement studies designed to minimize all effects other than those of the local atmosphere were conducted at EAFB to document the variability of sonic boom signatures at the ground. A total of 34 F-104 supersonic flights were made at constant Mach and altitude over an 8000-foot linear array of microphones at different times of the day for 8 days over a period covering 2 months. Figure 2.25 (ref. 2.24) presents the results of two such flights made about 1 month apart and at different times of the day.

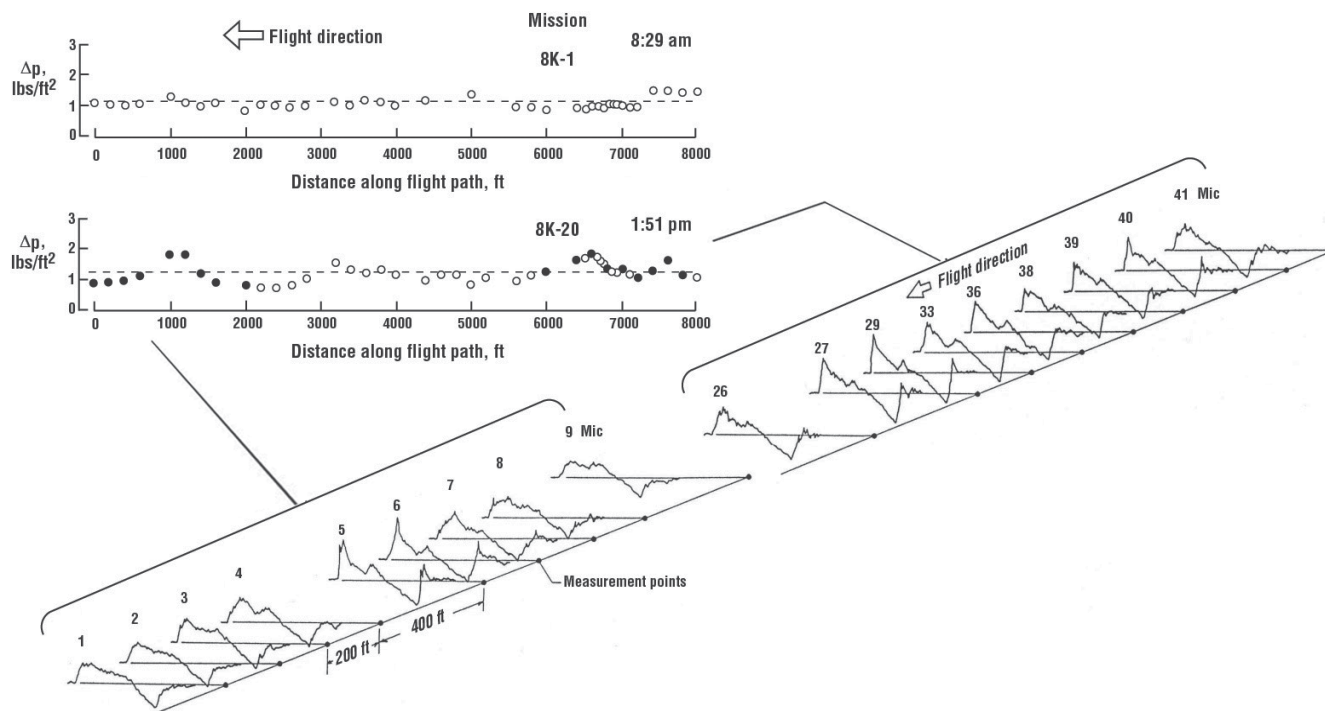


Figure 2.25. Variability in sonic boom overpressures and signature shapes of an F-104 aircraft flying above EAFB at Mach 1.3 and an altitude of 30,500 feet. This variability was measured along an 8000-foot array (adapted from ref. 2.24).

In the upper left of the figure, the peak overpressures obtained from the microphone systems of the array with separation distances ranging from 50 feet to 200 feet for each flight are plotted as a function of distance along the 8000-foot array. Each data point represents the maximum positive peak overpressure reading from a particular microphone of the array. Also shown in each of the two cases is a horizontal dashed line representing the calculated nominal overpressure for the average flight conditions of the test and for standard atmospheric conditions.

It can be seen that a rather small variability in the overpressure values was present for the early morning flight (flight 8K-1) when the lower layer of the atmosphere was fairly stable. In the case of the early afternoon flight (flight 8K-20), when the lower atmosphere was becoming more unstable, considerable variability in boom levels was observed and the data plot has a cyclic or wavelike appearance where measured overpressure values included those markedly higher than, and lower than, the calculated nominal value.

In order to define better the nature of the overpressure variations just noted for flight 8K-20, some signature data are included. The signatures correspond to the overpressure data points shown by the solid symbols. These solid symbol data points are associated with a group of microphones for which the separation distance was generally 200 feet. Note that the highest overpressure values are associated with the peaked waveforms, whereas the lower overpressure values are associated with the rounded waveforms. In the case of flight 8K-20, there is an orderly progression of the wave shape between the lower overpressure and higher overpressure signatures. During the January 2004 SSBE flight tests (ref. 2.20) a supersonic run was performed over a 12,500-foot linear array of 26 ground microphones, spaced 500 feet apart, in the afternoon time period when the lower layer of the atmosphere is normally unstable. Figure 2.26 presents the measured boom signatures along the linear array for flight 19-2 on January 14, 2004 at 1347 hours local time.

The F-5E aircraft flew steady level at Mach 1.4 and an altitude of about 32,000 feet. Although the boom signatures show some evidence of turbulence influences, they are all generally N-wave in character and the variation in boom levels and bow-shock rise time are not as great as those observed on the 8K-20 flight shown in figure 2.25. The above results suggest the possible existence of a characteristic structure of the atmosphere that is changing as a function of time, but has characteristic dimensions of a few hundred to a few thousand feet.

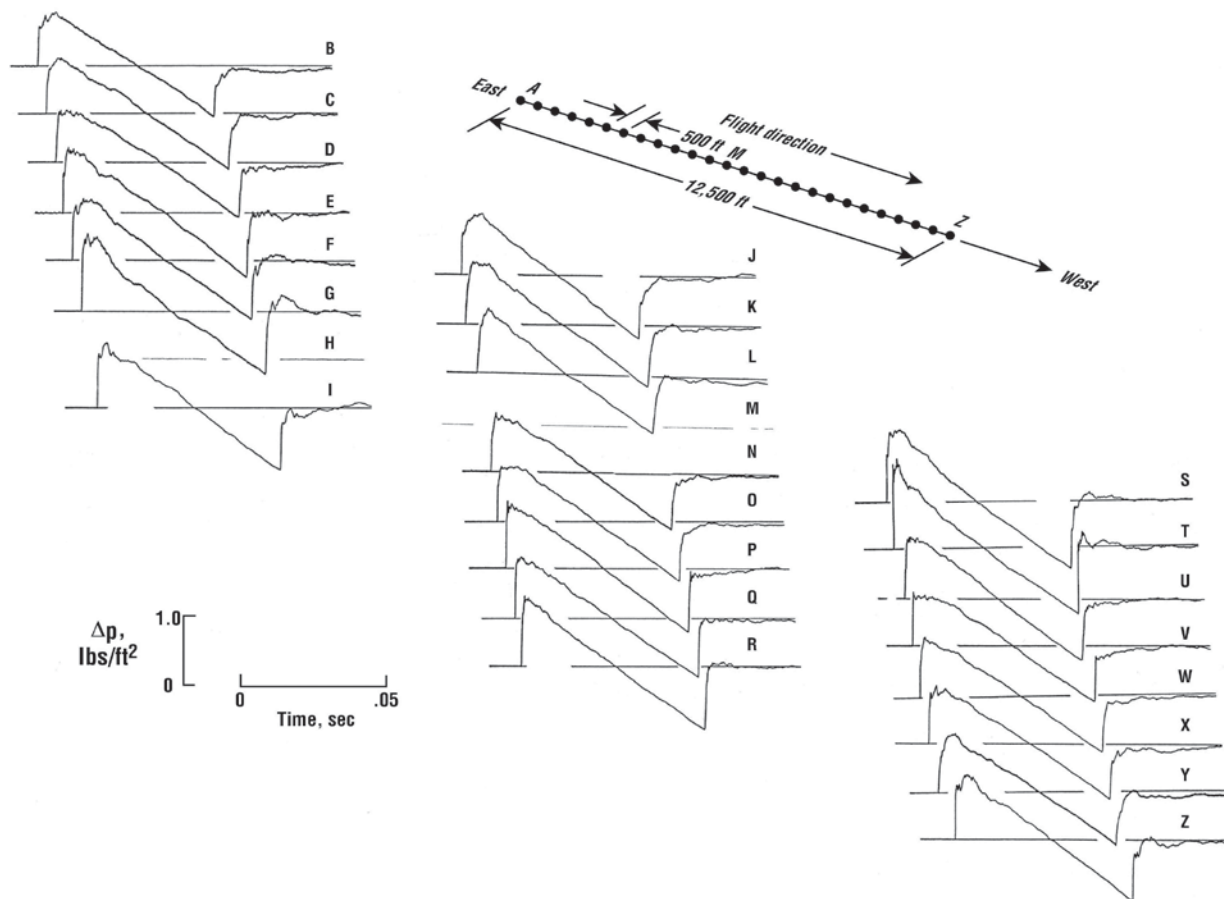


Figure 2.26. Measured sonic boom signatures from the F-5E along a 12,500-foot array of 26 ground microphones spaced 500 feet apart. Flight 19-2 on January 14, 2004 at 1347 hours local time (adapted from ref. 2.20).

Turbulence and Gust Structure

Garrick and Maglieri (ref. 2.25) pointed out that the characteristic length of turbulence in the lower atmosphere below 1000 to 2000 feet depends on the height above terrain. An interesting detailed view of the vortex structure near the ground is afforded by figure 2.27 (from ref. 2.26), which shows equal velocity contours, or isotachs, obtained from measurements taken during 25 seconds of gusty winds. The horizontal section shows the isotachs obtained from measurements taken at eight stations along an array of 50-foot poles equally spaced over a linear distance of 420 feet. The vertical section shows the isotachs obtained from measurements taken at five equally spaced stations up a 250-foot high tower. In each section, the ordinate represents distance along the array or up the tower and the abscissa is time. During the sampling period, the average wind traversed a distance of over 1000 feet. The vortex structure depicted in figure 2.27 was acquired in an open unobstructed area. One can imagine a completely different vortex structure associated with areas in which cluster homes are located between and among high-rise structures and in valleys and on hilly terrain. It is obvious that the influence of such wide-ranging atmospheric situations on the boom signatures that propagate through them will be different.

Turbulence in the upper atmosphere has been probed by instrumented airplanes (ref. 2.27). Typical results of measurement for moderate turbulence are shown in figure 2.28 as the variation of power spectral density of vertical velocity with wave number (1/wavelength).

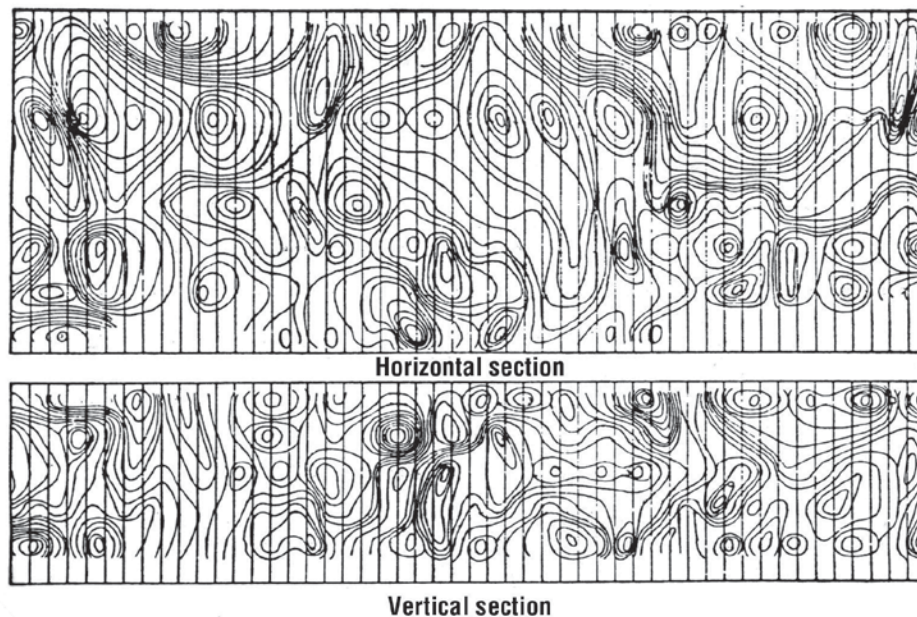


Figure 2.27 Gust structure near the ground as revealed by isovelocity contours (adapted from ref. 2.26).

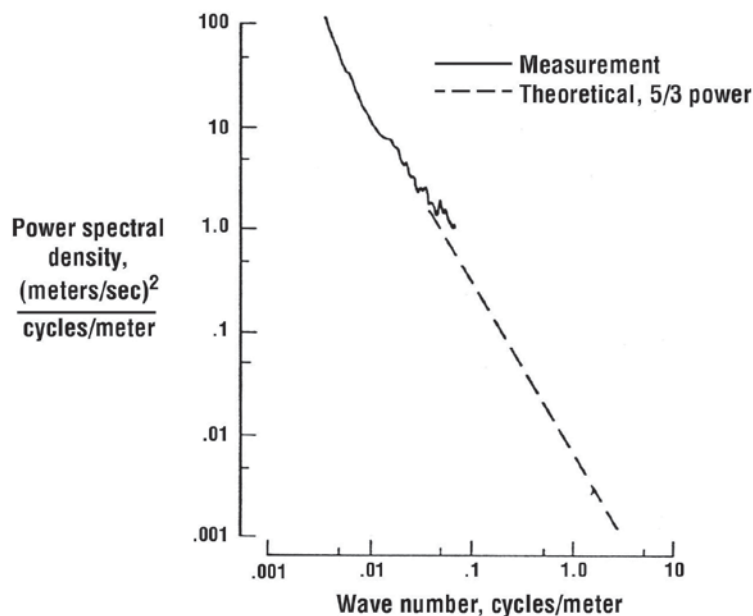


Figure 2.28. A spectrum of atmospheric turbulence (adapted from ref. 2.27).

The dashed extension to the measurements follows the theoretically expected $5/3$ power of the wave number. The shape of this curve tends to be relatively invariant while the amplitude is a function of the severity of the turbulence. The curve shows the distribution of power in the various wavelengths and the area under the curve yields the total power. This same type of figure can also apply approximately near the ground with relatively less power in the longer wavelengths. It may be noted that a sonic boom pressure signature of 0.3 to 0.4 seconds duration covers acoustic wavelengths that range from about 1000 meters to fractions of a foot. Thus, the interaction of the pressure signature and the turbulence occurs over the entire spectrum shown and includes acoustic wavelengths less than and greater than the characteristic vortex sizes.

As previously noted, the atmosphere, particularly the first few thousand feet of the earth's boundary layer, plays a significant role relative to the sonic boom signature waveforms for a given aircraft. It has also been found that these atmospheric influences appear to have similar effects on aircraft signatures independent of aircraft size (i.e., signature duration). Figure 2.29 (ref. 2.25) presents examples of sonic boom waveforms that were measured at different times and on different flights in the primary carpet for three different types of aircraft. The measured

waveforms for the 55-foot long F-104 aircraft are for a time duration (Δt) of about 0.10 second and are seen to differ from the nominal N-wave shape, varying from a sharply peaked to a gently rounded shape. Similar tracings are shown for the B-58 (about 98 feet long) and XB-70 (about 185 feet long) aircraft. The B-58 signatures are roughly 0.2 second in duration and the XB-70 signatures are approximately 0.30 second in duration. The main differences between the boom signatures for a given aircraft occur at the time of the rapid compressions (i.e., the bow and tail shocks of the N-wave signature). The largest overpressures (Δp) are generally associated with the sharply peaked waves, whereas the lower pressures are associated with the rounded waveforms, which display longer rise times (τ).

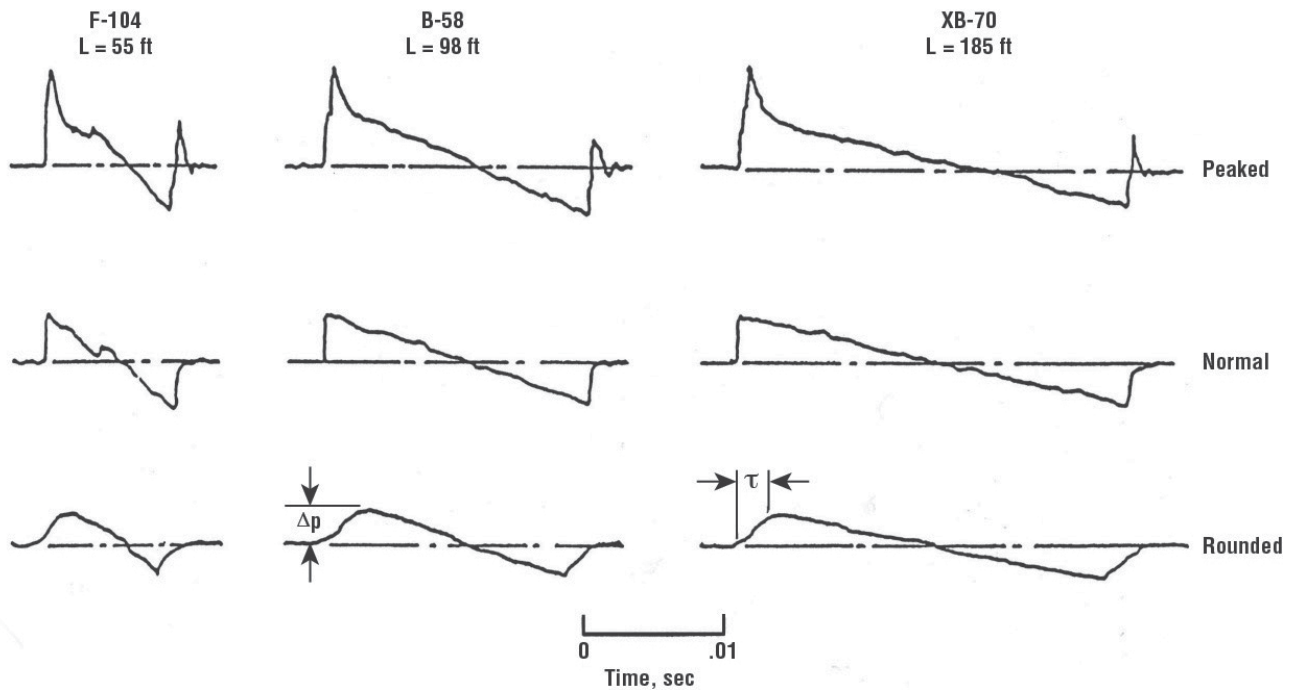


Figure 2.29. Influence of atmosphere on boom signatures from different size aircraft (adapted from ref. 2.25).

Initially, rise time was defined as the time from the onset of the shock from ambient pressure to the maximum overpressure. Further definitions included the rise time to the 1/2 and 3/4 overpressure amplitude. Today, the preferred description of a boom signature rise time is the time from the 10 percent of the overpressure amplitude from ambient pressure to the 90 percent value of the overpressure. As will be discussed in later chapters of this report, rise time (τ) plays a significant role in human response both outdoors and indoors to sonic booms and also to the response of building structures to booms.

Also of significance is the fact that distortions displayed on the bow shocks are duplicated at the tail shock and are independent of the signature length or duration for the three cases shown of about 0.10 to 0.30 second.

The fact that virtually all N-wave signatures of 300 msec or less exhibit the same turbulence distortion patterns of the bow and tail shocks suggests certain features of the turbulence structure can be considered frozen within this time-space regime. It has also been found that as the N-wave signature durations grow larger, as for the case of measurements from the Shuttle Orbiter on reentry at high Mach-altitude conditions, that this bow-tail shock duplication is not evident.

Measured results from 10 sonic boom sites in the California area that were located along and laterally from the ground track on STS-26 reentry, are illustrated in figure 2.30 (ref. 2.28). Also shown on the figure are the Mach number and altitude at which the boom was generated. Note that the ten signatures cover the range of Mach numbers from 4.57 to 3.18 and altitudes from about 115,000 feet to 95,000 feet, respectively.

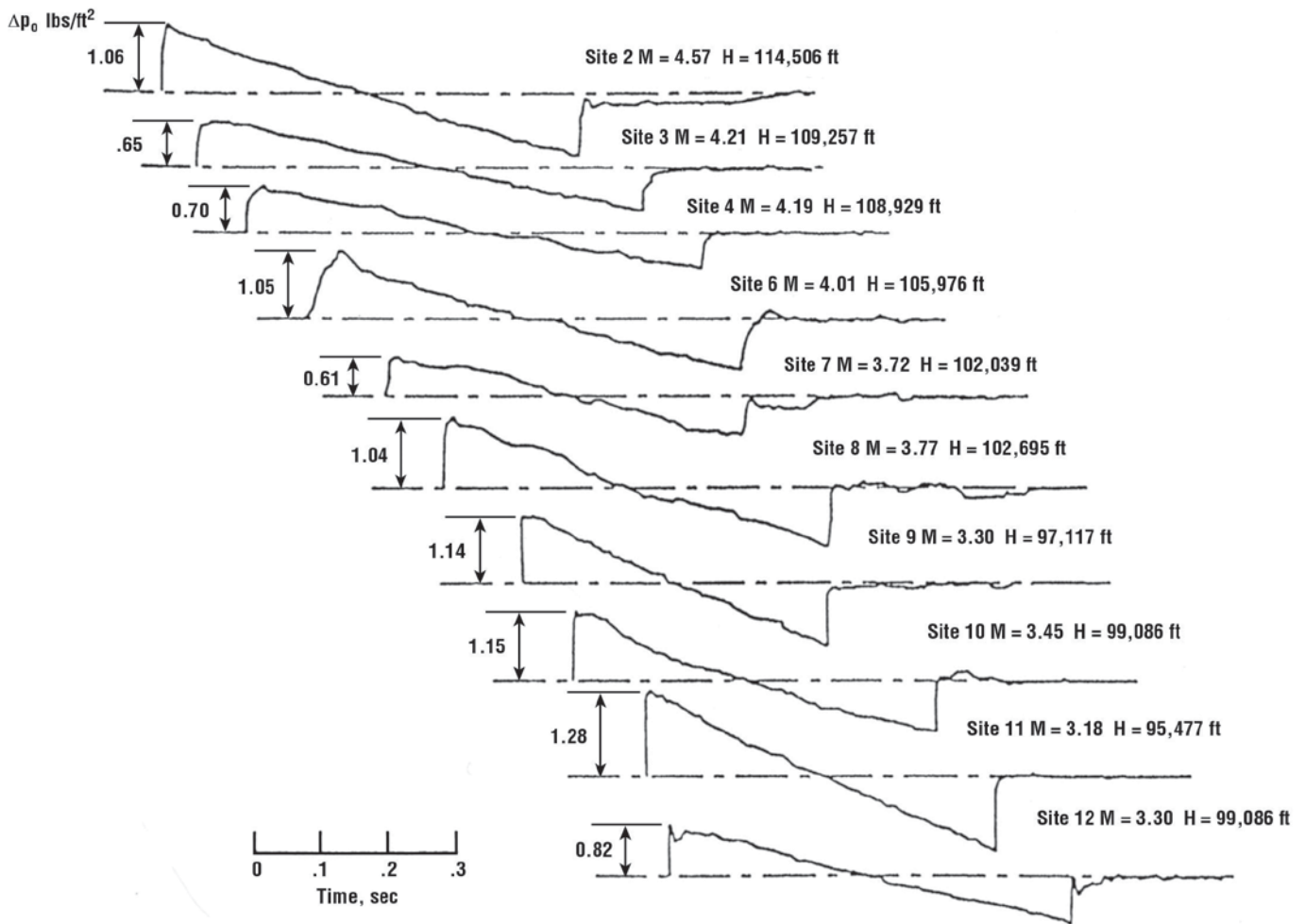


Figure 2.30. Comparison of sonic boom pressure signatures from STS-26 reentry as measured at 10 sites in California (adapted from ref. 2.28).

It can be seen that all signatures are similar, being N-wave in shape with fairly rapid rise times on most of the signatures. Durations vary from about 0.45 second to 0.68 second and overpressures from 0.61 to 1.28 lbs/ft². There are indications of atmospheric effects on the signatures, in particular, sites 4, 6, 7, and 12, but all 10 signatures remain N-wave in character.

It should be noted, however, that at the high Mach-altitude conditions, where the signature durations are large, the nature of the bow and tail shocks may differ and that whatever peaking or rounding of the bow shock resulting from atmospheric turbulence in the lower layers of the atmosphere is not exactly repeated at the tail shock (for example, site 2 vs site 12). A similar observation is evident for the first two high Mach-altitude on-track measured signatures on STS-1 reentry (ref. 2.29). This fact suggests that the previously mentioned assumption of a frozen atmosphere does not apply in all cases when the signature lengths are larger than the scale of the atmospheric disturbances.

Effect of Microphone Orientation

It has been shown that shock wave signatures with similar spikey characteristics on both the bow and tail waves can be realized as a result of microphone orientation. Garinther and Moreland (ref. 2.30) investigated several transducers that were considered for use in evaluating the hearing hazard of pressure waves that small arms produce. Although muzzle blast was foremost in the study, measurements were also made of the shock waves associated with the supersonic passage of the rifle bullet past the microphone, which was oriented at various angles from normal (0° incidence) to grazing (90° incidence). The results from BRL 250-kc microphone are shown in figure 2.31.

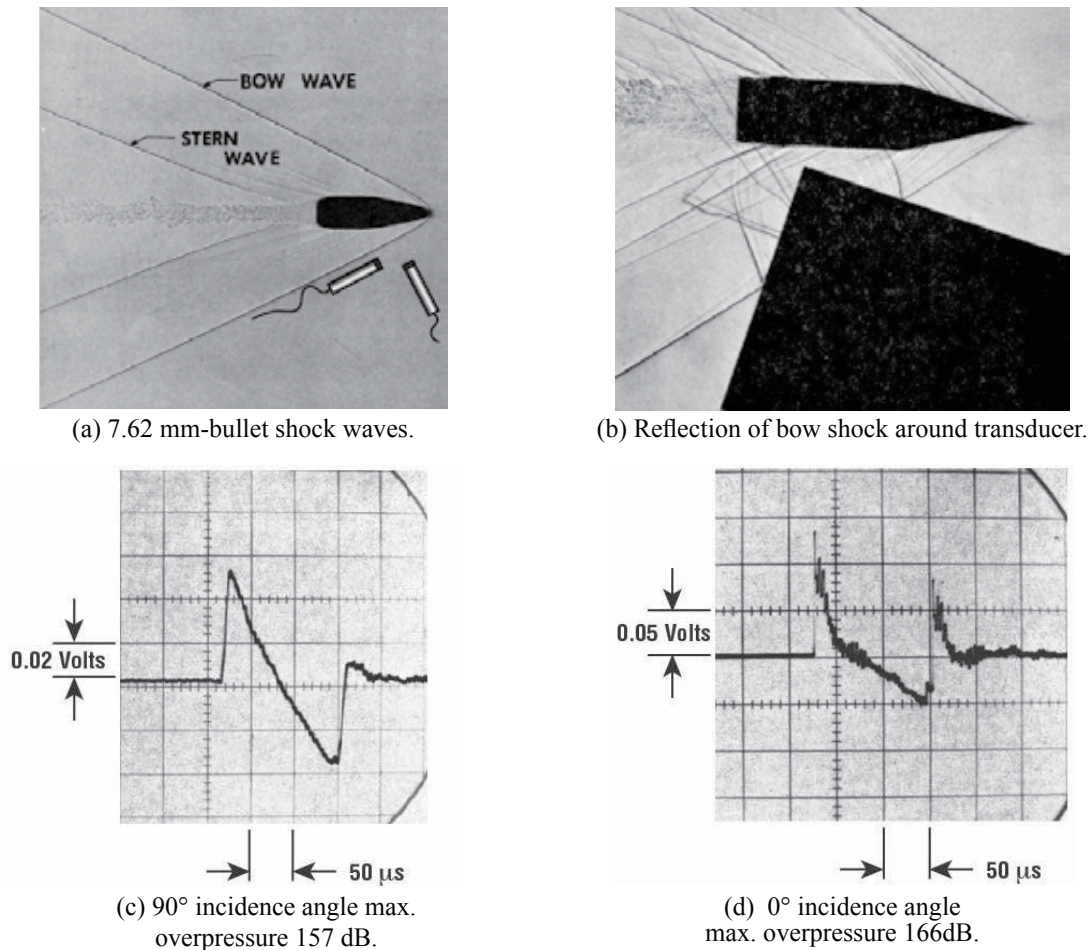


Figure 2.31. Influence of microphone orientation on bullet shock wave signature (adapted from ref. 2.30).

Figure 2.31(a) shows the shock waves associated with the 7.62 mm rifle bullet traveling at 2870 feet per second with microphones about 1 meter from the shock pattern at 0° and 90° incidence to the shocks (normal and grazing, respectively). Figure 2.31(b) illustrates how the bow shock reflects around the simulated transducer, which is oriented at about a 45° incidence angle to the shock. Note the very large difference between the thickness of the shocks as compared to the size (1.20-in. diameter) of the microphone diaphragm. In the case of boom signature measurements resulting from the shocks off the aircraft, the reverse is true (i.e., the shocks are usually an order of magnitude thicker than the size of the microphone diaphragm).

Figure 2.31(c) and figure 2.31(d) show the significant difference in the measured N-waves from the bullet shock system. The signature measured with the microphone at grazing incidence in figure 2.31(c) results in the expected N-wave without distortions due to reflections or refractions about the transducer. However, at normal incidence, the bow and tail shocks are peaked and spikey, similar to what has been observed during sonic boom measurement and attributed to atmospheric effects.

However, for the aircraft boom case, the thickness of the shock is much greater than the size of the microphone used to measure the signatures. As such, microphone orientation should not play a role in defining the boom signature characteristics. In order to establish that the boom signature distortions (spiking and rounding of bow and tail shocks) are truly a result of atmospheric influences and are not a result of the orientation of the microphone measurement systems, a special boom overflight test was conducted during the 1966–67 sonic boom experiments (ref. 2.22).

Figure 2.32 depicts the test setup and resulting boom signature measurements. Six of the Photocon microphone systems (ref. 2.31) were arranged on a 4-foot square ground board in a cluster about one foot in diameter and isolated from any vibrations. One was flush mounted with its diaphragm parallel to the ground, four were oriented

about 6 inches above the board with their diaphragms at an incidence angle of 45° to the ground plane in a cruciform array parallel and perpendicular to the aircraft ground track. A sixth microphone was located in the same plane and with its diaphragm parallel to and facing the ground.

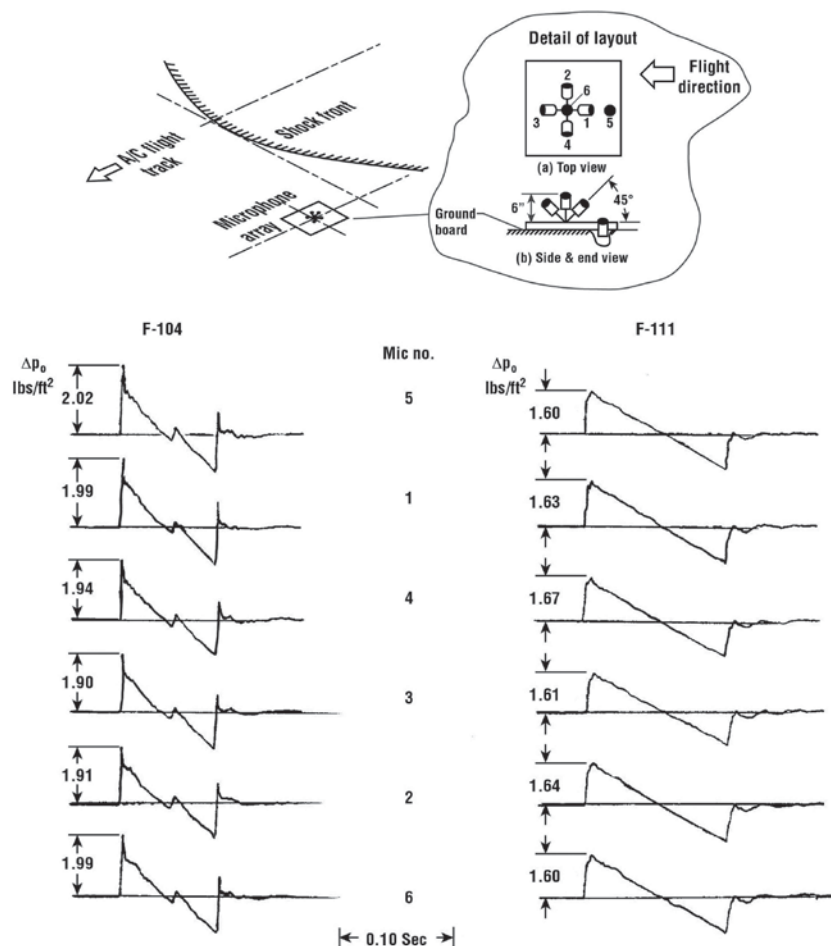
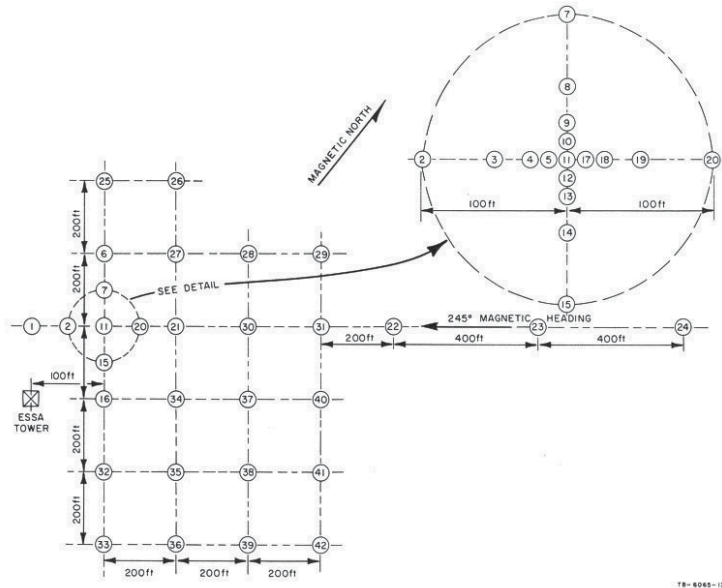


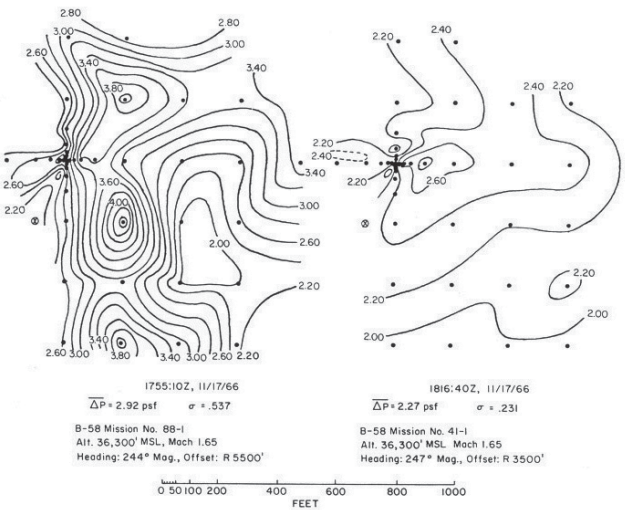
Figure 2.32. Effect of microphone orientation on sonic boom signature shape.

Two passes were made on 2 consecutive days, one in the afternoon with the F-104 at Mach 1.3 and 21,000 feet altitude and offset from the microphone array by about 5 miles. The second pass was made in the morning of the second day by an F-111 at Mach 1.92 and an altitude of 40,000 feet almost directly overhead of the array. Examination of the measured signatures indicate that for the F-104 afternoon flight, atmospheric influences are evident in the measured boom signatures in that they are spikey, whereas for the F-111 morning flight, when the lower layer of the atmosphere were quiescent, near normal N-waves were measured. In both cases, any distortions that occurred for the bow shock were also present on the tail shock. More importantly, however, is that for each flight, the measurements made by all six microphones are essentially identical regardless of diaphragm orientation. Thus, the signature distortions associated with aircraft generated sonic booms result from atmospheric effects. A similar microphone orientation checkout test was conducted in 1987 by the U. S. Air Force during the development of their digital Boom Event Analyzer Recorder (BEAR) system (ref. 2.32). Once again, six microphones were arranged in the same fashion as for the 1967 EAFB tests and the results were similar.

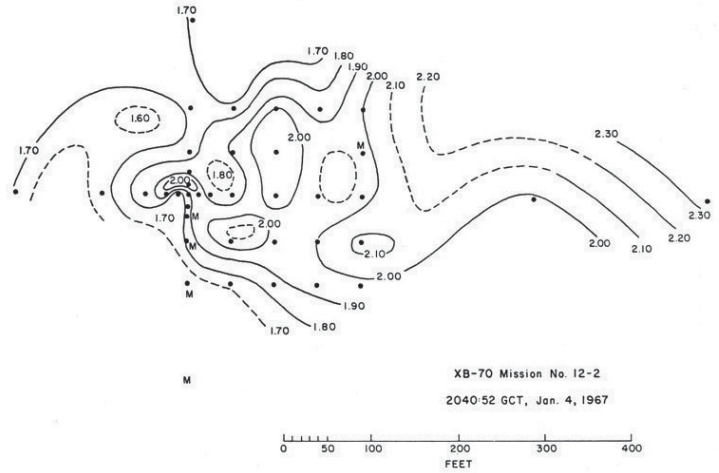
Earlier in this chapter (figs. 2.16 and 2.32) it was shown that sonic boom signatures acquired with the microphones grouped within a foot or so were essentially identical. It was also shown that as the separation distance between microphones increased beyond 50 feet, the boom signatures differed from one another (see figs. 2.17, 2.18, 2.25, and 2.26). Some studies conducted by the Environmental Science Services Administration (ESSA) during the 1966 EAFB National Sonic Boom Program sought to establish a more solid relationship between the atmosphere and its influence on sonic boom signatures. Figure 2.33 (ref. 2.33) shows the designed layout of 42 microphone measurement systems located near the aircraft ground track and with a spacing of from 12.5 feet to 200 feet along with contours displaying the distribution of overpressure patterns for two supersonic overflights.



(a) Microphone array for ESSA studies – Site 9.



(b) Distribution of overpressure patterns for Missions 88-1 and 41-1, 200-ft grid array.



(c) Distribution of overpressure patterns for Mission 87-1, 50-ft grid array.

Figure 2.33. Microphone layout and overpressure patterns acquired during 1967 NSBEO ESSA meteorological investigation (adapted from ref. 2.33).

During these tests, it was observed that at the microphone array arranged in concentric circles out to a 100-foot radius (microphones 2 through 20 in figure 2.33(a)), the microphones that were within 25 feet of the center of the circle (microphones 4, 5, 9, 10, 11, 12, 13, 17, and 18) were correlated (i.e., all the signatures were essentially the same). As the distance from the center of the circle increased to 50 feet (microphones 3, 8, 14, and 19) the correlation ceased to exist and all the signatures were different from each other.

A similar observation was made during the 2003 SSBD flight program (ref. 2.34) and is shown in figure 2.34 (ref. 2.35). It can be seen that the two boom signatures from the F-5E aircraft measured at microphones 1 and 2 are 25 feet apart and essentially identical in all aspects.

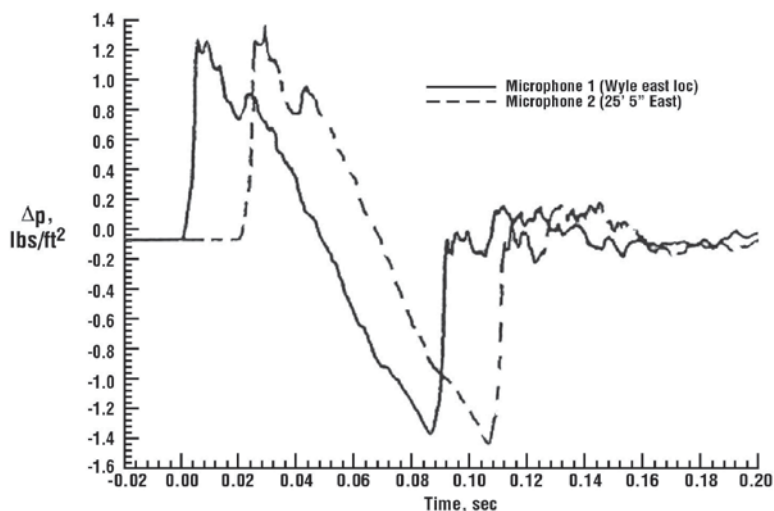
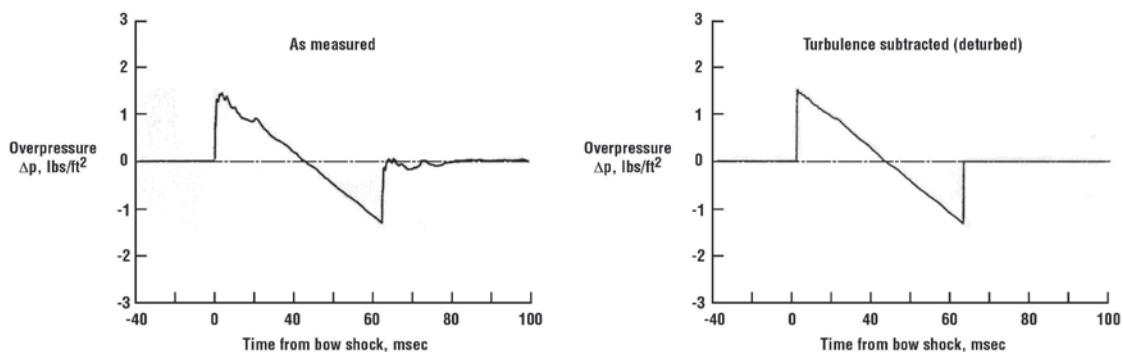


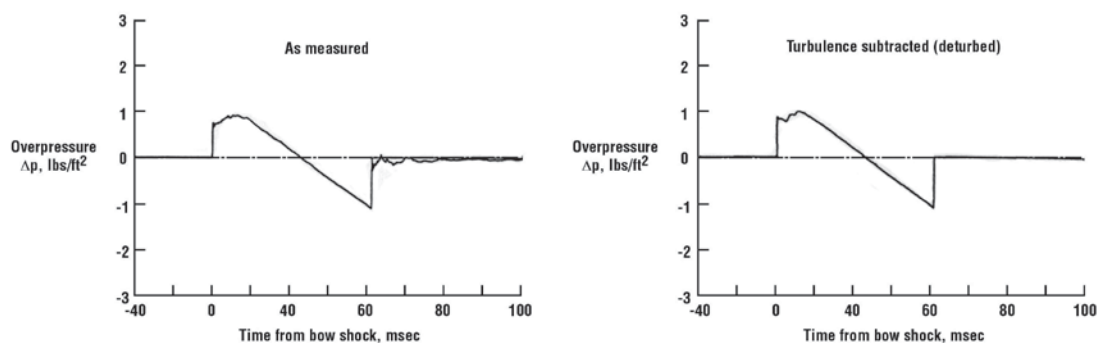
Figure 2.34. Signatures from microphones positioned 25 feet apart (ref. 2.35).

Signature Deturbing

The fact that atmospheric distortions to the sonic boom signatures affect the bow and tail shocks equally, on waveforms of up to 300 msec in duration, allows one to assume that the turbulence structure of the atmosphere is essentially frozen during the time period in which the shock propagates through it to the ground. Boom signatures measured for the SSBD and F-5E aircraft of about 90 msec in duration are also short enough that the frozen turbulence assumption should apply. A deturbing procedure was therefore applied (refs. 2.20, 2.36, and 2.37). The process consisted of superposing a clean step function on the rear shock and subtracting that from the measured boom following the shock. The resulting difference was then subtracted from both the front and rear shocks. Figure 2.35 (from ref. 2.20) shows the results. Figure 2.35(a) shows a measured F-5E boom on the left and the same signature with turbulence subtracted on the right. The rear shock (by definition) becomes a simple step. With the influence of turbulence on the bow shock removed, the full signature is close to a perfect N-wave. This process was found to work for virtually all of the N-wave booms.



(a) F-5E signatures.



(b) SSBD signatures.

Figure 2.35. Examples of boom signature cleanup. The flights of 1/15/04 were at 16:20 hrs and 18:17 hrs (adapted from ref. 2.20).

This turbulence subtraction algorithm was applied to the measured SSBD boom shown in figure 2.35(b). The turbulence-subtraction analysis showed that the original signature variations were due to turbulence. Removal of turbulence results in extremely consistent measured results for the N-wave and shaped boom.

It is interesting to note that sonic boom signature deturbing was first looked at by Kane and Palmer in 1964 (ref. 2.1) when they noted that if there is turbulent scattering of the shock wave, the changes of the turbulent structure of the atmosphere between the instant of passage between the bow shock wave and the aft shock wave are very small (i.e., one can assume that the turbulence is frozen for that time period) and the front and aft shock waves should be affected in the same way. Thus, they performed the following experiment to test this deduction. First they made a tracing of the distorted N-wave signature. Then, they placed this tracing below the original trace so that the axis corresponding to time is parallel to the original N-wave signature, as shown in figure 2.36. Next, the trace is translated to the left so that the point where the aft shock wave begins and the front shock wave begins coincide vertically. Next, they perform an algebraic-graphical subtraction in which values below the zero Δp_z line are treated as negative. This procedure, illustrated in the figure, restored the original form of the N-wave.

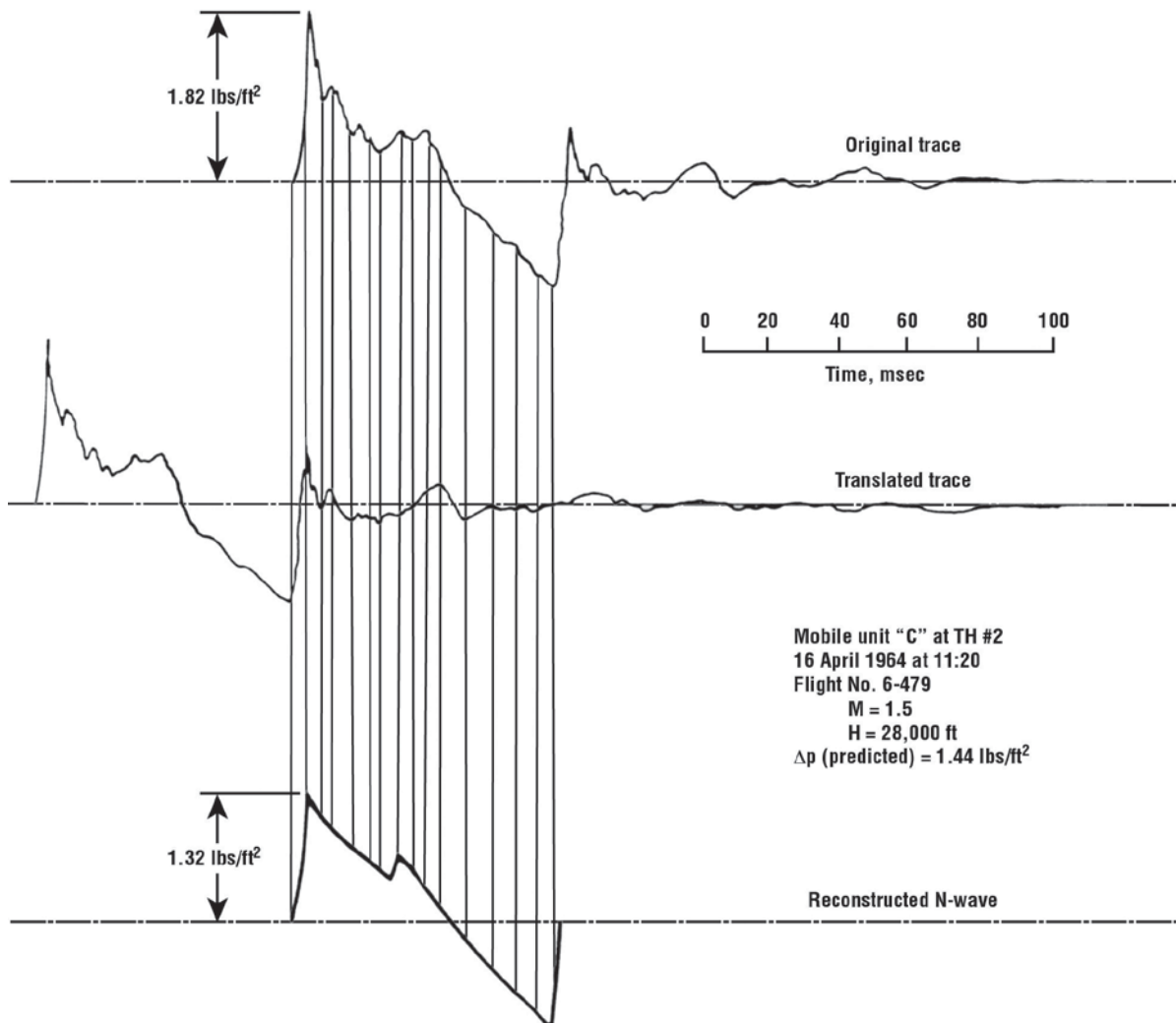


Figure 2.36. Reconstruction of wave signature by graphical method (adapted from ref. 2.1).

Off-Track Variability

Signature variability is not only observed along the aircraft flight track, but also at lateral distances out to and beyond the cutoff depending upon the state of the atmosphere, particularly in the lower layers. An illustration of such an occurrence is presented in figure 2.37 (ref. 2.9) for steady level flights of an F-104 at the EAFB test site during fairly stable and unstable conditions of the atmosphere. The four flights were made at about the same Mach and altitude conditions.

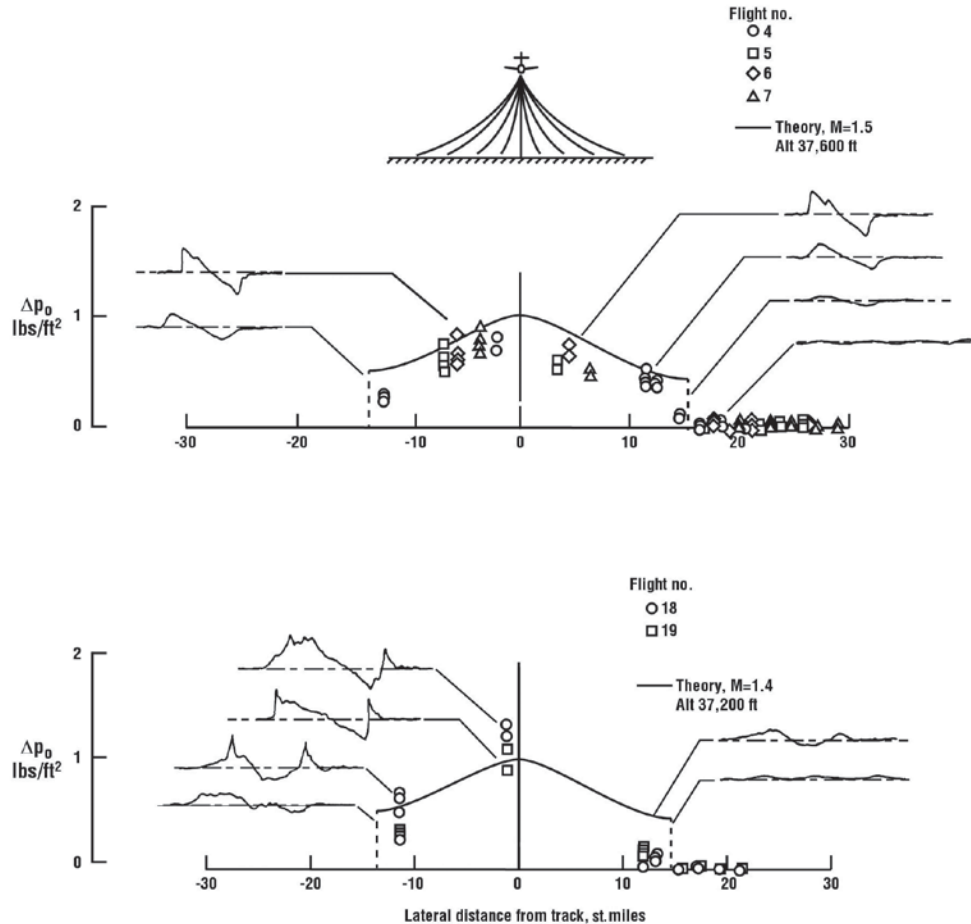


Figure 2.37. Effects of atmosphere on lateral boom signatures (ref. 2.9).

The lateral spread results shown at the top of the figure represent four flights under fairly calm surface and lower layer conditions. Note that similar waveforms were obtained for about the same distances to each side of the airplane ground track and the bow-shock overpressure decreases while the rise time increases (wave becomes more rounded) as the lateral cutoff is approached. Beyond this point, the boom signatures lose their identity and are observed as a rumbling noise as depicted by the low frequency pressure time histories.

Lateral-spread results, presented in the lower part of figure 2.37, were obtained in the same manner as those in the upper half of the figure, only during a day in which the atmosphere was known to be more active, that is, high surface winds, cloud cover, and overcast. The results presented are for two steady-level passes of the F-104. Solid symbols represent no disturbances observed or measured. Also shown are sketches of the type of pressure signatures measured at the various recording stations. The most significant feature of these latter results are the shapes of the signatures. Note that a nominally shaped N-wave does not appear – rather the wave signatures are greatly distorted into peaked and rounded waveform shapes with accompanying wide ranges of overpressure. In fact, one of the signatures near the lateral cutoff has the appearance of a U-shape (double positive peaks) associated with focusing as observed for Mach cutoff (see fig. 5.7 of Chapter 5).

Statistical Variations

Peaking and rounding of sonic boom signatures is statistical in nature and occurs as a function of either time or distance. A summary of the variations of the on-track overpressures resulting from the atmosphere for steady level flight is given in figure 2.38 (ref. 2.38). This statistical analysis comprises most of the planned sonic boom experiments that have been conducted in the United States. Data are included for a wide range of aircraft, a Mach number range of 1.2 to 3.0, and an altitude range of about 10,000 to 80,000 feet. A total of 12,406 data samples have resulted from the 1,625 supersonic flights.

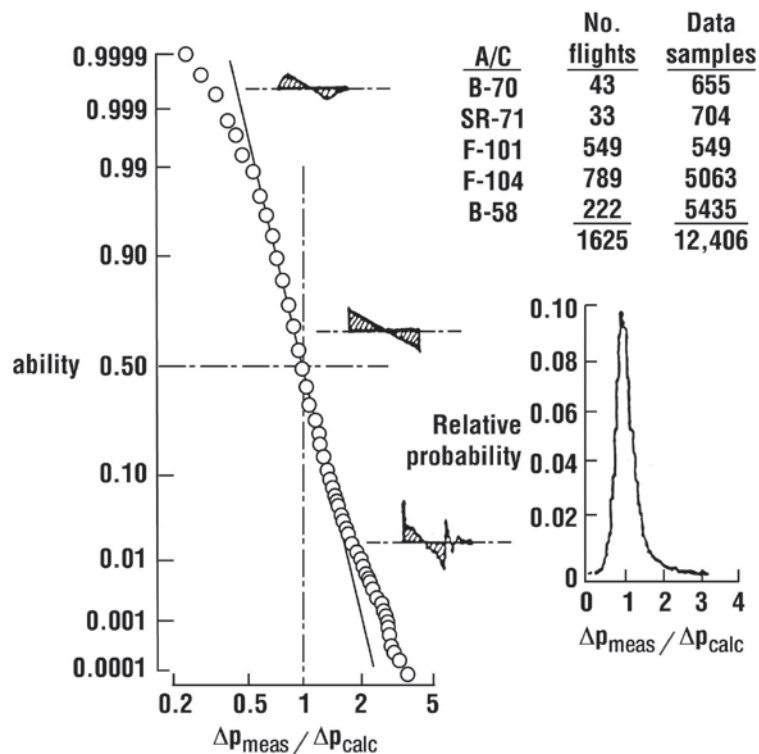


Figure 2.38. On-track statistical variation (adapted from ref. 2.38).

Plotted on figure 2.38 is a cumulative frequency distribution and histogram for on-track measurements showing the probability of equaling or exceeding the ratio of the measured overpressure to the predicted overpressure for steady flight in standard atmosphere with no winds. For this type of presentation, all the data would fall in a straight line if the logarithm of the data fit a normal distribution. Rounded signatures of the waveform sketched in the chart are usually associated with overpressure ratios less than 1.0. Nominal or N-wave signatures are observed on the average and peaked signatures of higher overpressures are observed usually at ratios greater than 1.0.

The data indicate that variation in the sonic boom signatures, as a result of the effects of the atmosphere, can be expected during routine operations. For example, one boom in a thousand is expected to exceed the nominal value by a factor of about 3.0, at least for N-wave designed aircraft.

Effect of Mach Number

It has also been found that sonic boom variability is dependent upon flight Mach number. Higher Mach numbers result in less variability of the N-waves. This is illustrated in figure 2.39 (ref. 2.24), which shows the statistical variation observed in the sonic boom overpressures for an F-104 airplane flying at a constant altitude of about 30,000 feet at Mach numbers of 1.3 and 1.6 over an 8000-foot linear array of microphones and an illustration of the shock-ray patterns for both the low and high Mach number situation as they propagate to the ground. Note that for the lower Mach case, the ray path is longer and, thus, spends more time in the lower layers of the atmosphere as compared to the higher Mach case. As a result, as will be noted from the probability distributions that are shown on the left-hand side of the chart, the longer the dwell time in this layer of the atmosphere the greater the variability. As the variability increases, the chance of encountering large excursions and thus higher boom levels, on occasion, is increased.

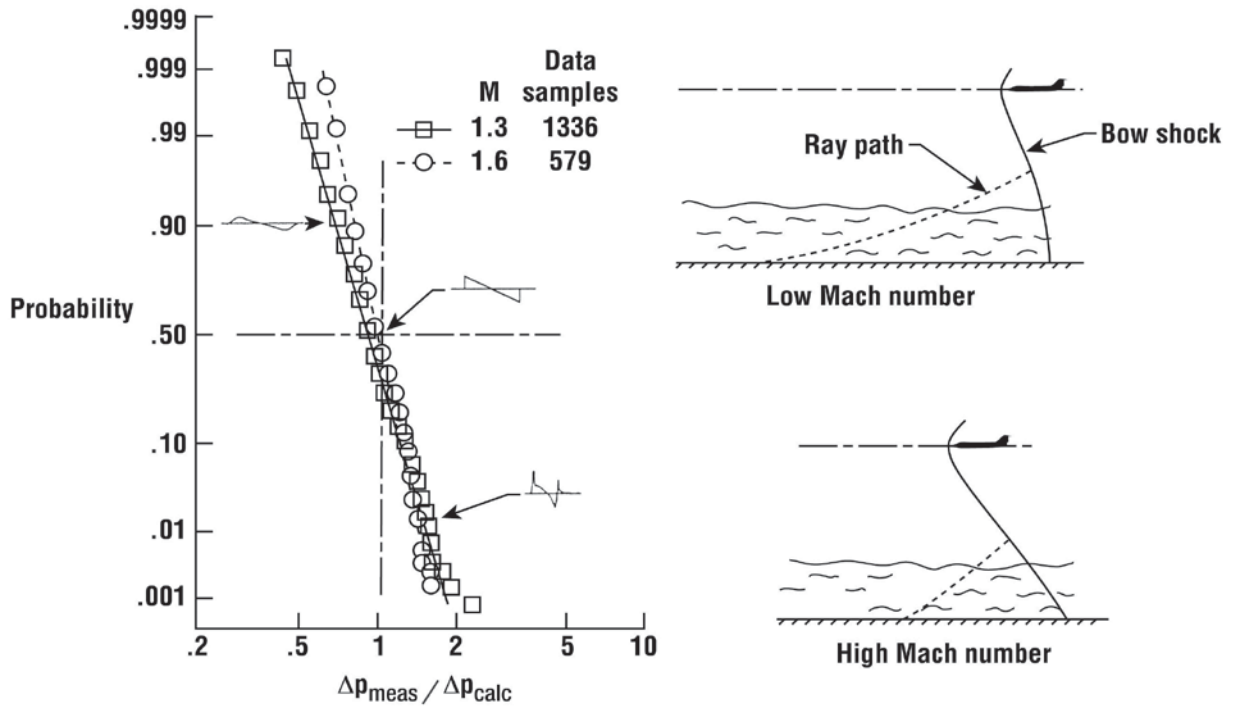


Figure 2.39. Effect of aircraft Mach number on sonic boom variability (F-104 at 30,000 ft MSL), (adapted from ref. 2.24).

Effect of Lateral Distance

A comparison of the variability of the overpressures for a given set of flight conditions for flights of the XB-70 for locations on track and at a large distance from the flight track are given in figure 2.40 (ref. 2.15). Data for measurement locations about 13 miles off the flight track (diamond symbols) are compared with those on the track (circle symbols) for flights at an altitude of 60,000 feet and Mach numbers of 1.8 to 2.5.

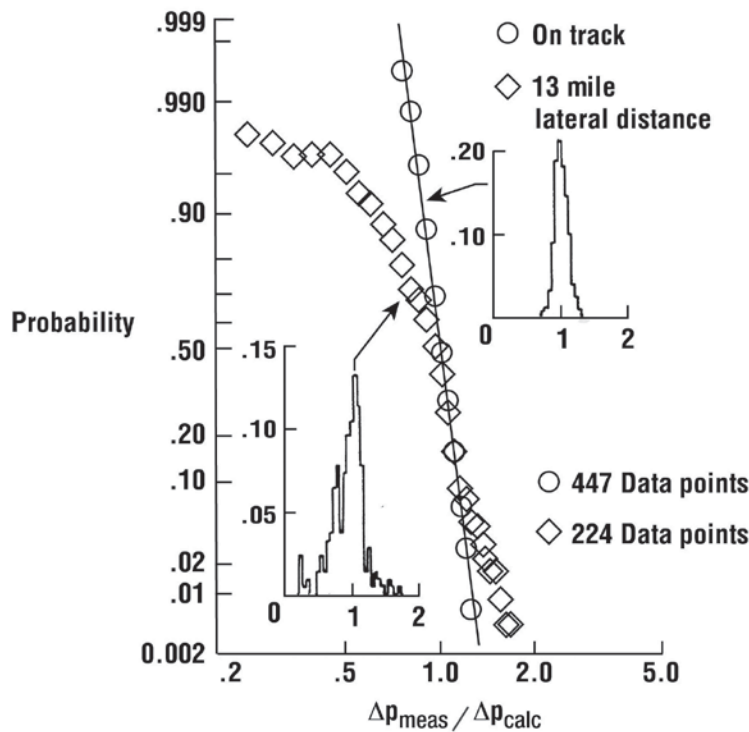


Figure 2.40. Effect of lateral distance on sonic boom variability; XB-70 at Mach 1.8–2.5 at 60,000 feet (adapted from ref. 2.15).

In addition to the probability curves, histograms are also included. It can be seen that the probability distribution for the measurements obtained at distances out to 13 miles shows larger variability. This, of course, would be expected as a result of the longer ray paths traveled by the waves in the lower layers of the atmosphere before reaching the lateral measurement stations.

Rise Time Variability

The possibility that the rise times tend to increase with increasing flight altitude is suggested by the data in figure 2.41 (ref. 2.39). The various data points are individual rise times (τ_{Max} or $\tau_{1/2}$) measured on-track when aircraft are flying at a given altitude. Scatter of the data is a clear indication of the effects of turbulence and small-scale atmospheric phenomenon. If the trend indicated by the data is real, then one is confronted with an as yet unexplained inconsistency with the generally accepted notions that (1) the magnitude of the rise times is caused by atmospheric perturbations, and turbulence in particular (2) the bulk of such perturbations are within 3000 feet of the ground and (3) any accumulative creation of finite rise times by higher-altitude variations should be negated by nonlinear steepening effects. It will be shown later in these discussions that the influence of atmospheric absorption dominated by the molecular relaxation of O_2 and N_2 can play a nontrivial role in signature rise time. As it stands, the data suggest that N-wave sonic boom signatures produced by aircraft flying at an altitude of 50,000 to 60,000 feet will realize about a 3–6 milliseconds rise time under most conditions.

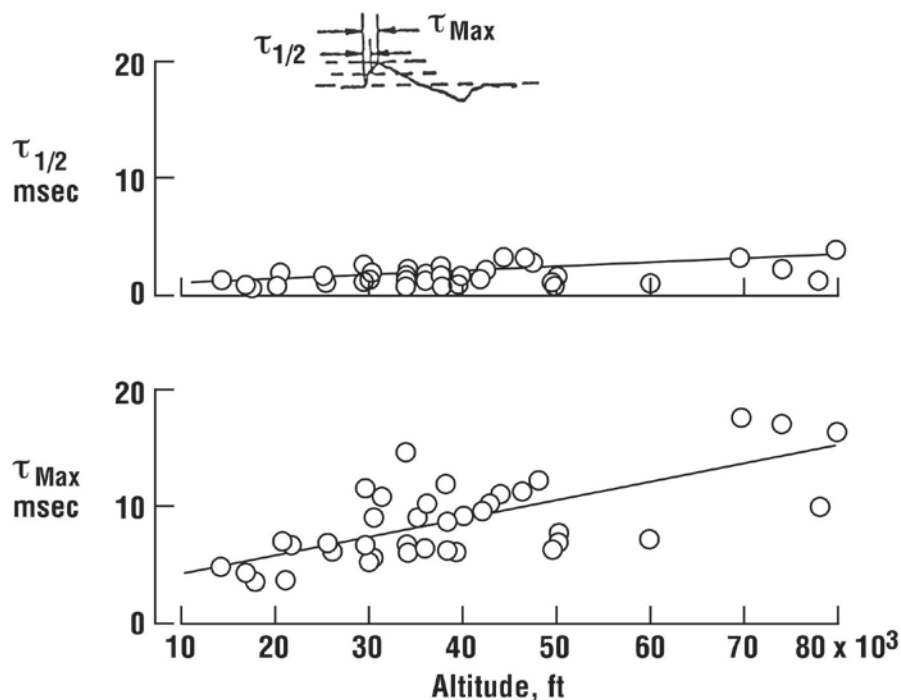


Figure 2.41. Variation of rise time with altitude (on track) (adapted from ref. 2.39).

It has been shown that signature variability increases with increasing lateral distance since these ray paths, which the shock travels along, spend more time in the lower layers of the atmosphere. Thus, one would expect that the signature shock rise time would also increase as lateral distance increases. The plots of the rise time relative probabilities shown in figure 2.42 (ref. 2.39) are based on data taken for F-104 airplanes flying in the altitude range of 28,000 feet to 32,000 feet at a Mach number of about 1.5 during the Oklahoma City tests (ref. 2.40) and are similar to other rise-time histograms. This particular figure illustrates the general observation that larger rise times may be expected when the lateral distance from the ground track is increased. Once again, as was shown in the previous figure, rise times, to the half and maximum amplitudes are presented for measurements made on the ground track and at lateral locations of 5 and 10 miles. Note that both the mean rise times and the relative probability of larger rise times increase as lateral distance is increased.

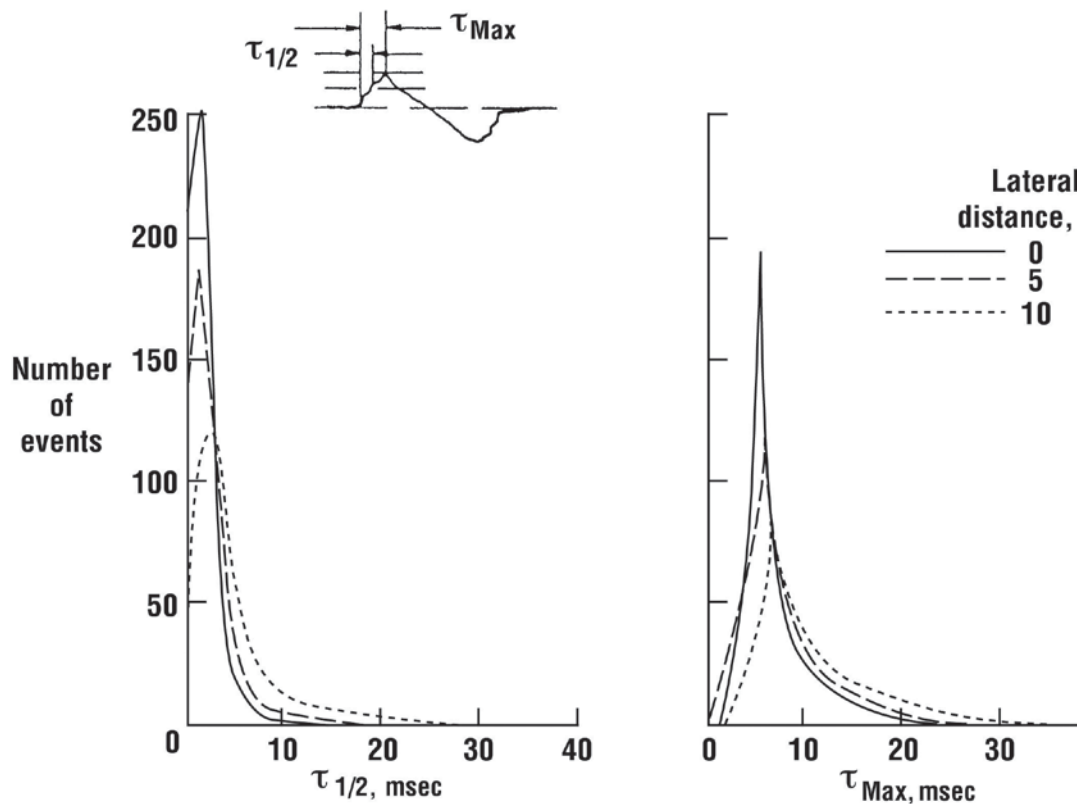


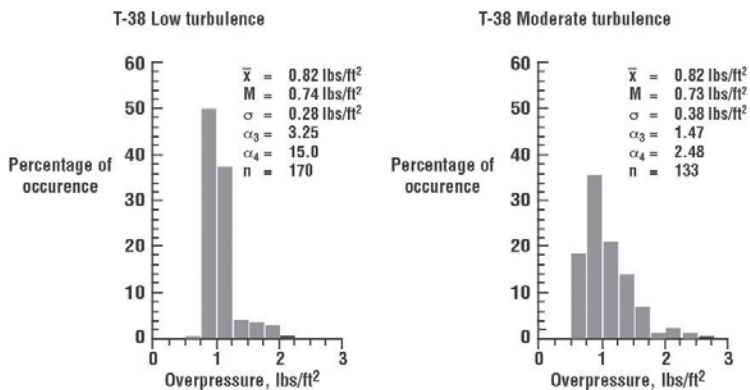
Figure 2.42. Variation of signature rise time with lateral distance (adapted from ref. 2.39).

Joint Acoustic Propagation Experiment (JAPE) Sonic Boom Experiments

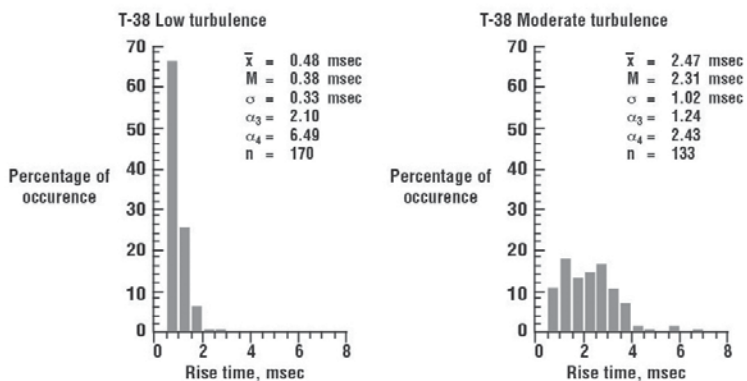
In August 1991, a sonic boom propagation experiment was conducted at the White Sands Missile Range (WSMR), New Mexico, as part of the North Atlantic Treaty Organization (NATO) JAPE. The sonic boom propagation experiment was added to JAPE to take advantage of the extensive meteorological instrumentation gathered to perform the JAPE experiment (refs. 2.41 and 2.42).

The sonic boom propagation experiment consisted of flying three types of aircraft supersonically over a ground-based microphone array with concurrent measurements of turbulence and other meteorological data. The test aircraft were a T-38, F-15, and F-111, and were flown at speeds of Mach 1.2 and 1.3, and at an altitude of 30,000 feet above a 16 element, linear microphone array with an inter-element spacing of 200 feet. In 2 weeks of testing, 57 supersonic passes of the test aircraft were flown from early morning to late afternoon.

Histograms of the percentage of occurrence of peak bow-shock overpressure and rise time for a T-38 and an F-15 for low and moderate turbulence conditions are presented in figure 2.43 and figure 2.44, respectively (from ref. 2.41). Typically, during the WSMR sonic boom experiment there was little cloud cover. Temperature inversions with light winds were the norm in the morning. By afternoon the desert floor had heated up, the morning inversion had been replaced with an increased lapse rate, and the winds had increased in speed. Thus, it is assumed that the morning time period was associated with low turbulence and the afternoon time period with moderate turbulence. The average (\bar{x}) and median (M) overpressure, rise time values, standard deviation (σ), skewness (α_3), kurtosis (α_4), and the number of data points (n) for each histogram are listed in the histogram legends. Skewness is a measure of the degree of symmetry of a distribution and Kurtosis is a measure of the peakedness.

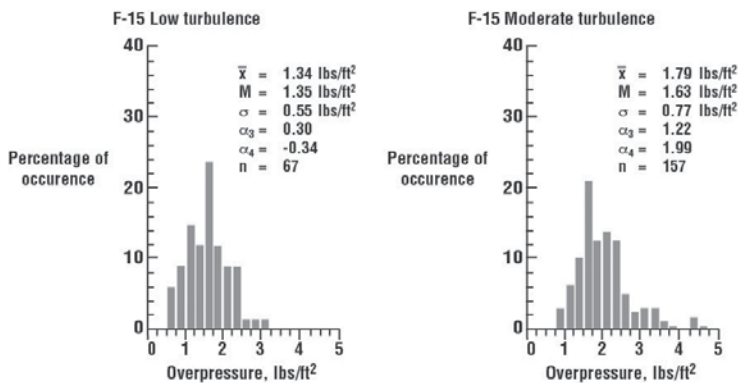


(a) Low and moderate turbulence bow-shock overpressure distributions.

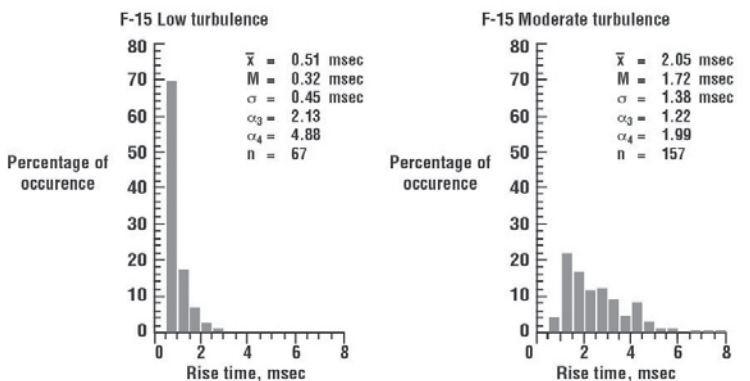


(b) Low and moderate turbulence rise time distributions

Figure 2.43. Histograms of sonic boom overpressure and shock rise for T-38 aircraft obtained during JAPE (ref. 2.41).



(a) Low and moderate turbulence bow-shock overpressure distributions.



(b) Low and moderate turbulence rise time distributions.

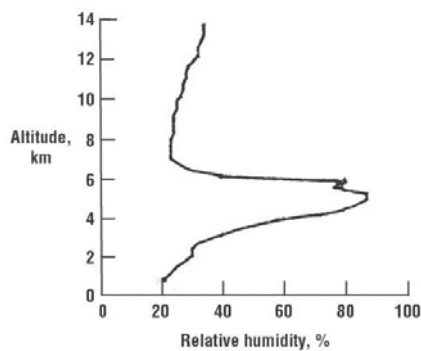
Figure 2.44. Histograms of sonic boom overpressure and shock rise time for F-15 aircraft obtained during JAPE (ref. 2.41).

Examination of the results in both figures show that the moderate turbulence overpressure and rise time distributions from both T-38 and F-15 flights are more skewed and thus less peaked than for the low turbulence conditions. The bow shock overpressure distributions were skewed positively indicating large positive deviations. The majority of measured data indicated that the mean and standard deviation of the bow-shock overpressure distributions increased from the low turbulence condition to the moderate turbulence condition. As turbulence increased, the difference between the median and the mean increased indicating larger positive overpressure deviations. The effect on rise time is more readily seen in the rise time distributions. In general, the moderate turbulence rise time distribution mean values were larger by a factor of 4 from the low turbulence conditions and the standard deviations were larger by a factor of 3.

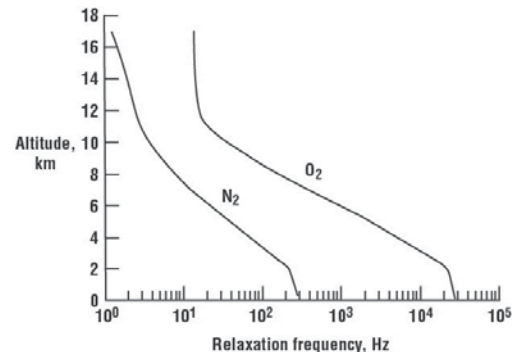
The authors noted that little of the extensive meteorological data collected were available for inclusion in these data. It should also be noted that the earlier flight-test results regarding the statistical variations in sonic boom overpressure resulting from the atmosphere and shown in figure 2.38 is presented in a different format than the JAPE findings.

Atmospheric Absorption

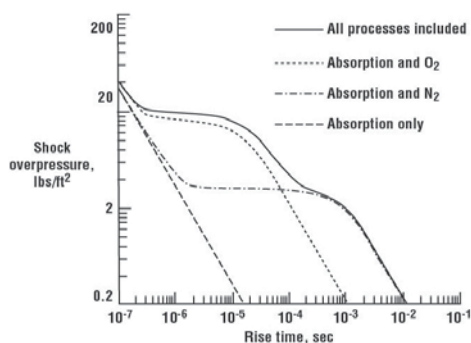
Absorption of sound by the atmosphere is a process consisting of thermo-viscous dissipation (classical absorption) and molecular relaxation that is dominant. Since 99 percent of the atmosphere is composed of nitrogen and oxygen, it is the relaxation of these molecules in the presence of water vapor that controls the atmospheric absorption of sound. In the absence of turbulence, the rise time of a perfect N-wave is determined by absorption. Figure 2.45(a) shows a typical variation of relative humidity with altitude and the figure 2.45(b) variation of relaxation frequencies with altitude. Figure 2.45(c) illustrates two findings. The first is that the rise time increases with decreasing shock overpressure, reflecting the diminished effect of non-linear steeping. The second is the dominance of molecular relaxation relative to classical absorption.



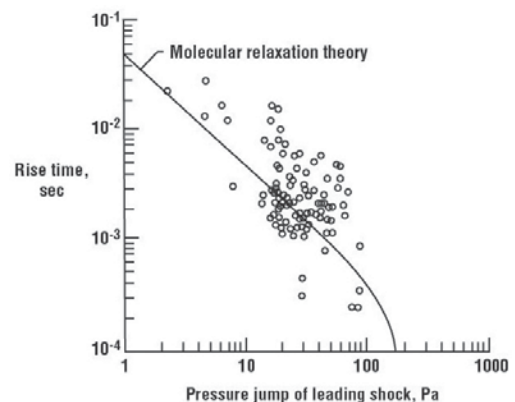
(a) Distribution of relative humidity in atmosphere (ref. 2.43).



(b) O₂ and N₂ relaxation frequencies (50 percent RH at ground) (ref. 2.44).



(c) Contribution of classical absorption, O₂, and N₂ relaxation to rise time (ref. 2.45).



(d) Variation of shock rise time with shock overpressure (ref. 2.43).

Figure 2.45. Role of molecular relaxation and classical absorption on sonic boom rise time.

Note the strong influence of O_2 and N_2 in increasing shock rise time as compared to classical absorption effects. In figure 2.45(d), a comparison of the rise times of measured sonic boom signature overpressures to the steady state shock overpressure predicted by the molecular relaxation model is shown. Theory and measurements show increasing shock rise times with decreasing shock overpressures. Such rounded, or long rise time boom signatures, have been observed on some SR-71 (ref. 2.46) and Shuttle reentry flights (refs. 2.28 and 2.29) where boom levels of 1.0 lb/ft^2 and less were experienced.

The ZEPHYRUS computer model (ref. 2.2) calculates sonic boom distortion during propagation through the atmosphere. Non-linear effects, attenuation, dispersion refraction, and wind are accounted for, but not distortion due to turbulence. Of particular interest is its ability to include the effects of absorption in the calculation of the boom signature. A brief overview of the program outputs is presented in figure 2.46 (ref. 2.2). The initial waveforms represent those that would be calculated in the near field below the aircraft. All of the data are plotted to the same scale for comparison.

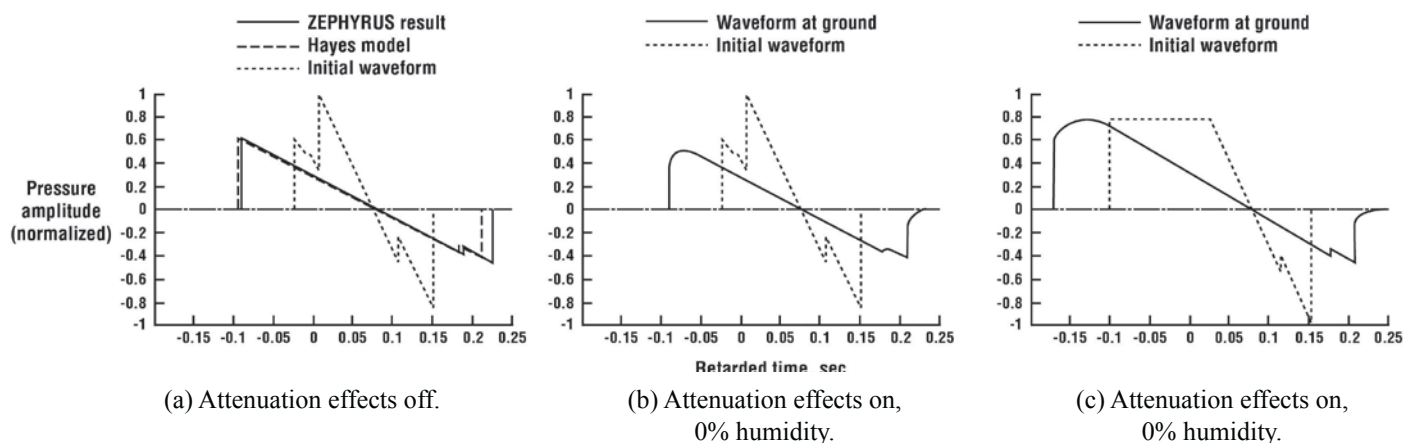


Figure 2.46. Influence of molecular relaxation and atmospheric absorption and initial signature shape on shock rise time (ref. 2.2).

To validate the ZEPHYRUS model, its output was compared to that of the ARAP (Hayes model) program (ref. 2.47) that has been used for many years to predict sonic booms. ARAP does not include absorption but only models nonlinear effects. In order to compare ZEPHYRUS with ARAP, the attenuation effects were turned off. The comparison, shown in figure 2.46(a), indicates that the ZEPHYRUS results agree quite well with ARAP. Figure 2.46(b) presents the results from ZEPHYRUS propagating the same initial signature to the ground with full nonlinear and attenuation effects turned on for zero percent relative humidity at the ground. Note that the general N-wave shape is essentially unchanged but the attenuation produced rounding at the bow and tail shocks. Sonic booms measured on quiescent days in the desert area, where low humidity is common, do show this shock front rounding. In higher humidity areas, the measured signatures display less rounding. Figure 2.46(c) presented an interesting finding regarding the dependence of rise time on initial signature shape. In figure 2.45(c) it is noted that rise times depend on the magnitude of the shock and, as such, the remaining waveform is relatively unimportant. To investigate this, a flat-topped initial waveform was selected (fig. 2.46(c)) and propagated in ZEPHYRUS for the zero percent humidity case. The amplitude of the initial waveform was reduced so that the bow shock amplitude of the waveform at the ground would be comparable to the results in figure 2.46(b). Note that the rise time of the ground signature from the initial flat-topped signature is at least 1.5 times that of the saw-tooth one shown in figure 2.46(b), thus, indicating that waveform shape does have a strong influence on rise time.

In 1989, Pierce (ref. 2.45) showed that shock waves below about 0.4 lb/ft^2 would have rise times longer than what might be expected of stronger shocks and, hence, would be particularly quiet. This expectation was also suggested in the previous two figures. The relaxation theory upon which this is based is sufficiently well established so as to be standardized (ref. 2.48) and has been successfully applied to sonic boom calculations (ref. 2.49). The results agree well with available sonic boom flight-test data (ref. 2.50).

Sonic boom signatures in available flight-test data tend, however, to be in the 1 to 2 lbs/ft² range. Boom signatures below 0.4 lb/ft² are rare and when generated by conventional aircraft tend to occur near lateral cutoff, where they are distorted by the effects of turbulence and ground interference.

In 2004, a series of sounding rocket tests (unrelated to sonic boom research) were conducted. Pre-flight analysis indicated that low-amplitude N-wave booms would occur under the reentry flight track. The opportunity was taken to acquire measurements of the sonic boom signatures to examine weak boom shocks structures after they had propagated through a real atmosphere (ref. 2.51). Several NASA Dryden Boom Amplitude and Shape Sensor (BASS) sonic boom recorders were deployed within the expected ground footprint and acquired an extraordinarily clean 0.2 lb/ft² N-wave that provided a shock structure used by Plotkin, Haering, and Murray (ref. 2.51) to quantitatively compare with relaxation theory. The results are presented in figure 2.47 (ref. 2.51).

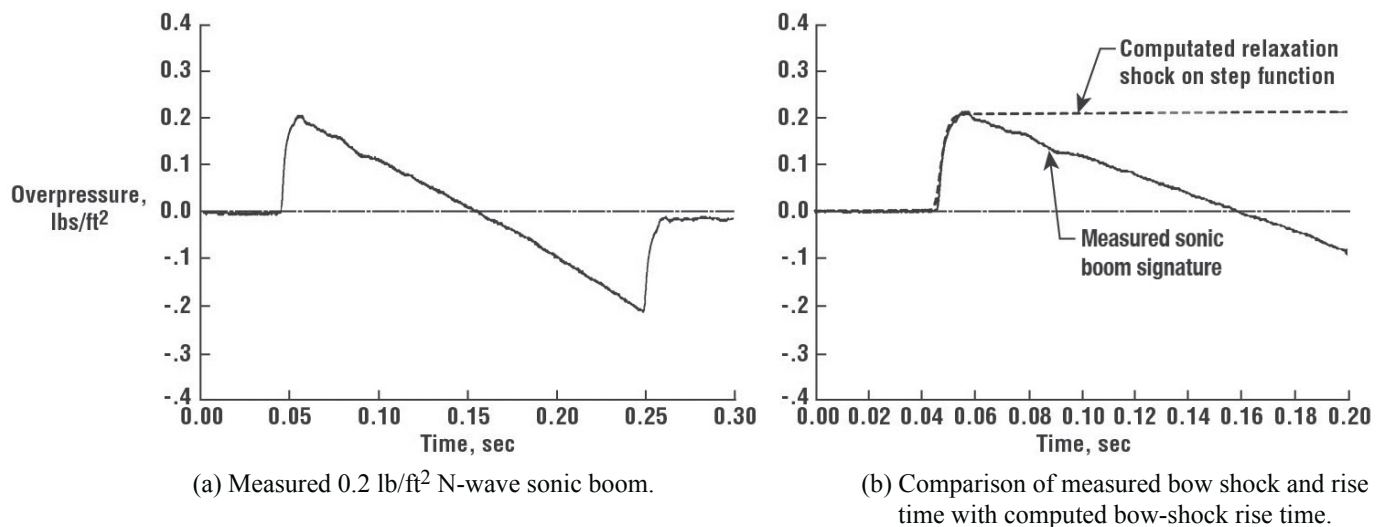


Figure 2.47. Example of the influence of atmospheric relaxation on a low-amplitude sonic boom (adapted from ref. 2.51).

Figure 2.47(a) shows the measured 0.2 lb/ft² N-wave. Note that the front and rear shock waves have the same shape and that the shape qualitatively appears similar to that of absorption on shocks presented in references 2.49 and 2.50. Figure 2.47(b) shows a detailed comparison of the measured shock structure with a theoretical relaxation shock. This is the measured bow shock from the boom shown in figure 2.47(a) with the time scale expanded and the computed shock overlaid. The agreement is excellent, confirming the expectation that relaxation shock theory applies to weak sonic booms in the real atmosphere.

Recently, Baudoin, Coulouvrat, and Thomas (refs. 2.52 and 2.53) noted that although atmospheric absorption may have a huge impact on the sonic boom annoyance by reducing the amplitude and increasing the rise time, the standard absorption due to the vibrational relaxation of molecular nitrogen and oxygen do not allow for an estimate of the influence of clouds where scattering by water droplets occurs. They also pointed out that as clouds cover more than 50 percent of the earth's surface and that test flights performed in the former Soviet Union in 1967–1968 indicated a strong impact. The authors applied an existing model for acoustical propagation in a polydispersed air-vapor-droplet suspension by Gubaidullin and Nigmatulin (ref. 1 of ref. 2.52) to conditions prevailing in atmospheric clouds to determine the impact of clouds on reducing the amplitude and increasing the rise time of sonic boom signatures. Their results show a dramatic increase of sound attenuation and dispersion, as shown in figure 2.48.

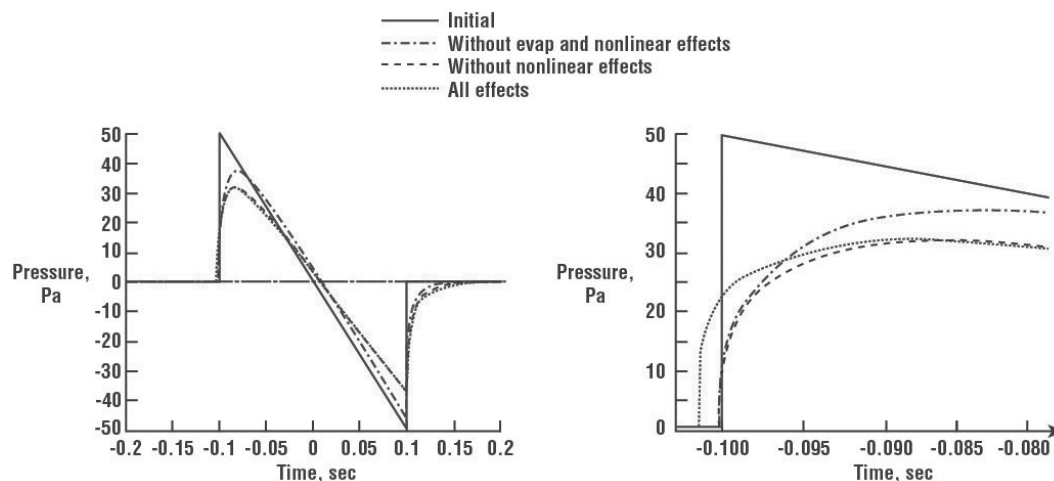


Figure 2.48. Influence of clouds on sonic boom N-wave (adapted from ref. 2.52).

The study considered the propagation of a 0.2 second duration N-wave of maximum overpressure of 50 Pascals (about 1 lb/ft²) into a typical cumulus cloud 2000 m high and 2000 m deep and with a water liquid content of 1 gram/cu meter and mean radius of 10 mm. The calculation is performed with all propagation mechanisms (dotted curve), nonlinear effects (dashed curve), and without evaporation and nonlinear effects (dashed dotted curve). Examination of the results of figure 2.48 show that after propagating through the cloud layer, the pressure maximum is only 64 percent of its initial value and the rise time is increased up to 4.6 msec. The authors noted that their results are in accordance with some test flights performed in the Soviet Union in 1967–1968 that observed a smoothing of the wave profile and diminution of about 40 percent of the pressure maximum for similar conditions.

Secondary Booms

Secondary booms (see figures 1.2 and 1.3 in Chapter 1) are an inescapable consequence of supersonic flight. Each of the major sonic boom flight programs sent secondary booms propagating through the upper atmosphere. The secondary booms went essentially unnoticed until the 1977 to 1978 time period, when the Naval Research Laboratory (NRL) investigated the East Coast acoustic disturbances (ref. 2.54), which were initially reported to be strange and mysterious in origin. The Concorde had entered into commercial service in mid-1976 and scientific use was being made of its secondary boom, which was a consistent and known source for determining the characteristics of the upper atmosphere (refs. 2.55 and 2.56). Concorde secondary booms thus became more evident and complaints to this effect were received. However, in every case of Concorde-generated secondary sonic booms, rerouting of the flight tracks and changes in operating conditions, depending upon atmospheric and seasonal variations, mitigated the problem. A more recent study that correlates seasonal and diurnal atmospheric fluctuations of the upper atmosphere to variations in the arrival time, trace velocity, and arrival azimuth of the infrasonic signals from Concorde are given in reference 2.57.

The secondary sonic boom carpet and the disturbances experienced within this carpet are not as well defined as for the primary sonic boom. Only fragmentary observations and measurements are available. These disturbances are known to involve both the upper and lower levels of the atmosphere during propagation, to have very low overpressure values, and to have a very low frequency content. Propagation distances greater than 100 miles are observed and relatively large ground areas are exposed, but the significance from a community response standpoint has not been established.

Secondary sonic booms, or so-called over-the-top boom disturbances (refs. 2.55, 2.56, and 2.58–2.61), are quite distinct from primary booms, not only in the manner in which they are propagated from the aircraft to the ground, but also in the way their signatures are shaped. The characteristics of these secondary sonic booms are illustrated in figure 2.49 (ref. 2.61). An overall pressure time history from the Concorde secondary boom is shown in figure 2.49 and is seen to be complex in that numerous disturbances are observed (some 13 minutes or so after passage

of the aircraft) at this particular measurement location over a period of 1.5 minutes with a maximum peak-to-peak pressure of about 0.2 lb/ft². Three sections of the overall pressure signature at A, B, and C are presented with expanded time scales on figure 2.49(b) to figure 2.49(d), to provide an indication of the frequency content of these signals. Note also that the fundamental frequency is about 1.5 to 2.0 Hz. For secondary boom signatures, the pressure changes very slowly and is in the sub-audible frequency range, and may or may not be heard.

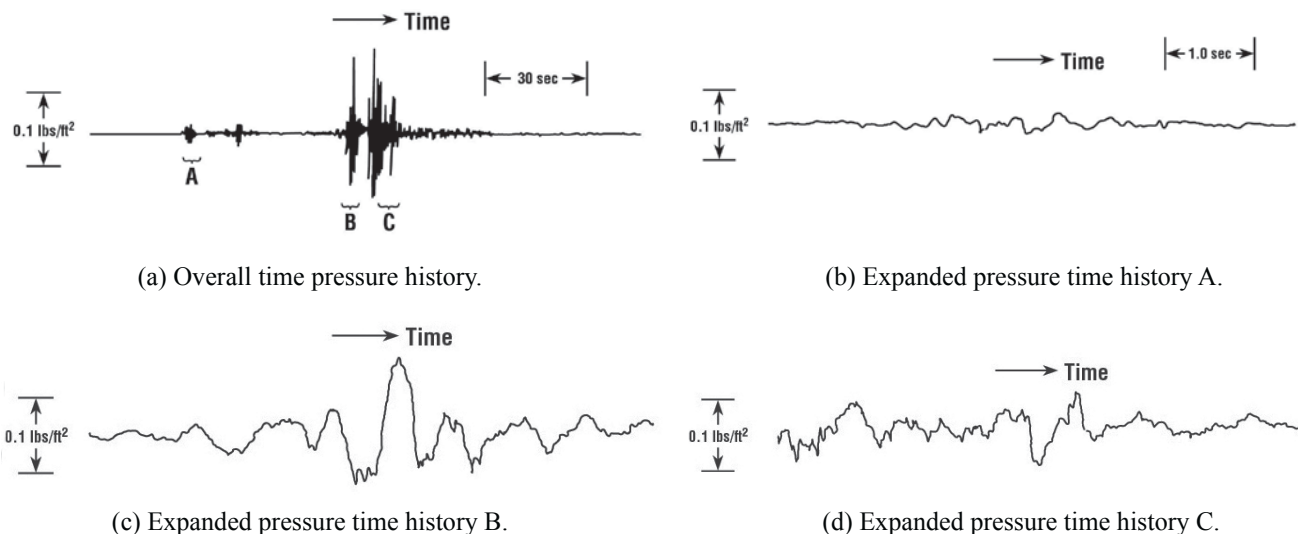


Figure 2.49. Characteristics of secondary sonic booms (adapted from ref. 2.61).

An appreciation of the distinct differences between secondary and primary boom signatures may be obtained with the aid of figure 2.50. At the top left of the figure is shown the cruise carpet boom signature from Concorde (ref. 2.62) and to the right the resulting secondary boom signature (ref. 2.61). The two signatures are plotted to the same pressure and time scales. Note that the Concorde secondary boom signature is considerably different in character and lower in overpressure than the primary boom N-wave signature.

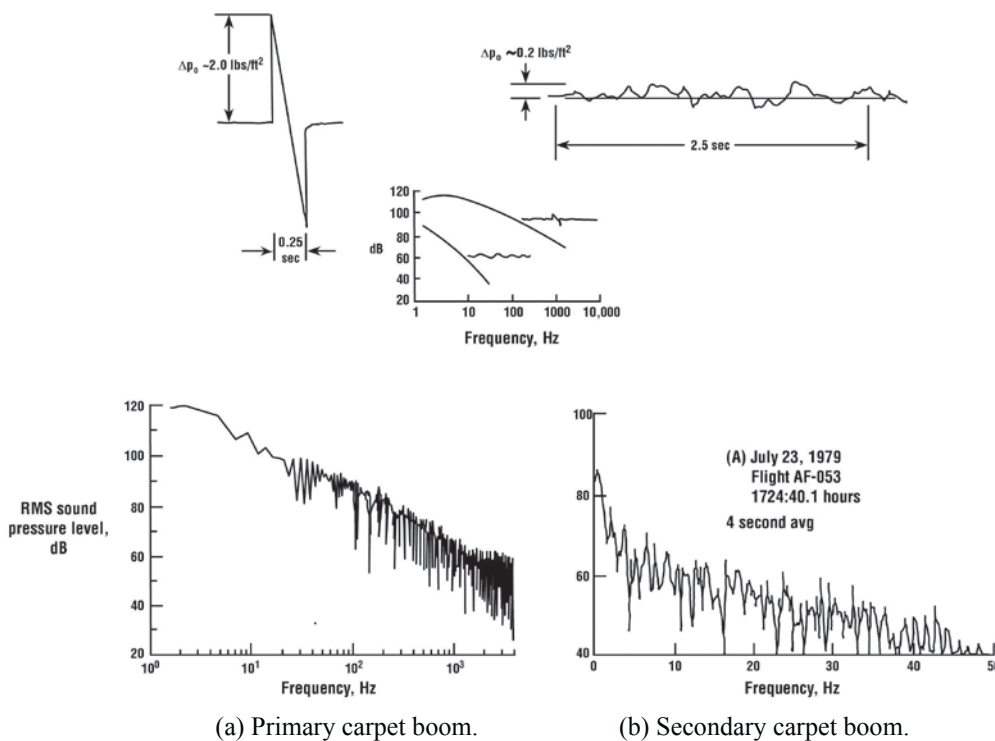


Figure 2.50. Comparison of primary and secondary sonic boom signatures and spectra for Concorde.

A further indication of the significant difference between the secondary and primary boom signatures may be obtained by comparing their frequency spectra as shown in the lower portion of figure 2.50. Note that the primary N-wave boom spectrum (ref. 2.62) contains a considerable amount of energy out beyond 1000 Hz, whereas the secondary boom energy (ref. 2.61) is confined to frequencies below about 50 Hz. As such, the secondary boom disturbances are in the sub-audible range and observed as muffled thumps and low frequency rumbles. As a result, secondary booms are difficult to sense outdoors, but noticeable indoors, since buildings respond to these low frequencies that are near the natural frequency of vibration of the building structural components.

Currently, three computer programs are capable of secondary sonic boom propagation, TRAPS, ZEPHYRUS, and PCBoom 6 (ref. 2.64). TRAPS (ref. 2.63), added the capability of ray path reversal and secondary booms to the Hayes ARAP program (ref. 2.47). A more recent program, ZEPHYRUS (ref. 2.2), includes air absorption and molecular relaxation effects on sonic boom propagation. The current version of PCBoom (ref. 2.64) computes boom signatures at an over-the-top caustic passage and at ground caustic intercepts and also includes absorption effects.

The TRAPS ray tracing was used by Gardner and Rogers (ref. 2.58) to predict the secondary boom levels associated with Concorde flights. The results of this research are presented in figure 2.51 (ref. 2.58). Figure 2.51 shows the predicted ground pressures for the initially upward and initially downward waves, as a function of distance from the ground track. The solid lines show the combined linear and nonlinear results, while the dashed lines show the result obtained using nonlinear theory alone. The latter can be considered to be an upper bound for the ground pressure. The dominant signal is from the initially downward wave. The highest pressure (about 0.008 lb/ft²) will occur about 200 nmi from the ground track. The pressure measured on the ground track is a minimum and will be about 0.003 lb/ft² for the initially downward wave. This is in contrast to the carpet boom, where the pressure is a maximum (about 2.0 lbs/ft²) along the ground track and decreasing to zero at the lateral cutoff. The reason the secondary boom levels are at a minimum on the ground track is because the ray paths along which the shocks propagate are less steeply inclined at lateral locations as compared to on-track. Thus, on-track rays extend to much higher altitudes, travel longer ray paths, and are subject to more atmospheric attenuation resulting in lower pressure amplitudes. The sharp cutoffs, indicated by the vertical dashed lines at about 200 nmi, are due to shadow zone formation similar to the lateral cutoff overpressure of the primary carpet.

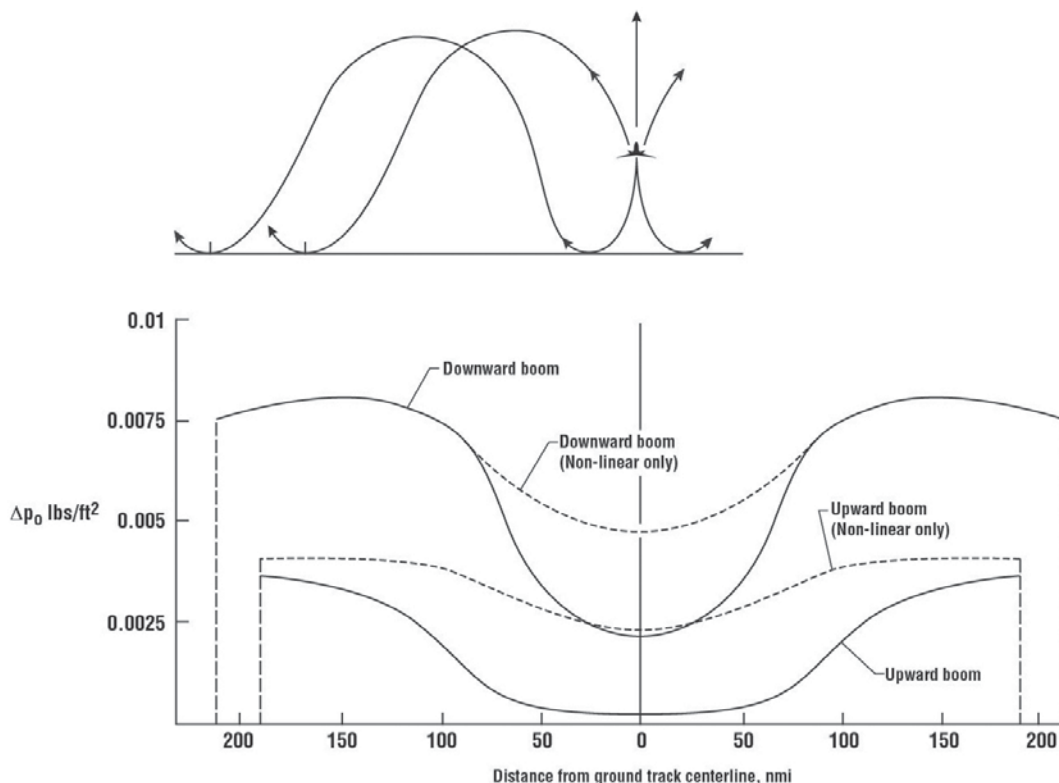


Figure 2.51. Variation of secondary sonic boom levels with lateral distance (adapted from ref. 2.58).

It should be noted that the predicted secondary sonic boom levels are at least an order of magnitude less than those that have been observed (ref. 2.61). The difference may be in the difficulty of accurately determining atmosphere characteristics and wave front angles of propagation. The studies of Pichon et al. and Poling (refs. 2.57 and 2.65) respectively, illustrated the impact of weather and flight conditions on secondary booms. The Blanc-Benon et al. (ref. 2.66) signature model was used to predict the amplitude and frequency of the secondary booms. They attribute the bursts to the arrivals of direct and indirect rays and the rumble noise to the presence of gravity waves or other fine scale effects in the atmosphere.

It has been shown that secondary booms, sometimes referred to as over-the-top booms, are associated with every supersonic flight (ref. 2.58). The disturbances, which arrive at the ground some 10–15 minutes after passage of the aircraft, are known to involve both the upper and lower levels of the atmosphere during propagation. Propagation distances of over 100 miles are observed and relatively larger ground areas are exposed and the pressures are higher at lateral locations than on-track. Secondary sonic booms are quite distinct from primary booms not only in the manner in which they are propagated from the aircraft to the ground but also in the way their signatures are shaped. For secondary boom signatures, the pressure changes very slowly and its frequency content is in the sub-audible range, both about an order of magnitude lower than for the primary boom. This lack of audibility combined with the very low amplitudes makes secondary booms difficult to sense outdoors, but they can be noticeable indoors. The secondary sonic boom carpet and the disturbances experienced within it are not as well defined as those for the primary boom and only fragmentary observations and measurements are available.

Chapter 2 Summary Remarks

The atmosphere plays a significant role in establishing the characteristics of the primary sonic boom signature. Primary booms result from shocks that propagate through only that part of the atmosphere below the aircraft. Pressure, temperature, and wind profiles can be classified as macro effects and are responsible for defining the intensity, location, and lateral extent of the sonic boom ground footprint. Above Mach 1.5, these macro effects have a relatively small effect on boom intensity and signature shape.

Turbulence in the lower layer of the atmosphere has a significant influence on altering N-wave boom signature shape. The peaking and rounding of the boom signatures can be expected during supersonic flight operations. Higher overpressures are observed from peaked signatures and lower values from rounded signatures.

Current sonic boom prediction codes can account for non-standard atmosphere with winds and atmospheric absorption but cannot account for the influence of turbulence in the lower layers of the atmosphere.

Aircraft shock waves that propagate through the atmosphere at altitudes higher than the aircraft are responsible for the secondary booms, also referred to as over-the-top booms. They are of low amplitude and frequency, and therefore difficult to sense outdoors but are noticeable indoors. These disturbances extend well beyond the primary boom footprint. As a result, meteorological conditions play an important role in secondary boom long distance propagation. Existing prediction codes can define the ground footprint but underestimate the pressure levels.

Chapter 2 References

- 2.1 Kane, Edward J. and Palmer, Thomas Y.: Meteorological Aspects of the Sonic Boom. SRDS Report No. RD 64-160, FAA, ASTIA No. AD 610463, 1964.
- 2.2 Robinson, Leick D.: A Numerical Model for Sonic Boom Propagation Through an Inhomogeneous, Windy Atmosphere. NASA CP-3172, Feb. 1992, pp. 7–30.

- 2.3 Coulouvrat, Francois; Blumrich, Reinhard; and Heimann, Deitrich: Meteorologically Induced Variability of Sonic Boom of a Supersonic Aircraft in Cruising or Acceleration Phase ISNA 17 AIP Conf. Proceedings, Vol. 838, Melville, NY 2005, pp. 579–586.
- 2.4 Maglieri, D. J.; Hilton, D. A.; Huckel, V.; Henderson, H. R.; and McLeod, N. J.: Measurements of Sonic Boom Signatures From Flights at Cutoff Mach Number. NASA SP-255, Oct. 1970, pp. 243–254.
- 2.5 Lundberg, W. R.: Seasonal Sonic Boom Propagation Prediction. AL/OE-TR-1994-0132, March 1994.
- 2.6 Dressler, Robert and Fredholm, Nils: Statistical Magnifications of Sonic Booms by the Atmosphere. FFA Rept. 104, Aeronau. Res. Inst. Sweden, 1966.
- 2.7 Lundberg, Bo K; Dressler, Robert F.; and Lagman, Sven: Atmospheric Magnification of Sonic booms in the Oklahoma Tests. FFA Rept. 112, Aeronau. Res. Inst. Sweden, June 1967.
- 2.8 Haglund, George T. and Kane, Edward J.: Flight Test measurements and Analysis of Sonic Boom Phenomena Near Shock Wave Extremity. NASA CR-2167, Feb. 1973.
- 2.9 Maglieri, D. J.; Hilton, D. A.; and McLeod, N. J.: Further Experiments on the Effects of Atmospheric Refractions and Aircraft Accelerations on Sonic Boom Ground Pressure Patterns, NASA TN-D 3520, July 1966.
- 2.10 Onyeowu, Ronald O.: Diffraction of Sonic Boom Past the Nominal Edge of the Corridor. J. Acoust. Soc. Am., Vol. 58, No. 2, Aug. 1975.
- 2.11 Hubbard, H. H.; Maglieri, D. J.; and Huckel, V.: Variability of Sonic Boom Signatures With Emphasis on the Extremities of the Ground Exposure Patterns. NASA SP-255, Oct. 9–30, 1970, pp. 351–359.
- 2.12 Pierce, Allan D.: Atmospheric Propagation at Larger Lateral Distances From the Flight Track. NASA Conf. Pub. 3279, Oct. 1994.
- 2.13 Coulouvrat, Francois: Sonic Boom in the Shadow Zone: A Geometrical Theory of Diffraction. J. Acoust. Soc. Am., Vol. III, No. 1, Pt. 2 of 2, Jan. 2002.
- 2.14 Walker, E. J. and Doak, P. E.: Effects of Ground Reflections on the Shape of Sonic Bangs. 5th Congress International D'Acoustique, Liege, Sept. 7–14, 1965, paper L55.
- 2.15 Maglieri, D. J.: Sonic Boom Flight Research - Some Effects of Airplane Operations and the Atmosphere on Sonic Boom Signature. NASA SP-147, 1967, pp. 25–48.
- 2.16 Maglieri, Domenic J. and Hubbard, Harvey H.: Ground Measurements of the Shock-Wave Noise From Supersonic Bomber Airplanes in the Altitude Range from 30,000 to 50,000 Feet. NASA TN D-880, 1961.
- 2.17 Hubbard, Harvey H.; Maglieri, Domenic J.; Huckel, Vera; and Hilton, David A.: Ground Measurements of Sonic Boom Pressures for the Altitude Range of 10,000 to 75,000 Feet. NASA TR R-198, 1964.
- 2.18 Hilton, David A.; Huckel, Vera; Steiner, Roy; and Maglieri, Domenic J.: Sonic Boom Exposures During FAA Community Response Studies Over a Six-Month Period in the Oklahoma City Area. NASA TN D-2539, 1964.
- 2.19 Hilton, D. A.; Huckel, Vera; and Maglieri, D. J.: Sonic Boom Measurements during Training Operations in the Chicago Area. NASA TN D-3655, 1966.
- 2.20 Plotkin, K. J.; Haering, E. A., Jr.; Murray, J. E.; Maglieri, D. J.; Salamone, J.; Sullivan, B. M.; and Schein, D.: Ground Data Collection of Shaped Sonic Boom Experiment Aircraft Pressure Signatures. AIAA-2005-0010, Jan. 2005.

- 2.21 Haering, E.; Murray, J.; Purifoy, D.; Graham, D. H.; Meredith, K. B.; Ashburn, C. E.; Stucky, M.: Airborne Measurements of Shaped Sonic Boom Demonstration Aircraft Pressure Signatures with Comparison to CFD. AIAA-2005-0009, 2005.
- 2.22 Maglieri, D. J.; Hilton, D. A.; and McLeod, N. J.: Summary of Variations of Sonic Boom Signatures Resulting from Atmospheric Effects. National Sonic Boom Evaluation Office: Sonic Boom Experiments at Edwards Air Force Base. NSBEO-1-67 (Contract AF 49(638) 1758, Stanford Research Inst., July 28, 1967, Part 1, Annex C, pp. C-1-1 to C-1-125.
- 2.23 Wetmore, Joseph W. and Reeder, John P.: Aircraft Vortex Wakes in Relation to Terminal Operations. NASA TN D-1777, 1963.
- 2.24 Maglieri, Domenic; Huckel, Vera; Henderson, H. R.; and McLeod, Norman, J.: Variability in Sonic Boom Signatures Measured Along an 8000 Foot Linear Array. NASA TN-5040, 1969.
- 2.25 Garrick, I. E. and Maglieri, D. J.: A Summary of Results on Sonic Boom Pressure Signature Variations Associated With Atmospheric Conditions. NASA TN D-4588, 1968.
- 2.26 Sherlock, R. H.; Stout, M. B.; Dow, W. G.; Gault, J. S.; and Swinton, R. S.: Storm Loading and Strength of Wood Pole Lines and a Study of Wind gusts. Edison Elec. Inst., c. 1936.
- 2.27 Houbolt, John C.; Steiner, Roy; and Pratt, Kermit G.: Dynamic Response of Airplanes to Atmospheric Turbulence Including Flight Data on Input and Response. NASA TR-R-199, 1964.
- 2.28 Maglieri, Domenic J.; Henderson, Herbert R.; Stansbery, Eugene G.; and Massey, Steven J.: A Compilation of Space Shuttle Sonic Boom Measurements. NASA CR 2011-217080, April 2011.
- 2.29 Garcia, Frank J.; Jones, Jess H.; and Henderson, Herbert H.: Correlation of Predicted and Measured Sonic Characteristics from the Reentry of STS-1 Orbiter. NASA TP-2475, 1985.
- 2.30 Garinther, G. R. and Moreland, J. B.: Transducer Techniques for Measuring the Effect of Small-Arms Noise on Hearing. U.S. Army Tech. Memo. 11-65, July 1965.
- 2.31 Hilton, D. A. and Newman, J. W., Jr.: Instrumentation Techniques for Measurement of Sonic Boom Signatures. J. Acoust. Soc. Am. 39, S31-S35, 1966.
- 2.32 Lee, Robert A.: Air Force Boom Event Analyzer Recorder (BEAR): Comparison With NASA Boom Measurement System. AAMRL-TR-88-039. July 1988.
- 2.33 Roberts, C.; Johnson, W.; Herbert, G.; and Hass, W. A.: Meteorological Investigations. National Sonic Boom Evaluation Office: Sonic Boom Experiments at Edwards Air Force Base, NSBEO-1-67 (Contract AF 49 (638), 1758), Stanford Research Inst., July 28, 1967, Part 1, Annex D. DD-D-1 through D-11 (also A-10 and A-14).
- 2.34 Pawlowski, Joseph W.; Graham, David H.; Boccadoro, Charles H.; Coen, Peter G.; and Maglieri, Domenic J.: Origins and Overview of a Shaped Sonic Boom Demonstration Program. AIAA 2005-0005, Jan. 2005.
- 2.35 Morgenstern, J. M.; Arslan, A.; Lyman, V.; and Vadyak, J.: F-5 Shaped Sonic Boom Demonstrator's Persistence of Boom Shaping Reduction Through Turbulence, AIAA-2005-0012, Jan. 2005.
- 2.36 Plotkin, Kenneth J.; Maglieri, Domenic J.; and Sullivan, Brenda M: Measured Effects of Turbulence on the Loudness and Waveforms of Conventional and Shaped Minimized Sonic Booms. AIAA-2005-2949, May 2005.

- 2.37 Plotkin, Kenneth J.; Maglieri, Domenic J.; and Sullivan, Brenda M.: Measured Effects of Turbulence on the Loudness of Sonic Booms. Proc. of 17th Int. Smp. on Non-Linear Acoustics, AM Inst. of Phys. Melville, NY, July 2005, pp. 627–630.
- 2.38 Maglieri, Domenic J. and Kenneth, J.: Sonic Boom, Chapter 10: Aeroacoustics of Flight Vehicles, Theory and Practice. NASA RP 1258, Vol. 1 and WDRC TR 80-3052, Aug. 1991.
- 2.39 Pierce, Allan D. and Maglieri, Domenic J.: Effects of Atmospheric Irregularities on Sonic Boom Propagation. J. Acoust. Soc. Am., Vol. 51, No. 2, (Part 3), 1972, pp. 702–721.
- 2.40 Maglieri, Domenic J. and Sothcott, Victor E.: Summary of Sonic Boom Rise Times Observed During FAA Community Response Studies Over a 6-Month Period in the Oklahoma City Area. NASA CR-4277, April 1990.
- 2.41 Willshire, W. L., Jr. and DeVilbiss, D. W.: Preliminary Results from the White Sands Missile Range Sonic Boom Propagation Experiments. NASA CP-3172, Feb. 1992, pp. 137–150.
- 2.42 Willshire, William L., Jr.; Garber, Donald P.; and DeVilbiss, David W.: Flight Test Measurements of the Effect of Turbulence on Sonic Boom Peak Overpressure and Rise Time. J. Acoust. Soc. Am., Vol. 92, Issue 4, 1992, pp. 2329–2330.
- 2.43 Cleveland, Robin O.; Hamilton, Mark F.; and Blackstock, David T.: Effect of Stratification and Geometrical Spreading on Sonic Boom Rise Time. NASA CP-3279, Oct. 1994, pp. 19–38.
- 2.44 Robinson, Leick D.: A Numerical Model for Sonic Boom Propagation through an Inhomogeneous, Windy Atmosphere. NASA CP-3172, Vol.1, Feb. 1992, pp. 7–30.
- 2.45 Pierce, Allan D.: Weaker Sonic Booms May be Considerable More Quiet. J. Acoust. Soc. Am. 85, 1989, p. 581.
- 2.46 Maglieri, Domenic J.; Huckel, Vera; and Henderson, Herbert R.: Sonic Boom Measurements for SR-71 Aircraft Operating at Mach Numbers to 3.0 and Altitudes to 24,384 Meters. NASA TN D-6923, 1971.
- 2.47 Hayes, Wallace D.; Haefeli, Rudolph C.; and Kulsrud, H. E.: Sonic Boom Propagation in a Stratified Atmosphere With Computer Program. NASA CR-1299, 1969.
- 2.48 Method for the Calculation of the Absorption of Sound by the Atmosphere. ANSI SI-26-1978, American National Standards Institute.
- 2.49 Chambers, James P.; Cleveland, Robin O.; Bass, Henry E.; Blackstock, David T.; and Hamilton, Mark F.: Comparison of Computer Codes for the propagation of Sonic Booms Through Realistic Atmospheres Utilizing Actual Acoustic Signatures. NASA CP 3335, July 1996, pp. 151–175.
- 2.50 Kang, J.: Nonlinear Acoustic Propagation of Shock Waves through the Atmosphere with Molecular Relaxation. PH.D. Thesis, The Pennsylvania State University, May 1991.
- 2.51 Plotkin, K. J.; Haering, E. A.; and Murray, J. E.: Low-Amplitude Sonic Boom From a Descending Sounding Rocket. Proc. of 17th Inst. Symp. on Non-Linear Acoustics, AM. Inst. of Phys. Melville NY, July 2005, pp. 615–618.
- 2.52 Baudoin, M.; Coulouvrat, F.; and Thomas, J. L.: Absorption of Sonic Boom by Clouds. Proc. of 17th Int. Symp. on Non-Linear Acoustics, AM. Inst. of Phys. Melville NY, July 2005, pp. 619–622.
- 2.53 Baudoin, M.; Coulouvrat, F.; and Thomas, J. L.: Sound, Infrasound, and Sonic Boom Absorption by Atmospheric Clouds. J. Acoust. Soc. Am. 130(3), Sept. 2011, pp. 1142–1153.

- 2.54 Dept. of Navy: NRL Investigations of East Coast Acoustics Events 2 December 1977 – 15 February 1978, March 10, 1978.
- 2.55 Balachandra, Nambath K.; Donn, William L.; and Rind, David H.: Concorde Sonic Booms as an Atmospheric Probe. *Sci.*, Vol. 197, No. 4298, July 1, 1977, pp. 47–49.
- 2.56 Donn, William L.: Exploring the Atmosphere with Sonic Booms. *Am. Sci.*, Vol. 66, No. 6, Nov.–Dec., 1978, pp. 724–733.
- 2.57 Pichon, Alexis Le; Garces, Milton; Blanc, Elisabeth; and Barthelemy, Maud: Acoustic Propagation and Atmospheric Characteristics Derived From Infrasonic Waves Generated by the Concorde. *J. Acoust. Soc. Am.* 2002, pp. 629–641.
- 2.58 Gardner, John H. and Rogers, Peter H.: Thermospheric Propagation of Sonic Booms From the Concorde Supersonic Transport. NRL Memo. Rept. 3904, U. S. Navy, Feb. 14, 1979 (Available from DTIC as AD A067 201).
- 2.59 George, A. R. and Kim, Y. N.: High-Altitude Long Range Sonic Boom Propagation. *J. Aircraft*, Vol. 16, No. 9, Sept. 1979, pp. 637–639.
- 2.60 Liszka, Ludwik: Long-Distance Focusing of Concorde Sonic Boom. *J. Acoust. Soc. Am.*, Vol. 64, No. 2, Aug. 1978, pp. 631–635.
- 2.61 Rickley, Edward J. and Pierce, Allan D.: Detection and Assessment of Secondary Sonic Booms in New England. FAA-AEE-80- 22, May 1980.
- 2.62 Holbeche, T.: Measurements of Sonic Bangs From the Prototype Concorde 002 During Supersonic Development of Flying in the United Kingdom. Royal Aircraft Establishment Tech. Memo. Aero. 1405, 1972.
- 2.63 Taylor, A. D.: The TRAPS Sonic Boom Program. NOAA Tech. Memo. ERL ARL-87, July 1980.
- 2.64 Page, J. A.; Plotkin, K. J.; and Wilmer, C.: PCBoom Version 6.6 Technical Reference and User Manual. Wyle Report WR 10-10, March 2010.
- 2.65 Poling, Hugh W.: Impact of Weather and Flight Condition on Secondary Booms. NASA CP 3335, July 1996, pp. 136–150.
- 2.66 Blanc-Benon, Phillipe; Dallios, Laurent; Scott, Julian; Erger, UWE; and Allwright, David: Ray Theory Analysis and Modeling of the Secondary Boom Propagation for Realistic Atmospheric Conditions. ISNA 17 AIP Conf. Proc., Vol. 838, Melville, NY 2006, pp. 187–192.

CHAPTER 3 INFLUENCE OF MANEUVERS

In this chapter, sonic booms associated with maneuvers of aircraft are discussed including dives, climbout pushovers, turns, and linear accelerations. Unlike the carpet booms associated with steady supersonic flight that are dragged along behind the aircraft, maneuver booms are single occurrences, where multiple booms may be observed at the ground with boom intensities greater or less than the corresponding carpet boom. Military operations may, of course, include all of the above, whereas commercial operations would involve milder turn and pushover maneuvers. Both military and commercial flights must transition from subsonic to supersonic speeds and descend and decelerate from supersonic to subsonic speeds. Questions regarding focus booms from maneuvering flight include whether they can be avoided or minimized and controlled to the extent of the focus area and magnitude of the focused boom. Descent decelerations are not touched upon in this section since flight planning can eliminate focusing at the ground either by decelerating to subsonic speed at constant altitude or scheduling Mach decrease and descent to preclude focusing. This chapter concludes with a discussion of sonic booms that can occur from aircraft flying at relatively low altitudes and high subsonic Mach numbers and in a subsonic dive-pull-up maneuver.

Nature of Focus Patterns

Any rapid deviation of a vehicle from steady, level supersonic flight conditions can produce considerable modifications in the location, number, and intensity of the ground shock wave patterns. This maneuvering phenomenon is illustrated in figure 3.1 (ref. 3.1), which shows the shock wave ground-intersection patterns for two flight conditions of an aircraft. For simplicity, only the bow shock wave is shown.

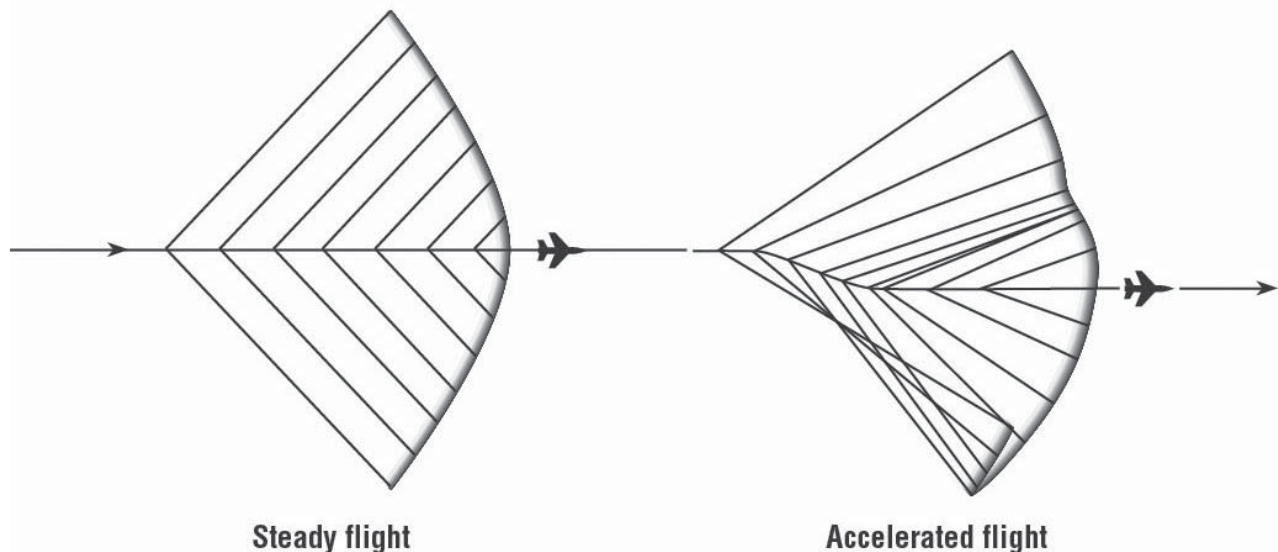


Figure 3.1. Nature of ray path-shock wave ground footprint from steady and accelerated flight (ref. 3.1).

At the left, the shock wave ground-intersection pattern for an aircraft in steady, level flight is shown. The ray paths from the aircraft to the ground, represented by the angled lines, are generally parallel to each other and the bow shock wave ground-intersection pattern, as represented by the heavy shaded line, is essentially hyperbolic in shape. The pattern to the right is for an aircraft experiencing a level lateral acceleration. The ray paths are no longer parallel. In fact, in some regions they tend to converge and in others to diverge. Likewise, the shock wave ground intersection pattern is no longer hyperbolic and contains some irregularities, including a shock fold in which multiple booms would be observed and a cusp formation in which the pressures are higher than for steady flight conditions. Such pressure increases are indicators of focused booms.

Another example of boom focusing due to maneuvering flight is presented in figure 3.2 (ref. 3.2). Shown on the figure is a three-dimensional view of both the vertical cross section and the ground pattern for an aircraft in a dive of about 20° beginning at Mach 1.2 at 40,000 feet and terminating at about 20,000 feet and Mach 1.6. Only the bow shock is illustrated. The ground pattern is symmetric with respect to the flight path so that only the part on the right side of the flight track is shown. The bow shock that develops into a folded three-shock system in the vertical plane spreads laterally when intersecting the ground and extends about 6 miles and results in multiple booms over an appreciable ground area. As the aircraft proceeds along the low-altitude level portion of the flight path, the complicated shock pattern produced by the dive hits the ground and vanishes. The ground shock is left with a fold that gradually unravels as the aircraft continues so that the end result is the normal hyperbolic-shaped ground shock. Everywhere there is a shock, a boom will be observed and wherever a folding of a shock front occurs would be a pressure enhancement (focus).

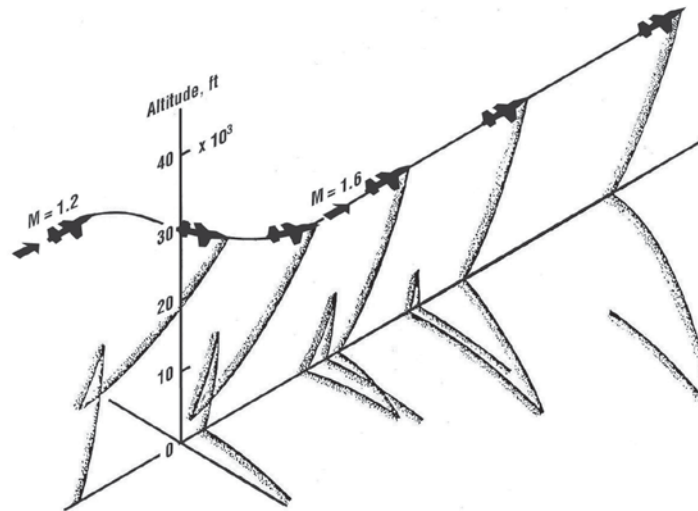


Figure 3.2. Schematic of shock wave and ground pattern for an aircraft in a dive (ref. 3.2).

Once it became obvious that supersonic flight would become commonplace, especially for military aircraft, some early cursory flight experiments were conducted to assess the nature of booms associated with steady and maneuvering flights. In 1959, Kerr (ref. 3.3), in addition to reporting on the booms from steady-level flight, also reported on sonic booms associated with level flight acceleration from Mach 0.98 to 1.2 at an altitude of 10,000 feet, supersonic acceleration and deceleration, and a 2-g supersonic turn at Mach 1.5 at 40,000 feet. Hubbard et al. (ref. 3.4) reported on 63 supersonic flights conducted at EAFB in 1961 with emphasis on the influence of lift (i.e., aircraft weight) on boom levels. Twenty-three of the flights dealt with maneuvers. Included were dives, turns, and linear accelerations. Increases in boom levels of about 2, 3, and 4 times the boom levels from steady flight were observed for a linear acceleration, pull-up-push-over, and circular turn, respectively (refs. 3.1 and 3.5).

Military Operations

In the next series of figures, boom signature overpressure observations will be shown for various types of maneuvers performed by military aircraft and include a dive, climb/pushover, turn and turn entry, and finally longitudinal accelerated transition flight from subsonic and supersonic speeds. Each of these non-steady flights can result in non-uniform sonic boom ground patterns, which could include focus and non-focus regions where boom levels may be intensified or decreased respectively. Most of these military maneuvers are avoidable, especially in the case of commercial flight operations with the exception of the transition focus boom.

Four air combat type maneuvers were studied and included a diving acceleration, a climbout-pushover, constant g turn, and a level linear acceleration. Some results of each of these four types of maneuvers will be presented in subsequent figures. A major part of the results to be shown were acquired during the Have BEARS flight-test program conducted by the USAF Test Pilot School in April 1994 (ref. 3.6). This study had three main objectives – (1) to test the ability of pilots to control the placement of the focus region, (2) to validate prediction methods,

and (3) to evaluate the effects of atmospheric turbulence on focusing. An F-16B (similar to the airplane shown in fig. 3.3) served as the test aircraft.



(U.S. Air Force photo)

Figure 3.3. General Dynamics F-16B Fighting Falcon.

Dives

For the diving accelerations, performed during the USAF Have BEARS flight-test program, the F-16B aircraft attained stability at Mach 0.9 and an altitude of 20,000 feet. At the maneuver point, the pilot selected full afterburner, rolled inverted, and performed a 4-g pull-down to a 30° nose low attitude on the flight path marker. No course corrections were provided after initiation of the maneuver. The maneuver was terminated as the aircraft reached Mach 1.2 or descended below an altitude of 13,000 feet. A profile view sketch of the dive maneuver and the on-track measured results are shown in figure 3.4 (ref. 3.6). Examination of the signature development indicates that the focus boom location was somewhere in the region up-track from the target point (about -2000 feet) where the signature was observed with an overpressure of 6.0 lbs/ft². The maximum overpressure of 7.2 lbs/ft² occurred at the target point, which was in the post-focus region as indicated by the N-wave U-wave signature. Within the focus region, the peak overpressure of 7.2 lbs/ft² was amplified over the average carpet boom overpressures of about 3.7 lbs/ft², which resulted in a focus factor of about 2.0 for the flight data.

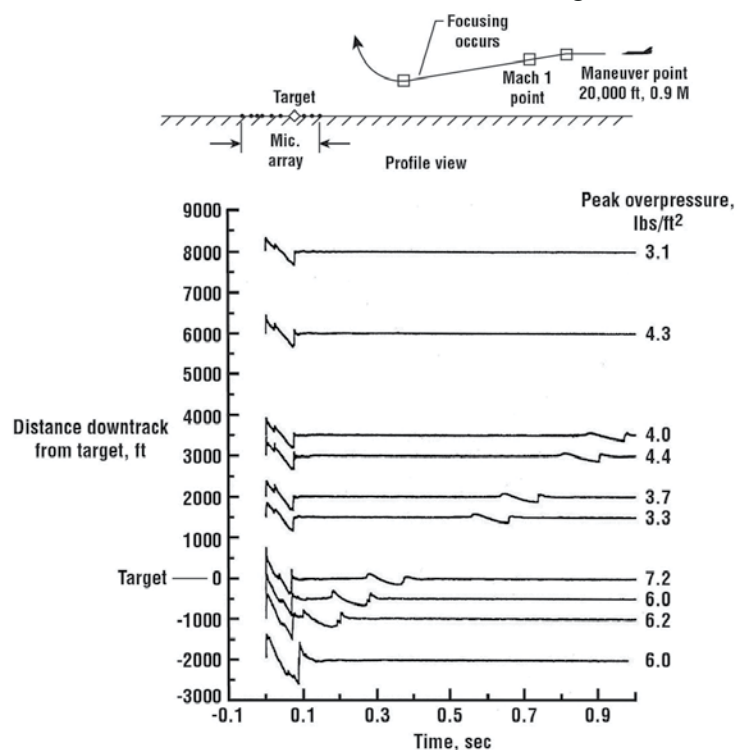


Figure 3.4. Measured sonic boom signatures from aircraft in a 30° accelerating dive (adapted from ref. 3.6).

Climbout/Pushover

For the climbout/pushover maneuver performed during the USAF Have BEARS flight-test program (ref. 3.6), the aircraft would start a 10° climb at Mach 1.2 and an altitude of 10,000 feet. At the pushover point, the pilot pushed the aircraft over to a load factor of -0.5 g to the level flight attitude while maintaining constant Mach number. The maneuver was terminated as the aircraft reached the level flight attitude. A profile view sketch of the climb/pushover maneuver along the on-track booms measured from this flight is shown in figure 3.5 (ref. 3.6). The maximum peak overpressure was 11.6 lbs/ft² and occurred 2000 feet down-track of the predicted focus point (target point). This boom was amplified by a factor of 4 as compared to the average overpressures observed in the pre-and post-focus regions. For this flight, a second signature was not observed in the post-focus region, only slight disturbances appeared to trail behind the N-wave.

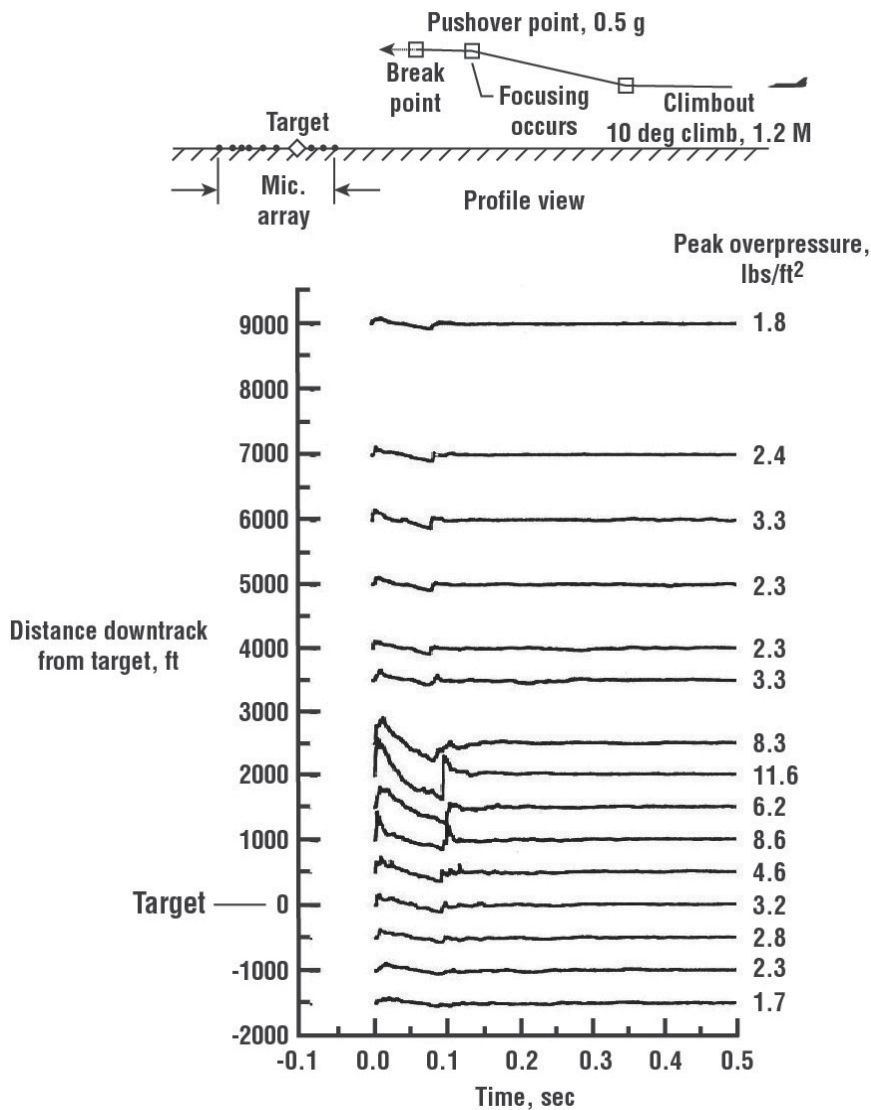
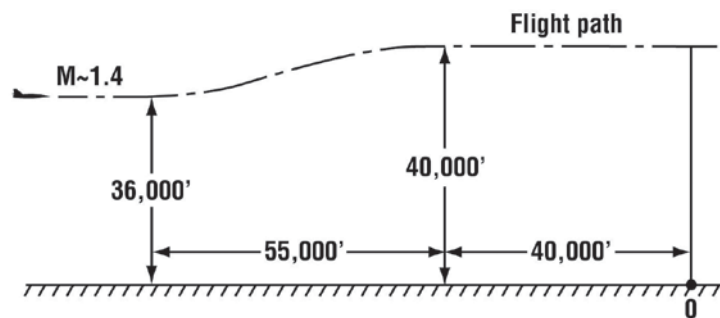
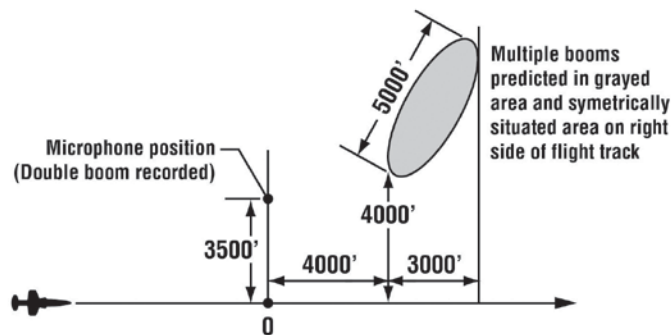


Figure 3.5. Measured sonic boom signatures from aircraft in -0.5-g climbout/pushover (adapted from ref. 3.6).

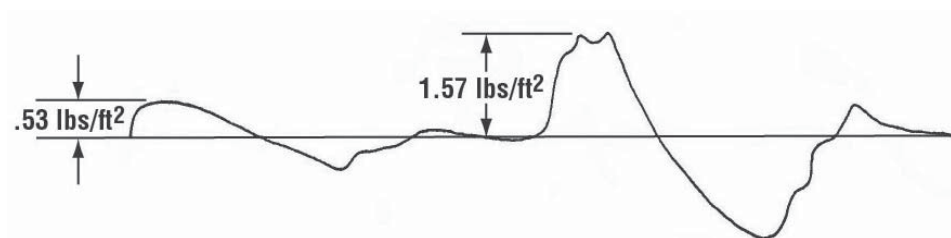
Figure 3.6 (ref. 3.5) shows a profile and plan view of a constant Mach number pull-up/climb/pushover, which was also carried out by NASA and the USAF in the vicinity of Rogers Dry Lake at EAFB. The results presented in figure 3.5 for the climbout/pushover maneuver present the boom signatures and focus development along the ground track of the aircraft. Focusing can also occur at locations lateral to each side of the ground track, as shown in figure 3.6. The flight path was essentially confined to a vertical plane and had the approximate dimensions shown in figure 3.6(a). Radar tracking and weather information were obtained, but ground pressure measurements were recorded by only one microphone, which was slightly off the flight track, as indicated in figure 3.5(b). Note that in this case the second signature to arrive had the highest overpressure by about a factor of 3.0. Theory predicted multiple booms and normal overpressures in the grayed elliptical region shown on the figure and in a similar symmetrically situated region on the other side of the flight track. The shock waves, which fell within these two areas, originated from the pushover and level-out portion of the maneuver.



(a) Profile view of maneuver.



(b) Plan view of maneuver.



(c) Measured sonic boom pressure signature.

Figure 3.6. Sonic boom signatures measured near focus region from climbout/pushover maneuver (ref. 3.5).

Turns

For the constant-g turn flown during the USAF Have BEARS flight program, a load factor of 4 g was chosen as a maximum sustainable load factor for the turn maneuver while trying to maintain Mach 1.2. Before the maneuver, as shown in the plan view sketch of the turn maneuver (fig. 3.7), the aircraft was stabilized at Mach 1.2 and an altitude of 10,000 feet. At the start of the turn, the pilot selected full afterburner and initiated a 4-g level turn. The maneuver was terminated after a 50° turn.

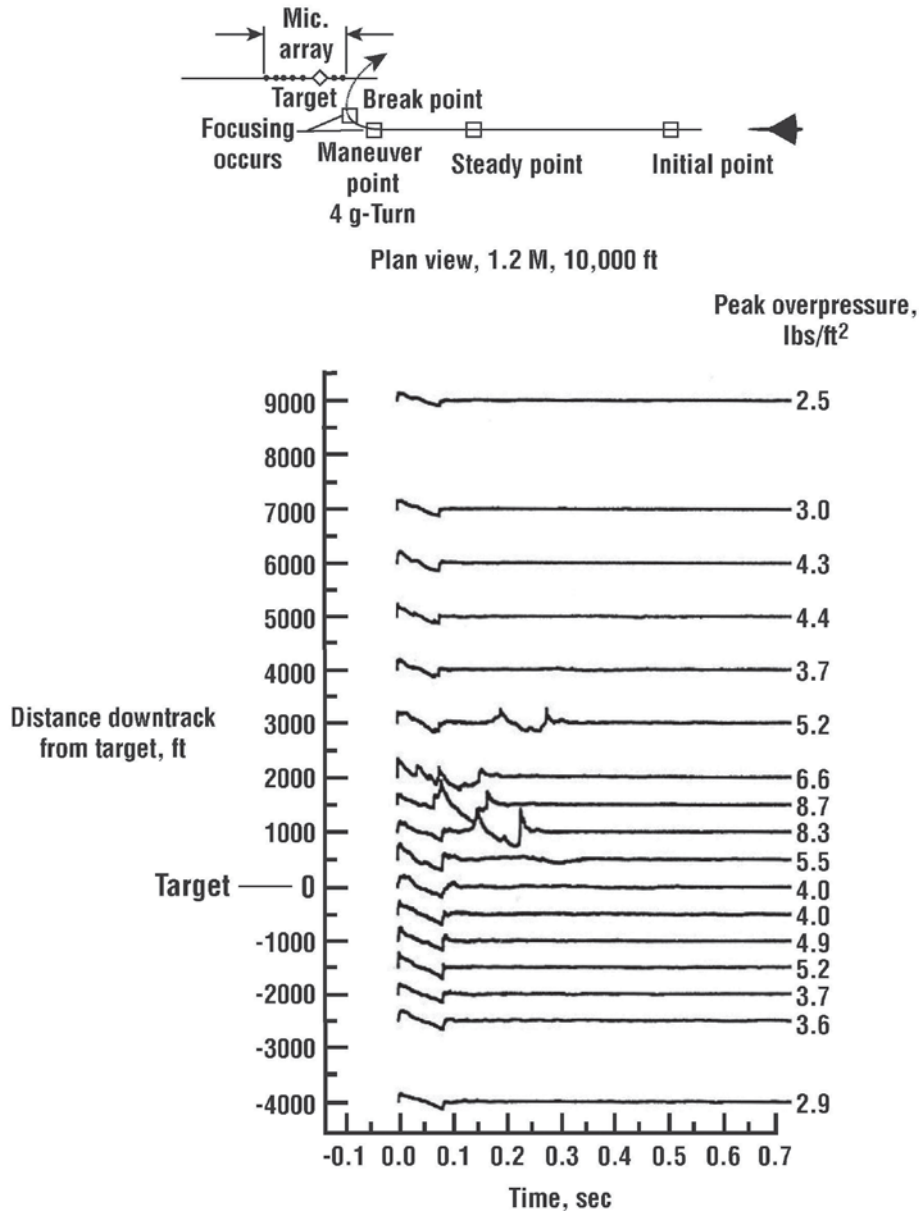


Figure 3.7. Measured sonic boom signatures from aircraft in constant 4-g turn (adapted from ref. 3.6).

The flight path was aligned with the array so that the array would capture the focal line from the steady part of the turn and not the superfocus region generated by the initiation of the turn. The measured booms are shown in figure 3.7 (ref. 3.6). At the first part of the array, the measured booms were from the steady portion prior to the maneuver point. Focusing was measured within a band of 2500 feet about the target point with the maximum overpressure measured at 1500 feet from the target. This showed that the focal line was very narrow for this maneuver. The maximum overpressure was 8.7 lbs/ft². Post-focus signatures or disturbances appeared in both directions. The measured focus boom from the turn amplified the boom by a factor of about 2.5.

As shown in figure 3.7, during a turn maneuver the measurements were in the vicinity of the focus line from the steady part of the turn and not near the superfocus generated by the initiation of the turn where two focus lines merge. The superfocus region on the ground was very small in area and challenging to capture. A superfocus recording was, however, successfully accomplished as part of the French Operation Jericho Carton flight test (ref. 3.7). At an altitude of 33,000 feet, a Mirage IV flew a 2-g turn entry at Mach 1.7. Figure 3.8 shows the measured results and supporting focus analysis.

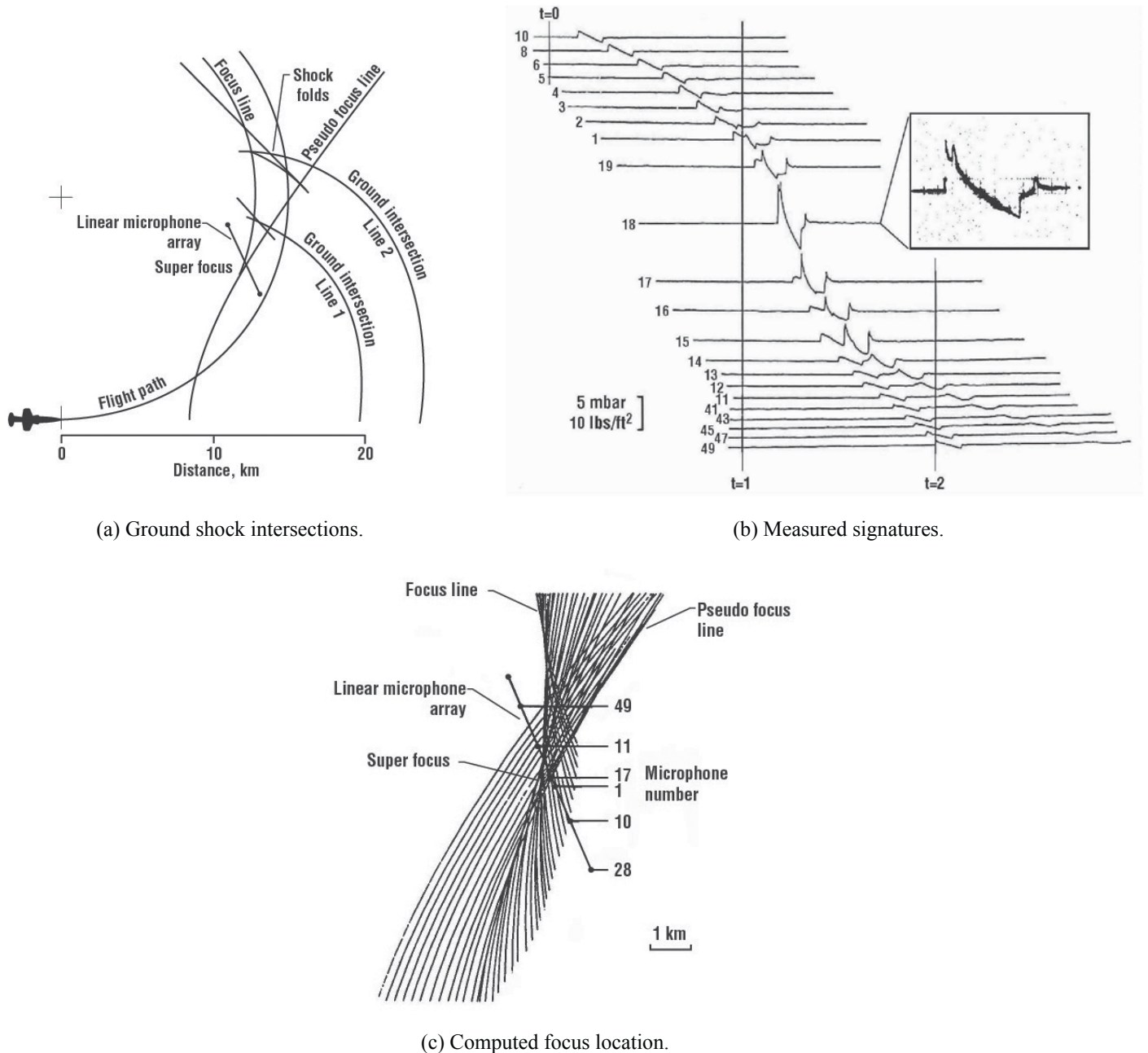


Figure 3.8. Superfocus boom from turn-entry maneuver at Mach 1.7 and at an altitude of 33,000 ft (adapted from ref. 3.7).

In figure 3.8(a), the predicted ground shock-interaction and shock folding of the turn entry is presented. At the tip of the shock folds, two focus lines develop – one due to the steady portion of the turn and the pseudo focus line due to the turn entry. Where those two focus lines join is known as the superfocus location. Also shown is the designed ground location of the 4.8 km linear array of 50 microphones with respect to the aircraft path. Figure 3.8(b) presents the sonic boom signature measurements. The three vertical lines are located 1 second apart. Examination of these signatures suggests that they were obtained between the two focus lines and very near the superfocus location. On microphone 18, the maximum value of the overpressure was obtained. From the

oscillograph trace of the signature from microphone 18, it can be seen that the first peak was higher and sharper than the second one. The intensity of the overpressure was about 15 lbs/ft², which gave a focus factor of about 9.0. The existence of the two peaks on the bow shock, as opposed to one, indicated that the measurement was not at the exact superfocus location. This conclusion is confirmed by the signatures from microphones 15 and 19, where the existence of several shocks is shown. The conclusion is also confirmed by the post-analysis graph of this particular flight given in figure 3.8(c), which shows that the two focus lines cross the measurement line in its middle at about 1 or 2 km away from the superfocus. It is important to appreciate that the superfocus influences a very small area on the ground on the order of a few hundred feet.

Transition Flight

Supersonic cruise flight requires that the aircraft transition from subsonic to supersonic speeds and, as such, will always have associated with it a focus region. This transition (accelerated flight) may occur at constant altitude or during a climb-acceleration profile. In either case, focusing will always occur. Since all vehicles will generate the transition boom, which incidentally is usually the first boom to reach the ground, a brief review of the nature of its occurrence and significance in terms of boom level is in order.

Figure 3.9 (ref. 3.8) is intended to illustrate the nature of the transition focus boom. An aircraft in level flight, from left to right, accelerates through Mach 1. A uniform atmosphere is modeled so that the rays are straight. As the aircraft accelerates, rays converge to focus. The distance to the focal point varies with the aircraft position, so the focus is a coalescing of rays on a line called a focus (caustic). Crossing rays away from the caustic are separate booms, but a focused boom condition exists where they converge along the caustic. A maximum focus boom occurs along the caustic and is of particular interest where it intersects the ground, while multiple signatures (at least two – an N-wave and a post-focus U-wave) occur at positions down track. The focus point on the ground is very small and is a one-time occurrence; that is, it is not dragged along with the vehicle as is the case for the carpet boom.

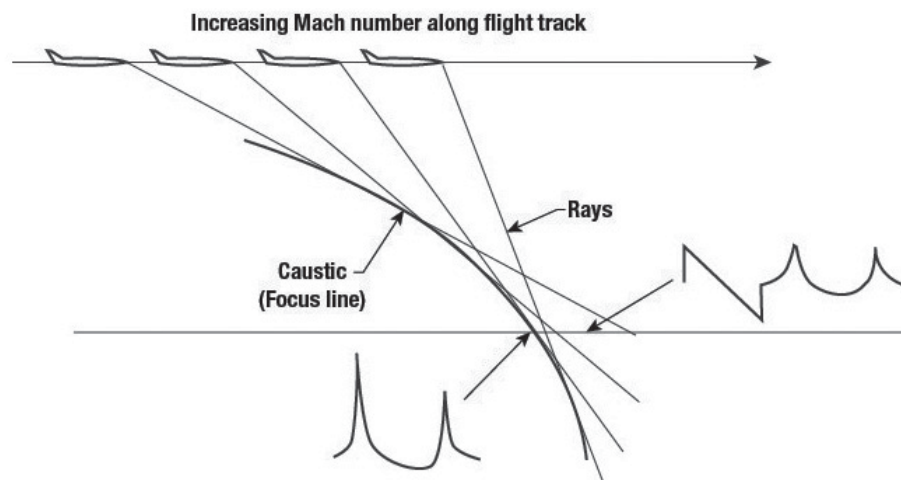


Figure 3.9. Nature of transition focus boom (adapted from ref. 3.8).

While figure 3.9 shows straight rays and a curved caustic, the wave behavior close to the caustic is very similar for cutoff caustics shown later in figure 5.5. The governing equations of boom behavior at a focus and a key scaling law were developed by Guiraud (ref. 3.9). A key parameter in focus scaling is the curvature of the caustic. Another property of the caustic is that it forms an envelope (boundary) of the rays. It is clear from figure 3.9 that a transition focus caustic forms a boundary between the region where there is no boom and where the boom carpet begins.

The governing equation written by Guiraud (ref. 3.9) is the nonlinear Tricomi equation:

$$\varphi_{yy} - (y/R + \varphi_x) \varphi_{xx} = 0 \quad (3.1)$$

where φ is the perturbation velocity potential, x is a local coordinate along the caustic, y is a local coordinate normal to the caustic, and R is the relative radius of curvature between the caustic and the ray. This equation applies locally, within a diffraction layer along the caustic. The $\varphi_x \varphi_{xx}$ term is nonlinear, the same second order steepening quantity that is represented by Whitham's rule (ref. 3.10). The remaining linear terms are hyperbolic (supersonic) at positive y and elliptic (subsonic) at negative y , consistent with the caustic forming a boundary. There is a subsonic evanescent wave (shown in fig. 5.5) on the shadow side.

Guiraud developed a scaling law for a step function shock. Because there is only one length scale, R , involved, the scaling law is universal so that a single step shock result (experimental or numerical) can be applied to focusing of any single shock. Gill and Seebass (ref. 3.11) and Gill (ref. 3.12) developed a numeric solution for the peak factor in Guiraud's solution. This was exploited by Plotkin and Cantril (ref. 3.8) to incorporate focal zones in a prediction code that evolved into PCBoom (ref. 3.13). Plotkin and Cantril's analysis showed that Gill and Seebass's numeric peak focus result matched the N-wave flight-test results of Operation Jericho (ref. 3.7) and the ballistic range experiments of Sanai et al. (ref. 3.14).

For N-wave booms, it is common to refer to a focus factor as being the ratio between shock amplitude at the focus and shock amplitude for an equivalent carpet boom. This is typically in the range of 2.5 to 5 (refs. 3.7 and 3.15). This focus factor should not be confused with the universal peak factor required by Guiraud's similitude.

On-Track

While figure 3.9 shows the transition focus from the perspective of sonic boom rays and is oriented on the caustic, figure 3.10 shows the transition focus from the perspective of wavefronts and is oriented to the perspective of observers on the ground. In the upper portion of the figure is a sketch showing the development of the on-track pre-focus, focus, and post-focus carpet boom regions associated with an accelerated flight of an aircraft transitioning from subsonic to supersonic speed. The aircraft is flying from left to right. Also shown is the development of the bow shock and focus caustic line and their intersection with the ground as the aircraft accelerates from Mach 0.9 to 1.5. The sonic boom pressure signatures that would be observed at various positions along the ground within the pre-focus, focus, post-focus, and carpet regions are also shown.

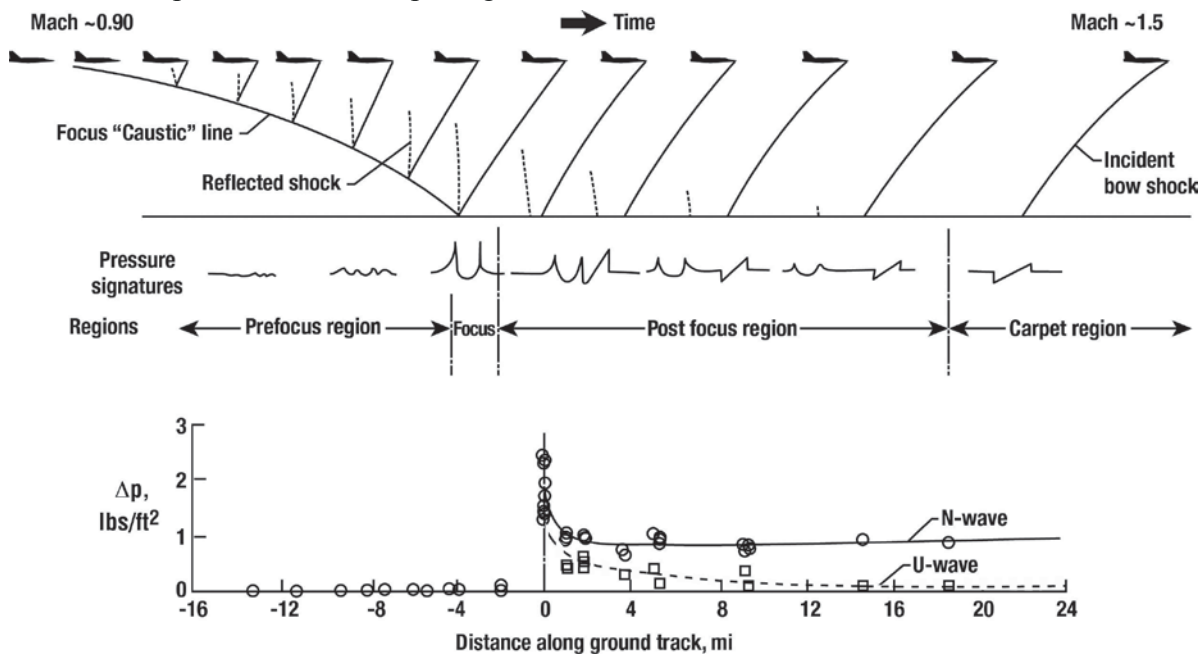


Figure 3.10. Measured boom overpressures along ground track for aircraft in transition flight, Mach 0.9 to 1.5 at 37,000 feet (adapted from ref. 3.15).

In the pre-focus region, ahead of the focus caustic line, the nature of the pressure disturbances are low frequency noise signatures such as rumbles that increase in amplitude as the focus is approached. Within the focus region, which may be on the order of 100 – 200m in width, an observer would experience the intense U-shaped focus signature as a loud bang-bang. In the post-focus region that follows the focus, anywhere from 3 to 4 shocks may be experienced at intensities less than at the focus and an observer would hear a bang-bang pop-pop. The time between these two events increases as the carpet boom region is approached. Once the carpet boom region is entered, the U-wave disappears due to atmospheric refraction and an observer experiences only the lower level bang-bang of the carpet N-wave.

In the lower portion of figure 3.10 (ref. 3.15) is shown the results of sonic boom ground-pressure measurements along the ground track for three longitudinal aircraft accelerations from Mach number Mach 0.9 to about Mach 1.5 at a constant altitude of 37,000 feet with an array of microphones extending about 23 miles. The data at the 0 on the abscissa of figure 3.10 represent the so-called focus boom conditions where pressure amplifications occur. The data for the three separate flights were normalized by plotting the highest measured ground overpressure, Δp_o , at this zero position. The direction of the aircraft is from left to right, as indicated by the sketches at the top along with corresponding tracings of measured signatures. The data points represent peak overpressures as defined in the sketch. The low value points to the left are observed as rumbles. The high points near the center correspond to measurements that are very close to the focus point and thus represent what are conventionally described as focus booms. To the right of the focus point are two distinct sets of signals that relate to the region of multiple booms. For convenience in illustrating the trends of the data, solid and dashed lines are faired through the data points. The data points that cluster about the solid curve relate to the bow shock overpressure of the first signature to arrive, in all cases, and this eventually develops into the steady-state signature of the carpet boom. The data points that cluster about the dashed curve relate, in all cases, to the bow shock overpressure of the second signature to arrive. These values generally decrease as distance increases and eventually this second signature ceases to exist due to atmospheric refraction.

The highest overpressures are measured in an extremely localized region. These values are as high as 2.5 times the maximum value observed in the multiple-boom region. The main multiple-boom overpressure values are of the same order of magnitude as those predicted for comparable steady-state flight conditions.

The locations of the focus boom and multiple-boom regions are readily predictable provided such information as flight path, altitude, and acceleration rate of the aircraft is available. Based on this experience, it was believed at the time that the focus boom could be placed at a position on the ground to within about ± 5.0 miles of the desired location and would be improved if more detailed weather information was available.

During the USAF Test Pilot School 1994 Controlled Focus Boom (ref. 3.16) Project (also called Have BEARS in ref. 3.6), a set of transition flights were performed both under radar guidance and autonomously using on-board guidance capabilities within an F-16B aircraft for placement of the focus boom at a ground target.

Figure 3.11 (ref. 3.6) presents a comparison of the predicted and measured signatures along the ground track of an F-16 aircraft during transition flight from Mach 0.9 to 1.2 at a constant altitude of 10,000 feet and under calm atmospheric conditions. The predicted signatures shown on the left hand side of the chart were computed from PCBoom3 (ref. 3.13) using the aircraft acceleration profile and rawinsonde weather information near the time of flight. Corresponding measured signatures are shown on the right hand side of the figure. The boom signatures are aligned in relative time to the leading shock. It will be noted that the first boom recorded, figure 3.11(b), was 500 feet up-track of the target point and had a peak overpressure of 10.8 lbs/ft². However, the maximum peak overpressure of 19 lbs/ft² occurred at the target point. Note also the increased separation between the N-wave and U-waves with distance from the focus region. In this post-focus region, the N-wave signature boom levels (about 6.0 lbs/ft²) are settling down to the carpet boom values associated with steady flight at a higher Mach number while the U-wave signatures continue to decrease in boom level until they disappear due to atmospheric refraction. For this particular flight, an amplification (focus factor) of about 3.0 was observed. Good agreement existed between the predicted and measured signatures, and boom placement on the target was excellent.

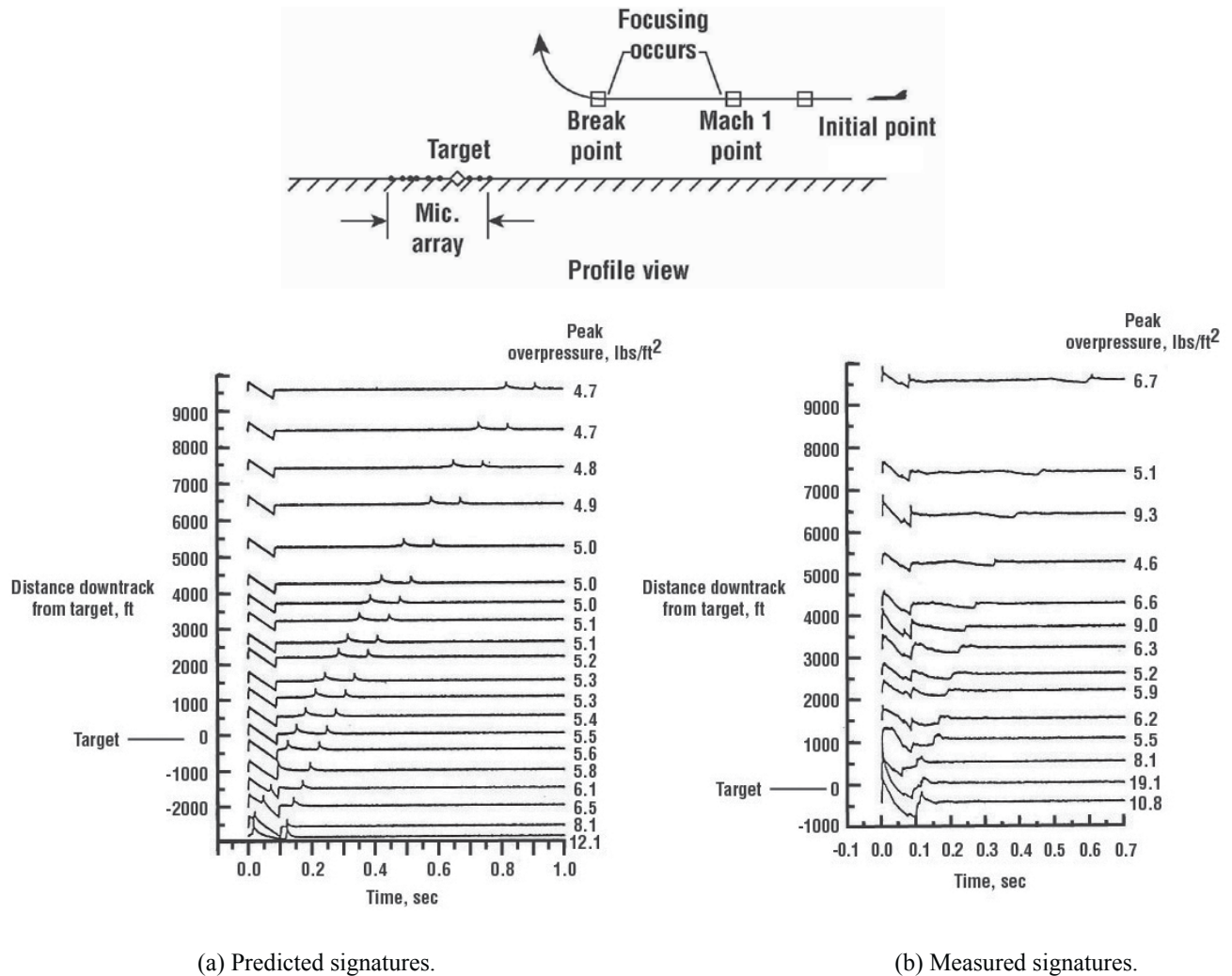


Figure 3.11. Comparison of on-track predicted and measured sonic boom signatures during transition flight, level acceleration of F-16 from Mach 0.9 to Mach 1.2 at 10,000 ft (adapted from ref. 3.6).

The results presented in figure 3.11 from the USAF Have BEARS flight-test program (ref. 3.6) have shown that this transition focus region can be placed to within plus or minus 1000 feet of the desired location if the vehicle performance and atmospheric conditions are known. It would be expected that for maximum focusing to take place, the atmosphere must be stable. Atmospheric turbulence, which is random in nature, would tend to upset this required in-phase condition and, thus, act to reduce the chances for maximum focusing or even eliminate it in some cases (refs. 3.6 and 3.15).

The predicted focus boom region during transition flight of the SR-71 from Mach 0.9 to about Mach 1.2 at an altitude of 30,000 feet in a standard atmosphere is presented in figure 3.12 (ref. 3.17).

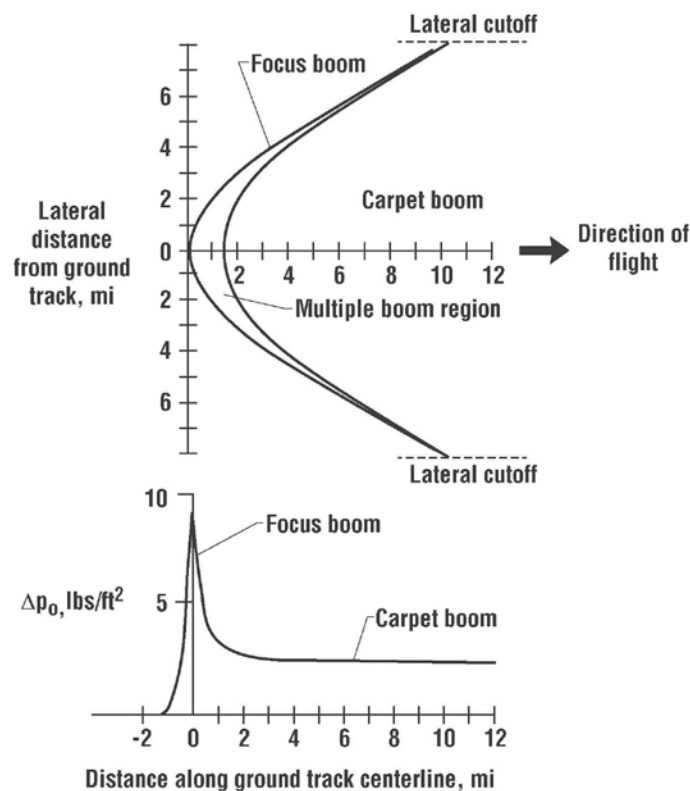


Figure 3.12. Predicted focus boom region during SR-71 transition flight distance along ground track, mi (adapted from ref. 3.17).

A plan view of the focus region for the aircraft moving from left to right is depicted in the upper right portion of the chart. The lower part of the figure shows a profile of the N-wave bow shock overpressures along the airplane ground track. It can be seen that the highest overpressures, about 9.0 lbs/ft² occur along the focus boom line and decrease rapidly as distance along the ground track increases. The nominal, or carpet boom, beyond the focus and multiple boom regions and along the ground track is shown to be 2.5 lbs/ft². This results in a focus factor along the ground track of about 3.5. Other flight-test measurements suggested that the focus factor can vary from 2.5 to 5.0. It was also shown that the focus line extended laterally out to the cutoff.

A unique set of flight experiments regarding focus booms associated with transition flight at low altitude were conducted at Istres, France in 1967 (ref. 3.18). A Mirage IIIB (fig. 3.13) served as the flight-test fighter aircraft and was flown at an altitude of 2000 feet (610 m) to minimize the influence of the atmosphere, accelerating from Mach 0.97 – 1.06 over a 3 km array of 28 ground microphones spaced some 100 m apart. Results from one of the transition flights are shown in figure 3.14. Bow-shock overpressures are plotted for each of the measured signatures, along with 5 measured signatures representing the pre-focus (microphones 3 and 6), focus (microphone 9), and post-focus (microphones 12 and 15) regions. There are three observations of significance that deserve discussion. First, a maximum overpressure of 28 mbars (about 58 lbs/ft²) was observed at the focus (microphone 9). The average overpressure associated with the post-focus region (microphones 12 through 27) is about 5.5 mbars (about 11.5 lbs/ft²). This results in a focus factor, on the bow shock, of about 5.0. The second observation is that the maximum overpressure is quite localized, drops off to half amplitude during the next 100 m, and becomes equal to the carpet boom within the next 300 m. Also, the signatures measured at the focus (microphone 9) show that the area (impulse) under the positive phase of the signature is much less than that associated with an equivalent N-wave of equal amplitude and period. The third observation is the character of the measured

signatures in the pre-focus region as illustrated in the traces from microphones 3 and 6. These types of signatures have been observed on airfoils in wind tunnels and aircraft in flight, wherein the free-stream flow is at very high subsonic Mach number (see, for example, fig. 25 of ref. 3.19) but the flow about the aircraft in some locations may be supersonic. Although the bow shock overpressure is 5.6 mbar, as the flow accelerates about the aircraft, the tail shock amplitude increases to about 21 mbar (44 lbs/ft²).



(U.S. Air Force photo)

Figure 3.13. Dassault-Breguet Mirage III.

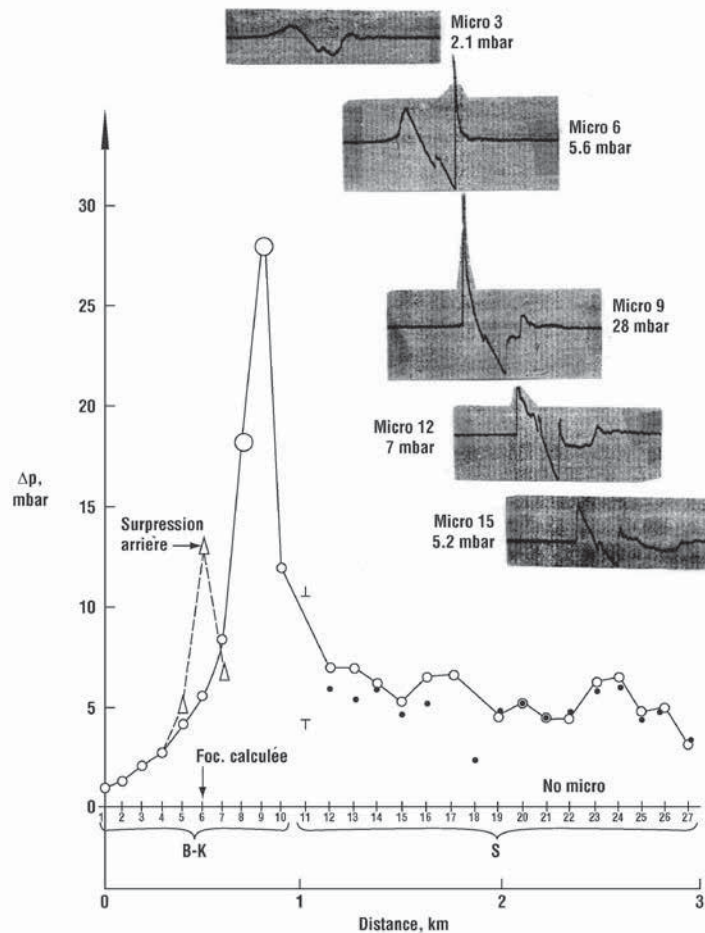


Figure 3.14. Low-altitude transition focus boom measurements (adapted from ref. 3.18).

The cut-off Mach number, where the aircraft speed over the ground is less than the speed of sound at the ground, associated with the Mirage IIIB flights for a standard atmosphere is about 1.02. The focus boom will be associated with the transition region from about Mach 0.95 to Mach 1.04. As altitude increases, Mach cutoff also increases (M_{co} at 30,000 ft is about 1.12, while at the tropopause (an altitude of about 36,000 feet) and above Mach cutoff is about 1.16). Such subsonic-transonic signatures are usually refracted before reaching the ground.

Lateral Locations

Measurements designed to gain insight into the overpressures and focus factor associated with the laterally extended focus line for transition flight have also been conducted. Figure 3.15 (ref. 3.7) presents this set of measurements that were conducted in the 1967 time period in France. To the left of the figure is a schematic of the test setup showing the focus region and a set of lateral measurement locations (indicated by the dashed lines) where measurements were taken. This lateral displacement was accomplished by offsetting the aircraft flight track from the linear microphone array. The measured results are presented at the right of the figure. Focus overpressures are shown as a function of lateral distance from the flight track. The circles representing each measurement include the accelerations associated with each flight. In an attempt to reduce the data scatter, the overpressure Δp , is shown as the ratio of $\Delta p/(M^2-1)^{1/8}$, where M is the Mach number corresponding to the shock wave focusing on the measurement line.

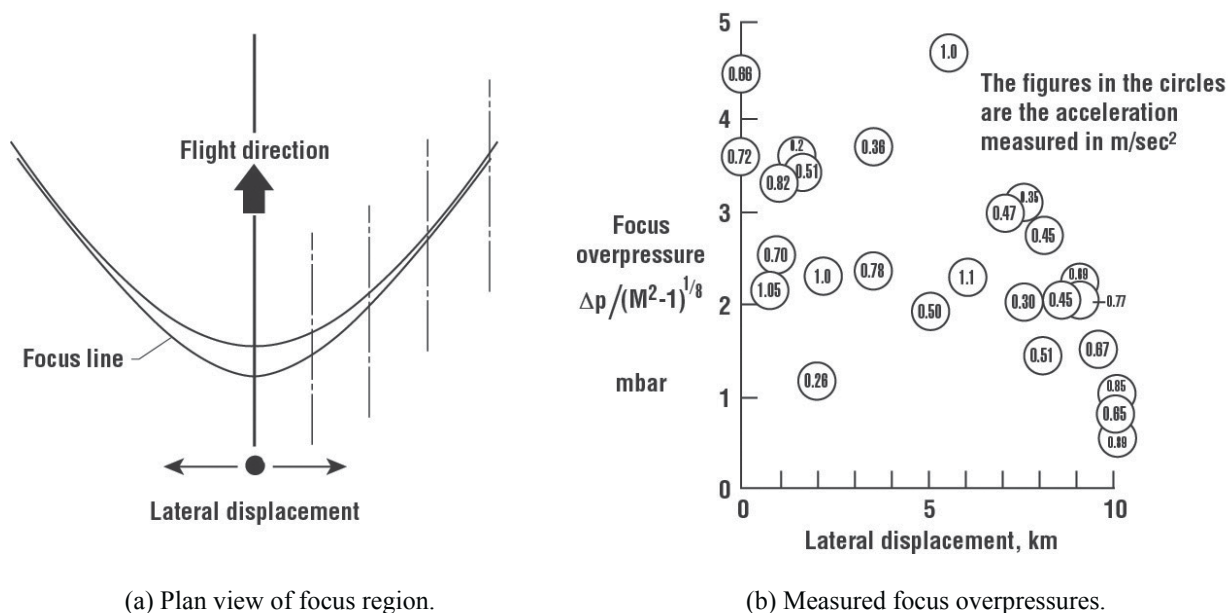


Figure 3.15. Measurements of focus booms at various lateral distances from ground track, rectilinear flight of Mirage IV at 33,000 feet (adapted from ref. 3.7).

Examination of the results show that the focus overpressures decrease as lateral distance increases and occurs in the same fashion as for steady-level flight. This may suggest that the focus factor remains constant with lateral distance out to cutoff. These are the only known published results of this nature and more research is required regarding the lateral focus factor. It is expected that the caustic curvature, rather than the distance and acceleration, plays a key role in scaling.

Modeling Focus Boom Footprint

Since these experimental data were obtained, considerable progress has been made relative to the state-of-the-art of sonic boom modeling (see ref. 3.20). All of the sonic boom models provide signatures at the ground. For many applications, the user needs a full footprint of some overall quantity, typically the maximum overpressure on the ground. Figure 3.16 (ref. 3.20) shows a schematic footprint (contour chart of peak overpressure) for a focal zone corresponding to a transition acceleration maneuver performed in level flight at a fixed acceleration rate.

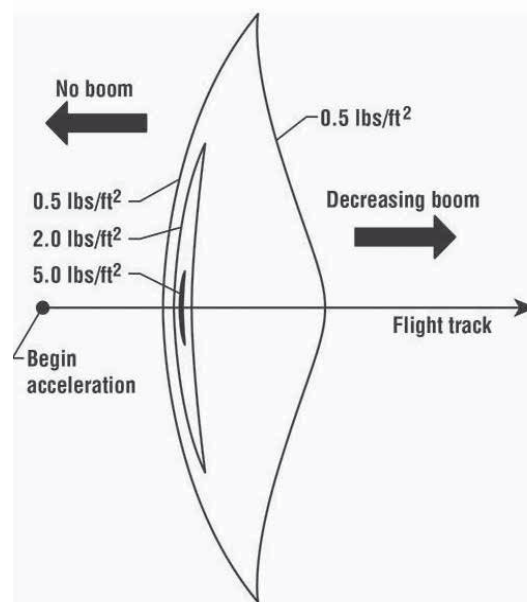


Figure 3.16. Transition focus boom footprint showing overpressure contours in the focal zone along the ground track and laterally (not to scale)(ref. 3.20).

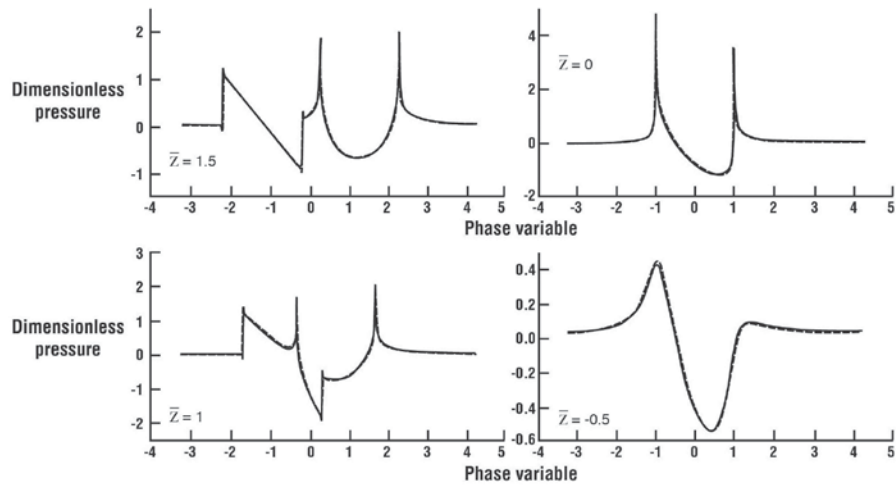
At one time, due to computer capabilities, creating a footprint like that shown in figure 3.16 was a significant undertaking. Using the early version of PCBoom3 (ref. 3.16) in the mid-1980s, such a footprint took several days to generate. Calculating the boom at enough points on the ground would take one or two (sometimes three) overnight computer runs. Runs were pieced together manually and contours were then drawn using a custom-written plotting program. Today, the computations for a footprint, as shown in figure 3.16, take only a few seconds from start to finish.

Influence of Signature Shape

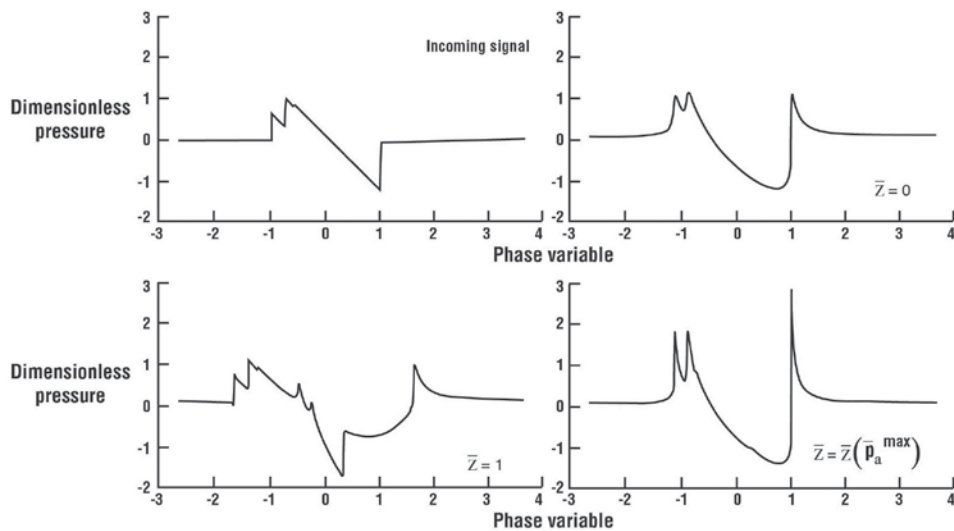
While PCBoom's mid-1970s application of the Gill-Seebass shock solution was quite successful for N-wave booms, it carried the assumption that each shock was an independent entity and behaved as an isolated step. A major advance occurred 25 years later, when Auger and Coulouvrat (ref. 3.21) and Marchiano and Coulouvrat (ref. 3.22) obtained a new numeric signature length. An iterative pseudospectral algorithm was used to solve for the full boom signature throughout the diffraction zone in the vicinity of the caustic. Their solution showed that signature shape, and the interaction between multiple shocks, can have a significant effect on the focus factor.

Two cases are presented in figure 3.17 (ref. 3.21) for transition flight in a standard atmosphere and at a constant altitude of about 12 km and an acceleration rate of 0.6 m/sec^2 , one assuming the incoming signature to be an N-wave (fig. 3.17(a)) and the other a multi-shock signature of Concorde at the same altitude (fig. 3.17(b)). For the N-wave case, predicted sonic boom pressure time histories are shown for four distances from the caustic. The distance is indicated as nondimensional $\bar{z} = z/\delta$, where z is distance above the caustic and δ is the diffraction thickness of the focal zone. The locations include the evanescent shadow zone region ($\bar{z} = -0.5$), at the focus ($\bar{z} = 0$), at the edge of the diffraction zone where the N and U-waves are just separate ($\bar{z} = 1.0$), and outside the diffraction zone where the N and U-waves have separated ($\bar{z} = 1.5$). It can be seen that at the focus location ($\bar{z} = 0$), the maximum bow and tail shock overpressures are about 4.5 times the amplitude of the incoming N-wave signature bow and tail shocks.

In the case of the three-shock Concorde incoming signature (fig. 3.17(b)), the maximum bow shock overpressure at $\bar{z} = \bar{z}(p_a^{\max})$ is only about twice that of the incoming bow shock pressure. However, it is important to point out that the amplification of the tail shock for the Concorde case is about four times that of the incoming bow shock.



(a) N-wave incoming signature.



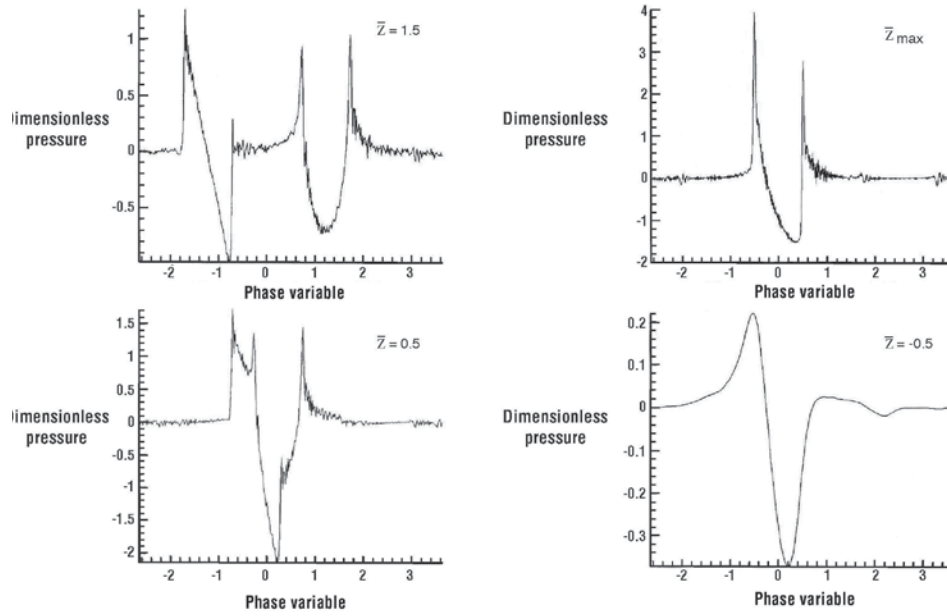
(b) Concorde incoming signature.

Figure 3.17. Influence of incoming sonic boom signature on focus boom during transition flight (ref. 3.21).

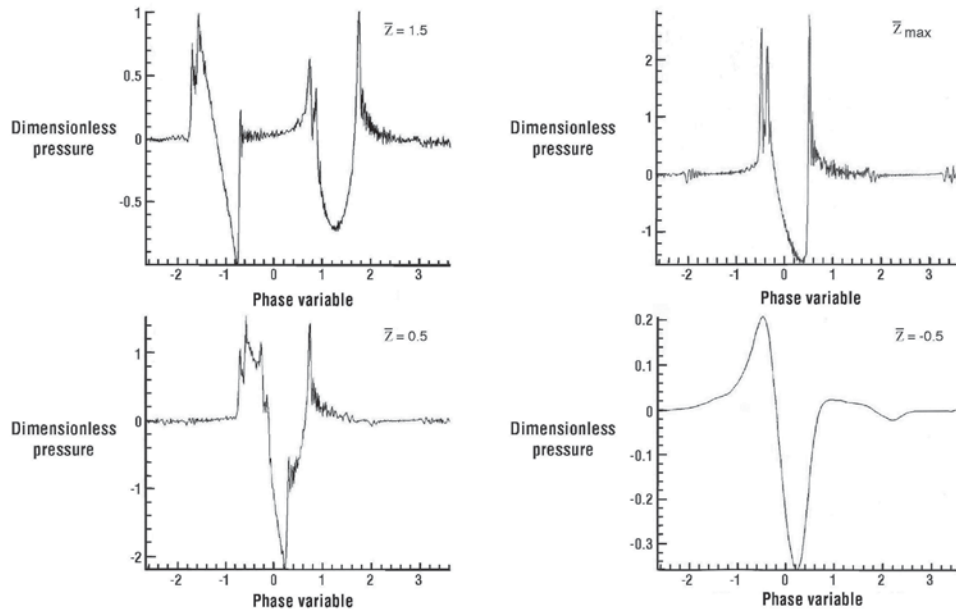
Since it has been shown that boom signature shape can influence transition focus boom levels, the question arose as to whether future aircraft designed to exhibit low-boom shaped signatures during cruise flight would also result in lower focus levels during transition from subsonic to supersonic Mach numbers. In order to answer this question, a numerical code was developed by Kandil and Zheng (ref. 3.23, Appendix 4 “Development and Application of a Sonic Boom Focusing Computer Code”) that would replicate the Auger-Coulouvrat (ref. 3.21) results so that one could examine the influence of several shaped boom signatures on transition focus booms.

Computational runs, computed with the full nonlinear Tricomi equation, were made for the case of an incoming N-wave and on an incoming three-shock saw-tooth representing a Concorde signature during transition flight and for the same operating conditions as assumed in figure 3.17. The results are presented in figure 3.18 for similar shadow zone, caustic, and above caustic locations (\bar{z} values). Comparison of the predicted focus signatures at the

\bar{z} position where maximum amplitude occurs, figure 3.17 for $\bar{z} = \bar{z}(p_a^{\max})$ for the Auger-Coulouvrat and figure 3.18 at $\bar{z} = \max$ for the Kandil code, indicate that the Kandil code does indeed replicate the Auger-Coulouvrat results.



(a) N-wave incoming signature.



(b) Concorde three-shock saw-tooth incoming signature.

Figure 3.18. Predicted signatures for level transition flight using Kandil numerical code (ref. 3.23).

Next, the Kandil-Zheng numerical code was used to predict the signatures in the vicinity of the transition focus boom for four low-boom shaped cruise signatures that included the asymmetrical and symmetrical flat-top and initial shock ramp type. A summary of the focus factors for both the bow and tail shocks for all six incoming signatures that were examined is provided in figure 3.19 (ref. 3.23).

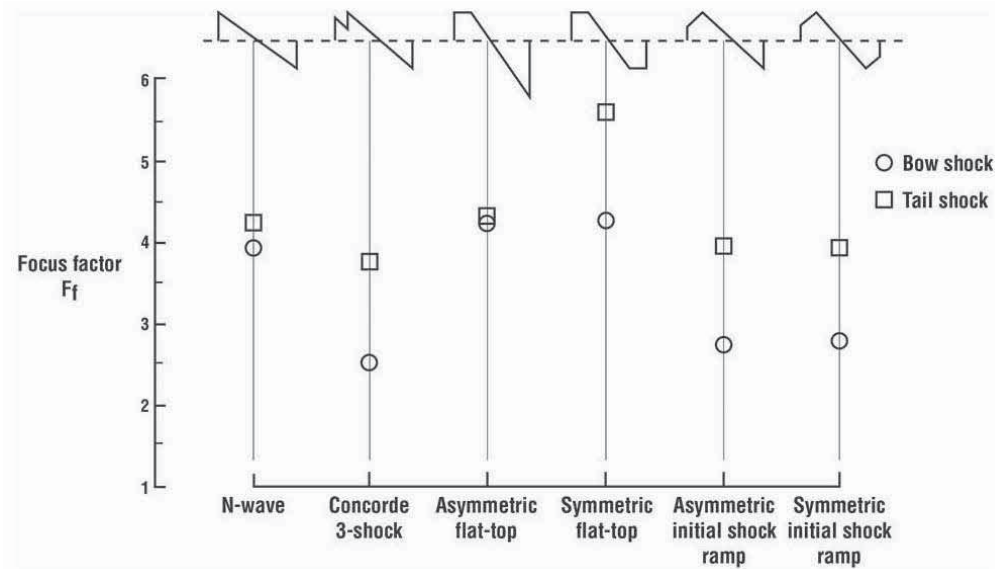


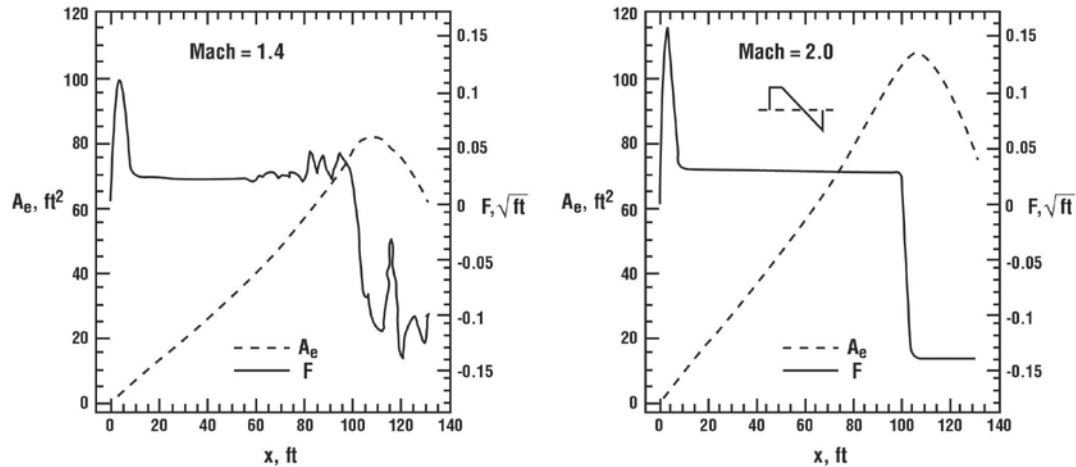
Figure 3.19. Influence of incoming sonic boom signature shape on focus factor for linear acceleration at constant altitude of 12 km at 0.6 m/sec² (ref. 3.23).

It can be seen from the figure that the lowest focus factors of the bow shock are associated with the Concorde type multi-shock and asymmetric and symmetric initial shock ramp signatures. Note also that the tail shock focus factors are greater than the bow shock focus factors for all six incoming signatures with a maximum of about 5.6 for the symmetric flat-top incoming signature. In the post focus region all six of the incoming signatures considered show that the reflected waveforms are still U shaped. Although not included in reference 3.23, the predicted focus signature for an incoming symmetrical ramp signature of 0.5 lb/ft² overpressure, 150 msec period, and 30 msec rise times the refracted waveform is also U shaped.

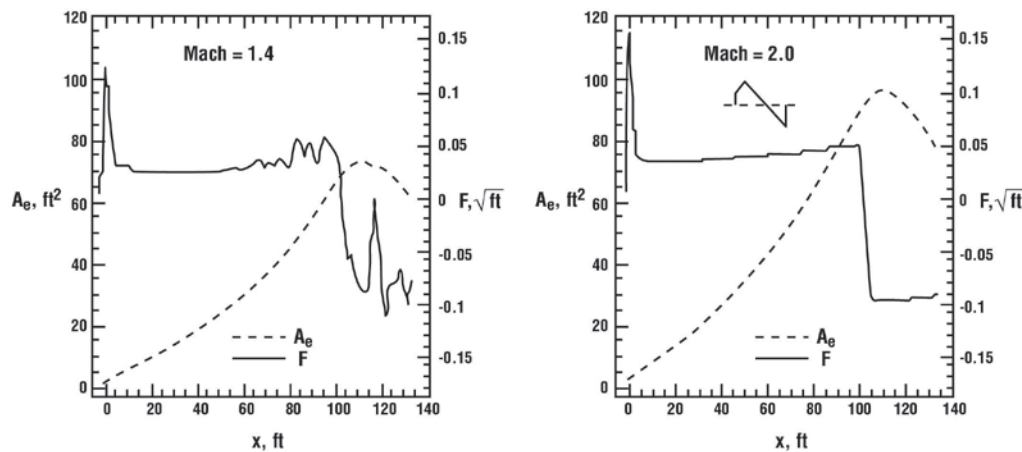
Design Cruise and Incoming Transition Signatures

The next question that arose concerned the relationship, if any, that a shaped signature designed for cruise flight may have with its incoming signature during the transition phase of operation. Bobbitt and Massey (ref. 3.23, Appendix 1) provide a simple method for calculating the lift distribution that allows the effective area distribution, due to volume at the design Mach number, to be rapidly evaluated. This code permits calculation of the equivalent volume at other Mach numbers using the design Mach number volume distribution plus the lift distribution methodology. Effective area distributions and F-functions were presented for Mach numbers from 1.8, or 2.0 down to 1.2 for both asymmetrical flattop and initial shock ramp type pressure signatures. Mach 1.0 cuts (actual geometry) of the area distributions for these two types of signatures are also given. Some results are presented in figure 3.20.

The design F-function (F) and effective area (A_e) for an asymmetric flat-top and initial-shock ramp configuration at Mach 2.0 along with the same quantities calculated for Mach 1.4 are shown in figure 3.20. It can be seen that the F-functions for both Mach 2.0 and Mach 1.4 vary in amplitude as expected but are quite similar in shape. Although the effective area distributions at Mach 1.4 show fluctuations in the aft portions of the flat-top and ramp F-functions, when compared to the Mach 2.0 cruise case they are surprisingly similar. In reference 3.23, it was concluded that shaped cruise signatures may be viewed as the incoming signature for the transition flight case.



(a) Asymmetric flat-top configuration.



(b) Asymmetric initial-shock ramp configuration.

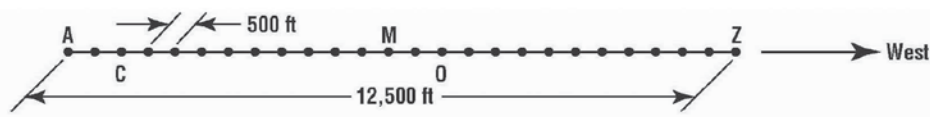
Figure 3.20. Comparison of F -functions and equivalent area distributions for two configurations at Mach 1.4 and Mach 2.0 (ref. 3.23).

In an attempt to gain some early insight into the design cruise and incoming transition signatures, the Shaped Sonic Boom Demonstrator (ref. 3.24), which generates a nominal flat-top boom at its design condition, appeared to provide an opportunity to measure focusing of a non-N-wave signature. Accordingly, plans were made to incorporate a focus condition flight in the January 2004 SSBE Flight Test Program (ref. 3.25).

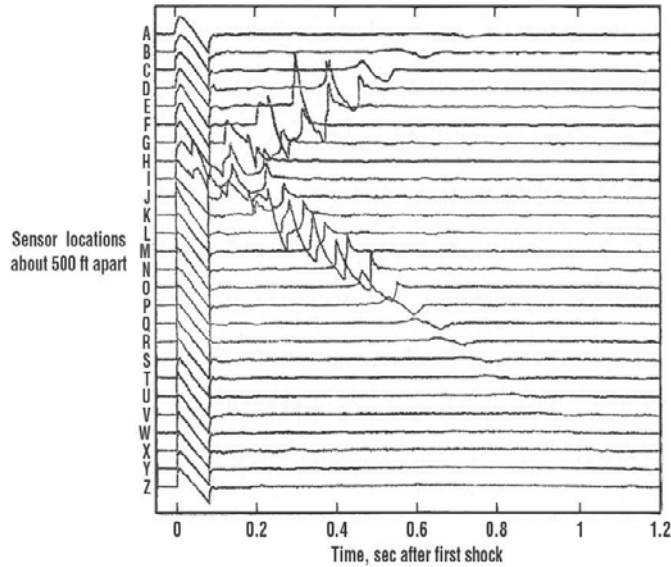
There are four types of maneuvers that will generate focal zones and include – (1) flight near sonic cutoff, (2) linear acceleration, (3) turn, and (4) pushover-dive. SSBD's shaped minimal boom design point is Mach 1.4 at an altitude of 32,000 feet. That eliminated maneuver type (1) as a possibility, since SSBD's low amplitude sonic boom would end up an N-wave. Maneuver type (2) was not possible because the aircraft's acceleration capability around Mach 1.4 is limited. That left maneuver types (3) and (4), so PCBoom4 (ref. 3.26) was exercised for turn and pushover-dive maneuvers beginning from steady-level flight at the design condition. It was found that a level turn could generate a focus, but would involve bank angles in excess of 40° . The g-load would be within the load limits of the aircraft, but the increased induced drag would reduce the aircraft's Mach number to less than 1.4.

The pushover-dive focus was examined. It was found that a pushover rate of one degree per second would

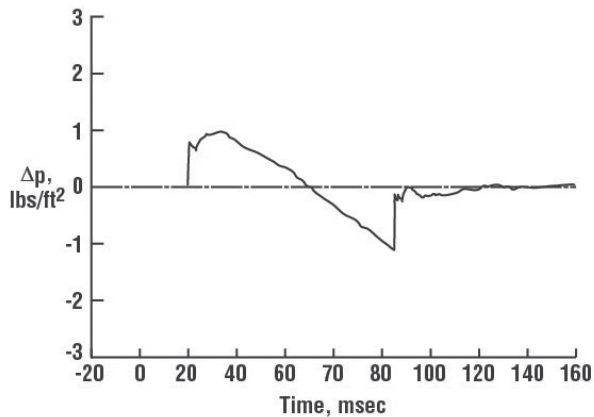
generate a focus at the ground as the aircraft passed through a flight path angle of minus one to two degrees. The results from flight 27 are presented in figure 3.21 (from ref. 3.27).



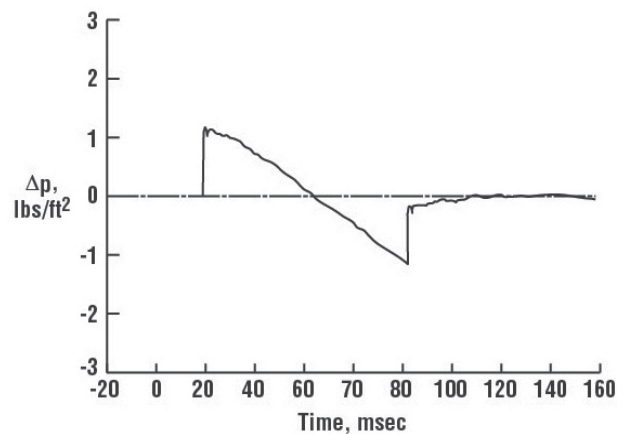
(a) Linear array of ground-based microphones.



(b) Measured boom signatures along microphone array.



(c) Recorded boom signature at sensor C.



(d) Recorded boom signature at sensor O.

Figure 3.21. Sonic boom signatures associated with SSBD pushover maneuver Flight 27 (adapted from ref. 3.27).

Figure 3.21(a) illustrates the ground-based microphone array used for the flight test. The primary linear array is 12,500 feet long, with sensors located 500 feet apart. The intent was to place the geometric focus at the center of the array, near sensor M. Figure 3.21(b) shows the measured boom signatures along the microphone array for the pushover event. The plots are in the general format used in reference 3.6. They have been shifted in time so as to align the first shock at each sensor.

Results from Flight 27 indicate that the maximum focus occurs at the E sensor location. The SSBD's shaped bow shock is not apparent on the boom signatures at the scale of figure 3.21(b) but can be seen in figure 3.21(c) where the initial carpet wave from sensor C is plotted at an expanded time scale. The post-focus carpet boom signature measured at sensor O, shown at an expanded time scale in figure 3.21(c), which was expected to be a shaped boom, is actually an N-wave. Recall that the aircraft was unloaded to 0.25 g until it passed the end of the microphone array.

The carpet boom is thus from a flight condition where the lift load is one quarter that corresponds to the minimal boom design condition for SSBD. With that light a load (and correspondingly lower coefficient of lift) the shaping geometry that produced the flat-top bow shock was lost.

The focusing maneuver was successful, and it showed, as expected, that this pushover focusing maneuver was at a flight condition that does not yield the design low-boom cruise condition. That lesson is a useful result. Auger and Coulouvrat (ref. 3.21) showed that a lower focus factor is realized for the Concorde three-shock signature than that of a simple N-wave with only bow and tail shocks. They suggested that a deliberately complex signature could provide relief from focus superboms. The result of this flight test shows that focus conditions are well removed from the shaped minimal boom design point. While the off-design signature for the SSBD was a simple N-wave, the possibility of developing a suitable complex boom in the low Mach number transonic acceleration region of an operational low-boom supersonic aircraft may be realized. It is of interest to note, however, that Bobbitt and Massey (see Appendix 1 of reference 3.23) show that for transition flight from subsonic to supersonic speeds, the off-design signature is similar to that of design cruise Mach numbers as low as 1.2. However, the likelihood of realizing similar equivalent area distributions and F-functions of the transition phase of flight to the cruise design condition is yet to be determined.

Dedicated Flight Transition Experiments

Since acceleration to supersonic speed is an unavoidable maneuver for supersonic flight, the focus boom ground footprint associated with this transitioning has always been a serious obstacle to overland operations. It has been shown that the booms from transition flight can result in significant boom amplitude enhancements in the focal zones and that the potential exists for complex multi-signature patterns. Several transition focus boom flight tests have been conducted over the years aimed at defining the nature of this particular maneuver in order to seek ways to minimize its impact. A compilation of these nine flight tests (refs. 3.3, 3.4, 3.15, 3.16, 3.18, and 3.28 – 3.32) is presented in table 3.1, beginning with the earliest flight test, conducted in England in 1959, to the most recent flight test conducted in the United States in 2011. Information that provides an indication of the scope of each experiment in terms of flight conditions, microphone arrangement, and focus factors is also presented in the table.

Table 3.1. Compilation of Transition Flight-Test Experiments

Sponsor Item	England	NASA/USAF	NASA	French/Jericho			NASA/USAF Bren Tower	USAF Have BEARS	NASA SCAMP
Year	1959	1961	1964	1966	1967	1969	1970	1994	2011
Aircraft	Fairey Delta 2	F-104	F-104	Mirage III	Mirage IV	Mirage III & IV	F-104	F-16B	F-18B
No. Passes	7	7	5	12	5	23	26	31	70
Fit Alt ft	10,000	14,200	37,000	2,000	36,000	36,000	33,700	10,000	35,000 to 45,000
Mach Range	0.98 - 1.2	0.9 - 1.2	0.9 - 1.5	0.97 - 1.06	1.05 - 1.03	1.05 - 1.03	0.95 - 1.3	0.9 - 1.2	1.1 - 1.3
Acc Rates m/sec ²	Max A/B	Max A/B	Max A/B	3 Max A/B	0.3 - 1.2	0.2 - 1.2	1.1 - 1.6	Max A/B	
Linear Mic Array, ft	6,000	8,500	116,000	9,850	9,850	16,000	3,200	10,500 to 13,700	10,000
No of Mics	6	4	8	28	28	48	14	15 - 21	81
Mic Spacing, ft	1,300	2,800	5,000 10,000 20,000	330	330	394	200	500 & 2,000	125
Lateral Meas	None	None	None	None	None	To 6.2 mi One Side	0.34 Mile to Each Side	None	25°, 30°, 35° One Side
Above Ground Measurements	None	None	None	None	None	None	15 every 100 ft	None	2,500 ft & 7,500 ft
Meas Focus Factor	4.0	2.0 - 2.5	2.5	5	5.6	6.0	2.0 - 5.0	2.0 - 4.2	2.0 - 4.2
Focus Placed in Array	1/7 (?)	1 of 7	2 of 5	12 of 12	4 of 5	11 of 23	15/26	26 of 31	37 of 61
Max Focus Measured	None	None	None	2 of 2	None	1 of 23	None	None	
Reference	3.3	3.4	3.15	3.18	3.28	3.29	3.30 - 3.31	3.16	3.32

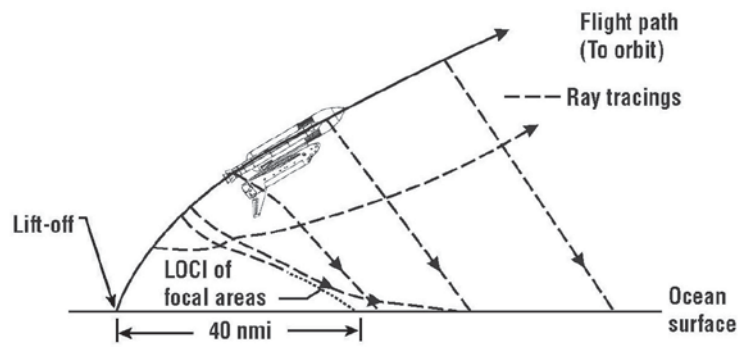
A common factor among the first eight of the nine transition flight-test studies was that the studies focused on the location of the focus, the condition that generated them, and the peak pressures of the focused N-wave signatures. Signature shapes were qualitatively noted, but other than the peak pressures, no comparison to theory was made. The ninth and most recent flight experiment, known as the Superboom Caustic Analysis and Measurement Program (SCAMP), had a primary goal of gathering a comprehensive empirical data set of focused sonic boom signatures suitable for validation of computer models for predicting sonic boom focal zones and signatures, and to apply these models to predict focus booms for low-boom aircraft designs.

SCAMP (ref. 3.32) consisted of 13 supersonic flights of an F-18, 11 of which had five to seven supersonic transition maneuvers. The objective was to obtain detailed signature data that could be compared to theoretical/numerical focus models. A variety of acceleration and pushover maneuvers were employed so as to vary caustic curvature (ref. 3.33). Forty focal zones were recorded along a 10,000-foot 81-microphone array (refs. 3.34 and 3.35). Ten focal zone signatures of various types were recorded on a powered glider about 5000 feet above the ground array. Two analytic models for focus signatures were evaluated. The first was a lossy nonlinear Tricomi equation (NLTE) solver (ref. 3.36). This was based on the methodology pioneered by Auger, Marchiano, and Coulouvrat (refs. 3.21 and 3.22) but extended to include atmospheric absorption. The rise time associated with absorption had been shown in ref. 3.8 to be significant for peak shock overpressures. NLTE results agreed very well with measured foci, matching the shock peaks and also the signature shapes throughout the focal zone. The second model was a Nonlinear Progressive Wave Equation (NPE) solver (ref. 3.37), a more general wave propagation code. NPE provides good qualitative agreement with measured booms, but required external scaling and in its current form does not include absorption losses.

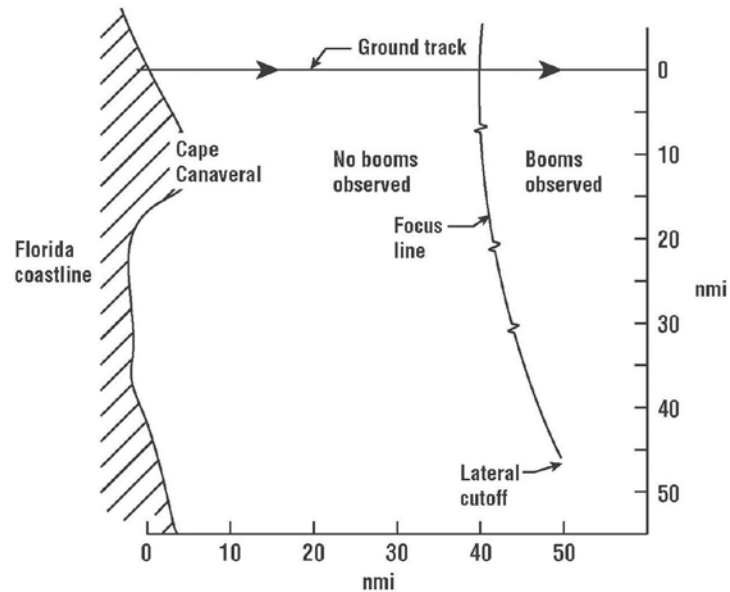
The validated NLTE codes was applied to prediction of transition focus for several low-boom aircraft configurations (ref. 3.38). Interactions between shocks, similar to those seen in figure 3.17(b), were observed. General indications of the effects of Mach number, altitude, and maneuver on focus factor were observed.

Launch Vehicle Transition Focus Boom

Transition focus booms were also experienced during the launch-ascent phase of mission operations with vehicles such as the Saturn-Apollo rocket/capsule combination vehicles and the Space Transportation System (STS)/Space Shuttle Orbiter. An illustrated description of the launch-ascent focus boom region is presented in figure 3.22 (ref. 3.39). The origin of the launch-ascent focus boom region is shown schematically in the figure. When, for example, the Saturn-Apollo vehicles and the Space Shuttle first achieved supersonic velocities, they were in nearly vertical flight and the propagation of the disturbances was upward, away from the ground. As the vehicles continued to accelerate and pitch over, the flight path angle decreased sufficiently so that the disturbance propagation path intersected the ground surface. The combination of angular and linear acceleration rates resulted in a region some 40 nmi or so from the launch site in which the acoustical energy was focused, as indicated by the loci of focal areas shown in the profile view presented in figure 3.22(a). These loci define a focus line on the ocean surface that is parabolic in shape as depicted in figure 3.22(b) and extends laterally approximately 40 nmi or so to each side of the vehicle ground track out to the lateral cutoffs. Beyond the lateral cutoff, the pressure wave is refracted up by the atmosphere and does not intersect the ground. Behind (downrange from) the focus line, the post-focus region overpressure peaks originating from different points on the flight path reach the surface at different times, producing signatures with multiple peaks. In front of the focus line (the pre-focus region), no sonic boom reaches the ground. The highest peak overpressure is obtained at the focus line beneath the flight path and falls off both laterally from the ground track and downrange from the focus line.



(a) Origin of launch-ascent focus boom.



(b) Plan view of launch-ascent focus boom region.

Figure 3.22. Description of launch-ascent focus boom region (adapted from ref. 3.39).

The pre-focus, near-focus, and post-focus signatures observed from measurements acquired during the launch-ascent of the Saturn-Apollo 17 (ref. 3.39) mission are shown in figure 3.23. Six U. S. Naval vessels were located in the Atlantic Ocean directly under the flight path of the launch vehicle and were positioned to cover the extent of the focus region. Note that although two of the measurements were near the focus line, the chart suggests that the values measured do not represent the maximum overpressures within the focus line.

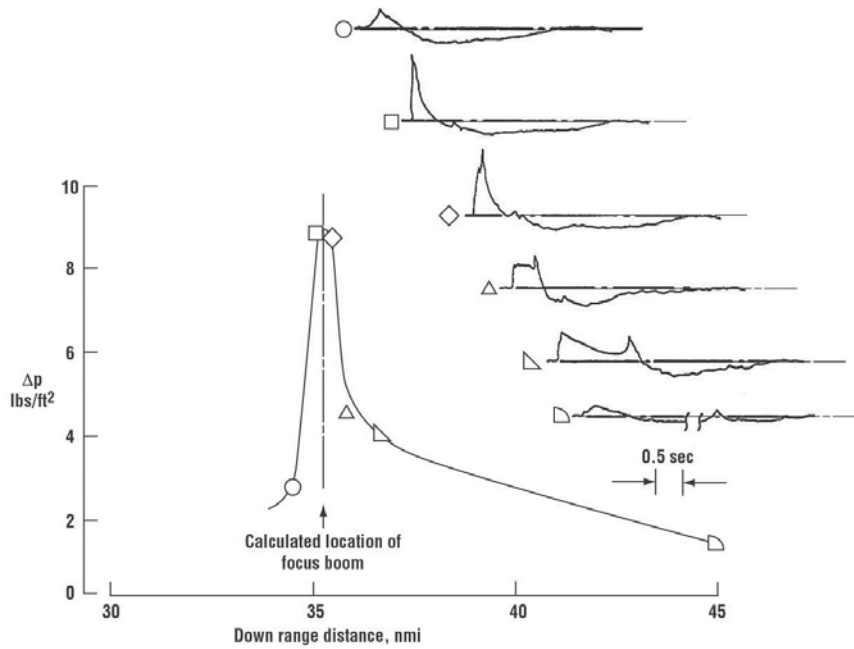


Figure 3.23. Saturn-Apollo 17 launch-ascent sonic boom signatures within focus region (ref. 3.39).

Sonic boom signatures representative of those measured within the STS launch-ascent focus region are shown in figure 3.24 (ref. 3.39) and are similar to those observed from the Saturn-Apollo launch-ascent. Note the change in the time scale associated with each set of measured signatures. The uppermost signature was measured at a location in the pre-focus region slightly up-track (before) the focus line. The signature shown at the center of the figure was measured within the focus line and is seen to consist of a sharp signal shock of large amplitude, which may not represent the maximum value. A considerable database on focus booms associated with supersonic aircraft suggests that the downrange thickness of the focus line is on the order of a few hundred feet. Down-track, behind the focus line, and in the post-focus region the measured signature shown at the bottom of figure 3.24 also displays a two-shock trace, the initial shock being attributed to the direct boom and the second the reflected shock arriving at a slightly later time and from a slightly different location along the ascent trajectory.

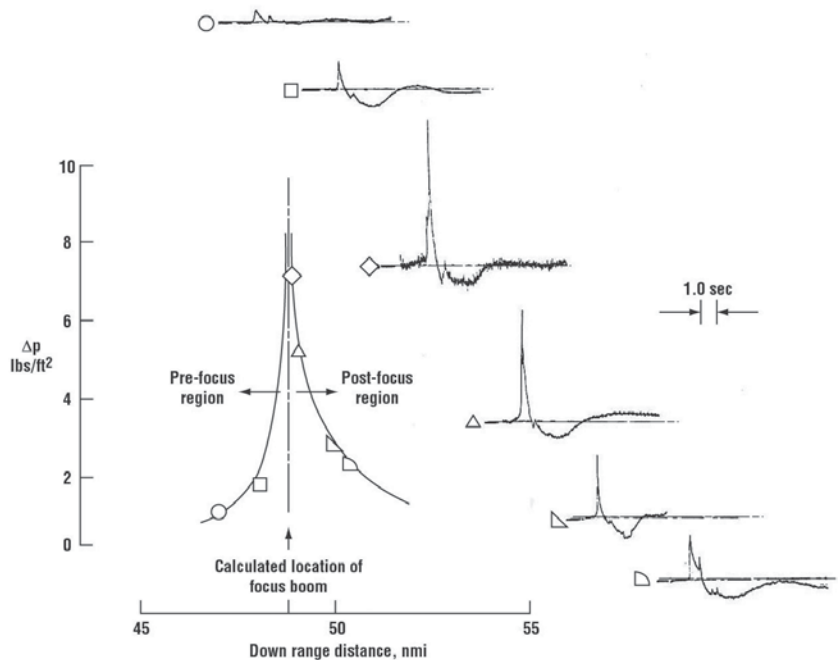


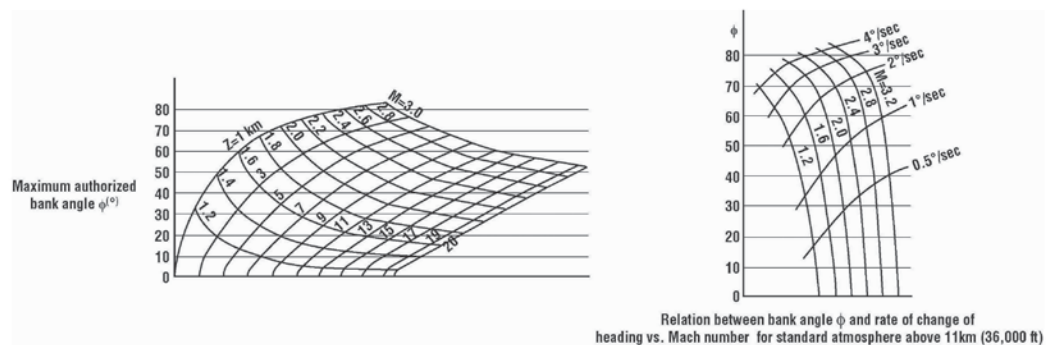
Figure 3.24. STS launch-ascent sonic boom signatures within focus region (ref. 3.39).

It is quite observable that the measured sonic boom ground signatures associated with the Saturn-Apollo and STS Shuttle launch ascents are quite different in character than the N-wave shapes associated with aircraft and the Space Shuttle Orbiter. Note from figures 3.23 and 3.24 that the boom signatures measured in the post-focus region (i.e., down-track of the focus line) consist of an initial bow shock followed by a long expansion similar to signatures associated with explosive charges. Thus, only a single boom is observed. In addition, the boom signature period is on the order of 4.0 seconds. Although Saturn-Apollo and STS Shuttle vehicles (in their launch configurations) were large, the initial shock resulted from the enormous rocket engine exhaust plumes.

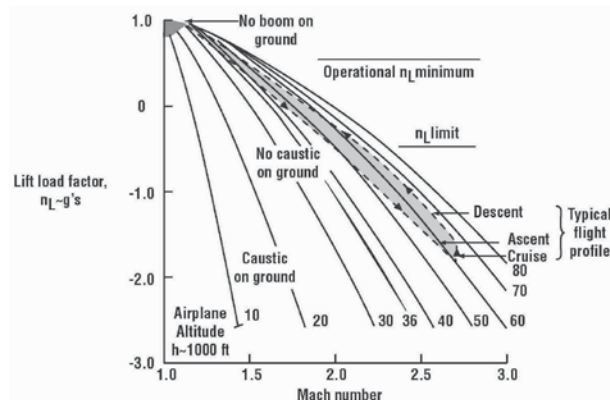
Current coastal launch sites allow for the placement of the transition focus region to impact over water. Future space exploration efforts may be located at inland launch sites where sonic boom impact must be addressed with more consideration of the transition focus region.

Focus Boom Avoidance Charts

During the U.S. SST effort of the mid-1960s and also in preparation for the entry of Concorde into routine commercial flight service, information relating to the avoidance of flight maneuvers that could cause focus booms was obtained. Two examples of focus boom avoidance operational charts are provided in figure 3.25 (refs. 3.7 and 3.40). Wanner et al. (ref. 3.7) presented an operation chart regarding Concorde operations that avoids focus booms during turn maneuvers and is shown in figure 3.25(a). The maximum permissible bank angle in a steady turn for Concorde to not produce a focus on the ground is plotted as a function of altitude and Mach number. For a better understanding of these limits, the relation between bank angle and rate of change of heading versus Mach number is also shown. As an example, at Mach 2, the maximum authorized bank angle is 35° at an altitude of 36,000 feet (11 km) and 30° at an altitude of 52,500 feet (16 km). But on the other hand, the limit is much lower for low Mach numbers. At 32,800 feet (10 km), the maximum permissible bank angle at Mach 1.3 is only 10° .



(a) Maximum authorized bank angle in order to avoid focus during turning maneuvers (ref. 3.7).



(b) Pushover requirements for caustic formation on the ground (ref. 3.40).

Figure 3.25. Examples of focus boom avoidance operational charts.

A study by Haglund and Kane (ref. 3.40) of maneuvers typical of a large SST-type airplane showed that it is possible to perform normal SST flight operations without producing focus booms except during the transonic acceleration phase of flight. Thus, for commercially operated supersonic aircraft, maneuvers such as pull-up, pushovers, sideslips, and abrupt turns at supersonic speeds would be avoided and the proper deceleration-descent schedule would be employed to avoid focusing during decent. Figure 3.25(b) addresses the critical lift load factors n_L required for a caustic at the ground directly beneath the airplane during pushovers in the 1962 U.S. Standard Atmosphere with no wind. Note that caustics are most easily produced at the low supersonic Mach numbers. At speeds greater than about Mach 2, caustics are impossible to form operationally for an SST because of the load factor constraint on commercial flight. For passenger comfort the lift load factor n_L will be restricted to 0.5 g in pushovers, while the structural limit load factor minimum is about -0.5 g. A typical flight profile (Mach number-altitude variation) is also shown on the figure. For the operational minimum of 0.5-g load factor, caustics could be produced only at Mach numbers between 1.5 and the threshold value. Charts of this nature are very important in the operation of supersonic aircraft in order to avoid generating unnecessary focus booms during flight operations. In fact, such information could be integrated into an aircraft's onboard flight computer systems.

Haglund and Kane (ref. 3.40) also examined flight-test data involving acceleration rates of 0.04 g to 0.10 g that suggests that a method to alleviate the transonic accelerating caustic is to accelerate rather slowly. They concluded, however, that based upon current prediction methods at that time, there was no method available for calculating the variation of caustic intensity with acceleration magnitude even though the limited experimental data did suggest a pronounced effect of deceleration on caustic intensity. Recently, Auger and Coulouvrat (ref. 3.21) concluded that, for the limited acceleration rate and altitude examined, these factors had little influence on ground track focusing.

When the Space Shuttle Orbiter returned from orbit, most of its atmospheric descent was at supersonic speeds. The resultant sonic boom impinged on land areas in the United States, with the sonic boom carpet extending to the vicinity of the landing site. Prediction of sonic boom has been routinely performed as part of mission planning and these predictions have agreed well with measurements (ref. 3.39). There was some concern that maneuvers during the final stages of supersonic flight could, under anomalous atmospheric conditions, cause a focus boom to occur at some location on the ground. This concern was centered on the portion of descent around Mach 3, where the Shuttle made a significant S-turn. The finding of the Plotkin study of reference 3.41 indicates it does not appear that sonic boom focusing will occur in the Mach 3 range. Focusing is possible, but would require turn rates higher than those normally employed within the Orbiter's flight envelope. However, focusing can occur for turns at a Mach number below 2. This is outside the range that was of concern and is also in the range where sonic cut-off focusing is normally expected as the vehicle approaches subsonic speeds and the boom lifts from the ground.

Figure 3.26 is an example focus condition chart adapted from reference 3.41. The abscissa is turn rate and the ordinate is flight path angle rate. To the right are shown the Mach number, altitude, flight path angle, and Mach rate. These are nominal quantities, corresponding to the center of the ranges seen in several Shuttle-Orbiter reentries. The small rectangular area just above the center of the chart represents the flight envelope at that Mach number. The V-shaped lines represent the threshold of focusing. Within the V, no focus occurs. Outside (or below) the V, focus will occur. Three V contours are shown, the middle one corresponds to the nominal flight conditions to the right and the other two Vs are focus conditions computed at the extreme values of Mach rate. Focus charts similar to figure 3.26 are also presented in reference 3.41 for Mach numbers from 2 to 6 and for two atmospheres (the U. S. Standard Atmosphere and the EAFB Range Standard Atmosphere). These charts indicate that focusing was not expected to occur for Space Shuttle descent.

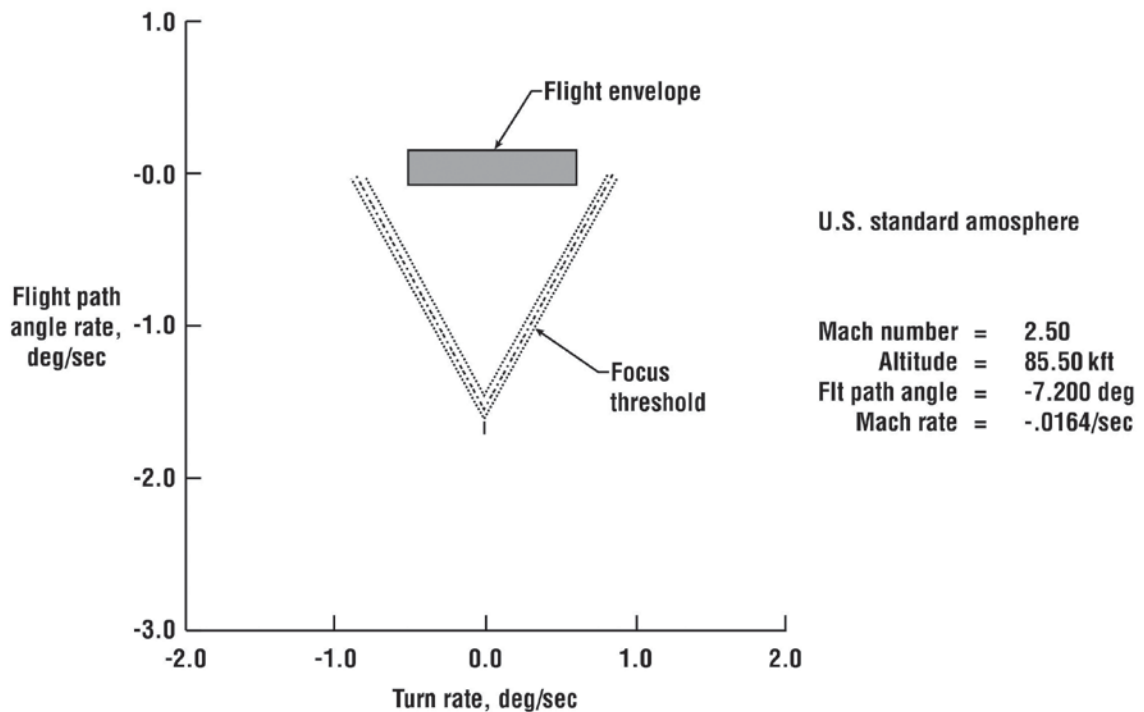


Figure 3.26. Space Shuttle Orbiter focus boom avoidance chart for descent (ref. 3.41).

As has been shown in the previous figures, sonic boom enhancement can result from a variety of aircraft maneuvers. Figure 3.27 is presented as a summary reminder that focus boom regions may be experienced when an aircraft performs three of the more common maneuvers and include a longitudinal acceleration, a 90° turn, and a pushover maneuver.

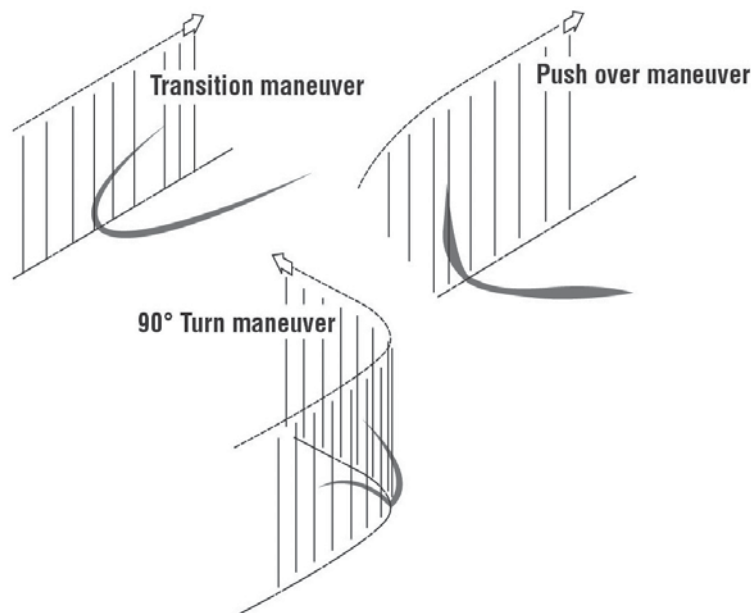


Figure 3.27. Focus boom regions on ground from three maneuvers.

In each maneuver, focus overpressure increases occur in the localized regions suggested by the shaded areas in the sketches. It is very important to remember that although the aircraft and shock waves are moving, these localized areas on the ground in which pressure enhancements occur are fixed and do not move with the aircraft. The localized regions, incidentally, are on the order of 1000 feet or less in width (thickness). The relative overpressure increases in these focus areas are a function of the type of maneuver and the acceleration

involved and are noted to be two to five times the boom carpet values and in some cases, as high as nine at so called superfocus locations, which are even smaller in extent. As noted previously, pressure buildups will always result for the longitudinal maneuver when the aircraft accelerates from subsonic to supersonic speeds. The overpressure increase areas associated with turns and pushover maneuvers can be minimized or avoided by reducing acceleration (or decelerating) or by simply avoiding the maneuver.

In scheduled commercial flight operations, longitudinal acceleration from subsonic to supersonic speeds is the only maneuver of significance from a ground exposure point of view. Focus boom during the deceleration-descent phase of flight can be avoided by proper arrangement of the aircraft Mach-altitude schedule. Recent experience has demonstrated that the focus boom region associated with this transition acceleration can be placed to within about ± 1000 feet of the designated area. However, experience with normal Concorde operations over a 1-year sampling has shown that meteorological induced variations in boom amplitude and focus location are experienced (ref. 3.42). It is important to note that any randomness of the atmosphere, which brings about waveform distortions, may decrease the focus factor value and, for certain situations, may eliminate the focus altogether as observed in references 3.15 and 3.16. Such occurrences, combined with a minimum boom design and flight transition profile, could render the focus boom ground footprint to a negligible issue.

Sonic Booms at High Subsonic Mach Numbers

It can generally be stated that as long as the aircraft speed over the ground is less than the speed of sound at the ground, boom-less flights at low supersonic Mach numbers at flight altitude can be achieved. It is often asserted that as long as the aircraft speed is less than Mach 1.00, no sonic booms should be experienced at ground level. However, it is known that sonic booms and, at times, damage has resulted from aircraft flights at relatively low altitudes and at high subsonic Mach numbers. Sonic booms were reported to have been observed from the subsonic XP-86 Sabre prototype (ref. 3.43), shown in figure 3.28, during a dive-pull-up maneuver several days before Chuck Yeager's level supersonic flight in the X-1 aircraft in 1947 when his support team in the NACA tracking van reported they heard what sounded like a distant rumble of thunder (ref. 3.44).



(U.S. Air Force photo)

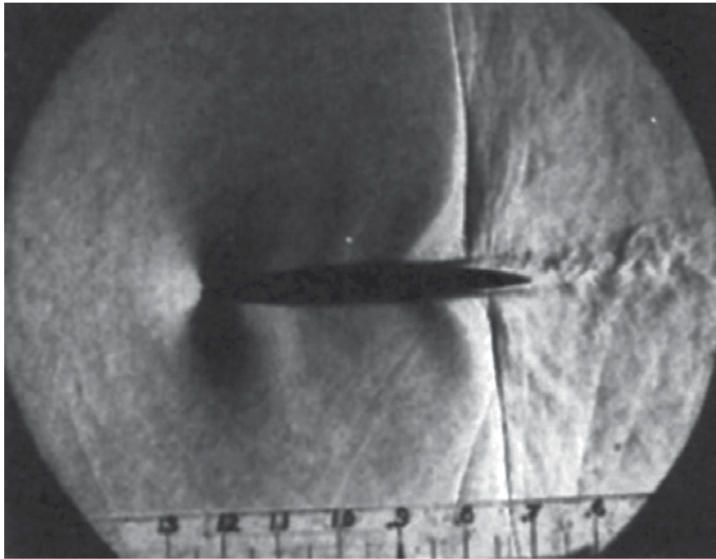
Figure 3.28. North American XP-86 Sabre prototype.

Booms from Low-Altitude Level Flight

Experience, confirmed by measurement (ref. 3.31) indicates that booms can be observed at ground level from aircraft in steady-level flight at Mach numbers from about 0.95 to 0.99 at altitudes of about 300 to 2000 feet above ground level. This phenomenon is similar to that observed for airfoils in wind tunnels (as shown in fig. 3.29(a) from ref. 3.19) at high transonic Mach numbers, for which localized shocks occur at the maximum thickness (where the flow accelerates beyond Mach 1.00 and then decelerates across a shock). These shocks extend for some distance from the airfoil before dissipating into acoustic disturbances. Extended shocks of this sort are also

shown in photographs of fighter aircraft in flight at high subsonic Mach numbers during low altitude passes such as shown in fig. 3.29(b) (refs. 3.45 and 3.46). The explanation of why the shock waves are visible is given in reference 3.45 (p. 4) as follows:

The freestream flow accelerates to supersonic speeds above and below the wing, causing the flow to condense in the expansion waves in the front portion of the condensation pattern. The aft end of the pattern is created by a shock wave through which the flow is decelerated back to subsonic speeds. The rapid temperature rise through the shock causes the condensed flow to evaporate.



(a) NACA 16-2122 airfoil in wind tunnel, Mach 0.90 (ref. 3.19).



(U.S. Navy photo, 050918-N-2328P-382)

(b) F/A-18F during a high-speed, low altitude pass.

Figure 3.29. Transonic flow fields.

The aircraft, like the airfoil has a maximum thickness (equivalent cross-sectional area distribution) such that the local flow can be equal to or exceed Mach 1.0 at some given free-stream transonic Mach number. These localized shocks have been observed to extend outward and downward as much as 30 airplane body lengths. The intensity of the shocks is substantial because of the very low altitudes and the signature (fig. 3.30), is considerably different in nature from the normally observed N-wave-type signature associated with a fully-developed supersonic flow field (see, for example, the discussion on a similar transonic signature presented in fig. 3.14).

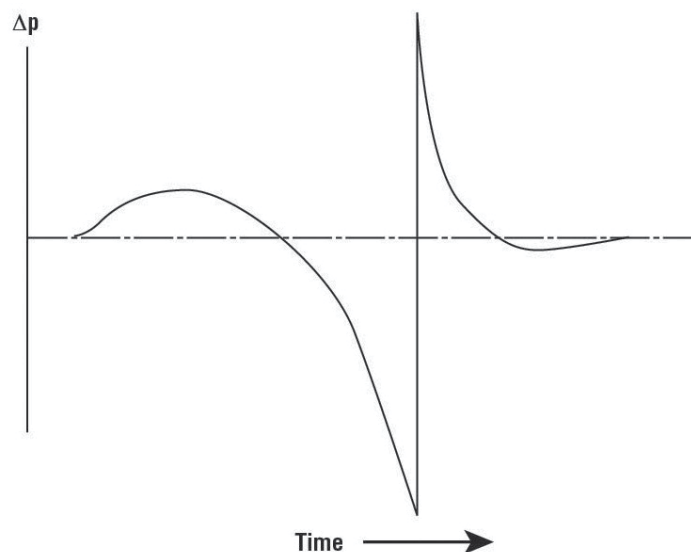


Figure 3.30. Character of transonic boom signature.

A detailed analysis of low-altitude transonic flight-test data (ref. 3.31) has indicated that existing meteorological conditions influence the vertical extent of attached shock waves produced at nearly sonic flight. Aircraft Mach number also has a direct influence on the strength and vertical extent of the attached shock waves. The extension of these attached shock waves to lower altitude may explain several accidental sonic booms produced by low-altitude, marginally subsonic aircraft (although Mach meter and altimeter errors may also be responsible).

Booms from Dive Pull-Up Maneuver

For aircraft in non-level flight, in a climbing or diving condition, the sonic boom propagation situation can change significantly as compared to that for level flights. The climb angle always directs or aims the shock wave and thus the boom away from the ground, whereas a dive angle directs or aims the shock wave and thus the boom toward the ground. The sketches presented in figure 3.31 can be useful in illustrating the influence of climb and dive angle on shock propagation. Figure 3.31 shows three aircraft all flying at the same high subsonic Mach number and altitude with the one on the left in level flight, the one in the center in a climb, and the one on the right in a dive. The shock wave and the ray path along which they propagate are also shown in the figure. Recall that it was stated earlier in these discussions that the ray always travel perpendicular to the shocks and at the local speed of sound. It is quite apparent from the three sketches in figure 3.31 that a climb angle essentially rotates the level flight shock-ray pattern upward, whereas the dive angle rotates the level flight shock rays downward. Another way of stating this from a propagation point of view is that a climb angle acts to effectively reduce the level flight Mach number, whereas a dive angle acts to effectively increase the Mach number.

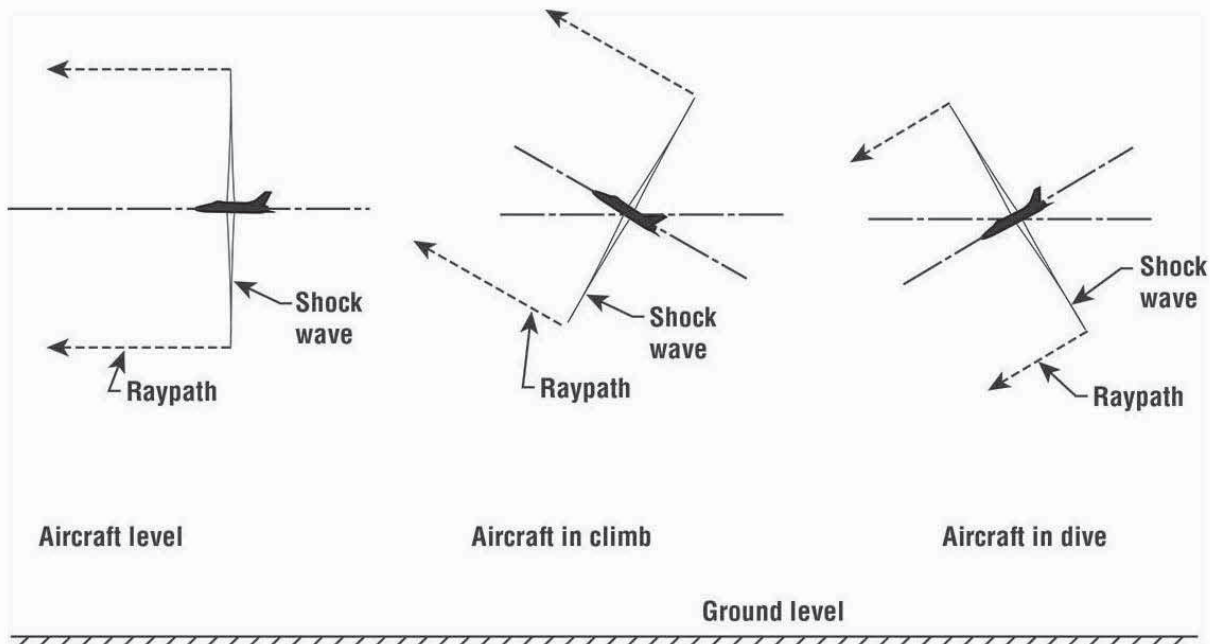


Figure 3.31. Nature of shock wave-ray paths of aircraft at a steady Mach number less than 1.0.

Now that the influence of dive angle has been presented, a discussion of the possibility of a sonic boom being observed on the ground during a high subsonic Mach number ($Mach < 1.0$) dive of an aircraft with a pull-up at relatively high altitudes (10,000 to 15,000 feet) is in order. A schematic illustration of such a situation is shown in figure 3.32.

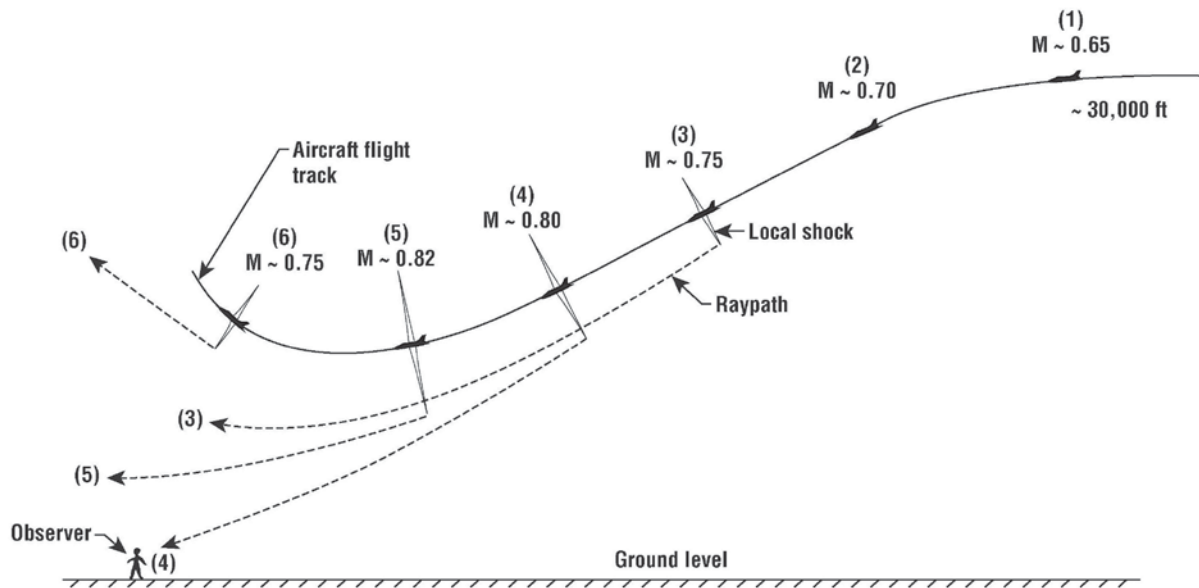


Figure 3.32. Schematic illustration of local shock waves and ray paths emanating from an aircraft in a 20° dive at Mach < 1.0 .

The aircraft is assumed to enter the dive from level flight in a standard atmosphere at about 30,000 feet and Mach 0.65 at position (1) indicated in figure 3.32. As the aircraft descends during the 15° to 20° dive it accelerates to about Mach 0.82 at the bottom of the dive at which time an 8-g pull-up is initiated and the Mach number then decreases to 0.75 at position (6). Note that during the dive, local shock waves appear and extend above and below the aircraft. The distance the shock waves extend from the aircraft increases as Mach number increases. For simplicity, only the ray paths associated with each of the local shocks that extend below the aircraft are shown. A similar picture would exist regarding the local shocks that extend above the aircraft. These ray paths start out perpendicular to the shock front and then begin refraction upward because of the refraction due to increasing temperature as they propagate towards the ground. There is only a short portion of the flight path between positions (3) and (5) where the shocks find favorable conditions (relative to shock angle-dive angle and ray path) to propagate the many thousand feet to the ground. It should be noted that the probability of these shocks reaching the ground is enhanced for the case of cooler temperatures at ground level and tailwinds at flight altitude. Likewise, warmer temperatures at ground level and headwinds at altitude would cause the shock to refract upward and away from the ground. Such weather situations are more influential in shallower dive angles than at steeper dive angles. Interestingly, Barger addressed these issues in a short technical note in 1967 (ref. 3.37).

Chapter 3 Summary Remarks

Rapid deviations of a vehicle from steady-level flight produce significant changes in ground shock patterns resulting in the observation of multiple booms and focused booms. These booms are one-time occurrences and are not dragged along the ground behind the aircraft like carpet booms.

Focus boom regions on the ground are extremely localized with typical focus factors on the order of two to five for transition booms. For commercial supersonic flight operations, most focus booms can be avoided or minimized except for the transition focus experienced during acceleration from subsonic to supersonic speeds. Placement of these focus booms to within ± 1000 feet of the desired location has been demonstrated.

The signature shape for transition flight is shown to have a significant influence in altering the focus boom levels. In addition, atmospheric turbulence at lower altitudes (< 5000 feet) also seems to diffuse focus boom levels.

Current prediction codes have matured sufficiently such that we can predict maneuver shock patterns on the ground and overpressure magnitudes, including focused boom regions.

Sonic booms have been experienced at ground level from relatively low-altitude flights at Mach numbers less than 1.0 and from steep dives from high altitude at high subsonic Mach numbers.

Chapter 3 References

- 3.1 Maglieri, D. J. and Lansing, D. L.: Measured Shock Wave Ground Pressure Patterns From Aircraft in Maneuvers. NASA TN D-2370, 1964.
- 3.2 Lansing, Donald L.: Some Effect of Flight Maneuvers on the Distribution of Sonic Booms. Proceedings of Symposium on Atmospheric Acoustic Propagation, Vol.1, June 14–15, 1961, pp. 24–43.
- 3.3 Kerr, T. H.: Experience of Supersonic Flying Over Land in the United Kingdom. AGARD Report 250, Sept. 1959.
- 3.4 Hubbard, Harvey H.; Maglieri, Domenic J.; Huckel, Vera; and Hilton, David A.: Ground Measurements of Sonic Boom Pressures for the Altitude Range of 10,000 to 75,000 Feet. NASA TR R-198, 1964.
- 3.5 Lansing, Donald J. and Maglieri, Domenic J.: Comparison of Measured and Calculated Sonic-Boom Ground Patterns Due to Several Different Aircraft Maneuvers. NASA TN D-2730, 1965.
- 3.6 Downing, Micah; Zamot, Noel; Moss, Chris; Morin, Daniel; Wolski, Ed; Chung, Sukhwan; Plotkin, Kenneth; and Maglieri, Domenic J.: USAF Flight Investigation of Focused Sonic Booms; Project “HAVE BEARs,” NASA CP-3335, July 1996, pp. 259–277.
- 3.7 Wanner, Jean-Claude; Vallee, Jacques; Vivier, Claude; and Thery, Claude: Theoretical and Experimental Studies of the Focus of Sonic Booms. *J. Acoust. Soc. Am.*, Vol. 52, No. 1, Pt. 1, July 1972.
- 3.8 Plotkin, K. J. and Cantril, J. M.: Prediction of Sonic Boom at a Focus, AIAA paper 76-2, Jan. 1976.
- 3.9 Guiraud, J. P.: *Acoustique Geometrique, Bruit Ballistique des Avions Supersoniques et Focalisation*, *J. Mechanique*, Vol. 4, 1965, pp. 215–267.
- 3.10 Whitham, G. B.: On the Propagation of Weak Shock Waves. *Journal of Fluid Mechanics*, Vol. 1, Part 3, Sept. 1956.
- 3.11 Gill, P. M. and Seebass, A. R.: “Non-Linear Acoustic Behavior at a Caustic: An Approximate Solution”, *AIAA Progress in Astron. Aeronautics*, Nagamatsu, H.J.T. (Ed.). MIT Press, 1975.
- 3.12 Gill, P. M.: “Nonlinear Acoustic Behavior at a Caustic”, Ph.D. Thesis, Cornell University, June 1974.
- 3.13 Plotkin, K. J.; Downing, J. M.; and Page, J.: USAF Single Event Sonic Boom Prediction Model: PCBoom. *J. Acoust. Soc. Am.*, 95(5), Part 2, May 1994, pp. 28–29.
- 3.14 Sanai, J.; Toong, T. Y.; and Pierce, A. D.: “Ballistic Range Experiments on Superbooms Generated by Refraction” and “Ballistic Range Experiments on the Super-boom Generated at Increasing Flight Mach Numbers”, *J. Soc. Am.*, 59(3), 1976, pp. 513–524.
- 3.15 Maglieri, D. J.; Hilton, D. A.; and McLeod, N. J.: Further Experiments on the Effects of Atmospheric Refractions and Aircraft Accelerations on sonic Boom Ground Pressure Patterns. NASA TN D-3520, July 1966.

- 3.16 Downing, Micah; Zamot, Noel; Moss, Chris; Morin, Daniel; Wolski, E.; Chung, Sukhwan; Plotkin, Kenneth; and Maglieri, Domenic J.: Measurement of Controlled Focus Booms from Maneuvering Aircraft. USAF/AL, AL-OE-WP-TR-1997-0185, Feb. 1998.
- 3.17 Plotkin, Kenneth J.: Sonic Boom Focal Zones from Tactical Aircraft Maneuvers, *Journal of Aircraft*, Vol. 30, No. 1, Jan.–Feb. 1993.
- 3.18 Vallee, J.: Operation Jericho-Focalisation, *Rapport D'Edute*, CEV, No. 272, Oct. 1967.
- 3.19 Maglieri, Domenic and Plotkin, Kenneth J.: Sonic Boom, Chapter 10, pp. 519-561, *Aeroacoustics of Flight Vehicles, Theory and Practice*. NASA RP 1258, Vol. 1 and WRDC TR 90-3052, Aug. 1991.
- 3.20 Plotkin, Kenneth J.: State of the Art of Sonic Boom Modeling. *J. Acous. Soc. Am.* 111(1), Part 2, Jan. 2002, pp. 520–536.
- 3.21 Auger, T. and Coulouvrat, F.: Numerical Simulation of Sonic Boom Focusing. *AIAA Jour.* Vol. 40, No. 9, Sept. 2002, pp. 1726–1734.
- 3.22 Marchiano, R. and Coulouvrat, F.: Numerical Simulation of Shock Wave Focusing at Fold Caustics with Application to Sonic Boom. *J. Acoust. Soc. Am.* 114(4), Pt. 1, Oct. 2003, pp. 1758–1771.
- 3.23 Maglieri, D. J.; Bobbitt, P. J.; Plotkin, K. J.; Kandil, O. A.; and Zheng, X.; and Massey, S. J.: Focused and Steady-State Characteristics of Shaped Sonic Boom Signatures: Prediction and Analysis. NASA CR 2011-217156, June 2011.
- 3.24 Pawlowski, J. W.; Graham, D. H.; Boccadoro, C. H.; Coen, P. G; and Maglieri, D. J.: Origins and Overview of the Shaped Sonic Boom Demonstration Program. AIAA-2005-0005, Jan. 2005.
- 3.25 Plotkin, K. J.; Haering, E. A., Jr.; Murray, J. E.; Maglieri, D. J.; Salamone, J.; Sullivan, B. M.; and Schein, D.: Ground Data Collection of Shaped Sonic Boom Experiment Aircraft Pressure Signatures. AIAA 2005-0010, Jan. 2005.
- 3.26 Plotkin, K. J. and Grandi, F.: Computer Models for Sonic Boom Analysis: PCBOOM4, CABoom, BOOMap, CORBoom. Wyle Report WR-02-11, June 2002.
- 3.27 Plotkin, K. J.; Martin, R.; Maglieri, D. J.; Haering, E. A., Jr.; and Murray, J. E.: Pushover Focus Booms from the Shaped Sonic Boom Demonstrator. AIAA-2005-0011, Jan. 2005.
- 3.28 Vallee, J.: Operation Jericho-Virage, *Rapport D'Etude*, CEV, No. 277, May 1969.
- 3.29 Vallee, J.: Operation Jericho-Carton, *Rapport D'Etude*, CEF No. 291, May 1973.
- 3.30 Haglund, George T. and Kane, Edward J.: Flight Test Measurements and Analysis of Sonic Boom Phenomena Near Shock Wave Extremity, NASA CR-2167, Feb. 1973.
- 3.31 Haglund, George T. and Kane, Edward J.: Analysis of Sonic Boom Measurement Near Shock Wave Extremities for Flight Near Mach 1.0 and for Airplane Accelerations. NASA CR-2417, 1974.
- 3.32 J. Page; K. Plotkin; E. Haering; D. Maglieri; Cowart, R.; Salamone, J.; Elmer, K.; Welge, H.; Ladd, J.: SCAMP: Superboom Caustic Analysis and Measurement Project Overview. AIAA-2013-0930, June 2013.
- 3.33 Plotkin, K. and Maglieri, D.: SCAMP: Experimental Design of a Sonic Boom Focus Flight Test. AIAA-2013-0931, January 2013.

- 3.34 Haering, E.; Cliatt, L.; Plotkin, K.; Maglieri, D.; Delaney, M.; Brown, J.: SCAMP: Rapid Focused Sonic Boom Waypoint Flight Planning Methods, Execution, and Results. AIAA-2013-0932, January 2013.
- 3.35 Page, J.; Hobbs, C.; Haering, E.; Maglieri, D.; Shupe, R.; Hunting, C.; Giannakis, J.; Franzeska, H.: SCAMP: Focused Sonic Boom Experimental Execution and Measurement Data Acquisition. AIAA-2013-0933, January 2013.
- 3.36 Salamone, J.; Sparrow, V.; and Cowart, R.: SCAMP: Solution of the Lossy Nonlinear Tricomi Equation for Sonic Boom Focusing. AIAA-2013-0935, January 2013.
- 3.37 Piacsek, A.: SCAMP: Application of Nonlinear Progressive-wave Equation to Sonic Boom Transition Focus. AIAA-2013-1064, January 2013.
- 3.38 Elmer, K.; Welge, H.; Salamone, J.; Cowart, R.: SCAMP: Supersonic Passenger Transport Transonic Acceleration Flight Profiles with Considerations of Focused Sonic Boom. AIAA-2013-1065, January 2013.
- 3.39 Maglieri, Domenic J.; Henderson, Herbert R.; Massey, Steven J.; and Stansbery, Eugene G.: A Compilation of Space Shuttle Sonic Boom Measurements. NASA CR-2011-217080, April 2011.
- 3.40 Haglund, G. E. and Kane, E. J.: Effect of SST Operational Maneuvers on Sonic Boom. *J. Acoust. Soc. Am.*, Aug. 1972, pp. 563–568.
- 3.41 Plotkin, Kenneth J.: Potential Sonic Boom Focal Zones From Space Shuttle Reentry. Wyle Research Report. WR 89-11, July 1989.
- 3.42 Coulouvrat, Francois; Blurich, Reinhard; and Heimann, Deitrich: Meteorologically Induced Variability of Sonic Boom of a Supersonic Aircraft in Cruising or Acceleration Phase. ISNA 17 AIAA Conf. Proc, Vol. 838, Melville, NY, 2006, pp. 579–586.
- 3.43 Blackburn, Albert: *Aces Wild: The Race for Mach 1*, Scholarly Resources Inc., 1998.
- 3.44 Yeager, C. and Janos, L.: *Yeager; An Autobiography*, Bantam Books, July 1985, p.130.
- 3.45 Campbell, James F.; Chambers, Joseph R.; and Rumsey, Christopher L.: Observation of Airplane Flow Fields by Natural Condensation Effects. AIAA 88-0190, Jan. 1988.
- 3.46 Vapor Condensation Makes F-14 Shockwaves Visible. *Aviation Week and Space Technology*, Vol. 107, No. 21, Nov. 21, 1977, pp. 46–47.
- 3.47 Barger, Raymond L.: Sonic Booms Attributed to Subsonic Flight. *AIAA Journal*, Vol. 5, May 1967, pp. 1042–1043.

CHAPTER 4 IN-FLIGHT FLOW-FIELD SIGNATURE MEASUREMENTS

Sonic boom prediction techniques benefit greatly from the experimental validation of the shock flow field surrounding an aircraft in supersonic flight. This validation can be acquired by means of wind tunnel and/or flight tests. In the former, there are limitations due to the fact that measurements are limited to the near- and mid-fields because of the tunnel test section and model size, as well as the fact that the medium surrounding the model does not represent the real atmosphere (i.e., it has uniform free stream conditions). Flight tests, on the other hand, provide a real environment and yield both near- and mid-field results along with the all important ground measurements. Near-, mid-, and far-field pressure signatures can be measured by probing aircraft or other means. In this section, several methods used to describe the flow field about an aircraft in supersonic flight will be presented along with a summary of the full-scale in-flight flow-field measurement database that has been acquired on aircraft over the last 60 years.

Review of Available Methods

An indication of the various methods used to describe the shock flow field about an aircraft in supersonic flight is schematically illustrated in figure 4.1. These methods include probe flights with instrumented supersonic aircraft, airborne measurements using very low-speed instrumented manned or unmanned aircraft, measurements taken with transducers located on high mountains, on blimps hovering high above the ground surface, on relatively high fixed towers, and at ground level. Schlieren photography has also been used to qualitatively describe the shock flow field about an aircraft in supersonic flight.

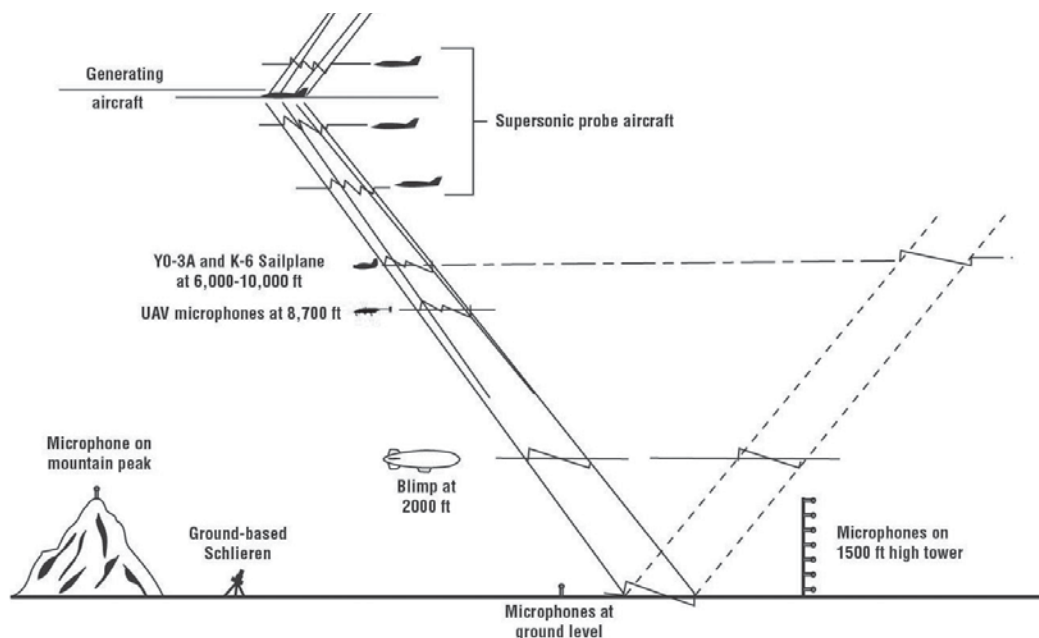


Figure 4.1. Methods used to measure shock flow field about an aircraft in supersonic flight.

Probing the near and mid flow field of the shock generating aircraft by means of an instrumented aircraft in supersonic flight passing or being passed at positions above, to the side, and below has been the most widely used research method and provides the clearest detail concerning the complex nature of the shock flow field near the aircraft.

Sonic boom measurements have been made on high mountains, but little, if any, data are available in existing literature. Sonic boom signatures have been measured by means of balloon-borne and tower-mounted microphones and provide considerable information on signature distortion due to turbulence in the few thousand feet of the earth's boundary layer, ground reflection coefficients and information regarding the extremities of shock waves

for flight operations at Mach cutoff and at lateral cutoff. Ground level measurements make up the majority of the sonic boom database.

Airborne and ground-based outdoor Schlieren methods and subsonic airborne in-flight techniques are recent and innovative approaches to defining the aircraft's supersonic flow field. These techniques are still undergoing development.

Application of the in-flight supersonic flow-field data acquired through any of the various methods/techniques just discussed is valuable for the design of an aircraft having a minimized boom waveform. As indicated in table 4.1, a description of the supersonic shock flow field will provide information on the number, location, and strength of the shocks contained in the flow field and can also show how many aircraft body lengths (h/l) it takes for these shocks to coalesce into their final form. Qualitative and quantitative information of this nature provides a means of validating the present computational fluid dynamic (CFD) prediction codes out to much larger distances than are attainable in wind tunnels using small models. This provides insight into determining when the flow field about the aircraft has developed such that it is approximately equivalent to a body of revolution when the ray tracing sonic boom propagation codes can be properly applied and correctly predict pressure signatures at all locations at ground level.

Table 4.1. Significance of In-Flight Supersonic Flow-Field Data

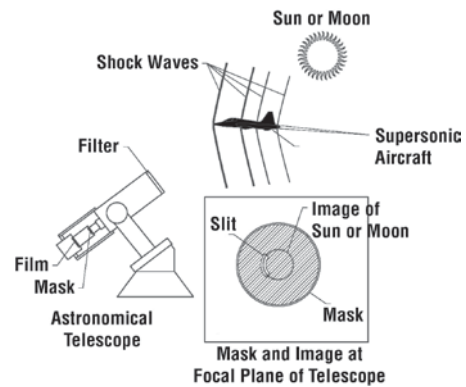
- | |
|--|
| <ul style="list-style-type: none">• Establishes number, location, strength of shocks.• Describes shock wave coalescence.• Validates prediction methods.• Provides insight into waveform persistence/aging.• Source of information on turbulence scale/waveform shape/shock rise time.• Describes atmospheric absorption.• Measured near- and mid-field signatures are not significantly contaminated by atmospheric instabilities. |
|--|

Measurement techniques, such as in-flight and ground-based Schlieren photography, also provide insight into the persistence of a sonic boom signature shock structure as it moves from locations very near the aircraft to many body lengths away as the local shocks age (move further away) and coalesce. Although the Schlieren observations are only qualitative in nature, they do provide excellent imagery of the shocks from the different aircraft components as distance from the aircraft increases.

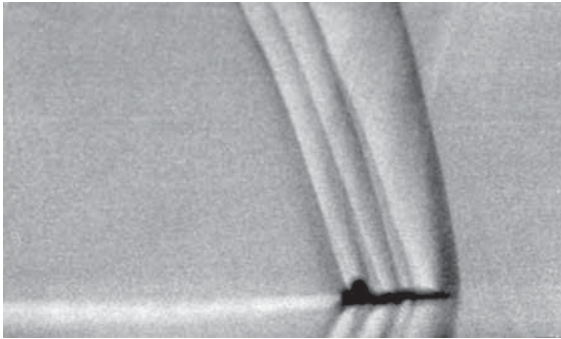
The concept and development of the ground-based Schlieren to obtain images of Aircraft in Flight (SAF), see figure 4.2 (ref. 4.1), was aimed at enhancing the understanding of the structure and development of the supersonic flow system about an aircraft. A photograph of the system is depicted in figure 4.2(a) and a schematic of its set-up for viewing aircraft in supersonic flight is presented in figure 4.2(b). The bottom two photographs, figure 4.2(c) and figure 4.2(d), are the results acquired by the ground-based Schlieren showing the shock systems emanating from a T-38 and F-18, respectively, in supersonic flight. In both photographs, the multiple shocks are clearly evident to h/l of about 2 to 5 and the exhaust stream boundaries are also well defined.



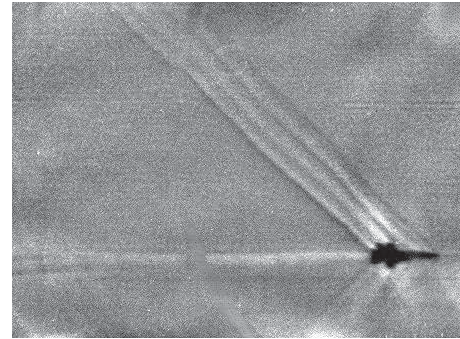
(a) SAF setup on runway at Wallops.



(b) Schlieren setup for aircraft in flight.



(c) SAF of T-38 at 32,000 ft slant range and Mach 1.1.



(d) SAF of F-18 at 60,000 ft slant range and Mach 1.4.

Figure 4.2. Description and results from ground-based Schlieren (adapted from ref. 4.1).

Whereas the ground-based Schlieren is aimed primarily at providing a visual picture of the shock system above and below the aircraft, an airborne aircraft system could provide significant close-up detail into the structure of the shock system surrounding the aircraft including wakes and exhaust systems. Continuing improvements and developments on the ground- and airborne-based Schlieren systems will tremendously enhance the database and, thus, the ability to properly handle the analysis of the near-, mid-, and far-field sonic boom characteristics of low-boom shaped vehicles.

Subsonic airborne measurement techniques also provide a source of information on atmospheric turbulence as it relates to signature distortions and shock rise times. Better definition of the influence of atmospheric absorption on shock smoothing (rise time) could also be inferred. Many of the shock flow-field observation techniques, especially the Schlieren photography and subsonic airborne systems, would provide a database regarding the initial conditions of the secondary (over-the-top) sonic boom. Finally, in-flight signature measurements are not as likely to be contaminated by atmospheric instabilities that are encountered in measurements at ground level.

Brief Review of Existing Database

A brief summary of the in-flight supersonic flow-field database that has been gathered over six decades is provided in table 4.2 and includes the test aircraft, location of the flow-field observation about the aircraft, number of body lengths (h/l) from the test aircraft, the technique used, type of results acquired, the time period of the observations, and the publication source. An examination of the information contained in the chart indicates that the present sonic boom flow-field database is a result of 13 experiments involving 12 different aircraft – the F-100, F-104, B-58, F-106, XB-70, F-18, SR-71, T-38, F-4, F-5E, SSBD, and F-15 Quiet Spike. The majority of flow-field experiments (identified in table 4.2) have been conducted using supersonic aircraft with instrumented probes and flying below the test aircraft at distances of from 0.4 to 95 body lengths, and also above and to the side of the test aircraft from 1 to 33 body lengths away (refs. 4.1 – 4.17).

Airborne measurements using transducers carried aloft on blimps (ref. 4.5) and stationary transducers located on a high tower (refs. 4.8 – 4.11) have provided very useful information but are most useful in measuring the far-field boom signatures due to their close proximity to the ground.

The most recent developments in flow-field definition techniques that can be used to describe the nature of the shock-flow field generated by an aircraft are the subsonic airborne systems (refs. 4.12, 4.13, 4.15 and 4.16). To minimize the non-stationary influences on measurements using sailplanes, their flights should be flown perpendicular to the generating aircraft flight track and directly under the aircraft. Subsequent figures provide details of measurements made on several of the configurations listed in table 4.2 and include those references (4.2 – 4.4, 4.6, 4.7, 4.12, and 4.14 – 4.17).

Table 4.2. In-Flight Supersonic Flow-Field Database

Test Aircraft	Observation Location	Separation Distance h/l	Method/ Technique	Data Format	Year	Reference
F-100	Below Side	2-41 2-33	Supersonic probe aircraft	Pressure signals	1956	4.2
F-100 F-104 B-58	Side Side Side	4-8 3-8 1-2	Supersonic probe aircraft	Pressure signals	1960	4.3
B-58	Above Below	17-20 14-96	Supersonic probe aircraft	Pressure signals	1963	4.4
F-106	Below	600	Blimp with airborne microphone	Pressure signals	1963	4.5
XB-70	Below Above	16 11-27	Supersonic probe aircraft	Pressure signals	1966	4.6 and 4.7
F-104	Below	600	1500 high BREN tower w/microphones	Pressure signals	1970	4.8-4.11
SR-71	Below	0.4-100	Supersonic probe aircraft and airborne platform	Pressure signals	1993	4.12
T-38	Above	0-2	Outdoor Schlieren	Photographs	1994	4.1
F-18	Above Below	0-4 0-59	Outdoor Schlieren	Photographs	1994	4.1
F-4	Below	38-86	Subsonic airborne platform	Pressure signals	1994	4.13
F-5E	Below	1.2-27	Supersonic probe aircraft	Pressure signals	2002	4.14
SSBD	Below Side	1.2-440 2.4	Supersonic probe aircraft and airborne platform	Pressure signals	2003-04	4.15 and 4.16
F-15 Quiet Spike	Above Below Side	4-8 1.4-10 2.7	Supersonic probe aircraft	Pressure signals	2006	4.17

Early Flight Tests

Insight into Nature of Flow Field

The first in-flight flow-field tests undertaken with the objective of determining and measuring the shock-wave pressure pattern surrounding an F-100 aircraft in steady-level supersonic flight was at Edwards Air Force Base in 1956 (ref. 4.2). At the time, the Century series jet fighter aircraft, capable of flying at supersonic speeds with ease, were being introduced and there was an urgent need to extend the general knowledge of the shock waves that generated the booming noise.

Time histories of the variation in static pressure caused by the shock waves were obtained by flying an F-100 aircraft, instrumented for static pressure measurements, through the shock waves generated by a second F-100. Fly-by passes were made to the right of and below the generating aircraft, which was flying at a speed of Mach 1.05 and an altitude of 35,000 feet. The separation distance between the two aircraft was varied from about 85 to 1700 feet. Several passes were also made below the generating aircraft flying at a speed of Mach 1.05 and an altitude of 25,000 feet with the separation distance varying between about 200 and 1000 feet.

The variations of static pressure experienced during the fly-by's were measured by the use of a differential pressure transducer and were recorded on a multiple channel oscillograph. A photo panel operated by the pilot recorded Mach number and altitude. Pressure transducers were located in the nose compartment of the F-100 and were connected to two static holes located on the test nose boom. Provisions were included to permit the pilot to close off one side of the pressure cell when the aircraft had been stabilized at the desired Mach number and altitude. This established a reference static pressure. During rapid climbs and descents both sides of the pressure cell were opened to preclude the possibility of overloading the cell. The separation distance between the aircraft was obtained by using a 35-mm movie camera mounted in the canopy of the instrumented aircraft. Continuous photographs were made of the shock generating aircraft during the passes. Then, using the known aircraft length, camera focal length, and measured image size it was possible to compute the range and azimuth.

Eighteen of the twenty signatures measured from these flight tests are shown in figure 4.3 (ref. 4.2). The variation in signature length is a result of the probing aircraft at different closure rates through the generating aircraft flow field. It can be seen that in the near field of the aircraft three or four shocks are evident and these are coalescing to an N-wave as distance from the aircraft increases. Signature overpressures varied from about 12 lbs/ft² at the close-in distances to about 2 lbs/ft² at the largest distances. Although only the nearest and furthest signatures are labeled with bow and tail wave overpressures, all the traces are to the same scale. Note also that in the near field, the tail shock pressures are greater than the bow shock pressures.

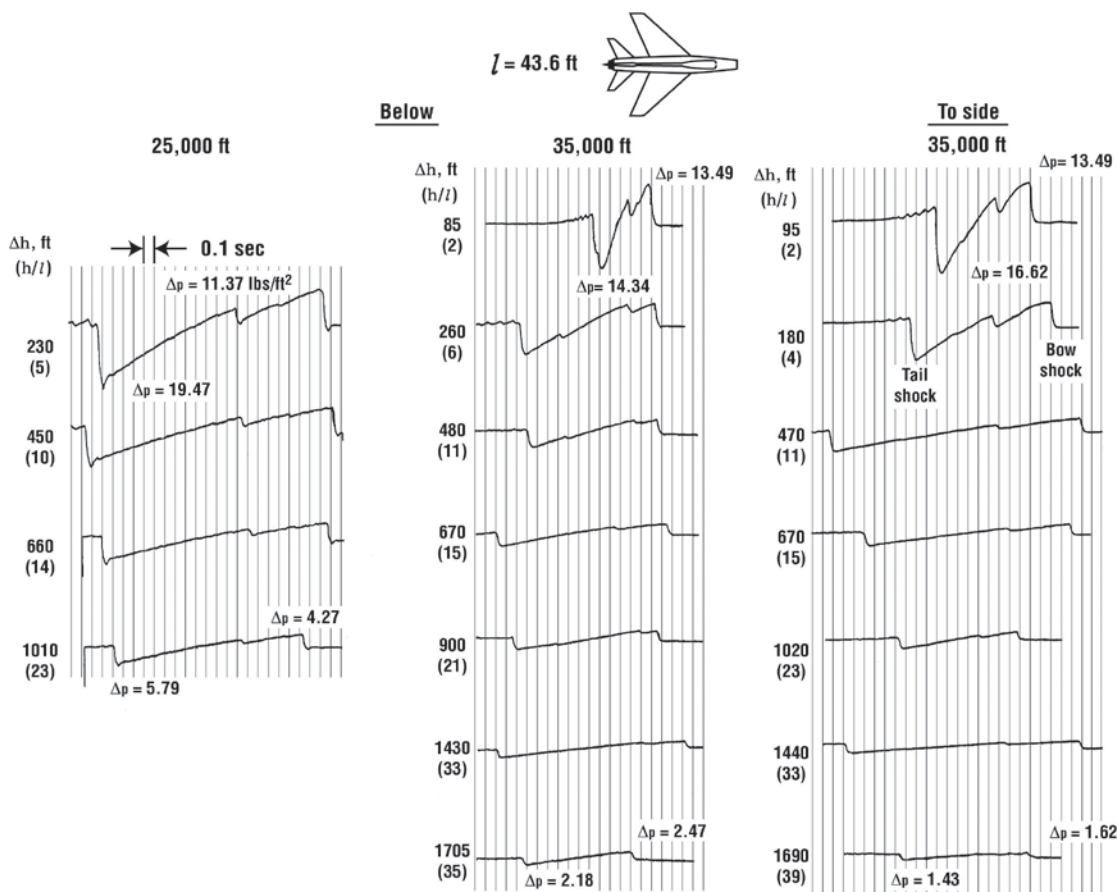


Figure 4.3. In-flight flow-field signatures measured below and to the side of an F-100 aircraft at Mach 1.05 (adapted from ref. 4.2).

It should be noted that these signatures lack fidelity in describing the shock rise times as a result of the measurement system frequency response. In addition, they were obtained at relatively low Mach numbers, separation distances are estimated, and aircraft weight is not provided. However, considerable amounts of information were gained from their analysis and include confirmation of current prediction codes in calculating the number and strength of local shocks and to confirm predictions of shock coalescence (ref. 4.18).

Measurements of Near-Field Shocks from Passing Aircraft

In 1960, a series of in-flight flow-field probe measurements were made to the side of an F-100, F-104, and B-58 at distances of from 120 to 425 feet (ref. 4.3). Data were obtained on the F-100 and F-104 at Mach 1.2 and on the B-58 at Mach 1.3 to Mach 1.8. The flow field to be measured was generated by the lead airplane, which was flown at a pre-selected Mach number. The passing airplane was flown through this flow field at a constant passing rate and variations in static pressure were measured by a sensitive pressure transducer mounted in the nose boom of the passing airplane. To determine the lateral-separation distance, a motion picture camera was mounted on the passing airplane to photograph the lead airplane. The flight altitude at which these flight tests were conducted is not given in the report nor is the weight of each aircraft. Figure 4.4 presents the measured signatures (ref. 4.3). Because of the experimental procedure used, the absolute lengths of the flow fields were not determined; therefore, the measured pressure signatures shown in figure 4.4 are presented in terms of non-dimensional distances between the front and rear shocks.

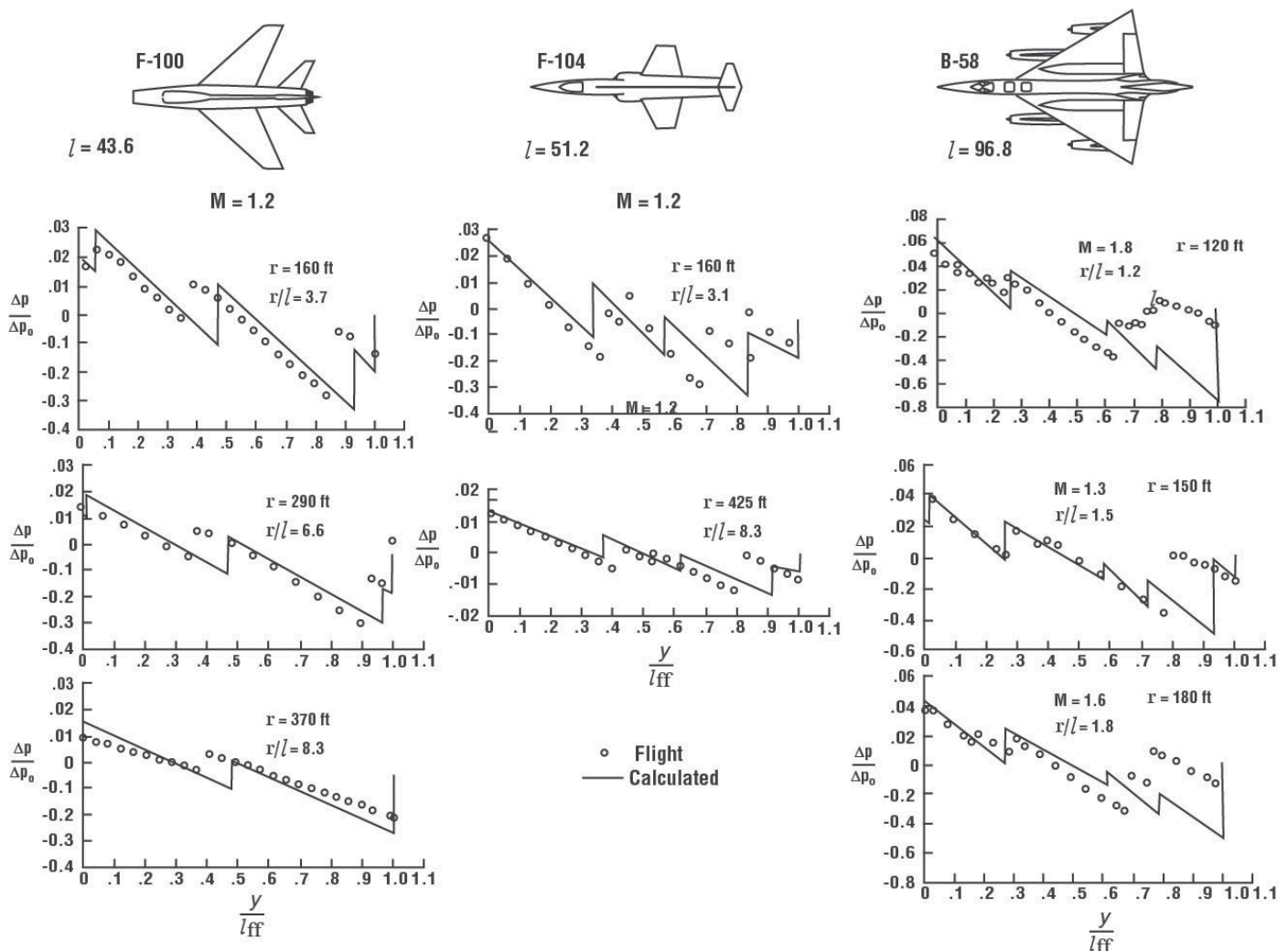


Figure 4.4. In-flight flow-field signatures measured to side of aircraft (adapted from ref. 4.3).

It can be observed that the measured signature data is a result of readings taken at discrete time intervals from the continuous pressure traces obtained with the transducer in the probe aircraft nose boom. As such, details of actual shock rise time and shock wave closure at the tail shock are not possible, although the actual number of shocks is shown. In addition, calculated boom signatures were also made, as shown by the solid traces on the chart, using the Whitham equivalent body analysis (ref. 4.19). Since the character of the signatures is volume dominated, one would expect fairly good correlation between prediction and measurements. It should be noted that the normal area distributions (i.e., Mach 1.0) were used in the calculations shown on the figure and they suffice for the low Mach cases. At the Mach 1.6 and 1.8 conditions for the B-58, large discrepancies were anticipated and observed in the vicinity of the tail shock. The correlation was greatly improved by using the area distributions associated with the flight Mach numbers.

Unlike the F-100 signatures, which were made over large distances (fig. 4.3), information regarding shock coalescence from the data in figure 4.4 does not yield much information. However, knowledge and lessons learned can be gleaned from data regarding the influence of inlet spillage and nacelle shocks on the boom signature.

Insight into Effects of Aircraft Lift

With the advent of the U. S. SST program, there was a need for in-flight flow-field measurements above and below a relatively large aircraft in order to assess existing boom prediction codes and their ability to account for both lift and volume effects on the sonic boom signature. Shock coalescence was also of interest regarding sonic boom signature freezing, a condition where Hayes' theory (ref. 4.20) predicts that signature shape beyond the point of freezing will persist indefinitely below the aircraft to the ground.

In response to the need for insight into the volume and lift effects on boom signatures, a series of in-flight flow-field measurements were conducted at EAFB in 1963 by NASA and the USAF involving the 96.8-foot long B-58 (shown in fig. 4.5) as the boom generating aircraft and a specially instrumented F-106 as the probing aircraft (ref. 4.4). The B-58 generating aircraft was flown at about Mach 1.6 in the altitude range of from 40,000 – 48,000 feet with gross weights varying from about 83,000 – 115,000 pounds.



(U.S. Air Force photo)

Figure 4.5. In 1963, a series of in-flight flow-field measurement investigations were conducted at Edwards Air Force Base involving the 96.8-foot long B-58 (shown above) as the boom-generating aircraft and a specially instrumented F-106 as the probing aircraft.

During the flight tests, both radar and optical (Askania) tracking were accomplished. The radar plotting-board tracks were used for ground control of the airplanes while they were getting into the proper position for the test run. The Askania tracking data were used in the data reduction process for determining the speeds and positions of the airplanes during the actual recording of data. One Askania network of three stations was used to track the generating airplane, and a second Askania network of three stations was used to track the instrumented airplane. Accuracy of space positioning was quoted as ± 1 foot and airplane velocity within an accuracy of ± 1 foot per second.

Seven penetrations were made and included two probings above the B-58 at distances of from about 1800 – 2000 feet and five probings below the aircraft at distances of about 1300 – 9000 feet. Measurements of the boom signature were also acquired at ground level. Figure 4.6 presents a schematic of the aircraft and shock flow field with actual tracings of the measured boom signatures above and below the aircraft flying at a speed of about Mach 1.6, an altitude of 48,000 feet, and a gross weight of about 115,000 pounds.

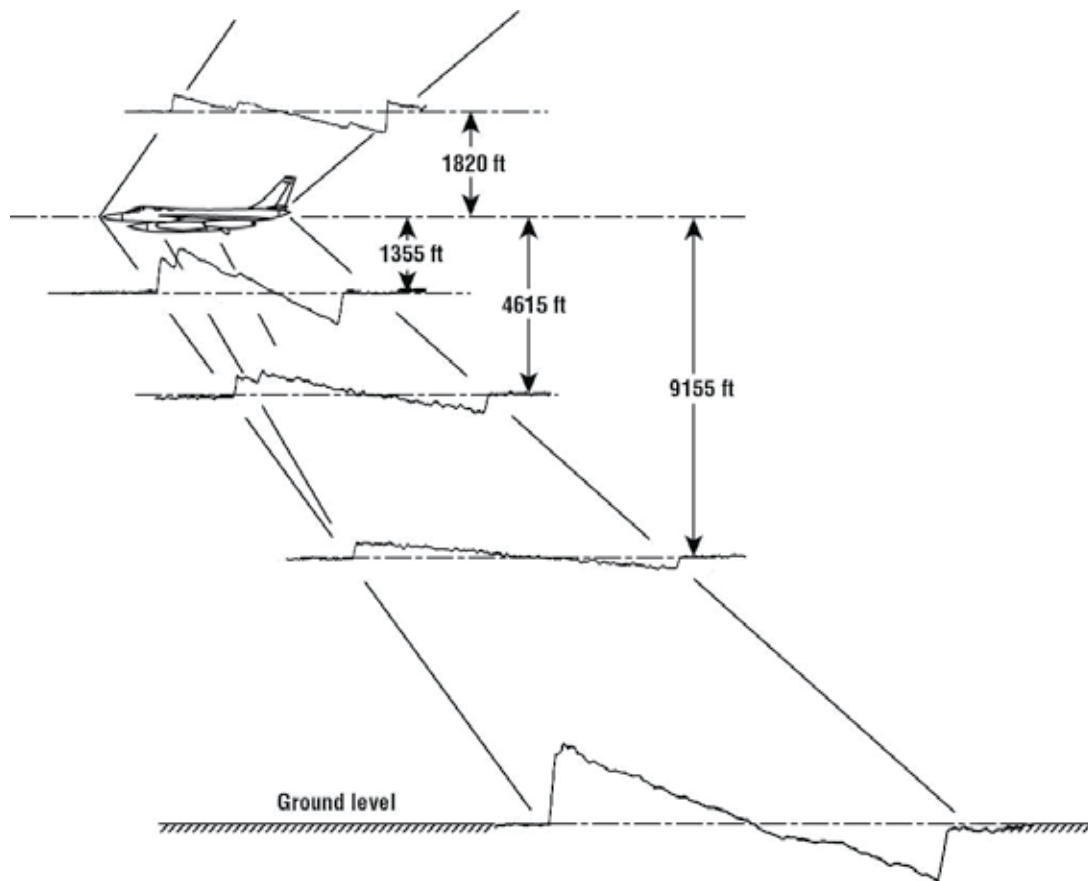


Figure 4.6. In-flight sonic boom signatures measured above and below a B-58 aircraft (adapted from ref. 4.4).

Examination of the signatures revealed several significant features. Below the aircraft at 1355 feet, the pressure signature contains four shocks – the bow and tail shocks plus the shocks off the front and rear of the MB-3 pod carried under the aircraft. As these shocks propagating downward below the aircraft they coalesce and the signatures progress from saw-tooth in character to an N-wave at about 9000 feet. Another obvious observation is that aircraft lift effects on boom signatures are evident when comparing the signatures measured above and below the aircraft at equal distances, especially in regards to the amplitude and location of the shocks.

The influence of lift on the sonic boom signature was further defined by flying the B-58 at 83,000 pounds gross weight at a lower altitude of 40,000 feet and about the same Mach number. The results of the two measurements obtained at about 1800 feet distance are given in figure 4.7.

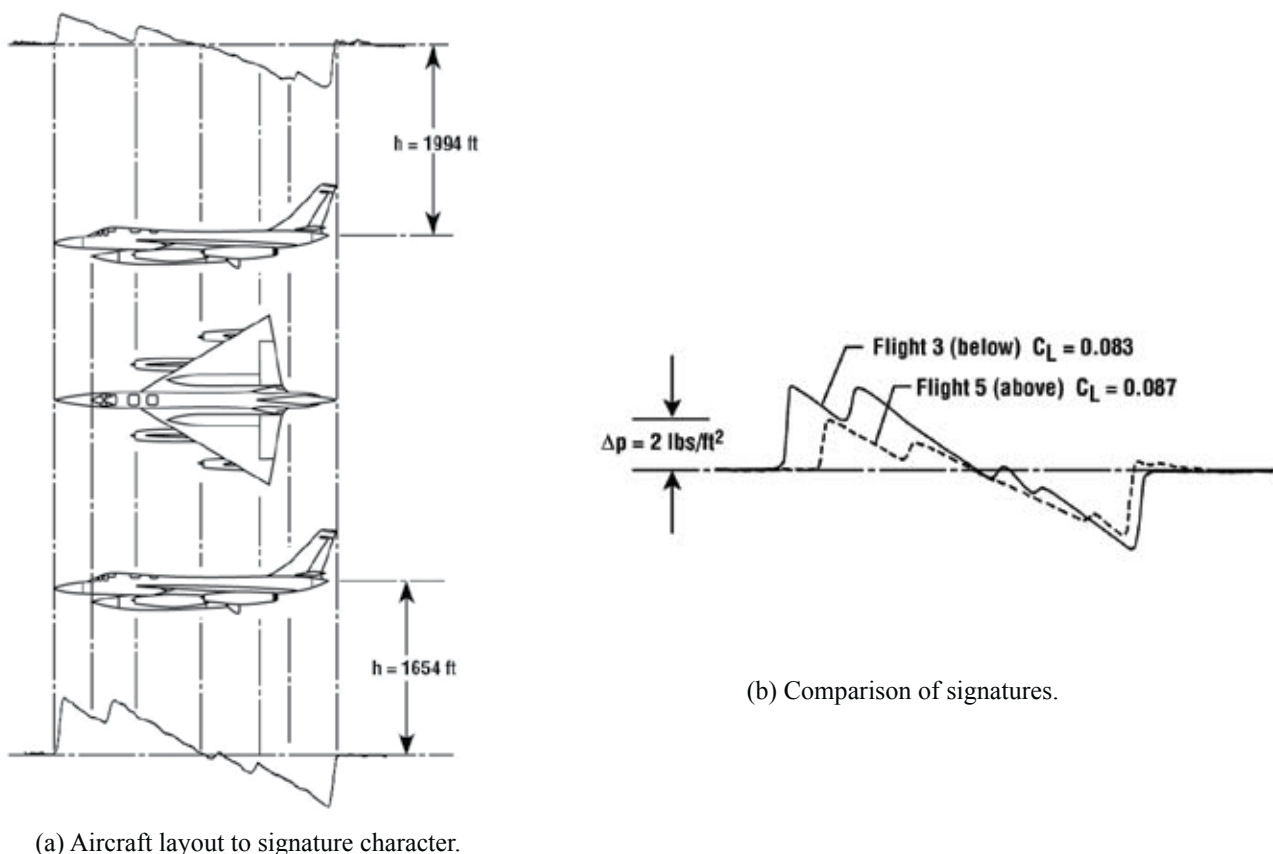


Figure 4.7. In-flight signatures measured above and below a B-58 at similar lift coefficients (adapted from ref. 4.4).

Referring to figure 4.7(a), a distinct difference in the above and below measured signatures, as related to the aircraft geometry, is evident in terms of the number of shocks. It can also be seen in figure 4.7(b) that, with the aircraft at nearly the same lift coefficient, the contrast between the two boom signatures measured at nearly the same separation distance above and below the aircraft is much greater below the aircraft due to the lift contribution.

Interestingly, with the exception of some unpublished correlations between the close-in measurements and prediction, this probing database has not been published before. Part of the reason is that a good geometric and wave drag description of the aircraft was not available at the time. Such information is now available (ref. 4.21).

During the 1966–67 U. S. National Sonic Boom Program (ref. 4.22), the opportunity was taken to obtain in-flight flow-field measurements on the 185-foot long delta-wing XB-70 aircraft (see figures 4.8 and 4.9) at EAFB. Sonic boom signatures were acquired above and below the XB-70, which was flown at an altitude of about 37,000 feet, a speed of Mach 1.5, and a weight of about 333,000 pounds. The probing aircraft was an F-104 instrumented with the same nose probe used previously on the F-106 probes of the B-58 (ref. 4.4). Six signatures were obtained including one measured at about 3000 feet above, but about 7000 feet laterally from the aircraft flight path centerline, and five signatures below the aircraft at distances of about 2000 feet and 5000 feet. Measurements

were also obtained at ground level. The same precision ground-based radar and optical (Askania) tracking that was used to position the B-58 and F-106 probing tests was used for the XB-70/F-104 probing tests.



(U.S. Air Force photo)

Figure 4.8. The North American XB-70A Valkyrie, escorted by a B-58 Hustler chase aircraft, making a landing approach at EAFB. The XB-70, in normal flight configuration, is showing paint job wear resulting from the rigors of the high-speed flight-test regime.



(NASA photo, ECN-2128)

Figure 4.9. During the 1966-67 U. S. National Sonic Boom Program, sonic boom signatures were acquired above and below the XB-70, which was flown at an altitude of about 37,000 feet, a speed of Mach 1.5, and a weight of about 333,000 pounds.

These measurements were highlighted at the time of the flight tests (ref. 4.6). A final analysis and documentation of the results are contained in reference 4.7. Three of the six in-flight measured signatures are shown in schematic form in figure 4.10 along with a signature measured at ground level.

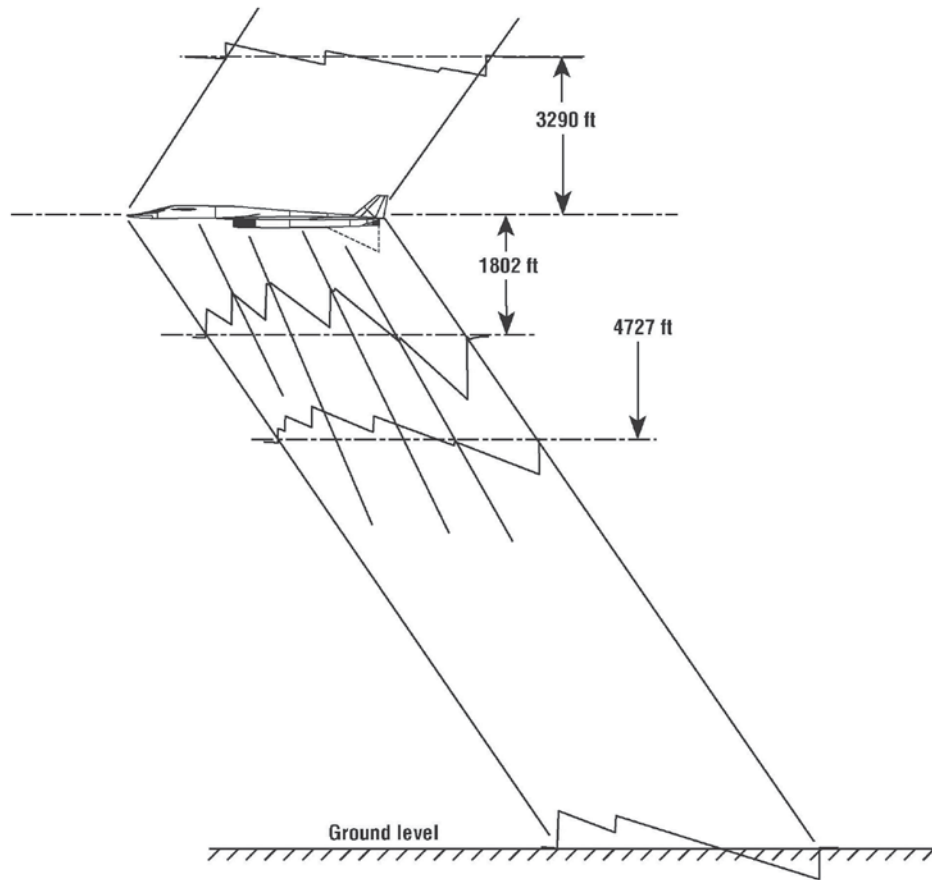


Figure 4.10. In-flight sonic boom signatures measured above and below the XB-70 aircraft (adapted from ref. 4.7).

It can be seen that the mid-field boom signatures are complex and have not yet coalesced to an N-wave at the ground ($h/l \sim 180$). Here again, as in the case of the B-58 flow-field measurements (ref. 4.4) previously discussed, the lack of XB-70 geometric and wave drag descriptions did not allow their use in CFD predictions. Details regarding XB-70 geometry, along with a wave drag description, are now available (ref. 4.21).

Validation of CFD Codes

SR-71 Aircraft

In-flight flow-field measurements below the 107-foot long NASA SR-71, shown at the top of figure 4.11, were accomplished as part of the NASA HSR Program. NASA Dryden Flight Research Center's (DFRC's) F-16XL, shown at the bottom of figure 4.11, was used as the probing aircraft and was fitted with an instrumented nose probe that measured the pressure field. Space positioning and separation distances between the SR-71 and the F-16XL (see figure 4.12) were provided through the use of ground-based precision radar and onboard GPS. Figure 4.12 presents a schematic of the flow-field measurements. The SR-71 was flown in the Mach range 1.25 – 1.48 and at altitudes of from 31,000 feet to 48,000 feet at gross weights varying from 74,000 pounds to 118,000 pounds. F-16XL probe measurements were acquired in the near- and mid-field at distances of about 500 feet to about 10,000 feet below the SR-71. In-flight measurements were also obtained at altitudes of about 10,000 feet above the ground using the quiet Y0-3A Quiet Star, a turboprop-powered glider aircraft, equipped with microphones. Boom signatures at ground level were also measured.



(NASA photo, EC95-430-24-2)

Figure 4.11. NASA's SR-71 and F-16XL ship #1 fly in formation on a sonic boom research mission.

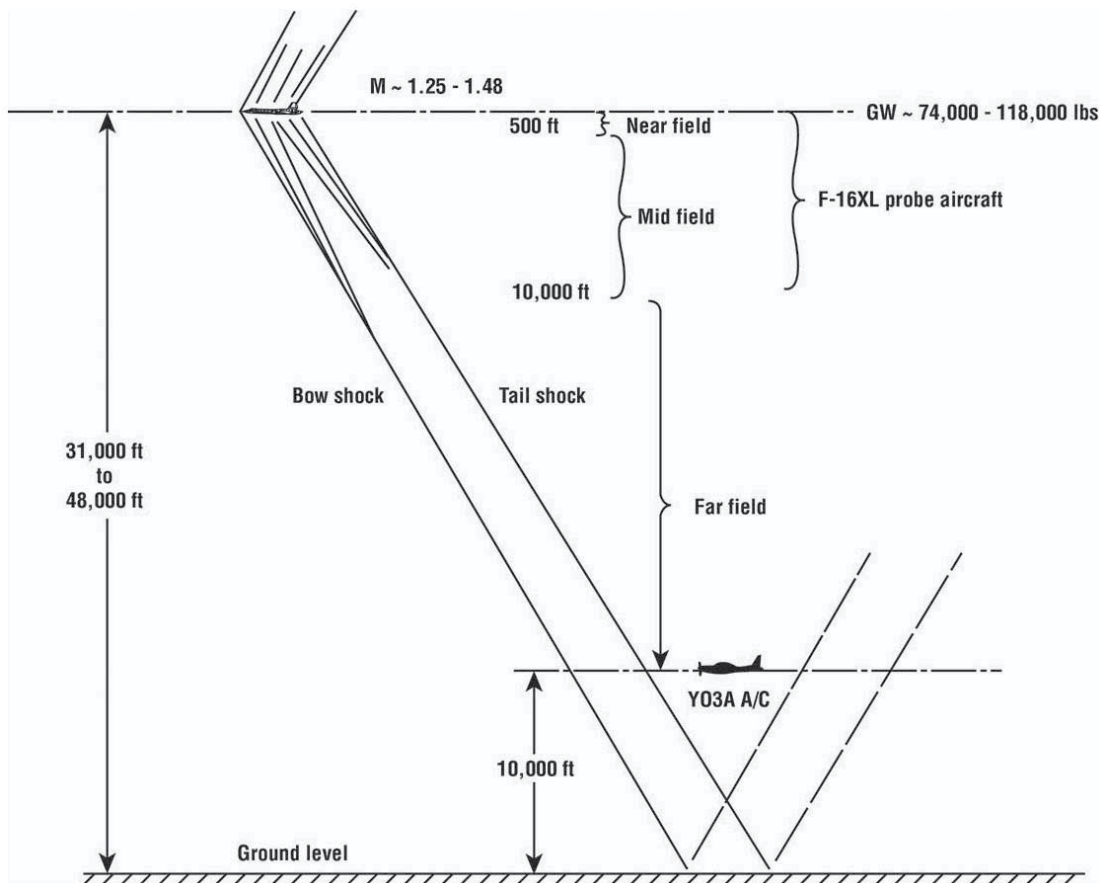


Figure 4.12. SR-71 shock flow-field measurement arrangement illustration.

At the time of these flight experiments, a significant effort in sonic boom minimization was taking place under the HSR program. CFD activities were widespread and there was a need for near-field in-flight signature measurements that would contribute to code validation. In particular, knowledge of how accurately the codes predicted shock coalescence as the complex near-field signature propagated to the ground was desired. The effect of inlet nacelle shocks, which had been shown in wind-tunnel tests to have a significant influence on shock coalescence, was especially important. Over 105 probe signatures were obtained.

Figure 4.13 shows a schematic of the flow field of the SR-71 with measured signatures (ref. 4.12) superimposed at various distances below the aircraft at about 500, 2000, 5000, and 8000 feet. The aircraft was flying at a speed of Mach 1.25, an altitude of 31,000 feet, and a gross weight of about 100,000 pounds. A complex sawtooth signature was observed at about five body lengths (~ 500 ft) from the aircraft with shocks emanating from the nose and canopy followed by a very strong inlet/nacelle wing shock that essentially dominated the front and mid-part of the flow field out to a distance of about 8000 feet ($h/l \sim 80$). Beyond this distance, an N-wave was established and continued to the ground.

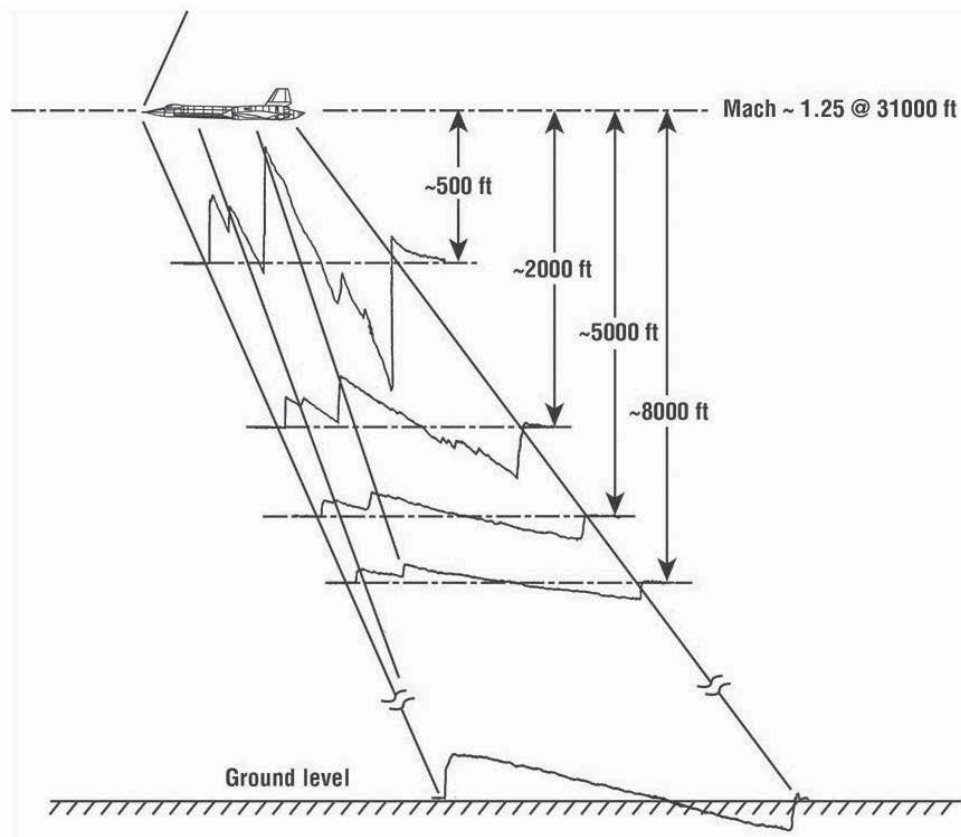


Figure 4.13. In-flight flow-field measurements below the SR-71 aircraft (adapted from ref. 4.12).

It is important to note that the SR-71 inlets were designed for full flow at the design flight conditions of Mach 3.0 at an altitude of 80,000 feet. Thus, at the off-design conditions at which the probe measurements were made, considerable inlet flow spillage occurs even though the inlets have a translating centerbody to control the flow. This spilled flow contributes significantly to shock strength and shock coalescence.

Figure 4.14 (ref. 4.12) represents the same data as in figure 4.13 but the various signatures are superimposed to better visualize the changes with probe separation distances. The figure shows the measured in-flight SR-71 sonic boom signatures where all the bow shocks are aligned. Several trends are noteworthy. As vertical separation between the SR-71 and F-16XL probe aircraft was increased, the overall signature length increased, the overpressures decreased, and the inlet and canopy shocks moved toward the bow shock. One interesting and unexpected trend concerned the plume pressures aft of the tail shock. All of the plumes from each signature collapsed to one curve.

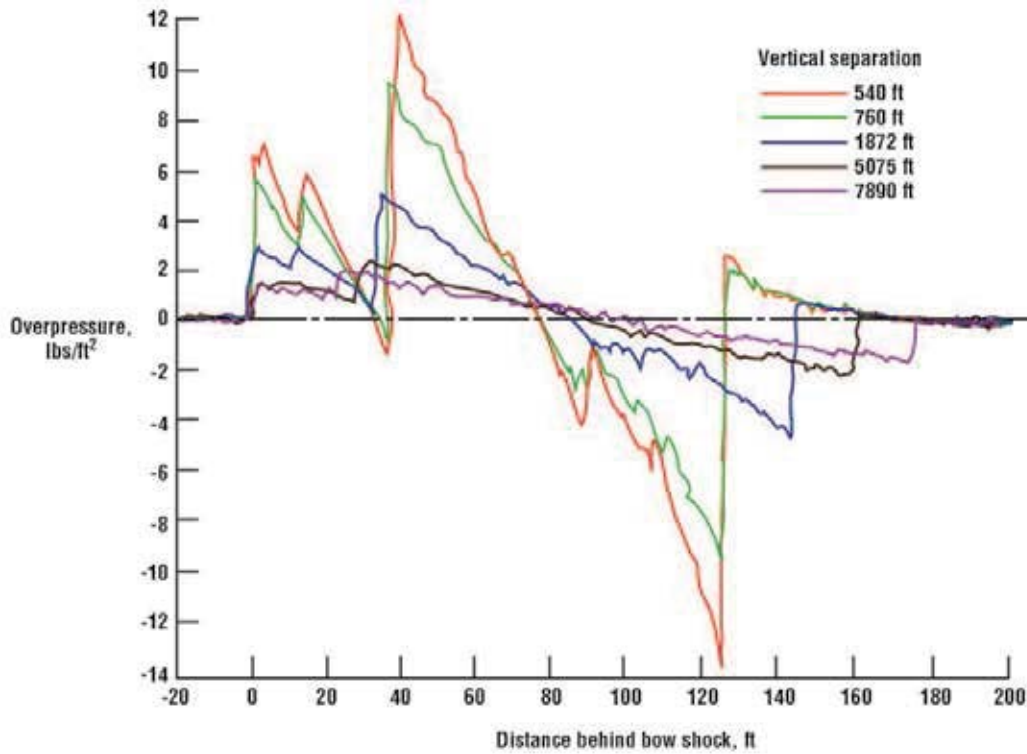


Figure 4.14. Data probes for an SR-71 at Mach 1.25 and an altitude of 31,000 feet (adapted from ref. 4.12).

A comparison of flight-test data and the computed pressure signatures by Fouladi (ref. 4.23) are presented in figure 4.15 for the SR-71. The MDBOOM code (ref. 4.24) was used to propagate the computed signature to the distance at which the flight measurements were made.

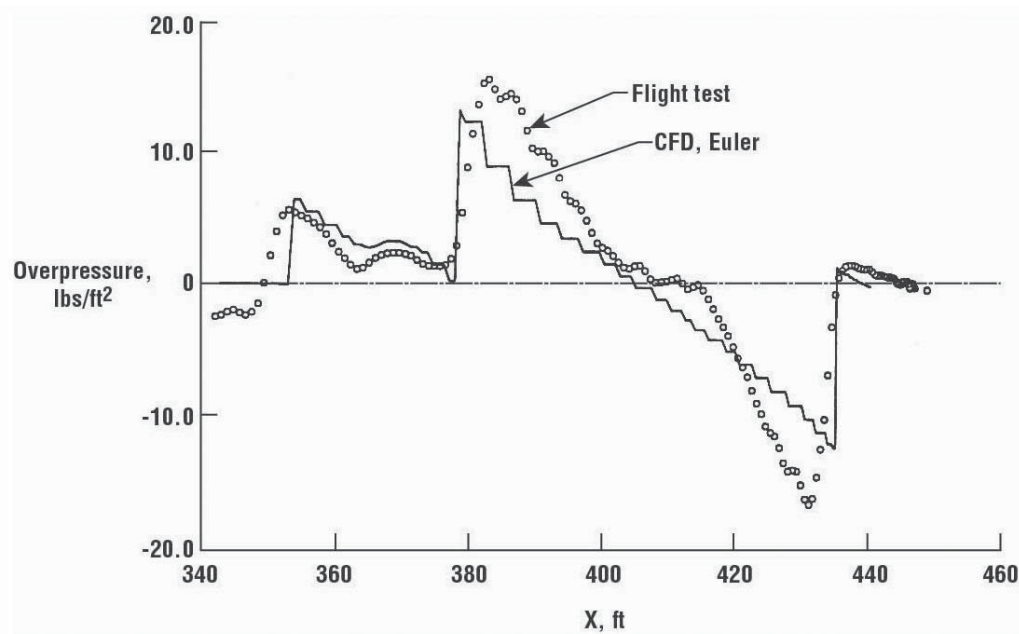


Figure 4.15. Comparison of measured and predicted in-flight SR-71 boom signature (adapted from ref. 4.23).

The comparison shows reasonable agreement, particularly in the first half of the signature. The pressure peak in the inlet region was under-predicted in the computed signature. This may have been due to the lack of modeling of some features such as by-pass doors on the engine in the CFD computations.

F-5E Inlet Spillage Shock Measurements (ISSM)

The F-5E Tiger II in-flight probe measurements flight-test program of 2002 was conducted to define the supersonic flow field below the F-5E at various distances and with particular emphasis on the performance of the aircraft's inlets and the amount of air spillage associated with certain flight conditions. This effort was given the name the Inlet Spillage Shock Measurements (ISSM) test and provided information that was crucial to the design of the Shaped Sonic Boom Demonstrator (SSBD), a modified version of the F-5E Tiger II that would produce a flattop boom signature (ref. 4.25) and is subsequently discussed. The success of the SSBD program depended on the accuracy of CFD as a predictive tool and thus high correlation was necessary between the measured and predicted signatures on the F-5E.

The ISSM test was conducted at EAFB using an instrumented NASA F-15B aircraft to probe the F-5E flow field (see fig. 4.16) at a nominal Mach number of 1.4 at an altitude of about 32,000 feet.



(NASA photo, EC02-0041-3)

Figure 4.16. An instrumented NASA F-15B aircraft probes an F-5E supersonic flow field on an Inlet Spillage Shock Measurements (ISSM) flight test high above the Mojave Desert at Edwards Air Force Base, California in 2002.

Fifty-six pressure signatures were collected during four flight tests. Of the 56 pressure signatures collected, four met the criteria for CFD validation based upon the criteria used in determining acceptable signatures. These four criteria were:

1. Small vertical separation distance from the F-5E (optimally 50 to 200 feet)
2. Fairly constant separation distance
3. Fairly steady-state flight conditions for the F-5E (no maneuvers by the F-5E)
4. F-15B generally directly beneath the F-5E (no large off-track variation of the relative flight paths)

Some results are presented in figure 4.17 (ref. 4.14) that show a comparison of signature 47, measured 94 feet below the aircraft, with CFD predictions assuming three inlet mass-flow conditions, one 10 percent greater and 10 percent less than the design case of 58.6 lbs/sec.

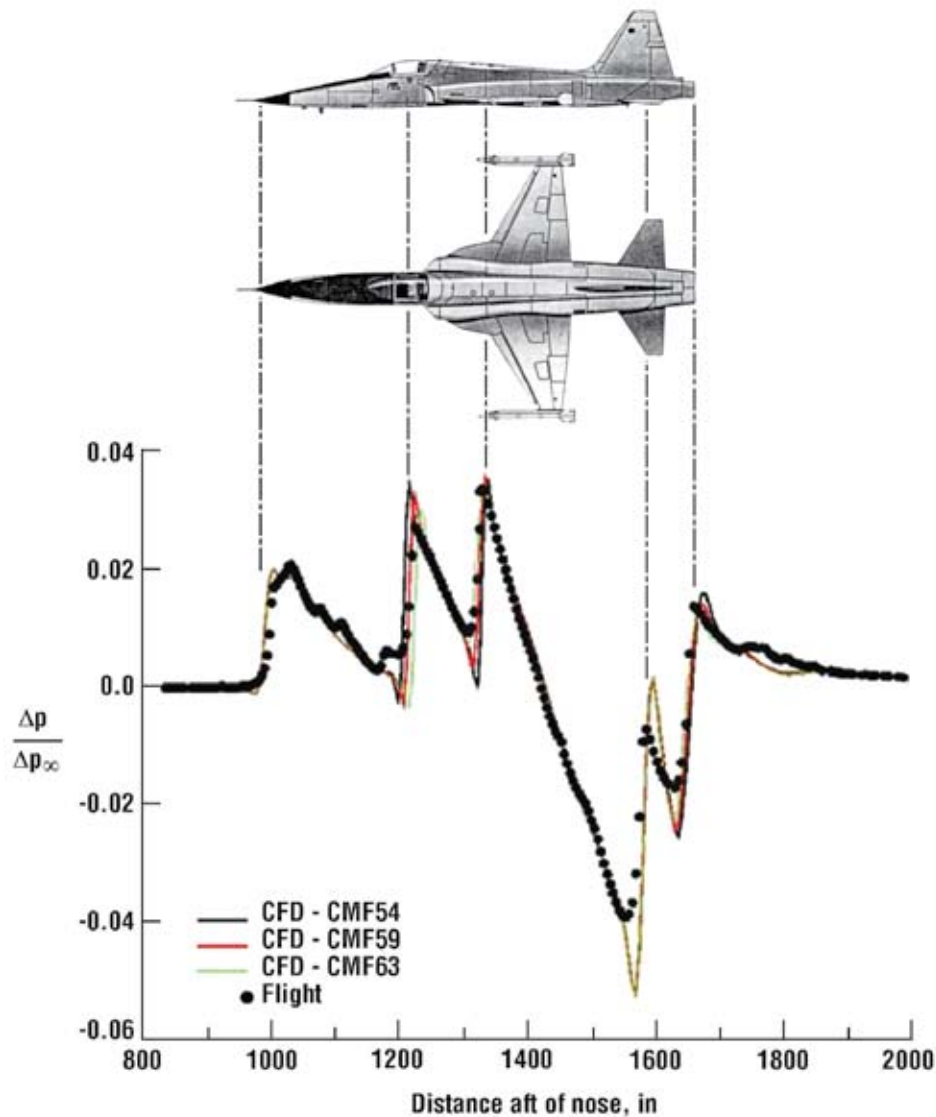


Figure 4.17. F-5E pressure signature comparison for various inlet mass flow rates. Signature 47/CFD translated 10 in aft (adapted from ref. 4.14).

Two major findings were evident. The CFD results matched the measured signature in regard to the number, location, and magnitude of the shocks, especially of the nose, inlet, and wing shocks and it was also established that the pressure signature was not significantly sensitive to the inlet mass flow. The inlet and wing shocks moved aft and decreased in amplitude as mass flow was increased and moved forward and increased in magnitude as mass flow was decreased. Comparing the location of the computed shocks with the measured flight-test data showed that the nominal value of 58.6 corrected mass flow (CMF) matched best, which validated the pre-test prediction of inlet mass flow. Such findings assured confidence that the modifications to the SSBD design would provide the desired flat top signature.

Shaped Sonic Boom Demonstrator (SSBD) Aircraft

In 1988, a 2-day Sonic Boom Workshop (ref. 4.26) was held to assess the state of the art in sonic boom physics, methodology, and understanding and to determine areas in which additional sonic boom research was needed. Three priority research areas were identified – (1) establishing the criteria for an acceptable sonic boom waveform, (2) designing a viable aircraft to a desired shaped waveform, and (3) quantifying the atmospheric effects on shaped waveforms. Maglieri, Sothcott, and Keefer (ref. 4.27) suggested a fourth need – demonstrating the persistence of shaped boom signatures to the ground from an aircraft flying in the real atmosphere. Recognition of this latter need led to the SSBD program (ref. 4.25), which utilized an F-5E aircraft modified as shown in figure 4.18 to produce a

flat-top shaped signature at the ground. Modifying the F-5E aircraft to produce a flat-top bow shock was found to be the most straightforward modification to the aircraft and such a signature would be more distinguishable after propagating the large distance between the aircraft and the ground. Additional discussion of signature shaping for boom minimization will be presented in Chapter 5.



(NASA photo)

Figure 4.18. Shaped Sonic Boom Demonstrator (SSBD) aircraft.



(NASA photo, EC03-0229-6)

Figure 4.19. The Shaped Sonic Boom Demonstrator (SSBD) aircraft (top) performs a research flight while a U.S. Navy F-5E flies chase.

A detailed flight program to describe the near-mid and far-field boom signatures associated with the baseline F-5E and SSBD aircraft (see fig. 4.19) was conducted at EAFB in 2002–2004 (refs. 4.14, 4.15, and 4.16 respectively). The measurement setup was similar to that involved during the SR-71 boom measurements (fig. 4.12), except that the F-15B was used to probe the near- and mid-field (from about 1.5 to 15 body lengths below the aircraft) and an L-23 sailplane was used to obtain measurements of the incident and reflected signature in the far field 6000 to 8000 feet above the ground. An illustration of the F-5E and SSBD flow field measurement arrangement is shown in figure 4.20.

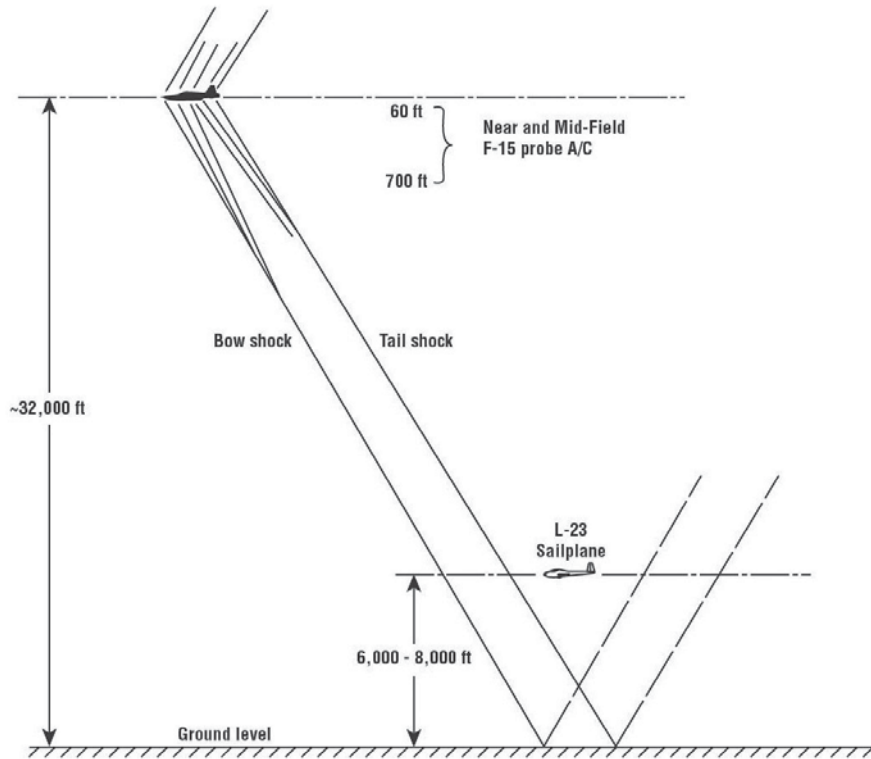


Figure 4.20. Illustration of the F-5E and SSBD shock flow-field measurement arrangement.

Both aircraft were flown at a design Mach number of 1.4 and at an altitude of about 32,000 feet. Aircraft gross weight at the time of probing was about 13,000 pounds. A total of 56 in-flight pressure signatures were obtained on the F-5E (ref. 4.14) and 68 on the SSBD (ref. 4.15).

An illustration of the characteristics of the signatures observed for the SSBD aircraft is presented in figure 4.21 (ref. 4.15). Three signatures are shown – one measured in the near-field at about 80 feet below the aircraft, one measured using the L-23 sailplane flying at about 5500 feet above the ground, and one at ground level.

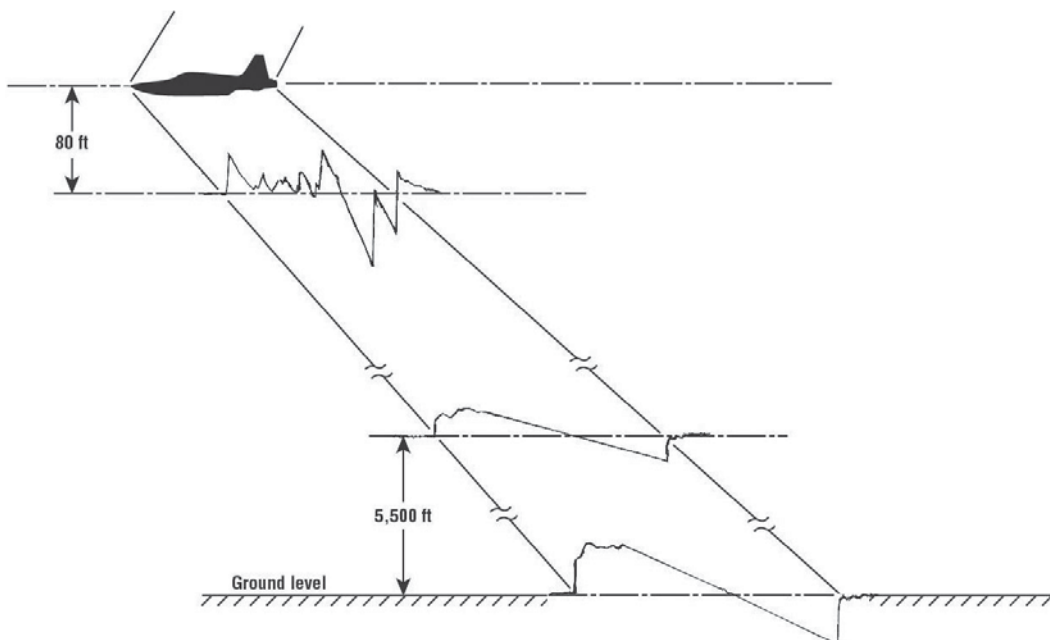


Figure 4.21. In-flight flow-field measurements below SSBD aircraft (adapted from ref. 4.15).

The modifications to the F-5E aircraft were designed to alter regions just downstream of the bow-shock portion of its N-wave ground signature into a flat-top shape while leaving the aft portion of the N-wave signature unaltered. Comparison of the SSBD near-field signature (shown in fig. 4.21) with that of the unmodified F-5E (shown in fig. 4.17) illustrates the nature of the change that results in the SSBD near-field signature shape. Note that from the inlet shock rearward, both the F-5E and SSBD near-field measured signatures are essentially the same. The character of the SSBD near-field signature behind the bow shock, however, is altered as a result of the reshaping of the F-5E forebody. Such a change in the near-field signature results in the nearly flat-top shape observed in figure 4.21 for the far-field at the sailplane location and at ground level.

A more detailed look at the SSBD near-field signature is provided in figure 4.22. Figure 4.22 shows the signature below the SSBD measured in flight from the NASA F-15B probe aircraft at about 80 feet below the SSBD, which is flying at Mach 1.4 and an altitude of 32,000 feet. Also shown in figure 4.22 is a computed signature from a CFD calculation at the same separation distance. The source of each shock is identified including – the bow, forebody, canopy, inlet, leading-edge extension, wing leading edge, wing trailing edge, horizontal tail leading edge, recompression shock, and the expansion caused by the exhaust plume.

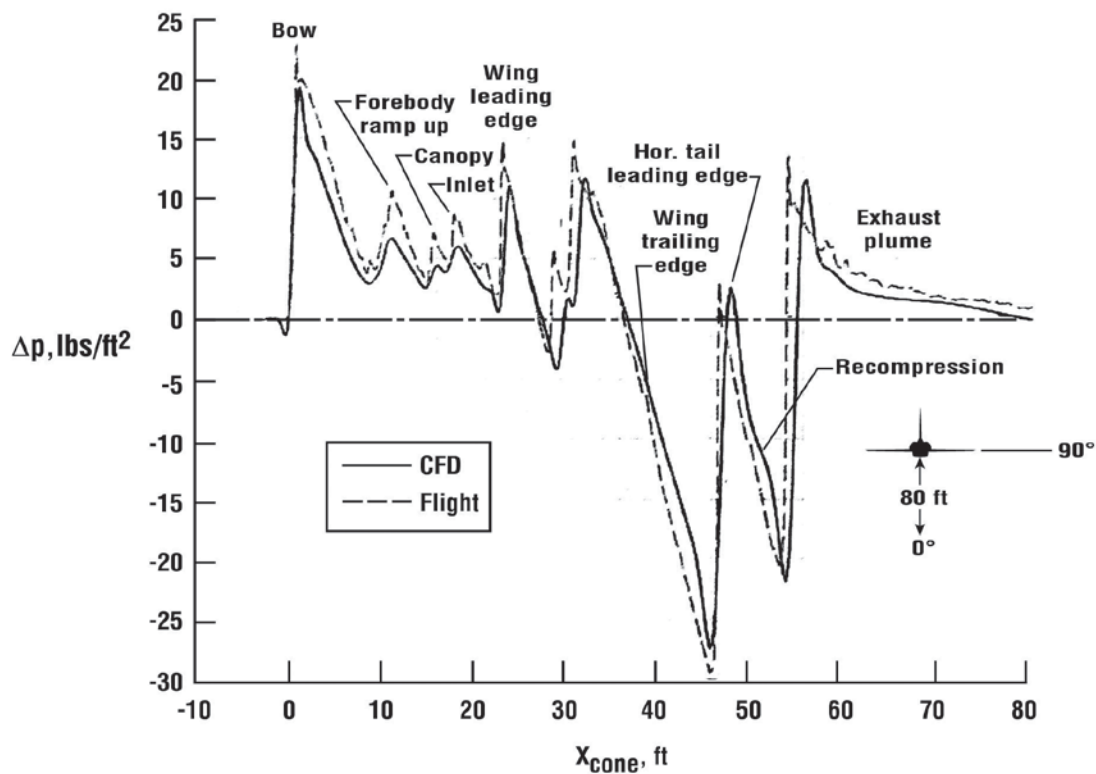


Figure 4.22. SSBD pressure signature comparison between flight test and CFD analysis, for separation distance about 80 feet below the aircraft (~1.6 body lengths) (adapted from ref. 4.15).

The design modifications were such as to provide for a strong bow shock that would prevent the following shocks, especially from the inlet, leading-edge extension (LEX), and wing leading edge, from moving forward as the signature propagated towards the ground. The two shocks located between the bow and inlet shock are associated with the slight ramp up of the nose forebody just ahead of the canopy and the canopy shock. Other minor features of the aircraft such as the airdata probe at the nose, nose gear doors, and total temperature probes were not included in the CFD analysis. On the whole, however, the computed pressure signature captured all of the measured shocks and at the correct locations. An excellent match was also observed for the maximum overpressures at the inlet, wing, and tail shocks. This provided further evidence that the design changes to the SSBD were proper in that the desired initial flat-top signature was observed in the far field. Results similar to those of figure 4.22 are derived in reference 4.28 as well as ground signatures.

The reshaping of the SSBD was focused on assuring that the shaped flat-top boom signature would result at a location directly below the aircraft. It was also believed that the shaping influence would extend to some distances laterally to each side of the aircraft. In order to assess the robustness of the design changes, near-field flow-field probe measurements were made at several azimuthal angles below and to the side of the SSBD.

In figure 4.23 (ref. 4.15) the near-field measurement of an in-flight signature at about 85 feet below and 45° to the side of the aircraft is presented. In comparing this signature to that measured directly below the SSBD (fig. 4.22) it is first noted that they have similar shock structures. Closer examination shows that the shock structure is different on the forebody region and the inlet shock has become more dominant at the 45° location. Measurements made at ground level and off track about 20° indicate that the benefit of the shaping effect was still evident. These measurements suggest that designing minimum shaped signatures must include consideration of off-track locations out to lateral cutoff.

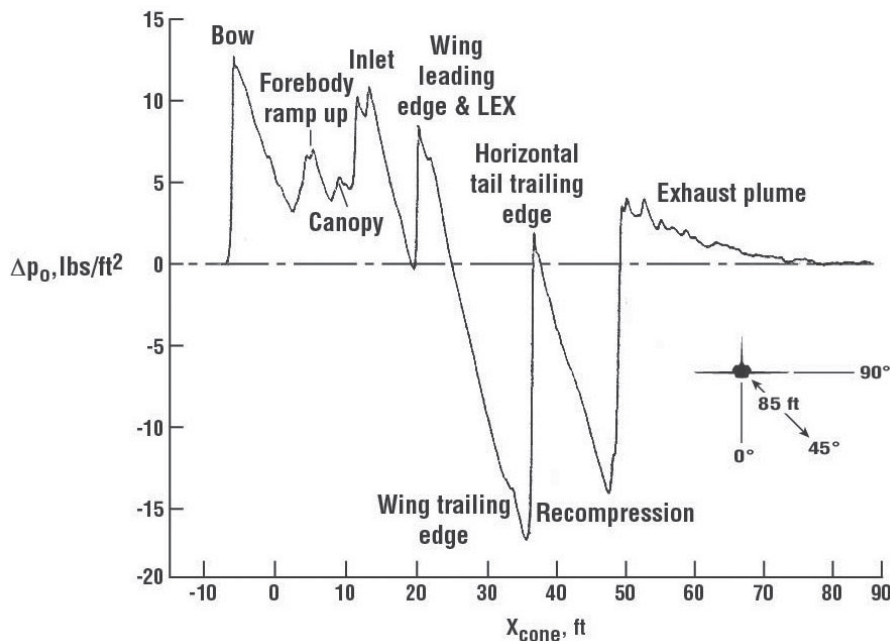


Figure 4.23. Near-field sonic boom signature measured at about 85 feet below and 45° to the side of the SSBD aircraft (adapted from ref. 4.15).

F-15B Quiet Spike™ Aircraft

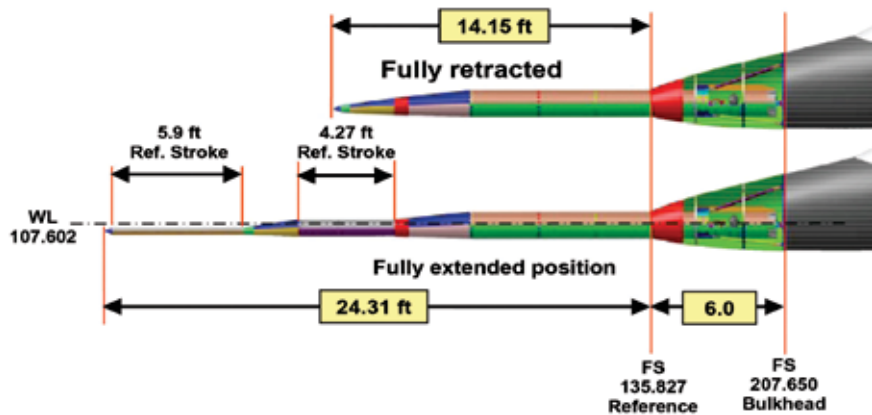
From April 2004 to February 2007, Gulfstream and NASA DFRC engaged in a flight-test program to validate the technical feasibility of the Quiet Spike™ (ref. 4.29), a Gulfstream-patented sonic boom mitigation device. The Quiet Spike was adapted to the NASA F-15B flight research aircraft and a total of 32 research flights were conducted between August 2006 and February 2007.

The arrangement and description of the Gulfstream Quiet Spike adapted to the NASA F-15B is presented in figure 4.24 (ref. 4.29). The NASA F-15B Quiet Spike flight research aircraft, with the spike fully extended, is shown in figure 4.24(a), figure 4.24(b) provides details of the Quiet Spike geometry, and figure 4.24(c) shows the F-15B Quiet Spike flight research aircraft in flight with the Quiet Spike fully retracted and extended. These flight tests had two objectives – the first was to assure the structural integrity of the Quiet Spike design throughout its operating envelope and the second was to acquire a description of the supersonic flow field near the aircraft associated with the Quiet Spike in its fully extended mode.



(NASA photo, ED06-0111-08)

(a) NASA F-15B #836 with fully extended Quiet Spike installed and prepared for SMI testing.



(b) Quiet Spike geometry.



(NASA photo, ED06-0149-23)



(NASA photo, ED06-0184-10)

(c) NASA F-15B #836 and Quiet Spike during first flight and first extension flight.

Figure 4.24. Arrangement and description of the Gulfstream Quiet Spike™ adapted to the NASA F-15B flight research aircraft (adapted from ref. 4.29).

The Quiet Spike was designed such that the series of weak shocks generated by each of the telescoping sections would not coalesce into an N-wave but propagate to the ground in parallel fashion. When the Quiet Spike is integrated into a low-boom designed configuration it provides the appropriate equivalent area distribution that would result in a shaped signature at the ground having an initial ramp shape rather than the abrupt N-wave shock (see for example refs. 4.30 and 4.31).

In December 2006, over 30 near-field probe measurements using the NASA F-15 #837 aircraft were made below, to the side of, and above the test aircraft flying at a speed of Mach 1.4 and an altitude of 40,000 feet at distances from about 95 to 630 feet to confirm the Quiet Spike aerodynamic shaping theory and the coalescence rates of the canopy, wing, and inlet shocks on the front end of the F-15B Quiet Spike configuration as the shocks propagate away from the aircraft.

Because of the strength and persistence of the F-15B shock flow field behind the three shock system from the Quiet Spike, it was predicted that the Quiet Spike's bow shock minimization would not be observable on the ground. CFD analysis had shown that the series of shocks from the Quiet Spike would persist to a sufficient distance from the F-15B aircraft before being overtaken by the F-15B flow field. However, the CFD analysis also predicted that the benefit could be realized on the ground signature when the Quiet Spike is incorporated on a low-boom shaped vehicle.

In figure 4.25 (ref. 4.17), an F-15 Quiet Spike near-field signature, measured 95 feet below the aircraft, and a comparison with a hybrid CFD calculation are presented. Each of the major shocks associated with the Quiet Spike and F-15B flow field are also identified.

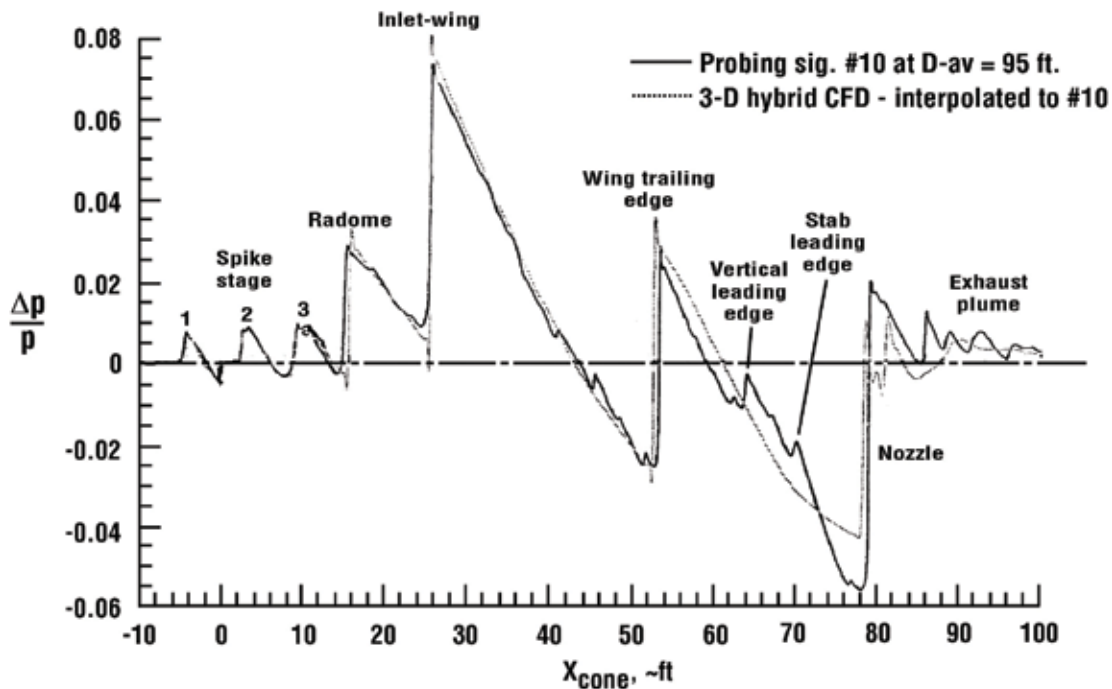


Figure 4.25. F-15B Quiet Spike near-field signature measured 95 feet below the aircraft and a comparison with hybrid CFD calculation (adapted from ref. 4.17).

The comparison of measured and predicted shocks, the location of the shocks, and magnitude of the shocks are excellent, with the exception of the events following the wing trailing-edge shock. In addition, the three shocks off the Quiet Spike (stages 1, 2, and 3) are clearly evident and generated as designed. Results of the probing test and CFD calculations confirmed that parallel propagation of the Quiet Spike weak shocks persisted out to 10 body lengths below the F-15.

In addition to the near-field probing directly below the F-15 Quiet Spike aircraft, off-track measurements were also made. These measurements were obtained in order to quantify the Quiet Spike shock strength as a function of azimuthal position since the Quiet Spike was designed to have steeper sloping transitions on the top side of the conical transitions than on the bottom (see fig. 4.24). Early analyses showed that weak shock waves generated by the lesser sloping design on the bottom of the spike would propagate downward and persist into the mid field to achieve the desired ground signature.

Sixteen off-track signatures were measured, four of which are presented in figure 4.26 (ref. 4.17) – one measured below the aircraft at a distance of about 377.5 feet, one at about 45° to the side 279.5 feet, one at about 90° to the side and 426.6 feet, and one at about 115° to the side and above the aircraft at 484.3 feet.

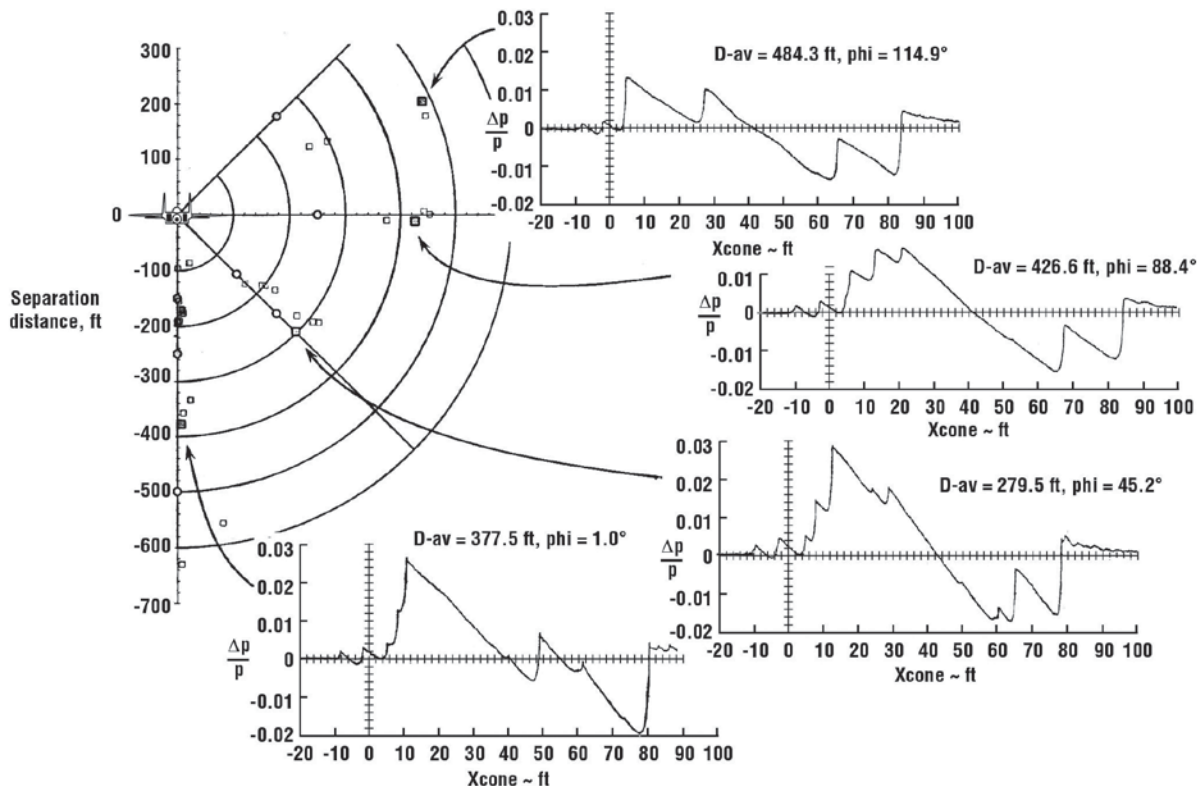


Figure 4.26. F-15B Quiet Spike near-field signatures measured below, to the side of, and above the aircraft (adapted from ref. 4.17).

Note that at about 380 feet below the aircraft, the measured signature exhibits the expected three shocks associated with the Quiet Spike design, but the third shock is being overridden by the F-15B nose shock at this distance. A similar situation is observed at the 45° position. At the position nearly abreast and above the aircraft, only the first and second Quiet Spike shocks are evident. Large changes in the character of the F-15B shock system are evident, as expected, as one moves from observations below, to the side of, and above the vehicle due to both geometric and lift changes.

The Quiet Spike has proven that it can play a significant role in achieving the desired area distribution for a low-boom vehicle. Since the Quiet Spike is being carried throughout the flight mission, it would be of interest to examine whether Quiet Spike could play a beneficial role at off-design conditions, in particular during the transition phase of flight to minimize the focus boom signature.

Flow-Field Database Utilization

Before concluding this chapter, it is useful to briefly review the utilization of all the in-flight flow-field probe measurements that have been acquired over the past 50 years in validating/updating the prediction codes.

Shown in figure 4.27 are the sketches of the planforms of the eight aircraft for which in-flight boom signatures were obtained. Below these sketches is an indication as to whether the signatures were measured in the near, mid, or far field. This is followed by a listing of the known individuals who have made use of the database, the number of signatures utilized, and whether the correlations with theory have been made and published.

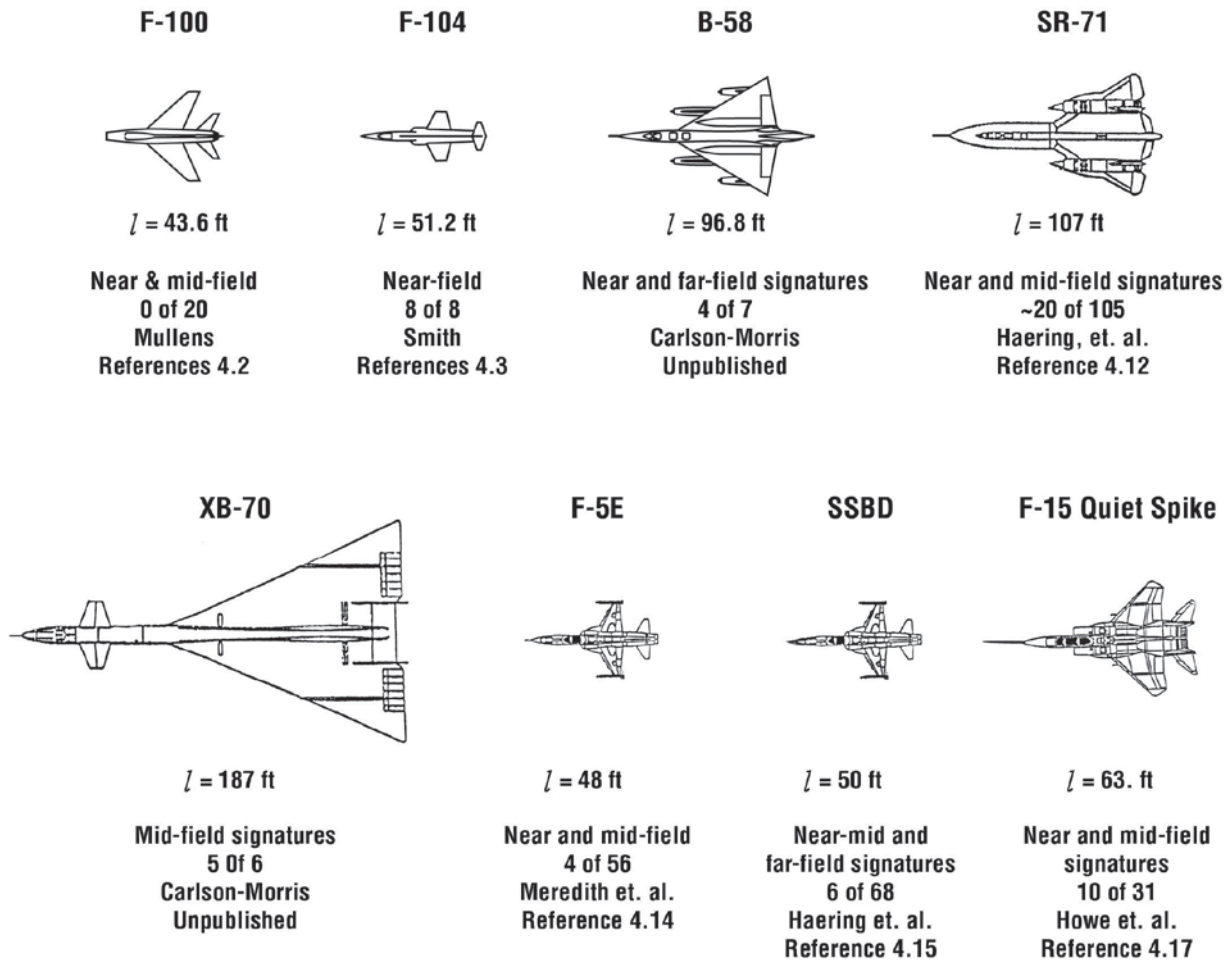


Figure 4.27. Utilization of in-flight flow-field measured signatures with prediction code.

Boom theory was in its infancy and CFD for sonic boom did not exist in 1956 when Mullens (ref. 4.2) completed the measurements on the F-100 aircraft. The primary objective of these measurements was to gain knowledge into the nature of the shock flow field surrounding an aircraft at supersonic speeds and extend the general knowledge of the shock waves that produce the booming noise. Even though the 1960 measurements on the F-104 were focused on examining the influence of the supersonic flow field on the stability and control of other aircraft, Smith (ref. 4.3) did show that the signatures calculated using the Whitham equivalent body analysis (ref. 4.19) correlated well with the measured signatures (ref. 4.3).

By the time that flow-field measurements were conducted on the B-58 and XB-70 (1963 and 1966, respectively), sonic boom theory was greatly advanced as a result of the U. S. SST effort and although CFD was well underway it was not focused on the sonic boom arena. Here again, the primary objective of these two measurement efforts was to establish the influence of lift on sonic boom and although Carlson and Morris applied existing boom codes for comparison with the measured signatures and showed good correlation, the results were never formally published.

It was not until the late 1980s and 1990s that a renewed effort was launched to quantitatively describe the near- and mid-field flow fields from aircraft in supersonic flight for use in confirming the newly developed CFD sonic boom prediction codes. This effort began with the SR-71 sonic boom flight program of 1995 (ref. 4.12) in concert with the NASA HSR Program (ref. 4.32) with increased emphasis stemming from the DARPA QSP effort (ref. 4.33) and followed by the F-5/SSBD and Quiet Spike flight programs (refs. 4.25 and 4.29) of 2002 to 2004 and 2006, respectively.

Chapter 4 Summary Remarks

Knowledge of the flow field surrounding a supersonic aircraft is paramount to the verification of prediction codes and to the design of an aircraft with an acceptable sonic boom signature. Description of the shock flow field is needed to provide information on the number, location, and strength of the shock field and describes how the shocks coalesce into final form in the far-field ground signature.

Several techniques are available to measure the flow field around a supersonic aircraft. These include probing the near and mid flow fields by means of an instrumented aircraft; the use of instrumented sailplanes, blimps, and towers to describe the far-field signatures; and airborne and ground-based Schlieren photography methods that can provide useful qualitative information.

Probing the near and mid flow field of the shock generating aircraft by means of an instrumented aircraft in supersonic flight has been the most utilized flight research method and provides the clearest detail as to the complex nature of the shock flow field near the aircraft.

Sonic boom signatures measured in the far field by means of airborne microphones provide considerable information about signature distortion from turbulence in the last few thousand feet near the ground.

Chapter 4 References

- 4.1 Weinstein, L.; Stacy, K.; Vieira, J.; Haering, E., Jr.; and Bowers, A.: Imaging Supersonic Aircraft Shock Waves. *Journal of Flow Visualization and Image Processing*, Vol. 4., No. 3, 1997, pp. 189–1990.
- 4.2 Mullens, Marshall E.: A Flight Test Investigation of the Sonic Boom. AFFTC TN 56-20, Air Research and Development Command, U. S. Air Force, May 1956.
- 4.3 Smith, Harriet J.: Experimental and Calculated Flow Fields Produced by Airplanes Flying at Supersonic Speeds. NASA TN-D 621, 1960.
- 4.4 Maglieri, Domenic J.; Ritchie, Virgil S.; and Bryant, John F., Jr.: In-Flight Shock Wave Pressure Measurements Above and Below a Bomber Airplane at Mach Numbers from 1.42 to 1.69. NASA TN-D-1968, Oct. 1963.
- 4.5 Maglieri, Domenic J.: Sonic Boom Flight Research, Some Effects of Airplane Operations and the Atmosphere on Sonic Boom Signatures. NASA SP-147, 1967, pp. 25–48.
- 4.6 Maglieri, D. J.; Huckel, V.; Henderson, H. R.; and Putnam, T.: Preliminary Results of XB-70 Sonic Boom Field Tests During National Sonic Boom Evaluation Program. National Sonic Boom Evaluation Office: Sonic Boom Experiments at Edwards Air Force Base. NSBEO-1-67 (Contract AF 49(638)-1758, Stanford Research Institute, July 28, 1967. Part II, Annex C, pp. C-II-1 to C-II-17.
- 4.7 Maglieri, Domenic J.; Henderson, Herbert R.; and Tinetti, Ana F.: Measured Sonic Boom Signatures Above and Below the XB-70 Airplane Flying at Mach Number 1.5 and 37,000 Feet. NASA/CR 2011-217077, April 2011.
- 4.8 Maglieri, Domenic J.; Hilton, David A.; Huckel, Vera; and Henderson, Herbert R.: Measurements of Sonic Boom Signatures From Flight at Cut-Off Mach Number. NASA SP-255, Oct. 1970, pp. 243–254.
- 4.9 Hubbard, H. H.; Maglieri, D. J.; and Huckel, V.: Variability of Sonic Boom Signatures With Emphasis on the Extremities of the Ground Exposure. NASA SP-255, Oct. 1970, pp. 351–359.
- 4.10 Haglund, George T. and Kane, Edward: Analysis of Sonic Boom Measurements Near Shock Wave Extremities for Flight Near Mach 1.0 and for Airplane Accelerations. NASA CR-2417, 1974.

- 4.11 Haglund, George T. and Kane, Edward, Jr.: Flight Test Measurements and Analysis of Sonic Boom Phenomena Near Shock Wave Extremity. NASA CR-2167, Feb. 1973.
- 4.12 Haering, Edward A., Jr.; Ehernberger, L. J.; and Whitmore, Stephen A.: Preliminary Airborne Measurements for the SR-71, Sonic Boom Propagation Experiment. NASA TM 104307, Sept. 1995.
- 4.13 Stansbery, Eugene; Baize, Daniel; and Maglieri, Domenic J.: In-Flight Technique for Acquiring Mid- and Far-Field Sonic Boom Signatures. NASA CP-1999-209699, Dec. 1999, pp. 249–268.
- 4.14 Meredith, K.; Dahlin, J.; Graham, D.; Haering, E.; Maline, M.; and Page, J.: Flight Test Measurement and Computational Fluid Dynamics Correlation of F-5E Off-Body Pressures. AIAA-2005-0006, Jan. 2005.
- 4.15 Haering, E.; Murray, J.; Purifoy, D. D.; Graham, D. H.; Meredith, K. B.; Ashburn, C. E.; Stucky, J.: Airborne Measurements of Shaped Sonic Boom Demonstration Aircraft Pressure Signatures with Comparison to CFD. AIAA 2005-0009, Jan. 2005.
- 4.16 Plotkin, K.; Haering, E.; Murray, J.; Maglieri, D.; Salamone, J.; Sullivan, B.; and Schein, D.: Ground Data Collection of Shaped Sonic Boom Demonstration Aircraft Pressure Signatures. AIAA 2005-0010, Jan. 2005.
- 4.17 Howe, D. C.; Waithe, K.; and Haering, E. A.: Quiet Spike™ Near Field Flight Test Pressure Measurements with Computational Fluid Dynamics Comparison. AIAA 2008-0128, Jan. 2008.
- 4.18 Hicks, Raymond M. and Thomas, Charles L.: A Preliminary Report on Shock Coalescence. NASA SP-255, Oct. 1970, pp. 297–305.
- 4.19 Whitham, G. B.: The Flow Pattern of a Supersonic Projectile. Computational Pure and Applied Mathematics, Vol. V, No. 3, Aug. 1952, pp. 301–348.
- 4.20 Hayes, Wallace D.; Haefeli, Rudolph C.; and Kulsrud, H. E.: Sonic Boom Propagation in a Stratified Atmosphere, With Computer Program. NASA CR-1299, 1969.
- 4.21 Tinetti, Ana F.; Maglieri, Domenic J.; Driver, Cornelius; and Bobbitt, Percy J.: Equivalent Longitudinal Area Distributions of the B-58 and XB-70-1 Airplanes for use in Wave Drag and Sonic Boom Calculations. NASA/CR-2011-217078, March 2011.
- 4.22 National Sonic Boom Evaluation Office: Sonic Boom Experiments at Edwards Air Force Base. NSBEO-1-67 (Contract AF 49(638)-1758), Stanford Research Institute, July 28, 1967.
- 4.23 Fouladi, Kamran: CFD Predictions of Sonic-Boom Characteristics for Unmodified and Modified SR-71 Configurations. NASA CP-1999-209699, Dec. 1999, pp. 219–236.
- 4.24 Plotkin, K. J.: Calculation of Sonic Boom From Numerical Flow-Field Solutions: MDBOOM Version 2.2, Wyle Research Report WR 92-14, July 1992.
- 4.25 Pawlowski, J. W.; Graham, D. H.; Boccadoro, C. F.; Coen, P. G.; Maglieri, D. J.: Origins and Overview of the Shaped Sonic Boom Demonstration Program. AIAA 2005-0005, Jan. 2005.
- 4.26 Darden, C. M.; Powell, C. A.; Hayes, W. D.; George, A. R.; and Pierce, A. D.: Status of Sonic Boom Methodology and Understanding. NASA CP3027, Jan. 19–20, 1988.
- 4.27 Maglieri, D. J.; Sothcott, V. E.; and Keefer, T. N., Jr.: Feasibility Study in Conducting Overflight Measurements of Shaped Sonic Boom Signatures Using the Firebee BQM-34E, RPV. NACA CR189715, Feb. 1992.

- 4.28 Kandil, Osama A.; Ozcer, Isik A.; Sheng, Xudong; and Bobbitt, Percy J.: Comparison of Full Potential Propagation-Code Computations with the F-5E “Shaped Sonic Boom Experiment” Program. AIAA 2005-0013.
- 4.29 Cowart, R. and Grindle, T.: An Overview of the Gulfstream/NASA Quiet Spike™ Flight Test Program. AIAA 2008-0123, Jan. 2008.
- 4.30 Howe, D. C.: Improved Sonic Boom Minimization with Extendable Nose Spike, AIAA 2005-1014, Jan. 2005.
- 4.31 Howe, D. C.: Sonic Boom Reduction Through the Use of Non-Axisymmetric Configuration Shaping. AIAA 2003-0929, Jan. 2003.
- 4.32 Committee on High Speed Research, ASEB, NRC: U.S. Supersonic Commercial Aircraft: Assessing NASA’s High Speed Research Program, National Academics Press, March 1958.
- 4.33 Wlezien, R. and Veitch, L.: Quiet Supersonic Platform. AIAA Paper 2002-0143, Jan. 2002.

CHAPTER 5 APPROACHES TO SONIC BOOM MINIMIZATION

This chapter presents a review of sonic boom minimization approaches through aircraft operations, aircraft shaping, and alterations of the airstream around an aircraft. Aircraft operations include changes in flight altitude and Mach number, increasing flight path angle, flying at cut-off Mach number where the speed of the aircraft over the ground is less than the speed of sound at the ground, tailoring the flight path during cruise, and flying an unsteady flight path as a form of active control. Aircraft shaping includes changing the configuration planform such that the volume and lift distributions and propulsion integration are arranged in such a manner as to produce a ground signature that is either a substantially reduced N-wave or typically a non-N signature with increased rise time and/or reduced overpressure. The goal is to soften the boom's loudness to the point where it is not objectionable, potentially not even heard. This is considered to be the most common approach to boom minimization, and is discussed in detail in Chapter 7.

The most extreme approaches to boom minimization alter the airstream surrounding the aircraft so as to increase its effective length and fineness ratio. The goal is similar to shaping, but is accomplished without a physical aerodynamic body. Other exotic approaches that have been investigated include propulsion-airframe integration schemes and unique arrangements of vehicles to essentially increase the equivalent vehicle length or shield the shocks from ground observers. Each of these minimization approaches are designed to alter the boom signature intensity and shape and in some cases perform supersonic flights that are referred to as boomless. It is appropriate, therefore, to begin with a brief discussion of the term "boomless".

Boomless Flight

Throughout most of the studies related to boom minimization via shaping and particularly airstream alterations, the term "boomless flight" is mentioned. A brief discussion of the meaning of this term and how it translates in terms of boom loudness and building response follows.

Schematic of Flight Situation

In figure 5.1, two aircraft flight situations are schematically shown that will aid in discussion of boomless flight. The situation to the left of figure 5.1 is for an aircraft flying steady-level at a low supersonic Mach number such that its speed over the ground (V_g) is less than the speed of sound at the ground (a_g). Thus, the aircraft is flying at a speed below Mach cutoff (M_{CO}) – that is, the flight Mach number at which the shocks terminate and reflect back upwards. Acoustic disturbances are only observed if the termination point is within a few hundred feet of the ground. Thus, flights below M_{CO} can be classed as boomless even though they are obviously not shock free.

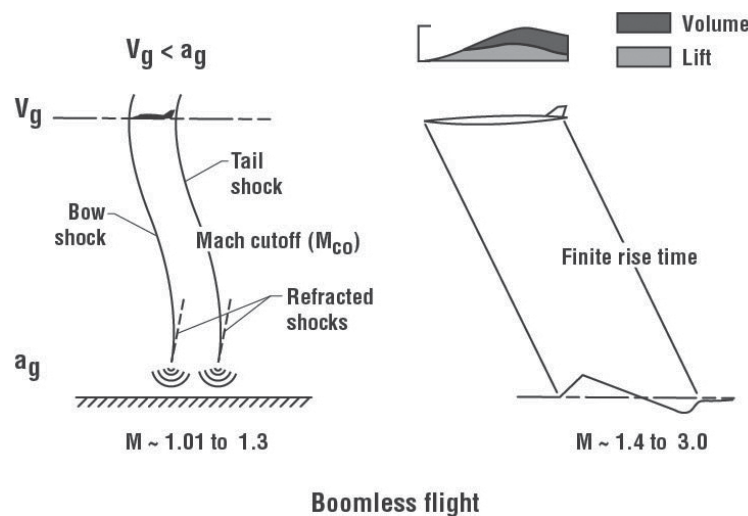


Figure 5.1. Understanding the meaning of boomless flight.

It will be shown later on in this chapter that the practical range for M_{CO} flight (i.e. where the shocks do not reach the ground, fig. 5.1) is in the Mach 1.01 to Mach 1.3 range and that, at the shock termination, a caustic (focus) condition exists wherein the boom overpressures can be as much as 3.0 times the boom levels generated by the aircraft flying at the same altitude at Mach numbers above cutoff Mach number M_{CO} .

The schematic to the right of figure 5.1 is for the case of very long and slender (~600 to 900 feet) aircraft having very high fineness ratios of about 60 to 80 as compared to about 16 to 20 for supersonic transport designs and 8 to 10 for subsonic aircraft. The fineness ratio is defined as the fuselage length divided by the fuselage maximum diameter. High fineness ratios are desirable for supersonic vehicles in order to reduce wave drag. Acquiring such extreme lengths had been the focus of the majority of the airstream alteration (phantom body) concepts, which will be discussed later in this chapter. The flight Mach number of these studies ranges from about 1.4 to 3.0. The resulting boom signature at the ground is no longer the classical N-wave but one with very long shock rise times, almost approaching a sine-wave. Since the ear responds to rapid changes in pressure, a signature of the sort shown on the right side of figure 5.1 would be less likely to be heard by outdoor observers. Once again, as for the M_{CO} case, a long vehicle producing a finite rise time signature is boomless flight (only for outdoor observers – as will be shown on the next figure) but not shock free flight.

Boom Responses

Sonic booms are experienced by people both outdoors and indoors, and, as will be discussed in Chapter 8, their responses can differ considerably. In fact, it has been found that objections to booms can be greater for those observing them indoors as compared to outdoors. The thrust of all sonic boom minimization activities is to design an aircraft that produces a boom signature with a shape and maximum overpressure that is acceptable both outdoors and indoors.

Loudness (the magnitude of the sound) is one measure of boom acceptance. The influence of altering the sonic boom signature's shape on observed loudness is presented on the left hand portion of figure 5.2 (ref. 5.1). Relative loudness is shown for four boom signatures, all having the same maximum overpressure of 1.0 lb/ft². They have varying levels of the initial shock strength from 1.0 lb/ft² (for the N-wave) to 0.125 lb/ft² followed by ramps up to the maximum $\Delta p = 1.0$ lb/ft². Note that the initial shock on the left has zero rise time. It is apparent that decreasing the initial shock strength decreases loudness. Because the human ear responds to rapid changes in pressure, humans consequently hear only the actual shock. Note that there is an 18 dB reduction in loudness for a shaped signature having a 0.125 lb/ft² initial shock (with 1.0 lb/ft² maximum level) as compared to the N-wave having an initial shock of 1.0 lb/ft² (also the maximum level). If one carries the rise time analogy a step further to a sine wave signature of the same amplitude and period as the N-wave, it would be inaudible outdoors. The sine wave signature would not be heard indoors either. It should be noted that even though these experiments were done on subjects outdoors and indoors with windows opened and closed, the subjects were only rating boom loudness. The indoor signatures that subjects were exposed to were re-shaped as compared to the outdoor signature in order to account for the changes due to transmission losses through the building walls and windows. Subjects were not exposed to the other stimuli experienced indoors, such as building vibrations and rattling, that also cause annoyance.

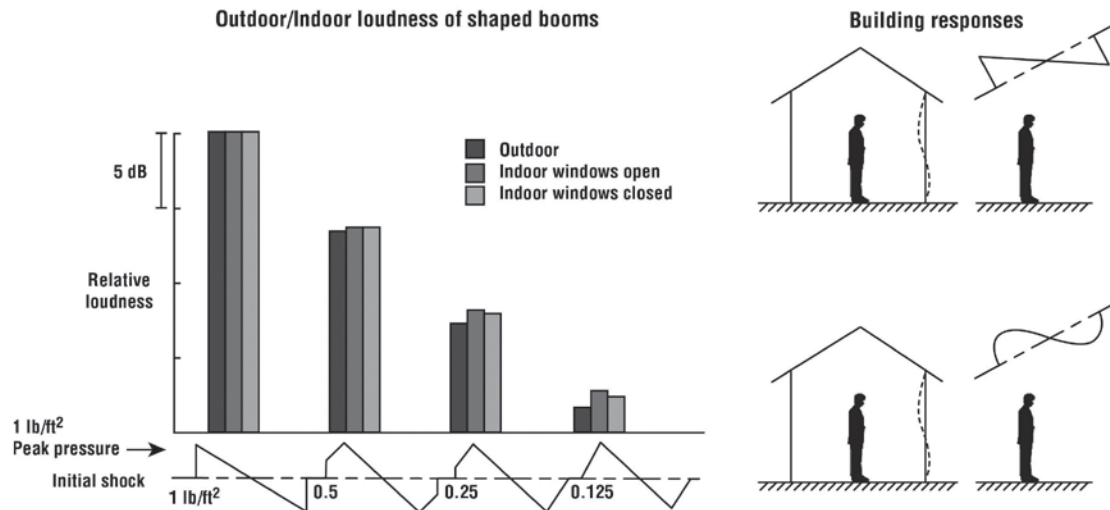


Figure 5.2. Sonic boom loudness and building response (adapted from ref. 5.1).

To the right side of the figure is a schematic illustrating a building structure response to an N-wave and sine wave of the same overpressure level and duration. Also shown on the schematic is an outdoor and indoor observer. Outdoors, the observer would not hear the sine wave signature because of its extremely low frequency but definitely would hear the booms from the N-wave. Indoors, the observer would respond to the building vibration and rattling of windows and bric-a-brac, etc., for either the N-wave or sine wave. In Chapters 8 and 9 of this publication, it will be shown that a sine wave is more efficient exciting a building structure than an N-wave. Therefore, when shaping a boom signature to reduce loudness, it is also desirable to reduce its overpressure and increase rise time.

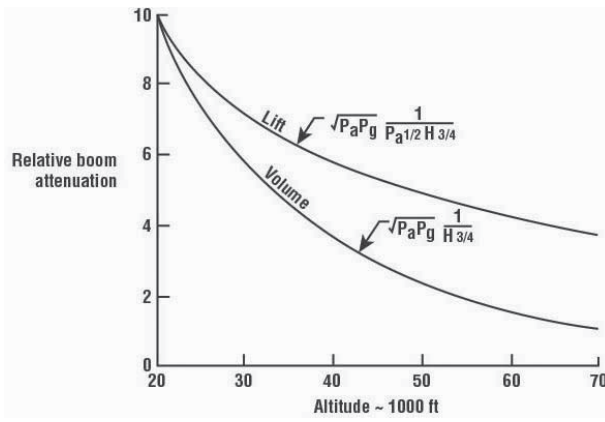
Boom Minimization through Aircraft Operations

In this section, sonic boom minimization by means of altering aircraft flight operations will be reviewed and include the demonstrated benefits associated with flight altitude and Mach number, those resulting from altering flight path angle and the no boom cut-off Mach number flight operation. Two additional aircraft operations aimed at reducing the boom observed at the ground will also be discussed, both of which may be considered beyond the realm of current practice – Ferri's tailoring the aircraft flight path (ref. 5.2) and Crow's active control – unsteady flight path (ref. 5.3).

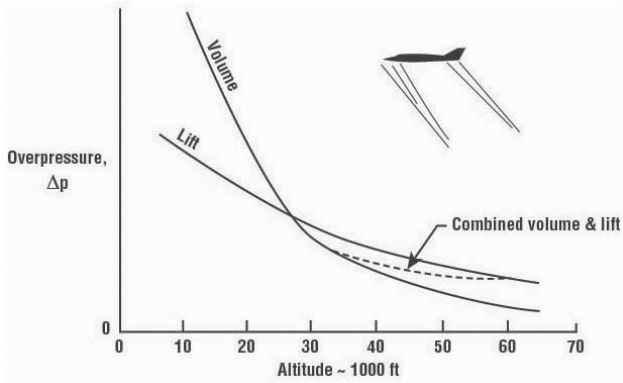
Influence of Altitude and Mach Number

Aircraft flight altitude and Mach number play a significant role in determining the magnitude of the boom as shown in figure 5.3 (ref. 5.4). Figure 5.3(a) shows the relative boom attenuation as a function of the flight altitude for two aircraft in steady-level flight at the same Mach number – (1) a lightweight fighter whose boom is due primarily to its volume and (2) a heavyweight bomber whose boom is due primarily to the weight (lift) it is carrying. The sonic boom of an aircraft is made up of the boom generated by its volume and the boom generated by the lift it carries. Thus, aircraft size and weight play a significant role in establishing boom intensity. The attenuation is, of course, a function of both altitude (H) and atmospheric pressure at the flight altitude (P_a) and at the ground (P_g). It can be seen that increasing altitude will result in significant attenuations of the boom depending upon the amount of volume and lift carried by the vehicle.

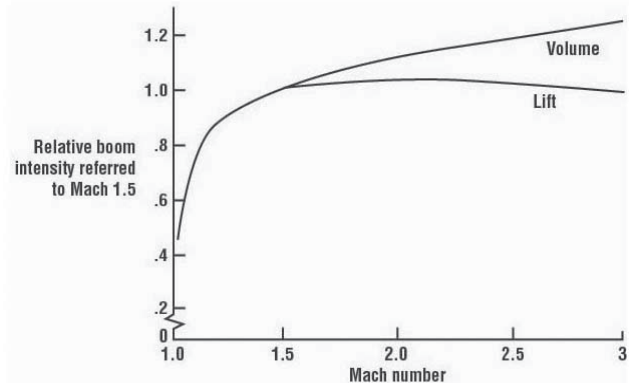
Another view on the influence of increasing altitude at a constant Mach number and weight is shown in figure 5.3(b). Overpressure is plotted as a function of flight altitude. Two curves are shown, one for volume only and the other for lift only. The plot shows that for a fixed Mach number at low altitudes, the volume contribution is dominant. As the airplane is flown at higher altitudes and at a given Mach number, the angle of attack must increase in order to maintain the lift equal to the weight, thus producing a stronger shock wave.



(a) Sonic boom attenuation with altitude.



(b) Contribution of aircraft lift and volume on boom level.



(c) Influence of Mach number on boom level.

Figure 5.3. Influence of altitude and Mach number on sonic boom (ref. 5.4).

The variation of shock strength with Mach number is given in figure 5.3(c). In the case of the lower-weight vehicle where the boom intensity is primarily due to its volume, the shock strength increases with increasing Mach number. For the heavyweight vehicle where the boom intensity is primarily due to the lift it is carrying, shock strength increases with Mach number up to about a value of 1.5 and then begins to decrease. The decrease is due to the fact that as speed is increased, the vehicle angle of attack decreases in order to maintain the same lift. This, in turn, reduces the vehicle drag and thus the boom due to vehicle volume. Thus, the effect of speed for the lift contribution is somewhat different than that for the volume contribution for a fixed weight.

In addition to the influences of changes in altitude and Mach number discussed above, both also play a key role in the design of aircraft for low-boom shaped signatures, as will be addressed later in this section.

Flight Path Angle

Another operational procedure that can be used to minimize the boom at ground level is through the use of flight path angle (γ) to delay its arrival until the aircraft has reached higher altitudes. Figure 5.4 has been assembled to illustrate this situation.

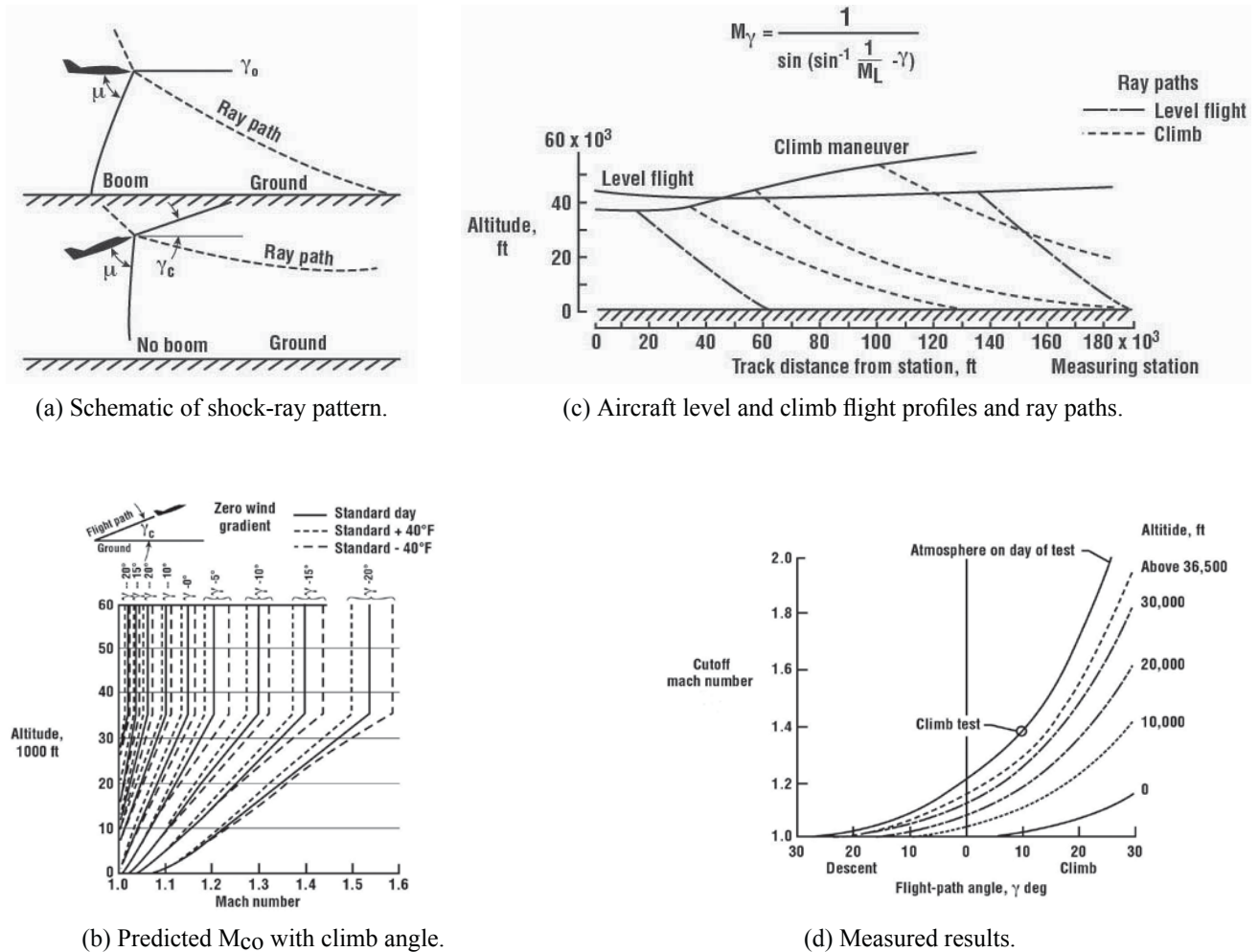


Figure 5.4. Effect of climb angle on cut-off Mach number (adapted from refs. 5.5 and 5.6).

Figure 5.4(a) illustrates two aircraft (both flying at constant Mach number) – one in level flight (γ_o) and the other at a given flight path angle (γ_c). Only the bow shock waves are shown. For the level flight case γ_o , the Mach-altitude is such that the speed of the aircraft over the ground is greater than the sound speed at the ground and the bow shock reaches the ground and is observed at the ground. In the climb case γ_c , the climb angle is selected so that as the aircraft passes through the same altitude, the bow shock becomes normal to the ground causing it to terminate before reaching the ground. The flight path angle γ can be viewed as an effective change in Mach number, positive climb angles being beneficial regarding boom minimization on the ground while negative climb angles (dives) are detrimental.

The theoretical cut-off Mach (M_{CO}) for various climb and descent angles for a standard atmosphere with no winds and also for a standard day $\pm 40^\circ\text{F}$ are provided in figure 5.4(b) (ref. 5.5). It can be seen that an aircraft in a 20° climb in a standard atmosphere with the proper Mach schedule can delay booming the ground until it reaches about Mach 1.55 at the tropopause (36,000 feet).

In order to determine experimentally whether cut-off Mach number is affected in a manner indicated by the equation shown on figure 5.4(c), a flight investigation was conducted involving level flight followed a short time later by one that included a pull-up and climb maneuver (ref. 5.6). The Mach number was 1.4 for level flight, but varied from the 1.4 planned Mach to between 1.4 and 1.34 in the 10° climb maneuver. The flight paths for the two test flights, taken from the radar plot board, are shown in figure 5.4(c) along with the ray paths for both the level and climbing flights represented by the dot-dash and dashed lines respectively. In figure 5.4(d), the calculated M_{CO} is shown as a function of flight path angle for flights at various altitudes in a standard atmosphere. Also shown is

the calculated M_{CO} for the atmosphere on the test day. The climb test data point is also shown and is seen to be in good agreement with prediction.

Climb angle has been used during military operations to delay the arrival of the transition focus boom to a more suitable location further down the flight track along with its corresponding lower overpressures as a result of the higher altitude at which the boom is produced.

Mach Cut-Off Operations

It has been suggested that overland supersonic operations be flown at so-called cut-off Mach numbers, that is, relatively low Mach numbers at which the aircraft shocks and thus booms do not reach the ground. This might be accomplished by operating a conventional SST at low supersonic speeds, by developing a low Mach number SST (ref. 5.7), or by designing an advanced low-boom supersonic transport. However, as noted in the previous discussion on boomless flight, at the termination of the shocks during Mach cutoff (M_{CO}), a caustic (focus) condition exists wherein the boom overpressure can be as much as 3 times the boom level generated by the aircraft flying at the same altitude at a high Mach number. This caustic is carried along with the aircraft during the entire flight at M_{CO} .

Figure 5.5 shows the focusing situation caused by refraction when steady flight is just below the M_{CO} . As shown in figure 5.5(a), the rays are curved and the caustic is straight. A bow shock is shown illustrating how it appears to be reflected from the caustic. The reflection corresponds to rays continuing after passing their tangent point along the caustic. Notice that the rays approach their tangent point and the area between the consecutive rays decrease and approach zero at the caustic. Figure 5.5(b) shows a more detailed view of the Mach cut-off caustic, from a pressure signature perspective, showing the types of waveforms expected. The N-wave signature to the left has not yet reached the caustic, and far above it will be a conventional boom. Since the ray tube area at the caustic is zero, geometric acoustics state that the pressure goes to infinity. The caustic is an edge and violates the geometric acoustics condition since the gradient length scale of P is large compared to wavelength, so diffraction serves to limit the signature amplitude at the caustic. Diffraction tends to limit low frequencies more than high, so the bow and tail shocks amplify more than the expansion portion of the N-wave boom signature, hence, an incoming N-wave will transform into a U-wave shape at the caustic (its maximum). The other waves have interacted with the caustic, with the post-focus U-wave reflected and low frequency evanescent waves passing below the caustic.

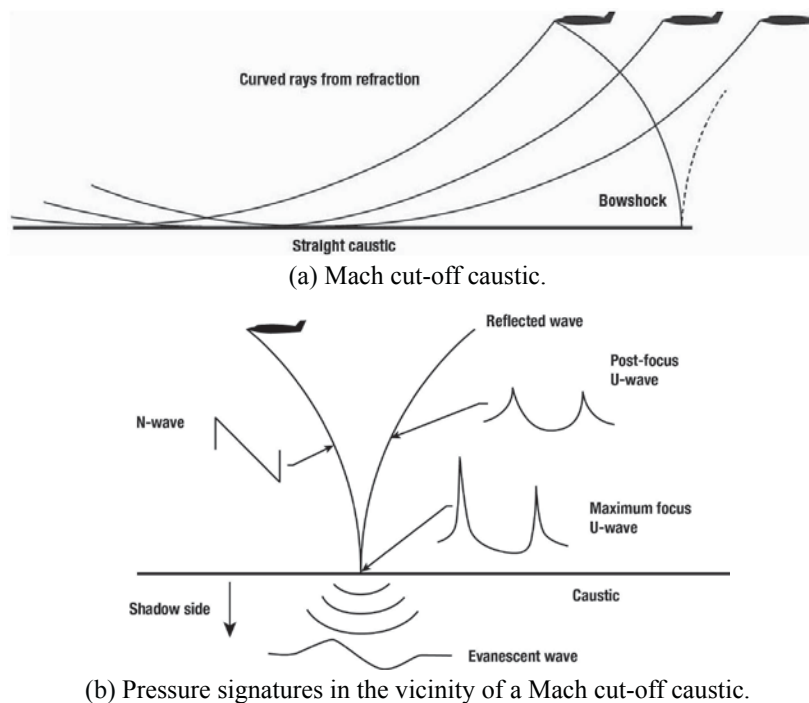


Figure 5.5. Focus due to steady-level flight at Mach cutoff (M_{CO}).

A pictorial of the sonic boom behavior for steady-level flight near Mach cutoff (M_{CO}) is illustrated in figure 5.6. The shock profiles in four conditions of flight are shown and include operations at M_{CO} , near M_{CO} , slightly above M_{CO} , and well above M_{CO} . At M_{CO} , the bow and tail shocks terminate and reflect back on themselves prior to reaching the ground, since the speed of the aircraft over the ground is less than the sound speed at the ground. Booms are also not observed at locations lateral to the aircraft ground track for M_{CO} flight. An acoustic disturbance may be observed at a few hundred feet below the shock extremities. As the Mach number is increased, the bow and tail shocks propagate further down towards the ground to the point where they may touch the ground. In this case, a U-shaped focus boom signature is experienced. It can have up to three times the intensity of the boom from a steady flight at a high Mach and at the same altitude. Such a focus or caustic could be experienced throughout much of the M_{CO} flight mission. This focus signature will also be observed a very short distance lateral to the track, as illustrated by the sketch. At Mach numbers slightly above and well above M_{CO} , the boom signature and intensity is approaching that associated with the normal carpet boom and is N-wave in character with the lateral extent of the boom being about 1 mile in width for each 1000 feet of flight altitude. The plot of overpressure with flight Mach number, shown at the top of figure 5.6, positions these various flight Mach conditions and clearly shows the pressure buildups for operations near M_{CO} . The risk of operating below M_{CO} is that if the Mach number inadvertently exceeds the cutoff condition, there can be an extensive focus boom region on the ground.

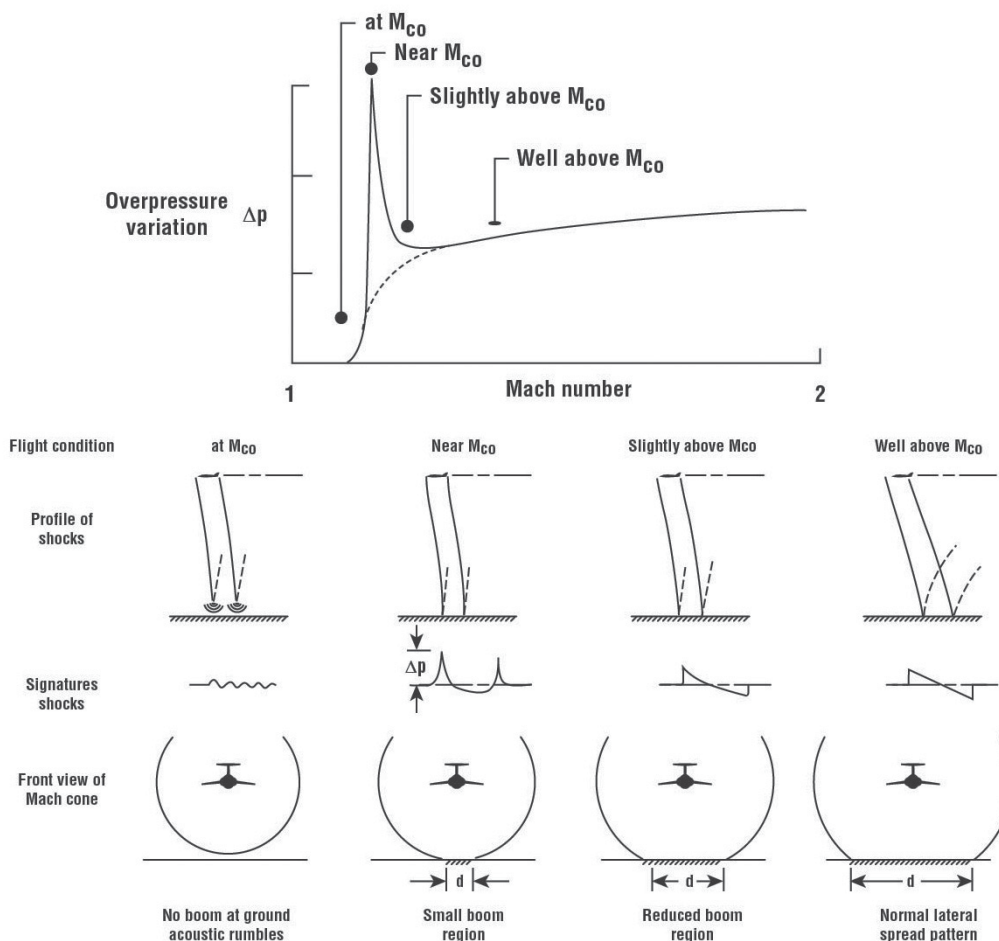


Figure 5.6. Pictorial of sonic boom behavior for level flight near Mach cutoff.

In the 1970 time period, a series of flight-test experiments (ref. 5.8) were conducted by NASA, the Atomic Energy Commission (AEC), the National Oceanic and Atmospheric Administration (NOAA), the USAF, and the Department of Transportation (DOT)/Federal Aviation Administration (FAA) to investigate the nature of sonic booms at flight operations at Mach cutoff (M_{CO}). Use was made of the 1500-foot high Bare Reactor Experiments, Nevada (BREN) tower at the AEC test site Jackass Flats, Nevada to locate microphones every 100 feet from ground level to the top. Microphones were also located at 200-foot spacing on the ground along the flight track.

Flights of F-104 aircraft, vectored and tracked by ground-based precision radar crews, were made at an altitude of 33,700 feet and at speeds near M_{CO} ranging from about 1.1 to 1.3 (based upon atmospheric sounding data near flight times) over the tower such that the shocks terminated somewhere within the 1500-foot tower height. Flights were also made at Mach numbers well above M_{CO} . The results are presented in figure 5.7 (refs. 5.8, 5.9, and 5.10) and include schematics of the ray-path and shock field diagrams, signature shapes, and boom level.

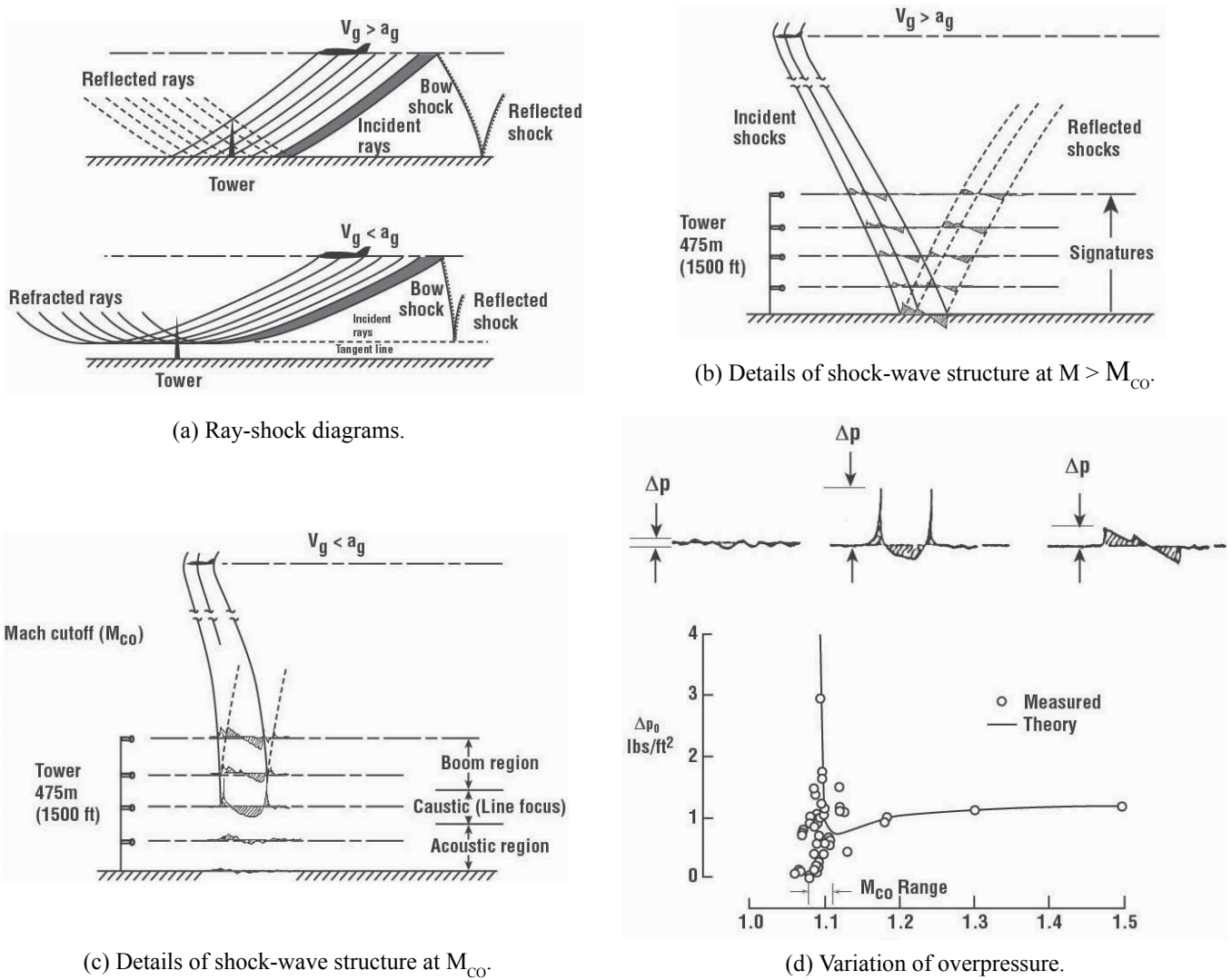


Figure 5.7. Nature of sonic boom for steady flight near cut-off Mach (M_{CO}) (adapted from ref. 5.8).

Figure 5.7(a) shows the ray paths for a flight where the aircraft speed over the ground V_g is greater than the sound speed, a_g , at the ground and also where it is less than M_{CO} . The aircraft is shown moving in a direction from right to left and, for simplicity, only the bow wave is shown. In the case where $V_g > a_g$, the bow shock wave extends to the ground and is reflected upward. As the disturbances that form this shock wave are emitted from the aircraft, they travel toward the ground along ray paths indicated by the solid lines. These rays intersect the ground and are reflected upward, as illustrated by the dotted lines. Note that two consecutive rays are essentially parallel and tend to converge only slightly as they approach the ground. When $V_g < a_g$, the bow shock extends downward below the aircraft until its speed becomes less than the speed of sound at the ground and reflects back on itself before reaching the ground. Note that the rays have a greater curvature and are totally refracted at an altitude above the ground. The areas between adjacent rays, as indicated by the shaded region, decrease until they theoretically approach zero where the rays become tangent and the ray tube area between them goes to zero, where boom pressures are expected to markedly increase. Thus, a caustic, or line focus, is formed where the rays become tangent at the cut-off altitude.

Sketches of sonic boom signatures measured on the tower and ground for the flight at Mach 1.3 ($M > M_{CO}$) are shown in figure 5.7(b). At the top of the tower, both incident and reflected N-wave signatures are observed. The incident and reflected signature are similar in shape and are about equal in amplitude. At ground level, these two signatures are coincident and only a single signature is observed and depending on the ground surface characteristics, could have about twice the amplitude of the free air pressure signatures. At the top of the tower, therefore, one would observe four distinct booms, whereas at ground level only two booms would be observed and they would be twice the intensity of the free air boom.

For the case of the grazing condition (M_{CO}), shown in figure 5.7(c), at the top of the tower, a normal N-wave signature was measured that included the incident bow and tail shocks and their reflections. At midtower, which was the approximate location of the shock wave extremity, it is noted that a U-shape (caustic) signature is measured for which the amplitudes are larger than those associated with N-wave signatures observed in the supersonic flow region. Near the base of the tower, below the shock extremity, the signatures are rounded or sinusoidal in shape and indicate acoustic disturbances.

The overpressures associated with the BREN tower signatures are presented in figure 5.7(d). A theory curve is also shown (refs. 5.11–5.15). At Mach < 1.10 , very low boom levels were measured, and these were associated with the acoustic type of signature. At Mach numbers above 1.10, normal N-wave types of signatures were observed from which the pressure increased gradually with increasing Mach number as predicted by theory. Near Mach 1.10, U-shape waveforms were generally observed. The U-shaped measured caustic signatures generally indicate overpressure enhancement compared to those associated with the higher Mach numbers. The highest enhancement factor measured is 3. On a final note, the shock wave was found to be quite sensitive at its extremity to local atmospheric conditions (winds, turbulence, etc.).

The range of Mach numbers and altitudes over which operations at cut-off Mach number can be performed is shown in figure 5.8. Looking first at the case of a standard atmosphere with no winds (fig. 5.8(a), ref. 5.16) for steady-level flight at Mach numbers to the left of the M_{CO} line will result in no booms reaching ground, whereas flights at Mach numbers to the right of the line will result in booms reaching the ground. The highest speed at which the aircraft could operate above the tropopause, in a standard atmosphere with no wind without producing booms at the ground, is about Mach 1.16. In a real atmosphere, variations in the effective speed of sound do exist because of temperature and winds, as shown in figure 5.8(b) and figure 5.8(c) (refs. 5.17 and 5.12). Note that cut-off Mach numbers of as high as 1.5 are possible with a 200-knot headwind at altitude. Conversely, with a 50-knot tailwind at the aircraft, flights above the tropopause would have to be flown at Mach < 1.05 . Climb or descent angles would also permit an increase or decrease in M_{CO} , respectively.

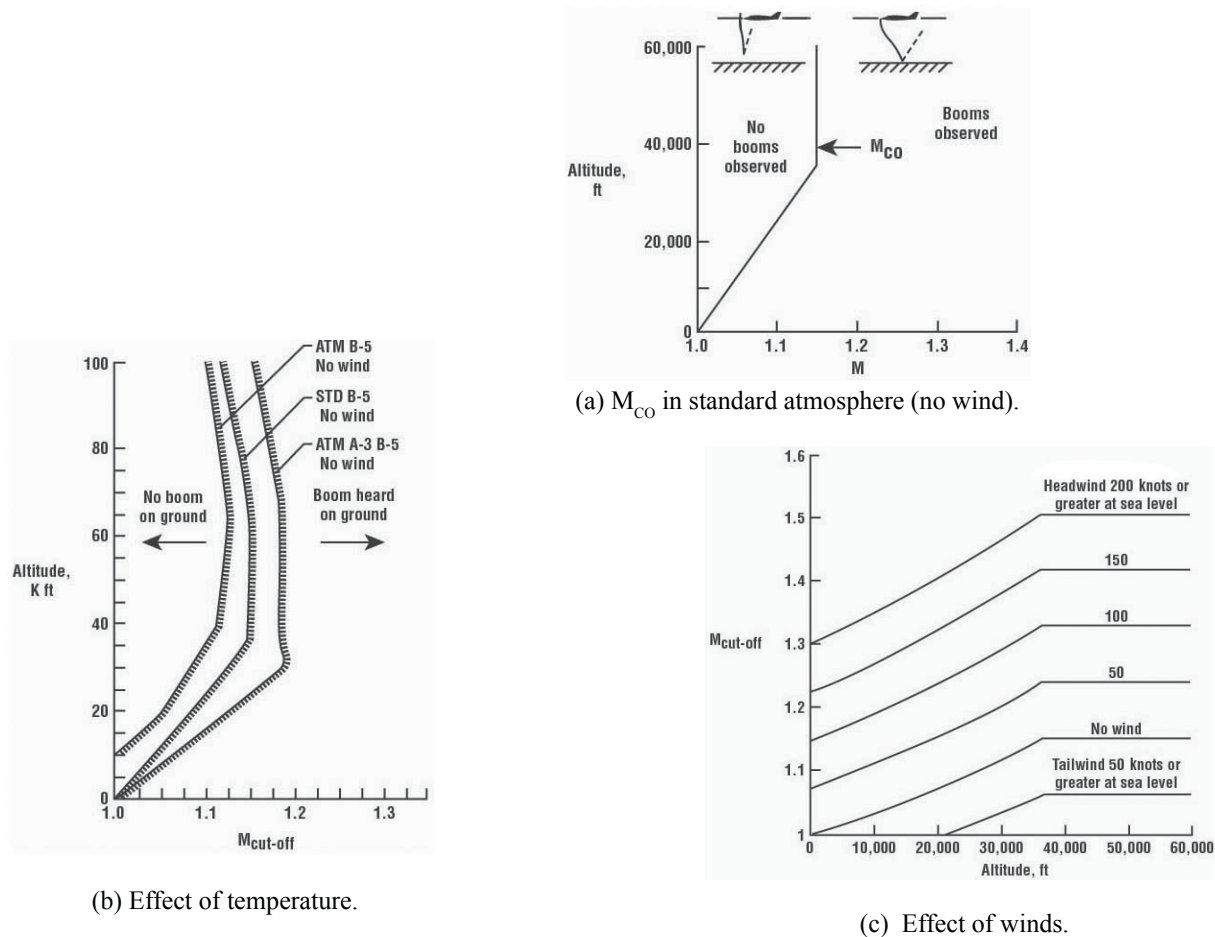


Figure 5.8. Influence of temperature and wind gradients on Mach cutoff (adapted from refs. 5.12, 5.16, and 5.17).

Flight near M_{CO} played an important role as to whether a sonic boom was observed at the ground from Chuck Yeager's famous X-1 (fig. 5.9) flight of October 14, 1947, in which he was the first person to pilot an aircraft that broke the sound barrier in level flight. According to his book (ref. 5.18, p. 130), the X-1 was in level flight at 42,000 feet and achieved Mach 1.07 during the flight. He stated that a sonic boom was observed on the ground by his test group. This boom was the first ever produced by an aircraft in level flight and supposedly the first ever generated by an aircraft. Shock wave booms have been produced by projectiles, rifles, and cannons long before aircraft booms were observed. With respect to the X-1 boom, in looking back on it and what is known today regarding M_{CO} , it would have been fortunate that it was observed, since for a standard atmosphere (no wind), the cutoff Mach number for level flight at 42,000 feet is about 1.16. The X-1 only attained Mach 1.07. Thus, no boom would be observed at ground level because of atmospheric refraction. If the atmosphere was non-standard (i.e., cooler temperatures) and there was a tailwind gradient of at least 50 knots at altitude, then the predicted Mach cutoff would have been about 1.06. Thus, at Mach 1.07, a sonic boom would have been observed, and since it was so near to cutoff, it would sound more like a rumble than a distinct double boom. Yeager noted that the NACA tracking van reported a distant rumble of thunder. However, records show that the flight was heading northwest over Victorville and upper air weather soundings taken at Bakersfield, California on that day show that the winds at altitude were from the northwest at 50 knots. Thus, Yeager's X-1 would have encountered headwinds and not tailwinds, and as such the Mach cutoff would have been more like 1.24, resulting in the shocks terminating without even reaching the ground.



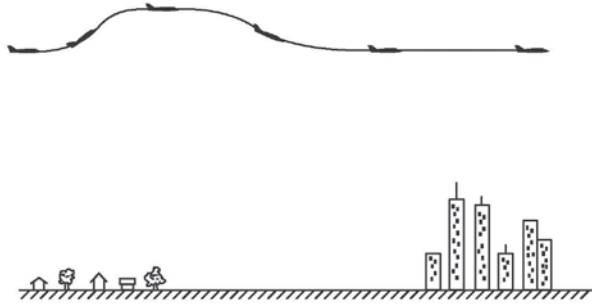
(C-1959-49476)

Figure 5.9. On October 14, 1947 Chuck Yeager piloted the Bell X-1 past the sound barrier, exceeding Mach 1.0 in level flight.

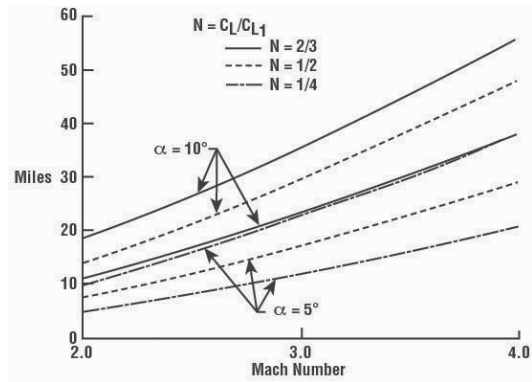
Two points should be made about boomless flight operations. Boomless flight is independent of aircraft configuration and is a function of the aircraft operating conditions and the atmosphere. Aircraft configuration is, of course, important from the standpoint of efficiency of operation at these low Mach numbers; for example, flying a high Mach cruise design at the off-design M_{CO} is less desirable than flying an aircraft designed to operate at Mach 1.15. In either case, boomless flight operations, unlike the stationary focus from an aircraft maneuver, always result in a continuous caustic or focal line where the overpressures can be higher than those of the steady flight boom from the aircraft flying at the same altitude but at the higher cruise Mach number. Therefore, in order to assure the shocks and thus the boom for flight at M_{CO} will terminate at some safe height above ground level, a margin of safety in the form of reduced Mach number is required (refs. 5.9 and 5.10). A practical range of M_{CO} above the tropopause flight is probably no greater than 1.3. Studies have been conducted in the past (see ref. 5.19) and are continuing to examine the possibility of overland boomless flight operations involving the Mach cut-off concept as a means of decreasing travel time.

Tailoring Flight Path

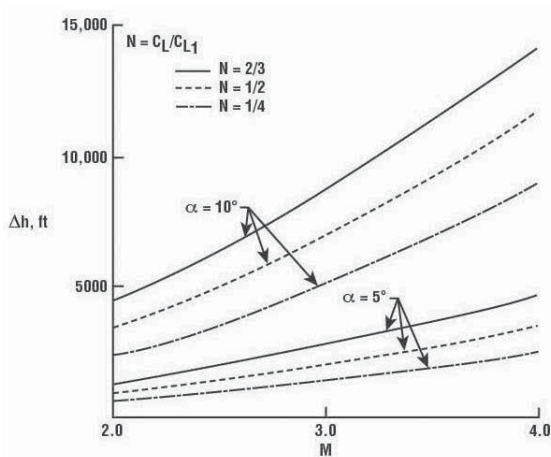
Since overland supersonic flights would include operations over heavily populated areas, Ferri (ref. 5.2) examined the possibility of substantially reducing the sonic boom when flying over cities. As illustrated in figure 5.10(a), reducing the aircraft lift can be accomplished by means of a maneuver. An airplane flying at high velocity could perform a pull-up maneuver of a few degrees before reaching the point where its cruise sonic boom level will be minimized and then fly a lower lift trajectory to effectively reduce the boom over the selected point. The airplane could then fly for several miles producing a signal that is substantially reduced.



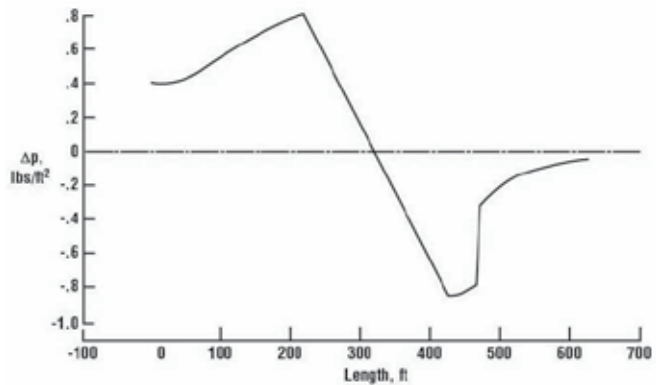
(a) Schematic of pull-up maneuver.



(b) Distance over which boom is reduced.



(c) Maximum Δh reached.



(d) Resulting boom signature.

Figure 5.10. Local reduction of sonic boom by maneuvering aircraft (adapted from ref. 5.2).

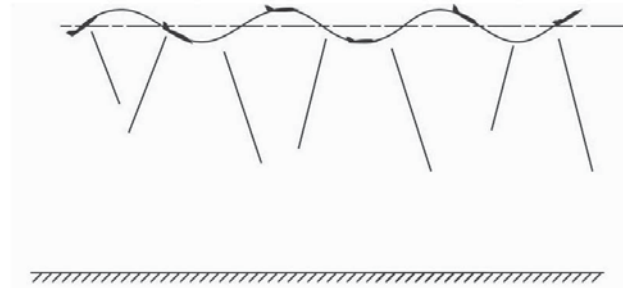
The distance over which the reduced boom levels would be realized is given in figure 5.10(b) as a function of Mach number and for different values of, the pull-up or pushover maneuver angle and for varying values of N , and the ratio of the aircraft C_L during the maneuver to the cruise C_L . The maneuver starts at an altitude of 40,000 feet (see fig. 5.10(a)) where the airplane makes a pull-up maneuver of α degrees and then flies a trajectory at constant C_L , equal to N times the C_L for cruise, with constant velocity. The airplane first increases altitude, then descends, and reaches 40,000 feet again at the same angle α . The maximum altitude reached is given in figure 5.10(c). Two values of initial angle of the trajectory have been considered – one corresponding to $\alpha = 5^\circ$ and the second to $\alpha = 10^\circ$. The maximum value of the discontinuous Δp produced by the sonic boom decreases strongly when the flight altitude decreases and C_L decreases.

The maneuver therefore can alleviate substantially the disturbances produced by sonic boom. For example, initial Δp for the C_L corresponding to the two-thirds of the horizontal value at an altitude of 40,000 feet can be as low as 0.4 lb/ft² and ramping up to about 0.8 lb/ft², as shown by the signature in figure 5.10(d). The boom signature corresponds to an airplane having a weight of 460,000 pounds and a length on the order of 300 feet. The takeoff weight of the airplane is between 650,000 and 700,000 pounds. Whether or not tailoring cruise flight path to include pull-up pushover maneuver to reduce lift and thus Δp as the aircraft approaches populated areas is yet to be evaluated as being practical or usable.

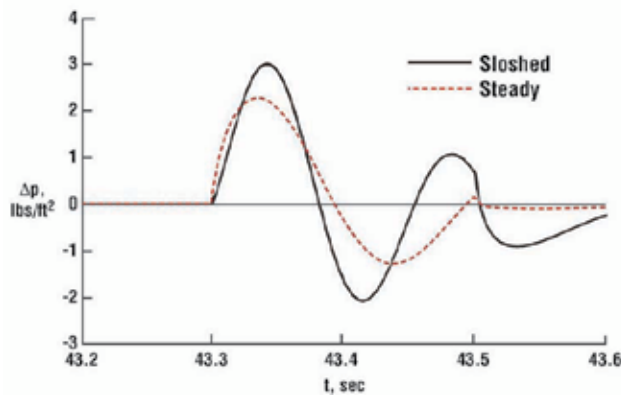
Active Control-Unsteady Flight Path

Figure 5.11 presents some results of a study by Crow and Bergmeier (ref. 5.3) of sonic booms produced by aircraft in non-steady flight. The goal was to find whether “slosh”, a non-steady source phenomena where the longitudinal

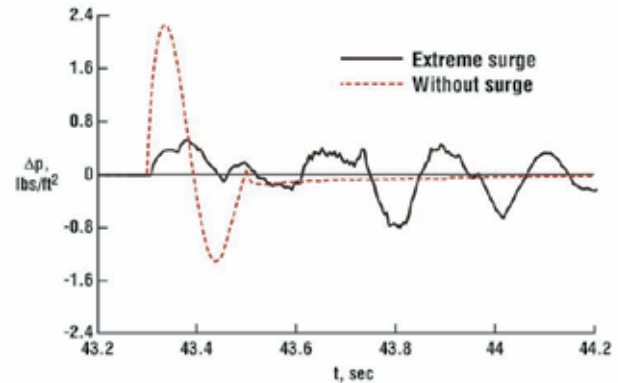
flow of lift back and forth from the middle of the aircraft to the nose and tail, and surge, a periodic acceleration of the aircraft along its flight path, can scramble or attenuate sonic booms heard by listeners on the ground as schematically is illustrated in figure 5.11(a). Such source phenomena would constitute active sonic boom control. Active sonic boom control must somehow prevent the pressure waves generated by a supersonic aircraft from coalescing into compact and coherent wave at large distances. The control methods must work for listeners located anywhere on the ground.



(a) Periodic flight profile.



(b) Sonic boom from a sloshed lift distribution.



(c) Sonic boom from an aircraft subject to extreme periodic surge.

Figure 5.11. Active sonic boom control using non-steady flight (adapted from ref. 5.3).

The first example of a periodic source is slush. An aircraft with three lifting surfaces could implement slush by oscillating control surfaces at the three trailing edges with the canard and tails synchronized and the wing 180° out of phase. Alternatively, an elongated delta or quarter sine wing could have piezoelectric leading edges capable of bending into S-shapes, thereby altering the longitudinal distribution of cambers. Figure 5.11(b) displays sonic booms arising from periodic slush. The darker curve is the boom at zero phase, while the red dashed curve is the boom of the steady source. It was concluded from the plot that slush alters the boom profoundly but does not reduce its pressure level.

The second example of a periodic source is surge – a periodic acceleration of the aircraft along its flight path. In principle, engine thrust variations could implement surge. A deliberately excited phugoid oscillation could do so also, with the complication of small periodic changes in altitude. Neither mode of implementation was recommended for commercial supersonic transports. Sonic booms from the surging aircraft are stretched and attenuated, as shown in figure 5.11(c). The sonic boom of the steady source (red dashed line) has collapsed into waves of low amplitude resembling broad band noise. The waves seem oddly complicated in view of their origin from a simple aircraft undergoing a simple sinusoidal surge.

As stated by Crow and Bergmeier (ref. 5.3, p. 108), “Unfortunately the assumed surge amplitude is anything but practical; its position oscillates at an amplitude of 400 feet and frequency of 0.5 Hz. The amplitude of speed oscillations is 1257 ft/sec, so the speed varies from 73 ft/sec to 3257 ft/sec in the course of a cycle. Acceleration oscillations have amplitudes of 3948 ft/sec², about 123 times the acceleration of gravity.”

The authors also point out that the speed and acceleration amplitudes diminish as the frequency falls, but so too does the efficacy of surge as a means of reducing sonic boom intensity. At a frequency of 0.1 Hz, the amplitude of acceleration is 4.9 times gravity, but the sonic boom is hardly changed from the case of steady flight. Surge with more moderate accelerations shifts the boom back and forth without chopping it to pieces. The phase-averaged boom is still weak, but the weakness reflects only boom displacements, not intensity reductions that a listener would notice.

In this section, five approaches to sonic boom minimization through the use of flight operations have been discussed including – (1) the influence of altitude and Mach number, (2) flight path angle, (3) Mach cut-off operations, (4) tailoring the flight path, and (5) active control-unsteady flight path. The first three approaches are considered to be practical while the last two may be considered beyond the realm of current practice. Increasing altitude, using a climbing flight path angle, operating at speeds that are less than the speed of sound at the ground, and M_{CO} can play a role in reducing the boom levels at the ground. Other than flight below M_{CO} eliminating the boom at the ground (or making it worse if cutoff condition is slightly exceeded), these flight parameters do not change the character of the boom. In 1965, McLean (ref. 5.20) pointed out that booms propagating to the ground could be “mid field” and not necessarily asymptotic far-field N-waves. That led to the development of the concept of the mainstream approach to boom minimization.

Boom Minimization through Aircraft Shaping

Following McLean’s concept of mid-field signatures, considerable research efforts have been made aimed at reducing or eliminating sonic boom by shaping. These efforts have been classified as two types of studies – (1) aerodynamic modification studies and (2) exotic configuration studies. As stated by Seebass and George (ref. 5.21, pp. 687–688), “We will call aircraft configurations that leave total enthalpy of the flow essentially unchanged aerodynamic configurations. ... Configurations that change the total enthalpy of a significant fraction of the flow past them, as well as those that rely on physics beyond our comprehension, we will term exotic configurations.”

In this section, minimization by way of aerodynamic modifications that leave the total enthalpy of the flow essentially unchanged will be discussed. A presentation of several configurations/planforms that have been set forth aimed at minimizing the sonic boom and the role that the aircraft volume and lift distribution play in shaping the vehicle boom signature is included. Substantial quantitative analysis of shaping has utilized Whitham’s equivalent body concept. Chapter 7 presents details of the application of this concept to shaping, together with an extensive review of shaping configuration studies. A brief review of this concept is presented in this chapter. This is followed by a discussion of the role two configuration components, wing planform and wing dihedral, play in boom minimization. Application of the various boom approaches aimed at designing low-boom concepts is presented as applied to numerous supersonic transport and supersonic business jet concepts.

Configuration/Planform

The concepts illustrated in figure 5.12 involve vehicle shaping for boom minimization. Their objective is generally to reduce the amplitude of the shock waves either by stretching an N-wave signature and trading length for amplitude, or to create a non-N-shape such as a flat-top or ramp.

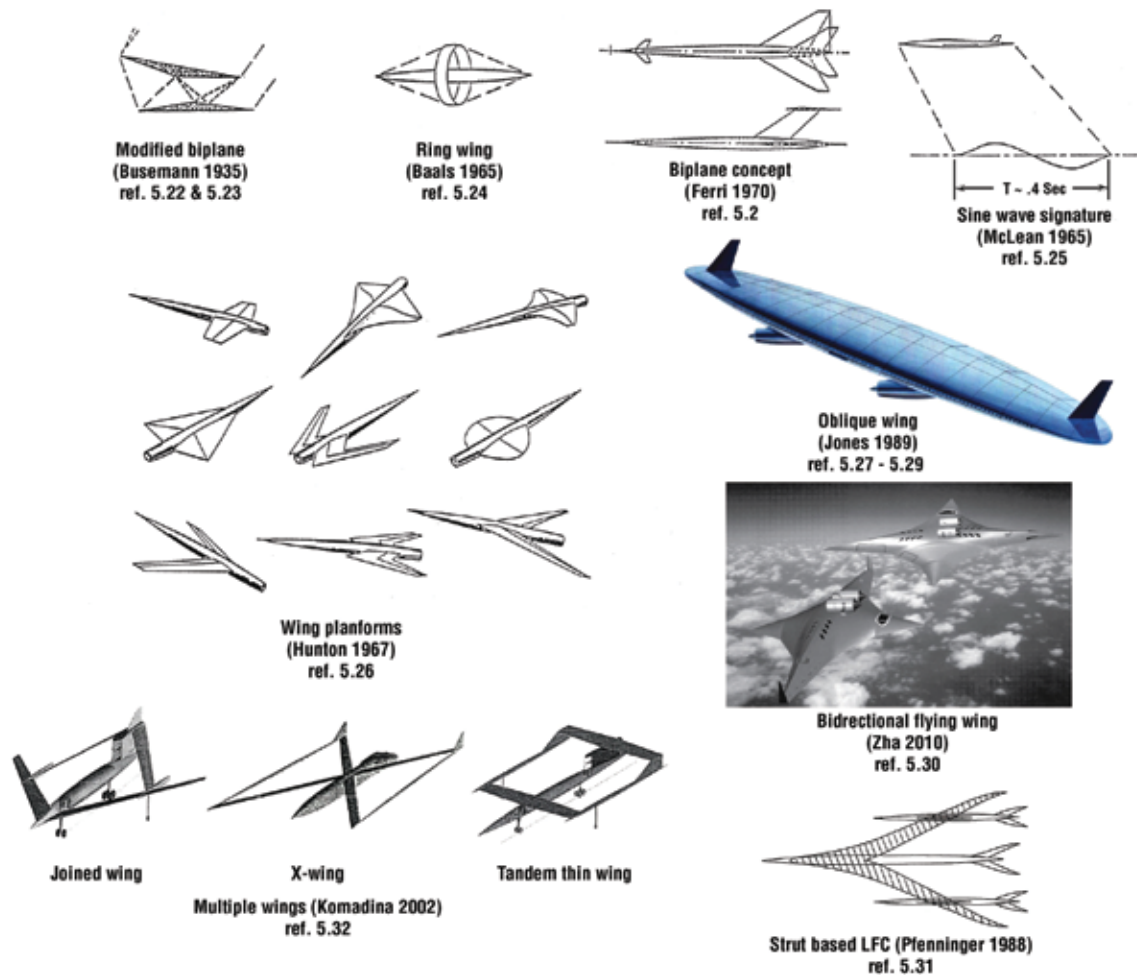


Figure 5.12. Boom minimization concepts involving vehicle shaping.

The Busemann biplane concept of 1935 (fig. 5.12, top left) is a concept where for one specific Mach number at zero lift, the wave drag can be made zero with no external shock waves (ref. 5.22). Twenty years later (ref. 5.23), Busemann noted that no satisfactory solution for the lifting case depicted has yet been devised. The ring wing (ref. 5.24) is essentially the Busemann wing wrapped around a contoured fuselage. It is also ineffective for the lifting case. A practical version of the supersonic biplane with reduced booms has been investigated by Ferri (ref. 5.2) and is a unique way to increase the effective lifting length of the vehicle. In the mid 1960s, McLean (ref. 5.25) noted that for supersonic transports of practical length, the signature at the ground need not be the far-field N-wave. He observed that the mid-field region could extend several hundred body lengths. One could envision a large (500-foot long) SST flying low enough to be within the near field. If the volume and lift distributions are optimized, the sonic boom signature could be a sine wave and, thus, not easily observed by a person outdoors.

Several wing configurations that were examined by Hunton in regards to the effect of wing planform, dihedral, and camber on sonic boom (ref. 5.26) are shown in the center left of figure 5.12. The oblique wing was a concept developed in Germany in 1942 and flight proven during the 1980s in the form of the subsonic AD-1 by NASA under the direction of Jones (ref. 5.27). Li, Seebass, and Sobieczky (ref. 5.28) noted that this configuration was designed to fly efficiently at subsonic speeds and also overland at Mach numbers of 0.9 to 1.10 where there is no sonic boom at the ground. This concept combines the volume and lift distributions to have a long lifting length and to alter boom signature both below the aircraft and at lateral distance from the ground track. Early studies (ref. 5.29) suggested that the oblique wing concepts may be limited to ~Mach 1.4. Speeds higher than Mach 1.4 are possible with more wing sweep, but, as stated in reference 5.28 (p. 754), “the wing’s control becomes increasingly difficult with 60° being judged acceptable in previous studies.”

A recent novel idea for a 70-passenger supersonic transport, shown at the middle right of figure 5.12, having an operational range of 2000 nmi, that is claimed to achieve low sonic boom and high subsonic and supersonic performance is the supersonic Bi-Directional (SBiDir) flying wing (ref. 5.30). This Mach 1.6 vehicle, which has a wing loading of 15.3 lbs/ft², is said to achieve its high efficiency subsonically and supersonically by performing a mode change from subsonic to supersonic and vice versa using one of two options – (1) to turn the engines through a mechanical system or (2) by using the aerodynamic forces on the wing to turn the airplane under the engines. They considered the latter since it was found to be the most energy efficient method. Pfenninger’s long-range supersonic laminar flow design (ref. 5.31), shown in the lower right of figure 5.12, incorporated highly swept strut-braced wings and was to offer high cruise L/D’s and low sonic boom overpressures. Several multiple wing configurations studied by Northrop Grumman (ref. 5.32) during the Defense Advanced Research Projects Agency (DARPA)/Quiet Supersonic Platform (QSP) program (ref. 5.33) are shown at the bottom left of figure 5.12. These highly unconventional vehicle concepts were thought to be more accommodating in fulfilling the QSP goals and requirements, particularly in the 6000-nmi range. This DARPA effort was aimed at advancing the technologies necessary to enable the development of efficient and environmentally acceptable overland supersonic aircraft. So there are a multitude of supersonic aircraft concepts, but most except for the Concorde and various fighter aircraft have not evolved enough in terms of their design maturation to determine their viability.

Volume and Lift Distribution

Sonic boom signature minimization through aircraft shaping is based upon the equivalent body concept established by Whitham and Walkden (refs. 5.34 and 5.35) and is illustrated in figure 5.13 (ref. 5.36). The message to be conveyed is that for sonic boom purposes, if the actual airplane wind-tunnel model shown in the upper left of the figure is replaced by an equivalent body of revolution (upper right) having the same effective area distribution (A_e) as shown by the center plot, then similar sonic boom signatures will result. The two sonic boom signatures shown at the bottom of the figure confirm the validity of the theory. Some slight variations are noted to exist between the tail shock recompression (negative) phase of the waveform, but these are primarily a result of the body-sting support termination.

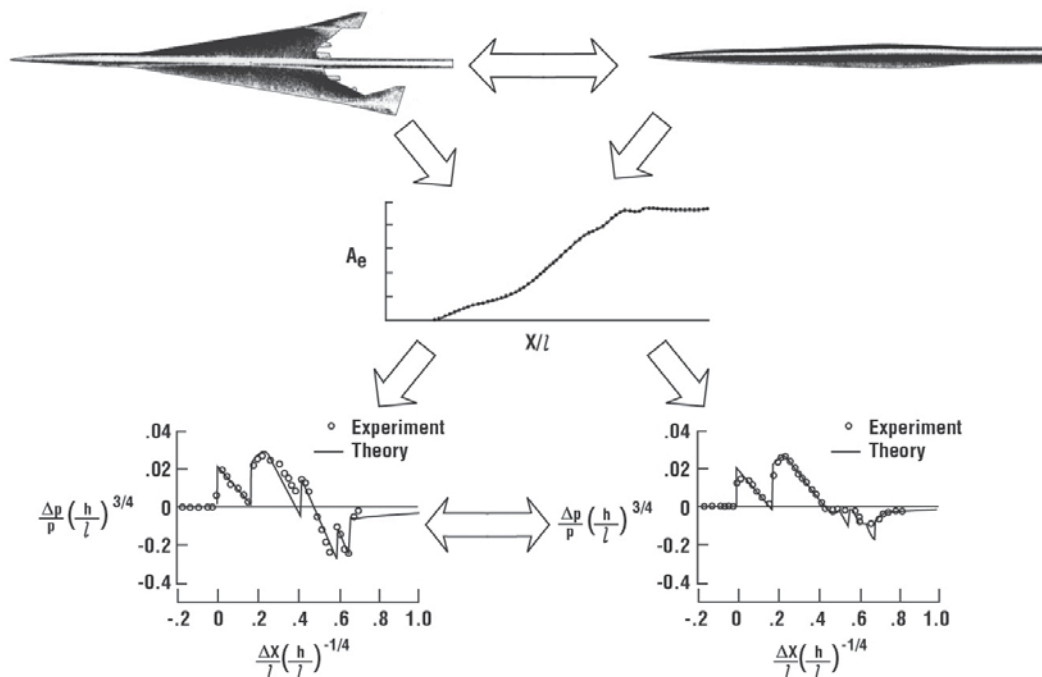


Figure 5.13. Illustration of the equivalent body concept, Mach 1.41, $C_L = 0.1$, $h/l = 10$ (adapted from ref. 5.36).

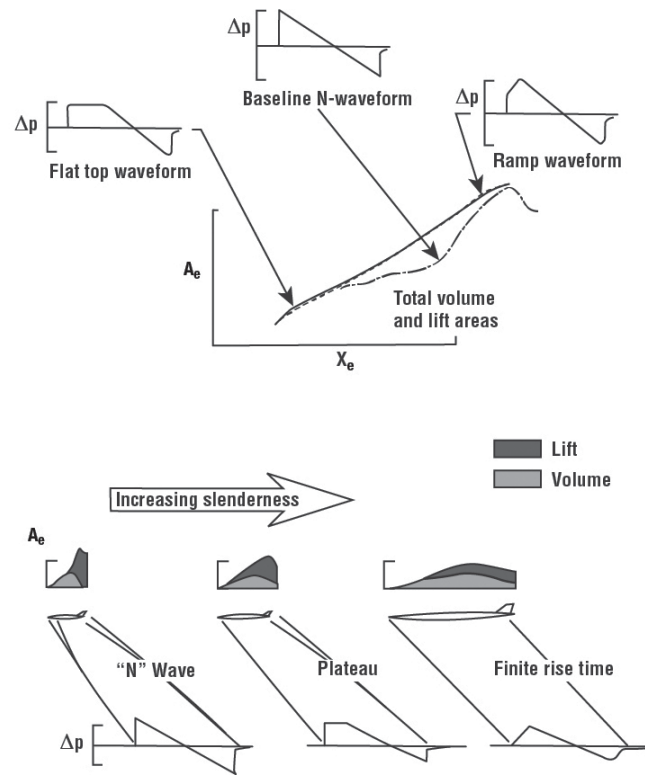


Figure 5.14. Relationship of signature shapes to vehicle area development.

Illustrations of some general signature characteristics and airplane shaping considerations for sonic boom minimization are illustrated in figure 5.14. Three equivalent area distributions (A_e) and the resulting far-field boom signatures are shown in the lower part of the figure. All of the past and current supersonic aircraft, which are not designed for boom minimization, have their volume and lift arranged in such a manner as to produce an N-wave on the ground. Designs where the aircraft volume and lift are arranged so as to produce a smooth optimum progression of A_e from the nose to the maximum value result in a boom signature that can either be a flat-top or an initial shock ramp type waveform as illustrated by the two top A_e curves. Note that very little change in A_e (at the nose and near the maximum value) is necessary to change from a flat-top to an initial shock-ramp signature.

In order to reduce the overpressure for a given design, the equivalent area must be spread so as to increase the slenderness ratio as illustrated by the three sketches shown in the lower part of figure 5.14. It will be noted that the N-wave signature is associated with an A_e development that is irregular resulting in the classical N-wave. As the A_e development is smoothed and stretched out over a longer length with a lesser A_e maximum, a flat-top (plateau) signature of reduced Δp results. Spreading A_e smoothly over an even longer length and even lower A_e maximum could result in a finite rise time signature approaching a sine wave. As will be shown later in this section, vehicle length on the order of 500 feet or greater would be required for this latter case. Two important lessons learned from the discussion are that the signature overpressure is set by the maximum area carried and the signature shape is determined by the shape of the A_e curve.

Vehicle Shaping – Wind-Tunnel Results

The area shaping concept was first validated by Carlson et al. in 1966 on two models tested in the wind tunnel (ref. 5.36) that had equivalent area distributions similar to the N-wave signature and Plateau (asymmetric flat-top) signature depicted in figure 5.14. The test results are provided in figure 5.15. Measured sonic boom signatures for two vehicle configurations are shown for various distances from the models – one vehicle configuration consisting of a basic body designed to produce an N-wave signature in the far field and another vehicle configuration

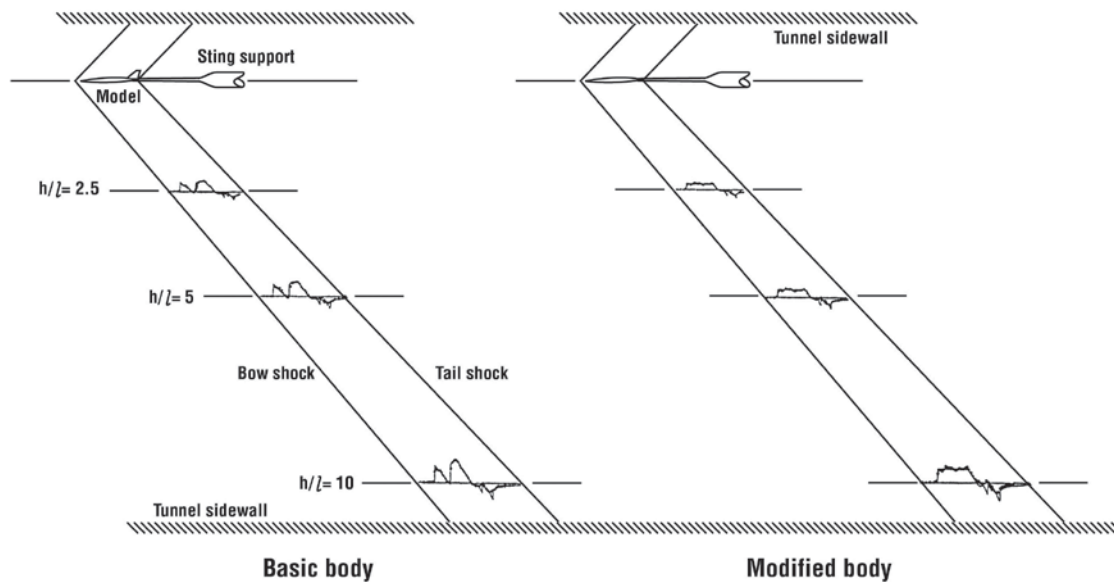


Figure 5.15. Measured sonic boom signatures on a basic and modified equivalent body of revolution in the wind tunnel, Mach 1.41, $C_L = 0.1$ (adapted from ref. 5.36).

consisting of a modified body designed to produce a flat-top signature in the far field. Signature measurements at 2.5, 5, and 10 body lengths (h/l) from the model illustrate the development of the waveforms for the two models. Note that the basic configuration signature sketches shown to the left, which result in an N-wave in the far field, still retain the multiple saw-tooth shock characteristic out to 10 body lengths. However, the signatures shown on the right side of figure 5.15 are produced by a model, that was designed to produce a flat-top signature in the far field, and show flat-top waveforms at all three measurement positions. Tunnel test section/model size constraints limit the furthest measurement – in this case, to 10 body lengths from the model. Measurements at larger h/l either require smaller models, which then begin to lose geometric fidelity, or larger tunnels. Wind-tunnel model near-field signatures of the type shown in figure 5.15 are then inserted into a sonic boom prediction program and propagated to distances/body lengths equivalent to full-scale aircraft flying at cruise altitudes.

Vehicle Shaping – Flight Test Results

Although theory, supported by wind-tunnel measurements, predicted that a shaped signature from a real aircraft would persist to the ground while propagating through the real atmosphere, the consensus of the technical community was that this process would have to be demonstrated.

In 2002, Northrop Grumman had the opportunity to demonstrate this area shaping concept on an existing aircraft to produce a shaped sonic boom signature. This aircraft modification and test was designed to produce a flat-top signature on the ground and thus, if successful, would confirm that a shaped signature would persist through a real atmosphere to the ground. This program (ref. 5.37), named Shaped Sonic Boom Demonstrator (SSBD), was carried out as part of DARPA's QSP program (ref. 5.33). Theory predicted that a shaped wave would persist to 300–600 body lengths. Wind-tunnel measurements similar to those of figure 5.15 have been acquired on models designed to have shaped waveforms out to the walls of the test section, some 20 body lengths.

To demonstrate persistence, only the positive phase of the aircraft's N-wave needed to be modified. This is fortunate, since modifying the complete N-wave signature would be virtually impossible. An initial study had shown that it was feasible to modify the F-5E series aircraft to produce a shaped boom signature in a relatively short time frame and at a reasonable cost. Detailed boom analysis, including CFD, provided the required design modifications. A brief view of both aircraft and the shaping change along with the measured flight-test signatures are given in figure 5.16 (ref. 5.37) and figure 5.17 (refs. 5.38, 5.39, and 5.40). Referring to figure 5.16, on the left side of the figure is shown the basic F-5E Tiger II aircraft and its associated equivalent area distribution (A_e)

which is known to produce an N-wave at the ground. To the right of the figure is shown the SSBD aircraft with its re-shaped equivalent area distribution (A_e) designed to produce a flat-top signature at the ground.

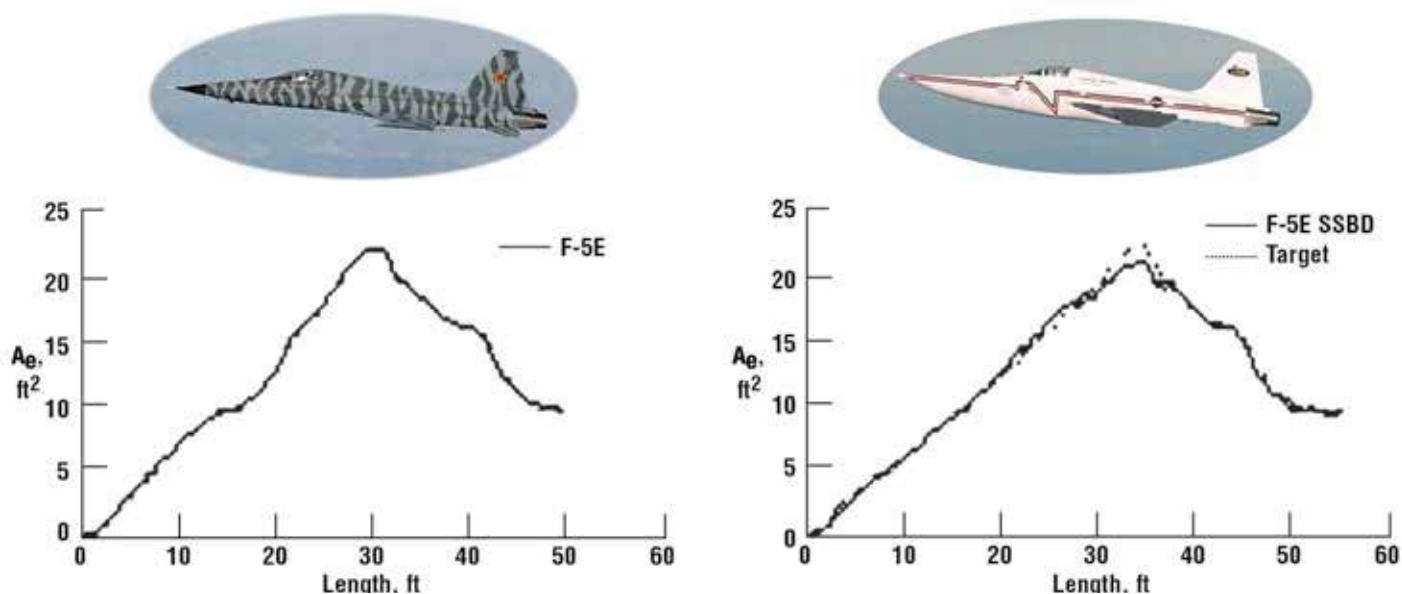


Figure 5.16. Modification of F-5E into the Shaped Sonic Boom Demonstrator (SSBD) (adapted from ref. 5.37).

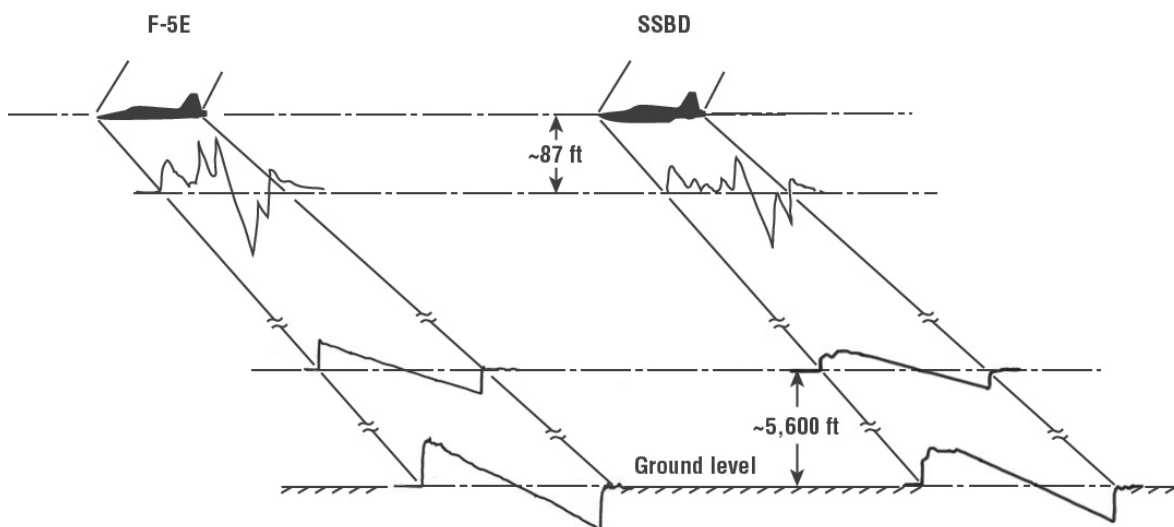


Figure 5.17. In-flight and ground measurement of shock flow field below the F-5E and SSBD (adapted from refs. 5.38, 5.39, and 5.40).

In-flight probings of the F-5E and SSBD were performed to describe the near- and mid-flow field below each aircraft. Signature measurements were also acquired in the far field using a sailplane flying at about 6,000 ft above ground level and with microphones at ground level. The results of these flight tests are given in figure 5.17 (refs. 5.38, 5.39, and 5.40).

For both the F-5E and SSBD, the near-field signatures contain several shocks from the various components of each aircraft. The results of the modifications to the SSBD are evident when comparing the front portion of the signatures to that of the F-5E. Note too that the three shocks at the rear of the signature are similar since no changes were made to the aft end of the F-5E. At ground level, the F-5E signature has developed into a classical N-wave and the SSBD signature has developed into the flat-top wave as designed. In figure 5.18, the ground measured boom signatures for the F-5E and SSBD are compared. The aircraft were flying about 45 seconds apart at about the same altitude, Mach number, and flight track.

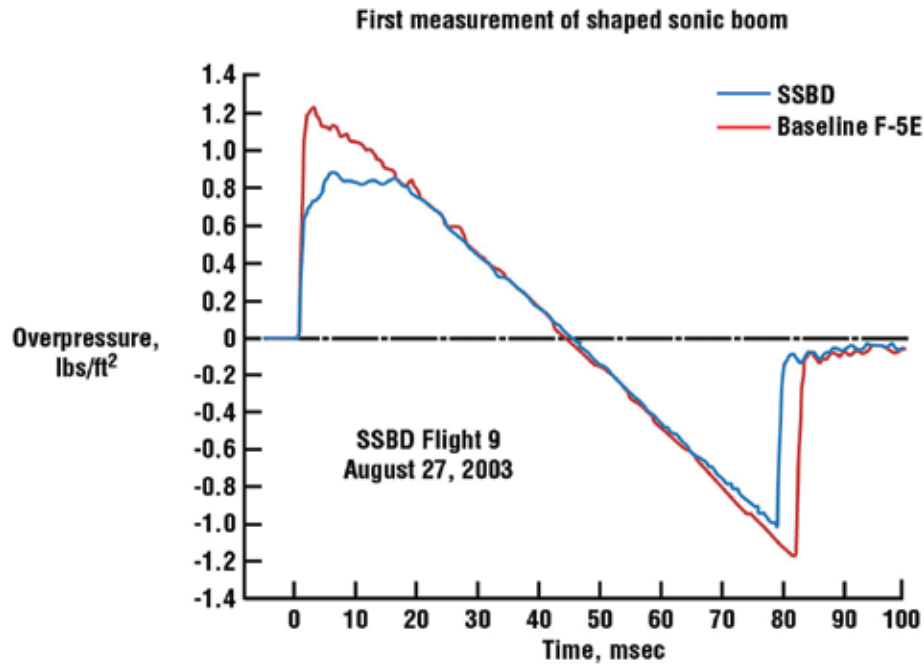


Figure 5.18. First measurement of a shaped sonic boom (ref. 5.37).

Exhaust/Aft Shock Interaction – Flight Test Results

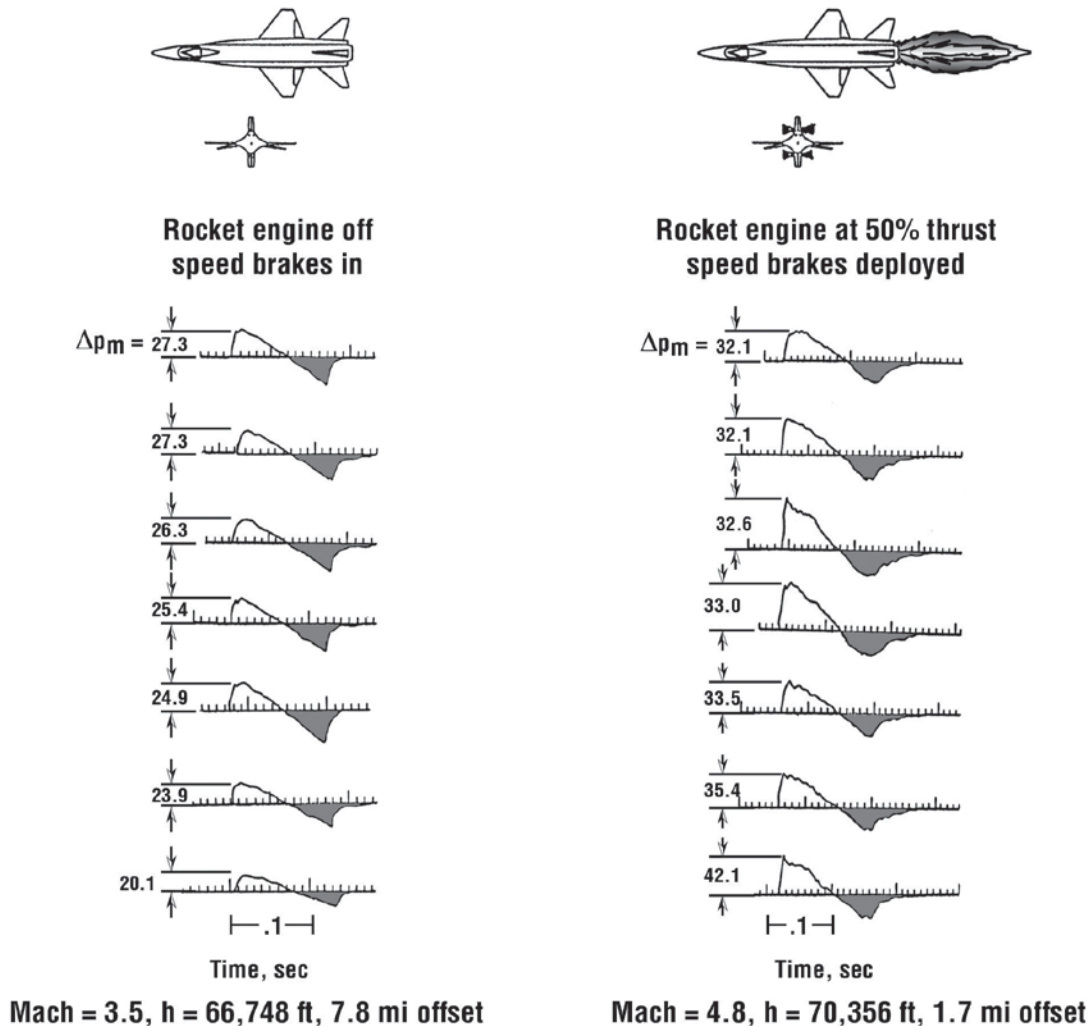
Current prediction codes take into account the aircraft engine exhaust flow and include it as an area addition in developing the equivalent area distribution (A_e) for given flight conditions. In some configurations, because of engine placement, the exhaust influences the A_e during its rise to the maximum area – an undesirable feature. Other configurations have the exhaust adding beyond A_e max can smooth the area distribution and reduce the aft shock, which can be a desirable feature relative to its influence on the far-field boom signature.

Sonic boom measurements were acquired on the X-15 hypersonic research aircraft (fig. 5.19(a)) and are reported in reference 5.41. An interesting set of data was obtained concerning the influence of the X-15 aft flow field, specifically the exhaust plume and speed brake deployment, on the sonic boom signatures. The results are shown in figure 5.19(b).



(U.S. Air Force photo)

(a) North American X-15 hypersonic research aircraft.



(b) Effects of X-15 rocket engine plume and speed brakes at Mach~4 and altitude of about 70,000 feet (adapted from ref. 5.41).

Figure 5.19. The North American X-15 hypersonic research aircraft and influence of rocket engine plume and speed brakes on X-15 sonic boom signatures.

Two sets of boom signatures are presented – the signatures on the left are for the X-15 without the rocket engine thrusting and speed brakes retracted, and the signatures on the right are for the aircraft with the rocket engine thrusting at 50 percent and its four speed brakes deployed. The boom signatures from the seven microphones separated by about 100 feet have been drawn to the same overpressure and time scale. The important point to be made regarding the two sets of signatures relates to the manner in which the tail shock (recompression wave) returns to ambient pressure. For the non-thrusting case and speed brakes retracted, shown to the left, the bow and tail (recompression) shock fronts have rapid recoveries. As such, two cracks or booms were heard. In the case

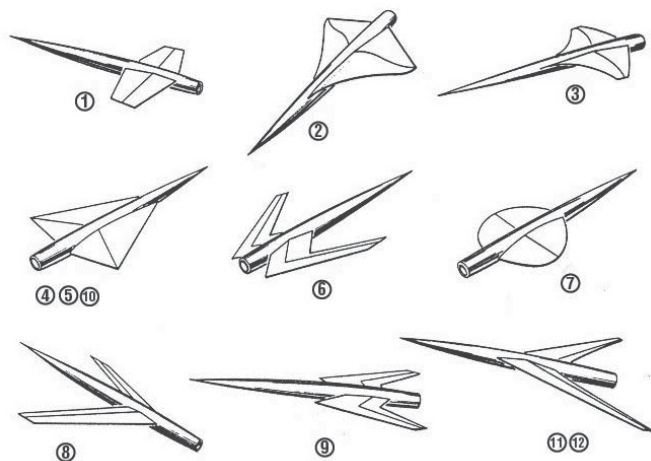
of the engine thrusting 50 percent and speed brakes deployed (shown to the right of the figure), the tail shock recovery is very gradual with a considerably longer rise time. This stretching of the negative phase of the boom signature is due to the influence of exhaust plume and wake from the speed brakes, which are acting to increase the effective length of the vehicle. An observer would hear only a single crack associated with the bow shock in this latter case.

The results of figure 5.19(b) suggest that consideration be given to examining the possibility of favorably altering the aft shock flow-field exhaust design to minimize the influence of the tail shock regarding people and building response. For the current vehicle designs that produce N-wave signatures in the far field on the order of 1 lb/ft² to 3 lbs/ft², the influence of the engine exhaust flow plays a second order role in the boom intensity and signature shape. However, in the design of low-boom shaped signature vehicles, the exhaust flow will play a more important role. A more in-depth discussion on the influence of engine exhausts on boom signatures is provided in Chapter 7.

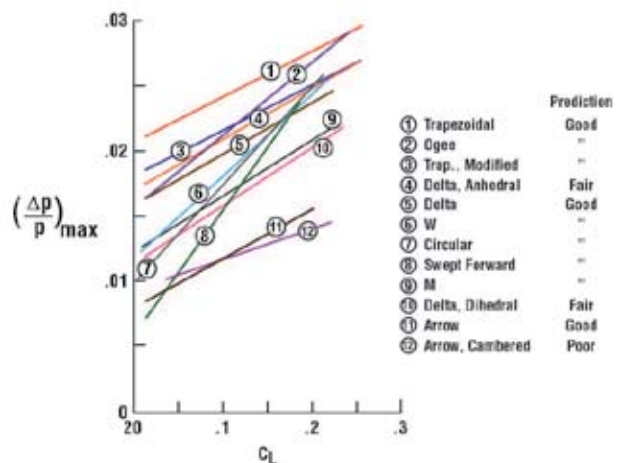
Wing Planform

Shocks due to volume effects are minimized by having volume distributions that are as close to optimum as possible. In Chapter 7 of this publication, the virtues of volume distributions that provide a fast pressure recovery followed by a shock are discussed. Lift distributions can also be used to control the strength and location of shocks by means of planform changes, wing section thickness, wing twist, and wing camber and dihedral. It is important to note that the volume and lift contributions to the effective area distribution are superimposed such that the two contributions must be optimized together to obtain the optimum results. An interesting set of wind-tunnel tests of various wing configurations was conducted in the mid 1960s (ref. 5.26) to examine wing configurations that were to some extent unconventional at the time in order to search out possible new design concepts for boom minimization that may have been overlooked in earlier studies.

Shown in figure 5.20(a) (ref. 5.26) are sketches of wing configurations examined. Each had been selected to feature some particular arrangement of the wing shock system – such as intersecting, curved, or vertically displaced shocks to explore various shock system combinations. In addition to these symmetrical configurations, the arrow wing was also tested with a cambered airfoil section and the delta wing studied with wing dihedral of $\pm 10^\circ$.



(a) Study configurations.



(b) Summary of wing peak overpressures.

Figure 5.20. Influence of wing configurations on sonic boom, Mach 1.4, $h/l = 4$ (adapted from ref. 5.26).

A summary of the overpressure characteristics measured for these various wings in the presence of the simple body is provided in figure 5.20(b). Maximum peak overpressures resulting from the wing as a function of lift coefficient are presented for 12 wings for Mach 1.4 and at a distance of four body lengths. The assigned numbers, in addition

to identifying the curves, can be seen to indicate the general progression of overpressure from the highest to the lowest level at the approximate lift coefficient for transition flight of 0.15. Also shown is a table on the right that is intended to summarize, in somewhat gross terms, the measure of success in which the characteristics of these several wings could be predicted by theory at the time.

The principle conclusions that were drawn from the study are as follows:

1. A relatively large spread in overpressures was obtained for this series of wings ranging from the unswept trapezoidal down to the highly sweptback arrow and the limits of this spread were predicted by theory.
2. Camber for the arrow wing was advantageous at the higher lift coefficients and warranted further detailed study. This effect was not predicted by theory.
3. The variation in lift effectiveness on the overpressure, as evidenced by the differences in the slopes of the curves, is quite large and preliminary estimates of these effects were generally successful.
4. Wing dihedral on the delta configuration showed a surprisingly large reduction of the overpressure, which was predicted with only fair success.

Wing Dihedral

Sonic boom minimization, when realized to its fullest extent, will include consideration of the complete ground footprints. Thus, minimum boom concepts will attempt to not only reduce boom levels directly below the aircraft but also laterally to each side of the ground track out to cutoff. Wing dihedral has been shown to be effective in providing boom relief for both on- and off-track locations, as shown in figure 5.21.

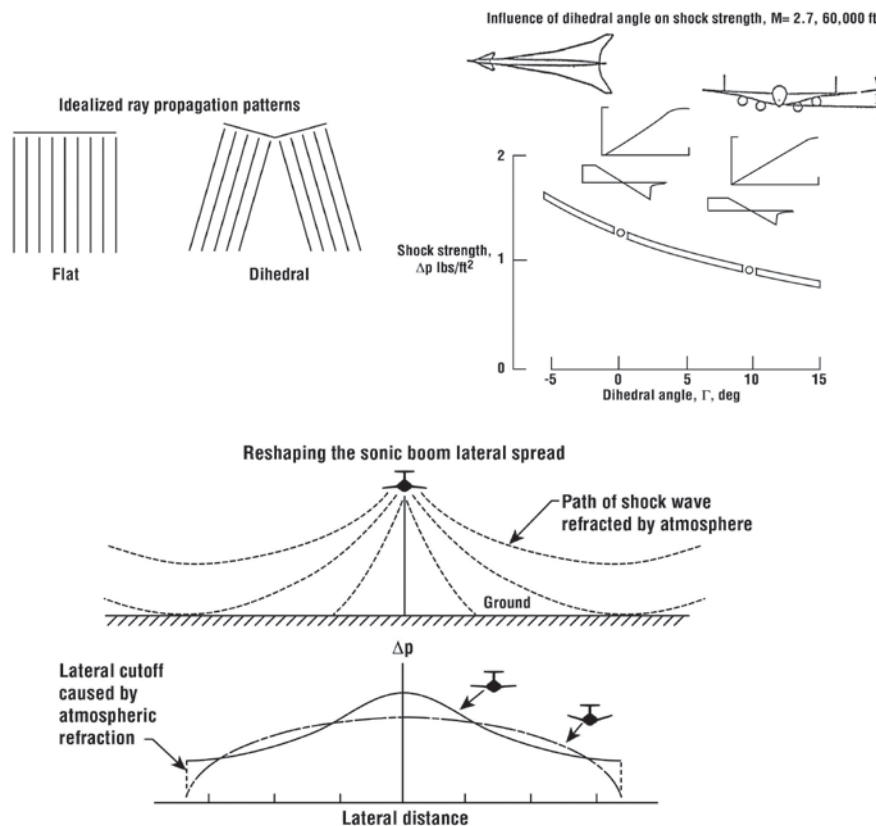


Figure 5.21. Influence of dihedral on boom reduction.

The idealized ray propagation patterns for a flat wing and one with dihedral, illustrating the influence of dihedral, are shown at the top left of figure 5.21. In the top right of the figure, the influence of dihedral on a large SST type concept (ref. 5.42) is shown. As can be seen, dihedral angle is an extremely important design consideration. Dihedral angle is defined as shown in the sketch of the rear view of the configuration at its design attitude. A dihedral angle of 0° would result in an on-track shock strength of about 1.25 lbs/ft². Increasing the dihedral angle to about 9.5° permits the trailing edge of the wing tip to lie in the same horizontal plane as the wing apex such that when developing the equivalent area distribution, A_e , the 9.5° dihedral is equivalent to about a 40-foot increase in the wing overall length. This results in a 28-percent reduction on-track shock strength to about 0.9 lb/ft². Increased dihedral could lead to greater gains. However, as wing dihedral increases, so too does the aircraft roll-yaw coupling increase leading to aircraft stability problems. There is thus a strong incentive for solution of the problem of roll-yaw coupling for wings with large positive dihedral. In the lower part of figure 5.21 are two sketches that describe the lateral distribution of sonic boom overpressures. The solid line curve represents the expected falloff of Δp with lateral distance out to the lateral cutoff due to atmospheric refraction of the shock waves. The dashed curve suggests a more uniform redistribution of the overpressures through the use of wing dihedral. Since the lateral cutoff is independent of the vehicle configuration and only a function of the aircraft operating conditions and the atmosphere (ref. 5.12), then the normal Δp distribution represented by the solid line can be considered as being flexible and since boom levels are less off track than under the aircraft, a flattening of the curve would provide for more uniform boom levels laterally across the ground boom footprint. Reduced levels are experienced under the aircraft and increased levels laterally.

An informative set of wind-tunnel tests relative to anhedral and dihedral were conducted as part of the wing configuration studies presented on figure 5.20 (ref. 5.26) and the results are shown in figure 5.22. Three models were tested (as shown by three curves on the left side of the figure) – (1) a flat wing, (2) a wing with 10° anhedral, and (3) a wing with 10° of dihedral at Mach 1.7 and a lift coefficient of 0.2. First note the small silhouette of the test configuration, which is scaled to show the relative size and distance of the model from the probe station located at ground level as tested in the wind tunnel that is equivalent to a distance of 4.5 body lengths. Also shown on the left are the peak overpressures measured as a function of lateral to vertical distance ratio for the three values of wing dihedral.

It can be seen that for -10° anhedral, higher overpressures are experienced over those for the flat wing (0°). On the other hand, for 10° of dihedral a significant reduction in overpressure is realized as compared to the flat wing. Also note, however, that these separated curves are nearly parallel, which was interpreted to mean that the effect of dihedral in these tests is attributed primarily to a volume effect, presumably from the vertical displacement of the wing volume and not to any favorable lift effect since the lift coefficient was the same.

The curves on the right of figure 5.22 are intended to show the attenuation of the centerline maximum overpressures for the three wings out to large distance ratios that are commensurate with flight. Note that at an h/l of 50 or more, N-waves begin to form and at h/l of 200 or so, representative of flight altitudes for SST size configurations, the effects of anhedral and dihedral are no longer evident. These results have been derived from the measured centerline signatures on the assumption that these near-field characteristics, measured at an $h/l = 4.5$ would remain orderly out to any distance. At the time of these tests, this assumption was questioned and it was recommended that further experimental investigation was needed (i.e., measurement at greater h/l 's). It is now understood, as will be shown in the next figure, that care must be exercised during boom minimization efforts that near-field signatures must be extended to much larger h/l 's for certain configurations before propagating them to the ground. This is especially true for those configurations designed to alter the lateral distribution of the pressures on the ground.

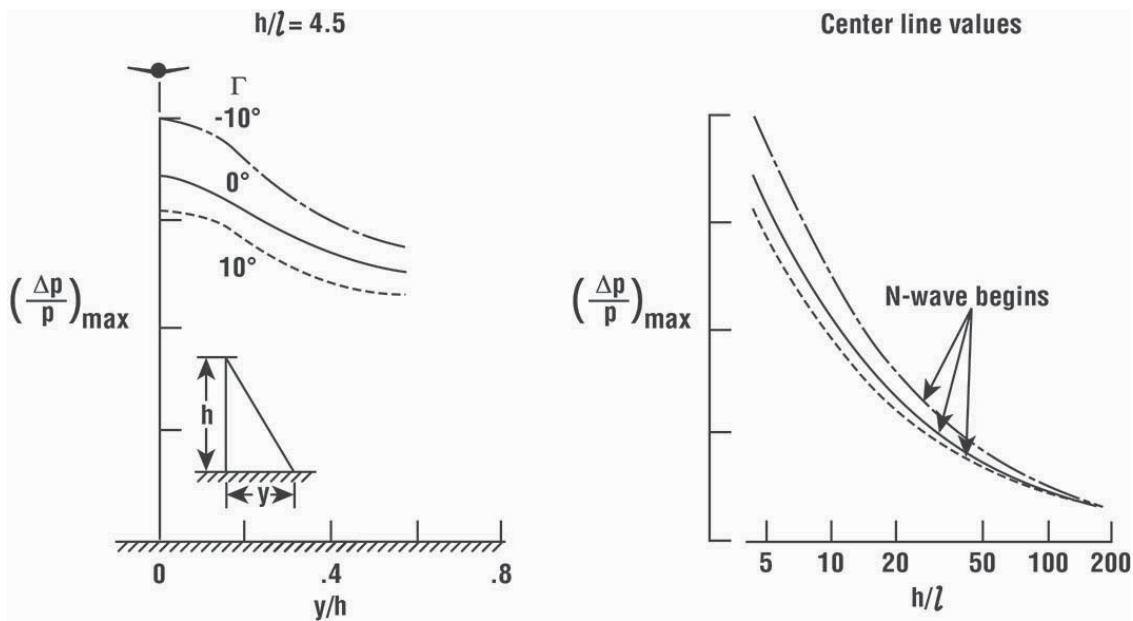


Figure 5.22. Measured and predicted effects of anhedral and dihedral on sonic boom (ref. 5.26).

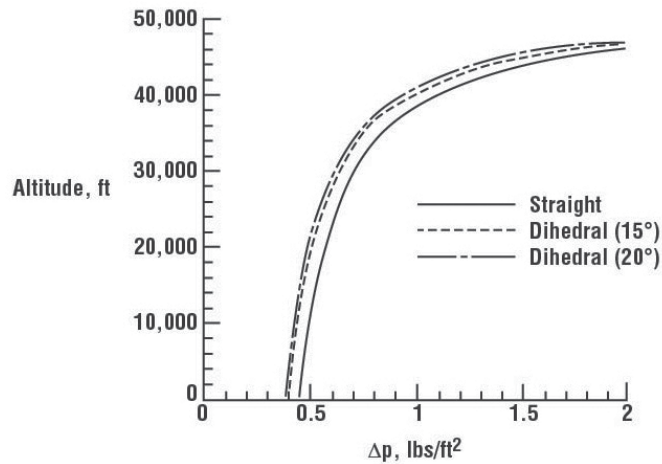
As an integral part of the NASA HSR program, an assembly of present and past sonic boom experts in the areas of boom generation, propagation, predicting, and effects met to establish the state-of-the-art needs and opportunities regarding boom minimization (ref. 5.43). In an overview of theoretical aspects of sonic boom, W. D. Hayes provided considerable insight into the concerns regarding lateral redistribution and axisymmetry.

Hayes first made the point that when sonic booms are calculated at an azimuthal angle other than at 90° (on-track) under the flight path, a rough approximation of the cosine of the azimuthal angle often is used as a factor to correct the lift contributions. For accuracy, the actual cuts for volume and lift at that azimuthal angle should be determined and the canonical procedure for predicting the sonic boom should be followed. Predictions and minimization calculations are most often done at an azimuthal angle of 90° , since boom levels are most often a maximum there. The lateral distribution of the boom should be accurately calculated when the flight track boom has been minimized, since those off track may be larger.

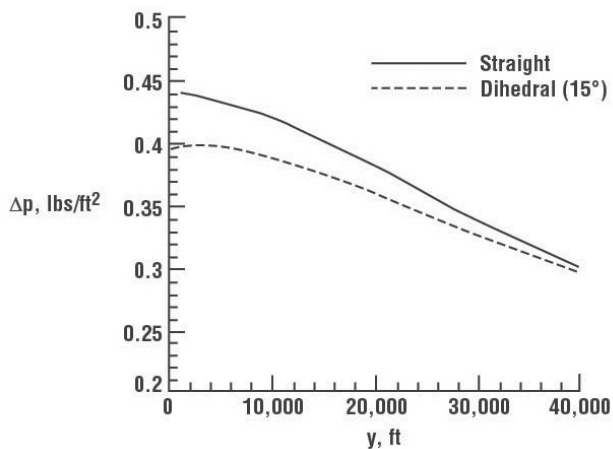
In reference 5.43 (p. 12), Hayes further stated:

...Ray-tracing or linear theory methods are only valid where the flow can be assumed to be locally axisymmetric, therefore, the nonlinear codes like MMOC must be modified to calculate in all azimuthal directions. Flow field codes would have to calculate further radially than they do currently so they could match the ray-tracing codes. Otherwise, experimental data for extrapolating from the near field to the mid field would have to be obtained from tests of wind tunnel models in large tunnels.

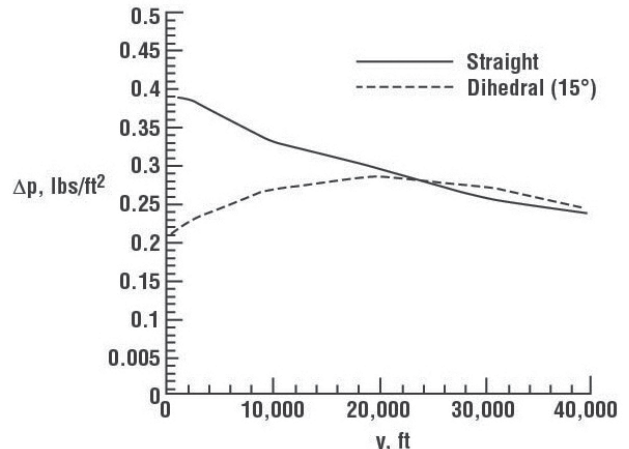
In reference 5.44, Bobbitt, Kandil, and Yang looked at the effects of wing dihedral on sonic boom using the 3-D-Full-Potential Propagation code of reference 5.45. The motivation for this study was the perception that the beneficial effects of dihedral may have been underestimated in the past due, in part, to the deficiencies of the propagation codes in use. Test cases included three 60° delta wings, two with dihedral of 15° and 20° and the third was straight (flat, no dihedral). One delta wing has a 5 percent biconvex airfoil section and a second was slab sided. The lift coefficient was maintained at the same value for both the plain (straight) and dihedral wings by varying angle of attack. Some results of this study are presented in figure 5.23 (ref. 5.44) for the straight delta wing (no dihedral) with a chord of 60 feet and similar delta wings with dihedrals of 15° and 20° . The flight conditions are for Mach 2 at 50,000 feet and at lift coefficients of 0.077.



(a) Variation of initial (bow) shock strength below wings.



(b) Variation of initial (bow) shock strength with lateral distance.



(c) Variation of trailing (tail) shock strength with lateral distance.

Figure 5.23. Effect of wing dihedral on sonic boom overpressure for a delta wing have 5 percent biconvex section and 60-foot chord flying at Mach 2 at 50,000 feet and a $C_L = 0.077$ (adapted from ref. 5.44).

Figure 5.23(a), which shows the on-track variation of the initial (bow) shock strength with altitude, in contrast with the results in figure 5.22, indicates that the benefits of dihedral persist all the way to ground from 50,000 feet (833 body lengths). Figure 5.23(b) and figure 5.23(c) show the variation of the initial (bow) shock strength and trailing (tail) shock strength, respectively, as a function of lateral distance from the flight track. It can be seen that for the initial (bow) shock (fig. 5.23(b)), the strength of both straight and 15° dihedral wing decrease with lateral distance and the difference in their strength also decreases. The trailing (tail) shock for the straight wing (fig. 5.23(c)) also decreases as lateral distance increases. For the 15° dihedral wing, the reduction in the trailing shock on track is much larger than that realized on the initial (bow) shock and this beneficial effect only persisted to about half the lateral distance realized for the bow shock. This indicates that there is a lift effect as well as a volume effect.

It should be noted that the lateral extent of the sonic boom footprint for the given flight conditions is about 135,000 feet lateral to the ground track. Thus, the lateral extent of the results in the figure (40,000 feet) suggests that the effects of dihedral beyond 40,000 feet and out to lateral cutoff for the cases shown are small.

Wing dihedral has been shown to be effective in providing boom relief for both on- and off-track locations on the ground. Reductions of from 18 percent to 28 percent of the on-track boom levels have been predicted for vehicles having 10-15° dihedral and continue at lesser benefits out to about 1/3 of the distance to lateral cutoff. Dihedral does not influence the extent of the lateral cut-off distance, which is independent of vehicle configuration and is only a function of altitude, Mach number, and the atmosphere.

Low-Boom Concepts

In principle, an aircraft can be designed to produce almost any type of sonic boom signature. Such a design, if it is to fly supersonic over land, must result in a viable aircraft with an acceptable low-boom shaped signature. It is known that aircraft configuration and technology advances are key players in attaining such a vehicle. Aircraft size (which is driven by the number of passengers) where boom levels tend to decrease as the vehicle decreases in size is also a key factor in producing a viable aircraft design that generates a low-boom shaped signature. Thus, a 10-passenger supersonic business jet has a much better chance of producing an acceptable boom than a 300-passenger commercial transport.

One illustration of the significance of aircraft configuration on sonic boom minimization is given in figure 5.24 (ref. 5.42). Sonic boom levels are shown as a function of aircraft weight at the beginning of cruise for four transcontinental vehicles of equal lengths of 290 feet with planforms varying from a delta-wing vehicle with tail to a tailless highly swept arrow wing with a canard. Sketches are used to show modified effective area developments and signatures corresponding to each of the four configurations.

An important consideration that often arises in discussions of sonic boom minimization is the advantage that can be taken of across-the-board technology advances. As such, each of the four design point airplane weights were also evaluated for combined empty weight and specific fuel-consumption reductions of 10 to 20 percent, as shown in figure 5.24. Overpressures of 1.0 lb/ft² and less are usually associated with the highly swept arrow wing planforms. It can be seen that, although technology advances offer appreciable gains in terms of reduced sonic boom level, these gains are not comparable with those potentially attainable through the employment of low-boom design approaches.

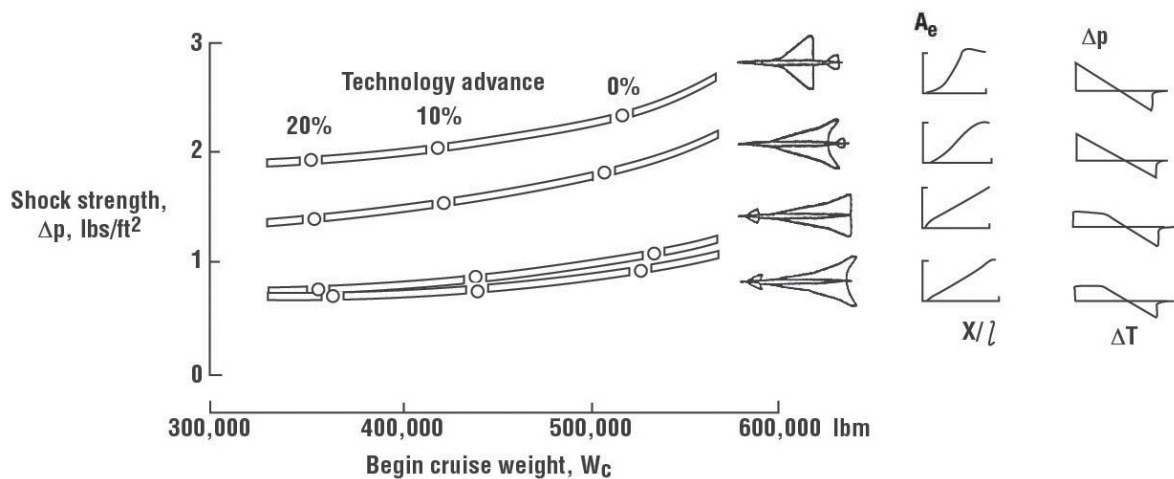
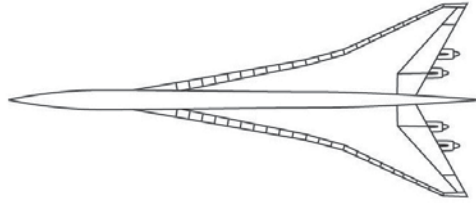


Figure 5.24. Significance of aircraft configuration and weight on sonic boom minimization, Mach 2.7, 60,000 ft, 2500 nmi, 234 PAX (adapted from ref. 5.42).

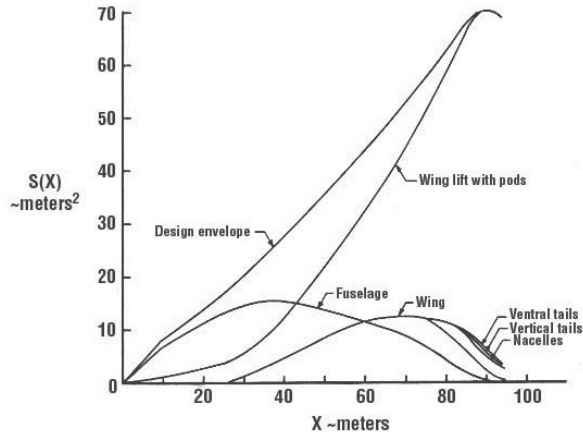
In the following sections, several configuration studies will be presented for supersonic transports and supersonic business jet size vehicles.

Supersonic Transports

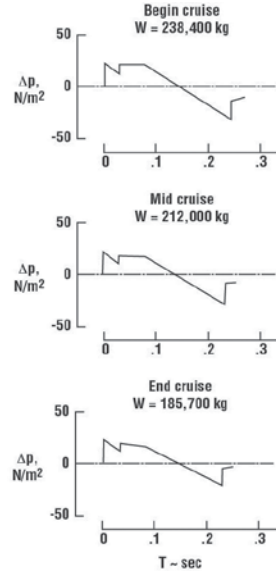
In 1972, Kane conducted a study (ref. 5.46) to determine if an airplane designed to produce a low-boom shaped signature represented a feasible supersonic transport. It was found that, in principle, sonic boom designed configurations represent a potentially realistic concept assuming technology advances. Two goals were chosen, a high-speed $\Delta p = 1.0$ lb/ft² or less for a supersonic cruise of Mach 2.7, an altitude of 55,000 feet (fig. 5.25), and a mid-Mach $\Delta p = 0.5$ lb/ft² for a supersonic cruise of Mach 1.5 and altitude of 45,000 feet (fig. 5.26).



(a) Configuration layout.

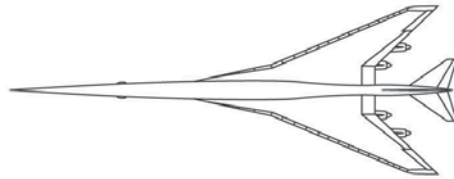


(b) Design point area distribution.

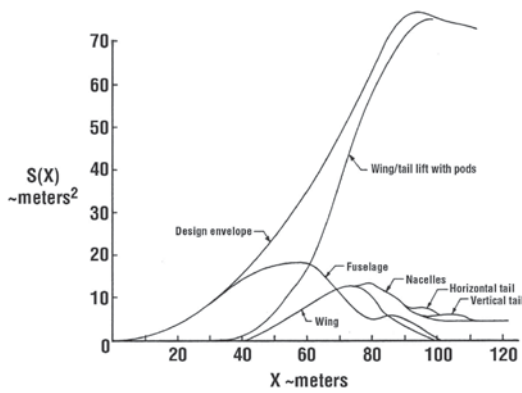


(c) Predicted boom signatures.

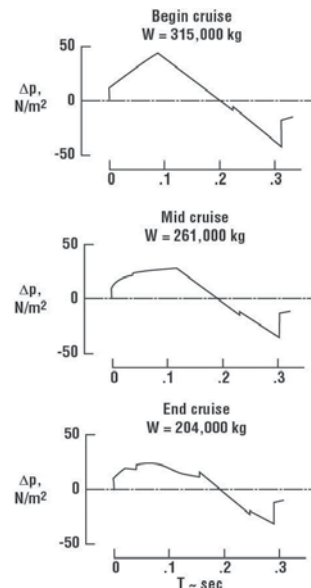
Figure 5.25. Characteristics of low sonic boom supersonic transport concept – high-speed design, Mach 2.7, $l = 307$ ft, design $\Delta p = 1.0$, MTW = 775,000 lbs, PAX = 151, constant altitude cruise of 55,000 ft (adapted from ref. 5.46).



(a) Configuration layout.



(b) Design point area distribution.



(c) Predicted boom signatures.

Figure 5.26. Characteristics of low sonic boom supersonic transport concept – Mid-Mach design, Mach 1.5, $l = 350$ ft, design $\Delta p = 0.5$ lb/ft², MTW = 750,000 lbs, PAX = 180, constant altitude cruise of 45,000 ft (adapted from ref. 5.46).

The high-speed design goal was achieved with a blended arrow wing configuration with dihedral and with pod-mounted engines at the wing trailing edge, shown in figure 5.25(a). A folding canard was also used at low speed. An overall equivalent area distribution based on the design point is shown in figure 5.25(b) and follows the desired $3/2$ power law slope to provide a flat-top signature for cruise altitude of about 60,000 ft. The nose of the area envelope was blunted to reduce the amount of fuselage ahead of the wing. This aircraft was designed to have the capability of carrying 151 passengers 3220 nmi.

In figure 5.25(c), the estimated sonic boom signatures are as shown for the Mach 2.7 constant altitude cruise at beginning, middle, and end of cruise. Two observations may be made. Although the $\Delta p = 1.0$ lb/ft² design goal was achieved, the signature shocks have not completely coalesced and, as such, the flat-top signature was not realized. Also, the tail shocks (recompressions) at the beginning and mid cruise were somewhat greater than 1.0 lb/ft². It was stated (ref. 5.46) that the most critical problem with this configuration was the stability at subsonic speeds and low weights.

The Mach 1.5 design of the 1972 Boeing study (ref. 5.46) had a goal of $\Delta p = 0.5$ lb/ft² (24 N/m²) for a flight at Mach 1.5 and an altitude of 45,000 feet. Figure 5.26 (ref. 5.46) presents the characteristics of this concept. The mid Mach was chosen because preliminary data indicated that a reasonable size and weight aircraft could be designed to produce cruise boom signatures of 0.5 lb/ft².

The design was also a blended arrow-wing configuration with dihedral and with pod-mounted engines on the wing trailing edge shown in figure 5.26(a). In figure 5.26(b), the design point equivalent area (A_e) distribution, which was to follow the quadratic law in shape in order to produce a ramp signature, is shown. Note that the airplane is quite slender at the nose to maintain the front shock Δp within the design criteria and this led to the arrow wing and an up-loaded (not normal) horizontal tail for longitudinal balance and trim.

Sonic boom signatures calculated for this baseline airplane are shown in figure 5.26(c) for beginning, middle, and end of cruise; all at constant Mach and altitude. All three signatures are of the ramp type where the initial bow shock is about 0.25 lb/ft² ramping to almost 2.0 lbs/ft² at beginning cruise and to about 1.0 lb/ft² at end of cruise. In addition, the tail (recompression) shock is about 0.75 lb/ft² and could not be reduced further without some extreme aft body contouring and attendant drag increase. The aircraft would have been capable of carrying 180 passengers 3220 nmi.

As mentioned earlier in this section, a reduction in sonic boom loudness outdoors (via ramp signature with large shock rise time) without a reduction in maximum overpressure, Δp , may not reduce annoyance of indoor observers as compared to an N-wave of equal maximum overpressure. A final observation is that this Mach 1.5 configuration is designed to have a lower boom than the high-speed design of the previous figure by being longer and flying at a lower altitude and Mach number. It is important to point out that, as shown in this study, the slope of the aircraft equivalent area distribution (the $3/2$ power, $5/2$ power, quadratic, linear, etc.) establishes the desired shaped boom signature. Also, as will be noted in Chapters 6 and 7 of this publication, the slope of A_e buildup depends upon the Mach number, flight altitude, and airplane length, l . The larger the aircraft length (l), the more linear the buildup of the equivalent area distribution (A_e) must be. As distance from the aircraft increases, ramp type signatures will, as they propagate to the ground, want to develop into N-waves. Thus, ramp signatures may be more compatible to long aircraft flying at low-Mach altitude. Flat-top signatures, on the other hand, usually allow aircraft to fly at high altitude, which in turn dictates higher Mach numbers.

In sonic boom minimization, the total length of the airplane has proven to be a design parameter of extreme importance. Ferri (ref. 5.2) took advantage of the fact that the required length of the airplane can be interchanged with the height of the airplane. This tradeoff suggested a biplane concept, one having wings that do not interfere at supersonic speeds and do not choke at transonic speeds, with potential to minimize the boom.

Figure 5.27 (ref. 5.2) presents a possible biplane configuration and corresponding predicted boom signature at the ground. This vehicle is also designed to fly at a lower Mach-altitude cruise such that the desired near-field

signature is realized at ground level. As such, the aircraft is long (290 feet) and slender with the upper wing 45 feet above the fuselage centerline. Cruise is at Mach 1.5 and an altitude of 40,000 feet.

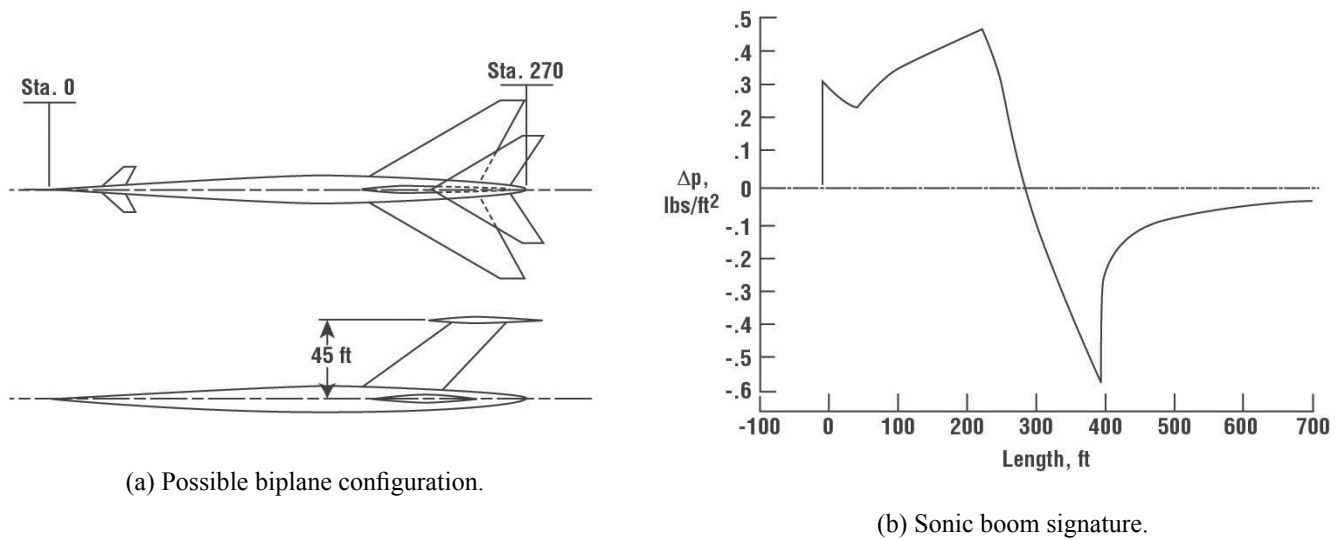


Figure 5.27. Possible biplane configuration and predicted boom signature, Mach 1.5 at 40,000 ft, $l = 290$ ft, $w_{cruise} = 320,000$ lbs, 250 PAX, 2800 mile range (adapted from ref. 5.2).

Figure 5.27(b) illustrates the boom signature predicted for the biplane concept. Note that it is a ramp type with an initial shock Δp of 0.3 lb/ft² ramping to about 0.45 lb/ft². Here again, as noted on the previous Boeing mid-Mach design (fig. 5.26), the tail (recompression) shock has a $\Delta p = 0.6$ lb/ft². However, if the calculated signature would be realized in actuality (i.e., rear shock does not recompress to ambient pressure but gradually trails away to ambient pressure) then an outdoor observer would only hear a boom of about 0.4 lb/ft². Here again, indoor observers would experience the annoyance of the 0.6 lb/ft² recompression shock.

As mentioned earlier in this section, flight altitude and airplane weight play key roles in the determination of the sonic boom signature. Figure 5.28 (ref. 5.2) illustrates the influence of these two parameters. Figure 5.28(a) shows the predicted boom signatures for a biplane configuration flying at altitudes of 40,000 feet and 60,000 feet at Mach 2.7. The airplane is 300 feet long and is similar in shape to the configuration shown in the previous figure. Note that both signatures are ramp type with initial shocks of $\Delta p = 0.3$ lb/ft² for a flight at an altitude of 40,000 feet and $\Delta p = 0.4$ lb/ft² for an altitude of 60,000 feet. Both signatures then ramp up to about 0.6 lb/ft² and 0.8 lb/ft², respectively. More importantly, the boom signature for the vehicle flying at the lower altitude has a lower boom level and shorter length than at an altitude of 60,000 feet due to lift effects.

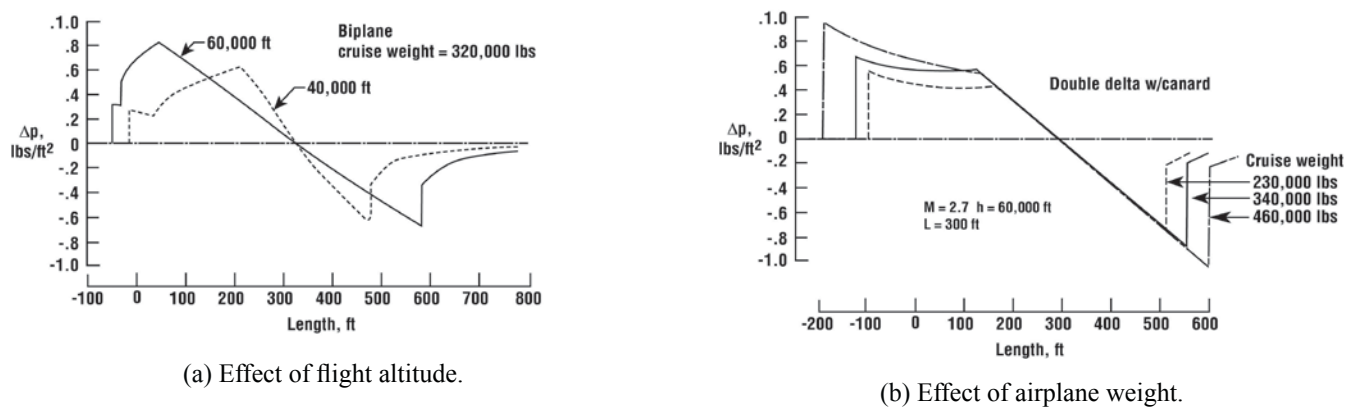


Figure 5.28. Influence of altitude and cruise weight on boom signatures (adapted from ref. 5.2).

Some interesting comments made by Ferri (ref. 5.2) regarding this situation reveal that if the equivalent area distribution selected on the basis of sonic boom optimization requires too large a fuselage in the front part of the vehicle, the requirement can be satisfied by using highly swept-back wings. However, if the flight Mach number increases at constant altitude or the flight altitude decreases for the same Mach numbers, then the maximum fuselage cross section permitted corresponding to the total area distribution selected decreases. As a consequence, solutions are obtained that do not have practical applications because the permissible fuselage is too small. Because the cross section and volume of the fuselage required for a vehicle are dictated by the mission, the apparent advantage from the point of view of reduced sonic boom of low-altitude flight (below 40,000 feet), as indicated by generalized optimization studies, cannot be achieved when realistic requirements of volume, area, and length of the fuselage are introduced even if the large reduction of airplane performance, due to the decrease of flight altitude, could be accepted.

Airplane weight and hence wing lift can exert a powerful influence on the sonic boom signature. Predicted signatures for three airplanes at Mach 2.7 and a cruise altitude of 60,000 feet having the same length (300 feet) and same distribution of cross-sectional area but at cruise weights of 230,000 pounds, 340,000 pounds, and 460,000 pounds are shown in figure 5.28(b) (ref. 5.2). The configuration is a double-delta planform with canard. Note that the signatures, at least at the lower weights, are flattop in character as dictated by the area development for this configuration. It can be seen that a decrease in weight decreases substantially the Δp . In fact, a halving of the weight decreases the bow shock by about 40 percent.

It has been shown thus far that cruise boom levels on the order of 1.0 lb/ft² or less may be possible for SST-size concepts that are on the order of 300-feet long, weigh about 600,000 to 700,000 pounds at takeoff, and have fineness ratios (length divided by equivalent diameter based on A_c) of about 30. Concorde was about 200-feet long and weighed about 400,000 lbs at takeoff, and had a fineness ratio of about 20.

Supersonic Business Jets

It is of interest to also look at a vehicle of smaller size and weight with regard to sonic boom. In 1995, a study was made (ref. 5.47) to provide a compilation of all documented supersonic business jet activities from 1963 to 1995 by universities, industry, and NASA. One of the configuration studies, conducted in the 1986 time period, documented the effects of emerging technology on a dual use Business/Interceptor Supersonic Cruise Jet. A three-view of the study configuration is shown in figure 5.29.

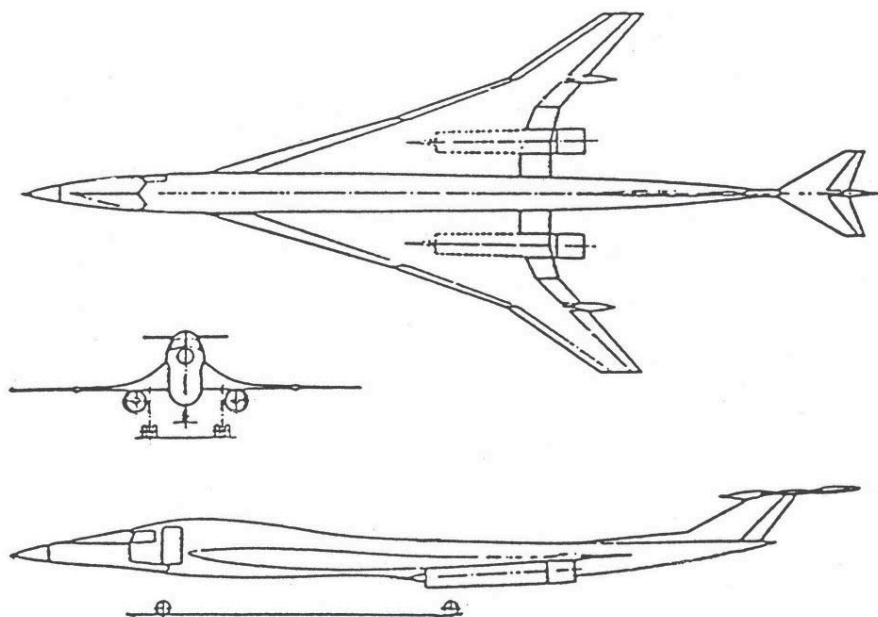


Figure 5.29. Convertible Business Interceptor supersonic cruise aircraft configuration, Mach 2.0, $l = 103$ ft, alt = 55,000 ft, PAX = 8, Range = 3622 nmi, MTW = 61,600 lbs (ref. 5.47).

This 1986 study was initiated to assess the feasibility of an eight-passenger, supersonic cruise long-range business jet aircraft that could be converted into a military missile carrying interceptor. The baseline passenger version had a flight crew of two with cabin space for four rows of two passenger seats plus baggage. The ramp weight was 61,600 pounds. Range was 3,622 nautical miles at Mach 2.0 cruise. Balanced field take-off distance was 6,600 feet and landing distance was 5,170 feet at 44,737 pounds. The passenger section from aft of the flight crew station to the aft pressure bulkhead in the cabin was modified for the interceptor version. Bomb-bay type doors were added and volume was sufficient for four advanced air-to-air missiles mounted on a rotary launcher. One of the main constraints established for this study was that the external geometry of the concept would be retained so the aerodynamic performance would be the same for both missions. No attempt was made to design this vehicle for minimum boom. Wing loading was about 63 lbs/ft² and the L/D at mid cruise about 7.0. This aircraft had a fineness ratio of about 17 and the N-wave boom signature at mid cruise was about 0.9 lb/ft².

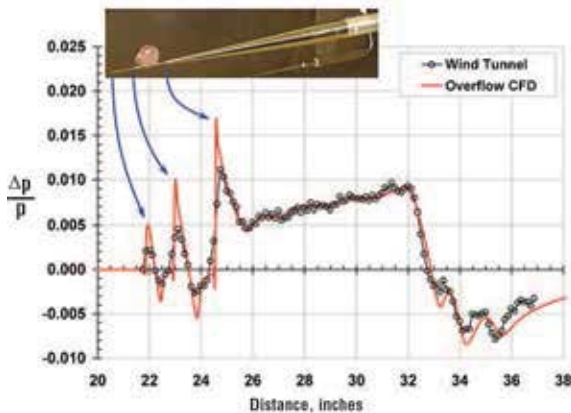
When boom minimization becomes a first order concern, the vehicle design requires an entirely different approach that may incorporate unique features in order to achieve the low-boom goal. For example, variable swept aft wings were employed on several SSBJ concepts discussed in reference 5.47 and more recently by Gulfstream (ref. 5.48). A study by the Japan Aerospace Exploration Agency found that a variable swept forward wing was considered to be a suitable configuration for an SSBJ (ref. 5.49). A most interesting and unique effort by Gulfstream Aerospace Corporation and their desire to bring a quiet civil supersonic aircraft to market involved a configuration employing their quiet nose spike, as shown in figure 5.30 (refs. 5.50 – 5.53) to acquire a low-boom equivalent area distribution. Figures 5.30(a) and 5.30(b) show the vehicle with the nose spike in the deployed and stowed position.



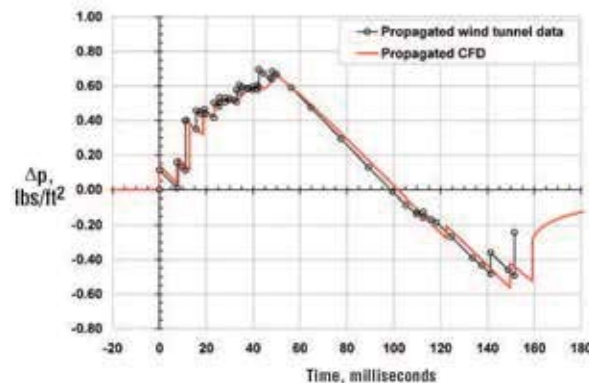
(a) High-speed concept with deployed quiet spike.



(b) Low-speed concept with stowed quiet spike.



(c) Wind-tunnel/CFD near-field signatures.



(d) Propagated wind-tunnel/CFD ground signatures.

Figure 5.30. A Gulfstream supersonic business jet concept employing Quiet Spike (adapted from refs. 5.50 and 5.51).

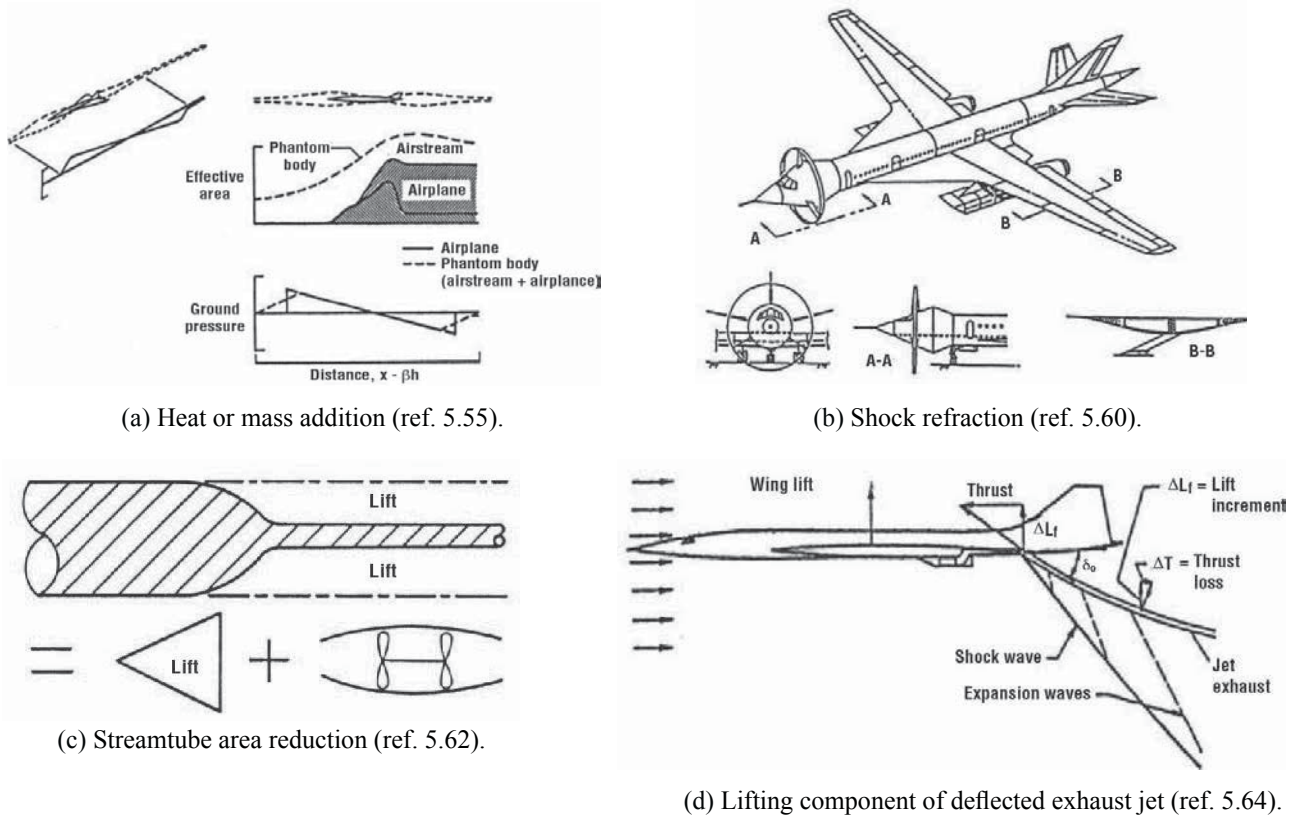
Gulfstream’s efforts began in 2004 with CFD analyses followed by wind-tunnel tests in the NASA Unitary Tunnel (ref. 5.51). These results confirmed that a ramp-shaped boom signature would result at ground level as indicated by the near- and far-field ground signature results shown in figures 5.30(c) and 5.30(d). A full-scale flight version of the Quiet Spike was then adapted to the NASA F-15B and in-flight and near-field probe measurements were acquired in 2006 that further confirmed its performance (ref. 5.50). See also figures 4.24 – 4.26 in Chapter 4 of this publication for additional details of the quiet nose spike.

A final note of interest regarding the Quiet Spike cited in Chapter 4 is whether it could play a beneficial role at off-design conditions, in particular during the transition phase of flight to minimize the focus boom signature. Howe (ref. 5.54) has shown that placement of the engines above the wing can benefit the sonic boom by partially shielding the inlet shocks thereby influencing shock coalescence to allow shaped signatures to reach the ground. A detailed discussion of engine placement is presented in Chapter 7.

In this section, boom minimization by way of aerodynamic modifications that leave the total enthalpy of the flow essentially unchanged was discussed. A presentation of several configurations/planforms aimed at boom minimization, a discussion of the role that the volume and lift distribution of an aircraft play in shaping the boom signature, and a brief review of the equivalent body of revolution concept were included. Wind-tunnel and flight-test results were presented that confirm the persistence of a shaped signature from an aircraft to the ground. It was shown that wing dihedral plays a role in reducing the boom intensity on track and redistributing the boom levels on each side of the aircraft ground track to provide a more uniform boom exposure pattern. Several low-boom concepts of supersonic transports and supersonic business jets were shown and discussed that demonstrate that low-boom shaped signatures can be produced by properly arranging the aircraft volume and lift distributions to acquire the desired equivalent area distribution (A_e).

Boom Minimization through Exotic Concepts

The previous discussion addressed aircraft configurations that leave the total enthalpy (a measure of the total energy of a thermodynamic system) of the flow essentially unchanged and assigned them the term “aerodynamic configurations” (ref. 5.21). In the remainder of this section, discussion will be focused on configurations or techniques that change the total enthalpy of a significant fraction of the flow past them as well as those that rely on physics beyond present comprehension and assign them the term “exotic concepts”. Four such concepts are illustrated in figure 5.31. These concepts include – (1) those that alter the airstream (phantom body) to increase the effective length through heat or mass addition as per Miller and Carlson (refs. 5.55 and 5.56), Batdorf (refs. 5.57 and 5.58), and Swigart and Lubard (ref. 5.59), as shown in figure 5.31(a), and (2) those that employ shock refraction from artificial changes in acoustic impedance as per Rethorst et al. (ref. 5.60) and Henderson (ref. 5.61), as shown in figure 5.31(b), and (3) the Resler (ref. 5.62) concept, which examined the premise of eliminating the boom due to lift through thermodynamic processes by achieving a reduced area stream tube as shown in figure 5.31(c) (accomplished by the incorporation of special engine designs), and (4) the concept examined by Galanis (ref. 5.63), who calculated some of the practical consequences of the streamtube area reduction method and the heat or mass addition phantom body concept as well as the Goethert and Gruska scheme (ref. 5.64, fig. 5.31(d), pp. 2.157 – 2.180) of using the lift component of a deflected exhaust jet to increase the lifting length of the vehicle and thus reduce the boom.



(a) Heat or mass addition (ref. 5.55).

(b) Shock refraction (ref. 5.60).

(c) Streamtube area reduction (ref. 5.62).

(d) Lifting component of deflected exhaust jet (ref. 5.64).

Figure 5.31. Some exotic concepts for boom minimization.

Heat or Mass Addition

The phantom body exotic concept shown in figure 5.31(a) has been the exotic concept most aggressively researched and studied. The nature of the airstream alterations required to produce the phantom body in order to achieve the highly desirable finite rise time signature will be discussed along with an estimate of the power requirements necessary to attain the low overpressure and large shock rise times for boomless signatures. Use of a thermal fin as a means of altering the airstream will be discussed.

Airstream Alteration

An effective area development (solid line curve) of an airplane that would produce an N-wave as well as a phantom body area development (dashed curve), resulting from a combination of the airplane and altered airstream, are depicted in figure 5.31(a). These area developments would also produce a boomless signature on the airplane ground track. The difference between the area development of the phantom body and that of the airplane defines the required airstream alterations that must be created using a carefully controlled heat or force field extending well ahead of and behind the airplane. At ground positions away from the flight track, the airplane effective area development assumes a different shape and magnitude. Thus, boom elimination at all ground positions would require a carefully controlled azimuthally as well as longitudinally altered airstream. As will be shown in a later figure, the phantom body must be much longer than the actual aircraft in order to acquire the desired finite rise time signature. However, if the vehicle slenderness ratio is not increased, the added effective area produced by the phantom body will actually increase the maximum sonic boom overpressure over that of the basic airplane.

In figure 5.31(a), it was noted that the phantom body length is the primary factor upon which the sonic boom signature characteristics as well as the power requirements depend. Figure 5.32 (ref. 5.55) shows how the rise time τ increases and the maximum ground overpressure Δp_{\max} decreases as the phantom body area development

is stretched out. In selecting a reasonable body length, no values less than 900 feet are considered because lengths less than that do not produce a finite rise time. As expected, the power requirements increase with increasing length. The desired rise time is the primary factor for defining the necessary phantom body length and the maximum power requirements. A rise time of 30 msec and a corresponding body length of 975 feet were chosen for the example to provide a near minimum power requirement while offering significant sonic boom benefits and a margin against possible adverse effects of atmospheric distortion (i.e., nonlinear shock steepening).

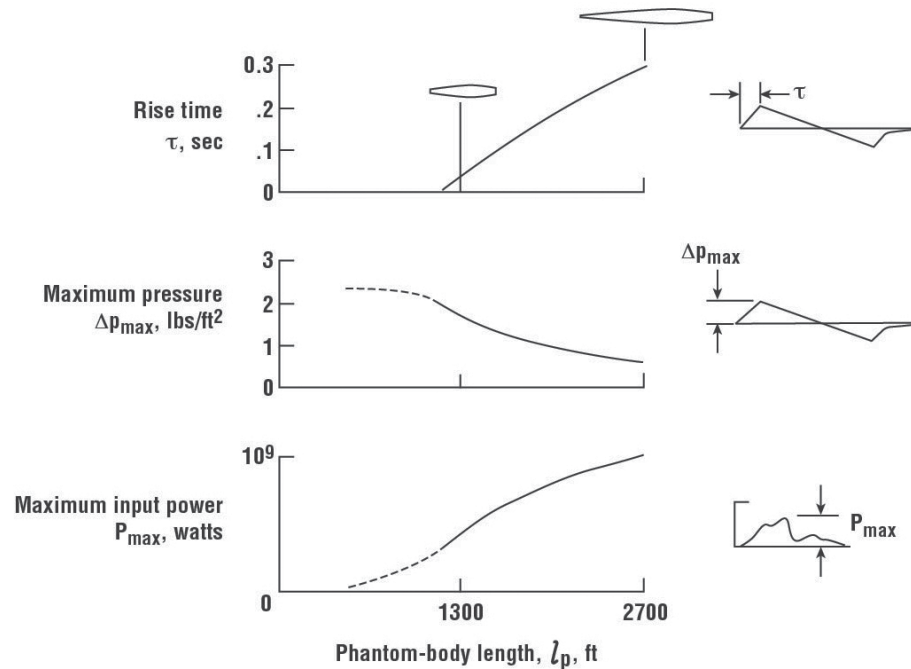


Figure 5.32. Phantom body length consideration (adapted from ref. 5.55).

The results of studies reported in reference 5.55 indicate that power requirements become less for lower Mach numbers, but not to the extent that the scheme appears to be more practical. For high Mach numbers, which are more attractive from an economic standpoint, the power requirements are greater. For a given Mach number, power requirements are not significantly less at altitudes above or below those normally selected for cruise economy.

The requirements for elimination of the front shock (i.e., obtaining significant shock rise time) has been examined by Lipfert (ref. 5.65) and the results are shown in figure 5.33. It can be seen that in order not to exceed the baseline aircraft overpressure, a phantom body length of about 550 feet is required as compared to the 298-foot length of the actual aircraft. Note too that a shock rise time of only 0.10 seconds (100 msec) is acquired. Thus, it is necessary to triple the aircraft length in order to achieve a finite rise time without increasing the overpressure. Large penalties in terms of increases in effective area and signature impulse are also incurred. On first impression, it would appear the airstream alteration concept has been applied to an N-wave designed aircraft with already undesirable lift and volume characteristics. It would be of interest to apply the concept to a configuration that has already been minimized through aircraft shaping.

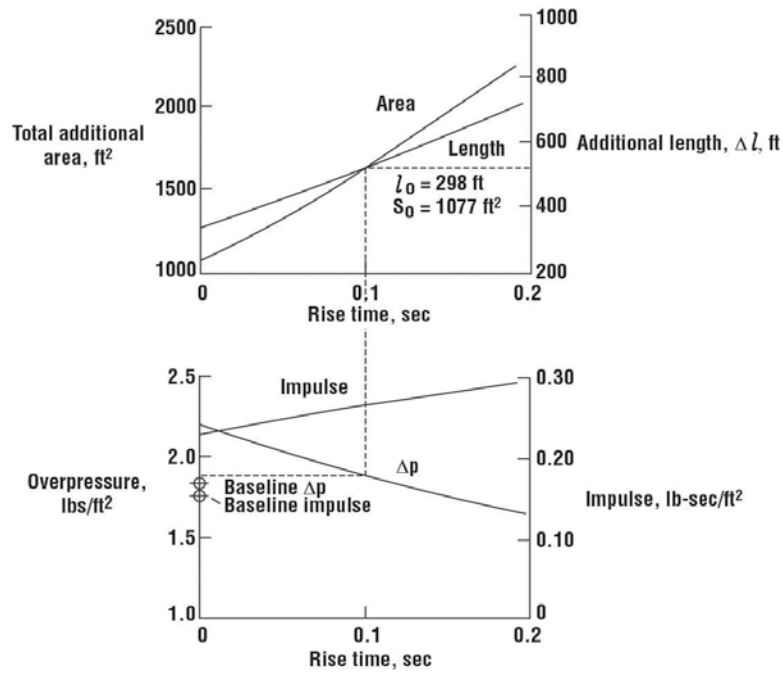


Figure 5.33. Front shock elimination requirements (ref. 5.65).

Thermal Fins

The thermal fin (refs. 5.57 and 5.59) is one of many approaches that have been proposed regarding airstream alterations to produce a phantom body and may be described with the aid of figure 5.34. The unique features of the thermal fin are the direct burning of fuel to produce the heat field and the introduction of the heat below the airplane itself. Batdorf (ref. 5.57, p. 336) points out that “with direct burning of jet fuel, the power requirements for bow shock elimination are not necessarily prohibitive” and that “locating the heat field below the airplane would be attractive from the standpoint of airplane thermal environment and safety.”

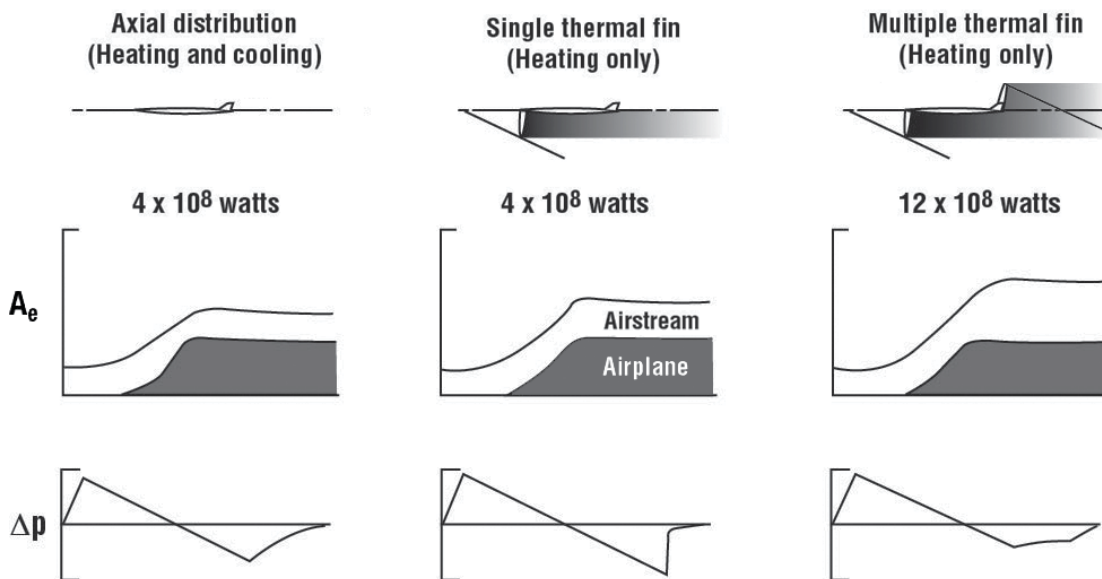


Figure 5.34. Thermal fin concept (ref. 5.55).

As stated by Miller (ref. 5.55, p. 337):

The conceptual single thermal fin arrangement illustrated at the center of figure 5.34 is compared with an un-implemented axial distribution of heating and cooling shown at the left. Because the thermal fin as presently conceived provides for heat addition only, the airplane must be reshaped and the phantom body forepart must be extended an additional 27 ft to provide an airstream that requires no heat removal. For the single thermal fin, no significant increase in power over the basic axial concepts is required. With direct burning during the supersonic portion of a coast-to-coast flight, it is estimated that power requirements can be met with about a 20-percent increase in onboard fuel. It should be noted that the single thermal fin would be effective in eliminating only the bow shock, and the tail shock would remain unless some means is provided for properly shaping the rear portion of the phantom body. The possibility of employing a second thermal fin for tail shock suppression was considered and is illustrated on the right in the figure. Estimates indicate that total shock elimination employing thermal fins would require about 60 percent additional onboard fuel, with no account being taken of the weight and performance penalties of the system.

It is obvious that the thermal fin that must extend about 80 feet below the airplane would pose severe if not insurmountable problems related to aircraft performance, stability, structure, and weight.

Six models were used in the wind-tunnel test program conducted in the NASA Langley 4- by 4-foot Supersonic Wind Tunnel as illustrated in figure 5.35. The design and construction of models, data reduction, analysis, and reporting was conducted by Aerospace Corp. (ref. 5.66) under contract to NASA.

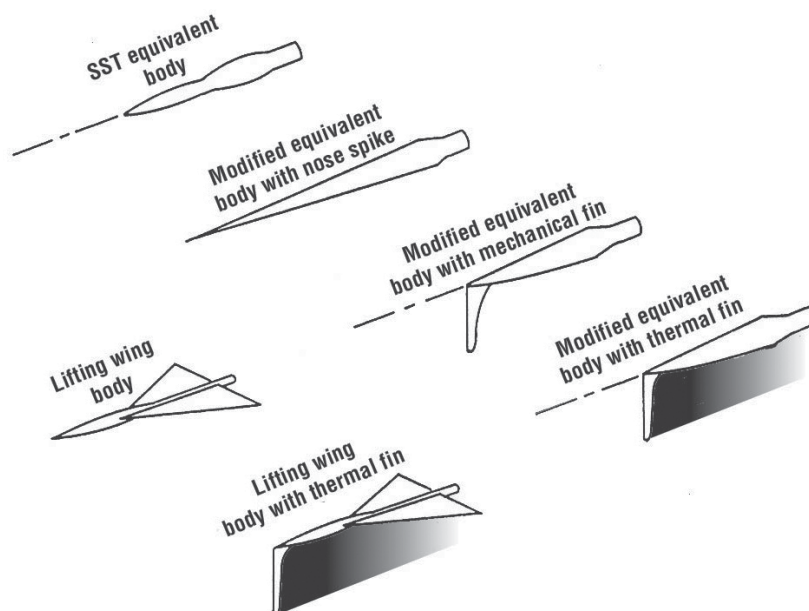


Figure 5.35. Models for wind-tunnel program (ref. 5.55).

The test program was divided into two parts. The first part consisted of testing the four non-lifting bodies shown diagonally across the top of the figure. The basic model in this series was a 10-inch long body of revolution having an effective area development representative of an SST at cruise speeds. The second model was essentially an isentropic spike modification of the basic model with an additional length of 6 inches, which was designed to produce a finite rise time signature. Each of the remaining two models in this series had a vertical fin extending about 4 inches below the model nose. The fin models were designed to have identical effective area developments and thus produce identical signatures as the isentropic spike model. The solid mechanical fin was about 40 percent larger than the thermal fin – this difference being simulated by means of hot gas ejection. The second part of the test program involved the testing of two lifting wing-body models shown at the lower left of the figure. The basic wing body model produced a lift-induced sonic boom pressure signature with shocks. The wing-body model

with the thermal fin was designed to suppress the shocks. In the actual tests, the wing-body model configuration included the solid fin rather than the thermal fin with flow.

For each of the models, signatures were measured at Mach 2.01 for a minimum of two model-probe separation distances. The thermal fin model design incorporated instrumentation necessary for measuring the properties of the gas being emitted. Some of the results of the experimental program carried out in the NASA Langley 4- by 4-foot Supersonic Wind Tunnel at Mach 2.01 to investigate the validity of the heat-field concept for sonic boom alleviation are presented in figure 5.36 (ref. 5.66). To the left of the figure are shown three of the six configurations that were tested and included the basic body of revolution (fig. 5.36(a)), having a nominal length of 10 inches and representative of a 1/360 scale SST configuration; the basic body plus solid fin (fig. 5.36(b)) designed so that the slope of the area distribution at the test Mach number follows the 5/2 power law so as to provide the finite ramp signature; and the basic body and so-called thermal fin (fig. 5.36(c)) in which about 40 percent of the solid fin model is replaced by a heat field designed to have an area distribution equivalent to that of the basic body and solid fin. The heat field is generated by passing nitrogen through a 1/8-inch diameter heating tube that continues through the model into a nozzle whose exit plane is at the rear of the fin. In order to accommodate the 1/8-inch heating tube in the fin section, the scale of the thermal fin model was increased by a factor of 1.5 over its solid counterpart. Hence, the basic body portion of the thermal fin model has a nominal length of 15 inches.

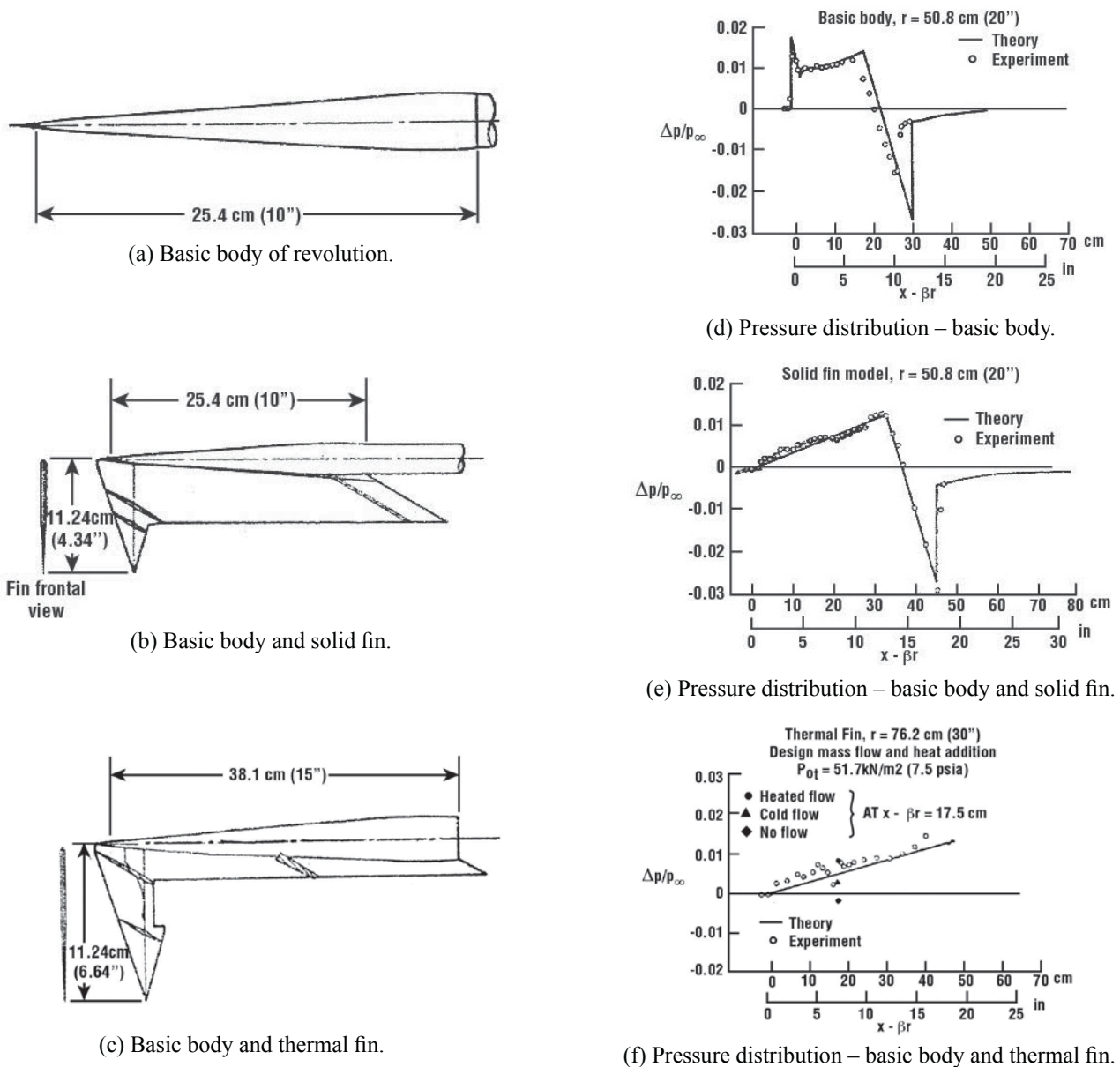


Figure 5.36. Wind-tunnel results for thermal fin concept (adapted from ref. 5.66).

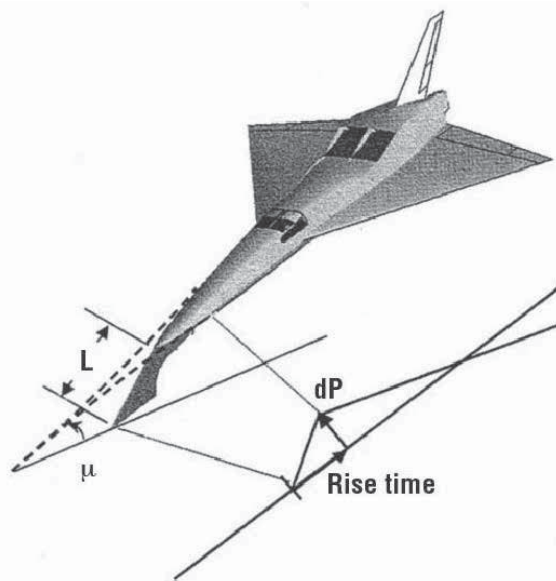
The resulting pressure signatures for all three models are shown on the right hand side of figure 5.36. Figure 5.36(d) presents the measured and calculated signature for the basic body at a distance of two body lengths ($h/l = 2.0$). Good agreement existed between the measured and predicted signatures, which is typical of an N-wave design aircraft. The measured and predicted signature (fig. 5.36(e)) for the basic body and solid fin, also at two body lengths, displayed the finite rise time signature associated with a $5/2$ power law shaped area distribution. Again, good correlation existed between theory and measurement. The important question is whether any local compression regions will cause a shock wave to develop. Two such regions are seen in the signature shown in figure 5.36(e) – one at the beginning and one toward the end of the linear pressure rise region. When the signature was measured at three body lengths, no significant steepening occurred for the compressive region at the beginning and the one toward the end of the linear region has nearly disappeared. It was noted that even if shock waves developed from these compressions, they would account for no more than 10 percent of the total pressure rise.

The measured signature for the basic body plus thermal fin (fig. 5.36(f)) shows the results of passing heated nitrogen through the fin at the design mass flow rate and temperature (ref. 5.66). Note the large expansion and subsequent recompression ($\sim x-\beta r = 6$ in.). This portion of the signature corresponds to disturbances generated by the nozzle region of the fin, expansion being generated by the growing area deficit through the nozzle region, and the recompression caused by this deficit becoming constant at the end of this region. Visual examination of the model after the test indicated that the nozzle slot did not remain constant in width during the test, but bowed at the center when the flow was turned on, giving a mass (and hence area) deficit in the lower region of the fin. This is the probable cause of the expansion recompression region noted in the signature. Further, note the two points marked cold flow and no flow. These points were obtained by turning the heater power and then the nozzle flow to the off position. In this manner, the effects of the flow and heat are separated and it is seen that they both contribute about equally to the overpressure at this point.

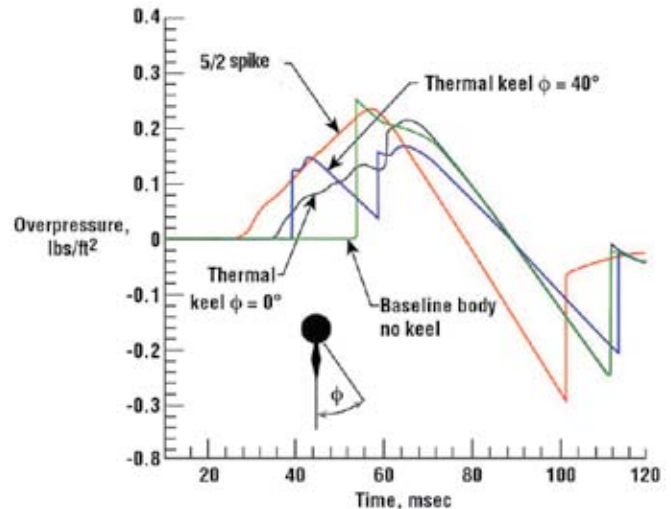
Forward Swept Keel

The concept of an isentropic spike projected by energy addition was revisited during the DARPA/QSP program. A detailed numerical investigation to further advance the keel concepts of Batdorf and Swigart using high fidelity computational methods in the application of aft-axis volume control for sonic boom mitigation was performed by Marconi, Bowersox, and Schetz in 2003 (ref. 5.67). It was also based on Marconi's earlier work of 1998 (ref. 5.68). Two equivalent bodies of fineness ratio 17.1 and 10.1 having a $5/2$ spike area distribution and a forward swept solid and thermal keel were investigated at Mach 2.4. The computations were made assuming a vehicle of 85 feet in length flying at an altitude of 57,000 feet.

Four specific goals were pursued – (1) examining both on- and off-track boom mitigation, (2) developing techniques for a design of thermal keel heating distributions, (3) examining the use of alternate keel orientations (length and shape) to minimize overall size, and (4) producing tailored ground signatures for single and multiple keel flow fields. A depiction of the forward swept keel and some numerical results are presented in figure 5.37 (ref. 5.67).



(a) Pressure distribution – basic body and thermal fin.



(b) Predicted ground signature comparisons.

Figure 5.37. Schematic of forward swept keel concept and ground signature comparisons for a 17.1 body fineness ratio, a 5/2 spike, and thermal keel on- and off-flight track (adapted from ref. 5.67).

Figure 5.37(b) illustrates the significant benefit of vehicle length amplification resulting from the addition of off-axis volume. In the optimum case of a keel swept forward normal to the Mach plane, a keel length L can be used to produce the same effect as a spike of length $Mach \times L$. Sweeping the keel forward so that its leading edge is perpendicular to the free-stream Mach line also results in the minimum length of the device. Figure 5.37(b) also shows the predicted sonic boom ground pressure signatures for the baseline body, the baseline body with the phantom spike, and the forward swept thermal keel for both an on-track and 40° off-track location.

The first observation is that all of the modified signatures are more acceptable than the baseline body as a result of the increased shock rise times for the 5/2 spike and thermal keel at $\phi = 0^\circ$ and the two lower amplitude shocks on the thermal keel at $\phi = 40^\circ$. Note the on-track signature from the thermal keel closely matches the 5/2 power area distribution having a spike signature rise time of about 35 msec and is also lower in overall magnitude. The off-track keel signature displays two small shocks but lacks the beneficial rise time of the spike and thermal keel on track.

It is of interest to note that in this study (ref. 5.67), the improvements from thermal keel having a 10:1 fineness ratio body were not as beneficial as for the thermal keel having a 17:1 fineness ratio body. Recall that the fineness ratios of most of the SST and supersonic business jets (SSBJs) is in the 17 to 19 range with some of the QSP concepts being as high as 22.

Focused Microwave Energy

Another concept of an isentropic spike projection by energy addition funded under the 2000 DARPA/QSP program was the work of Miles et al. at Princeton University (ref. 5.69). This study explored the possibility of achieving significant reductions of sonic boom by combining dynamic aft-body energy addition and/or near-field shock focusing with vehicle shape optimization. Various antenna configurations were analyzed to establish their ability to focus microwave energy to the required field strengths. One example is shown in figure 5.38 (ref. 5.69), suggesting a four-array configuration mounted under the aircraft, which focuses the 49 megawatts of microwave energy about 46 meters ahead of the vehicle. They also note that this location can be rapidly moved by changing the relative phases of the transmitting elements.

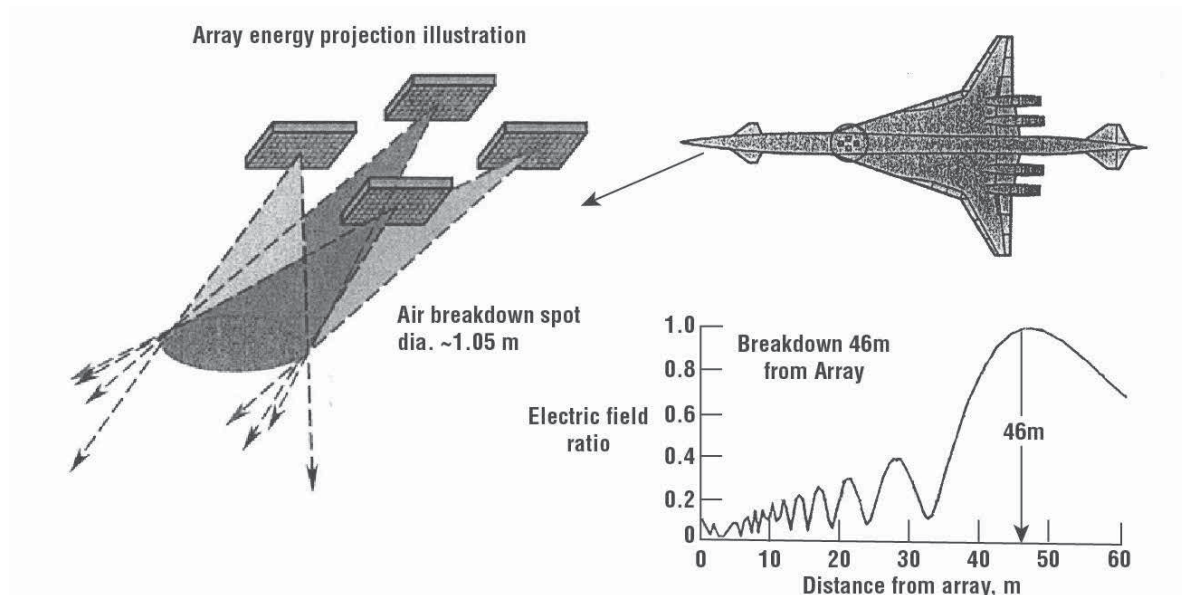
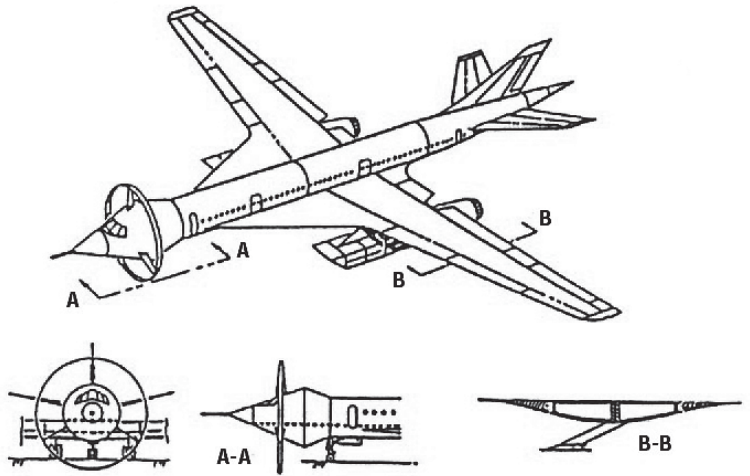


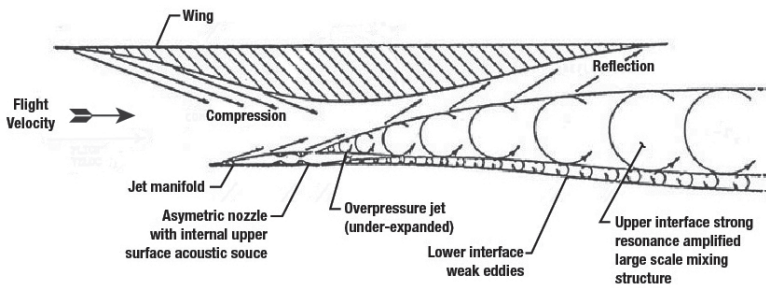
Figure 5.38. Model of microwave focusing to a 1-meter diameter spot, 46 meters below the aircraft with four 2-meter multi-element arrays emitting at 3.0 GHz, and located on the underside of the aircraft, as shown in the diagram. The arrays deliver 49 MW to the breakdown regime (ref. 5.69).

Shock Refraction

The Rethorst concept, which employed shock refraction from artificial changes in acoustic impedance to alter the airstream, was first examined in the mid-1960s during the U.S. SST Program (ref. 5.60). In the mid-1980s, Rethorst's Vehicle Research Corporation (VRC) claimed to have discovered a practical approach for no or low-boom supersonic flight and patented the concepts shown in figure 5.39. Note that two engine arrangements are proposed for a basically similar aircraft configuration – one of underwing pods as shown in figure 5.39(a) and the other of tail-mounted pods as shown in figure 5.39(c). For each case, a very large circular ring is located forward near the cockpit to provide a sheet of air that envelopes the complete vehicle. The wing/jet system is shown in figure 5.39(b).

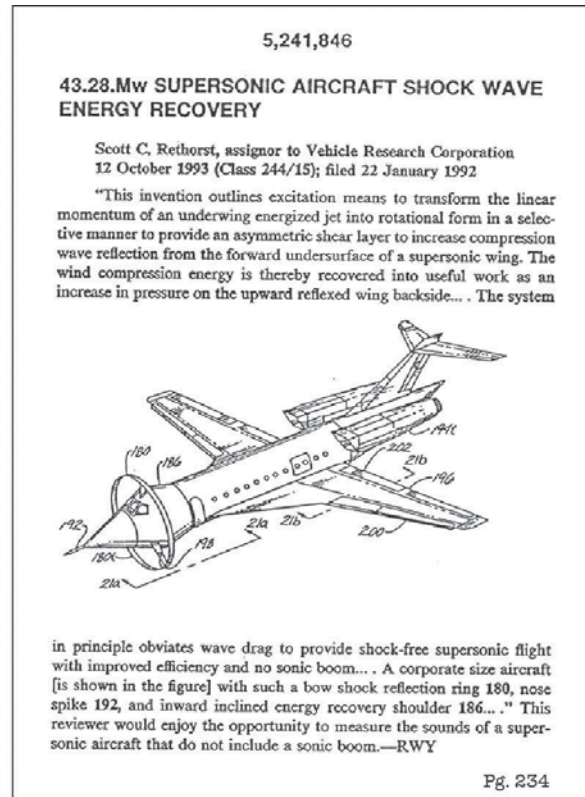


(a) Boomless configuration with underwing engines.



(b) Wing/jet system with shock wave energy recovery mechanism.

Figure 5.39. Shock reflection from artificial changes in acoustic impedance (adapted from refs. 5.60 and 5.70).



(c) Patent review (tail mounted engines).

As described in the patent, the system discharges a portion or all of the propulsive jet, usually fan air, as a planar sheet below and apart from the wing, thereby providing a variable energy flow. The jet sheet comprises a pneumatic shield to contain the underwing pressure, reflecting the compression waves generated by the forward concave-down wing underside upwards against the contracting aft portion of the wing, producing a lift and thrust component. As shown in figure 5.39(b), an asymmetric nozzle with an internal upper surface acoustic source is located below the wing. A review of the 1992 Rethorst supersonic aircraft shock wave Energy Recovery Patent (ref. 5.70) is provided in figure 5.39(c). Essentially, all who have examined this concept agree that minimization and even elimination of the boom due to aircraft volume can be accomplished. However, eliminating boom due to lift is not possible.

Exhaust Jet Sheet Deflection

Another application of the aircraft engine exhaust was investigated in the early 1970s by Goethert and Gruska (ref. 5.64, pp. 2.157–2.180). Some results are provided in figure 5.40. Their research showed that a slot-type engine exhaust has the unique capability of shifting lift from the solid surfaces of the wing to the region behind the wing. The critical lift is produced by wing pressures and the lift forces produced by the engines. There is no lift on the engine or wing wake. Due to lift produced by the engines, the angle of attack can be reduced and the level of pressure on the wing reduced. These results were developed for two dimensional flow conditions. Not only is there a shifting (reduction) of the lift on the main wing and an associated reduction of the sonic boom, but also favorable effects on the performance of the aircraft in certain flight regimes (usually at relatively high Mach numbers). It was shown that slotted nozzle engine exhausts have the unique capability to shift lift from the solid surface of the wing to the region behind the wing, with the resulting increase in lifting length and reduction in boom intensity.

In figure 5.40(a) and figure 5.40(b), it is shown that the sonic boom signature spreads over a larger distance and has a smaller pressure peak when the lifting surface has a larger chord; that is, when lift is spread over a larger distance in the flight direction. The study showed that the distribution of the lift in the flight direction can occur not only by means of stretching the wing chord, but also by having part of the total lift produced by the deflected exhaust of the jet engine(s) as illustrated in figure 5.40(c). The deflected jet exhausts produce lift, thus reducing the lift required of the wing.

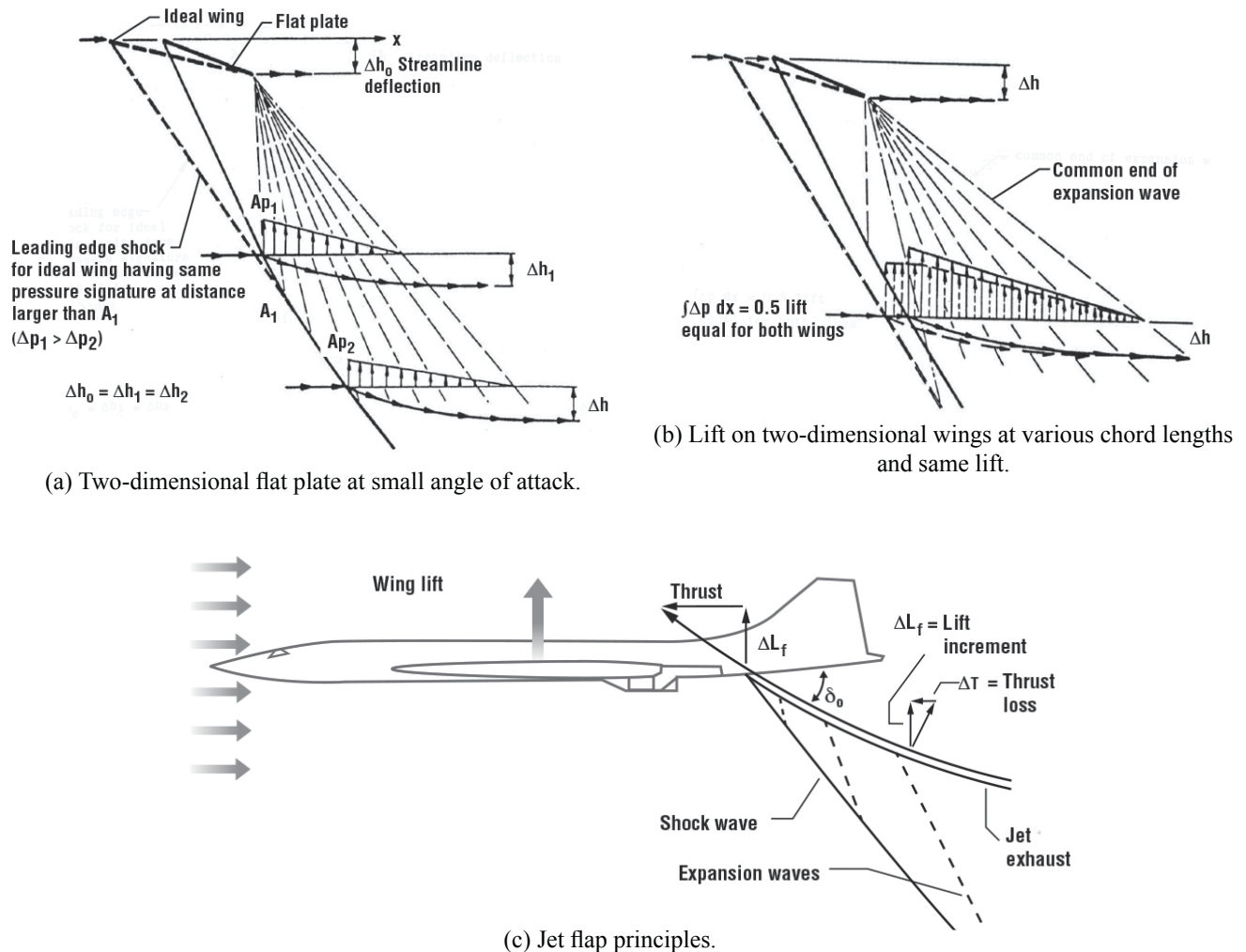


Figure 5.40. Sonic boom minimization by means of deflected exhaust jets (adapted from ref. 5.64).

Virtually no mention has been made of the boom reductions to be realized with the concept nor the penalties associated with its implementation. It was stated that at Mach 3 the jet flap would be identical in effectiveness to a mechanical flap with a flap chord of about 35 percent of the main wing.

Other Unique Exotic Minimization Schemes

In 1972, Lipfert (ref. 5.65) conducted a study that considered all identifiable means of altering the flow near the aircraft that could improve the boom at ground level and to include a realistic assessment of the penalties incurred by these various means. It was shown that weight penalties of the order of the baseline aircraft were incurred but that smaller weight penalties would result if one could create a precursor signal that would warn of the impending boom and, as such, reduce the startle effect. In figure 5.41(a), two approaches are put forth relative to this concept (i.e., to create a precursor disturbance) – (1) the use of a small drone aircraft or (2) a laser focused to a remote upstream spot.

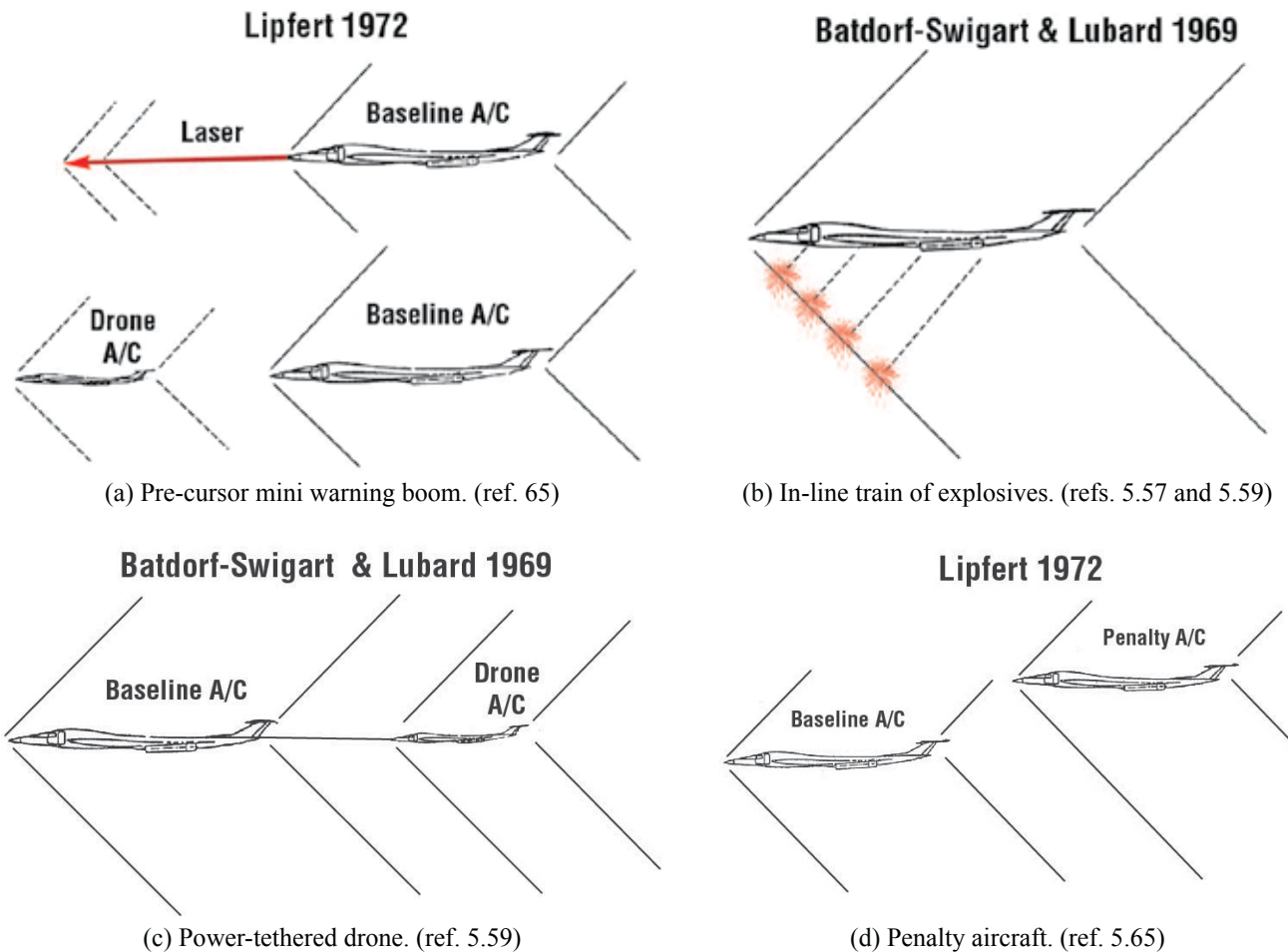


Figure 5.41. Other unique exotic minimization techniques.

However, as will be shown in Chapters 8 and 9, although startle plays a significant role in outdoor response, a precursor signal warning of the impending boom does not necessarily condition the observer to the oncoming boom. For example, even though one anticipates thunder following a lightning strike, he or she is still startled. Likewise, in the case of aerial fireworks, one expects a loud boom following a mortar shell burst at altitude, but is still startled by the burst.

Several other methods for boom reduction have been set forth by Batdorf (ref. 5.57) and Swigart and Lubard (ref. 5.59) and include the use of a continuous in-line train of explosive pellets that are ignited upon launch from the aircraft, as depicted in figure 5.41(b) and the use of a powered tethered drone. The fuel for propulsion and heating of this drone would be supplied through the tether as shown in figure 5.41(c).

The concept of a penalty aircraft, put forth by Lipfert (ref. 5.65) and shown in figure 5.41(d), calls for the use of a penalty aircraft that would fly in close proximity to the baseline aircraft (so that the sonic booms interfere) and relieve the necessity of increasing the baseline aircraft gross weight. The additional weight would be borne by the penalty aircraft and its lift distribution would be tailored to provide, in part, the desired low-boom signature. A logical question arises as to the benefits to be gained from such an arrangement. Obviously, both aircraft must maintain position in three dimensions very accurately and for the complete range of the mission. While this scheme was not considered quantitatively, the favorable trend may be seen by considering Seebass's criterion (ref. 5.21) that indicated doubling of the weight (W , baseline plus trailing penalty aircraft) and length (l , baseline plus trailing penalty aircraft) results in a reduction of the boom.

Overview of Exotic Concepts

A listing of the various exotic schemes relating to sonic boom minimization, that have been discussed are listed in table 5.1. Included is a listing of the individuals, the approximate time of their entry into the field, reference to the work, and the mechanism involved. In the discussions following table 5.1, assessment of these activities is presented and include those by Lipfert (ref. 5.65), Miller and Carlson (ref. 5.56), and Seebass and George (ref. 5.21).

Table 5.1. Brief Overview of Exotic Concepts to Minimize Sonic Boom

Participants	Year	Reference	Mechanism/Device
Rehorst	1965	5.60	Shock refraction
Cahn and Andrews	1968	5.71	Electrodynamics
Resler	1968	5.62	Steamtube reduction
Cheng and Goldberg	1969	5.72	Electrodynamics
R.L. Chuan	1969	5.73	Mass removal
Miller and Carlson	1969 1970	5.55, 5.56	Heat or mass addition
Batdorf, Swigart, Sweigart and Lubard	1969 1970 1975	5.57, 5.58, 5.59, 5.66	Heat or mass addition
Galanis	1970	5.63	Steamtube reduction
Henderson	1970	5.61	Shock refraction
Newman	1972	5.64	Cryogenic cooling
Kohl	1972	5.64	Focused laser beam
Goethert and Gruska	1972	5.64	Deflected jet exhaust sheet
Kunhardt et. al.	1998	5.74	Plasmas
Marconi et. al.	1998 2002	5.68	Heat or mass addition
Miles et. al.	2002	5.69	Focused microwave beam

In a controversial paper written in 1968, Cahn and Andrews (ref. 5.71) proposed an electrostatic scheme of creating reduced shock wave strength by means of static charges. Their proposed research method was then analyzed by Cheng and Goldberg (ref. 5.72), who assigned unit weight penalties for the electrical equipment required for the scheme. Apparently, their analysis did not include a realistic assessment of the effects of the electrical forces on the boom signature.

Chuan's patent (ref. 5.73) dealt with mass removal from the airstream through air condensation into the aircraft boundary layer. This would affect a fractional reduction of the boom due to volume but provide no benefit to the portion due to lift.

Both heat and force fields were considered in the Miller-Carlson study (ref. 5.56). However, in order to completely cancel the shocks, it was found necessary to both add heat in some regions and remove it in others. Larger quantities of heat may readily be added through combustion, but no such potentially light-weight mechanisms existed for cooling. In earlier discussions of references 5.57, 5.58, 5.59 and 5.66, a thermal keel was proposed as a means

of altering the airstream and forming a phantom body. Wind-tunnel tests were conducted and demonstrated the concept. The propulsive and control implications of this scheme were not considered.

Another class of boom alleviation was concerned with streamtube contraction by the propulsion system. Resler (ref. 5.62) noted that a negative volume effect could be used to cancel a portion of the lift effect if an engine could be designed with exit cross-sectional area less than the inlet. His approach may be considered as an extreme application of the phantom body concept in which a constant area body would be created by streamtube reduction only. If this could be accomplished, no disturbance of any kind would be felt outside the phantom body boundaries. It was also noted that the drag for a given lift using this scheme is three times what it would be for an ordinary wing with the same lift. Galanis (ref. 5.63) examined the concomitant engine requirements, concluding that a new cycle with airstream cooling was required using the fuel as a heat sink. Rethorst's concept (ref. 5.60) was similar in that power plant streamtube contraction was also required, albeit implicitly. Also, both concepts involved wing configurations with lift from the top surface only. Such wings provide only half the lift at the same wave drag.

Newman (cited in ref. 5.64, p. 1.4) conducted a brief assessment of using air liquidation to suppress the boom. It was found early on that the additional power required to maintain large external surfaces at cryogenic temperatures in high Mach number flow fields was excessive and the work was discontinued. Kohl (cited in ref. 5.64, pp. 2.127–2.156) advanced the idea to use current or future lasers to deflect the airflow about the aircraft and thus create a phantom body. The laser beam would be focused at distances of 100 feet or more ahead of the aircraft. Interest has also risen regarding the use of plasmas for boom minimization; the reasoning being if plasmas reduce drag, then it might be possible to delay the onset of sonic booms. Kunhardt et al. conducted a series of shock tube experiments to obtain shock wave modification data by the use of plasmas (ref. 5.74). Goethert and Gruska (ref. 5.64, pp. 2.157–2.180) proposed employing the lifting component of deflected jet exhausts to essentially increase the aircraft lifting length to spread the boom signature and thereby decrease the overpressure. Marconi, Bowersox, and Schetz (ref. 5.67) recently revisited the Batdorf-Swigart thermal keel approach by way of a forward-swept keel and Miles et al. (ref. 5.69) revisited the Kohl laser approach by way of a microwave focusing array mounted under the aircraft.

In this section, minimization and elimination of the sonic boom by means of configuration or techniques that change the total enthalpy of a significant fraction of the flow past them as well as those that rely on physics beyond present comprehension and classify them as “exotic concepts” have been discussed. Included are the alteration of the airstream about a vehicle to create a phantom body through the use of heat or mass addition, those that employ shock refraction from artificial changes in acoustic impedance, those that achieve streamtube reduction through aerodynamic means, and those that use the lift component of a deflected exhaust jet to increase vehicle lifting length. Other unique exotic minimization schemes include electro-aerodynamics, cryogenic cooling, focused laser or microwave beams, and use of plasmas.

Support for these exotic schemes began in the late 1960s and early 1970s as part of the U.S. SST effort and the schemes were revisited in the early 2000s as part of the DARPA/QSP effort. In general, it was found that all of the above approaches to boom minimization or elimination carried with them large penalties in terms of either large increases in power amounting to more than the aircraft's propulsion power output or a weight increase of the order of the baseline gross weight, or drag increases, for a given lift of about three times that for an ordinary wing with the same lift.

Chapter 5 Summary Remarks

Boom reduction through aircraft operations can be obtained by increasing altitude, use of a climbing flight profile, and flying at speeds that are less than the sound speed at the ground. Achieving Mach cutoff (M_{CO}) is generally limited to $Mach < 1.3$ depending upon winds and temperatures.

Sonic boom minimization by means of aircraft shaping to produce non-N-wave shaped signatures has been shown to be feasible and validated in wind tunnels and in full-scale flight. Recent developments in CFD codes allow

for the proper management of the aircraft volume, lift distributions, and engine exhaust flows so as to yield the equivalent area distribution (A_e) required to produce a low-amplitude shape boom signature at ground level.

Wing planform and dihedral has been shown to be effective in providing boom relief for both on- and off-track locations on the ground. Dihedral does not play a role in establishing the boom lateral cut-off distance that is independent of vehicle configuration and only depends on altitude, Mach number, and atmospheric conditions. Engine/nacelle locations above the wing provide partial shielding of the inlet shocks and alter the coalescence of the near-field shocks.

Numerous studies have been conducted involving exotic concepts – those that change the total enthalpy of the flow as well as those that rely on physics beyond present comprehension. In general, all of these schemes have large power, weight, or drag penalties.

Chapter 5 References

- 5.1 Shepherd, K. P.; Sullivan, B. M.; Leatherwood, J. D.; and McCurdy, D. A.: Sonic Boom Acceptability Studies. First Annual High Speed Research Workshop, NASA CP-10087, Part 3, April 1992, pp. 1295–1311.
- 5.2 Ferri, Antonio: Airplane Configurations for Low Sonic Boom. NASA SP-255, Oct. 1970, pp. 255–275.
- 5.3 Crow, Steven C. and Bergmeier, Gene G.: Active Sonic Boom Control. NASA CP-3335, July 1996, pp. 68–111.
- 5.4 Kane, Edward J. and Sigalla, Armand: Effect of Sonic Boom on Supersonic Transport Design and Performance. Fifth Conference on Applied Meteorology of the American Meteorological Society; Atmospheric Problems of Aerospace Vehicles, March 2-6, 1964, Atlantic City, NJ. Also available as Boeing Doc. D6-8614, Feb. 1964.
- 5.5 Patterson, Donald W.: Sonic Boom Limitations on Supersonic Aircraft Operations. Aero/Space Engineering, July 1960, pp. 22–24 and pp. 40–45.
- 5.6 Lina, Lindsay J. and Maglieri, D. J.: Ground Measurements of Airplane Shock Wave Noise for Mach Numbers to 2.0 and Altitudes to 60,000 Ft., NASA TN-D-235, 1960.
- 5.7 Bradley, E. S.; Johnson, W. M.; and Von Keszycski, C. H.: Passenger Transport at Low Supersonic Speeds. AIAA paper No. 69-776, 1969.
- 5.8 Maglieri, D. J.; Hilton, D. A.; Huckel, V.; Henderson, H. R.; and McLeod, N. J.: Measurements of Sonic Boom Signatures from Flights at Cutoff Mach Number. NASA SP-255, Oct. 1970, pp. 243–254.
- 5.9 Haglund, George T. and Kane, Edward J.: Flight Test Measurements and Analysis of Sonic Boom Phenomena Near Shock Wave Extremity. NASA CR-2167, Feb. 1973.
- 5.10 Haglund, George T. and Kane, Edward J.: Analysis of Sonic Boom Measurements Near Shock Wave Extremities for Flight Near Mach 1.0 and for Airplane Accelerations. NASA CR-2417, 1974.
- 5.11 Seebass, R.: Nonlinear Acoustic Behavior at a Caustic. NASA SP-255, Oct. 1970, pp. 87–120.
- 5.12 Randall, D. G.: Methods for Estimating Distributions and Intensities of Sonic Bangs. R&M, No. 3113, British A.R.C., 1959.
- 5.13 Friedman, Manfred P. and Chou, David C.: Behavior of the Sonic Boom Shock Wave Near the Sonic Cutoff Altitude. NASA CR-358, 1965.

- 5.14 They, C.: Refraction Atmospherique et Reflection au Sol Des Bangs. AGARD Conf., Proc. No. 42, May 1969.
- 5.15 Guiraud, J. P.: On the Intensity Value of Sonic Boom in the Neighborhood of a Caustic. C.R.H. Acad. Sci., Vol, 256, No. 8, Feb. 18, 1963 (A63-16929).
- 5.16 Maglieri, Domenic J. and Plotkin, Kenneth J.: Aeroacoustics of Flight Vehicles: Theory and Practice. NASA RP 1258, Vol, 1 and WRDC TR 90-3092, Aug. 1991, pp. 519–561.
- 5.17 Kane, Edward J. and Palmer, Thomas Y.: Meteorological Aspects of the Sonic Boom. SRDS Report No. RD 64-160, FAA, ASTIA No. AD 610 463, 1964.
- 5.18 Yeager, Chuck: Yeager: An Autobiography. A Bantam Book, July 1985, p. 130.
- 5.19 Perley, Richmond: Design and Demonstration of a System for Routine Boomless, Supersonic Flights. Report No. FAA-Rd-77-72, April 1977.
- 5.20 McLean, F. E.: Some Non-Asymptotic Effects on the Sonic Boom of Large Airplanes. NASA TND-2877, June 1965.
- 5.21 Seebass, R. and George, A. R.: Sonic Boom Minimization. Jour. Acous. Soc. of Am., Vol. 51, 1972, pp. 686–694.
- 5.22 Busemann, A.: Aerodynamischer Auftrieb bei Überschallgeschwindigkeit, Volta Congress, 1935, pp. 315–347.
- 5.23 Busemann, A.: The Relation Between Minimizing Drag and Noise at Supersonic Speeds, High-Speed Aeronautics. Polytechnic Institute of Brooklyn, Brooklyn, NY, 1955.
- 5.24 Baals, Donald D. and Foss, Willard E., Jr.: Assessment of the Sonic Boom Problems for Future Air-Transport Vehicles. Jour. Acous. Soc. of Am., Vol. 39, No. 5, part 2, 1966, pp. S-73-S80.
- 5.25 McLean, Edward F.: Configurations Designed for Specified Pressure Signature Characteristics. NASA SP-180, May 1968, pp. 37–45.
- 5.26 Hunton, Lynn W.: Current Research in Sonic Boom. NASA SP-180, May 1968, pp. 57–66.
- 5.27 Sims, Alex G. and Curry, Robert E.: Flight Characteristics of the AD-1 Oblique-Wing Research Aircraft. NASA TP-2223, March 1985.
- 5.28 Li, P.; Seebass, R.; and Sobieczki, H.: The Sonic Boom of an Oblique Flying Wing. CEAS/AIAA-95-107, June 1995.
- 5.29 Kulfan, Robert M.: High-Transonic-Speed Transport Aircraft Study - Summary Report. NASA CR-2465, Sept. 1974.
- 5.30 Espinal, Daniel; Im, Hongsik; Lee, Brian; Dominquez, Joanna; Sposoto, Hannah; Kinard, Daniel; and Zha, Ge-Cheng: Supersonic Bi-Directional Flying Wing, Part II: Conceptual Design of a High Speed Civil Transport. AIAA Paper 2010-1393.
- 5.31 Pfenninger, Warner and Vemuru, Chandra S: Design Aspects of Long Range Supersonic LFC Airplanes with Highly Swept Wings. SAE paper 881397, Oct. 1988.
- 5.32 Komadina, S. and Drake, A.: Development of a Quiet Supersonic Aircraft with Technology Applications to Military and Civil Aircraft. AIAA paper 2002-0519, Jan. 2002.

- 5.33 Wlezien, R. and Veitch, L.: Quiet Supersonic Platform. AIAA Paper 2002-0143, Jan. 2002.
- 5.34 Whitham, G. B.: The Flow Pattern of a Supersonic Projectile, *Commun. Pure and Appl. Math*, Vol. V, No. 3, 1952, pp. 301–348.
- 5.35 Walkden, F.: The Shock Pattern of a Wing-Body Combination, Far from the Flight Path. *Aero. Quarterly*, Vol. IX, May 1958, pp. 164–194.
- 5.36 Carlson, Harry W.; McLean, Edward F.; and Shrout, Barrett L.: A Wind Tunnel Study of Sonic Boom Characteristics for Basic and Modified Models of a Supersonic Transport Configuration. NASA TM X-1236, 1966.
- 5.37 Pawlowski, Joseph W.; Graham, David H.; Boccadora, Charles H.; Coen, Peter G.; and Maglieri, Domenic J.: Origins and Overview of a Shaped Sonic Boom Demonstration Program. AIAA 2005-0005, Jan. 2005.
- 5.38 Meredith, K.; Dahlin, J.; Graham, D.; Haering, E.; Maline, M.; and Page, J.: Flight Test Measurement and Computational Fluid Dynamics Correlation of F-5E Off-Body Pressures. AIAA-2005-0006, Jan. 2005.
- 5.39 Plotkin, K.; Haering, E.; Murray, J.; Maglieri, D.; Salamone, J.; Sullivan, B.; and Schein, D.: Ground Data Collection of Shaped Sonic Boom Demonstration Aircraft Pressure Signatures. AIAA-2005-0010, Jan. 2005.
- 5.40 Haering, E.; Murray, J.; Purifoy, D. D.; Graham, D. H.; Meredith, K. B.; Ashburn, C. E.; and Stucky, J.: Airborne Measurements of Shaped Sonic Boom Demonstration Aircraft Pressure Signatures and Comparisons to CFD. AIAA-2005-0009, Jan. 2005.
- 5.41 Green, Karen S. and Putnam, Terrill W.: Measurements of Sonic Booms Generated by an Airplane Flying at Mach 3.5 and 4.8. NASA TM-X-3126, Oct. 1974.
- 5.42 Carlson, Harry W.; Barger, Raymond L.; and Mack, Robert J.: Application of Sonic Boom Minimization Concepts in Supersonic Transport Design. NASA TN D-7218, 1973.
- 5.43 Darden, Christine M.; Powell, Clemans A.; Hayes, Wallace D.; George, Albert R.; and Pierce, Allan D.: Status of the Sonic Boom Methodology and Understanding. NASA CP 3027, 1988.
- 5.44 Bobbitt, P. J.; Kandil, O. A.; and Yang, Z.: The Beneficial Effects of Wing Dihedral on Sonic Boom. AIAA 2003-3273, May 12–14, 2003.
- 5.45 Kandil, O. A.; Yang, Z.; and Bobbitt, P. J.: Prediction of Sonic Boom Signature Using Euler-Full-Potential CFD with Grid Adaptation and Shock Fitting. AIAA 2005-2543, June 2002.
- 5.46 Kane, Edward J.: A Study to Determine the Feasibility of a Low Sonic Boom Supersonic Transport. NASA CR-2332, Dec. 1972.
- 5.47 Maglieri, Domenic J.: A Compilation and Review of Supersonic Business Jet Studies from 1963 through 1995. NASA CR-2011-217144, May 2011.
- 5.48 Woltz, R.: A Summary of Recent Supersonic Vehicle Studies at Gulfstream Aerospace. AIAA Paper 2003-0558, Jan. 2003.
- 5.49 Harinouchi, Shigeru: Conceptual Design of a Low Sonic Boom SSBJ. AIAA Paper 2005-1018, Jan. 2005.
- 5.50 Cowart, R. A. and Grindle, T.: An Overview of the Gulfstream/NASA Quiet Spike Flight Test Program. AIAA-2008-0123, Jan. 2008.

- 5.51 Howe, D. C.; Simmons, F., III; and Freund, D.: Development of the Gulfstream Quiet Spike for Sonic Boom Mitigation, AIAA 2008-0124, Jan. 2008.
- 5.52 Howe, D. C.: Improved Sonic Boom Minimization with Extendable Nose Spike, AIAA 2005-1014, Jan. 2005.
- 5.53 Howe, D. C.; Waithe, K.; and Haering, E. A.: Quiet Spike™ Near Field Flight Test Pressure Measurements with Computational Fluid Dynamics Comparison. AIAA 2008-0128, Jan. 2008.
- 5.54 Howe, D.: Engine Placement for Sonic Boom Mitigation. AIAA 2002-0148, Jan. 2002.
- 5.55 Miller, David: Status of Research on Boom Minimization through Airstream Alteration. NASA SP-255, Oct. 1970, pp. 325-340.
- 5.56 Miller, D. S. and Carlson, H. W.: A Study of the Application of Heat or Force Fields to the Sonic Boom Minimization Problem. NASA TN D-5582, Dec. 1969.
- 5.57 Batdorf, S. B.: A New Approach to the Alleviation of the Sonic Boom. Aerospace Corporation Rept. No. ATR-70 (S9990)-1, Sept. 1969.
- 5.58 Batdorf, S. B.: An Alleviation of the Sonic Boom by Thermal Means. AIAA Paper 70-1323, 1970.
- 5.59 Swigart, R. and Lubard, S.: Sonic Boom Studies. Aerospace Corporation Rept. No. ATR-69 (S8125)-1, May 1969.
- 5.60 Rethorst, S.; Alperin, M.; Behrens, W.; and Fujita, T.: Reduction of Shock Wave Strength by Means of Nonuniform Flow. AFFDL-TR-69-62, Pt. 1, 1-103, 1969.
- 5.61 Henderson, L. F.: On Shock Impedance. *Journal of Fluid Mechanics*, 40, 1970, pp. 731–732.
- 5.62 Resler, E. L., Jr.: Reduction of Sonic Boom Attributed to Lift. NASA SP-180, May 1968, pp. 99–106.
- 5.63 Galanis, N. T.: Power Plant Design for the Reduction of the Sonic Boom Generated by Supersonic Transport Aircraft. Ph.D. Thesis, Cornell University, June 1970.
- 5.64 Goethert, B. H.: Fundamental Research on Advanced Techniques for Sonic Boom Suppression. Rept. FAA-RD 73-4, University of Tennessee, Nov. 1972.
- 5.65 Lipfert, R. W.: An Analytical Study of Some Possible Sonic Boom Alleviation Schemes. AIAA Paper 72-653, June 1972.
- 5.66 Swigart, Rudolph J.: Verification of the Heat-Field Concept for Sonic Boom Alleviation. *AIAA Journal of Aircraft*, Vol. 12, NO. 2, 1975, pp. 66–71.
- 5.67 Marconi, F.; Bowersox, R. D. W.; and Schetz, J. A.: Sonic Boom Alleviation Using Keel Configurations. *AIAA Journal of Aircraft*, Vol. 40, No. 2, March–April 2003.
- 5.68 Marconi, F.: An Investigation of Tailored Upstream Heating for Sonic Boom and Drag Reduction. AIAA Paper 98-0333, Jan. 1998.
- 5.69 Miles, R.; Martinelli, L.; Macheret, S.; Shneider, M.; Girgis, I.; Zaidi, S.; Mansfield, D.; Siclari, M.; Smereczniak, P.; Kashuba, R.; and Vogel, P.: Suppression of Sonic Boom by Dynamic Off-Body Energy Addition and Shape Optimization. AIAA Paper 2002-0150, Jan. 2002.
- 5.70 Young, Robert W.: Supersonic Aircraft Shock Wave Energy Recovery (5,241,846), Review of Acoustical Patents. *J. Acoust. Soc. Am.*, 95(3), March 1994, p. 1700.

- 5.71 Cahn, M. S. and Andrew, G. M.: Electro-Aerodynamics in Supersonic Flow. AIAA Paper No. 68-24, Jan. 1968.
- 5.72 Cheng, S. and Goldberg, A.: An Analysis of the Possibility of Reduction of Sonic Boom by Electro-Aerodynamic Devices. AIAA paper No. 69-38, Jan. 1969.
- 5.73 Chaun, R. L.: Sonic Boom Amelioration. U.S. Patent 3510095.
- 5.74 Kunhardt, E.; Saeks, R.; Mankowski, J.; and Suchomel, C.: One Dimensional Shock Characteristics in Weakly Ionized Gases. AIAA Paper 99-4941, Nov. 1999.

CHAPTER 6 THEORETICAL CONSIDERATIONS AND APPLICATIONS

This chapter addresses the theoretical developments since the mid 20th century relevant to the analysis of sonic booms. It begins with the early ideas of Whitham, Landau, Walkden and other scientists based on linear theory with nonlinear corrections and ends with an analysis of hypersonic theory based primarily on blast wave methodology. Also presented are the methods for calculating the propagation of pressure signatures based on Whitham's F-function and Thomas's waveform parameter method. Research utilizing Whitham's F-function method led to the development of the "age parameter" and a phenomenon that became known as "freezing". These theoretical factors are discussed in detail in this chapter.

Since most near-field flow calculations made today use CFD codes based on Euler equations, the difficulties of matching these data to the linear far-field propagation codes are presented. In addition, the lateral variations of sonic booms as well as the lateral extent of sonic booms on the ground are discussed. Finally, several theory and experiment comparison plots are presented that indicate how well the predictive methods work.

Fundamental Boom Theory

Early speculation was that sonic booms were associated with a Doppler singularity at Mach 1 (engine noise bunching up as the sound barrier was broken). Researchers soon realized that sonic booms were the same phenomenon as ballistic waves, the properties of which had been understood for some time, quantified through the work of DuMond et al. (ref. 6.1), Whitham (refs. 6.2 and 6.3), and others, including Landau's work on the asymptotic form of weak shock waves (ref. 6.4). Building on this work and on Hayes's linearized flow theory (ref. 6.5), the basics of sonic boom analysis were laid down by Whitham (refs. 6.2 and 6.3), Walkden (ref. 6.6), Warren (refs. 6.7 and 6.8), Randall (ref. 6.9), and others. Contributions and improvements have been made over the years by a host of researchers and were documented in several summary papers (see refs. 6.10 to 6.15).

The Whitham theory is based on the concept that linear theory provides the correct first order values along a characteristic, but the location of the linear theory characteristics is correct only to the zeroth order. He developed a procedure to correct the characteristic location to the first order, thus obtaining a uniform first order solution – which is formally equivalent to second order. The Whitham methodology began with the acoustic solution for the flow field around a supersonic projectile.

$$\delta p(x - \beta r) = p_a \frac{\gamma M^2 F(x - \beta r)}{(2\beta r)^{1/2}} \quad (1)$$

which is often written as

$$\delta p(\chi) = p_a \frac{\gamma M^2 F(\chi)}{(2\beta r)^{1/2}} \quad (2)$$

where χ is the location on the axis of the equivalent body of the Mach plane translated field point, where

a = Speed of sound

F = Source function

M = Mach number = U/a

p_a = ambient pressure

$$\delta p = p - p_a$$

r = radial coordinate

U = free stream velocity

x = axial coordinate parallel to flight path

$$\beta = \sqrt{M^2 - 1}$$

γ = ratio of specific heat

$$\chi = x - \beta r$$

The meaning of the coordinate $\chi = x - \beta r$ is sketched in figure 6.1. Lines of constant χ are simply the Mach waves originating at axial position x along the body.

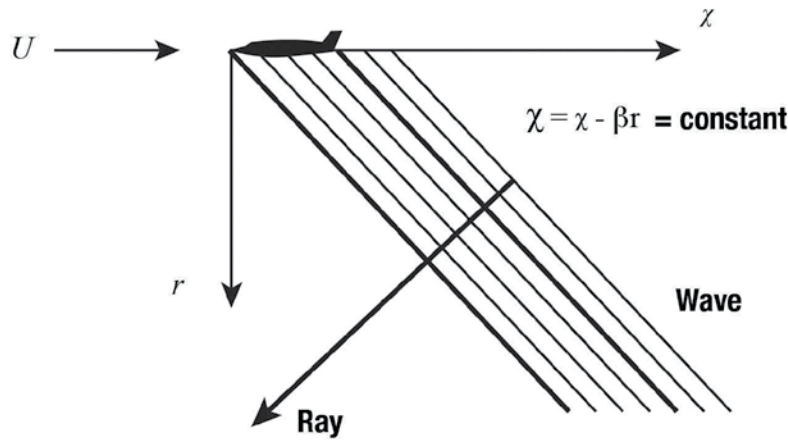


Figure 6.1. Coordinate system and definition of χ .

Equations (1) and (2) are essentially the acoustic propagation of a locally axisymmetric source. This generally means that r is far enough from a vehicle that near-field cross-flow effects have become negligible, and that the amplitudes are small enough that propagation is linear.

The F-function in equations (1) and (2) for an axisymmetric body is related to its geometry by

$$F(x) = \frac{1}{2\pi} \int_0^x \frac{A''(\bar{x})}{\sqrt{x - \bar{x}}} d\bar{x} \quad (3)$$

where A is the cross sectional area of the body and $A''(\bar{x})$ denotes the second derivative. The area A is the normal projection of cuts made at the Mach angle (i.e., slices along lines of χ). For slender bodies, A is often approximated by the cross-sectional area.

Equations (2) and (3) are written for an axisymmetric vehicle. They can apply to a non-axisymmetric vehicle if the flow field is such that it can be considered as locally axisymmetric, i.e., at any given azimuthal angle θ the flow behaves as if it was axisymmetric, so equation (2) can be generalized to

$$\delta p(\chi, \theta) = \frac{p_a \gamma M^2}{(2\beta r)^{1/2}} F(\chi, \theta) \quad (4)$$

Walkden (ref. 6.6) determined the θ dependence for a wing-body combination, accounting for the volume of the fuselage, the volume and lift of the wing, and interference between the body and wing. Walkden's result for the F -function can be written in terms of a single volume term, including any interference effects and a single lift term including lift interference effects as

$$F(x, \theta) = \frac{1}{2\pi} \int_0^x \frac{A_v''(\bar{x}, \theta) + \beta/2q_\infty L'(\bar{x}, \theta)}{\sqrt{x - \bar{x}}} d\bar{x} \quad (5)$$

$L'(x, \theta)$ can be approximated by $\cos\theta L'(x)$ and written so that the θ direction component of total integrated lift from the leading edge up to station x is defined as

$$L(x, \theta) = \cos\theta \int_0^x L'(\bar{x}) d\bar{x} \quad (6)$$

and the ' and '' indicate first and second derivatives with respect to x , where

θ = direction component of lift, it is zero in head down direction

q_∞ = free stream dynamic pressure = $\frac{1}{2} \rho U^2$

ρ = ambient density

$L(x, \theta)$ = lift on a spanwise strip per unit chordwise length

$A_v(x, \theta)$ = longitudinal area distribution

The A_v'' term is the volume contribution in equation (5) and is determined by the cross sections measured by cutting planes aligned with the Mach angle. The L term is the contribution due to lift as noted and should really be determined along Mach cutting planes. Except for extremely slender wing planforms, the use of equation (6) based on the longitudinal lift distribution is a more serious approximation than the use of simple cross sections for volume cuts. The numerator of the integral in equation (5) before differentiation is referred to as the effective area A_e .

$$A_e(x, \theta) = A_v(x, \theta) + \frac{\beta}{2q_\infty} \int_0^x L(x, \theta) d\bar{x} \quad (7)$$

Thus, equation (4) for $\delta p(x, \theta)$ uses F from equation (3) with A_e replacing A .

$$F(x, \theta) = \frac{1}{2\pi} \int_0^x \frac{A_e''(\bar{x}, \theta) d\bar{x}}{\sqrt{x - \bar{x}}} \quad (8)$$

As noted earlier, for a slender body, $A_v(x, \theta)$ can be approximated by the normal cross-sectional area at station x . For an aircraft in level flight or in a coordinated turn, lift is normal to the wing span head up and θ is zero in the head down direction. Total lift is the integral of $\cos\theta L'(x)$ over the vehicle length. The cosine form for the azimuthal direction is a reasonable, practical approximation, much like normal area cuts rather than Mach cuts, but it should be remembered that the lift portion of equation (7) is best performed along Mach cuts at each θ . It should also be remembered that the volume and lift components properly include the interference components identified by Walkden (ref. 6.6).

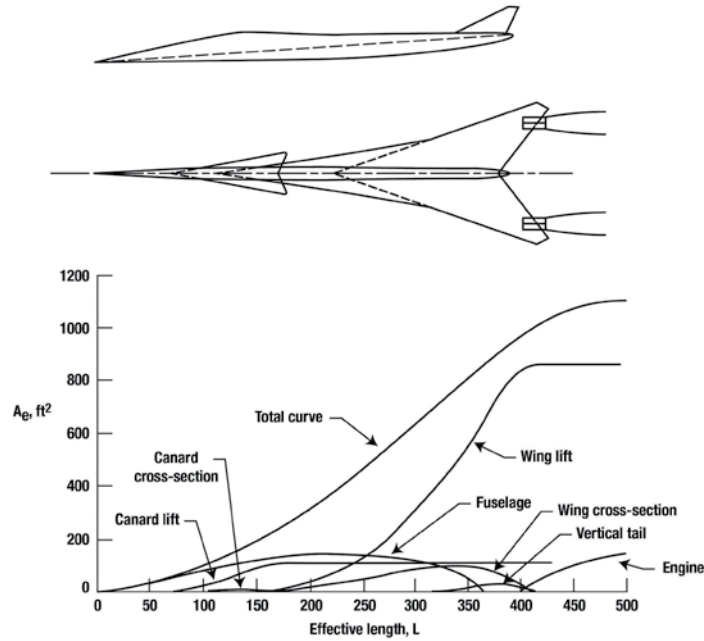


Figure 6.2. Equivalent area distribution corresponding to airplane configuration. Mach 2.7, symmetry plane cuts (ref. 6.16).

A typical build up of lift and volume contributions to an A_e distribution is shown in figure 6.2 for an SST (ref. 6.16) with a 300-foot-long fuselage (actual length).

Early researchers (refs. 6.1 and 6.2) found that the far-field decay of shock strength in a uniform atmosphere follows a $r^{-3/4}$ law. Whitham (refs. 6.3 and 6.17) derived the following expression for the far-field shock jump

$$\Delta p_s = p_a \left[2c_a \int_0^{\tau_0} F(\tau) d\tau \right]^{\frac{1}{2}} \left[\frac{\gamma+1}{2\gamma} S \int_0^s \frac{1}{\sqrt{S}} ds \right]^{-\frac{1}{2}} \quad (9)$$

where p_a and c_a are the ambient pressure and speed of sound, γ is ratio of specific heats and S is the geometrical acoustic ray-tube area. Whitham noted that S could be further generalized to include acoustic impedance and refraction.

The integration limit τ_0 is the value of τ that makes $F(\tau_0) = 0$ and $\int_0^{\tau_0} F(\tau) d\tau$ a maximum. This usually corresponds to the initial positive phase of the F -function. As pointed out in references 6.17 and 6.18, for a uniform atmosphere, $S \sim s \sim r$ and equation (9) yields the $r^{-3/4}$ behavior. The uniform atmosphere form of the Whitham-Walkden-Randall theory (refs. 6.3, 6.6, and 6.9) is thus

$$\Delta p_s = \frac{2^{\frac{1}{4}} p_a \gamma \beta^{\frac{1}{4}}}{(\gamma+1)^{\frac{1}{2}} \left(\frac{r}{l}\right)^{\frac{3}{4}}} \left[\int_0^{\tau_0} F(\tau) d\tau \right]^{\frac{1}{2}} \quad (10)$$

or

$$\Delta p_s = \frac{2^{\frac{1}{4}} \gamma \beta^{\frac{1}{4}} \sqrt{p_a \rho g}}{(\gamma+1)^{\frac{1}{2}} \left(\frac{h}{l}\right)^{\frac{3}{4}}} \left[\int_0^{\tau_0} F(\tau) d\tau \right]^{\frac{1}{2}} \quad (11)$$

where $\sqrt{p_a p_g}$ is used in equation (11) instead of P_a (eq. (10)) to approximate the effect of the acoustical impedance differences in the atmosphere between the ground and the aircraft.

A more general formulation of boom theory includes the actual ray tube area, S , as contained in equation (9) and acoustical impedance rather than approximating it with p . If atmospheric winds are included, then the impedance and ray tube area factors are combined into the general form derived by Blokhintzev (ref. 6.19). Additionally, in the general theory, the upper limit of the F-integral is $\tau(s)$, rather than the τ_0 , so that mid-field as well as far-field booms can be computed. The general theory is presented later in this chapter.

A further representation of equation (10) is found in reference 6.11

$$\Delta p_{max} = P_a \frac{K_r(\beta)^{\frac{1}{4}}}{\left(\frac{h}{l}\right)^{\frac{3}{4}}} \left(K_s \frac{D}{l}\right) \quad (12)$$

where

$$K_s \frac{D}{l} = \left\{ \frac{2^{\frac{1}{4}} \gamma}{(\gamma + 1)^{\frac{1}{2}}} \left(\int_0^{\tau_0} F(\tau) d\tau \right)^{\frac{1}{2}} \right\} \quad (13)$$

and K_r is the ground reflection factor normally taken as 1.9 or 2.0.

In subsequent publications (refs. 6.20 and 6.21) equation (11) evolved into

$$\Delta P_{max} = \frac{K_p K_r \sqrt{p_a p_g} (\beta)^{\frac{1}{4}}}{\left(\frac{h_e}{l}\right)^{\frac{3}{4}}} K_s \quad (14)$$

where K_p is a factor accounting for the difference between uniform atmosphere propagation and propagation in the real atmosphere. The shape factor K_s includes both volume and lift contributions while h_e , the effective altitude, accounts for the effect of flight-path and ray-path-azimuth angles on propagation distance. Signature duration is determined in a similar fashion and is given by

$$\Delta t = K_t \frac{3.42}{c_a} \frac{Ml}{(M^2 - 1)^{3/8}} \left(\frac{h_e}{l}\right)^{1/4} K_s \quad (15)$$

where K_t is a factor, similar in concept to K_p , that adjusts for propagation in a real atmosphere and is given in reference 6.21, and c_a is the speed of sound at the aircraft's altitude.

In addition to laying out the calculation procedure for Δp_{max} and Δt , reference 6.21 provided several illustrative boom calculations. Figure 6.3, from reference 6.21, depicts some typical results that show good agreement of Δp_{max} and Δt predictions with experiment. A note of caution is in order – the method of reference 6.21 only applies to conventional aircraft that yield N-wave sonic boom signatures as opposed to tailored minimum boom signatures.

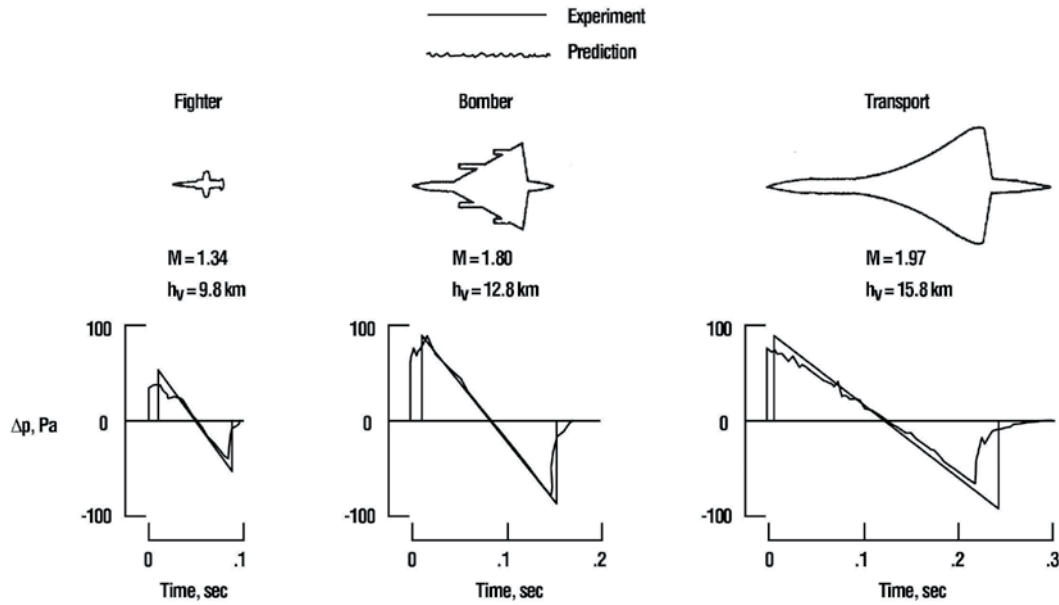


Figure 6.3. Correlation of predictions with measurements covering a range of airplane types (ref. 6.21).

A further cautionary note – equation (8) properly applies to configurations that have smooth shapes (i.e., without slope discontinuities). Reference 6.3 discusses an F-function integral, denoted as the h function, that applies to both smooth and non-smooth area distributions and is more accurate in the latter case.

Signature Evolution

Equations (1), (2), and (4) do not require that F be obtained from equations (5) or (8) since it is simply an acoustic source function. The only requirement is that the wave have locally plane wave behavior, such that χ is the appropriate combination of x and r and that amplitude changes over gradient scales that are large compared to the signal wavelength. Whitham (ref. 6.17) wrote a general form of equation (1) in simpler form as

$$\frac{\delta p}{p} = \frac{F(\tau)}{\sqrt{B}} \quad (16)$$

where B is a generalization of r to represent any slowly varying amplitude change and τ is a time based equivalent of χ . Whitham wrote S rather than B , specifying that S could be a constant (plane wave), s (propagation distance, cylindrical wave), or s^2 (propagation distance squared, spherical wave). He also noted that S could represent a general ray tube area and could include acoustic impedance variations. B is used here to represent that general form. Ray tracing, ray tube area and acoustic impedance, based on Blokhintzev's theory (ref. 6.19), will be discussed later in this section.

In equation (16) the time based variable

$$\tau = t - \frac{s}{a} \quad (17)$$

represents phase along a ray that is normal to the wavefronts sketched in figure 6.1, where s is the propagation distance along the ray and a is the ambient sound speed. $F(\tau)$ and $F(\chi)$ are not the same function, since one is a function of time and the other of length, but both forms are used in the literature with length units generally applied to external scaling of both forms. The arrival time of wavefront of phase τ is $t = \tau + s/a$. If the propagation medium has varying sound speed a_0 , the arrival time generalizes to

$$t = \tau + \int_0^s \frac{ds}{a_0} \quad (18)$$

The appearance of N-waves at the ground, rather than near-field waves that closely mimic the aircraft configuration, is a consequence of propagation not actually being linear. Whitham (refs. 6.2 and 6.3) proposed that the linear solution gave the correct wave amplitude to first order, but that the wave shapes (or ray arrival times) were only correct to the zero order. A uniformly valid first order solution could be obtained by adjusting propagation speed to first order. a_0 in equation (18) is replaced with $a_0 + \delta a + \delta u$, where δa is the perturbation to sound speed and δu is the local volume velocity associated with the acoustic wave. From the acoustic equations, these are

$$\begin{aligned} \delta a &= a_0 \frac{\gamma - 1}{2\gamma} \frac{\delta p}{p_0} \\ \delta u &= a_0 \frac{1}{\gamma} \frac{\delta p}{p_0} \end{aligned} \quad (19)$$

so that

$$a_0 \Rightarrow a_0 + a_0 \frac{\gamma + 1}{2\gamma} \frac{\delta p}{p_0} = a_0 + a_0 \frac{\gamma + 1}{2\gamma} \frac{F(\tau)}{\sqrt{B}} \quad (20)$$

Equation (17) for the arrival time is updated to

$$t = \tau + \int_0^s \frac{ds}{a_0} - F(\tau) \frac{\gamma + 1}{2\gamma} \int_0^s \frac{ds}{a_0 \sqrt{B}} \quad (21)$$

which can be written as

$$t = \tau + \int_0^s \frac{ds}{a_0} - F(\tau) \Lambda(s) \quad (22)$$

where

$$\Lambda(s) = \frac{\gamma + 1}{2\gamma} \int_0^s \frac{ds}{a_0 \sqrt{B}} \quad (23)$$

is denoted the age parameter. This is equivalent to the age variable defined throughout the course of sonic boom theory development. Hayes (ref. 6.12) has noted that Landau (ref. 6.4) first presented this for a uniform medium (where it was just the distance), and Whitham was the first to present it for a non-uniform medium (ref. 6.22). Hayes et al. (ref. 6.23) wrote the age variable, with different notation than used here, for downward ray propagation in a horizontally stratified atmosphere.

Applying the age parameter to equation (16)

$$\frac{\delta p}{p} = \frac{F(\tau - \Lambda(s)F(\tau))}{\sqrt{B}} \quad (24)$$

so that wavefront τ arrives early by the amount ΛF (i.e., the age parameter times its F-function waveform steepens as sketched in figure 6.4 for three successive times).

If continued indefinitely, geometric construction of steepening leads to triple valued regions, as sketched in figure 6.4(c). When the waveform slope approaches vertical, however, a shock wave will form, as sketched in figure 6.5. The wave speeds up behind a weak shock and is given by linearizing the Rankine-Hugoniot equations, and (for zero pressure before it) is

$$u_s = a_0 + a_0 \frac{\gamma + 1}{4\gamma} \frac{\Delta p}{p_0} = a_0 + a_0 \frac{\gamma + 1}{4\gamma} \frac{F(T(s))}{\sqrt{B}} \quad (25)$$

where Δp is the shock pressure, and $T(s)$ is the phase of the wavefront about to enter it. Note that a weak shock's speed increment above ambient is half that of the increment for an isentropic compression wave of the same strength. This leads to the area balance algorithm for fitting shocks to a folded-over construction such as figure 6.4, wherein the folded-over region is replaced with a shock such that the area of the waveform is preserved. This is illustrated in figure 6.6.

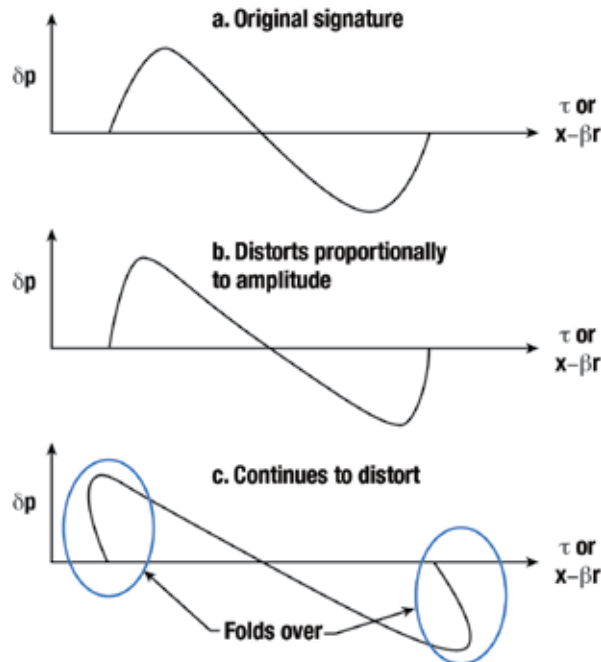


Figure 6.4. Nonlinear distortion of boom signature. Each point advances by ΛF .

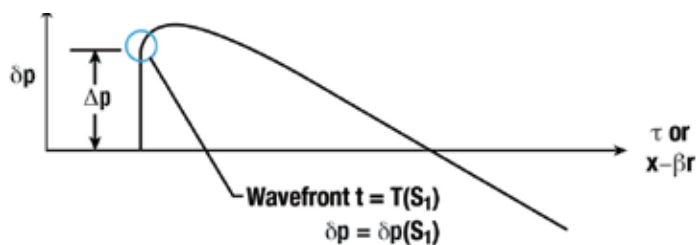


Figure 6.5. Shock formation at wavefront $T(S_1)$.

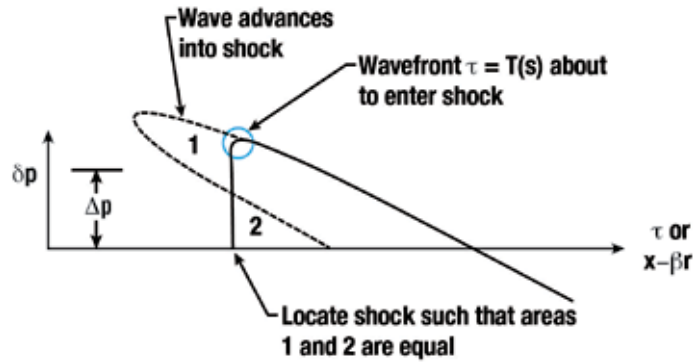


Figure 6.6. Shock fitting by area balance.

The arrival time $T(s)$ at distance s of the shock for a simple waveform as shown in figures 6.4-6.6 is given by equation (26) with $T(s)$ replacing τ (see equation (22))

$$t_{shock} = T(s) + \int_0^s \frac{ds}{a_0} - F(T(s))\Lambda(s) \quad (26)$$

If equation (26) is differentiated once with respect to s , it gives dt_{shock}/ds , which is the reciprocal of the shock speed given by equation (25). Whitham combined these equations, obtaining a differential equation for $T(s)$, which he then integrated to obtain

$$F(T(s)) = \left[2 \int_0^{T(s)} F(t) dt \right]^{1/2} [\Lambda(s)]^{-1/2} \quad (27)$$

Equation (27) provides F behind the shock, hence the shock pressure. This is an implicit relation, since $T(s)$ appears as a limit to the integrand of F on the right hand side. Whitham (ref. 6.17) noted that at large distances most of the original F -function will be engulfed in the shock, and $T(s)$ will be very close to τ_0 , the zero at the end of the positive phase of the F -function. In the far-field, the shock overpressure will thus be

$$\Delta p = \frac{p_0}{\sqrt{B}} \left[2 \int_0^{\tau_0} F(t) dt \right]^{1/2} \Lambda^{-1/2} \quad (28)$$

Because only a small portion of the original F -function is left, the shock will be followed by a linear expansion, hence an N-wave shape, with positive duration given by the advance time to the shock, which he found to be

$$\Delta t = \left[2 \int_0^{\tau_0} F(t) dt \right]^{1/2} \Lambda^{1/2} \quad (29)$$

For plane, cylindrical, and spherical waves the asymptotic behavior is

$$\Delta p \propto \begin{cases} s^{-1/2} & \text{Plane} \\ s^{-3/4} & \text{Cylindrical} \\ (\log s)^{-1/2} & \text{Spherical} \end{cases} \quad (30)$$

$$\Delta t \propto \begin{cases} s^{1/2} & \text{Plane} \\ s^{3/4} & \text{Cylindrical} \\ (\log s)^{1/2} & \text{Spherical} \end{cases} \quad (31)$$

The cylindrical results are the well known $r^{-1/2}$ law, so that the amplitude of an N-wave boom decays more rapidly than the $r^{-1/2}$ decay of a cylindrical acoustic wave. Note that the additional $1/4$ power results from the slope of the N being absorbed into the shock. The shock of a flat-top boom discussed in the minimization chapter decays at the acoustic rate of $r^{-1/2}$, and the shock of a ramp boom would decay slower than $r^{-3/4}$ since the portion of the wave entering the shock has an upward slope.

Not all booms are asymptotic in the far-field, and many real world F-functions are complex with multiple shocks possible. The area-balancing rule illustrated in figure 6.6 can be used to locate shocks. Figure 6.7 illustrates how this can be done, either after steepening the signature (top sketch) or before steepening (bottom sketch). Either way the shock position is iterated until the areas are balanced.

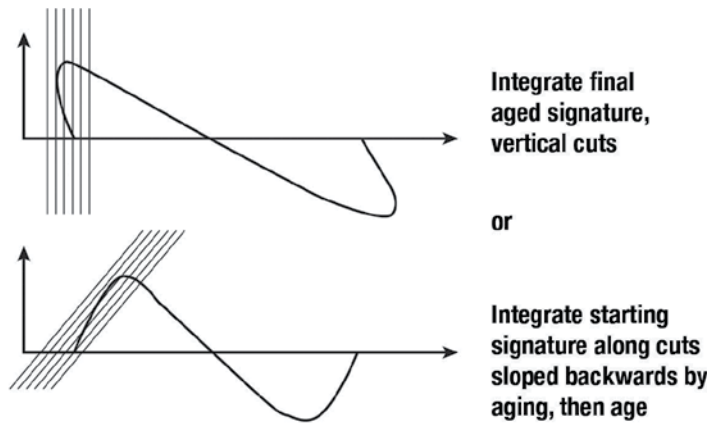


Figure 6.7. Shock fitting by area balancing.

Iterative shock balancing can be tedious to implement, particularly if there are multiple shocks in a signature. A general algorithm for shock fitting was developed by Middleton and Carlson (ref. 6.24) and by Hayes (ref. 6.23). In this method, a function S is defined that is the integral of the F-function:

$$S = \int_0^x F(\tau) d\tau \quad (32)$$

The function is computed for the age-strained τ , i.e., $\tau - F \Lambda$, as illustrated in figure 6.8.

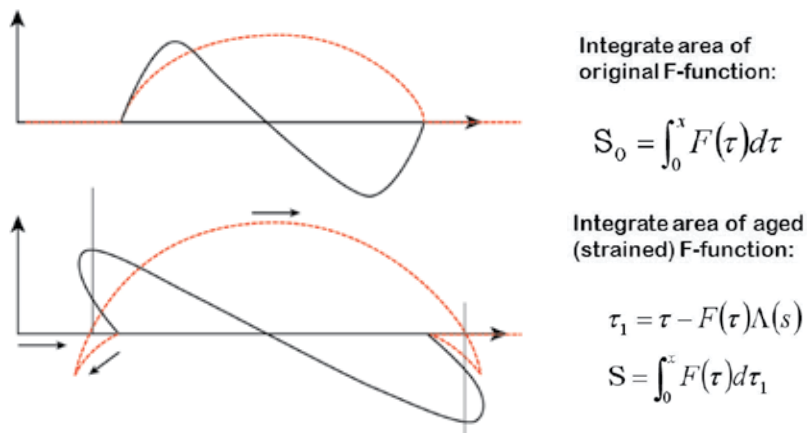


Figure 6.8. Shock fitting by crossings of the S function.

Because S is the integral of F , it represents areas of F , so area balancing is equivalent to places where F crosses itself. Note in figure 6.8 that triple valued regions of F correspond to regions where S reverses its direction, then after progressing in the original direction crosses itself. Shocks are located where forward-running segments of S cross. Middleton and Carlson (ref. 6.24) define the algorithm, and provide step-by-step procedures for its implementation. Those steps include rules for dealing with situations where there can be multiple overlaps in a region. Hayes et al. (ref. 6.23) shed further rigor on the underlying mathematics in their presentation.

An alternate method of aging a signature and managing shock formation is the waveform parameter method developed by Thomas (refs. 6.25 and 6.26). In that method, the signature is divided into several segments and shocks, as shown in figure 6.9. The per-segment quantities that define the waveform parameters are shown in the figure. Thomas’s implementation works directly with the pressure signature, rather than the F -function, but that is just a matter of scaling and (despite the title of ref. 6.25) is an equivalent definition. Thomas’s method uses Whitham’s rule to compute the advance of each x_i in the signature, and the corresponding lengths λ_i and slopes m_i . The shock jumps Δp_i are computed by a generalization of the process Whitham used to compute the shock jump for an N-wave. The software implementation of this method advances the signature at nominal time or distance steps along a ray. If a shock forms within a step, or if two segments coalesce within a step, the step is shortened to match the shock formation or coalescence point. The waveform parameters are reformulated to include the new shock and/or to eliminate the merged segment, and the process continues.

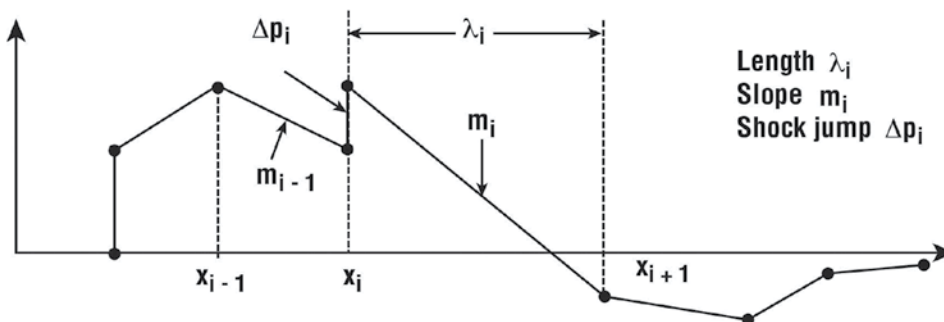


Figure 6.9. Representation of boom signature by waveform parameters.

A weakness of Thomas’s original implementation is that the code only expected one shock formation or coalescence at a time. If a complex signature with a large number of points is specified, there is an increasing chance that two such events could happen simultaneously, causing a failure of the calculation. This becomes a problem when using CFD data as F -function inputs, since such solutions tend to have numerous points on a fine mesh, increasing the likelihood of simultaneous coalescences. This is an issue for the Thomas code and its descendants, which included earlier versions of PCBoom (ref. 6.27). A multi-coalescence update was made to a proprietary code (ref. 6.28).

Signature Aging and Shock Coalescence

Early sonic boom analyses concentrated on far-field signatures and the Landau-Whitham result that N-waves were inevitable. There was a major conceptual advance in 1965 when McLean (ref. 6.29) pointed out that N-wave booms were not inevitable. He noted that when real atmosphere effects (derived in the next section) were considered, the boom at the ground would not be far field, but would be mid-field and did not have to be an N-wave. This signature freezing phenomenon was further explained by Hayes (ref. 6.12) and explored by Seebass (refs. 6.10 and 6.30) and George (ref. 6.31). Hayes defined an age variable (ref. 6.23) that in an isothermal atmosphere reaches an asymptotic value at a distance of $\pi H/2$ where H is the scale height of an isothermal atmosphere.

While the term freezing was coined, figures 6.10 and 6.11 from reference 6.25 show that, for both uniform and standard atmospheres, an example two-shock signature from an aircraft at an altitude of 60,000 feet never freezes. There is a distinct difference in the rate of coalescence as both signatures move continuously toward an N-wave. The interest is, of course, in the boom at the ground, and not what it would be if it propagated indefinitely. It would appear that if that same airplane had been flying at lower altitude, say at 45,000 feet, then the two-shock configuration would have reached the ground yielding a smaller Δp_{\max} .

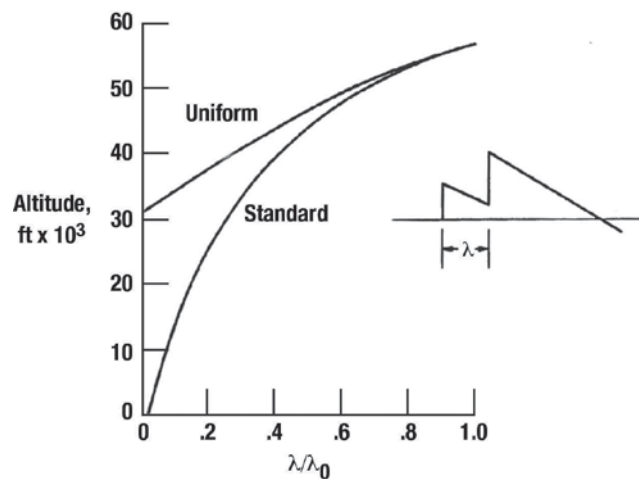


Figure 6.10. Effect of atmospheric gradients on shock coalescence for an ogee wing at Mach 1.69 and $C_l = 0.136$ (ref. 6.25).

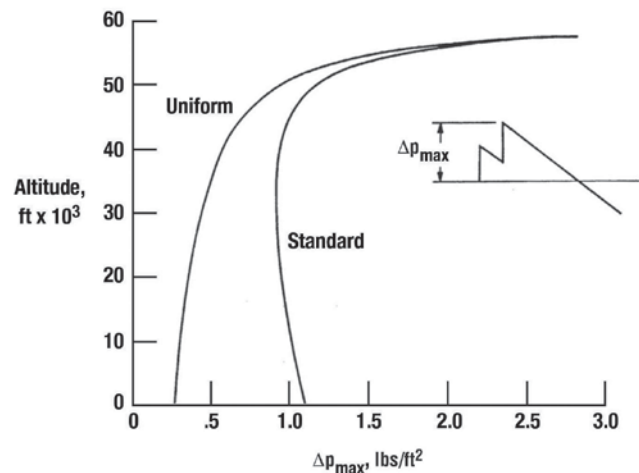


Figure 6.11. Effect of atmospheric gradients on wave amplitude for an ogee wing at Mach 1.69 and $C_l = 0.136$ (ref. 6.25).

While true freezing does not occur in the real atmosphere (refs. 6.32 – 6.38) and the phenomenon might better be called chilling, it is important to note that mid-field signatures are the rule for larger aircraft. By controlling shock-strength, pressure-recovery rates (see fig. 6.12), and altitude, non-N-wave signatures on the ground can be achieved.

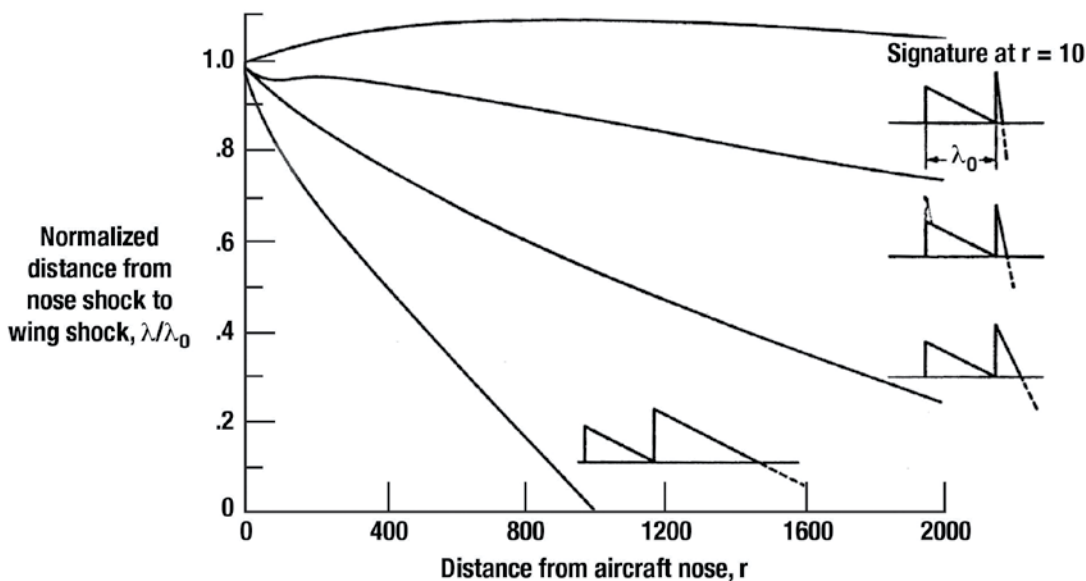


Figure 6.12. Effect of slope behind wing shock on coalescence at Mach 3 (ref. 6.32).

Pressure Signature Propagation in a Real Atmosphere

The theory development presented in equations (16) through (32) has been for propagation through a uniform atmosphere, although the potential for atmospheric gradients has been discussed and the parameter B introduced in equation (16) provides a place for those effects. Atmospheric gradients are addressed by the method of geometrical acoustics. The formulation employed is that of Blokhintzev (ref. 6.19), which addresses wind, sound speed, and density gradients. An equivalent simpler derivation for a windless atmosphere, following that of Officer (ref. 6.39) is presented in detail below, with Blokhintzev’s full result shown afterwards.

Ray Tracing

Consider propagation through an atmosphere with variable ambient sound speed and density, with no wind velocity and neglecting gravitational buoyancy. The wave equation is

$$\frac{\partial^2 p}{\partial t^2} - \rho_o \alpha_o^2 \vec{\nabla} \cdot \frac{1}{\rho_o} \vec{\nabla} p = 0 \tag{33}$$

where p now is termed the acoustic overpressure α_o and ρ_o are the ambient sound speed and density.

A solution is sought of the form

$$p(x, y, z, t) = P(x, y, z) e^{i\omega \left[t - \frac{W(x, y, z)}{a_o} \right]} \tag{34}$$

where

ω = frequency

a_∞ = fixed reference sound speed

$P(x,y,z)$ = amplitude function

$W(x,y,z)$ = wavefront function

$t - W/a_\infty$ is a generalization of the earlier phase relation $t - s/a$, and P is a generalization of the $1/\sqrt{B}$ amplitude relation (see eq. 16).

Substituting equation (34) into equation (33) and separating the real and imaginary parts, the following two equations are obtained:

$$1 - \frac{a_o^2}{a_\infty^2} (\nabla W)^2 = \frac{a_o^2}{\omega^2} \left(\frac{\vec{\nabla} \rho_o}{\rho_o} \bullet \frac{\vec{\nabla} P}{P} - \frac{\vec{\nabla}^2 P}{P} \right) \quad (35)$$

$$\nabla^2 W + \vec{\nabla} W \bullet \left(2 \frac{\vec{\nabla} P}{P} - \frac{\vec{\nabla} \rho_o}{\rho_o} \right) = 0 \quad (36)$$

Note that the only terms dependent on ω are on the right hand side of equation (35). Those terms are of the order $(\lambda/L)^2$, where λ is the wavelength of the signal and L is the scale length of atmospheric gradients and amplitude changes. If the short wavelength limit, $\lambda \ll L$, is taken, equation (35) becomes

$$1 - \frac{a_o^2}{a_\infty^2} (\nabla W)^2 = 0 \quad (37)$$

so that there is no frequency dependence, and the system is non-dispersive. Equation (35) is the eikonal equation, familiar from geometrical optics, and states that the gradient of W is proportional to the local index of refraction. Propagation is along geometrical rays orthogonal to wave fronts W .

Since equation (34) is written for a harmonic wave, the $\lambda \ll L$ limit is really taken as $\omega \rightarrow \infty$. Keller (ref. 6.40) presented an alternate derivation written in terms of shocks, where taking the shock thickness as small (formally $\lambda \ll L$) yielded the same result as the harmonic formulation. Because sonic booms are shocks, some authors (e.g., Friedman, Kane, and Sigalla in ref. 6.41) cite Keller rather than Blokhintzev. Once a ray field is computed, $\vec{\nabla} W$

may be written $\frac{\alpha_\infty}{\alpha_0} \hat{n}$ where \hat{n} is the unit vector field representing ray direction. Equation (36) may be

written as

$$\vec{\nabla} \bullet \left(\hat{n} \frac{P^2}{\rho_o a_o} \right) = 0 \quad (38)$$

which has the form of a continuity equation. Defining a ray tube as a bundle of rays, equation (38) integrates to

$$P \left(\frac{S}{\rho_0 a_0} \right)^{1/2} = \text{constant} \quad (39)$$

where S is the ray tube area. Figure 6.13 is a sketch of a ray tube and its cross sectional area (note that S is not the same as the function defined in equation (32)). Notations in sonic boom literature are not entirely consistent. A is often used for ray tube area, and should be not confused with A used for body cross sectional area in the F-function definition. The quantity $\rho_0 a_0$ is the acoustic impedance, and equation (39) represents conservation of energy within a ray tube.

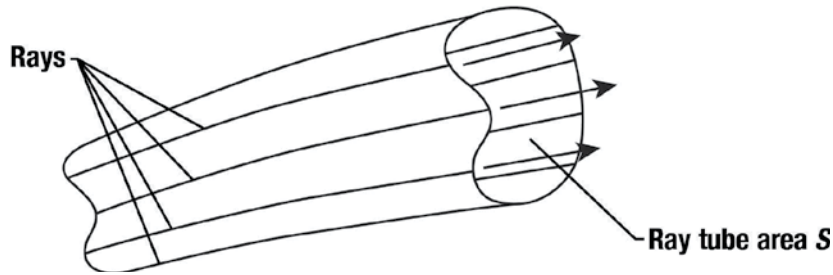


Figure 6.13. Ray tube and ray tube area.

When winds are present, the acoustic equations are considerably more complex. The acoustic velocity, density, and sound speed perturbations do not fall out until the short wave limit is taken. Because of convection, the ray paths do not necessarily coincide with wave normals. Blokhintzev derived the eikonal and amplitude for an inhomogeneous moving medium, and obtained (with notation slightly different from that used here)

$$q^2 - \frac{a_0^2}{a_\infty^2} (\nabla W)^2 = 0 \quad (40)$$

$$\vec{\nabla} \cdot \left[\left(\hat{n} + \frac{\vec{u}_0}{a_0} \right) \frac{P^2}{q \rho_0 a_0} \right] = 0 \quad (41)$$

where

$$q = \left(1 + \frac{\vec{u}_0 \cdot \hat{n}}{a_0} \right)^{-1} \quad (42)$$

$\vec{u}_0 = \text{ambient wind velocity}$

Equation (41) integrates to

$$\frac{P^2}{q^2 \rho_0 a_0} S = \text{constant} \quad (43)$$

along a ray tube defined by trajectories

$$\vec{c} = a_0 \hat{n} + \vec{u}_0 \quad (44)$$

It is straightforward to match equations (2) and (16) to equation (39) or (43) to obtain the proper form of the generic amplitude $1/\sqrt{B}$. Rays can be traced by any of the familiar methods from optics, including Fermat's principle and Snell's law. Ray tracing begins with an initial ray on a ray cone generated at any given time at the aircraft. Figure 6.14 illustrates a ray cone and an initial ray at azimuth ϕ (Note that ϕ is about the aircraft's roll axis, as is body-oriented azimuth θ as in equation (4), but is relative to earth referenced down rather than aircraft coordinates. The two angles differ by the bank angle).

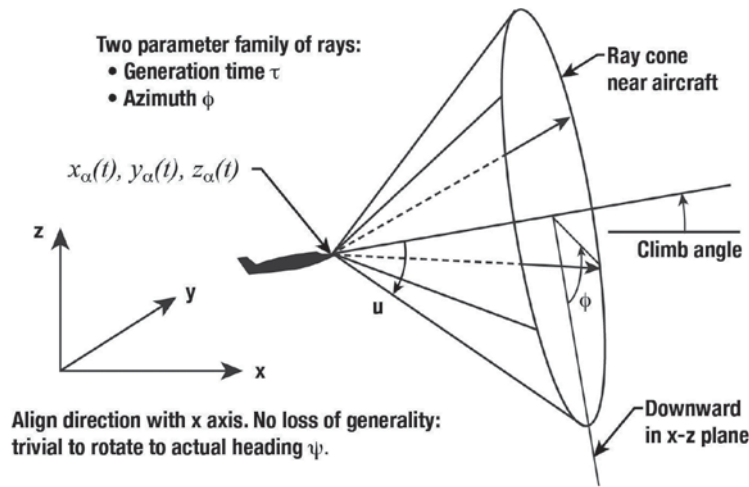


Figure 6.14. Ray cone at time t and initial ray at azimuth ϕ .

The independent variables for selecting a ray are aircraft time t and the azimuth ϕ . In software implementations of boom theory, it is typical to use four rays, separated by small increments in t and ϕ . There are two widespread styles in use. The first is that in the ARAP program (ref. 6.23), where differential relations are developed for the ray path and ray tube area. Those relations are in the form of quadratures, which then are evaluated numerically. The second is that used in the Thomas program (ref. 6.26) where each ray is traced numerically and the ray tube areas obtained by differences between them.

As might be surmised by the division of theory within this chapter, numeric implementation of sonic boom theory is modular. Figure 6.15 shows the logical flow. For a given point on the aircraft's flight path, the F-function is obtained from aerodynamics and geometry. Geometry and area rule are set off in the chart since the F-function (or initial p vs s signature, depending on scaling tastes) can come from any suitable source, such as CFD. Rays are traced, depending only on the flight path kinematics and the atmosphere. Ray tube areas and the age parameter are part of the ray tracing analysis, which is independent of the vehicle source characteristics. Finally, the initial signature is merged with ray tracing and aging to obtain the boom signature at the ground or any location along the ray path. Figure 6.16 shows the same process in graphical format.

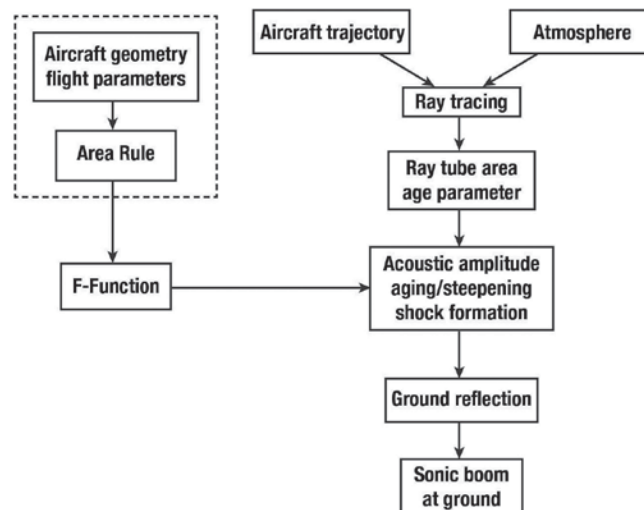


Figure 6.15. Logical flow of sonic boom calculation.

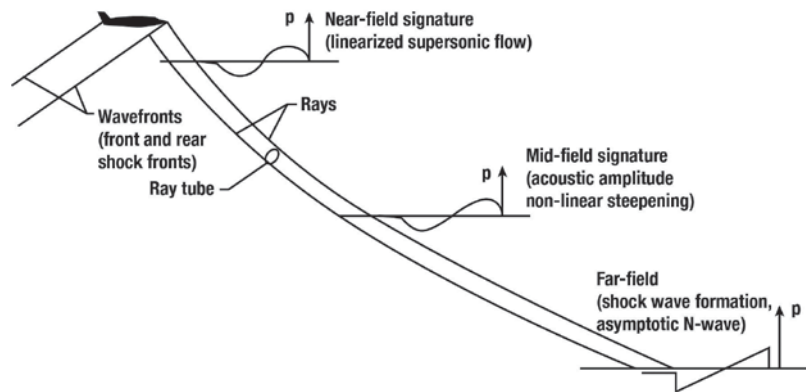


Figure 6.16. Sonic boom generation, propagation, and evolution.

Pressure Signature Propagation Codes

As noted earlier, there are several methods/computer codes available for predicting the evolution of an aircraft's pressure signature as it propagates to the ground through a real stratified atmosphere. One of the most used codes in the United States for many years, when F-function methodology was dominant, was the Hayes code (refs. 6.23, 6.42, and 6.43). Rao (ref. 6.44) formulated a methodology for maneuvering aircraft in a homogeneous atmosphere and Randall (ref. 6.45) for steady-state flight in a stratified atmosphere.

The Hayes code was based on geometrical acoustics as derived by Blokhintsev (ref. 6.19). Details of the method are given in reference 6.23; the computer code (often called the ARAP code) is also described in this reference. There are other propagation codes based on the Hayes methodology that go by various names. Improved user friendly inputs are typical; some may have a more accurate maneuver capability. Another propagation code based on ray tracing concepts was documented in references 6.46 and 6.47 by Friedman et al. As with the Hayes code, this program allowed for flight paths that are curved, climbing, or diving. Example results were given for the effects on sonic boom of some atmospheric effects as well as flight path curvature and acceleration.

An alternate method with limited utility was formulated by Schorling (ref. 6.48). He noted that while the ray tracing codes include the effects of nonlinear distortions they are essentially linear in nature and are not adequate for handling such nonlinear effects as shock focusing or cut-off Mach number. In his method of characteristics based on analysis, the nonlinear system of partial differential equations for supersonic flow were solved for large distances by using a perturbation method developed by Tsien Poincaré, Lighthill, and Kuo (see ref. 6.49). The analysis of reference 6.48 was for a homogeneous atmosphere; reference 6.50 extends this work to a stratified atmosphere.

Another propagation code (and its derivatives) frequently used today is the Thomas code (refs. 6.25 and 6.26). The Thomas code is based on geometrical acoustics as derived by Blokhintsev (ref. 6.19) but does not use an F-function to represent the near-field signature. In reference 6.25 (p. 206), Thomas asserts that,

The approach used is to describe the waveform of the sonic boom wave by several waveform parameters and then to obtain equations for the parameters as functions of time. This approach has the advantages that: (1) the theory is simpler and more intuitive than the Whitham theory, (2) it provides a more convenient method for extrapolating experimental signatures because the pressure signature is dealt with directly, rather than through the use of an F-function, and (3) shock locations are determined by a much neater method than the classical area balancing technique used in F-function extrapolations.

As noted earlier, Thomas's wave parameter formulation is actually a generalization of Whitham's analytic formulation summarized in equations (20) – (27). His initial waveform corresponds to beginning with the left hand side of equation (1) rather than the right hand side, which is appropriate if the F-function itself has not been computed or directly measured. The formulation of the method is rather elegant, but in some situations lends itself to complexity in practical implementation.

The effects of aircraft acceleration and atmospheric temperature, pressure, and wind gradients are included in the theory and in the computer program (ref. 6.26). Several other codes with the acronym SHOCKN and THOR, developed at the University of Mississippi and University of Texas respectively, are described and applied in reference 6.51.

One of the most widely used codes is PCBoom (ref. 6.27). It originated as an extension of the Thomas code, with algorithms to compute signatures within focal zones. It has evolved into a multi-featured program, accepting a variety of source definition types and computing complete footprints. The current version also computes over-the-top booms and accounts for the actual ellipsoidal earth, rather than flat earth. Because of the instabilities of the waveform parameter method for complex signatures, the current version of PCBoom has abandoned the waveform parameter in favor of the age parameter and Middleton-Carlson shock fitting. PCBoom retains the feature of beginning with δp at a reference r rather than the F-function.

Siclari (ref. 6.52) and Fouladi (ref. 6.53) compared ground pressure signatures calculated with an early version of MDBOOM (ref. 6.54) and Thomas (ref. 6.26). As seen in figures 6.17 and 6.18, the MDBOOM code yielded a higher Δp and longer signatures than that of Thomas. This indicates that the mid-field pressure signature did not decay as fast with the MDBOOM prediction as the near-field decay of the Thomas code. Siclari also states that MDBOOM results show significantly less sensitivity to extrapolation distances in comparison to the Thomas code. Certainly the vertical distance from the aircraft where the propagation code is matched to the Euler solution is critical. Nevertheless, the differences are puzzling since MDBOOM is also based on the Thomas methodology. The signatures compared in both references 6.52 and 6.53 are those for the symmetry plane (on track) of conceptual configurations. It would be useful to have a comparison of these methods for a configuration where real data exists, such as shown in figure 6.3, for the Carlson methodology.

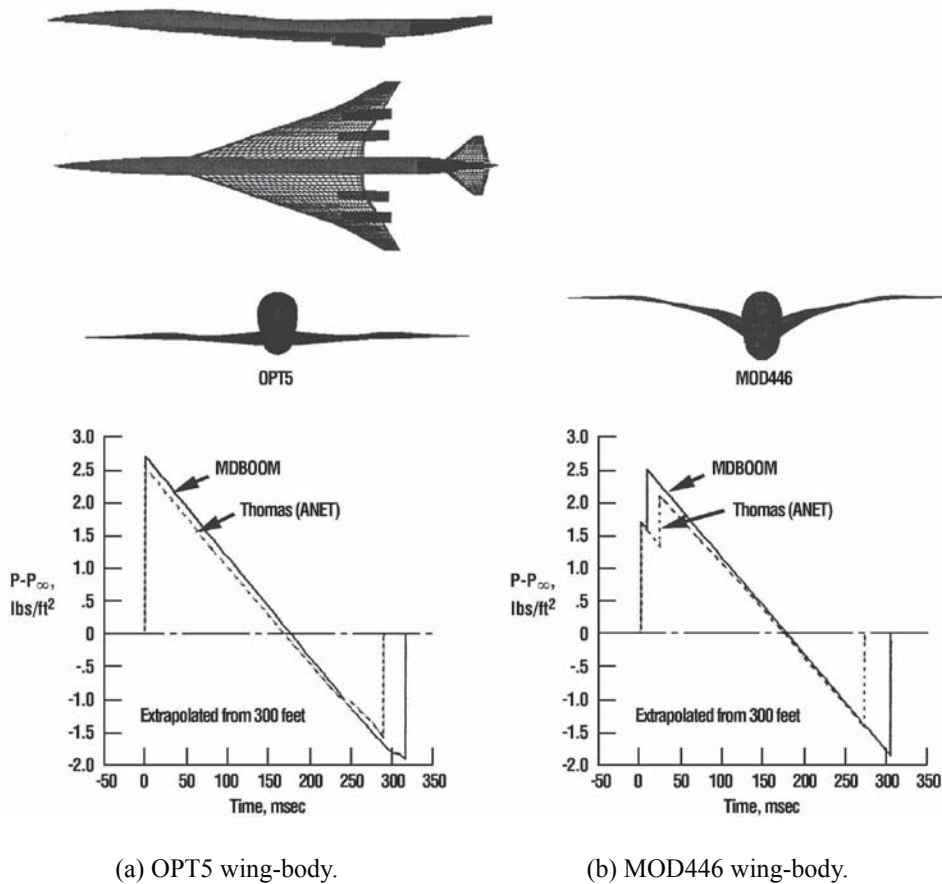


Figure 6.17. Comparison of MDBOOM and Thomas ANET predictions of ground pressure signatures (ref. 6.52).

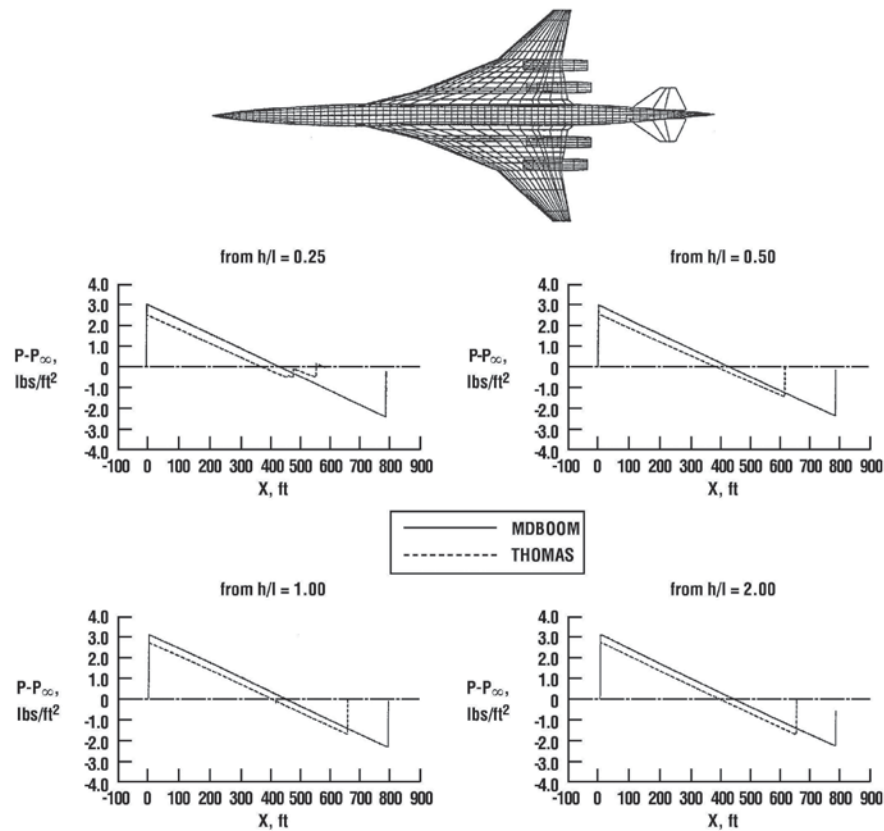


Figure 6.18. Comparison of the ground pressure signatures of the baseline configuration MDBOOM versus Thomas, Boeing 1080-1122 baseline configuration (ref. 6.53).

There are several codes based on the Thomas code methodology in circulation, so apparently MDBOOM was based on a different version than that used by Siclari. It is worth noting that the equations in references 6.25 and 6.26 differ from each other, one being based on signature time and the other on signature length.

One area where most of these propagation codes break down is when a focus exists. Factors that are neglected (diffraction and nonlinear effects) in the development of geometric acoustics become important and limit pressures at these singularities to finite values. Three types of focused booms and the maneuvers that produce them are detailed in reference 6.55 along with the methodology required to predict their geometry and magnitude. Modifications to a version of the Thomas code were made to include the focused boom, or caustic geometry analysis, and example calculations are given. Other analyses of the booms of maneuvering aircraft are given in references 6.56 to 6.59. Related studies of the sonic boom behavior near a caustic are discussed and listed in reference 6.55. See Chapter 3 for additional discussion of the effect of maneuvers on sonic boom.

The most used boom codes employed in the United States do not consider the secondary or over-the-top booms. Gardner and Rogers (ref. 6.60) provide details of a nonlinear theory for the long-range propagation of sonic booms through the thermosphere. Results are presented for the case of the Concorde SST in straight, level, and steady flight at an altitude of 17.5 kilometers and a speed of Mach 2. Taylor (ref. 6.61) describes the TRAPS code that added secondary boom capability to the ARAP (or Hayes) code. ZEPHYRUS (ref. 6.62) is another code that has secondary boom capability and includes absorption effects as well. A comparison of the two aforementioned codes (refs. 6.61 and 6.62) is given in reference 6.63, which examined the impact of weather and flight conditions on the secondary boom (see also discussion in Chapter 2). It is interesting that while both TRAPS and ZEPHYRUS account for the passage of an over-the-top boom through a caustic, neither actually computes boom signatures at a caustic. The current version of PCBoom (ref. 6.64) does compute boom signatures at an over-the-top caustic passage and at ground caustic intercepts and also includes absorption effects.

The Near-Field/Mid-Field Dilemma

It is convenient to break down the volume of air surrounding a supersonic aircraft into three regions – a near field, a mid field, and a far field (see figure 6.19). The near field may be calculated using linear theory or, most likely today, using a CFD code based on the Euler equations. In the near field, Euler equation case, the actual geometry would have been modeled including the fuselage, wing, tail, and engines. Normally in treating the engine, boundary conditions are placed on the inlet and exhaust planes to calculate the flow around and downstream of the engines. In some cases, investigators have allowed flow through the engine but no energy is added. Reference 6.65 by Siclari and Fouladi is an example of the former procedure.

In the use of Euler equations for near-field calculations there will normally be nonlinear and non-axisymmetric effects. To get to a radial location where the CFD solution can be properly matched to locally axisymmetric ray tracing propagation codes, the Euler calculation may have to extend out to the far field. Today high-fidelity Euler-equation calculations beyond a billion points or nodes, and the extension of a high fidelity calculation to the far field is possible, but not yet practical for general use. The original Whitham formulation modeled source and propagation as a single zone. Using CFD for the near field becomes a two-zone problem, and attention must be paid to matching the zones.

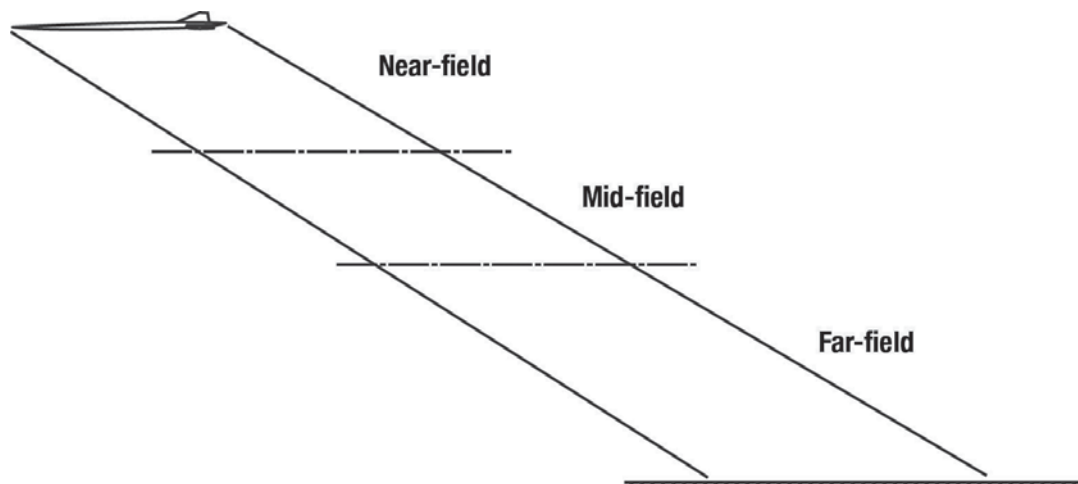


Figure 6.19. Radial breakdown of pressure variations from near field to far field.

Another more accurate option would be to use a three-zone formulation, where a mid-field code that matches the CFD calculations at a small radius can continue propagation out to the far-field locally axisymmetric region, where ray tracing codes like ARAP (ref. 6.23) or Thomas (ref. 6.26) would complete the propagation. Real near-field flow fields are not locally axisymmetric or linear, so the CFD calculation must be matched to a mid-field code that models similar flow physics.

Shock Smearing and Fitting

When calculating the near field of an aircraft using a CFD Euler code, one will find that the shock jumps are consistent with the Rankine-Hugoniot equations. With this constraint there are shocks of different shape and strength followed by pressure recoveries of different strengths (rates of recovery). Normally, CFD calculations are made with grids that are stretched radially as one moves to the outer boundaries, since the flow gradients become smaller, and far-field boundary conditions can be imposed. Outer boundaries are typically placed one to two body lengths from the centerline depending on the Mach number and shape. Solution schemes are generally of the shock capturing variety. All of this combines to smear the shocks and reduce their maximum pressure jumps from their proper value at the outer boundary. Figures 6.20 and 6.21 from references 6.66 and 6.65, respectively, show the smearing of shocks caused by the solution algorithms and grids and how the smearing becomes worse as the radial distance is increased (fig. 6.21). It should be noted that the HFLO3 (fig. 6.20) calculations, at an h/l of 0.25, involve an adaptive grid and the AIRPLANE calculations used a high resolution unstructured grid.

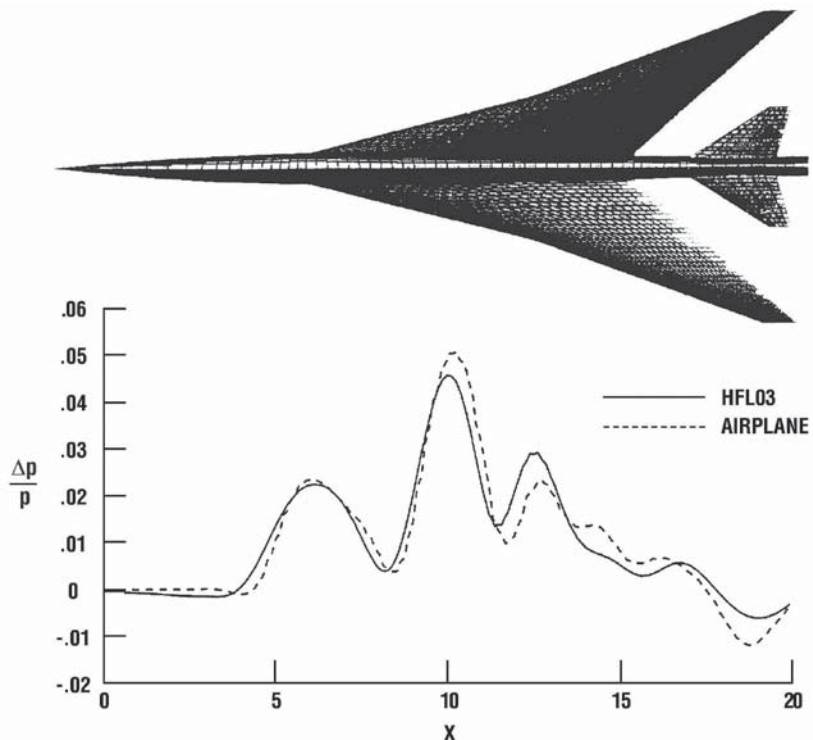


Figure 6.20. Comparison of AIRPLANE and HFL03 near-field pressure signatures. Mach 2.0, $\alpha = 2.75^\circ$, $h/l = 0.25$ (ref. 6.66).

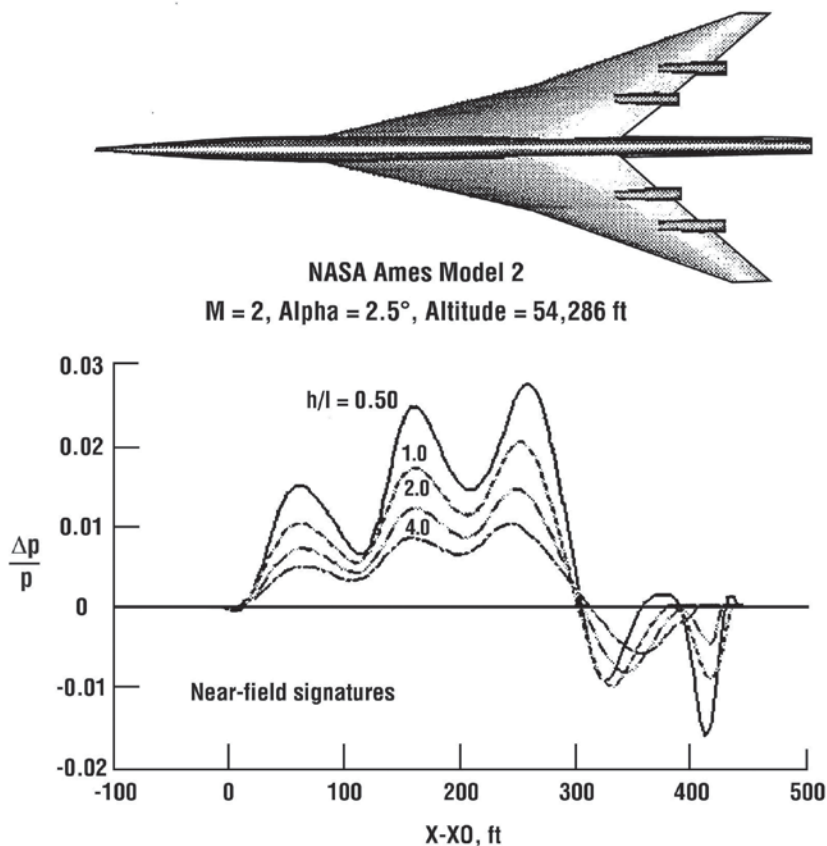


Figure 6.21. Near-field pressure signatures for the Ames Model 2 design (ref. 6.65).

Shock fitting schemes are another option and have been available for many years. However, they are not normally used or needed where the primary interest is the pressures on the configuration itself. Whether a

procedure can be formulated to recover an accurate finite shock jump at the near-field boundary from a smeared one is not clear. Lacking a shock fitted Euler (or Navier-Stokes) code it is desirable to use a grid that conforms as close as possible to the shocks and to have as high a concentration of grid points in the vicinity of the shocks as can be accommodated. The latter is desirable since shock jumps are usually resolved in three or four grid points. The use of a grid adaptation scheme in an Euler code with a shock capturing solution algorithm is one way of further improving resolution. The combination of shock capturing and shock fitting is the preferred or ideal approach. The latter provides a procedure for explicitly computing the jump conditions across shocks. It locates the shocks and treats them as boundaries between regions where the solution is regular. Moretti (ref. 6.67) developed a method known as floating shock fitting where shocks float during the iterative calculation. Several papers treating the Euler equations with shock fitting have been published over the years (refs. 6.68 to 6.71) and the technique is fairly well established. Shock fitting has also been applied to various versions of the potential equations for both transonic and supersonic flows (refs. 6.72 and 6.73). Where the near-field shocks are smeared (not fitted) one would like to employ a mid-field calculation that starts as close to the aircraft as possible. This places strong demands on the matching method of a two-zone scheme.

Mid-Field Pressure Propagation Methods

Page and Plotkin (ref. 6.74) describe a shock fitting Euler code (SCRAM) that has been coupled with the multipole linear scheme of George (ref. 6.75). The multipole pressure field is matched to the CFD solution at some radius and converts it to an equivalent locally axisymmetric source, so that a ray tracing code can be applied to take the pressure pulse to the ground. While this is clearly a more accurate method to propagate the pressure signature than connecting the ray tracing code directly to the CFD solution, there is still a concern. The multipole method still assumes the sources are concentrated along the vehicle axis, so the further one can take the CFD solution (larger radial distance) into the mid field where the ratio of wingspan to distance is small, the more accurate will be the multipole solution. While reference 6.74 presents the multipole results only for a simple triangular wing configurations and the SCRAM code, it has been successfully applied in various studies to more complex configurations and other CFD codes. Application of the multipole mid-field methodology, along with the SCRAM Euler code, to a complex canard configuration is discussed in reference 6.76. Improvement to the multipole scheme by Morgenstern was noted by Siclari in reference 6.52 (p. 158). There are other papers, though seldom referenced, that describe the multipole approach to boom minimization authored by Y. S. Pan. In references 6.77 and 6.78, he developed the propagation equations and applied them to the calculation of the flow about several bodies of revolution.

Another methodology that would serve as a mid- to far-field propagation methodology or as a near-field to ground methodology was given in reference 6.79. This methodology was based on the full potential equation (FPE) and matched to the near-field Euler solution point for point to the full potential solution, across three planes of data, thus capturing the lateral and radial gradients as well as shock jumps. While the FPE did not duplicate Euler equation results exactly, the difference is small. The method uses both grid adaptation and shock fitting to maintain accurate shock-pressure jumps and is capable of calculating the propagation of the three-dimensional pressure wave all the way to the ground. For example, calculations for ground pressure signatures for delta wings with biconvex and slab-sided sections flying at Mach 2.01 and an altitude of 52,000 feet are given in reference 6.79. The method has also been used to show the merits of dihedral wings in reference 6.80. FPE code predictions for a delta-wing configuration have also been compared to the experimental data of Cliff (ref. 6.66) and to flight data for a modified F-5 in reference 6.81.

At the start of the calculation, the FPE method discussed in reference 6.79 uses an interpolation routine that determines the flow variables on the unstructured grid of the FPE propagation codes from those of the structured grid of the near-field Euler calculation. Reference 6.82 has added an additional interpolation routine that enables an unstructured grid near-field Euler calculation (ref. 6.83) to be used. This modification was demonstrated in reference 6.82 for a double-cone configuration along with experimental data comparisons.

In the utilization of a FPE methodology for a mid-field code, or extending the near-field Euler calculation to the far

field, there is a question of where to initiate the far-field ray tracing code calculation. While the pressure signature calculated by the mid-field or Euler codes is normally input, and continuity of its magnitude is preserved, the radial gradient may not be preserved. Lacking a theoretical prescription, the mid-field or Euler calculation can be extended to several different radial distances, then exercising for each distance the far-field propagation code to see if the starting location, or match point, makes a difference in the ground signature. At the radial distance, where a further increase in radial location of the match point has only a trivial effect on the ground signature, one should assume a proper match point has been found.

Another mid-field possibility is that of Hicks and Mendoza in reference 6.84. While its title purports to predict the sonic boom from experimental near-field results, the method could be used to extrapolate near-field Euler calculations based on Whitham's F-function, which in turn is based on his h-function (ref. 6.3) and is capable of calculating the pressures of bodies with discontinuities in the shape of their area and lift distributions. The method is illustrated using experimental results for an XB-70 model (see fig. 6.22) taken at two radial positions of r/l of 1.0 and 4.5 and lift coefficients from 0.04 to 0.19 as illustrated in figures 6.23(a) and 6.23(b). A comparison of the calculated ground signature for the XB-70 (fig. 6.22) at Mach 1.8 and an r/l of 280, using wind-tunnel pressure signatures measured at an $r/l = 1.0$ (fig. 6.23) is compared with flight data in figure 6.24.

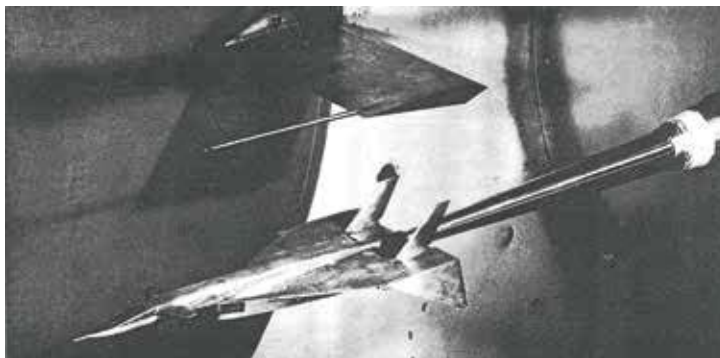


Figure 6.22. Model and related test equipment installed in the 9- by 7-foot wind tunnel (ref. 6.84) (model rotated 90° from running position).

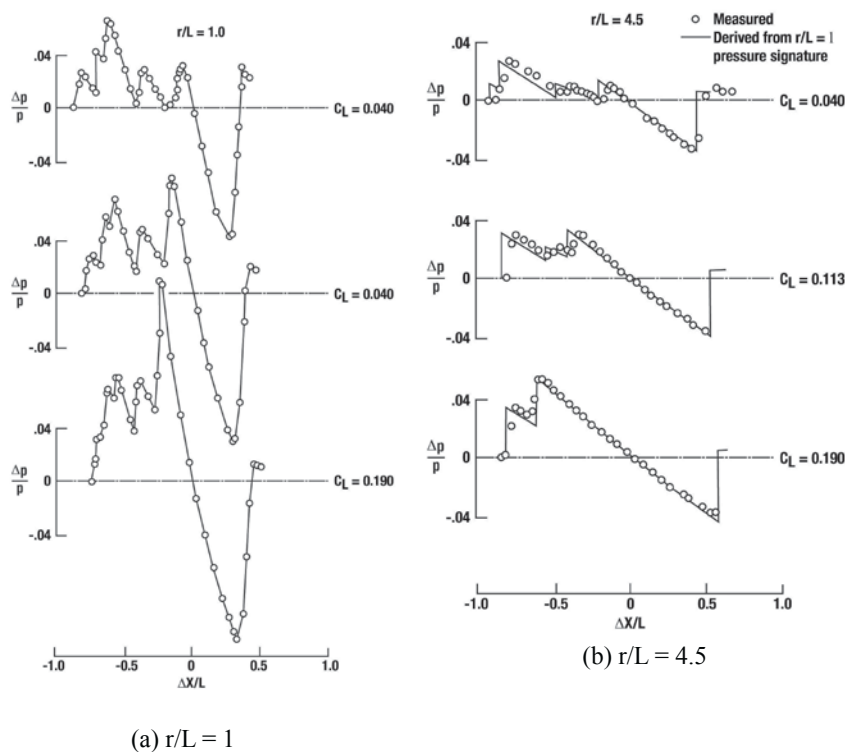


Figure 6.23. Wind-tunnel test results for an XB-70 model recorded at two radial positions of r/l varying lift coefficients (ref. 6.84).

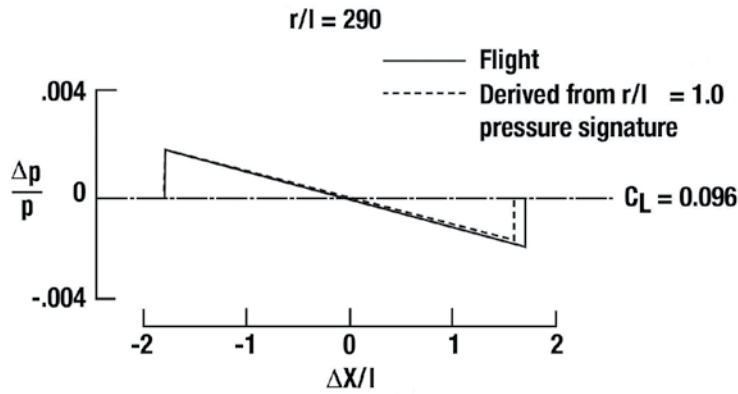


Figure 6.24. Comparison of flight and wind-tunnel derived pressure signatures at $r/l = 1.0$ and Mach 1.8 (ref. 6.84).

The flight data was obtained from an XB-70 airplane test at Edwards Air Force Base using an average of three separate pressure signatures for the airplane. These measured results were the only data available a Mach 1.8 where the ground track of the aircraft was sufficiently close to the ground measurements.

As can be seen, the agreement between the wind-tunnel derived data taken at an r/l of 1.0 and the flight pressure signature is good except for the small discrepancy in the location of the rear shock. This discrepancy is primarily attributed to two factors. First, no attempt was made to simulate the flow of hot exhaust gases in the wind-tunnel tests. Second, the sting support used with the wind-tunnel model was too short to allow for an accurate measurement of the decay of the pressure signature downstream of the rear shock (see fig. 6.22). In order to balance area for the determination of the rear shock strength and location on the experimental F-function at an r/l of 290, it was necessary to extrapolate the wind-tunnel pressure signatures of figure 6.23 downstream for several model lengths. As a mid-field code, the question of where to make the match with the ray tracing code is a concern, just as for the FPE or Euler equation solutions. However, the F-function methodology used in reference 6.84 is capable of calculating the pressure signature all the way to the ground.

Lateral Variation and Extent of Sonic Boom Signatures

Considerable attention has been given to defining the lateral variation and extent of the primary boom carpet for steady flights of aircraft at various Mach numbers and altitudes. References 6.41, 6.85, 6.86 provide equations for the former, but Kane and Palmer in reference 6.87 did a simple analysis that was based on the result that, in a uniform atmosphere, the magnitude of an N-wave sonic boom varies inversely as the $3/4$ power of the distance from the airplane to the ground.

Given

$$D = \sqrt{y^2 + h^2} = h \sqrt{1 + \left(\frac{y}{h}\right)^2} \quad (45)$$

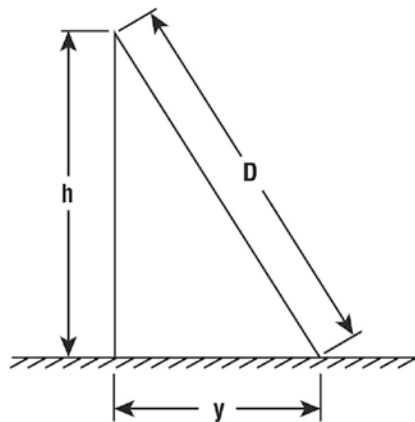


Figure 6.25. Geometry nomenclature used for distance calculation.

the expression for Δp at some lateral position relative to Δp under the flight track is

$$\frac{\Delta p}{\Delta p_{\text{under flight track}}} = \left(\frac{h}{D}\right)^{3/4} \left[\frac{I(y_o, \theta)}{I(y_o, -90^\circ)} \right]^{1/2} \tag{46}$$

Equation (46) can be rewritten using equation (45) as

$$\frac{\Delta p}{\Delta p_{\text{under flight track}}} \left[\frac{I(y_o, -90^\circ)}{I(y_o, \theta)} \right]^{1/2} = \left[1 + \left(\frac{y}{h}\right)^2 \right]^{-3/8} \tag{47}$$

where

$$I(y_o, \theta) = \int_0^{y_o} F(y, \theta) dy \tag{48}$$

and the F-function is defined by equation (5). See equations (9), (10), and (11) for the relationship of $I(\tau_o, \theta)$ to Δp . A plot of equation (47) for the lateral variation of the boom strength compared to those calculated by the method of references 6.41, 6.85, and 6.86 is shown in figure 6.26. As reference 6.87 (p. 8) notes,

The above results indicate that in the standard atmosphere, the variation of boom strength with lateral distance may be very closely approximated by equation (47) with Δp under flight track being obtained by the methods of the first section of this chapter. The lateral distribution of sonic boom strength predicted by this method should be suitable for most routine calculations.

In the early stages of sonic boom studies, concern was expressed regarding the nature of sonic boom exposure patterns near the lateral cutoff. It was believed by some (ref. 6.88 and 6.89) that boom focusing would occur at the lateral extremities of the primary boom carpet as a result of atmospheric refraction during steady-level flight. Some boom prediction codes, based on linear acoustic theory, show rapid increases in boom level as a result of ray tube areas going to zero at the lateral cutoff (ref. 6.90). However, in 1959, Randall (ref. 6.9) developed the following equation for the lateral cutoff for altitudes below the tropopause (~36,000 feet).

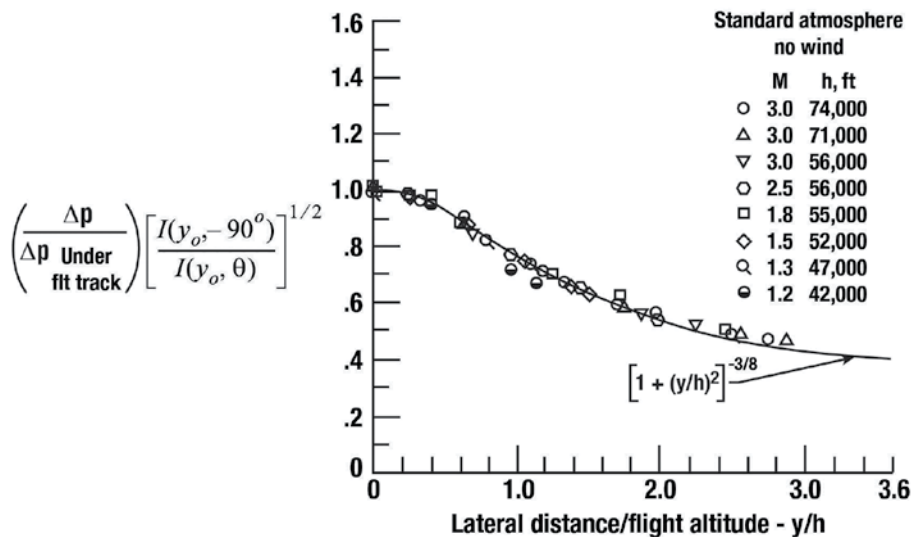


Figure 6.26. Variation of boom strength with lateral distance for U.S. Standard Atmosphere in 1962 (adapted from ref. 6.87).

$$y_{max} = \pm h \left[\frac{a_g + a_a}{a_g - a_a} \right]^{1/2} (1 - a_g^2/V^2)^{1/2} \quad (49)$$

and with $V = a_a M$

$$y_{max} = \pm h \left[\frac{a_g + a_a}{a_g - a_a} \right]^{1/2} \left(1 - \frac{a_g^2}{a_a^2 M^2} \right)^{1/2} \quad (50)$$

Where

h = altitude

a_g = speed of sound at the ground

a_a = speed of sound at the altitude of flight

V = velocity of airplane at flight altitude

Randall evidently derived the equation required for above the tropopause but did not provide its equation (ref. 6.9). A plot of the variation of the cutoff distance with Mach number for altitudes up to 65,000 feet is provided in figure 6.27.

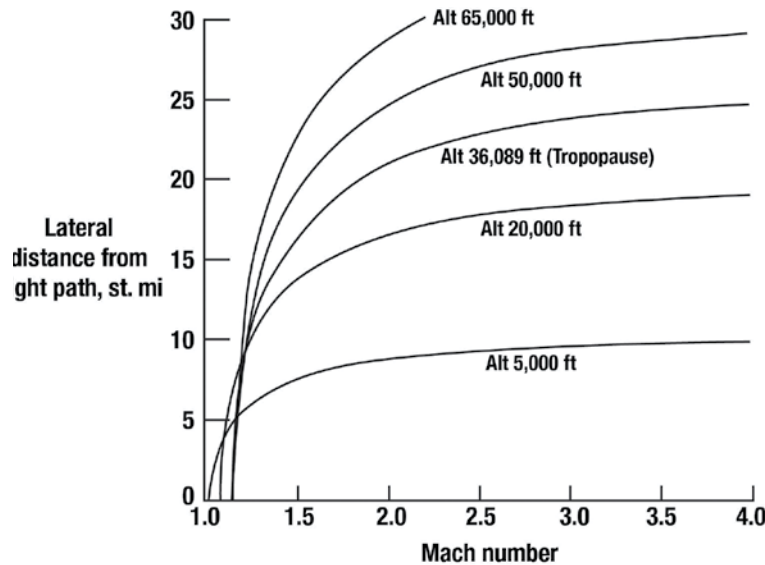


Figure 6.27. Lateral spread of sonic bangs produced by an aircraft in steady level flight, measured from flight track (adapted from ref. 6.9).

In 1964, Kane and Palmer (ref. 6.87) developed lateral cutoff equations that, for altitudes below the tropopause, are the same as Randall's equation. For altitudes above the tropopause (36,000 feet) and below 65,000 feet, reference 6.87 adds an additional term to equation (50) so that y_{max} becomes

$$y_{max} = \pm \left\{ 36,000 \left[\frac{a_g + a_{36}}{a_g - a_{36}} \right]^{1/2} + (h - 36,000) \frac{a_{36}}{(a_g^2 - a_{36}^2)^{1/2}} \right\} \left\{ \left[1 - \frac{a_g^2}{a_{36}^2 H^2} \right]^{1/2} \right\} \quad (51)$$

where a_{36} indicates the value of the speed of sound a at 36,000 feet (the tropopause) and h is the altitude above 36,000 feet. A plot of equations (50) and (51) (ref. 6.87) is given in figure 6.28. This plot contains the same type of data as in figure 6.27 but in a different format. An equation that gives the value of y_{\max} for altitudes above 65,000 feet was also provided in reference 6.87.

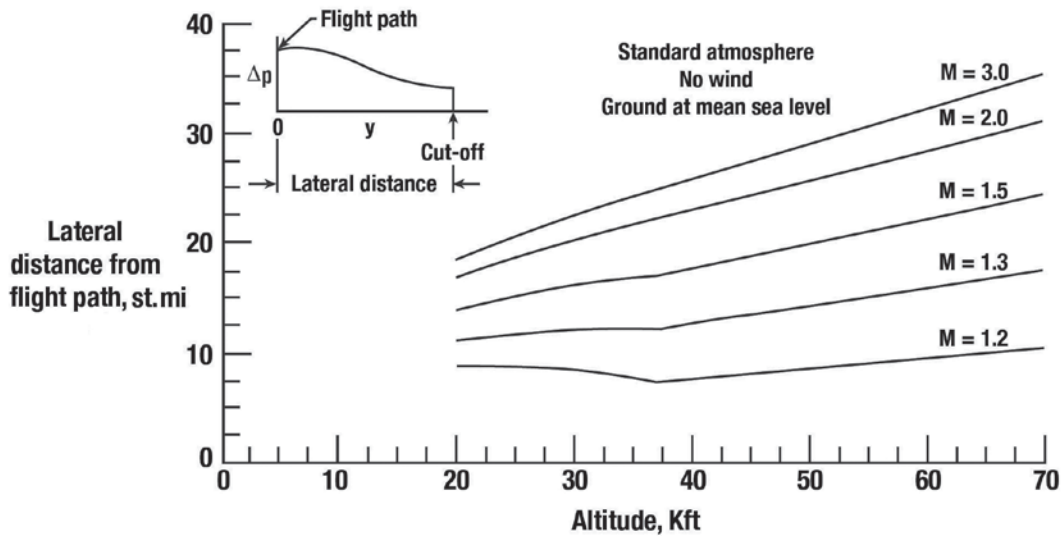


Figure 6.28. Lateral location of sonic boom cutoff in U.S. Standard Atmosphere (1962) (ref. 6.87).

In the 1960s and 1970s, special effort was taken to obtain a more accurate pressure distribution near the extremity of the shock wave pattern on the ground (refs. 6.91 and 6.92). Some sample data are shown in figures 6.29, 6.30, and 6.31. Particular emphasis was placed on the cut-off region where a grazing condition exists because of atmospheric refraction, as suggested by the ray-path sketch at the top of figure 6.29. As evident from equation (50) and (51) the lateral cut-off point is independent of aircraft type and is only a function of the aircraft altitude, the Mach number, and the characteristics of the atmosphere below the aircraft (ref. 6.9).

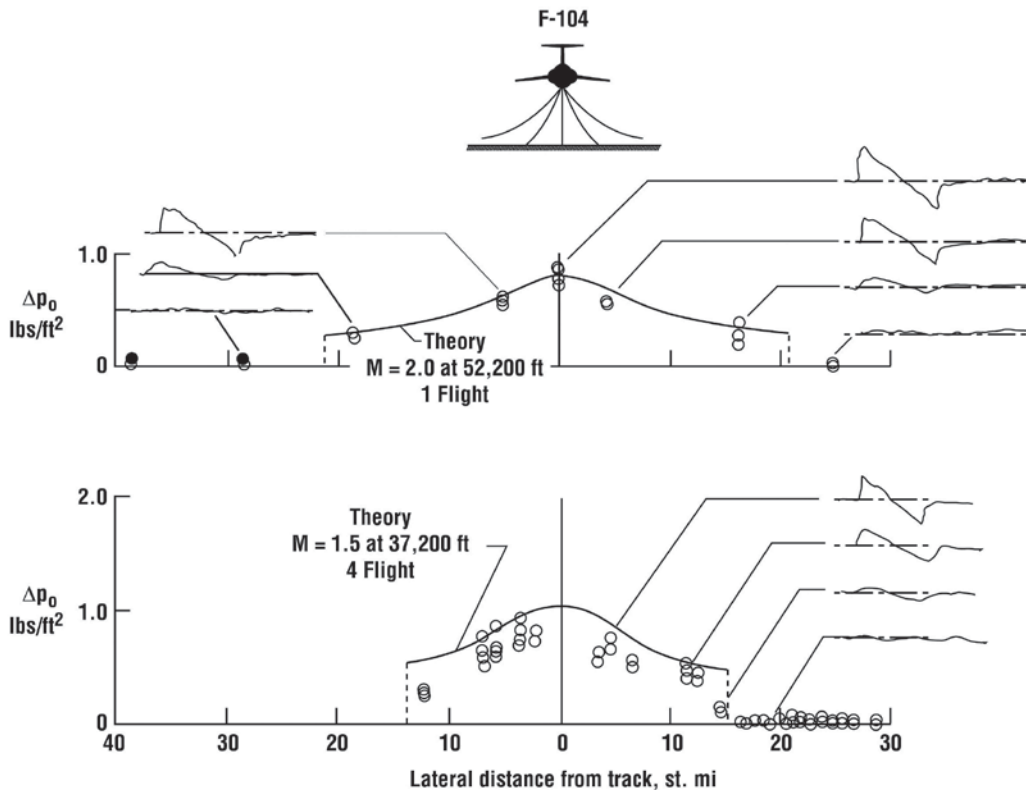


Figure 6.29. Measured lateral spread patterns for a fighter aircraft at two different altitudes (ref. 6.91).

Flights were made at altitudes of 52,200 feet and 37,200 feet and Mach numbers of 2.0 and 1.5, respectively, during quiescent atmospheric conditions and the results are compared with theory in the data plots of figure 6.29. The results from the flight at 52,200 feet and a Mach number of 2.0 show that the pressures generally decrease as lateral distance increases (solid symbols indicate that no boom was observed). The fact that measurements were obtained beyond the theoretically predicted cut-off distance led to more definitive studies at 37,200 feet and a Mach number of 1.5. These data, which were obtained from four flights involving various lateral displacement distances of the airplane from the overhead position, are similar and, in fact, beyond the predicted cut-off distance of 15 miles zero signals are indicated. Note that a figure similar to figure 6.29 was also used in the discussion of atmospheric effects in Chapter 2.

A better understanding of this phenomenon may be obtained from examination of measured waveforms taken at two different altitudes, as seen on the right hand side of figure 6.29. Sharply defined shock-wave type signatures exist generally for the region predicted by the calculations. Near the predicted lateral cutoff the rise times are noticeably longer. At distances beyond the predicted cutoff the signatures lose their identity and associated observations indicate the existence of rumbles, as previously described. These rumbles are noise that emanates from the extremity of the shock wave beyond the cutoff as it propagates through the air in the vicinity of the measuring stations.

Data similar to those shown in figure 6.29 were obtained on a large supersonic aircraft, the XB-70, at two altitudes and Mach numbers, and are presented in figure 6.30 (ref. 6.91). In figure 6.30, overpressure measurements are plotted as a function of lateral distance to each side of the ground track. The data at the top of the figure relate to four flights made at 37,000 feet and a Mach number of 1.5. The data at the bottom are taken from 13 flights at an altitude of 60,000 feet and a Mach number range of 1.8 to 2.5. The data points are coded to represent the averages of from 3 to 40 microphones as indicated on the figure. Also shown are calculated curves using the generalized theory of references 6.9, 6.21, and 6.93 for a standard atmosphere where the centerline values are determined using the latter two references. The cut-off points due to atmospheric refractions are shown as vertical dashed lines (ref. 6.9). It can be seen that the overpressures are a maximum on the track and decrease with increasing lateral distance as predicted generally by theory. The measured and calculated values of overpressure are in good agreement with the exception of the region near the lateral cutoff where the measured data falls below the theory. This discrepancy is due in part to the fact that only the areas from the Mach cutting planes for locations directly below the aircraft (symmetry plane) were utilized in the theory and lift was assumed to fall off as cosine θ .

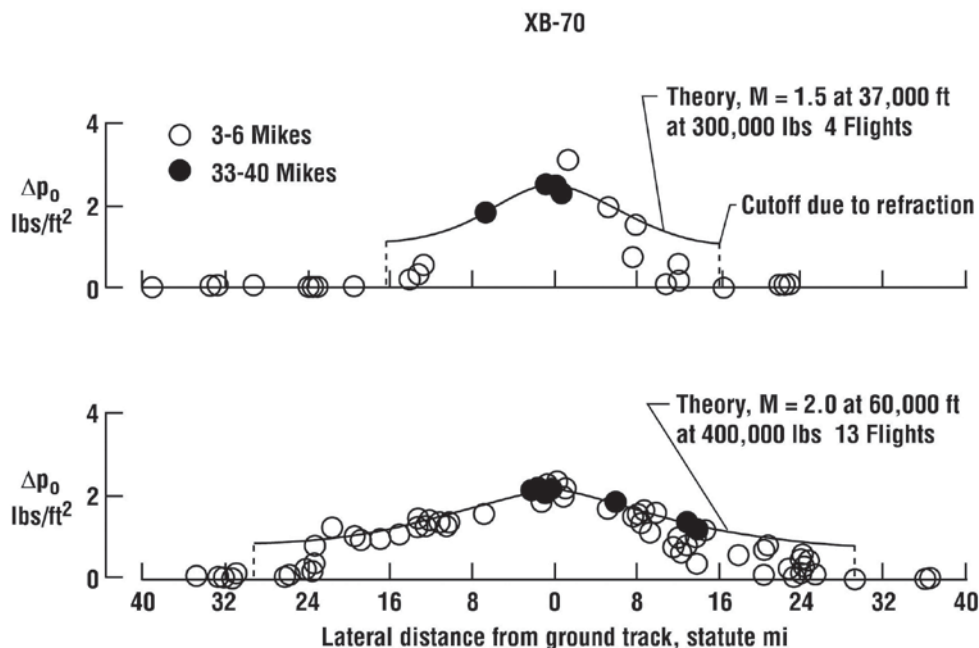


Figure 6.30. Sonic boom overpressures for the XB-70 aircraft as a function of lateral distance for two different flight conditions (ref. 6.91).

Another set of lateral spread measurements acquired for the SR-71 aircraft at altitudes from about 50,000 feet to 80,000 feet are presented on figure 6.31 (from ref. 6.94). Each symbol represents an individual mission, the solid symbols represent the average of the measurements obtained on 15 to 46 microphones and the open symbols the average of the measurements obtained from 3 to 10 microphones. The circle symbols represent data from flights made during the November 1966 to January 1967 time period for which atmospheric conditions observed to be somewhat more quiescent than those represented by the diamond symbols which were made during the June 1966 time period. Once again, overpressures are a maximum on track and decrease with increasing lateral distance, as predicted by theory (refs. 6.9 and 6.93).

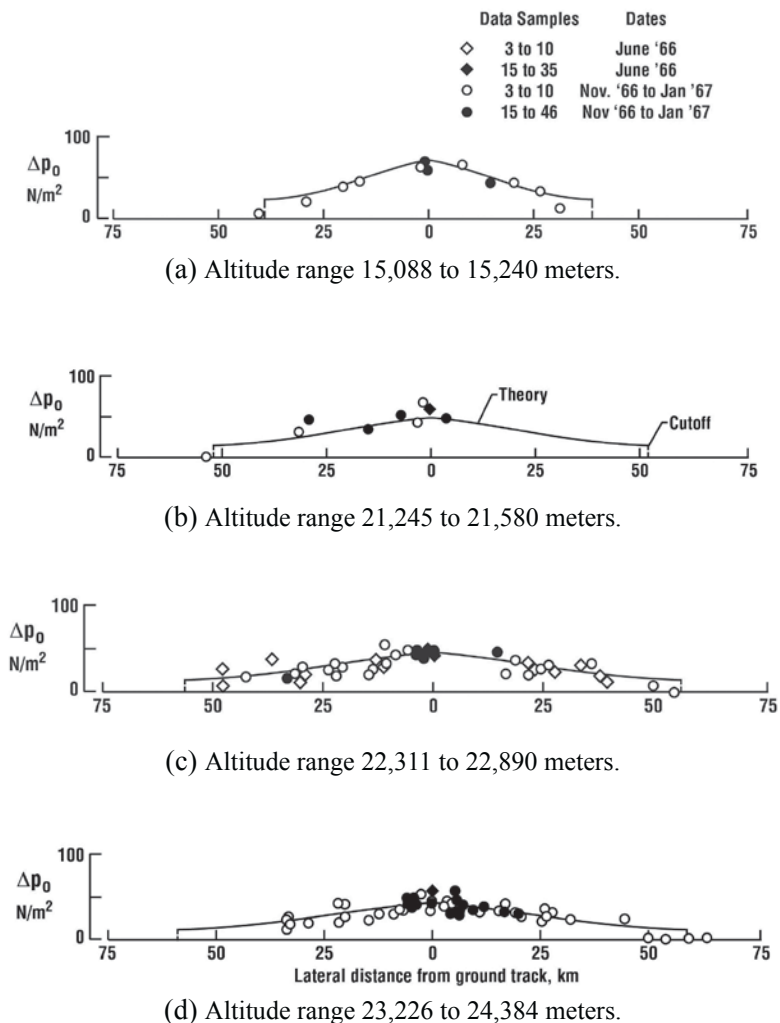


Figure 6.31. Sonic boom overpressures as a function of lateral distance for various altitude ranges for the SR-71. Mach number ranges from 1.92 to 3.0 (ref. 6.94).

Comparisons of the calculated and measured lateral extent of the sonic boom patterns as a function of aircraft altitude and Mach number for steady flight in a standard atmosphere are given in figure 6.32 (refs. 6.18 and 6.95). The data points represent averages of several measurements involving various aircraft. The width of the sonic boom carpets on the ground increase with increasing altitude and Mach number. For example, at an altitude of 20,000 feet and Mach 1.5 the total width of the pattern is about 22 nmi. At 60,000 feet and Mach 2.0 the pattern width is about 55 nmi. The two sketches at the top of the chart illustrate the fact that supersonic flights at low altitudes result in narrow carpets having higher overpressures, whereas at higher altitudes the carpet widths are much broader and the ground overpressures are lower. In this chart, good agreement exists between measured and calculated values. Note that the entire width of the ground signature is plotted in figure 6.32 and not the semi span as in figure 6.27 and 6.28. Also, nautical miles are used in figure 6.32 and statute miles in figures 6.27 and 6.28.

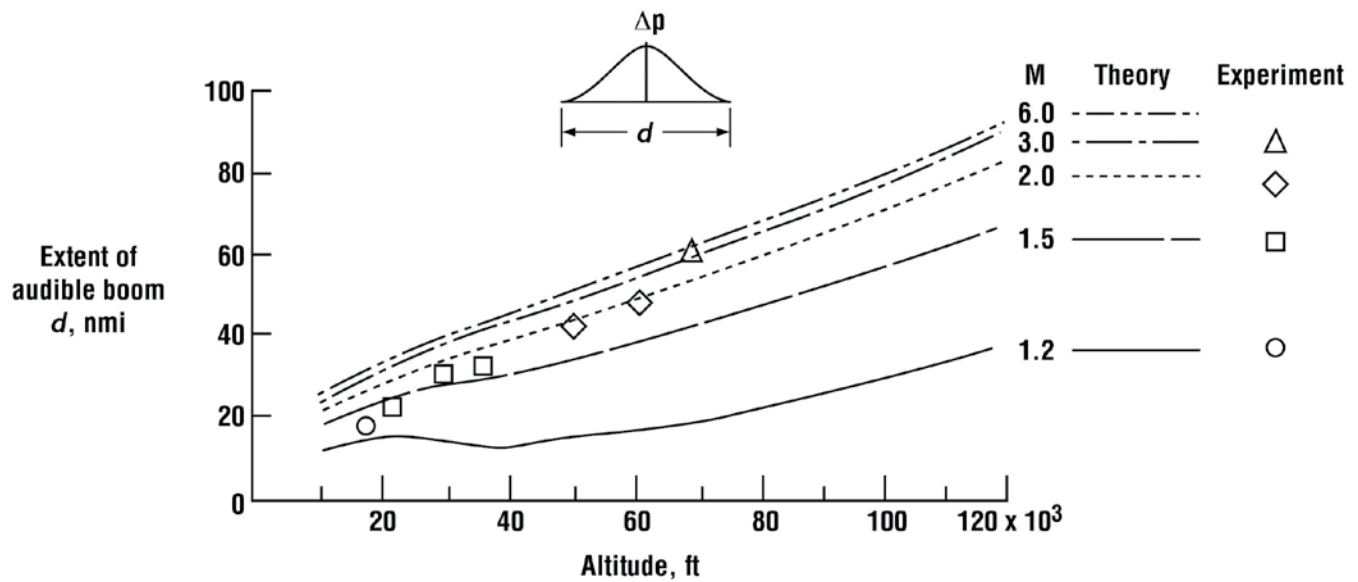


Figure 6.32. Width of primary sonic boom pattern on ground (adapted from refs. 6.18 and 6.95).

Additional discussion of the boom lateral variation and cutoff is given in Chapter 2. Included in these discussions are other works of significance regarding sonic boom beyond the lateral cutoff (in the shadow zone), including diffraction effects (refs. 6.96 through 6.99).

Hypersonic Sonic Boom Methodology

By 1970, there was an increased interest in the prediction of sonic booms at hypersonic speeds. Three-dimensional Euler or Navier-Stokes methodology was available at that time, but not the computers to run 3-D nonlinear codes, hence, analytical or empirical solutions were required. In 1970, A. Richard Seebass, while at the Boeing Scientific Research Laboratory developed a method for hypersonic strong-shock propagation based, in part, on blast wave theory. Seebass noted that an instantaneous release of energy per unit radian, E , produces a shock wave with a shock pressure rise Δp for the strong shock regime (ref. 6.100 by Sakurai)

$$\frac{\Delta p}{p_o} = \frac{2\gamma}{\gamma + 1} \left[\frac{(r/R)^{-2}}{a} + b \right] \quad (52)$$

where p_o is the ambient pressure, γ is the ratio of specific heats, r is the radial distance of the shock from the origin and effective radius

$$R = \sqrt{E/p_o} \quad (53)$$

The numerical constants a and b have the values of 0.877 and 0.989 respectively for $\gamma = 1.4$.

Realizing that for large values of r that $\Delta p \sim r^{-3/4}$, equation (52) was modified to

$$\frac{\Delta p}{p_o} = \frac{2\gamma}{\gamma + 1} \left\{ \beta \left[(1 + \alpha r^2/R^2)^{3/8} - 1 \right] \right\}^{-1} \quad (54)$$

where

$$\alpha = 16 ba/5 \quad (55)$$

and

$$\beta = 5/6b \quad (56)$$

With the above values for a , b , and for α and β , and with the effective radius R set equal to $(D/2\pi p_o)^{1/2}$ equation (54) becomes

$$\frac{\Delta p}{p_o} = 1.39 \left[\left(1 + 17.4 \frac{p_o r^2}{D} \right)^{3/8} - 1 \right]^{-1} \quad (57)$$

Since there is a great variation of the drag, D , with Mach number, Seebass found it convenient to rewrite equation (57) using

$$D = C_D \frac{1}{2} \rho V^2 \frac{\pi d^2}{4} \quad (58)$$

and with a non-dimensional area in the drag equation as the body cross section $\pi d^2/4$. Using equation (58) for drag, equation (57) becomes

$$\frac{\Delta p}{p_o} = 1.39 \left[\left(1 + \frac{31.7}{M^2 C_d} \left(\frac{r}{d} \right)^2 \right)^{3/8} - 1 \right]^{-1} \quad (59)$$

Equation (59) can also be cast in a somewhat different and more accurate form by noting that to go from a homogeneous atmosphere to an isothermal atmosphere (see ref. 6.10) the following equation applies

$$\frac{\Delta p}{p_g} = \frac{1}{\sqrt{p_g/p_o}} \left[\frac{2h \cos^2 \theta}{\pi H} \right]^{1/4} \left(\frac{\Delta p}{p_o} \right)_{p_o \text{ homogeneous}} \quad (60)$$

where θ is the angle between the normal to flight path trajectory and the vertical (see fig. 6.33). For an isothermal exponential atmosphere with $p_o/p_g = e^{-h/H}$, equation (60) becomes

$$\frac{\Delta p}{p_g} = 0.893 e^{-h/2H} (h/H)^{1/4} (\cos \theta)^{1/2} \left(\frac{\Delta p}{p_o} \right)_{p_o \text{ homogeneous}} \quad (61)$$

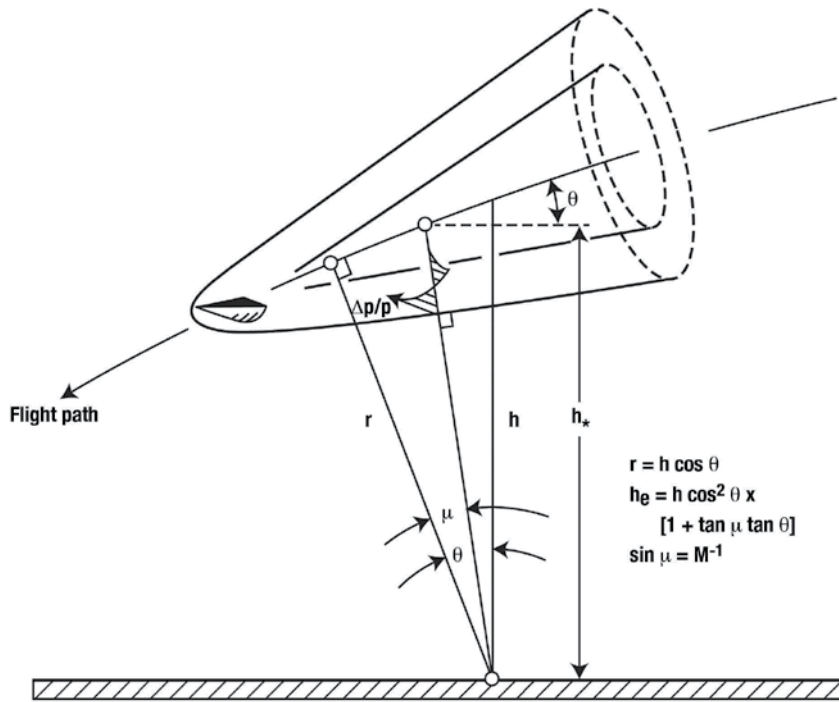


Figure 6.33. Sketch defining symbols used to analyze flight trajectory of hypersonic vehicles.

Confining one's interest in equation (57) to cases where $\frac{17.4p_0r^2}{D} \gg 1$ and where $\left(\frac{17.4p_0r^2}{D}\right)^{3/8} \gg -1$, equation (57) becomes

$$\frac{\Delta p}{p_0} = \frac{0.476D^{3/8}}{(p_0r^2)^{3/8}} \quad (62)$$

If one sets $p_0 = \frac{p_0}{p_g} p_g = e^{-h/H} p_g$ in equation (62) and inserts it in into equation (61) with r

equal to h , the atmospheric scale height $H = 25,000$ feet, $p_g = 2116$ lbs/ft², D normalized by 10^5 , and $\theta = 0$, and a ground reflection factor of 2.0, it becomes

$$\Delta p_g = \frac{3.83(D/10^5)^{3/8}}{e^{h/(8H)}(h/H)^{1/2}} \quad (63)$$

This is identical to the equation Seebass derived except for the multiplicative factor, which he set at 4.2 instead of 3.83. It is also similar to that given by Seebass and George in a later paper (ref. 6.101, p. 8). A plot of Δp as a function of h/H using Seebass' 4.2 factor is given in figure 6.34. Note that it is a drag dominated result and for an aircraft where Mach is large and Mach $\times \tau$ is the order of 1, where τ is the slenderness ratio.

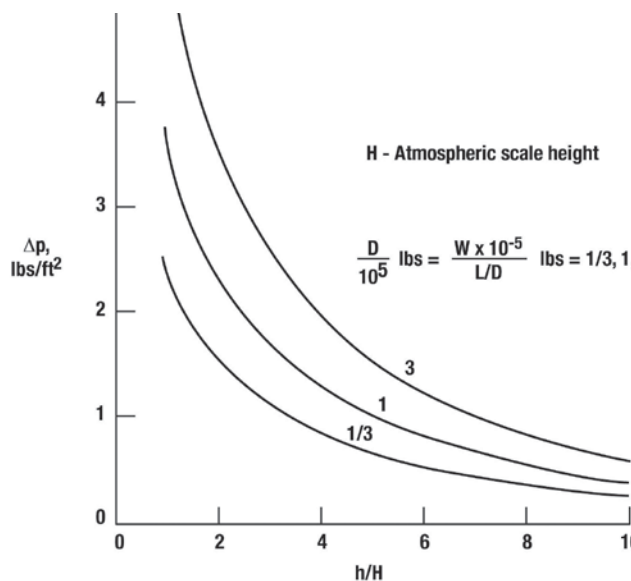


Figure 6.34. Cruise overpressure versus altitude for hypersonic vehicles (ref. 6.101).

A second version of figure 6.34 is given in reference 6.101 (p. 8) that includes plots of the impulse as well as the overpressure. A third version of this figure is contained in reference 6.18. Plotkin has added the overpressure and impulse for a nominal 400,000 pound supersonic transport (HST) at Mach 2.7 to that of reference 6.101 (see figure 6.35). It tends to make the point that a hypersonic transport may be more boom friendly than a supersonic transport (SST). However, it has been pointed out in reference 6.18 that the theory is a volume only model that does not account for vehicle lift. Almost 40 percent of the boom from an SST such as Concorde is due to lift. The drag-dominated theory implicitly assumes a short body, which results in short signature durations and correspondingly lower impulse.

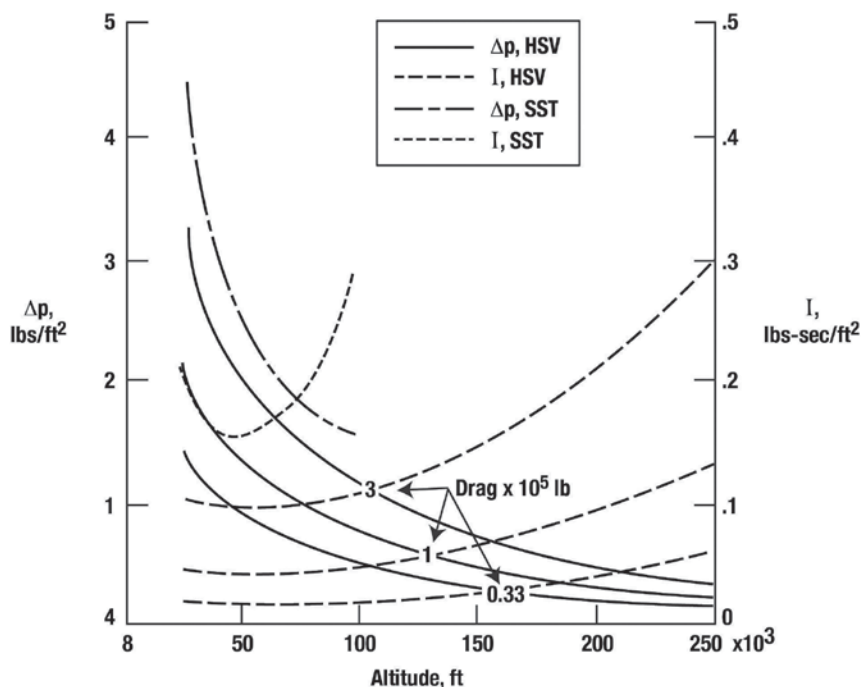


Figure 6.35. Overpressure and impulse as function of altitude for drag-dominated hypersonic vehicle. A conventional SST is shown for comparison (ref. 6.18).

M. N. Plooster, also during the 1970 time period (see ref. 6.102), investigated the shocks resulting from an instantaneous energy release along a line in a quiescent atmosphere. He utilized an empirical relationship between shock overpressure and radius suggested by Jones, Goyer, and Plooster (ref. 6.103) of the form

$$\frac{2(\gamma + 1)}{\gamma} \frac{\Delta p}{p_o} = \left\{ \alpha [1 + \beta \lambda^2]^{3/8} - 1 \right\}^{-1} \quad (64)$$

where

$$\alpha = (3/8)^{3/5} c^{8/5} \quad (65)$$

$$\beta = (8/3)^{-8/5} c^{-8/5} \quad (66)$$

$$\lambda = r/R \quad (67)$$

$$R_o = (4E_o/b\gamma p_o)^{1/2} \quad (68)$$

For air with $\gamma = 1.4$, Jones, in reference 6.104, finds $b \approx 3.94$ in the equation for R_o .

Substituting the above definitions into equation (64) yields

$$\frac{\Delta p}{p_o} = 0.291 \left\{ 0.555 c^{8/5} \left[\left(1 + 4.8 c^{-8/5} \left(\frac{r}{R_o} \right)^2 \right)^{3/8} - 1 \right] \right\}^{-1} \quad (69)$$

This equation approaches $\left(\frac{r}{R_o} \right)^{-2}$ as $\frac{r}{R_o} \rightarrow 0$ and for large $\frac{r}{R_o}$ it approaches $[(r/R_o)^{-3/4}]$,

for the strong and weak shock solutions, respectively.

With $E_o = D$, R_o becomes $0.85156 (D/p_o)^{1/2}$ and equation (69) can now be written as

$$\frac{\Delta p}{p_o} = 0.291 \left\{ 0.555 c^{8/5} \left[\left(1 + 6.62 c^{-8/5} \frac{r^2}{D} p_o \right)^{3/8} - 1 \right] \right\}^{-1} \quad (70)$$

Setting

$$\frac{D}{p_o} = C_D M^2 \frac{\gamma \pi}{8} d^2 \quad (71)$$

equation (69) can be recast as

$$\frac{\Delta p}{p_o} = 0.291 \left\{ 0.555 c^{8/5} \left[\left(1 + 12 c^{-8/5} \frac{r^2/d^2}{C_D M^2} \right)^{3/8} - 1 \right] \right\}^{-1} \quad (72)$$

Thus, for a homogeneous atmosphere and large r/d

$$\frac{\Delta p}{p_o} \sim \frac{1}{[r/d]^{3/4}} \quad (73)$$

For $\frac{12c^{-8/5} r^2/d^2}{C_D M^2} \gg 1$ and $\left(\frac{12c^{-8/5} r^2/d^2}{C_D M^2} \right)^{3/8} \gg -1$ equation (72) can be simplified to

$$\frac{\Delta p}{p_o} = \frac{0.206 M^{3/4} (C_D)^{3/8}}{c(r/d)^{3/4}} \quad (74)$$

Jones, Goyer, and Plooster (ref. 6.103) assumed $c \sim 1$. However, to agree with the results of Pan and Sotomayer (ref. 6.105) and Tiegerman (ref. 6.106), c should be 0.844 and to agree with Seebass equal to 0.545. In reference 6.102, Plooster noted that equation (64) could better approximate the strong shock solution at small radii by including a δ^{-1} factor in the definition of β . This accounts for the efficiency that the system utilizes the input energy (to produce shock waves) at substantially less than 100 percent efficiency.

Consequently, the equation for β is

$$\beta = (8/3)^{8/5} \frac{c^{-8/5}}{\delta} \quad (75)$$

With a value of c of 0.95 and $\delta = 2.62$, equation (68) for $\Delta p/p_o$ with the above modification, becomes

$$\frac{\Delta p}{p_o} = 0.57 \left[(1 + 1.99 \lambda^2)^{3/8} - 1 \right]^{-1} \quad (76)$$

and is plotted and compared to data from three primacord tests in figure 6.36. As evident from the figure, the modified Δp equation gives a very accurate representation of the experimental results.

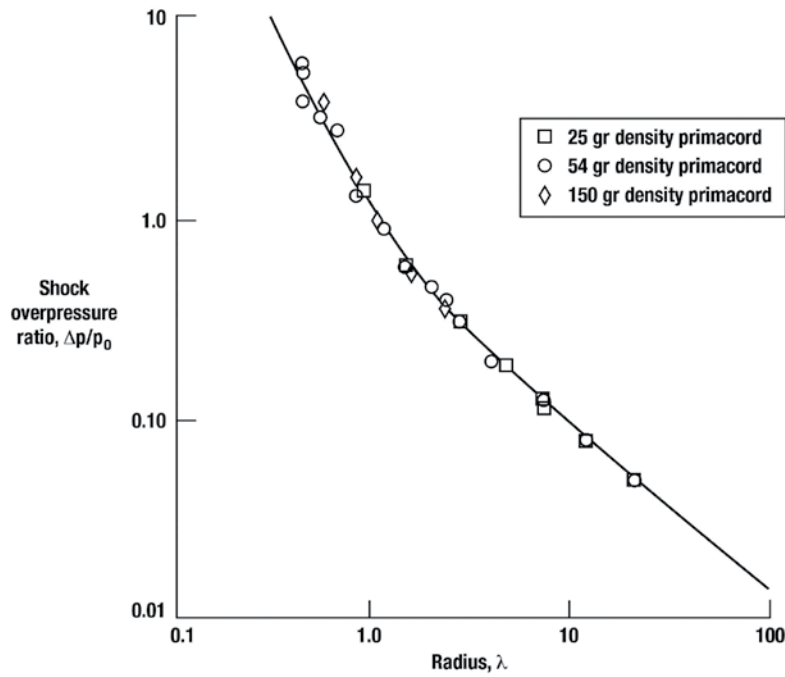


Figure 6.36. Radial dependence of shock wave overpressure from detonation of long charges of high explosive (Primacord). The curve through the data points is from equation (75) (ref. 6.102).

Using the definitions of λ and R_o , given by equations (67) and (68), equation (76) may be written in terms of more physical quantities as

$$\frac{\Delta p}{p_o} = 0.57 \left[\left(1 + 5 \frac{(r/d)^2}{C_D M^2} \right)^{3/8} - 1 \right]^{-1} \quad (77)$$

If it assumed that $5 \frac{(r/d)^2}{C_D M^2} \gg 1$ and $\left(5 \frac{(r/d)^2}{C_D M^2} \right)^{3/8} \gg -1$

Equation (77) becomes

$$\frac{\Delta p}{p_o} = 0.312 \frac{M^{3/4} (C_D)^{3/8}}{(r/d)^{3/4}} \quad (78)$$

for a homogeneous atmosphere.

For an isothermal atmosphere, equation (78) is substituted in equation (60) and with C_D replaced by its definition from equation (58) for large r ($r = h$), it becomes

$$\Delta p_g = \frac{3.16(D/10^5)^{3/8}}{(h/H)^{1/2} e^{h/(8H)}} \quad (79)$$

with $H = 25,000$ feet, $p_g = 2116$ lbs/ft², $\theta = 90^\circ$ and a ground reflection factor of 2.0. Equation (79) is identical to equation (63) of Seebass, except for the multiplicative factor.

Pan and Sotomayer (ref. 6.105) presented the results of an approximate method, based on hypersonic small disturbance theory, for calculating the sonic boom strength $\left(\frac{\Delta p}{p_o}\right)_s$, normalized position τ and positive phase duration l_x . The equations they gave for these quantities are

$$\left(\Delta p/p_o\right) = 0.343[\lambda(\lambda^{1/2} - 0.908)]^{-1/2} \quad (80)$$

$$\tau = \lambda - 0.160 - 0.588(\lambda^{1/2} - 0.908)^{1/2} \quad (81)$$

$$l_x = 0.588M(\lambda^{1/2} - 0.908)^{1/2} \quad (82)$$

where

$$\tau = (C_o t)/R_o = \frac{x_s}{MR_o} \quad (83)$$

$$\lambda = r/R_o \quad (84)$$

and

$$l_x = L_x/R_o \quad (85)$$

with C_o being the speed of sound of the undisturbed flow, R_o being a characteristic radius $(E/b\gamma p_o)^{1/2}$, E being the energy released per unit length of the line source, and $b = 0.985$ for air with $\gamma = 1.4$. Note that equation (80), for $\Delta p/p_o$, has a different form from Plooster's equation (64) and Seebass' equation (54). With the above definitions and setting

$$R_o = \left(\frac{E}{b\gamma p_o}\right)^{1/2} = \left(\frac{D}{b\gamma p_o}\right)^{1/2} = \left(\frac{\pi C_D}{8} \frac{C_D}{b} M^2 d^2\right)^{1/2} \quad (86)$$

or

$$R_o = 0.63(C_D)^{1/2} M d \quad (87)$$

equations (80), (81), and (82) can be written as

$$\frac{\Delta p}{p_o} = 0.243 \left(\frac{M \sqrt{C_D}}{r/d} \right)^{1/2} \left[\frac{\sqrt{r/d}}{M^{1/2} C_D^{1/4}} - 0.721 \right]^{-1/2} \quad (88)$$

$$\frac{x_s/d}{M^2 \sqrt{C_D}} = \frac{r/d}{M^2 \sqrt{C_D}} - 0.101 - 0.416 \left(\frac{\sqrt{r/d}}{\sqrt{M} (C_D)^{1/4}} - 0.721 \right)^{1/2} \quad (89)$$

$$\frac{L_x/d}{M^2 \sqrt{C_D}} = 0.416 \left(\frac{\sqrt{r/d}}{\sqrt{M} (C_D)^{1/4}} - 0.721 \right)^{1/2} \quad (90)$$

Note that the 0.243 factor in equation (88) is at variance with the factor used in reference 6.106, which has it as 0.306, but is consistent with equation (80) and the definition of R_o . The 0.306 factor was required by Pan and Sotomayer (ref. 6.105) to make it compatible with the Plooster data (fig. 6.36) for a $\Delta p/p_o = 0.1$, i.e., so that at

$$\frac{r/d}{M \sqrt{C_D}} = 5.628 \text{ (or } \lambda = 8.933), \frac{\Delta p}{p_o} \text{ equals } 0.1. \text{ Thus,}$$

$$\frac{\Delta p}{p_o} = 0.306 \left(\frac{M \sqrt{C_D}}{r/d} \right)^{1/2} \left[\frac{\sqrt{r/d}}{M^{1/2} C_D^{1/4}} - 0.721 \right]^{-1/2} \quad (91)$$

Also, note that the 0.343 factor in equation (80) must be increased to 0.433 to be consistent with equation (91).

A plot of $\Delta p/p_o$ from equation (91) along with those of Seebass (equation (59)) and Plooster's (equation (77)) is given in figure 6.37.

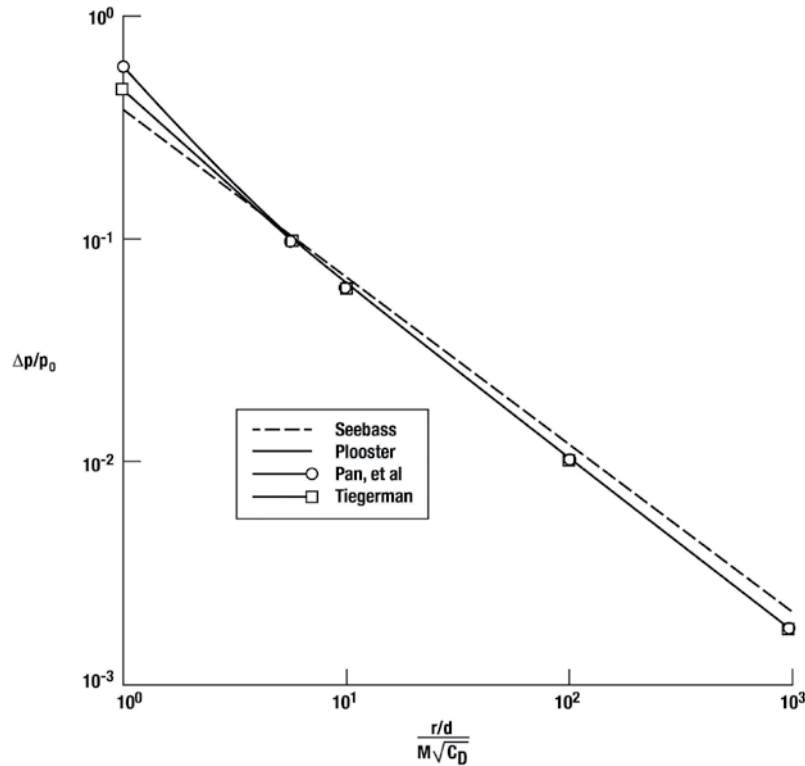


Figure 6.37. Variation of $\Delta p/p_0$ with $r/d/M\sqrt{C_D}$.

In 1975, Tiegerman's thesis entitled "Sonic Booms of Drag Dominated Hypersonic Vehicles" (ref. 6.106) was published. This thesis, which built on Seebass's formulation, contains the background and development of the hypersonic far-field theory for sonic booms. Like the earlier investigations, it relies on similar length and time scales. The equation for $\Delta p/p_0$ for a homogeneous atmosphere that Tiegerman derived is

$$\frac{\Delta p}{p_0} = \frac{A_1}{\bar{R}} [\sqrt{\bar{R}} - A_2]^{1/2} \quad (92)$$

where $A_1 = 0.6079$ and \bar{R} is given by

$$\bar{R} = \frac{r}{\sqrt{D/(2\pi p_0)}} \quad (93)$$

and with

$$\frac{D}{2\pi p_0} = \frac{C_D M^2 \gamma d^2}{16} \quad (94)$$

\bar{R} can be recast as

$$\bar{R} = \frac{3.38 r/d}{M\sqrt{C_D}} \quad (95)$$

Using this definition, equation (92) for $\Delta p/p_o$ becomes

$$\frac{\Delta p}{p_1} = 0.244 \frac{M\sqrt{C_D}}{r/d} \left[\frac{\sqrt{r/d}}{\sqrt{M}(C_D)^{1/4}} - \frac{A_2}{1.8386} \right]^{1/2} \quad (96)$$

The value of A_2 was given as -0.55 when second order terms were included. However, reference 6.106 also states that it should be positive, so its value was never conclusively established although it was discussed in some detail.

If $\frac{\sqrt{r/d}}{\sqrt{M}(C_D)^{1/4}} \gg \frac{A_2}{1.8386}$, then

$$\frac{\Delta p}{p_o} = 0.244 \frac{M^{3/4}(C_D)^{3/8}}{(r/d)^{3/4}} \quad (97)$$

showing again the $(r/d)^{-3/4}$ behavior in the far field for a homogeneous atmosphere. A second and interesting form of equation (92) can be developed for the case where $\sqrt{\bar{R}} \gg A_2$,

$$\frac{\Delta p}{p_1} = \frac{A_1}{(\bar{R})^{3/4}} \quad (98)$$

using equation (93) for \bar{R} equation (98) for $\Delta p/p_o$ becomes

$$\frac{\Delta p}{p_o} = \frac{0.3052(D)^{3/8}}{r^{3/4}(p_o)^{3/8}} \quad (99)$$

With Seebass' equation (60), the homogeneous atmosphere equation above for $\Delta p/p_o$ can be converted to the following one for the pressure jump on the ground ($r = h$) in an isothermal atmosphere

$$\Delta p_g = \frac{2.46(D/10^5)^{3/8}}{e^{h/(8H)}(h/H)^{1/2}} \quad (100)$$

In this derivation p_g was set equal to 2116 lbs/ft², H to 25,000 feet, and a ground reflection factor of 2.0 was employed. Equation (100) is the same as that prescribed by Seebass (eq. (63)) except for the multiplicative factor, which is 2.46 versus 3.83. If the same empirical factor is used for Tiegerman's equation (96) as for Pan's equation (91), i.e., 0.306, and if A_2 is set equal to -1.8569, equation (96) becomes

$$\frac{\Delta p}{p_o} = 0.306 \frac{M\sqrt{C_D}}{r/d} \left[\frac{\sqrt{r/d}}{\sqrt{M(C_D)^{1/4}}} + 1.01 \right]^{1/2} \quad (101)$$

As for equations (77) and (91) with $\frac{r/d}{M\sqrt{C_D}} = 5.628$, equation (101) will yield a $\frac{\Delta p}{p_o}$ of 0.1.

A plot of this equation versus those of Plooster's, Pan's, and Seebass' is provided in figure 6.37 and labeled Tiegerman. As is evident from this figure, all of the Δp equations for the homogeneous atmosphere (with the empirical corrections) reduce to essentially the same result. In reference 6.106, Tiegerman also derived equations for the axial and radial lengths of the positive phase (L_x and L_r) for a homogeneous atmosphere. The equations are

$$\frac{L_x}{M\sqrt{D/(2\pi p_o)}} = \frac{L_r}{\sqrt{D/(2\pi p_o)}} = (1.042) \left[1 + \frac{B_z}{[r/\sqrt{D/2\pi p_o}]^{1/2}} \right]^{1/2} \left[\frac{r}{\sqrt{D/2\pi p_o}} \right]^{1/4} \quad (102)$$

Using

$$\frac{D}{2\pi P_o} = \frac{C_D 1/2 \rho_o V^2 S}{2\pi P_o} = \frac{C_D M^2 \gamma d^2}{16} \quad (103)$$

with the reference area defined as $\frac{\pi d^2}{4}$, equation (102) for L_x and L_r becomes

$$L_r = \frac{L_x}{M} = 0.4179 dM \sqrt{C_D} \left[\left(\frac{r/d}{\sqrt{C_D} M} \right)^{1/2} + 0.5439 B_2 \right]^{1/2} \quad (104)$$

With $B_2 = A_2$ and using the same empirical value for A_2 as for equation (101), i.e., -1.8569, equation (104) becomes

$$L_r = \frac{L_x}{M} = 0.4179 dM \sqrt{C_D} \left[\left(\frac{r/d}{\sqrt{C_D} M} \right)^{1/2} - 1.01 \right]^{1/2} \quad (105)$$

Recall that the main virtue of this empiricism (the value of A_2) was it enabled the agreement of $\Delta p/p_o$ with the data of Plooster. Except for the B_2 term, equation (104) for L_x/M is essentially the same as Pan and Sotomayer's equation (90).

Equations for an L_x and the positive phase impulse I_x for an isothermal atmosphere were also given in reference 6.106. They are listed below in a slightly different form.

$$L_x = 31.27 (D / (10^5))^{3/8} e^{3h/8H}, ft \quad (106)$$

$$I_x = 0.0345 (D / 10^5)^{3/4} e^{h/(4H)}, lb \text{ sec}/ft^2 \quad (107)$$

In deriving these formulas, H was set equal to 25,000 feet, p_g to 2116 lbs/ft² and the speed of sound a_g to 1117 ft/sec.

Tiegerman's result was recast as an effective F-function and incorporated into PCBoom (ref. 6.27) for two applications – the boom generated by high altitude under-expanded rocket plumes and the boom generated by blunt reentry bodies. This was used to very successfully predict the boom from a re-entering comet probe (ref. 6.107) with predicted and measured peak overpressures agreeing within 1 percent and arrival time within 1.25 seconds.

To date, the combinations of Euler and FPE codes have not been applied to a hypersonic case. The strong shock extrapolation procedure of reference 6.108 may prove useful in extrapolating the high amplitude sources to a radius where ray tracing codes can continue propagation to the ground. Finally, there is not an analytical method at hypersonic speeds for calculating sonic boom parameters that includes lift. The various methods documented for drag dominated vehicles have different forms, but for large radial distances reduce to essentially the same results when they are empirically matched to the Plooster data and the excellent agreement of a Tiegerman-based prediction to the measured Stardust reentry boom data (ref. 6.107).

Boom Predictions and Correlations with Experiment

Up until the late 1980s, boom prediction methodology was primarily F-function based. Near-field pressures provided by the F-function were fed into the Hayes or Thomas ray-tracing propagation codes to determine the ground pressure signatures. Since that time, the use of Euler CFD codes has been the preferred method for near-field calculations. The ingredients contained within F-function-based sonic boom prediction codes, i.e., equivalent axisymmetric-body methods, along with the CFD approach, are schematically illustrated in figure 6.38. Also indicated is the use of near-field wind-tunnel data. In this latter case, due to the lack of three-dimensional data, the calculation must proceed directly to the ray-tracing propagation code.

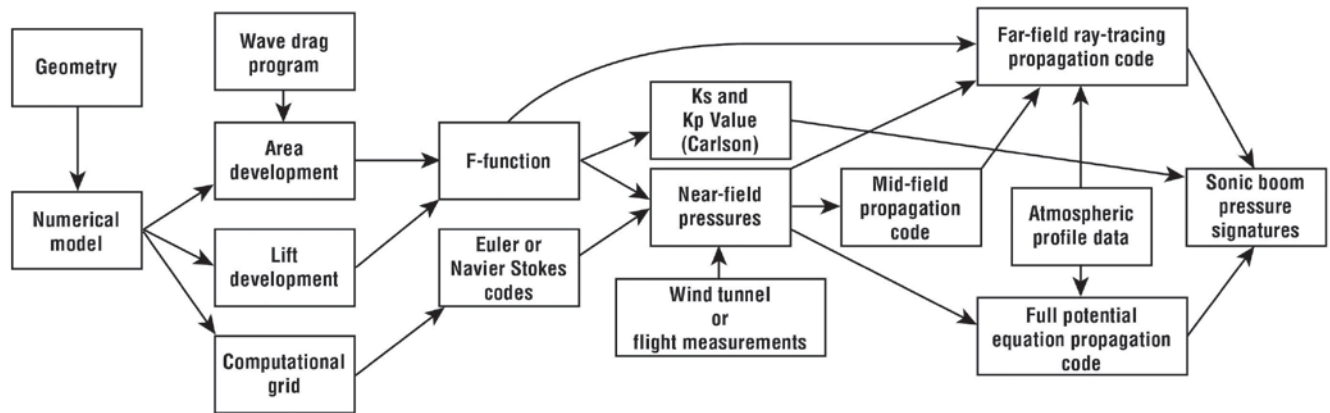


Figure 6.38. Ingredients of sonic boom prediction programs.

For the Euler or Navier-Stokes codes, a computational grid is required. Ideally, the code will have an adaptive grid capability to concentrate the grid in the vicinity of shocks, or a shock fitting routine, since shock jumps tend to smear as distance from the configuration increases (noted earlier). In most cases, Euler equation codes are used since, for vehicles at cruise conditions, viscous effects are second order. Boom predictions using this technology are included throughout subsequent sections.

The path for the F-function approach begins with the geometry of the vehicle that is converted into a numerical model. Area developments for the desired Mach number and azimuth angle are obtained through use of a computing program, which is also used in the evaluation of airplane wave drag. Lift development is also normally provided by a computer program. The resulting equivalent area distributions evolve into the Whitham F-function and then into the near-field signature. This near-field signature is then input to the atmospheric propagation program (ray-tracing) or a mid-field propagation code that better accounts for nonlinear or three-dimensional effects. The output of this latter program is then input to the ray-tracing code providing the detailed sonic boom signatures at ground level for standard or actual (non-standard) atmospheres. A third path is indicated where the K_s , K_p , and K_t factors are obtained using the Carlson methodology of reference 6.21.

The wind-tunnel path in the sonic boom prediction program was developed in order to use the near-field signatures measured on small sonic boom models. These models, in themselves, provide the same inputs as the primary path (geometry, volume, lift, etc.). This alternate path is particularly valuable when sonic boom information is required for non-standard configurations, for vehicles operating at extreme conditions, and particularly at relatively high Mach numbers.

It should be noted that the most frequently used sonic boom prediction method in use today has been developed and improved upon over several decades. The basic Whitham (ref. 6.3) method has been enhanced by the works of many individuals, including Carlson (ref. 6.21), Hayes (ref. 6.23), Thomas (ref. 6.26), and Plotkin (ref. 6.54). Application of computer programs by the authors to essentially all classes of vehicles for both steady and non-uniform flight operations in standard or non-standard atmosphere has provided good correlation with actual measured signatures.

Correlation of Boom Predictions for Aircraft

A considerable amount of theory/experiment correlations work has been done using flight-test data. The bulk of the signatures measured in the usual flight-test programs display some form of deviation from nominal or average signatures as a result of atmospheric disturbances (discussed in Chapter 2). However, complete sets of relatively disturbance-free signatures have been obtained by some programs in which a deliberate attempt was made to minimize these factors by selection of test site, season, and time of day.

An interesting set of signatures for the 55-foot long Lockheed F-104 Starfighter supersonic jet fighter is shown in figure 6.39 (ref. 6.109). Note the wide variety of altitudes and Mach numbers at which the various flight tests were conducted. For the on the deck flight at 60 feet ($h/l \sim 1$), the signature is very complex and the overpressure is of the order of 100 lbs/ft². Except for the bow shock (where the measured peak overpressure at the bow shock was clipped when the measurement system was over-driven), the signature shape is well represented by the theory. It is also evident that the signature approaches a simple N-wave as altitude (and h/l) is increased. At 48,000 feet ($h/l \sim 873$) an N-wave has formed and the overpressure is less than 1 lb/ft². The agreement of theory and experiment is good except in the vicinity of the tail wave, where the predicted signature has a longer period (Δt). In the above discussion, h and l are the symbols for the respective altitude and aircraft length.

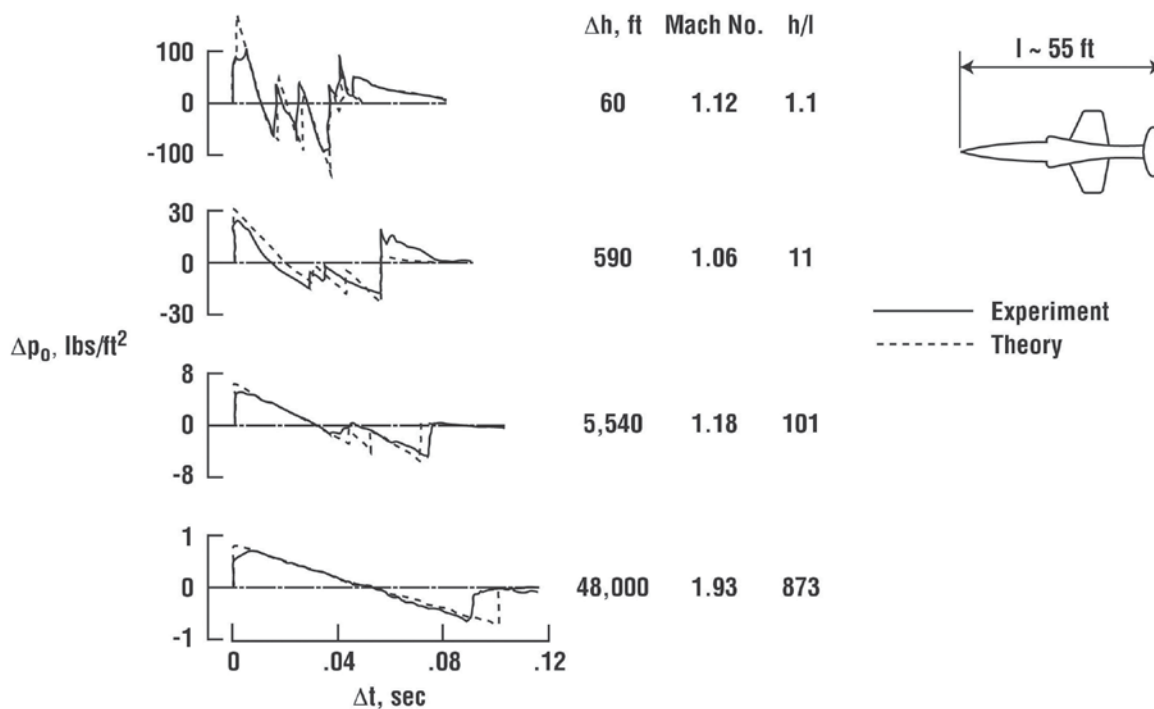


Figure 6.39. Measured and predicted sonic boom signatures for F-104 aircraft (on-track) (ref. 6.109).

Far-field ground signatures for Mach numbers near 3.0 for the XB-70 and the SR-71 were also obtained. Figure 6.40 shows an experiment/theory comparison (ref. 6.110) for the XB-70 at a Mach number of 2.84, an altitude of 70,300 feet, and a gross weight of 304,500 pounds. Data for three microphones are plotted and compared to the predicted signature. All show that the theory predicts the shock strengths very well but that the predicted signature length exceeds that of the measurement. Since the bow shock was made to line up with the experimental one, it is not clear if the difference in signature length is a front or back-end problem or simply a theory shortcoming. It is worth noting that the weight, and thus the lift, is substantial. The magnitude of the measured bow shocks range from 1.6 lbs/ft² to 1.9 lbs/ft² and the signature length is about 0.30 sec.

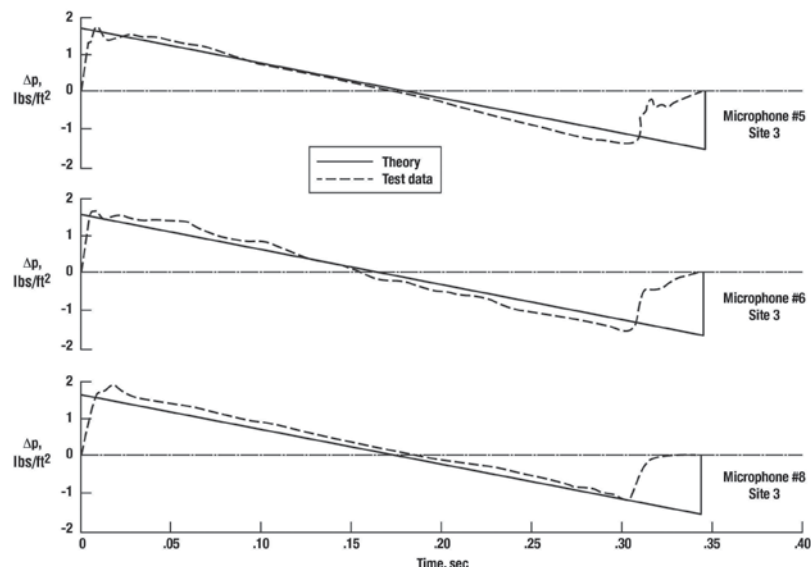


Figure 6.40. Sonic booms measured by three microphones for the XB-70-2, Mach 2.84, $h = 70,300$ feet (ref. 6.110).

There are also flight measurements for the SR-71 aircraft at a Mach number of 3.0 and an altitude of 80,000 feet (refs. 6.94 and 6.111). Figure 6.41 shows this measurement as well as those for Mach numbers of 1.35 and 2.0. All of the theoretical predictions are in agreement with experiment both for the shock jumps and the length of signature. However, the SR-71 is a smaller and lighter (80,000 to 100,000 pounds) aircraft than the XB-70 and effectively more slender at 105 feet in length. It is also noteworthy that the earlier calculations (figs. 6.29-6.31) for the wind-tunnel models were made using Whitham's F-function near-field methodology as interpreted by Carlson, McLean, and Shrout (ref. 6.93) and the flight prediction for the SR-71 was based on the F-function, plus Hayes' propagation code (ref. 6.23), calculations.

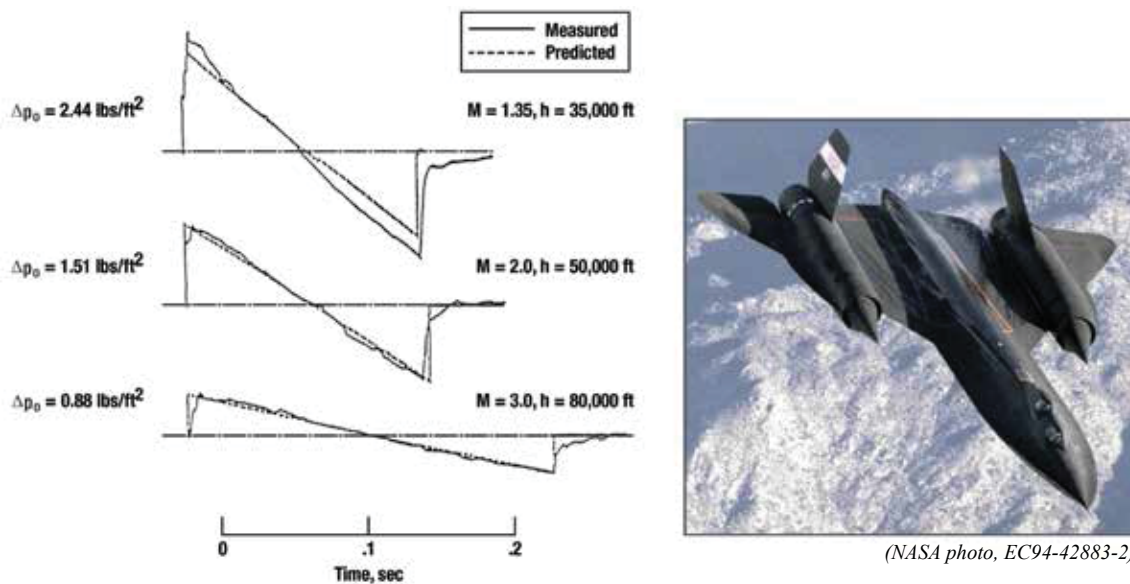


Figure 6.41 Measured and predicted sonic boom signature for the SR-71 aircraft (on-track) (adapted from ref. 6.111).

Bodies of Revolution

As Mach numbers increase beyond 3 or 4, the linear methods normally used for sonic boom predictions begin to have problems. In the near field, where nonlinear effects are most important and become increasingly so as Mach number increases, linear lifting-surface methods and Whitham's F-function methodology start to break down. With the near-field predictions becoming more inaccurate the mid- and far-field estimates also suffer. It should be noted, however, that the sharper (pointed) and more slender a configuration, the higher the Mach number and radial distance may be before these methods falter.

Some evidence of these problems can be seen in reference 6.112, which contains data for some slender bodies of varying bluntness (see fig. 6.42) for Mach numbers from 1.41 to 4.63. They are defined by simple $r \sim x^n$ equations, where the n values used are 1.0, 0.5, and 0.25 as noted by the equations on the figure. Bow-shock pressures, in the form of $\frac{\Delta p_{max}}{p} \left(\frac{h}{l}\right)^{3/4}$, and impulses for these bodies are plotted as a function of n in figures 6.43 and 6.44.

The pressure-parameter plots for Mach numbers of 2.96, 3.83, and 4.63 show fair agreement for all Mach number and n values. The impulse plot, on the other hand, shows that the predictions deteriorate with increasing Mach number and bluntness. This reflects the differences in the lengths of the positive phase of the pressure signatures. Note that all of these data are for zero angle of attack.

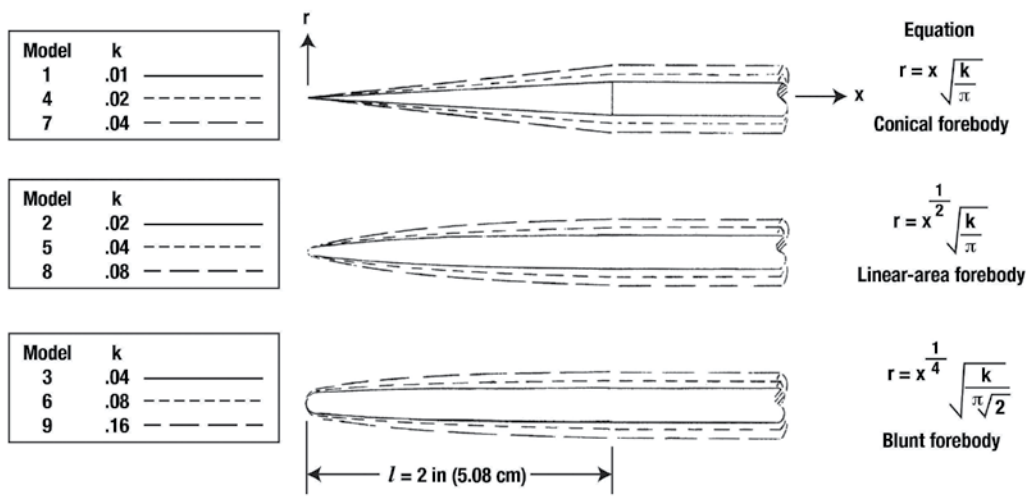


Figure 6.42. Models with equations for model radii (ref. 6.112).

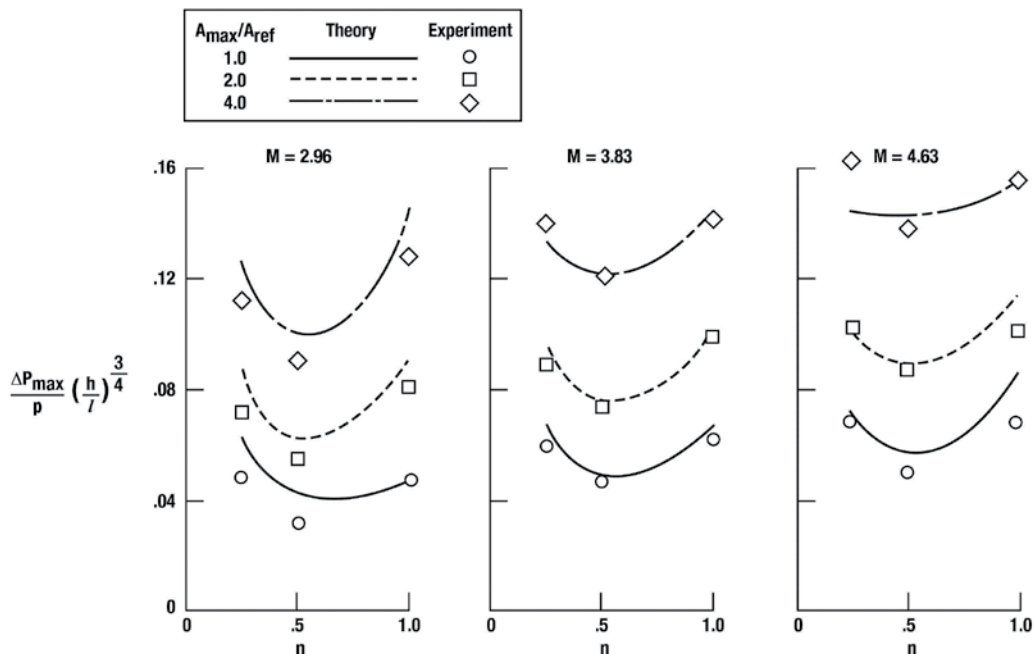


Figure 6.43. Variation of maximum overpressure parameter with bluntness parameter, $h/l = 5$ (ref. 6.112).

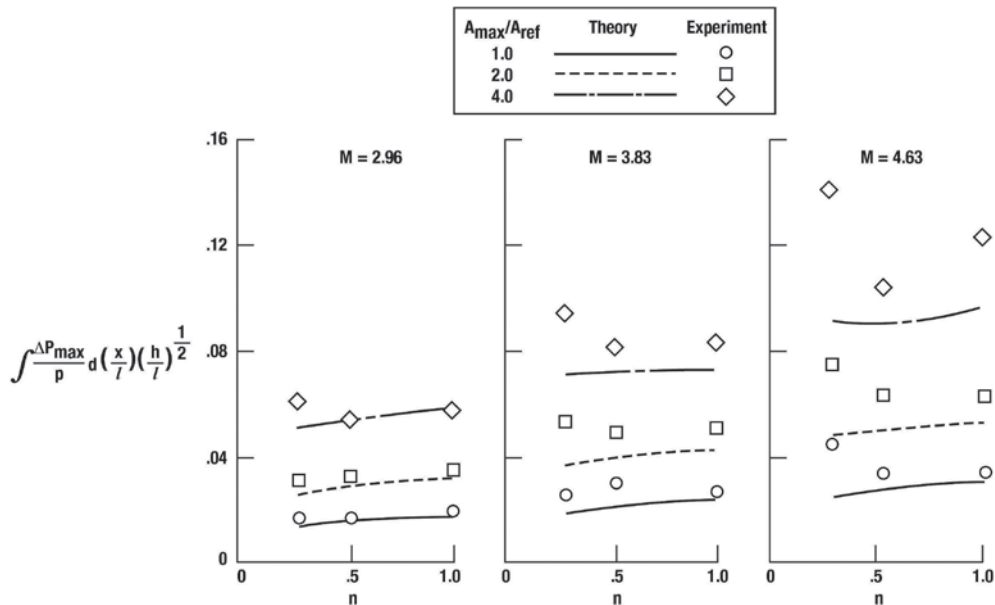


Figure 6.44. Variation of signature impulse parameter with bluntness parameter (ref. 6.112).

Whitham’s method (ref. 6.3) is used for these pressure-signature and shock-strength predictions for a smooth body. However, for a conical forebody with its sharp shoulder, the authors applied the non-smooth-body equation of Whitham (also ref. 6.3). They also looked at the effects of the effective lift and boundary layer, as shown in figure 6.45. The former is due to the asymmetric pressures on the Mach-cut planes. It is evident from the figure that the non-smooth method provided a better result in the aft regions of the signature and that the addition of the boundary layer improved the agreement of the theoretical bow-shock strength with experiment.

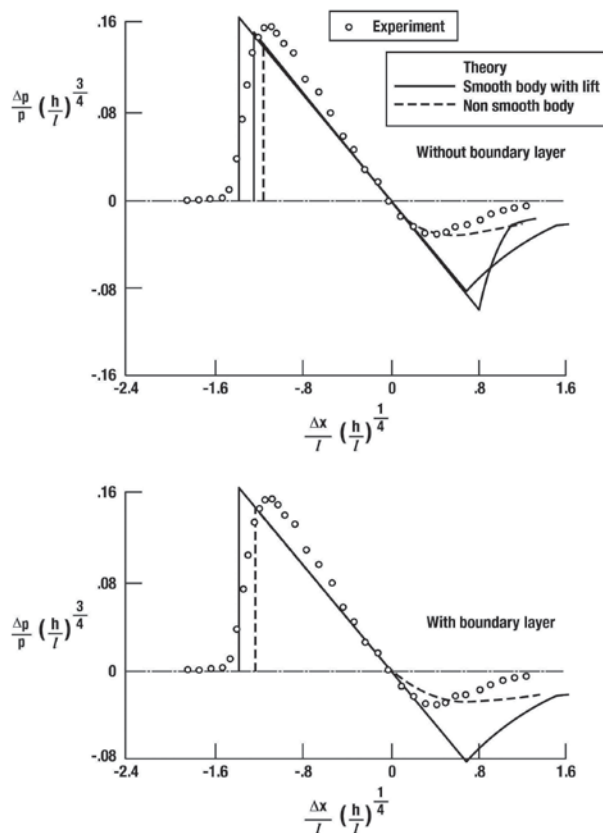


Figure 6.45. Comparison of smooth-body program with lift and non-smooth-body program, with and without boundary layer. Model 7, Mach 4.63, $h/l = 5$ (ref. 6.112).

Diamond Cross-Section, Body and Wing Body

Normally, at hypersonic Mach numbers, one expects to see the predicted impulse of signatures to be larger than those measured. This is attributed primarily to the fact that most signatures contain lift effects and lifting effects on signature length are generally not as well predicted as volume effects. Several models were tested in 1970 and reported in reference 6.113 that shed some light on this phenomenon. In this paper, flow field surveys of two configurations, shown in figure 6.46, were carried out. One configuration consisted of a body with a diamond cross-section and a leading-edge sweep of $\sim 80^\circ$ (model A), while the other configuration consisted of a body with a wing of 64.5° sweep (model B). Figures 6.47 and 6.48 give pressure distributions for these models in the form of $(\Delta p)(h/l)^{3/4}$ for three Mach numbers (2.3, 2.96, and 4.63). Data for both non-lifting and lifting attitudes is provided.

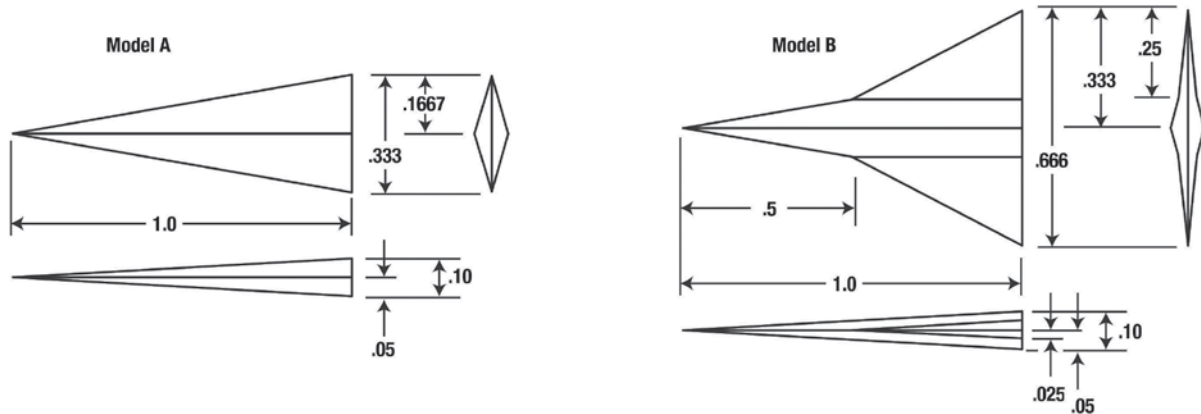


Figure 6.46. Sonic boom test models. All dimensions are non-dimensionalized with respect to model length l of 7.62 cm (3 in.) (ref. 6.113).

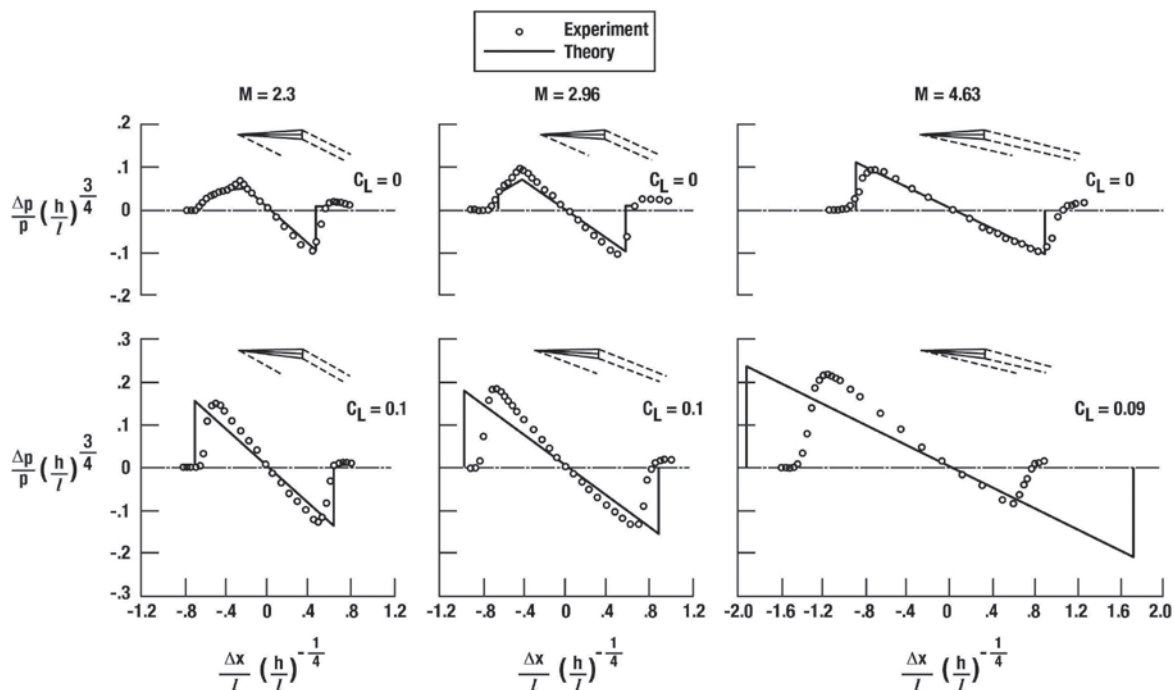


Figure 6.47. Experimental and theoretical pressure signatures for model A at selected values of M and C_L , $h/l = 4$ (ref. 6.113).

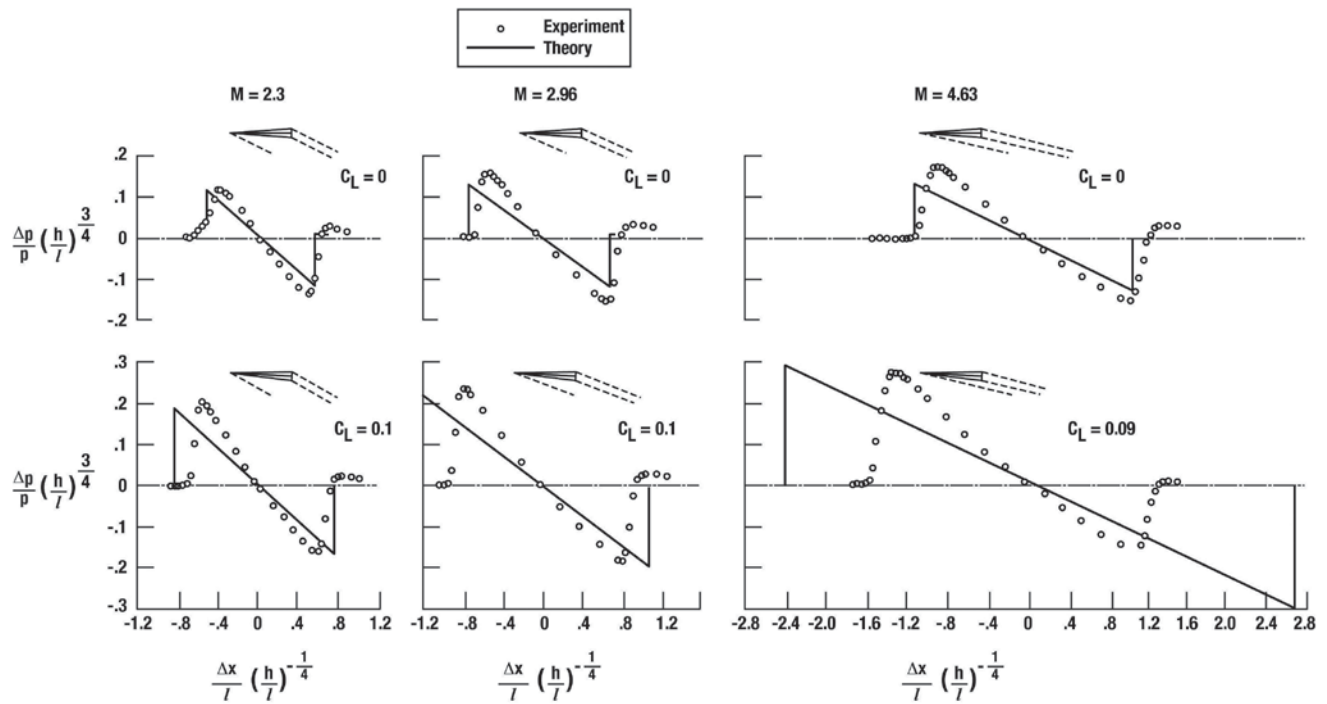


Figure 6.48. Experimental and theoretical pressure signatures for model B at selected values of M and C_L , $h/l = 4$ (ref. 6.113).

The theoretical predictions were made using Whitham's methodology as interpreted by reference 6.93. Figure 6.47 for model A shows for $C_L = 0$ that the theoretical pressures agree quite well with experiment for all three Mach numbers. At a $C_L \sim 0.1$, the magnitude of the measured and predicted pressures are still in good agreement, however, the signature-length predictions become progressively worse as Mach number increases. While the difference in signature length between the theoretical prediction and experiment for Mach numbers 2.3 and 2.96 might be minimized by accounting for viscous effects, the difference at a Mach number of 4.63 is clearly a failure of the quasi-linear method. Figure 6.48 for model B shows similar data but the predictions of the magnitude of the pressure parameter at $C_L = 0$ deteriorate as the Mach number increases from 2.3 to 4.63. Curiously, for the lifting calculation at a $C_L \sim 0.1$, the magnitude of the pressure parameter is fairly well predicted but the signature-length predictions exceed the measured ones as for model A.

Apollo Capsule

In the area of ground sonic boom measurements, there is also data for the Apollo capsule during the atmospheric entries of Apollo 15 and Apollo 16 (refs. 6.114 and 6.115). Application of the prediction methodology of reference 6.21 to these cases are shown in figure 6.49. Illustrative theory/experiment comparisons for four Mach numbers from 1.75 to 15.0 are plotted. Predictions for the magnitudes of the bow, or leading, shocks range from fair to good. Signature length estimates are generally longer than those measured. However, the effective length of the capsule due to flow separation over the after body was not accounted.

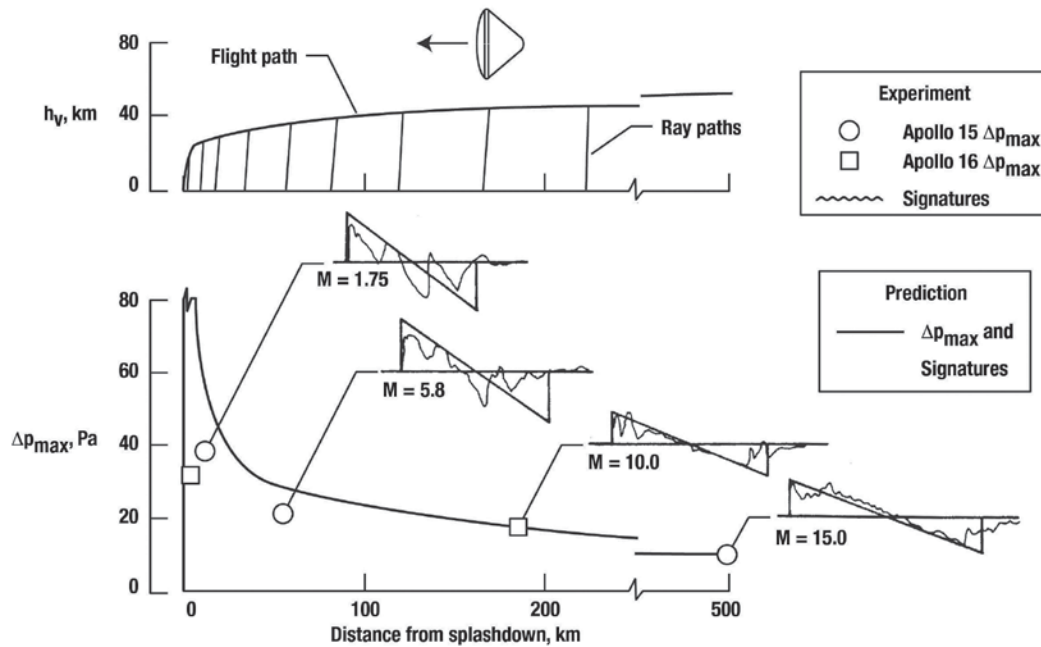


Figure 6.49. Correlation of predictions with measurements made during reentries of Apollo 15 and 16 (ref. 6.21).

Similar calculations for Apollo 15 and Apollo 16 were carried out at the Ames Research Center (ARC) during the early 1970s and documented in references 6.116 and 6.117. The wind-tunnel data was obtained on a 0.016-scale model of the Apollo 15 command module (fig. 6.50) at Mach numbers from 1.5 to 10 in the Jet Propulsion Laboratory (JPL) supersonic and hypersonic wind tunnels and were reported in reference 6.117. Data for Mach numbers of 1.16 and 4.57 and an h/l of 2.85 are shown in figure 6.51. Bank angles consistent with the flight conditions at those Mach numbers were used. The tunnel signature for Mach 1.16 was obtained by extrapolating the data of reference 6.118 from Mach 1.5. This extrapolation is justified because the signature parameters have been found to change very little between these Mach numbers. It was also necessary to interpolate between the bank angles for which data were presented in reference 6.118 to obtain the signatures shown in figure 6.51.

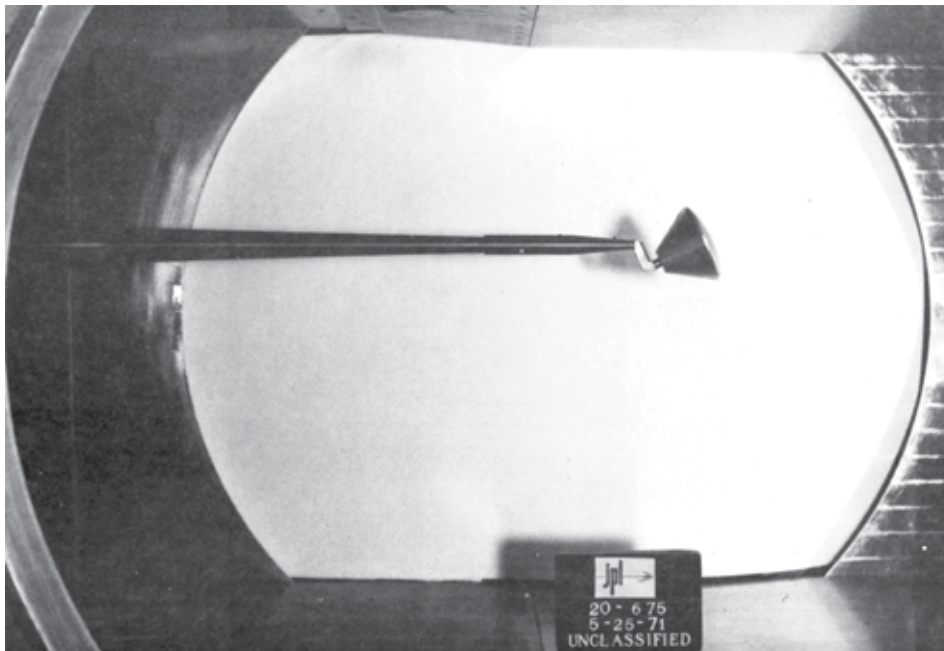


Figure 6.50. Installation photograph showing an Apollo capsule model in 20-inch Supersonic Wind Tunnel at the Jet Propulsion Laboratory (ref. 6.117).

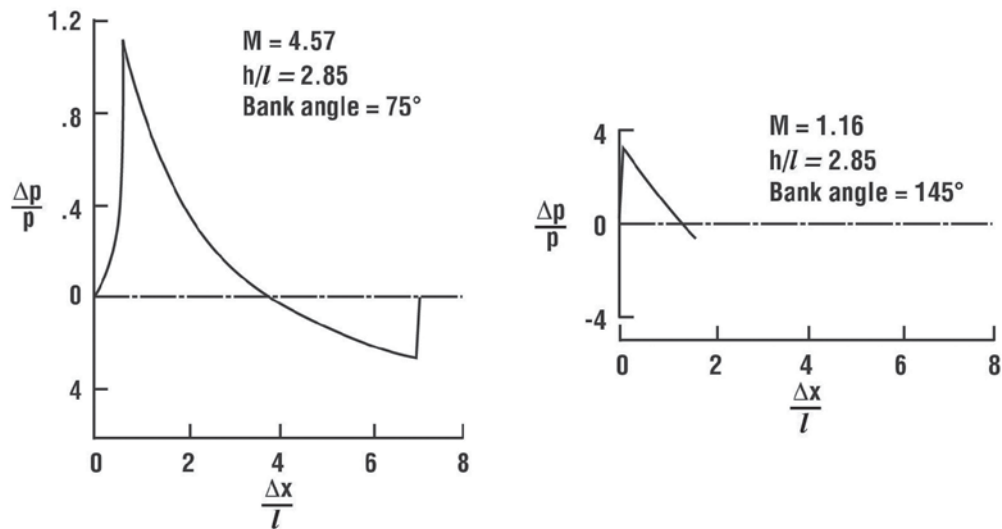
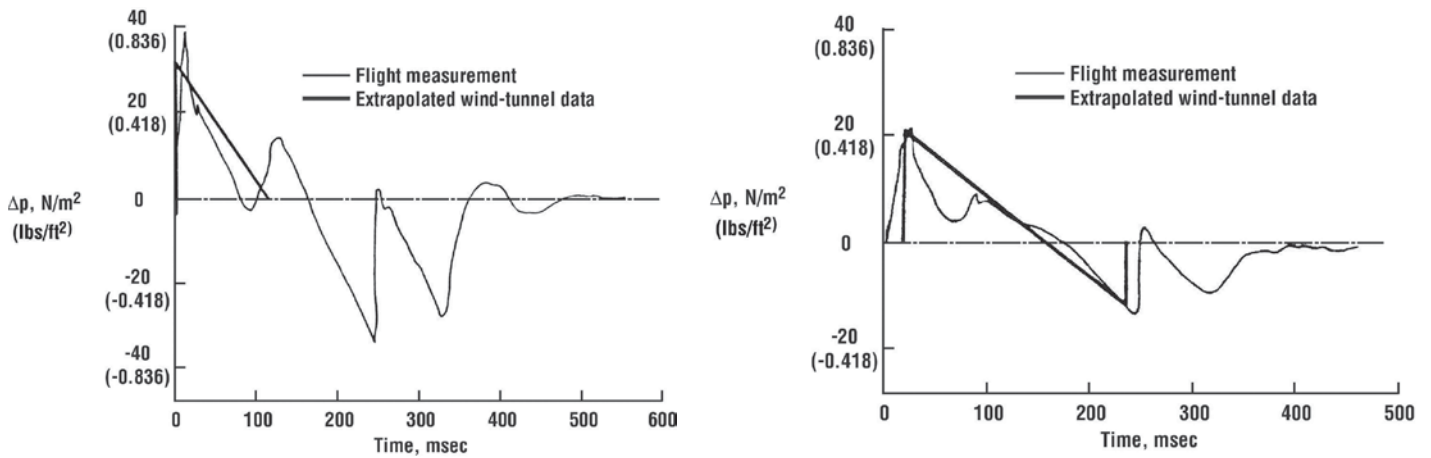


Figure 6.51. Apollo Command Module wind-tunnel pressure signatures (ref. 6.116).

Calculation of the ground overpressures required the determination of the point-of-origin on the flight path of the pressure signals received by the sensors located on two ships (USS *Kawishiwi* and USS *Okinawa*) positioned north of Hawaii. With the point-of-origin determined, the propagation methodology of Thomas (refs. 6.25 and 6.26) was utilized to calculate the ground signatures shown in figure 6.49. Comparison of the calculated pressure signatures (extrapolated from wind-tunnel data) with the measured ones shown on figures 6.52(a) for Mach 1.16 and figure 6.52(b) for Mach 4.57 indicate good agreement – similar to those shown earlier for the Carlson technique. Only the positive portion of the wind-tunnel signature has been shown at Mach 1.16, since shock-wave reflections from the floor of the wind tunnel prevented the recording of the full pressure signature at the lowest Mach number of the test described in reference 6.118. The possible effects of temperature and winds on these measurements are discussed in reference 6.116. Apollo command module wind-tunnel data is also contained in reference 6.108 along with a method for extrapolating strong shock waves.



(a) $M = 1.16$, $h = 19,580$ m (64,253 ft), $\psi = 37.6^\circ$, $\gamma = -49.36^\circ$,
 $\dot{M} = -0.0213/\text{sec}$, $\dot{\psi} = 0.94^\circ/\text{sec}$, $\dot{\gamma} = -1.75^\circ/\text{sec}$,
 bank angle = -145° , $\phi = 50^\circ$

(b) $M = 4.57$, $h = 34,450$ m (110,304 ft), $\psi = 51.3^\circ$, $\gamma = -10.1^\circ$,
 $\dot{M} = -0.0812/\text{sec}$, $\dot{\psi} = 0.4^\circ/\text{sec}$, $\dot{\gamma} = -0.3^\circ/\text{sec}$,
 bank angle = 75° , $\phi = 0^\circ$

Figure 6.52. Apollo 15 Command Module wind-tunnel in-flight correlation (ref. 6.116).

Saturn V Launch Vehicle

Booms produced by the Apollo ascent vehicles, shown schematically in figure 6.53, have also been measured and, in a few cases, have been compared to predictions. Reference 6.114 provides Apollo 15 measured signatures (see fig. 6.54) from the two ship stations shown in the schematic of figure 6.55. The first signature, measured aboard the USS *Salinan*, is for a Mach number of 6.07 and an altitude of ~209,000 feet. The second was measured aboard the USS *Austin* and is for a Mach number of 16.13 at an altitude of 586,392 feet. The Mach 6.07 measurement was for the S-1C vehicle configuration while a Mach number of 16.13 was measured for the S-11 stage. As noted, no predictions were made of the pressure signatures for these two cases. Similar data is described in reference 6.115 for the Apollo 16 mission. Ascent measurements for the flight were made at three ship stations. As in Apollo 15, no predictions were made of the pressure signatures.

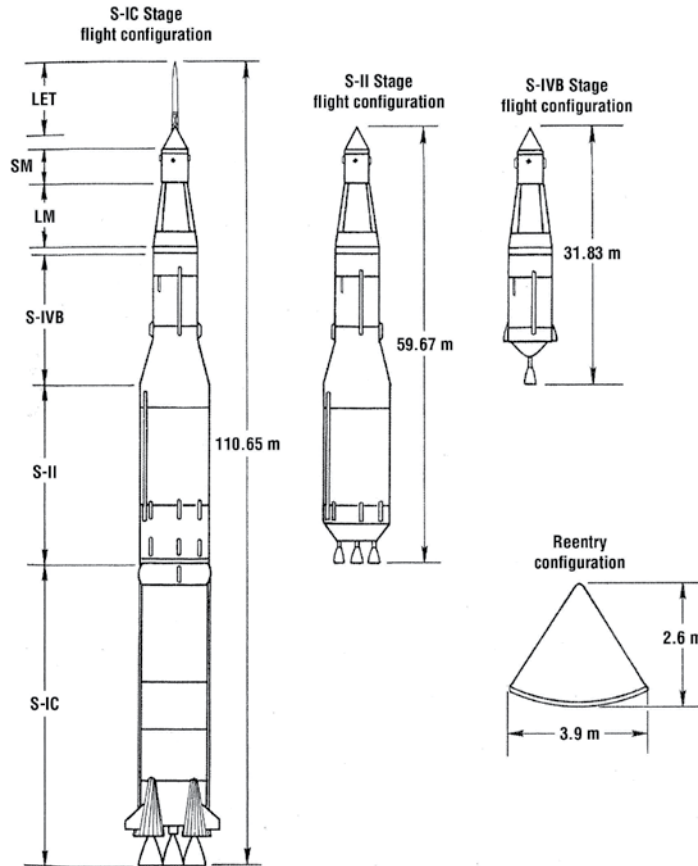
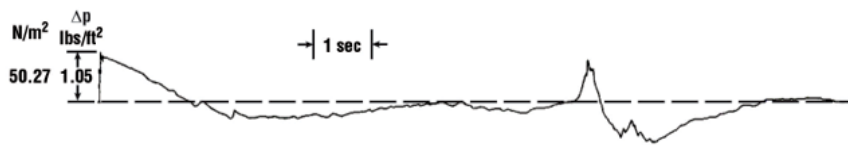


Figure 6.53. Schematic diagram of Apollo/Saturn V launch vehicle and reentry vehicle configurations (ref. 6.115).



(a) Measured on USS *Salinan*, Overhead Conditions: Velocity = 2210 m/sec and Altitude = 63,422 meters.



(b) Measured on USS *Austin*, Overhead Conditions: Velocity = 4762 m/sec and Altitude = 178,778 meters.

Figure 6.54. Measured sonic boom signatures during ascent as recorded at positions 87 km and 970 km from the launch site, along the Apollo 15 ground track (ref. 6.114).

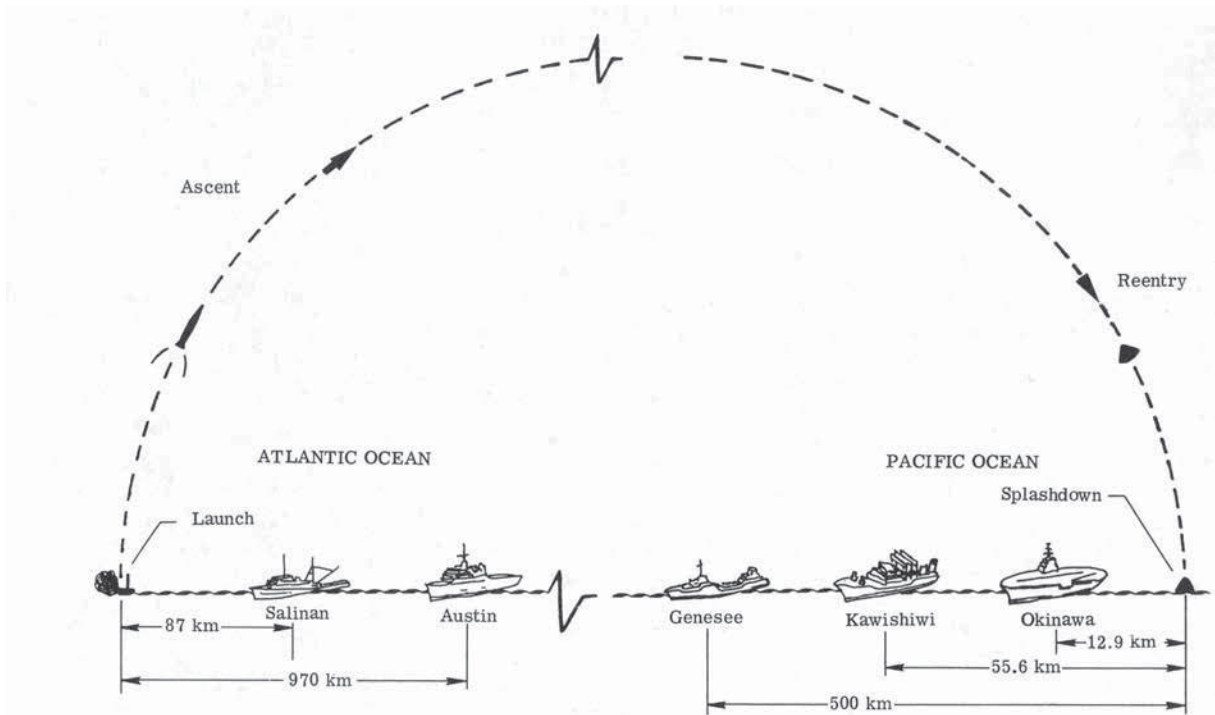


Figure 6.55. Schematic showing ship position for data acquisition during launch and reentry (ref. 6.114).

From a measurement standpoint, Apollo 17 (ref. 6.119) was more detailed than Apollo 15 and Apollo 16, having a total of six measuring stations. Figure 6.56 (ref. 6.119) shows the relative ship locations. Signatures from these six stations are given in figure 6.57 (ref. 6.119). These stations were located to lie within the focus regions associated with the flight path angle and acceleration profile of the space vehicle during ascending flight. Listed in the figure are the velocity and the altitude of the launch vehicle recorded along the flight path at the time that the initial sonic boom was generated for each of the measurement stations.

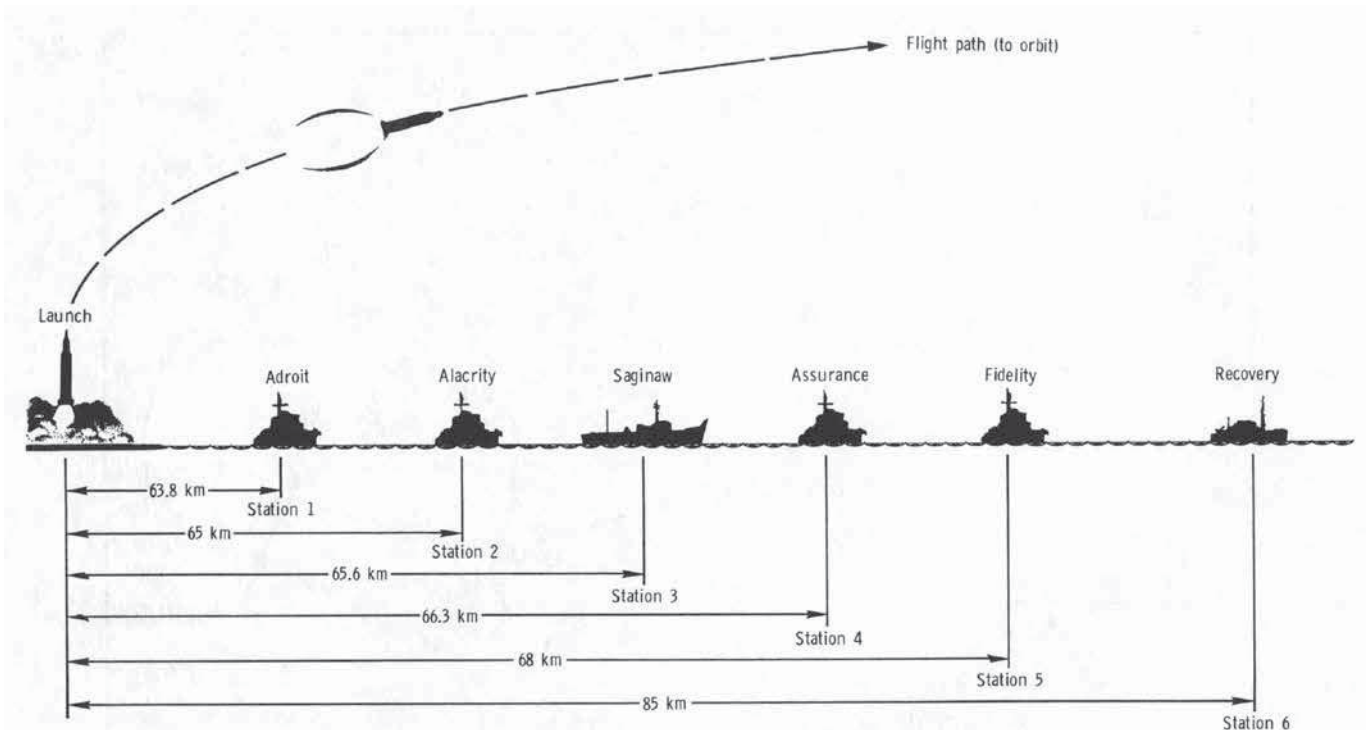


Figure 6.56. Schematic showing ship position for data acquisition during ascent (ref. 6.119).

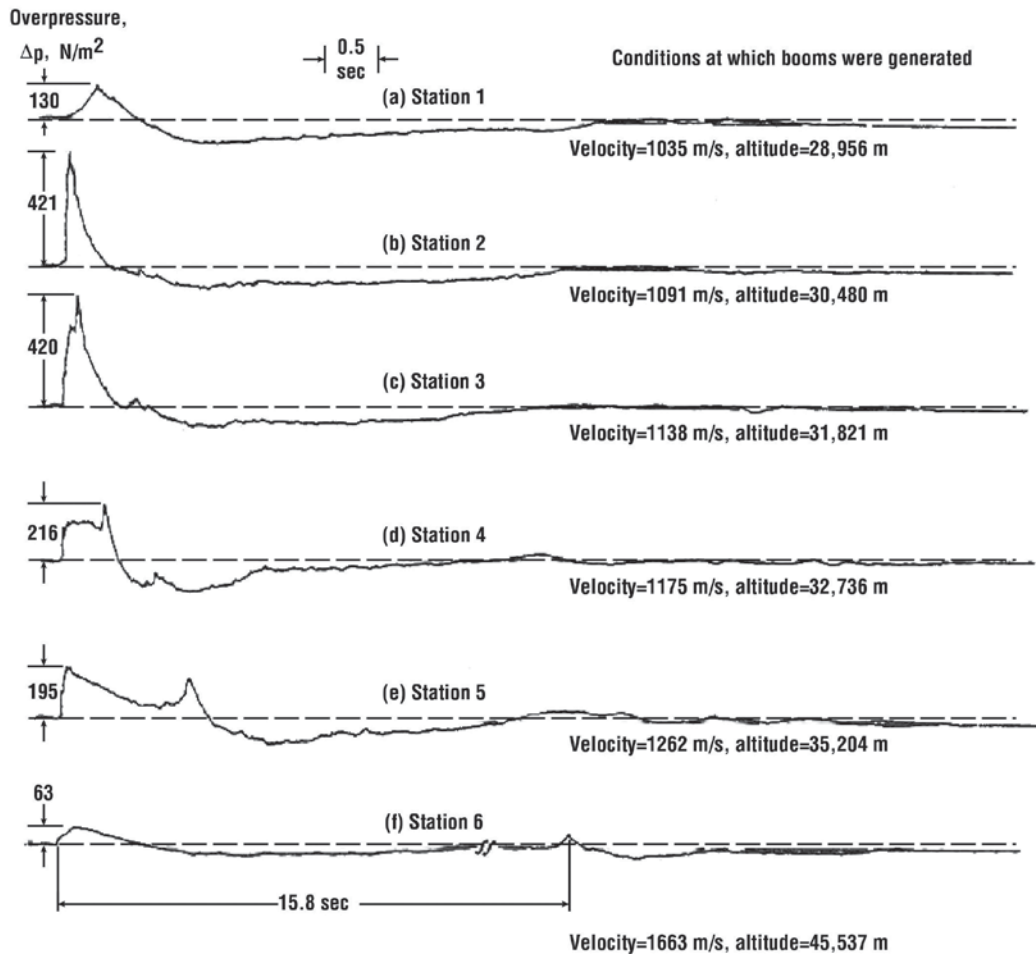


Figure 6.57. Sonic boom signatures measured during ascent of Apollo 17 as recorded at stations 1 to 6 (ref. 6.119).

In contrast to the Apollo 15 and Apollo 16 data, predictions of the shock overpressures were made and are shown in figure 6.58. This figure was taken from reference 6.119, which, in turn, was taken from reference 6.120. Clearly, the agreement is quite remarkable. No indication is given in these references of the methodology used to obtain results, but most likely they utilized the experimental data of references 6.108 and 6.121, the strong shock propagation procedures of reference 6.108 and the wave form propagation method of Thomas (refs. 6.25 and 6.26).

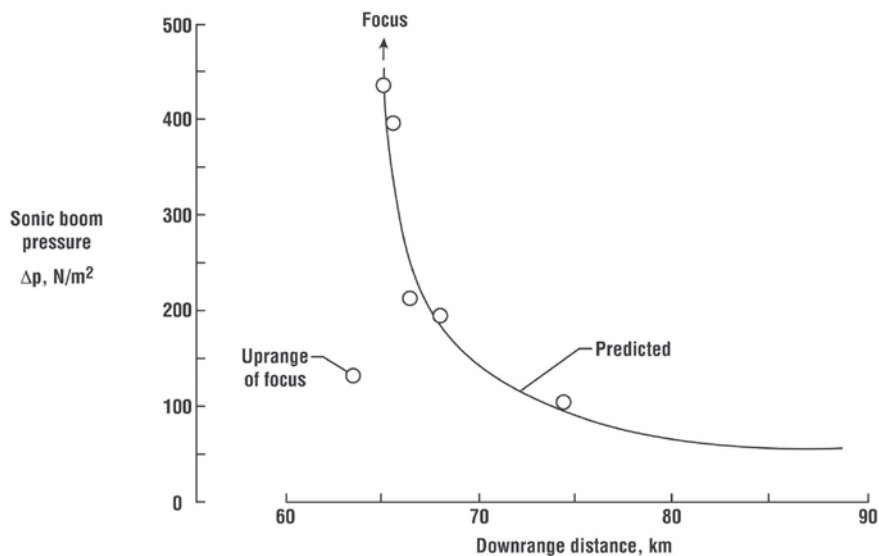


Figure 6.58. Overpressure data as a function of downrange distance as measured in the focus boom region during ascent of Apollo 17 (ref. 6.119).

Space Shuttle

Pressure signature measurements and boom predictions for early versions of the Shuttle and booster date back to the early 1970s. For example, references 6.122, 6.123, and 6.124 contain data on early straight- and delta-wing orbiter concepts. Reference 6.125 contains data and sonic boom predictions for a fly-back booster and orbiter shown in figure 6.59. Tests were conducted with and without a solid exhaust plume simulation. Figure 6.60 shows a Schlieren for Mach numbers of 3.0 and 4.0 of the ascent configuration with the simulated exhaust plume and the strong shock that the latter generates. Boom predictions and correlations were made using Thomas' method and the near-field measured pressures contained in the report. An illustrative example is given in figure 6.61 for the flight conditions listed in the legend, where α is the angle of attack, ϕ is bank angle, and Ψ is heading angle. It gives the variation of ΔP_{\max} with the rate of change of flight path angle, for the launch configuration with and without plume and the fly-back booster without plume. For values beyond ~ -0.5 deg/sec, there is a focus region. The label "trajectory value" is the value for the example trajectory given in the paper at a Mach number of 3.0. The other plots provided in reference 6.125 illustrate the effects of flight path angle and its rate of change.

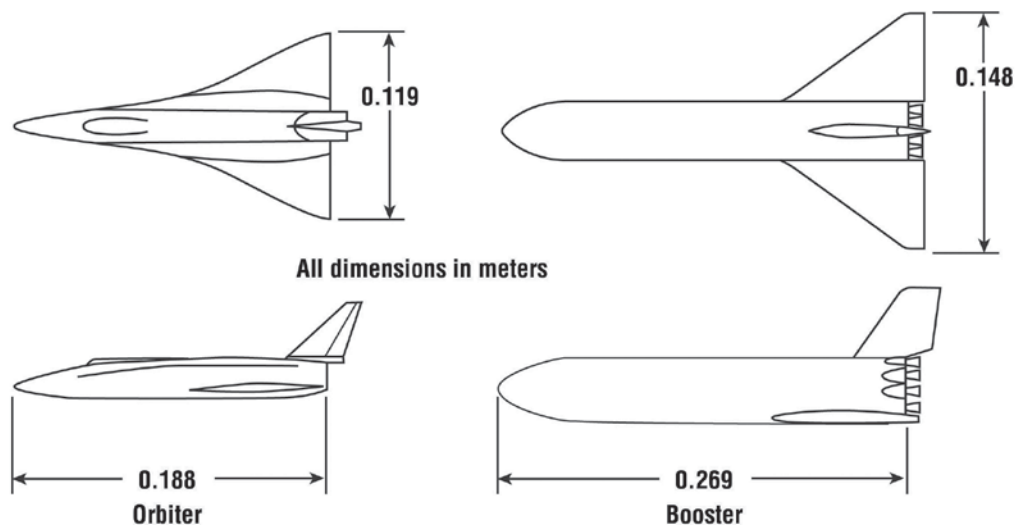
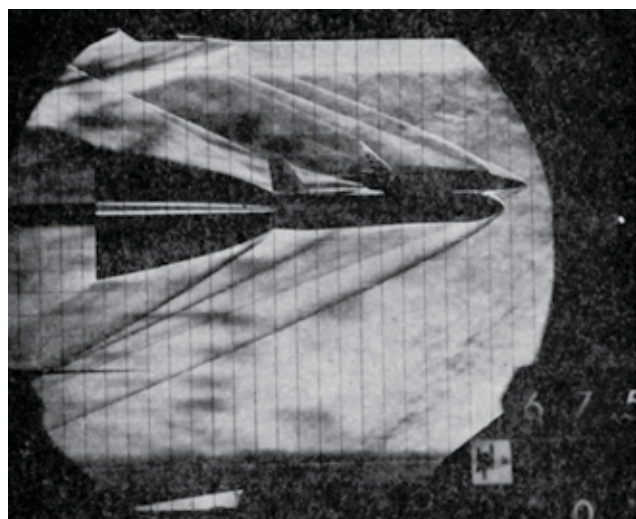
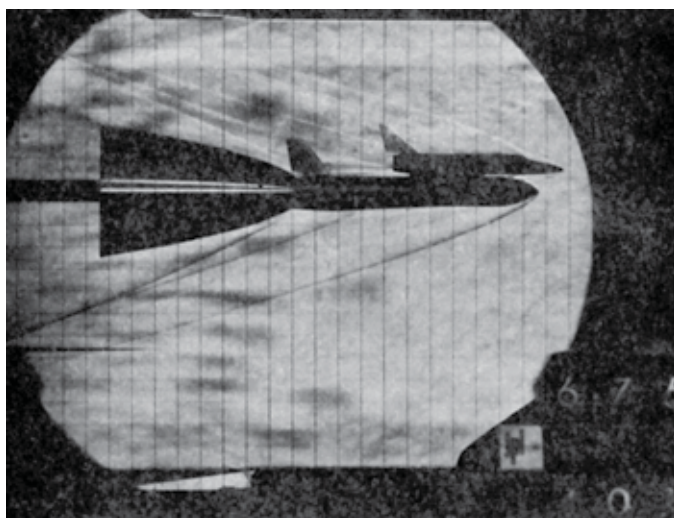


Figure 6.59. Fly-back booster and orbiter configurations (ref. 6.125).



(a) Launch configuration with simulated plume (Mach 3).



(b) Launch configuration with simulated plume (Mach 4).

Figure 6.60. Shadowgraphs taken during tests in JPL 0.508 meter (20-inch) supersonic wind tunnel, $\alpha = 0^\circ$, (ref. 6.123).

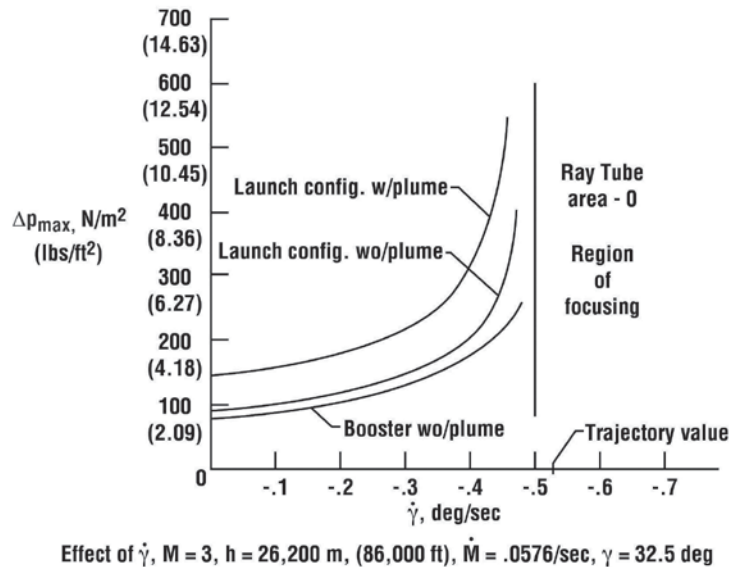


Figure 6.61. Sonic boom during ascent $\alpha = 0$ degrees, $\phi = 0$ degrees, $\dot{\psi} = 0.0105$ degrees/second (ref. 6.125).

Subsequent to the publication of reference 6.124, the Space Shuttle Orbiter was heavily modified. As a result of these design modifications, a wind-tunnel investigation that used a 0.0041 scale model of the latest (final) Space Shuttle Orbiter (see figure 6.62) to determine the effects on the ground overpressure characteristics due to changes in the geometry and the aerodynamic characteristics of the Orbiter was conducted. The results of the investigation were presented in 1975 in a paper (ref. 6.126, p. 1) written by Mendoza. The abstract for this paper states,

Pressure signatures for a 0.0041-scale model of a space shuttle orbiter were measured in a wind tunnel at Mach numbers from 1.30 to 3.02. The model was tested at 10° and 25° angles-of-attack and roll angles were varied from 0° to 180° in 30 degree increments. Comparisons of sonic boom levels were made for a delta-wing configuration and for the latest space shuttle orbiter, which were assumed to have identical lengths and entry trajectories.

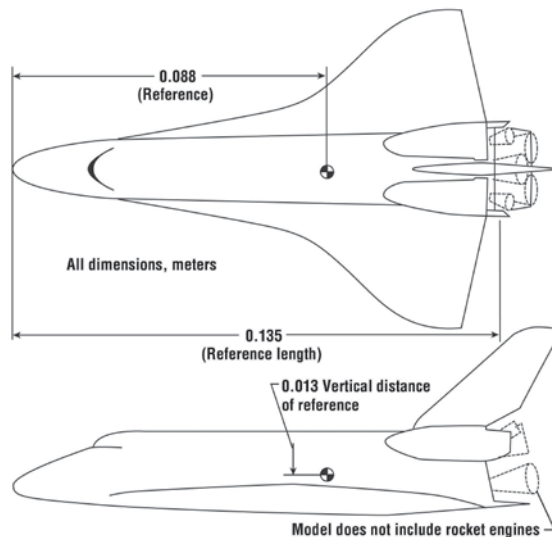


Figure 6.62. The 0.0041 scale model of the latest Space Shuttle Orbiter (ref. 6.126).

Calculations were made for two trajectories (actually two modified trajectories) using the waveform method of reference 6.126. These trajectories, shown in figure 6.63, are for space shuttle entry and cover a range of Mach numbers from 2.7 down to 1.2. A comparison of sonic boom footprints for the Space Shuttle and earlier versions of the shuttle for trajectory A are shown in figure 6.64. Figure 6.64 shows that the longest delta-wing space shuttle had the highest pressure and the 32.6 m delta wing shuttle the lowest. Similar results for trajectory B are given in reference 6.126.

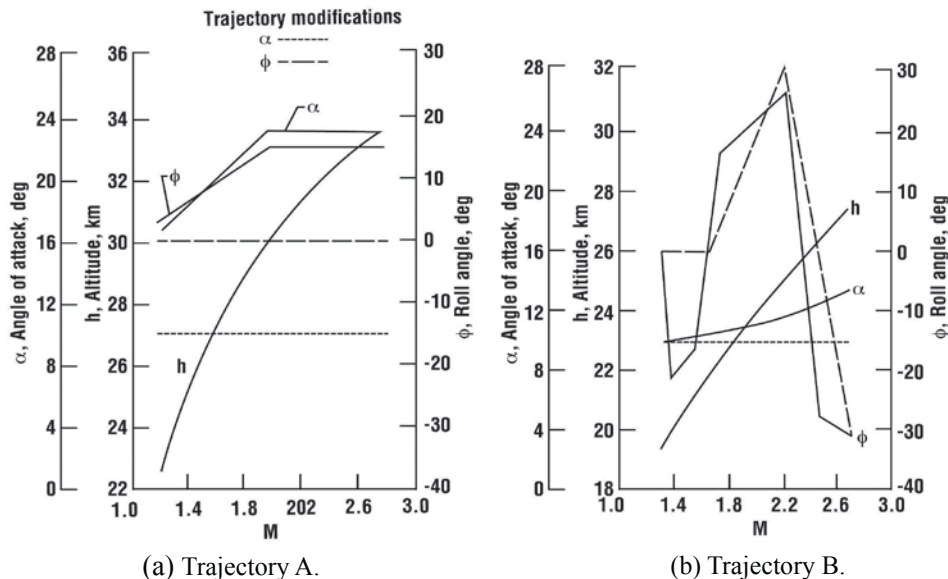


Figure 6.63. Space Shuttle entry trajectory parameters (ref. 6.126).

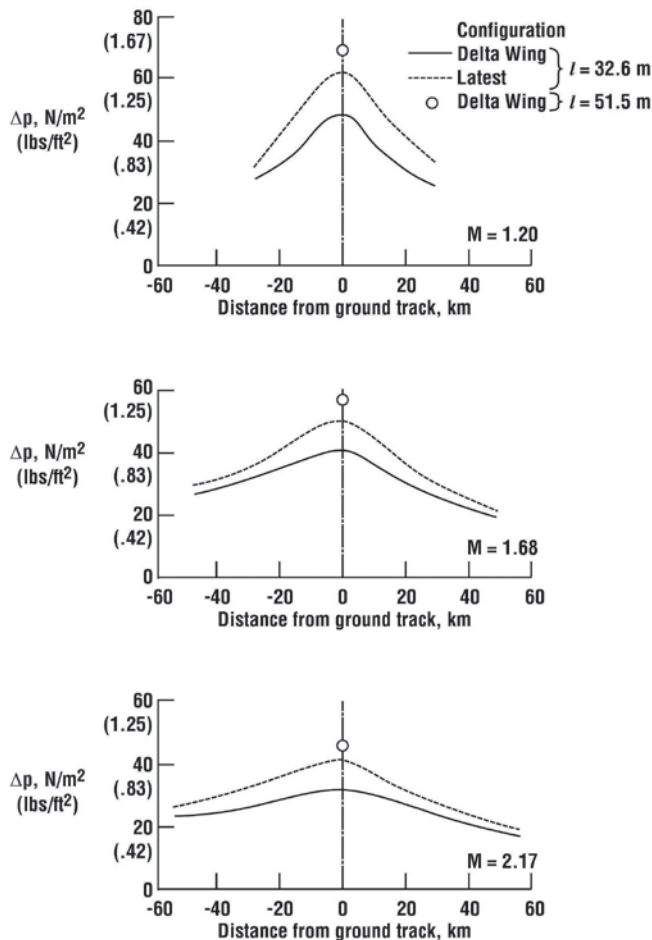


Figure 6.64. Comparisons of the sonic boom footprints for the various space shuttle vehicles, $K_r = 1.9$ for trajectory A (fig. 6.63(a), ref. 6.126).

Variations of the maximum Δp with Mach number for the two modified trajectories in figure 6.63 for the shuttle orbiter and for delta-wing and straight-wing orbiters are provided in figure 6.65. It is evident that the trajectory B of Δp values are larger than those for trajectory A and that the latest orbiter Δp values are higher than those of the delta-wing version. The highest value is for the straight-wing orbiter with a Δp of 95 N/m² at a Mach number of 1.2 (see ref. 6.122).

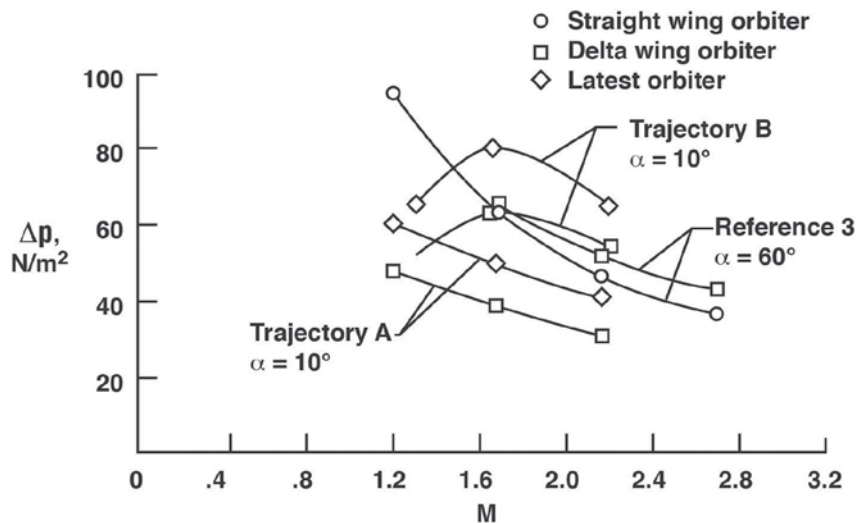


Figure 6.65. Ground track sonic boom levels for three orbiter configurations (ref. 6.126).

The 1973 paper by Holloway et al. treated both the shuttle orbiter and ascent vehicle booms (see ref. 6.120). Also, it analyzed both Western Test Range (WTR) and Kennedy Space Center (KSC) launches. Thomas' methodology (ref. 6.26) used in these calculations was augmented by the near-field strong shock extrapolation procedure of reference 6.108. Figure 6.66 (adapted from ref. 6.120) shows the ground-track overpressure variation during shuttle ascent.

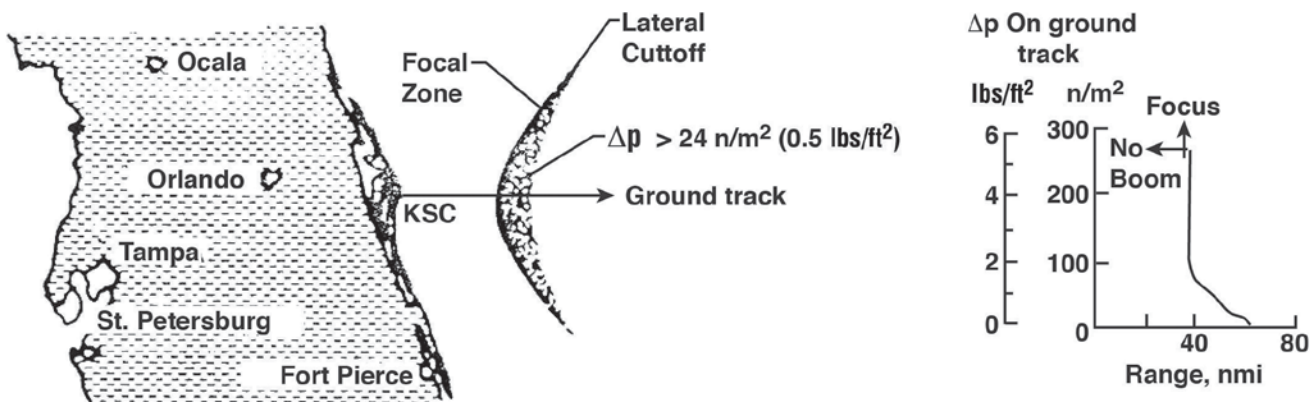


Figure 6.66. Ground track overpressure variation during shuttle ascent (adapted from ref. 6.120).

As shown earlier for the Apollo ascent (fig. 6.58), there is a focal region followed by a rapid decline in overpressure. Maximum pressures at the focus may be in excess of 200 n/m² (4.0 lbs/ft²). Focused energy may be expected to extend to about 45 nmi on either side of the ground track. The general characteristic of the focus zone is that it is longest near the ground track and becomes narrow near the outer edge. Analysis of the Saturn V data from Apollo 17 suggests that the longitudinal extent of the focal zone will be less than 2 nmi at its widest point.

Overpressures during orbiter entry are plotted in figures 6.67 and 6.68 (ref. 6.120). The lateral distributions, pictured in figure 6.67, have the typical bell shape and are a maximum at a Mach number of 2.0. Figure 6.68, a plot of the maximum values, shows that the overall maximum is around 1.4 lbs/ft² and occurs at a range to landing of ~ 30,000 feet. Further details are given in reference 6.120.

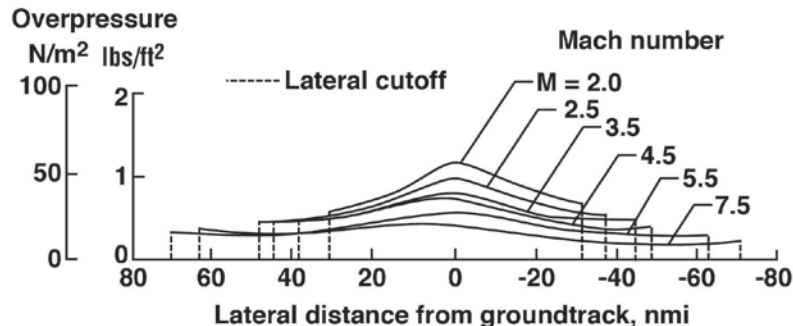


Figure 6.67. Lateral overpressure variation during orbiter entry (ref. 6.120).

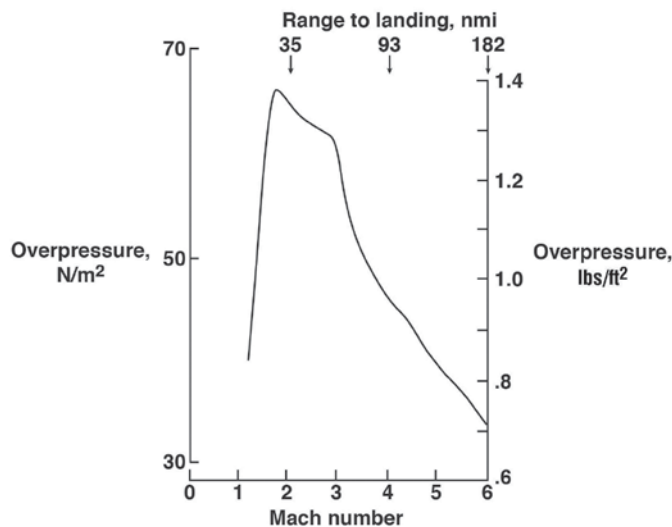


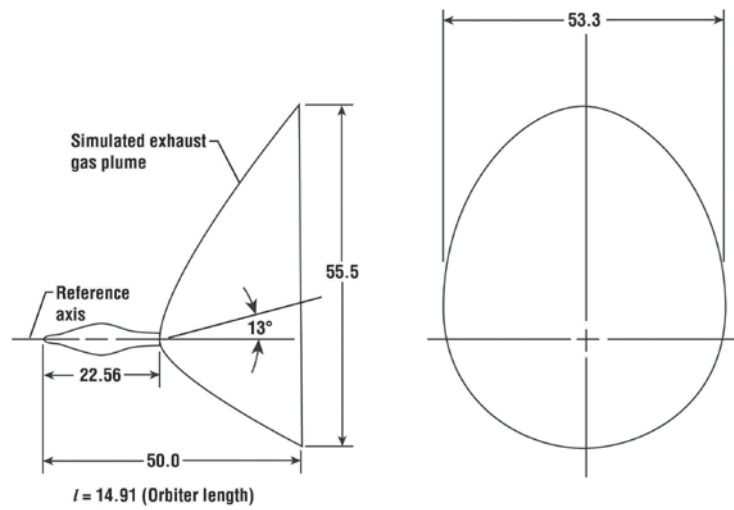
Figure 6.68. Orbiter entry overpressure variation along the ground track (ref. 6.120).

The near-field pressure signatures of the space shuttle launch and orbiter vehicle were further studied by Ashby in 1979 in reference 6.127 (p. 7),

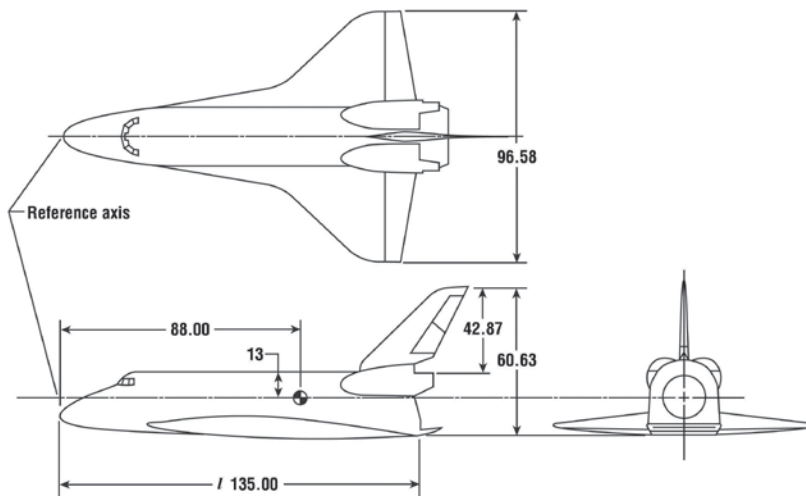
Static-pressure signatures parallel to the flight path of the launch and entry configurations of the spaceshuttle were measured in the Langley 20-inch Mach 6 tunnel in air at selected distances from the flight path. The launch configuration, consisting of an equivalent body of revolution (representing the orbiter and external fuel tank) with a solid exhaust gas plume attached, was tested at an angle of attack of 0° . The entry configuration (Orbiter alone) was tested over an angle-of-attack range from 10° to 40° .

The simulated plume body represents the area distribution of the gaseous exhaust plume plus the mixing region between the plume inner shock and the external flow. Its shape and size were determined in a manner described in reference 6.128.

Figure 6.69(a) shows the dimensions and shape of the launch configuration model as well as that of the orbiter (fig. 6.69(b)). A schematic of the test setup is shown in figure 6.70. Measured values of $\Delta p/p$ are tabulated in the paper for a range of azimuths from 68.5° to 180° at an h/l of 10.65 and a Mach number of 6.0. Plots and calculated signatures are given for azimuth angles of 150° and 90° . A plot of the 150° data and predictions based on the methods of references 6.129 and 6.130 are presented in figure 6.71. Experimental pressures were determined using both static and pitot probes at an h/l of 10.65.



(a) 0.000456-scale model of equivalent body of revolution (orbiter and external fuel tank) with solid exhaust gas plume (Mach 6).



(b) 0.0041-scale model of 0898 orbiter.

Figure 6.69. Delta-wing Space Shuttle Orbiter test model. All linear dimensions are in millimeters (ref. 6.127).

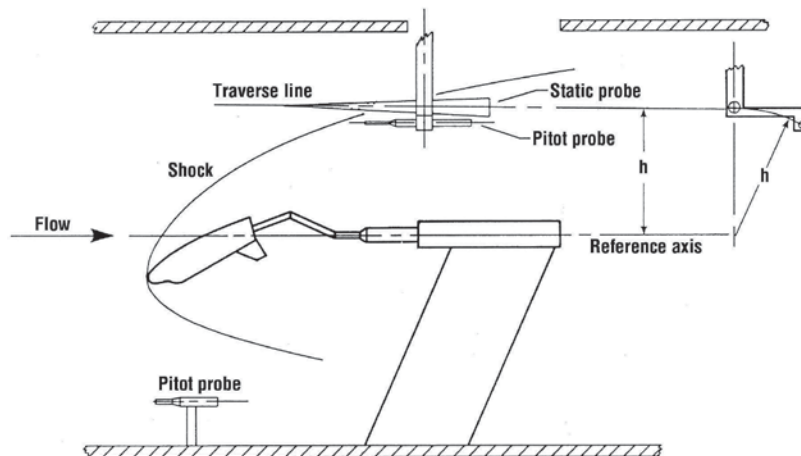


Figure 6.70. Schematic of test setup (ref. 6.127).

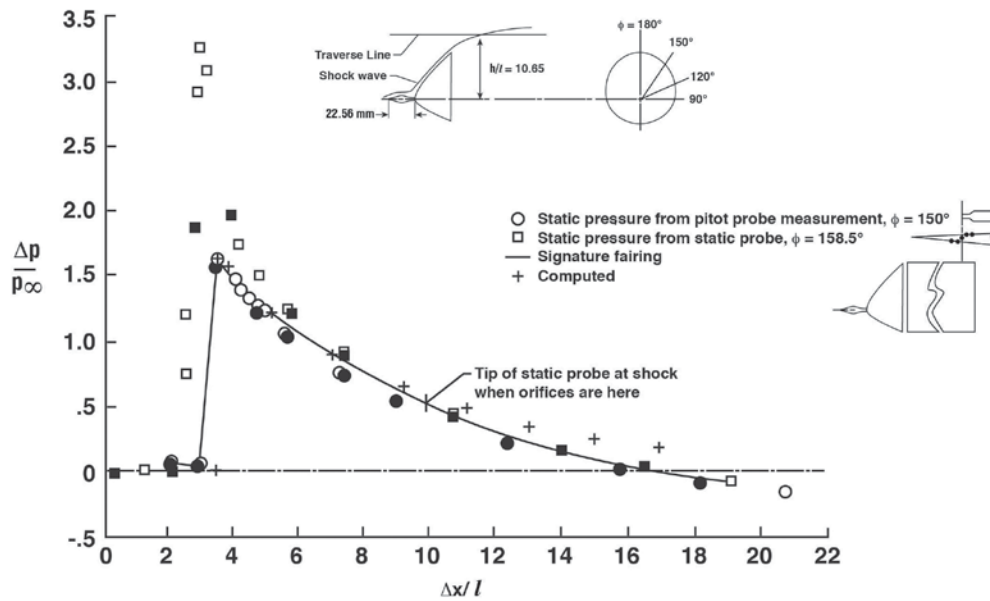


Figure 6.71. Pressure signatures for 0.000456-scale model of equivalent body of revolution (orbiter and external fuel tank) with solid exhaust gas plume (Mach 6) at two meridional angles of 150° . Filled symbols are from forward traverse. Origins were shifted for plotting, $\alpha = 0^\circ$ (ref. 6.127).

The computations were carried out for the geometry illustrated in the key. The geometry has a cylindrical wake downstream of the plume. Data for both forward and reverse traverses are also provided. It is noteworthy that the static probe sensed the pressure bump (bow shock) first and its measured maximum value is about twice that of the pitot probe. A similar relationship exists between the calculated pressures jump and the static probe measurements. If one assumes that the static probe measurement is the most accurate, then it would appear that the actual viscous expansion about the simulated plume model was greater than that of the inviscid calculation (refs. 6.129 and 6.130) for the model with the cylindrical wakes.

The presentation of the orbiter experimental results in reference 6.127 is more extensive than the presentations of experimental results for the ascent vehicle. The experimental results for the geometry presented in figure 6.69 are provided for the lower symmetry plane (0° azimuth angle) and angles of attack of 10° , 20° , 30° , and 40° . The computer code had limitations in how far downstream and radially the flow could be computed. As stated in reference 6.127 (p. 6),

The computer program would not run far enough downstream for the shock to be at the required h/l , and could not compute the flow field for angles of attack greater than 25° . Since only the flow field of the windward surface is of interest, the upper surface can be judiciously contoured to make the program run for an angle of attack of 30° , but only for a small distance beyond the length of the configuration. To make the program run the required distance for the shock to be at the desired h/l , an established experimental observation was utilized. It has been shown (refs. 6.131 and 6.132) for a delta wing configuration at angles of attack above 20° , a body of revolution generated by the lower surface contour in the plane of symmetry has, at an angle of attack of 0° , approximately the same flow field as the delta wing configuration does in that plane. Therefore, such an equivalent body of revolution was used in the program to calculate the flow field for an angle of attack of 30° .

This prediction is shown in figure 6.72 and is in good agreement with the pitot probe measurements, but much lower than those for the more accurate static probe. Neither probe is able to account for the large flow angles present in the flow field at such high angle of attack and small h/l values. Present-day Euler codes do not have these limitations.

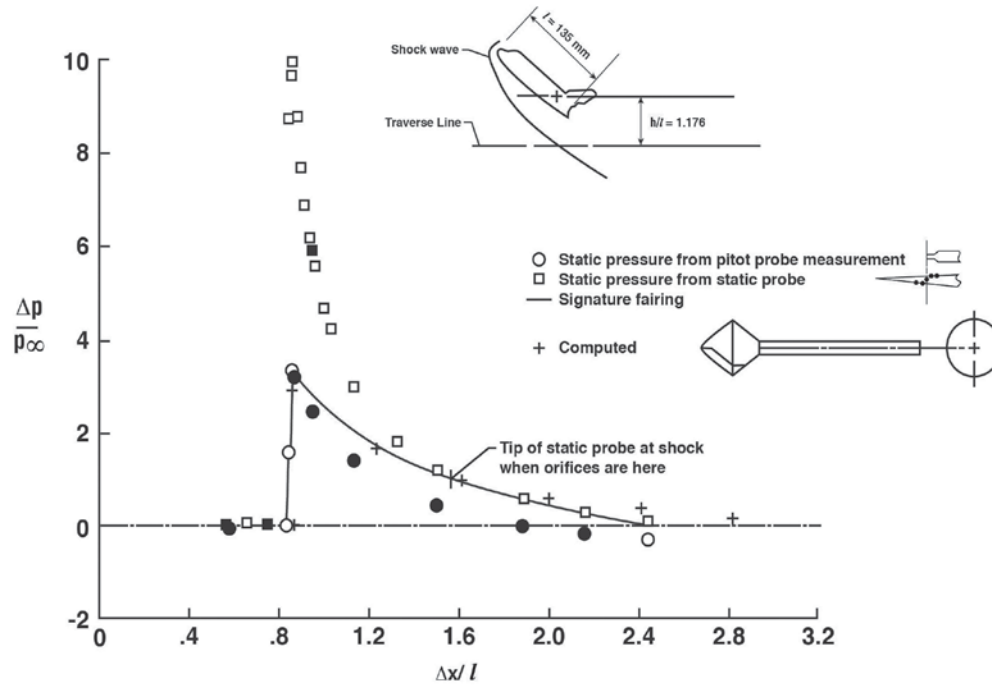


Figure 6.72. Pressure signatures along plane of symmetry of 0.0041-scale model of the 089B orbiter at an angle of attack of 30° . Filled symbols are from forward traverse. Origins were shifted for plotting, $\phi = 0^\circ$ (ref. 6.127).

Reference 6.133 focuses on correlations of ground measured pressure data with sonic boom predictions for the space shuttle STS-1 orbiter during reentry. Forty-four sonic boom pressure signatures recorded at 11 locations during the reentry of the Orbiter *Columbia* are compared to signatures extrapolated from flight altitudes using near-field wind-tunnel pressure data for Mach numbers of Mach 1.23 to 5.87. Pressure signatures were recorded by microphones positioned at ground level and simulated ear level near the descent ground track along the California corridor. Only the ground level data was used for the theory/experiment correlations. Station locations, meteorological data, signature duration, and shock-rise-time information are tabulated in ref. 6.133.

The ground signature measurements taken at the 11 stations are shown in figure 6.73. While all are N-wave type signatures, several of the leading shocks have rounded peaks (instead of sharp corners) and the last two, for Mach numbers of 1.40 and 1.23, have a spiked shock. The time duration of the signatures vary from 0.693 second at Mach 5.87 to 0.375 second at Mach 1.23.

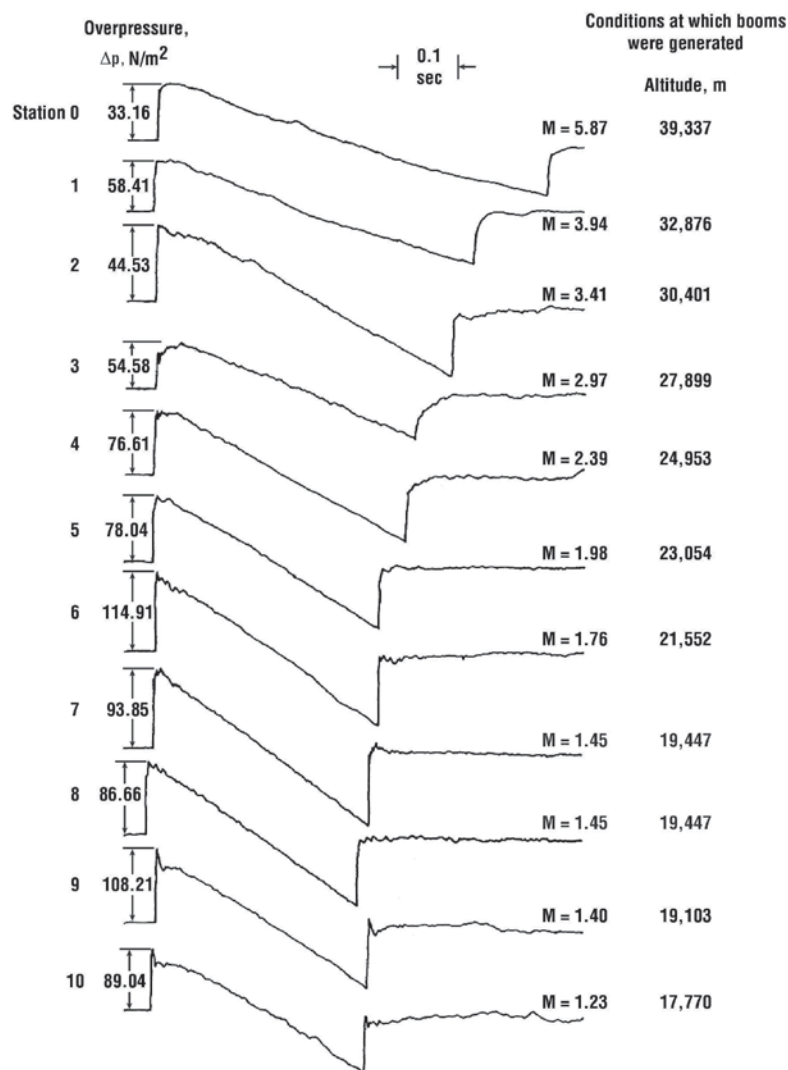


Figure 6.73. Measured sonic boom signatures recorded at 11 measurement sites located under and lateral to the STS-1 reentry ground track (adapted from ref. 6.133).

The sonic boom predictions were made using Thomas' extrapolation methodology (ref. 6.26) and the wind-tunnel data from references 6.126 and 6.127. Mach number, angle of attack and h/l combinations used in the reference 6.126 tests are provided in the table included with figure 6.74 below. Roll angles ranged from 0° to 180° in 30° increments. Tests were at a Mach number of 6.0 and the h/l was 1.176 (ref. 6.127). Angles of attack ranged from 10° to 40° and roll angles from 0° to 68.5° or 90° depending on whether the data was taken by the pitot probe or static pressure probe, respectively. The estimated roll angle and angle-of-attack variation with Mach number during the reentry of the STS-1 orbiter are given in figure 6.74. In order to make ground sonic boom predictions for the flight conditions of the signatures of figure 6.73 interpolations and extrapolations of the data (i.e., roll angle, angle of attack, and Mach number) contained in the above references were required. With these data, Thomas' wave-form propagation code was used to make predictions of all 11 signatures shown in figure 6.73.

M	1.30	1.64	2.21	2.61	3.02
α	10°	10°	10°	10°/ 25°	25°
h/l	1.55 and 1.36	1.36	1.36	1.36 and 0.99	0.99

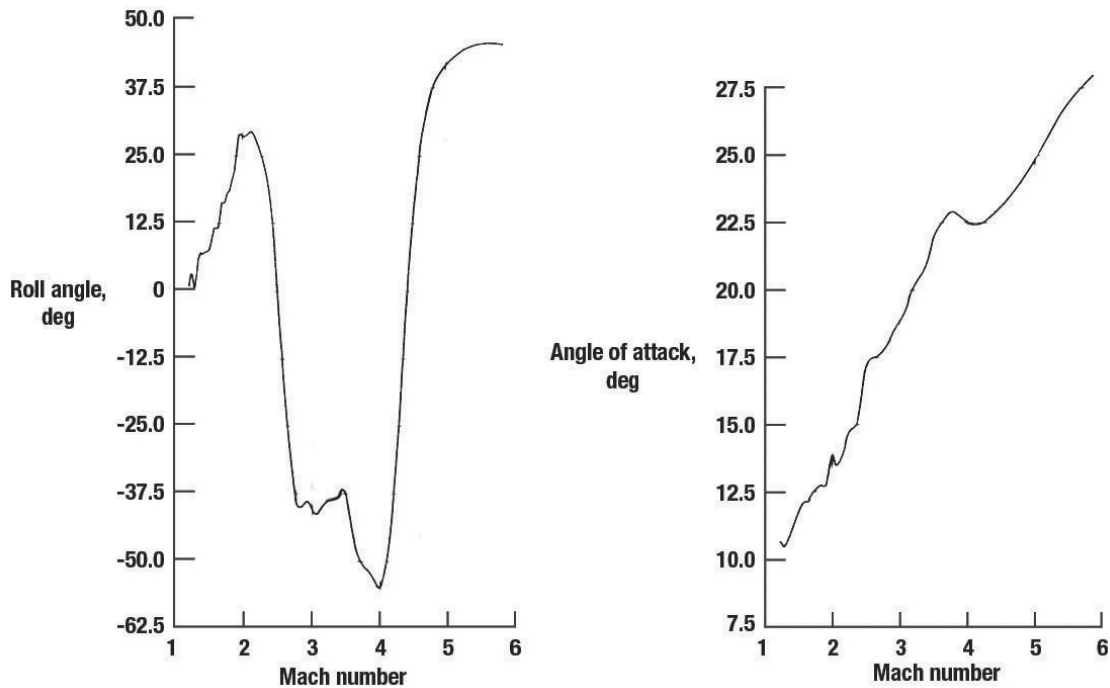


Figure 6.74. Estimated roll angle and angle of attack during reentry of STS-1 orbiter (ref. 6.133).

Since most of the wind-tunnel data are limited to the positive phase of the signatures, predictions were only made for the positive phase. Two examples are provided in figure 6.75; one for station 0 at a Mach number of 5.87 and the other for station 3 at a Mach number of 2.97. The agreement of the prediction with experiment is good in both cases, as it was for the other 9 cases (not shown).

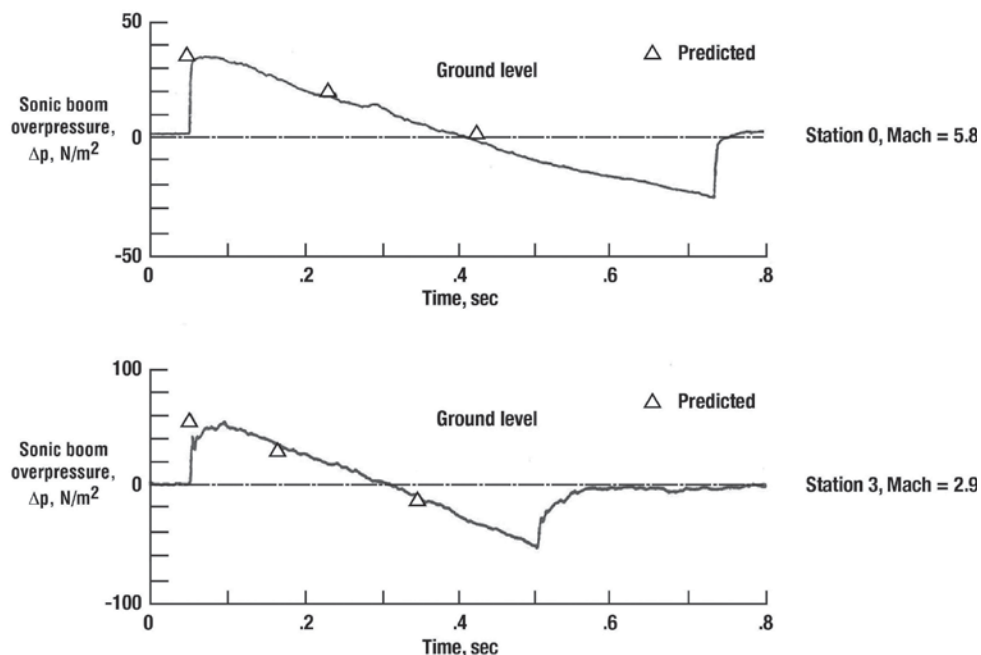


Figure 6.75. Predicted and measured sonic boom signatures for the Space Shuttle at Mach 5.87 and 2.97, and respective altitudes of 39,337 and 27,889 meters (ref. 6.133).

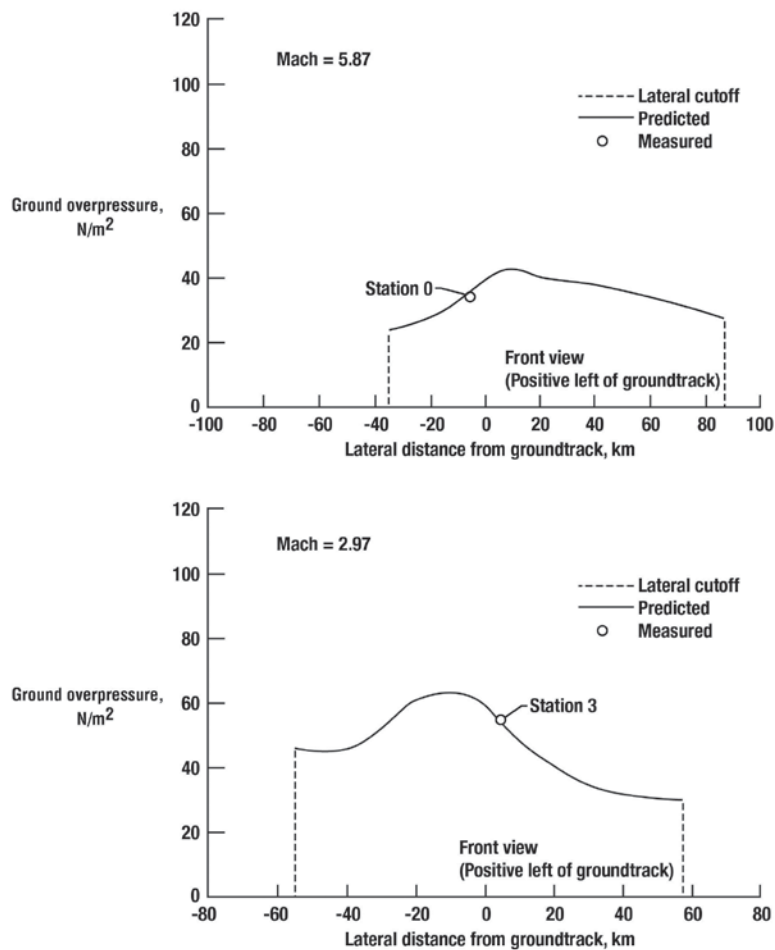


Figure 6.76. Lateral distribution of reentry overpressures along shock/ground intersections (ref. 6.133).

The authors of reference 6.133 also calculated the lateral distributions of the maximum pressures at the ground for the 11 stations. As with the longitudinal distributions, the results for stations 0 and 3 are shown in figure 6.76. It is apparent that the roll angle at station 0 (Mach 5.87) (see figure 6.74) is about $+45^\circ$, while that at station 3 (Mach 2.97) is approximately -40° . Also, the angle of attack at station 0 is $\sim 25.5^\circ$ and 16.25° at station 3. Thus, one would assume that the character of the ground signature at station 0 would be quite different from that at station 3. This is clarified in figure 6.76. Also note that the lateral extent of the ground signatures for station 0 is slightly greater than that for station 3 with Mach number and altitude effects tending to offset one another.

Peak Overpressure Predictions

Numerous studies aimed at defining the peak amplitudes (overpressures) of the signatures for primary boom carpets for a wide range of vehicles and flight conditions have been conducted. A summary of the results from these studies for generally quiescent atmospheric conditions is depicted in figure 6.77 (ref. 6.134). Predicted and measured on-track sonic boom overpressures are plotted as a function of altitude for several aircraft of various sizes and weights (including Concorde) and for Apollo and Shuttle launch and reentry vehicles. The data represent predominately on-track measurements (i.e., those within ± 3 nmi of the vehicle ground track).

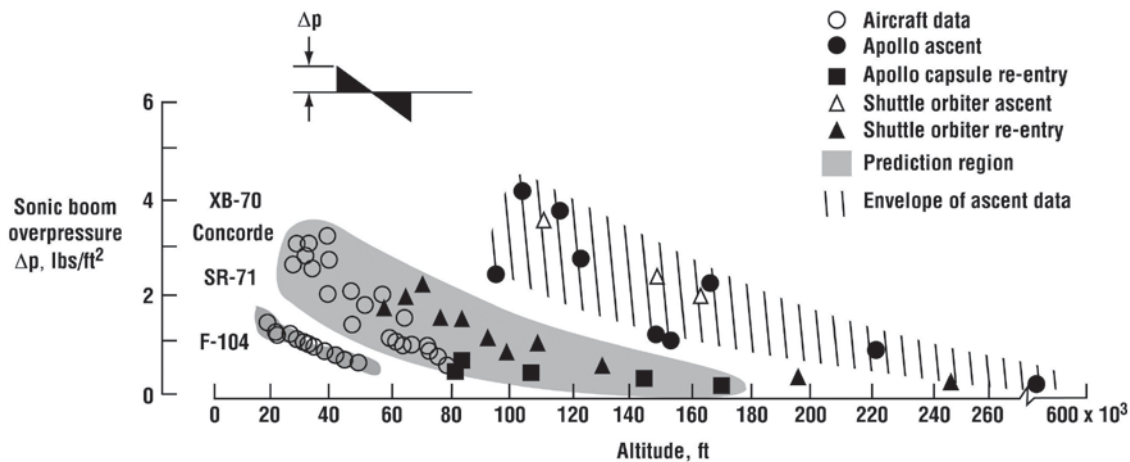


Figure 6.77. Summary of measured and predicted sonic boom overpressures near the ground track for various aircraft and spacecraft (ref. 6.134).

It can be seen that the predicted trend of decreasing sonic boom overpressure with increasing altitude is reflected in the aircraft data up to 80,000 feet, in the Apollo capsule measurements up to 174,000 feet, and in the Space Shuttle Orbiter results up to altitudes of about 250,000 feet. The two Space Shuttle Orbiter data points at altitudes of about 195,000 feet and 250,000 feet were at offset distances of about 33 nmi and 75 nmi respectively. Note that the larger the vehicle, the greater the overpressure, varying from about 3.5 lbs/ft² for the large XB-70 to about 1.0 lb/ft² for the smaller F-104 fighter at the same altitude and to 0.2 lb/ft² for the even smaller Apollo capsule. Space Shuttle Orbiter overpressures vary from about 2.5 lbs/ft² at 70,000 feet to about 0.7 lb/ft² at 129,000 feet. In all cases, the data, particularly for the Space Shuttle Orbiter, closely match the data obtained from the performance of aircraft in flight tests over the past four decades.

The sonic boom overpressures measured during the launch-ascent of the Saturn-Apollo vehicle and Space Shuttle do not include overpressures very near or on the focus line. In addition, the ascent boom data are plotted at the approximate altitude at which the boom originated. Previous plots, similar to figure 6.77 (ref. 6.134), are plotted at altitudes corresponding to the vehicle overhead position.

In general, the measured overpressures for the launch and ascent portion of spacecraft flights indicate the same trend of decreasing pressure with increasing altitude. However, the magnitudes of the overpressure values during ascent are much greater than those of the reentry vehicle. Since the launch vehicle is considerably larger than the reentry vehicle, higher boom levels can be expected. The largest portion of the overpressure from launch vehicles results from the “effective body” produced by the rocket exhaust plume. It is noteworthy that disturbances from Apollo rockets in space were measured at ground level for the vehicle operating at altitudes up to about 600,000 feet (ref. 6.135). Simplified methods for prediction of spacecraft launch and reentry sonic booms are discussed in references 6.21, 6.136, 6.137, and 6.138.

Chapter 6 Summary Remarks

The Whitham F-function methodology is still useful in the estimation of sonic booms of supersonic aircraft whether in an exact or semi-empirical scheme. In supersonic design and analysis, the use of F-function methods

prior to the application of Euler-equation CFD codes can lead to a better understanding of the flow field and its shocks, and thus to more meaningful and efficient Euler calculations.

With today's computer capabilities, Euler or Navier-Stokes CFD codes can be used to define a configuration's flowfield out to where near-field effects are small. Ideally, one would use shock-fitted Euler codes for near-field calculations to eliminate shock-smearing, and thus provide more accurate shock pressure jumps at large radial distances. If computer limitations do not allow the Euler CFD code calculations to extend out to where near-field effects are small, several other options are available. The use of George's multipole analysis for the mid-field calculations, closely coupled with the CFD can affect an overall improvement as demonstrated by Page and Plotkin. A second and more accurate option would be the use of a mid-field code based on the full-potential equation. With this approach, lateral gradients of the flow quantities can be matched at the interface with the near-field code calculations and accuracy improved.

Understanding how the pressure signature aging and freezing during its propagation to the ground is useful in the design of low-boom supersonic aircraft. The magnitude of the pressure gradients following shocks in the near field dictates their subsequent strength, including those in the ground pressure signature (sonic boom).

Numerous ray tracing codes are available for the prediction of the pressure signatures, or sonic boom, on the ground. All are based on geometrical acoustics as derived by Blokhintsev. Some are F-function dependent, while others use Thomas' waveform approach. All treat the steady-state, or constant-velocity, boom. Several can predict the focused booms that result from maneuvers and acceleration, as well as non-standard atmospheres with winds. Several computer codes are capable of calculating the secondary, or over-the-top booms. Only a few propagation codes treat the effect of air absorption.

Wind-tunnel and flight data from low Mach numbers to near orbital speeds are presented along with predictions based primarily on methods developed for supersonic application. At hypersonic speeds, the boom intensities are fairly well predicted, but predicted signature lengths are usually longer than measured. Hypersonic boom methodology is based primarily on blast wave theory and consequently applies to drag-dominated vehicles.

Chapter 6 References

- 6.1 DuMond, W. M.; Cohen, E. R.; Panofsky, W. K. H.; and Deeds, E.: A Determination of the Wave Forms and Laws of Propagation and Dissipation of Ballistic Shock Waves. *J. Acoust. Soc. Am.* 18, 1946, pp. 97–118.
- 6.2 Whitham, G. B.: The Behavior of Supersonic Flow Past a Body of Revolution Far from the Axis. *Proc. Roy-Soc. A.* Vol. 201. No. 1064, March 1950, pp. 89–109.
- 6.3 Whitham, G. B. : The Flow Pattern of a Supersonic Projectile. *Communications on Pure and Applied Math*, Vol. V, No. 3, Aug. 1952, pp. 301–348.
- 6.4 Landau, L.: On Shock Waves at Large Distances from the Place of Their Origin. *J. Phys. USSR*, Vol. 9, No. 6, 1945, pp. 496–500.
- 6.5 Hayes, W. D.: Linearized Supersonic Flow. Thesis, California Institute of Technology, 1947; Reprinted as North American Aviation Report AL-222; Available as Princeton University AMS Report 852, 1968.
- 6.6 Walkden, F.: The Shock Pattern of a Wing-Body Combination, Far from the Flight Path. *Aero. Quarterly*, Vol. IX, May 1958, pp. 164–194.

- 6.7 Warren, C. H. E.: Sonic Bangs: A Qualitative Explanation. R.A.E. Tech. Note Aero. 2192, ARC 15,540. Sept. 1952.
- 6.8 Warren, C. H. E.: Addendum and Corrigenda to Above. R.A.E. Tech. Note. Aero 2192a. A.R.C. 15,541. Oct. 1952.
- 6.9 Randall, D. G.: Methods for Estimating Distributions and Intensities of Sonic Bangs. ARC Technical Rept. R&M No. 3113, Aug. 1959.
- 6.10 Seebass, R.: Sonic Boom Theory. *Journal of Aircraft*, Vol. 6, No. 3 (May-June 1969), pp. 177–184.
- 6.11 Carlson, H. W.; Mack, R. J.; and Morris, O. A.: Sonic Boom Pressure-Field Estimation Techniques. *J. Acoust. Soc. Am.*, Vol. 39, Number 5, Part 2, 1966, pp. 510–518.
- 6.12 Hayes, Wallace D.: Brief Review of the Basic Theory. *Sonic Boom Research*, A. R. Seebass, ed., NASA SP-147, 1967, pp. 3–7.
- 6.13 Carlson, H. W. and Maglieri, D. J.: Review of Sonic-Boom Generation Theory and Prediction Methods. *J. Acoust. Soc. Am.*, Vol. 51, No. 2 (Part 3), 1972, pp. 675–685.
- 6.14 Darden, Christine M., et al.: Status of Sonic Boom Methodology and Understanding. NASA CP 3027, Jan. 1988.
- 6.15 Plotkin, K. J. and Maglieri, D. J.: *Sonic Boom Research: History and Future*. AIAA-2003-3575, Orlando, FL, June 23, 2003.
- 6.16 Ferri, Antonio and Schwartz, Ira R.: *Sonic Boom Generation, Propagation, and Minimization*. AIAA Paper No. 72-194, Jan. 1972.
- 6.17 Whitham, G. B.: On the Propagation of Weak Shock Waves. *Journal of Fluid Mechanics*, Vol. 1, pt. 3, Sept. 1956.
- 6.18 Maglieri, D. J. and Plotkin, K. J.: *Aeroacoustics of Flight Vehicles: Theory and Practice*. NASA RP1258, Vol. 1 and WRDC TR 90-3052, Aug. 1991, pp. 519–561.
- 6.19 Blokhintzev, D. I.: The Propagation of Sound in an Inhomogeneous and Moving Medium1. *J. Acoust. Soc. Am.*, Vol. 18, 1946, pp. 322–328: Also “Acoustics of Non-Homogeneous Moving Medium,” *Gostekhiyat*, Moscow, USSR, 1946 (translated as NACA TM-1946).
- 6.20 Jackson, C. M. and Carlson, Harry W.: Nomograms for Determining Sonic Boom Overpressure. *Journal of Aircraft* 3, 1966, pp. 74–76.
- 6.21 Carlson, Harry W.: *Simplified Sonic Boom Prediction*. NASA TP 1122, March 1978.
- 6.22 Whitham, G. B.: The Propagation of Weak Spherical Shocks in Stars. *Communications of Pure Applied Math*, Vol. 6, 1953, pp. 397–414.
- 6.23 Hayes, W. D.; Haefeli, R. C.; and Kulsrud, H. E.: *Sonic Boom Propagation in a Stratified Atmosphere With Computer Program*. NASA CR-1299 (1968).
- 6.24 Middleton, W. D. and Carlson, H. W.: *A Numerical Method for Calculating Near-Field Sonic Boom Pressure Signatures*. NASA TN D-3082, 1965.
- 6.25 Thomas, Charles L.: *Extrapolation of Wind-Tunnel Sonic Boom Signatures without Use of a Whitham F-Function*. NASA SP-255, 1970, pp. 205–217.

- 6.26 Thomas, Charles L.: Extrapolation of Sonic Boom Pressure Signatures by the Waveform Parameter Method. NASA TN D-6832, June 1972.
- 6.27 Plotkin, K. J.: PCBoom3 Sonic Boom Prediction Model - Version 1.0e, Wyle Research Report WR 95-22E, October 1998.
- 6.28 Plotkin, K. J. and Page, J. A.: MDBOOM and MDPlot Computer Programs for Sonic Boom Analysis and Design. Wyle Research Report WR 02-02, Aug. 2002.
- 6.29 McLean, F. E.: Some Non-Asymptotic Effects on the Sonic Boom of Large Airplanes. NASA TN D-2877, June 1965.
- 6.30 Seebass, R.: Minimum Sonic Boom Shock Strengths and Overpressures. *Nature* 221 (1969), pp. 651–653.
- 6.31 George, A. R.: Lower Bounds for Sonic Booms in a Midfield. *AIAA Journal* 7, 1542 (1969).
- 6.32 Hicks, Raymond M. and Thomas, Charles L.: A Preliminary Report on Shock Coalescence. NASA SP 255, Oct. 1970, pp. 297–305.
- 6.33 Cleveland, R. O. and Blackstock, D. T.: Waveform Freezing of Sonic Booms in the Atmosphere. *J. Acoust. Soc. Am.* 92 (4) (A), 1992, pp. 23–31.
- 6.34 Cleveland, R. O.; Hamilton, M. F.; and Blackstock, D. T.: Effect of Stratification of the Atmosphere on Sonic Boom Propagation. Proceedings of the 6th International Conference on Long-Range Propagation. Ottawa, Canada (1994), pp. 59–76.
- 6.35 Plotkin, K. J.: On the Aging of Sonic Booms. *J. Acoust. Soc. Am.* 93 (1993), p. 2407 (A).
- 6.36 Cleveland, R. O.: Propagation of Sonic Booms through a Real, Stratified Atmosphere. Ph.D. Dissertation. Department of Mechanical Engineering, the University of Texas at Austin (1995).
- 6.37 Cleveland, R. O.: Effects of Atmospheric Stratification on Sonic Boom Propagation. *J. Acoust. Soc. Am.* 97, 3257 (A) (1995).
- 6.38 Cleveland, Robin O. and Blackstock, David T.: Waveform Freezing of Sonic Boom Revisited. NASA CP 3335. Vol. I, July 1996, pp. 20-40.
- 6.39 Officer, C. B.: Introduction to the Theory of Sound Transmission, with Application to the Ocean, McGraw-Hill, New York, 1958.
- 6.40 Keller, J. B.: Geometric Acoustics. I. The Theory of Weak Shock Waves, *Journal of Applied Mechanics*, 25(8), 1955, pp. 938–947.
- 6.41 Friedman, M. P.; Kane, E. J.; and Sigalla, A.: Effects of Atmosphere and Aircraft Motion on the Location and Intensity of a Sonic Boom. *AIAA Journal* 1 (6), 1963, pp. 1327–1335.
- 6.42 Haefeli, R. C.: Effects of Atmosphere, Wind, and Aircraft Maneuvers on Sonic Boom Signatures. NASA CR 66756, April 1969.
- 6.43 Hayes, Wallace D. and Runyan, Harry L., Jr.: Sonic Boom Propagation through a Stratified Atmosphere. *J. Acoust. Soc. Am.*, Vol. 51, No. 2 (Part 3) 1972, pp. 695–701.
- 6.44 Rao, P. S.: Supersonic Bangs. *Aeronautics Quarterly* 7 (1956), pp. 21–44 and pp. 135–155.
- 6.45 Randall, D. C.: Sonic Bang Intensities in a Stratified, Still Atmosphere. *Journal of Sound Vibrations* 8 (1968), pp. 196–214. Also RAE Tech. Rept. No. 66002 (1966).

- 6.46 Friedman, M. P.; Kane, E. J.; and Sigalla, A.: Effects of Atmosphere and Aircraft Motion on the Location and Intensity of a Sonic Boom. *AIAA Journal*, Vol. 1, No. 6, June 1963, pp. 13–27 and pp. 1327–1335.
- 6.47 Friedman, Manfred P.: A Description of a Computer Program for the Study of Atmospheric Effects on Sonic Booms. NASA CR-157, February 1965.
- 6.48 Schorling, Michael: Calculation of Supersonic Flows at Large Distances from Slender Lifting Bodies. NASA TN D-6446, August 1971.
- 6.49 Tsien, H. S.: The Poincaré-Lighthill-Kuo Method. Vol. IV of *Advances in Applied Mechanics*, H. L. Dryden and Theodore Von Kármán, eds., Academic Press, Inc., 1956, pp. 281–349.
- 6.50 Schorling, Michael: A Nonlinear Theory for Sonic-Boom Calculations in a Stratified Atmosphere. NASA TN D-7105, March 1973.
- 6.51 Chambers, James P.; Cleveland, Robin O.; Bass, Henry E.; Blackstock, David T.; and Hamilton, Mark F.: Comparison of Computer Codes for the Propagation of Sonic Booms through Realistic Atmospheres Utilizing Actual Acoustic Signatures. NASA CP 3335, July 1996, pp. 151–175.
- 6.52 Siclari, Michael J.: Sonic Boom Prediction and Minimization of the Douglas Reference OPT5 Configuration. NASA/CP-1999-209520, December 1999, pp. 138–161.
- 6.53 Fouladi, Kamran: Langley’s Computational Efforts in Sonic Boom Softening of the Boeing HSCT. NASA/CP-1999-209520, December 1999, pp. 47–72.
- 6.54 Plotkin, K. J.: Calculation of Sonic Boom from Numerical Flow Field Solutions: MDBOOM, Version 2.2, Wyle Research Report WR-92-14, July 1992.
- 6.55 Plotkin, Kenneth J. and Cantril, Jerry M.: Prediction of Sonic Boom at a Focus. AIAA Paper No. 76-2, 1976.
- 6.56 Barger, Raymond L.: Some Effects of Flight Path and Atmospheric Variations on the Boom Propagated from a Supersonic Aircraft. NASA TR R-191, 1964.
- 6.57 Lansing, Donald L.: Application of Acoustic Theory to Prediction of Sonic Boom Ground Patterns from Maneuvering Aircraft. NASA TN D-1860, October 1964.
- 6.58 Lansing, Donald L. and Maglieri, Domenic J.: Comparison of Measured and Calculated Sonic-Boom Ground Patterns Due to Several Different Aircraft Maneuvers. NASA TN D-2730, April 1965.
- 6.59 Onyeowu, R. O.: A Numerical Study of the Effects of Aircraft Maneuvers on the Focusing of Sonic Booms. UTIAS Report No. 192, November 1973.
- 6.60 Gardner, John H. and Rogers, Peter H.: Thermospheric Propagation of Sonic Booms from the Concorde Supersonic Transport. NRL Memorandum Report 3904 (February 14, 1979).
- 6.61 Taylor, A. D.: The TRAPS Sonic Boom Program. NOAA Technical Memo ERL ARL-87, July 1980.
- 6.62 Robinson, L. D.: Sonic Boom Propagation through an Inhomogeneous Windy Atmosphere. Ph.D. Dissertation, Department of Physics, The University of Texas at Austin (1991).
- 6.63 Poling, Hugh W.: Impact of Weather and Flight Condition on Secondary Booms. Baize, Daniel G., Editor. NASA CP 3335, July 1966, pp. 136–150.
- 6.64 Page, J. A.; Plotkin, K. J.; and Wilmer, C.: PCBoom Version 6.6 Technical Reference and User Manual, Wyle Report WR 10-10, March 2010.

- 6.65 Siclari, M. J. and Fouladi, Kamran: A CFD Study of Component Configuration Effects on the Sonic Boom of Several High-Speed Civil Transport Concepts. NASA CP 10133, Vol. II, Ames Research Center (May 12-14, 1993), pp. 277–300.
- 6.66 Cliff, Susan E.: On the Design and Analysis of Low Sonic Boom Configurations. NASA CP 10133, Vol. II, Ames Research Center (May 12-14, 1993), pp. 37–80.
- 6.67 Moretti, G.: Thoughts and Afterthoughts about Shock Computations. Poly Technical Institute of Brooklyn, PIBAL Report 72-37, December 1972.
- 6.68 Salas, Manuel D.: Shock Fitting Method for Complicated Two-Dimensional Supersonic Flows. AIAA Journal, Vol. 14, No. 5, May 1976.
- 6.69 Verhoff, A. and O’Neil, P. J.: A Natural Formulation for the Numbered Solution of the Euler Equations. AIAA Paper 84-0163, January 1984.
- 6.70 Hartwich, P. M.: Fresh Look at Floating Shock Fitting. AIAA Journal, Vol. 29, No. 7, 1991, pp. 1084–1091.
- 6.71 Hartwich, Peter M.: Comparison of Coordinate-Invariant and Coordinate-Aligned Upwinding for the Euler Equations. AIAA Journal, Vol. 32, No. 9, September 1994.
- 6.72 Hafez, M. M. and Murman, E. M.: A Shock Fitting Applied to Relaxations of Transonic Small-Disturbance Equations. AIAA Journal, Vol. 15, No. 6, 1977, pp. 786–793.
- 6.73 Hafez, M. M. and Murman, E. M.: A Shock Fitting Algorithm for the Full Potential Equation. AIAA Paper 77-632 (1977).
- 6.74 Page, Juliet A. and Plotkin, Kenneth J.: An Efficient Method for Incorporating Computational Fluid Dynamics into Sonic Boom Prediction. AIAA Paper 91-3275, 1991.
- 6.75 George, A. R.: Reduction of Sonic Boom by Azimuthal Redistribution of Overpressure, AIAA Paper No. 68-159, 1968.
- 6.76 Camacho, Peter: CFD Analysis of the MDC Mach 2.4/1.8 Low Boom Wind Tunnel Model. NASA CP 10133, Vol. II, May 1993, pp. 169–194.
- 6.77 Pan, Y. S.; A Method for Wind Tunnel Investigations of Sonic Boom Based on Large Models. AIAA Journal, Vol. 10, No. 11, 1972, pp. 1408–1414.
- 6.78 Pan, Y. S.; Wang, K. T.; and Varner, M. O.: Extension of the Current Sonic Boom Theory and Development of a Wind Tunnel Testing Method Based on Large Models. Fundamental Research on Advanced Techniques for Sonic Boom Suppression. Goethert, Dr. B. H., Editor, Report FAA-RD 73-4, University of Tenn., November 1972.
- 6.79 Kandil, O. A.; Yang, Z.; and Bobbit, P. J.: Prediction of Sonic Boom Signature Using Euler-Full Potential CFD with Grid Adaptation and Shock Fitting. AIAA 2002-2543, June 2002.
- 6.80 Bobbitt, P. J.; Kandil, O. A.; and Yang, Z.: The Beneficial Effects of Wing Dihedral on Sonic Boom. AIAA 2003-3273-CP, May 2003.
- 6.81 Kandil, Osama A.; Ozcer, Isik A.; Sheng, Xudong; and Bobbitt, Percy J.: Comparison of Full Potential Propagation-Code Computations with the F-5E “Shaped Sonic Boom Experiment” Program. AIAA 2005-0013, 2005.

- 6.82 Kandil, Osama and Ozcer, Isik A.: Sonic Boom Computations for Double-Cone Configuration Using CFL3D, FUN3D, and Full-Potential Codes. AIAA 2006-0414, 2006.
- 6.83 Anderson, W. K. and Bonhaus, D. L.: An Implicit Upwind Algorithm for Computing Turbulent Flows on Unstructured Grids. *Computers and Fluids*, Vol. 23, No. 1, 1994, pp. 1–22.
- 6.84 Hicks, R. M. and Mendoza, J. P.: Prediction of Aircraft Sonic Boom Characteristics from Experimental Near Field Results. NASA TM X-1477, 1967.
- 6.85 Kane, E. J.: Propagation of Sonic Boom through a Non-Uniform Atmosphere. Boeing Doc. D6-8979, May 1962.
- 6.86 Brown, J. R.: Sonic Boom Propagation –Nonhomogeneous Atmosphere, TA-90. Boeing Doc. DC-2315TN, September 1964.
- 6.87 Kane, Edward J. and Palmer, Thomas Y.: Meteorological Aspects of the Sonic Boom. SRDS Report No. RD 64-160, FAA, ASTIA No. AD 610463, 1964.
- 6.88 Dressler, Robert and Fredholm, Nils: Statistical Magnifications of Sonic Booms by the Atmosphere. FFA Rept. 104, Aeronautical Research Institute of Sweden, 1966.
- 6.89 Lundberg, Bo K.; Dressler, Robert F.; and Lagman, Sven: Atmospheric Magnification of Sonic Booms in the Oklahoma Tests. FFA Rept. 112, Aeronautical Research Institute of Sweden, June 1967.
- 6.90 Haglund, George T. and Kane, Edward J.: Flight Test Measurements and Analysis of Sonic Boom Phenomena Near Shock Wave Extremity. NASA CR-2167, February 1973.
- 6.91 Maglieri, D. J.: Sonic Boom Flight Research – Some Effects of Airplane Operations and the Atmosphere on Sonic Boom Signature. NASA SP-147, 1967, pp. 25–48.
- 6.92 Maglieri, D. J. and Hilton, D. A.: Experiments on the Effects of Atmospheric Refraction and Airplane Accelerations on Sonic Boom Ground Pressure Patterns. NASA TN D-3520, July 1966.
- 6.93 Carlson, Harry W.; McLean, Edward F.; and Shrout, Barret L.: A Wind Tunnel Study of Sonic Boom Characteristics for Basic and Modified Models of a Supersonic Transport Configuration. NASA TM X-1236, 1966.
- 6.94 Maglieri, Domenic J.; Huckel, Vera; and Henderson, Herbert R.: Sonic Boom Measurements for SR-71 Aircraft Operating at Mach Numbers of 3.0 and Altitudes to 24,384 Meters. NASA TN D-6823, 1971.
- 6.95 Kane, Edward J.: Some Effects of the Atmosphere on Sonic Boom. NASA SP-147, April 12, 1967, pp. 49–63.
- 6.96 Hubbard, H. H.; Maglieri, D. J.; and Huckel, V.: Variability of Sonic Boom Signatures with Emphasis on the Extremities of the Ground Exposure. NASA SP-255, October 1970, pp. 351–359.
- 6.97 Onyeowu, Ronald O.: Diffraction of Sonic Boom Past the Nominal Edge of the Corridor. *J. Acoust. Soc. Am.*, Vol. 58, No. 2, August 1975.
- 6.98 Pierce, Allan D.: Atmospheric Propagation at Larger Lateral Distances from the Flight Track. NASA CP 3279, October 1994, pp. 99–122.
- 6.99 Coulouvrat, Francois: Sonic Boom in the Shadow Zone: A Geometrical Theory of Diffraction. *J. Acoust. Soc. Am.*, Vol. III, No. 1, Pt. 2 of 2, January 2002.

- 6.100 Sakarai, A.: On the Propagation and Structure of Blast Waves, I and II, J. Phys. Soc., Japan 8 and 9, 1953 and 1954, pp. 662–669 and pp. 256–266.
- 6.101 Seebass, A. R. and George, A. R.: Sonic Boom Reduction through Aircraft Design and Operation. AIAA Paper No. 73-241, 1973.
- 6.102 Plooster, Myron N.: Shock Waves from Line Sources. Numerical Solutions and Experimental Measurements. Phys. of Flds., Vol. 13, No. 11, Nov. 1970.
- 6.103 Jones, D. L.; Goyer, G. A.; and Plooster, M. N.: Shockwave from a Lightning Discharge. Journal of Geophysical Res. 73, 3121, 1968.
- 6.104 Jones, D. L.: The Energy Parameter B for Strong Blast Waves, NBS TN 155, July 1962.
- 6.105 Pan, Y. S. and Sotomayer, W. A.: Sonic Boom of Hypersonic Vehicles. AIAA Journal, Vol. 10, No. 4, 1972.
- 6.106 Tiegerman, B.: Sonic Booms of Drag Dominated Hypersonic Vehicles. Ph.D. thesis, Cornell Univ., 1975.
- 6.107 Plotkin, K. J.; Franz, R. J.; and Haering, E. A., Jr.: Prediction and Measurement of a Weak Sonic Boom from an Entry Vehicle (A). J. Acoust. Soc. Am., Vol. 120, Paper 2a PA3, 2006, p. 3077.
- 6.108 Hicks, Raymond M.; Mendoza, Joel P.; and Thomas, Charles L.: Pressure Signatures for the Apollo Command Module and the Saturn V Launch Vehicle with a Discussion of Strong Shock Extrapolation Procedures. Ames TM X-62,117, April 6, 1972.
- 6.109 Carlson, Harry W.: Experimental and Analytic Research on Sonic Boom Generation at NASA. NASA SP-147, 1967, pp. 9–23.
- 6.110 Kane, Edward: The Boeing Company, Private Communication to D. J. Maglieri. March 15, 1967.
- 6.111 Carlson, H. W. and Maglieri, D. J.: Review of Sonic Boom Generation Theory and Prediction Methods. J. Acoust. Soc. Am., Vol. 51, No. 2(Part 3), 1972, pp. 675–685.
- 6.112 Shrouf, Barrett L.; Mack, Robert J.; and Dollyhigh, Samuel M.: A Wind-Tunnel Investigation of Sonic-Boom Pressure Distributions of Bodies of Revolution. NASA TN D-6195, April 1971.
- 6.113 Miller, David S.; Morris, Odell A.; and Carlson, Harry W.: Wind-Tunnel Investigation of Sonic Boom Characteristics of Two Simple Wing Models at Mach Numbers from 2.3 to 4.63. NASA TN D-6201. April 1971.
- 6.114 Hilton, David A.; Henderson, Herbert R.; and McKinney, Royce: Sonic Boom Ground Pressure Measurements from Apollo 15. NASA TN D-6950, 1972.
- 6.115 Henderson, Herbert R. and Hilton, David A.: Sonic-Boom Ground Pressure Measurement from the Launch and Reentry of Apollo 16. NASA TN D-7606, 1974.
- 6.116 Hicks, Raymond M.; Mendoza, Joel P.; and Garcia, Frank Jr.: A Wind Tunnel-Flight Correlation of Apollo 15 Sonic Boom. Ames TM X-62,111, SSPD 71, Jan. 28, 1972.
- 6.117 Garcia, Frank, Jr.; Hicks, Raymond M.; and Mendoza, Joel P.: A Wind Tunnel Flight Correlation of Apollo 16 Sonic Boom. NASA TM X-62,073, SSPD-90, Feb. 5, 1972.
- 6.118 Mendoza, Joel P. and Hicks, Raymond M.: Wind Tunnel Pressure Signatures for an 0.016 Scale Model of the Apollo Command Module. NASA TM X-62,047, July 14, 1971.

- 6.119 Henderson, Herbert R. and Hilton, David A.: Sonic-Boom Measurements in the Focus Region during the Ascent of Apollo 17. TN D-7806, Dec. 1974.
- 6.120 Holloway, Paul F.; Wilhold, Gilbert A.; Jones, Jess H.; Garcia, Frank, Jr.; and Hicks, Raymond M.: Shuttle Sonic Boom – Technology and Predictions. AIAA Paper No. 73-1039, 1973.
- 6.121 Hicks, R. M. and Mendoza, J. P.: Pressure Signatures for a 0.0053 Scale Model of the Saturn V - Apollo Launch Vehicle with Simulated Exhaust Plumes. NASA TM X-62, 129, July 23, 1973.
- 6.122 Hicks, R. M.; Mendoza, J. P.; and Levy, L. L., Jr.: An Investigation of Sonic Boom for Straight- and Delta-Wing Space Shuttle Orbiters. NASA TM X-62, 030, April 1971.
- 6.123 Hicks, R. M. and Mendoza, J. P.: Wind-Tunnel Pressure Signatures for a Delta Wing Space Shuttle Vehicle. NASA TMX-62,040, May 1971.
- 6.124 Hicks, Raymond M. and Mendoza, Joel P.: Wind-Tunnel Pressure Signatures for a Delta Wing Space Shuttle Vehicle and a Space Shuttle Fuel Tank. NASA TM X-62,119, April 1972.
- 6.125 Hicks, Raymond M. and Mendoza, Joel P.: A Brief Study of the Space Shuttle Sonic Boom during Ascent. NASA TM X-62,050, July 23, 1971.
- 6.126 Mendoza, Joel P.: Wind Tunnel Pressure Signatures for a 0.0041-Scale Model of the Space Shuttle Orbiter. NASA TM X-62,432, May 1975.
- 6.127 Ashby, George C.: New-Field Boom Pressure Signatures for the Space Shuttle Launch and Orbiter Vehicles at Mach 6. NASA TP-1405, April 1979.
- 6.128 Hicks, Raymond M. and Mendoza, Joel P.: An Investigation of the Feasibility of Simulating Gaseous Exhaust Plumes with Solid Bodies in Sonic Boom Studies. NASA TMX-62,62131, 1973.
- 6.129 Marconi, Frank; Salas, Manuel; and Yaeger, Larry: Development of a Computer Code for Calculating the Steady Super/Hypersonic Inviscid Flow Around Real Configurations. Vol. I, Computational Technique. NASA CR-2675, 1976.
- 6.130 Marconi, Frank and Yaeger, Larry: Development of a Computer Code for Calculating the Steady Super/Hypersonic Inviscid Flow Around Real Configurations. Vol. II, Code Description. NASA CR-2676, 1976.
- 6.131 Keyes, J. Wayne and Ashby, George C., Jr.: Calculated and Experimental Hinge Moments on a Trailing-Edge Flap of a 75 Degree Swept Delta Wing at Mach 6. NASA TN D-4268, 1967.
- 6.132 Ashby, George C., Jr. and Helms, Vernon T., III: Flow Field Surveys on the Windward Side of the NASA 040A Space Shuttle Orbiter at 31-Degree Angle of Attack and Mach 20 in Helium. NASA TM X-3560, 1977.
- 6.133 Garcia, Frank J.; Jones, Jess H.; and Henderson, Herbert H.: Correlation of Predicted and Measured Sonic Characteristics from the Reentry of STS-1 Orbiter. NASA TP-2475, 1985.
- 6.134 Maglieri, Domenic J.; Henderson, Herbert R.; Massey, Steven J.; and Stansbery, Eugene G.: A Compilation of Space Shuttle Sonic Boom Measurements. NASA CR2011-217080, April 2011.
- 6.135 Cotton, Donald and Donn, William L.: Sound from Apollo Rockets in Space. Science, Vol. 171, No. 3971, Feb. 12, 1971, pp. 565–567.
- 6.136 Carlson, Harry W. and Mack, Robert J.: A Study of the Sonic-Boom Characteristics of a Blunt Body at a Mach Number of 4.14. NASA TP-1015, 1977.

- 6.137 Ashby, George: A Study of Sonic Boom Characteristics of a Blunt Body at a Mach Number of 6. NASA TP-1787, 1980.
- 6.138 Carlson, Harry W. and Mack, Robert J.: A Wind-Tunnel Study of the Applicability of Far-Field Sonic Boom Theory to the Space Shuttle Orbiter. NASA TP-1186, June 1978.

CHAPTER 7 SONIC BOOM MINIMIZATION FOR VARIOUS AERODYNAMIC CONFIGURATIONS

In this chapter, minimization methods based on the Whitham F-function are discussed, as well as results based on the more complex optimization schemes employing CFD Euler codes. In addition, the utility of having a fast pressure recovery (rapid expansion) following an initial shock as well as embedded shocks is discussed. Also presented in this chapter, in some detail, are the effects of engine nacelles and engine exhausts on sonic booms. Finally, a section in this chapter is devoted to a discussion of the features of numerous supersonic jet concepts proposed and promoted in publications over the years as well as the 300-passenger commercial aircraft designs conceived in the NASA SCAR and HSR programs.

F-Function Boom Minimization

The minimization of sonic boom by theoretical methods started with the development of the first propagation equation and included linear aerodynamics and homogeneous atmosphere techniques. Most researchers credit L. B. Jones (ref. 7.1) with the first analytical approach. It is based on equation (5) of Chapter 6, using the Whitham/Walkden area rule F-function integral. Jones noted that by treating this equation as an Abel integral equation and since $A'_v(x)$ and $L(x)$ are continuous in the range of $0 \leq x \leq l$ its inverse is

$$A''_v(x) + \frac{\beta}{2q_\infty} L'(x) = 2 \frac{d}{dx} \int_0^x \frac{F(y)}{\sqrt{x-y}} dy \quad (1)$$

a = speed of sound

F = source function

M = Mach number = U/a

U = free stream velocity

x, y = axial coordinate parallel to flight path

$$\beta = \sqrt{M^2 - 1}$$

$L(x)$ = lift on a spanwise strip per unit chordwise length

$A'_v(x)$ = longitudinal variation of cross-sectional area

q_∞ = free stream dynamic pressure = $1/2 \rho U^2$

ρ = ambient density

The ' and '' indicate first and second derivatives with respect to x . Note that this methodology is based on the smooth-body form of the F-function.

Integrating equation (1) (which assumes axial symmetry) yields

$$A'_v(x) + \frac{\beta}{2q_\infty} L(x) = 2 \int_0^x \frac{F(y)}{\sqrt{x-y}} dy \quad (2)$$

and when integrated again with respect to x gives

$$A_e(x) = A_y(x) + \frac{\beta}{2q_\infty} \int_0^x L(y) dy = 4 \int_0^x F(y) \sqrt{x-y} dy \quad (3)$$

with the total lift, L , given by

$$L = \int_0^l L(y) dy \quad (4)$$

where l is the length of the aircraft.

Since $A_e(0) = 0$, the left hand side of equation (3) can be designated as the effective area A_e .

Equation (3) is the basis for Jones' (refs. 7.1, 7.2, and 7.3) minimum-boom analyses. Jones (ref. 7.2) determined that the far-field minimum N-wave shock pressure jump for lift at any distance is given by the lift distribution

$$\frac{L(x)}{\rho U^2} = \frac{1}{2\sqrt{l}} \left(\frac{L}{\rho U^2} \right) \frac{1}{\sqrt{x}} \quad (5)$$

except near the origin. For a non-lifting body with a given base area, the area distribution yielding the minimum pressures jump was obtained as

$$A_v(x) = A(l) \sqrt{\frac{x}{l}} \quad (6)$$

The optimum lift and area distributions for other constraints are given in tables 7.1 and 7.2, respectively, from reference 7.2. Optimums for combined lift and area distribution are given in table 7.3 also from reference 7.2.

In these tables, the following additional symbol definitions apply:

V = volume of aircraft

$$J = \int_0^{x_0} F(x) dx$$

x_0 = location of the zero of Whitham's F-function

x_{cp} = location of center of pressure

Table 7.1. Non-Lifting Bodies (ref. 7.2)

Constraints	J	A(l)	Necessary condition
V	$\frac{3}{8} \frac{V}{l^{3/2}}$	$\frac{3}{2} \frac{V}{l^{3/2}} \sqrt{x}$	---
A(l)	$\frac{1}{4} \frac{A(l)}{\sqrt{l}}$	$A(l) \sqrt{\frac{x}{l}}$	---
V,A(l)	$\frac{3}{8} \frac{V}{l^{3/2}}$	$\frac{3}{2} \frac{V}{l^{3/2}} \sqrt{x}$	$3V \geq 2lA(l)$

Table 7.2. Lifting Wing Without Volume (ref. 7.2)

Constraints	J	L(x)	Necessary condition
L	$\frac{\beta}{4\sqrt{l}} \left(\frac{L}{\rho U^2} \right)$	$\frac{L}{2\sqrt{l}} \frac{1}{\sqrt{x}}$	-----
L, x _{cp}	$\frac{3\beta}{16\sqrt{l}} \left(\frac{L}{\rho U^2} \right) (1+x_{cp})$	$\frac{3}{8} \frac{L}{\sqrt{x(l)}} \left(1 + \frac{x_{cp}}{l} \right) + \frac{1L}{8x} \left(\frac{l}{x} \right) \left(\frac{3x_{cp}}{l} - 1 \right)$	$\frac{1}{3} \leq \frac{x_{cp}}{l} \leq 1$
l, x _{cp}	$\frac{3\beta}{8\sqrt{l}} \left(\frac{L}{\rho U^2} \right) (1-x_{cp})$	$\frac{3}{4} \left(\frac{L}{\sqrt{x(l)}} \right) \left(1 - \frac{x_{cp}}{l} \right)$	$\frac{x_{cp}}{l} \leq \frac{1}{3}$

Table 7.3. General Configuration (ref. 7.2)

Constraints	J	Necessary condition
L, V, A(l)	$\frac{1}{4\sqrt{l}} \left[A(l) + \frac{\beta}{\rho U^2} L \right]$	$\frac{x_{cp}}{l} = \frac{1}{3} + \frac{V \rho U^2}{\beta l} \frac{2A(l) \rho U^2}{3 \beta L}$
L, A(l)	$\frac{1}{4\sqrt{l}} \left[A(l) + \frac{\beta L}{\rho U^2} \right]$	-----
L, x _{cp} , A(l)	$\frac{1}{4\sqrt{l}} \left[A(l) + \frac{\beta}{\rho U^2} L \right]$	$V = \frac{2}{3} l A(l) + \frac{\beta l L}{3 \rho U^2} \left(3 \frac{x_{cp}}{l} - 1 \right)$
L, V	$\frac{1}{4\sqrt{l}} \frac{\beta L}{\rho U^2}$	$A(l) = 0; x_{cp} = \frac{1}{3} + \frac{V \rho U^2}{\beta l L}$
L, x _{cp} , V, A(l)	$\frac{3}{8l^{3/2}} \left[V + \frac{\beta L}{\rho U^2} \left(1 - \frac{x_{cp}}{l} \right) \right]$	$V \geq \frac{2}{3} l A(l) + \frac{1}{3} \frac{\beta l L}{\rho U^2} \left(3 \frac{x_{cp}}{l} - 1 \right)$
L, x _{cp} , V, A(l)	$\frac{3}{16l^{3/2}} \left[2lA(l) - V + \frac{\beta l L}{\rho U^2} \left(1 + \frac{x_{cp}}{l} \right) \right]$	$V \leq \frac{2}{3} l A(l) + \frac{1}{3} \frac{\beta l L}{\rho U^2} \left(3 \frac{x_{cp}}{l} - 1 \right)$
L, x _{cp} , V	$\frac{3}{8l^{3/2}} \left[V + \frac{\beta l L}{\rho U^2} \left(1 - \frac{x_{cp}}{l} \right) \right]$	$V \geq \frac{1}{3} \frac{\beta l L}{\rho U^2} \left(3 \frac{x_{cp}}{l} - 1 \right)$
L, x _{cp} , V	$\frac{3}{16l^{3/2}} \left[\frac{\beta l L}{\rho U^2} \left(1 + \frac{x_{cp}}{l} \right) - V \right]$	$V \leq \frac{1}{3} \frac{\beta l L}{\rho U^2} \left(3 \frac{x_{cp}}{l} - 1 \right)$

Jones's minimization results are for far-field booms. With N-waves considered to be inevitable, his near-field signatures are in the form of delta function pulses, so that shock waves would quickly form. This exploited the dissipation of energy by the shocks and their higher decay rate of $1/r^{3/4}$ versus $1/r^{1/2}$ for isentropic acoustic waves. However, while shock and/or impulse could be minimized, this class of signatures would have shocks that were not expected to be acceptable to the public.

A major conceptual advance occurred in 1965 when Mclean (ref. 7.4) pointed out that the boom from a large aircraft flying at normal operational altitude in the real atmosphere would not reach asymptotic far-field conditions. The boom would thus not necessarily be an N-wave, so that shapes other than N-waves became possible. The concept of mid-field shaped booms was born.

Figure 7.1 shows a range of the types of mid-field signatures that could be considered if the goal is to reduce shock overpressure. Compared to a regular N-wave shown in figure 7.1(a), Jones's solutions yielded N-waves with lower peak pressures (figure 7.1(b)). A sine-like boom shown in figure 7.1(c) would remove the audible high frequency energy. While shock formation may be avoidable, aging tends to generate signatures with linear segments. Therefore, a signature like the shockless boom shown in figure 7.1(d) may be more feasible to generate. If a shock is unavoidable, minimum shock (figure 7.1(e)) or flat-top (figure 7.1(f)) booms are expected to be favorable. Psychoacoustic experiments reviewed in Chapters 8 and 9 have shown that shaped booms, particularly ramp (shockless or minimum shock) are indeed quieter than N-wave booms.

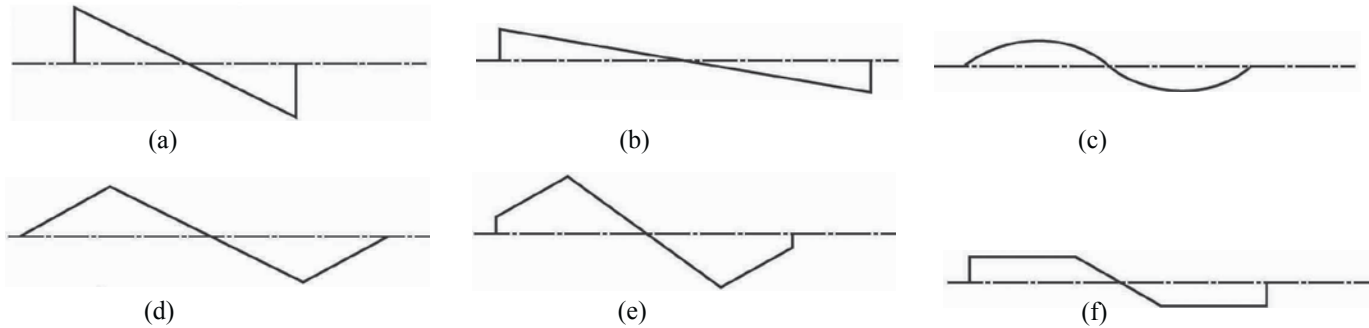


Figure 7.1. Ground overpressure signatures.

Another significant advancement occurred in the late 1960s, when George (ref. 7.5) developed a basic quantitative approach to minimized shaped-boom design. He noted that Jones's delta function solution for a minimum asymptotic N-wave was optimal at any N-wave distance. Once that existed, there could be a further pressure signature behind this solution as shown in figure 7.2. In the figure, Λ is the age parameter, F_1 and F_2 are the F-function values at those two points, I_0 is the positive impulse of the pressure signature t , t_0 , and T_0 are time, and τ is the shock rise time.

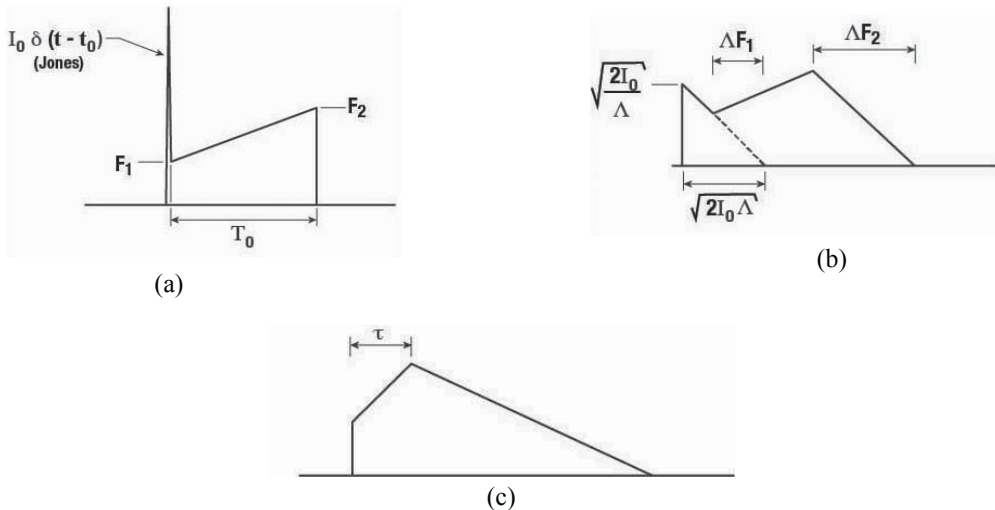


Figure 7.2. Aging of a Spiked Ramped Signature (adapted from ref. 7.5).

The signature at the aircraft begins with a spike according to Jones' N-wave solution as shown in figure 7.2(a). There can be an additional signature behind this solution, but with compression regions having small enough slopes such that they will not steepen into shocks. When the signature is partially aged as shown in figure 7.2(b), the spike has steepened into a partial N-wave, with the expansion of the partial N-wave sketched as a dashed line. At the fully aged design point (fig. 7.2(c)), the bow spike has decayed to match the isentropic wave behind it and the forward part of a ramp minimum shock boom has evolved.

George and Seebass completed the theory with the aft part of the boom and showed that their solution yielded the minimum possible shock pressures for a given weight aircraft (refs. 7.6, 7.7, and 7.8) with the optimal F-function given by equation (7a) and sketched in figure 7.3 (ref. 7.8).

$$F(y) = \begin{cases} A\delta(y) + By + C, & 0 \leq y \leq \lambda \\ By - D, & \lambda \leq y \leq l \end{cases} \quad (7a)$$

Here A , B , C , and D are constants yet to be determined and $\delta(y)$ is the delta function. The corresponding equivalent area development using equation (3) is

$$A_e(x) = 4Ax^{1/2} + \frac{15}{16}Bx^{5/2} + \frac{8}{3}Cx^{3/2} - l(\lambda) \frac{8}{3}(C + D)(x - \lambda)^{3/2} \quad (7b)$$

where $l(\lambda)$ is the unit step function.

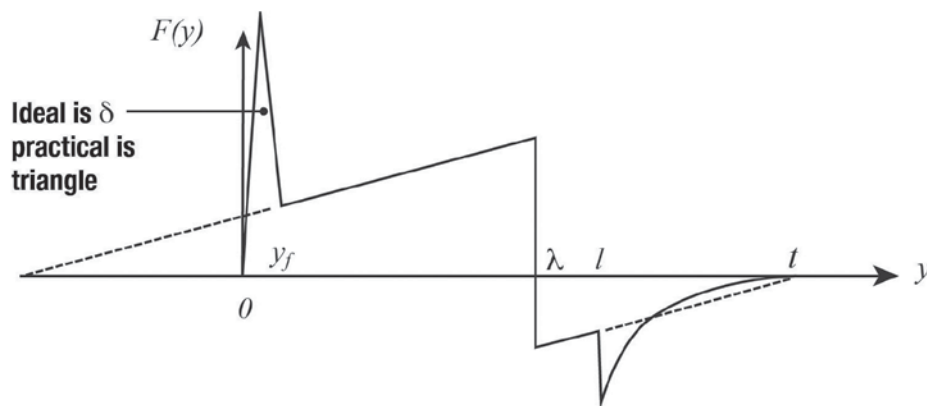


Figure 7.3. Whitham F-function for minimizing various signature parameters (adapted from ref. 7.8).

A key part of their solution was that the F-function was defined algebraically as shown in equation (7a). When this solution was applied to the inverse Abel transform (equation (3)), the result is also algebraic as shown in equation 7(b).

Mid-field shaped methodology became the workhorse of boom minimization and was used and extended in studies such as references 7.9, 7.10, and 7.11. Reference 7.9 includes an excellent review of minimization studies from the 1960s through the early 1970s, spanning the time from before the concept of shaping through the first few years of the George-Seebass Theory. Darden's Reference 7.10 contains a practical application of the methodology and serves as the basis of systematic shaping studies.

The methodology of Darden (ref. 7.10) has the ability to define either flat-top or ramp pressure signatures for a real atmosphere. Figure 7.4 (ref. 7.10) depicts the effective area distribution, F-function, and pressure signature and associated quantities that must be specified or determined.

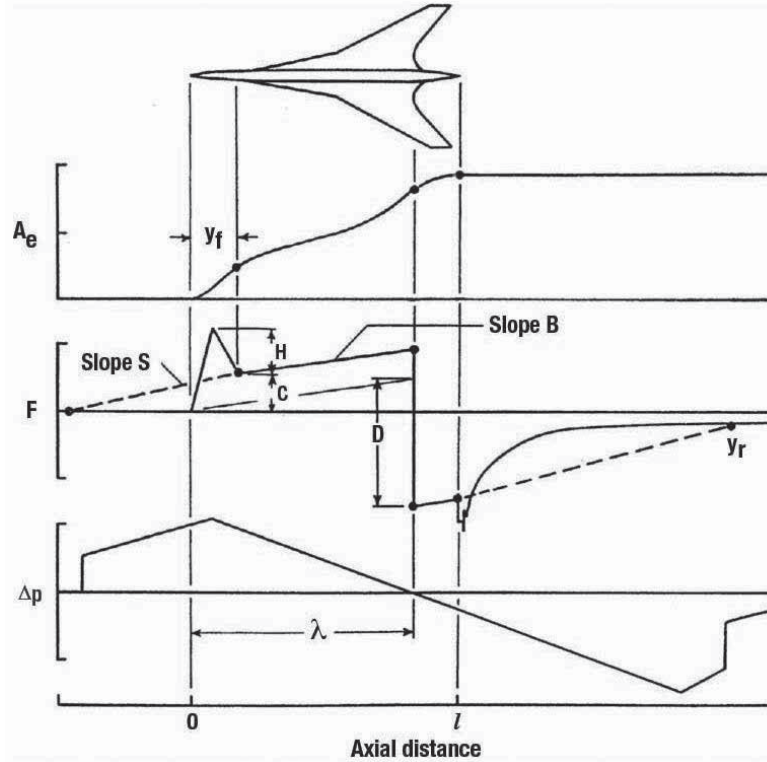


Figure 7.4. Illustration of the theoretical concepts of near-field sonic boom (ref. 7.10).

Darden’s F-function is defined below, where for $B = 0$ a flat-top signature results, and for $B \neq 0$ a ramp-type signature or N-wave may result, depending on the values of l , y_f and H .

$F(y)$	y	
$2yH/y_f$	$(0 \leq y \leq y_f/2)$	(7a)
$(2y/y_f - 1) - H(2y/y_f - 2)$	$(y_f/2 \leq y < y_f)$	(7b)
$B(y - y_f) + C$	$(y_f \leq y < l)$	(7c)
$B(y - y_f) - D$	$(l \leq y < l)$	(7d)

In these equations, H , B , C , D , and l are unknown coefficients, which are determined by the cruise conditions of the aircraft, by nose length, by the prescribed ratio of bow to rear shock strength, and by the type of signature being minimized.

Substituting equations (7) for the F-function into equation (3) for A_e yields

$$\begin{aligned}
 A_e(x) = & \frac{32H}{15y_f}x^{5/2} - 1\left(x - \frac{y_f}{2}\right)\frac{16}{15}\left(x - \frac{y_f}{2}\right)^{5/2}\left(\frac{2H-C}{y_f/2}\right) \\
 & + 1(x - y_f)\frac{16}{15}(x - y_f)^{5/2}\left(\frac{2H-2C}{y_f} + B\right) - 1(x - l)\frac{8}{3}(x - l)^{3/2}(C + D)
 \end{aligned}
 \tag{8}$$

where $I(x - y_f/2)$ and $I(x - y_f)$ and $I(x - l)$ are Heaviside unit step functions.

A critical parameter is the width of the forward spike, y_f , and its effect on the initial pressure jump, impulse, and drag. Figure 7.5 from reference 7.10 shows that as y_f is increased, drag goes down and the flat-top pressure levels, and ramp maximum pressures increase. For the conditions given in the legend of figure 7.5, most of the drag benefits are realized by the time y_f/l has reached a value of 0.05. It should be noted that reference 7.10 also includes a description of a computer code that calculates the Whitham F-function and the corresponding equivalent area distribution, which produce the minimum overpressure (flat-top) or minimum-shock (ramp) signatures.

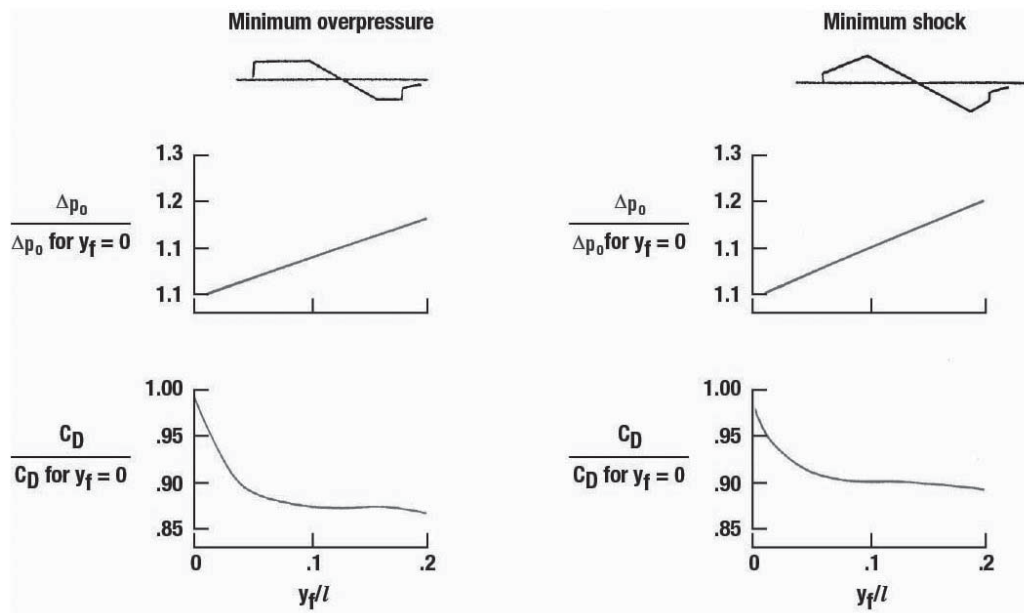


Figure 7.5. Estimated drag increments associated with configuration changes for sonic boom minimization. Mach = 2.7, $h = 18,288 \text{ m}$ (60,000 ft), $W = 272,155 \text{ kg}$ (600,000 lbs), $l = 91.44 \text{ m}$ (300 ft) (ref. 7.10).

The results given in figure 7.5 are for an altitude, $h = 60,000$ feet, and an aircraft length of $l = 300$ feet or an h/l of 200. A 100-foot long aircraft flying at an altitude of 50,000 feet yields an h/l of 500. Few papers present results for h/l values beyond 300. The work of Hague and Jones (ref. 7.12) is an exception. Figure 7.6 (ref. 7.12) shows that as h/l increases, the shape of body that produces the minimum pressure jump changes.

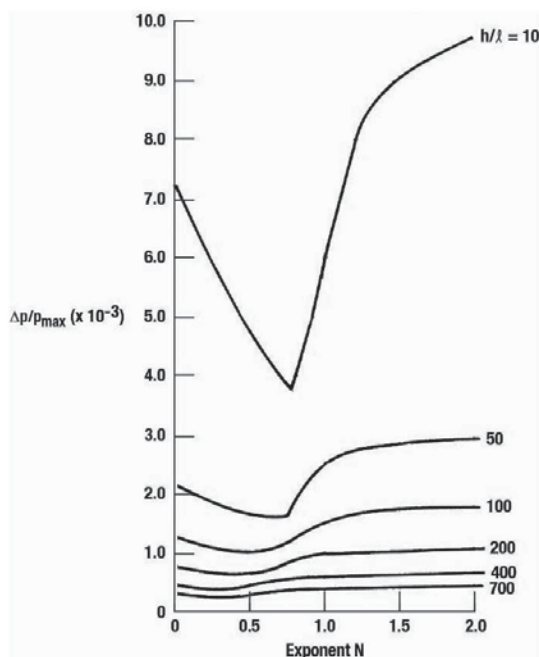


Figure 7.6. Effect of distance on single power arc solutions with length and base constrained, Mach = 2.2 (ref. 7.12).

For power law bodies (i.e., $r = Ax^N$), the exponent N that yields the minimum Δp decreases from ~ 0.75 at an h/l of 10 to ~ 0.3 at an h/l of 700. Of course, Mach number as well as the constraints imposed will have an effect on the minimum shape. Clearly for configurations on the order of 100-foot length, like small business jets, and with h/l values approaching 500, this is a phenomenon that needs to be understood and used to the greatest advantage.

An even further modification of the optimum F-function, which might be termed a hybrid, was made by Haglund and Mack (refs. 7.13 and 7.14), as shown in figure 7.7, that has both flat-top and ramp features following the initial shock. The effect of hot and cold days on the length of the nose spike to achieve a given pressure level behind the initial shock is discussed in reference 7.14. Additional modifications to this initial area development (nose geometry) are given by Mack in reference 7.15, which illustrates the options available using the F-function for maintaining a near-optimum pressure distribution.

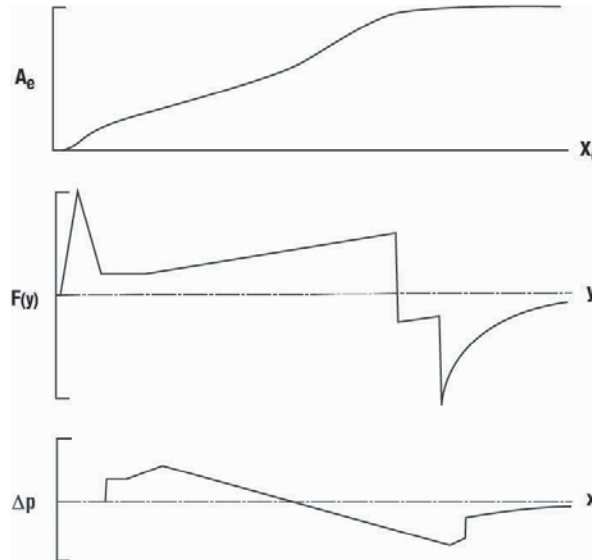


Figure 7.7. Haglund-modified equivalent areas, F-function, and pressure signature (adapted from ref. 7.13).

The Rapid Pressure Recovery/Expansion

Referring back to equations (5) and (6), we see that the derivative of $A_v(x)$ (i.e., $dA_v(x)/dx$ from equation (6) and $L(x)$ from equation (5) of Jones' minimum boom analysis both have the same behavior. The front-loaded lift distribution (eq. (5)) and the blunt body (eq. (6)) resulting from this behavior yield a strong shock followed by a rapid recovery/expansion. This has certain advantages as can be seen from the pressure jump equation from Thomas (ref. 7.16) for a uniform atmosphere where Δp varies inversely as m , the rate of change of pressure recovery/expansion. Clearly, the more negative the value of m (note that m is negative in the sketch of fig. 7.8) the faster the pressure jump decreases. This same phenomenon applies for embedded shocks as well, such as those from a nacelle or inlet shock.

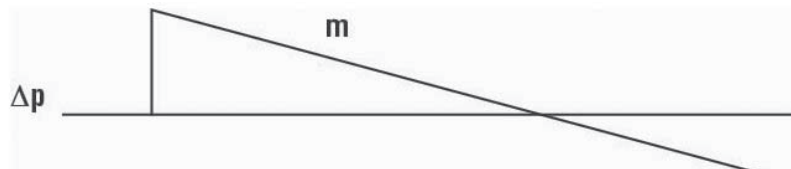


Figure 7.8. Typical N-wave sonic boom.

Aside from the advantage of a rapid shock-strength reduction, the fast recovery of an embedded shock also reduces its ability to move forward and coalesce with the bow shock. Hicks and Thomas (ref. 7.17) studied this effect along with the effect of several other parameters on shock coalescence using the uniform atmosphere equations of reference 7.16. Figure 7.9 shows the faster the pressure recovery of the wing shock, the lower the convergence with bow shock.

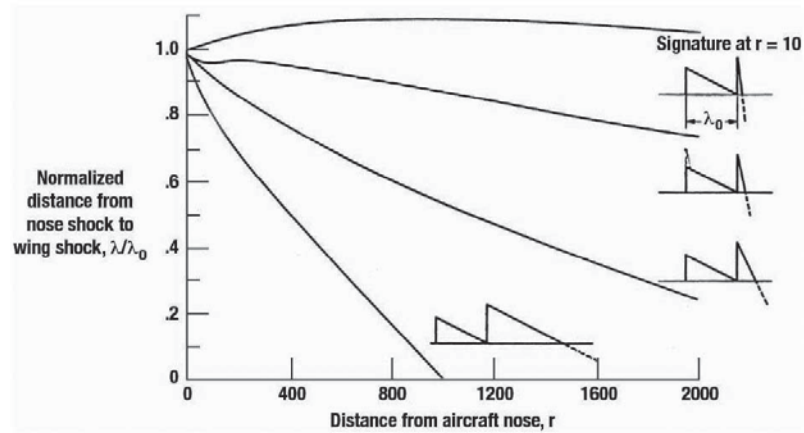


Figure 7.9. Effect of slope behind wing shock on coalescence, Mach = 3 (adapted from ref. 7.17).

Minimization of Sonic Boom Using Various Optimization Schemes

The minimization of sonic booms using F-function methodology was discussed in the previous section of this chapter and will be addressed to a lesser degree in the next section, entitled “The Effect of Engine Nacelles on Sonic Booms”. While sonic booms can be minimized using F-function methodology and effective area distributions, they are calculated and minimized more precisely using the Euler-equations, real aircraft geometries, and a mathematical optimization technique. However, there are studies that use an optimizer in combination with the F-function and linear-lifting methodology, or Euler-equation, flow-field solutions. Numerous papers have been published over the past decade using these approaches. Some of these papers will be discussed in the following pages.

One of the first studies to use the Euler equation, along with an optimizer, also utilized the F-function (see ref. 7.18). However, the optimization technique, named NPSOL (see ref. 7.19), did not operate directly on the configuration’s geometry but on the F-function, defined initially by nine variables. The number was later increased from 9 to 10 variables because the flat-top F-function originally sought was not feasible with the volume constraints imposed. Consequently, a combination flat-top and ramp F-function was required. This type of F-function is plotted and the segments labeled in figure 7.10.

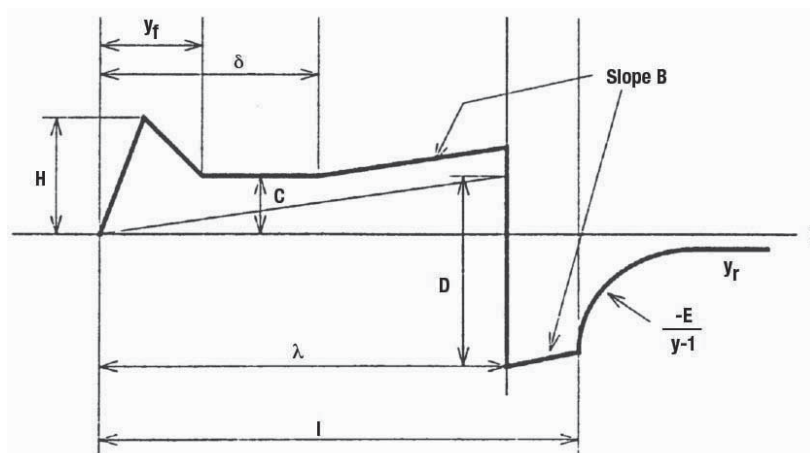


Figure 7.10. Combination flat-top and ramp signature (ref. 7.18).

In Cheung’s method (ref. 7.18), the F-function is extracted from the near-field pressure signature (usually at one body length) and the associated effective-area distribution from this F-function. The procedure was applied to the Boeing 911 configuration shown in figure 7.11 with the wing geometry fixed.

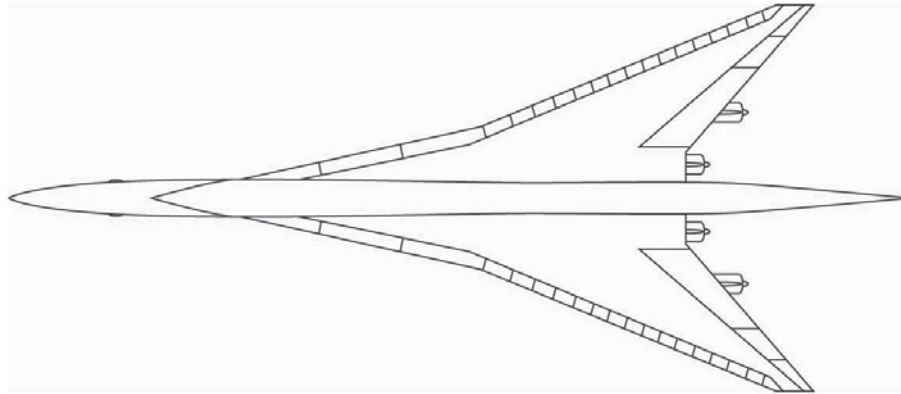


Figure 7.11. Boeing 911 configuration (ref. 7.18).

Thus, the fuselage area distribution was actually the target of the optimization. Figure 7.12 gives a plot of the original effective area distribution and the one that resulted from the optimization procedure (modified). A similar optimization could have been done with the lift distribution using camber as a variable.

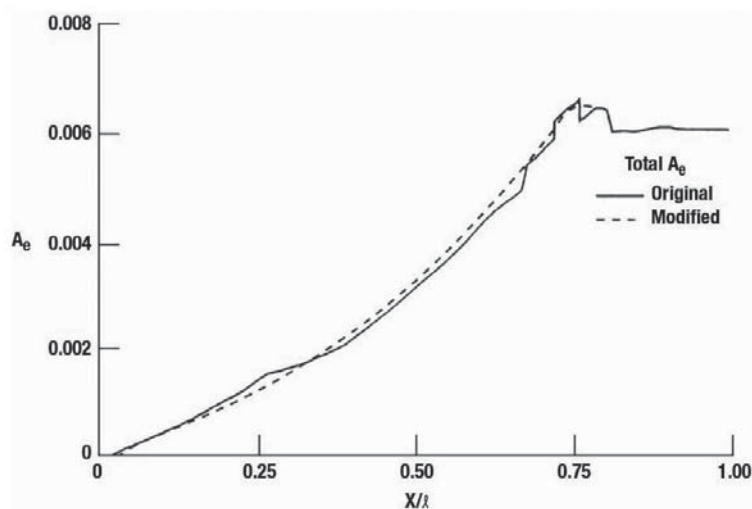


Figure 7.12. Equivalent area distributions for original and modified Boeing 911 configuration (ref. 7.18).

The sonic boom improvement that resulted from the modification to the A_e distribution is evident in the plot of figure 7.13. It shows that the second shock at a time of ~ 0.12 second has been eliminated and a near flat-top signature was achieved.

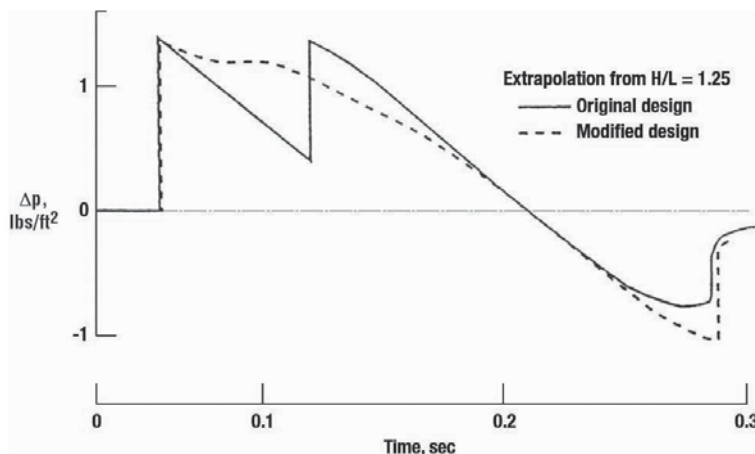


Figure 7.13. Original and modified sonic boom signatures for the Boeing 911 configuration, $h/l = 133$, $Mach = 1.7$, $\alpha = 4.0^\circ$, Altitude = 44,000 ft (adapted from ref. 7.18).

The optimizer NPSOL (ref. 7.19) was used by Siclari (ref. 7.20) where fuselage volume and camber distributions were optimized for four different configurations. The Euler calculations were carried out by a very efficient multi-block three-dimensional finite volume marching code (MIM3DSB). In addition, as noted in reference 7.20 and later in this chapter, a unique grid topology is used to accurately capture shocks several body lengths downstream of the aircraft. Additional details of MIM3D are given in reference 7.21. Once the pressures are determined, those below the aircraft become input to a waveform parameter propagation code (ref. 7.16) that extrapolates these near-field signatures to the ground through a specified atmosphere.

The design system used in reference 7.20 for optimizing one or more geometric features of an aircraft concept is depicted in figure 7.14. This system seeks to minimize the objective function in terms of its derivative and not the function itself. There may be local minima, which may not be the best solution, and there may be cases when the solutions are not smooth. Therefore, there has to be operator involvement, particularly in selecting and changing the initial estimate. Cubic splines are used to describe the geometric design variables such as fuselage volume distribution or camber. The number of design variables might be as little as three or as many as 15. The gradient based optimization method will require one or two evaluations of the objective function for each design variable depending upon whether one-sided or central derivatives are used to evaluate the objective function gradients. Hence, for example, if 10 design variables are used, the design methodology will require 10 to 20 CFD runs to evaluate the objective function gradients. If 10 global iterations of the design method are implemented, this could add up to 100 to 200 CFD runs.

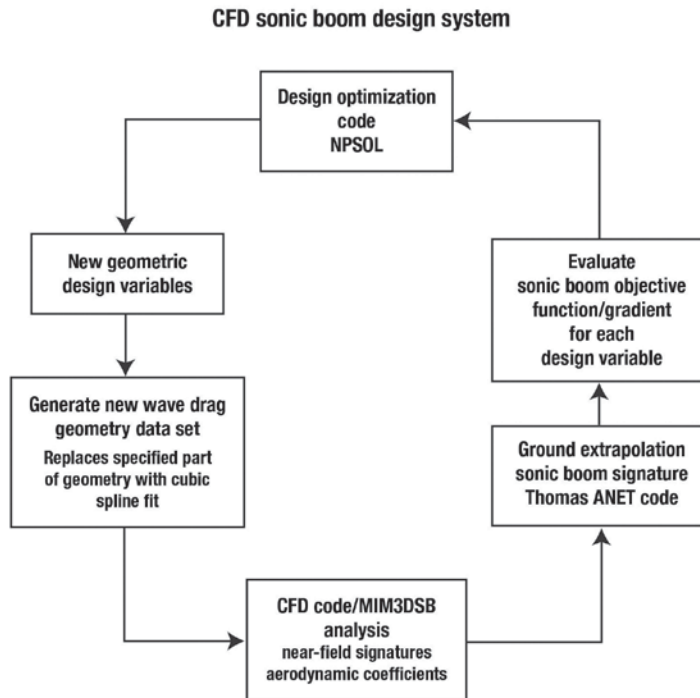


Figure 7.14. CFD sonic boom design system (ref. 7.20).

One of the four configurations analyzed in reference 7.20 was the LB18-10B, pictured in figure 7.15. It was designed using F-function techniques to have a ramp sonic boom signature when cruising at Mach 1.8 and at an altitude of 48,600 feet. When subjected to CFD analysis, the near-field pressure signatures in figure 7.15 are the result. These signatures, for h/l values of 0.5, 1.0, and 2.0 are also used to produce the ground sonic boom signatures shown on the right side of the figure. Clearly, these signatures are not ramp type, although the pressure level is comparable to that of the target ramp signatures.

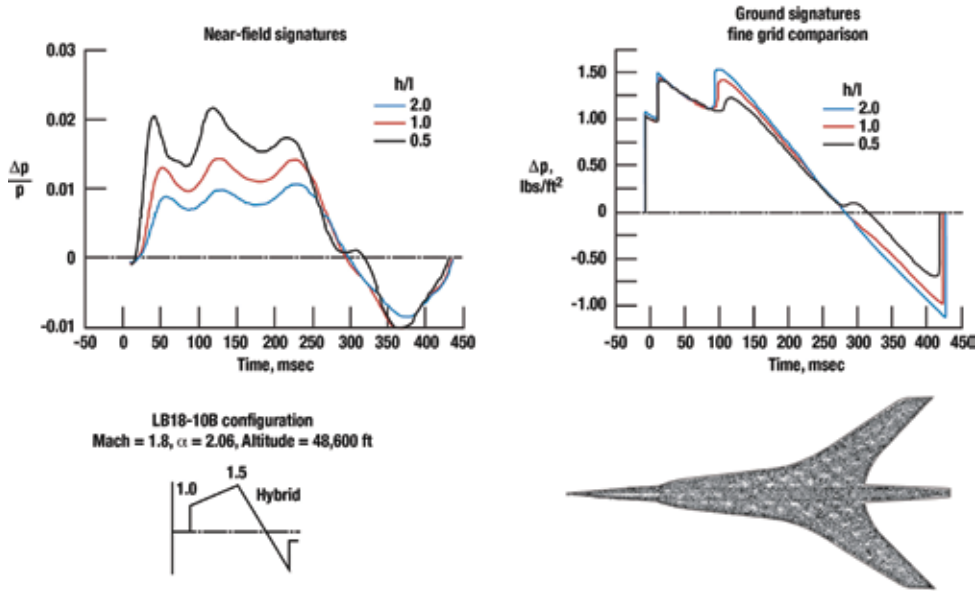


Figure 7.15. CFD analysis of near-field and extrapolated ground signatures for the LB18-10B (adapted from ref. 7.20).

Four separate design computer runs were made using different fuselage stations and target ramp pressures (see figure 7.16). Overall, these design runs required over 100 CFD runs. Fuselage cross-sections are ellipses and the major and minor axes were design variables. The starting or initial signature for each run, along with the final signature and the target ramp signatures, are plotted for each run. Run 4 resulted in an excellent wavy approximation of the target ramp.

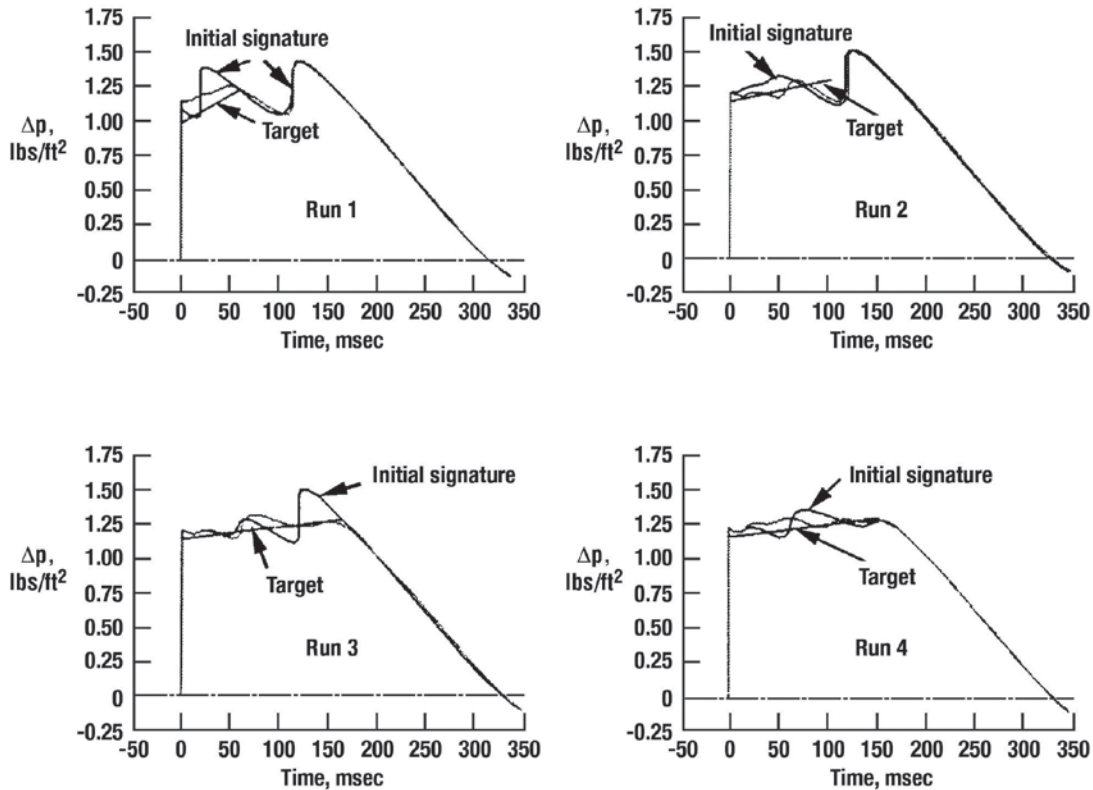


Figure 7.16. Fuselage volume modifications and target signatures for the LB-18-10B configuration (adapted from ref. 7.20).

Due to computation time, the grid used for the production runs was not the finest possible. So, a finer grid calculation of the run 4 configuration was performed. Sonic booms using the near-field signatures at $h/l = 1.0$ and 2.0 for the finest grid are shown in figures 7.17 and 7.18. In figure 7.17 for an h/l of 1.0 , the finest grid calculation is compared to the one using the production or design grid.

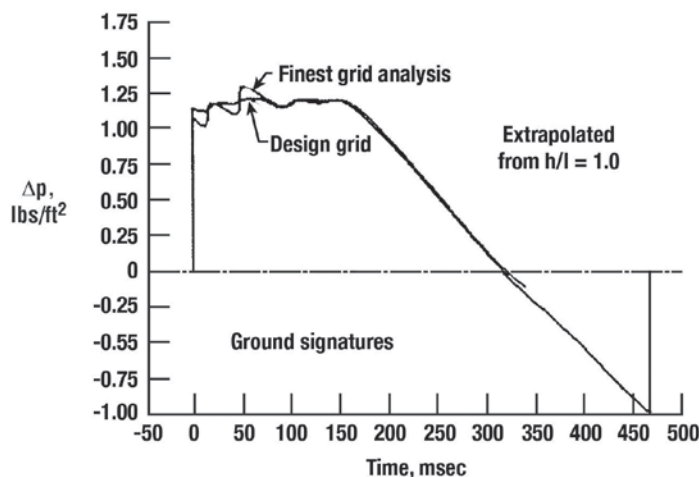


Figure 7.17. Comparison of ground signatures for crude design and fine grid analysis of modified LB18-10B extrapolated from $h/l = 1.0$, $M = 1.80$, $\alpha = 2.06^\circ$, Altitude = 48,000 ft (ref. 7.20).

Note that the finest grid analysis yields higher amplitude oscillations than that of the lower resolution design grid. Nevertheless, they are smaller in amplitude than that of the original signatures (see fig. 7.18) and, consequently, are a better approximation of the target ramp signature. Thus, the optimization procedure did reduce the magnitude of the sonic boom produced by the LB18-10B configuration. Similar results are given in reference 7.20 for the other configurations.

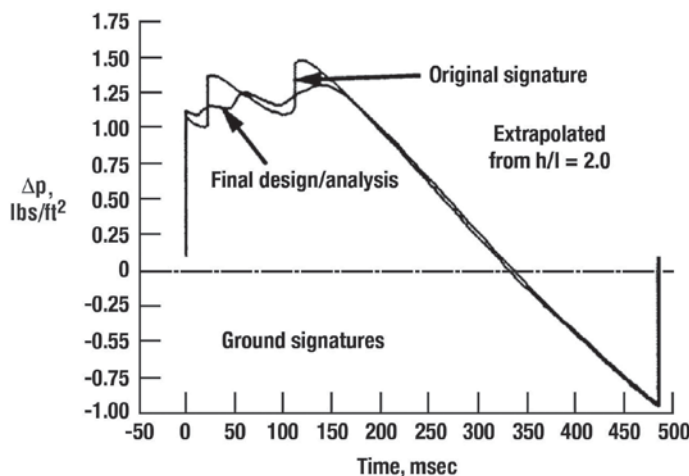


Figure 7.18. Comparison of ground signatures for modified and original LB18-10B configuration extrapolated from $h/l = 2.0$ (adapted from ref. 7.20).

The F-function was also used in reference 7.22 by Makino et al. to provide an optimum target near-field pressure at an h/l of 2.0. The axial distribution of fuselage radii is perturbed in their scheme to minimize the difference in the calculated and target near-field pressures. The near-field flow calculations were made using a fully 3-D Euler CFD code. The optimization method is based on the least-squares technique of Lee and Eyi (ref. 7.23). The low-boom configuration fuselage depicted in figure 7.19 is the prime subject of the minimization effort, particularly the aft part.

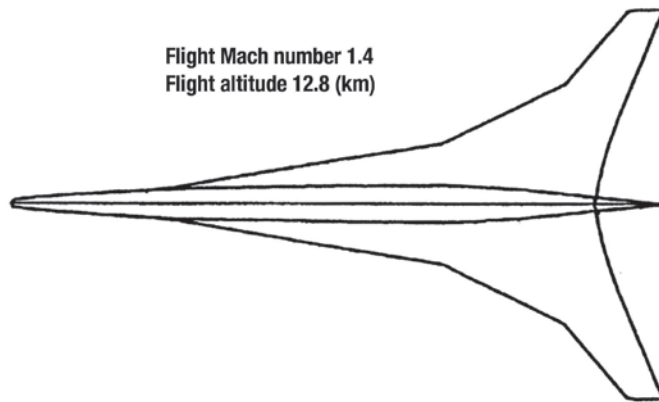


Figure 7.19. Low-boom configuration (ref. 7.22).

Initially, this configuration had an equivalent area distribution close to the designed optimum and where the small differences from the optimum are beyond an x of 70 meters (see fig. 7.20).

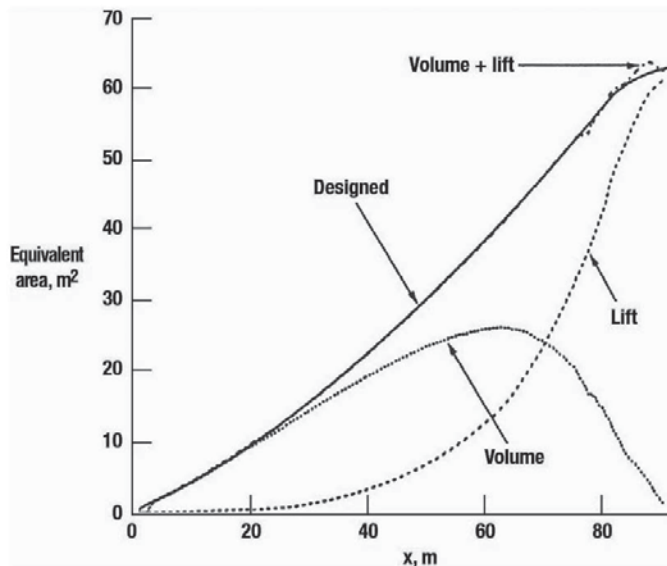


Figure 7.20. Equivalent distributions (ref. 7.22).

However, the shock they produced at a time of ~ 125 msec on the ground signature (see fig. 7.21) is far from optimum. Application of the minimization process eliminated this shock and resulted in the near flat-top optimized ground signature shown in figure 7.21.

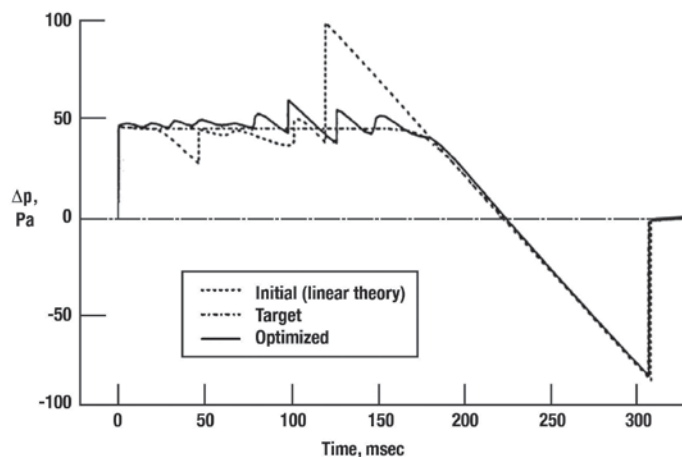


Figure 7.21. Optimized ground pressure signature (adapted from ref. 7.22).

The equivalent area that resulted from the optimization (volume plus lift) is plotted in figure 7.22 and shows an increase in the area of the fuselage over most of its length. Figures 7.21, 7.22, and 7.23 demonstrate that there are effects that F-function methods do not account for that must be overcome to achieve a real optimum. Thus, the nonlinear Euler equations, when coupled to an optimization scheme with the necessary logic, can produce a more realistic low-boom configuration.

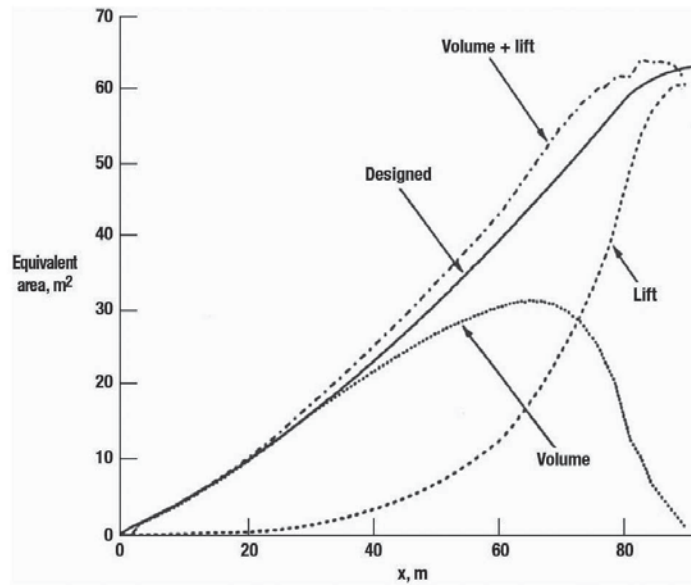


Figure 7.22. Optimized equivalent-area distributions (ref. 7.22).

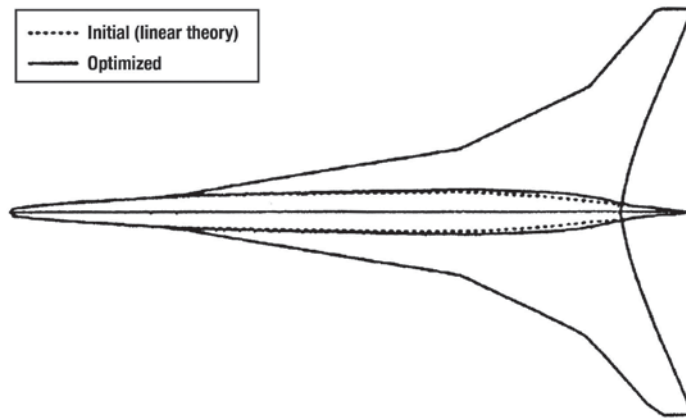


Figure 7.23. Optimized fuselage geometry (ref. 7.22).

Makino et al. (ref. 7.22) also applied the least-squares optimizer to a simple delta-wing/body configuration with excellent results. Finally, loudness calculations were made for the initial and optimized ground pressure signatures of the low-boom configuration, which showed a 2dBA reduction (77.4 versus 79.4) for the latter.

An entirely different optimization scheme is used in reference 7.24 to reduce the sonic boom of a slightly swept wing configuration appropriate for a supersonic business jet. An adjunct method is used that was originally developed (see ref. 7.25) to optimize the shape, pressure distribution, and associated aerodynamic coefficients of a configuration. It was later extended in reference 7.26 to calculate non-co-located sensitivities. It is this capability that was applied in reference 7.24 to the sonic boom reduction problem. The remote inverse adjunct approach developed in reference 7.24 modifies the true geometry not by altering its planform but its current shape grid point by grid point. Gradients are calculated for each point on the surface of the wing and fuselage, and modifications are made based upon a simple steepest descent algorithm.

The business jet configuration studied is shown in figure 7.24. As stated in reference 7.24 (p. 5),

It was sized to accommodate between 6 to 8 passengers with a gross takeoff weight of 100,000 pounds and a fuselage length of 100 feet. The supersonic flight condition at which all designs were calculated is Mach 1.5. The fuselage is cylindrical and the maximum diameter occurs at 31% measured from the nose of the fuselage. The wing has a biconvex wing section with a 7.125 degrees leading edge sweep, an aspect ratio of 3.0 and a taper ratio of 0.218.

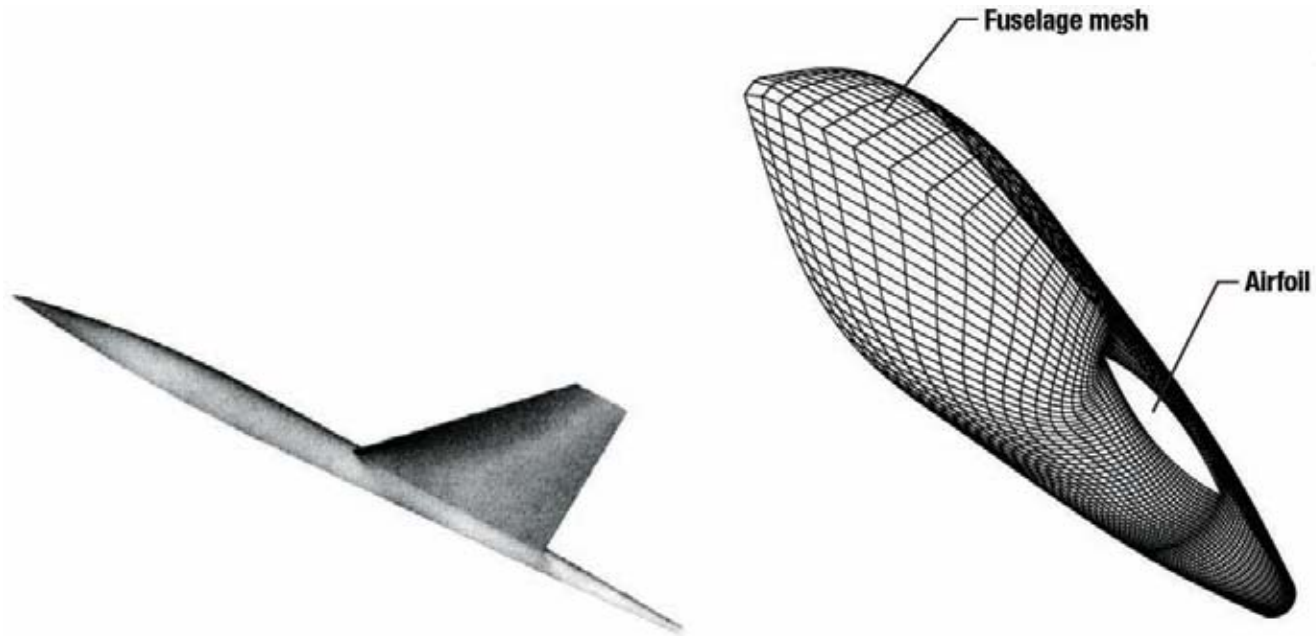


Figure 7.24. Business jet configuration studied in reference 7.24.

The flight altitude was not given, but based on some of the discussions, is probably around 50,000 feet. As stated in reference 7.24 (p. 6),

The root airfoil is a 3% thick biconvex airfoil and the tip is 1.5%. The biconvex profile in the center sections was obtained by interpolating between the root and tip. The airfoils were constructed to accommodate thick spars at the 10 and 80% chord locations. The baseline wing does not have geometric twist. The computational mesh has eight blocks with 193x49x33 nodes on a C-H grid. The fuselage has 25 points in the cross-streamwise direction and 144 points in the streamwise direction. The wing contains 97 points in the streamwise direction and 17 sectional cuts in the spanwise direction.

Calculations were made with and without a lift constraint. The target pressure distribution was obtained by re-scaling the initial calculated near-field pressure distribution. Figure 7.25 shows the initial and final wing-root airfoil geometries for the unconstrained lift case. However, the wing thickness is constrained. To maintain the wing thickness distribution, the upper surface profile is modified to maintain the spar locations at the 10 percent and 80 percent chord locations. At the end of each design cycle, the minimum permissible thickness constraint is imposed at each chordwise cut between the 10 percent and 80 percent chord locations.

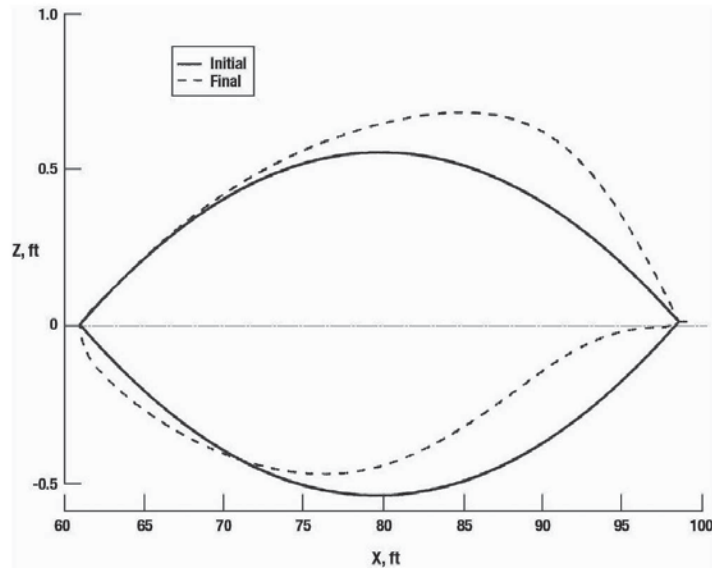


Figure 7.25. Initial and final root airfoils at $M = 1.5$ (adapted from ref. 7.24). Note the difference in ordinate and abscissa scales.

The shape modifications, illustrated by the root airfoil modification in figure 7.25, yield a 40 percent reduction in the wing shock and a 35 percent reduction in the trailing shock of the near-field pressure distribution shown in figure 7.26. Different scales are used for the ordinate and abscissa in figure 7.25 to better show the shape change. On the ground (fig. 7.27), there is about a 23 percent reduction in the wing shock. Since lift is not constrained, C_L is reduced from 0.1 to 0.073. When the wing lift coefficient is constrained at a value of 0.1, the geometry modification that results is less than that for the unconstrained lift (as seen in fig. 7.28). However, figure 7.29 shows that the fuselage near-field peak pressure has been reduced by almost 18 percent of its initial value. The wing peak pressure was reduced by 22 percent as opposed to the 4 percent reduction in the unconstrained case. With the wing lift coefficient constrained at 0.1, the angle of attack rose from 1.62° to 2.39° and the drag coefficient increased from 0.00568 to 0.00574. Modest decreases on the order of 10 percent were obtained for the fuselage, wing, and trailing shocks of the ground signature (see fig. 7.30).

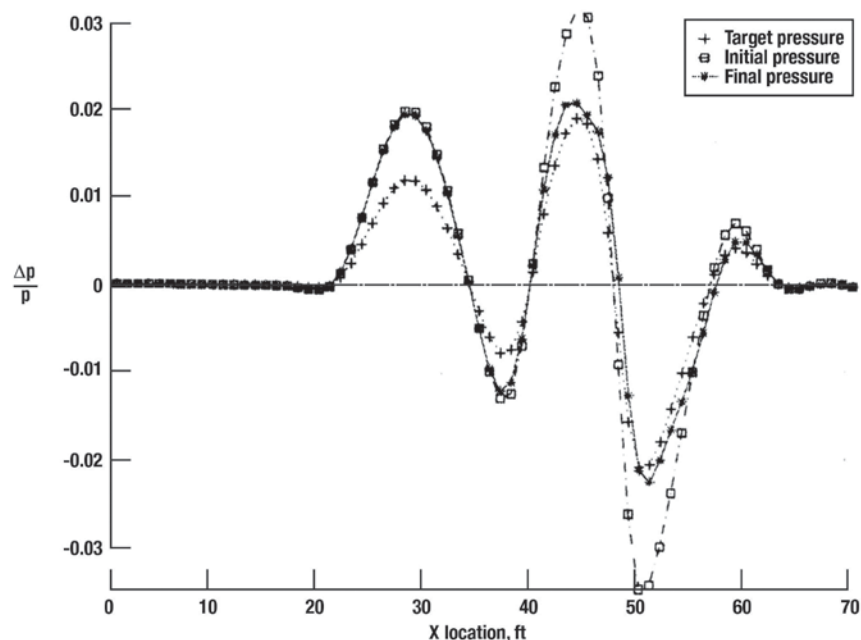


Figure 7.26. Sonic boom reduction: target, initial, and final near-field pressure distribution after 50 design cycles, $Mach = 1.5$, $\alpha = 1.62$ deg, lift not constrained (adapted from ref. 7.24).

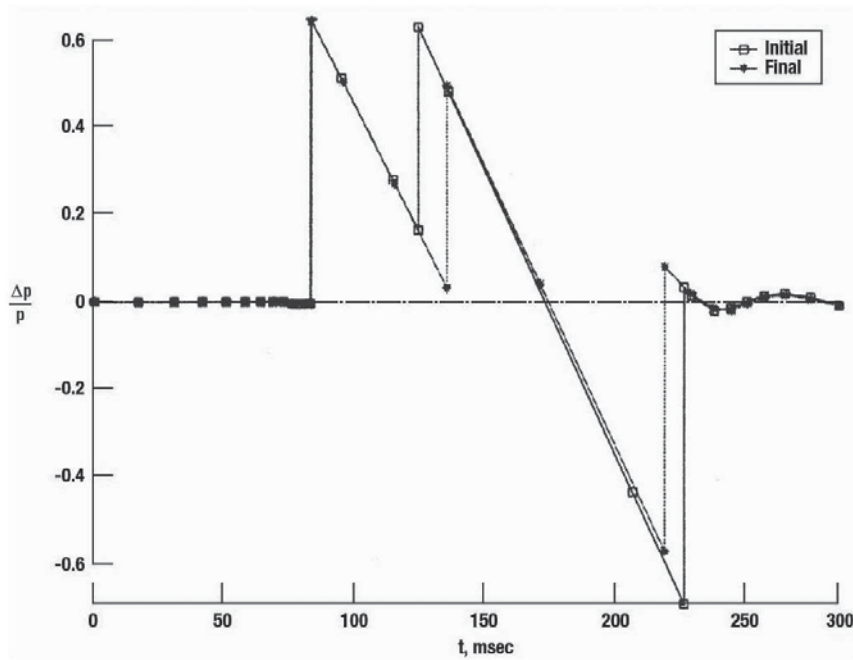


Figure 7.27. Sonic boom reduction: initial and final ground signatures after 50 design cycles, Mach = 1.5, $\alpha = 0^\circ$, lift not constrained (adapted from ref. 7.24).

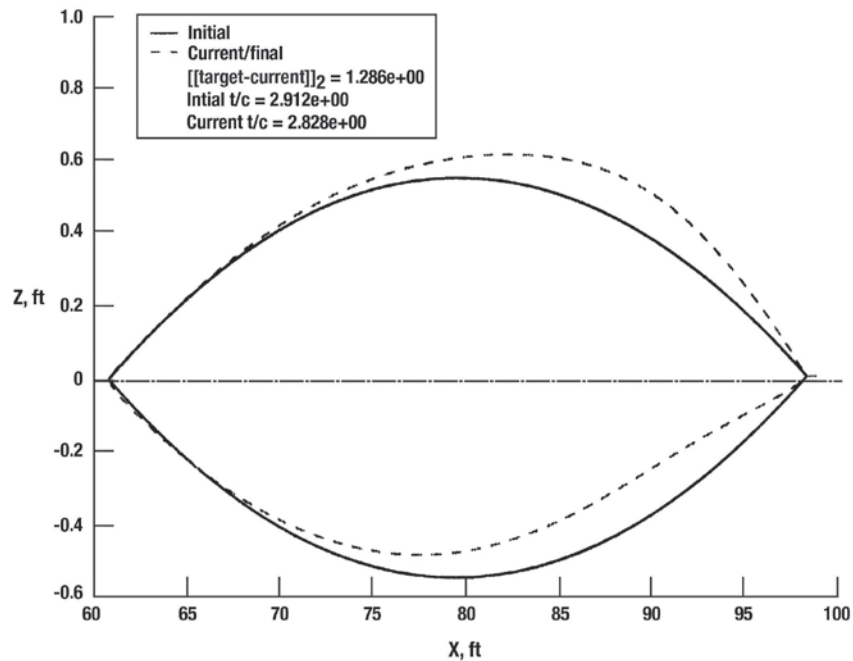


Figure 7.28. Initial and final root airfoils, Mach = 1.5 (adapted from ref. 7.24). Note the difference in ordinate and abscissa scales.

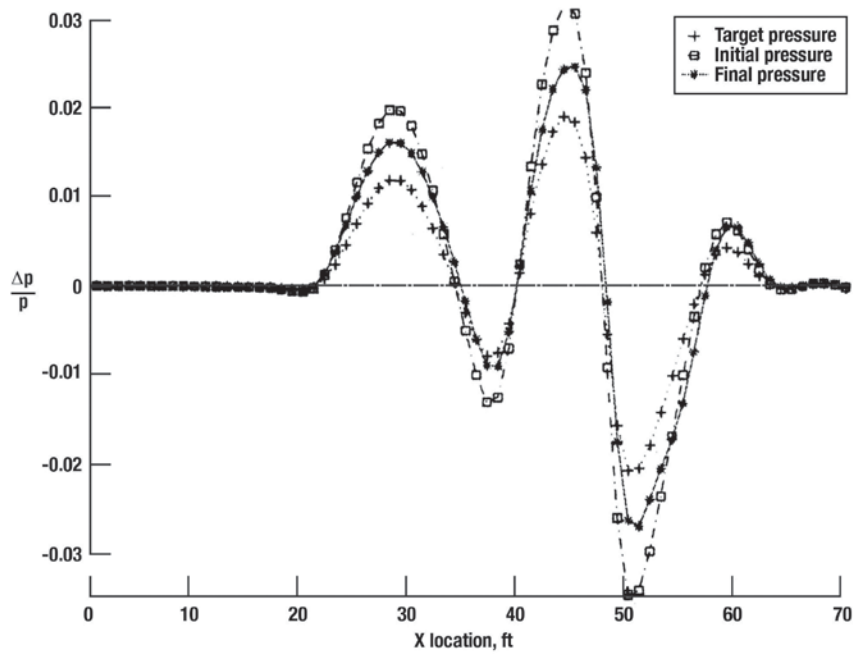


Figure 7.29. Sonic boom reduction: target, initial and final near-field pressure distribution after 50 design cycles, $Mach = 1.5$, $\alpha = 2.39^\circ$, $C_L = 0.1$ (adapted from ref. 7.24).

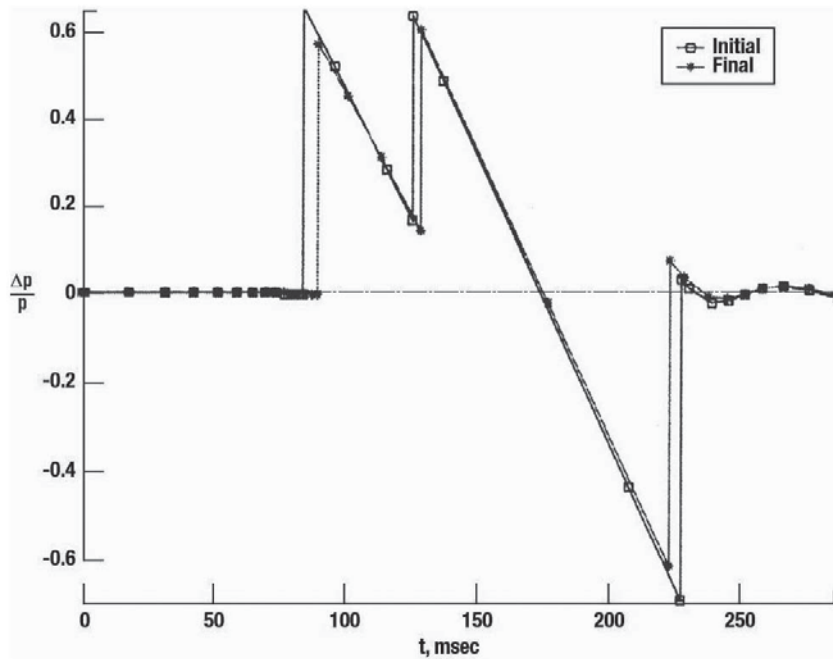


Figure 7.30. Sonic boom reduction – initial and final ground signatures after 50 design cycles, $Mach = 1.5$, $\alpha = 2.39^\circ$, $C_L = 0.1$ (adapted from ref. 7.24).

A 2008 paper by Li, Shields, and Le (ref. 7.27) introduced a computer program named BOSS (Boom Optimization using Smoothest Shape modifications). As noted in reference 7.27 (p. 1381), BOSS,

was intended to help designers find the right configuration among the infinite number of possible configurations that are equally good using any numerical figure of merit. BOSS uses the smoothest shape modification strategy for modifying the fuselage radius distribution at 100 or more longitudinal locations to find a smooth fuselage shape that reduces the discrepancies between the design and target equivalent area distributions over any specified range of effective distance.

The authors also noted in reference 7.27 (p. 1381) that using BOSS “within a few hours, a designer can either generate a realistic fuselage shape that yields a supersonic configuration with a low-boom ground signature or quickly eliminate any configuration that cannot achieve low-boom characteristics with fuselage shaping alone.” Further details of the BOSS methodology are given in ref. 7.27.

In the authors’ sonic boom minimization efforts, F-function technology is employed using equivalent area distributions for lift and Mach cuts to acquire the area distributions (see equation 3). The fuselage has circular cross-sections and is defined by 120 equally spaced longitudinal locations. The vertical and horizontal tails and engine nacelles are accounted for in the volume distribution.

The starting configuration for the BOSS minimization study is shown in figure 7.31. Boom considerations were not employed in its design. It has a take-off weight of 100,000 pounds, a balanced field length of 7000 feet, and a cruise Mach number of 1.8. The nacelles are located atop the wing and based on Howe’s analysis (ref. 7.28) in a near-optimum location. The equivalent area distribution is given in figure 7.32(a) along with its lift and volume components. Also shown is the hybrid signature target (i.e., a compromise between low-drag and low-boom area distributions). As one might expect, the sonic boom of the performance low-drag concept, figure 7.32(b), is not anywhere near the desired optimum.

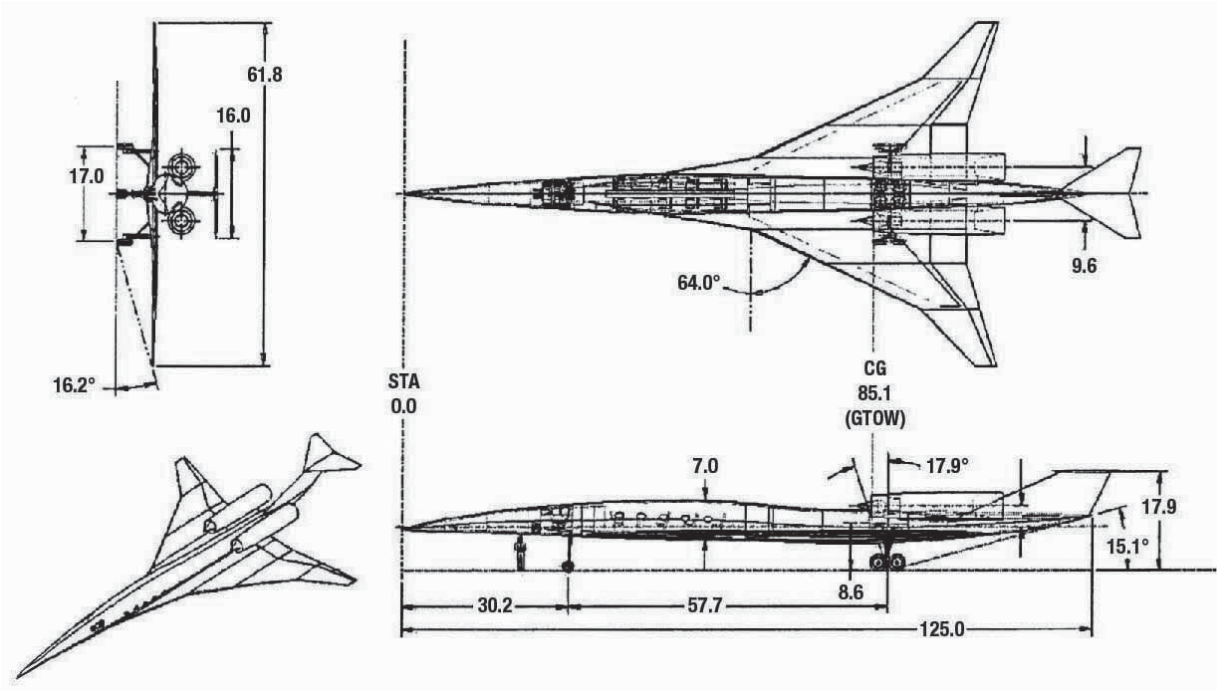
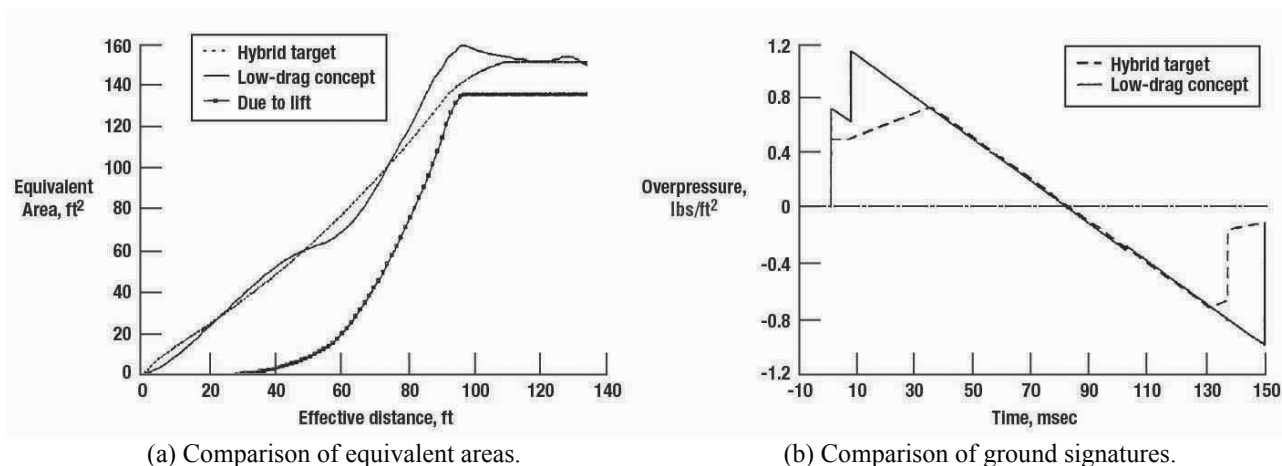


Figure 7.31. Three-view depiction of a supersonic business jet concept designed for optimum performance (ref. 7.27).



(a) Comparison of equivalent areas.

(b) Comparison of ground signatures.

Figure 7.32. Equivalent area distribution and ground signature of a low-drag supersonic concept (adapted from ref. 7.27).

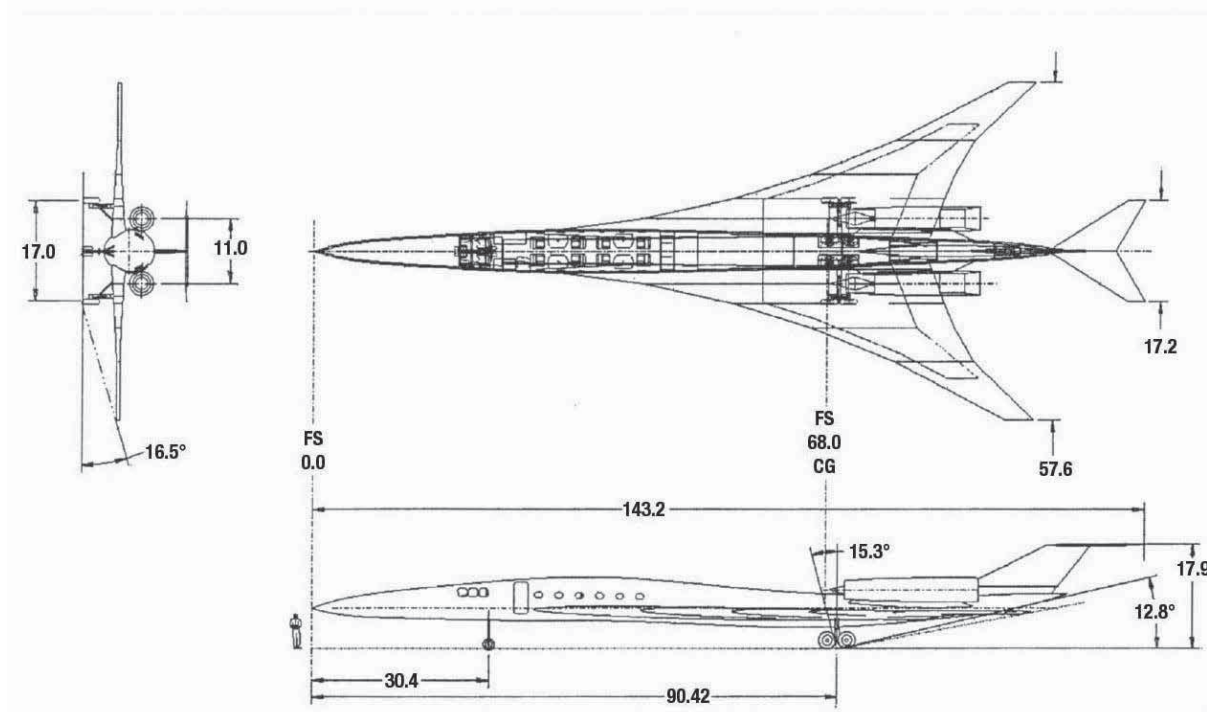


Figure 7.33. Three-view depiction of a low-boom supersonic business jet concept (ref. 7.27).

A second configuration was developed and is depicted in figure 7.33.

As noted in reference 7.27 (p. 1390),

The final A_e distribution in figure 7.34(a) is a low-boom area distribution derived by a designer, via a trial-and-error approach using planform modifications and fuselage shaping in succession, to best match the unmatchable target area distribution. This process usually takes several days to complete.

Clearly, a better approximation of the target hybrid equivalent area distribution was achieved (see fig. 7.34(a)) as well as the ground ramp-type signature shown in figure 7.34(b). The resulting low-boom fuselage shape (dashed lines) is plotted in figure 7.35. Note the difference in the ordinate and abscissa scales.

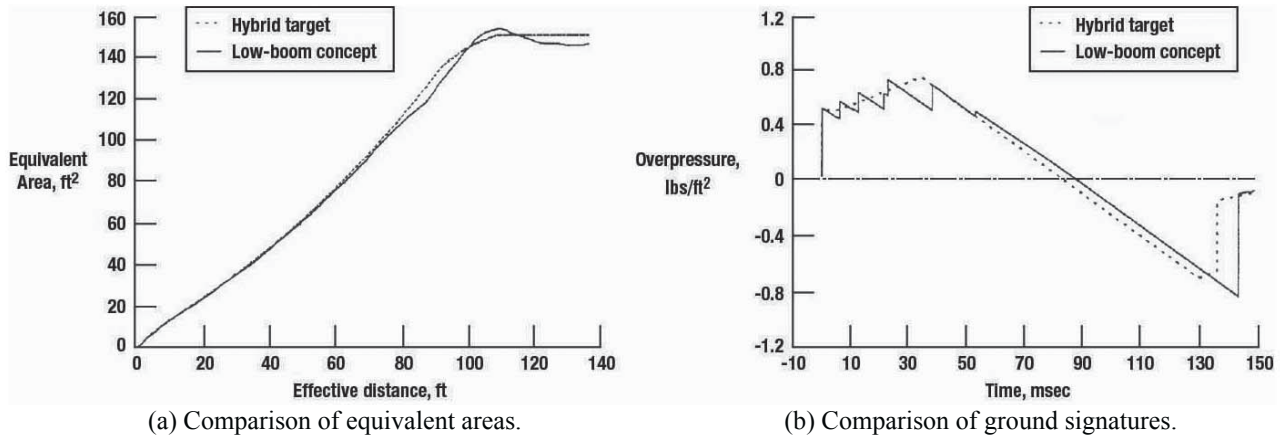


Figure 7.34. Equivalent area distribution and ground signature of low-boom signatures (adapted from ref. 7.27).

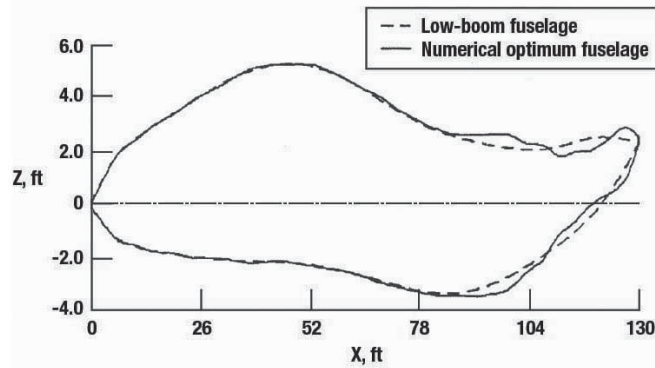


Figure 7.35. Side view of low-boom fuselage and numerically optimum fuselage (adapted from ref. 7.27).

Subsequently, the linear methodology and BOSS were applied to modify the fuselage shape in order to better approximate the hybrid ramp target signature. The resulting equivalent area distribution or numerical optimum (fig. 7.36) shows the close agreement achieved with the hybrid target equivalent area distribution. The sonic boom signature achieved relative to the hybrid target is shown on the right side of figure 7.36. It is evident that this is an improvement over that of the low-boom concept of figure 7.34(b). Figure 7.36 gives the fuselage shape for the numerical optimum that evolved compared to that for the low-boom configuration. With its irregularities it is not as practical as the low-boom shape but, with its optimum ramp signature, does point the way to further refinement.

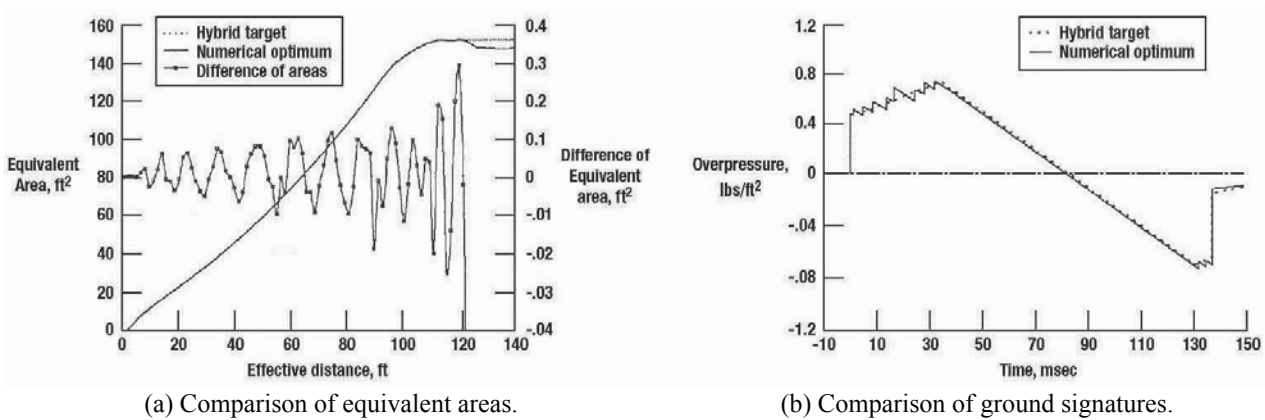


Figure 7.36. Equivalent area distribution and ground signature of a numerically optimum concept (adapted from ref. 7.27).

The use of BOSS to analyze and optimize the sonic boom signatures of a configuration through the modification of its fuselage geometry was demonstrated in reference 7.27. As stated in reference 7.27 (p. 1381),

To summarize, BOSS allows one to examine the differences between the design and target equivalent areas, decide which part of the design equivalent area curve needs to be modified, choose a desirable rate for the reduction of the discrepancies over the specified range, and select a parameter for smoothness control of fuselage shape.

Then BOSS “will then generate a fuselage shape based on the designer’s inputs in a matter of seconds.”(ref. 7.27, p. 1381) Further, as stated in reference 7.27 (pp. 1394-1395), “If the generated solution is not acceptable, the designer can work on a different part of the equivalent area curve, change the rate of reduction, or relax the smoothness control until a desirable solution is found.”

Minimization of the sonic boom of a supersonic jet without consideration of its aerodynamics, the mission constraints, structure, take-off and landing distances, cabin volume, etc., normally yields an optimistic result. Studies that examine boom-minimum designs as well as performance-based designs always show higher booms for the latter. Understanding and applying practical constraints and performance goals in the design of a low-boom aircraft is highly desirable. As stated by Choi, Alonso, and Kroo in reference 7.29 (p. 1), they have utilized a:

Multi-disciplinary aircraft synthesis tool (PASS) that incorporates highly-tuned low-fidelity models of all the relevant disciplines and computes the complete mission profile of the aircraft, and a hierarchical multi-fidelity environment for the creation of response surfaces for aerodynamic performance and sonic boom loudness (BOOM-UA) that attempts to achieve the accuracy of an Euler-based design strategy.

Some of the factors considered in PASS are – drag estimation, weights and c.g., propulsion, low-speed analysis (including takeoff and landing), and mission analysis.

CFD tools used include the A502/Panair and AirplanePlus flow solvers, the Centaur Mesh Generation System, and the PCBoom software (an early version of ref. 7.30) for propagation of the acoustic signatures. Details of the PASS system are given in the paper as well as a discussion of the accuracy of the A502/Panair code relative to AirplanePlus Euler solver. Another feature of reference 7.29 is that it concentrates on minimizing the loudness of the sonic boom (in dBA) rather than the maximum shock strength in lbs/ft². The baseline configuration from reference 7.29 was a design that fell short of the desired range (4500 nmi) by almost 1000 miles. Its geometry is provided in figure 7.37 with other pertinent details listed in table 7.4. A reduced target range of 4000 nmi was established. To achieve this range, the weight was increased and with it the target balanced field length, which was increased from 5000 feet to 6500 feet.

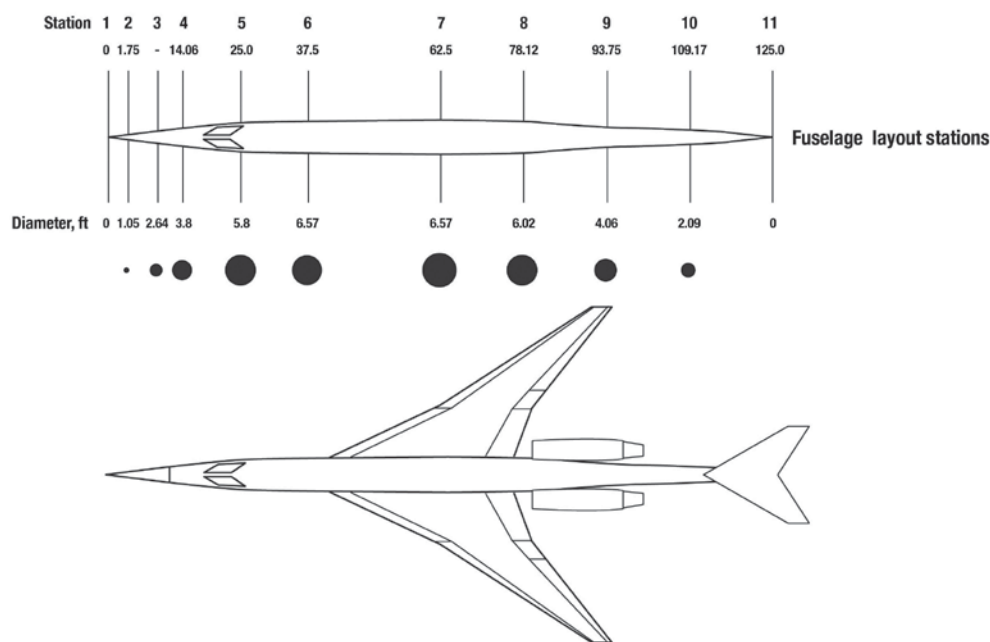


Figure 7.37. Summary of baseline configuration (adapted from ref. 7.29).

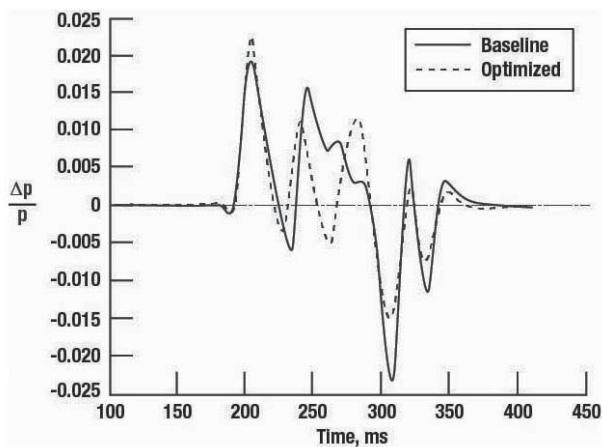
Table 7.4. Results of PASS + Response Surface Analysis of the Baseline Configuration (ref. 7.29)

Range	3,650 nmi
BFL	5,482 ft
MTOGW	92,018 lbs
Ground signature (dBA)	86.15

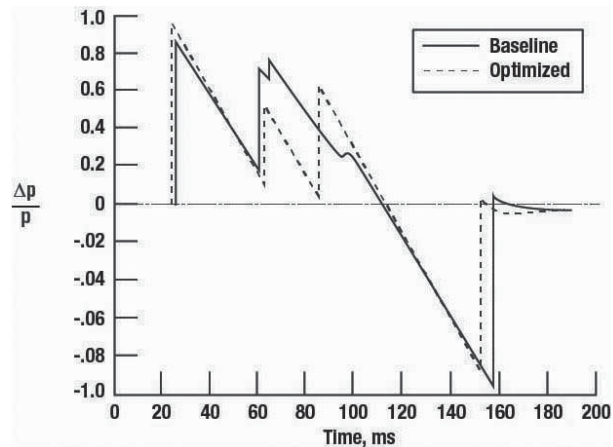
A PASS optimization was carried out using the new targets. The resulting performance and aircraft geometry details are listed in table 7.5. The near-field pressure distributions and ground boom signatures of the baseline and optimum configurations are given in figure 7.38. It is obvious from figure 7.38(b) that the initial shock strength of the ground signature of the optimized design was increased by about 10 percent from that of the baseline. On the other hand, the mid-field shock at 60 msec is reduced significantly leading to a loudness reduction from 86.15 dBA to 78.87 dBA.

Table 7.5. Results of PASS + response surface optimization for boom minimization (ref. 7.29)

Performance	
Cruise Mach	1.6
Range	4,000 nmi
BFL	6,500 ft
MTOGW	97,130 lbs
Ground signature (dBA)	78.87
Wing and Tail Geometry	
Wing reference area	1,155 ft ²
Wing aspect ratio	4.2
Wing quarter-chord sweep	55°
Leading edge extension	0.55
Trailing edge extension	0.026
Wing root leading edge	0.23
Root section t/c	3.0 percent
Break section t/c	2.56 percent
Tip section t/c	2.0 percent



(a) Near-field pressure distribution.



(b) Ground boom signature.

Figure 7.38. Comparison of optimized and baseline designs (adapted from ref. 7.29).

However, Choi, Alonso, and Kroo (ref. 7.29) were not satisfied with the wing geometry and some additional changes were implemented. As they note in reference 7.29 (p. 13),

Minor reductions in reference area (from 1,155 ft² to 1,100 ft²), aspect ratio (from 4.2 to 3.7) and sweep (55° to 54°) were manually applied to the above (optimum) design to return the wing to a more reasonable shape. The resulting configuration suffered only a modest gain in boom strength, while still managing to meet all other constraints, as can be seen in table 7.6 and figure 7.39.

Table 7.6. Results of PASS + Response Surface Optimization for Boom Minimization with Small Manual Modifications (ref. 7.29)

Range	4,021 nmi
BFI	6,255 ft
MTOGW	95,000 lbs
Ground signature (dBA)	80.3
Wing and Tail Geometry	
Wing reference area	1,100 ft ²
Wing aspect ratio	3.7
Wing quarter-chord sweep	54°
Leading edge extension	0.23

In addition to the boom minimization, reference 7.29 presented the results for a case where take-off gross weight is minimized. It increased the loudness level of the ground pressure signature by 4.6 dBA and decreased the TOGW by 253 pounds.

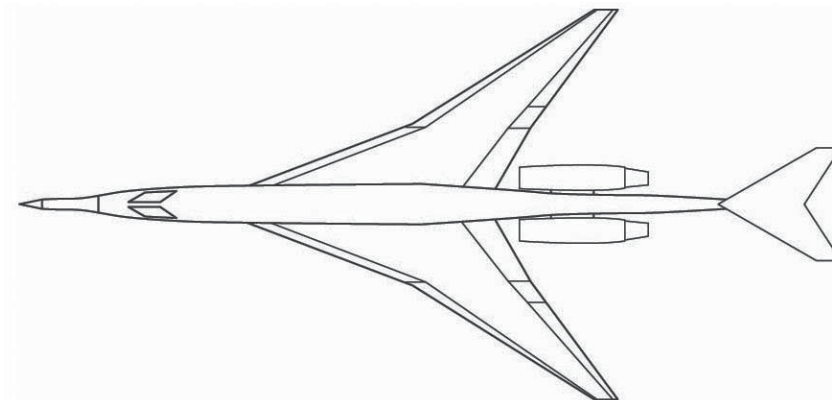


Figure 7.39. Boom optimized configuration plus small manual modifications (adapted from ref. 7.29).

Finally, reference 7.29 presents the results of an array of computational tools that have been integrated and applied in such a way that a multi-disciplinary optimization can be performed with numerous constraints. An interesting difference between this study and most others that attempt boom minimizations is that it keys on loudness rather than bow- and/or trailing-shock strengths. Another interesting aspect is that this study starts with a design that is more performance than boom oriented. However, if one starts with a lower boom design, like one based on linear optimization theory, it might yield a configuration with a lower boom and still have the range required.

In summary, several sonic boom reduction schemes exist that vary in complexity and utilize different optimization methodologies. Some use a combination of linear and nonlinear (Euler) flow codes, while others rely entirely on Euler codes. Most studies only treat the aerodynamic characteristics and sonic booms of their configurations. However, some studies also treat the structural and mission consequences of going from a performance to a low-boom design.

The Effect of Engine Nacelles on Sonic Booms

One of the most complex and challenging problems faced by designers of civil supersonic aircraft is the placement of the engines. Large 300-passenger transports studied in NASA's SCAR, HSCT, and HSR programs generally had four engines – two mounted on each side, under the wing, and near the trailing edge. Supersonic business jet (SBJ) concepts are usually powered by two engines, placed below the wing in some configurations and above the wing or on the vertical tail in others. Depending on the location, the engines may cause an increase in strength of the bow or trailing shocks of the sonic boom signature or produce discrete shocks somewhere in between. The wing geometry, fuselage shape and/or engine locations can be configured such that they will do the least damage to the effective area distribution and the resulting sonic boom at the cruise Mach number. It is important to note that when a configuration is optimally designed with the engines in place, engine relocation may cause additional shocks to appear in the near-field and ground signatures that did not previously exist.

The magnitude of the shocks produced by the engines will depend on their size as well as the details of the inlet and the exit. Also, the exhaust plume may have a significant effect on the shocks produced depending primarily on the pressure ratio. Exhaust effects will be discussed in detail in the next section. The flow spillage from engines that are not operating at optimal conditions can also enhance the strength of the shock or shocks emanating from the forward portion of the engine nacelle. It is normally assumed in analytical studies, at the design conditions, that the engines are operating without spillage. Pylons that hold the engines to the wing or fuselage are usually accounted for, particularly in the CFD studies already performed.

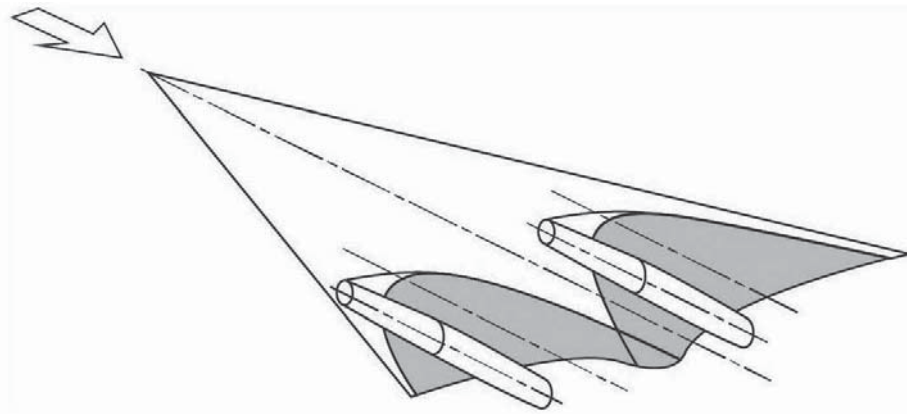
Several theoretical studies using F-function methodology or Euler CFD codes have been conducted that examine propulsion integration problems. In most cases, the engine's geometry is idealized as well as that of the inlet and exhaust flows. In the following discussion, a description of some of these studies will be provided.

F-Function Methodology

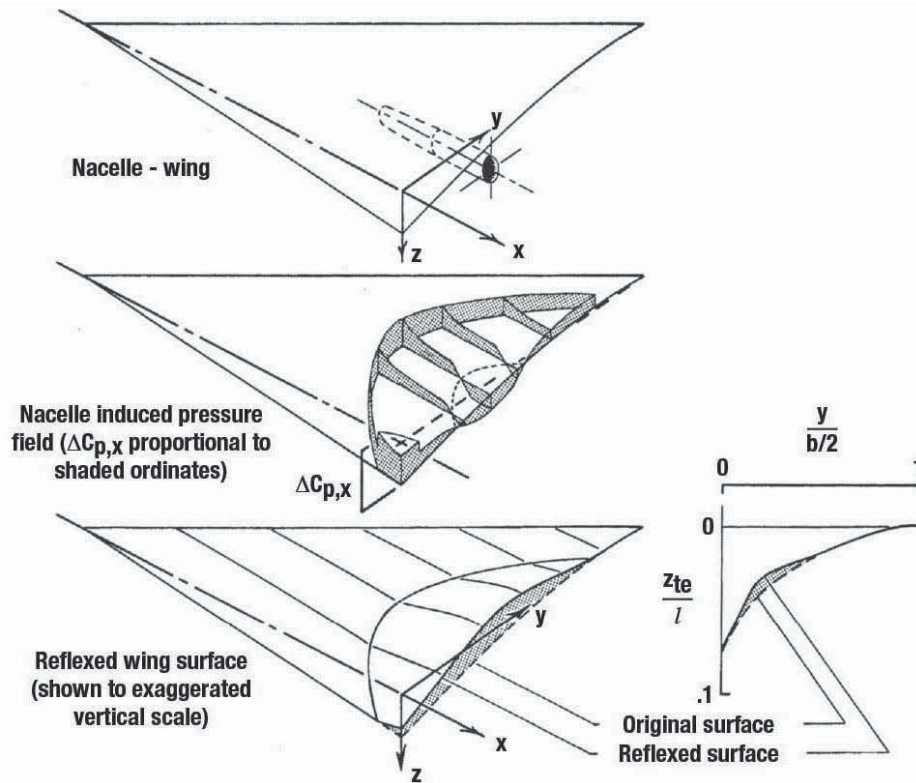
F-function methods for sonic boom prediction, which were prevalent in the 1950s and 1960s, rely on the effective area distribution of a configuration (see equations (5) and (7) of Chapter 6). The latter, in turn, is derived using Mach cuts of the proposed geometry or from an analytical method aimed at producing an optimal distribution (refs. 7.6 and 7.10). One of the first methods used to analyze the incremental effects of engines was based on a combination of the F-function and linear-potential-theory methodologies and documented in reference 7.31. In this reference, a computer code is described that calculates:

- The interference pressures and associated lift and drag on a wing adjacent to a nacelle
- The calculation of the local wing camber (reflex) required to cancel out all, or a portion of, the interference effect of a nacelle

A schematic of the nacelle-wing interference problem is shown in figure 7.40(a). A typical result is also shown in figure 7.40(b), including the nacelle-induced pressure field and the wing deformation or reflex required to cancel out this effect. The small plot in the right-hand corner shows the original trailing-edge geometry along with that of the reflexed surface.



(a) Pictorial representation of nacelle-wing interference problem (shaded area indicates interference region).



(b) Nacelle pressure field at surface of twisted and cambered wing and reflex surface required for 100 percent cancellation.

Figure 7.40. Sketch of nacelle-wing interference problem, pressure field, and reflexed surface to cancel out the induced pressure (ref. 7.31).

The integrated or force effect of the interference pressures is illustrated by the lift-drag polar shown in figure 7.41 along with the associated moment coefficient. It is evident that at low C_L there is a drag penalty while at design C_L there is none. The effect on moments of the interference pressures is to make them more negative, as indicated in the C_m vs C_L plot on the right side of figure 7.41.

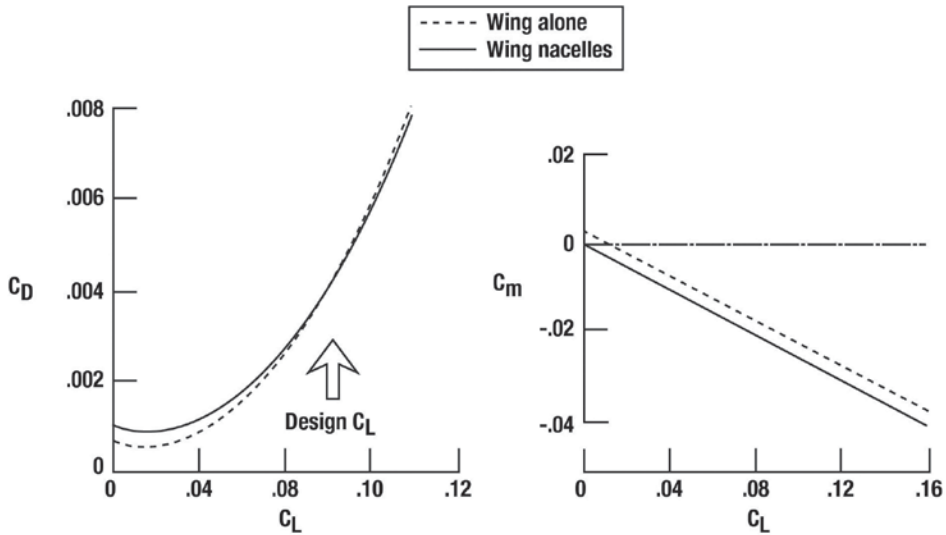
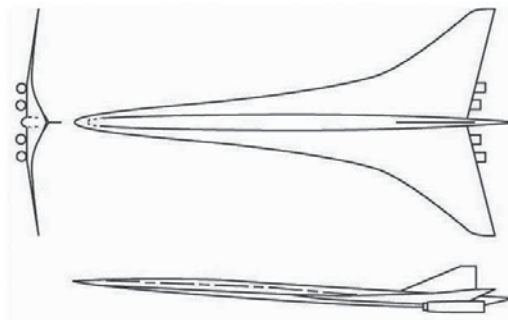
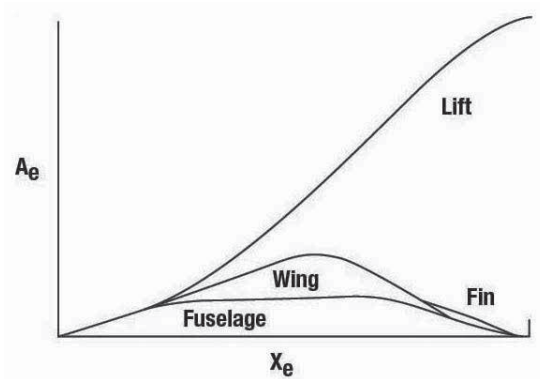


Figure 7.41. Aerodynamic characteristics of twisted and cambered wing-nacelle combination for 0 percent reflex (adapted from ref. 7.31).

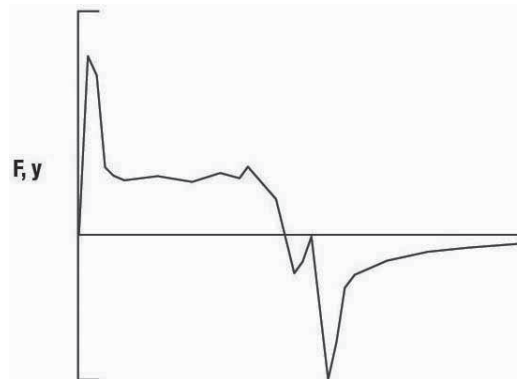
Several papers contain analyses that highlight the adverse effects of the engine nacelles on sonic boom signatures. In a study by R. Mack (ref. 7.32), the issue of nacelle integration was addressed and provided an improved analysis, which contained all of the pieces that go into an F-function including the isolated and interference effects of nacelles. Figure 7.42 from this study (ref. 7.32) shows the configuration used to illustrate the method (fig. 7.42 (a)) as well as its effective area distribution (fig. 7.42(b)) and associated F-function (fig. 7.42(c)). Note that the nacelle effects are not included in the F-function plotted in figure 7.42(c). Figure 7.43 shows the effective areas due to the interference lift produced by the nacelles, the corresponding F-function, and incremental effect that the interference lift of the nacelles has on the configuration's F-function distribution.



(a) Conceptual aircraft.

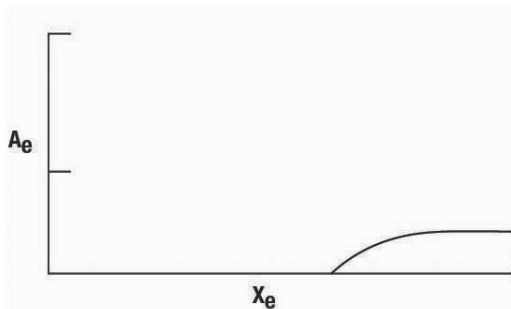


(b) Effective area distribution.

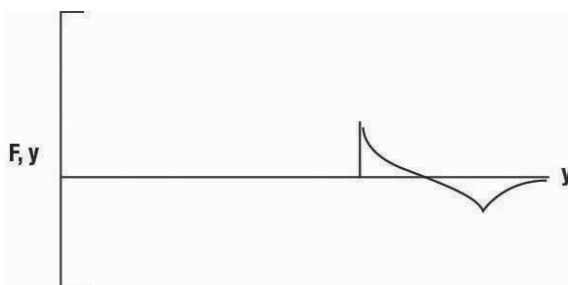


(c) F-function.

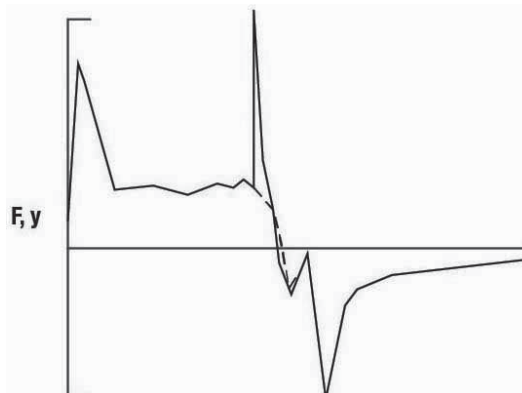
Figure 7.42. Three-view depiction of the conceptual aircraft, its effective area distributions, and associated F-function (ref. 7.32).



(a) Effective area due to wing nacelle interference.



(b) F-function due to wing nacelle interference.



(c) Total configuration F-function.

Figure 7.43. Effective area due to wing-nacelle interference and the corresponding F-function as well as the total configuration F-function, including that due to the interference lift (ref. 7.32).

The additional effective area created by the volume effects of the nacelles is illustrated in figure 7.44 along with the associated F-function distribution. The result of adding all component F-functions together is given in figure 7.45. This figure can be compared to the distribution shown in figure 7.42 to see the large incremental effect the nacelles had on the basic F-function.

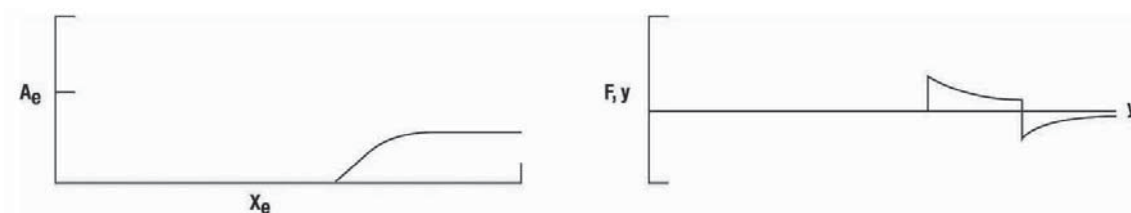


Figure 7.44. Equivalent area and F-function for an isolated nacelle (ref. 7.32).

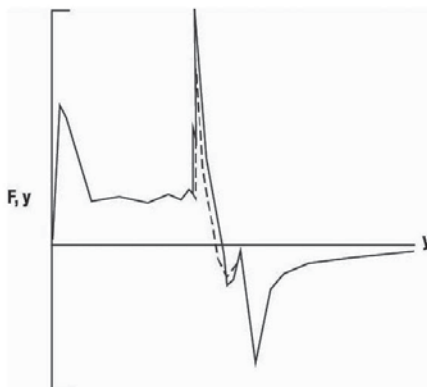


Figure 7.45. F-function of all aircraft components. The dashed lines show the F-function before the increments from figure 7.43 were added (ref. 7.32).

While the F-function effects of the nacelle shocks may be strong, they are usually followed by a rapid recovery. As noted earlier in this chapter, the shock strengths diminish very rapidly when followed by a rapid recovery so that the effect of the nacelle shock on the F-function may not be indicative of its effect on the sonic boom.

F-function distributions for a slightly different configuration (fig. 7.46), with and without nacelles, are shown in figure 7.47 (ref. 7.33). This configuration is for cruise at Mach 1.8 overland and 2.4 over water, thus, the prime concern for the boom is at Mach 1.8. The large peak in the F-function at an x of 275 feet, due to the nacelles, is clearly on the down slope or expansion region of the F-function, which helps minimize the adverse effects of the engines on the sonic boom ground signature, as seen in figure 7.48. The F-function distribution in figure 7.47 is for the start of cruise at Mach 1.8.

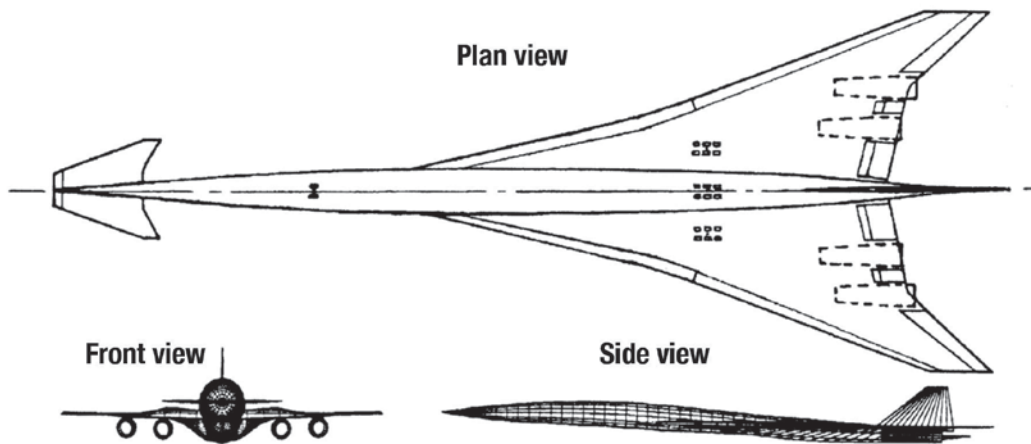


Figure 7.46. Mach 2.4/1.8 Configuration general arrangement (ref. 7.33).

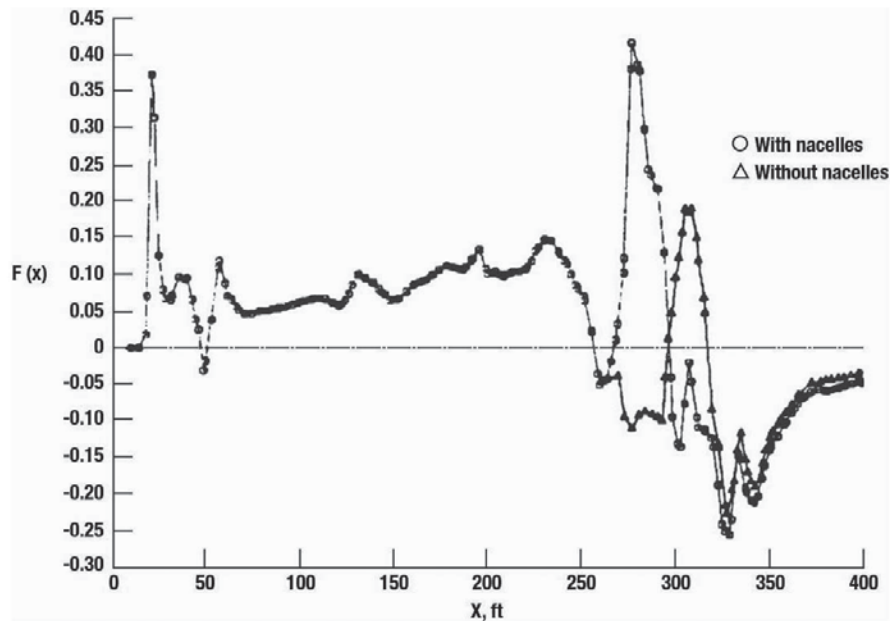


Figure 7.47. MDBOOM predicted F-function at Mach 1.8 beginning of cruise (adapted from 7.33).

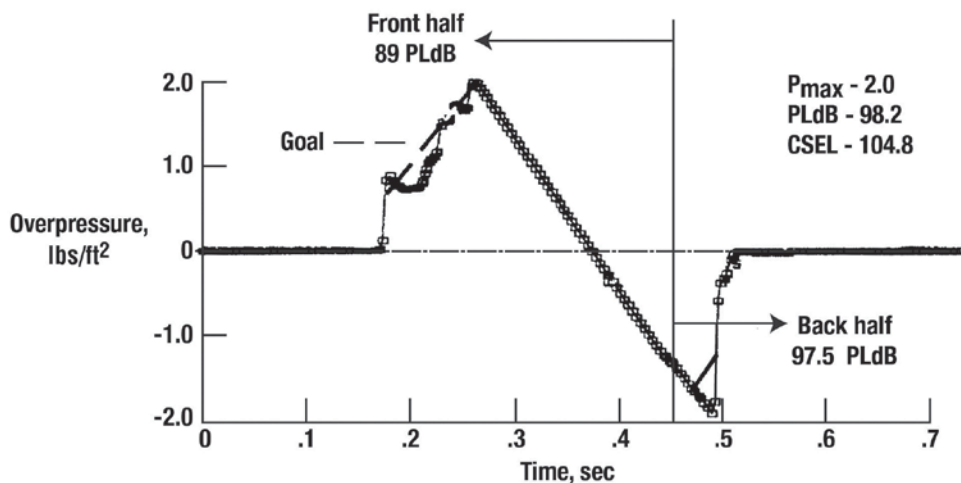
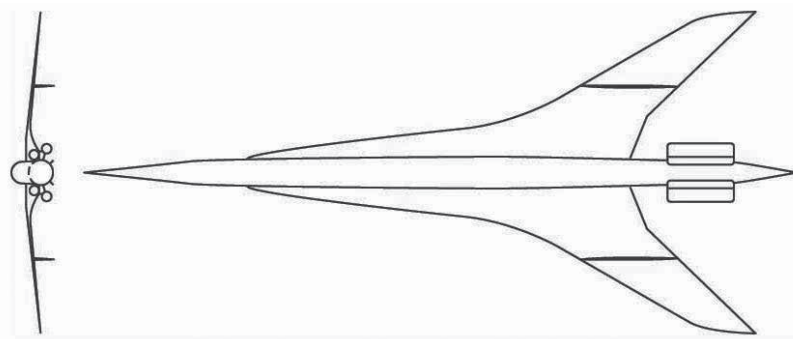
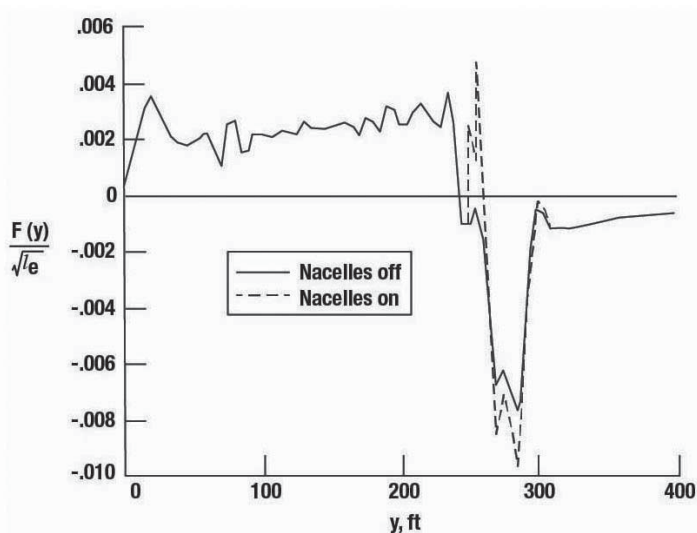


Figure 7.48. Mach 2.4/1.8 Configuration ground under-track waveform at Mach 1.8 beginning of cruise (ref. 7.33).

A different engine installation is illustrated in figure 7.49 along with its F-function (ref. 7.34). The four engines are mounted on the aft end of the fuselage (see fig. 7.49 (a)) and produce incremental effects to the F-function (see fig. 7.49 (b)) that are lower than those seen on most wing-mounted engine configurations. The sonic boom signature created by this concept flying at Mach 1.8 at an altitude of 48,000 feet and a start of cruise weight of 618,000 pounds is shown in figure 7.50 along with the ramp-type ideal signature. The small shock at an $(x - \beta h/l)$ of 0.6 is due to the engines and its low magnitude is a result of the optimal location of the engines.



(a) Front and top view of the HSCT-10B wind-tunnel model.



(b) Whitham F-function.

Figure 7.49. Three-view depiction and Whitham F-function of the complete HSCT-10B wind-tunnel model (adapted from 7.34).

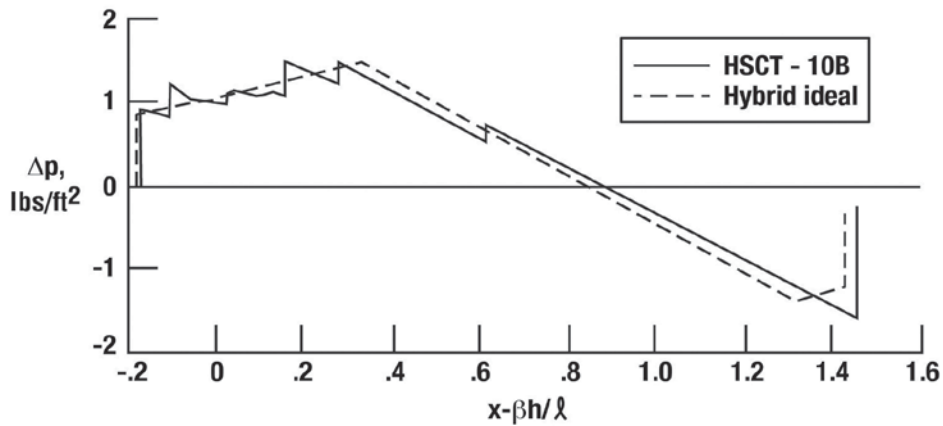


Figure 7.50. Predicted ground-level pressure signature from the HSCT-10B cruising at $M = 1.8$, $h = 48,600$ feet and start-of-cruise weight of about 618,000 pounds (ref. 7.34).

In reference 7.35, Cliff documented an analysis of three supersonic cruise configurations using CFD codes with both structured and unstructured grids. The configurations were analyzed without engines and with four or three engines. A drawing of the configuration, designated LBWT, is shown in figure 7.51. The symmetry-plane grids for this configuration are shown in figures 7.52 and 7.53, with the former for the HFLO structured-grid code and the latter for the unstructured-grid AIRPLANE code. AIRPLANE unstructured, surface grids for the empennage of three- and four-engine versions of the LBWT are shown in figures 7.54 and 7.55.

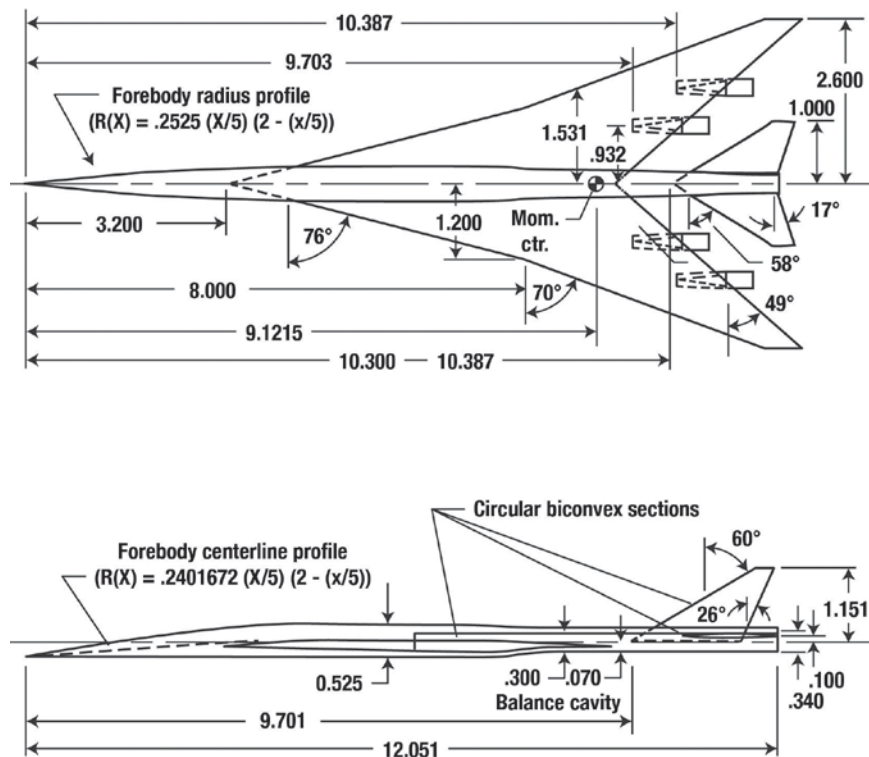


Figure 7.51. LBWT wind-tunnel model (ref. 7.35).

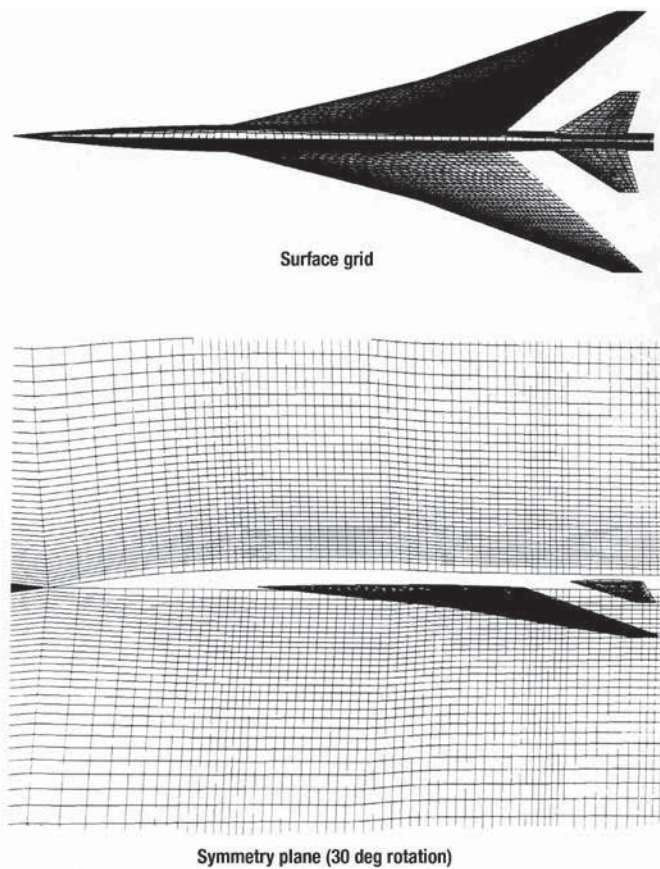


Figure 7.52. HFL04 computational grid (ref. 7.35).

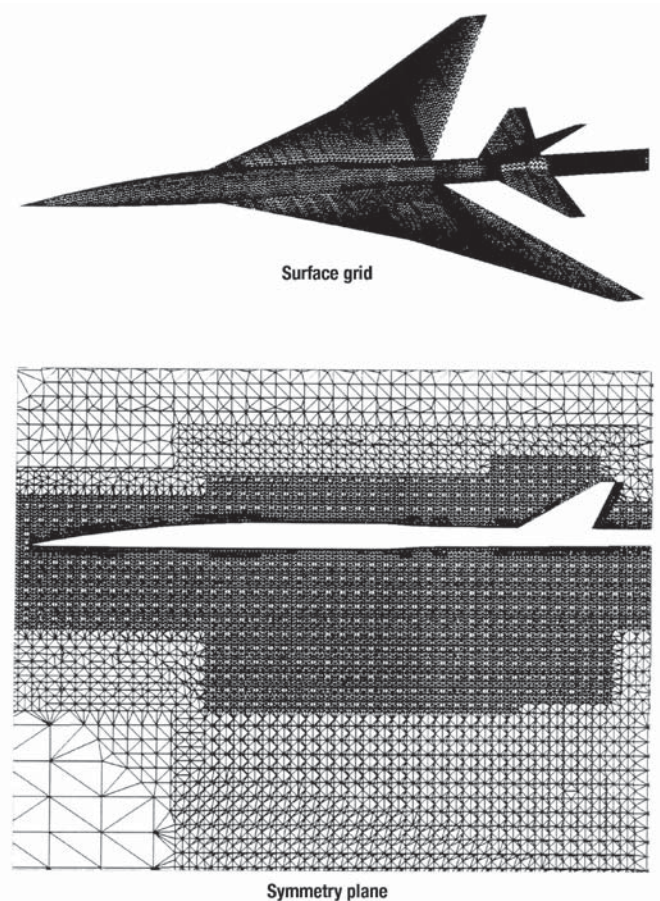


Figure 7.53. AIRPLANE unstructured tetrahedral grid for the LBWT without engines (ref. 7.35).

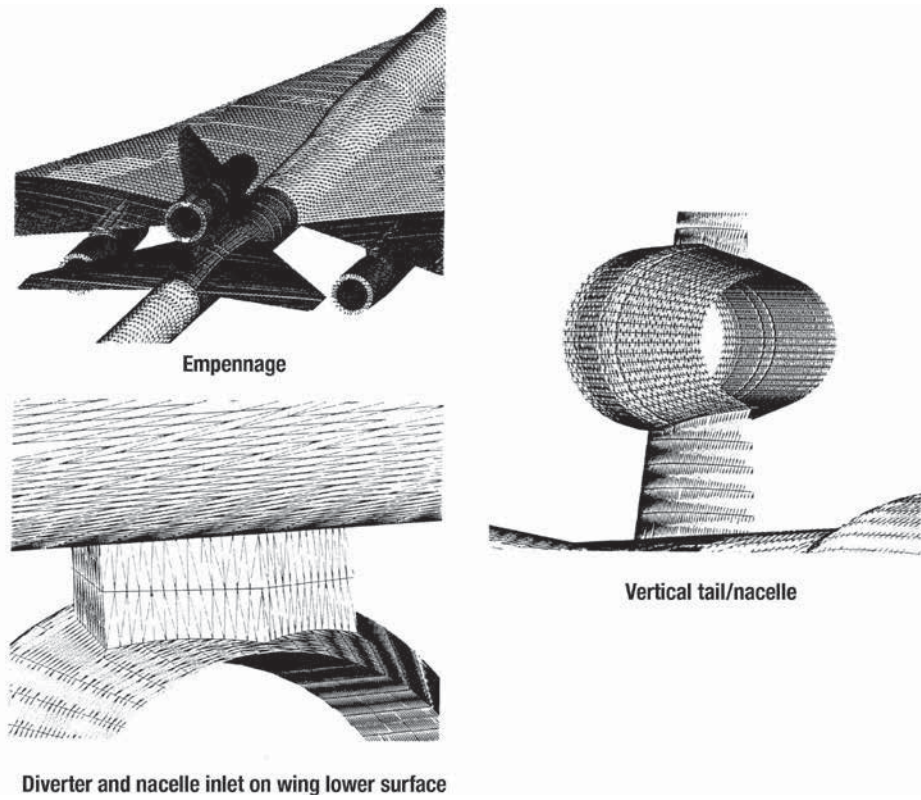


Figure 7.54. AIRPLANE unstructured surface grid for the LBWT with three nacelles (ref. 7.35).

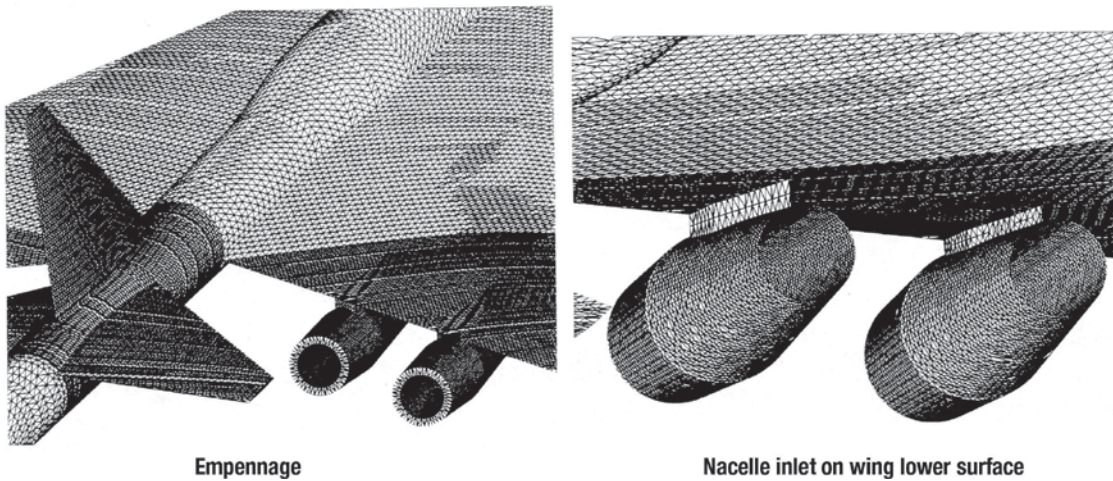


Figure 7.55. AIRPLANE unstructured surface grid for the LBWT with four nacelles (ref. 7.35).

Near-field pressure signatures at an h/l of $1/3$ for the LBWT configuration with three and four nacelles using these grids are plotted in figure 7.56. The incremental effects of the three and four engines on the pressure near $x = 16$ inches are quite evident. When these pressure signatures are propagated to the ground from an altitude of 60,000 feet and a Mach number of 2.0, the result is depicted in figure 7.57.

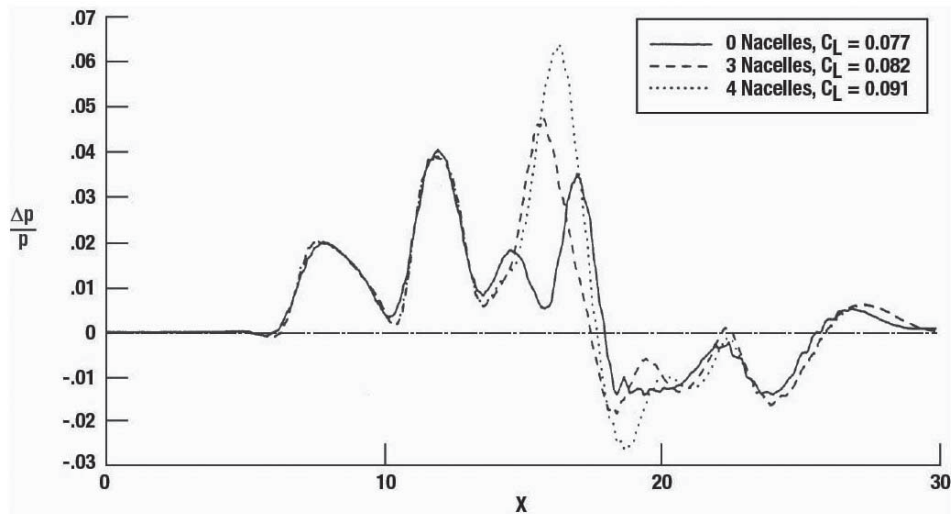


Figure 7.56. AIRPLANE near-field pressure signatures for the LBWT, Mach = 2.0, $\alpha = 2.50^\circ$, $h/l = 1/3$ (adapted from ref. 7.35).

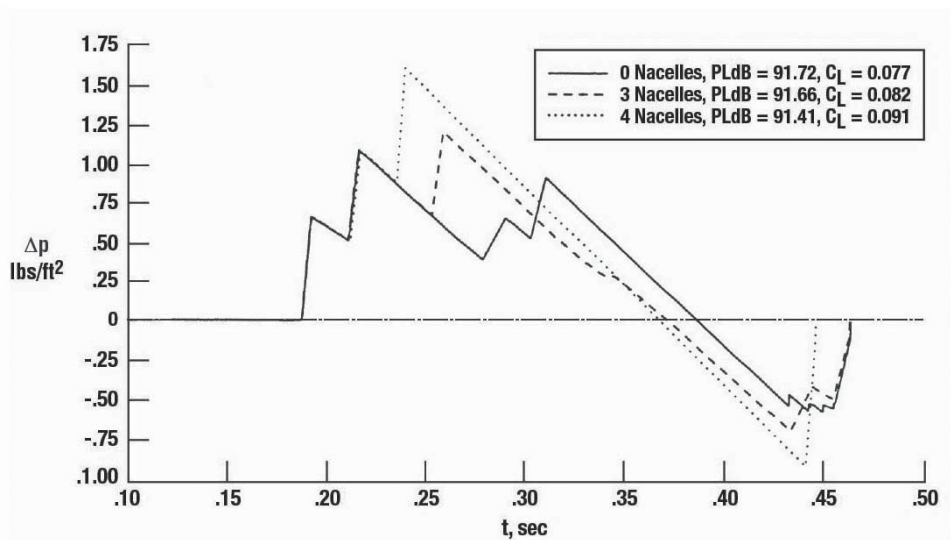


Figure 7.57. Ground pressure signatures for the LBWT using AIRPLANE/ANET/ADDRISE computational data extrapolated from $h/l = 1/3$, Mach = 2.0, $\alpha = 2.5^\circ$, $h = 60,000$ feet (adapted from ref. 7.35).

This figure shows that both three and four engine concepts cause increases to the maximum pressure with the latter raising the level from ~ 1.1 lbs/ft² (no engines) to 1.6 lbs/ft². Similar results for a canard version of LBWT (LBWC) and for the configurations without the empennage (LBW) are given in reference 7.35.

Another study, documented in the same workshop proceedings (ref. 7.21), also looked at the incremental effects of engine installations. The relative sonic boom merits of five configurations were explored using a very efficient 3-D Euler, finite-volume marching code (MIM3DSB) perfected by Siclari and Fouladi. As they stated in reference 7.21 (p. 227),

In addition, a unique grid topology is used to accurately capture shocks several body lengths downstream of the aircraft. This unique grid topology has been sometimes referred to as the “donut grid” and consists of modeling the inner boundary downstream of the aircraft as a Mach cone surface. This approach takes advantage of the Mach cone characteristics associated with supersonic flow and reduces grid spreading and the resultant smearing of shock waves that would occur with the use of a normal relaxation method type of grid.

Near-field signatures were extrapolated to the ground using the Thomas wave-form parameter method (ref. 7.16).

The planform geometry of the five concepts (ref. 7.21), along with the cruise-flight conditions utilized is given in figure 7.58 with the front-view geometries shown in figure 7.59. These designs were sized for carrying 300 passengers 5000 nautical miles and are 300-feet long. Sample results will be given here for the Langley LB16 and the Ames Model 3 configuration.

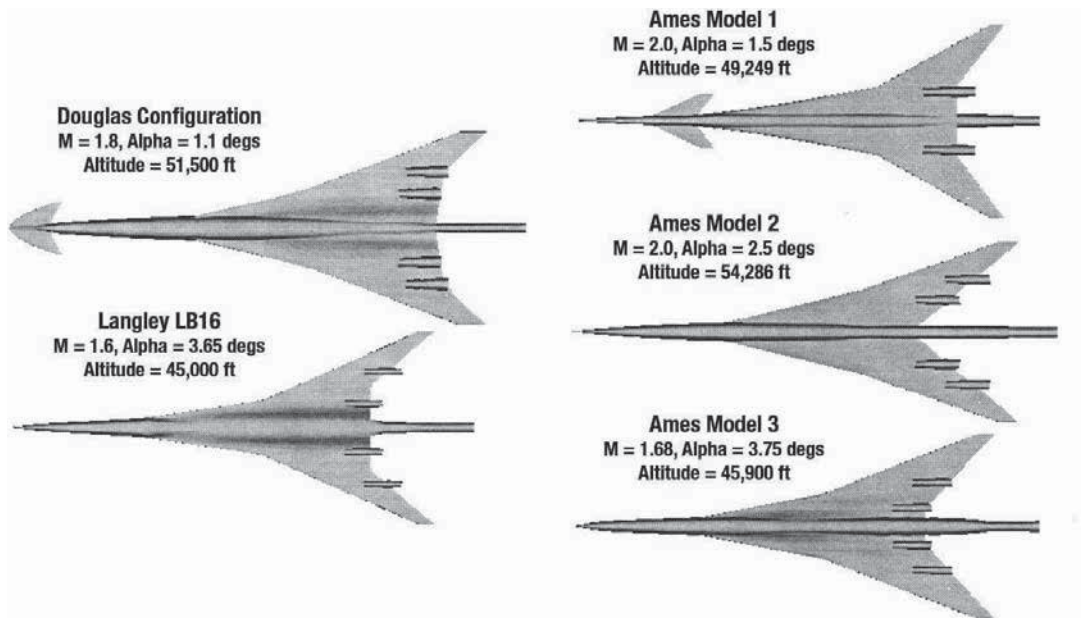


Figure 7.58. Planform view of CFD geometry models for five low-boom aircraft (ref. 7.21).

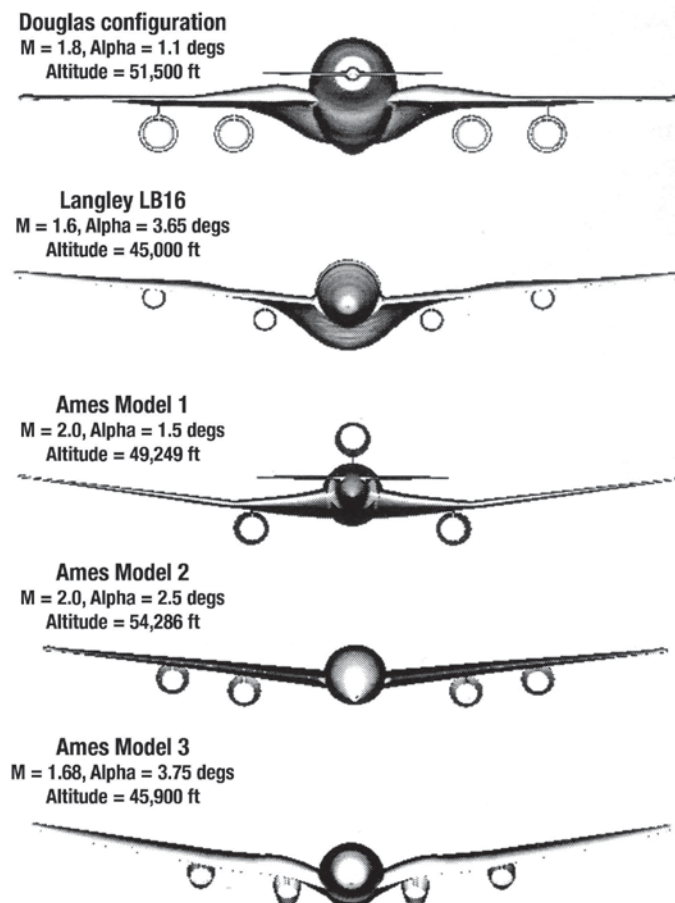


Figure 7.59. Front view of CFD geometry models for five low-boom aircraft (ref. 7.21).

As stated by Siclari and Fouladi in reference 7.21 (p. 231),

The nacelles are treated in a similar fashion for all five configurations. The inlet face is treated as a discontinuity in the geometry and the assumption is made that all of the mass flow encompassed by the inlet face is captured with no spillage. The internal geometry of the engine nacelles was not modeled. The engine exits are also treated as discontinuities and grid points lying within the engine exhaust area are assigned free-stream values. This was done in order to approximately simulate flow-through nacelles. More realistic engine exhaust conditions can also be simulated by MIM3DSB.

The MIM3DSB realistic engine exhaust condition simulations will be demonstrated in the next section with the aid of reference 7.36. The type of grid used to calculate the characteristics of these configurations is illustrated by the cross section of the grid, used for the Langley LB16 design (fig. 7.60) and the Ames Model 3 design (fig. 7.61).

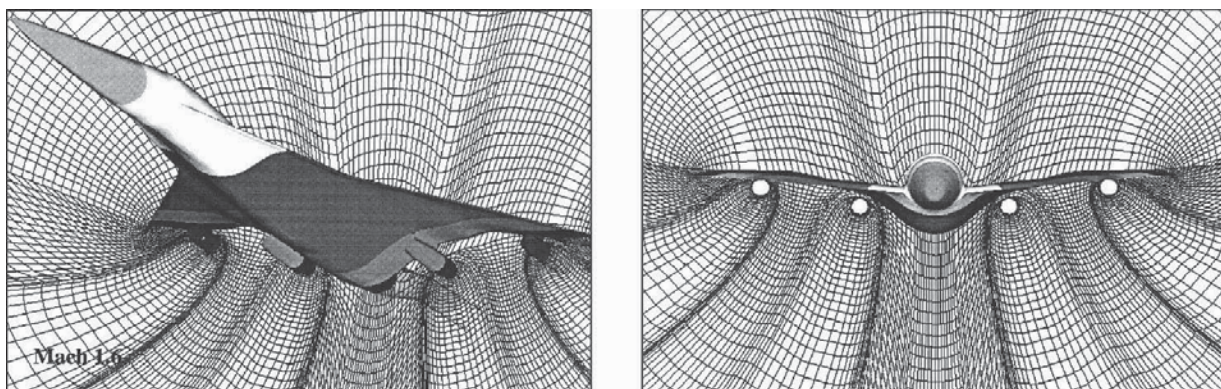


Figure 7.60. Grids and blocking structure for the Langley LB16 design (adapted from ref. 7.21).

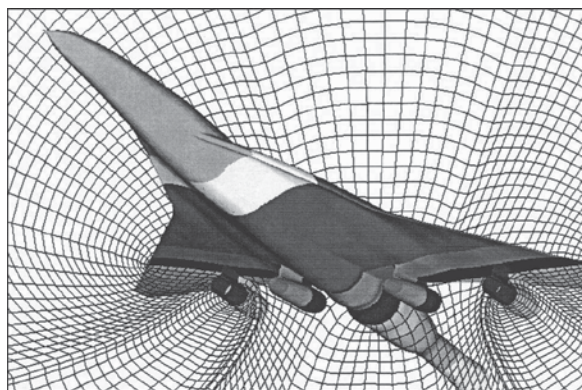


Figure 7.61. Grids and blocking structure for NASA Ames Model 3 (adapted from ref. 7.21).

Lift, drag, and moment coefficients along with L/D are calculated for each configuration and both near-field and ground-pressure signatures were determined. The authors noted that to adequately describe the geometry of the five aircraft designs, including the nacelles, 7 to 11 axial grid blocks were typically required. Three grid blocks were needed to model a staggered pair of nacelles.

The effect of nacelles on the near- and far-field pressure signatures for the Langley LB16 design at Mach 1.6 and $h = 45,000$ feet is given in figure 7.62. Shown on the left hand side of the figure are the near-field pressure distributions at a distance of 300 feet below the aircraft ($h/l = 1$) for the nacelle on and off configurations. It can be seen that, even at the close-in distances, the incremental effects of the engines are to reduce the shock that occurs without the engines. Similarly, on the ground (fig. 7.62 right side), the shock due to the nacelles is much weaker than of the nacelles-off shock and the bow or trailing shocks as well. This is an indication that the engines were well placed and that the geometry was properly tailored.

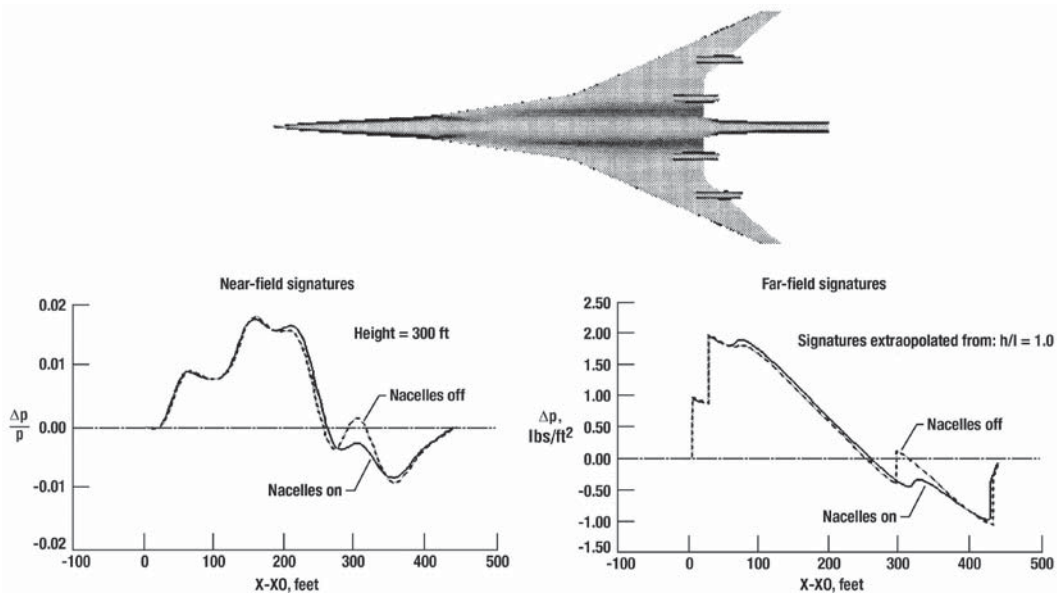


Figure 7.62. Effect of nacelles on the near- and far-field signatures of the Langley LB16 design, X_0 is the location of the initial shock (ref. 7.21).

A plot similar to figure 7.62 is given for the NASA Ames Model 2 and is shown in figure 7.63. This configuration, like LB16, has an arrow wing with four engines placed to provide as smooth an area distribution as possible. However, at Mach 2 the results are not the same. The incremental pressure due to the engines at a distance of 300 feet is higher than the incremental pressure without engines and, consequently, there is adverse impact on the ground pressures (fig. 7.63).

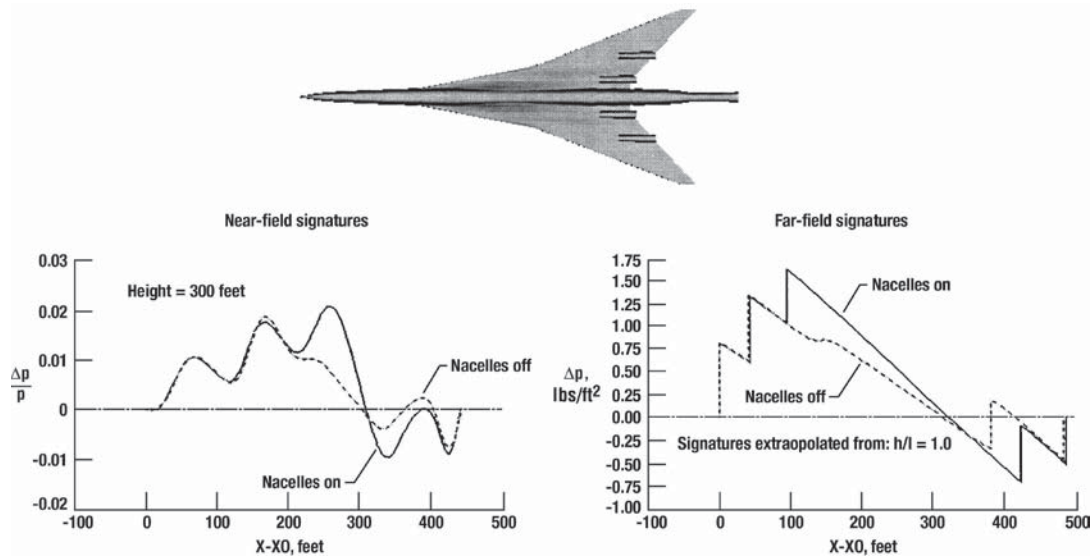


Figure 7.63. Effect of nacelles on the near- and far-field pressure signatures for the Ames model 2 design, Mach = 2.0, $\alpha = 2.5^\circ$, $h = 54,286$ feet (ref. 7.21).

Calculations for the Ames Model 3 geometry (see fig. 7.64) at Mach 1.68 show near-field and ground pressure signatures due to engine installation that are similar in magnitude to those of the LB16 design at Mach 1.6, indicating that the engine integration task produced better results at the lower Mach number.

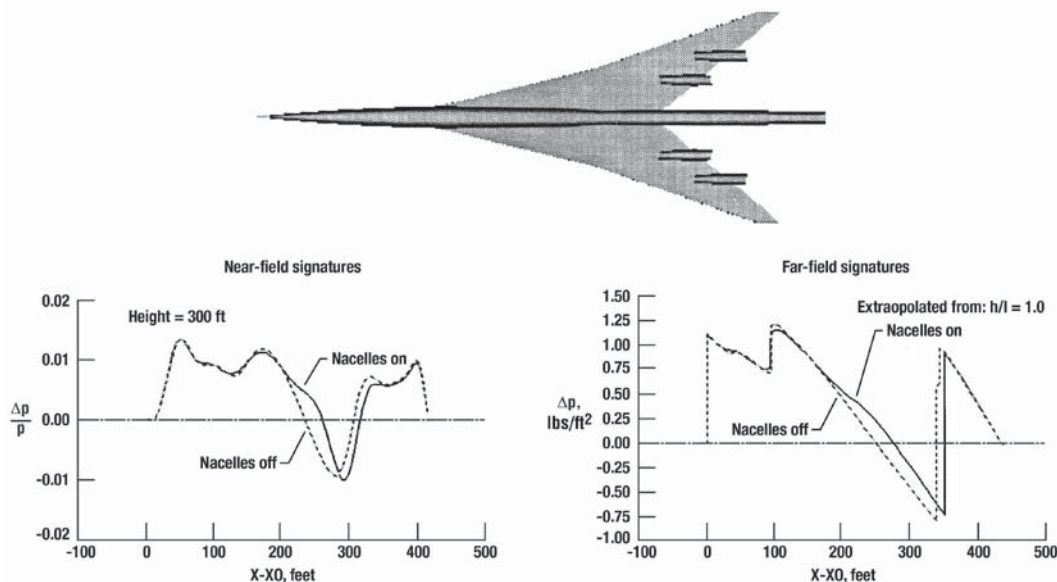


Figure 7.64. Effect of nacelles on the near- and far-field pressure signatures of the Ames Model 3 design, Mach = 1.68, $\alpha = 3.75^\circ$, $h = 45,900$ feet, X_0 is the location of the initial shock (adapted from ref. 7.21).

A few of the studies that address the sonic boom of supersonic business jets focus on the incremental effects of engine installation. In 2002, however, Howe (ref. 7.28) specifically focused on the engine placement problem using a generic wing-fuselage geometry and engines placed at three locations above the wing and the same three longitudinal locations below the wing. Adjustments to the wing and fuselage geometries were made to achieve the near-optimum area distribution shown in figure 7.65. A schematic of the wing-fuselage and the engine longitudinal placements is shown in figure 7.66. The ground signature for the baseline geometry is plotted in figure 7.67 and shows an initial $\Delta p/p$, for a standard atmosphere of 0.00032 and a peak $\Delta p/p$ of 0.00034, which convert to a Δp of 0.677 lb/ft² and 0.72 lb/ft² for a sea level pressure of 2116 lbs/ft².

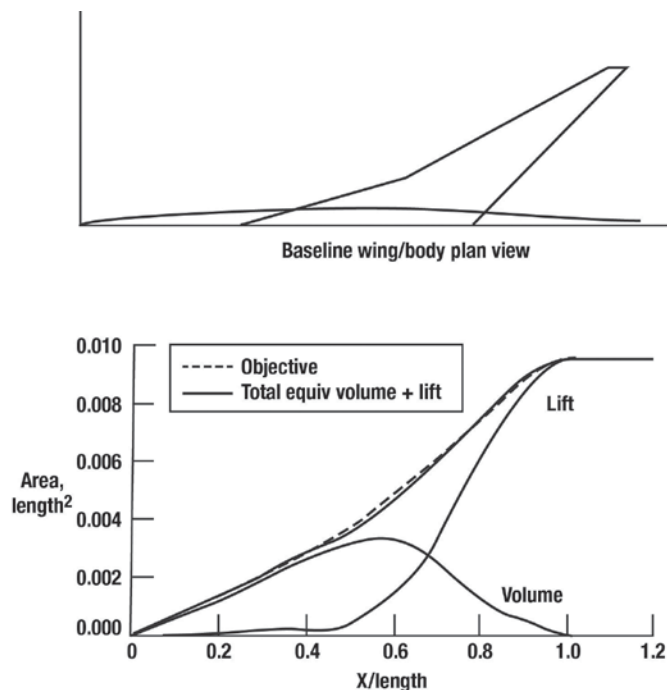


Figure 7.65. Baseline configuration and equivalent area distributions (ref. 7.28).

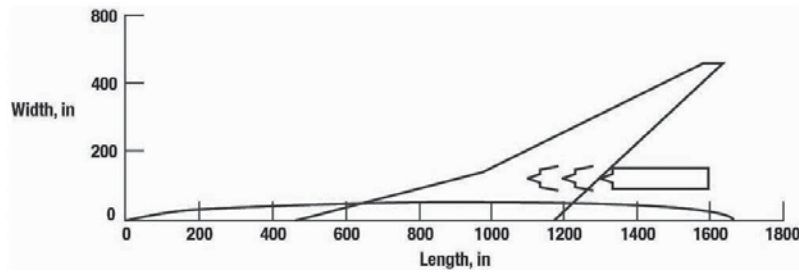


Figure 7.66. Inlet/nacelle axial positions (ref. 7.28).

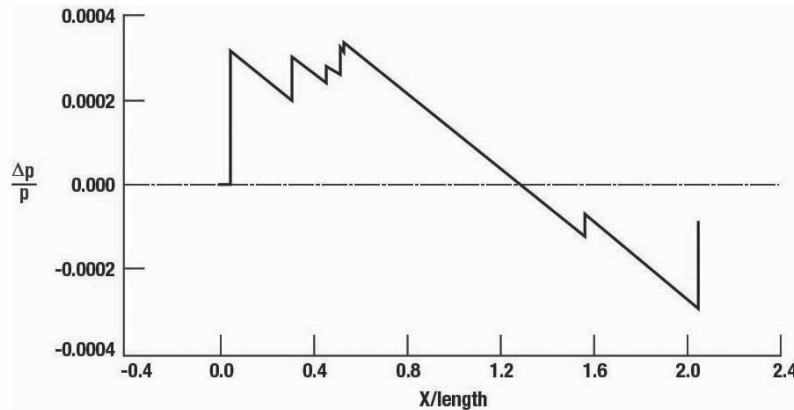


Figure 7.67. Baseline wing-body ground signature (adapted from ref. 7.28).

Near-field flow calculations were made using the OVERFLOW solver (ref. 7.37) where grid blocks for nacelles or other components are embedded and point-to-point alignment is not required. Far-field pressure-wave propagations are made using Thomas' waveform parameter method (ref. 7.16). Figure 7.68 shows a view from the underside of the wing of the OVERFLOW grid, including the block containing the nacelle. As stated by Howe in reference 7.28 (p. 6), it shows the position of a:

... large block which is added to resolve the near field pressures below the configuration for later signature extraction and sonic boom propagation. This block is swept along the Mach angle and has grid points clustered in the vicinity of the shocks and strong pressure gradients. Also, this block extends down past one body length below the configuration and intersects both the nose block and the under nacelle block to avoid smearing the solution by the more coarsely gridded wing/body or outer blocks.

About 10 million grid points were used for the under-wing nacelle configurations and 11 million for the over-wing nacelles. Pressure-wave propagation calculations were made starting with the Euler solution at one body length below the fuselage.

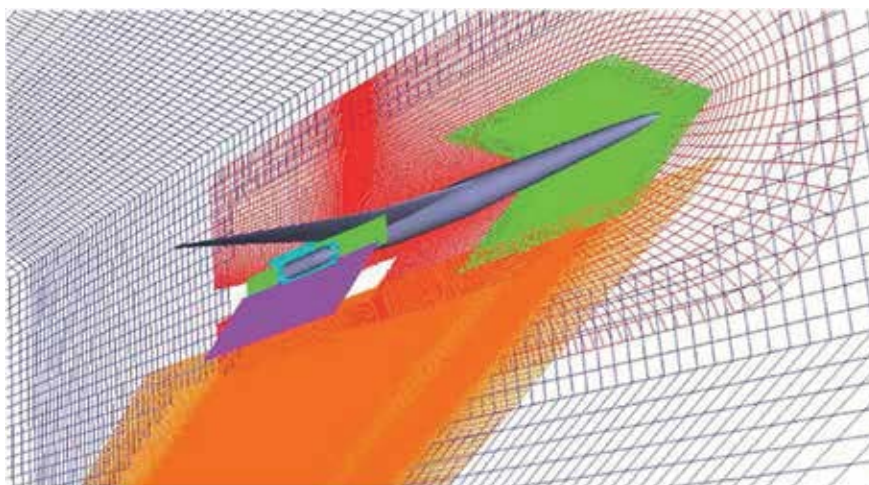


Figure 7.68. Overall view of the OVERFLOW grid (ref. 7.28).

Two inlet geometries, an external compression inlet and a mixed compression inlet, were utilized for each of the six engine locations. The differences in geometry of these engine inlets (fig. 7.69) produced different shock strengths and patterns and thus cause different interference effects, drags, and lifts as well as sonic booms. Near-field pressure and sonic booms for the mid-axial position of the external compression engine are given in figures 7.70 and 7.71, respectively. Clearly, in this location, the under-wing location of the nacelle produces the stronger shock. This carries over to the ground signature where the under-wing nacelle shock has coalesced with the bow shock to form a slightly higher $\Delta p/p$ than that produced by the over-wing nacelle location (fig. 7.71 (a)).

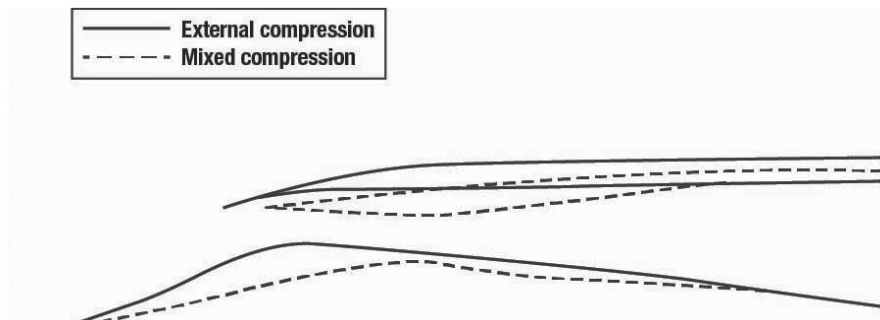


Figure 7.69. Inlet geometry comparison (ref. 7.28).

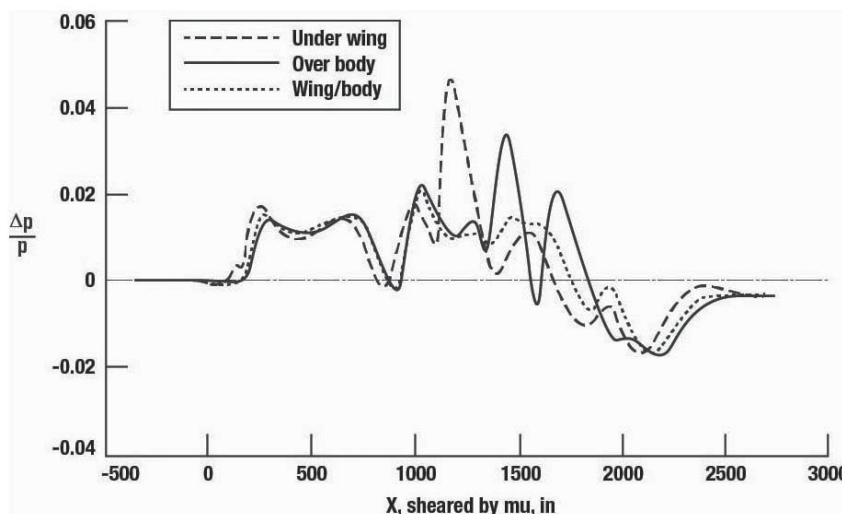
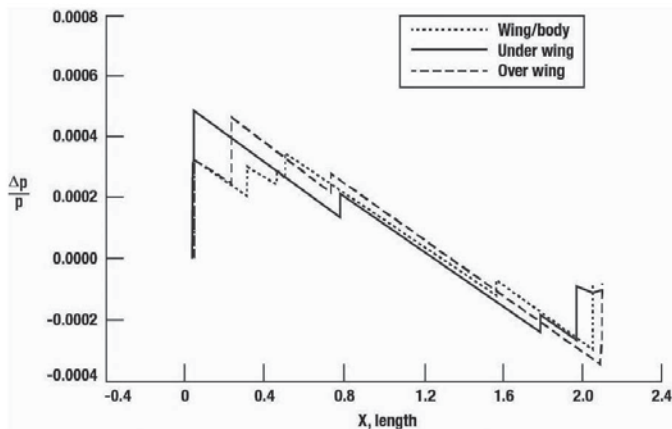
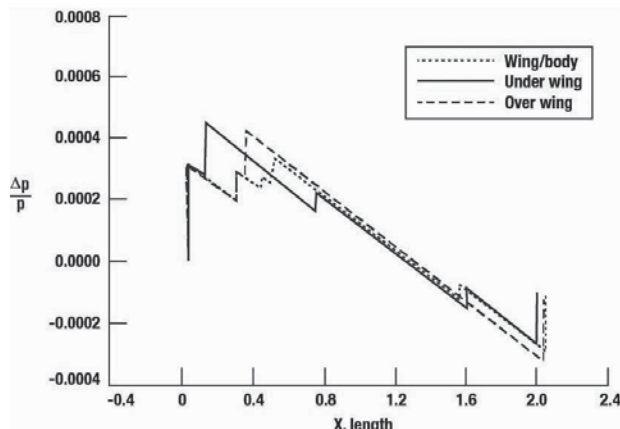


Figure 7.70. Near-field pressure comparison for external compression inlet (adapted from ref. 7.28).



(a) External compression signatures.



(b) Mixed compression signatures.

Figure 7.71. External and mixed compression inlet ground signatures (ref. 7.28).

Ground pressure signatures for the mixed compression inlet seen in figure 7.71(b) are similar to those for the external compression inlet with the exception that the under-wing nacelle's shock does not quite coalesce with the bow shock. The flight conditions and configuration data for these calculations are given below in table 7.7.

Table 7.7. Flight Conditions and Configuration Data for Figures 7.65 through 7.71

Mach number	2.20
Altitude	56,000 ft
Wing Area	1800 ft ²
Fuselage length	140 ft
Weight	101,000 lbs

A low-boom supersonic business jet (SBJ) configuration was designed and analyzed by Mack and the results are documented in reference 7.38. It has its engines mounted on the vertical tail, a canard for take-off rotation, and a wing with a curved (versus straight-line segments) leading edge. Several different canards and canard locations were studied to improve the take-off characteristics and meet the 6000-foot take-off distance specification. The three-view depiction in figure 7.72 is the SBJ with the original canard. Other canard geometries and locations were examined in reference 7.38 to increase rotation rate and decrease take-off distance. The effective area distribution of this configuration is shown in figure 7.73 along with the target low-boom distribution (dashed line). X_e is the effective distance along the longitudinal direction.

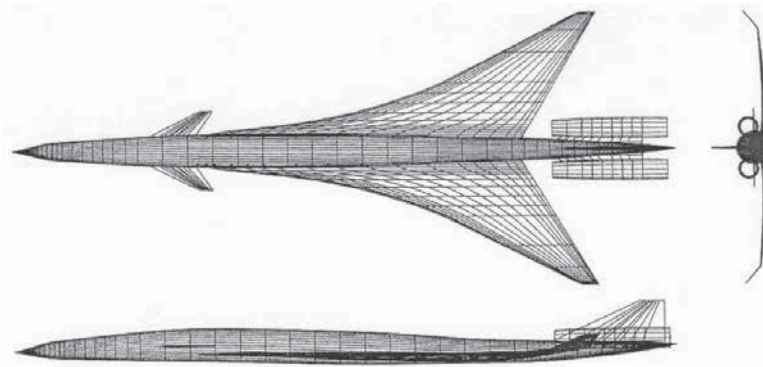


Figure 7.72. Three-view depiction of low-boom SBJ concept (ref. 7.38).

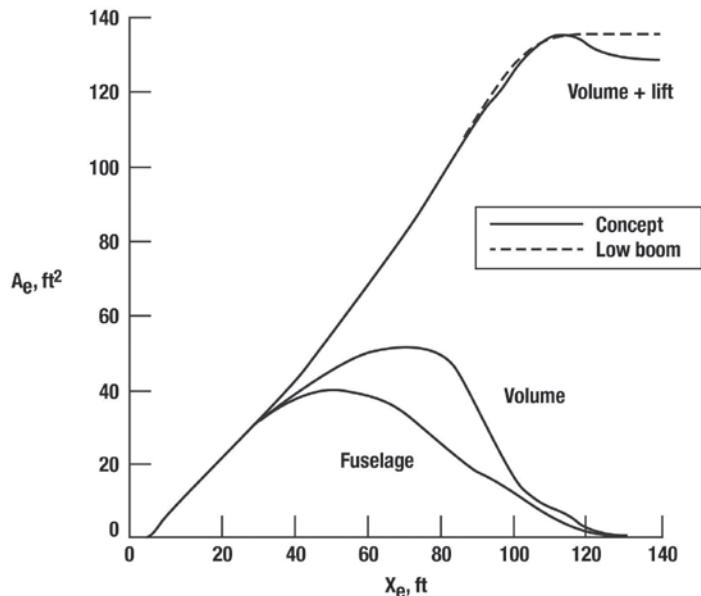


Figure 7.73. Summed equivalent areas, excluding nacelles, of the SBJ concept shown above. Mach = 2, $W_c = 88,497$ lbs, and $h = 53,000$ feet (ref. 7.38).

The F-function for the nacelles was calculated by the method of reference 7.31 and is plotted in figure 7.74 where y is the spanwise direction or Whitham F-function effective length parameter. When this is added to the basic wing-fuselage F-function the result is shown on the left of figure 7.75. Note that the increment due to the nacelle starts at a y value of around 100 feet. A slightly better result might have been achieved had the nacelles and the start of the expansion been a bit closer. Mack notes in reference 7.38 (p. 18),

Ideally, the nacelle volume F-function would be added to the fuselage-wing-fin volume and wing-lift F-function at the longitudinal distance where the fuselage-wing F-function expansion began. However, the nacelles off F-function in figure 7.75(b) shows the ideal was not completely achieved. Better agreement between the SBJ concept's wing/fuselage/fin/nacelle F-function and its theoretically ideal F-function might have been achieved by expending more effort in the fuselage tailoring and/or by using more stations in the volume and lift distribution.

Nevertheless, the ground pressure signature for the configuration with and without nacelles, plotted in figure 7.76, does not show a large increment due to the nacelles. There is a small increase in the tail shock and a small shock at an $(x-\beta h)/l_c$ of 0.3.

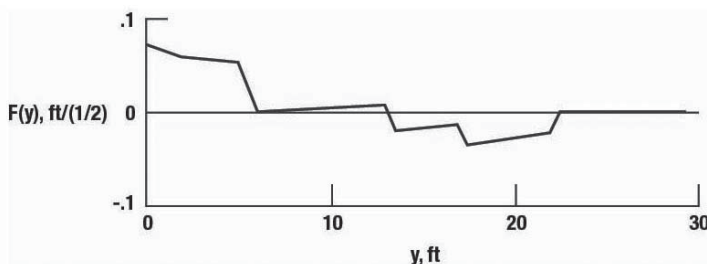
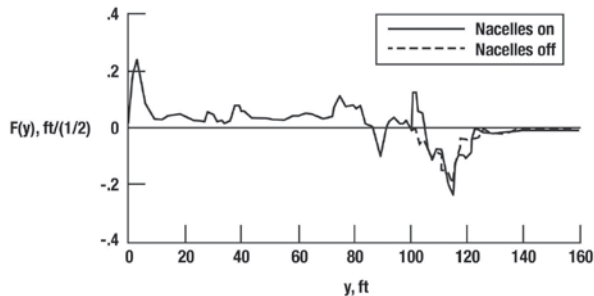
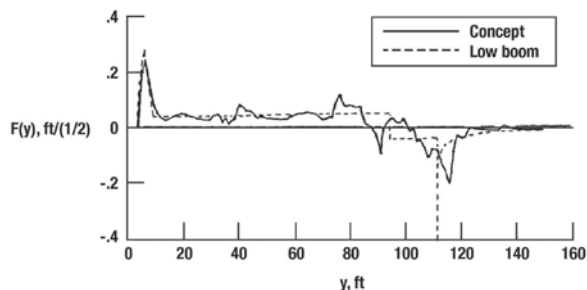


Figure 7.74. F-function of the nacelle for the concept's low-bypass ratio engine (ref. 7.38).



(a) Comparison of nacelle-on and nacelle-off F-functions.



(b) Comparison of ideal and calculated F-functions – nacelles off.

Figure 7.75. Nacelle-on and nacelle-off F-functions of the SBJ concept at beginning of cruise. As well as nacelles off F-function compared to that of ideal low-boom concept (ref. 7.38).

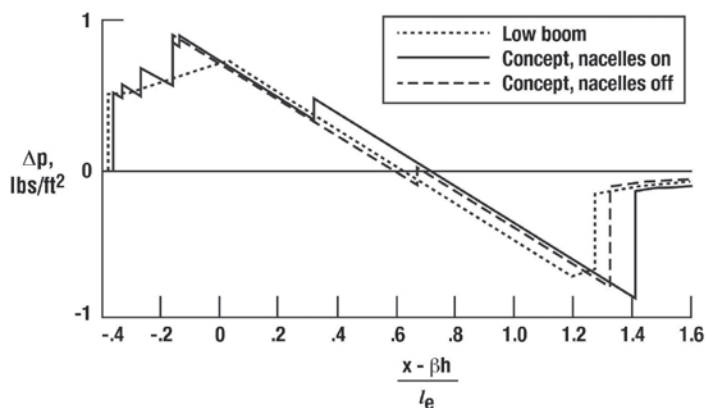


Figure 7.76. Predicted ground signatures from the SBJ concept with the canard at zero lift. Mach = 2, $W_c = 88,497$ lbs, and $h = 53,000$ ft (ref. 7.38).

In summary, there are published studies that address the effect of nacelles on sonic booms. Sample results from some of these studies have been presented. It is clear that the incremental effect of engine nacelles on the sonic boom produced by a supersonic cruise aircraft is highly dependent on the aircraft's geometry and the locations of engine nacelle placement. Changes in wing planform and fuselage longitudinal area distributions can usually be made to reduce the adverse effects of an engine installation. Using F-function equivalent area distributions to make adjustments to the area distribution and/or locate nacelles can be most useful in a qualitative sense. Generally, these adjustments should be validated and fine-tuned using CFD.

The Effect of Engine Exhausts on Sonic Booms

The origin of the trailing or rear shock of a sonic boom is substantially more complicated than that of the leading or bow shock. This is due to the geometric complexity of the rear areas of most configurations. Vertical and horizontal tails, engines, wing trailing edges, and the aft portion of fuselages all contribute to establishing the aft portion of the boom signature. Most of these aircraft components are usually accounted for in sonic boom predictions whether the flow field analysis is made using the Euler equations or the linear effective area F-function approach. However, there is one item that is frequently ignored independent of the method used – the contribution of engine exhaust plume. This is most likely because engine exhaust is not part of the aircraft's geometric definition and an accurate calculation of the plume shape, for a real engine, may be beyond most analysts' capabilities. During the 1950s and 1960s, the convenient assumption was usually made that the effective exhaust shape was cylindrical. However, there were methods available for estimating the effective boundary of jets exhausting into a supersonic stream (refs. 7.39 to 7.41). Reference 7.42, published in 1969, documented the first study that analyzed both the real and effective (solid body) shape of jet plumes, as well as their possible effect on sonic booms. Experimental data for a series of seven nozzles was provided (see figure 7.77 for details) along with calculations for the inviscid jet boundary using the linear method of reference 7.43. Also, the jet equivalent solid body shapes were calculated using the method detailed in the study.

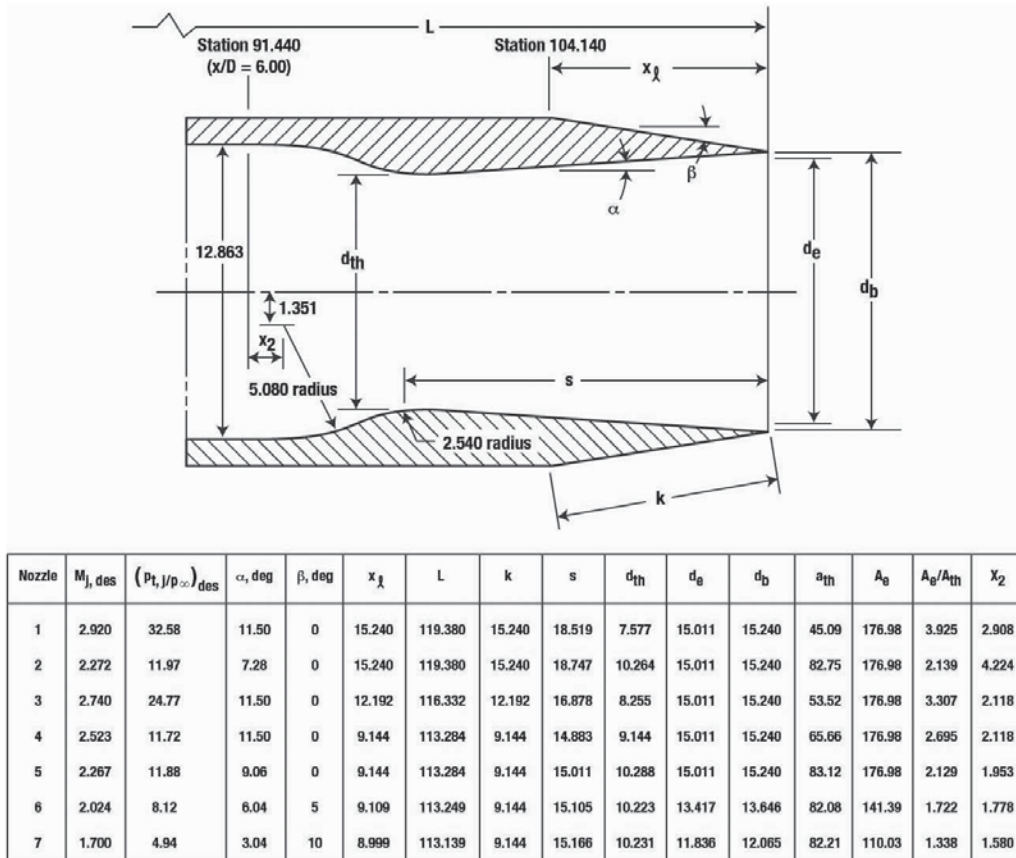


Figure 7.77. Details of nozzles. All dimensions are in cm except as noted. Areas are in cm^2 (ref. 7.42).

Figure 7.78 shows illustrative jet-equivalent solid shapes for nozzle 4 and for a series of pressure ratios. The solid body plumes shown in this figure were used for the near-field pressure signature calculations shown in figure 7.79. These calculations were made for two aircraft configurations – a podded engine fighter and a four-engine supersonic transport. Results for Mach 2.2 and a range of pressure ratios up to 2.326 are given in figure 7.79 (ref. 7.42).

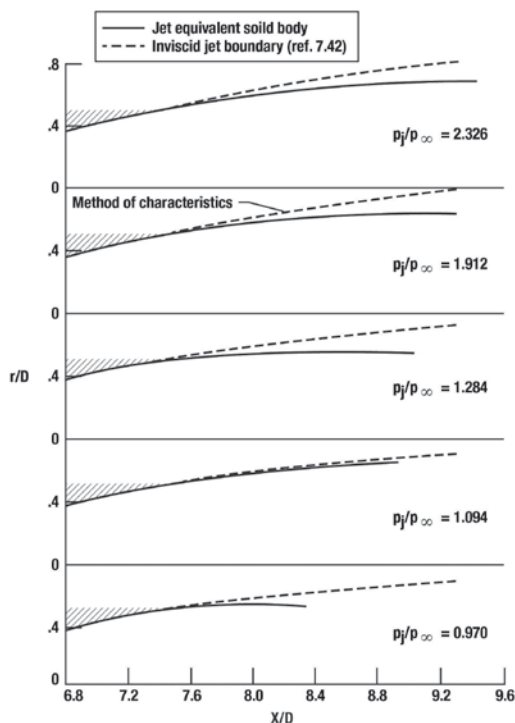
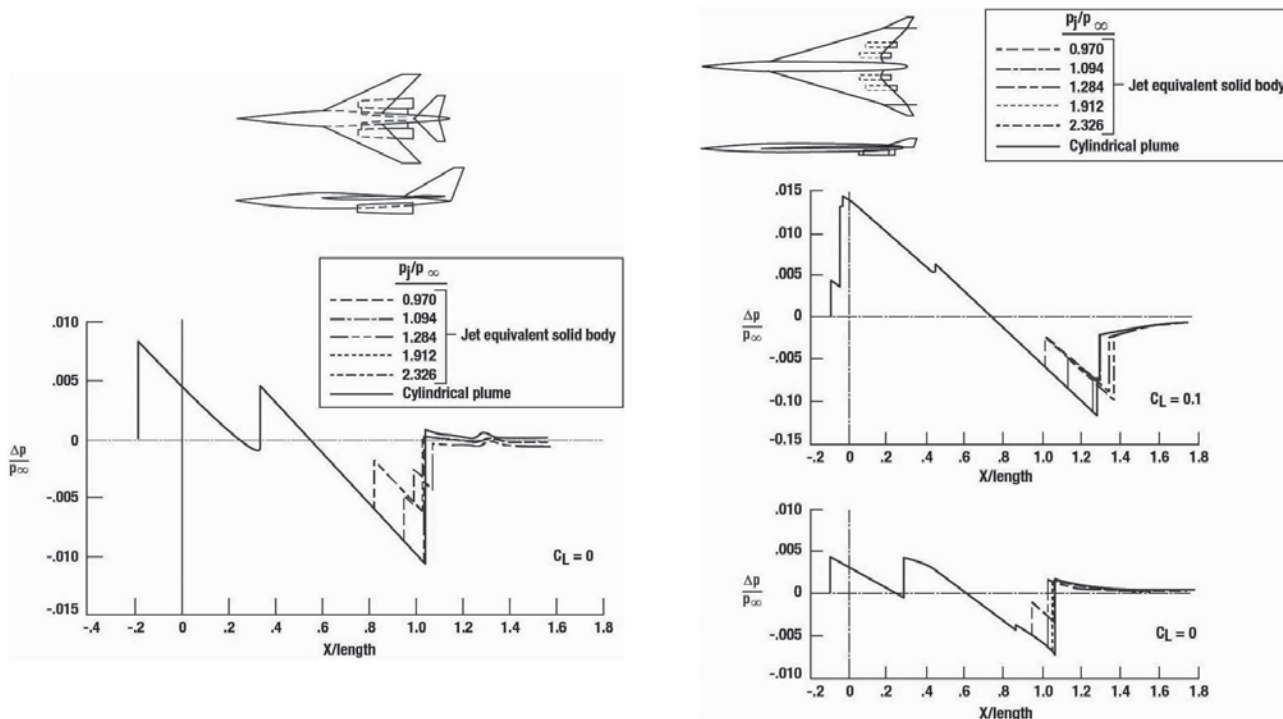


Figure 7.78. Comparison of jet equivalent solid body with inviscid jet boundary for jets exhausting from nozzle 4 at several jet static-pressure ratios, Mach = 2.2 (adapted from ref. 7.42).



(a) Fighter airplane with two podded engines.

(b) Supersonic transport airplane with four podded engines.

Figure 7.79. Effect of jet plume on sonic boom pressure signature of podded-engine fighter airplane and supersonic transport airplane with nozzle 4, Mach = 2.20 (adapted from ref. 7.42).

Putnam and Capone note in reference 7.42 (p. 17) that these calculations,

Indicate that there is considerable effect on the trailing-shock-wave system resulting from the jet plume with the effects increasing with jet pressure ratio. However, these effects are a near field effect, and calculations of the far field N-wave pressure signatures indicated that for the cases considered there would be no effect of the jet plume.

There are no data or sonic boom signatures given to support this conclusion.

Additionally, in 1992 Barger studied the exhaust problem mentioned in reference 7.44 using the numerical technique of Salas (ref. 7.45) for plume shape calculations. Most of his results were for the low-boom design configuration depicted in figure 7.80. Sonic booms were computed for this configuration at several Mach numbers with both cylindrical and computed plume shapes. The calculated plume and shock for Mach 2.1 and an altitude of 55,000 feet is shown in figure 7.81. No numbers are given for the pressure ratios or for the Mach number ratio M_j/M_∞ for this plume.

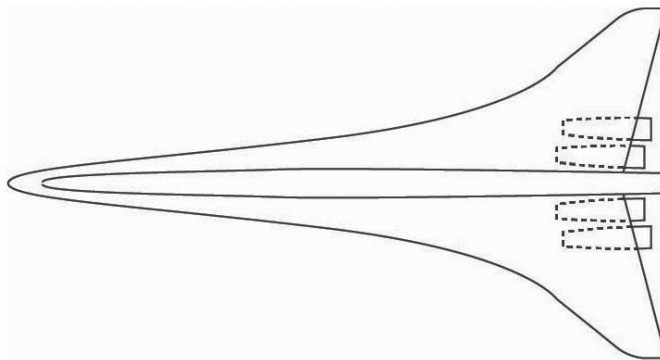


Figure 7.80. Supersonic cruise, low sonic boom design (ref. 7.44).

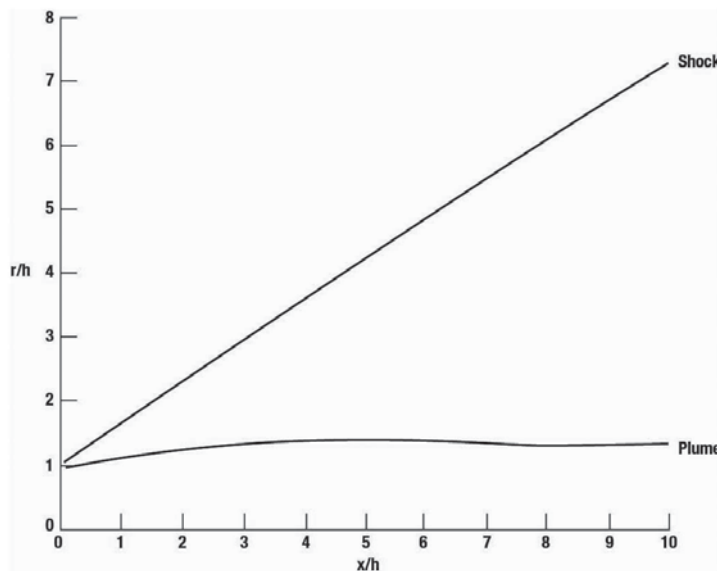


Figure 7.81. Computed plume shape for flight at Mach = 2.1 and altitude of 55,000 feet (ref. 7.44).

F-function methodology was used for the boom calculations and is given along with the sonic boom pressure distributions in figure 7.82 for both cylindrical (fig. 7.82(a)) and calculated plumes (fig. 7.82(b)). Clearly, the calculated plume provided a significant hump in the F-function beyond an x/L of 0.7 and it, in turn, caused an increase in the strength of the secondary shock from 1.2 to ~ 1.8 lbs/ft² (fig. 7.82(b)). This increase caused the secondary shock to become the dominant noise source. After analyzing the results for altitudes of 45,000, 55,000, and 60,000 feet, Barger (ref. 7.44, p. 4) concluded that “for flight at altitudes above 60,000 ft, the plume effects were dominant; but for altitudes below 55,000 ft, they were significant but not dominant.”

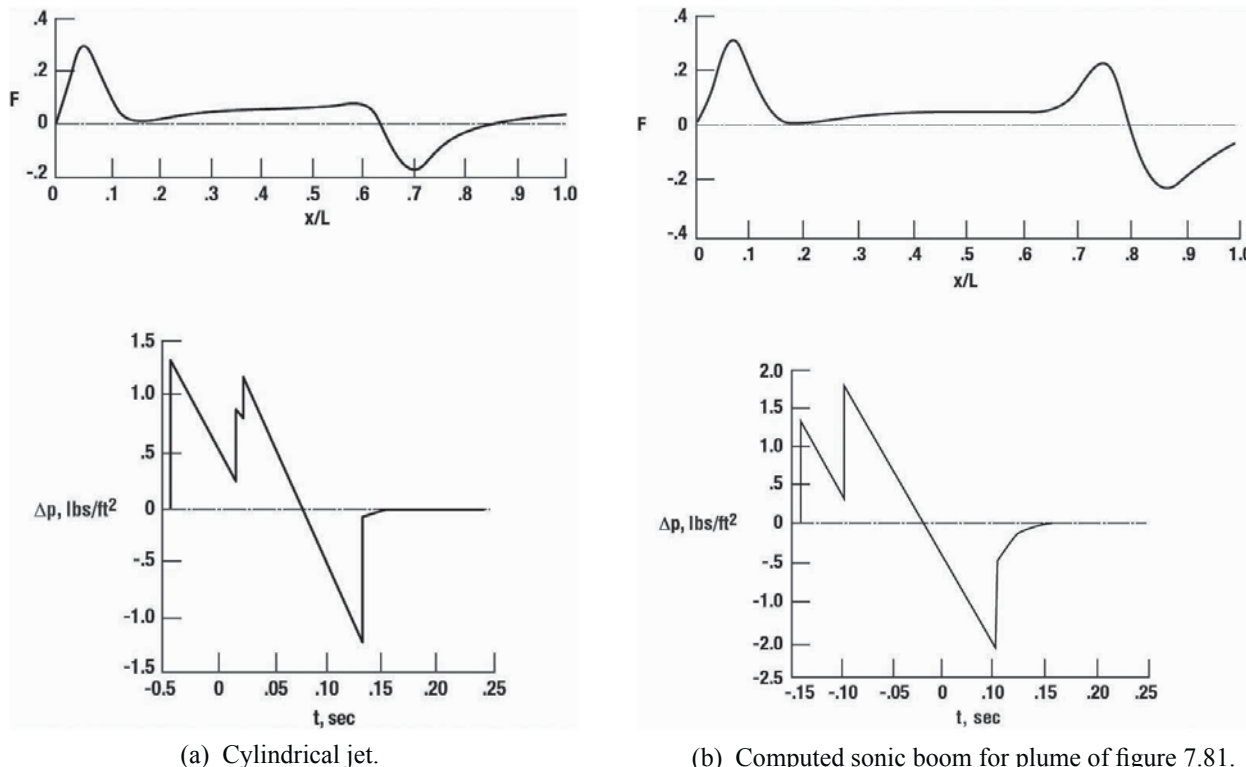


Figure 7.82. F-functions and ground level signatures for low-boom configuration with cylindrical jet and computed plume shown in figure 7.81, $M = 2.1$ and altitude of 55,000 feet (adapted from ref. 7.44).

The results of a third study, carried out by Siclari, attempted to determine the effect of real exhaust plumes on the sonic boom of a configuration was published in 1992. In his Euler-equation calculations, discussed in reference 7.36 (p. 187), Siclari stated that,

The inlets were initiated by assuming that all of the mass entering the face of the engine is swallowed or zero spillage is assumed. The exhaust of each nacelle was simulated by injecting mass into the flow and by assuming the flow was no longer isoenergetic. In other words, the enthalpy downstream of the engines was no longer assumed to be constant. The actual engine operating conditions for the Mach 2 aircraft obtained from NASA and used in the computation were as follows:

$$\rho_j/\rho_\infty = 0.4796$$

$$V_j/V_\infty = 1.697$$

$$P_j/P_\infty = 1.0$$

The exhaust pressure ratio for the Mach 2 aircraft is matched with freestream. These conditions lead to exhaust jets with approximately a 2.4 Mach number.

Near-field and ground sonic boom pressure signatures for the Mach 2 configuration are plotted on the left side of figure 7.83 and show minimal effects on both. The bow and trailing shocks are not affected and the mid-signature shock that the plumes create is much less than that of the bow shock.

Calculations were also made in reference 7.36 at Mach 3 for the configuration shown on the right side of figure 7.83. The operating conditions for the engine were

$$\rho_j/\rho_\infty = 0.3904$$

$$V_j/V_\infty = 2.686$$

$$P_j/P_\infty = 1.048$$

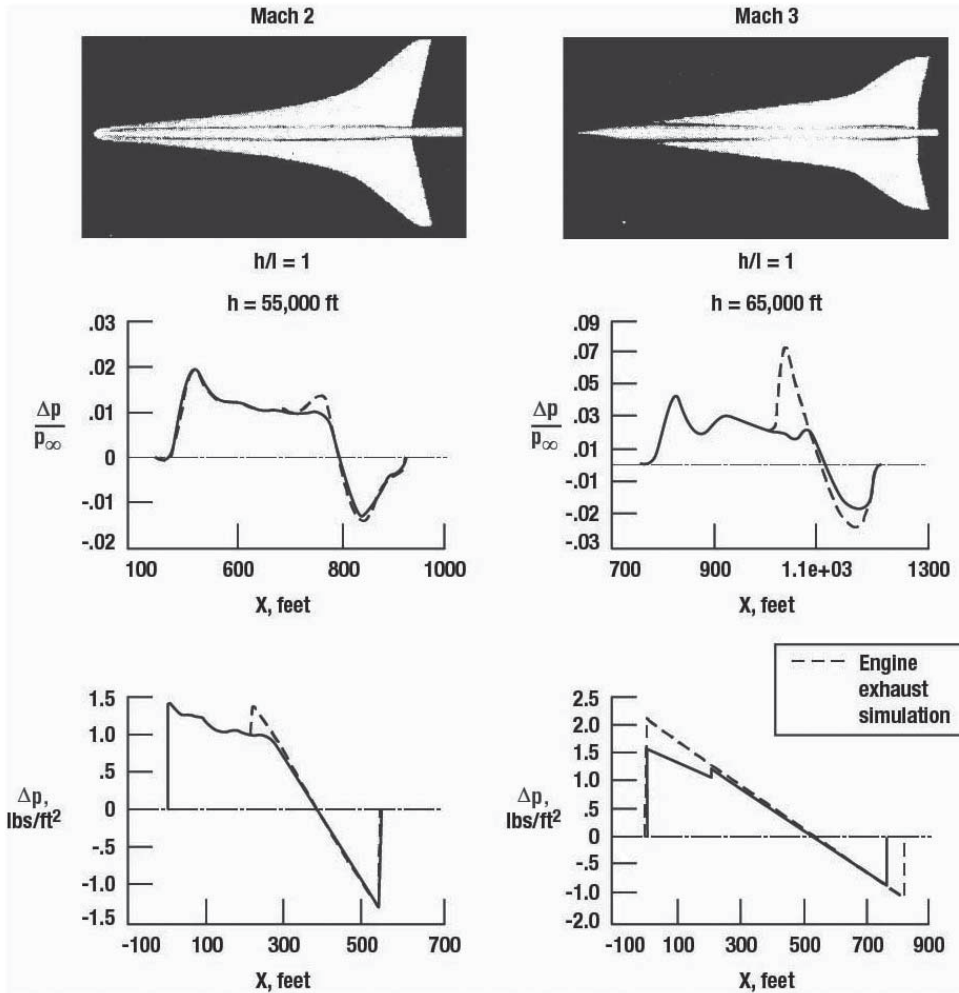


Figure 7.83. Comparison of $h/l = 1$ and extrapolated ground signatures for both flow-through nacelles and nacelles with engine exhaust simulation for the Mach 2 and Mach 3 configurations (ref. 7.36).

The jet plume is slightly under expanded and the jet exit Mach number for these conditions was computed as 4.92.

In reference 7.36 (p. 190), Siclari notes that “As a result of these conditions (i.e., under expanded jet and higher exhaust (Mach number)), it is expected that the engine exhaust for the Mach 3 aircraft will have a greater effect on the pressure field below the aircraft.” As seen in figure 7.83, the effect of the plumes on the near-field and ground sonic boom signatures is much larger. Both the bow and trailing shocks of the sonic boom are increased. Note that the cruise altitude for the Mach 3 case is 65,000 feet, while the cruise altitude for Mach 2 is 55,000 feet.

Calculated Results for Initial Slope and Contours of Jet Plumes

Both of the cases described above had static pressure ratios close to 1.0. As pressure ratio increases for the same flight conditions, the plume will be larger and the shock it generates will be stronger. Figure 7.78 for nozzle 4 illustrates the effect of increases in pressure ratio on plume size (fig. 7.84 from ref. 7.43 may be even more useful) since it highlights the initial slope of the plume. The latter calculations are for $\gamma_j = \gamma_\infty = 1.4$ and with the jet Mach

number equal to 2.0. The pressure ratio ranges from ~ 0.25 to 5.5 and Mach numbers from 2 to 9. As stated by Englert in reference 7.43 (p. 16),

The exact results were obtained by use of Prandtl-Meyer expansion curves for the expanding flow on one side of the jet boundary and by use of two-dimensional shock charts on the compression side of the boundary. A unique solution $\eta(0)$ is obtained, which yields continuity of pressure and velocity direction across the jet boundary.

It is also possible to calculate the exact values by solving the cubic equations for P_2/P_j and P_2/P_∞ simultaneously. Calculated values for $M_\infty = 2$ of the exact initial slope are given in figure 7.84 from reference 7.43 (solid lines) and are represented by the square symbols in the equation derived in the next section of this Chapter. As observed, the square symbols and the solid lines yield identical results. Even using only the terms up to $\eta(0)^2$ (i.e., eliminating the cubic term) provides a good approximation of P_j/P_∞ as seen by the circular symbols on figure 7.84. Finally, the linear equation results from reference 7.43 yield a good approximation of the exact $\eta(0)$ up to pressure ratios of 2.5. Whether these results are based on linear potential theory or exact theory, one can appreciate that for pressure ratios of 5 and 6 and plume initial slopes on the order of 0.25 (14°), the substantial impact exhaust plumes can have on the trailing shock of sonic booms.

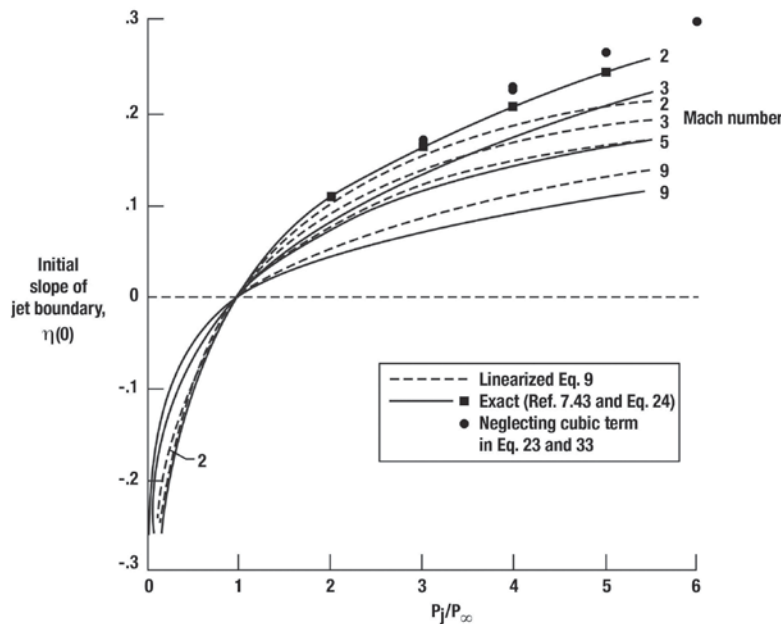


Figure 7.84. Comparison of linearized and exact initial slopes of jet boundary. Nozzle-exit and stream specific heat ratios, γ_j and $\gamma_\infty = 1.4$, nozzle wall and boat-tail angles = 0, $M_j = 2$ (ref. 7.43).

All of the theoretical results for jet plume shapes discussed were for air as the constituent gas, both for the exhaust and free-stream flows. The effect of real exhaust gases was not illustrated. The linear equation for the initial slope of the plume that produced (the dashed lines in figure 7.84) can also be used to get some idea of the effects of the exhaust gas on the initial slope and shape of the plume. The equation for $\eta(0)$ from reference 7.43 can be rewritten using the equation of state and the equation for the speed of sound as

$$\eta(0) = \frac{P_j/P_\infty - 1}{\frac{\gamma_j M_\infty^2}{\beta_\infty} \left[1 + \frac{\gamma_j M_j^2 \beta_\infty P_j}{\gamma_\infty M_\infty^2 \beta_j P_\infty} \right]} \quad (9)$$

While this is a linear result, it is most useful in a qualitative sense. Figure 7.85, derived from the above equation for $M_\infty = 2$ and $\gamma_j = 1.32$ shows (as expected) the strong dependence of the initial slope of the plume (i.e., $\eta(0)$) on

the value of the pressure ratio P_j/P_∞). Jet Mach number increases cause a decrease in plume slope while a realistic (reduced) ratio of the jet specific heats (i.e., 1.4 to 1.32) causes an increase.

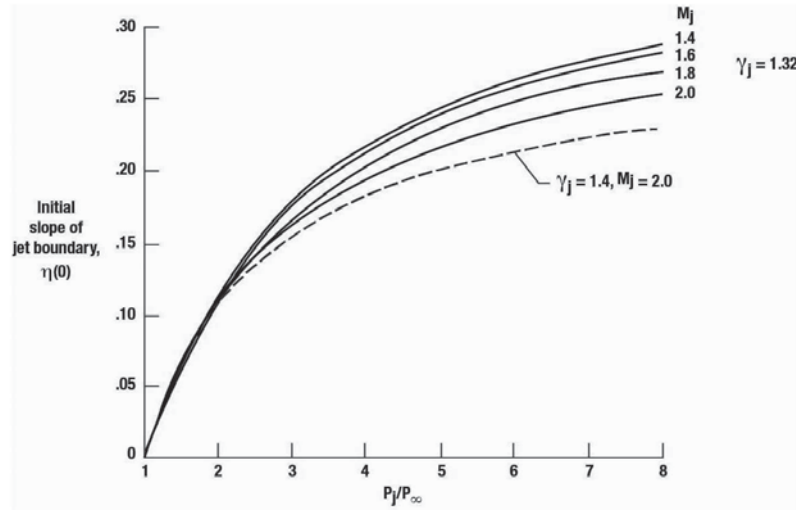


Figure 7.85. Initial slopes of jet plumes versus engine exhaust/free-stream pressure ratio for $M_\infty = 2.0$, $\gamma_j = 1.32$.

First and second order solutions of the linear potential equation for the shape of the plume are derived in reference 7.43. The first order solution is given by

$$\frac{r_b}{r_o} = 1 + \beta_\infty \frac{\eta(0) \sin K\bar{z}}{Ke b_1(\bar{z}/2)} \quad (10)$$

$$\bar{z} = \frac{Z}{\beta_\infty r_o} \quad (11)$$

$$K = \sqrt{b_2 - b_1^2/4} \quad (12)$$

$$b_1 = \frac{\frac{\gamma_j M_j^2 P_j}{\gamma_\infty M_\infty^2 P_\infty} \frac{\beta_\infty^2}{\beta_j^2} - 1}{2 \left[\frac{\gamma_j M_j^2 P_j}{\gamma_\infty M_\infty^2 P_\infty} \frac{\beta_\infty}{\beta_j} + 1 \right]} \quad (13)$$

$$b_2 = \frac{3}{8} \frac{\left[1 + \frac{\beta_\infty^3 \gamma_j M_j^2 P_j}{\beta_j^3 \gamma_\infty M_\infty^2 P_\infty} \right]}{\left[1 + \frac{\beta_\infty \gamma_j M_j^2 P_j}{\beta_j \gamma_\infty M_\infty^2 P_\infty} \right]} \quad (14)$$

These equations are slightly different in form, but equivalent to, those of reference 7.43. Note that z is the distance measured from the nozzle exit. As can be seen, the controlling exhaust gas parameters other than P_j/P_∞ are $\frac{\gamma_j M_j^2}{\gamma_\infty M_\infty^2}$ and $\frac{\beta_\infty}{\beta_j}$. A plot of the above equation for r_b/r_o versus \bar{z} as well as that for the second

order is given in figure 7.86 for $M_\infty = M_j = 2.0$ and a range of pressure ratios. Note that the first order solution varies little from that of the second, particularly for pressure ratios less than five. In reference 7.43 (p. 20), Englert notes that “The difference between the simpler solution (equation for r_b/r_0 above) and characteristics and experimental data was within 10 percent over the range investigated.” Thus, it is clear that for sonic boom calculations, based on the F-function methodology, the first order Englert equation is sufficient.

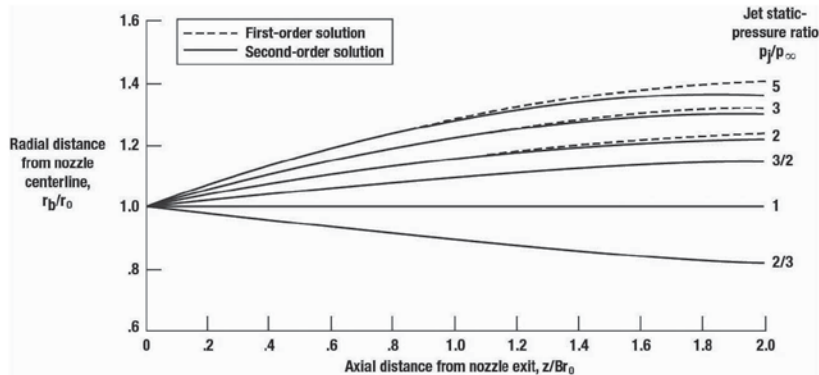
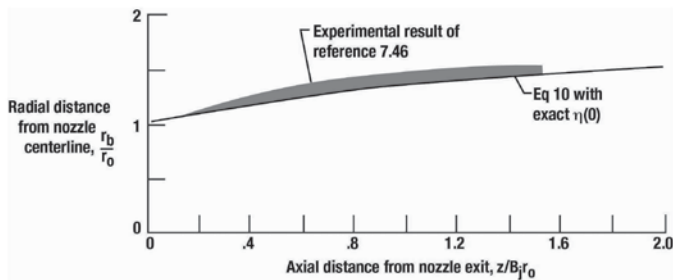
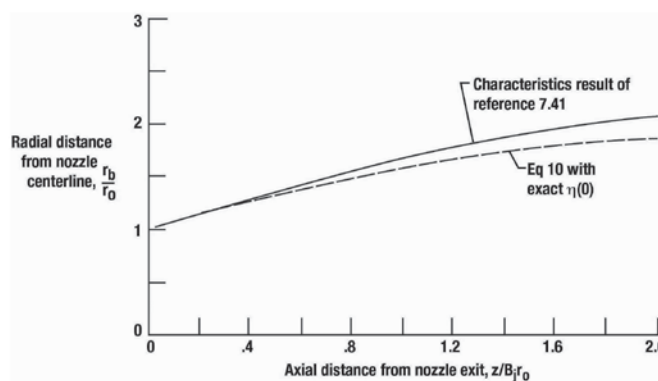


Figure 7.86. Comparison of first and second order theory for jet shape. Nozzle exit and stream specific heat ratios, γ_j and $\gamma_\infty = 1.4$, Nozzle-exit and stream Mach numbers M_j and $M_\infty = 2$ (adapted from ref. 7.43).

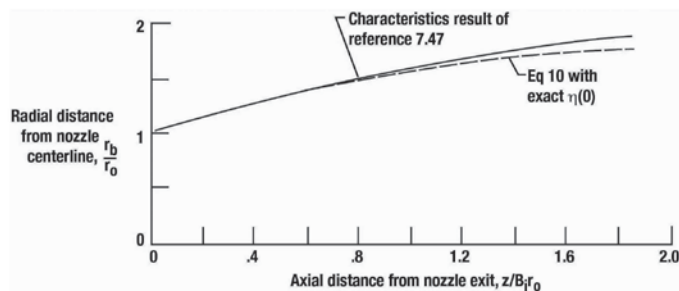
It is also of interest to compare the plume shape with the exact $\eta(0)$ in equation(10) to those calculated by the characteristics method. Figure 7.87 (ref. 7.43) shows such a comparison using data from three separate papers (refs. 7.41, 7.46, and 7.47). Clearly, there is excellent agreement between the two methods, particularly for the two lower jet Mach number cases. It is evident, then, that the linear plume-shaped equation with the exact $\eta(0)$ gives results comparable to characteristic equations for the plume shape just downstream of the nozzle for supersonic Mach numbers.



(a) $M_j = 2.29$, $M_\infty = 3.0$, $p_j/p_\infty = 2.0$, nozzle wall angle = 12° , boattail angle = 0° .



(c) $M_j = 3.0$, $M_\infty = 3.0$, $p_j/p_\infty = 12.23$, nozzle wall angle = 12.5° , boattail angle = 0° .



(b) $M_j = 2.38$, $M_\infty = 3.24$, $p_j/p_\infty = 8.96$, nozzle wall angle = 12.5° , boattail angle = 9° .

Figure 7.87. Jet contour for supersonic external flow (adapted from ref. 7.43).

Finally, all the analyses and data shown were for simple nozzles with uniform flow out of the nozzles. Plumes and associated shock systems for real engines with real exhaust gases, internal mixers, cowls with serrated trailing edges, by-pass air, and plugs have not been published in the open literature. The utility of the calculation methods for simple nozzles for approximating the plumes and shocks for the more complicated real engines has not been demonstrated.

Calculation of Exact $\eta(0)$

The equations defining the ratios of P_2/P_j and P_2/P_∞ (see fig. 7.88) are given below.

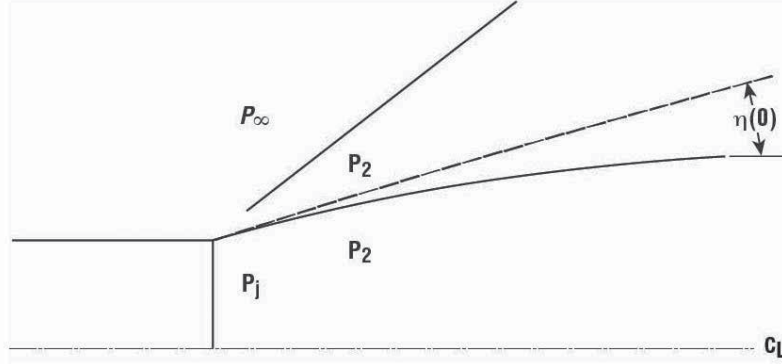


Figure 7.88. Sketch showing plume, plume shock, and pressures.

With A, B, C, D, E and F defined by

$$\frac{P_2}{P_j} = 1 - A\eta(0) + B\eta(0)^2 - C\eta(0)^3 \quad (15)$$

$$\frac{P_2}{P_\infty} = 1 + D\eta(0) + E\eta(0)^2 + F\eta(0)^3 \quad (16)$$

$$A = \frac{\gamma_j M_j^2}{\beta_j} \quad (17)$$

$$B = \gamma_j M_j^2 \left[\frac{(\gamma_j + 1)^2 M_j^4 - 4\beta_j^2}{4\beta_j^4} \right] \quad (18)$$

$$C = \frac{\gamma_j M_j^2}{2\beta_j^7} \left[\left(\frac{\gamma_j + 1}{6} \right) M_j^8 - \frac{(5 + 7\gamma_j - 2\gamma_j^2)}{6} M_j^6 + 5/3(\gamma_j + 1) M_j^4 - 2M_j^2 + \frac{4}{3} \right] \quad (19)$$

$$D = \frac{\gamma_\infty M_\infty^2}{\beta_\infty} \quad (20)$$

$$E = \gamma_\infty M_\infty^2 \left[\frac{(\gamma_\infty + 1) M_\infty^4 - 4\beta_\infty^2}{4\beta_\infty^2} \right] \quad (21)$$

$$F = \frac{\gamma_\infty M_\infty^2}{\beta_\infty^7} \left[\frac{(\gamma_\infty + 1)}{32} M_\infty^8 - \frac{(7 + 12\gamma_\infty - 3\gamma_\infty^2)}{24} M_\infty^6 + \frac{3}{4}(\gamma_\infty + 1) M_\infty^4 - M_\infty^2 + \frac{2}{3} \right] \quad (22)$$

Combining equations (15) and (16) yields

$$(P_j/P_\infty - 1) - \left(A \frac{P_j}{P_\infty} + D\right) \eta(0) + \left(B \frac{P_j}{P_\infty} - E\right) \eta(0)^2 - \left(C \frac{P_j}{P_\infty} + F\right) \eta(0)^3 = 0 \quad (23)$$

Solutions to this equation yields the required $\eta(0)$ and is given below

$$\eta(0) = -\frac{p}{3} + x \quad (24)$$

Where p and x are normally negative. The quantities p and x are determined through a series of equations starting with p , q , and r .

$$x = -2 \sqrt{\frac{a}{3}} \cot 2\phi \quad (25)$$

$$\phi = \tan^{-1} (\tan \psi)^{1/3} \quad (26)$$

$$\psi = \frac{1}{2} \tan^{-1} \left(\frac{b^2}{4} / \frac{a^3}{27} \right)^{-1/2} \quad (27)$$

$$a = \frac{1}{3}(3q - p^2) \quad (28)$$

$$b = \frac{1}{27}(2p^3 - 9pq + 27r) \quad (29)$$

$$p = \frac{-\left(B \frac{P_j}{P_\infty} - E\right)}{C \frac{P_j}{P_\infty} + F} \quad (30)$$

$$q = \frac{A \frac{P_j}{P_\infty} + D}{C \frac{P_j}{P_\infty} + F} \quad (31)$$

$$r = \frac{-\left(\frac{P_j}{P_\infty} - 1\right)}{C \frac{P_j}{P_\infty} + F} \quad (32)$$

$$\eta(0) = \frac{(AP_j/P_\infty + D) - \sqrt{\left(A \frac{P_j}{P_\infty} + D\right)^2 - 4\left(\frac{P_j}{P_\infty} - 1\right)\left(B \frac{P_j}{P_\infty} - E\right)}}{2\left(B \frac{P_j}{P_\infty} - E\right)} \quad (33)$$

Configuration Design/Analyses Concepts

The use of finite difference techniques to solve the three-dimensional Euler equations and full potential equation dates back to the 1960s. Wings, bodies, and wing-body configurations were treated in the 1970s using primarily single block grids. Improvements in grid technology, solution algorithms, and computers combined in the 1980s to allow the treatment of complex configurations (including nacelles, pylons, empennages, etc.) in a matter of hours. Purely supersonic flows that allowed the use of simple marching schemes could be solved in minutes. In addition, with the increased speed and storage capability of the large mainframe computers, the complexity of the Navier-Stokes could be accommodated and viscous effects assessed. The application of CFD and grid codes during the 1970s and 1980s seems to have been primarily to aircraft design analyses with an emphasis on aerodynamic characteristics.

Sonic boom analyses requiring a near-field signature for insertion in the Thomas propagation code, produced in 1972, could have benefitted from the application of CFD. However, the first concerted effort to take advantage of this fast improving technology started in the late 1980s. Several AIAA papers appeared in 1990 and 1991 (see refs. 7.48 to 7.52) and a handful of CFD sonic boom papers form the basis of Volume II of the Proceedings of the 1992 Sonic Boom Conference (ref. 7.53). Sonic boom workshops were also held in 1993 (ref. 7.54), 1994 (ref. 7.55), and 1995 (ref. 7.56) with each succeeding session producing design and methodology advancements. NASA Langley Research Center (LaRC), NASA Ames Research Center (ARC), Douglas, Lockheed, Grumman, and Boeing were the major participants.

Large Supersonic Commercial Transport Jet Studies

Most of the basic configuration geometries proposed for large supersonic commercial jets are contained in the first two NASA workshops (refs. 7.53 and 7.54). They are all either arrow-wing or cranked delta-wing designs. Subsequent workshops contain additional improvements to those configurations through trial and error or analytical optimization. Boom reduction to existing configurations is termed boom softening (see refs. 7.57 and 7.58). Comparisons of the maximum boom of several configurations following optimization are presented in reference 7.20. Performance assessments of several candidate configurations are contained in references 7.59 and 7.60. Figure 7.89 gives a sample result from the performance assessments of reference 7.59. It shows all of the configuration planforms and the characteristics table based on a 12,000-foot take-off field length constraint. Assessment of changes in various geometric features is the subject of other published studies. For example, table 7.8 lists some of the options studied by Morgenstern in reference 7.61.

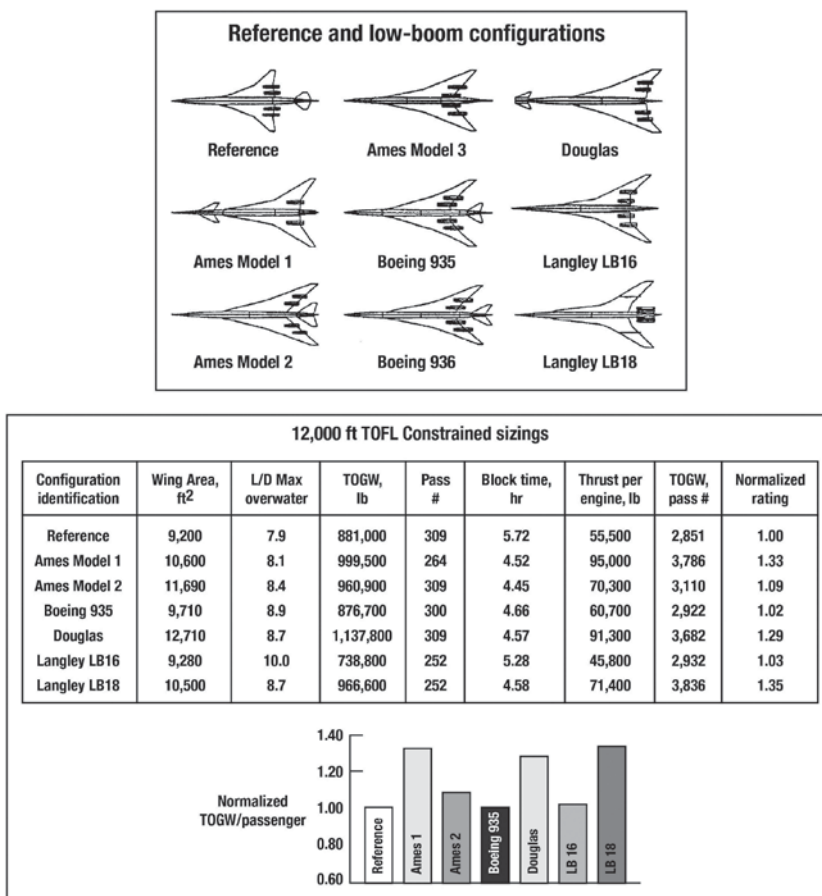


Figure 7.89. Performance assessments of six supersonic cruise low-boom configurations (ref. 7.59).

Table 7.8. Boom Softening Options (ref. 7.61)

Boom Softening Options
Small modifications
Different trim/tail loading
Wing dihedral
Fuselage camber
Outboard wing sweep (also in planform study)
Increased wing area
Moderate Modifications
Planform variations from planform study
Canard/3-surface
Fuselage length
Shaping of front shock using area/lift distribution

A summary of Haglund's assessment on sonic boom reduction possibilities of the Boeing HSCT based on his optimization studies presented in reference 7.60 is as follows:

1. The greater potential for sonic boom reduction rests on the tailoring of the lift distribution by modifications to the wing planform and size. Promising modifications include increased wing size (decreased wing loading), and increased wing slenderness, which may be achieved through increased wing leading-edge sweep and/or reduced span.
2. Wing dihedral shows promise for sonic boom reduction, but the adverse effects on the aerodynamics and structure must be understood and minimized.
3. The modifications that are most beneficial for reduced sonic boom aggravate the low-speed, take-off field length, and community noise problems.
4. The constraint imposed by the need for very small or no performance penalty is a severe one and will limit the range of boom-softening modifications.
5. For the 1080-444 configuration, with aggressive boom-softening and significant wing modifications, about 0.4 lb/ft² reduction in maximum over-pressure was achieved (from 2.97 to 2.57 lbs/ft²). This is at the expense of a 1 percent penalty in MUTATOR.
6. Technology advances that result in greater efficiencies in structures and propulsion will translate directly into reduced sonic boom provided that these advances produce a reduction in wing loading.

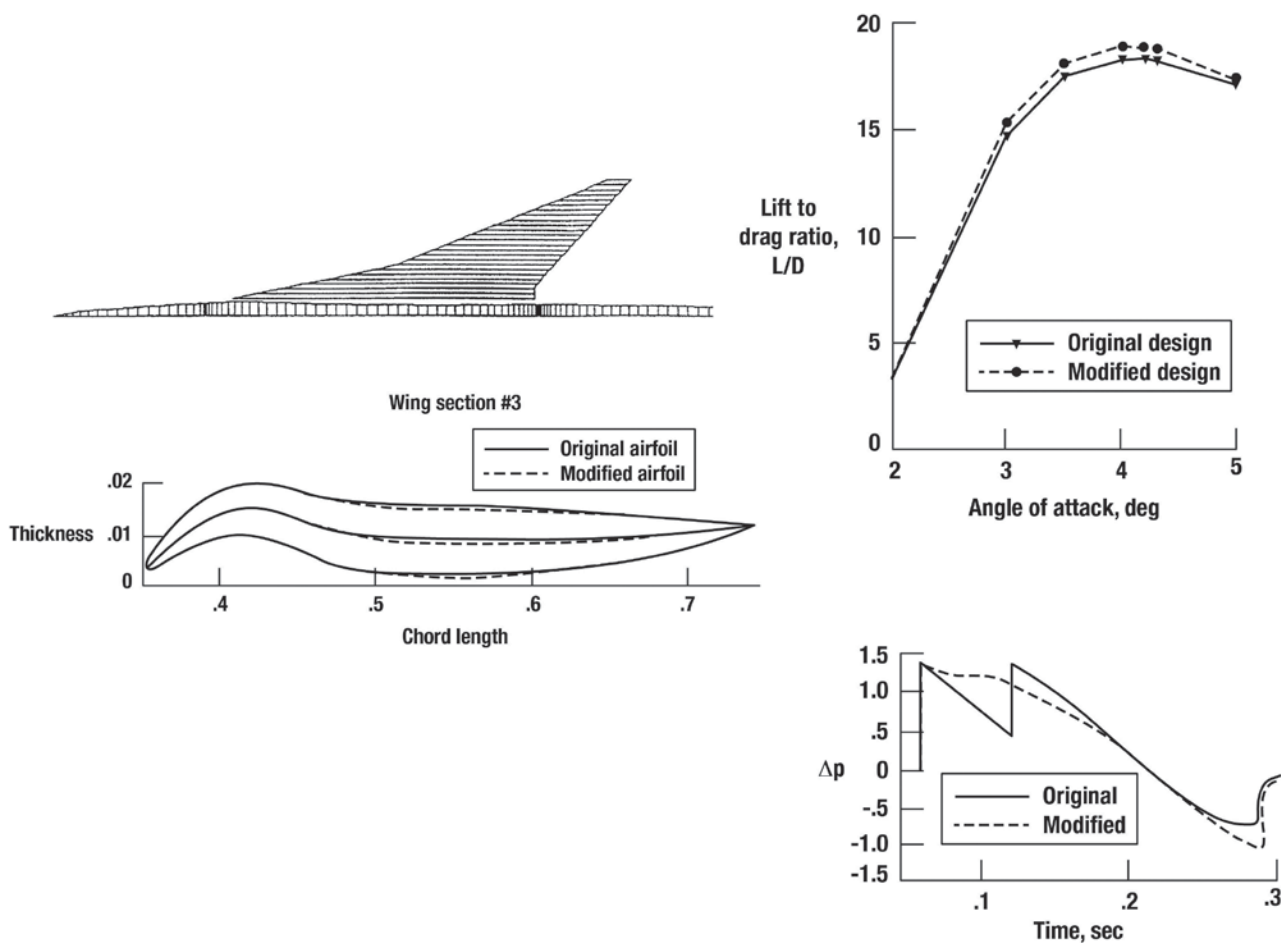
These conclusions also apply to the majority of the optimization results of other studies and, more importantly, provide a guide to current studies.

Finally, in order for the reader to get a better idea of the configuration geometries and analyses, sample geometries and results for large commercial jets are presented in the following sub-sections from references 7.53 and 7.54, along with a few comments to further define the content of the technical papers. In the last subsection, similar results for business jets are presented.

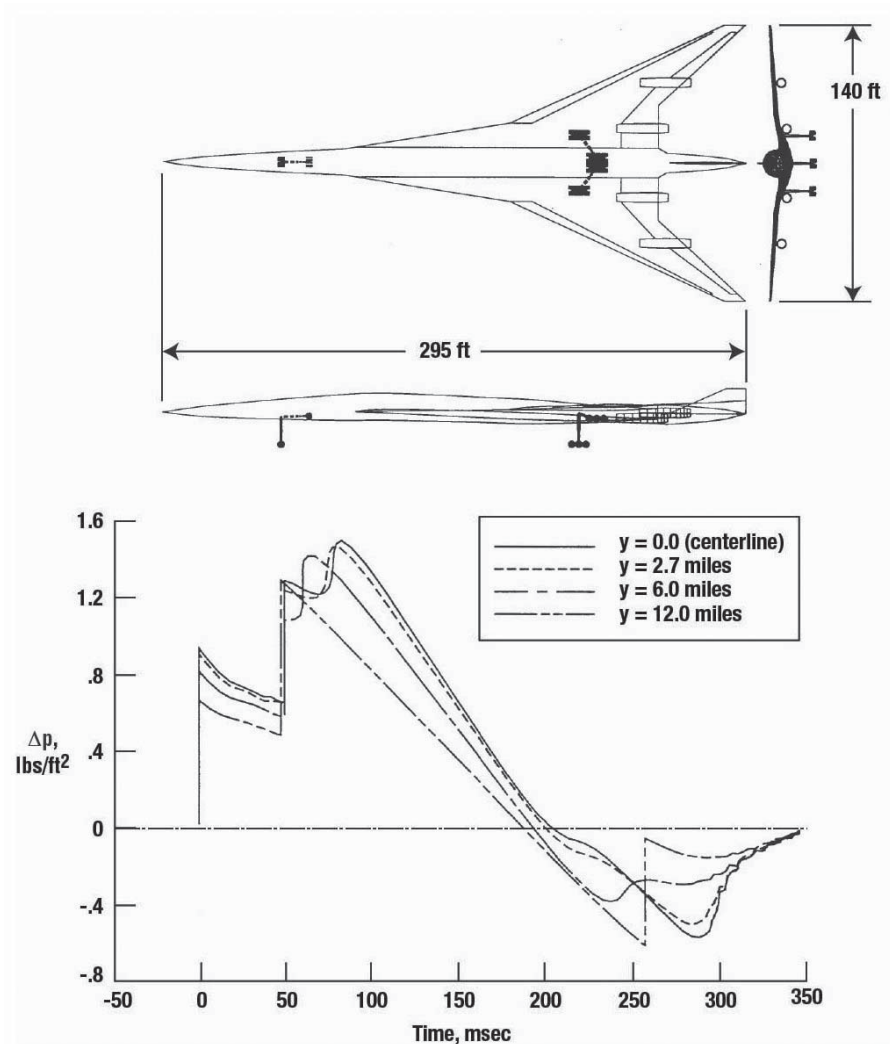
Supersonic Commercial Jets

The following sub-section contains depictions of the configuration concepts reported in NASA CP 3173 and NASA CP 10133 (refs. 7.53 and 7.54, respectively), along with a few sample result charts. The names of the authors, their affiliation, and a short list of comments to further indicate what is in the published study are provided for each configuration. NASA CP-1999-209699 (ref. 7.55) and NASA CP-1999-209520 (ref. 7.56) contain additional configuration studies. Other references report on further optimization of configurations in refs. 7.53 and 7.54. The four NASA reports are a valuable resource for anyone interested in the minimization of sonic boom and the tools utilized to perform this type of research.

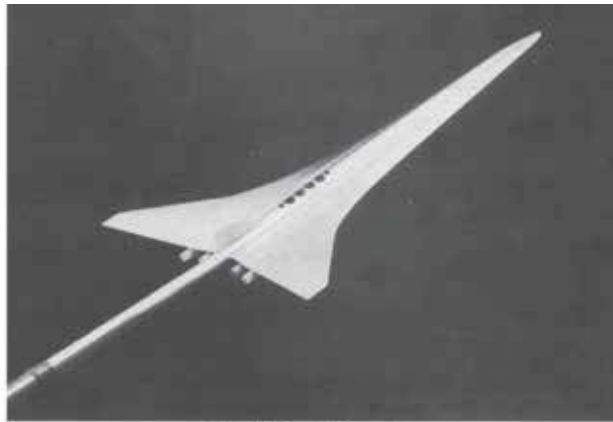
Configuration 1: Supersonic Airplane Design Optimization Method for Aerodynamic Performance and Low Sonic Boom	
Authors	Samson H. Cheung and Thomas A. Edwards
Organization	NASA Ames Research Center, Moffett Field, California
Report	High Speed Research: Sonic Boom, NASA CP 3173, Vol. II, Feb. 1992, pp. 31-44.
Comments	<ul style="list-style-type: none"> • Camber optimized to improve L/D (3.75%) • Euler version of UPS3D used for flow field calculation, NPSOL code for optimization • Darden F-function procedure for modest boom improvement • Mach 1.7, L = 330 ft, h = 44,000 ft • Boeing model 1080-911



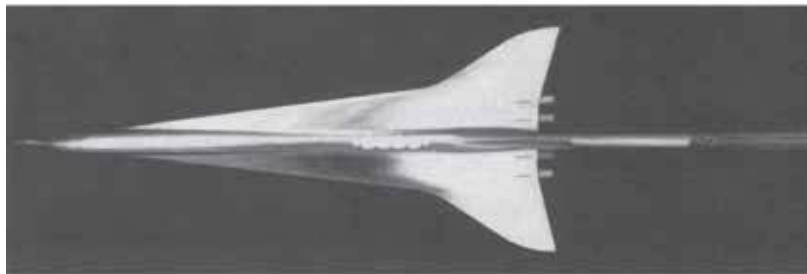
Configuration 2: CFD Predictions of Near-Field Pressure Signatures of a Low-Boom Aircraft	
Authors	Kamran Fouladi and Daniel Baize
Organization	Lockheed Engineering and Sciences Company, Hampton, VA NASA Langley Research Center, Hampton VA
Report	High Speed Research: Sonic Boom. NASA CP 3173, Vol. II, Feb. 1992, pp. 119-136.
Comments	<ul style="list-style-type: none"> • Hybrid signature design • Low-boom arrow wing • On and off-track signature • Near-field and ground signatures • $M = 1.6$, $h = 47,000$ ft • Near field calculated using MIM3DSB Euler-marching code • Grid resolution a possible problem



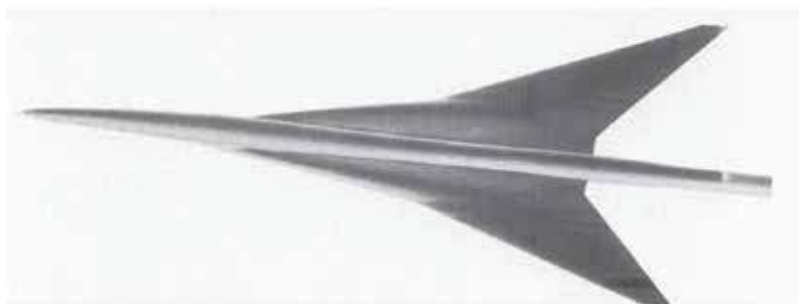
Configuration 3: Computational/Experimental Analysis of Three Low Sonic Boom Configurations with Design Modifications	
Author	Susan E. Cliff
Organization	NASA Ames Research Center, Moffett Field, CA
Report	High Speed Research: Sonic Boom. NASA CP 3173, Vol. II, Feb. 1992, pp. 89-116.
Comments	<ul style="list-style-type: none"> • Three low-boom configurations – two Mach 2.0 and one Mach 3.0 • Euler with structured and unstructured grids (Team and Airplane codes) • Theory and experiment for near field • Nacelle effects studies • Notes importance of grid resolution



Mach 2 configuration

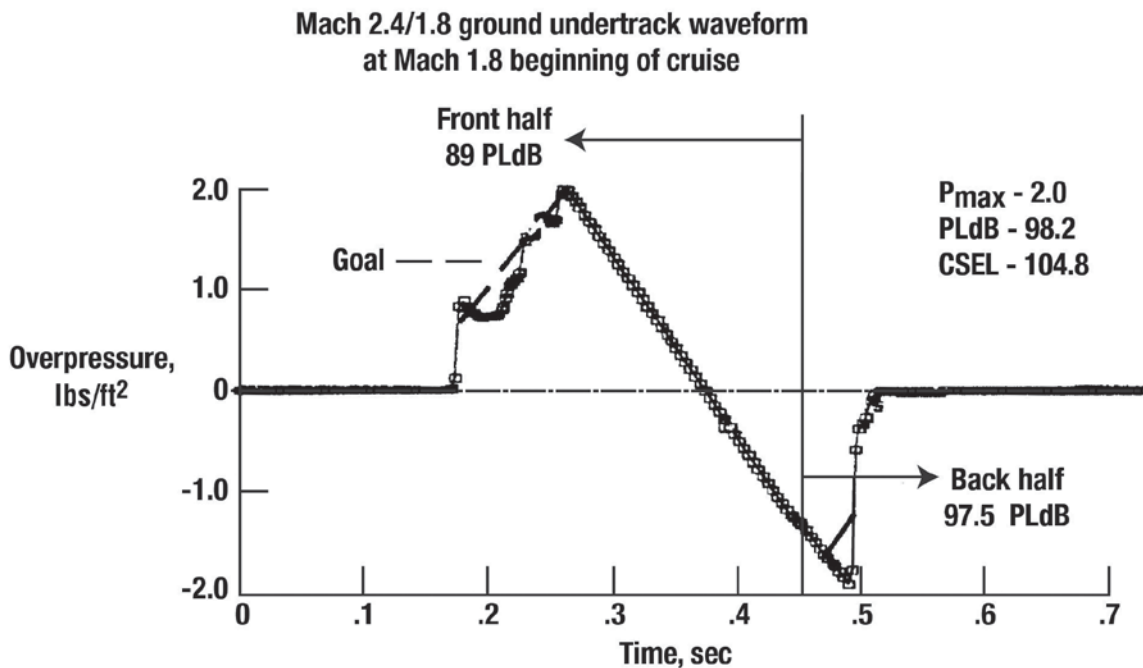
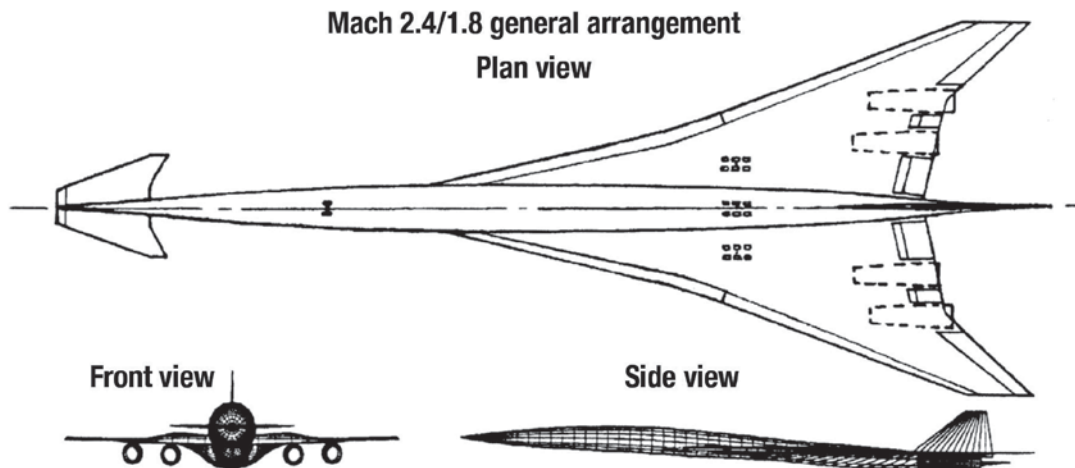


Mach 3 configuration

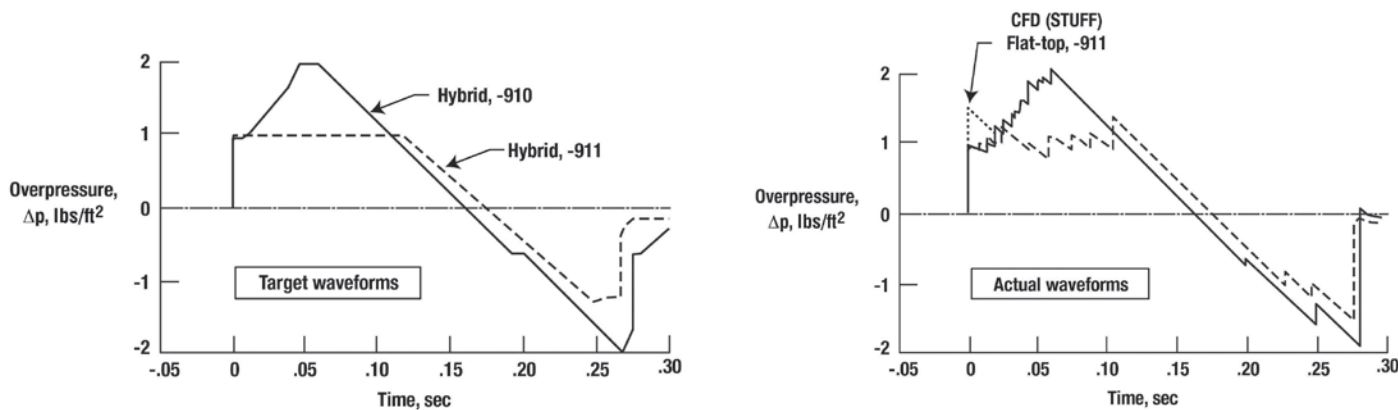
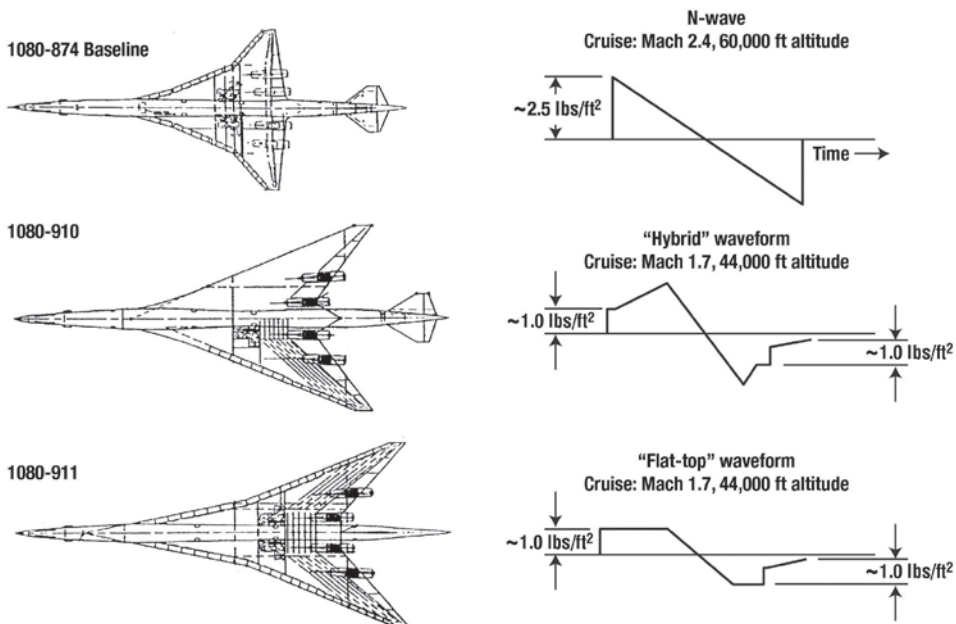


Isometric view of Haglund model, shaded to surface normals

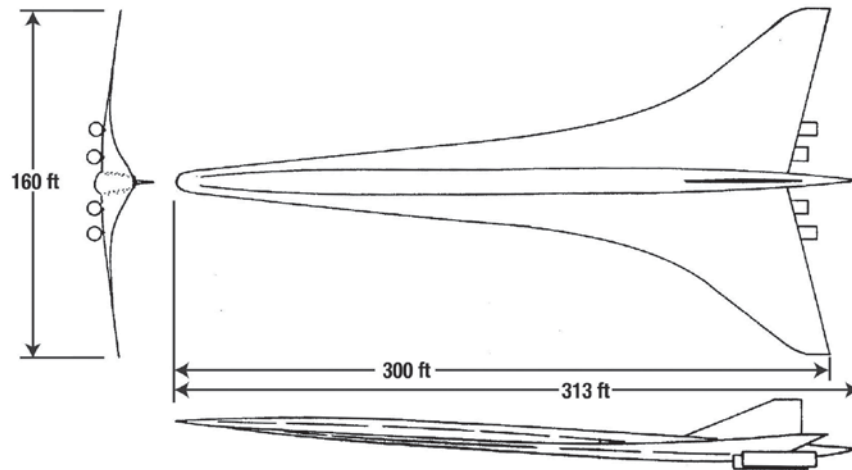
Configuration 4: Low Sonic Boom Design and Performance of a Mach 2.4/1.8 Overland High Speed Civil Transport	
Author	John M. Morgenstern
Organization	McDonnell Douglas Corporation, Douglas Aircraft Company, Long Beach, CA
Report	High Speed Research: Sonic Boom. NASA CP 3173, Vol. II, Feb. 1992, pp. 55-64.
Comments	<ul style="list-style-type: none"> • Canard configuration optimization • Various wing planforms, wing twist and camber, horizontal and vertical tails, canards fuselage and nacelle location studied • Ramp signature • Mach 2.4/1.8, L = 330 ft • On- and off-track signatures for M = 1.8 and M = 1.2



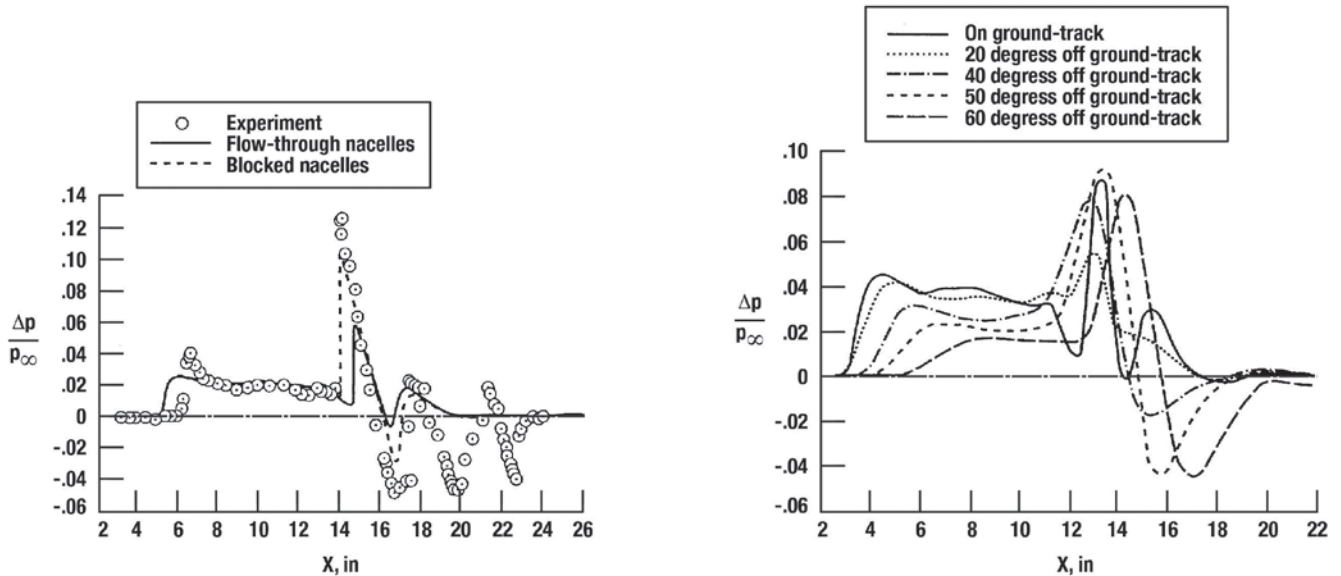
Configuration 5: Two HSCT Mach 1.7 Low Sonic Boom Designs	
Authors	George T. Haglund and Steven S. Ogg
Organization	Boeing Commercial Airplane Group, Technology and Product Development/ Aerodynamics Engineering, Seattle, WA
Report	High Speed Research: Sonic Boom. NASA CP 3173, Vol. II, Feb. 1992, pp. 65-88.
Comments	<ul style="list-style-type: none"> • Low sonic boom concepts for wind-tunnel study • Two low-boom concepts, ramp and flat top, and baseline studied • Blended Wing Body philosophy • Leading and trailing edge flaps vary for climb out and approach • Low-boom designs at $M = 1.7$ and 44,000-foot altitude • Suggestions for improved performance and low boom



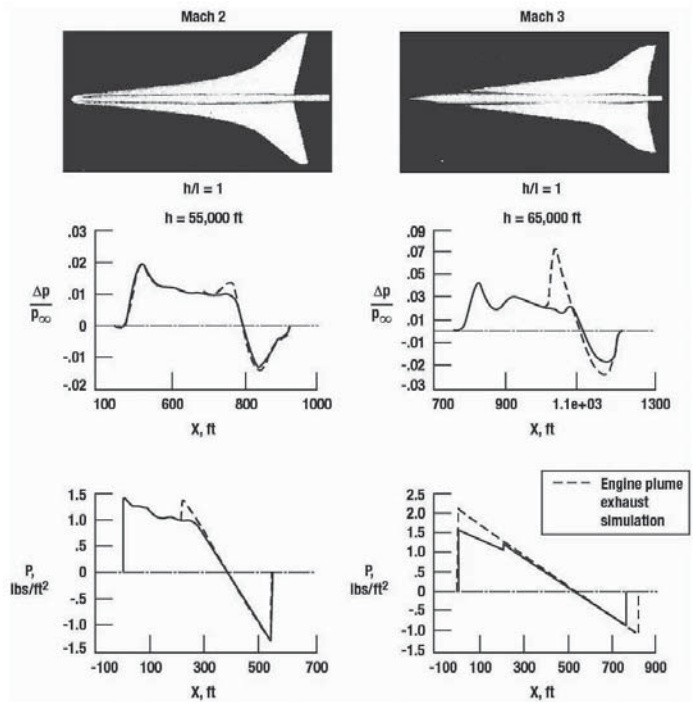
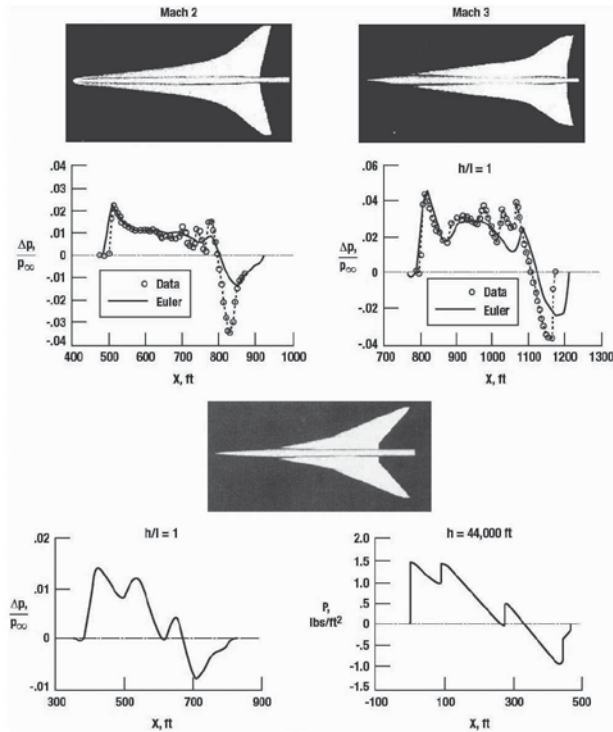
Configuration 6: Sonic Boom Prediction for the Langley Mach 2 Low-Boom Configuration	
Author	Michael D. Madson
Organization	NASA Ames Research Center, Moffett Field, CA
Report	High Speed Research: Sonic Boom. NASA CP 3173, Vol. II, Feb. 1992, pp. 157-174.
Comments	<ul style="list-style-type: none"> • Langley Mach 2 low-boom configuration • TranAir full-potential code use for near-field predictions • Theory experiment comparisons (on track) • On- and off-track predictions with/without nacelles



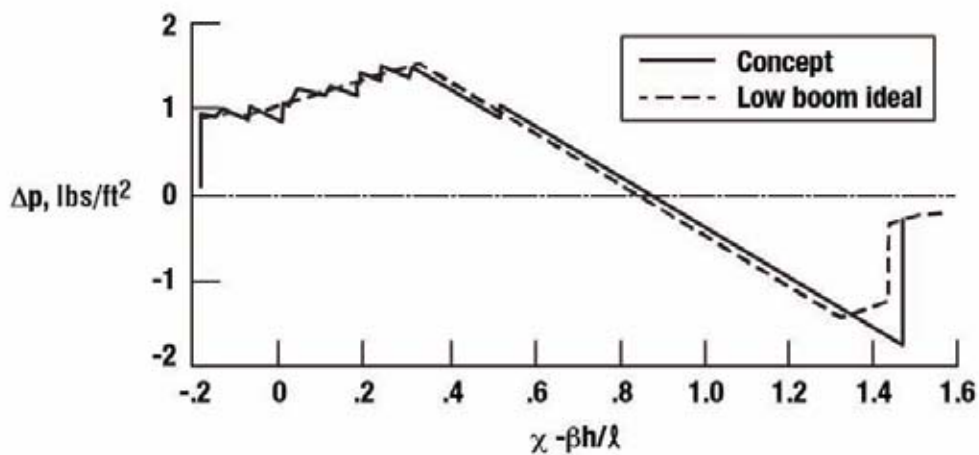
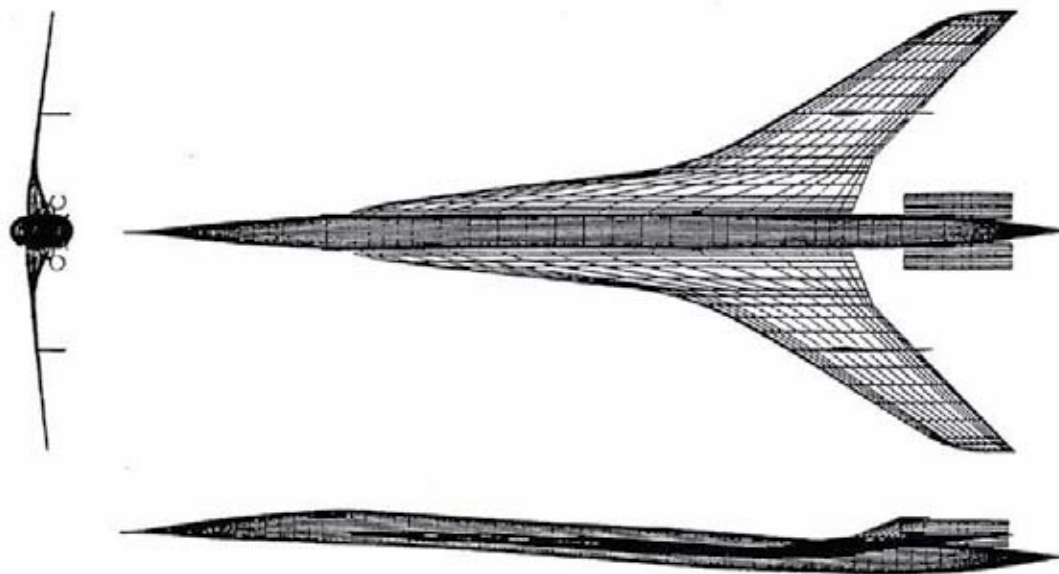
Three view drawing of the Mach 2 Model



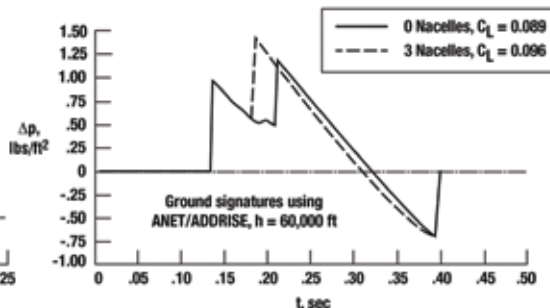
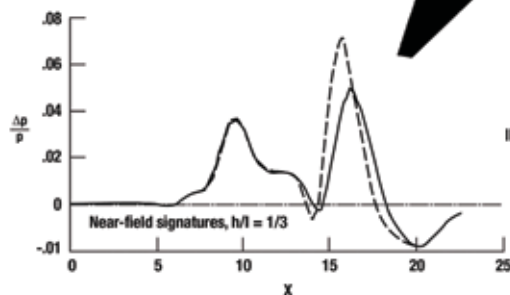
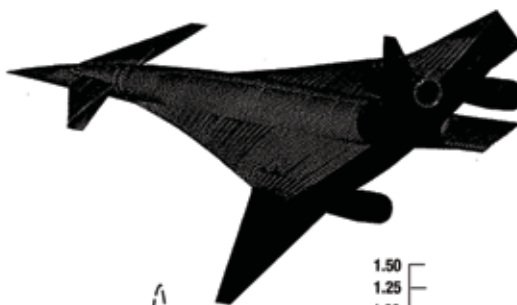
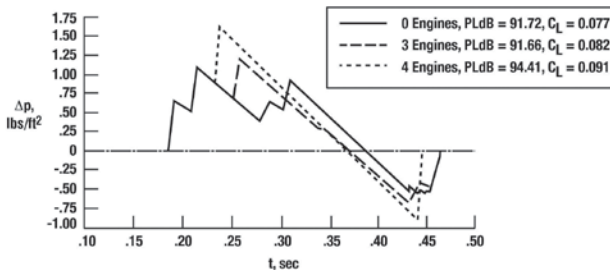
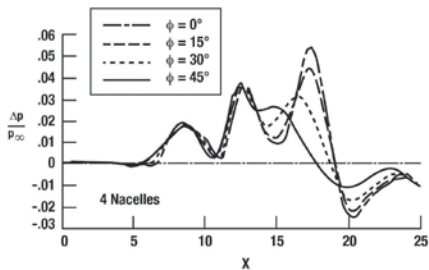
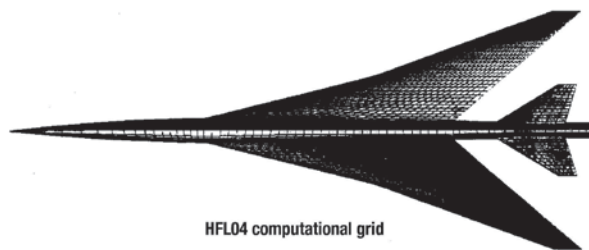
Configuration 7: Ground Signature Extrapolation of Three-Dimensional Near-Field CFD Predictions for Several HSCT Configurations	
Author	M. J. Siclari
Organization	Grumman Corporate Research Center, Bethpage, New York
Report	High Speed Research: Sonic Boom. NASA CP 3173, Vol. II, Feb. 1992, pp. 175-200.
Comments	<ul style="list-style-type: none"> Utilizes a multi-block Euler marching code developed by author. Includes innovative grid scheme for better shock resolution. NASA Mach 2 and 3 concepts as well as Boeing 911 low boom (Mach 1.7 configuration) studied Larger effect of real-exhaust on Mach 3 configuration boom (h = 65,000 ft) than on Mach 2 configuration (h = 55,000 ft) Higher pressures off track than on track shown for Mach 2 concept



Configuration 8: Low-Boom Aircraft Concept with Aft-Fuselage-Mounted Engine Nacelles	
Author	Robert J. Mack
Organization	NASA Langley Research Center, Hampton, VA
Report	High Speed Research: Sonic Boom. NASA CP 10133, pp. 17-36.
Comments	<ul style="list-style-type: none"> • Mach 1.8/2.4 concept developed using Haglund Hybrid F-function • TOGW 662,000 lbs, 328.4-foot length • Aft fuselage mounted engines • Start of cruise altitude = 49,300 ft, end of cruise altitude = 67,000 ft



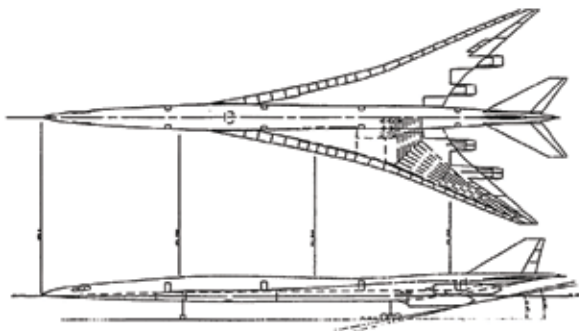
Configuration 9: On the Design and Analysis of Low Sonic Boom Configurations	
Author	Susan E. Cliff
Organization	NASA Ames Research Center, Moffett Field, CA
Report	High Speed Research: Sonic Boom. NASA CP 10133, Vol. II, May 1993, pp. 37-80.
Comments	<ul style="list-style-type: none"> • Low-boom design with three or four engines and with canard or horizontal tail • Developed using HFL03, HFL04, and airplane codes. The latter uses an unstructured grid, while the HFL codes use structured meshes • Cruise Mach numbers of 2.0 and cruise altitudes of 34,286 ft and 49,249 ft for tail and canard configurations, respectively • Boom, loudness, and performance results for various nacelle combinations • See also Cliff et al. paper in NASA CP-1999-209699



Configuration 10: Low Sonic Boom Studies at Boeing	
Author	George T. Haglund
Organization	Boeing Commercial Airplane Group, Advanced Development, HSCT Aerodynamics
Report	High Speed Research: Sonic Boom. NASA CP 10133, Vol. II, May 1993, pp. 81-94.
Comments	<ul style="list-style-type: none"> • Effort to improve Boeing 910 and 911 concepts using improved linear methodology • Modified model designed 935 and 936 are hybrid and flattop designs, respectively • Still concern for drag and weight penalties, rear shock strength, balance, trip and low-speed performance • One 1.0 lb/ft² flat top achieved • See also Haglund paper in NASA CP-1999-209699

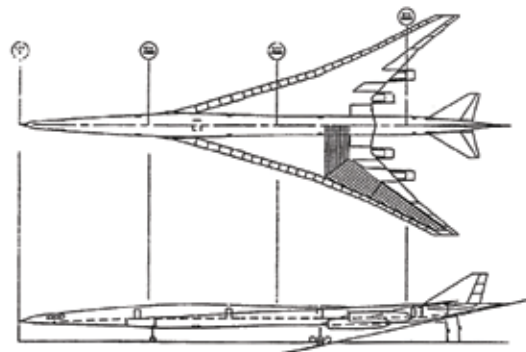
**Low-boom configuration, 1080-936
(Flat-top waveform)**

Fuselage length: 317.0 ft
 Wing span: 128.3 ft
 Wing area: 8799.0 ft²
 L.E. wing sweep: 78.7/68 deg
 Aspect ratio: 1.87
 Tri-class FAX: 325
 Cruise speed
 (overland/overwater): Mach 1.7 / 2.4

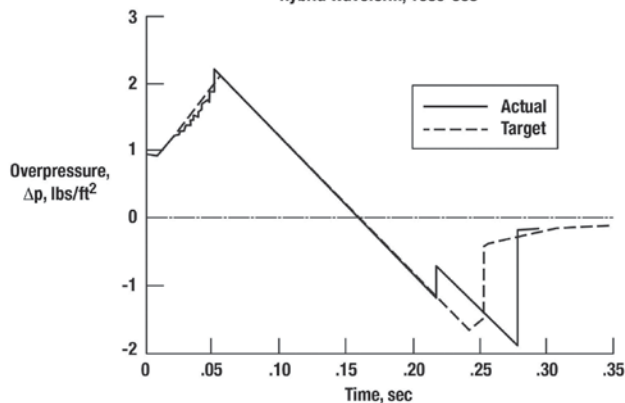


**Low-boom configuration, 1080-935
(Hybrid waveform)**

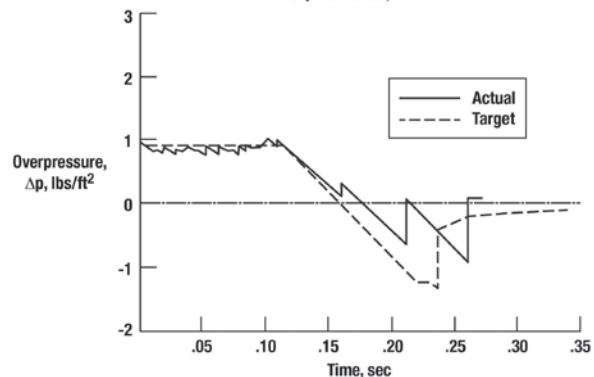
Fuselage length: 317.0 ft
 Wing span: 140.0ft
 Wing area: 9000.0 ft²
 L.E. wing sweep: 74.0/68.5/63.4 deg
 Aspect ratio: 2.18
 Tri-class FAX: 300
 Cruise speed
 (overland/overwater): Mach 1.7 / 2.4



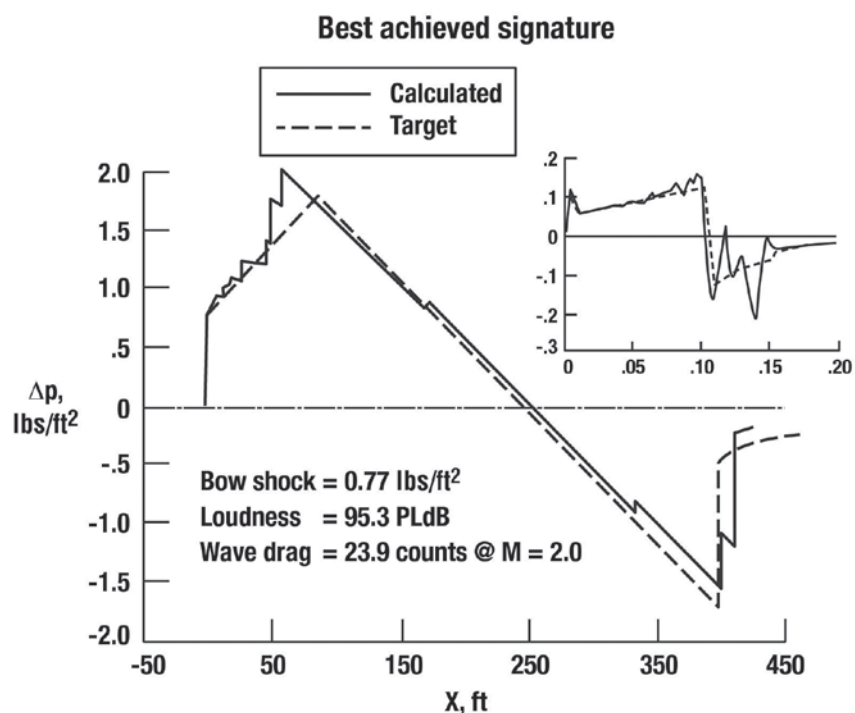
Hybrid waveform, 1080-935



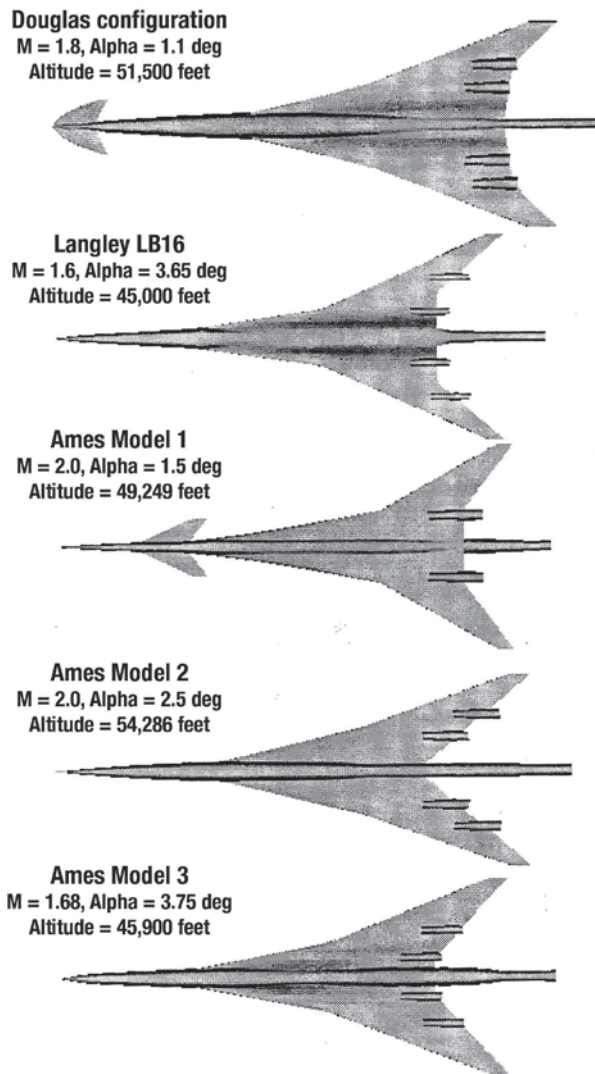
Flat-top waveform, 1080-936

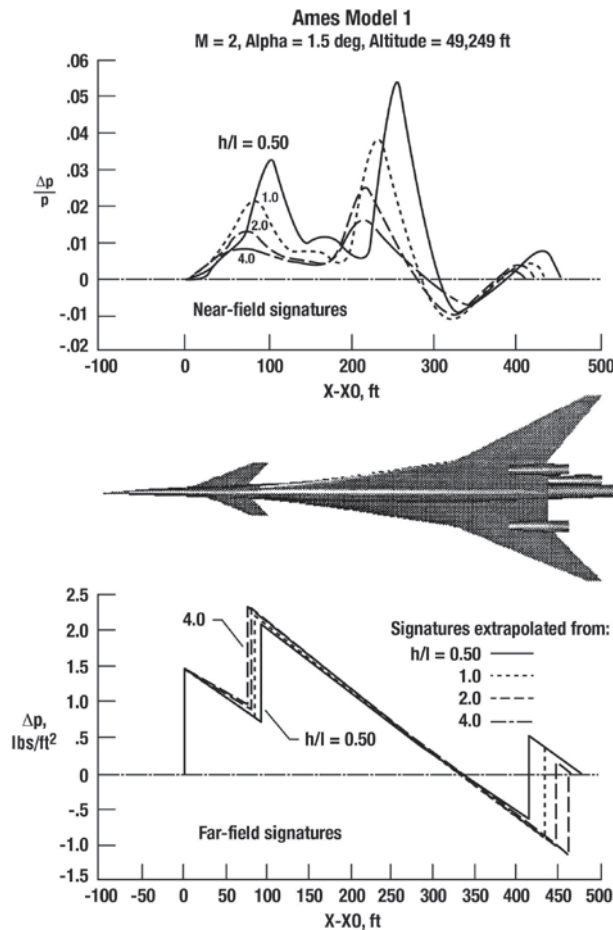
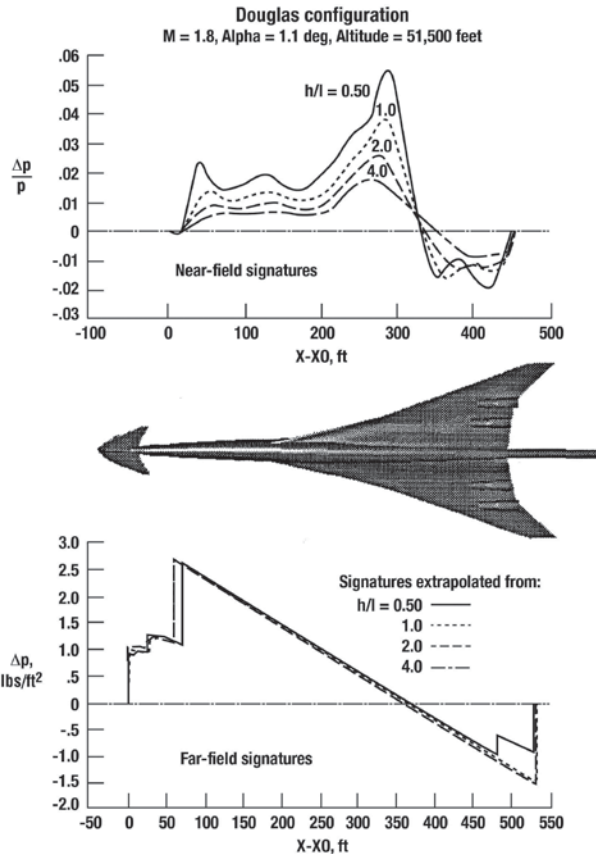


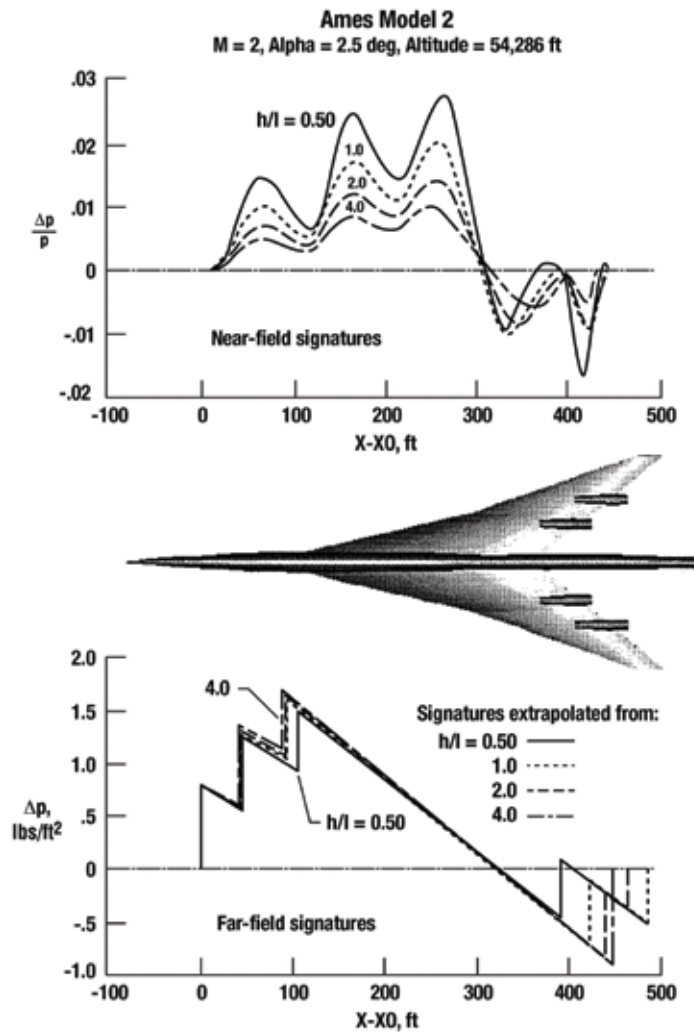
Configuration 11: A Mach 2.0/1.6 Low Sonic Boom High Speed Civil Transport Concept	
Authors	Daniel G. Baize and Peter G. Coen
Organization	NASA Langley Research Center, Hampton, Virginia
Report	High Speed Research: Sonic Boom. NASA CP 10133, Vol. II, May 1993, pp. 125-142.
Comments	<ul style="list-style-type: none"> • Appears to be further refinement of configuration of Fouladi and Baize (CP 3173) • Ramp F-function design • Minimized effect of nacelle integration



Configuration 12: A CFD Study of Component Configuration Effects on the Sonic Boom of Several High Speed Civil Transport Concept	
Authors	M. J. Siclari and Kamran Fouladi
Organization	Grumman Corporate Research, Bethpage, New York Lockheed Engineering and Sciences Company, Hampton, VA
Report	High Speed Research: Sonic Boom. NASA CP 10133, Vol. II, May 1993, pp. 227-300.
Comments	<ul style="list-style-type: none"> • Comparison of 5 configuration using Siclari-developed Euler code and grid topology. • Near- and far-field (boom) pressures as well as aerodynamic characteristics predicted and analyzed • Pressure results given for nacelles on and off • Results show error in ground pressures that can result from extrapolating from near-field pressures too close to airplane (e.g., less than one body length) • Extensive documentation, only a few sample results given here







Supersonic Business Jet Studies

There is general agreement that the first supersonic cruise aircraft to be produced for civil use will be a supersonic business jet (ref. 7.62). Over the past 45 years, conceptual studies have yielded business jets weighing from 8,400 to 134,000 pounds and having fuselage lengths from 40 to 135-feet long. A brief summary of several published business jet studies is presented in the following pages.

A design concept study of a small supersonic cruise vehicle by the University of Colorado in 1963 (ref. 7.63) was the first published study of such a vehicle. It is the smallest vehicle of the small supersonic cruise vehicle types to be proposed, having a 40-foot long fuselage and is by far the lightest, weighing in at 8,400 pounds at take-off ground weight (TOGW) (see figure 7.90).

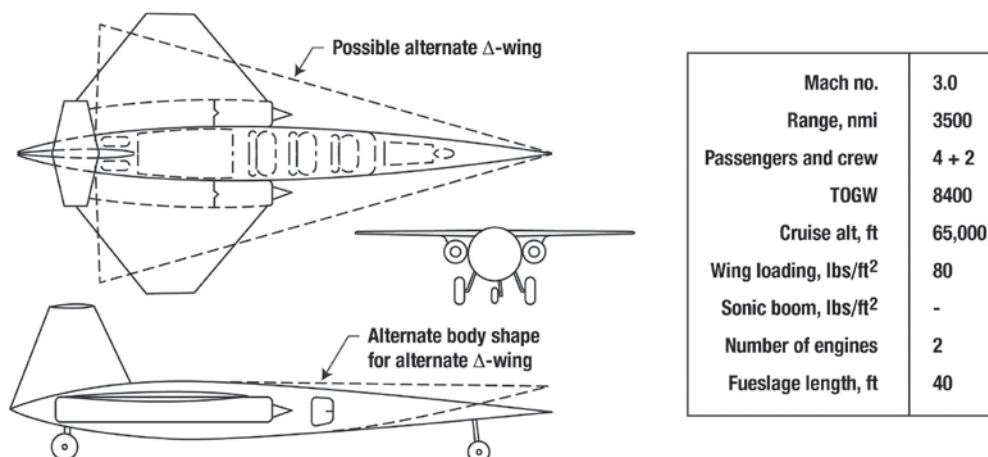


Figure 7.90. University of Colorado configuration, 1963 (ref. 7.63).

Up until recent years, the largest by weight (134,000 pounds TOGW) was a cranked arrow-wing concept developed in a study by Fairchild/Sweringen in 1982 (ref. 7.64). The baseline configuration for this study, shown in figure 7.91, has three engines. Business jet concepts were also developed under this study by Douglas, British Aerospace, and Lockheed. Their configurations give rise to the ranges for the various quantities provided in the adjacent table.

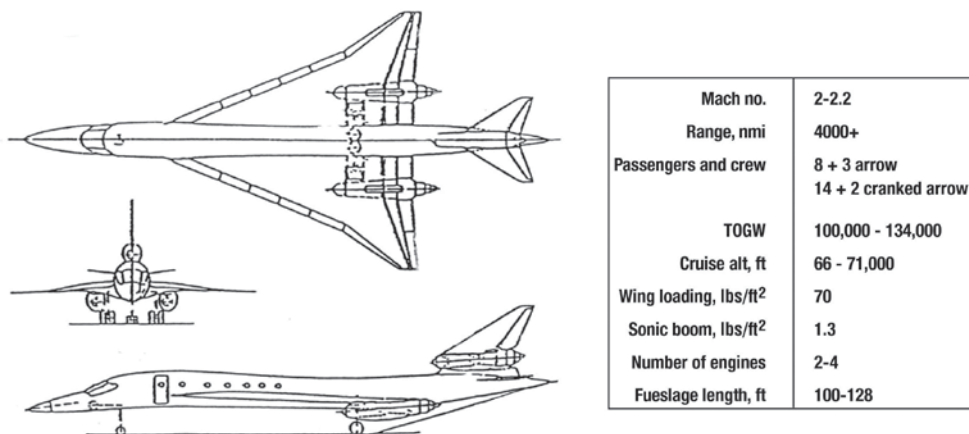


Figure 7.91. Fairchild/Sweringen baseline (ref. 7.64).

In addition to the University of Colorado and Fairchild/Sweringen configurations mentioned above (figs. 7.90 and 7.91), the characteristics of 23 business jet concepts, along with sketches of their geometries, are given in reference 7.64 by Maglieri. These concepts are typical of the configurations proposed in the 1970s and 1980s, and similar in most respects to those still being studied. More recent supersonic business jet studies are documented in the following pages.

Recent Supersonic Business Jet Studies

Since the publication of reference 7.64, there have been numerous studies that have produced low-boom supersonic cruise concepts of business jet size. One of the more significant efforts was DARPA’s Quiet Supersonic Platform (QSP) program (ref. 7.65), which was directed towards a dual use (commercial and military) 100,000-pound class aircraft. A goal of 0.3 lb/ft² was set by DARPA for the initial shock of the sonic boom. Several conceptual configurations are shown in reference 7.65, including the one pictured in figure 7.92. The QSP system goals versus those of the Concorde are also shown in figure 7.92.

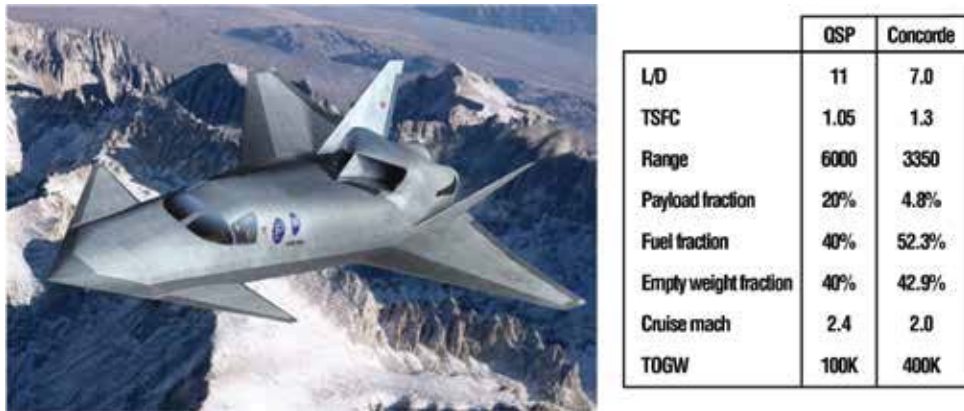


Figure 7.92. Quiet supersonic platform concept and design goals (ref. 7.65).

Komadina and Drake (ref. 7.66) describe a design approach that produced a dual-relevant vehicle concept that could be configured to satisfy the QSP Program goal of either a civilian business jet or a military strike aircraft. The geometry of the design is shown in figure 7.93 along with the design requirements in table 7.10 for the military strike version as well as those for the business jet and dual-relevant concepts.

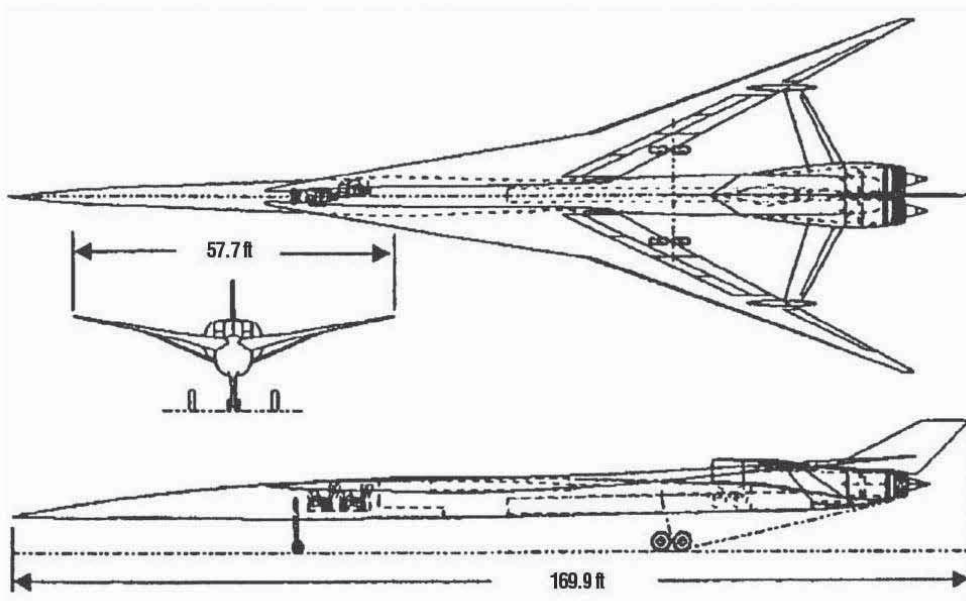


Figure 7.93. Dual-relevant vehicle (7.66).

Table 7.9. Vehicle Design Requirements (ref. 7.66)

	DARPA, QSP	Military Strike	Business Jet	Dual Relevant
Sonic boom	0.30 lb/ft ²	n/a	very low	0.30 lb/ft ²
TOGW	100,000-lb class	fallout	100,000-lb class	100,000-lb class
Range	6000 nm	QSP Consistent	4k - 6k nm	6000 nm
Cruise speed	M = 2.4	QSP Consistent	M \geq 1.8	M = 2.2
Payload	20% TOGW	QSP Consistent	6k - 8k lbs	20,000 lbs
TO/Landing noise	Stage 3	Stage 3	Stage 4	Stage 3
Cruise L/D	11	n/a	n/a	11
Cruise TSFC	1.05	n/a	n/a	1.05
Engine T/W	7.5	n/a	n/a	7.5
Takeoff BFL	n/a	8000 ft	6500 ft	7000 ft
X-wind land	n/a	30 kts	30 kts	30 kts
Cruise Altitude	n/a	\geq 60k ft	45k - 65k ft	60k - 65k ft

Note that the overall length of the design shown in figure 7.93 is approximately 170 feet. Figure 7.94 shows the equivalent area distribution and sonic boom signature of this configuration. Although several QSP system goals were established, the QSP had only one requirement that the initial shock strength be no greater than 0.3 lb/ft² (ref. 7.65). Note that in figure 7.94, the initial shock is \sim 0.3 lb/ft² but the maximum positive and negative shock strength is around 0.5 lb/ft².

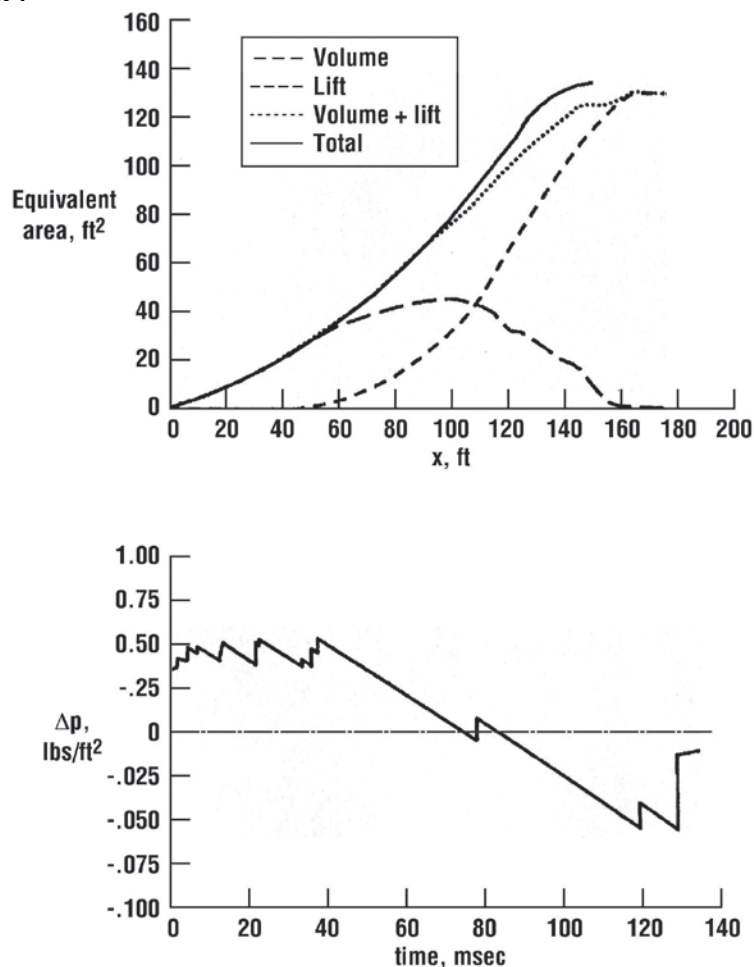


Figure 7.94. Equivalent area and sonic boom signature for dual-relevant vehicle (ref. 7.66).

The concepts developed in the QSP Program were designed to produce flat-top or ramp-type signatures. This concentration was the result of down-selecting from an initial slate of approaches that included concepts from unconventional (e.g., airflow modification) through the George-Seebass theory that had been the mainstay of conventional shaping analysis. The configuration studies included design exercises that verified a low-boom aircraft could be built. A follow on to the DARPA QSP Program was the Shaped Sonic Boom Demonstrator (SSBD) flight-test program that proved the persistence to the ground of a flat-top pressure signature. There were both DARPA and NASA components of this flight program and they are discussed in reference 7.67 and detailed in Chapter 5 of this publication.

A more recent SSBJ configuration design is discussed in reference 7.38 by Mack and shown in figure 7.95. It is noteworthy for its smooth, curved leading edge and its combination flat-top/ramp F-function definition. Near-field experimental pressure data is given for an h/l of 1.36. A sonic boom goal of 0.5 lb/ft^2 was achieved.

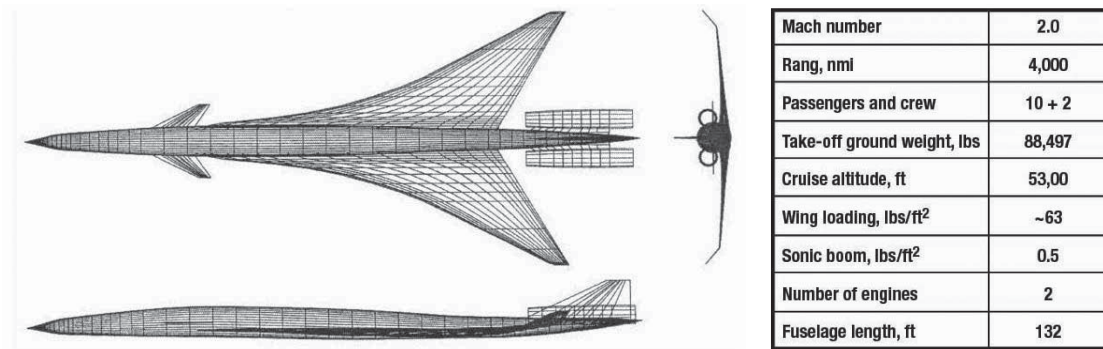


Figure 7.95. Three-view depiction of the Langley low-boom wind-tunnel model with large nacelles (ref. 7.38).

A study by Briceno et al. of the Georgia Institute of Technology (ref. 7.68) using a response surface methodology produced the optimized design of figure 7.96. The impact of 17 separate configurations, mission, aerodynamics, and environmental factors on 13 technologies are evaluated, along with the ability of 1025 separate configurations to meet the design goals/constraints. After the aircraft was sized, PBOOM (ref. 7.69) was used to calculate the sonic boom signature of the aircraft. For the optimized design initial shock strength of 0.68 lb/ft^2 was calculated versus the goal of 0.5 lb/ft^2 .

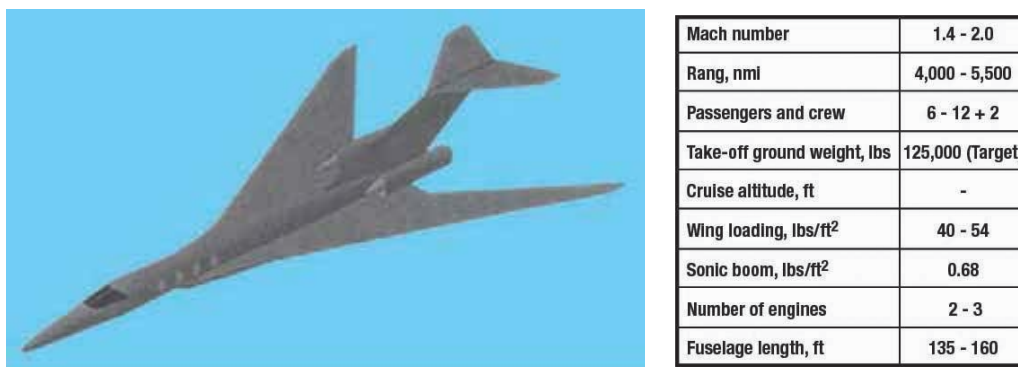


Figure 7.96. Georgia Tech Design (ref. 7.68).

A market study and accompanying environmental assessment were described in a 2003 AIAA paper by Wolz (ref. 7.70). The resulting Quiet Supersonic Jet (QSJ) configuration is shown in figure 7.97 as well as its geometric and weight characteristics.

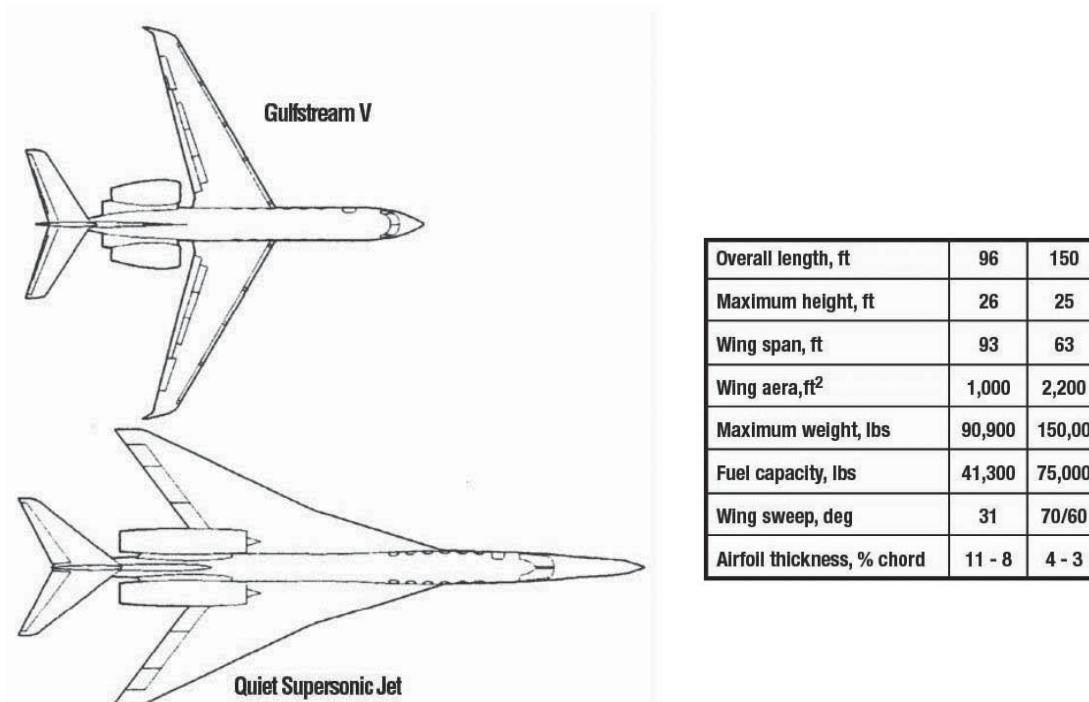


Figure 7.97. Baseline QSJ configuration (ref. 7.70).

In reference 7.70 (p. 8), Wolz concluded that:

- The QSJ will be well suited for a multitude of different civil and military missions.
- Establishing and meeting environmental standards for sonic boom, engine exhaust emissions, and airport noise are critical.
- Progress must be made to advance aerodynamic, propulsion, and structural system performance. Step improvements in all of these areas are needed to achieve the market-driven design requirements of a viable QSJ.

Further configuration studies by Gulfstream have led to the development of the Quiet Spike, discussed in Chapter 4 (see figures 4.24 – 4.26) and Chapter 5 (see figure 5.30). This is a retractable nose extension that allows aircraft length in supersonic flight to be longer than would be practical for ground and subsonic operations. The spike consists of telescoping sections where the diameters and lengths of the segments are such that the shocks from each step do not coalesce, but (when smoothed by atmospheric absorption during propagation to the ground) closely approximate an ideal shockless ramp shape.

Horinouchi of the Japan Aerospace Exploration Agency presented an AIAA paper in 2005 (ref. 7.71) that, in many respects, is similar to the study discussed by Wolz in reference 7.70. A mission study for both a supersonic business jet and small supersonic transport is described, along with payload and cabin size requirements. Other targets are given in table 7.11 below.

Table 7.10. Target Requirements for Supersonic Business Jet and Small Supersonic Transport (ref. 7.71)

Cruise speed	Mach 1.8 – 2.2
Range	3,500 nmi (as a minimum)
Payload	2 crew plus 8 passengers
Runway length	7,000 ft
Sonic Boom	0.3 – 0.5 lb/ft ²

A unique feature of reference 7.71 is its examination of a variable geometry forward swept wing along with a cranked arrow wing (see figure 7.98).

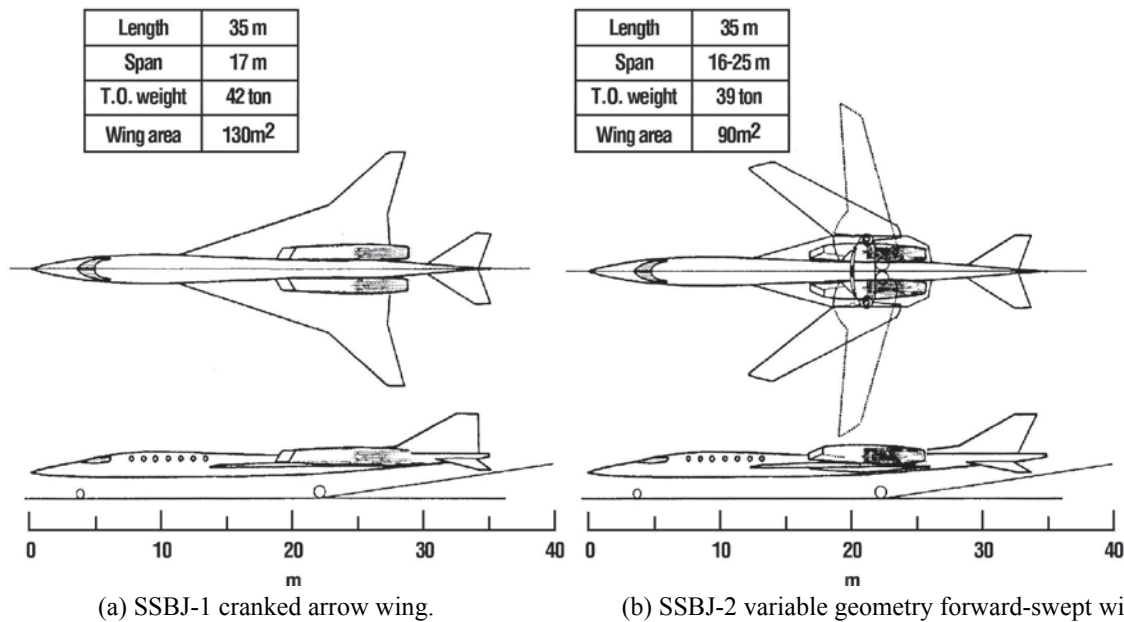


Figure 7.98. Cranked arrow and variable geometry forward-swept wings studied in reference 7.71.

Aside from the obvious low-speed advantages of the variable geometry forward swept wing configuration, reference 7.71 points out a possible sonic boom mitigation advantage as well. Below, figure 7.99 shows the effect area development of both cranked arrow and variable geometry forward swept wing configurations, and provides evidence of the potential for sonic boom mitigation benefits.

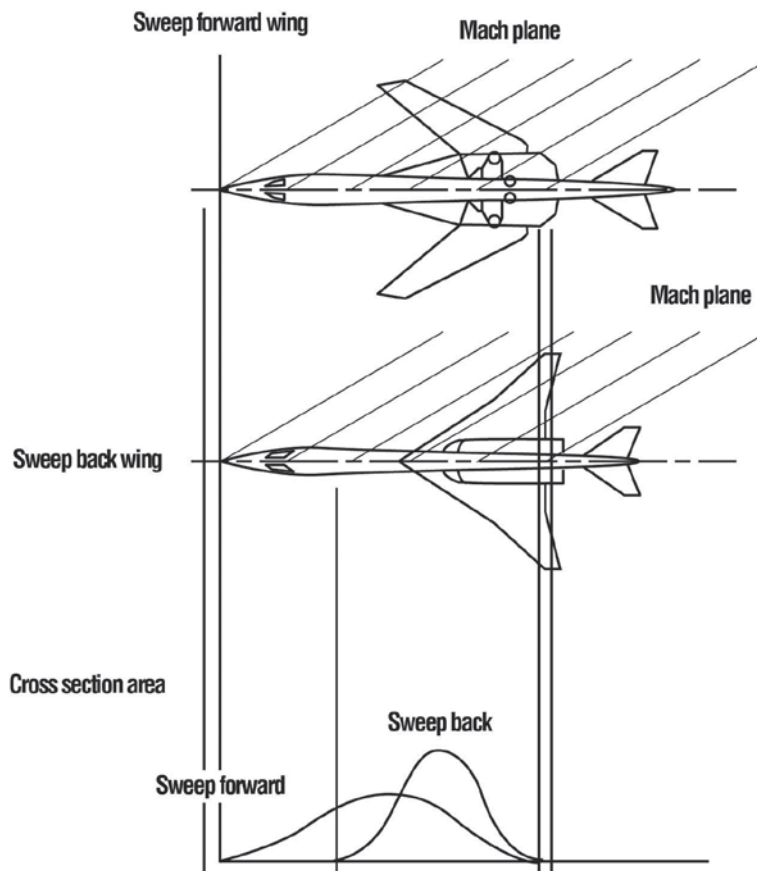
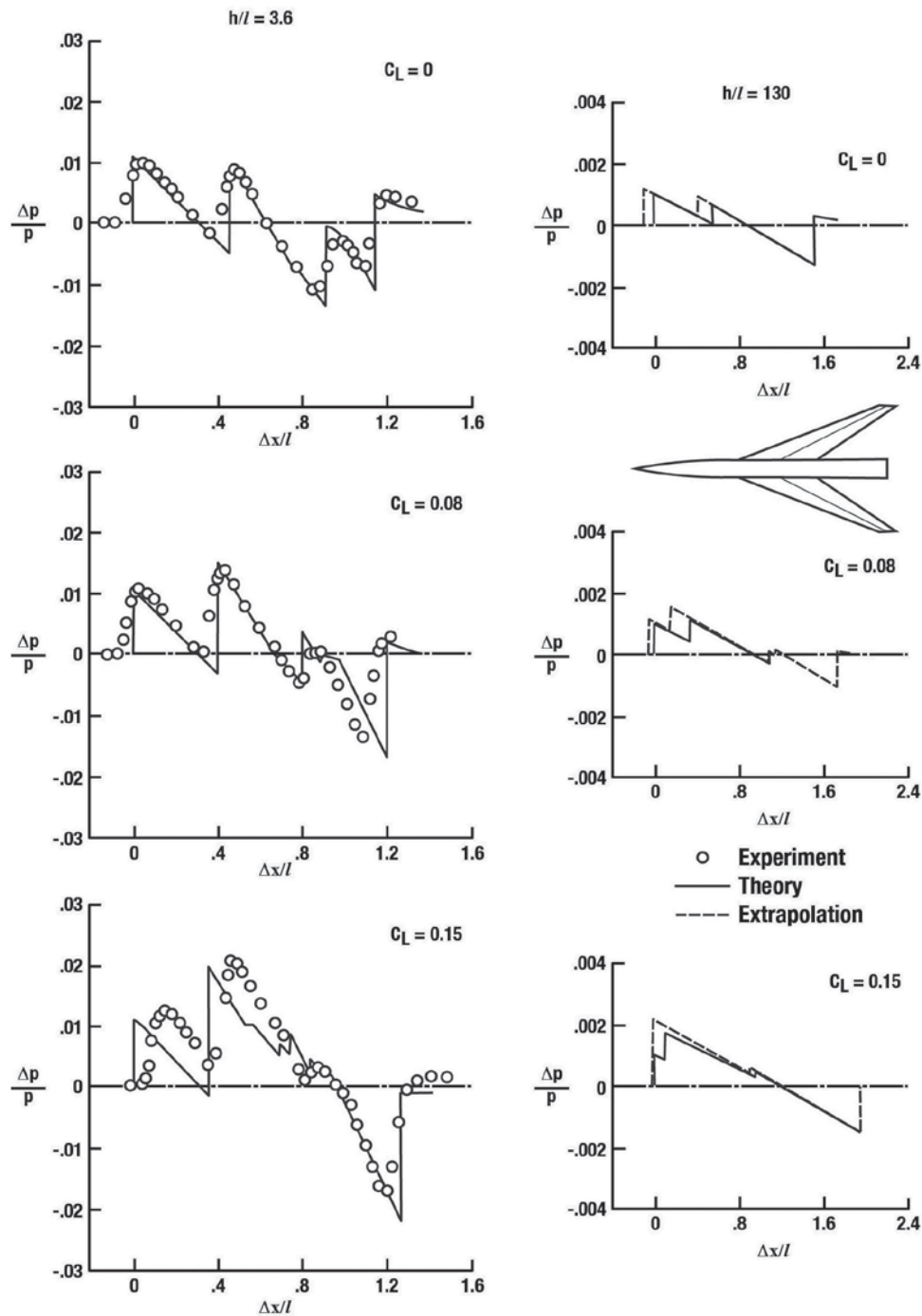


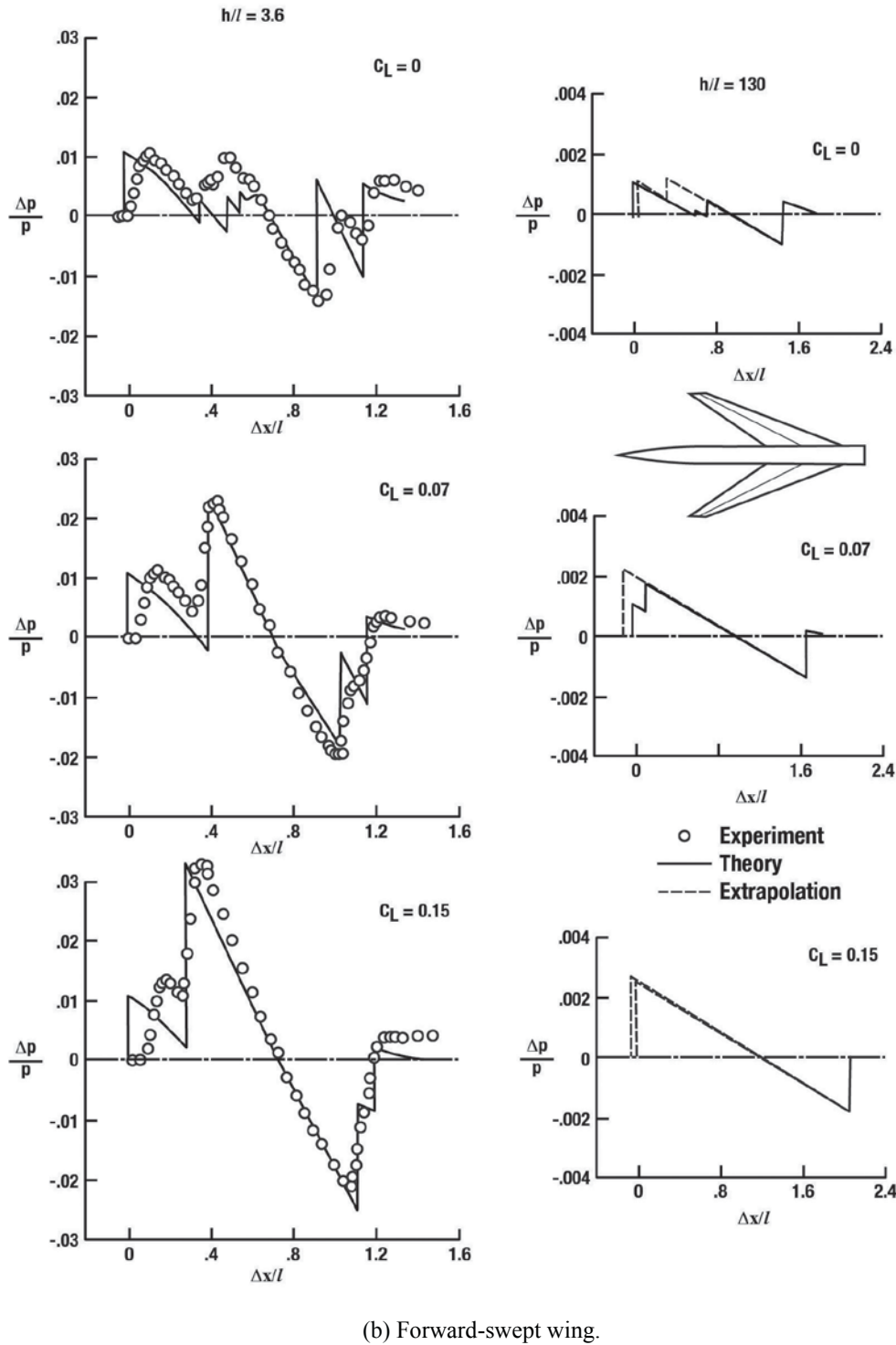
Figure 7.99. Mach cuts for swept back and forward swept wings (adapted from ref. 7.71).

Another paper that examined the virtue of a swept forward wing vis-a-vis that of an aft-swept wing is that of Hunton et al. (ref. 7.72). Figure 7.100, from this paper, shows the experiment results for three lift coefficients, compared to theoretical predictions for both aft-swept and forward-swept wings.



(a) Aft-swept wing.

Figure 7.100.(a) with following page 338, Comparison of experimental and theoretical pressure signatures for an aft-swept and forward-swept wing configuration at Mach 1.68 (adapted from ref. 7.72).



(b) Forward-swept wing.

Figure 7.100.(b) with previous page 337, Comparison of experimental and theoretical pressure signatures for an aft-swept and forward-swept wing configuration at Mach 1.68 (adapted from ref. 7.72).

Whitham's F-function methodology is used in the prediction of the pressure signature including an extrapolation procedure due to Hicks and Mendoza (ref. 7.73). The latter does not include the real atmosphere effects on shock coalescence as derived by Hayes, Haefeli and Kulsrud (ref. 7.74) or Thomas (ref. 7.16). Overall, the theory and experiment agreement at an h/l of 3.6 is good with the best results obtained for the aft-swept wing and the lower lift coefficients. At an h/l of 130, also shown in figure 7.100, sonic boom signatures for both the Whitham-based and extrapolation methods and they yield slightly different results for bow and wing shock strengths and wing shock locations.

Chapter 7 Summary Remarks

Boom minimization techniques based on Whitham's F-function are a valuable first-order tool in the conceptual design of low-boom supersonic aircraft. More complex configurations can be studied and boom reduction schemes can be utilized by applying the Euler CFD codes with numerical optimization. Several codes have been developed that automate the trade studies between boom minimization and performance, and deliver significant design improvements.

Minimization of the boom due to the forward part of a supersonic cruise aircraft is relatively straightforward due to the fact that the fuselage and the canopy are the main elements involved. The geometry of these components are relative simple and concentrated near the axis of the vehicle. On the other hand, the minimization of the aft shock, or boom, is a much more difficult task since the wing volume and lift, the empennage, aft fuselage, engines and engine exhaust plumes all contribute. The placement of the engine, and its exhaust plume relative to the other components, is critical to obtaining the lowest boom.

A variety of large supersonic commercial transport configurations and, more recently, supersonic business jet configurations have been studied over the years. In general, lower boom configurations have been achieved when the engines are integrated into the aircraft above the wing. In addition, the lower boom configurations tend to have higher drag than high-performance designs.

Chapter 7 References

- 7.1 Jones, L. B.: Lower Bounds for Sonic Bangs. *J. Roy. Aeron. Soc.* 65, 1-4 (1961).
- 7.2 Jones, L. B.: Lower Bounds for Sonic Bang in the Far-Field. *Aeron. Quart.* XVIII, Pt. 1, 1-21 (1967).
- 7.3 Jones, L. B.: Lower Bounds for the Pressure Jump of the Bow Shock of a Supersonic Transport. *The Acoustical Quarterly*, Vol. XXI, Feb. 1970.
- 7.4 McLean, F. E.: Some Non-Asymptotic Effects on the Sonic Boom of Large Airplanes. NASA TN D-2877, June 1965.
- 7.5 George, A.R., Lower Bounds for Sonic Booms in the Midfield, *AIAA Journal*, Vol. 7, No.8, Aug. 1969, pp. 1542–1545.
- 7.6 George, A. R. and Seebass, R.: Sonic Boom Minimization Including Both Front and Rear Shocks. *AIAA J.* 9, 2091-2093 (1971).
- 7.7 Seebass, R.: Minimum Sonic Boom Shock Strengths and Overpressures, *Nature* 221, 651-653 (1969).
- 7.8 Seebass, R. and George, A. R.: Sonic-Boom Minimization. *J. Acoust. Soc. Am.*, Vol. 51, No. 2 (pt. 3), Feb. 1972, pp. 686–694.
- 7.9 Carlson, H. W., Barger, R. L, and Mack, R. J., Application of Sonic-Boom Minimization Concepts in Supersonic Transport Design, NASA TN D-7218, June 1973.
- 7.10 Darden, Christine M.: Sonic Boom Minimization with Nose-Bluntness Relaxation. NASA TP 1348, Jan. 1979.
- 7.11 Mack, Robert J. and Darden, Christine M.: Wind-Tunnel Investigation of the Validity of a Sonic-Boom-Minimization Concept. NASA TP 1421. October 1979.
- 7.12 Hague, D. S. and Jones, R. T.: Application of Multivariate Search Techniques to a Design of Low Sonic Boom Overpressure Body Shapes. NASA SP 255, Oct. 1970, pp. 307–323.

- 7.13 Haglund, George T.: High Speed Civil Transport Design for Reduced Sonic Boom. Boeing Doc. No. Do-55430, NASA Cont. No. NAS1-18377, (1991).
- 7.14 Mack, Robert J. and Haglund, George T.: A Practical Low-Boom Overpressure Signature Based on Minimum Sonic Boom Theory. NASA CP-3173, Vol. II, Feb. 1992, pp. 15–30.
- 7.15 Mack, Robert J.: Additional F-Functions Useful for Preliminary Design of Shaped Signature, Low-Boom, Supersonic-Cruise Aircraft. NASA CP-1999-209699, Dec. 1999, pp. 1–12.
- 7.16 Thomas, Charles L.: Extrapolation of Wind-Tunnel Sonic Boom Signatures without Use of a Whitham F-Function. NASA SP 255, 1970, pp. 205–217.
- 7.17 Hicks, Raymond M. and Thomas, Charles L.: A Preliminary Report on Shock Coalescence. NASA SP 255, Oct. 1970, pp. 297–305.
- 7.18 Cheung Samson: Design Process of Ames Wind-Tunnel Model 3. NASA CP 10133, Vol. II, 1993, pp. 95–124.
- 7.19 Gill, P. E.; Murray, W.; Saunders, M. A.; and Wright, M. H: Users Guide for NPSOL (version 4.0): A FORTRAN Package for Nonlinear Programing. TR SOL 86-2, Jan. 1986, Dept. of Ops. Res., Stanford University.
- 7.20 Siclari, Michael J.: The Analysis and Design of Low Boom Configurations Using CFD and Numerical Optimization Techniques. NASA CP-1999-209699, Dec. 1999, pp. 107-128.
- 7.21 Siclari, M. J. and Fouladi, Kamran: A CFD Study of Component Configuration Effects on the Sonic Boom of Several High-Speed Civil Transport Concepts. NASA CP 10133, Vol. II, May 1993, pp. 227–300.
- 7.22 Makino, Y.; Aoyama, T.; Iwamiya, T.; Watanuki; and Kubota, H.: Numerical Optimization of Fuselage Geometry to Modify Sonic-Boom Signature. Journal of Aircraft, Vol. 36, No. 4, pp. 668–674.
- 7.23 Lee, D. K. and Eyi, S.: Aerodynamic Design via Optimization. Jour. of Aircraft, Vol. 29, No. 6, 1992, pp. 1012–1019.
- 7.24 Nadarajah, Siva K.; Jameson, Antony; and Alonso, Juan J.: Sonic Boom Reduction Using an Adjoint Method for Wing-Body Configurations in Supersonic Flow. AIAA 2002-5547, Sept. 2002.
- 7.25 Nadarajah, S. and Jameson, A.: A Comparison of the Continuous and Discrete Adjoint Approach to Automatic Aerodynamic Optimization. AIAA 2000-0667, Jan. 2000.
- 7.26 Nadarajah, S.; Jameson, A.; and Alonso, J.: An Adjoint Method for the Calculation of Remote Sensitivities in Supersonic Flow. AIAA 2002-0261, Jan. 2002.
- 7.27 Li, Wu; Shields, Elwood; and Le, Daniel: Interactive Inverse Design Optimization of Fuselage Shape for Low-Boom Supersonic Concepts. Jour. of Aircraft. Vol. 45, No. 4, July–Aug. 2008, pp. 1381–1397.
- 7.28 Howe, D.: Engine Placement of Sonic Boom Mitigation. Gulfstream Aero. Corp. AIAA Paper 2002-0148, Jan. 2002.
- 7.29 Choi, Seongim; Alonso, Juan J.; and Kroo, Ilan M.: Multi-Fidelity Design Optimization of Low-Boom Supersonic Business Jets. AIAA 2004-4371, Sept. 2004.
- 7.30 Page, J. A.; Plotkin, K. J.; and Wilmer, C. W.: PCBoom Version 6 Technical Reference and User Manual. Wyle Research Report WR 09-20, Aug. 2009.

- 7.31 Mack, Robert J.: A Numerical Method for Evaluation and Utilization of Supersonic Nacelle-Wing Interference. NASA TN 5057, March 1969.
- 7.32 Mack, Robert J.: Some Consideration of the Integration of Engine Nacelles into Low Boom Aircraft Concepts. NASA CP-3173, Vol. II, Feb. 1992, pp. 221–236.
- 7.33 Morgenstern, John M.: Low Sonic Boom Design and Performance of Mach 2.4/1.8 Overland High Speed Civil Transport. NASA CP-3173, Vol. II, Feb. 1992, pp. 55–64.
- 7.34 Mack, Robert J.: Wind-Tunnel Overpressure Signatures from a Low-Boom HSCT Concept with Aft-Fuselage-Mounted Engines. NASA CP-1999-209699, Dec. 1999, pp. 59-72.
- 7.35 Cliff, Susan E.: On the Design and Analysis of Low Sonic Boom Configurations. NASA CP 10133, Vol. II, May 1993, pp. 37–80.
- 7.36 Siclari, M. J.: Ground Signature Extrapolation of Three-Dimensional Near-Field CFD Prediction for Several HCST Configurations. NASA CP 3173, Vol. II, 1992, pp. 175–200.
- 7.37 Buning, P. G. et al.: OVERFLOW User's Manual, Version 1.8f, NASA Langley Research Center, 1998.
- 7.38 Mack, Robert J.: A Supersonic Business-Jet Concept Designed for Low Sonic Boom. NASA TM 2003-212435, Oct. 2003.
- 7.39 Wang, C. J. and Peterson, J. B.: Spreading of Supersonic Jets from Axially Symmetric Nozzles. *Jet Prop.*, Vol. 28, No. 5, May 1958, pp. 321–328.
- 7.40 Henson, J. R. and Robertson, J. E.: Methods of Approximating Inviscid Jet Boundaries for Highly Underexpanded Supersonic Nozzles. AEDC-TDR-62-7 (Contract No. AF-40(6))-800/S/A 24(61-73)) Arnold Eng. Dev. Ctr., May 1962.
- 7.41 Love, Eugene S.: An Approximation of the Boundary of a Supersonic Axisymmetric Jet Exhausting into a Supersonic Stream. *Jour. of Aero. Sci.*, Vol. 25, No. 2, Feb. 1958, pp. 130–131.
- 7.42 Putnam, Lawrence E. and Capone, Francis J.: Experimental Determination of Equivalent Solid Bodies to Represent Jets Exhausting into a Mach 2.20 External Stream. NASA TN D-5553, Dec. 1969.
- 7.43 Englert, Gerald W.: Operational Method of Determining Initial Contour of and Pressure Field about a Supersonic Jet. NASA TN D-279, 1960.
- 7.44 Barger, Raymond L.: Comparison of Jet Plume Shape Predictions and Plume Influence on Sonic Boom Signature. NASA TP 3172, 1992.
- 7.45 Salas, Manuel D.: The Numerical Calculation of Inviscid Plume Flow Fields. AIAA Paper No. 74-523, June 1974.
- 7.46 Englert, Gerald W. and Luidens, Roger W.: Wind-Tunnel Technique for Simultaneous Simulation of External Flow Field about Nacelle Inlet and Exit Airstreams at Supersonic Speeds. NACA TN 3881, 1957.
- 7.47 Love, Eugene S. and Grigsby, Carl E.: Some Studies of Axisymmetric Free Jets Exhausting from Sonic and Supersonic Nozzles into Still Air and into Supersonic Streams. NACA RM L54L31, 1955.
- 7.48 Cheung, Samson H.; Edwards, Thomas A.; and Lawrence, Scott L.: Application of CFD to Sonic Boom Near and Mid Flow-Field Prediction. AIAA Paper 90-3999, 1990.
- 7.49 Siclari, Michael J. and Darden, Christine M.: CFD Predictions of the Near-Field Sonic Boom Environment for Two Low Boom HSCT Configurations. AIAA Paper 91-1631, 1991.

- 7.50 Cliff, Susan E. and Thomas, Scott D.: Euler/Experiment Correlations of Sonic Boom Pressure Signatures. AIAA paper 91-3276, 1991.
- 7.51 Madson, Michael D.: Sonic Boom Predictions for Three Generic Models Using a Solution Adaptive Full-Potential Code. AIAA Paper 91-3278, 1991.
- 7.52 Haglund, George T.: HSCT Designs for Reduced Sonic Boom. AIAA paper 91-3103.
- 7.53 NASA CP 3173, High Speed Research: Sonic Boom, Vol. II, Feb. 25–27, 1992.
- 7.54 NASA CP 10133, High Speed Research: Sonic Boom, Vol. II, May 12–14, 1993.
- 7.55 NASA CP 1999-209699, Dec. 1999, High Speed Research: 1994 Sonic Boom Workshop.
- 7.56 NASA CP-1999-209520, 1995 NASA High-Speed Research Program Sonic Boom Workshop, Dec. 1999.
- 7.57 Cheung, Samson: Sonic Boom Softening of Reference-H, NASA CP-1999-209699, Dec. 1999, pp. 89-106.
- 7.58 Mack, Robert J.: Boom Softening and Nacelle Integration on an Arrow-Wing High Speed Civil Transport Concept NASA CP-1999-209520, Dec. 1999, pp. 121–137.
- 7.59 Baize et al.: A Performance Assessment of Eight Low Boom, High Speed Civil Transport Concepts. NASA CP-1999-209699, Dec. 1999, pp. 149-170.
- 7.60 Haglund, George T.: Potential for Sonic Boom Reduction of the Boeing HSCT. NASA CP-1999-209520, Dec. 1999, pp. 96–120.
- 7.61 Morgenstern, John M.: Potential for Sonic Boom Reduction of the 2.4 H5085 Arrow Wing HSCT. NASA CP-1999-209520, Dec. 1999, pp. 162–175.
- 7.62 National Research Council, Commercial Supersonic Technology – The Way Ahead, National Academy Press, Washington, DC, 2001.
- 7.63 Wood, K. D.: Aerospace Vehicle Design, Vol. I, Aircraft Design. Johnson Publishing, Co., Boulder, CO, 1963, pp. 41–61.
- 7.64 Maglieri, Domenic J.: Compilation and Review of Supersonic Business Jet Studies from 1963 through 1995. NASA CR 2011-217144, May 2011.
- 7.65 Wlezien, R. and Veitch, L.: Quiet Supersonic Platform Program. AIAA Paper 2002-0143. Jan. 2002.
- 7.66 Komadina, Steve and Drake, Aaron: Development of a Quiet Supersonic Aircraft with Technology Applications to Military and Civil Aircraft. AIAA Paper 2001-0519, Jan. 2002.
- 7.67 Pawlowski, Joseph W.; Graham, David H.; Boccadero, Charles H.; Coen, Peter G.; and Maglieri, Domenic J.: Origins and Overview of a Shaped Sonic Boom Demonstration Program. AIAA 2005-0005, Jan. 2005.
- 7.68 Briceno, Simon I.; Buonan, Michael A.; Fernandez, Ishmael; and Mavris, Dimitri: A Parametric Exploration of Supersonic Business Jet Concepts Utilizing Response Surfaces. AIAA Paper 2002-5828, Oct. 2002.
- 7.69 Coen, Peter: Development of a Computer Technique for the Prediction of Transport Aircraft Flight Profile Sonic Boom Signatures. Master's Thesis. GWU, 1991.
- 7.70 Wolz, R.: A Summary of Recent Supersonic Vehicle Studies at Gulfstream Aerospace. AIAA 2003-0558, Jan. 2003.
- 7.71 Horinouchi, Shigeru: Conceptual Design of a Low Sonic Boom SSBJ. AIAA 2005-1018, Jan. 2005.

- 7.72 Hunton, Lynn W.; Hicks, Raymond M.; and Mendoza, Joel P.: Some Effects of Wing Planform on Sonic Boom. NASA TN D-7160, 1973.
- 7.73 Hicks, Raymond M. and Mendoza, Joel P.: Prediction of Aircraft Sonic Boom Characteristics from Experimental Near Field Results. NASA TM X-1477, 1967.
- 7.74 Hayes, W. D.; Haefeli, R. C.; and Kulsrud, H. E.: Sonic Boom Propagation in a Stratified Atmosphere, with Computer Program. NASA CR-1299, 1969.

CHAPTER 8 RESPONSE TO SONIC BOOMS

This chapter begins with a description of the factors involved in boom exposure, including both human and building response. Outdoor and indoor stimuli include audible, vibratory, and visual cues. A discussion of damage complaints, relative to primary and secondary structural members, is given as a function of the range of boom exposure levels. Human response to booms includes startle, rattle, annoyance, effects on sleep, and long-term effects on health. Other effects of sonic booms are addressed including those on animals, terrain (avalanches and landslides), and other aircraft.

Factors Involved in Sonic Boom Exposures

There is considerable concern about the manner in which people and structures respond to sonic booms and how such responses will affect the acceptance of overland supersonic operations. The nature of the sonic boom response problem is illustrated in figure 8.1 (ref. 8.1). The sketch at the top of the figure suggests two different situations for people. In one case, the person is outdoors and is directly exposed to the shock waves. In the other case, the shock waves impinge on the building with the person inside the building. The building then acts as a filter that establishes the nature of the stimuli reaching the inside observer. The ingredients of this indoor exposure situation are included in the chain diagram at the bottom of the figure. The sonic-boom-induced excitation, which causes the building to vibrate, may arrive either through the air or through the ground. It is generally conceded that the air path is the more significant one in most cases and is thus designated the primary path on the figure. The ground transmission path is considered secondary and has not been found to be significant. Building vibrations can be perceived directly by the observer either through direct contact with the structure or visually, particularly in the case of window vibrations. A person may also observe vibration-induced noise, for example rattling of windows or, in the extreme case, associated superficial damage of the structure.

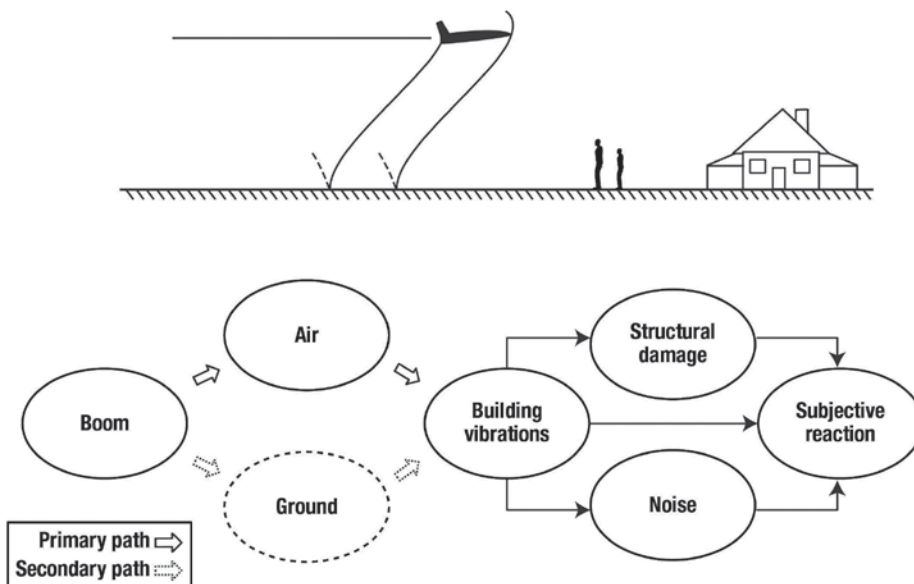


Figure 8.1. Factors involved in sonic boom exposures (adapted from ref. 8.1).

Loading on Buildings

A building is subjected to a variety of loading effects when a sonic boom wave pattern sweeps over it as illustrated in figure 8.2 (ref. 8.1). Shown schematically at the top of the figure is the N-wave pressure signature on the ground from a full-size N-wave supersonic transport. The pressure loading on the building, as the N-wave sweeps over it, at positions 1, 2, 3, and 4 is illustrated at the bottom half of the figure.

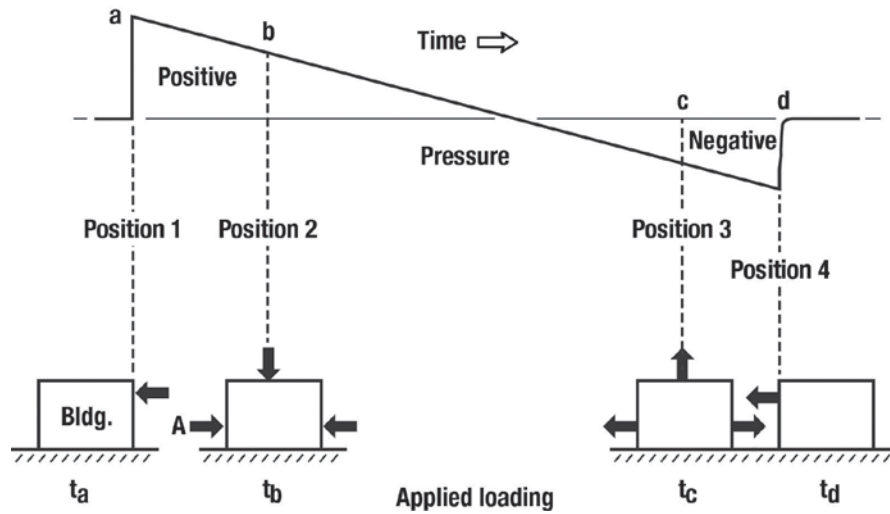


Figure 8.2. Factors involved in sonic boom exposures (adapted from ref. 8.1).

When the boom signature is at Position 1, the building would first be forced laterally as a result of the initial positive pressure loading on the front surface. Then, as the boom signature moves over the building (Position 2), it would then be forced inward from all directions, then pulled outward as the signature moves over it (Position 3) and finally displaced laterally again (Position 4) because of the negative pressures acting on the back surface. These loadings, which would be applied within a time period of about 0.1 to 0.3 second, can result in complex transient vibrations of the building.

The response of the structure will also depend upon the shape of the signature. Insight can be obtained through a simplified analysis that represents a building as a single degree of freedom, a spring mass system. A measure of structural response to transient inputs is the Dynamic Amplification Factor (DAF), which is the ratio of the maximum dynamic displacement to the displacement due to a static force (ref. 8.2). The higher the DAF, the greater the response of the structure to the transient input (the boom signature in this case). Figure 8.3 (refs. 8.2 and 8.3) illustrates the influence of signature shape on the DAF.

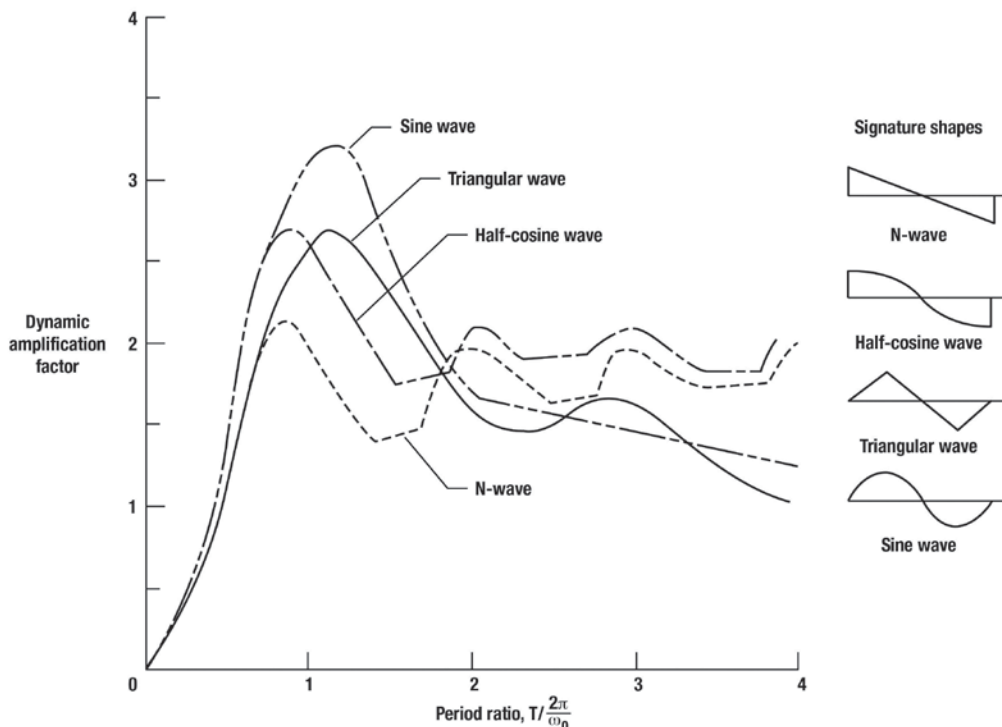


Figure 8.3. Influence of sonic boom shape on dynamic amplification factor (adapted from refs. 8.2 and 8.3).

Shown are the calculated DAFs on an undamped system plotted against the ratio of the duration of the signature, T , to the period of the oscillation $2\pi/\omega_0$ for four signature shapes that include an N-wave; a half-cosine wave, which is similar to a flattop signature; a triangular wave, which is representative of a finite rise time signature; and a sine wave. All signatures have the same maximum overpressure and duration.

The following discussion applies when the duration of the signature is roughly equal to the natural period of oscillation. It should also be noted that the effect of signature shape on complex buildings is more subtle (ref. 8.4 and 8.5) than the single degree of freedom analysis of figure 8.3. In this figure, the minimum value of 2.0 of the DAF is associated with the N-wave and the maximum value of about 3.0 is associated with the sine wave signature. This finding would be expected since the structure has inertia and would take some time to respond to the N-wave. On the other hand, since the sine wave signature loading begins gradually, the structure will be driven more efficiently. The DAF curve for the finite rise time signature will increase as rise time increases and eventually reach the sine wave value. The half cosine (flat-top) signature curve gives a DAF about midway between the N-wave and sine wave. The majority of the sonic boom database relating to structural response is for N-wave type signatures of overpressures of greater than 1.0 lb/ft^2 . Experimental data and analysis for N-wave and shaped signatures in the overpressure range of from about 0.2 lb/ft^2 to about 1.4 lbs/ft^2 provide considerably more insight into this question and will be discussed later in the next section.

The interaction of the structural components of the building as a result of the loading events is significant to the response of people indoors. The measured modal response of the floor, walls, and rooms of a two-story residence-type structure is presented in figure 8.4 (ref. 8.1). In the case illustrated for floor vibrations, it can be seen that a preferred phase relationship exists because of the manner in which interior wall structures are arranged. In regard to the wall structure, it was found that the panels between the vertical studs vibrated in a preferred manner such as that shown in the bottom left hand of the figure. Higher panel mode frequencies were also noted to exist and to be important. The sketch on the right-hand side of the figure suggests an interaction of the structure of the building and the enclosed air cavities within the rooms and attic spaces.

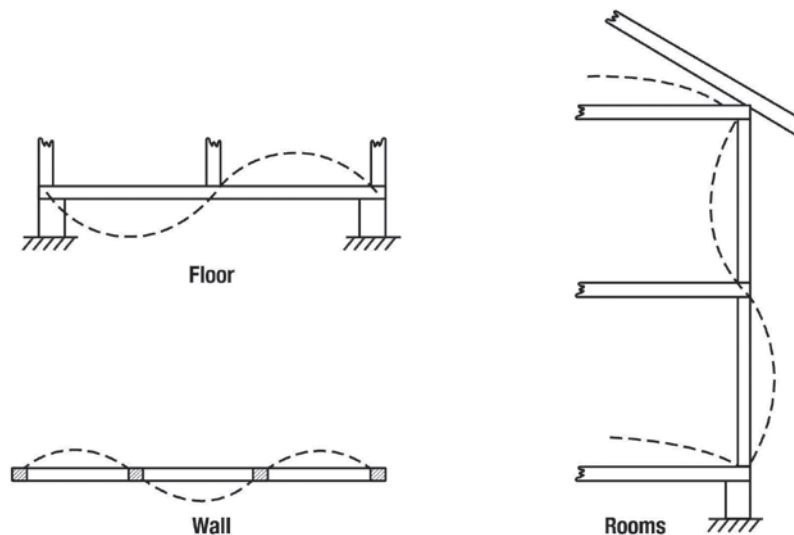


Figure 8.4. Measured modal responses for a two-story residence type structure (ref. 8.1).

Sonic Boom Stimuli

Inside the building, a person is exposed to a rather complex series of stimuli, including auditory, visual, and vibratory inputs. The nature of the auditory and vibratory inputs is illustrated in figure 8.5 (ref. 8.1). The top trace is the measured outdoor pressure time history. This signature is of the N-wave type, but it differs slightly from an N-wave in some of its details, as do many of the boom signatures measured outdoors as a result of atmospheric influences. The three bottom traces represent corresponding indoor exposure stimuli. The topmost of these traces represents the pressure variation inside the building owing to vibratory motions of the building and the cavity resonances. Although this is a pressure disturbance, it generally occurs in a frequency range that is not audible to

humans. The audible portion of this signal, as measured with a separate microphone system, has the characteristic shape of the middle trace and is an order of magnitude lower in amplitude. The audible portion of the pressure signal is associated with the rattling of the building structure and furnishings. Finally, the bottom trace represents the vibration of the floor that would be sensed by a person either directly or through the furniture. A person indoors, therefore, can be influenced because of an auditory, vibratory, or visual cue such as the movement of bric-a-brac on shelves and window movement. The indoor exposure situation is not understood well enough to permit the relative importance of each of these stimuli to be determined, although it was believed that in certain situations each one is significant. Presently, it is understood that the indoor pressure signature is composed of two parts, one due to the transmission of the boom and the other due to secondary sources such as rattles, squeaks, etc. Both parts are audible and their ratio depends on the characteristics of the structure.

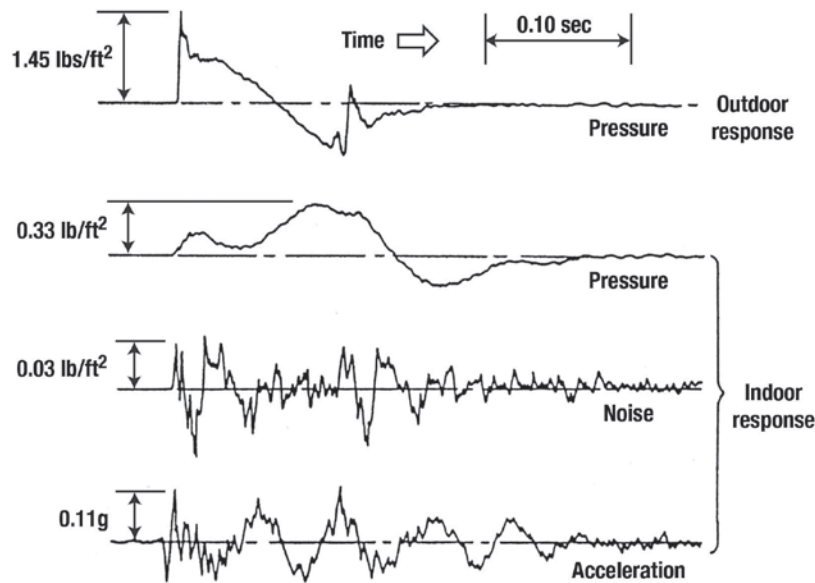


Figure 8.5. Outside and inside exposure stimuli due to sonic booms (ref. 8.1).

Human and building response is directly related to the frequency spectrum of the sonic boom signature. This is illustrated in figure 8.6, which shows the effect of boom signature time duration on the energy spectra of two sonic boom N-waves having the same overpressures but differing markedly in their time duration. The frequency ranges that are most important for human outdoor response and building response are indicated. It should be noted that these spectra result from N-waves with instantaneous (zero) shock rise times.

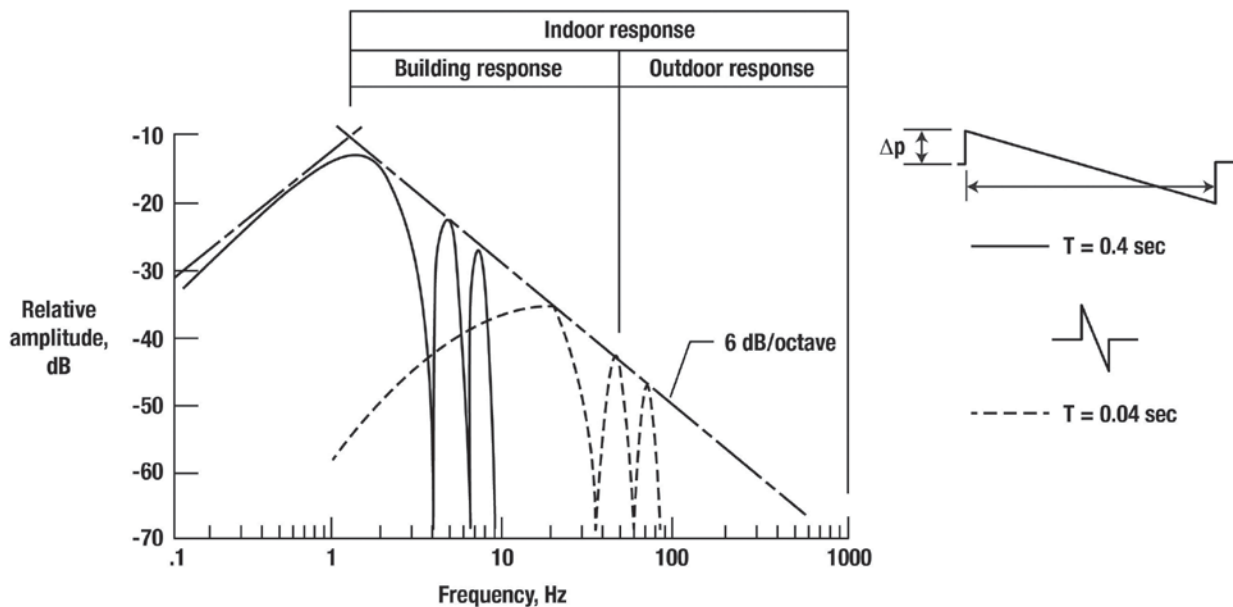


Figure 8.6. Effects of time duration on the energy spectra of sonic boom N-waves and their significance regarding responses (adapted from ref. 8.1).

Relative amplitudes of the component frequencies are shown in figure 8.6 by means of the spectrum envelope curves. Data for the short-duration wave from a small vehicle are shown by the curve of short dashes and those for the long-duration wave from an SST size vehicle are indicated by the solid curve. Although not shown in the figure, these spectrum envelopes continue out to higher frequencies. It is important to note that in each case the curves are tangent to a 6 dB per octave line that serves as a spectrum envelope for both waves. Examination of the figure shows that the relative amplitudes of the high frequency components from about 30 Hz - 1000 Hz are the same for the two signatures, which vary markedly in time duration. It is thus suggested that the human responses for outside exposure would be approximately the same from an overflight of a 350-foot SST size vehicle or a small vehicle. On the other hand, the low frequency components of the two signatures, which influence building response, vary markedly as a function of time duration. In particular, the low-frequency amplitudes from about 1 Hz - 20 Hz are considerably greater for an SST size vehicle boom signature of longer time duration. This result suggests that structural components having low vibration frequencies (e.g., larger building structures) would be excited by the SST size vehicle signature of longer duration and would not be significantly influenced by the much smaller vehicle's signature.

As indicated earlier, N-wave signatures having large rise times (τ) and of the same amplitude (Δp) and duration (ΔT) as a zero rise time N-wave will reduce outdoor, indoor, and building response because their spectral content is much reduced compared to that of an N-wave. This is illustrated with the aid of figure 8.7 (from ref. 8.4), which presents the envelopes of three frequency spectra: (1) one for a symmetrical N-wave of zero rise time, (2) the second for a symmetrical N-wave with an 8 msec rise time, and (3) the third for a symmetrical delayed ramp signature having an 8 msec rise to 0.5 lb/ft² followed by a 35 msec rise to 1.0 lb/ft². All three signatures have maximum boom levels (Δp) of 1.0 lb/ft² and a total duration (ΔT) of 350 msec.

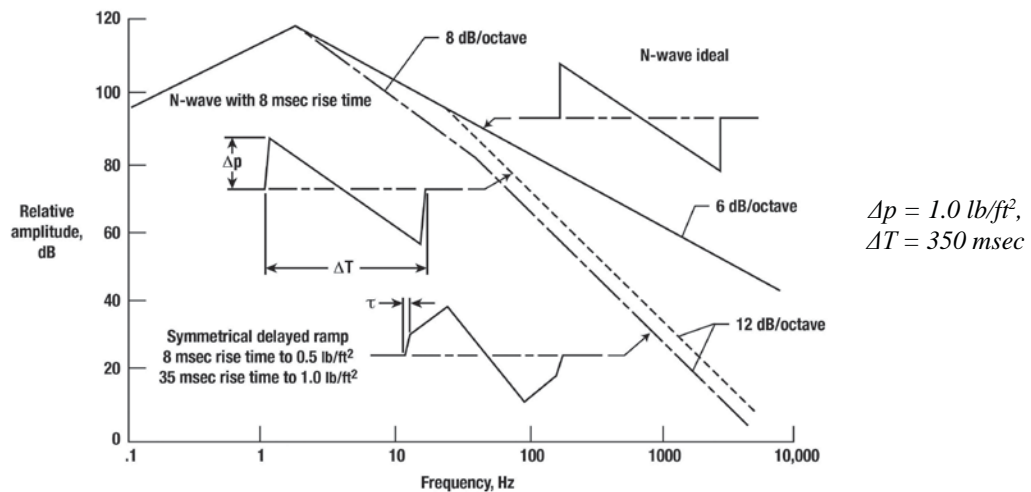


Figure 8.7. Frequency spectra of symmetrical sonic boom signatures (adapted from refs. 8.1 and 8.4).

It is evident that all three spectra peak in the sub-audible range of about 3 Hz (approximately the reciprocal of the signature period) and the levels decrease with frequency above this value. As previously mentioned for the ideal N-wave of zero rise time (figure 8.6), the decay is 6dB/octave. The N-wave with 8 msec rise time has an initial decay of 6dB/octave that transitions to 12 dB/octave at a frequency determined by the rise time (40 Hz for this example). Note the significant decrease in amplitude with frequency for the 8 msec rise time N-wave as compared to the zero rise time N-wave. For the delayed ramp signature with an 8 msec rise time on the initial shock, the spectrum shape is similar to the 8 msec N-wave spectrum but with a reduced amplitude of 6 dB due to the initial shock strength being 0.5 lb/ft² rather than 1.0 for the N-wave. Since the human ear is very sensitive to the higher frequencies, it follows that signatures with increased rise times will be more acceptable outdoors than zero rise time N-waves. Indoor response would also be expected to be more acceptable as a result of reduced building response associated with the reduced amplitudes at the lower frequencies for the shaped signatures. However, since shaped signatures were shown to increase the dynamic amplification factor (see fig. 8.3) over that predicted for an N-wave the benefits may be offset. An analytical study (ref. 8.5) on the effect of sonic boom shaping on booms heard indoors suggests otherwise and will be discussed later in the next section.

Structural Response

The relation between sonic booms and damage has the same complexity as the relation between sonic booms and structural response: a rigorous relationship depends on the frequency content of the boom and the frequency response of the structure. A practical, simple measure of the boom (for correlation with damage) would be the energy content in frequencies around the fundamental response frequency of structures, since this is where the greatest response occurs (refs. 8.6 and 8.7). For this reason, boom impulses, the area under the positive phase of the signature, as well as peak overpressures, are often reported. The fundamental frequency response of single frame residential buildings is typically 10 to 30 Hz (ref. 8.8). For the boom signature shown in figure 8.7, the energy spectral density at the dominant frequency of about 3 Hz is proportional to the overpressure times duration squared (ref. 8.9). Thus, boom impulse might be a reasonable estimation of structural response (refs. 8.10 and 8.11).

The vast majority of experience with sonic booms has been with N-waves of about 100 to 300 msec in duration. Usually only the overpressure has been reported or correlated with damage. One would, however, expect the relation between impulse, spectra, and overpressure to be fairly consistent for booms of such similar shapes (N-waves). As will be shown later in this section, care must be taken when these data associated with N-wave signatures are applied to significantly different types of boom signatures. However, these correlations of boom damage with overpressure are self-consistent and well worth examining.

Damage Complaints

Experience has shown that supersonic flights over communities have resulted in complaints regarding damage caused by sonic booms. The nature of the reported damage is fairly well represented in figure 8.8, which shows the percent of complaints with which certain types of damage are mentioned (ref. 8.12). Plaster cracks, the type of damage reported most frequently, are mentioned in 43 percent of the complaints. Other reported damage includes cracks in window glass, walls, and tile. Structures reportedly damaged by sonic booms are mostly brittle surfaces and are secondary structural components.

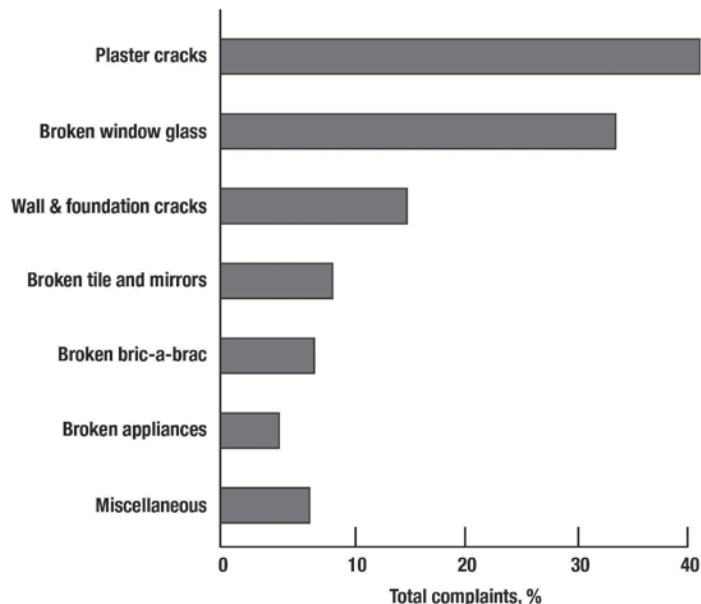


Figure 8.8. Sonic boom damage complaints (ref. 8.12).

Induced Damage

The majority of damage surveys have included all complaints made during the period of overflight, regardless of whether the damage was actually caused by sonic booms. During the St. Louis studies (ref. 8.12), wherein about 10 booms per month over a 7-month period were experienced, prompt investigations of the alleged damage

by architectural and engineering personnel indicated that only about 20 percent of the reported damage was considered likely to have been caused by a sonic boom. The remaining damage was considered to be due to natural causes, such as changes due to temperature, humidity, and aging. The results of such an engineering investigation are given in figure 8.9 (ref. 8.1). The overpressure range is indicated on the horizontal scale and the number of valid damage incidents per flight per million people is shown on the vertical scale. The four bars indicate the number of damage incidents associated with four different exposure areas (varying lateral distance from the ground track from 0 to 18 miles) for which the ranges of overpressure are indicated. It is obvious that the higher rate of occurrence was associated with the higher range of overpressures experienced at locations on or near the aircraft ground track. It may be significant that no damage incidents occurred for exposures below about 0.8 lb/ft² at the furthest lateral region, although it should be noted that a smaller number of data samples was available in this range. It is also important to note that the boom signature shapes at these lateral locations, in addition to having lower overpressures, can also have different frequency spectra due to increased shock rise times than those on or near the ground track.

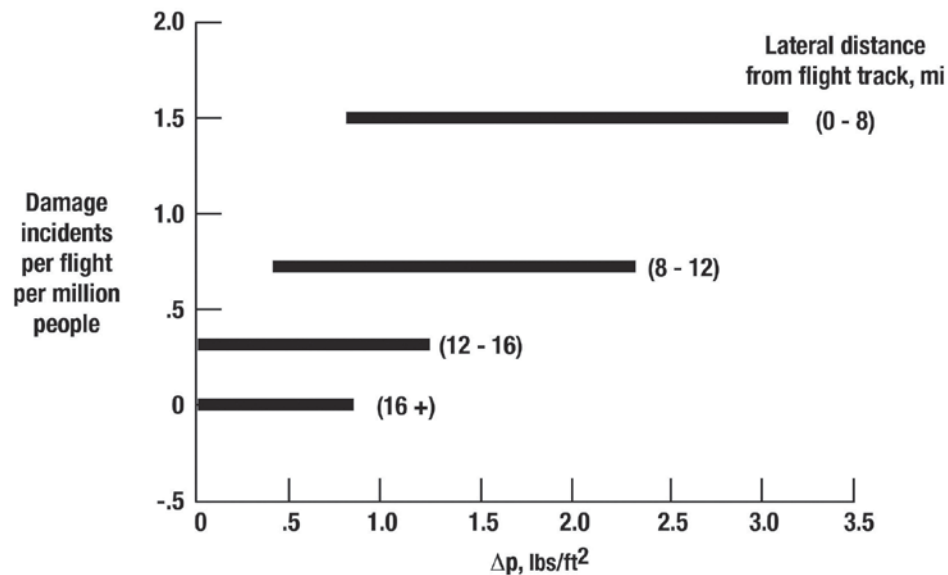


Figure 8.9. Sonic boom induced damage incidents for various overpressure ranges (adapted from ref. 8.1).

Damage Studies

In this section, brief summaries of the activities and findings regarding damage studies relating to plaster cracking, window breakage, and wall accelerations of conventional structures associated with N-wave sonic boom signatures will be presented. Some discussion will also be presented that addresses damage to buildings that are irreplaceable because of their historic nature.

In 1998, the USAF funded Haber and Nakaki (ref. 8.13) to review sonic boom damage to conventional structures. Concern regarding sonic boom damage to unconventional structures was also an important issue for the USAF and resulted in the summary work of Sutherland, Brown, and Goerner (ref. 8.14). In their assessment, unconventional structures involved historic national monuments or archaeological structures, Indian caves with ancient petroglyph drawings, older historic buildings, wells or large open water tanks, and radio telescopes/antenna. Ref. 8.14 contains a bibliography for the response of unconventional structures to sonic boom. Haber et al (ref. 8.15) describe the creation of a comprehensive database of the literature on the response of structures to noise and sonic boom. That database was incorporated into an archive denoted “International Bibliography On Noise” (IBON). IBON was not maintained and is no longer available.

Plaster Cracking

Archival information on the cracking of plaster has been documented from extensive building vibration studies made in connection with quarry blast operations (ref. 8.16). These 1942 data, summarized in figure 8.10 (ref. 8.17) as measured ceiling displacements versus response frequency, are still relevant today even though building designs, construction, and material have changed.

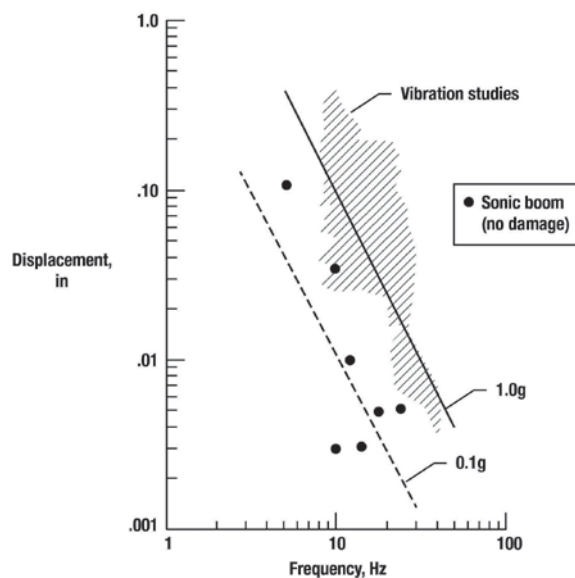


Figure 8.10. Summary of results from plaster vibration tests (ref. 8.17).

The envelope of the cross-hatched region encompasses the data points for which some plaster damage occurred during several building vibration tests. Associated 1-g and 0.1-g acceleration lines are shown for reference. The envelope indicates that the lowest amplitude at which damage occurs falls off as frequency increases and seems to follow roughly a constant acceleration line. Experience with buildings exposed to quarry blasting for which the acceleration amplitudes did not exceed 0.1 g resulted in no observable damage. The data points shown on the figure correspond to observations made during several sonic boom flight test programs and are associated with conditions of no observable damage. The limited sonic boom results are roughly consistent with the above vibration studies. The quarry blast vibration tests also produced many data points for which no damage occurred in the frequency range 5 to 40 Hz and at displacement amplitudes up to 0.3 inch. Definitive data on plaster damage are difficult to evaluate because of the many contributing factors such as variations in design, construction method, state of repair, environment, etc. (refs. 8.7 and 8.16). Approximately 40 such contributing factors relating to wall and ceiling cracks are listed in ref. 8.16.

The 1964-65 White Sands sonic boom overflights provided additional data regarding the cumulative crack length of plaster on wood lath in a two-story structure that occurred over a period of about 3 weeks of testing (ref. 8.18). Results are presented in figure 8.11 (taken from reference 8.2). Two curves are shown, one indicating the crack length growth for the no boom case and one associated with exposures to sonic booms. For the sonic boom case, nominal overpressures of 5 lbs/ft² were imposed the first 20 days and then increased in 2 lbs/ft² increments each day up to a maximum of 19 lbs/ft².

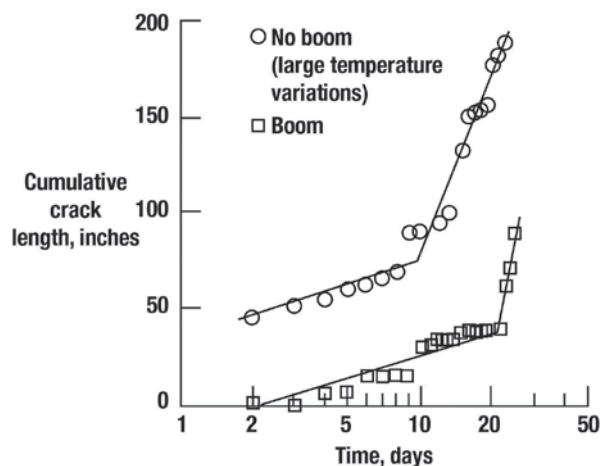


Figure 8.11. Cumulative crack length of plaster on wood lath observed during sonic boom tests (ref. 8.2).

For the no boom case (upper curve), two slopes are noted. The greater slope was attributed to the sizable changes in temperature between daytime and nighttime. The lower curve, representing the boom case, has two slopes also. The lesser slope almost parallels the no-boom case. However, after about 22 days of boom exposure, when the boom levels increase, the slope of the curve increases more rapidly than for the non-boom case. The authors concluded that for the two-story structure tested, the sonic booms caused damage when their level became greater than 11 lbs/ft².

In the early 1990 time period, the USAF funded a large-scale experimental and analytical effort on cumulative plaster damage (ref. 8.19). In these tests, full-scale plaster walls (8 ft by 10 ft) were subjected to many thousands of simulated booms of overpressures ranging from about 2 lbs/ft² to 20 lbs/ft². Three walls, including fixtures to simulate the boundary conditions that would exist in the actual structure of the ceiling, roof, and sidewalls were tested. Two were designated strong plaster wall and one weak plaster wall. Some of the results of these tests by Haber (ref. 8.20) are presented in figures 8.12 and 8.13.

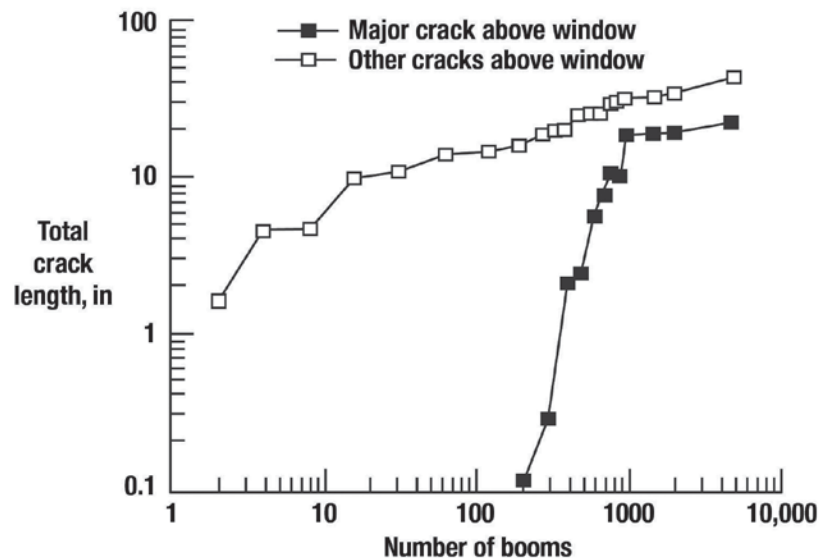


Figure 8.12. Total crack length in strong plaster wall versus number of simulated booms (ref. 8.20).

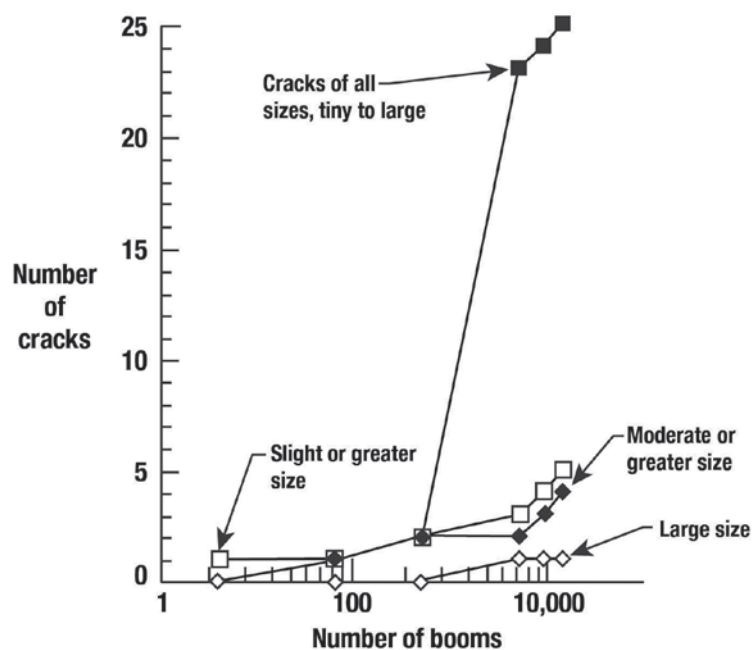


Figure 8.13. Number of cracks in weak plaster wall versus number of booms (ref. 8.20).

Total crack length versus number of simulated booms for the strong plaster wall is given in figure 8.12. Two curves are shown, both for observations of cracks above the window, with the lower curve designating major cracks and the upper curve designating all cracks except major ones. The tests consisted of 5000 simulated 20 lbs/ft² N-wave booms followed by 5000 booms of 1.8 lbs/ft².

Both curves show that crack length increases as the number of booms increases, with major cracks being initiated after some 200 booms and increase rapidly with increasing number of booms to a break point at about 1000 booms. At this point, the data fall in a horizontal line indicating no further damage.

A plot of the number of cracks versus number of booms for the weak plaster wall is given in figure 8.13 (from ref. 8.20). Four damage levels were defined to include tiny, slight, moderate, and large. For these tests, the test article wall was subjected to three sequences of 5000 simulated booms of 20 lbs/ft². The upper curve shows the number of observable cracks, regardless of size, and reaches a maximum of 25 after 5,000 booms. The other curves on the figure illustrate the number of cracks of various sizes. It is apparent that less than five cracks were observed with a size greater than tiny.

The key results of this study, as stated by the author of reference 8.20 (pp. 6-7), are as follows:

1. In the absence of stress raisers, pre-existing stresses, or pre-existing damage, no evidence was found for sonic boom damage at overpressures up to 20 lbs/ft².
2. Sonic booms or blast loads do cause progressive damage to plaster walls.
3. Sonic booms can produce cumulative damage given the right combinations of pre-existing stress and damage.
4. Damage to plaster from sonic booms is a result of the combined stresses introduced by the sonic booms together with environmental stresses.

As noted by Haber (ref. 8.20, p. 1):

Three concepts of cumulative damage are found in the literature: (1) any progressive damage from repeated sonic booms; (2) sonic boom damage in excess of that produced by environmental factors; and (3) sonic boom damage from repeated booms at an increasing damage rate.

Previous studies also established that plaster crack extensions can occur under repetitive sonic boom loads. As revealed by Haber (ref. 8.20, p.7), the present experimental study indicated that the sonic boom contribution to plaster damage occurs in three ways:

- Plaster that has been damaged by water or other factors may be weaker than well-maintained, properly constructed plaster. Sonic booms are one of many factors that may generate stress levels that can damage weakened plaster.
- Other natural and manmade forces may raise existing stress levels within plaster. Sonic booms may then act as a triggering mechanism for plaster failure.
- Plaster stress levels may be raised by other factors. The sonic boom levels may not be sufficient by themselves to trigger damage. They may, however, subject the plaster to fatigue cycles so that failure occurs when combined with pre-stresses and other cyclic stressors.

Window Breakage

Concern for glass window damage has existed long before the sonic boom issue came into being. In a 1964 paper by McKinley (ref. 8.21), it was noted that when a window pane has been abraded to the point of obscurity by weathering and diligent housekeeping, its strength to a uniform load is reduced to about half its original value.

Table 8.1 (ref. 8.21) indicates that it requires a loading of some 3000 lbs/in² to 30,000 lbs/in², depending on the type of loading and glass, to break large panes of glass.

Table 8.1. The Relationship of Load to Breaking Strength of Glass (ref. 8.21)

Typical Breaking Strength of Large Panes

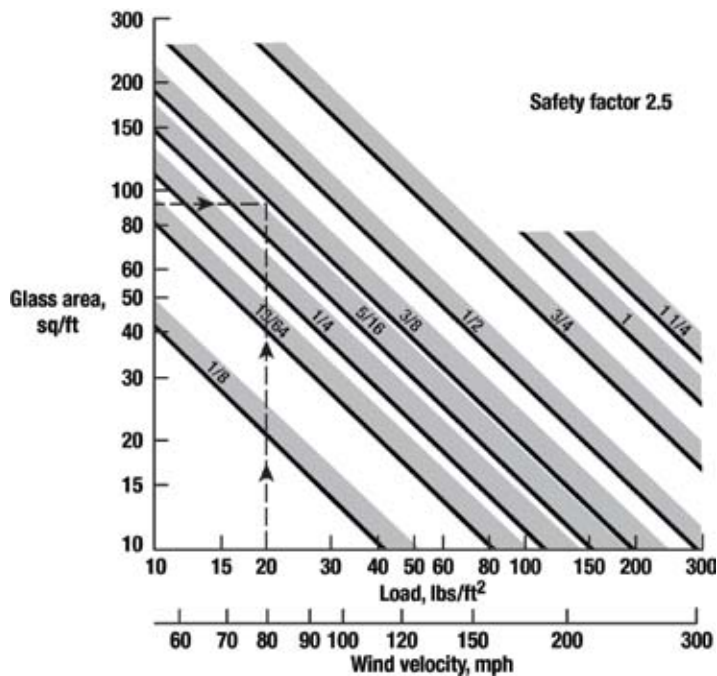
(Normal Surface Quality, As Glazed), lbs/in.²

Type of Loading	Approx. Load Duration	Regular Plate Glass	Regular Window Glass	Heat Strengthened	Fully Tempered (Herculite)
Sonic booms, blasts ^a	0.1 sec	6000	6600	15,000	30,000
Wind gusts	5-10 sec	5500	6050	13,750	27,500
Fastest mile wind ^b	1 min	4000	4400	10,000	20,000
Long-term	2 hours, indefinite	3000	3300	7500	15,000

^a The complex nature of these loads requires special engineering study when design criteria are to be established.

^b The term “fastest mile” denotes the average wind velocity over a 1-min period.

McKinley goes on to say that state and local building codes require glass of sufficient strength to resist wind loads to which outdoor walls are exposed. Figure 8.14, taken from reference 8.21, shows the recommended thickness of polished glass to meet wind load requirements.



Note: Solid lines are recommendations based on minimum thickness. Normal surface depreciation is taken into consideration. Shading suggests the possible performance of glass with newly formed surfaces. Velocities are averages for a 1-minute period. Support deflection not more than 1/175 of span at design load. Four edges glazed weather tight.

Figure 8.14. Recommended thickness of polished plate glass to meet wind load requirements – four sides supported (short side/long side not less than 1/3) (ref. 8.21).

The author points out that wind direction, local terrain, building geometry, and the position of the window in a facade may have considerable influence on the effective pressure to which glass in a particular opening may be exposed.

The 1960 USAF-NASA Project Little Boom flight-test experiments (ref. 8.22) included a study of window damage resulting from sonic booms of from about 5 lbs/ft² to 94 lbs/ft² overpressure and the findings are reported by Maglieri, Huckel, and Parrott (ref. 8.22) and Parrott (ref. 8.23). A series of test windows of plain and colonial style, most mounted in cubicles but some standing alone, were oriented under and lateral to the aircraft ground track. Some of the plain windows were tested statically and the results are given in figure 8.15 (refs. 8.22 and 8.23). The open symbols represent the typical behavior of a plain window. The solid symbols represent window failures that occurred in the 140 to 160 lbs/ft² range.

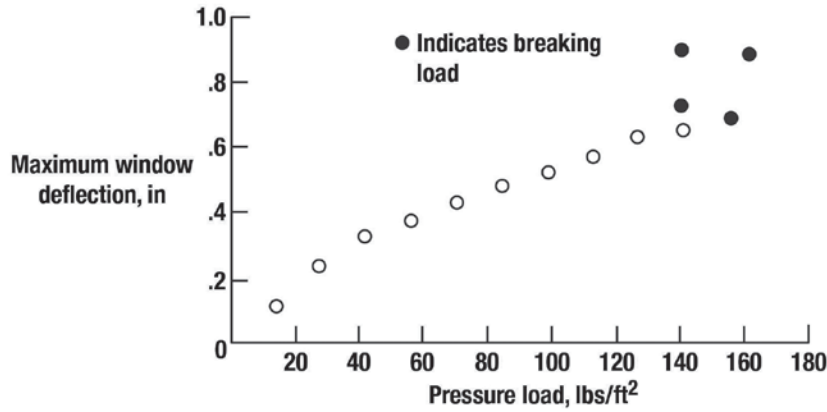


Figure 8.15. Maximum window deflection as static-pressure loading is increased to window failure indicated by solid symbols (refs. 8.22 and 8.23).

The results of similar tests on the colonial style windows resulted in considerably larger deflections for the same applied static pressure and the static breaking loads were about half that for plain windows. It was found that the wood mullions cracked before the glass failed. During the flight test program, 214 test windows were exposed to a range of sonic boom overpressures produced by two different aircraft (F-104 and F-105). The results are presented in figure 8.16 (refs. 8.22 and 8.23).

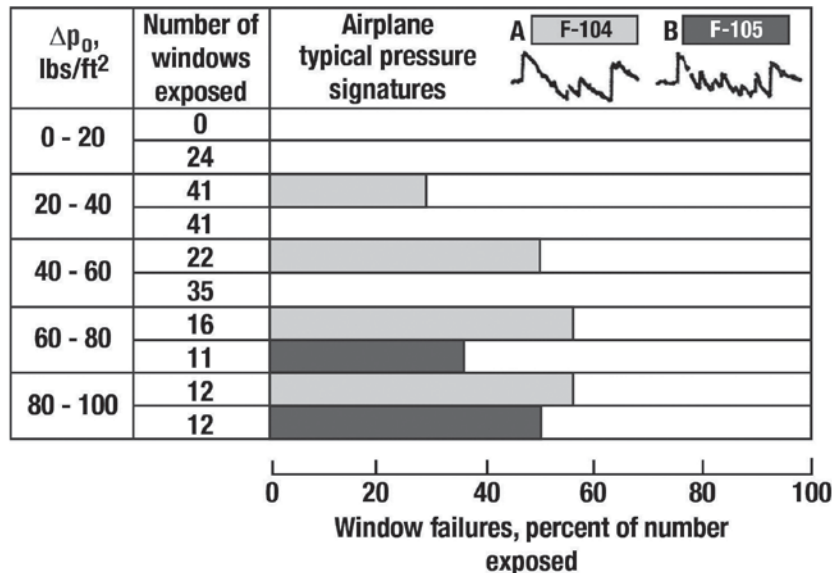


Figure 8.16. Summary of results from window-breakage tests (refs. 8.22 and 8.23).

More windows were damaged by airplane A, a Lockheed F-104 Starfighter, than for airplane B, a Republic F-105 Thunderchief, and no window damage occurred for airplane B at boom levels below 40 lbs/ft². While it appears that no damage occurred below an overpressure of 20 lbs/ft², it is to be noted that no windows were exposed to airplane A at boom levels below 20 lbs/ft².

The ability of airplane A to cause more damage at equal overpressures can be traced to a detail in the pressure signatures; namely the duration of the initial positive overpressure (referred to earlier as the positive impulse), which is somewhat greater than that for airplane B. Consequently, an attempt was made to correlate the available experimental glass breakage data for plain windows with the detailed characteristics of the initial positive phase of the pressure signature. These results are given in figure 8.17 (refs. 8.22, 8.23, 8.7, and 8.2).

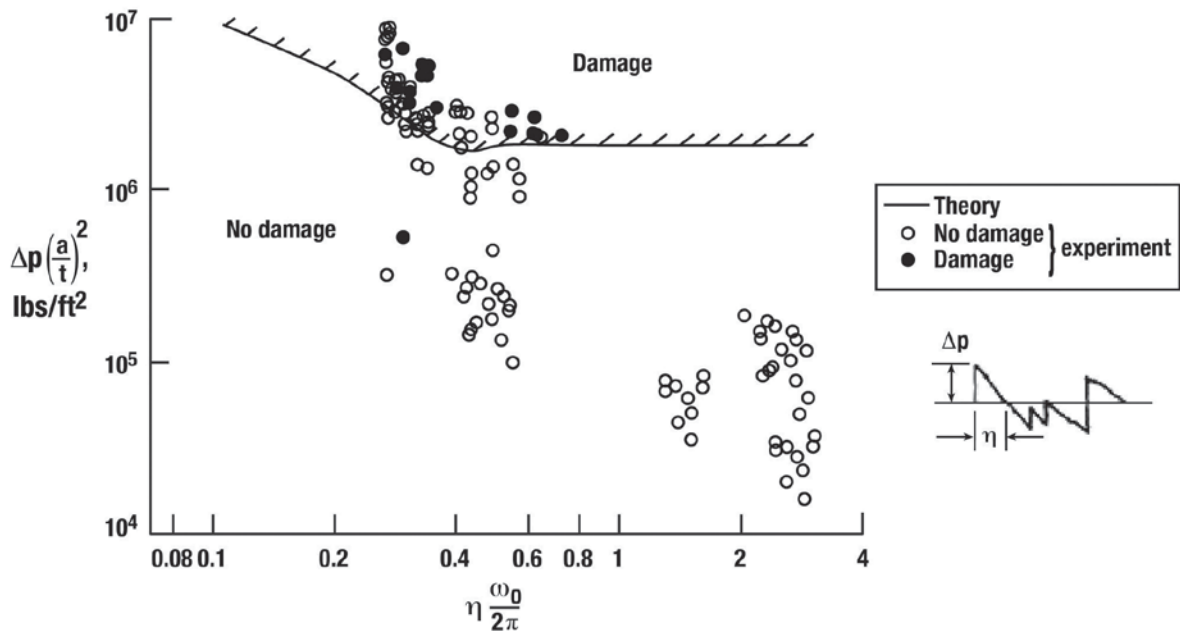


Figure 8.17. Summary of window-glass breakage due to sonic booms (refs. 8.22, 8.23, 8.7, and 8.2).

The ordinate represents a normalized loading parameter, where (a) and (t) are the window longest dimensions and glass thickness, respectively, and Δp the peak overpressure. The abscissa represents the duration of the positive phase of the boom signature (η) times the natural frequency of the window ω_0 . A damage boundary, taken from reference 8.7, is also shown. The solid symbols represent about 50 incidents of window glass breakage due to sonic booms from the low altitude tests.

It is to be noted that all but one of the damage data points for these square windows fall in the theoretical damage region. The only damage point to fall below the curve is associated with the 1959 sonic boom tests at Wallops Island, Va. (ref. 8.24), where a large plate glass store-front window was cracked at its lower left corner after a boom level of about 1.75 lbs/ft². This window, however, was believed to be pre-stressed in its mounting and made it vulnerable to damage from several loading inputs.

Hershey, Higgins, and Magrab (ref. 8.25) addressed the question of sonic boom glass breakage by posing a design question. As stated in reference 8.25 (p. 1009), the authors asked “what is the probability that a load having a certain statistical variation will cause a material having strength that varies in another statistical manner to fail?” They developed a response probability density function technique in a statistical model to estimate probability of glass breakage from sonic booms as a function of nominal boom levels and duration, aircraft flight path, window size, and whether the glass was in good condition or cracked. It was estimated that there would be 1.1 breaks per million panes in good condition boomed at a nominal overpressure of 1 lb/ft². The author’s noted that this agreed well with sonic boom claim data of 0.6 breaks per million panes boomed (ref. 8.25, p.1009).

Based on these findings, one can assume that window damage is generally predictable based on loading and structural information. It would also appear that damage to windows that are properly installed and well mounted

would not be expected from sonic booms resulting from normal high altitude supersonic flights. However, window breakage has occurred and will continue to occur, even at relatively low-boom levels (e.g., see ref. 8.15) due mostly to improper installation, weathering, aging, and previous cracking. In the same manner, glass of insufficient strength is weeded out to some degree by windstorms whenever they occur (McKinley, ref. 8.21). It should be expected that windows that are in disrepair or improperly installed will be weeded out as a result of sonic booms from supersonic operations overland.

Wall Damage

The peak values of measured stresses in a vertical stud due to various types of loading have been measured and the positive or negative value, whichever is higher, is plotted as stress versus peak overpressure in figure 8.18 (ref. 8.17).

Peak stress values are shown for sonic boom overpressures from 0.3 lb/ft² to about 3 lbs/ft², and the maximum stress is about 60 lbs/in². This is small compared to the design load stresses for the building and is of the same order of magnitude as the stress induced by such a common occurrence as a door closing. Also shown for comparison with this figure are data from explosive charges and rocket noise loadings. For extrapolated comparable peak overpressures for sonic booms, the stress response is somewhat lower for the explosive loading than for the sonic boom loading. The responses due to rocket engine noise at comparable peak pressures are markedly lower than those for the sonic boom. This is probably because most of the acoustic energy in the noise from the rocket was at frequencies above the natural frequency of the building components. Such results as those in figure 8.18 would suggest that there should be no concern for damage to primary structures due to sonic boom pressure loadings in the range shown.

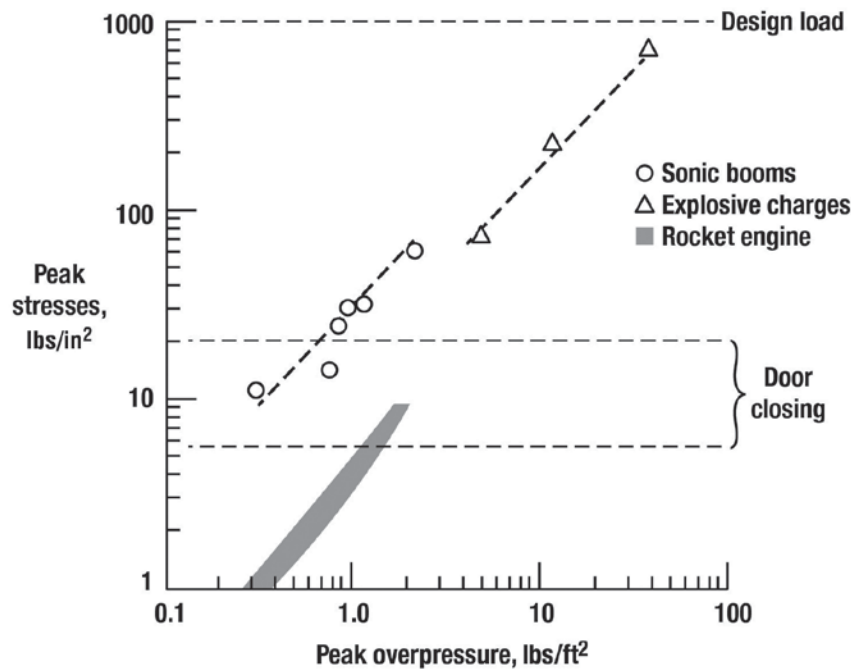


Figure 8.18. Peak vertical stud stresses as a function of peak overpressure for various types of excitation (ref. 8.17).

During the National Sonic Boom Program (ref. 8.26), peak acceleration amplitudes resulting from sonic booms associated with the F-104, B-58, and XB-70 aircraft were measured on a one-story residence structure and are presented as a function of overpressure in figure 8.19 (ref. 8.1).

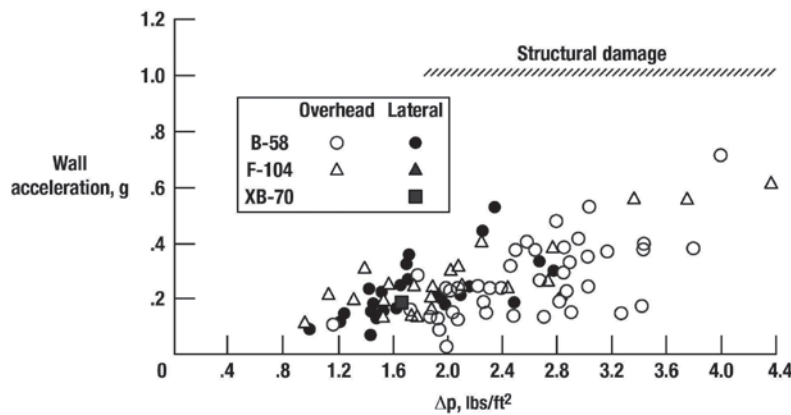


Figure 8.19. Maximum building wall acceleration amplitudes as a function of overpressure for three different airplanes (ref. 8.1).

The acceleration amplitudes are either positive or negative whichever is the largest for a particular test. The sonic boom outdoor overpressure value is the average of outdoor ground overpressures measured for that particular flight by an array of five microphones spaced 100 feet apart. Data were obtained from overhead flights and from flights displaced about 5 miles laterally. The horizontal cross-hatched line at the top of the figure represents the 1.0 g structural damage line shown in figure 8.10. It can be seen that acceleration amplitudes vary from about 0.1 g to about 0.7 g and that despite considerable scatter there is a general trend of increased wall acceleration level with increased overpressure. There seems to be no significant difference between overhead and lateral data points. There is thus the suggestion that the possible differences in wave angle and signature rise time due to the offset distance were not significant with regard to this particular measurement of building response. For the residence-type structure of the test, the dominant vibration responses were in a frequency range such that similar acceleration amplitudes were measured for both small, medium and large aircraft even though their signature durations ranged from 100 msec to 300 msec.

It is interesting to observe that if one were to extrapolate a line through the data set until it intersects the 1-g structural damage line, the resulting overpressure would be about 10 lbs/ft². As suggested by Clarkson and Mayes (ref. 8.2) and based on the extensive series of overflight tests, building structures in good repair should not be damaged at boom overpressures less than about 11 lbs/ft². Clarkson and Mayes also recognized that considerable loading variability occurs owing to atmospheric effects, and the residual strength of the structure varies according to usage and natural causes. The extreme statistical data required to predict the probability of damage to residential, commercial, and historical buildings are not available and cannot be obtained in a laboratory or limited overflight program.

Another perspective on the acceleration levels shown in figure 8.19 is presented in figure 8.20 (ref. 8.2) where they are compared with those experimentally determined (ref. 8.27) for other common events.

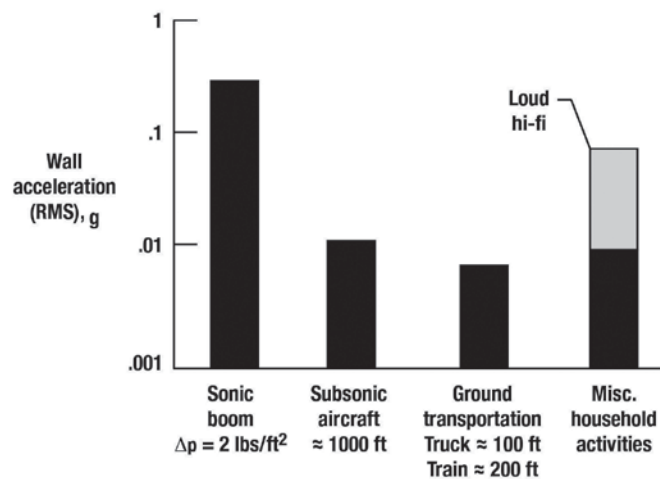


Figure 8.20. Maximum wall acceleration induced by various disturbances (ref. 8.27).

In figure 8.20, the ranges of measured wall acceleration for a sonic boom, subsonic aircraft, ground transportation, and miscellaneous household activities are represented by the vertical bars. The transient acceleration for a 2 lbs/ft² sonic boom overpressure is seen to exceed those observed for subsonic aircraft, trucks, and trains. The boom induced accelerations are comparable to those associated with loud hi-fi operations. Subsonic aircraft operations at about 1000 feet and heavy trucks and trains produce accelerations that are much lower in amplitude.

Damage to Historical Structures

In addressing the sonic boom issue regarding historical or unconventional structures (ref. 8.14), Sutherland et al. included historic natural monuments or archaeological structures, Indian caves with important older historic buildings, wells or large open water tanks, and radio telescopes/antenna. A field investigation concerning the vulnerability of Indian pictographs and petroglyphs to sonic booms from supersonic flights within the USAF Valentine Military Operating Area in Nevada was conducted and reported by Battis (ref. 8.28). It was demonstrated that damage is improbable for sonic boom levels of up to 5 lbs/ft² and signature durations from 100-200 msec. With regards to booms affecting satellite communication earth-station aerials, Duffy and Hatton (ref. 8.29), in their theoretical and empirical study, indicate that there was no damage or any interference with the facility under simulated booms of up to 6 lbs/ft² and durations of 250 msec.

In Europe, concerns focused on the potential damage to older buildings that are irreplaceable because of their historic connections; in particular, the many churches, cathedrals, and public and residential buildings that are several centuries old. Because of their ages, these buildings are generally in a poor structural state of repair compared with modern buildings. Windows were of predominant concern, especially the leaded stained glass windows that differ from ordinary windows. Also included were ornate plaster ceilings and walls with frescos and statues, which are all vulnerable to impulsive movements of the structure.

To assess the vulnerability of such structures, the Royal Aircraft Establishment (RAE), Farnborough, England, initiated a series of studies (ref 8.30) to measure the existing environment. Measurements were made of the response of major structural elements such as windows, walls, columns, ceilings, and spires of a range of cathedrals to their everyday noise and vibration environment. This included organ notes, bells, traffic, wind loading, thunder, and an artificial impulsive sound produced by a small explosive charge. In addition, several subsonic aircraft flyovers were performed. Typical results of this survey are shown in figure 8.21 (ref. 8.2). The limited overflight measurements that were made show that the predicted sonic boom response levels (see ref. 8.30) are greater than those produced by the normal environment.

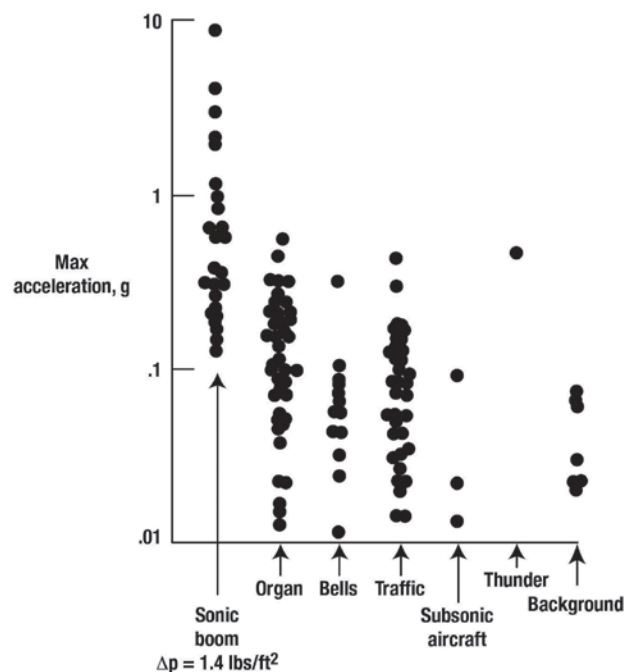


Figure 8.21. Response of cathedral windows to transient pressures (ref. 8.2).

The indications are that cathedral windows have more fatigue strength in reserve, but a definitive statement on this problem will require much more knowledge of the effects of other long-term natural forces such as settlement, temperature and humidity variations, weathering, etc.

An important aspect of the potential sonic-boom-induced damage problem as supported by the extensive N-wave signature database is illustrated schematically in figure 8.22 (ref. 8.1). The number of damage incidents for a given type of structure increases as the overpressure increases, and this is particularly evident at the higher overpressure values. Also shown in figure 8.22 is a schematic illustration of the amplitude distribution of the overpressures. Even though the nominal, or predicted, overpressure for a given aircraft at specific flight conditions may have a value that is lower than that at which building damage might be expected there is a distribution of pressure amplitudes such that a small percentage of them occur in the relatively high overpressure range. These high overpressure values, which occur occasionally because of either atmospheric effects or focus booms due to maneuvers, may be sufficient to trigger incipient damage in existing structures. It is obvious that shaped boom signatures having much lower nominal overpressure values and therefore more favorable probability distribution of overpressures are desirable in that it reduces the probability of causing building damage. However, low amplitude shaped boom signatures do not assure that the triggering of damage can be completely avoided, especially in structures in need of repair.

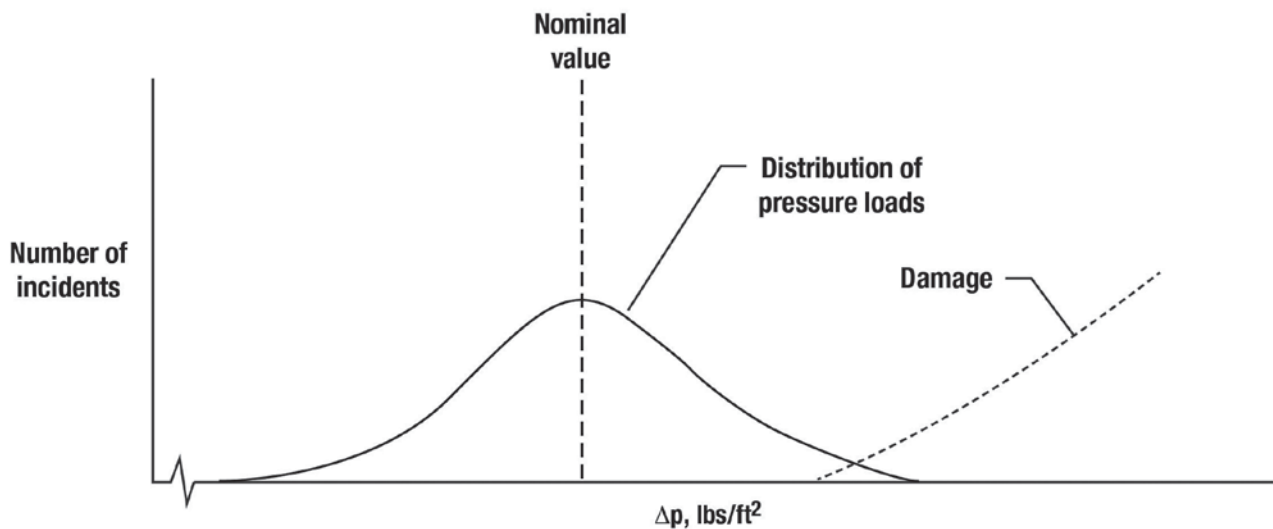


Figure 8.22. Nature of sonic boom induced damage problem (adapted from ref. 8.1).

The need to assure that future vehicles are designed to provide low amplitude shaped boom signatures that minimize the possibility of damaging structures and reducing annoyance were highlighted by the National Research Council 2001 study of reference 8.31 and in the DARPA 2002 QSP effort (ref. 8.32). Low-boom shaped signatures would shift the nominal value shown in figure 8.22 to the left. Shaped signatures whose spectra contain reduced levels of energy at the higher frequencies are expected to reduce the scatter due to atmospheric influences, thereby reducing the spread of the pressure load bell-shaped curve. Shifting the nominal overpressure to a lesser magnitude and tightening the pressure load distribution curve would significantly reduce the probability of building damage.

Building Response to Low Amplitude and Shaped Booms

In 2005, NASA, recognizing that little (if any) data existed regarding the response of structures and people in and out of doors to sonic boom levels of less than 1.0 lb/ft², initiated a series of low-boom flight tests at EAFB, California. Two series of low amplitude sonic boom tests were conducted in June 2006 and July 2007 to evaluate indoor/outdoor human response, structural acoustic building response and the effects of atmospheric turbulence for low amplitude sonic booms in the overpressure range of 0.1 to 0.6 lb/ft². In each test, a single family ranch-style home, one of older construction for the 2006 tests and a newer construction for the 2007 tests, was instrumented with numerous microphones and accelerometers.

The June 2006 tests (ref. 8.33) consisted of 112 booms during 6 flight days providing 14 conventional N-wave type signatures of nominal levels of about 1.4 lbs/ft^2 from straight and level flyovers of an F/A-18 (shown in figure 8.23) and 98 low-amplitude rounded type signatures of nominal levels of 0.1 lb/ft^2 to 0.6 lb/ft^2 generated by the F/A-18 performing a specially designed dive maneuver. The July 2007 tests (ref. 8.34) involved 72 booms over 5 flight days and consisted of 42 conventional N-wave types and 30 low-amplitude signatures. Example low overpressure signatures from two flights (Dive Numbers 3 and 5) are presented in figure 8.24 (ref. 8.35).



(NASA photo, EC00-0355-12)

Figure 8.23. In June 2006 and July 2007, NASA conducted low sonic boom flight tests of an F/A-18B Hornet at the NASA Dryden Flight Research Center (DFRC) in California.

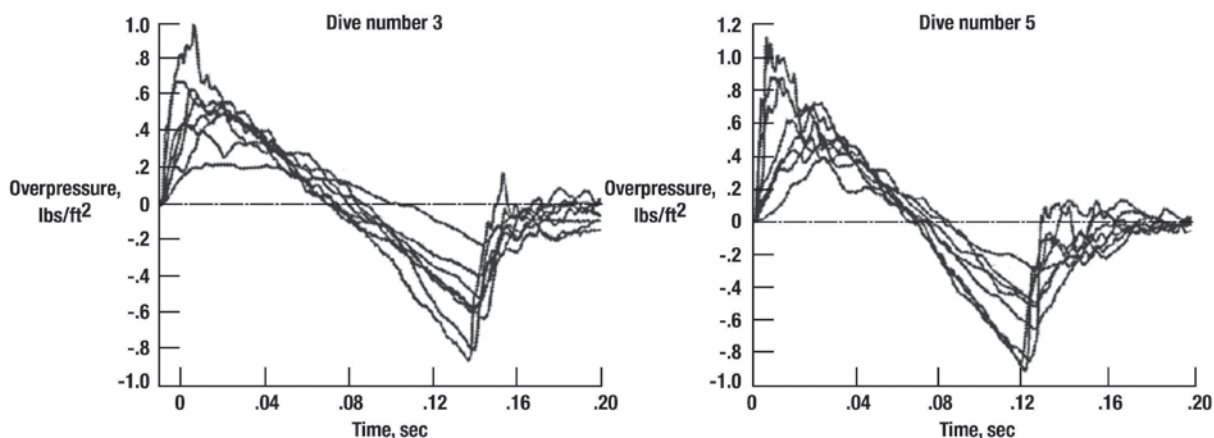


Figure 8.24. Ground-level sonic boom measurements from the F/A-18B aircraft in a supersonic low-boom dive maneuver (ref. 8.35).

Each signature represents a ground-level measurement from microphones spaced about one mile apart over six miles with one microphone placed 1 mile off track. It can be seen that the signatures vary in amplitude from about 0.2 lb/ft^2 to 1.0 lb/ft^2 and vary in waveform from a near N-wave to one approaching a sine wave. Signature rise times significantly increase as maximum overpressure decreases, as much as 40 msec for one signature. The influence of atmospheric turbulence is also evident on both the bow and tail shocks of all signatures shown.

A sample of the building response data obtained during the 2006 tests is presented in figure 8.25 (ref. 8.33). Wall acceleration time histories are shown for two sonic boom overflights; one from the F-18B in level flight producing an N-wave of a little over 1.0 lb/ft^2 and the other being a low-boom signature of a little less than 0.20 lb/ft^2 resulting from the dive maneuver flight.

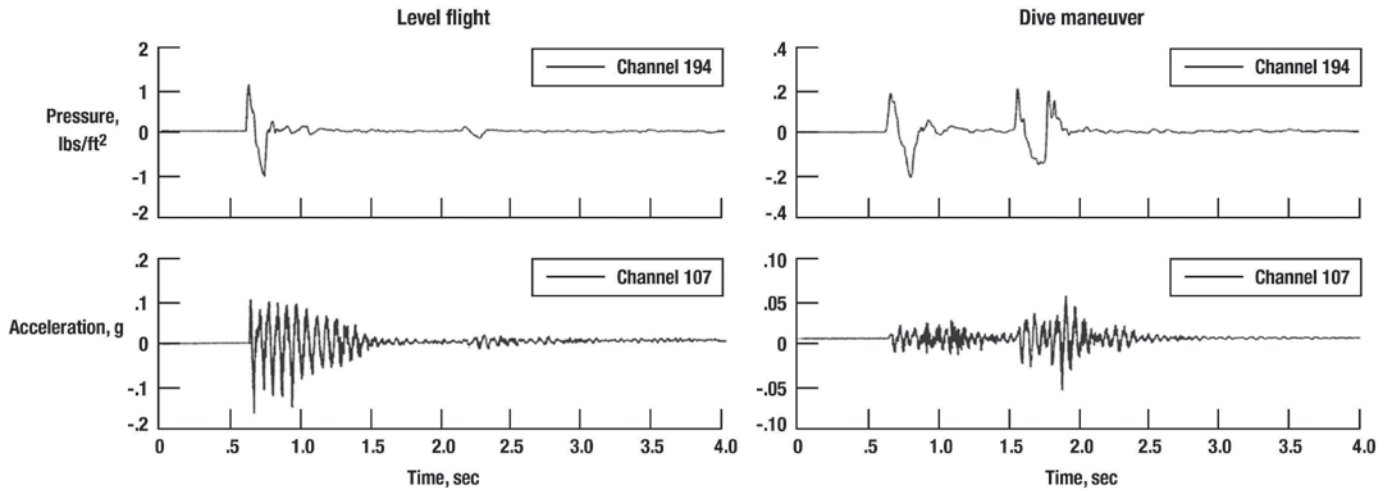


Figure 8.25. Time histories of transducer responses of an outdoor microphone and a wall-mounted accelerometer for a normal amplitude and a low amplitude sonic boom (ref. 8.33).

Note that the level flight boom signature time history, shown to the left in figure 8.25, has the remnants of the post-focus signature resulting from the acceleration to steady Mach occurring about 1.5 sec behind the carpet boom signature. The low-boom signature, shown on the right side of the figure, is followed by the expected post-focus boom about 1.0 sec later resulting from the dive maneuver. It can be observed that, in each case, the wall acceleration persists for about 1.0 sec following the boom arrival before damping out. In addition, it is interesting to note the differences in the nature of the wall acceleration time histories resulting from the normal N-wave boom, the low-amplitude N-wave signature followed by the post-focus boom. In the case of the 1.0 lb/ft² N-wave, the envelope of the wall acceleration peaks to ± 0.1 g and then decreases as time increases. One can also observe the very small response due to the refracted signature. The envelope of the wall response to the low boom N-wave type signature is about constant in amplitude whereas for the U-shape focus boom signature having the same overpressure, the wall acceleration builds to a maximum and then decreases as time increases.

Peak wall acceleration, whether positive or negative, measured at various locations on the single family ranch-style houses during the 2006 and 2007 tests as a function of outdoor sonic boom levels from the low-boom dive maneuvers and also from the straight and level flights of the F-18 aircraft are presented in figure 8.26 (refs. 8.33 and 8.34). These results are unique in that they fill in the large gap in the existing database as is evident in figure 8.19.

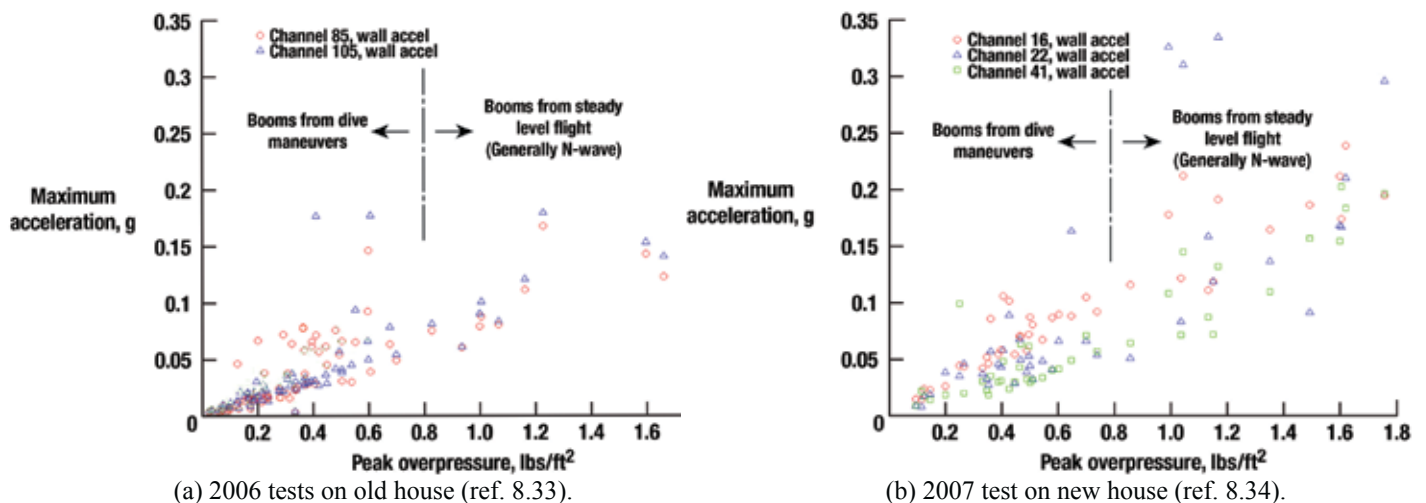


Figure 8.26. Maximum building wall acceleration amplitudes as a function of sonic boom overpressure (adapted from refs. 8.33 and 8.34).

It can be seen that wall accelerations observed in the 2006 tests (fig. 8.26(a)) ranged from about 0.05 for boom levels of 0.2 lb/ft² up to about 0.2g at boom levels of about 1.2 lbs/ft². For the 2007 tests (fig. 8.26(b)) slightly lower wall accelerations were observed and expected due to construction differences between the two houses.

It was shown in figure 8.24 that as the boom levels from the dive maneuvers decreased in level, the signature became more rounded with shock rise times increasing to about 40 msec. Since one would expect that rounded signatures would drive the structure more efficiently than an N-wave of equal amplitude and period, based on inertia considerations alone (see figure 8.3), one would also expect to see some sort of non-linearity in the variation of wall acceleration with sonic boom levels in the 0.2 lb/ft² to 0.6 lb/ft² range. However, the variation appears fairly linear, which is consistent with the results in figure 8.19 where the differences in wall acceleration resulting from the overhead flights to those resulting from flights that were offset about 5 mi lateral to the flight track were not significant. This finding was somewhat unexpected since the 5 mi offset flights produced signatures with larger rise times as compared to the on-track signatures and the angle of incidence at which the shock encounters the structure is also quite different.

A recent analysis was performed by Plotkin, Sizov, and Morgenstern (ref. 8.5) that describes the indoor perception of various shaped sonic boom signatures as compared to conventional N-waves. This study was aimed at determining which sonic boom shapes are best for minimizing the indoor perception and compare their indoor benefit for guidance in selecting the most acceptable low-boom signature shape.

The five low-boom shaped signatures, representative of those being considered by the technical community, are shown in figure 8.27 (ref. 8.5) and include a flat-top, ramp, and three multi-shock ramp approximations, together with a reference N-wave. Analyses of loudness, low frequency content, building tactile vibration, and rattle threshold were performed for each boom signature at six amplitudes. Building response was modeled as a single-degree-of-freedom (SDOF) system, with displacements governed by the Duhamel integral.

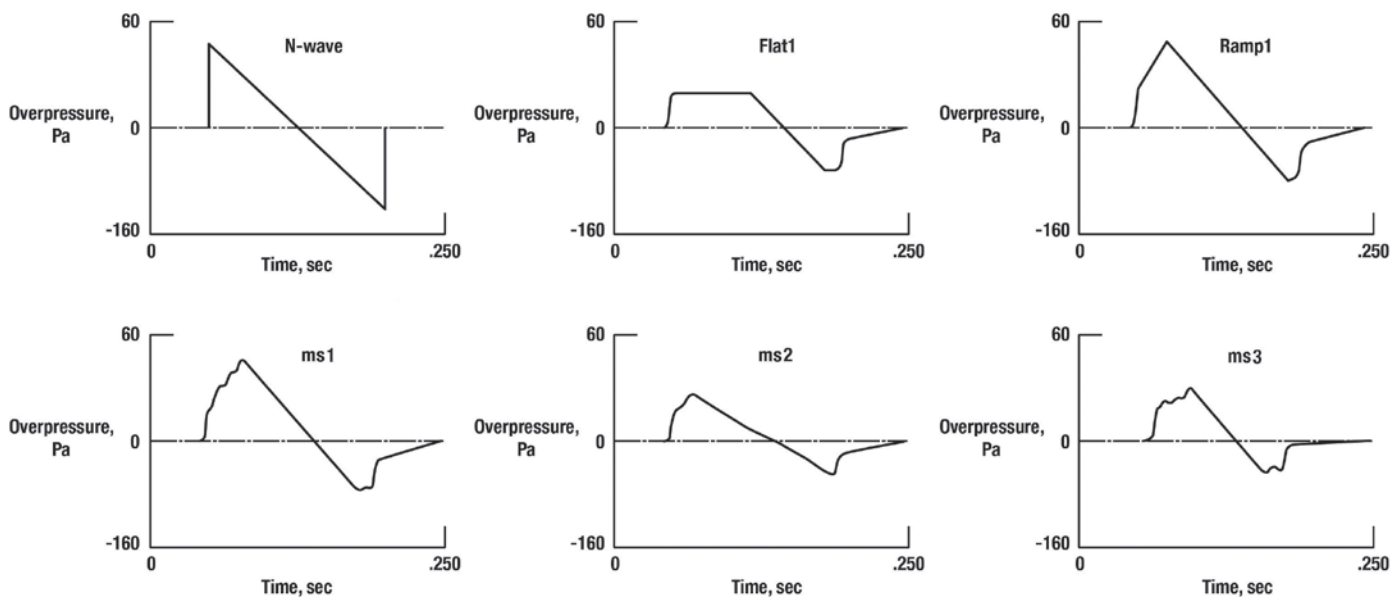


Figure 8.27. Type sonic boom signatures considered (adapted from ref. 8.5).

Wall accelerations as a function of peak overpressure for all six signatures are presented in figure 8.28 (ref. 8.5).

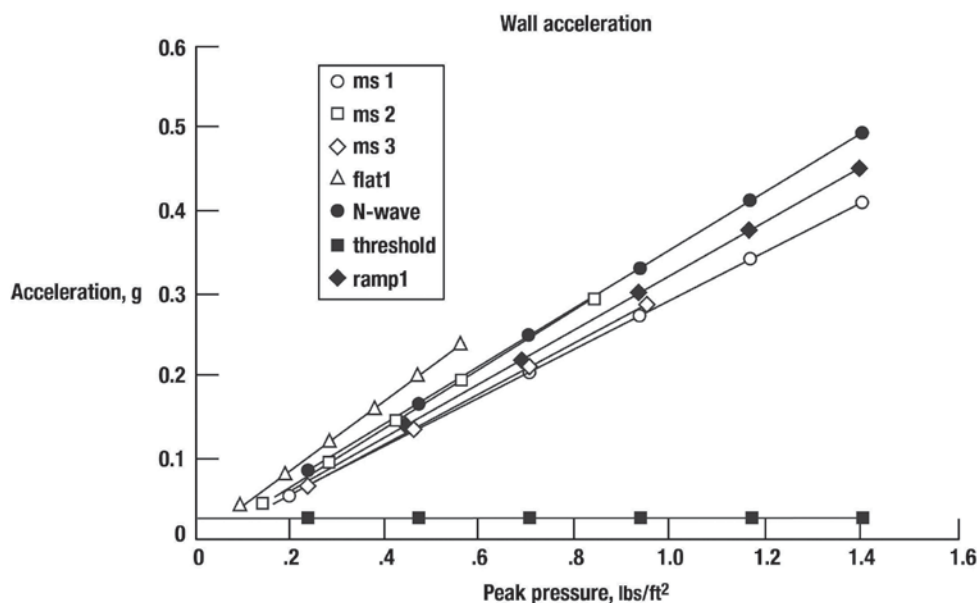


Figure 8.28. Predicted peak acceleration of wall for various sonic boom types and amplitude, compared with vibration threshold (ref. 8.5).

These results indicate that, at any given outdoor overpressure level, shaped signatures with larger rise times such as ramp1, ms1, and ms3 result in a lower wall acceleration than those resulting from an N-wave. Clarkson and Mayes (ref. 8.2) presented a summary of some measured responses of large windows and vertical studs due to N-wave type sonic boom loadings in the form of dynamic amplification factors. These results showed that the predicted values are generally conservative and, in particular, for the case of no damping encompass all of the measured data. In addition, it has been shown that the pressure loading on a building is lower for a signature having a longer rise time than for an equivalent N-wave in that the former has less energy at the higher frequencies (see figure 8.7) resulting in lower excitation of the structure.

In the section just concluded, discussions on structural response to sonic booms have been presented. Findings regarding damage complaints, induced damage, damage studies and building response to low amplitude shaped boom signatures were included. The majority of the data base is associated with N-wave signatures of amplitudes in the 1.0 lb/ft² to 3.0 lbs/ft² range with damage being confined to brittle surfaces and secondary structural components such as plaster and window cracks. Damage to those components is generally predictable based upon loading and structural information. As such, damage resulting from sonic booms from nominal high altitude flight would not be expected for structures in good repair.

In general, the vast majority of the sonic boom building response and damage to conventional and historical structures was acquired during the 1960s and 1970s in connection with the U.S. SST program effort and was a requirement to the environmental impact statements by the Department of Defense (DoD) for designating military operating areas (MOA's) in remote areas of the U.S. No controlled tests or analyses have been conducted on cluster homes as would be found in residential areas, nor have analyses or testing been conducted on high-rise structures or enclosed stadiums, all of which are of different design and construction methods with new materials.

Recent studies, analysis and full-scale overflight experiments indicate that low-amplitude shaped sonic boom signatures are more acceptable than N-waves of equal amplitude and duration regarding building response and indoor annoyance. It is shown that the pressure loading on a structure is lower for a signature having a longer rise time and thus has less energy at the higher frequencies resulting in lower excitation of the structure.

Human Response

The majority of the current database regarding sonic boom acceptability is based upon laboratory and overflight testing that was generated in the mid 1960s and early 1970s as part of the U.S. SST and Concorde development programs. The majority of these tests focused mainly on N-wave type sonic boom signatures in the range of about 1.0 lb/ft² to about 3.0 lbs/ft². Von Gierke and Nixon (ref. 8.36) provide an excellent review of the methods and results of these laboratory studies, controlled field studies, and uncontrolled overflight field studies on individual subjects, groups, and communities. The authors also stated that although much has been learned, it is possible that human responses measured during that time period may differ somewhat from those in the future. Indeed, that is likely the case since human attitudes are always in a state of change. Since the U.S. SST program was canceled and the Concorde was ultimately confined to over water operations, there was little opportunity or motivation for further studies. In the 1990s there was a renewed interest engendered by the potential for boom shaping and this period saw a flurry of activity on both laboratory and field studies.

As a result of this renewed interest, an extensive database has been generated by NASA regarding human responses to much lower level shaped sonic boom signatures, which include laboratory, in-home, and field studies. Sullivan (ref. 8.37) noted that laboratory studies have very good control over the sound stimuli that subjects hear but require a very abnormal listening environment. An in-home study, where sounds are played through loud-speakers in people's homes, improves the realism of the environment but at the same time reduces control over the sound field. Finally, field studies provide for a completely normal environment but suffer from very poor knowledge of the precise details of the sound exposure. Sullivan also states that the acceptability of, or annoyance, caused by a sound is affected by many factors. In a laboratory situation, while some of these factors are under control, others may be missing. Thus, laboratory studies allow sounds to be compared in a relative sense rather than in an absolute one. The in-home study moves closer to absolute measurements and the field studies measure absolute, real reactions. A compilation of the studies, complete with details of the findings, is provided by Leatherwood et al. (ref. 8.38).

The earliest studies on human response to sonic booms relied on overpressure as the parameter to describe a sonic boom. This was a reasonable approach since for an N-wave it represents the amplitude of the signature. However, the earliest laboratory studies established that the rise time of the signature was also important in determining human perception of sonic boom waveforms. The rise-time determines the mid- and high-frequency content of the signature. This is the frequency range of maximum sensitivity for human hearing. Thus, the use of various metrics, such as A-weighted sound exposure level and loudness-based metrics, has come into being.

However, there is a characteristic of sonic booms and other impulsive sounds – their low frequency content – that is able to vibrate buildings and create rattling sounds that must also be considered. All field studies of sonic booms have identified these phenomena as being important contributors to annoyance. As a result, C-weighted sound exposure level is used to assess high-energy impulsive sounds. The C-weighting emphasizes low frequencies relative to other metrics in an attempt to incorporate the effects of structural vibrations and the accompanying rattling of objects.

There is no consensus within the regulatory and scientific community regarding appropriate metrics and levels for sonic boom assessment. In large part this is due to the widespread prohibition of overland supersonic flight that resulted from the experience gained in the 1960s; an outright ban that required no consideration of metrics or levels. Despite this, there have been various proposals and attempts to develop assessment methods for sonic booms and other impulsive sounds. The general consensus is that selection of a final metric and level can not happen until a demonstration vehicle having a low-amplitude shaped signature is flown to assess its community acceptance.

An indication of some of the noise metrics that are being assessed is given in table 8.2. Leatherwood et al. (ref. 8.38) evaluated five of these metrics, the flat-weighted sound exposure level (FSEL), C-weighted sound exposure level (CSEL), A-weighted sound exposure level (ASEL), Stevens Mark VII Perceived Level (PL), and Zwicker loudness level (ZLL). The Leatherwood et al. (ref. 8.38) laboratory study was designed to: (1) quantify

loudness and annoyance response to a wide range of shaped sonic boom signatures and (2) assess these five noise descriptors as estimators of sonic boom subjective effects.

Table 8.2. Noise Metrics, Symbols, and Abbreviations

DNL	Day-Night Average Sound Level, dB
DNL(A)	Day-Night Average Sound Level, calculated using A-weighted sound pressure level, dB
DNL(C)	Day-Night Average Sound Level, calculated using C-weighted sound pressure level, dB
DNL(PL)	Day-Night Average Sound Level, calculated using perceived noise level, dB
ZLLd	Zwicker Loudness Level (diffuse field), dB
ZLLf	Zwicker Loudness Level (frontal field), dB
PL	Perceived Level (Stevens Mark VII procedure), dB
PNL	Perceived Noise Level, dB
ASEL	A-weighted Sound Exposure Level, dB
CSEL	C-weighted Sound Exposure Level, dB
FSEL	Flat-weighted Sound Exposure Level, dB

Based on the simulator studies, of the five metrics involved, Perceived Level (PL) proved to be the best choice for comparing booms with different shapes and amplitudes (see ref. 8.38). It was clearly a good metric for outdoor listening conditions and there are also some indications that it worked quite well indoors.

Loudness and Annoyance

For the outdoor situation, loudness and annoyance are a direct function of the sonic boom signature spectrum (see figs. 8.6 and 8.7). The sonic boom spectrum is defined by the signature shape, amplitude, and period or duration. Early laboratory studies involving N-waves revealed that perceived loudness or annoyance of sonic booms is primarily related to the peak overpressure and shock rise time (refs. 8.39, 8.40, 8.41, and 8.42). Peak overpressure is the dominant contributor, since the higher the boom level, the greater the judged loudness. Increasing rise times reduce loudness and annoyance, whereas signature duration had little influence as indicated in figure 8.29 (ref. 8.36).

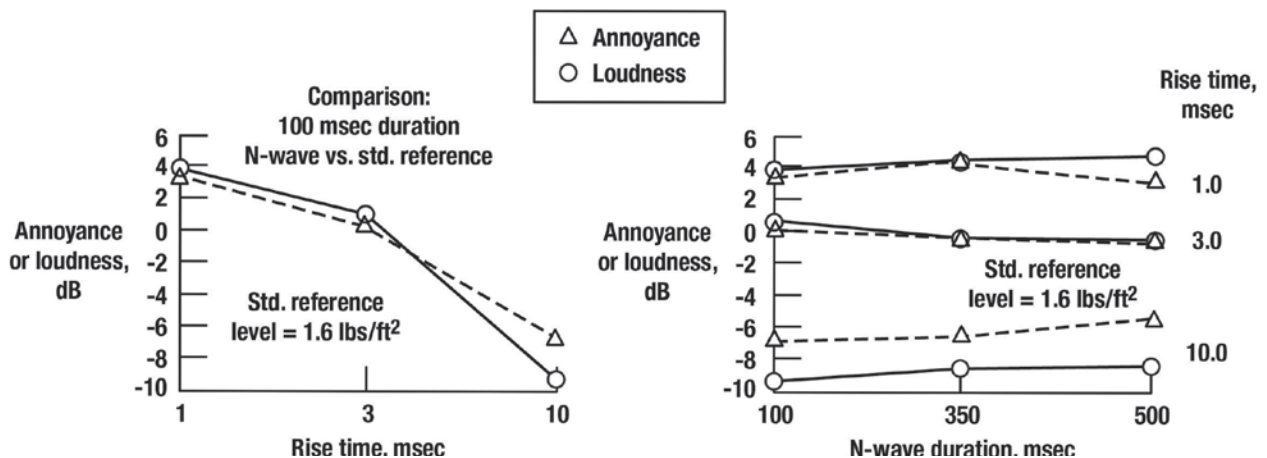


Figure 8.29. Relative loudness and annoyance versus boom signature rise time and duration. Laboratory free-field judgements (adapted from ref. 8.36).

It is seen that an increase in shock rise time from 1 msec to 10 msec decreases loudness and annoyance by about 13 dB. It should be noted that the findings presented in the figure are for a reference boom level of 1.6 lbs/ft². Similar results were observed at boom levels of 0.8 lb/ft² and 2.4 lbs/ft².

The procedure for loudness calculations has been applied to not only classical N-waves but also to low-boom shape signatures. For non N-wave shaped signatures, Niedzwiecki and Ribner (ref. 8.43) and Shepherd and Sullivan (ref. 8.44) showed that loudness is not only controlled by rise time and overpressure, but is also highly dependent upon the characteristic of the initial shock. They showed that loudness of booms could be reduced by replacing N-wave signatures with symmetrical signatures that achieved peak overpressure in two pressure steps instead of one. As can be seen from figure 8.7, booms shaped in this manner would contain significantly less high-frequency energy and be less loud than an N-wave of identical front shock rise time and maximum overpressure. This is illustrated in figure 8.30 (ref. 8.44), which shows the calculated loudness level of a shaped sonic boom signature observed outdoors.

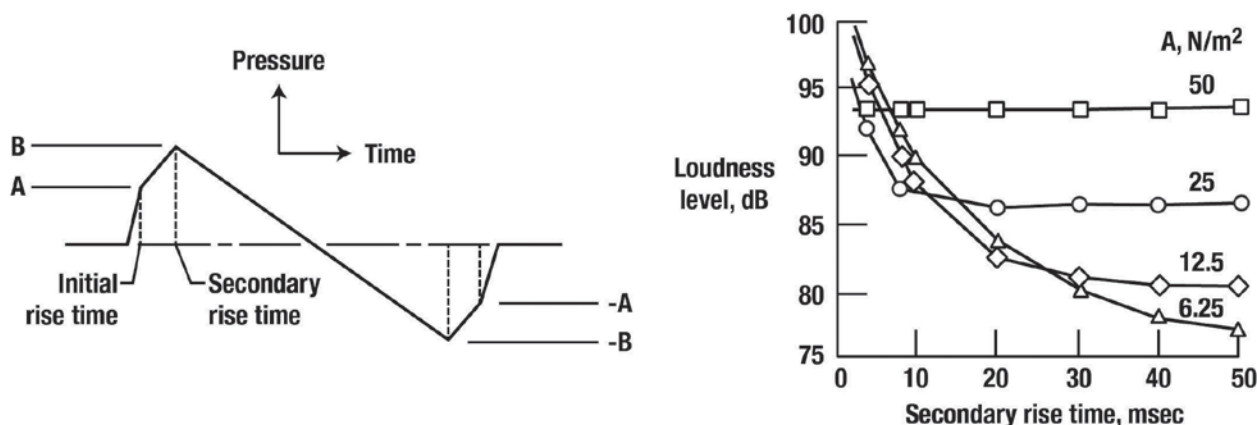


Figure 8.30. Calculated loudness level of shaped booms for outdoor listening conditions with peak overpressure of 50 N/m², duration of 350 msec and initial rise time of 2 msec (adapted from ref. 8.44).

The signature, shown to the left, has a duration of 350 msec and a peak overpressure (B) of 50 N/m² (about 1 lb/ft²) with an initial rise time of 2 msec (from zero to point A) with a secondary rise time from point A to point B, which is varied from 2 msec to 50 msec. Note that for a small value of the initial shock (A), say 6.25 N/m² (about 0.13 lb/ft²) and large secondary rise time (B) of say 40 msec, one realizes a reduction of about 16 dB in loudness as compared to a flat-top or N-wave signature of amplitude 50 N/m² (A = B = 50 N/m²) and a rise time of 2 msec. For an initial shock (A) of 25 N/m² and a rise time of 2 msec and a secondary shock rise time of 40 msec, one only realizes a reduction of about 7 dB in loudness compared to a flat-top or N-wave signature of 50 N/m² and a rise time of 2 msec. Thus, if the initial shock rise time is small, then it is desirable to keep the initial shock amplitude small (zero to A) and have a large secondary rise time from A to B. Conversely, if the secondary rise time is shorter than the initial rise time, then the pressure rise from A to B will control the loudness.

Shepherd and Sullivan (ref. 8.44) also made estimates of the loudness of sonic booms as they would be observed indoors of a building with windows open and also closed. However, as the authors noted, this assessment of indoor levels made no attempt to include the effects of structural vibrations or secondary acoustic radiation due to vibration-induced rattling of objects. Results of their study are illustrated in figure 8.31 (ref. 8.44).

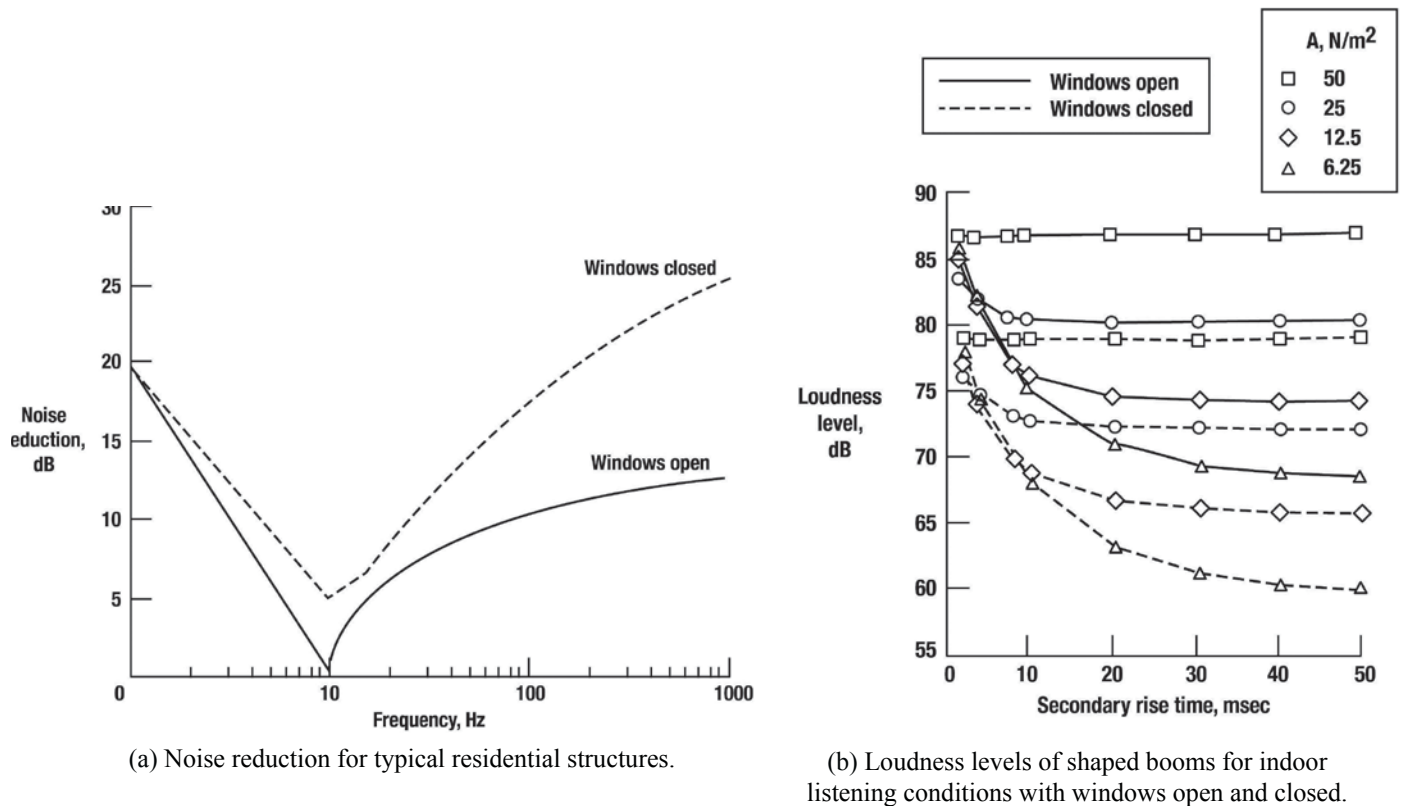


Figure 8.31. Estimates of the loudness of shaped sonic booms heard indoors with peak overpressure of $50 N/m^2$, duration of 350 msec and initial rise time of 2 msec (adapted from ref. 8.44).

In figure 8.31(a), the two curves of noise reduction were derived from measured data for a range of houses, both with windows open and closed. These noise reduction values were applied to the same range of booms described in figure 8.30.

As can be seen from figure 8.31(b), the trends of all the curves are similar for both cases of windows opened and closed. The authors also showed that there is a 10 dB decrease in loudness between the outdoor case and indoors with windows open.

Startle

Loudness calculations for sonic booms do not include the potentially important phenomena of startle to the outdoor observer and building vibration and rattle sounds that are experienced in an indoor listening environment. The outdoor observer not only experiences the audible aspects of the disturbance, but can also be startled. For example, during a thunderstorm when one observes lightning it is expected that thunder will follow. Despite this, thunder may still be startling. Sonic booms are, on occasion, said to sound like distant thunder. As shown in figure 8.32, the pressure signature of thunder is significantly different than that of an N-wave sonic boom signature. Ribner and Roy (ref. 8.45) modeled the lightning strike as a tortuous line emitting N-shaped pressure waves from points all along its length as illustrated in figure 8.32. Although emitted simultaneously, they arrive sequentially according to distance: the received pressure signature is essentially a convolution of an N-wave with a channel-shape function. Thus, the thunder spectrum approximates an N-wave spectrum modulated by another due to channel tortuosity.

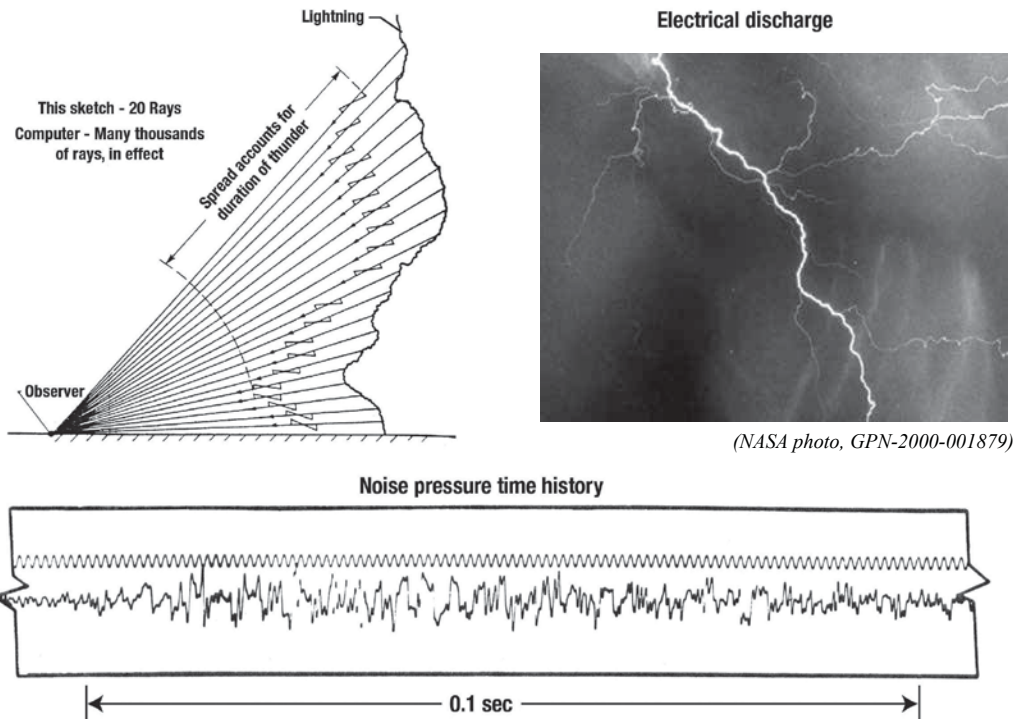


Figure 8.32. Measured pressure time history of thunder (adapted from ref. 8.45).

Another example of experiencing startle is associated with firework displays. Although observers are aware of, and are expecting, a loud burst following some aerial displays, they are still startled when the impulse noise reaches them. It is of interest to note that the overpressure levels associated with some of these aerial bursts are as high as 15 lbs/ft², as shown in figure 8.33 (ref. 8.46).

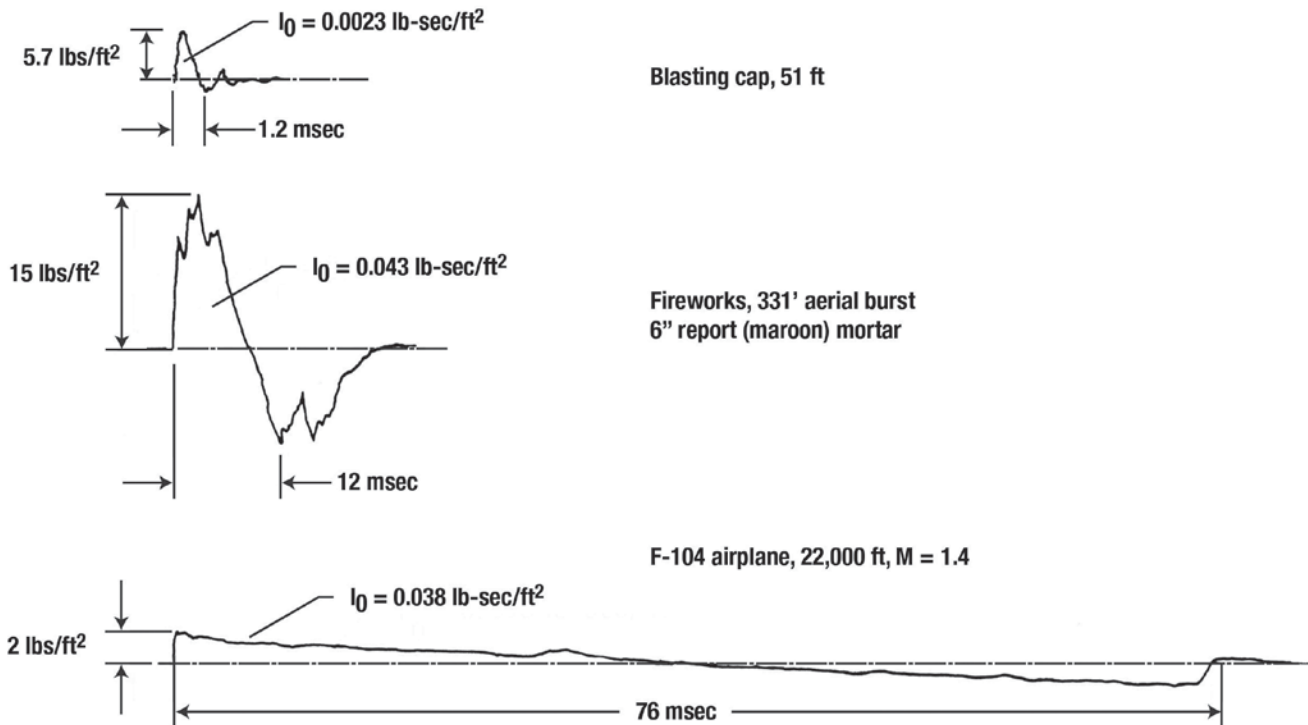


Figure 8.33. Waveform characteristics of three different impulsive noises (ref. 8.46).

In flight tests involving sonic boom measurements it has been found that even though the boom arrival times at the measurement locations were estimated to within ± 1 sec, the outdoor observer still experienced some startle when hearing the boom. Thus, a startle factor is inherent in the loudness and annoyance studies involving impulsive type disturbances.

Figure 8.34 (ref. 8.4) shows a summary of the types of interference including house shaking, being startled, sleep disturbance, interference with conversation, and interference with radio/television listening noted by respondents queried during the tests of community reaction to sonic booms conducted during the SST program in the 1960s (refs. 8.36 and 8.47). As indicated, house shaking was the most frequently cited type of interference from these exposure tests, with the startle factor close behind. The peak sonic boom pressures involved were in the range of 1.2 lbs/ft² for the Oklahoma City tests (ref. 8.47) and less than 3.1 lbs/ft² for the St. Louis (ref. 8.48) tests. Obviously, reducing overpressure would reduce the percentage of those annoyed by these various factors, especially the startle, rattle, vibration, and damage concerns.

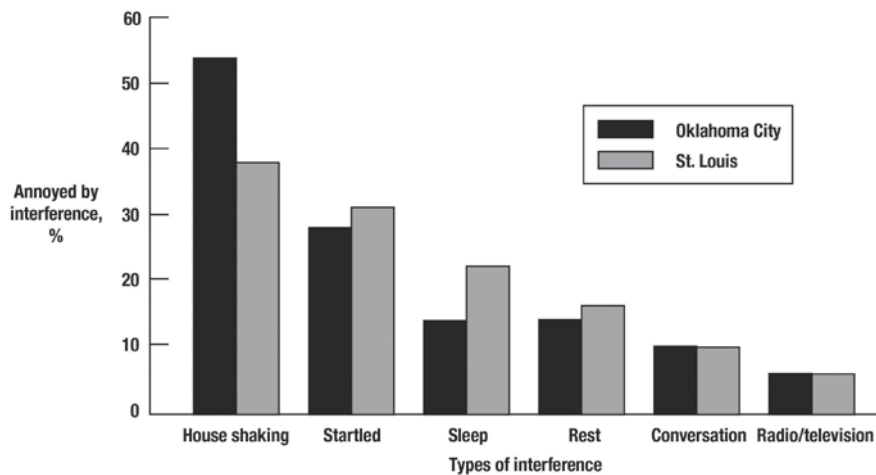


Figure 8.34. Types of interference from sonic boom community response tests (ref. 8.4).

Rattle

Schomer (ref. 8.49) states that one cannot overestimate the role that noise-induced rattle plays in sonic boom and blast noise annoyance. Figure 8.35 (ref. 8.49) shows the number of respondents annoyed by interference caused by artillery and street traffic noise to their normal daily experiences. These include sleep, rest/relaxation, care/concentration, radio/television, conversation, outdoors, rattles, startle, fright, and disturbing others in house.

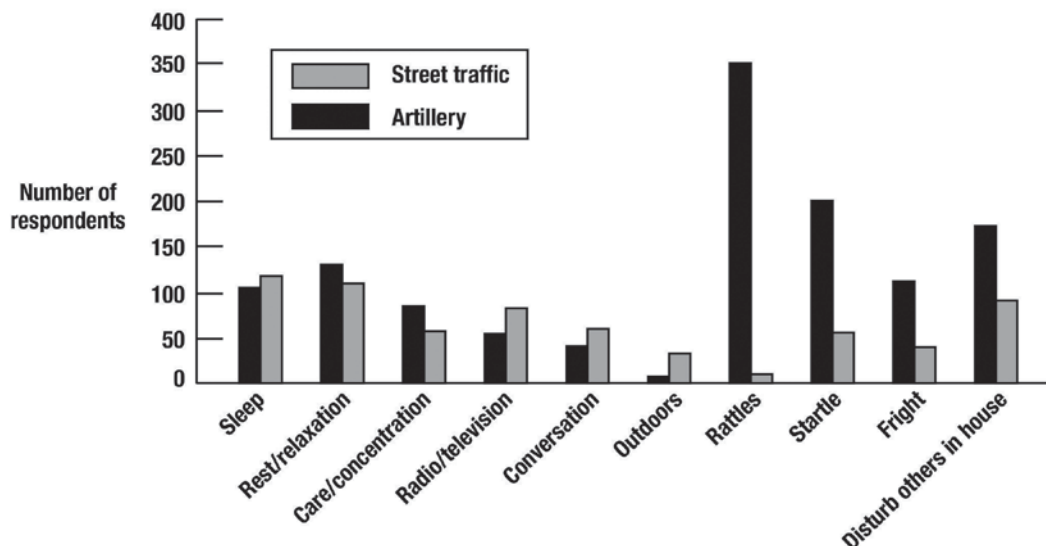


Figure 8.35. Number of respondents indicating annoyance to the factor indicated (ref. 8.49).

As can be seen, the prevalence of high annoyance to rattles was twice the rate of annoyance to startle, the second highest factor. Schomer also states that in contrast, speech interference and interference with listening to radio and television, two factors that depend on loudness, were 1/7th to 1/10th as important.

Sleep Interference

Von Gierke and Nixon (ref. 8.36) stated that sleep interference from nighttime booms could be a major determinant to public acceptance. They cite the laboratory 1968 and 1970 works of Lukas and Kryter (refs. 8.50 and 8.51) who examined the effects of simulated booms on sleep for boom levels of from 0.63 lb/ft² to 2.5 lbs/ft² and included age groups from 7 to 72 years of age. As stated by von Gierke and Nixon, all sonic booms in these laboratory studies were adequate stimuli for awakening subjects during their rapid eye movement (REM) state of sleep. REM is a normal stage of sleep that is characterized by the rapid movement of the eyes and occupies 20 to 25 percent of an adult's total sleep or some 100 minutes of a night's sleep. The study showed that 70 year old subjects were more likely to be awakened than younger subjects. They also noted that long-term effects on sleep of repeated nightly exposure to sonic booms are not known.

Two items of note should be mentioned at this point in the discussion. Although sleep interference is normally associated with nighttime sonic booms, there are those that work during nighttime hours and sleep during the day who would also be influenced by sonic booms. Second, no significant distinction is made regarding sleep interference in any of the major sonic boom community overflight programs of the past, some of which involved night time booms. For example, during the 1961-62 St. Louis overflights (ref. 8.12) in which interviews were conducted concerning 76 flights performed over a 7-month period, 45 of the total occurred between 9 P.M. and 4 A.M. The Oklahoma City overflight program (ref. 8.52), which ran from February 1964 through July 1964, involved no nighttime booms. All 1225 supersonic flights occurred between about 7 A.M. and 4 P.M. U.S. Air Force training flights over the Chicago area (ref. 8.53) during January-March 1965 involved a total of 49 supersonic runs, 22 of which boom measurements were obtained. Of these 22 flights, all occurred between about 12:30 P.M. and 3:45 P.M. Only damage complaints were reported. The two-phase National Sonic Boom Program at EAFB (ref. 8.26) that ran from June 1966 to November 1967 consisted of a total of 569 flights, all of which took place between 7 A.M. and 5 P.M. To summarize, there has been essentially no field tests with nighttime booms, with the exception of the 1961-62 St. Louis overflights, and thus there is little information available.

Acceptability

It has been shown that loudness and annoyance play an important role in establishing sonic boom acceptance. However, as pointed out by Von Gierke and Nixon (ref. 8.36), the acceptability of sonic booms must also include physiological, psychological, and sociological responses to regular commercial supersonic flights overland. They also state that based on the integrated results of past sonic boom overflight programs in the United States, United Kingdom, and France, a level of acceptable sonic boom exposure in the community has not been established, although some estimates of acceptable boom levels are in the range 0.1 to 0.75 lb/ft². Further, they point out that the wide variation in stimuli, immediate environs, and response behavior due to socio-psychological factors suggest that the concept of a range of acceptable levels is perhaps more appropriate than a single-value guideline. As such, a brief review of the past community overflight findings is in order.

A community survey was conducted at Edwards AFB in the 1966-1967 time period (ref. 8.26) that compared the attitudes of 793 persons toward sonic boom exposures prior to and during a special test period of boom activity that was increased over typical boom activity usually experienced by the residents. Prior to the test, the exposure was 4 to 8 booms per day at a mean overpressure level of 1.2 lbs/ft². During the tests (a 1-month period) 289 booms were generated at a mean peak overpressure level of 1.7 lbs/ft².

An additional finding from the study indicated that more than 50 percent of the respondents had experienced the 4 to 8 boom exposure schedule for over a year. Some adaptation to sonic boom exposure was suggested when one is exposed regularly on a daily basis to sonic booms, since 60 percent found the boom more acceptable after being regularly exposed to it before the tests. Ten booms per day at an overpressure level of 1.7 lbs/ft² was unacceptable for these respondents, as it was for the Oklahoma City residents (ref. 8.47).

Another survey of community reaction to sonic boom was conducted over six major metropolitan areas in the United States (Atlanta, Dallas, Denver, Chicago, Minneapolis, and Los Angeles) in relation to routine Air Force training flights in supersonic SR-71 aircraft (ref. 8.54). The boom exposures from the SR-71 overflights varied from an average number of one to three booms every 3 days at mean peak overpressures ranging from less than 1 lb/ft² to 2 lbs/ft². About 5000 pre-exposure, 500 during exposure, and 100 post-exposure personal interviews were completed. The post exposure interviews were taken from 4 to 5 months after the sonic booms had ceased. Although the different methodology limits comparisons, several findings are consistent with those of previous community studies. For example, respondents had a negative attitude towards sonic booms and the attitude increases rapidly in strength with increasing number of booms per day. Booms were ranked at the top of the most unwanted list of sounds. Ninety percent of complainants owned their own homes and felt that the booms damaged their homes.

The NASA HSR Program (ref. 8.55) required a revisiting and reassessment of previous sonic boom community overflight results in an attempt to establish the feasibility of overland supersonic flight. In order to update the database, a study was funded to examine the response of communities in a vicinity of Nellis AFB, Nevada (1992-93 time period) and Edwards AFB, California (1995 time period) to sonic booms associated with normal training/testing operations (ref. 8.56). A summary of these along with other findings is given in figure 8.36 (ref. 8.57).

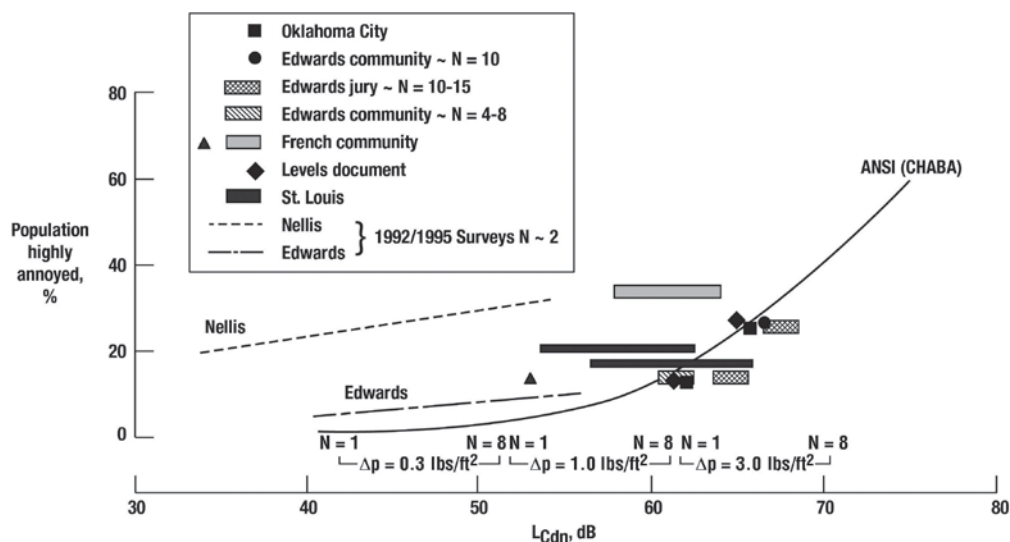


Figure 8.36. Predicted annoyance from supersonic flyovers compared to community observations. N = number of booms/day (adapted from ref. 8.57).

The percentage of the population highly annoyed by N-wave type sonic booms of various levels calculated using two metrics, the overpressure in lbs/ft² together with number of booms per day and the day-night average C-weighted sound level, is plotted in figure 8.36. C-weighting was selected by the Committee on Hearing, Bioacoustics, and Biomechanics (CHABA) (ref. 8.58) under the constraints that included common availability on standard sound level meters. LCdn is a cumulative aggregation based on the equal energy hypothesis, accounting for the number of events as well as their level. Also plotted in figure 8.36 is the CHABA curve (ref. 8.58), subsequently adopted by the American National Standards Institute (ANSI) (ref. 8.59) that provides an assessment of high-energy impulsive sounds with respect to residential communities. Examination of the data plotted in figure 8.36 shows that the early US-SST cruise boom level design target of 1.5 lbs/ft² is predicted to result in 10 to 30 percent of the population being highly annoyed by 1 to 8 booms/day, respectively. However, at boom levels of 0.3 lb/ft² to 0.5 lb/ft², the annoyance numbers are reduced to about 1 to 5 percent for the 1 to 8 booms/day.

The impulsive sounds addressed by CHABA include explosions, quarry blasts, artillery and gunfire, as well as N-wave sonic booms. The C-weighting metric selected is quite insensitive to rise time and mostly controlled by the magnitude of the overpressure and signature duration. As a result, it does not account for difference between the various types of impulsive sounds. For sonic booms, it does not recognize the reduced loudness of a shaped signature of the same overpressure and period but with a larger shock rise time. Studies using sonic boom simulators have shown that Perceived Level (also referred to as PLdB) is a better metric for assessing the loudness of N-wave and shaped signature booms observed outdoors and possibly indoors also (see table 8.2 and ref. 8.38). An illustration of the CSEL and PLdB sensitivity to rise time and signature shape is presented in figure 8.37.

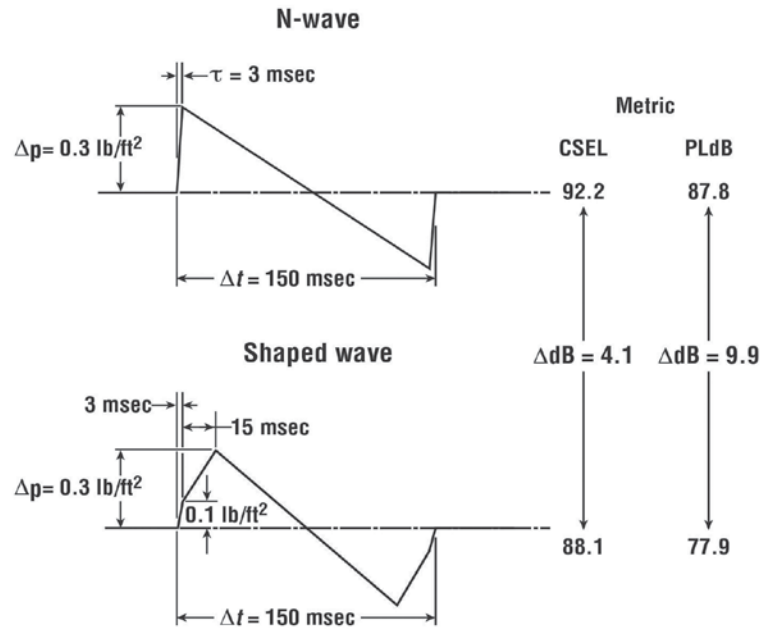


Figure 8.37. Comparison of the CSEL and PLdB loudness noise metrics for an N-wave and shaped wave boom signature.

Figure 8.37 shows two notional cruise boom signatures having the same overpressure (0.3 lb/ft^2) and period (150 msec). The top signature is an N-wave having a shock rise time of 3 msec. The bottom signature is a delayed ramp-type shaped signature having an initial shock rise time of 3 msec from 0 to 0.1 lb/ft^2 followed by a 15 msec rise time to the maximum overpressure of 0.3 lb/ft^2 . To the right of each signature are the calculated CSEL and PLdB. The CSEL metric indicates that the shaped signature (88.1 dB) is 4.1 dB lower in loudness level than the N-wave (92.2 dB). On the other hand, the PLdB metric shows the shaped wave (77.9 dB) is 9.9 dB quieter in loudness as compared to the N-wave (87.8 dB). It is obvious that the CSEL metric does not reflect the reduced loudness of shaped signatures having increased shock rise times. Thus, a shaped signature would always be more acceptable than an N-wave signature represented in figure 8.36 with the same overpressure and duration.

The Nellis and Edwards study (ref. 8.56) was a combined social survey and noise measurement program involving 14 communities that have been regularly exposed to sonic booms for many years. A total of 1573 interviews of community residents were completed. The least exposed communities averaged one measurable boom in 20 days and had less than one boom that was over 2.0 lbs/ft^2 in 100 days. The most exposed communities averaged 2 booms per day with about 1 boom per week over 2.0 lbs/ft^2 . The average number of booms per day of all overpressures for Nellis and Edwards was about 0.6 at a arithmetic mean overpressure of about 0.7 lb/ft^2 . Examination of the figure 8.36 shows that the reactions in the Edwards region, where supersonic flight operations are controlled and primarily of a research nature, are consistent with previous results, and fall on the ANSI/CHABA curve. On the other hand, the Nellis results indicate more severe reactions and fall well above the ANSI/CHABA curve. The author of the study stated that several potential explanations were explored, but none were able to satisfactorily explain the difference in reaction between the two communities.

These Nellis and Edwards sonic boom surveys (ref. 8.56) found that there were three aspects of sonic booms that were most disturbing, namely, being startled, noticing rattles and vibrations, and fearing the possibility of structural damage. This finding is consistent with previous community overflight findings (as will be shown on the next figure). Respondents report that the vibrations are not restricted to hearing rattles but also include noticing houses shake. A little over half of the startled respondents report that their startle reactions have not lessened from the time when they first heard the booms. More people fear the possibility of damage than believe that booms have thus far damaged their property.

Figure 8.36 is one interpretation of the available data relating residents' annoyance to their boom exposure. Another viewpoint on this question is provided by the data presented in figure 8.38 (refs. 8.57 and 8.60).

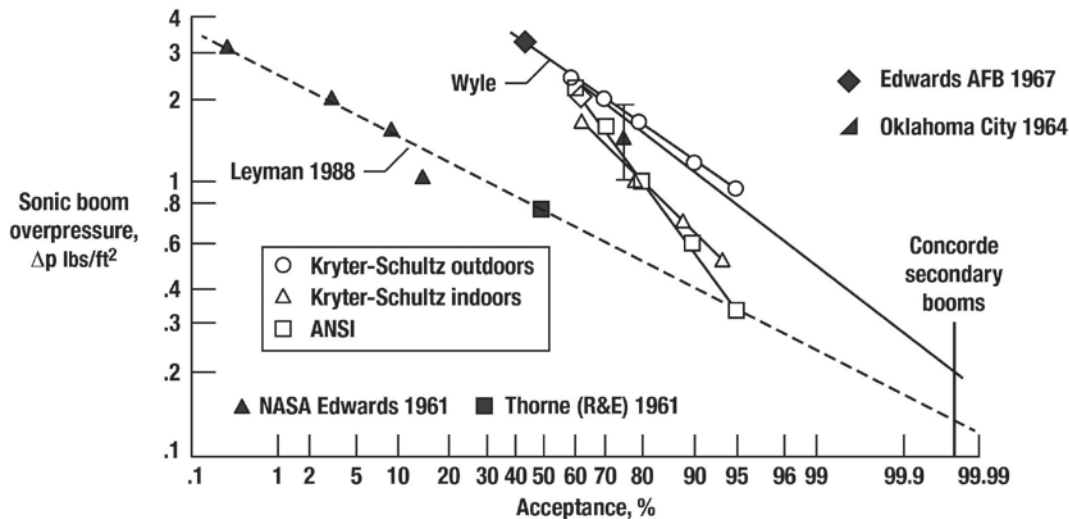


Figure 8.38. Predicted sonic boom acceptance (refs. 8.57 and 8.60).

Percentage acceptance on a probability scale is shown for a range of sonic boom overpressure levels. The straight lines marked Leyman and Wyle are two interpretations of the available data with particular emphasis on the 1966-67 Edwards results. Based on the assumption that percentage acceptance is equivalent to the inverse of highly annoyed, the lines marked Kryter-Schultz outdoors, Kryter-Schultz indoors, and ANSI are included for comparison.

The Kryter-Schultz outdoor line, which represents 16 booms per day exposure, is nearly coincident with the Wyle line. On the other hand, the ANSI and Kryter-Schultz indoor lines are in close agreement. Both data sets have markedly different slopes such that for sonic boom exposures less than 2.0 lbs/ft², the ANSI and Kryter-Schultz indoor lines would predict a lower rate of acceptance than do the Wyle and Kryter-Schultz outdoor lines. The Wyle interpretation (ref. 8.60) suggests that sonic booms with a peak pressure on the order of 0.8 lb/ft² would be expected to be acceptable about 95 percent of the time. The Wyle report further noted that it remains to be shown if shaped sonic booms would be expected to follow the same trend.

A final caution is in order before leaving this figure. The results of the 1992-93 Nellis and 1995 Edwards 6-month surveys, shown previously, are not included on this figure. Although the Edwards results would be close to the ANSI curve, the Nellis results would not be consistent with any of the curves, since annoyance was found to be far higher than in other studies.

Effects on Human Health

In an effort to determine if sonic boom exposure posed a threat to human health, the U.S. Air Force funded a study in the mid 1980s to examine long-term exposure to sonic booms and health data. The findings are presented in references 8.61 and 8.62. This study took place in the state of Nevada, since military supersonic operations have been carried out within its boundaries over a longer time than in any other area within the United States. Volume I

(ref. 8.61) presents the estimates of the sonic boom environment from 1969 to 1983. Although sonic booms were encountered as far back as 1955, the 1969 starting date was consistent with practical start dates for medical record acquisition. The subjects of this study were the residents of Nevada. Volume II (ref. 8.62) presents the results of the epidemiological study, which, as stated by the authors, “was built entirely on a state-wide epidemiologic evaluation of mortality for Nevada residents from 1968 to 1983, supplemented by hospital discharge morbidity data.” The study results indicated that no evidence was found to prove the existence of adverse health effects due to exposure to sonic booms.

Animal Responses

The proposed introduction of commercial supersonic transport travel in the early 1960s focused attention on the possible effects of sonic booms on animals. Earlier sonic boom damage claims associated with USAF training flights reflected that a small percentage of these involved animals. Concerns included possible changes in egg production from hatcheries, milk production of dairy herds, animal and bird reproduction, and stampeding and trampling. During the 1966 National Sonic Boom Program, conducted at EAFB, Casady and Lehman (ref. 8.63) conducted some preliminary investigations of the effects of booms on farm animal behavior for the purpose of deciding which common domestic and commercial animal species should be studied in greater detail at a later time.

Ten animal installations were selected and included a race horse breeding farm, two beef feeder lots, two turkey ranches, two chicken ranches, one sheep ranch, one commercial dairy, and one pheasant farm. The animal population of these installations was about 100 horses, 10,000 beef cattle, 125,000 turkeys, 35,000 chickens, 150 sheep, 320 dairy cattle, and 50,000 pheasants. About 104 booms over 3 weeks were experienced during morning hours Monday through Friday over a 3-week period. It was found that except for the avian species, the behavioral reactions to the sonic booms were considered minimal. In the case of the avian species, the most visible reactions occurred as a result of low-level subsonic flights, where noise was the disturbing factor.

One of the most commonly quoted evidences that sonic booms harm wildlife resulted from the 1969 study by Austin, Robertson, and Woolfender (ref. 8.64). Even though their evidence was admittedly circumstantial, they concluded that sonic booms had caused mass hatching failure of Sooty Terns on the Dry Tortugas, Florida. To explain the cause of failure, Austin, Robertson, and Woolfender considered and rejected many possible explanations, including predators, food shortages, pesticides, humans walking on the rookery, and abnormal weather conditions. An unusual growth of underbrush might also have been a contributing factor. They also discovered that although sonic booms were a common occurrence on the Dry Tortugas at the time, unusually intense booms were heard during the May nesting time period by the residents of the nearby National Park Service Station who stated that they were intense enough to shatter windows. As noted in the 1991 paper by Bowles, Aubrey, and Jehl (ref. 8.65), this hatching failure of the Sooty Terns was particularly startling since the Brown Noddies, nesting in the bushes in the same area fledged normal numbers.

In response to the findings above, the United States Air Force funded Bowles, Aubrey, and Jehl (ref. 8.65) to conduct a series of experiments to determine whether it was possible for very intense booms to crack eggs or damage embryos. They were also to review the literature on eggshell strength and resistance to accelerative damage. Since extremely low altitude flight required to produce the intense sonic booms would not be practical over the Dry Tortugas, the blasts were from small explosive pest-control devices to produce the test impulses. Although the overpressure levels associated with these test impulses (over 170 dB re: 20mPa) equalled and exceeded the 120 lbs/ft² sonic boom level from an aircraft flying at Mach 1.2 and an altitude of 90 feet, they differed from aircraft generated booms in several ways: the pressure time history was not N-wave in shape, the signature duration and shock rise times were shorter and the resulting noise spectrum is shifted to a much higher frequency range than that of an actual boom signature.

Test results showed that none of the infertile eggs developed cracks of any kind and several deliberately cracked eggs did not show sign of further damage. All remaining eggs hatched and there was no significant difference between controlled and exposed eggs hatchability, date, or weight.

In 1994, Bowles, Knobler, and Seddon (ref. 8.66) conducted another series of experiments to determine whether very high amplitude simulated sonic booms of long duration (period) could affect development of eggs and to measure egg resonance frequencies. Chicken eggs were used and are somewhat larger than Sooty Tern eggs. As a result, they were expected to have a greater tendency to resonate when exposed to sonic booms than Sooty Tern eggs. Use was made of the Bolt, Beranek, and Newman (BBN) Sonic Boom Test Facility that generated N-waves, via large speakers, of up to 30 lbs/ft² and duration of 100 msec, which closely simulates the sonic booms from an F-4E aircraft flying at $M = 1.1$ and altitudes of from 800 to 17,000 feet above the ground. Their findings did not provide any evidence of physical damage to egg shells such as cracking, or excessive embryonic deaths as a result of exposure to intense simulated sonic booms.

The 2002 study by Ting, Garrelick, and Bowles (ref. 8.67) was the first analytical study conducted to support the empirical work of Bowles, Knobler, and Seddon (ref. 8.66) by providing a mathematical analysis of avian eggs to sonic booms. Their study focused on chicken eggs since published data indicated that the structure and dimensions for eggs of a variety of bird species, including the Sooty Tern, are similar. The sonic boom was represented by an N-wave of 0.15 sec duration and two flight Mach numbers were chosen, Mach 1.2, the case most closely simulating an actual fighter aircraft flight, and the worst case of where the shock front would be parallel to the long axis of the egg resulting from an aircraft flying at an infinite Mach number. Peak eggshell stress and peak embryo acceleration were chosen as primary damage metrics. The authors also proposed a third criterion, the maximum allowable concentrated radial force that may be applied to the egg. The results of their analytical study indicated that no damage was predicted with any of the response metrics until sonic boom overpressures reached 250 lbs/ft² assuming flights at infinite Mach number. The maximum peak overpressure thus far recorded for an F-4E flight at $M = 1.2$ and 95 feet above ground level was 144 lbs/ft². Their calculations of the boom level required for damage to eggs assuming flight at $M = 1.2$ was 460 lbs/ft²; some 100 times greater than the sonic boom that would be associated with commercial supersonic operations. They thus conclude that even under the most extraordinary circumstances, sonic booms from practical aircraft maneuvers do not pose a threat to avian eggs.

It is curious that the Air Force devoted that much effort to assessing whether booms could crack eggs, since Austin et. al no evidence of physical damage but speculated more booms causing nest A controlled study on the effects of real and simulated sonic booms on farm-raised mink was conducted by Travis et al. in 1970 with funding from the FAA (ref. 8.68). These tests took place at three sites in Alaska. The conclusion drawn from these studies is that exposure of farm-raised mink to intense booms during whelping season had no adverse effect on their reproduction or behavior.

A comprehensive review of reports and studies of animal response to sonic booms was provided by Bell (ref. 8.69) in which he addresses USAF data relative to the reactions of domestic animals, mink, wild animals, and birds. He stated that, to date, it is difficult to make detailed interpretations of the effects of sonic booms on different animal species. Further, if aircraft are to continue flying supersonically over either populated or wilderness areas, further studies of the effect on animals should be conducted. He also stated that it may be necessary to utilize telemetry-type instrumentation to discern the impact of sonic booms on wildlife in its native habitat. In 1975, Lynch and Speake (ref. 8.70) conducted such a study involving 20 wild turkey hens equipped with transmitters and subjected them to both real and simulated booms. Their results indicated that sonic booms do not initiate any abnormal behavior in wild turkeys that would result in decreased productivity.

A more recent literature search of information pertaining to animal hearing and the effects of aircraft noise and sonic boom on domestic animals and wildlife can be found in reference 8.71. This effort, conducted by Mancini et al. of the National Ecology Research Center was a joint effort of the U. S. Air Force/U.S. Fish and Wildlife Service. Of the 60 species addressed, about one third were exposed to impulsive type noise (real and simulated booms, recorded thunderclaps, blasting, cannon fire, and exploding paper bags). Two hundred references were provided.

Other Responses

Seismic

During the U.S. SST activities of the 1960s and 1970s, there was a concern that sonic booms produced by aircraft moving at supersonic speeds would apply moving loads to the Earth's surface. Such a concern was expressed, even though it was known that the majority of the energy of the N-wave would be reflected due to the much higher sound speed (about 6500 ft/sec) in the ground, resulting in ground motions that might cause damage to residential structures, trigger earthquakes, and precipitate incipient avalanches or landslides in areas that are stressed to within a few percent of instability.

An extensive experimental database was established by Cook, Goforth, and Cook (ref. 8.72) and Goforth and McDonald (ref. 8.73) as part of the U.S. National Sonic Boom Program at EAFB, California (ref. 8.26), and involved 178 steady-level supersonic overflights for four aircraft: the F-104, B-58, SR-71, and XB-70. Five velocity-sensing seismographs were used and buried 1 m deep in the clay of a small dry lake bed and also on a nearby outcrop of quartz monzonite basement rock. Eight supersonic flights of the B-58 were also conducted over the Tonto Forest Seismological Observatory (TFSO) in Arizona, where a seismometer array, 9 km wide, was used to study the energy distribution outside and inside the sonic boom ground footprint and possibly focusing effects along the ground track of the aircraft. Three B-58 supersonic flights were flown over the Uinta Basin Seismological Observatory (UBSO) in Utah where seismometers were available at depths to 8000 feet to study attenuation with depth. These latter two locations afforded geology different than that at EAFB. The nature of the measured seismic signals associated with the B-58 sonic boom signatures measured at the ground for locations at EAFB, TFSO, and UBSO are presented in figure 8.39 (ref. 8.72).

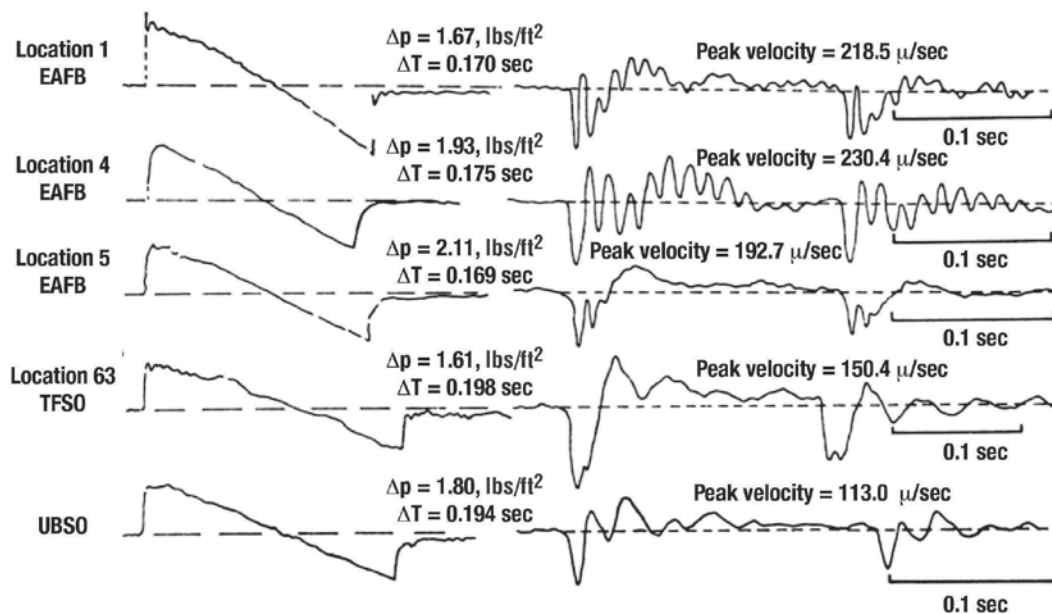


Figure 8.39. Variation of seismograms with variation of geological properties (ref. 8.72).

It can be seen that similar sonic boom N-waves resulted in very different seismic waveforms at each of the five locations. This effect, as stated in reference 8.72, is primarily due to the variation of the elastic parameters of the earth. Particle velocities vary from 113 μ /sec to slightly over 230 μ /sec. It was also observed that there was a rapid vertical attenuation at the USBO site, the maximum particle velocity at 13.4 m was only 1.3 percent of that near the surface. In all cases, the greatest particle velocities occurred in the two sharp downward peaks, which coincided with the bow and tail shock of the sonic boom N-wave. Regardless of aircraft type, the maximum particle velocity was roughly proportional to the boom overpressure, as shown in figure 8.40 (ref. 8.72) for XB-70 overflights.

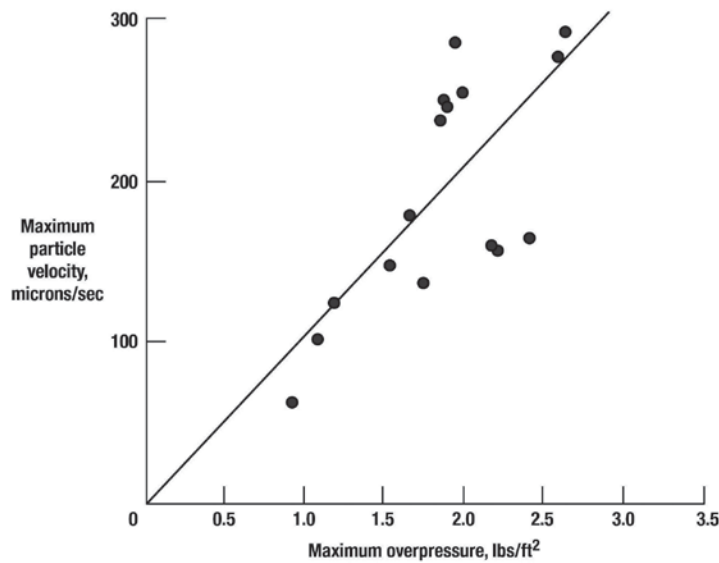


Figure 8.40. Variation of sonic boom level to peak earth particle vertical velocity, Clay Lake Bed (ref. 8.72).

The largest particle velocity measured during these tests was 340 μ /sec at a boom level of 2.5 lbs/ft², which amounts to less than 1 percent of the seismic damage threshold for residences established by the Bureau of Mines (ref. 8.74), which is 2.0 in/sec or 50,800 μ /sec.

During these measurements, forerunner waves were always seen at high gain settings. According to the authors, these waves had frequencies of the order of 2 Hz and amplitudes of 5 to 10 μ /sec and began as much as 7 seconds before the arrival of the sonic boom. Higgins (ref. 8.75) observed, during sonic boom tests, the continuous songs of birds in the field were completely silenced 4 to 8 seconds prior to the arrival of the audible boom.

As noted in reference 8.72, present quantitative theories for the major seismic effects agree reasonably well with the experiments. Underground effects of a sonic boom from aircraft are essentially confined to the top few meters of the ground and decrease rapidly with depth. Thus, the triggering of earthquakes by sonic booms is considered quite unlikely because earthquake foci are located at depths of at least 1 km. For aircraft traveling at hypersonic speeds above Mach 6.5 (i.e., faster than the speed of sound in the ground, 6500 ft/sec), this conclusion may no longer hold in that the shocks would no longer be confined to the top few meters of the ground and would propagate to greater depths.

Little experimental data exists regarding the effects of sonic booms in areas prone to avalanches and landslides. In March 1965, a sonic boom study was conducted near Leadville, Colorado to determine the effects of sonic boom overpressures on snow avalanches (ref. 8.76). Some 18 supersonic overflights producing measured overpressures of from 1.15 lbs/ft² to 5.02 lbs/ft² were generated and resulted in no avalanche activity. On one of the supersonic overflights, no measured overpressure was recorded but predictions based on the aircraft altitude and Mach number placed the overpressure at 10.35 lbs/ft². Forest Service personnel rated the avalanche hazard as low during the test period, resulting in the recommendation that further testing be conducted during periods of high avalanche hazard.

It is of interest to note that, in recent years, large existing seismograph networks have been used by Kanamori et al. (ref. 8.77) and Qamar (ref. 8.78) to detect sonic booms from aircraft and meteors. The seismic network in Southern California routinely detected booms from aircraft, such as the SR-71 and spacecraft such as the Shuttle Orbiter, and provide a unique opportunity to study the long-range propagation of primary and secondary sonic booms, as was done by Cates and Sturdevant (ref. 8.79). In addition to providing information on the vehicle ground speed, the array also provides information on the ground pressure patterns and vehicle altitude.

An interesting comparative study was made by Goforth and Rasmussen (ref. 8.80) of the frequency of occurrence,

severity, and spectral content of ground motions resulting from earthquakes and other natural and man-made sources with the motions generated by sonic booms. The data were recorded at the two seismic stations in Arizona and Utah and covered a period from 1963 through 1968. Of the 180,000 earthquake arrivals, some produced ground velocities of some 50 micron/sec. Quarry blast construction sites, oil well drilling and heavy river runoffs produced ground velocities less than about 10 microns/sec. No seismic signatures were observed due to thunder; possibly due to instrumentation response. Nuclear blasts from the Nevada test site produce peak ground velocities in excess of 50 microns/sec.

Marine Life

As was the case for booms impacting the earth, because of the large mismatch of the speed of sound in air (1116.4 ft/sec) and water (4800 ft/sec), the effect of sonic booms from vehicles in level flight at supersonic speeds over lakes and oceans was expected to be minimal since about 99 percent of the impinging energy would be reflected. Even so, there was a concern that certain sea life, especially marine mammals that spend most of their time in the first few hundred meters of the ocean, would be impacted by the sonic booms from commercial supersonic operations over water. A substantial database regarding this topic assuming a flat ocean surface was developed during the U.S. National Sonic Boom Program of the mid-1960s by Cook, Goforth, and Cook, and reported on in reference 8.72. Sawyers (ref. 8.81) and Cook (ref. 8.82) provided an analytical theory that was experimentally verified by Waters and Glass (ref. 8.83). Since then, substantial progress has been made regarding the penetration of sonic booms into the ocean to include realistic ocean surface, in homogeneous and arbitrary shaped waveforms, and a brief overview of these developments has been made by Sparrow (ref. 8.84).

The nature of the underwater sonic boom situation can be illustrated with the aid of figure 8.41 (ref. 8.84), which shows the predicted underwater waveforms at depths of 4, 16, and 64 meters from an F-15 sonic boom signature of about 1.7 lbs/ft² measured at the surface.

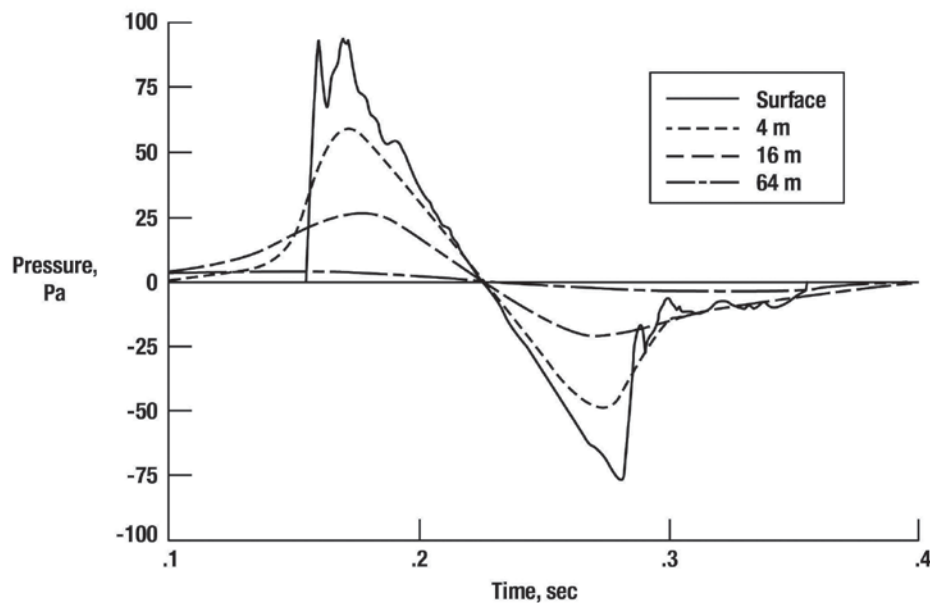


Figure 8.41. Underwater predicted waveforms from sonic booms (ref. 8.84).

Examination of the results of figure 8.40 show that sonic booms do not penetrate very far beneath the ocean's surface and the waveforms become increasingly rounded as depth increases. Also, as noted by Sparrow (ref. 8.84), the influence of focusing due to wind waves on the ocean and the effect of bubble plumes never increased or decreased the sound levels by more than 1.5 dB over those seen in a homogeneous flat ocean.

More recently, Sohn et al. (ref. 8.85) have performed careful field measurements of the sonic booms from an F-4 aircraft penetrating into the ocean at depths to 67 meters. Some measured and theoretically predicted pressure

time histories are given in figure 8.42 (ref. 8.85) for flight altitudes of 2000 feet and 20,000 feet above the water surface for Mach numbers of 1.07 and 1.26, respectively, show excellent agreement. For both flights it can be seen that the sonic booms do not penetrate to a significant depth, 7 meters in the cases shown, before becoming increasingly rounded, evanescent in character, as depth increases.

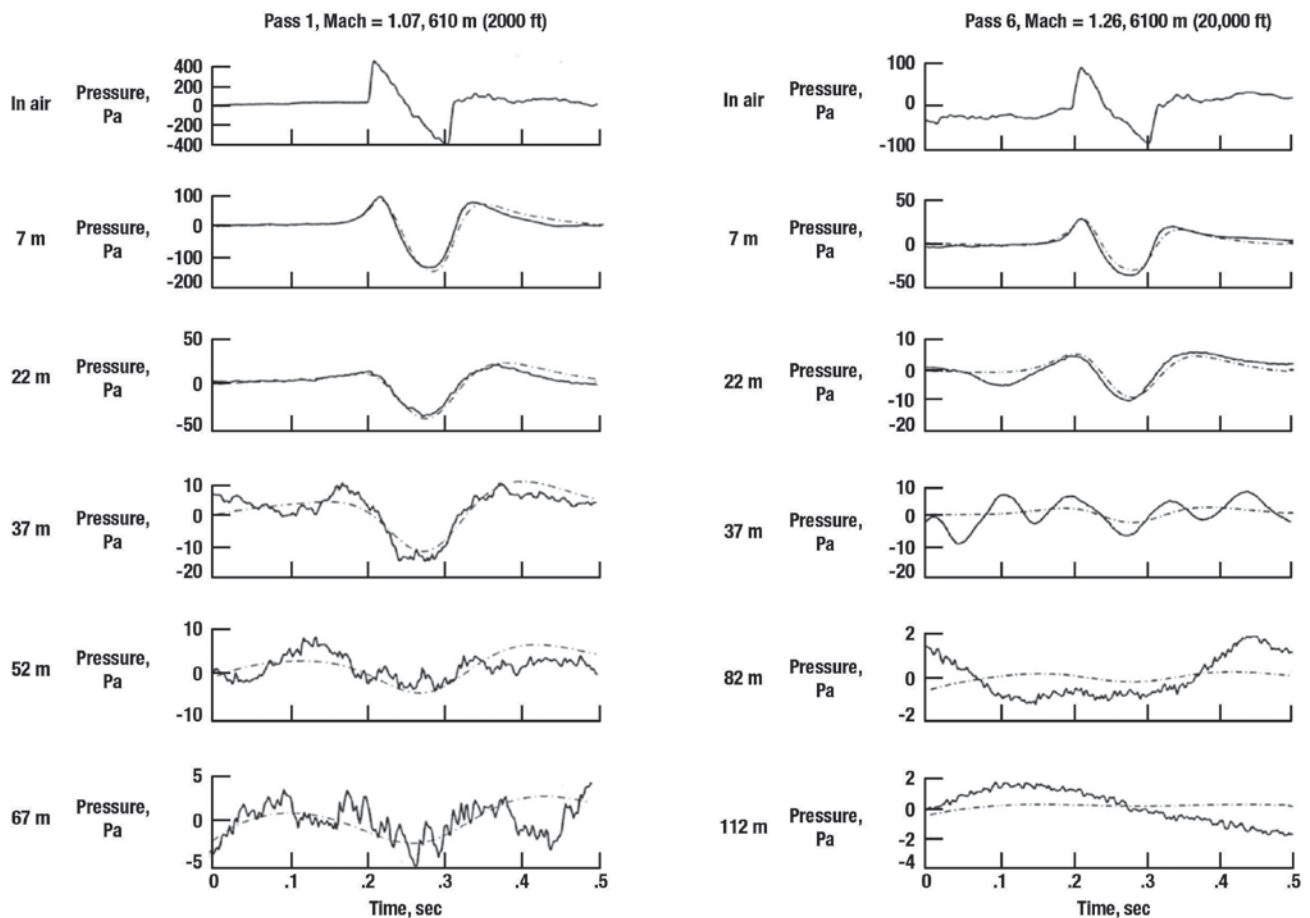


Figure 8.42. Comparison of measured (solid line) and predicted (dashed line) pressure time histories of sonic boom penetration from two flights into water of depths of 7m, 22m, 37m, 52m, and 67m (adapted from ref. 8.85).

Recently, an interesting study was conducted by Wang et al. (ref. 8.86) on the influence of extremely high sonic boom levels generated by low altitude flight of a supersonic cruise missile over the ocean surface. Overpressures of over 400 lbs/ft² were estimated at the ocean surface, about 50 times greater than was found in traditional studies. At a depth of 100 feet, they calculate that the maximum overpressure had fallen to about 1.44 lbs/ft², which is typical of the ocean surface conditions of traditionally high altitude studies.

It is worth noting that sonic booms will penetrate into water only when the boom shock wave angle, with respect to the water surface, is less than about 13.2° from the vertical, or faster than Mach 4.4 for a vehicle in level flight. The Intrieri and Malcolm experiments (ref. 8.87) were measured on an acoustic shock wave propagating into the water from projectile speeds above Mach 4.4. Sparrow also noted that an aircraft flying over the ocean at Mach 1.2 and diving at an angle steeper than 43.2° from level flight would produce a propagating wave into the ocean since the aircraft bow shock wave angle with respect to the water surface would be less than 13.2°.

Cook, Goforth, and Cook (ref. 8.72) compared the underwater pressure spectrum of a typical sonic boom signature overpressure of 2.5 lbs/ft² and a period of 100 msec from a Mach 1.5 flight with those of normal ambient noises, in sea stage 3 (moderate waves) and heavy ship traffic. Figure 8.43, taken from reference 8.72, is typical of the results in which the authors state that sonic boom pressures can be expected to momentarily exceed the ambient noise levels by up to 50 dB from the surface to depths of a few hundred feet between frequencies of 0.5 Hz to a

few hundred Hz. As such, sea life will be subjected to detectable amounts of momentary overpressures from the passage of the boom.

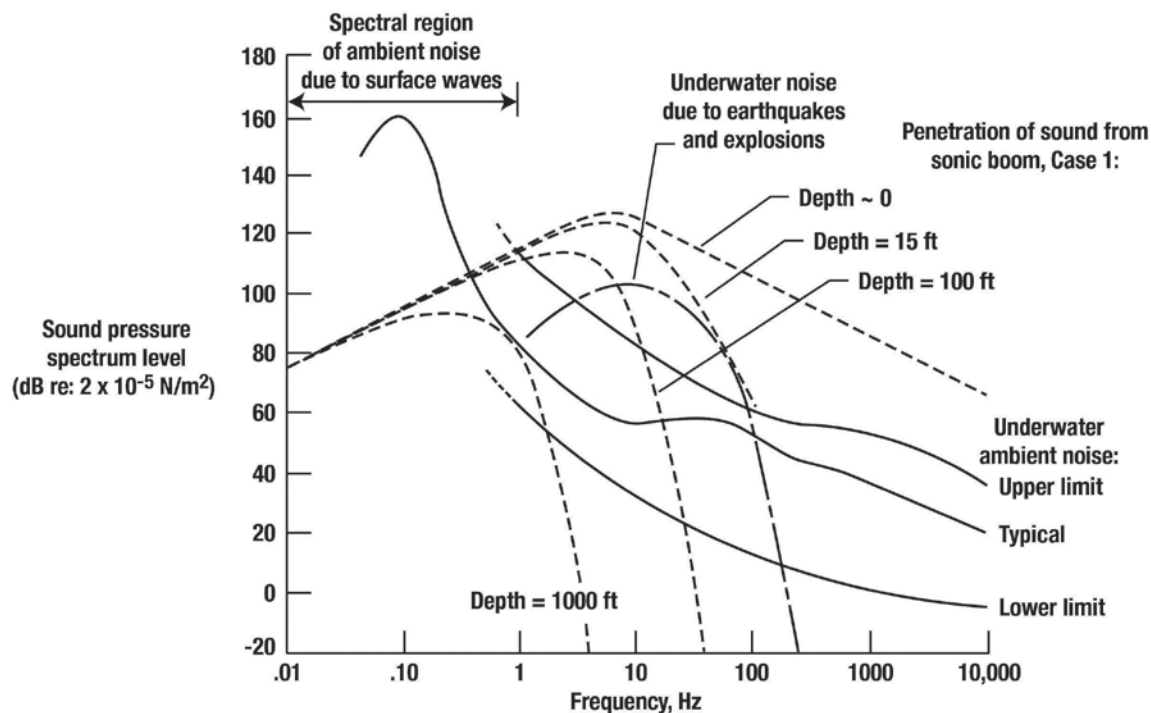


Figure 8.43. Comparison of underwater sound pressure spectrum levels for a sonic boom and ambient noise (ref. 8.72).

However, they further state that experiments in clear seawater with an underwater seismic pulse (electric sparker) have shown that the most sensitive small fish (anchovies and menhaden) are not stunned outside a radius of 1 meter from the spark of 2100 lbs/ft², about 600 times typical sonic boom overpressure levels.

Kemp has shown through experiments with explosive charges that oysters, blue crabs, and shrimp are less vulnerable to sonic booms than are fish (ref. 8.88). It is clear from the above findings that sonic booms from normal operations of supersonic aircraft will not harm these animals. In the early 1970s, the FAA in conjunction with the Department of Interior sponsored a program to conduct a field and lab study of the effects of sonic booms on fish and fish eggs during critical stages of development. Rucker (ref. 8.89) reported that egg and small hatched fish mortalities from eggs exposed to booms produced by military aircraft at overpressures up to 4.16 lbs/ft² caused no increase in mortality as compared to those for control groups of eggs spawned at the same time.

One of the potential launch sites for the Space Shuttle was Vandenberg Air Force Base in California. It was obvious that the sonic booms generated by the Shuttle launch would impact the California Channel Islands, which provide habitat for numerous forms of sea life. A 1980 study by Bowles and Stewart (ref. 8.90) was conducted to observe the effects of sonic boom disturbances to the pinnipeds and birds of San Miguel Island. They noted that dramatic disturbances can lead to an increased mortality rate for the habitat observed.

More recently, Perry, Boness, and Insley (ref. 8.91) conducted a study on the effects of Concorde sonic booms on breeding gray seals and harbor seals on Sable Island, Canada. These data were collected during the time period from January 1997 through May 1998. It is of interest to note that although the Concorde routinely passed the island on its daily trans-Atlantic flights, their reactions to these booms had never been documented. The study results showed relatively minor or no effects of the Concorde booms on breeding harbor and gray seals. It was also noted that they were unable to measure effects of sonic booms on animals in the water. They further state that the fact that booms penetrate water, there is the potential to affect animals that are in the water foraging or moving between foraging areas and breeding grounds.

Effect on Other Aircraft

A concern expressed during the U.S. SST studies of the mid-1960s related to the influence of sonic booms and associated shock waves on other aircraft. It was generally agreed that for subsonic aircraft due to the combination of high closure speeds and large separation distances, the effects would be negligible. For the case of a supersonic aircraft passing another aircraft flying supersonically, it was felt that adverse effects may be realized when the closure speeds are quite low and separation distances extremely small.

In 1963, the question of possible shock wave effects from a supersonic aircraft as it passes over a small subsonic aircraft was investigated. Two light aircraft, a small twin engine Beechcraft and a single engine Piper Cub, were instrumented with accelerometers and were overflown by an F-104 aircraft that produced sonic booms from 1.0 lb/ft² to 16.0 lbs/ft². Accelerations of the instrumented aircraft were also measured when it was parked on the ground and during maneuvering flights. Typical results of the sonic booms on the light aircraft are shown in figure 8.44 (refs. 8.92 and 8.93).

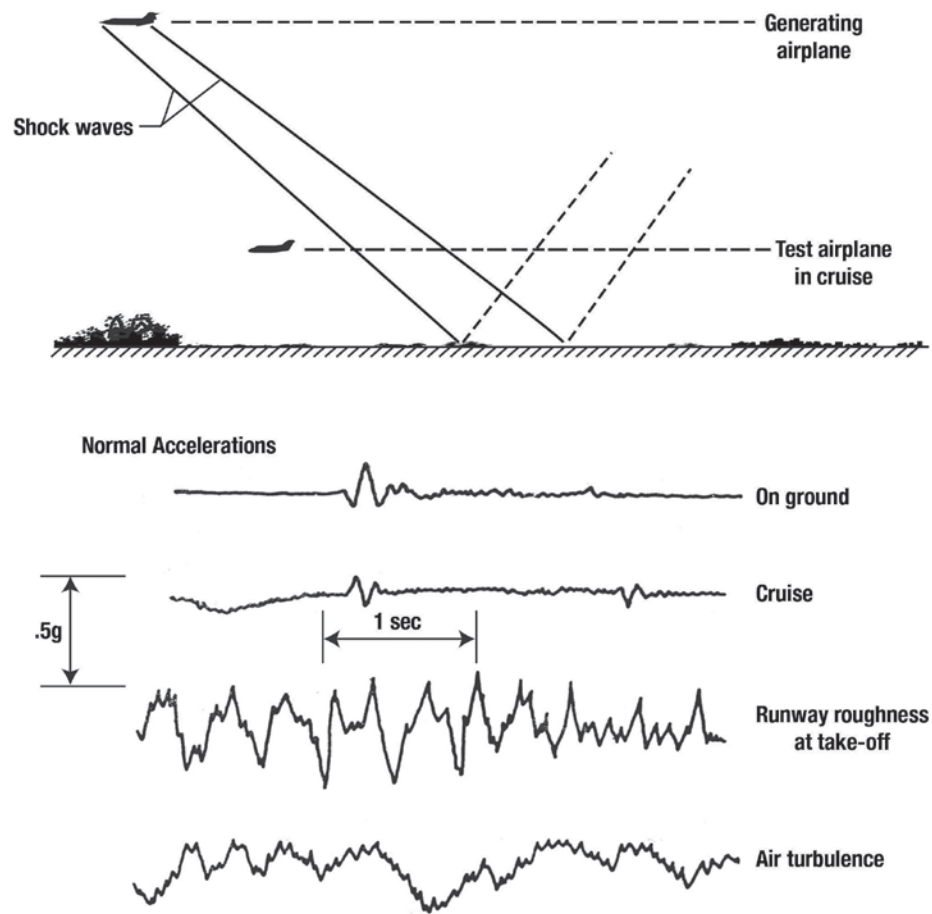
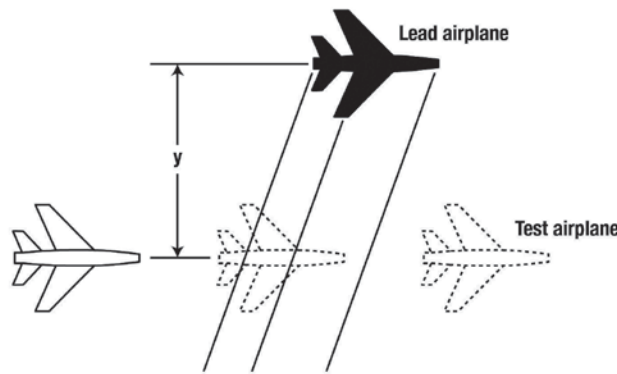


Figure 8.44. Sonic boom effects on light airplanes (adapted from refs. 8.92 and 8.93).

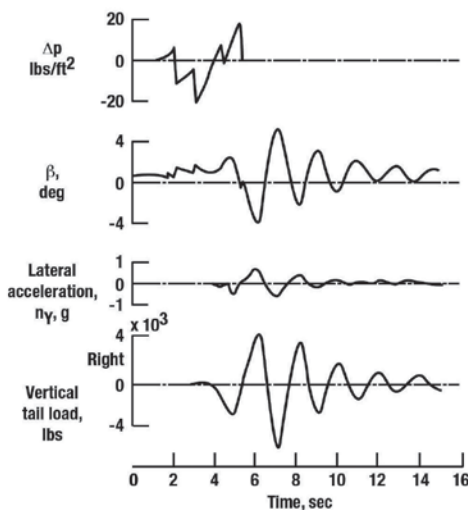
Acceleration levels for sonic boom induced levels experienced by the aircraft on the ground are observed to be approximately 0.3 g's whereas the aircraft in cruise experienced an appreciably smaller acceleration. By comparison, the accelerations when taxiing over a rough runway or in air turbulence are both shown in figure 8.44 and the latter accelerations are greater than those experienced during the sonic boom overflights. One observer in the aircraft noted that the estimated 16 lbs/ft² sonic boom was heard in cruise flight as a muffled sound and that the only visible effect on the aircraft was a slight movement of the window and vertical climb indicator. As a result of these tests, it was generally concluded that sonic booms do not constitute a hazard for other aircraft in flight or on the ground.

A limited experimental investigation was made on a subsonic transport and similar findings were observed (ref. 8.94). The supersonic aircraft was flown in a passing maneuver about 500 feet to the side and also below the transport-type airplane. Since the passing rates were very high, no airplane motion was expected. In both cases, the subsonic transport-type airplane experienced nothing more than a slight bump, with the airplane motions and loads being negligible. The only loading of concern would be the load induced by the flow field as it passes over the airplane. Thus, the pressure loading at separation distances of 100 feet or greater does not appear to be significant.

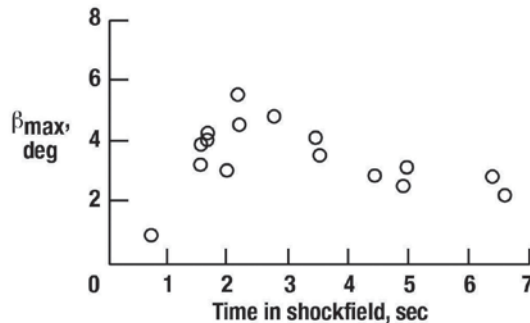
During the 1956 flight test to measure the pressure field surrounding an F-100 aircraft in supersonic flight at separation distances of from 2 to 33 body lengths (ref. 8.95), Mullens noted that during each supersonic pass the pilot of the overtaking aircraft said his aircraft was yawed considerably toward the other aircraft. Although no data were obtained at higher Mach numbers, pilot comments indicated that higher speed fly-by's could lead to considerable difficulty. It was also stated that aside from a risk of collision, it was known from similar tests by the NACA that vertical tail loads could become dangerously high (ref. 8.95). In 1959, Jordan (ref. 8.94) reported that at supersonic speeds, appreciable motions can be induced in an aircraft flying in close proximity to another aircraft. Some results of this flight test are presented in figure 8.45 (ref. 8.94) for a lateral separation distance of 100 feet (about 2 body lengths) at $M = 1.3$ and an altitude of 32,000 feet. The supersonic passing maneuver is illustrated in figure 8.45(a). Several passes were made to the side of the generating aircraft at various separation distances, closure rates, altitudes, and a Mach number of about 1.2. An indication of supersonic pressure field surrounding the generating aircraft can be found in reference 8.96.



(a) Supersonic passing maneuver.



(b) Time history of supersonic pass.



(c) Effect of passing rate on sideslip angle.

Figure 8.45. Formation flying at supersonic speeds (adapted from ref. 8.94).

Figure 8.45(b) presents a time history of the shock flow-field overpressure along with the corresponding responses of the aircraft including sideslip angle (β), lateral acceleration (n_y), and vertical tail shear load (F_y) as the aircraft passes through the flow field. It can be seen that a maximum side-slip angle, β , of 5.4° was produced and the lateral acceleration, n_y , at the aircraft center of gravity reached a maximum value of ± 0.7 g. The vertical tail shear loads (F_y), which are seen to be a function of sideslip angle, were approximately 50 percent of the design limit. The vertical tail loads attributed to the shock passage over the tail were less than 10 percent of the design limit. The influence of the time to pass through the shock flow field on sideslip angle (β) is shown in figure 8.44(c). At a slow passing rate, the yawing moment changes gradually and the aircraft tends to trim out and maintain a yawed attitude. The time to pass has an effect on the maximum sideslip angle, since the yawing-moment input is somewhat sinusoidal in shape and passing rates near the natural period of the airplane (about 2 sec) results in a dynamic response 2 to 3 times greater than for the static case. The fast passing rate resulted in negligible airplane motion and, thus, in relatively small vertical tail loads.

In addition to the formal tests on the effect of booms on aircraft, various subsonic vehicles have been used as platforms for elevating microphones above the ground surface in several flight tests described in Chapters 2 and 4. Numerous in-flight flow field probing tests have also been conducted and discussed in Chapter 4. No problems with the aircraft or aircrew occurred during any of those tests.

Observations from Intense Boom Levels

With the introduction of the Century series of military aircraft (F-100, F-101, F-102, F-104, F-105, and F-106) in the late 1950s and early 1960s, flights at supersonic speeds were easily obtainable. So too were flights at supersonic speeds at very low altitudes wherein very high sonic boom overpressures would be experienced. Two concerns became evident. The first related to the question as to whether these intense booms could be used for a variety of tactical purposes, from disabling sensitive electronic equipment to clearing mine fields, and second, that these overpressures would be high enough to harm humans. Two flight tests aimed at addressing those two concerns were conducted in 1960 during the joint NASA-USAF study Little Boom at Indian Springs, Nevada (ref. 8.22) and the 1965 U.S. Air Force flight maneuvers Joint Task Force II at Tonapah, Nevada (ref. 8.97). Altitudes from about 300 feet down to 50 feet above ground level were flown and overpressures as high as 120 lbs/ft² and 144 lbs/ft², respectively, were recorded.

With regard to the use of intense booms for tactical purposes, it was found that although numerous test windows were broken, little effect was observed on various ground equipment including a transport aircraft and Mace missile weapons system, the latter designed for operation under conditions of 864 lbs/ft² blast loadings. The primary reasons for this were that although the overpressures were high, the measured particle velocity behind the boom signature shocks was quite low (the order of 5 to 15 ft/sec), as compared to an explosive charge of equal overpressures and the exposure time was very short relative to the inherent inertia of the systems being exposed.

Regarding the question as to whether intense boom would harm humans, evidence suggests that effects on humans are limited to annoyance, startle, and sleep disturbance. During the very low-altitude supersonic flight tests in the Little Boom project, about 50 people, including experienced bioacoustic observers, were exposed to sonic boom overpressures of up to 120 lbs/ft² without any harm. Similar observations were made during the Tonapah flight tests where a 144 lbs/ft² boom level was recorded. Specific auditory observations made during these overflight programs are listed in table 8.3 (ref. 8.98).

Table 8.3. Observed and Predicted Auditory Responses to Sonic Booms**(Summary of all observations reported, from ref. 8.98)**

Nature of Auditory Response	Sonic Boom Experience or Prediction
Rupture of tympanic membrane	None expected below 720 lbs/ft ² None observed up to 144 lbs/ft ²
Aural pain	None observed up to 144 lbs/ft ²
Short temporary fullness, tinnitus	Reported above 95 lbs/ft ²
Hearing loss: permanent	None expected from frequency and intensity of boom occurrence
Hearing loss: temporary	None measured (1) 3-4 hours after exposure up to 120 lbs/ft ² (2) immediately after boom up to 30 lbs/ft ²
Stapedectomy	No ill effects reported after booms up to 3.5 lbs/ft ²
Hearing aids	No ill effects reported after booms up to 3.5 lbs/ft ²

Chapter 8 Summary Remarks

The vast majority of the community response database is for N-wave signatures having overpressures in the 1.0 lb/ft² to 3.0 lbs/ft² and durations of 100 msec to 300 msec. For this boom level range, 13 to 33 percent of the population was highly annoyed. Residences reported that startle, rattle, and vibrations and the possibility of damage are the most disturbing aspects of sonic booms. Little data exists on community response to nighttime booms, so the long-term effects on sleep are unknown.

The majority of the database regarding building response is associated with single dwelling structures. Little information exists regarding sonic boom effects on other modern structures and clustered homes in communities, or new design and construction methods and materials.

Sonic boom damage is confined to brittle materials and secondary structures in terms of plaster and window cracks. Damage is not likely to result from the normal sonic booms of high altitude operations for structures in good repair.

Seismic ground motions induced by some booms from supersonic flight are less than 1 percent of the damage threshold for residential structures. Booms have not triggered earthquakes but may precipitate incipient avalanches or landslides in areas already unstable. Sonic booms have been shown to have little effect on domestic and wild animals and aquatic life.

A level of acceptability of sonic booms has yet to be determined and may only be established by flying a demonstrator aircraft having a low-amplitude shaped signature over communities. Low-amplitude shaped signatures are shown to minimize annoyance both outdoors and indoors.

Chapter 8 References

- 8.1 Hubbard, Harvey H. and Mayes, William H.: Sonic Boom Effects on People and Structures. NASA SP-147, April 1967, pp. 65–76.
- 8.2 Clarkson, B. L. and Mayes, W. H.: Sonic-Boom Induced Building Structure Responses Including Damage. *J. Acoust. Soc. Am.*, Vol. 51:742-757, 1972.
- 8.3 Cheng, D. H. and Benveniste, J. E.: Dynamic Response of Structural Elements Exposed to Sonic Booms. NASA CR 1281, March 1969.
- 8.4 Brown, D. and Sutherland, L. C.: Evaluation of Outdoor-to-Indoor Response to Minimized Sonic Booms. NASA CR-189643, June 1992.
- 8.5 Plotkin, Kenneth J.; Sizov, Natalia V.; and Morgenstern, John M.: Examination of Sonic Boom Minimization Experienced Indoors. AIAA Paper 2008-57, Jan. 2008.
- 8.6 Cheng, D. H. and Benveniste, J. E.: Transient Response of Structural Elements to Traveling Pressure Waves of Arbitrary Shape. *Int. J. Mech. Sci.*, Vol. 8, No. 10, Oct. 1966, pp. 606–618.
- 8.7 ARDE Associates: Response of Structures to Aircraft Generated Shock Waves. WADC Tech. Rept. 58-169, U. S. Air Force, Apr. 1959. (Also available from ASTIA as AD-229-463L.)
- 8.8 Sutherland, Louis C.: Low Frequency Response of Structures. WR 82-18, Wyle Lab., May 1982.
- 8.9 Young, J. R.: Energy Spectral Density of the Sonic Boom. *J. Acoust. Soc. Am.*, Vol. 40, Number 2, 1966, pp. 496–498.
- 8.10 Maglieri, Domenic J. and Hilton, David A.: Significance of the Atmosphere and Aircraft Operations on Sonic Boom Exposure. NASA SP-83, May 1965, pp. 245–256.
- 8.11 Seebass, R. and George, A. R.: Sonic Boom Minimization. *J. Acoust. Soc. Am.*, Vol. 51, pp. 686–694, 1972.
- 8.12 Nixon, C. W. and Hubbard, H. H.: Results of USAF-NASA-FAA Flight Program to Study Community Responses to Sonic Booms in the Greater St. Louis Area. NASA TN D-2705, May 1965.
- 8.13 Haber, Jerald and Nakaki, David: Sonic Boom Damage to Conventional Structures. SAF HSD-TR-89-001, Feb. 1989.
- 8.14 Sutherland, Louis D.; Brown, Ron; and Gorener, Dawn: Evaluation of Potential Damage to Unconventional Structures by Sonic Booms. USAF HSD-TR-90-021, April 1990.
- 8.15 Haber, Jerald; Nakaki, David; Taylor, Craig; Knipprath, George; Kapparam, Vijay; and Legg, Mark: Effects of Aircraft Noise and Sonic Boom on Structures. USAF HSD-TR-89-002, Feb. 1989.
- 8.16 Thoenen, J. R. and Windes, S. L.: Seismic Effects of Quarry Blasting. U.S. Dept. of the Int., Bureau of Mines. Bulletin 442, 1942.
- 8.17 Mayes, W. H. and Edge, P. M., Jr.: Effects of Sonic Boom and Other Shock Waves on Buildings. *Material Research and Standards*, Vol. 4, No. 11, Nov. 1964, pp. 588–593.
- 8.18 Blume, John A. and Associates: Structural Reaction Program. National Sonic Boom Study Project. FAA Rept. SST 65-15, Vol. 1, April 1965.

- 8.19 Haber, Jerald M. and See, Alex: Cumulative Damage Plaster Tests. USAF AL/OE-TR 1994-0127, Oct. 1993.
- 8.20 Haber J.: Cumulative Sonic Boom Damage to Plaster. AIAA 93-4446, Oct. 1993.
- 8.21 McKinley, R. W.: Response of Glass in Windows to Sonic Booms. Materials Research and Standards, Vol. 4, No. 11, Nov. 1964, pp. 594–600.
- 8.22 Maglieri, Domenic J.; Huckel, Vera; and Parrott, Tony L.: Ground Measurements of Shock Wave Pressure for Fighter Airplanes Flying at Very Low Altitudes and Comments on Associate Response Phenomena. NASA TN D-3443, 1966 (formerly NASA TM X-611, 1961).
- 8.23 Parrott, T. L.: Experimental Studies of Glass Breakage Due to Sonic Booms. Sound-Its Uses and Control, May–June 1962.
- 8.24 Maglieri, Domenic J.; Hubbard, Harvey H.; and Lansing, Donald L.: Ground Measurements of the Shock-Wave Noise from Airplanes in Level Flight at Mach Numbers to 1.4 and at Altitudes to 45,00 Feet. NASA TN D-48, Sept. 1959.
- 8.25 Hershey, Robert L.; Higgins, Thomas H.; and Magrab, Edward B.: Application of the Response Probability Density - Function Technique to Predicting the Probability of Sonic-Boom Glass Breakage. J. Acoust. Soc. Am., Vol. 55, No. 5, May 1974, pp. 1009–1017.
- 8.26 National Sonic Boom Evaluation Office: Sonic Boom Experiments at Edwards Air Force Base. NSBEO-1-67 (Contract AF 49(638)-1758, Standford Res. Inst. July 28, 1967.
- 8.27 Carden, H. D.; Findley, D. S.; and Mayes, W. H.: Building Vibrations Due to Aircraft Noise and Sonic Boom Excitation. Presented at Symp on Machinery Noise, ASME Annual Mtg., Los Angeles, CA, Nov. 16–21, 1969.
- 8.28 Battis, J. C.: Siesmo-Acoustic Effects of Sonic Booms on Archeological Sites. Valentine Military Operations Area. A. F. Geophysics Laboratory. AFGL-TR-83-0304, Nov. 1983, AD A139581.
- 8.29 Duffy, P. S. J. and Hatton, J. D.: Concorde Over Goonhilly. The Post Office Electrical Engineers, July, Vol. 64(3), 1971, pp. 172–176.
- 8.30 Warren, C. H. E.: Recent Sonic-Bang Studies in the United Kingdom. J. Acoust. Soc. Am., 51:783-789, 1972.
- 8.31 National Research Council: Commercial Supersonic Technology: The Way Ahead, Nat. Act. Press, Wash. DC, 2001.
- 8.32 Wlezien, R. and Veitch, L.: Quiet Supersonic Platform. AIAA Paper 2002-0143, Jan. 2002.
- 8.33 Klos, J. and Buehrle, R. D.: Vibro-Acoustic Response of Buildings Due to Sonic Boom Exposure, June 2006 Field Test, NASA TM-214900, Sept. 2007.
- 8.34 Klos, J.: Vibro-Acoustic Response of Buildings Due to Sonic Boom Exposure: July 2007 Field Test. NASA TM-2008-215349, Sept. 2008.
- 8.35 Haering, E. A., Jr.; Smolka, J. W.; Murray, J. E.; and Plotkin, K. J.: Flight Demonstration of Low Overpressure N-Wave Sonic Booms and Evanescent Waves. Proc. of 17th Int. Symp. on Nonlinear Acoustics, Am. Inst. of Physics, Melville, NY, July 2005, pp. 647–650.
- 8.36 von Gierke, Henning E. and Nixon, Charles W.: Human Response to Sonic Boom in the Laboratory and the Community. J. Acoust. Soc. Am. 51, 766-782, 1972.

- 8.37 Sullivan, Brenda M.: Research on Subjective Response to Simulated Sonic Booms at NASA Langley Research Center. Proc. of 17th Int. Symp. on Nonlinear Acoustics, Am. Inst. of Physics, Melville, NY, July 2005, pp. 659–662.
- 8.38 Leatherwood, Jack D.; Sullivan, Brenda M.; Shepherd, Kevin P.; McCurdy, David A.; and Brown, Sherilyn A.: Summary of Recent NASA Studies of Human Response to Sonic Booms. *J. Acoust. Soc. Am.* 111 (1), Pt. 2, Jan. 2002, pp. 586–598.
- 8.39 Harel, J. R. P. and Zepler, E.: The Loudness of Sonic Booms and Other Impulsive Sounds. *J. Sound Vibration*, 1965, pp. 249–256.
- 8.40 Shepherd, L. J. and Sutherland, W. W.: Relative Annoyance and Loudness Judgments of Various Simulated Sonic Boom Waveforms. NASA CR 1192, 1968.
- 8.41 Johnson, D. R. and Robinson, D. W.: Procedure for Calculating the Loudness of Sonic Bangs. *Acustica* 21, 307–318, 1969.
- 8.42 Niedzwiecki, A. and Ribner, H. S.: Subjective Loudness of N-Wave Sonic Booms. *J. Acoust. Soc. Am.* 64, 1617–1621 (1978).
- 8.43 Niedzwiecki, A. and Ribner, H. S.: Subjective Loudness of “Minimized” Sonic Boom Waveforms.” *J. Acoust. Soc. Am.* 64, 1622–1626 (1978).
- 8.44 Shepherd, K. P. and Sullivan, B. M.: A Loudness Calculation Procedure Applied to Shaped Sonic booms. NASA TP 3134, 1991, pp. 1–10.
- 8.45 Ribner, Herbert S. and Roy, Dipankar: Acoustics of Thunder: A Quasilinear Model for Tortuous Lightning. *J. Acoust. Soc. Am.*, 72(6), Dec. 1982, pp. 1911–1925.
- 8.46 Maglieri, Domenic J. and Henderson, Herbert R.: Noise From Aerial Bursts of Fireworks. *J. Acoust. Soc. Am.*, Vol. 54, No. 5, 1973, pp. 1224–1227.
- 8.47 Borsky, P. N.: Community Reactions to Sonic Booms in the Oklahoma City Area. National Opinion Res. Ctr., AMRL Rept. TR-65-37, Repts. I and II, 1965.
- 8.48 Nixon, C. W. and Borsky, P. N.: Effects of Sonic Booms on People: St. Louis, Missouri, 1961–1962. Aerospace Medical Res. Lab. Rept., AMRL-Rept. TR-65-196, 1965.
- 8.49 Schomer, Paul D.: Some Important Factors in Community Response to Sonic Booms, Noise-Con. 2004, July 12–14, 2004.
- 8.50 Lukas, J. S. and Kryter, K. D.: A Preliminary Study of the Awakening and Startle Effects of Simulated Sonic Booms. NASA CR-1193. Sept. 1968.
- 8.51 Lukas, J. S. and Kryter, K. D.: Awakening Effects of Simulated Sonic Booms and Subsonic Aircraft Noise on Six Subjects 7 to 72 years of Age. NASA CR-1599, May 1970.
- 8.52 Hilton, David A.; Huckel, Vera; Steiner, Roy; and Maglieri, Domenic J.: Sonic-Boom Exposures during FAA Community Response Studies over a Six-Month Period in Oklahoma City Area. NASA TN D-2539, 1964.
- 8.53 Hilton, David A.; Huckel, Vera; and Maglieri, Domenic J.: Sonic Boom Measurements during Training Operations in the Chicago Area. NASA TN-D-3655, Oct. 1966.
- 8.54 Tracor Inc.: Public Reactions to Sonic Booms. NASA CR-1665, Sept. 1970.

- 8.55 National Research Council: U.S. Supersonic Commercial Aircraft – Assessing NASA’s High Speed Research Program, Nat. Acad. Press, Washington, DC, 1997.
- 8.56 Fields, James M.: Reactions of Residents to Long-Term Sonic Boom Noise Environments. NASA CR 201704, June 1997.
- 8.57 Hubbard, Harvey H. and Shepherd, Kevin P.: Comparisons of Methods for Predicting Community Annoyance Due to Sonic Booms. NASA TM 110289, Nov. 1996.
- 8.58 Anonymous: Assessment of Community Response to High Energy Impulsive Sounds. Rept. of Working Group 84, CHABA, Nat. Aca. Press, Washington, DC, 1981.
- 8.59 Anonymous: American Standard Method for Assessment of High Energy Impulsive Sounds with Respect to Residential Communities. ANSI S12.4, 1986.
- 8.60 Brown, David and Sutherland, L. C.: Sonic Boom (Human Response and Atmospheric Effects) Outdoor-To-Indoor Response. Proceedings of the First Annual High-Speed Research Workshop, NASA CP 10087, Part 3, April 1992, pp. 1345–1363.
- 8.61 Kamerman, C. S.; Sutherland, L.; and Plotkin, K.: Exploratory Study of the Potential Effects of Exposure to Sonic Boom on Human Health, Vol. 1, Sonic Boom Environment. AAMRL-TR-86-020, June 1986.
- 8.62 Anton-Guirgis, H.; Culver, B. D.; Wang, S.; and Taylor, T. H.: Exploratory Study of the Potential Effects of Exposure to Sonic Boom on Human Health, Vol. 2, Epidemiological Study. AAMRL-TR-86-020, June 1986.
- 8.63 Casady, R. B. and Lehman, R. D.: Response of Farm Animals to Sonic Booms. Sonic Boom Experiments at EAFB, NSBE 0-1-67 Interim Rept., Annex H, Sept. 1966.
- 8.64 Austin, O. L., Jr.; Robertson, W. B., Jr.; and Woolfender, G. E.: Mass Hatching Failure in Dry Tortugas Sooty Terns. Proc. Int. Ornithological Cong. 15:627, 1970.
- 8.65 Bowles, A. E.; Aubrey, F. T.; and Jehl, J. R.: The Effect of High Amplitude Impulsive Noise on Hatching Success. A Reanalysis of Sooty Tern Incident. Noise and Sonic Boom Impact Technology Program, OL-AC HSD/YAH Rept. No. HSD-TP-91-0006, 1991.
- 8.66 Bowles, A. E.; Knobler, M.; and Seddon, M. E.: Effects of Simulated Sonic Booms on the Hatchability of White Leghorn Chicken Eggs. Occupational and Environmental Health Directorate, AL-OE-TR-1994-0179.
- 8.67 Ting, Carina; Garrelick, Joel; and Bowles, Ann: An Analysis of the Response of Sooty Tern Eggs to Sonic Boom Overpressures. J. Acoust. Soc. Am. 111(1), Part 2, Jan. 2002, pp. 562–268.
- 8.68 Travis, Hugh F. et al.: An Interdisciplinary Study of the Effects of Real and Simulated Sonic Booms on Farm-Raised Mink (*MUSTELA Vison*). FAA Eq.-72-2, Aug. 1972.
- 8.69 Bell, Wilson B.: Animal Response to Sonic Booms. J. Acoust. Soc. Am. 51, 758–765, 1972.
- 8.70 Lynch, Thomas E. and Speake, Dan W.: The Effect of Sonic Boom on the Nesting and Brood Rearing Behavior of the Eastern Wild Turkey. Rept. No. FAA-RD-75-2, Jan. 1975.
- 8.71 Mancini, Karen M.; Gladwin, Douglas N.; Vilella, Rita; and Cavendish, Mary G.: Effects of Aircraft Noise and Sonic Booms on Domestic Animals and Wildlife. A Literature Synthesis. AFESC TR 88-14, June 1988.

- 8.72 Cook, J. C.; Goforth, T.; and Cook, R. K.: Seismic and Underwater Responses to Sonic Boom. *J. Acoust. Soc. Amer.* 51, 729–741, 1972.
- 8.73 Goforth, T. and McDonald, J.: Seismic Effects of Sonic Booms. NASA CR-1137, 1968.
- 8.74 Duvall, W. I. and Fogelson, D. C.: Review of Criteria for Estimating Damage to Residences from Blasting Vibrations. TN 23, U.7, NO. 5963, U.S. Dept. of the Interior, Bureau of Mines, 1962.
- 8.75 Higgins, Thomas H.: The Response of Songbirds to the Seismic Compression Waves Preceding Sonic Booms. Report No. FAA-RD-74-78, May 1974.
- 8.76 Lillard, D. C.; Parrott, T. L.; and Gallagher, D. C.: Effect of Sonic Booms of Varying Pressures on Snow Avalanches. FAA Rept. SST 65-9 AD 468 794, August 1965.
- 8.77 Kanamori, H.; Mori, J.; Sturtevant, B.; Anderson, D.; and Heaton, T.: Seismic Excitation by Space Shuttles, *Shock Waves* 2, 89–96, 1992.
- 8.78 Qamar, A.: Seismic Excitation by Atmospheric Disturbances: The Dec. 1992 Space Shuttle and a Fireball in Jan. 1989. SSA Abstract, April 1993.
- 8.79 Cates, Joseph E. and Sturtevant, Bradford: Seismic Detection of Sonic Booms. *J. Acoust. Soc. Am.* 111(1), Pt. 2, Jan. 2002, pp. 614–628.
- 8.80 Goforth, Tom T. and Rasmussen, Robert K.: Study of the Characteristics of Seismic Signals Generated by Natural and Cultural Phenomena. NASA CR 132606, Jan. 1974.
- 8.81 Sawyers, K. N.: Underwater Sound Pressure from Sonic Booms. *J. Acoust. Soc. Am.*, 523–524, 1968.
- 8.82 Cook, R. K.: Penetration of a Sonic Boom Into Water. *J. Acoust. Soc. Am.*, 47, 1430–1436, 1970.
- 8.83 Water, J. and Glass, R. E.: Penetration of Sonic Boom Energy Into the Ocean: An Experimental Simulation. Hydrospace Research Corp., Final Rept. on Contract FA-70-WAI-185, HRC TR 288, June 1970, available from NTIS/DTIC as AD 711 963.
- 8.84 Sparrow, Victor W.: Review and Status of Sonic Boom Penetration into the Ocean. *J. Acoust. Soc. Am.* 111(1), Pt. 2, Jan. 2002, pp. 537–543.
- 8.85 Sohn, R. A.; Vernon, R.; Hildebrand, J. A.; and Webb, S. C.: Field Measurements of Sonic Boom Penetration into the Ocean. *J. Acoust. Soc. Am.* 107, 3073–3083 (2000).
- 8.86 Wang, J. C. T.; Moody, D. M.; Griffice, C. P.; Edwards, J. R.; and Hashad, A. A.: Sonic Boom and Underwater Sound Pressure Induced by Low-Altitude Ramjet Cruise Missiles. AIAA Paper 2006-413, Jan. 2006.
- 8.87 Intrieri, P. and Malcolm, G.: Ballistic Range Investigation of Sonic-Boom Overpressures in Water. AIAA J.11, 510–516, 1973.
- 8.88 Kemp, R. J., Jr.: Do Seismographic Explosives Affect Marine Life?, Texas Game and Fish Austin, TX, 14, No. 9, 11–13, Sept. 1956.
- 8.89 Rucker, Robert R.: Effect of Sonic Boom on Fish,” Rept. No. FAA-RD-73-29, Feb. 1973.
- 8.90 Bowles, A. and Stewart, B.: Disturbances to the Pinnipeds and Birds of San Miguel Island, 1979-1980. Potential Effects of Space Shuttle Sonic Booms on the Biota and Geology of the California Channel Islands: Res. Repts., edited by J. R. Jehl, Jr. and C. F. Cooper, (Cent. Mar. Stud., San Diego State Un. and HSWRI, San Diego, CA, pp. 99–137.

- 8.91 Perry, Elizabeth A.; Boness, Darryl J.; and Insley, Stephen J.: Effects of Sonic Booms on Breeding Gray Seals and Harbor Seals on Sable Island, Canada. *J. Acoust. Soc. Am.* 111(1) Part 2, Jan. 2002, pp. 599–609.
- 8.92 Powers, John O.; Sands, J. M.; and Maglieri, Domenic J.: Survey of United States Sonic Boom Overflight Experimentation. *Aircraft Engine Noise and Sonic Boom*. FDP-PEP, CP 12, AGARD 1969, pp. 15–1 to 15–35.
- 8.93 Maglieri, Domenic J. and Morris, Garland J.: Measurements of the Response of Two Light Airplanes to Sonic Booms. NASA TN D-1941, 1963.
- 8.94 Jordan, Gareth H.: Some Aspects of Shock Wave Generation by Supersonic Airplanes. AGARD Rep. 251, North Atlantic Treaty Organization, Dec. 1959.
- 8.95 Mullens, Marshall E.: A Flight-Test Investigation of the Sonic Boom. AFFTC TN 56-20, Air Res. and Dev. Command, US Air Force, May 1956.
- 8.96 Smith, Harriet J.: Experimental and Calculated Flow Fields Produced by Airplanes Flying at Supersonic Speeds. NASA TN-D 621, 1960.
- 8.97 Nixon, C. W.; Hille, H. K.; Sommer, H. D.; and Guild, Elizabeth: Sonic Booms Resulting from Extremely Low Altitude Supersonic Flight: Measurements and Observations on Houses, Livestock and People. AMRL-TR-68-52, USAF, Oct. 1968.
- 8.98 von Gierke, H. E.: Effects of Sonic Boom on People: Review and Outlook. *J. Acoust. Soc. Am.* 39, 543–550, 1966.

CHAPTER 9 SONIC BOOM SIMULATION DEVICES AND TEST TECHNIQUES

Without question, sonic boom simulation devices have fulfilled a wide variety of sonic boom research needs that have led to a more complete understanding of sonic boom generation, propagation prediction, and responses. The development of experimental simulation techniques to generate sonic boom type disturbances have complemented the place of complex, lengthy, and costly supersonic flight operations.

In this section, we will review the simulation methods/devices listed in table 9.1, indicating the specific sonic boom issues they address and highlighting some of the experimental findings. The specific sonic boom issues to be discussed include validation of sonic boom design and prediction codes, the influence of atmospheric variability on boom signature distortions, quantifying focus boom intensities, underwater studies, sonic boom reflection and refraction by buildings and topography, indoor-outdoor subjective response, and building response.

In 1970, Edge and Hubbard (ref. 9.1) provided a review of the characteristics of the facilities and techniques of simulating sonic booms. Table 9.1 (ref. 9.1) lists the categories of simulators addressed along with an indication of research applications for each.

Table 9.1. Categories of Sonic Boom Simulators and their Research Application (from ref. 9.1)

Simulator Categories	Research Applications		
	Generation	Propagation	Response
Wind Tunnels	x	x	
Ballistic Ranges	x	x	
Spark Discharge		x	
Loudspeakers			x
Piston Systems			x
Shock Tubes		x	x
Explosives		x	x
Air Modulator Valves		x	x

The Edge-Hubbard summary of sonic boom simulators was updated in 1986 by Shepherd and Powell (ref. 9.2), who summarized the current status of boom simulators that might be used in future studies of the effects of booms on people, animals, and structures. Their study was confined to simulators in the United States and Canada, and indicated which of the simulators were fully operational, which required modest or major investment to bring to operational status, and those no longer in existence.

A majority of the sonic boom simulation devices listed in table 9.1 were not utilized beyond their initial application. However, recent and current activities in seeking vehicle designs having low-boom, non-N-wave shaped signatures required the continued use of several of these simulation devices. Wind-tunnel testing is still necessary for acquiring near-field pressure signatures for validation of the CFD codes used in numerous advanced vehicle designs and their shaped signatures. Loudspeaker test chambers, piston systems, and explosive charges have been utilized to assess the outdoor and indoor subjective response to these signatures and to establish the role of the visual, vibratory, and noise stimuli on indoor subjects. Building response studies utilizing linear charges, air modulation, and piston-driven devices and loudspeakers have also been carried out.

Validation of Sonic Boom Design and Predictive Codes

Measurements of the flow field characteristics surrounding the flight of a supersonic aircraft play a key role in the continuous development and validation of the design codes used to develop aerodynamically efficient low-boom vehicles of the future. The in-flight measurements of the pressure field about various aircraft presented in Chapter

4 of this publication were very instrumental in confirming the validity of past sonic boom prediction codes being applied to aircraft not designed for low sonic booms. The most recent flight tests involving the modified F-5E aircraft into the SSBD added additional credibility of the predictive codes for non-N-wave designs.

Although full-scale flight-test flow-field measurements will continue to be required for final confirmation of theory, such tests follow rather than lead the way. Small model testing in wind tunnels has long played a significant role in establishing the sonic boom characteristics of specific aircraft configurations and, thus, in the development of sonic boom design methodology and predictive codes. Another simulation technique – the use of a ballistic range to launch aircraft models – has also been examined. Each of these two simulation techniques will be briefly reviewed.

Wind Tunnels

Wind-tunnel studies of the sonic boom phenomenon have been conducted for over 50 years beginning with Carlson's work (ref. 9.3) in 1959 in the NASA LaRC 4- by 4-foot Supersonic Wind Tunnel. Since then, sonic boom wind-tunnel testing has been conducted in several NASA supersonic facilities, including the LaRC 4- by 4-foot Unitary Plan Supersonic Wind Tunnel, ARC 9- by 7-foot Supersonic Wind Tunnel, the 20-inch Mach 6 Tunnel, and the GRC 8- by 6-foot and 10- by 10-foot wind tunnels. Presently, the ARC 9- by 7-foot Supersonic Wind Tunnel and the GRC 8- by 6-foot Supersonic Wind Tunnel are the primary NASA facilities being used for sonic boom testing by NASA.

The success of sonic boom wind-tunnel tests is dependent upon the quality of the tunnel flow characteristics within the test section, the size and geometric fidelity of the model being tested, the devices and methods used to acquire the pressure measurements, and the manner in which the model is supported in the wind-tunnel test section. A schematic of a sonic boom wind-tunnel test setup of the mid-1960 time period is shown in figure 9.1 (ref. 9.4).

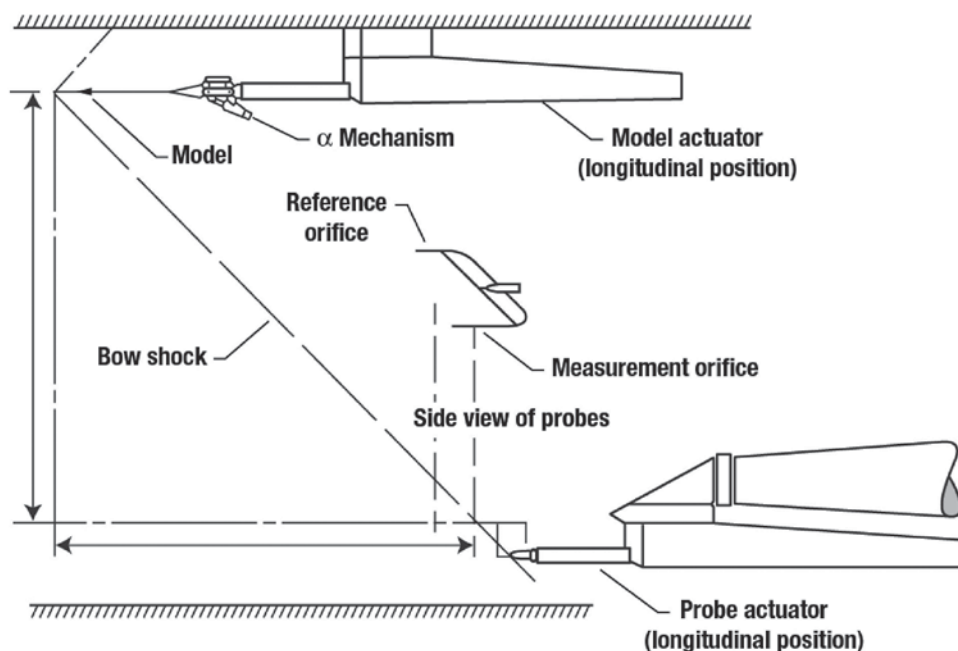


Figure 9.1. Wind-tunnel test setup of the mid-1960 time period (ref. 9.4).

During the past 50 years, wind-tunnel testing techniques have helped define the test model size, manner in which the model is mounted, and pressure measurement sensors necessary to describe the boom signatures about the model. These techniques were first set forth in 1967 by Carlson and Morris (ref. 9.4). They also advanced the methods used to minimize the influences of non-uniform and non-steady tunnel test conditions, model and measurement probe vibrations, and boundary-layer effects on the measured pressure signatures. In addition, they formulated procedures to adjust and correct the measurements. A typical measured pressure signature and its adjusted value is presented in figure 9.2 (ref. 9.4).

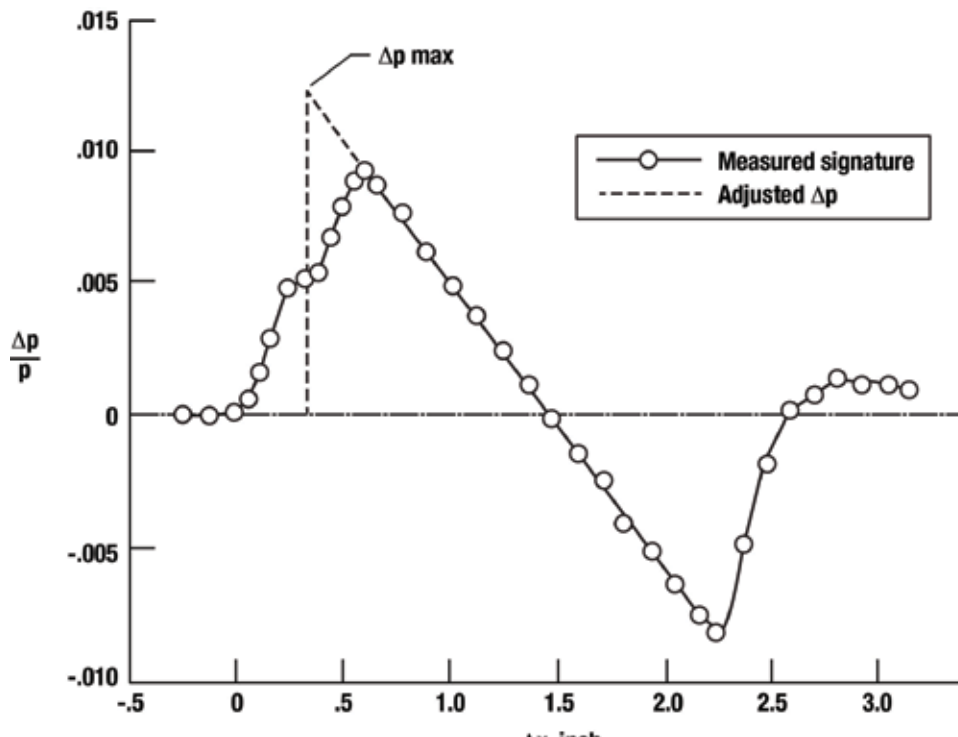


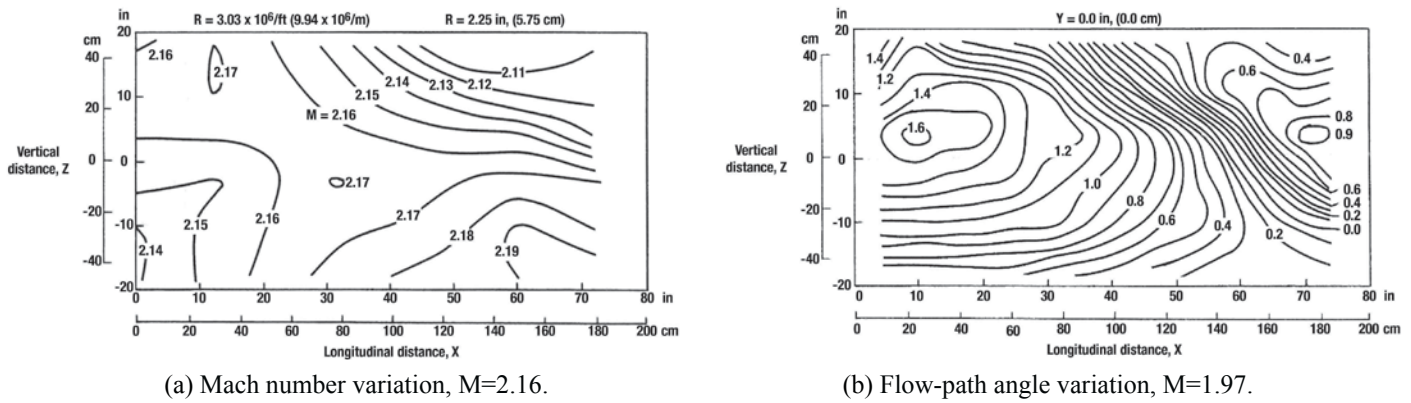
Figure 9.2. Typical measured sonic boom pressure signature of the mid-1960 time period (ref. 9.4).

The procedure for adjusting the measured signature, which has been smeared as a result of those influences, was to project a line along the expansion portion of the boom signature to the amplitude where the areas contained within the lower and upper parts of the initial shock were equal. As noted by the authors, the signature for this example was deliberately chosen to accentuate the departure from the N-wave shape. They further stated that such a departure from that of an N-wave is present to some degree in all tunnel signature measurements. In this section, discussions will be provided that address each of these concerns and include test section flow quality, models, pressure measurements, and model support.

Test Section Flow Quality

The tunnel measurement system for a sting-mounted model, as shown in figure 9.1, includes the geometric angle of attack, static and total pressures, and Mach number. As with any supersonic tunnel there are non-uniformities in all these quantities with the most uniform flow, hopefully, in the region where sonic boom models are mounted. Unlike wind-tunnel force tests, nonuniformities across the entire test section are of concern in regards to where in the test section the measurement probes are located. Measurements of the flow angle, Mach number, and pressure can be different due to the lateral, vertical, and longitudinal gradients of flow angle and Mach number across the test section.

A calibration of the flow qualities of a supersonic tunnel is always made prior to test operations. The NASA LaRC Unitary Plan Supersonic Wind Tunnel had two test sections that were used for many sonic boom model tests. Test section 1 was designed for testing at Mach numbers of 1.46 to 2.86 and test section 2 for Mach numbers of 2.30 to 4.63. The test sections are 4-feet wide (y) by 4-feet high (z) and 7-feet long (x). Reference 9.5 by Jackson et al. contains plots of the aforementioned non-uniformities for both test sections one and two. An example of the lateral and longitudinal variations of test section 1 in Mach number, M , and the flow angle Θ_v (measured in the vertical plane, deg) is presented in figure 9.3 (ref. 9.5).



(a) Mach number variation, $M=2.16$. (b) Flow-path angle variation, $M=1.97$.
 Figure 9.3. Mach number and flow-path angularity distributions in the NASA LaRC Unitary Plan Supersonic Wind Tunnel test section (adapted from ref. 9.5).

The surveys were made very near the horizontal centerline along the flow path at a distance $y = 2.25 \text{ in.}$ and $y = 0 \text{ in.}$ for Mach number and flow-path angle respectively. As observed in figure 9.3(a), the longitudinal Mach number variation across the test section centerline for a nominal tunnel Mach setting of 2.16 ranged from 2.11 to 2.18. The longitudinal variation of flow angle for a nominal Mach setting of 1.97 ranged from 0° to 1.6° . Such variations were also observed at different Mach and Reynolds numbers. As observed from this and other measurements for sonic boom testing, knowledge of the test section non-uniformities are very important as to determining whether to test, at what test conditions, and where to place the model and measurement devices.

Models

Wind-tunnel models have generally ranged in size from $\frac{1}{4}$ -inch to 30 inches in length depending upon the size of the wind-tunnel test section and the desire to acquire near-, mid-, or far-field flow conditions. A photograph of four 1-inch sonic boom models, shown in figure 9.4 (ref. 9.1), demonstrates the challenge between the size and fidelity of sonic boom models.



(NASA photo, Courtesy of Harry Carlson)

Figure 9.4. Small sonic boom wind-tunnel models tested in the wind tunnel (ref. 9.1).

For these models, pressure measurements were obtained at various distances from the sonic boom models ranging from about 1 to 50 body lengths. Larger models allow for more exacting geometric features such as flow-thru nozzles and exhaust simulation, put less demand on the measurement devices, provide higher test Reynolds numbers, and allow for more versatility of the model support. Flow-field measurements are usually restricted to distances close to the model (the near field) at about one to five body lengths (h/l).

Smaller models allow for flow-field measurements far from the model (mid- to far-field) at about 5 to 50 body lengths (h/l) and are more prone to flow-field contamination and model vibrations. In addition, flow-field measurements become more challenging as the measurement devices become large compared to the size of the model.

An extreme example of the influence of model size and perhaps vibration on three measured sonic boom signatures is presented in figure 9.5 (ref. 9.4).

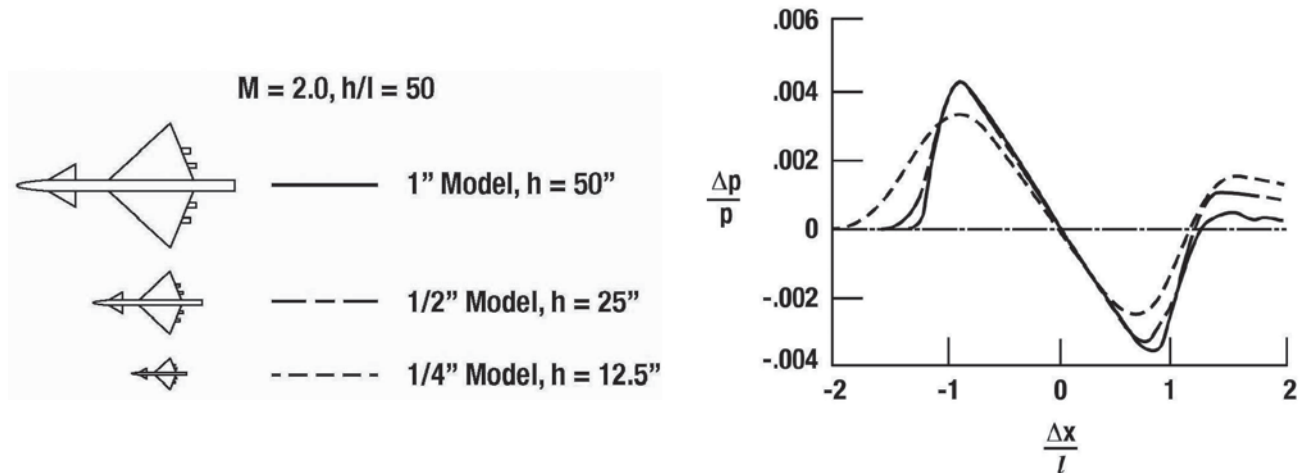


Figure 9.5. Effect of model size on measured signatures (adapted from ref. 9.4).

All three signatures were obtained at equal non-dimensionalized distances from models of a supersonic transport varying in size of 1-inch, 1/2-inch, and 1/4-inch. It can be seen that as model size decreases, the signature becomes more rounded. Recall that in order to acquire signatures further from the model into the mid- and far-field, smaller models were necessary. The results shown in figure 9.5 established that because of the deleterious effect of model size and vibration, and boundary layer buildup, models of 1/4-inch would no longer be used.

A comparison of the sonic boom signature measured in a wind tunnel from a 1-inch model of the B-58 aircraft with the ground measured signature of the full-scale 97-foot long aircraft in flight, is given in figure 9.6 (ref. 9.4). When the appropriate adjustments are made to the wind-tunnel signature, good agreement is established between wind-tunnel and flight results.

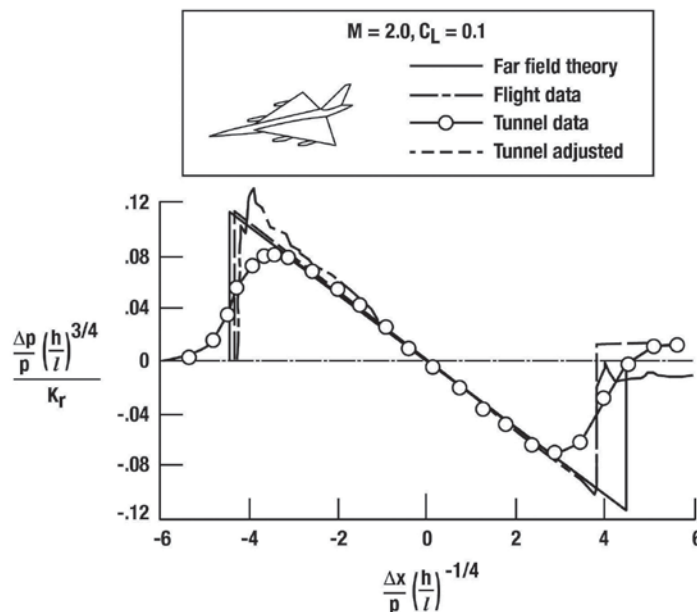


Figure 9.6. Correlation of wind-tunnel and flight-measured boom signatures (ref. 9.4).

The techniques employed to investigate the sonic boom phenomenon using wind tunnels have experienced little change in the past 50 years. Sting-mounted models and slender cone measurement probes and the associated signature adjustment methods were still in use in the early 2000 time period by Mack and Kuhn (ref. 9.6) for their sonic boom tests, as shown in figure 9.7.

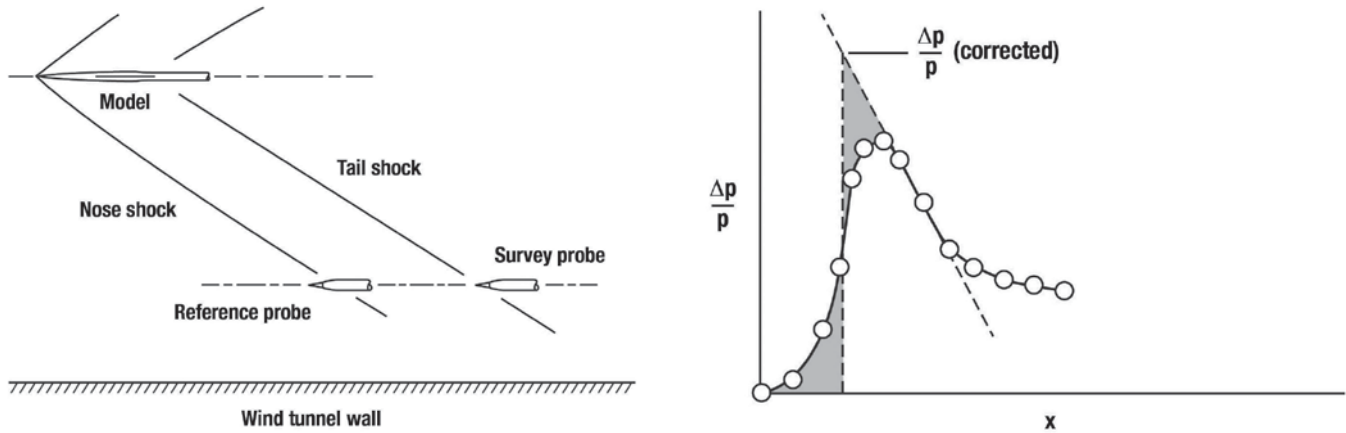


Figure 9.7. Wind-tunnel test setup of the early 2000 time period along with measured and corrected bow shock (ref. 9.6).

Shock smearing was still being experienced by Mack and Kuhn on their 10-inch long low-boom configuration shown in figure 9.8 (ref. 9.6).

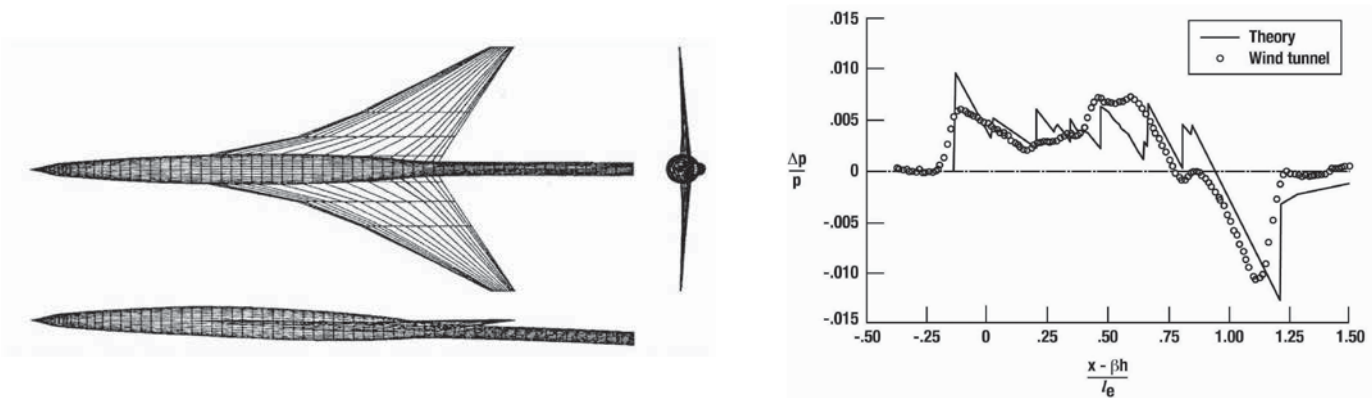
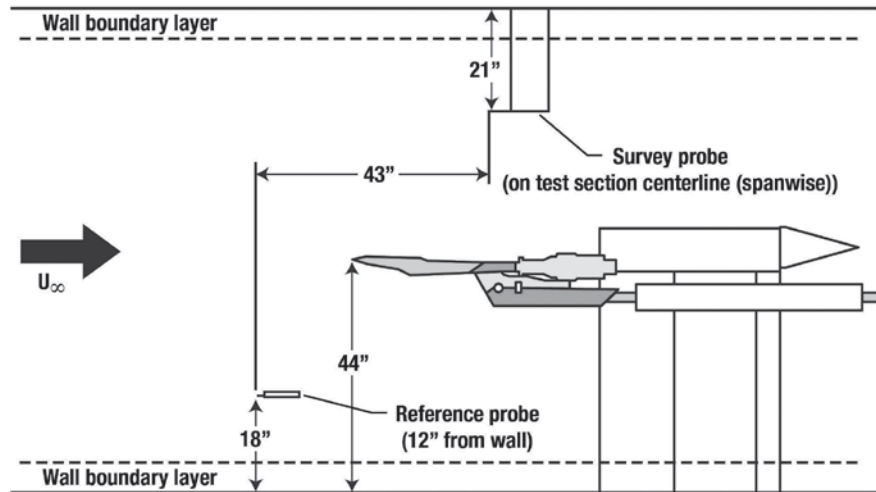


Figure 9.8. Three-view of 10-inch SLSLE model and results from wind-tunnel tests of the early 2000 time period, SLSLE model at $M = 2$, $C_l/C_{l_{cruise}} = 1.0$, and $h = 45$ inch (ref. 9.6).

However, as model size increases and measurements are acquired closer to the model, the accuracy and fidelity of the measurements improve considerably, as illustrated in figure 9.9 (ref. 9.7). Figure 9.9 shows the test setup in the NASA GRC 8- by 6-foot Supersonic Wind Tunnel and the measured and predicted near-field sonic boom signature at an h/l distance of 1.5 for the 2.49-foot SSBD model.

These tests also provided for model inlet flow-through nacelle effects. The model was mounted in the inverted position in the tunnel, as shown in figure 9.9, and attached to the tunnel sting support via a steel strut that replaced the vertical tail.



(a) SSBD model probe setup.

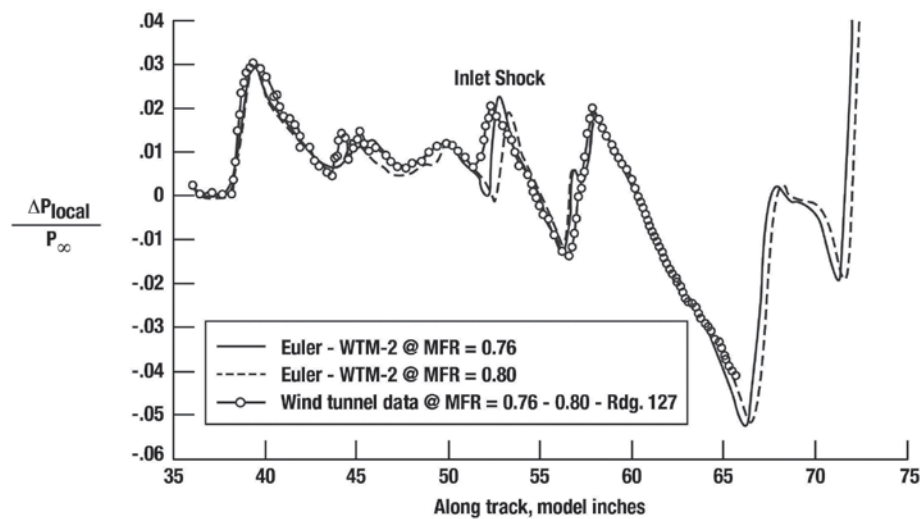
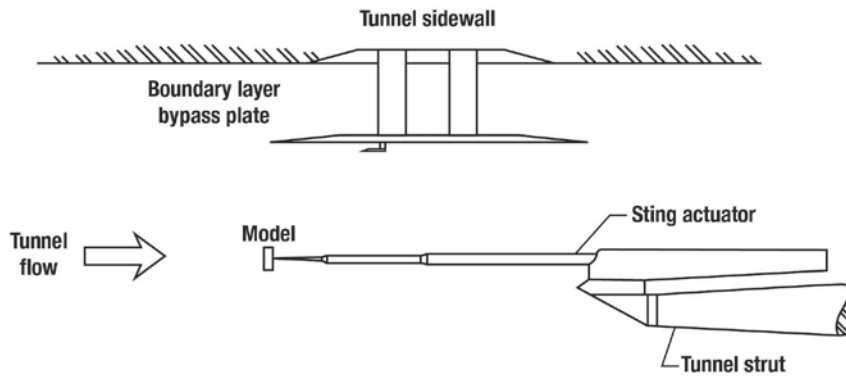
(b) Measured versus predicted centerline pressures for SSBD at design lift coefficient ($M=1.367$, $C_N=0.90$, $h/l=1.5$, $\phi=0^\circ$).

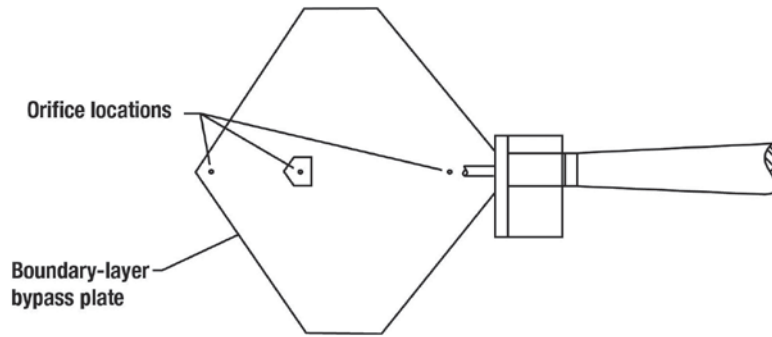
Figure 9.9. Schematic of SSBD sonic boom test setup in NASA GRC 8- by 6-foot Supersonic Wind Tunnel showing model and measurement probe locations with measured and predicted results (adapted from ref. 9.7).

Pressure Measurement Plate

Prior to 1960, the use of a stationary boundary-layer bypass plate was the preferred instrument for measuring flow-field pressure on sonic boom wind-tunnel models primarily because of its simplicity. A schematic of the wind-tunnel test setup that utilized a measurement plate and was used by Carlson (ref. 9.3) is depicted in figure 9.10.



(a) Schematic of tunnel test setup.



(b) Planview of boundary-layer bypass plate.

Figure 9.10. Description of wind-tunnel test section setup using stationary boundary-layer plate (ref. 9.3).

Measurements were obtained at pressure orifices on the surface of the plate. It was usually assumed that this flat plate would act as a perfect reflector producing a doubling of the pressure ratio $\Delta p/p$. In a subsequent test of this assumption, Carlson (ref. 9.8) conducted a systems check by obtaining measurements of the pressure field of the same model, first with the reflection plate and then with a small static probe. The results of this comparison are given in figure 9.11 (ref. 9.8).

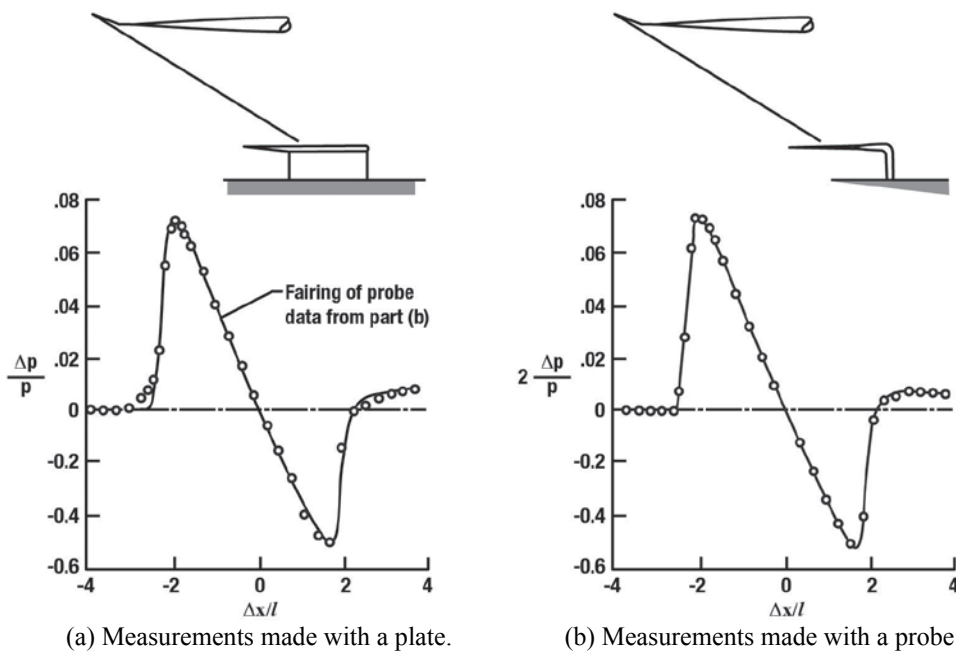


Figure 9.11. Comparison of pressure measurements made with a reflection plate and with a small static pressure probe (ref. 9.8).

The results indicated that, in general, the assumption of 2.0 as a reflection factor was substantiated. However, there is considerably more smearing of the onset of the bow shock due to shock-boundary-layer interaction as compared to that measured using the small static pressure probe. Because there was more boundary-layer smearing of the measured signature using the plate, subsequent wind-tunnel sonic boom flow-field pressure measurements were made using slender conical probes.

Pressure Measurement Probes

Use of a slender conical pressure measurement probe of the type shown in figure 9.12 (ref. 9.9) to define the shock flow field about a model in the wind tunnel has continued for the past 50 years with only slight variations as to the half cone angle, which varied from 1° to 2° . Four static pressure orifices were circumferentially spaced about 90° apart about half way from the tip of the 0.2-inch diameter conical probe.

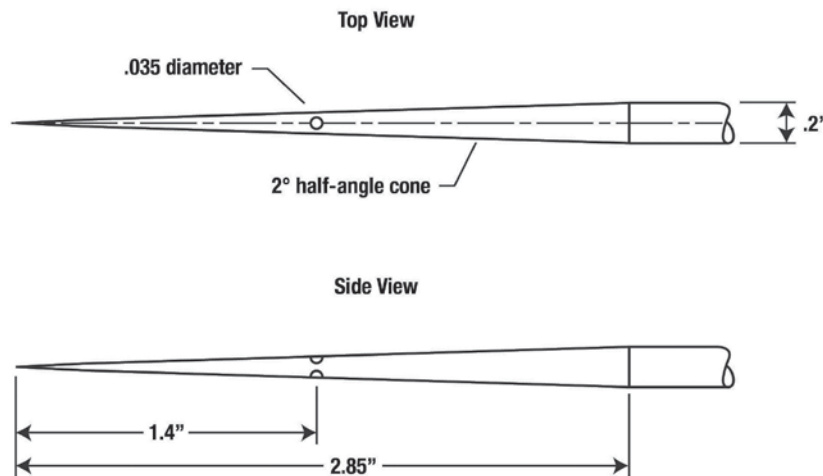


Figure 9.12. Geometry of conical (2° half-angle cone) pressure probe (ref. 9.9).

The static pressure orifices were arranged to lie in a Mach 1.4 plane originating from the model for the tests of reference 9.10 and in a Mach 2.92 plane for the tests of reference 9.11. This latter paper stated that the earlier tests (ref. 9.9), over a greater range of Mach angles, did not reveal any significant effects of the difference between the Mach angle and the vertically aligned orifices.

The long slender conical probe shown in figure 9.12 was used for the tests shown in figures 9.6 and 9.8, as well as the SSBD tests of figure 9.9. The higher stiffness of the large model, along with the more rigid model sting support arrangement, minimized model vibration effects on the signature measurements. However, there were still traces of shock smearing, smoothing, or rounding of the shocks in the measured signature. This was believed to be associated with the measurement probe; specifically, the shock off the tip of the conical probe, the boundary layer buildup from the probe tip to the measuring orifices, and the associated shock-boundary layer interaction (mentioned earlier) in the vicinity of the probe static orifices.

In 1959, Carlson (ref. 9.12) used a miniature conical probe in the LaRC 4- by 4-foot Supersonic Wind Tunnel to study the actual flow about wing-body combinations relative to store launches at supersonic speeds. The miniature conical probe was used again by Putnam and Capone in 1969 (ref. 9.13) in the 4- by 4-foot Supersonic Wind Tunnel to obtain local Mach, flow angle, and pressures in the flow field surrounding a cold jet exhausting into supersonic flow. A sketch showing the details of this conical probe are given in figure 9.13 (refs. 9.12 and 9.13). The five pressure orifices of the probe were connected to five Baldwin gages having a range of 15 lbs/in².

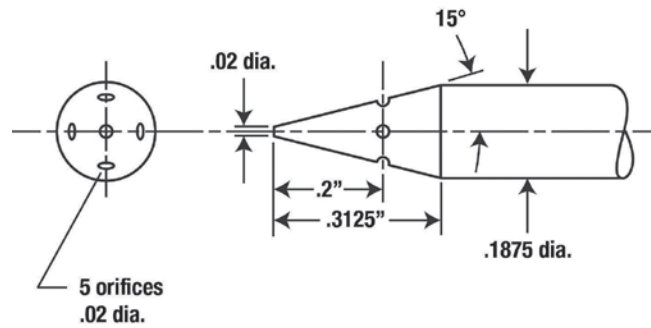


Figure 9.13. Detail of conical probe utilized in 1959 and 1969 wind-tunnel tests (refs. 9.12 and 9.13).

It is important to note that in each of these two tests, the Carlson model size was on the order of 3 ft in length with about 2-ft span and the Putnam-Capone jet nozzles were about 6 inches in diameter and 45 inches in length. Measurements were made at distances of from about 1 inch to 2 inches below the wing-body models and from the exhaust exit to about one nozzle diameter downstream for the jet flow tests. Some measured results are presented in figure 9.14(a) for the Carlson wing-model tests and in figure 9.14(b) for the Putnam-Capone jet nozzle tests.

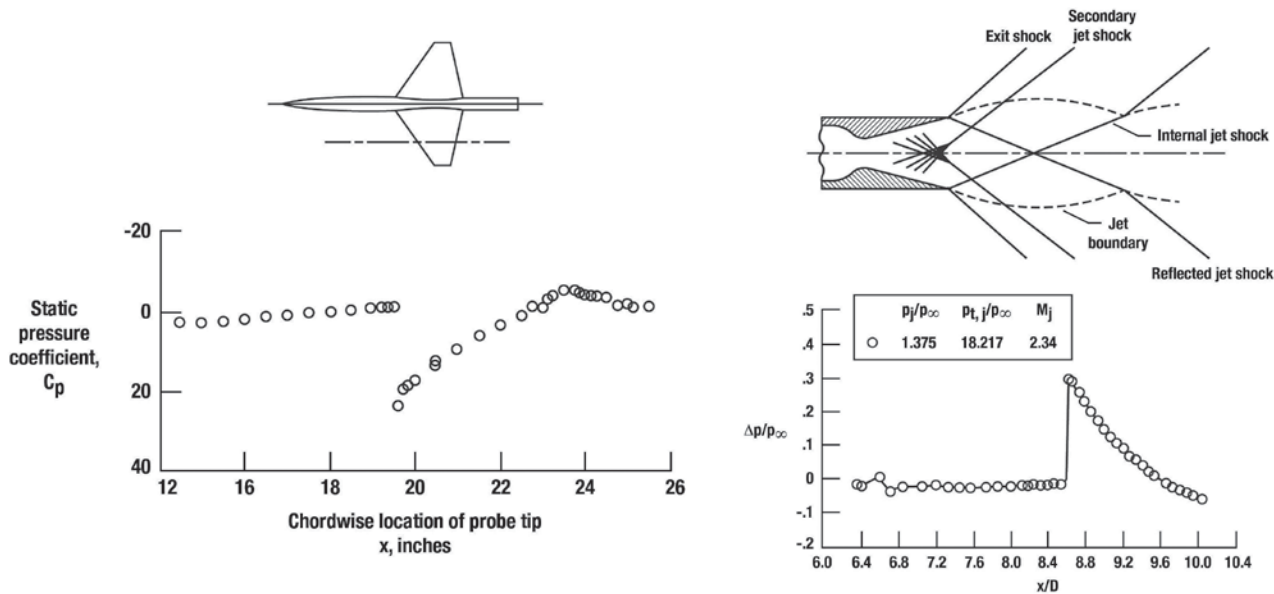


Figure 9.14. Flow-field pressure signatures obtained with the conical probes in 1959 and 1969 in the NASA LaRC 4- by 4-foot Supersonic Wind Tunnel.

Figure 9.14 shows that the conical probe is capable of sharply defining the initial shocks for both cases shown and that no rounding or smoothing of the shock is visible. In 2009, Bobbitt designed a conical probe, shown in figure 9.15 (ref. 9.14), for use in both wind-tunnel tests and flight to more completely and qualitatively describe the supersonic flow field surrounding a model or aircraft.

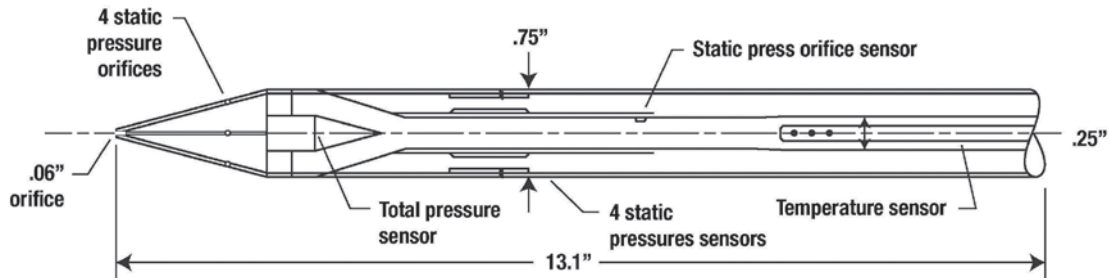
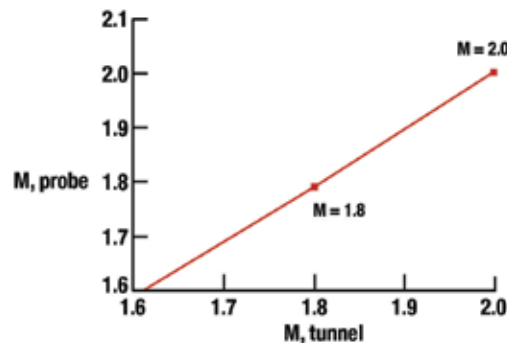


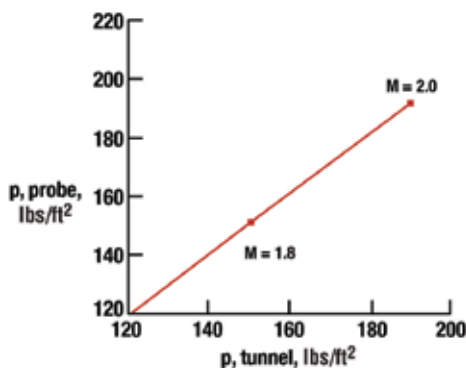
Figure 9.15. Schematic of conical probe with total temperature gage to provide free-stream pressure, Mach number, angle-of-attack, and free-stream velocity, static temperature, and speed of sound (ref. 9.14).

The version shown in figure 9.15 is for flight applications, a wind-tunnel version would be much smaller in diameter. The conical probe consists of miniature gages that measure static and total pressures from which Mach number and flow angle are obtained using the Euler equation solutions. The conical probe also contains a total temperature gage that will allow one to obtain sound speed and, thus, freestream velocity. Acceleration can be obtained by taking the time derivative of the velocity. The conical probe has several advantages over current probes as it can determine local Mach number, flow angle, total pressure and temperature, static pressure, velocity and speed of sound.

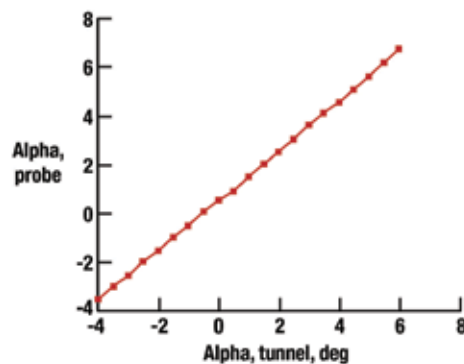
Some results of measurements acquired with the conical probe during wind-tunnel tests in the NASA LaRC 4- by 4-foot Supersonic Wind Tunnel (ref. 9.14) are presented in figure 9.16. It can be seen that the comparison between the conical probe values and wind-tunnel settings regarding tunnel Mach number (fig. 9.16(a)), pressure (fig. 9.16(b)), and angle of attack (fig. 9.16(c)) are in agreement.



(a) Probe versus wind-tunnel Mach number.



(b) Probe versus wind-tunnel pressure.



(c) Probe versus wind-tunnel angle of attack, Mach 1.6.

Figure 9.16. Comparison of conical probe measurements with tunnel settings (adapted from ref. 9.14).

In 1993, Bobbitt (ref. 9.9) invented a new type of wedge probe for use in acquiring sonic boom signatures in the wind tunnel and also for measuring the sonic boom signatures in the flow field surrounding an aircraft in flight. This device, shown in figure 9.17 (ref. 9.9), provides for the measurement of the flow-field pressure signatures in the wind tunnel free from shock and boundary layer influences.

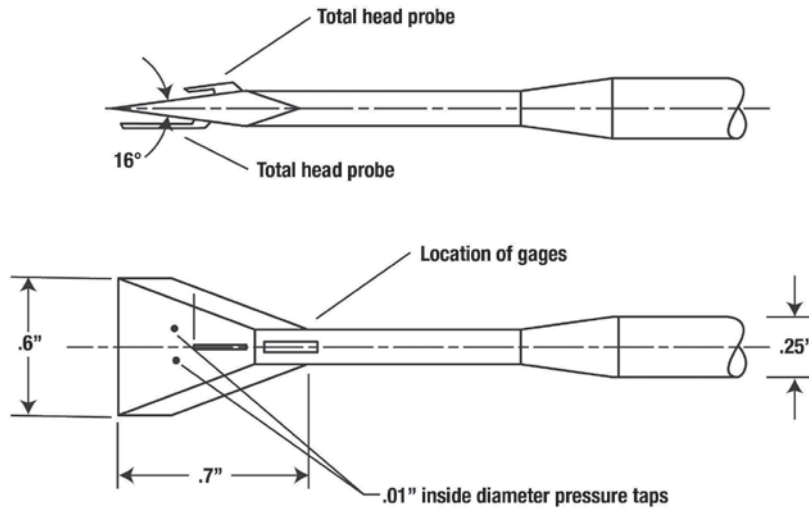


Figure 9.17. Supersonic wedge to provide Mach, angle-of-attack, and static pressure (adapted from ref. 9.9).

The wedge probe also provides flow Mach number and flow angularity. Initial tests of the wedge probe, using a sidewall mount, was conducted in the NASA LaRC 4- by 4-foot Supersonic Wind Tunnel and the results were compared with the wind-tunnel free-stream measurements. These comparisons are shown in figure 9.18 (ref. 9.9) and the correlation of the pressure and Mach number is excellent.

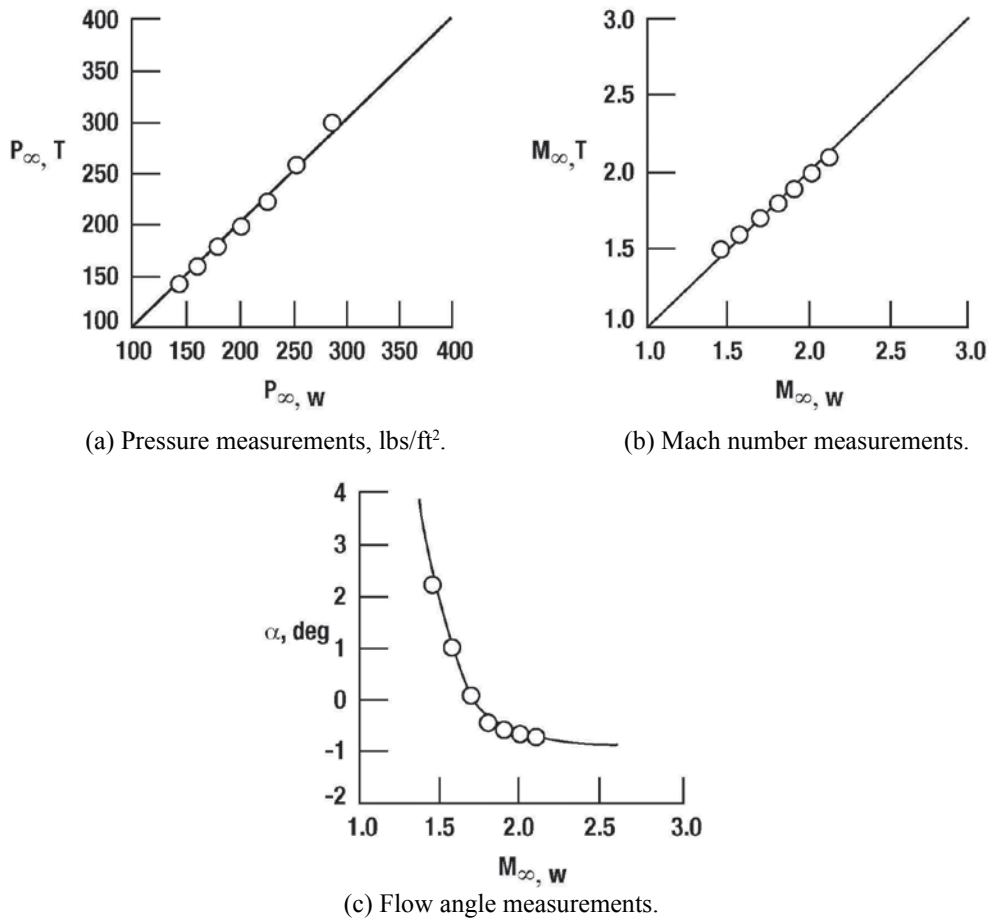
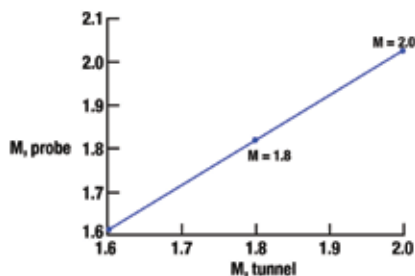
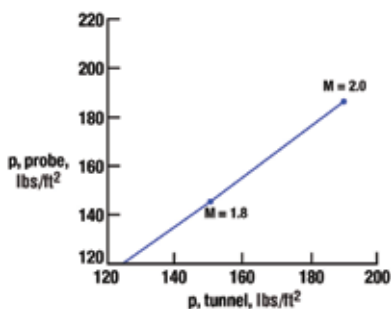


Figure 9.18. Comparison of wedge probe measurements with tunnel settings (adapted from ref. 9.9).

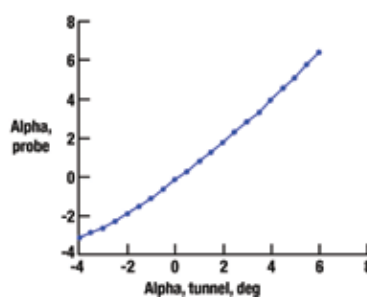
A larger-scale version of the wedge probe was built and tested in the NASA LaRC 4- by 4-foot Supersonic Wind Tunnel. Some results of measurements acquired with the wedge probe during wind-tunnel tests in the NASA LaRC 4- by 4-foot Supersonic Wind Tunnel (ref. 9.14) are presented in figure 9.19. It can be seen that the comparison between the wedge probe values and wind-tunnel settings regarding tunnel Mach number (fig. 9.19(a)), pressure (fig. 9.19(b)), and angle of attack (fig. 9.19(c)) are well correlated.



(a) Probe versus wind-tunnel Mach number measurements.



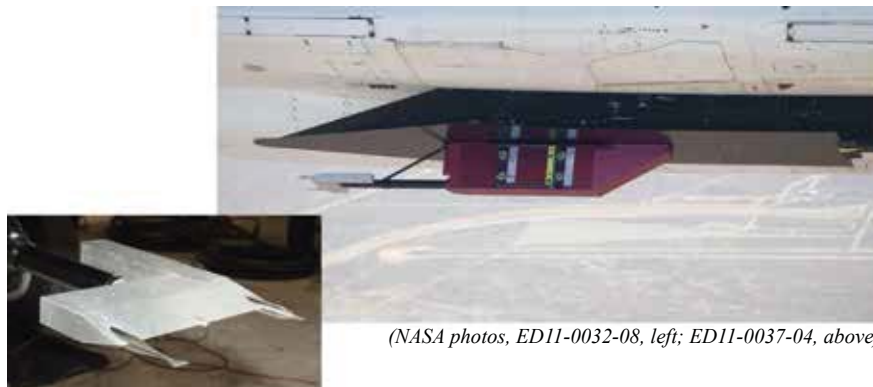
(b) Probe versus wind-tunnel pressure measurements.



(c) Probe versus wind-tunnel angle of attack, degrees, Mach 1.6.

Figure 9.19. Comparison of wedge probe and wind-tunnel free-stream flow qualities (adapted from ref. 9.14).

The conical and wedge probes were also installed on the NASA F-15B #836 testbed aircraft (ref. 9.14). They were located under the aircraft and mounted on the Centerline Instrumentation Pod (CLIP), as shown in figure 9.20. This arrangement was part of a structural integrity test of the probes. In the ultimate application of these probes, they would be mounted on the aircraft noseboom for the determination of all the free stream flow quantities.



(NASA photos, ED11-0032-08, left; ED11-0037-04, above)

Figure 9.20. Close-up of wedge and conical probe mounted on the NASA F-15 CLIP.

A sketch of the profile of this aircraft with major shocks emanating from the various components, which one would expect to occur, is shown in figure 9.21. As can be seen from the sketch, depending on whether the CLIP shock is ahead of, or behind the probes, there will be at least three or four strong shocks ahead of the probes. Thus, there is no possibility that the probes there can measure anything resembling free stream quantities. There are, however, measurements of some of these quantities by the airplane system and comparisons can be made to show the differences.

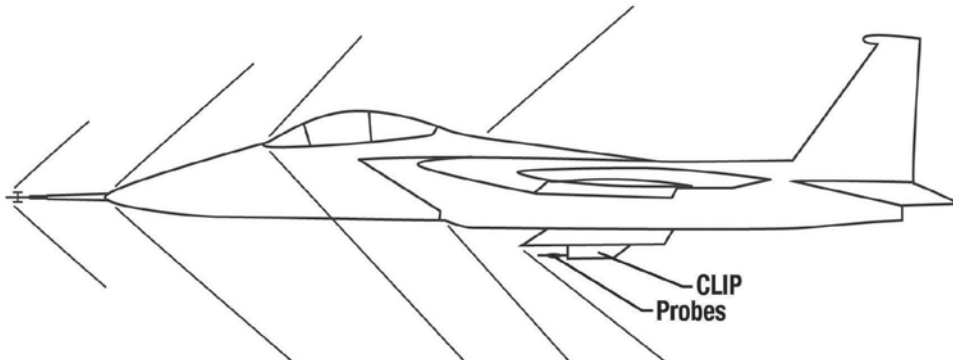


Figure 9.21 Sketch of F-15B aircraft showing the shocks off the various aircraft components ahead of the clip (adapted from ref. 9.14).

In figure 9.22 (ref. 9.14) are shown the measurements as a function of time for Mach number, total pressure, and angle of attack as measured by the conical and wedge probes along with similar measurements acquired with the aircraft system. The data were recorded during acceleration from Mach 1.3 to Mach 1.9 and deceleration from Mach 1.9 to Mach 1.3 at a constant altitude of 48,000 feet. Mach number data for the flight (see fig. 9.22(a)) shows the earlier time passage of the shocks off the CLIP edges over the wedge probe at ~116 seconds versus that for the conical probe at 150 seconds. Passage of these shocks in the other direction occurs at 320 seconds and 350 seconds for the conical and wedge probes respectively. There is also the pressure-gauge saturation limit for the wedge probe that was set at 10 lbs/in² that starts around 250 seconds and lasts until ~300 seconds (see figs. 9.22(a), (b), and (c)). Apparently, the 10 lbs/in² gauges in the conical probe were just below the saturation value set for those gages.

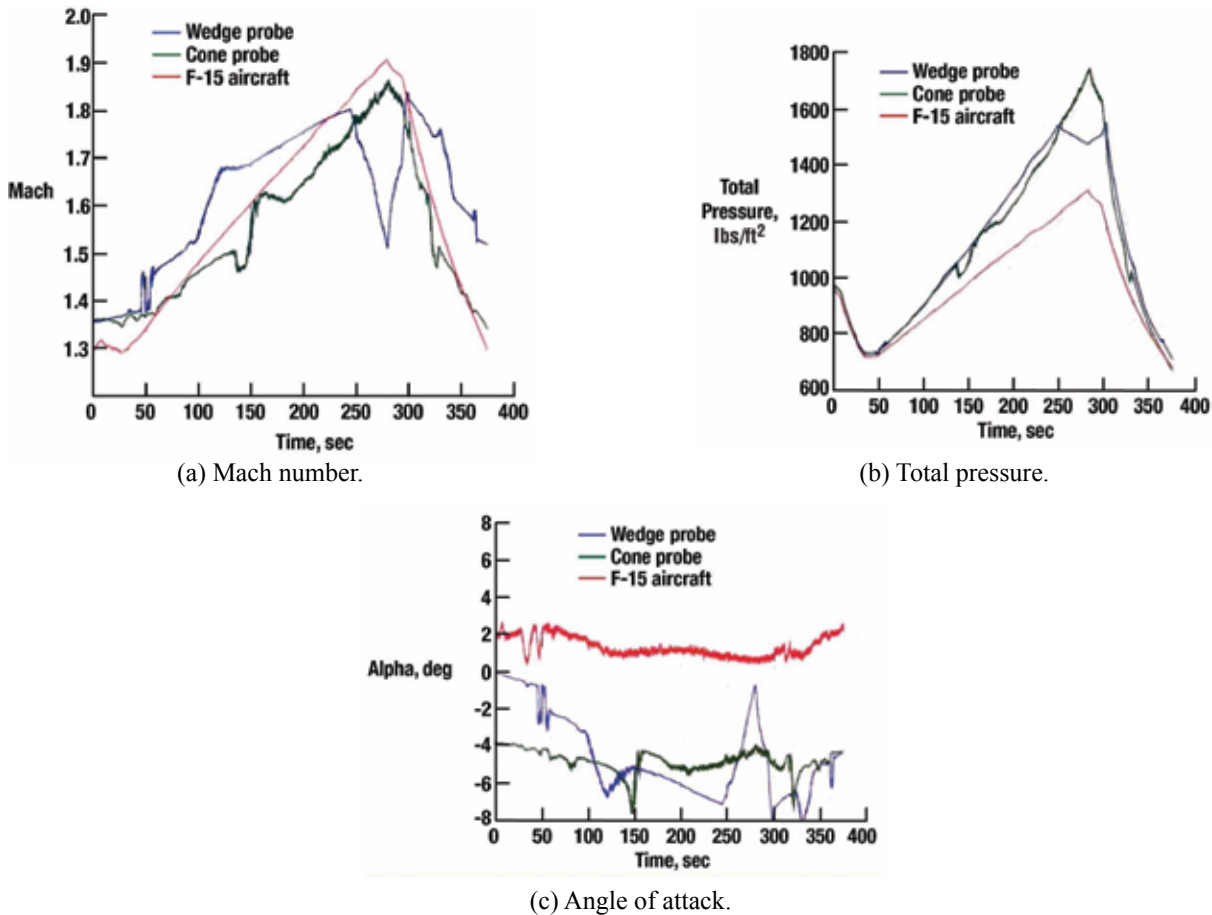


Figure 9.22. Comparison of computed time variation of Mach number, total pressure, and angle of attack for the conical and wedge probes (adapted from ref. 9.14).

The total pressure is essentially the same for the two probes (fig. 9.22(b)) consistent with the physics of fluid flow where no energy has been added or subtracted. Angle of attack for the two probes is plotted in figure 9.22(c). The differences mirror those of Mach number where the shock passage at times of 100 and 325 sec produce spikes in the variation of angle of attack.

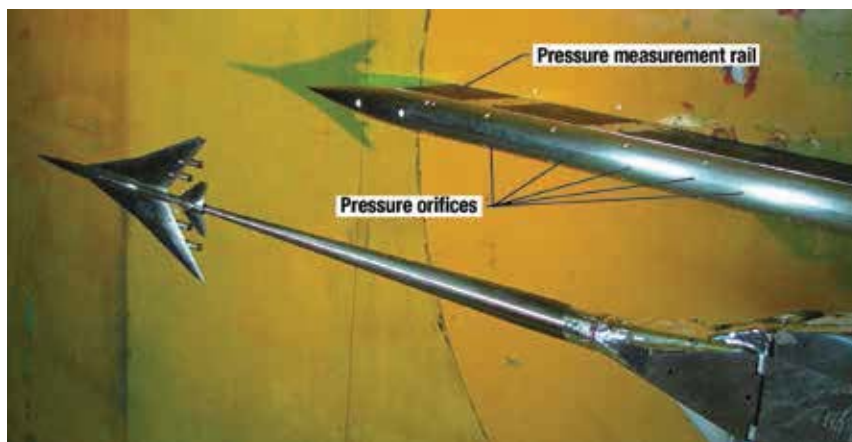
A significant feature of both the wedge and conical probes is that the measurement of Mach, angle-of-attack, pressure, and velocity are essentially instantaneous. As such, flow-field surveys, whether in wind tunnels or in full-scale flight, can be completed very rapidly thereby minimizing the influence of tunnel flow variations or aircraft motions on the measured pressure signature.

Pressure Measurement Rails

Slender conical measurement probes of the type shown in figure 9.12 are capable of acquiring pressure measurements with minimal flow interference, but obviously limit test measurements to a single location at a time. These singular measurements can limit test productivity and result in the measurement of a pressure signature over longer test times where changing tunnel conditions may occur. Researchers have developed and tested pressure measurement rails with closely spaced pressure taps over the length of the rail to measure a complete flow-field pressure signature. In a 2008 test in the ARC 9 - by 7-foot Supersonic Wind Tunnel, researchers investigated the use of pressure measurement rails versus the more traditional slender conical probes, as shown in figure 9.23 (ref. 9.15).



(a) Conical (2° half-angle cone) probe measurements (on- and off-track).



(b) Pressure measurement rail.

Figure 9.23. Pressure signature measurement devices mounted on the forward window blank at the Ames 9 - by 7- foot Supersonic Wind Tunnel (adapted from ref. 9.15).

While pressure measurement rails can address many of the limitations of singular conical probes, these devices can also introduce new measurement challenges such as flow interferences from the rail, pressure lag to the pressure sensors and longer tubing length required, and challenges with creating and determining a consistent reflection factor along the length of the rail. Conclusions from the 2008 tests at the ARC 9- by 7-foot Supersonic Wind Tunnel (ref. 9.15) indicated that while the pressure rails were far more efficient with respect to test time than the single conical probes, the probe data appeared to be less sensitive to tunnel flow variations such as humidity. Single probe data was more affected by non-uniformities in the flowfield during the longer test run and test efficiency due to the longer test times required. The results of the 2008 sonic boom study has led to a greater understanding of the issues related to pressure measurement rails.

In 2010, an improved pressure measurement rail called the RF 1.0 (reflection factor 1.0) rail was developed and is shown in figure 9.24 (ref. 9.16). Pressure signatures are measured on the apex of the rounded tip pressure rail with 420 axial static pressure orifices (0.015-inch diameter) along the length of the rail to obtain the sonic boom pressure signature. The rail was designed to have minimal flow disturbance and no reflection factor due a small edge radius (0.1-inch diameter), and minimize the reflections of the model signatures from the tunnel wall by the large standoff distance (14 inches).

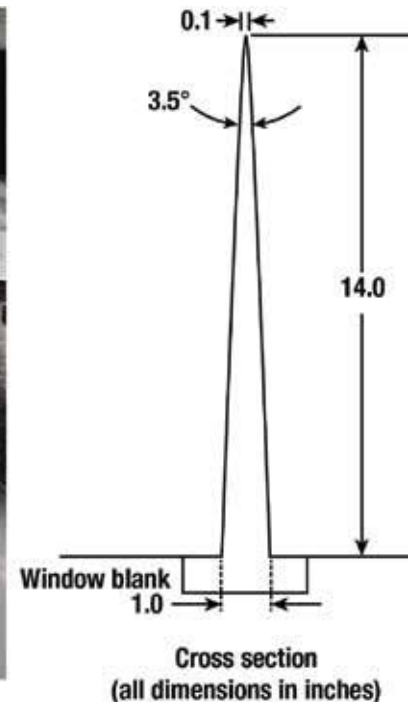


Figure 9.24. RF 1.0 pressure rail mounted on the aft window blank at the NASA ARC 9 - by 7-foot Supersonic Wind Tunnel (ref. 9.16).

Initial comparisons obtained in a 2008 test and presented in figure 9.25 (ref. 9.16) show reasonably good agreement between the RF 1.0 rail data, probe data, and CFD results for the forward pressure signature. Results for the aft signature are less conclusive, but the RF 1.0 rail appears to agree better with the CFD predictions than probe data. Final evaluation of the RF 1.0 rail and improvement of the test technique utilizing this rail are ongoing.

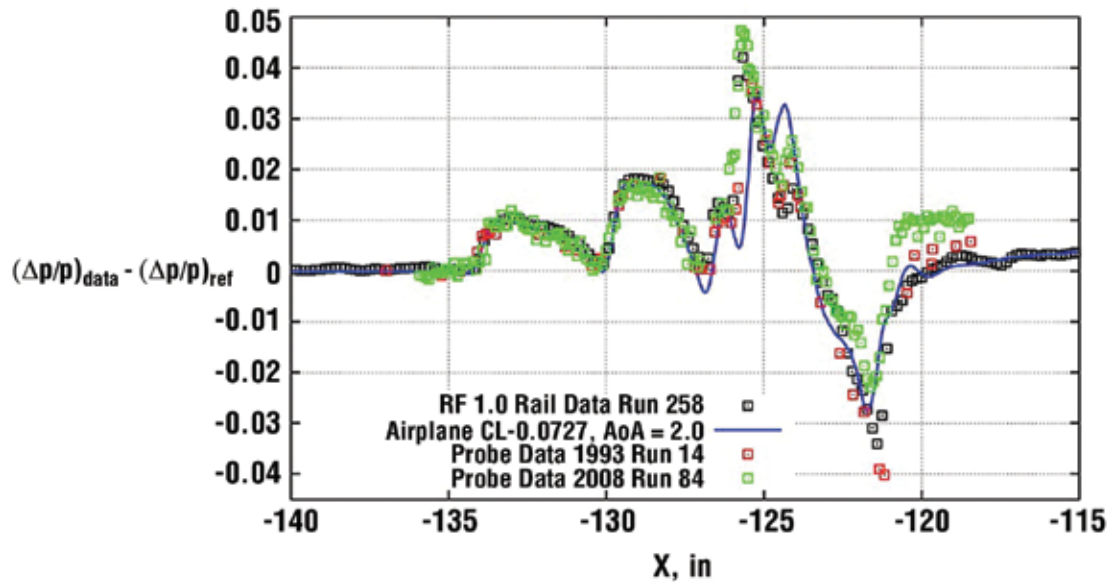


Figure 9.25. LBWT Configuration in NASA ARC 9- by 7-foot Supersonic Wind Tunnel (ref. 9.16), RF 1.0 rail data compared to conical probe data (1993 and 2008) and CFD results.

Model Support

The amount of effort that has been directed towards the reduction of the leading (bow) shock of a sonic boom signature as compared to the trailing (tail) shock is a natural consequence of an airplane's geometry. There are no control surfaces or engines up front on most supersonic cruise configurations, thus, the distribution of the fuselage's cross-sectional area and wing's lift and volume are the controlling elements. Due to the proximity of the model support and sting, an aft-end problem arises in wind-tunnel tests that are carried out to measure the pressure signatures below an aircraft. Exacerbating the problem is the fact that in order to make pressure measurements close to mid-field h/l 's of 5 to 10, where nonlinear effects are small, the model's length must be much less than the height of the tunnel (or if the wings are mounted vertically, much less than the width of the tunnel). Ferri and Wang (ref. 9.17) examined the effects of stings on pressure signatures to show that significant unrealistic effects can occur. Figure 9.26 from reference 9.17 gives an illustration of the modification that a sting can inflict on the rear shock of a pressure signature when propagated to the ground.

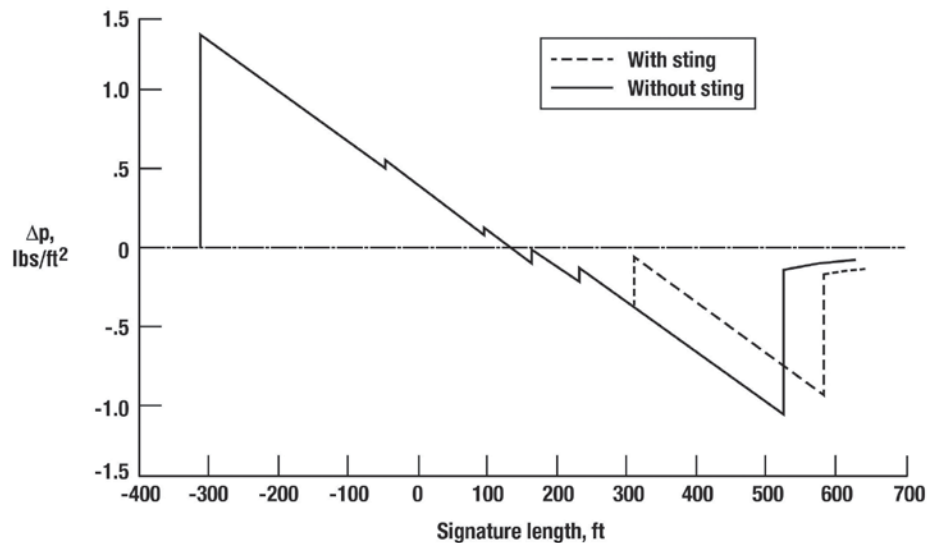
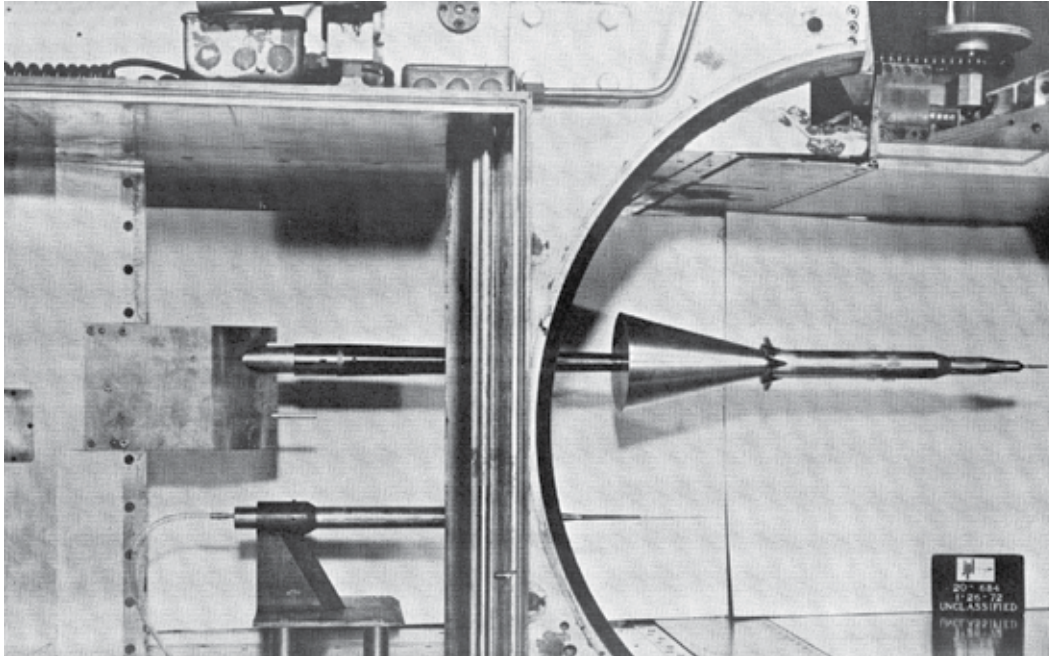
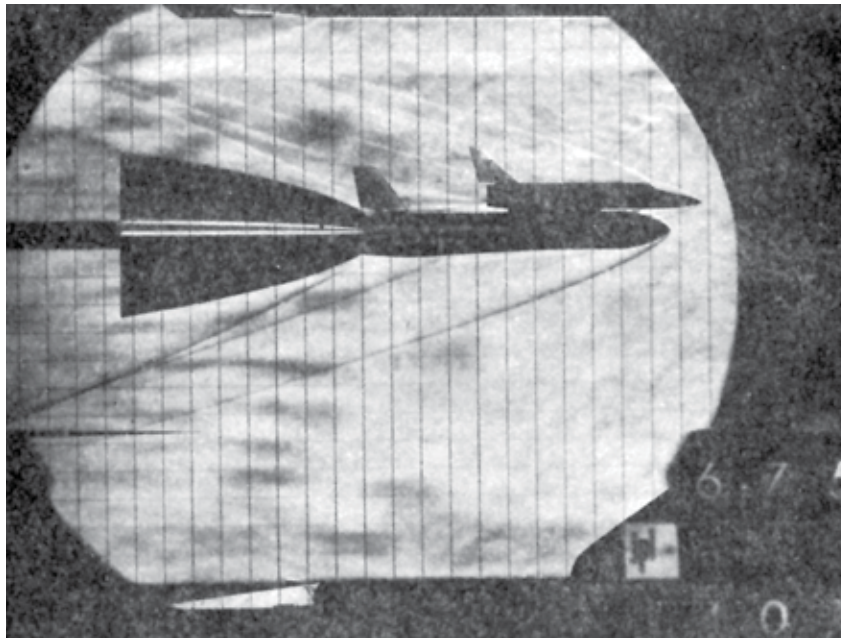


Figure 9.26. Effect of sting on a far-field signature (ref. 9.17).

One exception is the use of a sting, or stings, that have the geometry of the effective shape of the exhaust. In this case, the sting must be hollow to allow the flow from the flow-through nacelles on the aircraft model to pass through. Since each different engine has a different effective exhaust shape at a prescribed flight condition, the use of an exhaust-shaped sting has its limitations. Employing a series of stings representing different exhaust geometries could be an option. Simulation of the exhaust plumes associated with the ascent phases of flight of the Saturn V and Shuttle rocket-powered vehicles, as shown in figure 9.27 (refs. 9.18 and 9.19), present a much easier task relative to sting mounting arrangement.



(a) Model of Saturn V with simulated exhaust plume in JPL 20-inch tunnel (ref. 9.18).



(b) Shadowgraph of Shuttle launch configuration with simulated plume at Mach 4 (ref. 9.19).

Figure 9.27. Sting-exhaust plume simulation technique during tests in JPL 20-inch Supersonic Wind Tunnel.

There are wind-tunnel model mounts, other than ordinary stings, that may be used and are less intrusive with respect to the trailing shock and plume. As designers began to focus efforts on improved aft signatures and measurement of these aft signatures, the use of blade mounts for low-boom wind-tunnel models has emerged, as shown in figure 9.28 (ref. 9.20).



(a) Three-view drawing of wing-body-vertical low-boom aircraft concept with a blade mount.



(NASA photo)

(b) Installation at the NASA LaRC 4-by-4-foot Supersonic Wind Tunnel.

Figure 9.28. Gulfstream wind-tunnel model of low-boom aircraft concept with a blade mount (ref. 9.20).

Design of the blade mount becomes an integral part of the model design to minimize the effects of the blade mount on the aft signature of the wind-tunnel model. To date, blade mounts tend to exit the top of the model and swept with the Mach lines as much as possible to minimize the effect of the blade on both the off-body acoustic signature and model/mount interference effects. As one might expect, blade mounts are used to minimize cross-sectional area of the blade while meeting the structural requirements of the test facility. Data from the 2008 test of the Gulfstream wind-tunnel model with a blade mount are shown in figure 9.29 (ref. 9.20). Schlieren imagery and near-field pressures support the use of the blade mount and confirm that the aft features of the model were captured in the under-track signature.

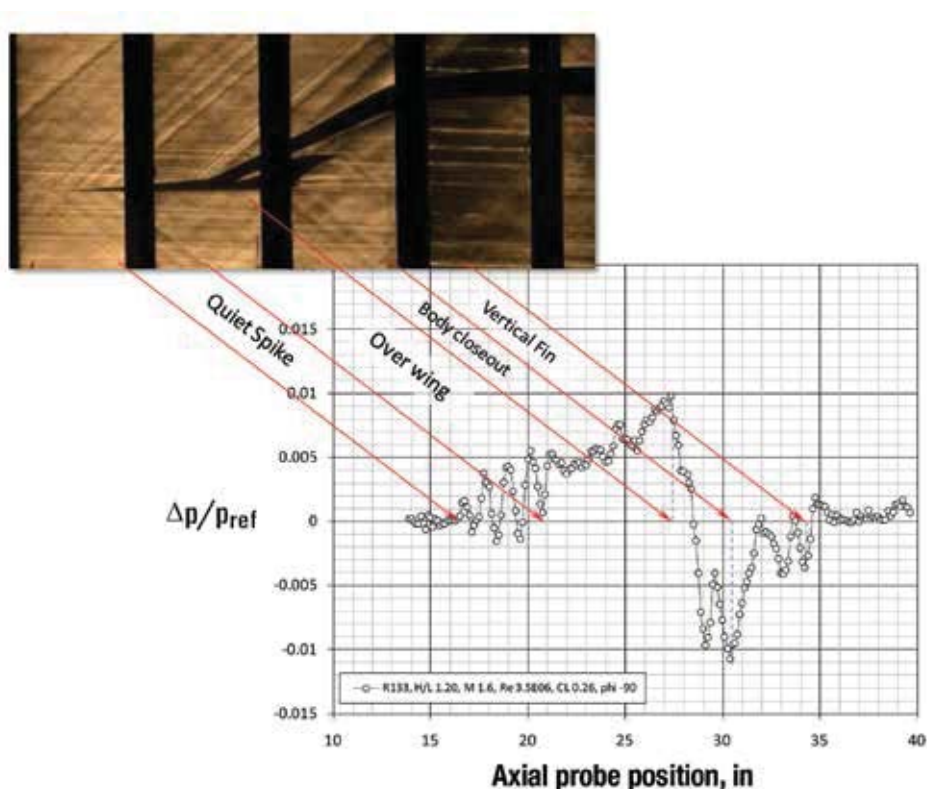


Figure 9.29. Schlieren and near-field signature data of Gulfstream wind-tunnel model with blade mount (ref. 9.20).

Due to the shift between the sting and model axis of revolution, test techniques must be adapted to obtain off-track measurements via adjustments to the wind-tunnel model angle of attack and roll angle in the tunnel. Overall, the use of blade mounts for low-boom models is likely to continue as an improved approach to achieve better understanding of the aft shock and plume features, and improve the fidelity of aft shock and plume modeling.

Ballistic Range – Free Flight Models

Another means of avoiding the trailing shock interference problems associated with sting-mounted wind-tunnel models is to launch free-flight models into a ballistic range. Such a simulation technique allows for much larger models, thus improving configuration fidelity and, in conjunction with a large ballistic range, allow for flow-field definition at larger distances from the model trajectory and permit the use of stationary microphones. The ability to vary the medium within the ballistic range is also a possibility as regards to investigating atmospheric influences or focusing effects.

A schematic of a light gas gun-ballistic range is shown in figure 9.30 (ref. 9.21). The major components are the pump tube, launch tube, an 8-foot diameter blast receiver tank and a range tank. A light gas gun, designed to generate high velocities, is used to propel the models at Mach numbers greater than 3. A large diameter piston is used to force a gas, helium or hydrogen, through a smaller diameter barrel containing the model aircraft enclosed in a sabot that breaks away after it leaves the barrel. The piston is powered by gun powder and a rupture diaphragm is used as the valve. At Mach 3 and lower, the gun is not used as a light gas gun. The range tank was 10 feet in diameter and 100 feet long and it operated at pressures of 10 atmospheres or evacuated to 3 mm Hg.

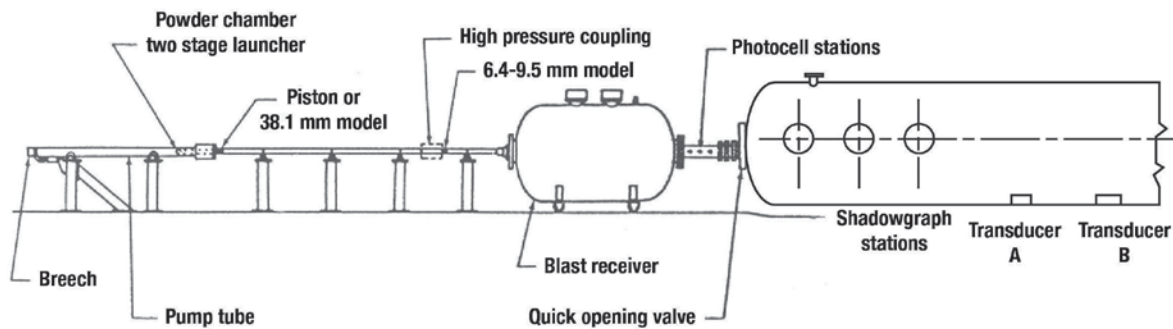


Figure 9.30. Sketch of light gas gun – ballistic range setup (adapted from ref. 9.21).

Three shadowgraph stations were available to record simultaneous horizontal and vertical shadowgraphs of the contour of the model and its angular orientation. Transducers were also located within the range tank downstream of the shadowgraph stations. A typical arrangement of the microphones can be seen in figure 9.31 (ref. 9.21).

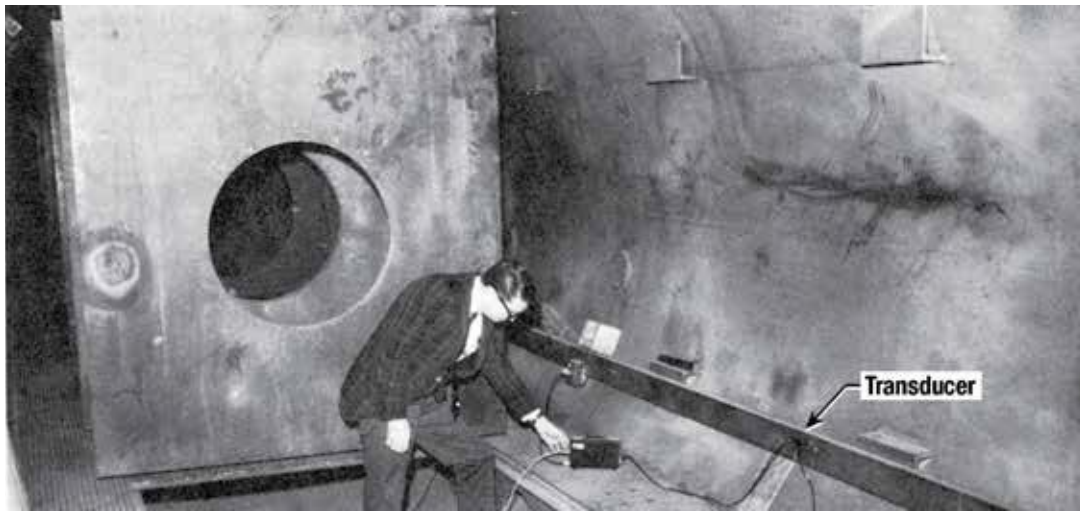
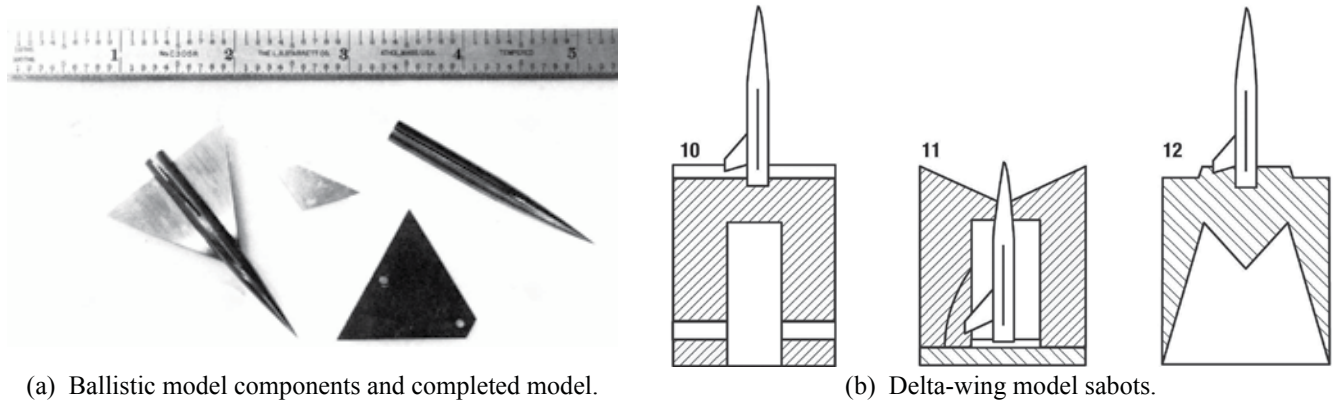


Figure 9.31. Test arrangement and microphone locations (ref. 9.21).

The model size was chosen to be compatible with the 38-mm diameter launch tube. A view of a delta-wing model and its components, along with the three sabot designs used to launch the models, is shown in figure 9.32 (ref. 9.21). The models (fig. 9.32(a)) had a length of about 2.0 inches and a span of about 1.3 inches. Considerable testing was performed to establish the best sabot design. The cantilever designs 10 and 12, shown in figure 9.32(b), failed completely in that the model was destroyed before it entered the range tank. It was found that Sabot 11, depicted in the center of figure 9.32(b), gave successful results with minimum contact with the model.



(a) Ballistic model components and completed model.

(b) Delta-wing model sabots.

Figure 9.32. Photographs of delta-wing model and sabot designs used in ballistic range tests (adapted from ref. 9.21).

Tests were conducted to assure there would be no danger of sabot impact damage to the transducer. The most promising results were obtained by launching the models into the range tank at low pressures. An example is shown in figure 9.33 (ref. 9.21). Because of the optical arrangement of the shadowgraph system, a double image of the model, as seen in the upper portion of figure 9.33, is sometimes acquired depending upon the model location in the field of view. The model flight was noted to be remarkably smooth with no observable pitch, yaw, or roll when the sabot was fully clear of the model.

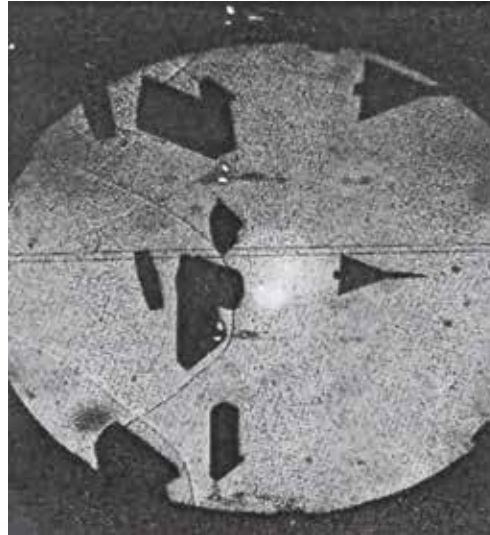


Figure 9.33. Shadowgraph of delta-wing launch and sabot breakaway (shot 34, Mach 3, tank evacuated to 20 mm Hg) (adapted ref. 9.21).

Considerable effort was expended on the selection of the proper transducer and its mounting arrangement. Of all the commercially available transducers, it was found that the capacitance type transducer was best suited for the research. An oscillograph trace of the sonic boom signature from the delta-wing model is provided in figure 9.34 (ref. 9.21).

The signature period observed in figure 9.34 is on the order of 175 μ sec with an overpressure level of about 65 lbs/ft². A slight ringing can be observed at the bow and tail shocks and a bow shock rise time of about 10 μ sec is noted, both attributed to the transducer limitations.

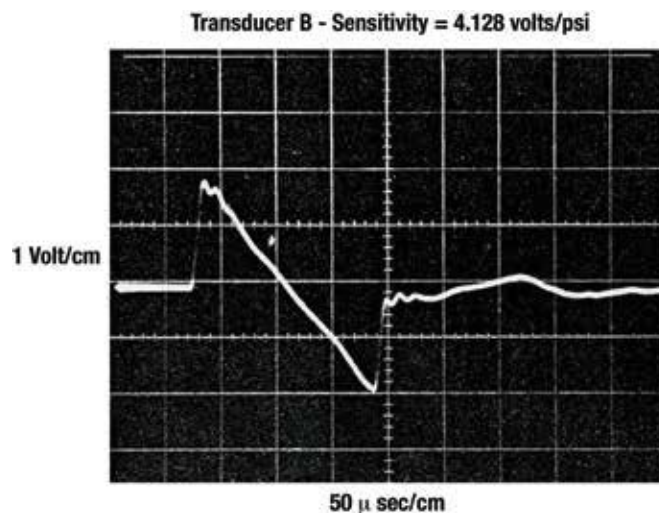


Figure 9.34. Oscillograph trace of sonic boom signature from delta-wing model. Shot 52, Mach 2.92 (adapted from ref. 9.21).

In figure 9.35, shadowgraphs of ballistic range shots of the delta-wing model are shown representing a successful launch, shown in figure 9.35(a), as compared to an unsuccessful launch shown to the right in figure 9.35(b). The results from both the horizontal and vertical shadowgraph views of the successful flight showed that the model flight trajectory experienced no pitch or yaw (fig. 9.35(a)) and although some roll was recorded, good pressure signatures were obtained. On the other hand, when similar launches were repeated (see fig. 9.35(b)) a roll rate of 300 deg/sec was recorded. It was concluded that the motion of the delta-wing models, which varied from smooth to highly erratic oscillatory in nature, was not attributable to model tolerances, sabot design, or light-gas gun tolerances. Attempts were made to arrest the models at the end of flight in order to minimize model fabrication costs, by using varying thicknesses of urethane foam. However, it was found that the model structural integrity could not be maintained.

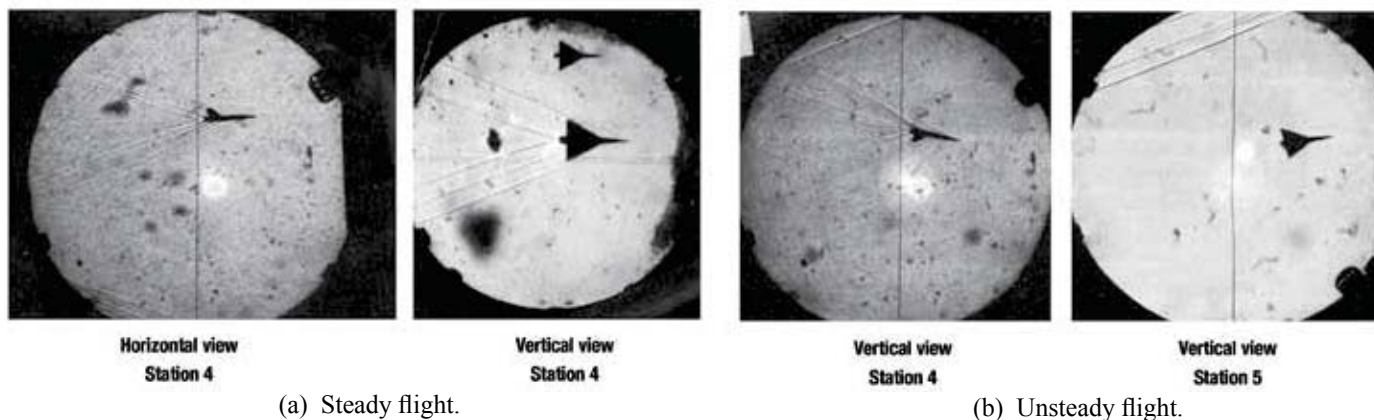


Figure 9.35. Shadowgraphs of delta-wing launch in ballistic range (adapted from ref. 9.21).

Testing of the wing-body models in the ballistic range was found to be impractical for several reasons, the foremost among them was the problem of launching stable flights. Model integrity relative to model recovery would be costly. Model size was such that a short duration N-wave signature (about 0.175 msec) would limit model geometric integrity and require transducers with very high frequency response.

However, some limited testing was conducted to explore the possibility of launching bodies of revolution representing the equivalent area distributions, A_e , of several shaped sonic boom signatures. It will be shown in the following section on modeling turbulence influences on sonic boom N-wave signatures that useful experiments on turbulence effects on shaped signatures could be acquired by launching bodies of revolution in the ballistics range.

Signature Distortions by Turbulence

Certain sonic boom issues are both difficult and costly to resolve by means of full-scale supersonic overflights and could require a lengthy time period to establish a credible research database. One such issue is the influence of the atmosphere on sonic booms, especially its turbulent nature in the initial 5000 feet of the earth's surface. Distortions of sonic boom signatures result in boom levels that are much greater than the predicted levels or much less.

Recall from Chapter 2, it took some 1625 supersonic flights and over 12,000 boom measurements, over about a quarter of a century, to acquire a sufficient database to establish the statistical variation of N-wave sonic booms. However, these results, which were obtained in specific areas of the United States, do not necessarily represent world-wide conditions of turbulence. More importantly, they apply only to N-wave type signatures and, except for the few flights of the SSBD, no database on the influence of turbulence on low-boom shaped signatures is available. It is possible that this particular sonic boom issue could be assisted through ground-based experimental simulation.

Experiments simulating turbulence effects have been performed in the past using a variety of techniques but always involving N-wave signatures. In this section, several different simulation techniques used in the past will be addressed, including – the use of ballistic ranges and projectiles to generate the N-wave and jet flows to simulate turbulence, use of a gas-filled soap bubble to refract and defract N-waves produced by spark discharges, use of a shock-tube horn-type sonic boom generator in conjunction with an air jet to simulate turbulence, shock-tube actuator and grid generated turbulence, firing projectiles into the real atmosphere, and use of a spark discharge to provide the N-wave and a fan-plenum chamber with slot jet discharge to simulate turbulence. Some of the key findings and limitations of each of these techniques will be presented.

Ballistic Range – Projectiles and Duct Flow Turbulence

The earliest model experimental study regarding the influence of turbulence in the lower layer of the atmosphere was performed by Bauer and Bagley in 1970 (ref. 9.22). The boom signature measurements with turbulence are of two basic types, those generated by jet interaction and those generated by thermal interaction. Every attempt was made to relate the model results to the full-scale flight measurements regarding shock thickness, turbulent scale, and sonic boom signature overpressure and period. In fact, the authors dedicate an entire section of the report on scaling laboratory sonic boom work.

Their experimental setup, shown in figure 9.36 (ref. 9.22) utilized the ballistic range at the McDonnell Douglas Aerophysics Laboratory at El Segundo, Calif. The range was enclosed within a barricade wall, with inside dimensions of 23 feet by 22 feet, and with a ceiling height of more than 10 feet. Sonic boom signatures were generated by firing projectiles at Mach numbers from about 1.5 to 3.0. Pressure signature measurements were made at three positions at approximately 6-inch spacing along a ground plane 15 feet below the projectile trajectory. Turbulence was generated from a jet flow duct exiting across the ground plane. Shadowgraph pictures were also obtained. A series of projectile shapes were used, as shown in figure 9.37 (ref. 9.22), and included 22, 30, and 46 caliber bullets and three machined projectiles of 0.22, 0.457, and 1.5 inches in diameter.

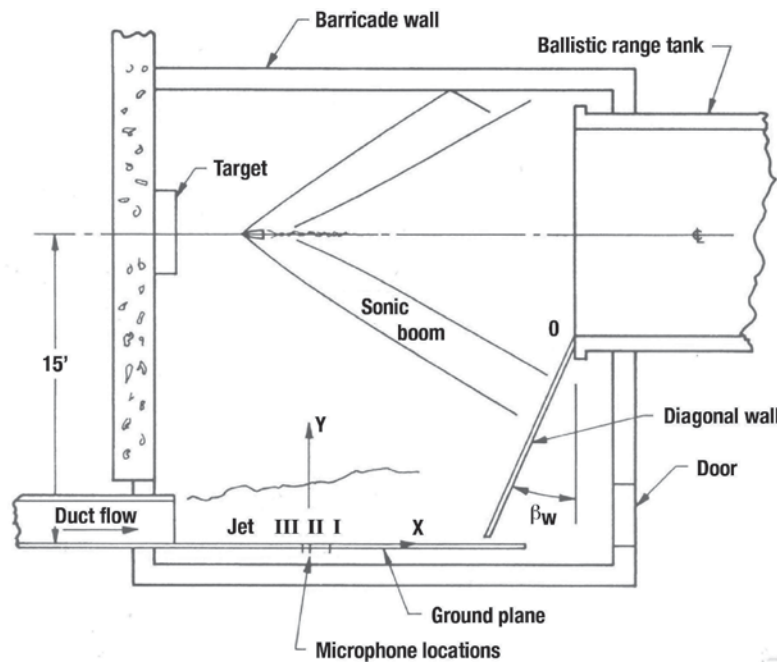


Figure 9.36. Schematic of ballistic range setup showing range tank, barricade, jet flow duct, ground plane, and measurement locations (view looking in the +z direction) (ref. 9.22).

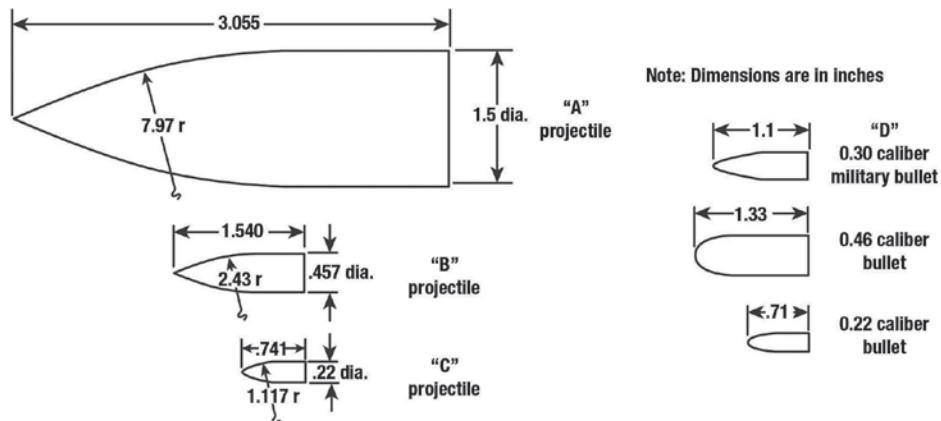


Figure 9.37. Bullet and projectile shapes used in experiment (measurement in inches) (ref. 9.22).

Projectile A was launched from a ballistic range light gas gun and the other projectiles and bullets were rifle launched. The Mach number was controlled by varying the powder charges. For the 15-foot distance at which measurements were taken, the ground plane reflected overpressure ranged from about 17 to 72 lbs/ft². Signature lengths were the order of 160 μ sec to 800 μ sec. The authors noted that the A projectile, which was more dangerous and difficult to fire, also generated overpressures many times larger than the full-scale values observed from full-scale flight tests and had a rather low sensitivity to turbulence because of the mismatch between the shock thickness and the model turbulence generated.

The duct that provided flow near the ground plane was 24 inches by 24 inches and was termed the “24-inch nozzle”. Four other nozzles were designed and attached to the end of the duct nozzle and these are depicted in figure 9.38. Each of the four nozzles has different contraction ratios and size, each producing different turbulence structures. The 4-inch nozzle terminated in a grid made up of 3/4-inch dowels on 4-inch centers. The 6-inch nozzle used a honeycomb grid with 6-inch cells. Two high-speed nozzles were designed, one that exited above the ground plane and the other at the ground plane. Flow velocities of from 82 ft/sec to about 240 ft/sec were acquired depending upon the nozzle inlet size.

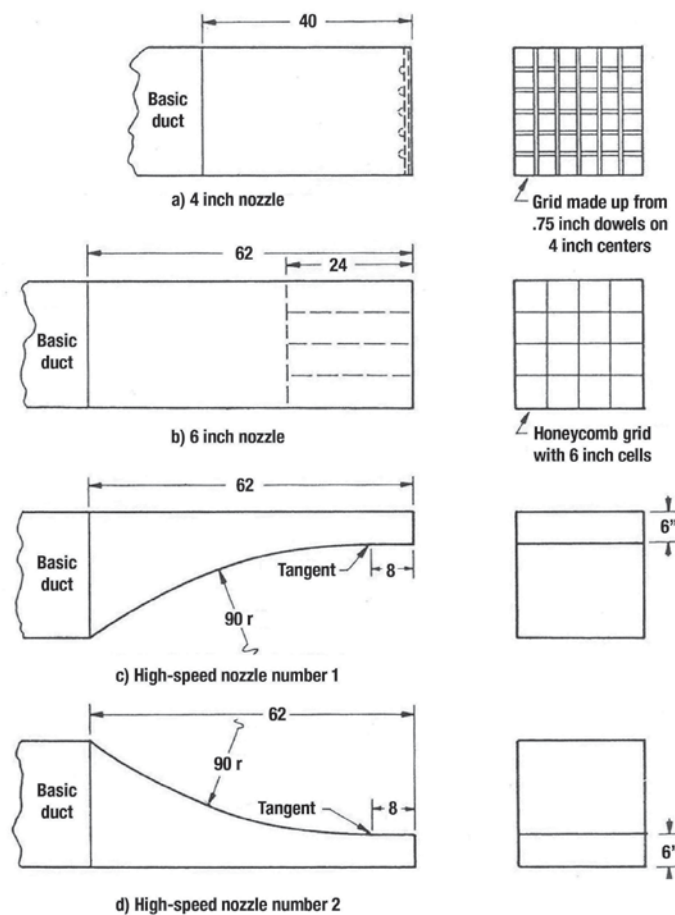


Figure 9.38. Sketches of various flow duct nozzles (ref. 9.22).

The authors noted that the design of the thermal generator presented a unique challenge regarding the upward velocity of the natural convection of the heated air possibly acting as a shear layer rather than a thermal interaction with the sonic boom. They finally designed the generator shown in figure 9.39 (ref. 9.22). Two such thermal generators were built and used in the experiments and were located in the z plane at 20 inches normal to the barrier floor and about 7 inches and 13 inches in the x and y axis respectively. Experiments related to the thermal work were also performed using a rising column of helium instead of heated air. The helium was injected vertically upward from a 0.031-inch nozzle attached to the plenum chamber. The low molecular weight of the helium was expected to alter the boom signature in much the same way as the hot air. The authors state that the advantage of the helium setup was in the small size of the nozzle compared to the large size of the thermal generator.

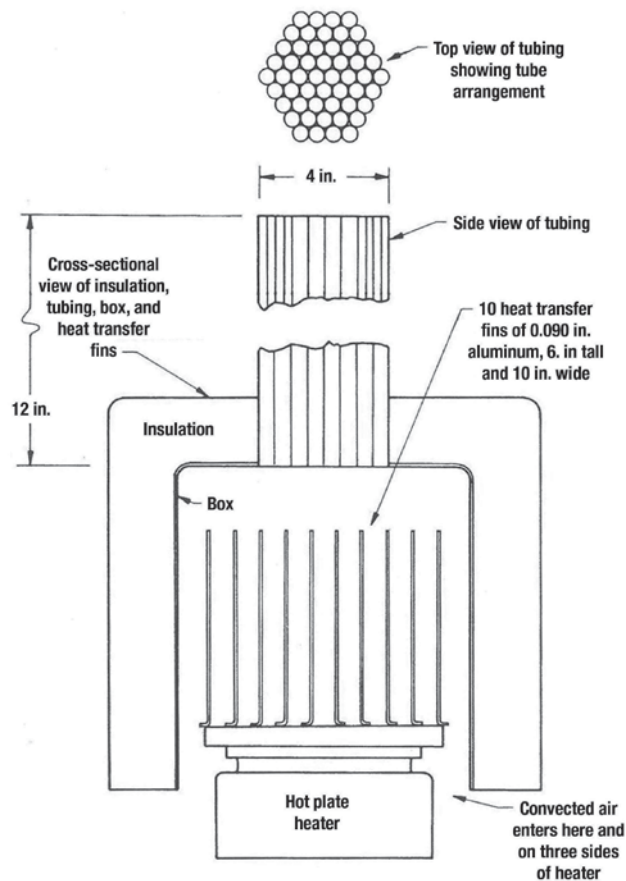


Figure 9.39. Thermal generator design (ref. 9.22).

Some sonic boom measurements with and without turbulence generated by jet interaction are presented in figure 9.40 (ref. 9.22) for microphones I and II spaced 6 inches apart along the ground plane. As expected for the no duct flow case (fig. 9.40(a)) the two measured no turbulence signatures retain their N-wave shape and have nearly the same overpressure of about 18 lbs/ft² and periods of 170 μsec. On the other hand, the N-wave signatures that have passed through the turbulence (fig. 9.40(b)) are distorted and vary in character from a peaked, almost spiked, to rounded wave forms with the overpressures varying from about 25 lbs/ft² down to about 12 lbs/ft². The distortions observed on the bow shock are repeated at the tail shock. Such activity is essentially replicating full-scale flight experience in the real atmosphere.

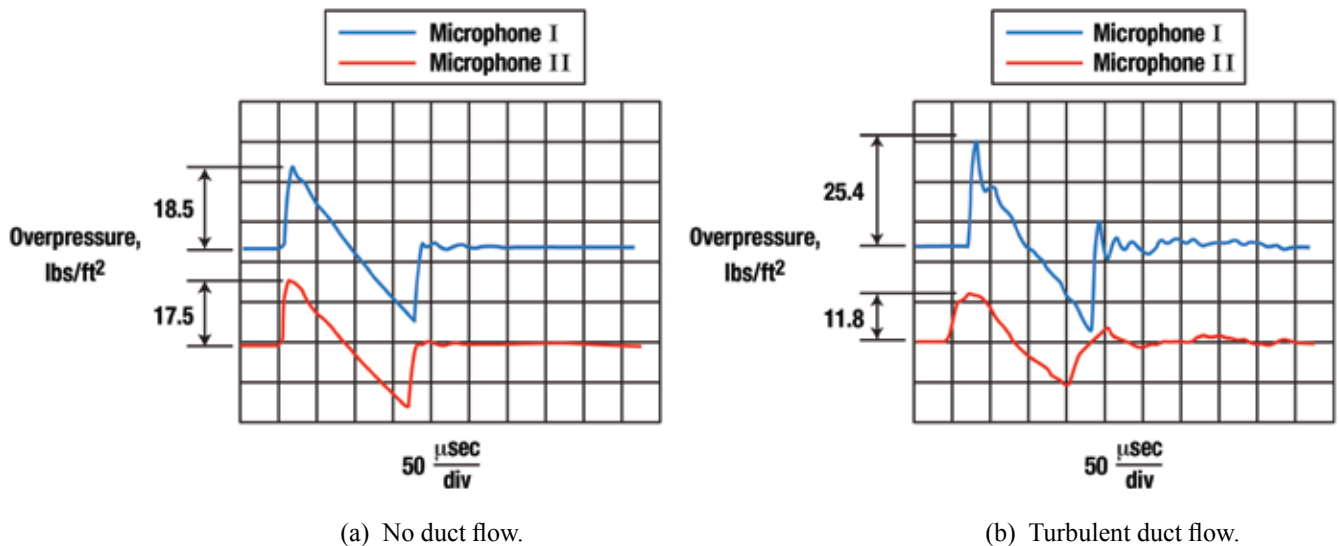


Figure 9.40. Sonic boom signatures from 0.22-caliber bullet at Mach 3 (adapted from ref. 9.22).

The probability distributions of the sonic boom signature overpressure and bow-shock rise time from many measurements on a 0.22-caliber bullet traveling at Mach 3.0 through three levels of duct flow generated turbulence are given in figure 9.41 (ref. 9.22). The authors stated that the slopes of the data regarding overpressure variability (fig. 9.41(a)) are generally less than corresponding data at Mach 1.6 for full-scale flight results. This would indicate that the experimental turbulence intensity created longer perturbations in the model scale than for full-scale results. Examination of the probability distribution of rise-times, shown in figure 9.41(b), indicate that for N-waves, turbulence increases the rise time and this finding is consistent with other model experiments and full-scale flight results. Sonic boom signatures measured with and without thermal interactions are presented in figure 9.42 (ref. 9.22). The projectile was a 0.46-caliber bullet at Mach 2.16.

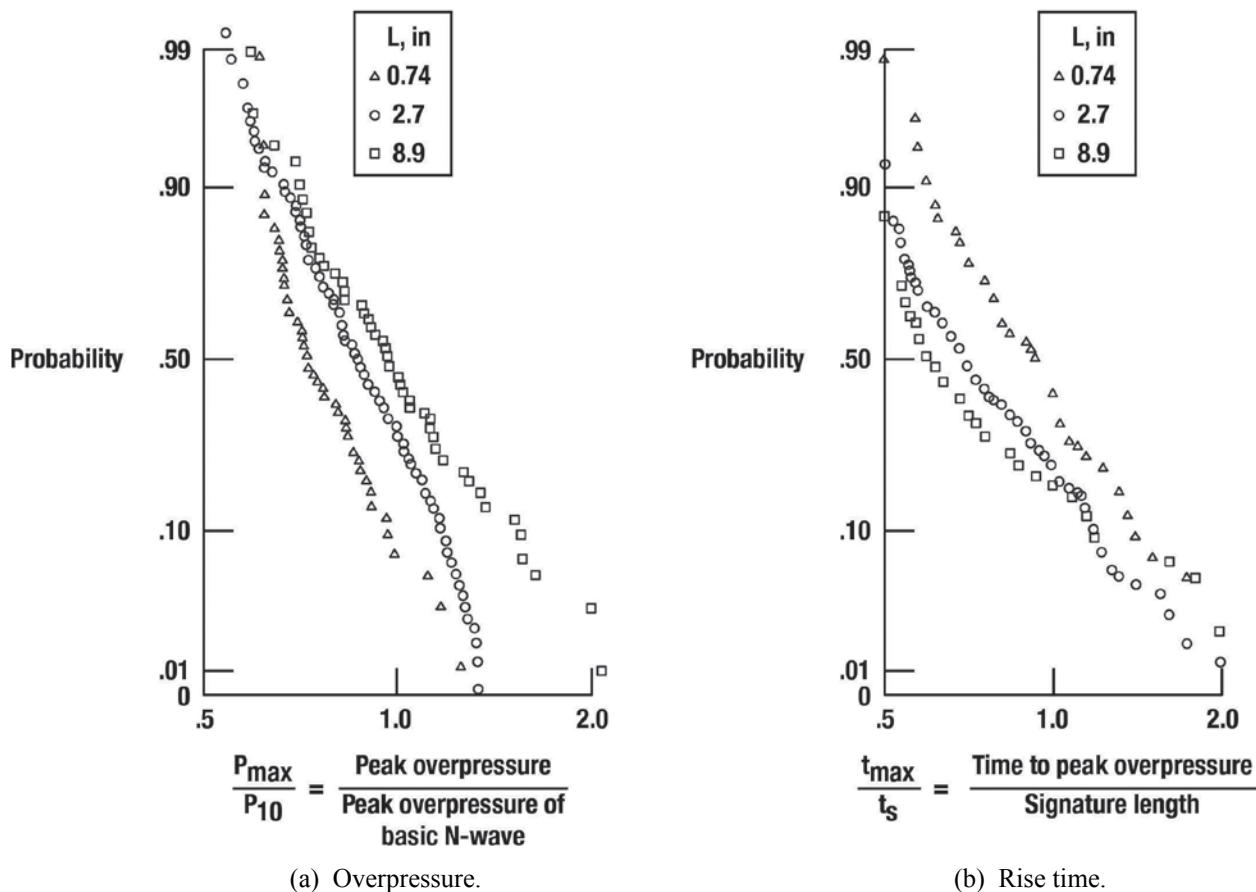


Figure 9.41. Probability distributions of overpressure and rise time from 0.22 caliber bullet at Mach 3.0 (adapted from ref. 9.22).

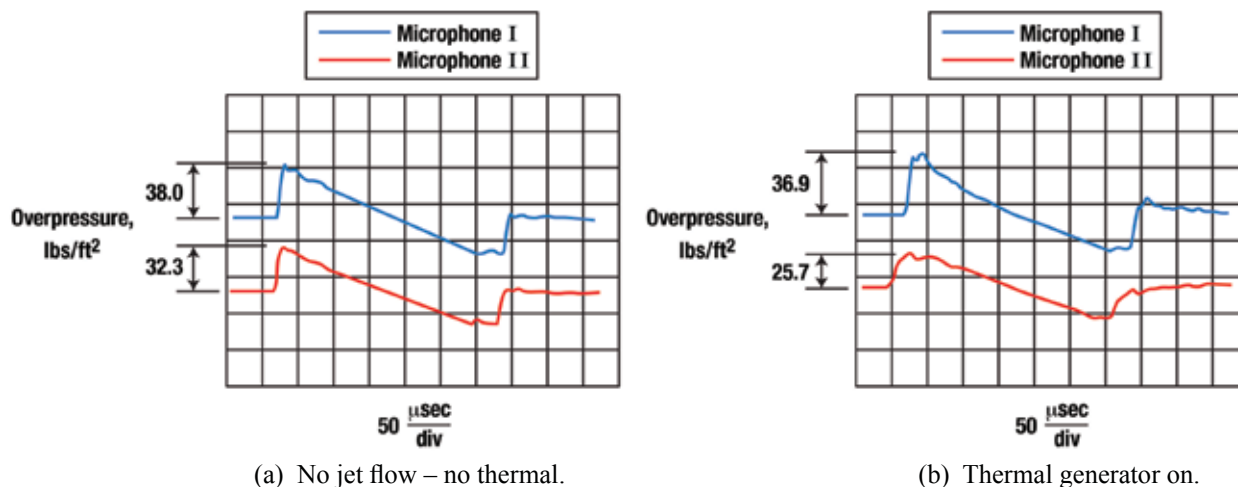


Figure 9.42. Sonic boom signatures from 0.46-caliber bullet at Mach 2.16 (adapted from ref. 9.22).

For the no-jet thermal case, figure 9.42(a), relatively clean N-wave type signatures are observed with overpressures of about 32 and 38 lbs/ft, and a period of 310 μ sec, both twice the values associated with the 0.22-caliber bullet (see fig. 9.40). When the thermal generators are operating (fig. 9.42(b)), the signatures vary from slightly peaked to rounded. In all of the thermal tests using generators or helium, none of the signatures were as peaked or spiked as compared to when the N-wave signature passed through the duct flow turbulence. Similar results were also observed during full-scale flight tests in the desert when it was determined that the non-steadiness lower layer of the atmosphere was predominately a result of thermal turbulent conditions (i.e., surface conditions were hot with no sustained winds and few minimal wind gusts) or mechanically turbulent conditions (i.e., mild surface conditions with sustained winds and gusts) (ref. 9.23).

In summary, the Bauer-Bagley (ref. 9.22) ballistic range tests to replicate the full-scale flight measurements showing the atmospheric turbulence influences on boom signatures showed that signature distortions that were seen on the bow shock are repeated at the tail shock of the N-wave and are in agreement with the Crow theory (ref. 9.24) of frozen turbulence. For the model signatures to be geometrically similar to full-scale flight results, the ratio of N-wave rise time to signature period needed to be preserved. The full-scale value of this ratio for a large supersonic transport is about 250. In these tests, this ratio was 450 for one series of tests and 270 for another. It is stated that the main problem using this particular size ballistic range and projectiles for these studies was the limitation in frequency response of the microphones and scaling of the turbulence. A larger ballistic range and larger projectiles would ease microphone requirements and make the task of providing the proper turbulent scales more achievable.

It is believed that there are even more advantages of the ballistic range projectile experimental setup. Unlike experiments where the N-wave signature is provided via a spark device or shock tube, projectiles can be modeled so as to generate cylindrical and non-N-waves (i.e., shaped signatures). Such shaping has been predicted by Hague and Jones (ref. 9.25) and is illustrated in figure 9.43 (ref. 9.25). The shaped projectile could be gun launched using sabots. A projectile fired down a ballistic range generates cylindrical waves, like an actual aircraft, rather than the spherical waves of a spark source or the plane wave of a shock tube. A significant, quantitative, and needed database could be established well before any low-boom shaped vehicles are flown and would play an important role in the development of computer codes designed to compute the alteration of the boom signatures that pass through various turbulence models.

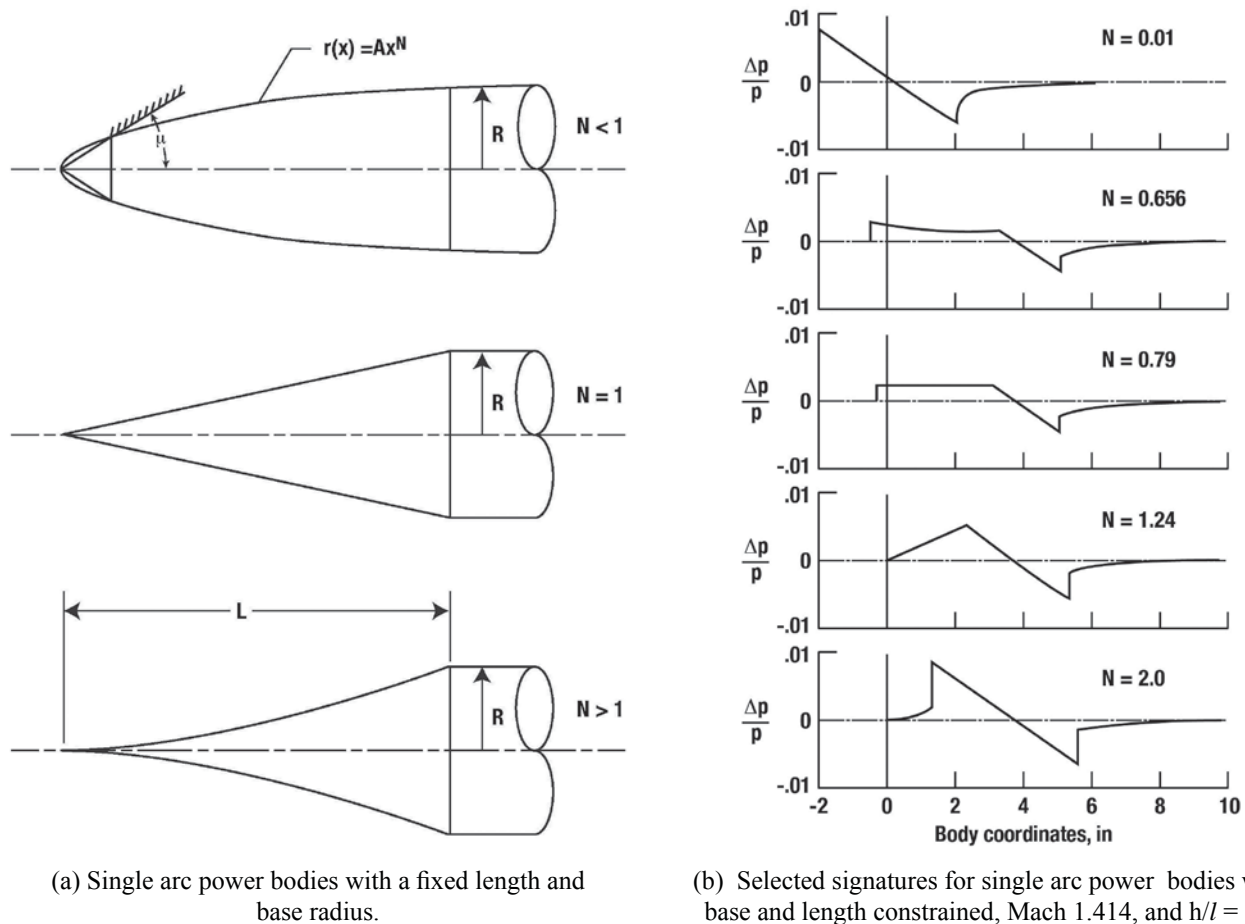


Figure 9.43. Examples of possible projectile shapes and resulting signatures (ref. 9.25).

Spark Discharge and Gas-Filled Bubble

About a year or so after the Bauer-Bagley experiments (ref. 9.22), Davy and Blackstock (ref. 9.26) conducted a set of model experiments to test Pierce's (ref. 9.27) explanation that sonic boom signature peaking and rounding are due to atmospheric non-homogeneities that act as converging and diverging lenses. They set out to observe the distortion of boom signatures resulting from speed of sound gradients in the atmosphere. Their experimental setup consisted of a gas-filled soap bubble to refract and diffract N-waves produced by an electric spark discharge. Figure 9.44 (ref. 9.26) illustrates the experimental setup, which consists of three main elements, a spark source, bubble, and microphones mounted on an optical bench. A gas laser (not shown in figure) was used for alignment. Each bubble was held by a ring of thin wire and surface tension caused the bubble to stick in the ring. Two different size rings were used to hold large (6.95 cm) and small bubbles, which permitted a variation in the propagation time of the N-wave through the two mediums. An example of measured signatures for the spark generated N-wave passing through a large argon and helium bubble along with the no bubble control shot is provided in figure 9.45 (ref. 9.26).

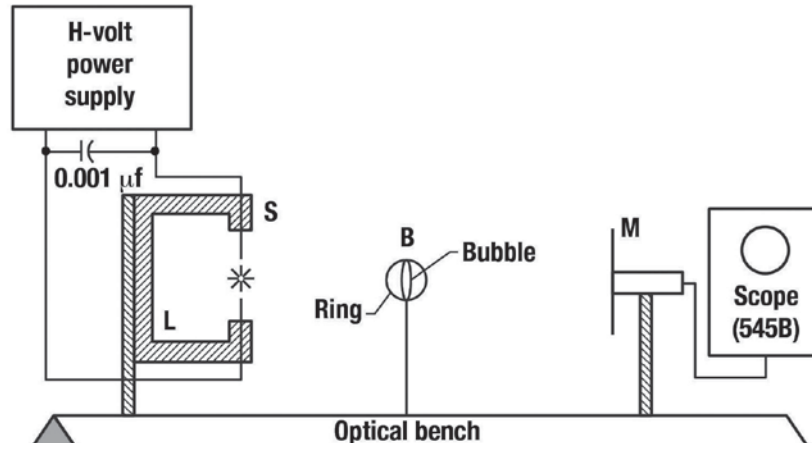


Figure 9.44. Sketch of apparatus. L is lucite mounting bracket, S is spark, B is bubble, and M is baffled microphone and preamplifier (ref. 9.26).

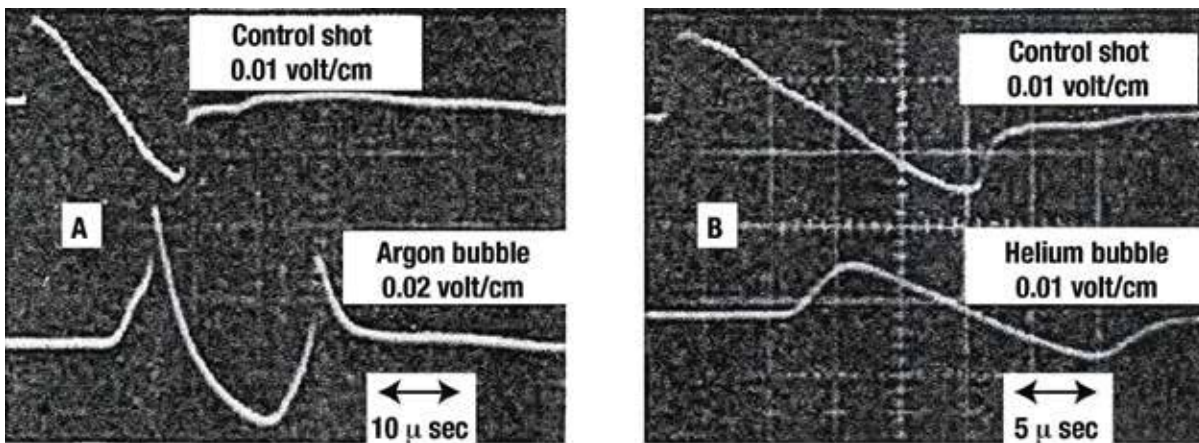


Figure 9.45. Waveforms received by microphones for large (6.35-cm diameter) bubbles. Upper trace in both A and B is control shot (no bubble in the wire ring). Bubble-microphone distance was 30 cm (ref. 9.26).

The top trace in each oscillograph trace is the control shot (no bubble) and it is seen that the signature is predominantly N-wave in shape. The experiment produced N-wave shapes with overpressures of about 34 lbs/ft² and a period of 20 μsec at a distance of 10 cm. At 60 cm, these values were about 4 lbs/ft² and a period of 26 μsec, respectively. Refraction and diffraction influences on the signature are noted by the authors – the argon filled bubble, acting as a converging lens, caused considerable peaking of the N-wave resulting in a three-fold increase in the overpressure. On the other hand, the helium filled bubble, acting as a diverging lens, resulted in considerable rounding of the N-wave and a reduced overpressure to about 70 percent of the control shot. In these experiments, they also stated that no rounded signatures were ever observed with the argon-filled bubbles. Notice also that the shock rise times are increased in both cases and that the signature distortions that occurred on the leading shock is repeated on the tail shock, as is found in all full-scale flight measurements. However, as the bubble is moved away from the microphone, the waveforms trend towards N-waves, as shown in figure 9.46.

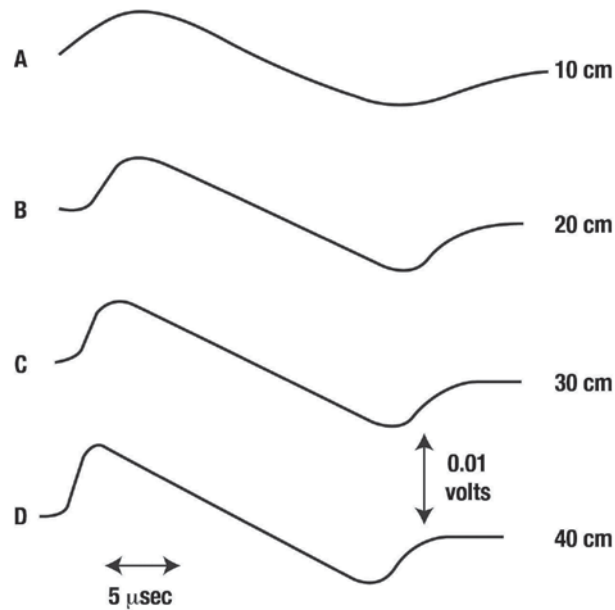


Figure 9.46. Waveforms observed for small (3.8 cm diameter) helium-filled bubble for various distances between microphone and bubble. The spark-microphone distance was held constant at 60 cm (adapted from ref. 9.26).

Figure 9.46 (ref. 9.26) shows four signatures that passed through small helium-filled bubbles. Measurements were made at 10 cm, 20 cm, 30 cm, and 40 cm from the bubble. Examination of these four signatures shows that they are trending towards an N-wave shorter rise time as the ring and bubble are moved further from the microphone. Traces for small argon bubbles showed similar features.

Shock Tube Horn and Air Jet

Ribner, Morris, and Chu (ref. 9.28) held the opinion that the peaking and rounding of sonic boom signatures due to disturbed atmospheric conditions was associated with turbulent eddies, somewhat jet-like, resulting from the speed-of-sound (temperature) or velocity gradients. The authors were aware of the work of Davy and Blackstock (ref. 9.26) who looked at the speed-of-sound effects in a laboratory using gas bubbles and, thus, focused their efforts on demonstrating the velocity gradient effect using air jets.

Their experimental setup, shown in figure 9.47 (ref. 9.28), utilized a horn-type sonic boom generator 80-feet long with a 10- by 10-foot opening at the end.

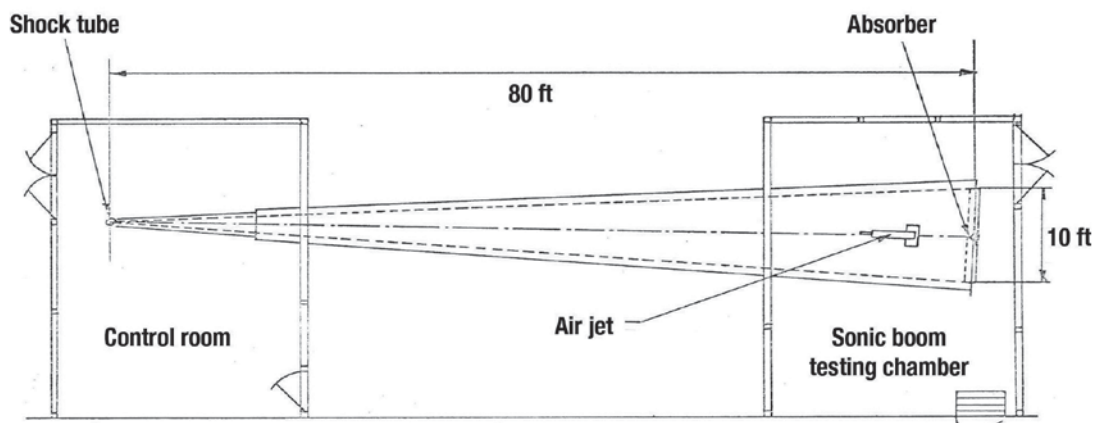


Figure 9.47. University of Toronto Institute for Aerospace Studies (UTIAS) horn-type sonic boom generator showing position of jet (ref. 9.28).

In reference 9.28 (p. 927), the authors state that:

A ½-inch nozzle air jet with a settling chamber was installed near the large end of the horn, pointing towards the small driver end (fig. 9.47). Several shock-tube drivers were used to produce quasi N-waves of 2 to 10 msec duration, roughly 2 to 10 feet in length. Thus, the length-scale factor of the experiments was about 1/50, and an effective zone of jet flow some 4-feet long would simulate a 200-foot atmospheric eddy.

These tests involved propagating the quasi N-wave signatures down the horn against, and with, the jet flow of varying velocities, thus producing turbulence at the far end of the conical horn. They also obtained measurements without the jet turbulence. Some results of their experiments are given in figure 9.48 (ref. 9.28) for the no-flow and a jet flow where the shock N-waves are traveling down the shock tube and against the jet flow of 340 ft/sec (see sketch at bottom of the figure).

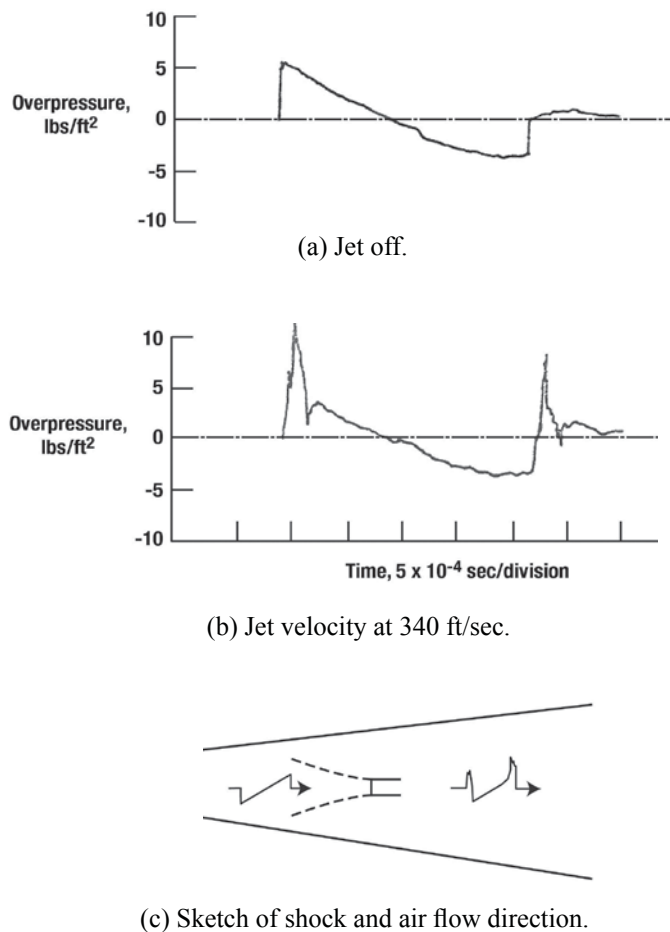


Figure 9.48. Spiked superboms produced by air jet in horn simulator; jet facing driver – (a) jet off and (b) jet velocity at 340 ft/sec (adapted from ref. 9.28).

The top trace, figure 9.48(a), represents the boom signature produced by the shock tube propagating down the tube having no jet flow. As can be seen, the signature closely resembles an N-wave except for slight asymmetry at the tail shock portion of the time history. Propagating this N-wave signature against the jet flow of 340 ft/sec is illustrated in figure 9.48(b). It can be seen that refraction, due to the mean flow pattern of the jet, caused the signature to become peaked, or focused, the bow and tail shocks showing similarity to what happens in supersonic flight-test measurements, and that the same peaking characteristics on the bow-shock show up at the rear shock. Note that the maximum overpressures for the no-flow case is about 5 lbs/ft² and for the turbulent spiked signatures it is about 12 lbs/ft².

When the air jet was turned around so that the jet flow was traveling in the same direction that the shock was traveling (see fig. 9.48(c)), rounded signatures were observed, as shown in figure 9.49 (ref. 9.28). Once again, the shock signature in the no flow condition (fig. 9.49(a)) is mostly N-wave in character with about 5.0 lb/ft² overpressure. At a jet flow velocity of 240 mph (fig. 9.49(b)) the boom signature is rounded and the bow and tail shocks have large rise times. Measurements of this sort were acquired at jet-flow velocities of 240, 340, and 420 ft/sec. Results show that as the jet flow velocity increases, so too does the peaking and rounding of the signature. From these initial experiments, the authors concluded that jets in the atmosphere can cause peaking and rounding of N-wave type sonic boom signatures. It should be noted that no details are given in reference 9.28 as to the turbulence scale or structure of the jet flow.

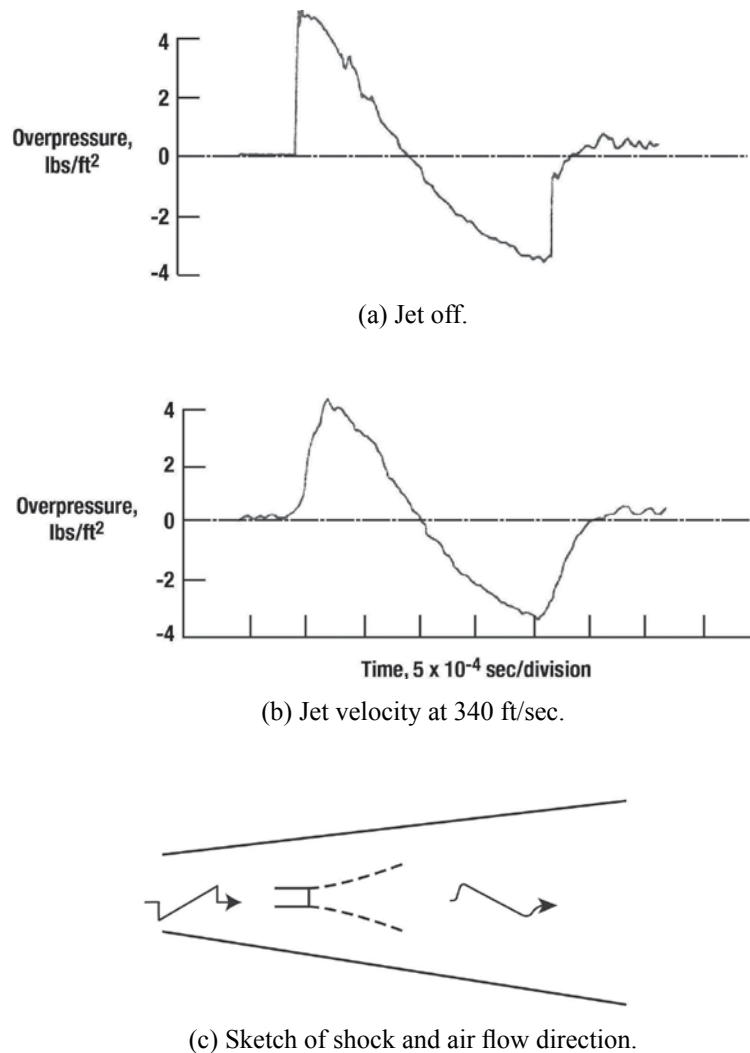


Figure 9.49. Rounded boom signatures produced by air jet in horn simulator, jet facing open end – (a) jet off and (b) jet velocity at 340 ft/sec (ref. 9.28).

Shock Tube and Grid Turbulence

Tubbs (ref. 9.29) undertook an experiment aimed at explaining why sonic boom shock thickness measured from full-scale flight tests were some 100 to 1000 times the theoretical (Taylor's) values. He conducted a series of laboratory experiments using a shock tube to generate the shock wave that passed through grid-generated turbulence. A shock tube is a device used to generate and direct a shock wave on to a test device. The shock wave inside the tube can be produced by developing a high pressure behind a diaphragm that is ruptured to allow the shock wave to propagate down the tube. A view of the test setup is given in figure 9.50 (ref. 9.29).

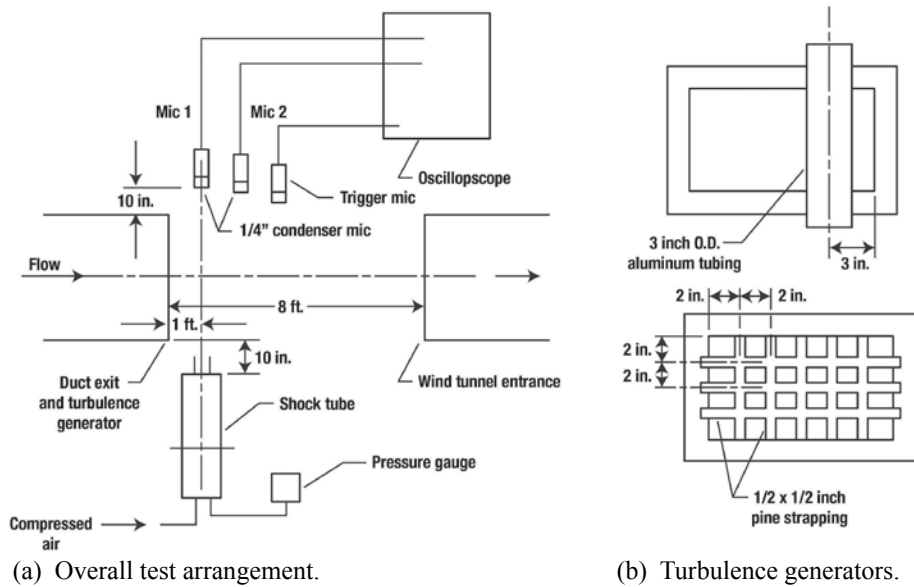


Figure 9.50. Schematic of experimental setup and two of six turbulence generators (adapted from ref. 9.29).

A weak shock, produced by a shock tube was passed at right angles through turbulent flow generated by placing obstructions at the exit of a wind-tunnel duct having an opening of 8 inches by 12 inches. Mean flow velocities of about 100 ft/sec were produced and turbulent velocities in the planetary boundary were the order of about 10 ft/sec. The turbulent path length was about one foot. Six turbulence generators were designed and used in the tests, two of which are shown in figure 9.50(b) representing the extremes in the designs.

Small rise times, the order of 10 μ sec or less, and low overpressures about 2 to 3 lbs/ft² were of paramount importance to the author. The authors decided to fire the boom across the turbulence in order to eliminate the spiking and rounding that Ribner, Morris, and Chu (ref. 9.28) observed when a jet was blowing against, and with, the shock. Two diaphragm materials were used – carbon paper and red zip (a cellophane about 4 μ m thick). Some 82 shocks through turbulence were made with the carbon paper diaphragms and 134 with the red zip. There was difficulty with the carbon paper not rupturing properly resulting in considerable scatter in the measured rise times. The red zip diaphragm ruptured well and produced consistent rise times. Samples of oscillograph traces for shock produced by the red zip diaphragms measured with microphone 1 and 2 are shown on figure 9.51 (ref. 9.29).

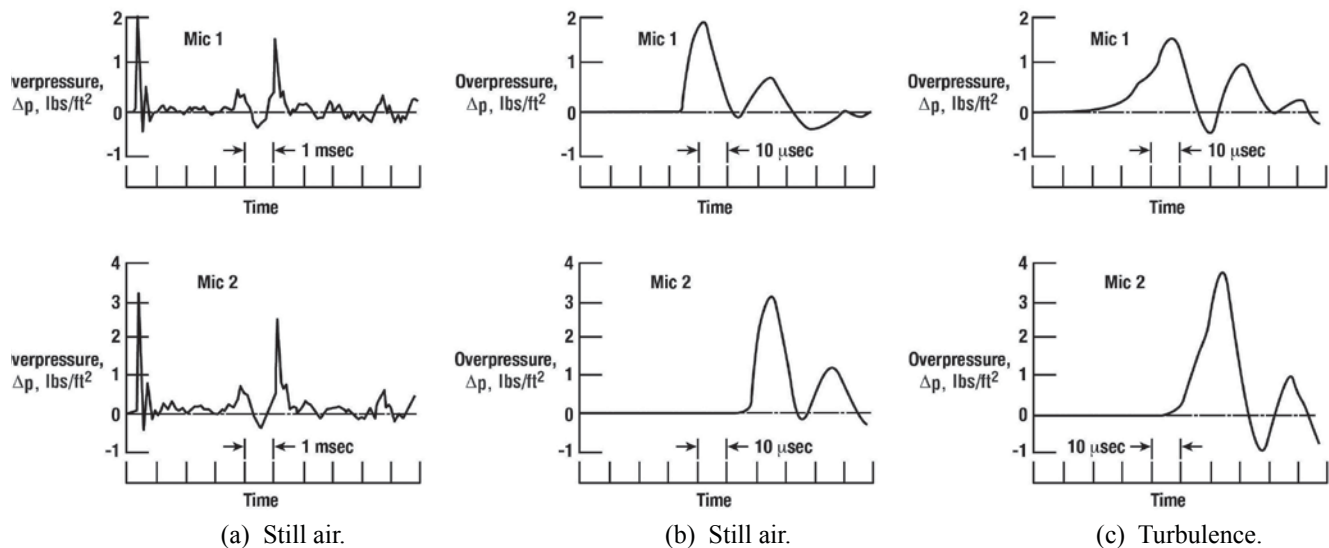


Figure 9.51. Typical oscillograph for shocks produced using red zip diaphragms. (a) and (b) reference shock (still air) and (c) shocks after passing through turbulence (adapted from ref. 9.29).

Figures 9.51(a) and 9.51(b) show the measured reference shock (still air with no turbulence) and figure 9.51(c) is the waveform after passing through turbulence (note the change in the pressure and time scales). It can be seen that signature rise times on the order of 10 μsec are observed for the still air with no turbulence case was achieved and overpressures of around 3 lbs/ft². Large increases in rise time on the order of 15-20 μsec are observed for the turbulent case.

A plot of frequency of occurrence against shock rise time is shown in figure 9.52 (ref. 9.29) for the red zip diaphragms. It was noted that these results are clearer than the carbon paper diaphragms – both showed that rise times with turbulent flow are higher. Also, this figure presents a statistical treatment of all the data, without regard to turbulence generators used.

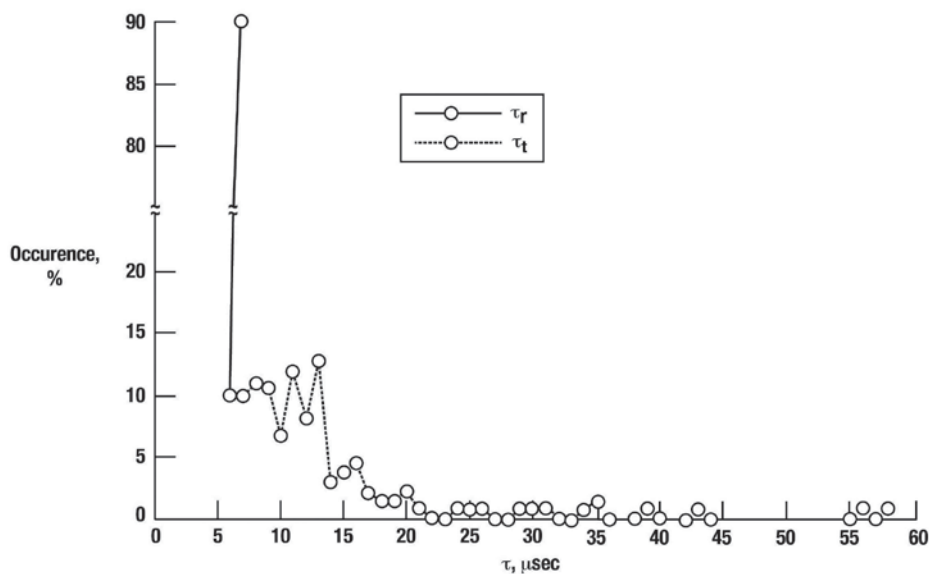


Figure 9.52. Distribution of reference rise time (τ_r) and rise time after passage through turbulence (τ_t) for shocks produced using red zip diaphragms (adapted from ref. 9.29).

Examination of figure 9.52 shows that a consistent reference rise time, τ_r , of about 7 μsec is altered by the turbulence, τ_t , indicating shock thickening. It is noted also that the frequency of occurrence, of the thinnest shock, decreases with turbulent flow and there was no instance of a shock thinner than the thinnest of the reference shocks observed. It further states that this would seem to indicate that turbulence is a shock thickening mechanism, but not a shock thinning mechanism.

Since Tubb's (ref. 9.29) work was directed towards explaining why sonic boom shocks had thicknesses 100 to 1000 times the Taylor shock thickness, he concluded his experiments were not successful in showing such large shock thickening by turbulence.

Projectiles into Atmospheric Turbulence

Bass et al. (ref. 9.30) conducted a model experiment to investigate the influence of real atmospheric turbulence on an N-wave sonic boom signature generated by supersonic projectiles. As will be shown, they were to experience the results of a mismatch in scaling between the projectile shock thickness and period, and the atmospheric turbulence. Recall that in the Bauer-Bagley ballistic range experiments (ref. 9.22), discussed earlier in this Chapter, it was found that as projectile size increased relative to the model turbulence scale, a rather low sensitivity to the turbulence was observed.

The Bass et al. experimental range is illustrated by figure 9.53 (ref. 9.30) and consists of a target into which the projectile was fired and microphone arrangement where the alignment of the microphone face to the Mach cone was considered to be very important for these experiments. Three outdoor ranges were used, range 1 on

which the projectiles were 30-06-caliber bullets with muzzle velocities of 1000 and 720 m/sec. The projectiles at range 2 were from a military tank firing projectiles in a sabot with muzzle velocities of 1460 m/sec. At range 3, the projectile source was a tank firing sabot and HEAT-T rounds at muzzle velocities of 1539 and 1173 m/sec. Although not stated, it is believed that these tank rounds were 105 mm in diameter. A fourth range was an indoor range with no air circulation or other sources of turbulence. The projectile used at range 4 (indoor) was 0.22 caliber with an average muzzle velocity of 1260 m/sec.

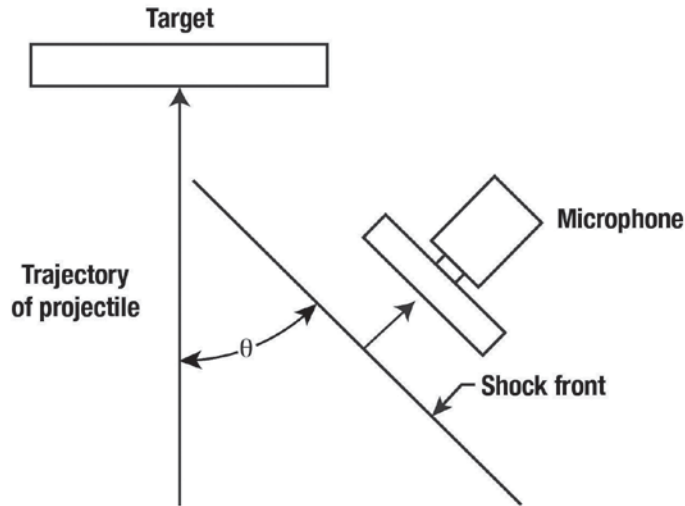


Figure 9.53. Typical experimental configuration. The angle θ is the Mach angle (adapted from ref. 9.30).

For each shot, two microphones at two locations recorded the waveforms simultaneously – one was near the projectile path, was not moved, and acted as the reference and trigger for the second microphone that was moved. A typical waveform, from the 30-06-caliber projectile at range 1 is presented in figure 9.54 (ref. 9.30). The signature is N-wave in character with an overpressure of 0.28 kPa, a period of 147 μsec and rise time of about 12 μsec . The range of N-wave values included in these tests ranged from 0.04 kPa to 2.8 kPa in overpressure, from about 76 μsec to 3.4 msec in period and from about 2 μsec to 18 μsec for the rise times. It was stated that the general form of the wave was reproducible, but not the fine structure. Propagation distance ranged from about 0.2 m to 92 m and a total of 43 rounds were fired during the tests.

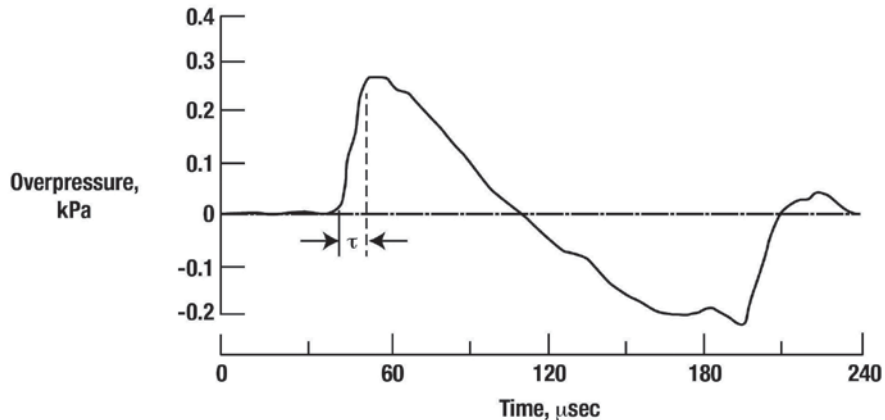


Figure 9.54. Typical recorded waveform at range 1 from the 30-06-caliber projectile (ref. 9.30).

The major results from the experiments are presented in figure 9.55 (ref. 9.30), which shows rise times as a function of N-wave overpressure. All of the rise time results acquired from the various projectiles, including the 22-caliber bullets, 30-06-caliber bullets, and 105-mm tank guns plotted on the figure. The associated scale of turbulence and turbulence strength of the real atmosphere ranged from about 1 m to 6 m and about 4×10^{-6} to about 24×10^{-6} , respectively. One major feature of this figure should be noted – as stated by the authors (ref. 9.30, p. 308), “...Specifically the measured rise times do not change in any specific way with turbulence strength, μ^2 . This observation suggests that turbulence plays a minor role, if any, in determining the rise time.”

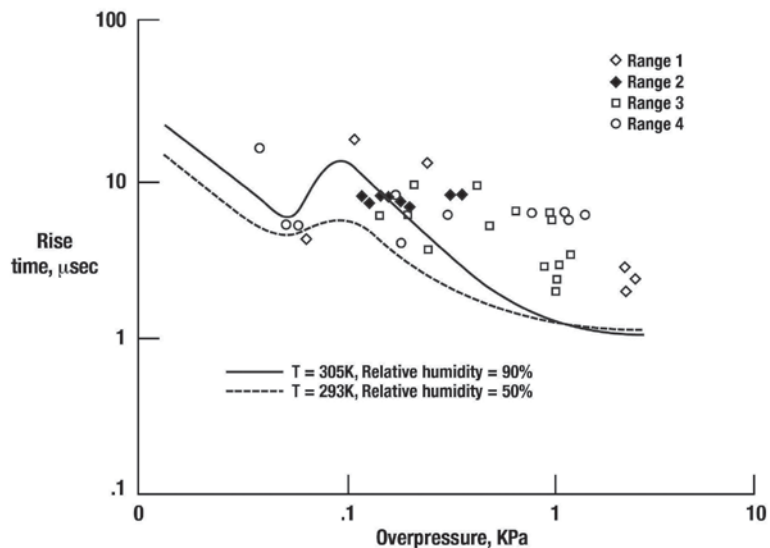


Figure 9.55. Experimental and computed rise times (ref. 9.30).

A second feature of figure 9.55 noted by the authors (ref. 9.30, p. 308) is: “The experimental rise time appears to reach a lower limit of about 2 μsec . This limit is most probably a result of experimental constraints, specifically, microphone alignment and bandwidth.”

In reference 9.30 (p. 306), the authors observed that “No correlation between measured rise times and the atmospheric turbulence was observed. This is in contrast to the findings of full-scale flight results and could have been expected because of the small scale of the projectiles used to generate the sonic boom.”

Spark Discharge and Fan Duct Turbulence

Lipkins and Blackstock (ref. 9.31) also performed a model experiment dealing with sonic boom propagation through turbulence by using an electrical spark to provide the N-wave signature and model turbulence generated by a plane jet. The authors took particular care to make the downscaling of the turbulence the same as that for the model N-waves – with a scale factor of about 10^{-4} . An illustration of the arrangement of the experimental setup is given in figure 9.56 (ref. 9.31).

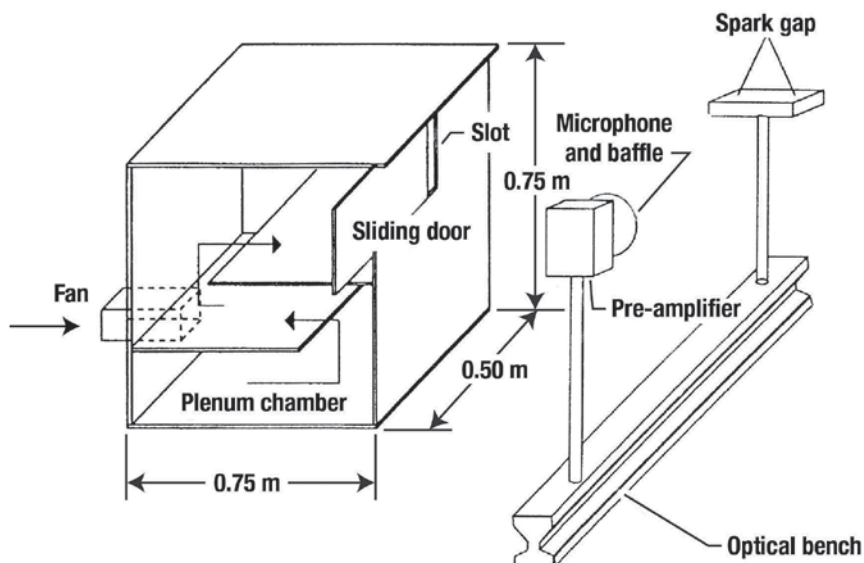


Figure 9.56. Arrangement of the experiment – plane jet source, spark source (without the parabolic reflector), and receiver. The dimensions shown are in meters (adapted from ref. 9.31).

The spark source and receiving systems were mounted on the optical bench. Both spherical and plane N-waves were used in the tests, the latter being generated by placing the spark gap at the focus of the parabolic reflector. The model turbulent velocity field was generated by a fan, plenum chamber, and rectangular nozzle to provide the plane jet. Flow exited a slot nozzle with a height of 0.25 m and a width that could be varied with the use of a sliding door, typically 25.4 mm for the experiments. Increasing the slot width increases the thickness of the turbulent flow. As such, the shocks are being influenced by the turbulence over a longer period of time. This situation is analogous to flight through the lower level of turbulence at a low or high Mach number, as was illustrated in figure 2.39 of Chapter 2. Measured boom signature variability was found to be increased for flights at Mach 1.3, as compared to flights at Mach 1.6 where the shock ray paths spent less time propagating through the turbulent lower layer. Reynolds numbers of about 53,000 were achieved at this open width and the N-wave propagation path was 0.7 m downstream where the jet velocity was about 30 m/sec.

An example of the signature of the spherical N-wave measured 400 mm from the spark is shown in figure 9.57 (ref. 9.31). It is seen that a nearly symmetrical N-wave is produced except that the tail shock is not as well formed as the bow shock. Overpressures of from 2 lbs/ft² to 4 lbs/ft² were produced from spherical N-waves and up to about 13 lbs/ft² from plane N-waves. The period and rise time of the N-wave signatures was about 15 μ sec and 0.5 μ sec, respectively. Such values place severe demands on the microphone receiving system. The authors used a system having a frequency response that was flat from 10 Hz to 2.25 MHz. Table 9.2 lists the nominal overpressure, period, and rise times for full-scale flight sonic booms and the experiment spark N-waves.

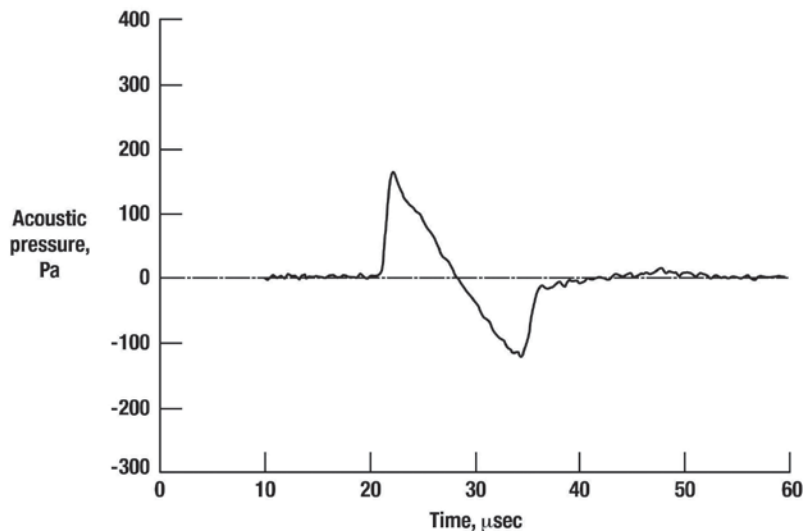


Figure 9.57. Example signature of a spherical N-wave measured 400 mm from the spark source (ref. 9.31).

Table 9.2. Typical Values of Rise Time τ , Peak Pressure Δp and Duration T for Sonic Booms and Spark-Produced N-Waves (ref. 9.31)

Parameter	Sonic Boom	Spark Produced N-wave
Δp	30-200 Pa	100-500 Pa
T	100-300 msec	10-30 μ sec
τ	2-10 msec	0.4-2 μ sec

For both the signature period and rise time, the ratio between full-scale and model experimental values is on the order of 5,000 to 10,000. Table 9.3 gives three characteristics of atmospheric turbulence, the design scale model values, and the actual measured values.

Table 9.3. Turbulence Parameters: Typical Atmosphere and Design and Achieved Values for the Model Experiment (ref. 9.31)

Characteristic Lengths for Atmospheric Turbulence	Atmospheric Turbulence	Model Exp. Turbulence Scaled Down	Model Exp. Turbulence Measured
Turbulent Boundary Layer Thickness	1000 m	0.1-0.2 m	0.05-0.3 m
Outer Length Scale (Large Eddies)	100-200 m	0.01-0.02 m	0.01-0.08 m
Inner Length Scale (Smallest Eddies)	10 mm	0.001 mm	0.1-0.01 mm

The author's note that except for the Kolmogorov inner length scale (small eddies), which is not important to these experiments, the measured values agree very well with the design values and thus conclude that the turbulence of the plane jet has about the right scale to mimic the role of the atmosphere where model N-waves are simulated sonic booms (ref. 9.31, p. 154).

Sets of 100 to 200 pressure waveforms were recorded, mostly using plane N-waves. Fewer measurements were recorded for spherical N-waves. However, the findings were qualitatively the same. The test procedure was to fire 100 spark-generated N-waves into quiet air, then turn the jet on and fire a second set of 200 N-waves. Several examples of waveforms of plane N-waves passing through the model turbulence to one with no turbulence are shown on figure 9.58 (ref. 9.31). The signature in the upper left of figure 9.58 is for the no-turbulence case. All the others are influenced by turbulence and vary from peaked and spiking to smoothing and rounding of the signature. Also, similar distortions are associated with the bow and tail shocks, as observed during supersonic flight in the atmosphere.

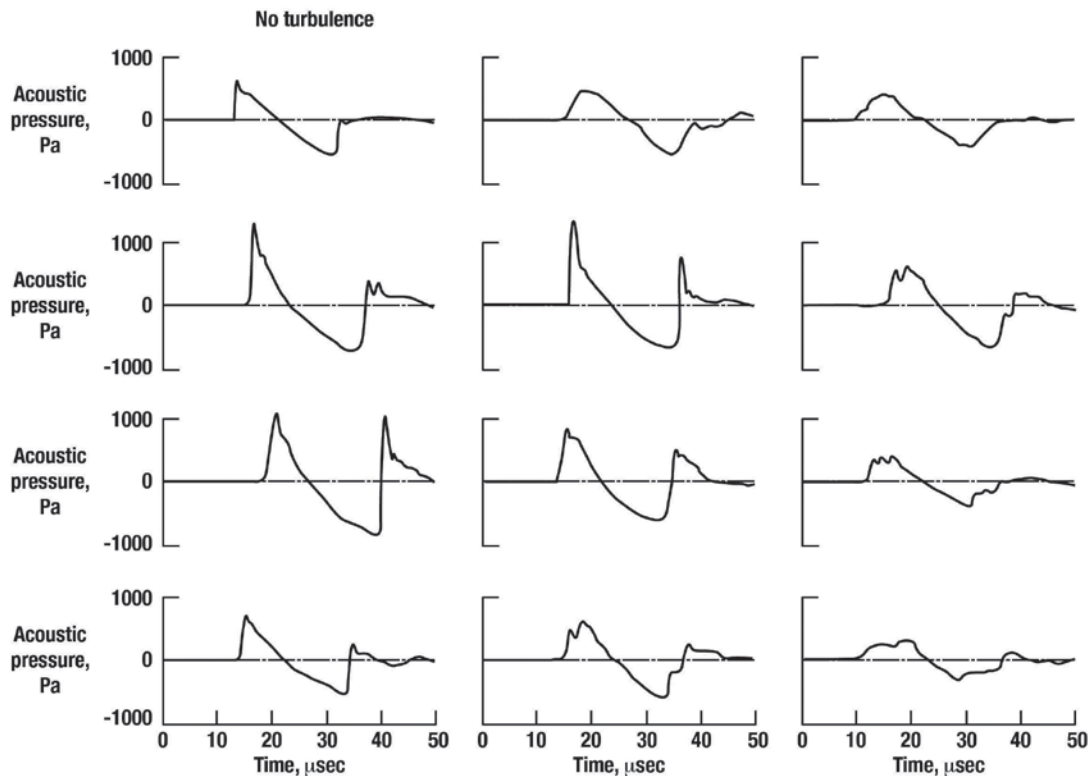


Figure 9.58. Waveforms of plane N-waves – the upper left trace is a reference N-wave recorded in the absence of turbulence; all others recorded after propagation through turbulence (ref. 9.31).

An illustrative display of recorded results of the distribution of overpressure and rise time also from reference 9.31 is provided in figures 9.59 and 9.60. Figure 9.59 shows the variability of the peak overpressure for 100 plane N-waves in still air and 100 plane N-waves into model turbulence. The dashed horizontal lines represent the average measurements with turbulence.

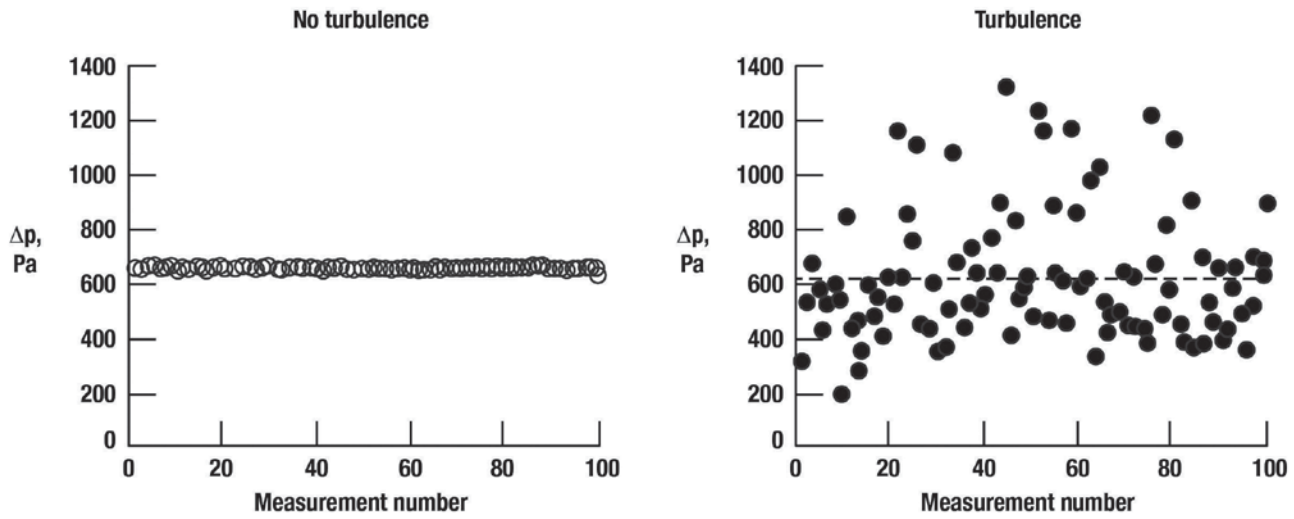


Figure 9.59. Values of peak pressure for 100 plane N-waves measured with and without turbulence. The dashed line shows the average for the measurements with turbulence (ref. 9.31).

For the no turbulence case, little variation is noted from the 600 Pa nominal plane N-wave overpressure throughout all 100 N-waves. A significant scatter is seen to result in the overpressure of N-waves passing through turbulence with a majority of the data points lying below the dashed line representing the difference between the average and median overpressure with turbulence.

Similar observations can be seen in the case of the plane N-wave rise times, as shown in figure 9.60 (ref. 9.31). Here, little variability in rise time is displayed for the no turbulence cases and considerable scatter in the data is seen for the turbulence runs. Most of the data points fall below the dashed line representing the average rise time measurement with turbulence.

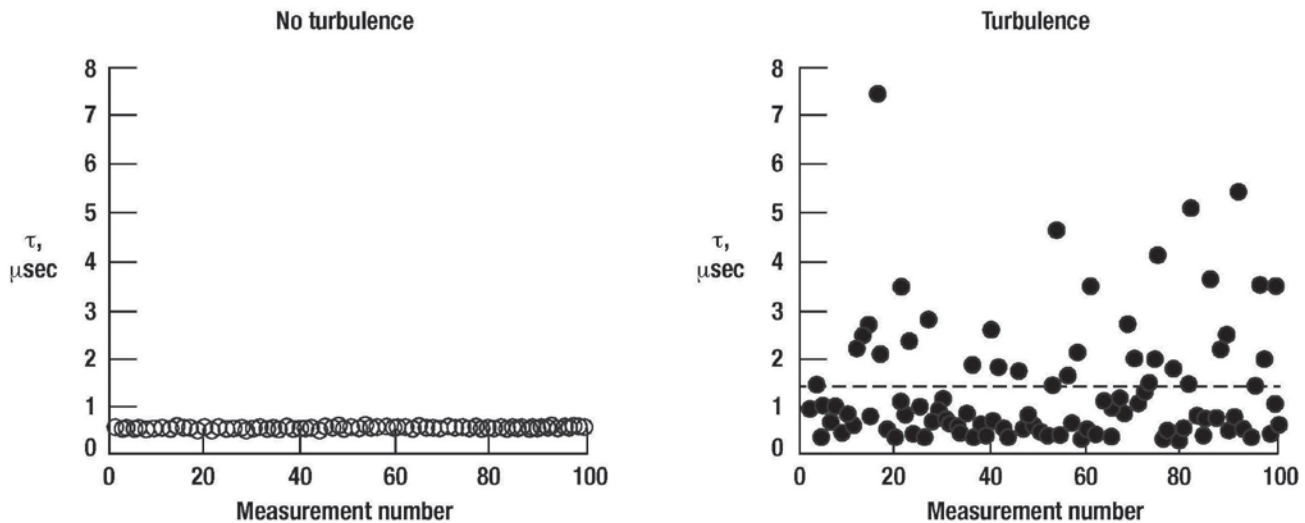


Figure 9.60. Values of rise time for 100 plane N-waves measured with and without turbulence. The dashed line shows the average for the measurements with turbulence (ref. 9.31).

From the measured results of overpressure variation due to turbulence, a cumulative probability plot of equaling or exceeding the no turbulence plane N-wave overpressure is presented in figure 9.61 (ref. 9.31). The authors note that the fact that these data fit a straight line on the log-normal scale illustrates that these results are similar to those for sonic boom in the atmosphere.

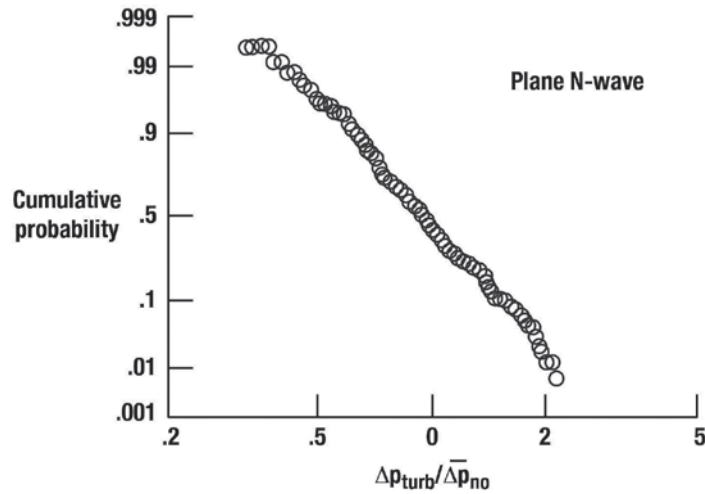


Figure 9.61. Cumulative probability curve of peak pressure of plane N-waves after propagation through turbulence. The curve is plotted on a log-normal scale and Δp_{no} is the average peak pressure measured in the absence of turbulence (ref. 9.31).

Regarding signature rise time, two interesting plots are presented by the authors of reference 9.31 and are shown in figure 9.62. They plotted the rise time cumulative probability function on an (a) linear and (b) log-normal scale.

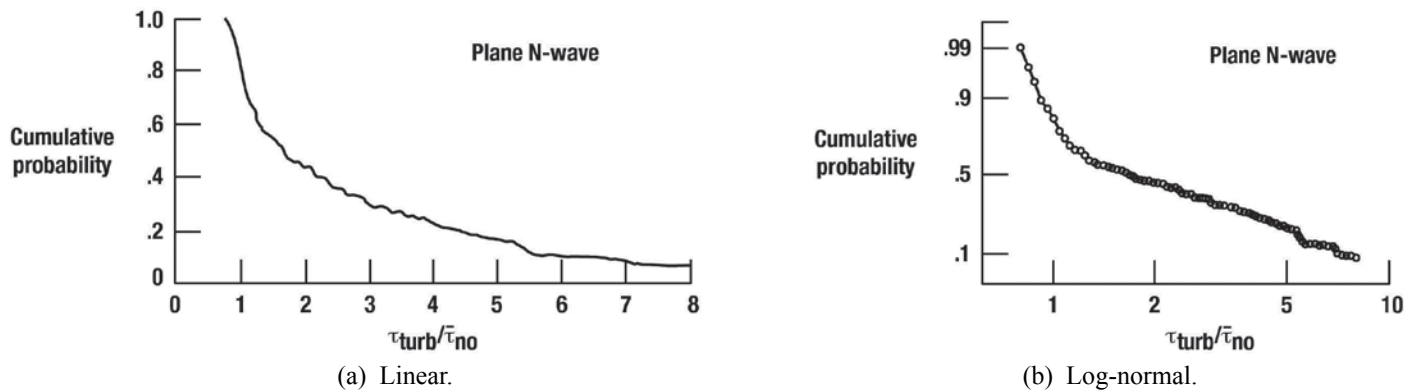


Figure 9.62. Cumulative probability curve of rise time plane N-waves after propagation through turbulence. $\bar{\tau}_{no}$ is the average rise time measured in the absence of turbulence (ref. 9.31).

The linear curve (fig. 9.62(a)) confirms that for plane N-waves, turbulence almost always increases signature rise time. The log-normal curve, figure 9.62(b) indicates a two-part behavior in that one can draw a straight line for rise time values greater than the no-turbulence average value and a second line for values smaller than the average.

As a result of this experiment, the authors concluded among other findings that they have successfully simulated sonic boom propagation through the atmosphere and that they reproduced waveform distortions both in scale and in character in this laboratory. Once again, the reduced scale of these experiments placed serious demands in the response of the measurement system with particular attention to the scaling of the spark N-wave and turbulence to a real atmosphere.

Quantifying Focus Boom Intensities

Sonic boom focusing is associated with certain flight conditions of an aircraft including steady level flight at cutoff Mach numbers (M_{CO}), transition flight from subsonic to supersonic speeds and maneuvering flight including supersonic turns, pull-ups, pushovers, and dives. Although acoustic theory provides for the location of the focus, it is not able to predict the intensity in that as the ray tube area approaches zero, the overpressure goes to infinity. Recent work by Auger and Coulouvrat (ref. 9.32) and Kandil and Zheng (ref. 9.33, Appendix D) now allows one to calculate the magnitude of the transition focus boom for a variety of in-coming boom signatures. However, the predicted levels from these computer codes require experimental validation.

Over the years, a substantial flight database has been established for each of these flight maneuvers (see Chapters 3 and 5). Acquiring boom signatures at the maximum focus during flight tests for any of these types of maneuvers is difficult and costly, requiring numerous microphone systems, knowledge of the aircraft operating conditions, careful execution of the particular flight maneuver, and detail information on the expected atmospheric conditions at the test site.

In response to the need for quantifying the boom intensity at a focus, several simulation techniques were developed and included ballistic ranges, a supersonic sled track, shock tubes, and spark discharges onto mirrors/refractors. A brief review of the application of each of these techniques to focusing conditions associated with steady-level flights at M_{CO} , transition flight from subsonic to supersonic speeds, and maneuvering flight involving accelerations and changes in flight path angle will be presented.

Mach Cutoff Focus Using Ballistic Range-Mixed Gases

It has been shown that steady-level flight at Mach cutoff (M_{CO}), where the aircraft speed over the ground is equal to the sound speed at the ground, will result in a focus at the shock extremity due to atmospheric refraction (see figs. 5.5, 5.6, and 5.7 in Chapter 5). In 1971, Peter et al. (ref. 9.34) conducted an experiment using a ballistic range and fired a projectile into a stratified medium of air and carbon dioxide. These results are briefly discussed by Wanner in reference 9.35. A focus factor of 1.7 was observed on the front shock that resulted in a focus factor of about 3.3 after a position correction, which compares to flight-test focus factors of about 3 (refs. 9.36 and 9.37). In 1974, Sanai, Toong, and Pierce (ref. 9.38) conducted a similar experiment to create refraction focus booms in a ballistic range firing projectiles at low supersonic speeds into a stratified medium of varying sound speed consisting of a homogeneous mixture of CO_2 and air. A schematic of this setup along with some measured results are presented in figure 9.63 (ref. 9.38). Pressure signatures were recorded by a fast response transducer inserted in the flow field. Dual Schlieren pictures were taken simultaneously during each run. A graphic summary of their findings is provided in figure 9.64 (from ref. 9.38). It can be seen from the figure that they too obtained a focus factor of 1.7 on the front shock, duplicating the values presented by Wanner et al. (ref. 9.35). It should be mentioned that experiments such as the one described herein where the shock signature is small and the range facility confined, one must contend with the difficulties associated with transducer size regarding response, shock diffraction, shock waves, and shock reflections.

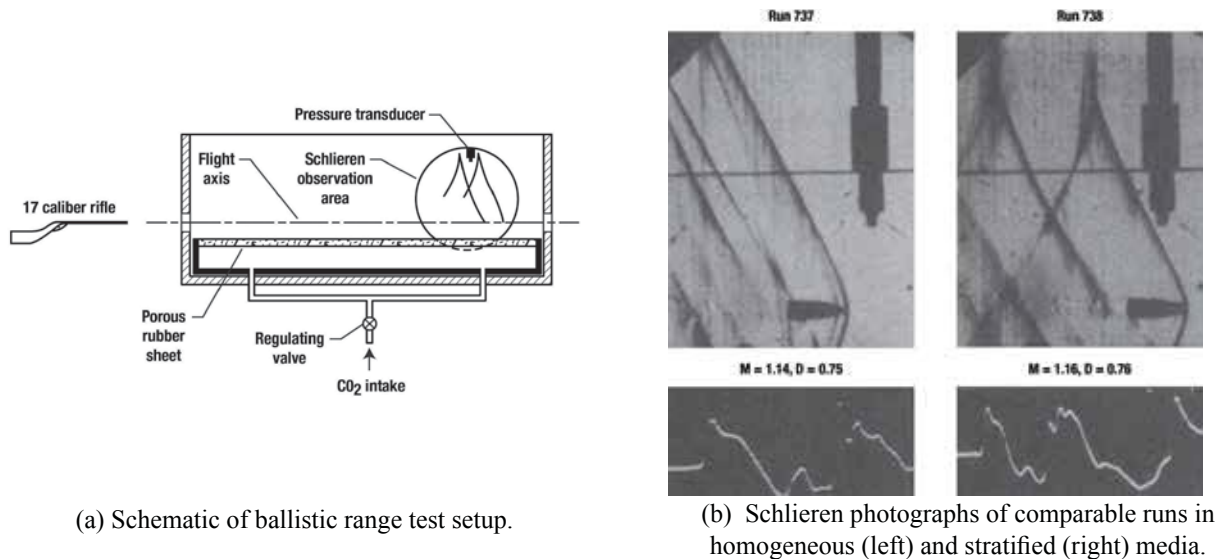


Figure 9.63. Schematic diagram and test results of experimental apparatus to measure sonic boom focusing due to atmospheric refraction (adapted from ref. 9.38).

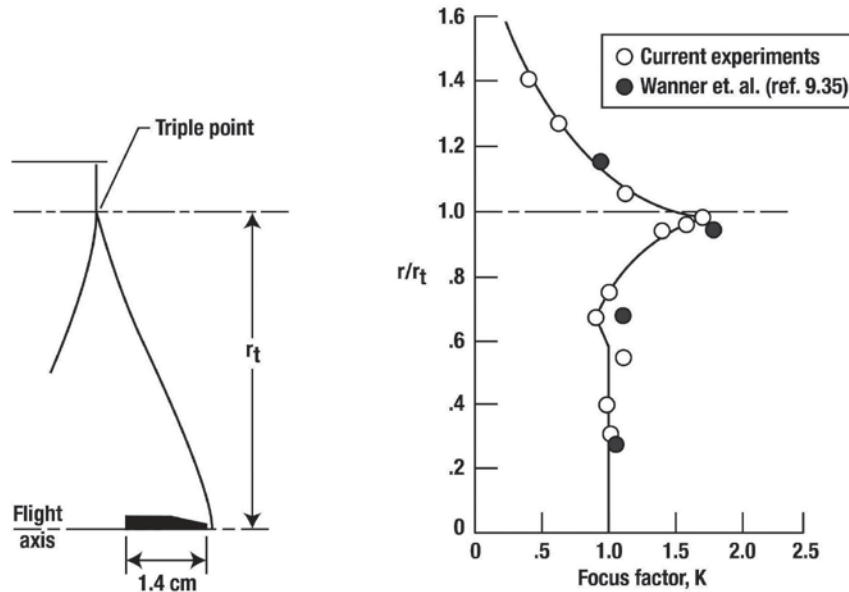
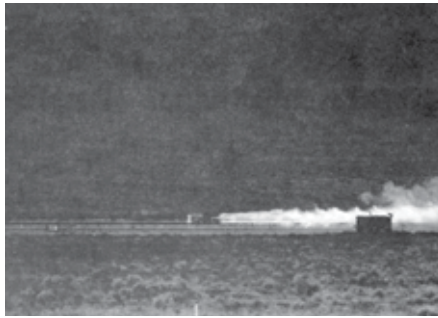


Figure 9.64. Radial variation of the focus factor for leading shock (adapted from ref. 9.38).

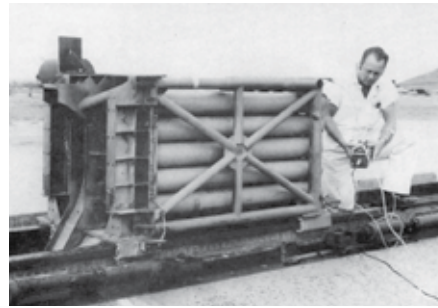
Transition Focus Utilizing a Rocket Sled Track

The focus boom resulting from an aircraft accelerating from subsonic to supersonic speeds cannot be eliminated or avoided. One can only influence the point at which the focus reaches the ground. In Chapter 3 of this publication, it is shown that transition focus booms can be placed to within ± 1000 feet of the desired location (see, for example, fig. 3.11) if the vehicle's performance and atmospheric conditions are known. As in the case of M_{CO} , focusing acoustic theory does not quantify the maximum overpressure experienced at the focus. However, as shown in Chapter 3, a computer code developed by Auger and Coulouvrat (ref. 9.32) and replicated by Kandil and Zheng (ref. 9.33, Appendix D) permits a prediction of the maximum focus value for a transition maneuver. Prior to this code development, an extensive flight database was generated in order to establish these maximum focus overpressure values and corresponding focus factors. Focus factors on the order of 2.5 to 5.0 have been experienced from N-waves (see figures 3.11–3.12 and 3.14 of Chapter 3). As noted earlier, obtaining focus boom measurements via flight tests is costly, difficult, and complex and requires great care and experience in their execution (see, for example, the work of Wanner et al. reported in ref. 9.35).

It is obvious that simulation techniques involving ballistic ranges, shock tubes, or spark discharge arrangements would not be suitable for addressing the transition focus concern, since the initial starting condition on each is already supersonic. A rocket sled track was believed to have applications and tests were made to determine its suitability. In 1974, Reed (ref. 9.39) conducted a series of tests using the Sandia 5000-foot long rocket sled track. Photographs of the sled track and carriage are shown in figure 9.65 (ref. 9.39).



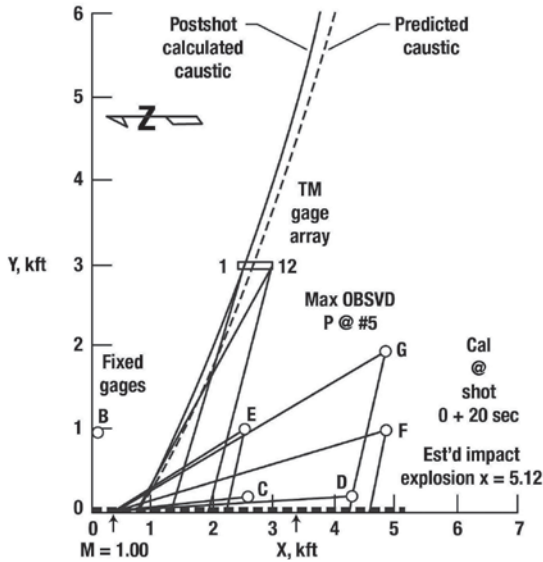
(a) Sled test.



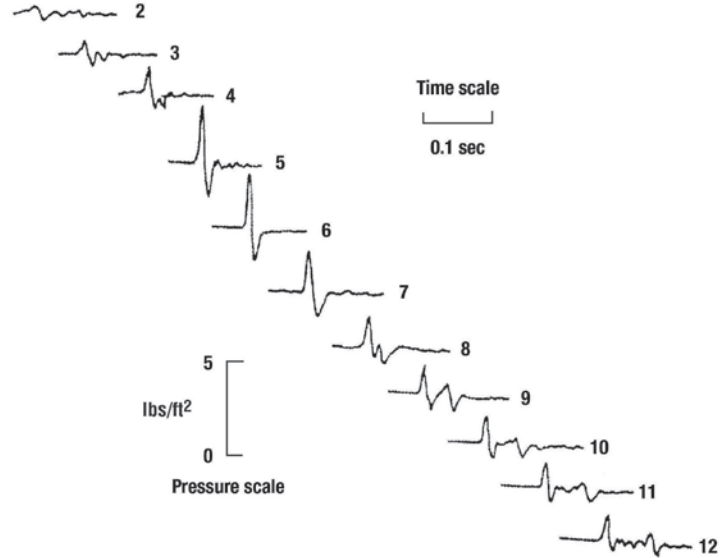
(b) Utility sled with 25 High Velocity Air-to-Ground Rockets (HVAR), 425-m/s maximum speed (1394 ft/sec).

Figure 9.65. Photographs of Sandia 5000-foot supersonic sled track (ref. 9.39).

The sled track has sufficient track length and supersonic capability to provide the necessary simulated conditions and also is of a size to allow for adaptation of fairly large-scale vehicles designed to produce N-wave type signatures and also shaped signatures. Some results of these tests obtained during a transition run are shown in figure 9.66 (ref. 9.39). The location of the 12-microphone array with respect to the predicted caustic (focus line) about 3000 feet lateral to the sled track is shown in figure 9.66(a). The overpressure scale is essentially the same for all signatures (fig. 9.66(b)).



(a) Location of microphone array to caustic.



(b) Microphone signatures.

Figure 9.66. Measured sonic boom signatures during transition of sled track from subsonic to supersonic speeds (adapted from 9.39).

The observed sonic boom signatures are typical of those measured in flight tests, that is, rumble type signatures are observed in the pre-focus region upstream of the focus line, a single N-wave within a focus region, and the N-wave carpet signature followed by the refracted (U-shaped) signature in the post focus region. A focus factor of about 2.2 is realized in figure 9.66(b). The maximum focus factor measured during these tests was about 3.3.

One of the major drawbacks of using the supersonic sled track for sonic boom simulation is the presence of the ground surface, which does not allow the boom signature to develop in three dimensions. In addition, the

atmosphere in which the boom is to be measured is horizontally stratified and influenced by the ground cover between the point of generation and measurement locations.

Maneuver Focus

In the two focus boom situations just presented – that of Mach cutoff (M_{CO}) and transition (the acceleration from subsonic to supersonic speeds) – the focus is associated with a single focus line or caustic. During aircraft flights involving both acceleration and geometric changes such as turns, dives, and pushover maneuvers, multiple focus lines (caustics) may be produced. At the point at which these focus lines merge, there is a superfocus. An excellent example of a superfocus resulting from turn-entry maneuver is presented by Wanner et al. (figs. 5, 15, and 17 of ref. 9.35 and also fig. 3.8 of this publication). A focus factor of 9 was observed. Simulation techniques, including spark discharges and parabolic and ellipsoidal reflectors, a shock tube, and a ballistic range, were utilized in laboratory experiments conducted with the objective of defining the maximum overpressures that could be experienced due to focusing of a sonic boom N-wave. A discussion of each of these techniques follows.

Spark Mirror Reflector

In 1969, Beasley, Brooks, and Barger (ref. 9.40) conducted a laboratory investigation of N-wave focusing using a spark to generate the N-wave and parabolic mirror as a reflector. Figure 9.67 depicts the lab test setup showing the arrangement of the spark, mirrors, and microphone. A comparison of the calculated and measured signatures of the initial N-wave, showing their shape at the focus and in the post focus region, is presented in figure 9.68. Although the summary presented in figure 9.69 shows the variation of peak overpressure with distance from the focus, it also indicates a maximum focus factor of about 3.0. The authors caution whether any conclusions concerning the maximum value could be drawn from such data. They further noted that although the data indicate significant amplitude in the vicinity of the focus, the very large amplitudes predicted by strict ray-tube theory were not obtained and that these large amplitudes are influenced by wave length, microphone response, mirror astigmatism, and mirror dimensions.

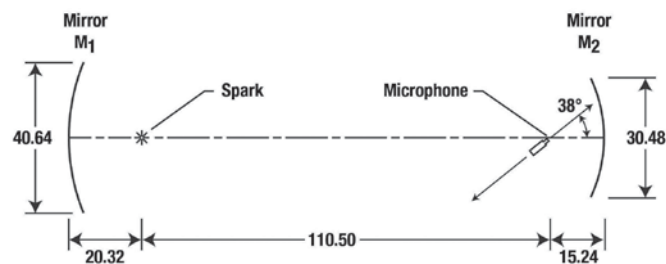


Figure 9.67. Schematic diagram of test apparatus for spark, mirror focus boom experiment. (Top view) All dimensions are in centimeters (ref. 9.40).

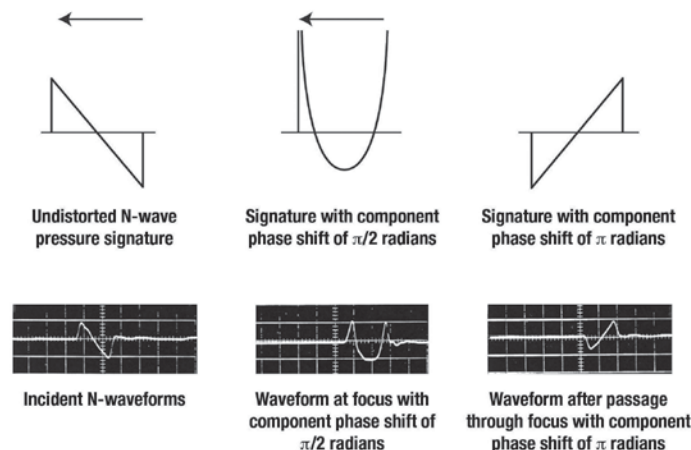


Figure 9.68. Calculated and measured shapes of the pressure signature as the wave passes through the focus. The arrow indicates the direction of wave propagation (adapted from ref. 9.40).

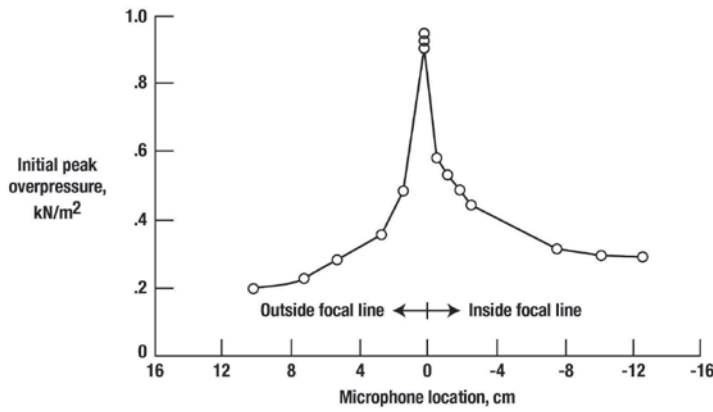


Figure 9.69. Laboratory test setup and results from spark with parabolic mirror focus boom experiment (ref. 9.40).

Laboratory tests similar to those just discussed were performed in 1972 by Cornet (ref. 9.41) utilizing the spark technique and a spherical mirror. Later on, Wright and Blackstock (ref. 9.42) conducted an experimental laboratory investigation of the focusing of intense, airborne pressure pulses (N-waves) by an ellipsoidal mirror. Three ellipsoidal reflectors (large, mid-size, and small) were used during these tests. All had the same major and minor axis and eccentricity as seen in figure 9.70(a). A schematic representation of the reflected (B) and edge-diffracted (C) wave fronts from the reflector are shown in figure 9.70(b). To the right of the exterior focus (F_2) is the pre-focus region and to the left is the post-focus region. The observed waveforms from one of the experiments is presented in figure 9.70(c) (ref. 9.42). Seven signatures are shown that represent measurements in the pre-focus (+12 cm), focus, and post-focus (-12 cm) regions. Each position corresponds to the arrival of the direct N-wave from the spark (A), reflected (B), and edge-diffracted (C) signals. For the case of the large reflector, a focus factor of over 10 is experienced. Reduced values of focus factor for the mid-sized and small reflectors were observed. Once again, the small scale of this experiment required considerable care and attention to maintain shock strength and consistency, and microphone size and frequency response. Since the spark-discharge method will always produce N-waves, an additional constraint is that focusing associated with shaped such as flattop or ramp signatures is not possible with this technique.

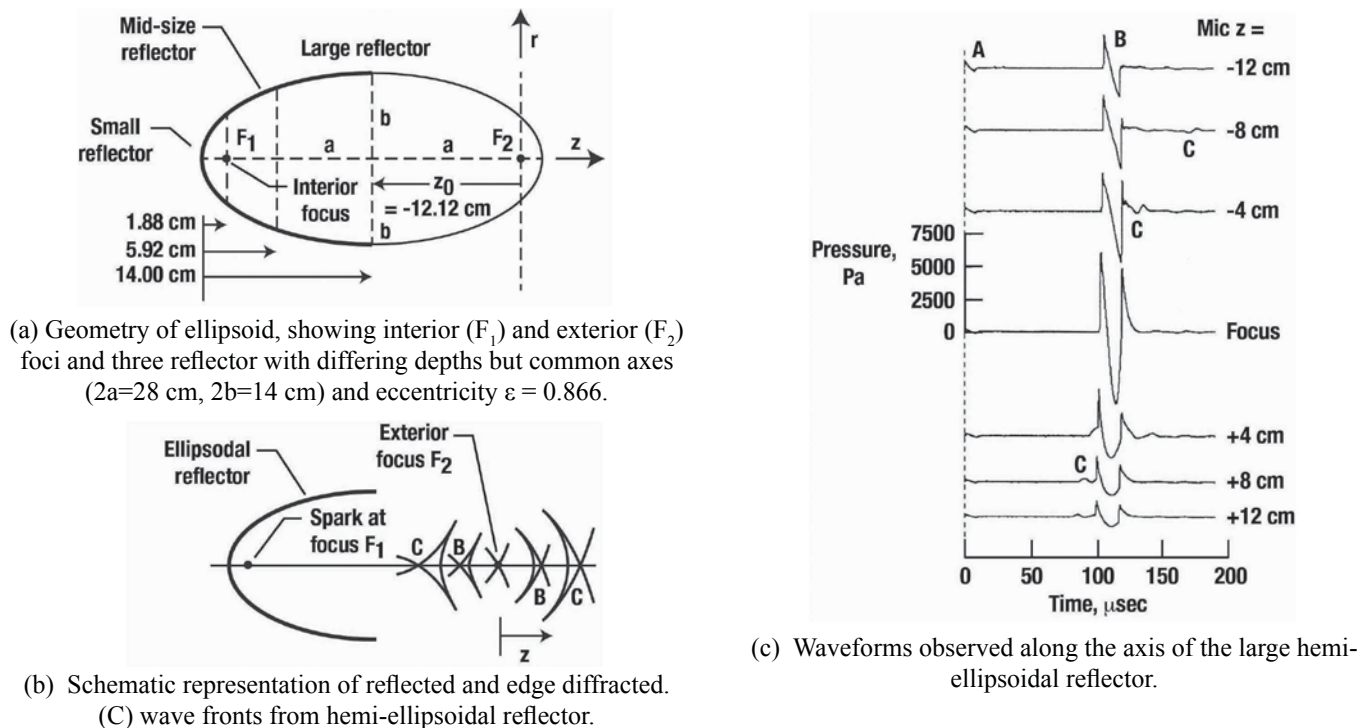


Figure 9.70. Laboratory test setup and results from spark and ellipsoidal mirror focus boom experiment (ref. 9.42).

Shock Tube Reflector

Distortion or wrinkling of the shock fronts, as illustrated in figure 9.71(a), by atmospheric anomalies or from non-steady flights were thought to cause boom focusing. Whitham (ref. 9.43) suggested that as the shock waves strengthen near the focus of, say, a concave curvature in the shock front, the converging rays bend away from each other and the concave front becomes convex and focusing would not occur. In 1973, Sturtevant (ref. 9.44) conducted an experiment to study shock waves focused from concave reflectors in a 17-inch diameter shock tube. In figure 9.71 (ref. 9.44) are shown the test arrangement and results from the shock tube experiment. It can be seen that as shock strength decreases, as a result of decreasing Mach number, the focus factor increases, varying from about 3 to 9.

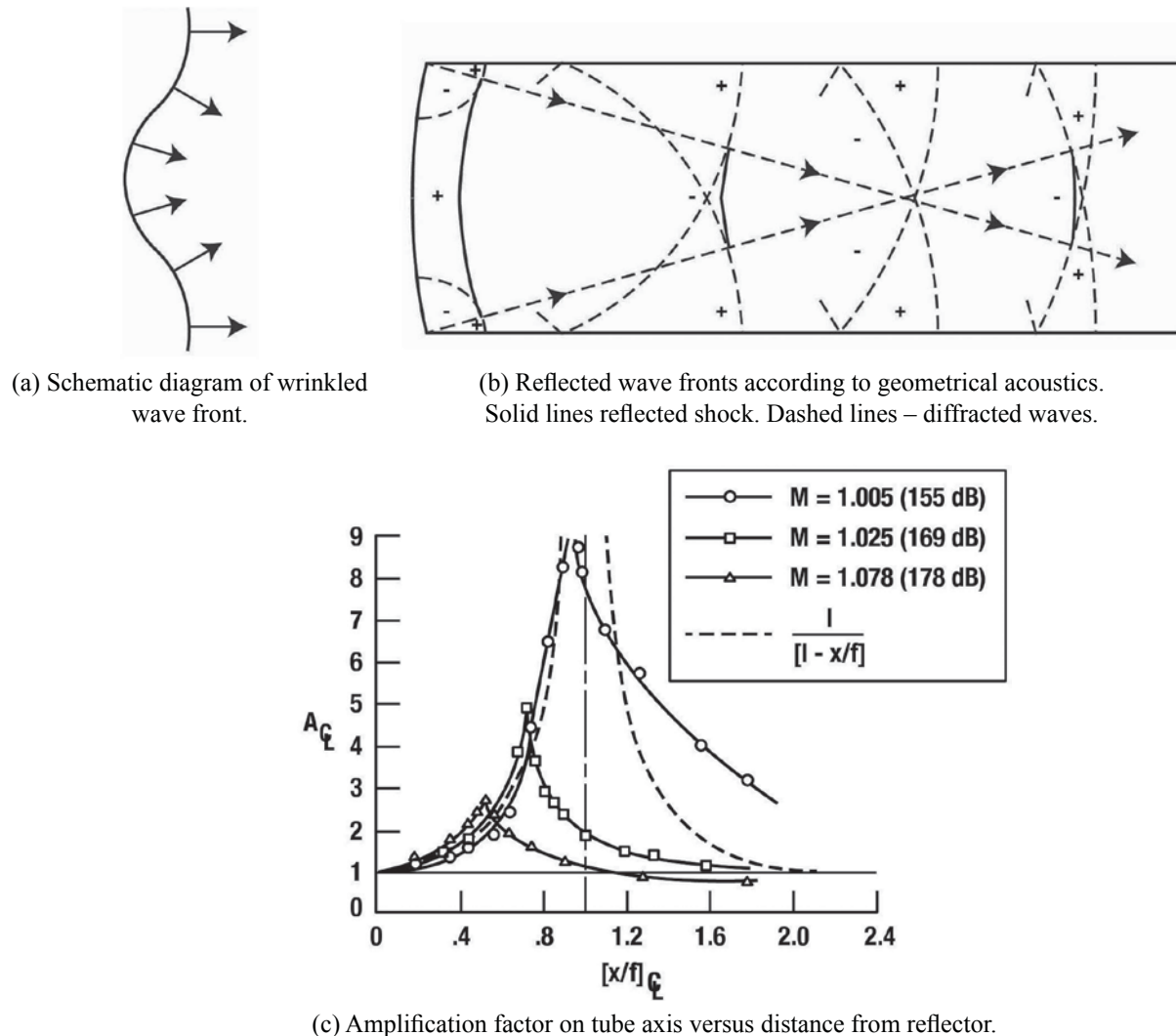


Figure 9.71. Arrangement and results from shock tube experiment on focusing of wrinkled wave front (adapted from ref. 9.44).

Ballistic Range-Mixed Gases

In an attempt to address superboms generated as a result of acceleration maneuvers, Sanai, Toong, and Pierce (ref. 9.45) made use of a dual Schlieren system and several fast response pressure transducers on the same small ballistic range that was utilized in the previous tests described in figure 9.63. The major difference was that the leak-proof gate, containing the gases of higher and lower sound speeds, was mounted vertically rather than horizontally, as shown in figure 9.72 (ref. 9.45).

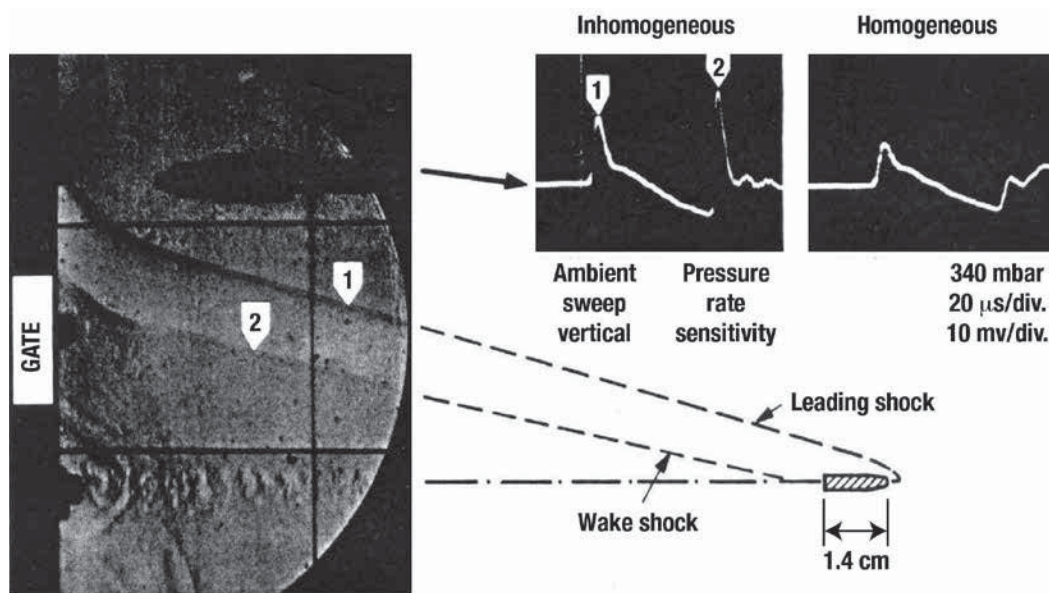


Figure 9.72. Results from ballistic range experiment to measure super booms from aircraft acceleration maneuvers (adapted from ref. 9.45).

Prior to the firing of the projectile, the gate is removed and the gases mix, creating a transition region of variable sound speed in the vicinity of the gate (black region at left of Schlieren picture). The projectile, passing through this medium, experiences increasing Mach number similar to an accelerating supersonic aircraft. Shown in the figure is a Schlieren photograph and simultaneous pressure signatures obtained from the shocks emanating from the bullet traveling 1235 m/sec from a helium-argon mixture into nitrogen causing the wavefronts to be concave. Comparison of the two pressure signatures show the magnification of the bow and tail shocks caused by the shock front concavity for the inhomogeneous case, as compared to the near N-wave shape in the homogeneous case. The largest focus factor obtained in these experiments was 2.0. The authors point out that this focus factor value of 2.0, with appropriate theoretical scaling to account for differences in shock overpressure ratios suggests that peak magnification of atmospheric sonic booms due to accelerated aircraft flight should be in the range of 6 to 13. These values bracket the results of field tests. Although the small ballistic range technique confronts difficulties associated with signatures of small size and response and shock waves and reflections, it does have an advantage over the spark-mirror systems in that signature shapes other than N-waves can be generated by proper shaping of the projectile. Focus factors other than these attributed to N-waves can be examined.

Underwater Studies

An analytical and experimental database has been generated since the late 1960s time period regarding the penetration of sonic booms into water and their impact on marine life in the oceans and seas of the world (see Chapter 8). A portion of the experimental database was generated by full-scale flight vehicles. As was noted in the discussion regarding the effect of sonic booms on marine life in Chapter 8, there is a large mismatch of sound speeds in air (1116 ft/sec) and water (4800 ft/sec). As a result of this large difference, the effect of sonic booms from vehicles in level flight at supersonic speeds over lakes and oceans was expected to be minimal since about 99 percent of the impinging energy would be reflected.

It is of interest to note that in the early years, only two documented experimental model studies regarding this subject were performed and they will be presented. The first was the scaled experiment by Waters and Glass (ref. 9.46) in 1970 using dynamite caps and a flooded quarry. In 1972, Intrieri and Malcolm (ref. 9.47) conducted scaled measurements using gun-launched projectiles over a water tank. Waters and Glass focused mainly on booms associated with supersonic flight and Intrieri and Malcolm investigated both supersonic and hypersonic speeds.

Blasting Caps/Flooded Quarry

The Waters and Glass (ref. 9.46) experiment was the earliest effort to investigate underwater sonic boom propagation. To accomplish this, they used an explosive charge detonated in the air over a small body of water. A schematic of their test setup is presented in figure 9.73 (ref. 9.46). The small body of water was a flooded quarry about 300 feet wide and 80 feet deep. The explosive charges, 6-grain dynamite blasting caps, were suspended from a high horizontal cable about 30 feet above the water. Two arrays of sensors were suspended in the area from a low horizontal cable and consisted of a microphone and hydrophone for the local array, directly under explosive charge, and a movable array consisting of a microphone and three hydrophones. All of the experiments were made with a flat water surface. No measurements were made to investigate effects of water roughness.

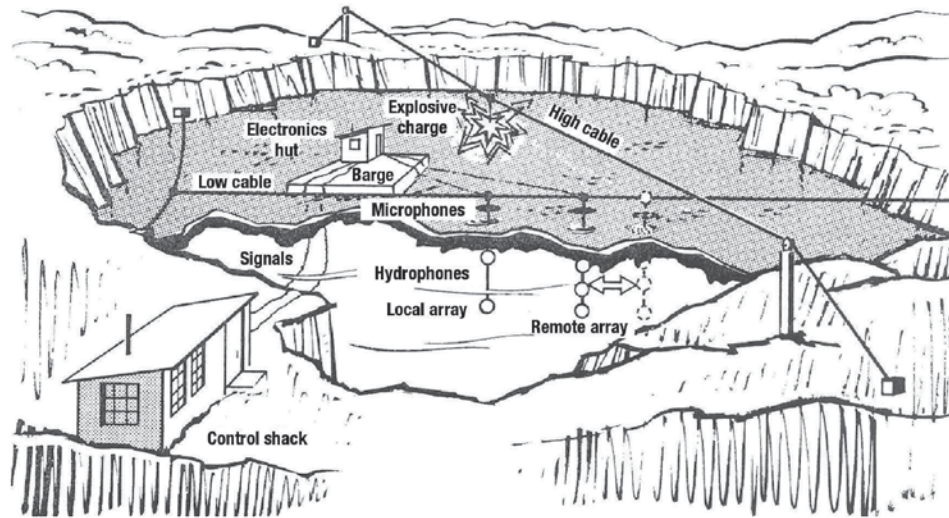


Figure 9.73. Geometry of sonic boom simulation experiment (ref. 9.46).

The explosive charges that produced a spherical spreading shock wave simulated the sonic boom upon the water surface, as shown in figure 9.74 (ref. 9.46). The indicated region of the spherical wave front was used to simulate the corresponding position of a conical wave front that a supersonic aircraft would generate. About 20 shots were made with the remote array positioned between 15 feet and 145 feet away from the local array, which was directly under the explosive charge. It was found that the optimum location, free from interference due to other transmitted signals, was from 2 to 60 feet from the local array. The location of the sensors is shown in figure 9.75 (ref. 9.46), which depicts the rays of sound within the critical angle that were transmitted across the air-water interface into the water. These rays were plotted in 5° increments in the water using Snell's law. The curves are wave fronts at successive intervals of time.

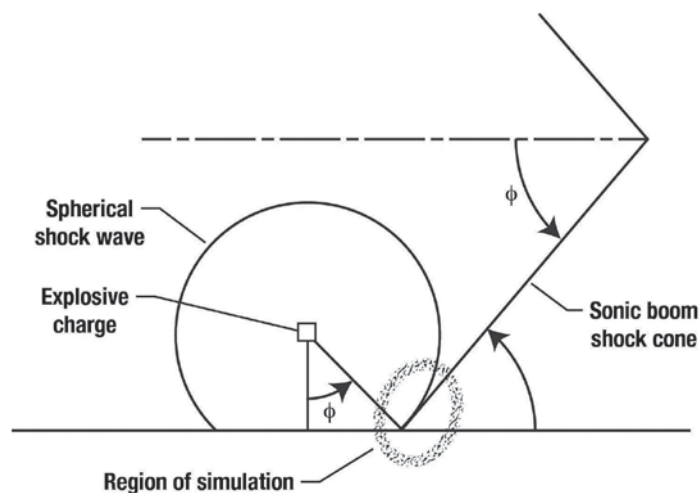


Figure 9.74. Simulation of region and shock cone using portion of spherical shock wave (ref. 9.46).

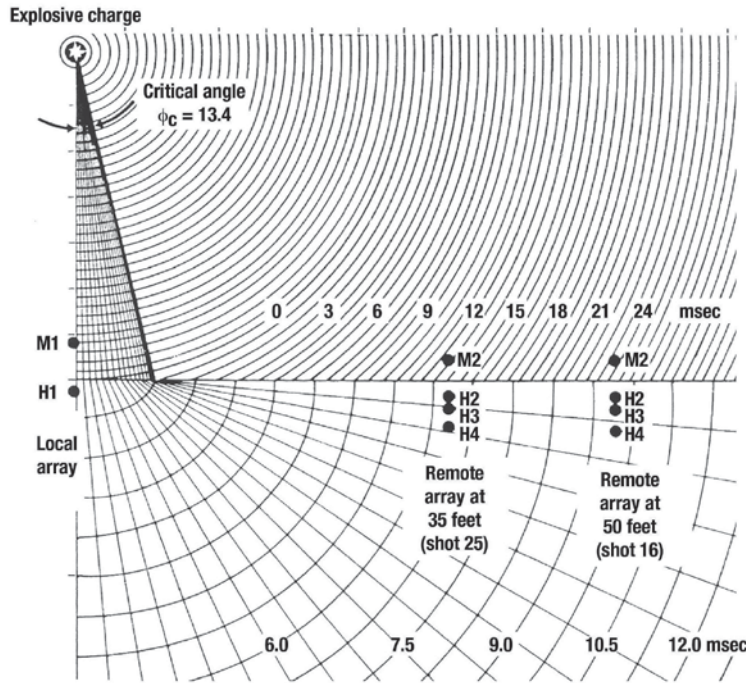


Figure 9.75. Locations of sensors for measurements of penetration of shock wave energy into water (ref. 9.46).

Figure 9.75 shows that the hydrophone directly below the explosive charge will be experiencing the shock penetrating the surface at speeds greater than the speed of sound in water (4800 ft/sec) and the remote hydrophone array positions will see shocks at Mach angles greater than 13.4° with effective velocities in the 1000 ft/sec to 2000 ft/sec range depending upon the location of the remote array from the overhead position. In an attempt to increase the width of the penetration measurement windows, a 16-foot square plywood reflector-absorber was suspended over the water directly under the explosive charge about 6 feet above the water surface to block out the shock wavefronts within the 13.4° cone. However, diffraction effects at the edge of the reflector-absorber resulted in its abandonment. In the initial stages of these experiments, inflated auto inner-tubes were used as floats to hold up the local and remote arrays rather than the overhead cables. However, it was found that the floats above the remote array were being excited by the incident airborne shock wave and were reradiating sound back into the water. This introduced signals that interfered with the desired measurements. Thus, all subsequent experiments were done without floats. A typical shock waveform measured 3.8 feet above the water by the local array microphones and is shown in figure 9.76 (ref. 9.46).

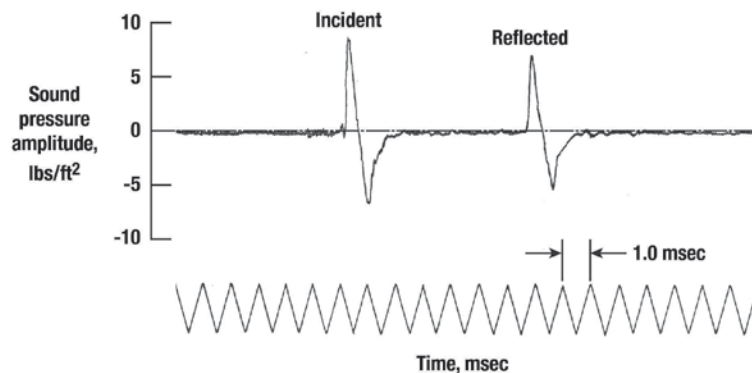


Figure 9.76. Airborne pressure N-wave due to 6-grain dynamite cap exploded at 3.8 feet above water surface (ref. 9.46).

Both the incident and reflected signatures of the airborne shock are shown. The dynamite cap pressure signature is a good approximation of an aircraft N-wave, except for the 10 lbs/ft² bow shock and a reduced level of the recompression tail shock (7 lbs/ft²). However, although the dynamite cap simulated the order of magnitude of a sonic boom of 2.0 lbs/ft², its signature duration of 1.8 msec was considerably shorter than the 100 to 300 msec measured from an aircraft. Since the dynamite cap shock signature duration is about 1 percent of that of a real

boom, the authors stated that the predicted water penetration for the experiment would only be 1 percent of that which would actually occur. In reference 9.46 (pp. 3-5), the authors went on to state:

But this amount of penetration, of the order of one foot in the experiment, did prove to be measurable. In retrospect, it is clear that if N-waves having durations of 100 msec to 300 msec had been used in the experiment, no meaningful measurements could have been made because of reverberations in the small body of water that was used. It would have been necessary to conduct the experiment in the deep ocean, which would have been a much more ambitious undertaking.

Placement of the hydrophones of the movable remote array was based on Sawyer's (ref. 9.48) theoretical expression for the penetration of an N-wave into the water and was found to be a few feet for the 1.5 msec duration of the dynamite cap explosive charge. The four hydrophones were set at 1, 1.5, 2.5, and 4.5 feet, the actual depth being somewhat greater than intended due to the catenary of the overhead cable suspension. The hydrophones and microphones had good frequency response, the hydrophones down to about 10 Hz and the microphones from about 1.0 Hz to about 10 KHz. The results of a measurement, including both transmission and penetration effects, are presented in figure 9.77 (ref. 9.46) for the local array directly below the explosive charge and the remote array, which was about 35 feet from the local array.

The measured results are quite interesting. Note that the signature measured by the local array of hydrophones directly below the explosive charge (see fig. 9.75) one foot below the water surface has the same characteristics as the airborne shock and is only slightly lower in overpressure. This was expected since the shock arrival angle to the water surface was within the critical angle (13.4°) resulting in a shock wave penetration speed greater than the sound speed in water. In contrast, for the remote location some 35 feet from the local array, the shock arrival angle to the water surface was well outside of and greater than the critical angle of 13.4° , which resulted in the shock front moving across the water surface at only 1600 ft/sec. The hydrophone measured signatures become more rounded and are an order of magnitude less than the airborne signature value, measured 2.4 feet above the water surface at the 35-foot remote array location, and decrease with increasing depth.

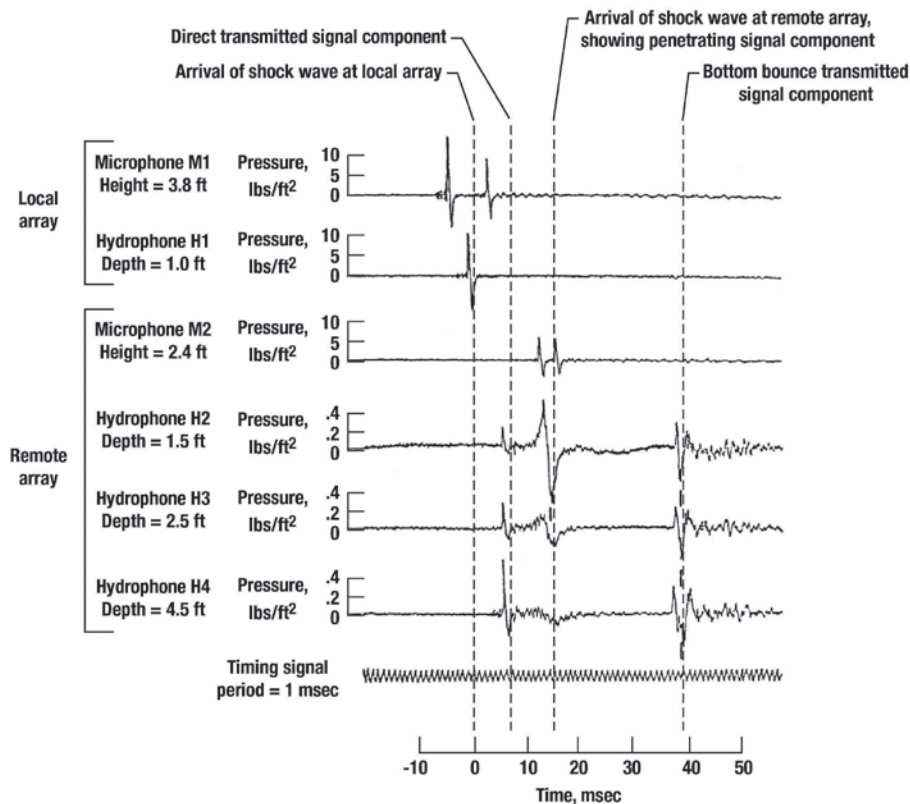


Figure 9.77. Airborne and underwater measurements of shock signature transmission and penetration at remote array 35 feet from local array (ref. 9.46).

A detailed comparison between the theoretical prediction provided in reference 9.46 for the test shot results shown in figure 9.77 is presented in figure 9.78 (ref. 9.46). The agreement between the predicted and measured signature is quite good, within a factor of two on both amplitude and signature duration. At the time of these experiments, during the early 1970s, the authors were satisfied that the experiment resulted in verification of predictions based on existing theory of N-wave penetration into a flat body of water. This simulation experiment, like others discussed in this chapter, had to address scaling concerns such as the explosive N-wave signature overpressures of about 10 lbs/ft² and periods of 1.5 msec and the water depth of 80 feet.

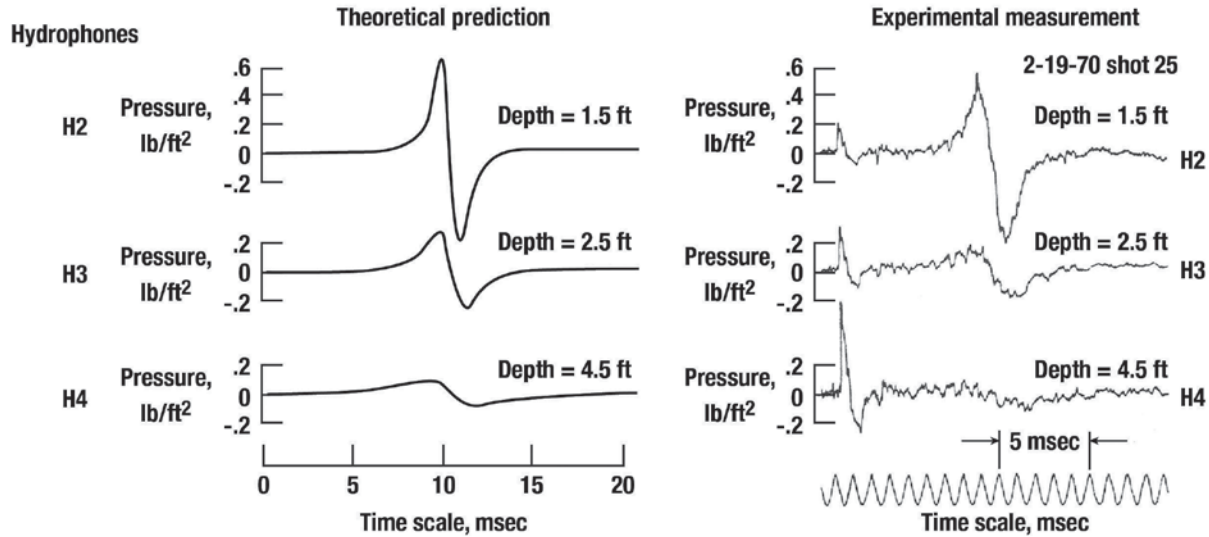


Figure 9.78. Comparison between theoretical prediction and experimental measurement of penetration of shock wave energy into water (adapted from ref. 9.46).

Ballistic Range Water Tank

Intrieri and Malcolm (ref. 9.47) conducted a unique experiment in investigating the penetration of sonic boom signatures moving over the water at speeds less than and greater than the speed of sound in water using the 10-foot diameter 300-foot-long NASA ARC Pressurized Ballistic Range and a gun-launched projectile over a large Plexiglas tank containing water. A sketch of the setup is shown in figure 9.79 (ref. 9.47).

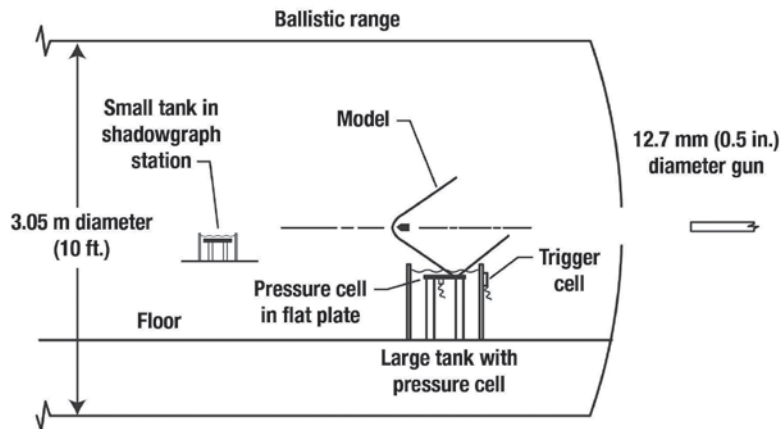


Figure 9.79. Sketch of test setup in ballistic range (ref. 9.47).

Two tanks were utilized in this experiment, the large tank in which pressure measurements were made and a smaller tank that was used for obtaining shadowgraphs of the shock behavior in air and water. These were placed directly under the flight path of the projectile. Details of the makeup of the large tank are given in figure 9.80 (ref. 9.47). The tank was a 24-inch by 24-inch by 12-inch open top container. The tank and the flat plate shown with the pressure cell could be moved vertically to vary the distance from the projectile flight path and the water level was also adjusted to vary the depth of the pressure cell beneath the water surface.

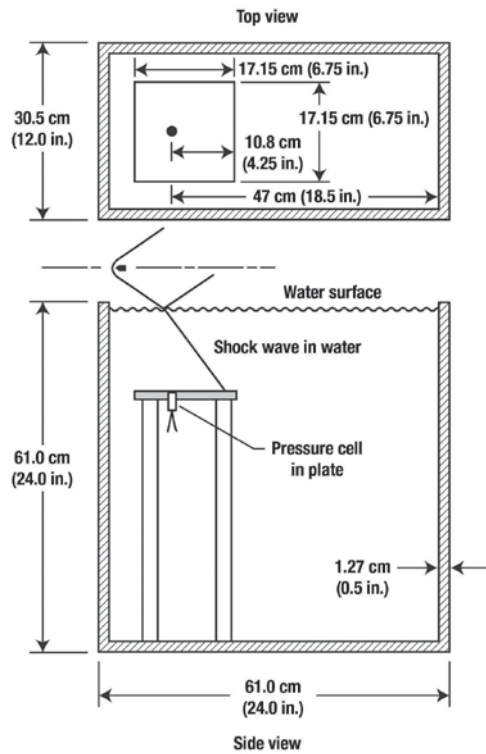


Figure 9.80. Dimensional sketch of large Plexiglas tank with pressure transducer (ref. 9.47).

A description of the projectile and resulting shock pressure signature is presented in figure 9.81 (ref. 9.47). A powder gas gun was used to launch the 45° half cone projectile, about 0.5 in., or 1.25 cm in diameter (fig. 9.81(a)) at Mach numbers of 2.7 and 5.7, corresponding to Mach numbers of 0.6 and 1.3 in water. The measured signature (fig. 9.81(b)) is N-wave in character with the tail recompression being significantly less in amplitude than the bow shock as a result of the large trailing wake on the projectile. Peak overpressures in air of from about 270 lbs/ft² to 1375 lbs/ft² were experienced at distances of about 34 inches to 8 inches, respectively. The signature period was 1.5 msec in duration.

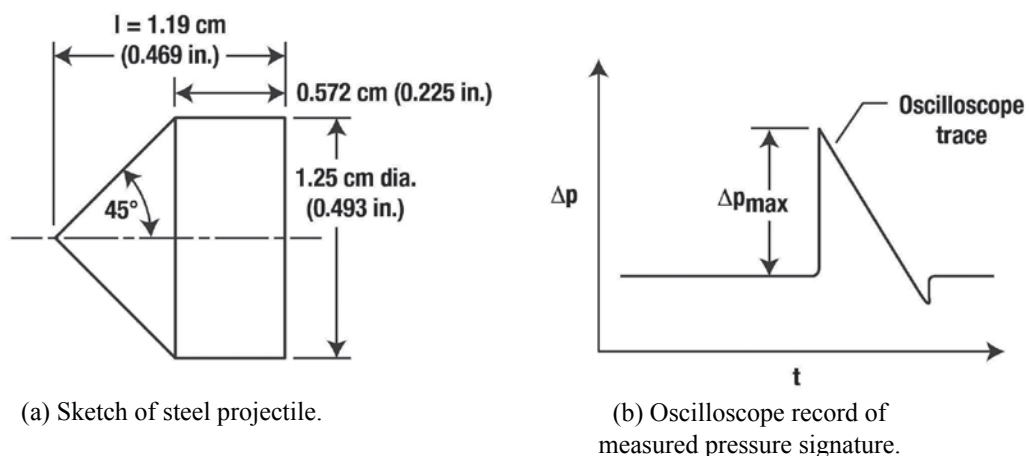


Figure 9.81. Description of projectile and shock pressure signature (adapted from ref. 9.47).

The shadowgraph of the projectile traveling over the water tank at Mach 2.7 is shown in figure 9.82 (ref. 9.47). Since the speed of the shock in air (i.e., Mach 2.7) is less in air than the speed of sound in water, which is about Mach 4.4, the bow and tail shocks are reflected off the surface of the water, as can be seen in figure 9.82. However, when the projectile is launched at Mach 5.7, the results are entirely different because airborne shocks do, in fact, penetrate below the water surface. These results are presented in figure 9.83 (ref. 9.47).

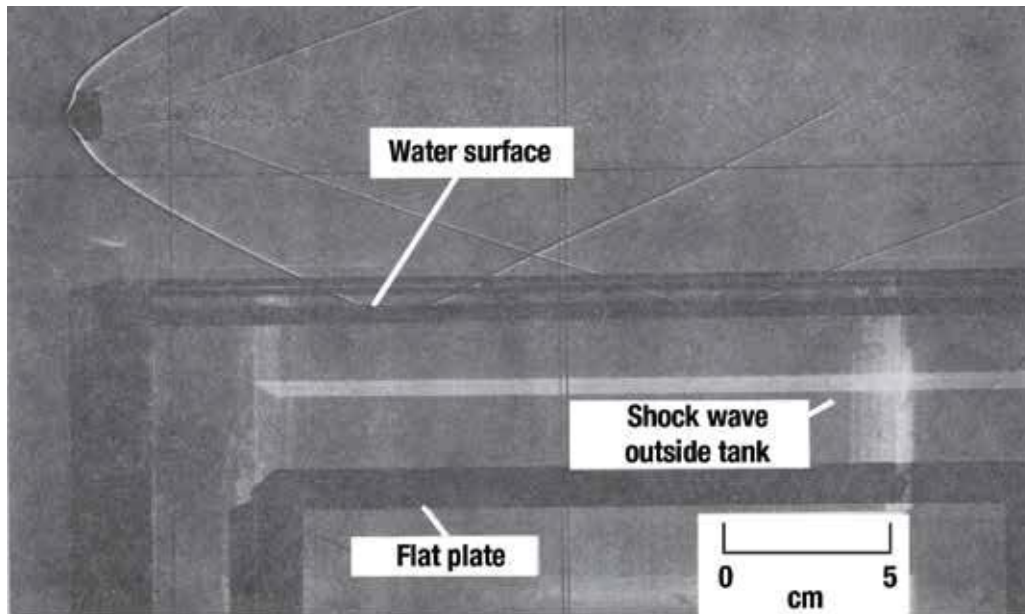


Figure 9.82. Shadowgraph picture of model flying over Plexiglas water-filled tank at Mach 2.7 in air $M_{water} = 0.6$ (ref. 9.47).

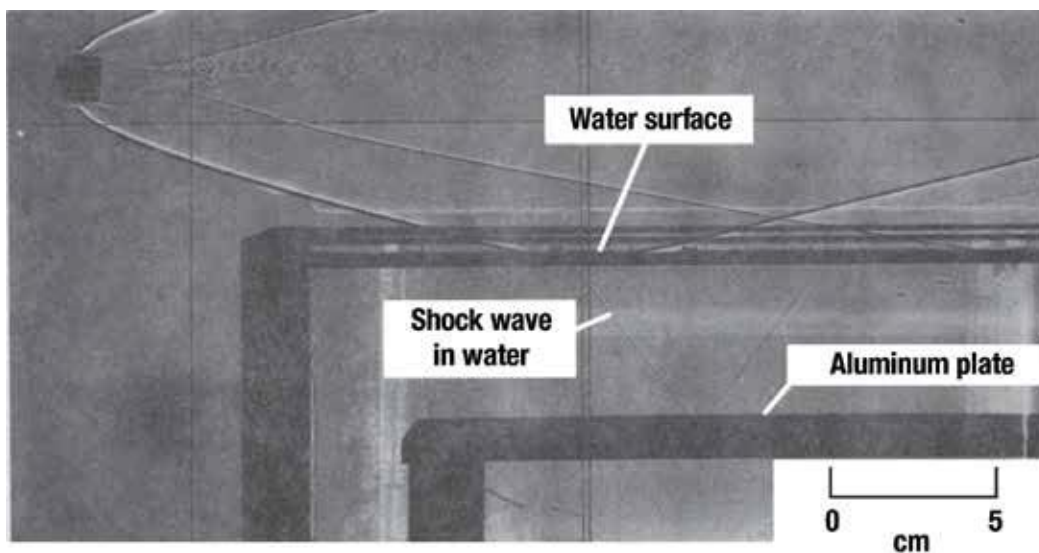


Figure 9.83. Shadowgraph pictures of model flying over Plexiglas water-filled tank at Mach 5.7 in air $M_{water} = 1.3$ (ref. 9.47).

The underwater shock resulting from the impingement of the projectile bow shock on the water surface is barely seen in the shadowgraph. Since the penetration of the projectile tail, or trailing shock, was significantly lower in overpressure than the bow shock, it is less visible in the shadowgraph, but still exists at shallow depths and will be shown in figure 9.84. The researchers found that when the aluminum plate was replaced with a Plexiglas plate, the shock wave propagating in water was not reflected by the plexiglass tank and bottom and passed through almost undisturbed. The authors stated that this occurred because the acoustic impedance (product of density and sound speed) of water and Plexiglas are nearly identical. Pressure signatures of the measurements obtained in air and underwater for the two cases shown on the above shadowgraphs (figs. 9.82 and 9.83) are presented in figure 9.84 (ref. 9.47).

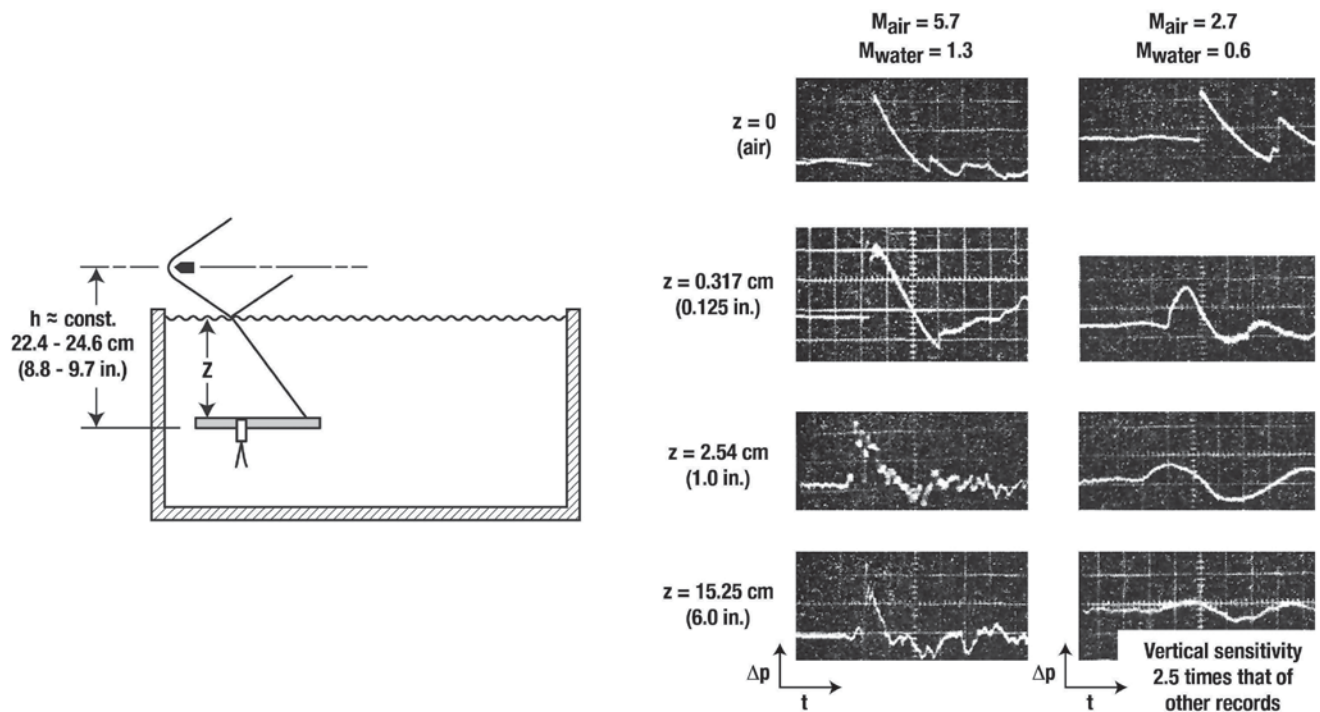


Figure 9.84. Oscilloscope records of pressure measurements in air and underwater (ref. 9.47).

A significant difference is apparent in the pressure signatures measured underwater between the subsonic and supersonic cases (Mach 2.7 and 5.7 in air, respectively). For the Mach 2.7 flights (subsonic case in water), there is a rapid decay in strength and a rounding of the signature with increasing water depth. For the Mach 5.7 flights (supersonic case in water), there is little loss in pressure amplitude and the signatures remain N-wave in shape, similar to the in-air case. Note too that the trailing shock, which was not too evident in the shadowgraph picture (fig. 9.83), is clearly evident in the measured pressure signature.

For the Mach 2.7 in-air case, the authors calculated the pressure signatures at various depths covering the range measurements of figure 9.84 using Sawyers' theory (ref. 9.48), and these are shown in figure 9.85 (ref. 9.47). The symbol δ is defined as the decay parameter for a sinusoidal plane wave underwater. In figure 9.86, the calculated maximum pressure variation with δ is shown. The reduction in peak pressure with water depth predicted by Sawyers is shown along with the measured results and the comparison is good. In fact, the authors state that these results (Intrieri and Malcolm) and those of Waters and Glass (see fig. 9.78) both support the theory even though they were conducted with completely different techniques and greatly differing time scales. The N-wave durations of 0.15 msec for the present tests and 1.5 msec for the Waters and Glass tests are an order of magnitude different and the shock overpressures are of about two orders of magnitude different for the Intrieri and Malcolm experiment than Waters and Glass.

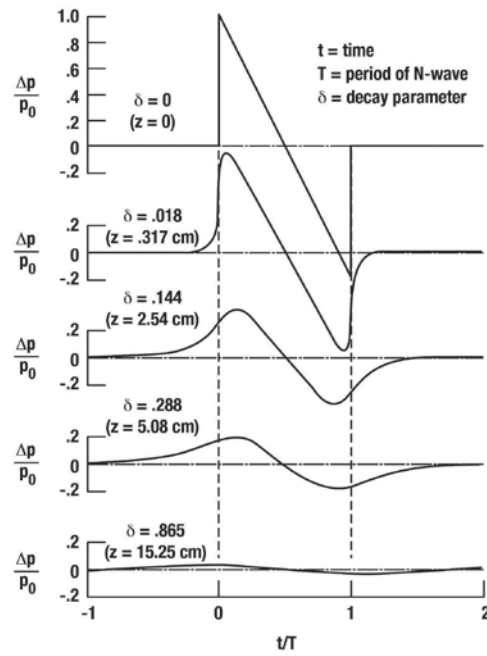


Figure 9.85. Calculated pressure signatures at various depths in water using theory of reference 9.48, $M=2.7$ in-air case (ref. 9.47).

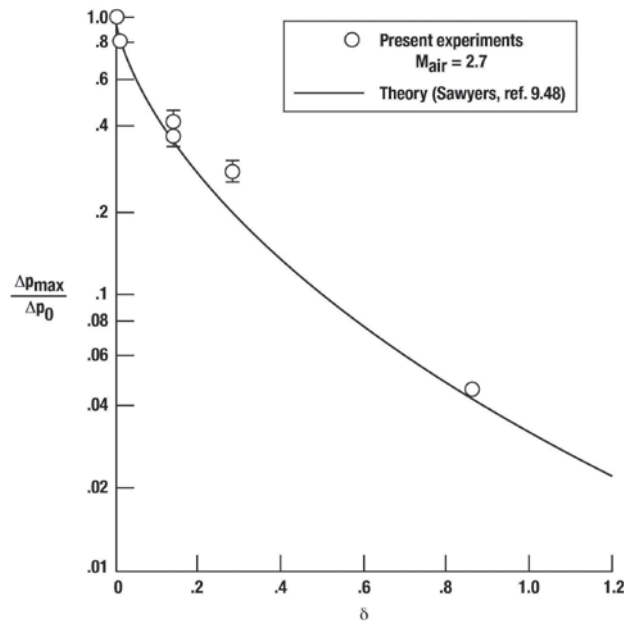


Figure 9.86. Variation of peak pressure from underwater sound waves with normalized depth parameter (ref. 9.47).

Recall that for the Mach 5.7 in-air case, shown in figure 9.84, the underwater pressure signatures changed little from the one measured in air at the water surface. The variation of the signature bow shock as a function of water depth for a constant distance of the projectile flight path above the water surface is shown in figure 9.87 (ref. 9.47). It can be seen that the maximum shock overpressure remains fairly constant with increasing water depth and is of the same level as the pressure at the water surface indicating essentially no loss in peak pressure due to water depth. This is further illustrated in figure 9.88 (ref. 9.47), which presents a variation of peak overpressure in air and underwater as a function of distance from the projectile flight path. Note that the variation in-air faired line, shown in figure 9.88(b), passes through data sets at all three depths at which measurements were obtained.

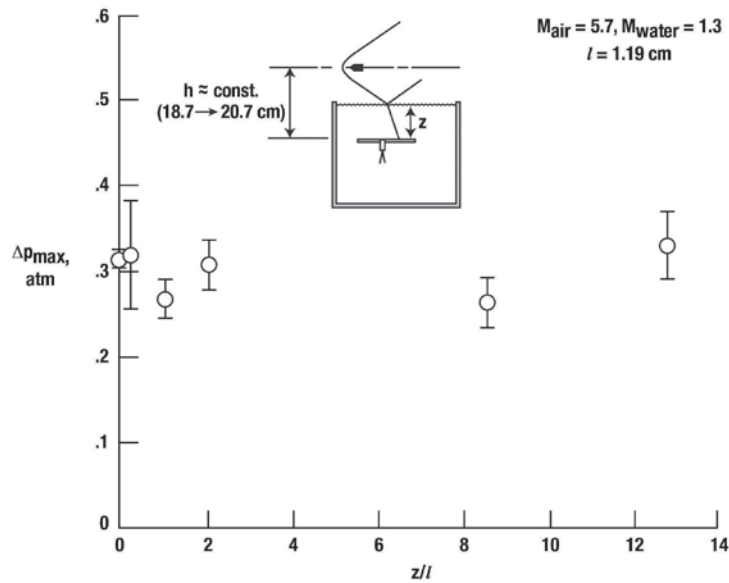


Figure 9.87. Variation of peak pressure with water depth using pressure cell mounted in flat aluminum plate (ref. 9.47).

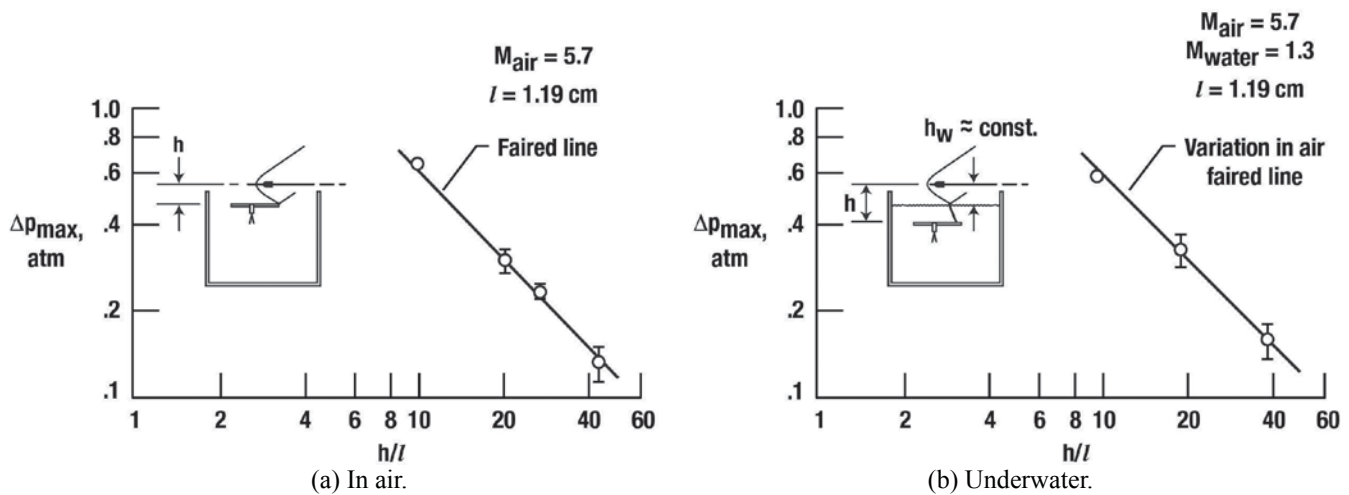


Figure 9.88. Variation of peak pressure with distance from flight path (ref. 9.47).

The simulation technique utilized by Intrieri and Malcolm also had to address the scaling concern of shock signature characteristics, water depth, transducer response, and measurement techniques. They did conduct an experiment to address the concern for the reflection and refraction of the shocks that may result with the pressure cell flush-mounted in a flat plate. The use of a ballistic range-projectile setup has great potential for examining the overwater sonic boom that will be associated with future vehicles designed to produce low-boom shaped signatures. Projectiles can be shaped to produce a variety of signature shapes, such as the bodies of revolution examined by Hague and Jones (ref. 9.25) and shown in figure 9.43.

Diffraction and Refraction of Sonic Boom Due to Buildings and Topography

Of the numerous environmental concerns contained within the sonic boom arena, the interaction between the sonic boom and topographical features such as buildings, mountains, rolling terrain, and canyons is one of the most interesting. Attention was brought to reflection and refraction concerns by Dini and Lazeretti in their 1969 paper (ref. 9.49), which showed incident boom overpressure could be enhanced from two to eight times depending upon the ground configuration, a few of which are illustrated in figure 9.89 (ref. 9.49).

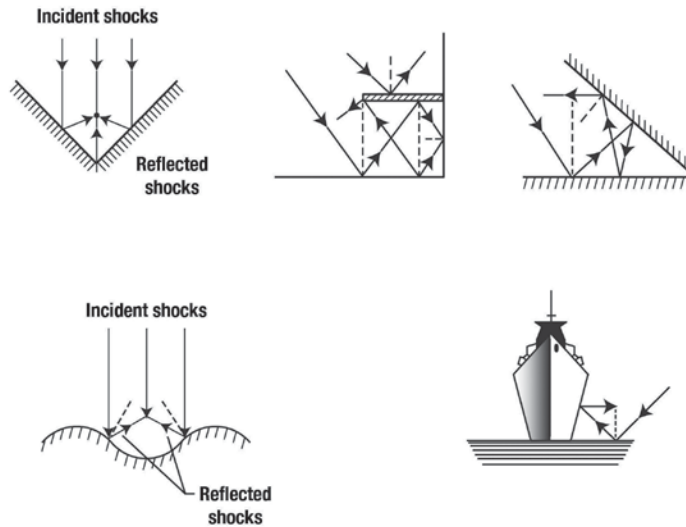


Figure 9.89. Schematics of incident and reflected shock patterns (ref. 9.49).

A substantial database has been established regarding this subject, but most relate to sonic boom loadings on commercial and residential structures (refs. 9.50 and 9.51) including the more recent work by Klos (ref. 9.52) and Cho and Sparrow (ref. 9.53). In each, however, these studies address various types of individual structures. No cluster of residential homes or multiple skyscraper arrangements have, as yet, been addressed. Several analytical efforts have been performed, i.e., Ting and Pan (ref. 9.54) and Ting and Kung (ref. 9.55), but these also deal with single structures.

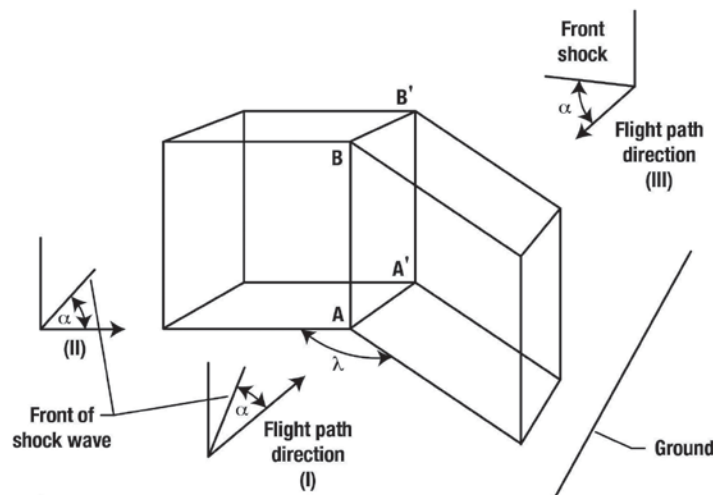


Figure 9.90. Three-dimensional diffraction of incident wave (ref. 9.54).

In their earlier study, Ting and Pan (ref. 9.54) looked at obtaining a near-field solution for the diffraction of a plane wave by a three-dimensional body and found one was not yet available. However, some partial information at the corners could be obtained using the averaging principle (ref. 9.56, p. 96), which states that “The intensification factor at the vertex of a cone with a solid angle λ is equal to the ratio of the solid angle of the flow field at the vertex without and with the cone, i.e., $4\pi/(4\pi-\tau)$.” Results from their study concerning a dimensional calculation for a V-shaped building shown in figure 9.90 (ref. 9.54) were obtained.

Three flight path approaches are indicated on the figure – direction I approaches the concave side of the V-shaped building, direction II is parallel to one leg of the V (which is, in effect, equivalent to a face-on boom to a single building), and direction III is opposite to I. The intensification factor (I.F.), calculated at the base of the V at position A for flight paths I and II and at position A' for flight path III, is provided in table 9.4 (ref. 9.54).

Table 9.4. Intensification Factors for a V-Shaped Building Arrangement Resulting from Supersonic Flight in Three Directions (ref. 9.54)

Intensification Factors (I.F.)

Corners	Flight Path					
	I		II		III	
	I.F.	$\lambda=\pi/2$	I.F.	$\lambda=\pi/2$	I.F.	$\lambda=\pi/2$
A	$4\pi/\lambda$	8	$4\pi(2\lambda)$	4	(a)	(a)
B	$4\pi(2\pi+\lambda)$	8/5	$4\pi(2\pi+\lambda)$	8/5	$4\pi(2\pi+\lambda)$	8/5
A'	(a)	(a)	$2\pi(2\pi-\lambda)$	4/3	$4\pi(2\pi-\lambda)$	8/3
B'	$4\pi(4\pi-\lambda)$	8/7	$4\pi/(4\pi-\lambda)$	8/7	$4\pi/(4\pi-\lambda)$	8/7

(a) Reached by diffracted waves from adjacent corners and edges.

Spark Discharge – Parabolic Mirror

In 1970, two laboratory simulations addressing boom refraction and diffraction were conducted. The first by Brooks, Beasley, and Barger (ref. 9.57), who used a spark discharge system and parabolic mirror to generate the sonic boom signatures and the second by Bauer and Bagley (ref. 9.22), who used a ballistic range and projectiles fired from a gun to produce the boom signatures. Brooks, Beasley, and Barger (ref. 9.57) describe a technique for simulating the fundamental phenomenon that occurs when a weak shock wave passes over a building and they present some representative data obtained using this technique. A schematic drawing of the apparatus is shown in figure 9.91 (ref. 9.57).

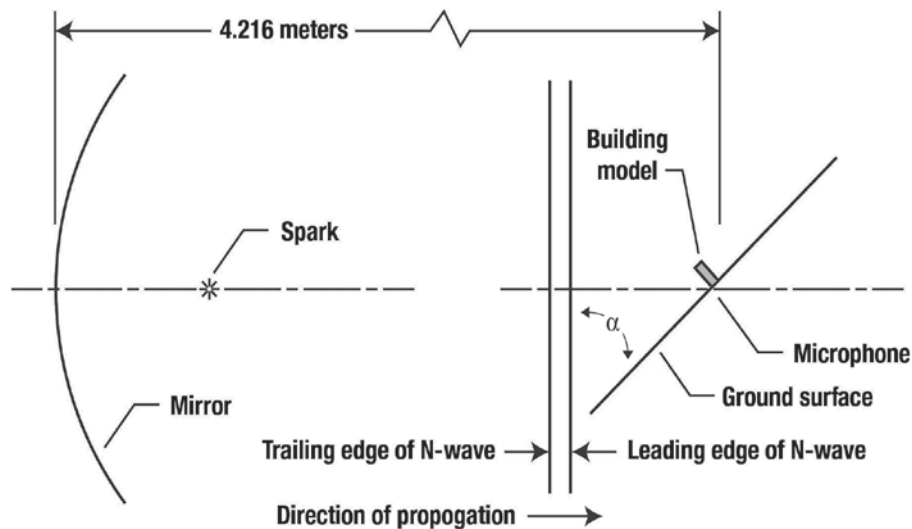


Figure 9.91. Diagram of test apparatus showing spark, mirror, ground surface, and building model (ref. 9.57).

The test setup consists of a spark device placed at the focus of a parabolic mirror so as to produce the sonic boom N-wave, which is then reflected from the mirror to the smooth ground surface plates, the latter made of 6.35-mm thick aluminum 41-cm wide by 51-cm long. Various building models were placed on this surface. The angle-of-incidence at which the shock impacts the model structure is varied by changing the ground plane angle with respect to the projectile trajectory. The distance between the mirror and model was 4.216

meters. A conventional off-axis Schlieren system (not shown) was used to photograph the shock waves. The author stated that the diffraction phenomenon resulting from an obstacle in the path of a sound wave depends primarily on the size of the obstacle to the wavelength of the sound pulse. As such, the models were scaled in accordance with the length of the N-wave. Various sizes of buildings were tested. They varied in height from 1/8 wavelength to 5 wavelengths and in width from 1/2 wavelength to a width greater than the mirror size.

They also chose to use ground shock angle (α in figure 9.90) rather than flight Mach angle ($\mu = \sin^{-1}(1/M)$) mainly due to the atmospheric effects. Shock tubes and projectile ranges were considered in the selection of a source to generate the N-wave but were discarded for the electric spark method. This latter method, which produces a plane wave rather than a conical wave, was found to be very consistent in both overpressures and wavelengths (period) and repeatable. The small size of the spark generated N-wave did present a limitation on the tests in that the microphone size relative to the signature period was large (microphone diameter is 3.22 mm or 1/8 wave length). The system had a flat response of ± 2 dB to 140 KHz.

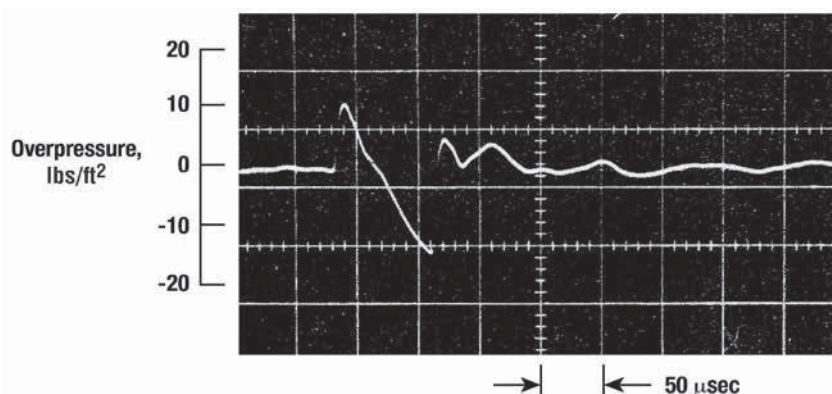


Figure 9.92. Typical signature of N-wave when microphone is mounted flush with ground surface. Oscilloscope sweep speed 50 $\mu\text{sec}/\text{cm}$ (adapted from ref. 9.57).

A typical signature of the N-wave produced by the spark and measured with a microphone flush-mounted in a ground plane is shown in figure 9.92 (ref. 9.57). The N-wave is quite representative of a sonic boom N-wave with the exception of the tail shock having somewhat greater amplitude than the initial bow shock. Boom overpressure of the bow shock is the order of 10 lbs/ft² and the signature period is about 100 μsec (wavelength of 2.5 cm).

In figure 9.93 (ref. 9.57), the general features of the wave pattern formed when the bow shock of the sonic boom N-wave passes over a two-dimensional building is shown. Shock wave passage is from left to right. Seven regions (see fig. 9.93) are identified and include: region 1 is the direct wave; region 2 is the wave reflected from the ground; region 3 is the wave reflected from the front face of the building; region 4 is a part of the direct wave that is diffracted around the upper rear corner of the building; region 5 consists of the compression wave diffracted from the upper front corner; region 6 is the expansion wave diffracted from the upper rear corner; and Region 7 is the wave refracted from the top of the building. The authors state that the wave pattern for a building of finite width is even more complex. Further examination of figure 9.93 (ref. 9.57) indicates that on the ground ahead of the building, the overpressure should be that of the direct wave with the ground reflection factor of 2.0. Near the top of the building front face, the overpressure should be the direct wave overpressure multiplied by the reflection factor for the building (also a factor of 2.0). As one approaches the base of the building, the wave reflected from the building overlaps the direct wave measured at the ground and at the base juncture, they are superimposed such that the overpressure is increased by a factor of 4.0.

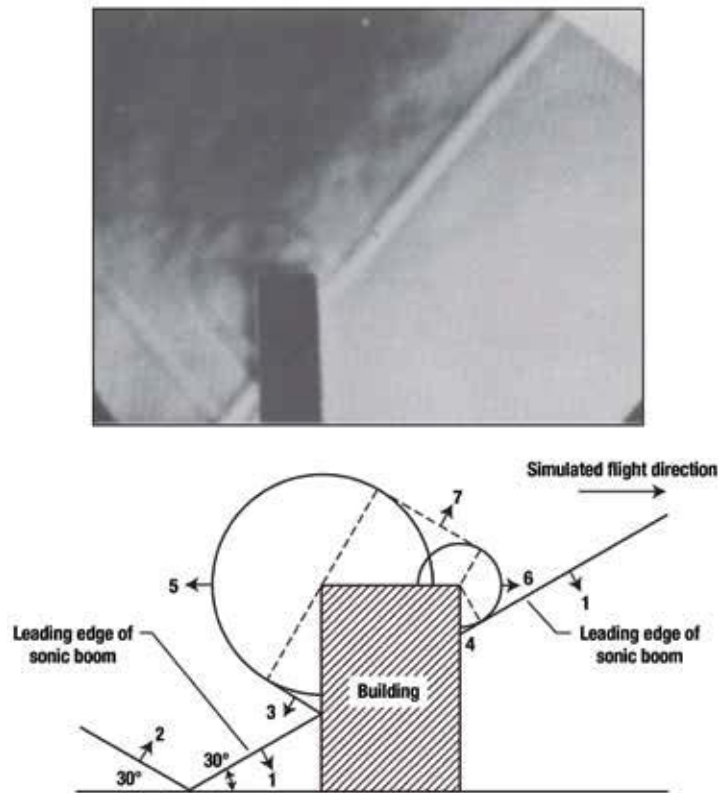


Figure 9.93. Reflection and diffraction of shock wave passing over a building. Arrows indicate direction of shock wave (ref. 9.57).

Test results from such an experiment is given in figure 9.94 (refs. 9.57). The overpressure measured on the ground at the base of a two-dimensional building of various heights is plotted as a ratio to the ground pressure p_g . It is noted that there is a small difference in the pressure ratio at the building base apex with the shock ground angle (i.e., simulated aircraft Mach number). In addition, the base apex overpressures are about 1.7 times those of the measured ground pressure rather than the factor of 2 for a perfect reflection case. This is due to diffraction effects and microphone size. The intensification ahead of and behind the intersection corners of an V-shaped building due to sonic booms at 30° and 60° incident angles is shown in figure 9.95 (ref. 9.57).

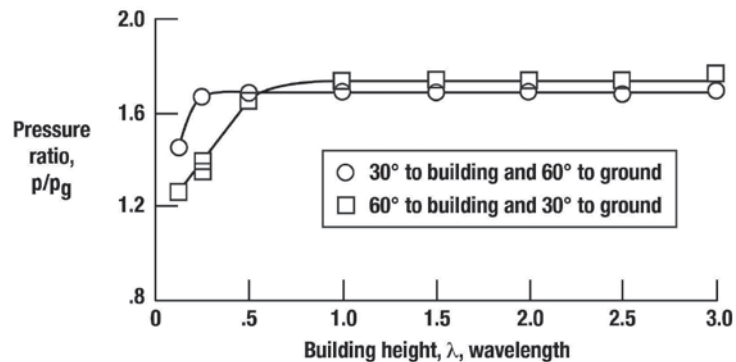


Figure 9.94. Maximum pressure to front base corner of building of various heights and infinite width due to sonic booms arriving at incident angles of 30° and 60° (ref. 9.57).

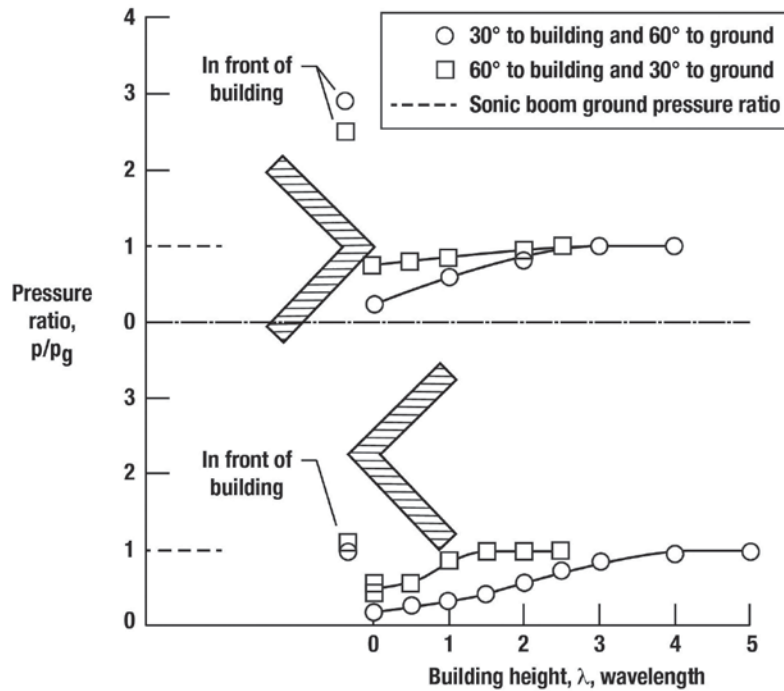


Figure 9.95. Ground pressure in front of and behind the intersecting corner of a V-shaped building 1 wavelength high and 1.5 wavelength on each side due to sonic booms at angles of 30° and 60° (ref. 9.57).

The experiments also examined whether unusual building shapes are better or worse than rectangular block shapes in regards to boom shielding or magnification. Results are presented for a V-shaped building in figure 9.95 (ref. 9.57). It can be seen that when the V-shaped building faces the incoming wave so that reflections from both sides and from the ground coincide at the base vertex, the amplitude, as expected, is magnified. When the wave is incident from the other direction, the pressure at the forward building base is lower and there is a significant amount of shielding on the inside of the L shape.

The influence of building cross-section, whether flat-faced or circular, is shown to have an effect on the pressure ratio that is realized on the front and behind the building. Some results for cylindrical buildings are shown in figure 9.96 (ref. 9.57).

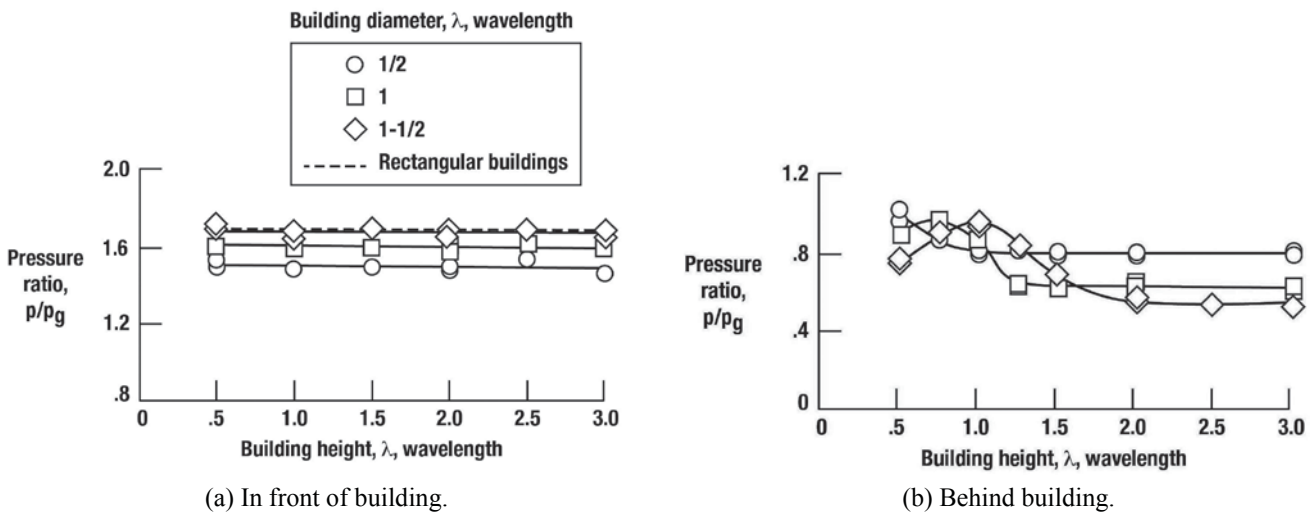


Figure 9.96. Pressure ratio on the ground in front of and behind cylindrical building due to sonic booms at an angle of 30° to the building and 60° to the ground (ref. 9.57).

It is shown in figure 9.96(a) that as the cylindrical building’s diameter decreases, the pressures also decrease from those measured for a rectangular building. This is a result of the beneficial effects of diffraction as the incoming

shock impacts and moves across the cylindrical building. As the building diameter increases from $\frac{1}{2}$ wavelength to $1\frac{1}{2}$ wavelengths, the beneficial effects of diffraction are reduced to the point where the shock front begins to see the cylindrical building as a rectangular flat surface. Behind the building (fig. 9.96(b)), the pressures depend on the phase relationships of waves coming over and around the cylindrical building.

In summary, this method of simulation proved to be of significant value giving results that are consistent with the previous analytical studies and suggest extending the scope to include clusters of building and some terrain topography. However, producing the sonic boom signatures using the spark discharge techniques, which results in an N-wave, does not allow for investigating the influence of low-amplitude shaped signatures.

Ballistic Range – Projectiles

The second of two experimental simulations regarding sonic boom reflection and diffraction on building structures and other topography was performed by Bauer and Bagley (ref. 9.22) using the same ballistic range and projectiles employed in their investigation of the influence of atmospheric turbulence on sonic boom signature distortions discussed early on in this chapter. The arrangement of the test setup is shown in figure 9.97 (ref. 9.22), which is the same arrangement as presented in figure 9.36 with the exception that the flow-duct is disabled and topographical models are placed on the ground plane. A sketch of one of these has been inserted to illustrate the arrangement. Their experimental setup shown in figure 9.97 (ref. 9.22) utilized an existing ballistic range enclosed within a barricade wall with inside dimensions of 25 feet by 22 feet with a 20-foot height.

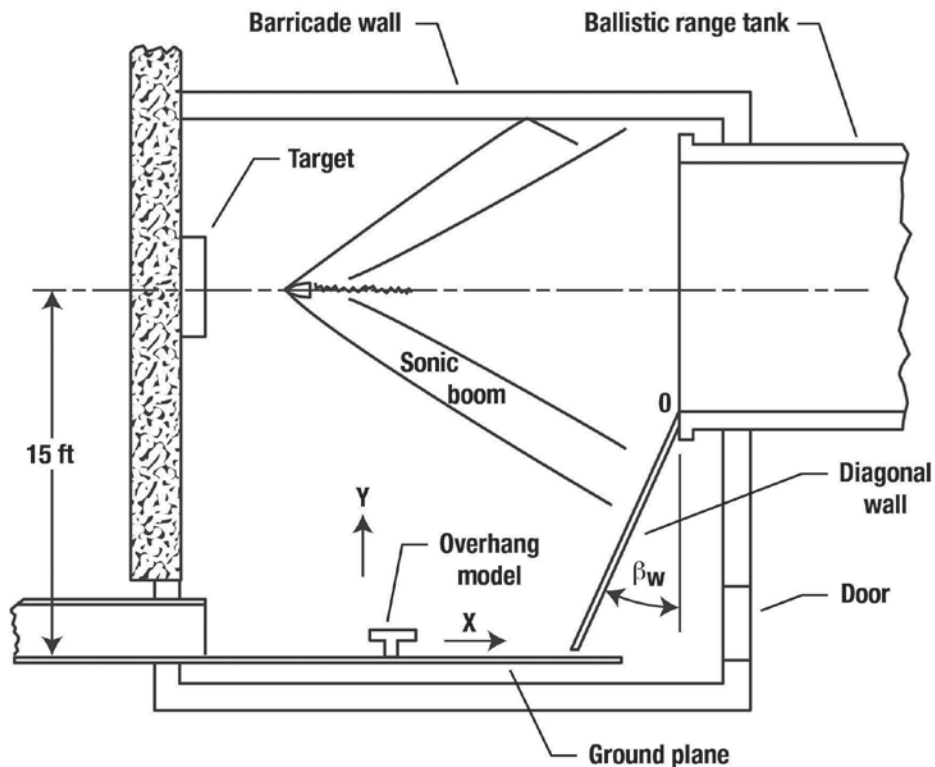


Figure 9.97. Plan view of barricade (adapted from ref. 9.22, see also fig. 9.36).

Sonic boom signatures were generated by firing projectiles at Mach numbers of from about 1.5 to 3.0. Pressure signature measurements of the projectile baseline signatures were made at three positions at around 6-inch spacing along a ground plane 15 feet below the projectile trajectory. The same series of bullets and projectiles used in the experiments on the influence of atmospheric turbulence on boom signature distortion discussed early on in this chapter were also used in the present experiment and are shown in figure 9.98 (ref. 9.22) and included 22-, 30-, and 46-caliber bullets and three machined projectiles of 0.22-, 0.457-, and 1.5-inch diameters.

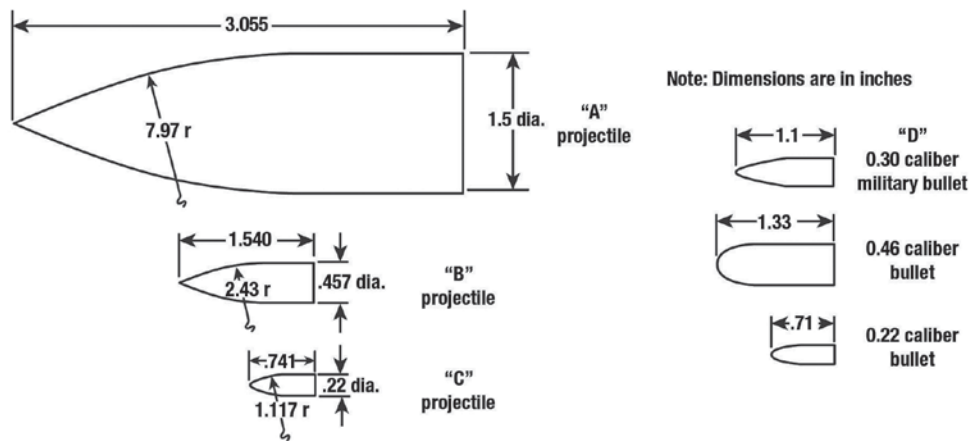
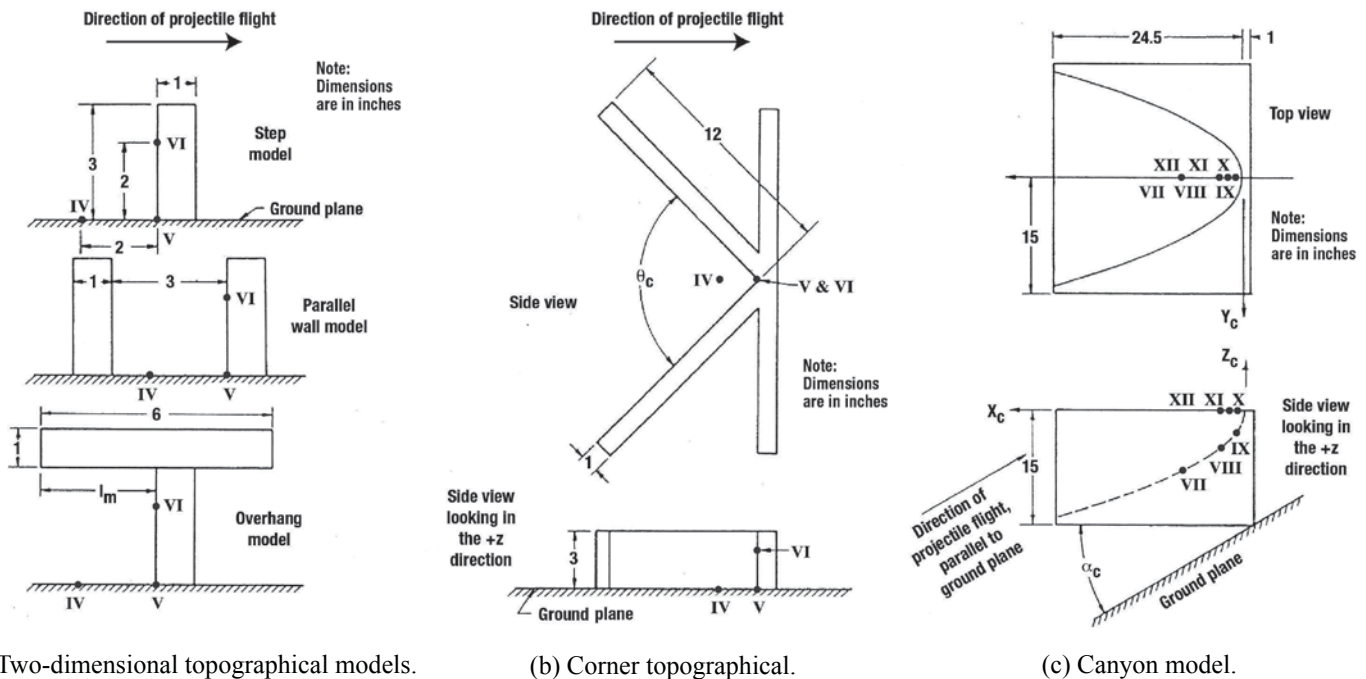


Figure 9.98. Bullet and projectile shapes used in experiment (ref. 9.22, see also fig. 9.37).

Projectile A was launched from a ballistic range light gas gun and the other projectiles and bullets were launched by rifle. Mach number was controlled during the experiment by varying the powder charges. For the 15-foot distance at which measurements were taken, the ground plane reflected overpressures ranged from about 17 to 72 lbs/ft². Signature lengths were on the order of 160 msec to 800 μ sec. Six topographical models having dimensions from 3 inches to 24 inches are shown in figure 9.99 (ref. 9.22). Included is a step model, parallel wall model, and overhang models shown in figure 9.99(a), a two-corner model (shaped) with apex angles of 45° and 90° (fig. 9.90(b)) and a canyon model (fig. 9.90(c)). For each model, the microphone locations are designated as IV through XII and are indicated on each sketch.



(a) Two-dimensional topographical models.

(b) Corner topographical.

(c) Canyon model.

Figure 9.99. Details of topographical models used in the tests (note dimensions are in inches, ref. 9.22).

Shadowgraphs were taken and played an important role in these tests, especially in positioning the models on the ground plane such that overpressure measurements from the incoming shock are made at the various microphone locations shown on figure 9.99. For the purpose of discussions, three models were chosen and include the step model, 2-inch overhang model, and the parallel wall model. Shadowgraphs of the N-wave shocks passing over each of the three models are presented in figure 9.100 (ref. 9.22).

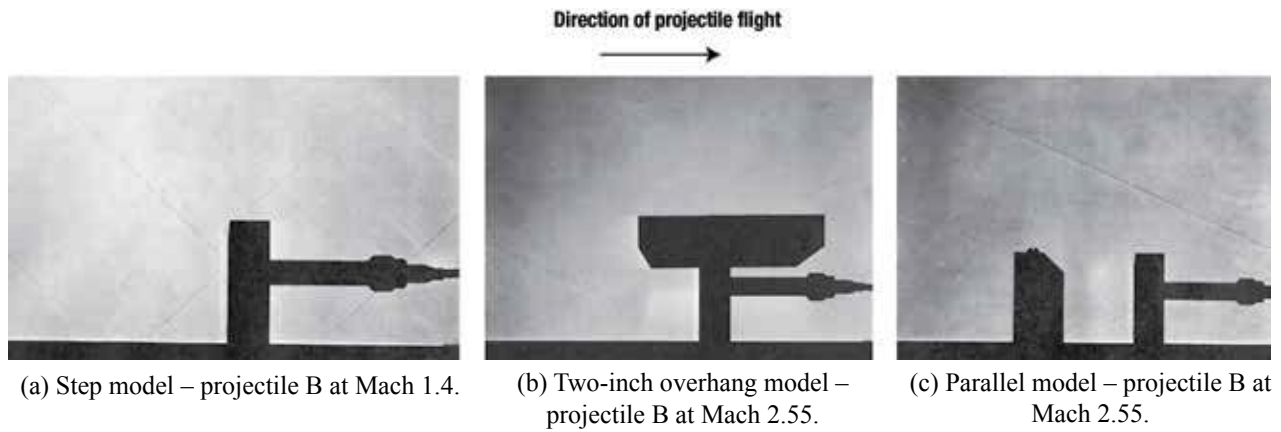


Figure 9.100. Shadowgraphs of three models and shocks from N-waves produced by Projectile B (ref. 9.22).

The two basic N-wave signatures generated by projectile B at Mach numbers 1.4 and 2.56, and measured at the ground board surface are shown in figure 9.101 (ref. 9.22). At Mach 1.4, the N-wave overpressure was 21.5 lbs/ft² and period was 300 msec, and at Mach 2.56, the overpressure was 25.0 lbs/ft² and period was 260 msec. Boom signatures measured on the step model at position IV (ground plane), V (apex of ground plane and step), and VI (on the step face at 2/3 the step height) for projectile B at Mach 1.4 are shown in figure 9.102 (ref. 9.22). As expected, an enhancement of the overpressure is realized at microphone V. Ting and Pan (ref. 9.54) predict a peak intensification factor (IF) of 4.0. Using 1/2 of the measured overpressure (i.e., the incident pressure) of 12.6 lbs/ft² and the 46.7 lbs/ft² of microphone V, the IF is about 3.7. At the 2/3 height location, microphone VI, three shocks are observed with the largest overpressure of 39.6 lbs/ft². Note also that the mid-shock of signature IV is at a different location than the location in figure 9.101(a) (which is near the trailing shock). In addition, there is a slight variation in the ground board signature overpressures between the two bow shocks at Mach 1.4 (i.e., 21.5 versus 25.3 lbs/ft²).

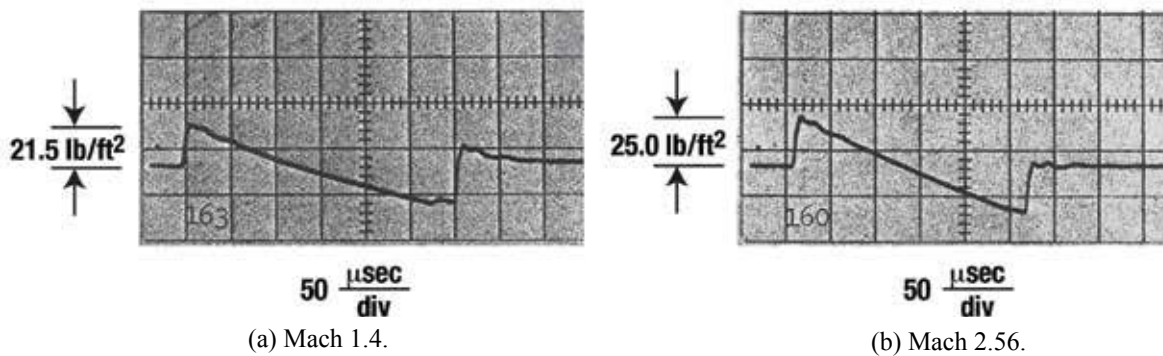


Figure 9.101. Basic signatures from projectile B (adapted from ref. 9.22).

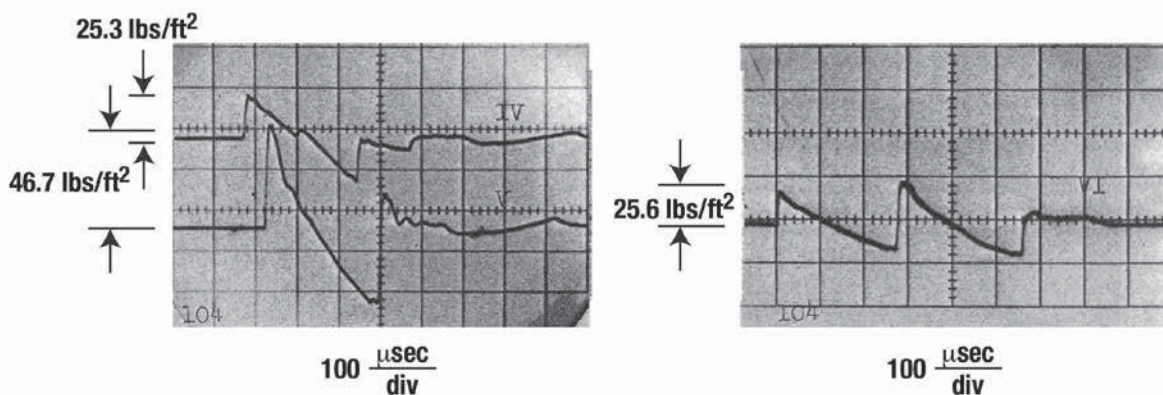


Figure 9.102. Signatures at location IV, V, and VI from projectile B at Mach 1.40 and the step model (adapted from ref. 9.22).

A quite complicated sonic boom signature is observed for the 2-inch overhang model shown in figure 9.103 (ref. 9.22). Note also the change in horizontal time scale on this plot. Multiple signatures were observed at all three microphone locations with the largest overpressure occurring at microphone V at the intersection of the ground plane and wall base with a value of 34.5 lbs/ft². The resulting IF is 2.62. Signatures associated with the parallel wall model, shown in figure 9.104 (ref. 9.22), are not too different than those measured on the step model (fig. 9.102). The signature measured at location IV with an overpressure of 15.7 lbs/ft² with the parallel wall model does not represent the direct ground pressure of 25 lbs/ft² for the step model seen in figure 9.101 due to the presence of the second simulated building. Thus, using the value of ground overpressure for the step model yields an IF of 3.9 associated with microphone V located at the intersection of the ground plane and the base of the second simulated building of the parallel wall model.

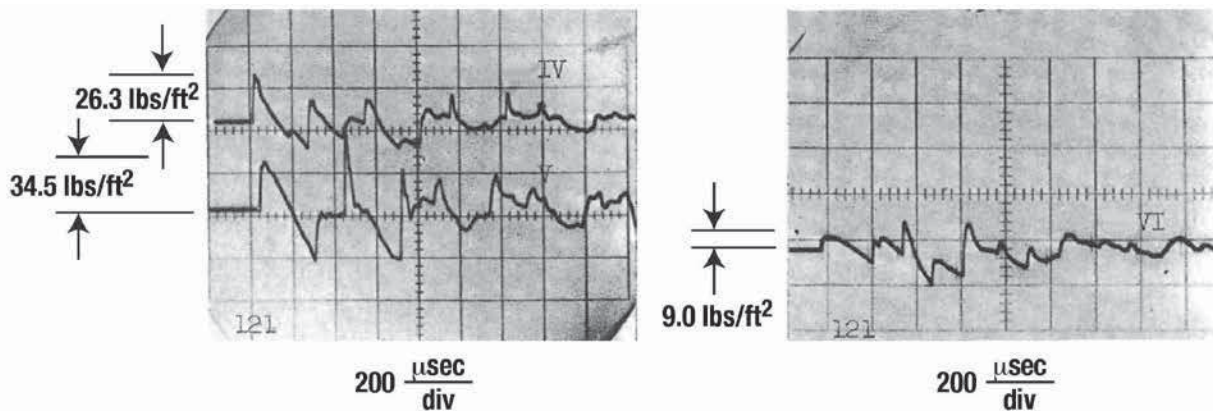


Figure 9.103. Signatures at location IV, V, and VI from projectile B at Mach 2.56 and the step model (adapted from ref. 9.22).

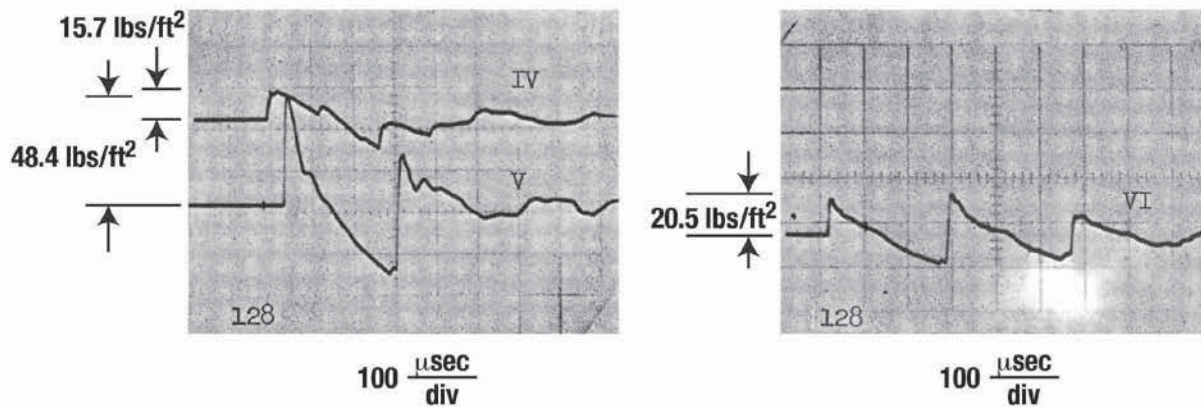


Figure 9.104. Signatures at locations IV, V, and VI from projectile B at Mach 2.56 and parallel wall model (adapted from ref. 9.22).

A summary of the IFs for all of the topographical models tested along with a canyon model is provided in tables 9.5 and 9.6 (ref. 9.22).

Table 9.5. Boom Intensification Factors Produced by Topographical Models (ref. 9.22)

Task	Shot No.	Model	Projectile	M	Intensification Factors Measured at Station		
					IV	V	VI
III	1-3	Step	D	2.5	--	3.70	1.72
III	3-3	Step	D	1.4	--	3.04	1.56(-1.66)
III	7-3	Step	B	2.6	--	3.22	1.78
III	4A-3	90° Cor.	D	2.5	--	4.14	2.80
III	5-3	90° Cor.	D	1.4	--	4.78	2.76
III	6B-3	90° Cor.	B	2.6	--	3.18	3.00
IV	104	Step	B	2.56	1.78	3.78	2.00
IV	111	Step	B	1.40	1.86	3.68	1.70
IV	133	90° Cor.	B	2.57	1.80(-2.40)	4.24	4.16
IV	137	90° Cor.	B	1.46	2.84(-3.06)	7.54	3.48
IV	138	45° Cor.	B	2.57	2.56(-2.74)	5.62	5.24
IV	142	45° Cor.	B	1.40	3.60(-3.94)	10.52	8.08
IV	122	1 in. O.H.	B	2.56	1.94	2.86	1.48(-1.80)
IV	121	2 in. O.H.	B	2.56	1.86	2.62	1.24(-1.58)
IV	127	3 in. O.H.	B	2.56	1.41	2.75	1.44
IV	124	4 in. O.H.	B	2.57	1.32	1.80(-1.92)	1.02(-1.04)
IV	123	1 in. O.H.	B	1.39	1.80	3.78	1.36(-2.42)
IV	116	2 in. O.H.	B	1.40	1.86	3.28	1.02(-1.51)
IV	126	3 in. O.H.	B	1.40	1.86	2.34	2.22(-2.34)
IV	125	4 in. O.H.	B	1.36	2.06	1.86(-1.88)	1.96
IV	128	Parallel	B	2.56	1.10(-1.16)	3.88	1.90
IV	131	Parallel	B	1.47	1.18	2.42	1.82

() for tail shock

Table 9.6. Boom Intensification Factors Produced by Canyon Model (ref. 9.22)

Shot Numbers	M	α_c (Degrees)	Intensification Factors Measured at Station					
			VII	VIII	IX	X	XI	XII
144, 146, 149, 150	2.57	0	2.68	3.70	2.14	1.04	1.04	1.14
145, 147, 148, 151	1.40	0	3.32	3.18	1.96(-2.42)	1.10	1.14	1.18
152, 154	2.56	66		2.28(-2.98)	3.48(-3.82)		13.8	
156	1.40	45		2.58(-3.18)	3.08(-3.88)		12.8	

Note that the largest value associated with the step, corner, overhang or parallel wall model was 10.52 and this was for the 45° corner. An even larger IF of 13.8 was measured on the canyon model from the B projectile at Mach 2.56 and at an angle of 66° from horizontal.

In summary, the simulation technique of using a ballistic range and firing projectiles is uniquely suited to experiments with clusters of model buildings and other topographical models. Further, as pointed out in the turbulence studies using this same simulation device, non N-wave boom signatures can be designed and launched via sabots. This would allow for examining the reflecting and diffraction of low-boom shaped signatures to establish the IF level.

Indoor-Outdoor Subjective Response

Research into the adverse environmental effects of sonic booms produced by aircraft goes back to the early 1960s. Laboratory and flight research has been performed (see Chapter 8) to define and understand how sonic booms affect structures, people, and animals. While flight experiments are the most realistic, they are also restricted in that they only apply to the particular aircraft used and the flight conditions flown. They are also expensive. Consequently, a variety of ground simulation devices have been developed and employed that yield realistic sonic booms to people, animals, and structures. They fall into four categories – (1) headphones, (2) loudspeakers inside closed booths, (3) piston systems, and (4) explosive charges. In subsequent paragraphs, short summaries of some of these systems and a sample of the research carried out using some of them will be discussed. The parameters of interest in the early days of developing sonic boom simulators are shown in figure 9.105 relative to the classical N-wave boom signatures.

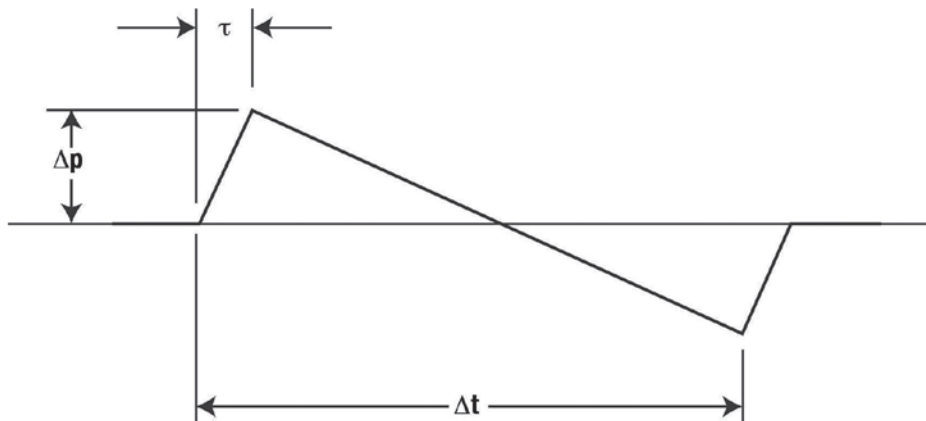


Figure 9.105. Illustration of sonic boom signature parameters that may be of interest for simulation. Wave-shape overpressure (Δp), duration (Δt), and rise time (τ) are depicted.

They include the magnitude of the leading-edge shock, the time it takes for the leading-edge shock to reach its maximum value (rise time), and the duration of the pressure signature. Since the mid-1960s, when the minimization of sonic booms became of prime interest to researchers, several new sonic boom signature shapes have become subjects of interest and three are illustrated in figure 9.106 along with the N-wave signature. One is termed a flat top or plateau, another called a finite rise time, and a third called minimum boom, or initial shock ramp signature. With the maximum shock magnitude and rise time added to the basic shapes there is almost an unlimited number of signatures that can be investigated. However, the three most investigated signature variables are initial and maximum shock strength, rise time, and signature duration.

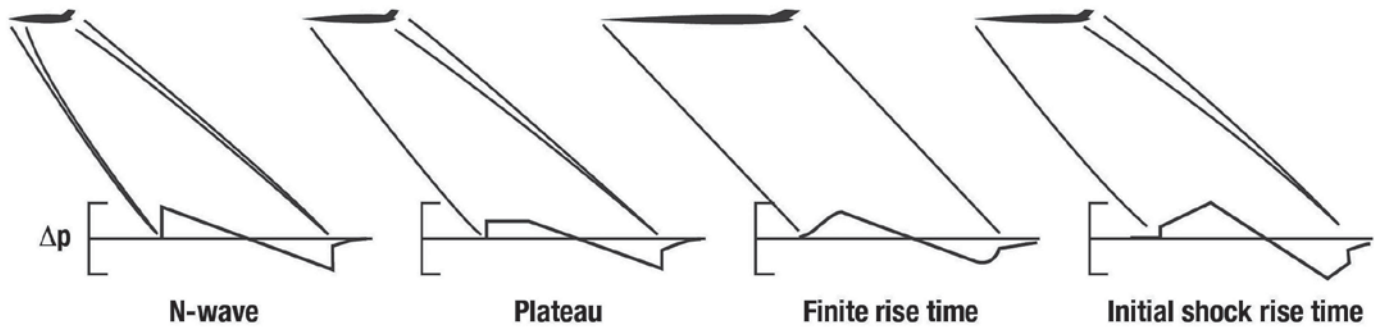


Figure 9.106. Airplane design for sonic boom minimization.

Most of the laboratory sonic boom testing has been devoted to determining the reaction of people to sonic booms. The major issues of concern are:

- How loud is the boom?
- How annoyed are the subjects?
- How startled are the subjects?
- What is the difference between indoor and outdoor reactions?
- What is the effect of rise time, boom intensity, and signature shape on the above variables?
- What simulator provides the most realistic sonic boom simulation?
- What metric best represents the subjects' opinions?

Headphones

One of the first simulation schemes (refs. 9.58 and 9.59) utilized custom headsets and electronic circuitry, as shown in figure 9.107. In their study of the subjective loudness of an N-wave, Zepler and Harel (ref. 9.60) set requirements for the headsets to be used in these tests. The headset included customized speakers (flat frequency responses in a range from a few Hertz to about 1500 Hz) and close attention to the fit of the headsets to keep out extraneous noises. The earphone cavities were 8 cm³ and the maximum pressure obtainable was 1 lb/ft². The relatively large earphone cavity was chosen to minimize the effect of different sizes of people's ears and also to reduce the effect of air leakage.

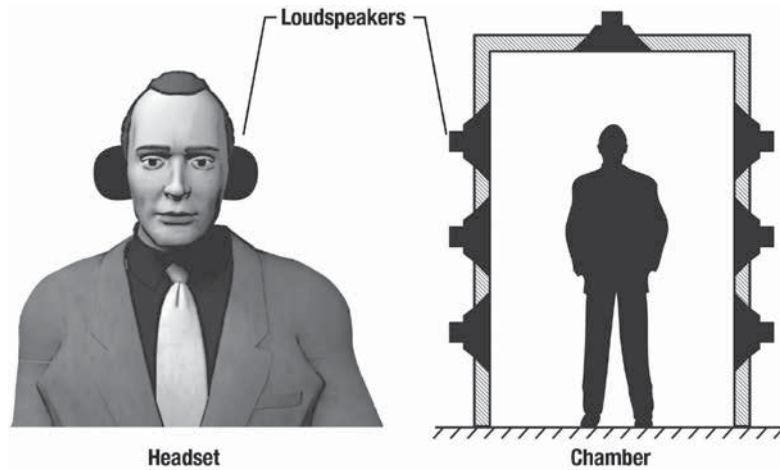


Figure 9.107. Illustrations of the application of earphone headset systems for simulating sonic booms (adapted from ref. 9.1).

The sonic boom variables investigated using the customized headsets were the same as those described earlier. The effect of these variables on loudness was determined. Figure 9.108 (ref. 9.60) shows both the pressure wave measured with an artificial ear in the headset and two sets of measurements (indicated by \circ and \square) where the loudness measurements in dB were obtained as a function of rise time with a constant maximum pressure. The pressure wave measured with an artificial ear is shown in figure 9.108(a). The slight deviation of the expansion portion of the signature from that of an N-wave, due to the headsets' lack of low frequency response, is not significant in regards to the loudness of the boom. Test subjects evaluated N-waves having fixed overpressure and a range of rise times. Each N-wave was compared to a 400 Hz tone, the amplitude of which was adjusted to be equal to the loudness of the N-wave. The experimental results for two series of tests are shown by the symbols in figure 9.108(b), and illustrate a decrease in loudness by increasing rise time. The solid lines represent predictions based on acoustic energy in the boom, frequency-weighted according to three different assumptions regarding loudness of impulsive sounds.

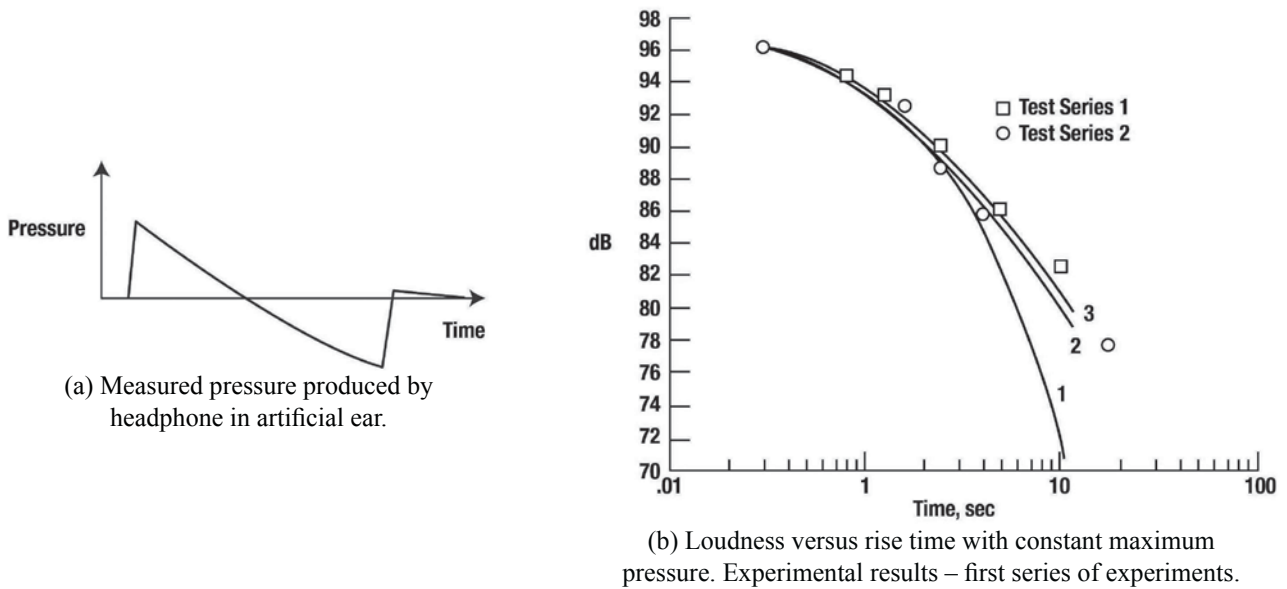


Figure 9.108. Results of N-wave loudness using headphones (adapted from ref. 9.60).

Loudspeaker Chambers

Some lack of realism is lost when only the ears are exposed to the simulated sonic boom. Whole body exposure to the transient sonic boom pressure field is clearly a more realistic simulation, especially for outdoors. To overcome this shortcoming, small closed chambers or booths equipped with loudspeakers were constructed by several organizations. Closed chambers or booths equipped with loudspeakers at the following locations will be subsequently discussed:

- Bolt, Beranek, and Newman (BBN) Chamber at Cambridge, Massachusetts (ref. 9.61)
- Bioacoustics Laboratory at Lockheed (Rye Canyon), California (ref. 9.62)
- University of Toronto, Canada (refs. 9.63, 9.64, and 9.65)
- NASA LaRC in Hampton, Virginia (ref. 9.66)
- Lockheed Martin in Palmdale, California (ref. 9.67)
- Gulfstream Aerospace Corporation in Savannah, Georgia (ref. 9.68)
- Laboratory of Mechanics and Acoustics in Marseilles, France (ref. 9.69)

BBN Chamber

Pearsons and Kryter (ref. 9.61) experimented with a 100 cubic-foot chamber to produce N-wave type pressure stimuli, as shown in figure 9.109. The room, constructed of 8-inch solid concrete block shown in figure 9.109, had inside dimensions of 3.5 feet deep by 3.5 feet wide by 7.9 feet high. The curtains shown in the figure were closed to cover the loudspeakers during the test. The door was 4 inches thick, with adequate sealing to provide a nearly airtight enclosure. Five 18-inch loudspeakers with center-tapped voice coils mounted in the walls and ceiling were used to produce the peak pressure associated with a sonic boom. The loudspeakers were driven by either a 75-watt McIntosh amplifier or a specially built power amplifier with push-pull output that used the loudspeaker center tap. A simulated outdoor sonic boom was generated by the speakers using a waveform generator called a photoformer. This device generated an electrical waveform by following a silhouette placed in the photoformer. The simulated indoor sonic boom, because of its complexity, was simulated from FM tape recordings made inside a house under the flight path of a jet aircraft flying at a supersonic speed.

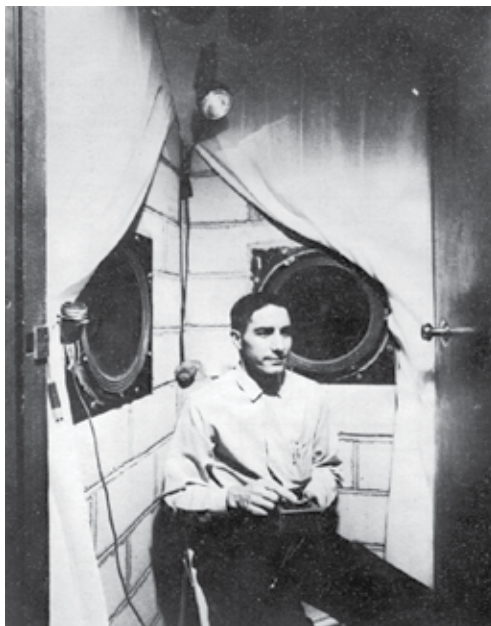


Figure 9.109. BBN Sonic Boom Test Chamber with curtains drawn to show low frequency speakers (ref. 9.61).

Using this chamber, the investigators studied the subjective acceptability of simulated sonic booms that would be heard outdoors and indoors and made comparisons with sounds of subsonic jet aircraft and bands of filtered white noise. The subjective acceptability of the booms was expressed in terms of equivalent perceived noise level in PNdB. When heard indoors, a sonic boom having an outdoor overpressure of 2.3 lbs/ft² was judged to be as acceptable as the sound of a subsonic jet heard indoors and having an outdoor level of 113 PNdB – the same boom heard outdoors was judged to be less noisy by an equivalent of 17 PNdB than the sound of a subsonic jet at 113 PNdB (ref. 9.61). The BBN Chamber is no longer in existence.

Lockheed Chamber

In the summer of 1965, the Bioacoustic Lab at Lockheed built a chamber similar to that of Pearsons and Kryter (see fig. 9.109). It was built to accommodate a single person, as shown in figure 9.110, and was later expanded to hold two people. The Lockheed system (ref. 9.62) used direct current amplifiers and servo system techniques to produce the low-frequency responses. Overpressures in the range of 0.5 to 5.0 lbs/ft², durations in the range of 100 to 500 msec, rise times from 1 to 50 msec, and a variety of fine-structure detail were capable of simulation. Sonic boom signature variables that were studied included those enumerated earlier for several other wave-shape changes.



Figure 9.110. Lockheed Sonic Boom Simulation Chamber – note hinged wall access (ref. 9.62).

Several results are provided in reference 9.62 that show the effects of rise times, N-wave duration, and shock magnitude on loudness. The relative loudness of 1/2 N-wave with several types of bow wave modifications are provided in figures 9.111 and 9.112. Figure 9.111 shows the effect on relative loudness of increasing the magnitude of the initial pressure rise of a 1/2 N-wave with a duration of 180 msec and a peak pressure of 1.6 lbs/ft². Note that the effect is substantial and the relative loudness increases almost linearly with the peak overpressure. For the two types of sawtooths (1/2 N-waves), figure 9.112 shows that the type 2 flat saw-tooth arrangement was not sensitive to inter-peak duration (i.e., the spacing between the sawtooth shocks) while the ramp-arrangement curve shows that for small spacings of less than 16 msec, there was a substantial reduction in relative loudness with respect to the standard 1/2 N-wave signature. The reference signature for figure 9.112 had a 150-msec duration with a peak pressure of 1.6 lbs/ft². This Lockheed Chamber is no longer in existence.

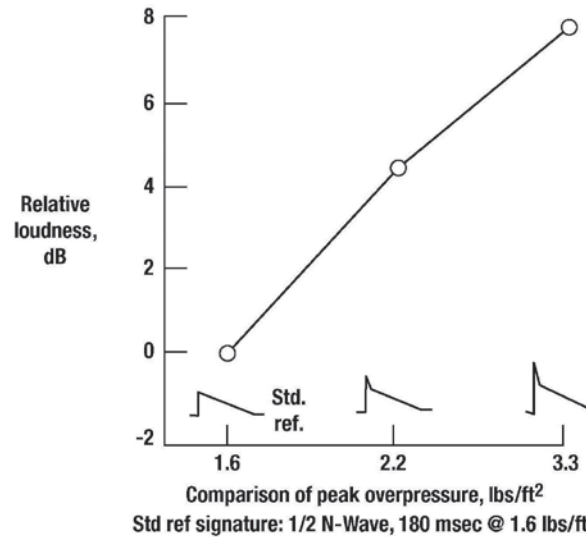


Figure 9.111. Relative loudness of 1/2 N-waves with bow wave modification (ref. 9.62).

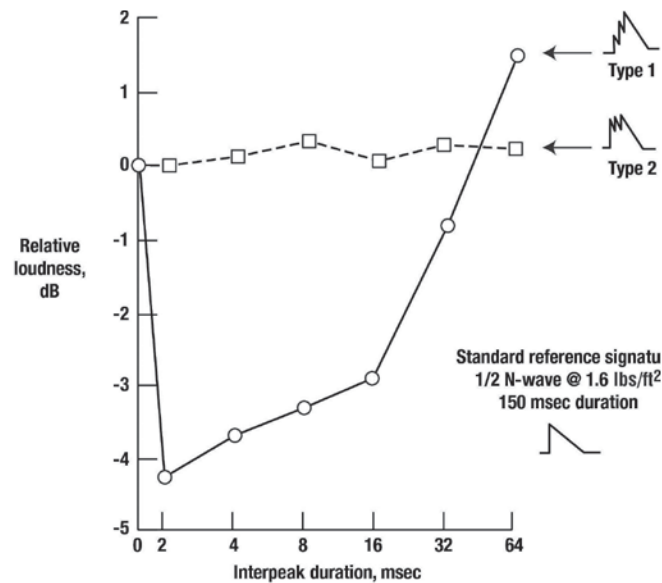


Figure 9.112. Relative loudness of 1/2 N-waves (types 1 and 2) with different saw-tooth spacing (ref. 9.62).

University of Toronto Institute for Aerospace Studies (UTIAS) Chamber

The University of Toronto's acoustic research concerning sonic booms began in the early 1970s and is documented in references 9.63, 9.64, 9.65, 9.70, and 9.71. This research was conducted in an airtight chamber with a volume of 2.1 m³ (74 ft³). The chambers had a double wall, plywood construction, and the inside was lined with sound-absorbing fiberglass. The chamber operating features are excerpted from reference 9.65 (pp. 1617-1618) and described below:

Six 15-inch low frequency loudspeakers and six 8-inch medium-frequency loudspeakers are used with a crossover network at 500 Hz. The electronic system consists of four d.c.-20,000 Hz 100 W amplifiers plus an equalizing network to compensate for speaker and booth coloration of the frequency response. The main element of the equalizing network is an Altec Lansing Model 729A "Acousta-Voiced" containing twenty-four one-third octave filters centered at frequencies from 12,000 Hz down to 63 Hz; each filter is adjustable over a range ± 12 dB. Additional filters utilizing summation circuitry are used to control the response of the system in the frequency range 0.1-60 Hz. Careful adjustment of these filters compensates for the major part of the non-uniform frequency response of the basic system, eliminating much of the waveform distortion.

The basic scheme of this sonic boom simulation system is shown in figure 9.113. Initially, the pressure signatures produced in the booth for the results of reference 9.64 had an unwanted oscillation just after the initial shock, as seen in figure 9.114. This is attributed to faults in the compensating filters. As noted by other investigators, the pressure signal has to be distorted in a very specific way to achieve the desired signal. Figure 9.115 shows examples of pressure signals recorded by microphones in the booth, both with (bottom) and without (top) the required distortion. Niedzwiecki and Ribner (ref. 9.65) investigated the effects of rise time and signature duration. A sample result is shown in figure 9.116 where an equal loudness curve is plotted as a function of rise time for 200 msec duration N-waves. It is clear from figure 9.116 that as rise time decreases, the overpressure (ΔP_{test}) can be increased and still maintain the same loudness. A similar curve for signature duration is also provided in reference 9.65.

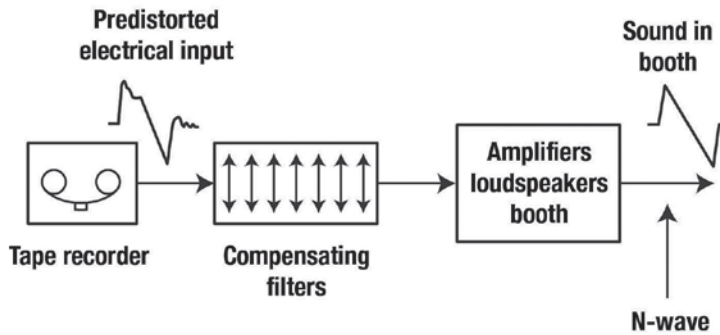


Figure 9.113. Schematic arrangement of UTIAS loudspeaker-driven sonic boom simulation booth (ref. 9.65).

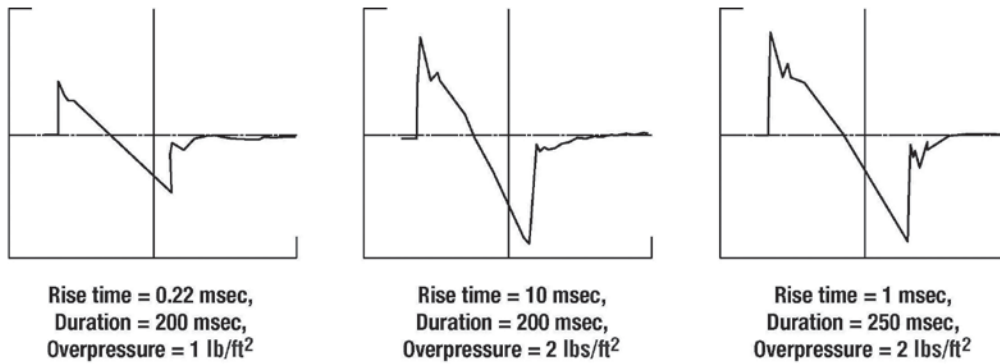


Figure 9.114. Reproduction of N-wave sonic boom signatures in UTIAS simulation booth (ref. 9.65).

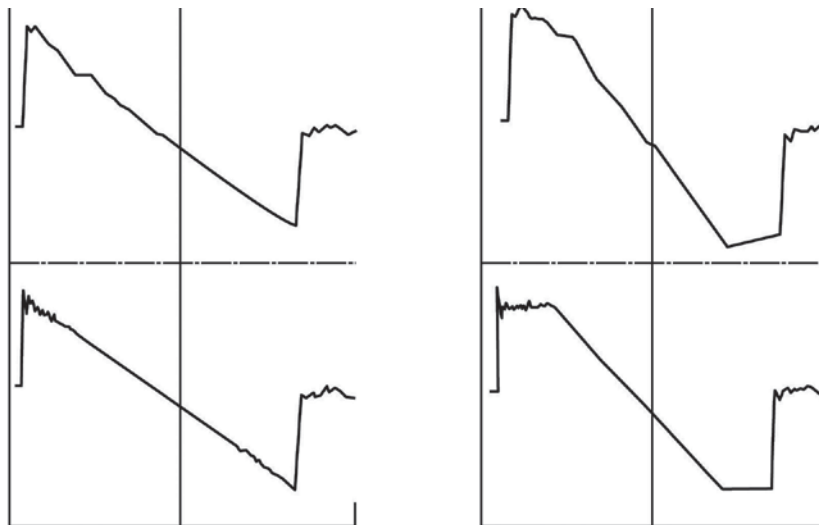


Figure 9.115. Examples of pressure signals recorded by microphone in UTIAS simulation booth without (top) and with (bottom) pre-distortion of input signal (ref. 9.65).

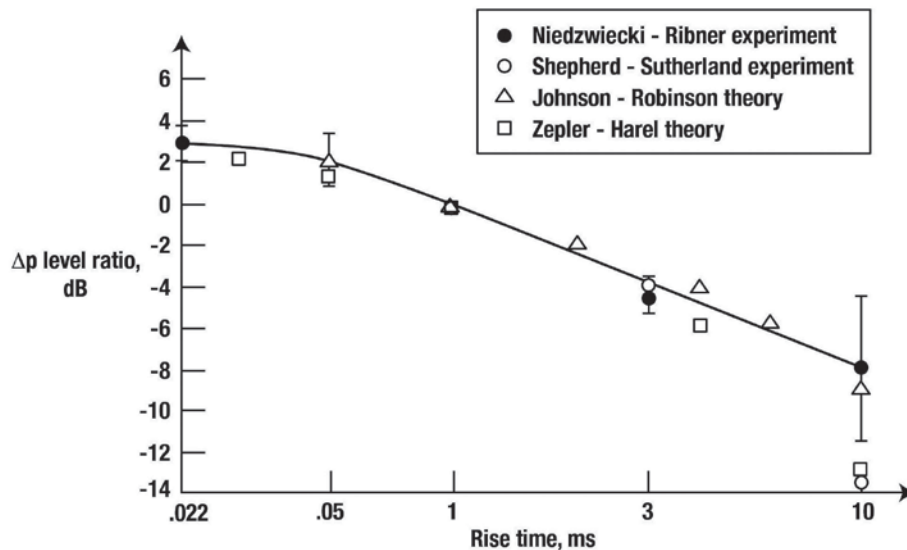


Figure 9.116. Equal loudness curve. Trade-off between overpressure level ratio ($-20 \log_{10} \Delta P_{test}/\Delta P_{ref}$) and rise time for 200 msec duration N-waves. $\Delta P_{ref} = 1 \text{ lb/ft}^2 (48 \text{ Pa})$, $t_{ref} = 1 \text{ msec}$ (ref. 9.65).

Another paper by Niedzwiecki and Ribner (ref. 9.70) detailed the results of an investigation into the effect of the low-frequency portion of the sonic boom spectrum on subjective loudness by using a high-pass filter. Two cut-off frequencies (25 and 50 Hz) were used and the resulting signatures are shown in figure 9.117.

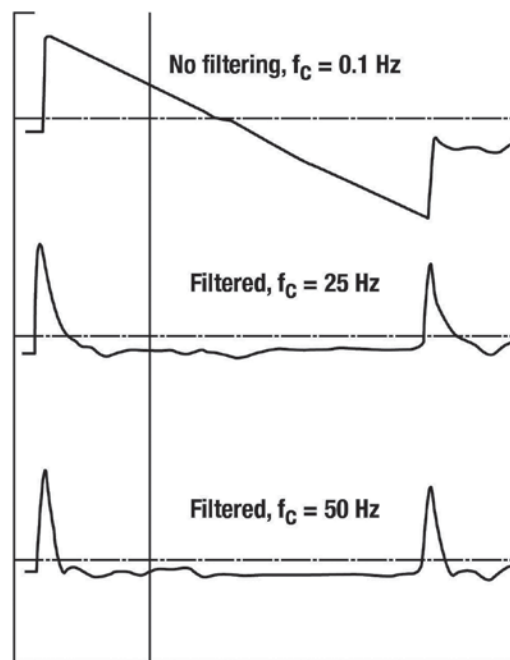


Figure 9.117. Effect of high pass filtering on sonic boom signal (pressure waveforms recorded in UTIAS simulation booth). N-wave signatures; $\tau = 1 \text{ msec}$; $D = 150 \text{ msec}$; $\Delta p = 48 \text{ Pa}$ (ref. 9.70).

As a result of this investigation, they concluded in reference 9.70 (p. 706):

The subjective tests reported herein permit the conclusion that the low-frequency content of the N-wave signature spectrum at typical levels has no significant influence on the subjective loudness. This is further supported by the observation that the changes in N-wave duration (which dominates the low-frequency content) have negligible influence upon the loudness. One practical inference follows: it may be unnecessarily rigorous to conduct subjective loudness tests on sonic-boom-like impulses in expensive

and complex simulation facilities like ours, facilities with extended low frequency response down to 1 Hz. A very high quality hi-fi system (preferable with both low phase and low amplitude distortion versus frequency) may be sufficient.

The UTIAS Chamber is no longer in existence.

NASA Langley Chamber

NASA LaRC's sonic boom simulator (ref. 9.66) came on line in 1991. Because this simulator is air tight, it can create low-frequency waveforms on the order of tenths of a Hertz. Thus, it has the capability to generate user-specified N-wave and other boom shapes having rise times as low as 0.5 milliseconds and peak overpressures up to 191 Pa (4 lbs/ft²). The design of the LaRC simulator was based upon the pre-distortion schemes described earlier and documented in references 9.64 and 9.71. However, several design enhancements were made to overcome some of the previous deficiencies through application of recent advances in electronic and computer technology (i.e., digital filters rather than analog filters). It has walls of 20 cm thick concrete block and a concrete ceiling and floor of thicknesses 13 cm and 10 cm, respectively (see fig. 9.118). The acoustical door is of foam-filled construction and has edge seals to maintain the booth as airtight as possible. The internal dimensions of the booth are 1.52 m high, 0.96 m deep, and 1.07 m wide, yielding a volume of 1.6 m³ (56.5 ft³). To reduce the effects of acoustic resonances the floor is carpeted and interior walls and ceiling are covered with 10 cm thick acoustical foam. This reduced the volume to about 1.1 m³. One wall contains a small window made of 2.5 cm thick Plexiglass. The window edges and the electrical wiring access holes were sealed with caulking material to maintain an airtight booth. The simulator door contains eight loudspeakers, four 38 cm low-frequency units and four 18-cm mid-range units. The speakers are protected from possible damage by a perforated metal screen.

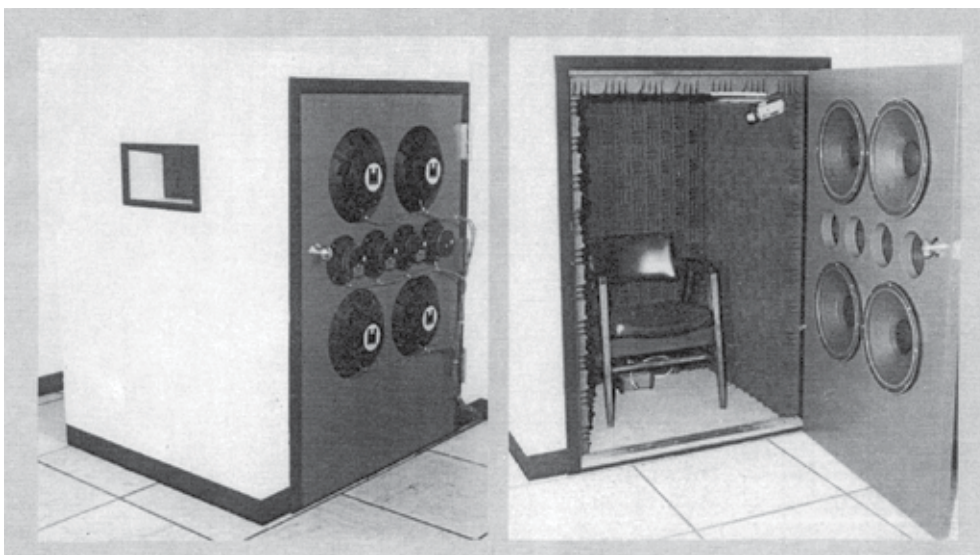


Figure 9.118. NASA LaRC Sonic Boom Simulator (ref. 9.66).

The major elements of the sound generation and monitoring system are shown in figure 9.119. The input signal originates from a computer-driven, 24-bit digital to analog converter and is then low-pass filtered to remove the digitizing frequency from the signal. A cross-over network (cross-over frequency set at 420 Hz) separates the high- and low-frequency components of the signal for input into the high- and low-frequency loudspeaker systems. Each set of four loudspeakers, connected in parallel, is powered by a DC-coupled amplifier rated at 200 watts when driving an 8 ohm load. For the reduced load of this loudspeaker arrangement, and for a low-duty cycle as required for sonic boom testing, the amplifiers are capable of generating more than 1000 watts.

Since human subjects are required in subjective response testing, a peak sound pressure level of 140 dB and an A-weighted limit of 95 dB(A) were enforced. Two microphones were located in the chamber (see fig. 9.119)

and two sound level meters are used to monitor the levels. As noted earlier, a pre-distorted sonic boom signature was input to the chamber in order to achieve the desired signature shape (ref. 9.66). Pre-distorted and measured shapes for the different desired shapes are shown in figure 9.120. Clearly, the digital broadband equalization filter, designed for the application (ref. 9.72), worked quite well.

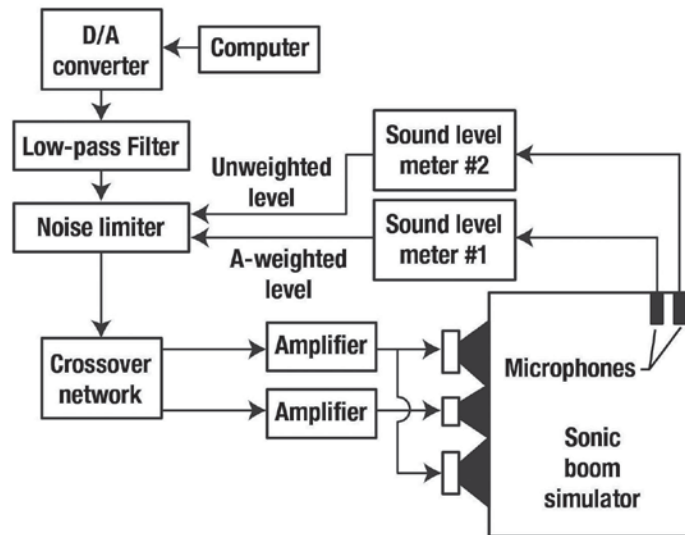


Figure 9.119. Sonic boom generation and monitoring system (ref. 9.66).

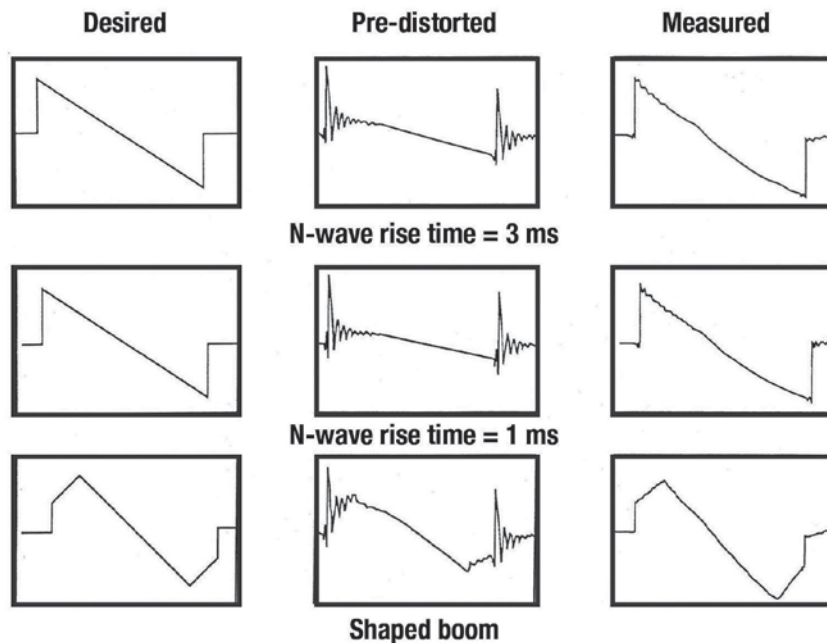


Figure 9.120. Examples of desired, pre-distorted, and measured sonic boom signatures (ref. 9.66).

One of the first tests of the LaRC simulator was to do an equal loudness test and compare the results to those of reference 9.65 (see fig. 9.116). In order to do this, adjustments had to be made to the data of reference 9.65 since the LaRC standard N-wave signature had a rise time of 3 msec and a peak overpressure of 49 Pa (1.03 lbs/ft²) and the reference 9.65 standard test had a rise time of 1 msec and a peak overpressure of 48 Pa (1.0 lb/ft²). As stated in reference 9.66 (p. 9):

Based on this, the increment in overpressure required to maintain constant loudness between a rise time of 1 msec (ref. 9.65, standard boom) and a rise time of 3 msec (standard boom in current study) was determined. This increment in overpressure was then subtracted from the reference 9.65 curve. This effectively resulted in a new equal loudness curve having loudness equal to that of the standard boom signature used in the present investigation.

Figure 9.121 shows the comparison, which is obviously quite good therefore lending credibility to both results. Test results for other signatures are provided in reference 9.66 using various metrics including C-weighted (SLC) A-weighted (SLA), and Perceived Level (PL(dB)).

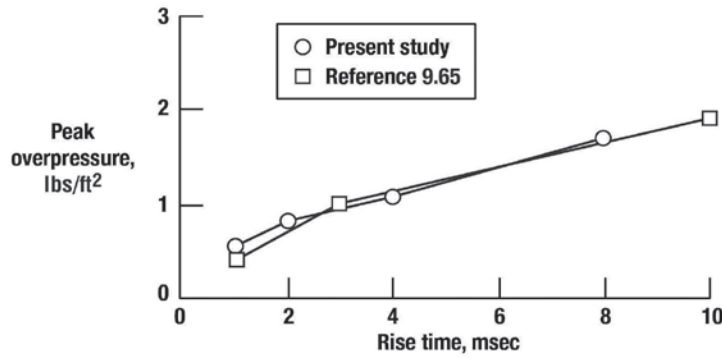


Figure 9.121. Comparison of equal loudness curves (ref. 9.66).

Lockheed Martin Chamber

This simulator was similar in design to the previously described NASA chamber in that it is an air-tight booth driven by loudspeakers located on the door surface of the enclosure (ref. 9.67).

Gulfstream Portable Chamber

The Gulfstream sonic boom simulator is different in many respects from the small airtight booths that have speakers in the doors (ref. 9.68). A major difference is that it is in a mobile trailer for demonstration purposes and is 32-feet long, 8.5-feet wide, and approximately 11.5-feet high. The trailer is divided into two sections, as seen in figure 9.122 – one for the operator and one for the test subjects. The speakers are located between the two sections.

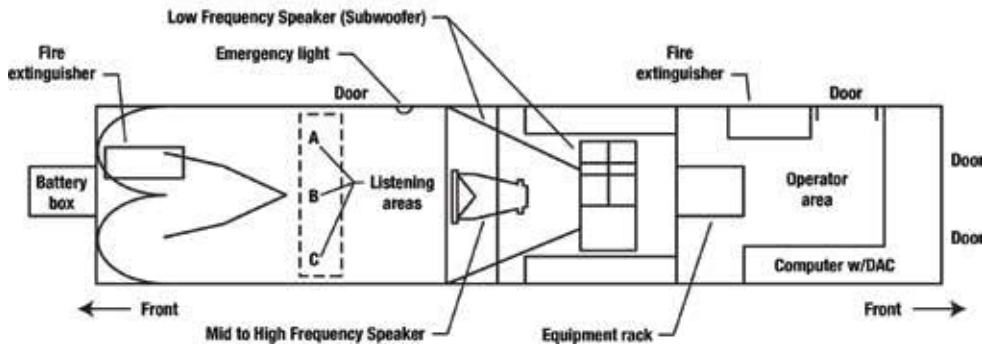
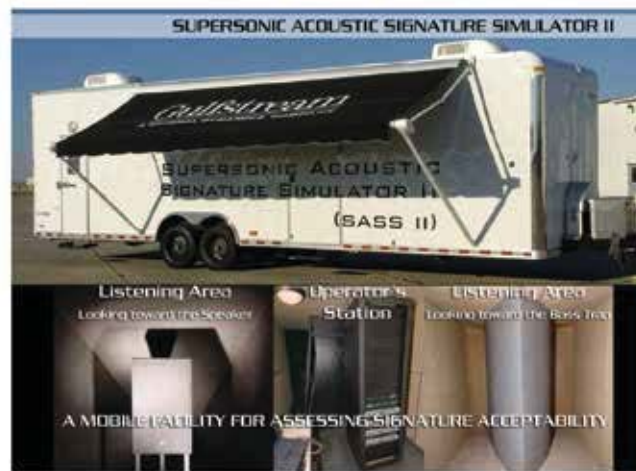


Figure 9.122. View and interior layout of the Gulfstream sonic boom simulator (adapted from ref. 9.68).

The overall setup and acoustics system, described in reference 9.68 (p. 668), was as follows:

The operator area contains the computing and audio hardware that produce the simulation. A laptop contains discrete-time data sampled at 24kHz that is output to the audio system via a data acquisition system. That hardware then sends an analog signal to the digital audio equalizer that is pre-programmed with the gains, filtering, and delays necessary for each power amplifier. Two power amplifiers supply signals to the four drivers in the wave-guided subwoofer and two power amplifiers supply signals to the four drivers in the mid/high frequency speaker. The full performance bandwidth of the system is 8 Hz to 18 kHz, but for sonic boom simulations the upper end of the system is reduced to 5 kHz.

The listening section in the simulator has interior dimensions of 6 feet wide, 7 feet high, and approximately 12 feet long. One to four people can stand in the designated listener area, which is roughly 5 feet wide and 2 feet deep. The sound travels from the speakers in the middle of the trailer, passes through the listener area, and into the anechoic termination at the front of the trailer. The anechoic termination, filled from floor to ceiling with fiberglass insulation, was constructed to absorb sound down to nearly 50 Hz. The walls and ceiling are thermally and acoustically treated with fiberglass insulation and absorptive open-cell foam. A thin sheet of perforated aluminum separates the foam and fiberglass. The foam has a thin, acoustically transparent cloth glued to its surface for aesthetics.

As with the other simulators, it was necessary to establish a transfer function between the input to the system and its output at several locations in the listener area. A multi-point equalization using time-domain Wiener filtering was computed that addresses the above mentioned problem. Additional details were provided in reference 9.68.

The Gulfstream simulator has a frequency bandwidth constraint, thus the target acoustic output is a band-pass filtered version of the full-fidelity waveform. The concern then is how well the system can match the target waveform in the time domain. Figure 9.123 compares the pressure versus time data for the full-fidelity waveform (dashed line), the band-pass filtered waveform (dotted line), and the simulator output (solid line) at listener position B for the measured N-wave. The simulator acoustic output closely matches the filtered version of the full-fidelity waveform.

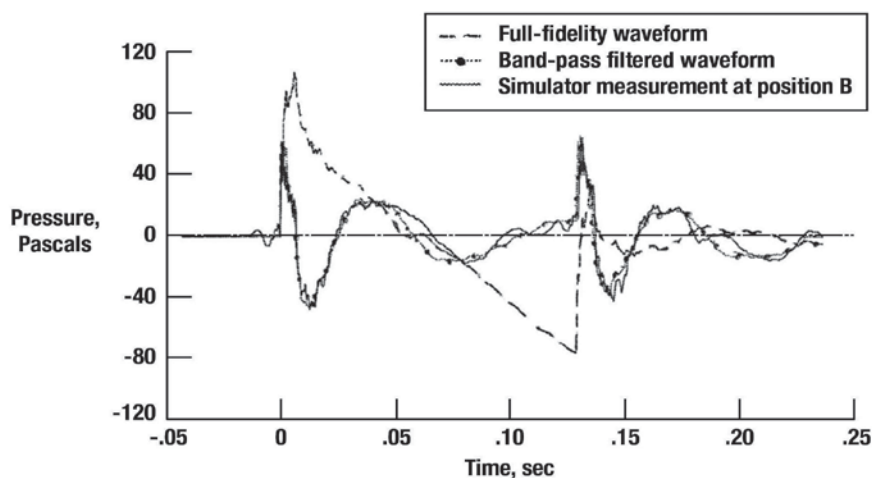


Figure 9.123. Time-domain comparison of the simulator acoustic output at listener position to the desired output and full-fidelity waveform (ref. 9.68).

Sullivan et al. (ref. 9.67) made comparative tests of the NASA, Lockheed, and Gulfstream simulators. Aside from the usual rise-time, peak-pressure, and pulse-duration studies, the effect of post-boom engine noise was studied in comparative tests of the Lockheed and Gulfstream simulators. Sullivan et al. (ref. 9.67, p. 156) note that:

Post boom noise (the “rumble” occurring after the boom) is essential for realistic simulation of sonic booms. The duration of the post boom noise should be at least about 1.5 sec. Longer duration does not improve realism ratings greatly, but shorter duration causes a rapid decrease in perceived realism.

Finally, Sullivan et al. (ref. 9.67, p. 156) conclude that:

Of the three simulators studies, the Gulfstream SASSII simulator was rated as somewhat more realistic than either the NASA or the Lockheed booths. The superior performance of the Gulfstream simulator could be due to its fundamentally different design or to subtle differences in the equalization filters.

Sound Restitution Cabin

The last simulation chamber to be described is the Laboratoire de Mécanique et d'Acoustique in Marseille, France (ref. 9.69, p. 664):

The simulation cabin has been built inside a room with concrete walls ensuring a very good insulation from outside noise. Its dimensions have been kept to a minimum, thus reducing the requirement on the sources, and shifting modal resonance toward higher frequencies. Cabin dimensions of 3 x 2 x 2 m have been considered adequate, and leave enough room for fitting 16 subwoofers at appropriate locations on the walls.

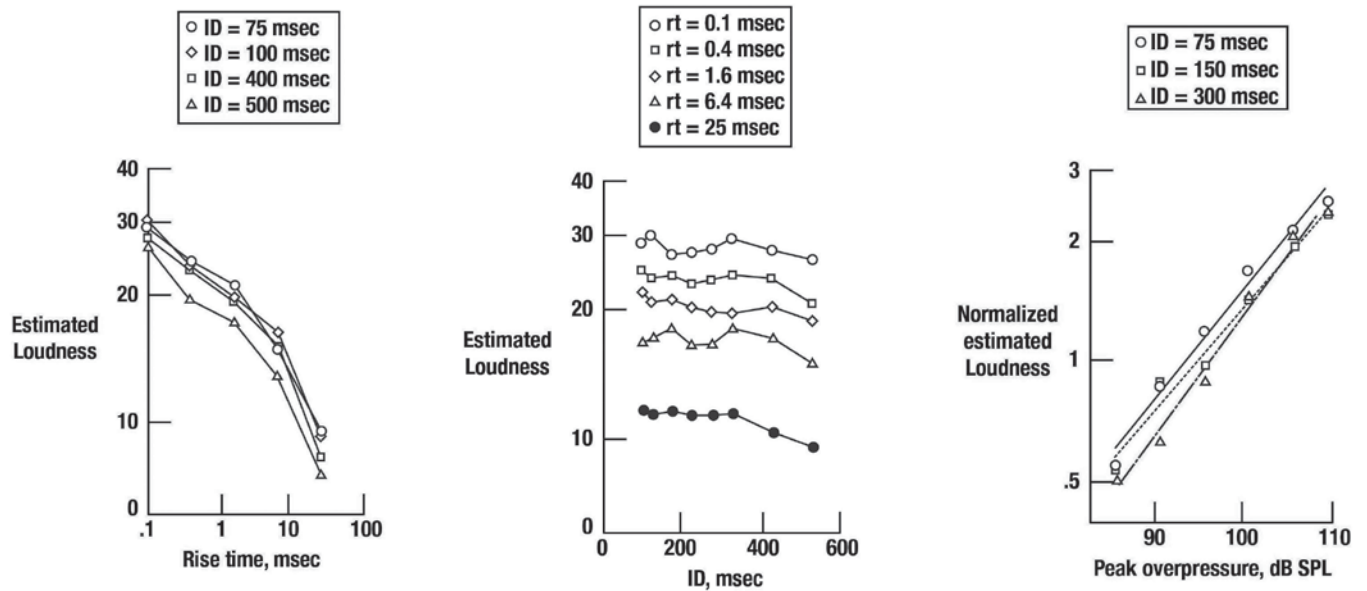
At very low frequencies, monopole subwoofers radiating inside an almost sealed room (pressure chamber) create a spatially uniform pressure. For increasing frequencies, the structure of the field is more complex, involving several degrees of freedom, but it may also be almost uniform with a suitable repartition and control of speakers. Conversely, at higher frequencies, a suitable lining on the walls allows one to consider the room as close to semi-anechoic. The whole frequency range is therefore driven by a triple control system, with different constraints for each frequency band.

More details about the cabin and loudspeaker design can be found in reference 9.73.

When reference 9.69 was being written, additional improvements were being undertaken to the simulator using active noise control techniques. As stated in reference 9.69 (p. 665):

A sound field reproduction strategy called Boundary Pressure Control (BPC) has been proposed (ref. 9.74), which is based on active noise control techniques. BPC intends to reproduce the required sound field inside a given volume via the active control of the acoustic pressure measured at some microphones placed over the whole boundary surface of the volume. Unlike other sound reproduction strategies, BPC is able to compensate efficiently for the room reflections, using adaptive filtering methods.

The results (fig. 9.124), were presented in reference 9.69 and show the effects of rise time, inter-peak durations (roughly signature length in milliseconds), and peak overpressure of synthesized N-waves. The results show, as have other investigations, that rise time and peak overpressures are the important quantities.



(a) Estimated loudness as a function of rise time (rt) for various values of the inter-peak over-pressure of 110 dB SPL. (b) Estimated loudness as a function of the inter-peak duration for various values of the rise time, with a peak over-pressure of 110 dB SPL. (c) Loudness function for various values of the inter-peak duration with a rise time of 2 msec.

Figure 9.124. Results of the perceptual assessment of N-wave signals synthesized in the simulation room (adapted from ref. 9.69).

The chambers previously discussed are best used for outdoor sonic boom responses. Indoor responses to booms are different due to the effects of the impedance of the walls, roofs, doors, and especially windows since the construction features of the windows and their window panel(s) are the most responsive features of a house. Also, the interiors of the house (including the room geometries, furniture, rugs, etc.) have an effect on what a person actually senses. Added to the above variables is what a person is doing at the time of exposure, e.g., he/she is watching the television, working on computers or asleep, etc. and secondary noises such as a “rattle”. Shepherd and Sullivan (ref. 9.75) described in detail a procedure that can be used to calculate the loudness of sonic booms. The procedure is applied to a wide range of sonic boom shapes. Of particular interest here is that estimates are made of the loudness of sonic booms, as they would be heard indoors, based on the measured noise reduction provided by typical dwellings. Indeed, calculations are presented with windows open and closed for a range of shaped booms. The difference in loudness between indoors and outdoors for a flat-top boom is about 8 dB. The noise reduction for typical residential structures as a function of frequency for these calculations is shown in figure 9.125.

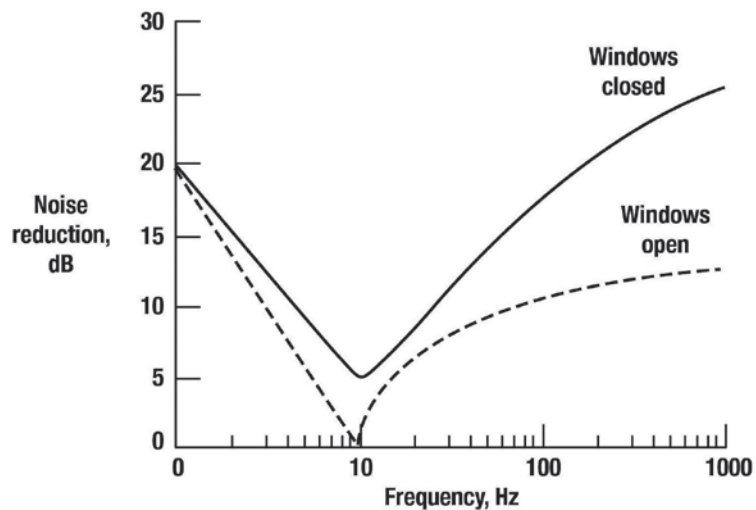


Figure 9.125. Noise reduction for typical residential structures (ref. 9.75).

Figure 9.126 illustrates the difficulty associated with the measurement and prediction of sonic booms indoors. This type of input (i.e., indoor sound levels, annoyance level, and activities affected) for each specific house of different shapes and construction features will be different. Added to these, the differences in the interior environment and the codification of the responses of people in different houses will clearly lead to average numbers for human responses with the large error bands.

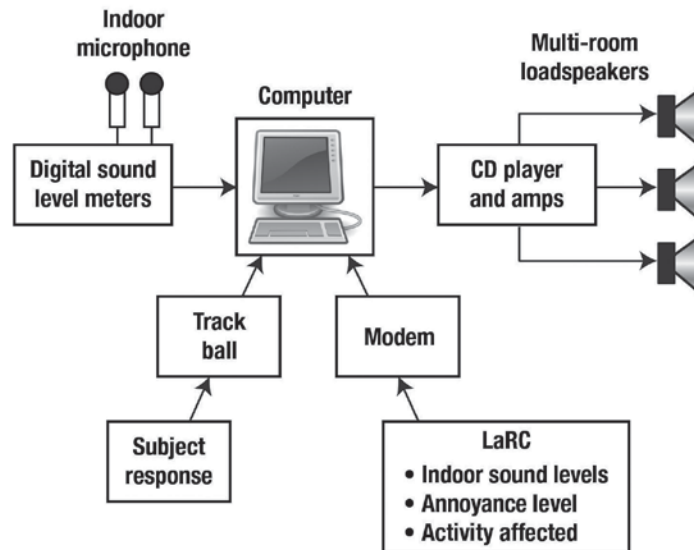


Figure 9.126. In-home noise generation/response system diagram (ref. 9.76).

In-Home Sonic Boom Simulation

The previously discussed simulators allow for the study of loudness and annoyance of a single sonic boom of a given amplitude, period, and shape. However, these findings reveal little about the reaction of people in communities exposed to multiple booms of a given amplitude, period, and shape over a period of time on a regular basis in their homes. In order to gain more insight to this question, McCurdy, Brown, and Hilliard (ref. 9.76, p. 1574) developed a computer-based system for studying the subjective response of people to the occurrence of multiple simulated sonic booms in their homes:

The apparatus developed for the present study, the in-home noise generation/response system (HONORS), is a computer-controlled audio system that generates simulated sonic booms, measures their levels, and records the test subject's ratings. Eight of the systems were rotated through 33 homes for 8 weeks in each home, providing a total of 1848 days of sonic boom exposures.

The system consisted of a computer and compact disc player that played the simulated sonic booms at randomly selected pre-programmed times through a preamplifier and amplifier into three or four loudspeakers located in different rooms of the house. No warning was given as to when the booms would occur. The two indoor microphones and sound level meters measured the levels of the booms as they occurred and also continuously measured the ambient noise levels in the home. The measurements were then transferred to the computer and stored on its hard disk. At the end of the day, the test subjects used the trackball to answer a series of questions about his/her activities during the day and his/her overall subjective response to the total sonic boom exposure for the day.

The arrangement of the test components in a subject's home is shown in figure 9.127. Only single family detached-dwelling homes were selected and covered the economic range from lower middle to upper middle class homes. The system components were located so as to minimize their disruption of the family's normal routines.



Figure 9.127. In-home noise generation/response system (ref. 9.76).

Three pressure signatures were used in the McCurdy, Brown, and Hilliard study (ref. 9.76). Two were outdoor signatures (an N-wave and a shaped wave) and the third was an indoor signature developed from an outdoor N-wave based on the noise reduction curves provided by typical dwellings (see fig. 9.125). All three wave shapes had an initial rise time of 4 msec. Three A-weighted noise levels were employed – 66, 70, and 74 dB. There were seven boom occurrence rates employed – 4, 10, 13, 25, 33, 44, and 63 per day.

Several result figures are presented in reference 9.76, two are shown here. The first, figure 9.128, shows the subjective annoyance rating versus the A-weighted sound exposure level of the individual sonic booms. Plots are provided for five exposure levels. Over the sound exposure levels from 63 to 77 dB, the annoyance ratings range from roughly 1 to 5, respectively. As one would expect, the annoyance rating goes down as the exposure level goes down and the annoyance level goes up with an increase in the number of occurrences.

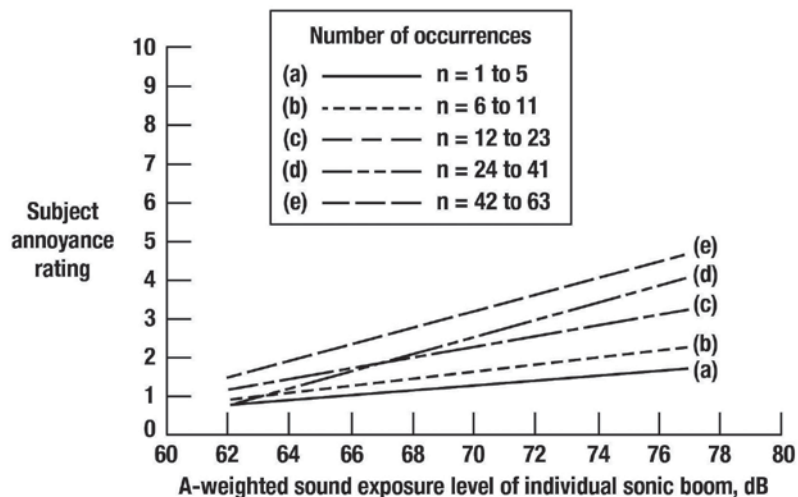


Figure 9.128. Effect of number of sonic boom occurrences on annoyance versus A-weighted sound exposure level of individual sonic booms (ref. 9.76).

Figure 9.129 shows the effect of sonic boom waveforms on annoyance for day-night average sound level based on perceived level. The figure shows the regression line of subjective annoyance rating DNL(PL) for each of the three waveforms used in the study. No significant difference in slope or intercept is evident. Results for other annoyance effects, such as startle, ambient noise level, subject activity, and subject adaptation to the booms are presented in reference 9.76. These experiments confirmed that the increase in annoyance resulting from multiple occurrences is commonly modeled by the addition of the term “ $10 \cdot \log(\text{number of occurrences})$ ” to the sonic boom level, as is commonly used for airport community noise assessment.

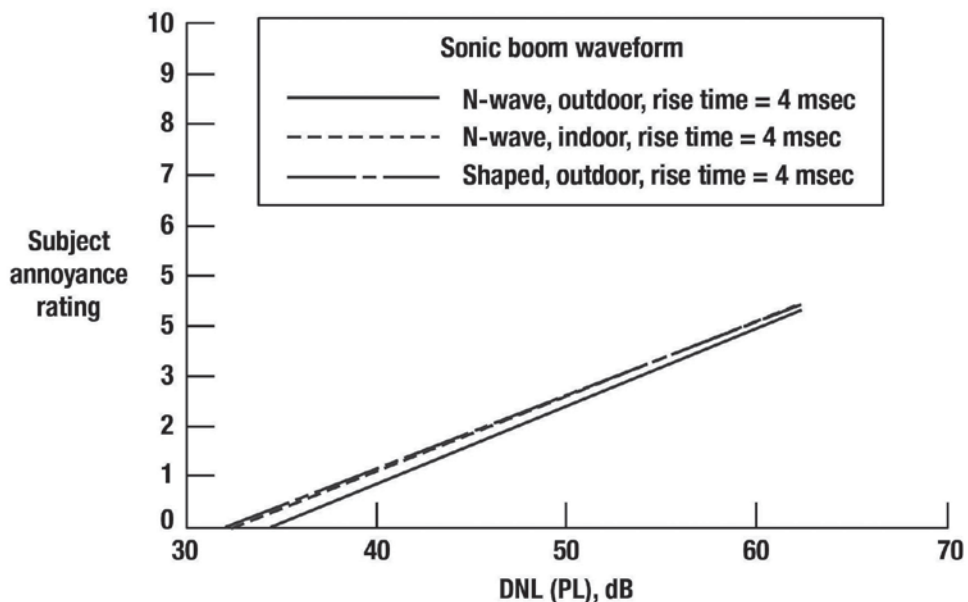


Figure 9.129. Effect of sonic boom waveform shape on annoyance versus day-night average sound level based on the perceived level noise metric (ref. 9.76).

Georgia Tech Simulator

In the early 1990s, Ahuja, et al. of Georgia Tech (ref. 9.77) set out to construct a facility so that human response to sonic booms and aircraft noise could be studied both indoors and outdoors. The facility consisted of unique low-frequency, high-power drivers and several more conventional loud speakers. This is an arrangement, when attached to a residential building, that allows for a range of from about 3 Hz to 4 KHz. Figure 9.130 shows a drawing of the test house and speaker complex, locations of indoor and outdoor subjects, and microphone measurement locations. As noted in reference 9.77, the suggested system is well suited to simulate realistic sounds of helicopters, tilt-rotors, trucks, trains, aircraft, and sonic booms of various shapes and durations. It can thus be used for human response, building response, sound propagation, and noise control studies. It was used to study the effect of sonic boom shaping on human response and reported in reference 9.78.

The simulator was set atop a raised platform and located in a large laboratory space at LaRC. The authors stated that the soundscape inside a house exposed to booms is primarily a result of two vibroacoustic phenomena, transmission of the boom through the structure and contact induced vibration sources such as window rattle. Both sources are simulated and independently controlled in this simulator. To simulate the transmission of a boom through the structure, the room is surrounded on two sides by 15-inch diameter subwoofer speaker arrays, 24 on the shorter wall, and 28 in the longer wall. Figure 9.132 illustrates this arrangement and also shows the support structure to hold the speakers.

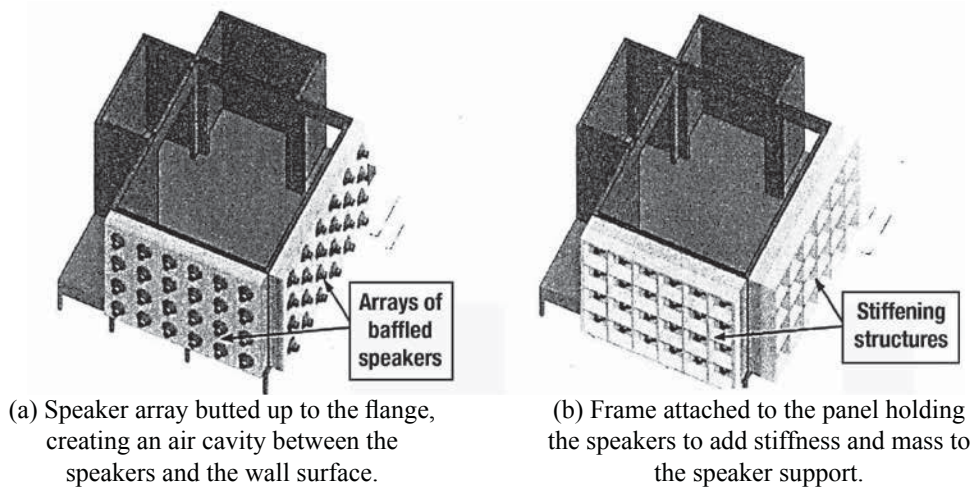


Figure 9.132. Arrangement of speakers and support system on NASA LaRC's indoor simulator (ref. 9.79).

The secondary sources that resulted from contact-induced vibration, such as rattle, squeak, and creak can be simulated with small speakers placed inside the room. Photographs of the completed facility showing an exterior and interior view are presented in figure 9.133. It is important to point out that simulating sonic booms using earphones or loudspeakers do not generate shock waves (i.e., no propagating acoustic wave, only a pressure change). However, the two pressure disturbances, when experienced in a small volume such as headphones or loudspeaker chambers, look the same as a sonic boom to a microphone or the human ear.

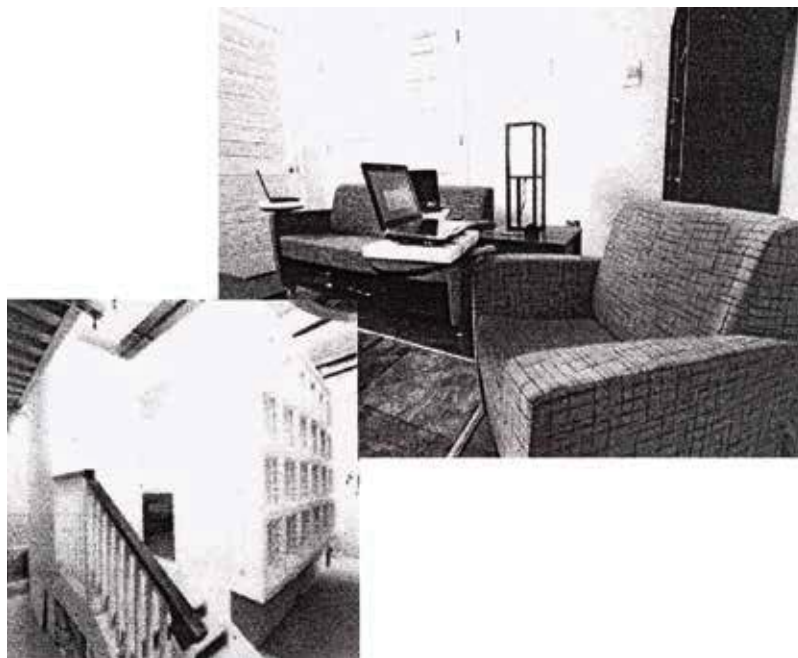


Figure 9.133. Exterior and interior views of NASA LaRC indoor sonic boom simulator.

Piston Systems

While acoustic booths are the most popular way of testing human response to sonic boom, there were several other devices that have been used for this purpose. A piston-driven facility (see fig. 9.134), developed at the Wright Patterson Air Force Base (ref. 9.80) and no longer in existence, had a chamber volume of 1.2 m³ and was developed specifically for testing human response to very low frequency noise (0.8 Hz to 10 Hz). A unique feature of the facility was that the position of the test chamber could be changed from vertical to horizontal so that the subject could be sitting, standing, or lying down during a test. Another piston-driven simulator (no longer in existence) was developed by the Stanford Research Institute (ref. 9.81) for the purpose of conducting sleep-awakening and startle-response studies on humans. This simulator consisted of a bedroom structure mock-up with a pressure chamber along one wall (see fig. 9.135). An electromechanical driver actuated a piston in the outside wall of the pressure chamber that provided a pressure load on the wall of the bedroom and thereby generated the desired acoustical and structural vibration environments within the room.

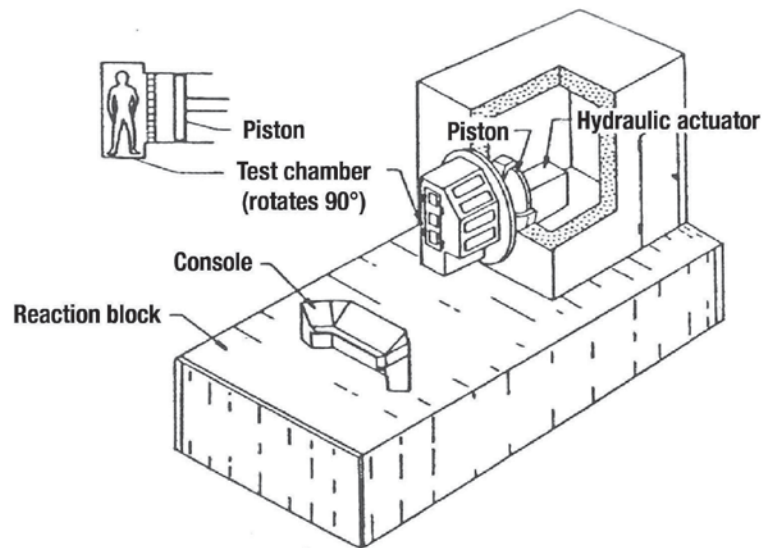


Figure 9.134. Perspective view sketch of the Aeromedical Research Laboratory dynamic pressure chamber (ref. 9.1).

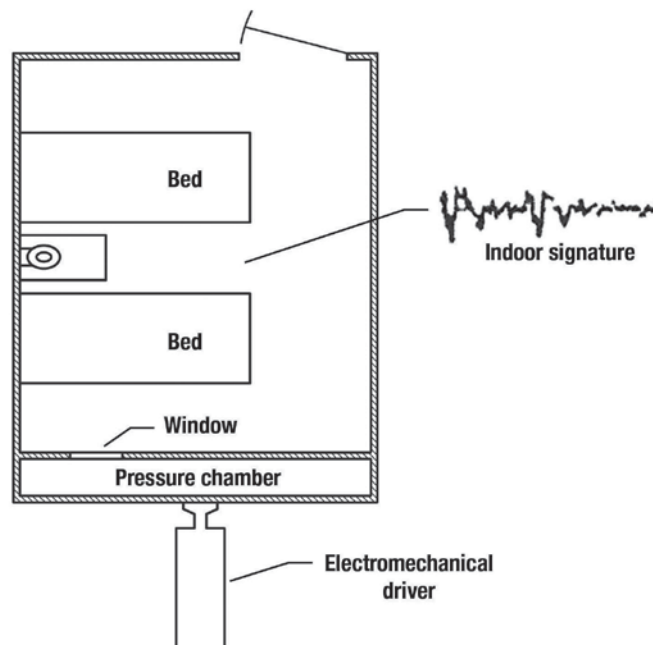


Figure 9.135. Plan view sketch of Stanford Research Institute setup for simulating indoor sonic boom environment for sleep awakening studies (ref. 9.1).

The boom simulator was intended to replicate the type of booms heard indoors, i.e., those that transmitted through building structures and windows. Further details of this facility and some illustrative results can be found in references 9.81 and 9.82.

Explosive Charges

Another method of simulating sonic booms is through the use of explosive charges, two of equal amplitude that could be detonated in series at a time interval equivalent to the duration of the sonic boom signature to be replicated. Although the boom signature overpressures and duration can be simulated using explosive charges, the spectra of the boom signature and explosive signatures are quite different, the latter lacking the low-frequency contribution associated with the expansion portion of the N-wave signature. This spectral difference means that although outdoors, booms and explosive charge simulations may not be observed as being different. Indoors, the observer would not realize the full extent of the vibratory and visual effects, only the acoustic aspects. Over the years, several experiments were performed that compared observer responses to booms from aircraft to those using explosive charge simulations. The findings of three such experiments are subsequently given.

Exercise Crackerjack

In July 1961, a series of tests were conducted by the Ministry of Aviation of the Royal Aircraft Establishment to provide bangs of nominal 1 lb/ft² and 2 lbs/ft² overpressures using the aforementioned explosive charges as well as using an English Electric Lightning F-3 aircraft (fig. 9.136). This program, called Exercise Crackerjack, exposed a group of listeners to the bangs created by these two disturbance sources. Researchers could then determine how tolerable the bangs were with ratings of 100 percent being completely tolerable (ref. 9.83). The exercise extended over 4 days with the listeners positioned in an open field and in a modern, one-story flat top laboratory building.



(photo courtesy of Adrian Pingstone)

Figure 9.136. English Electric Lightning F-3.

The outdoor and indoor signatures generated by the Lightning aircraft flying at Mach 1.4 at 43,000 feet are presented in figure 9.137 (ref. 9.83). These flight conditions were to generate a sonic boom with an initial shock strength of 1.0 lb/ft² on the ground out of doors. In this case, it only achieved a signature of about 0.8 lb/ft². The indoor leading-shock magnitude was only about 0.15 lb/ft². Other outdoor initial-shock values generated by the Lightning aircraft, intended to be a nominal 1.0 lb/ft², varied from 0.7 lb/ft² to 1.3 lb/ft². Similarly, the 2.0 lbs/ft² nominal signatures varied from 1.6 lbs/ft² to 2.7 lbs/ft². Some of the scatter from the nominal values can be attributed to adverse weather conditions in the form of wind and rain on 2 days of testing. Similar scatter was seen in the explosive charge bangs.

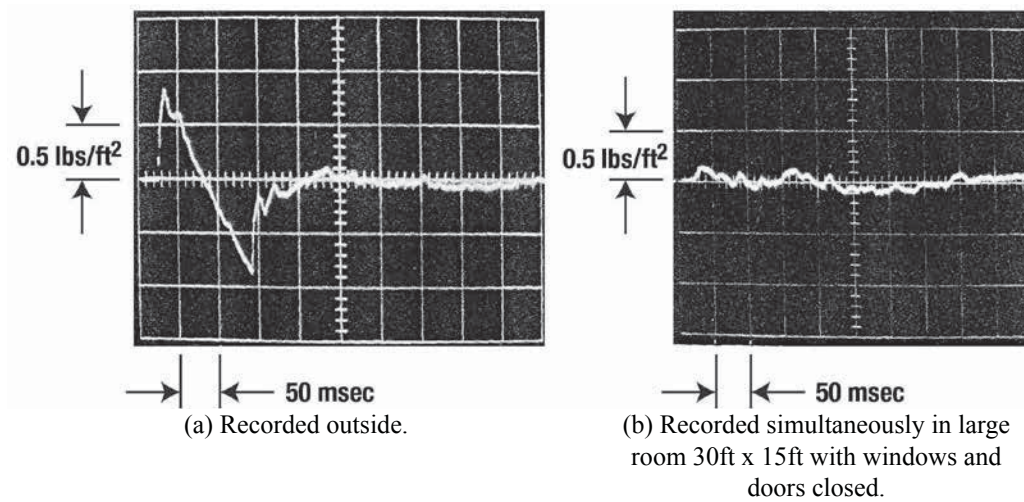


Figure 9.137. Sonic bang from Lightning flying at Mach 1.4 and an altitude of 43,000 feet (ref. 9.83).

A time variation of the overpressure caused by a single explosive charge, both outside and inside, is shown in figure 9.138. The left side plot of the figure shows a peak initial shock pressure similar to that of figure 9.137(a), except the pressure recovery is much faster. The indoor signature in the plot at the right side of the figure shows an oscillatory behavior much like that of figure 9.137(b). Double explosive-charge signatures for open air, and inside a large room, are shown in figure 9.139.

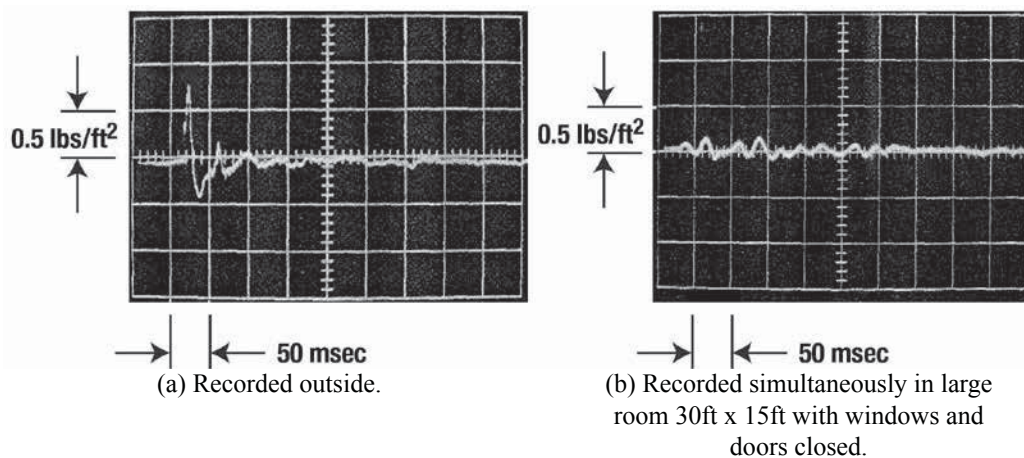


Figure 9.138. Explosive bang from single 11-ounce charge (ref. 9.83).

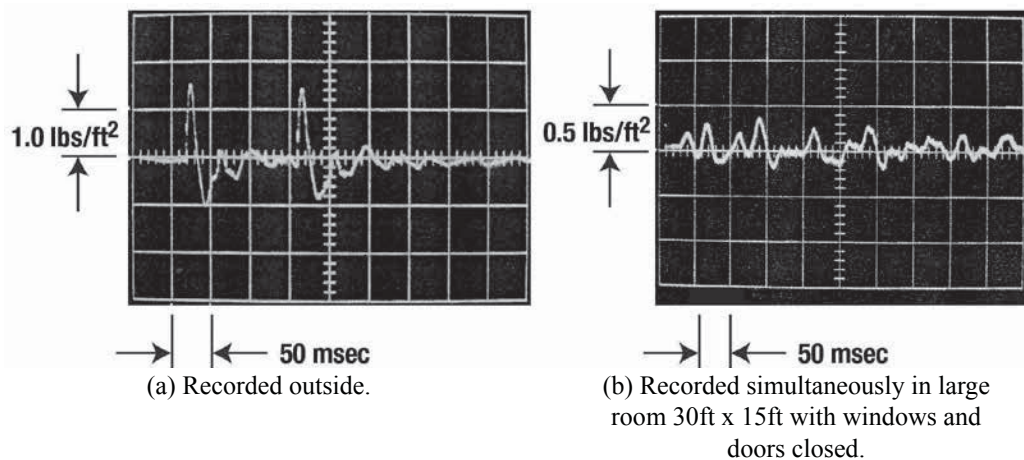


Figure 9.139. Explosive bang from double 3-pound charge (ref. 9.83).

Note that figure 9.139(a) represents an attempt to simulate a 2 lbs/ft² outside initial and trailing shock signature. Thus, the oscillations of pressure of the indoor signature, figure 9.139(b), achieve a magnitude of very roughly twice that of the figure 9.138(b), which simulated a 1.0 lb/ft² sonic boom. The degree to which humans tolerated the Lightning aircraft booms and explosive booms is shown in figure 9.140. The solid symbols are the explosive-charge data and the open symbols are the Lightning aircraft data.

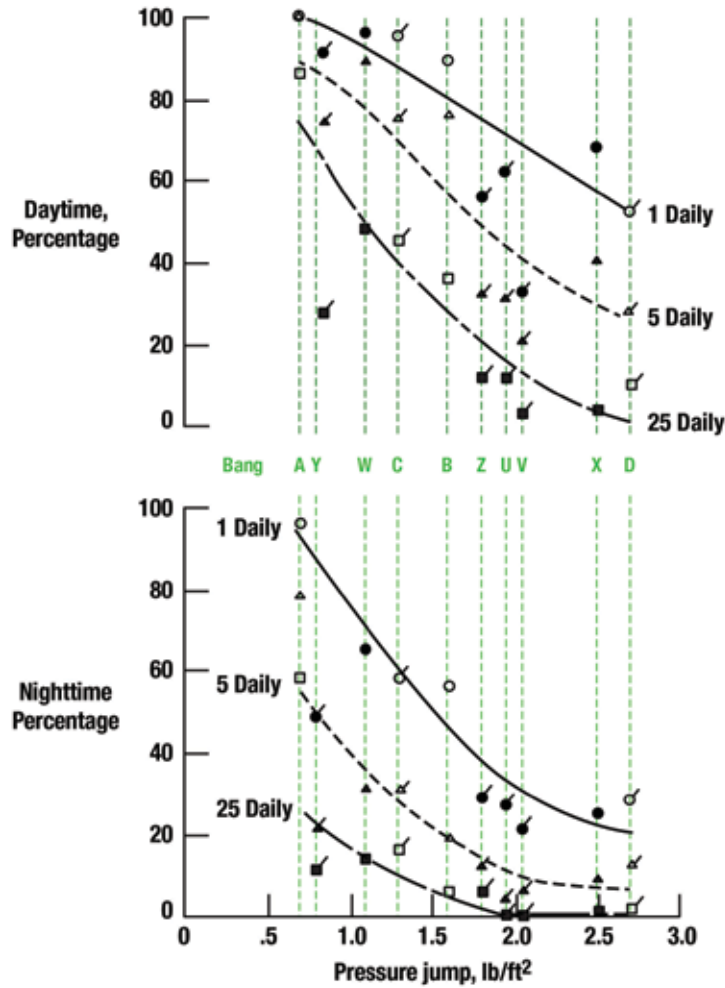


Figure 9.140. Percentages of those who would tolerate bangs of various pressure jumps at different frequencies during daytime and nighttime (adapted ref. 9.83, see tables 9.7 and 9.8 for bang or boom definitions).

The alphabetical key for the various shock simulations from figure 9.140 is given in tables 9.7 and 9.8 below.

Table 9.7. Morning - Listeners on the Mound (ref. 9.83)			
Identifying Letter	Disturbance Vehicle	Nominal Intensity, lb/ft ²	Actual Intensity, lb/ft ²
A	F-3 Lightning	1.0	0.7
W	Explosive	1.0	1.1
B	F-3 Lightning	2.0	1.6
X	Explosive	2.0	2.5

Identifying Letter	Disturbance Vehicle	Nominal Intensity, lb/ft ²	Actual Intensity, lb/ft ²
C	F-3 Lightning	1.0	1.3
Y	Explosive	1.0	0.8
D	F-3 Lightning	2.0	2.7
Z	Explosive	2.0	1.8
V	Explosive*	2.0	2.0
U	Explosive**	2.0	2.0
*Surprise explosive - double 3 lbs			
**Surprise explosive - single 3 lbs			

As noted in reference 9.83 (p. 6):

Great caution should be exercised in drawing conclusions from figure 9.140. We must remember that the percentages given are the percentages of people who consider they would tolerate bangs of the intensities and frequencies indicated. One wonders, for example, what percentage of people would have considered that they would have tolerated a network of railways being built all over Britain on witnessing the first journey of the Rocket from Stockton to Darlington in 1828: We must remember also that the sample of people was far from being representative of the community at large. Because of these reservations, it is not proposed to draw any conclusions of an absolute, quantitative, nature, but rather to make some relative, qualitative, observations.

Nevertheless, there are some aspects of the tests that are noteworthy. From figure 9.141 it is evident that there is not a significant difference between the Lightning aircraft's sonic bangs and the explosive bangs. As revealed in reference 9.83 (p. 6), answers to a questionnaire gave the impression that explosive bangs were not very different from the sonic bangs, particularly when heard indoors, and most particularly if made double. In fact, an appreciable percentage of those present thought that the unannounced bang V (see table 9.8) was a sonic bang, and several "did not know."

Exercise Westminster

A second test utilizing aircraft and explosives was conducted by the RAE and reported in 1965 (ref. 9.84). It was called Exercise Westminster since it was staged primarily for several members of Parliament. As with Exercise Crackerjack, both Lightning supersonic flyovers and explosive charges were used to provide the required disturbances. There were four supersonic flyovers, five explosion events and two subsonic flyovers by a DeHavilland Comet jetliner. The four supersonic flyovers were flown on successive days. Measurements were taken at 10 instrument stations.

There were listeners or juries involved in the tests, one jury group was assembled inside a tent and a second jury group was assembled inside of a Barrack Block building. The jury consisted of 61 voluntary listeners that were divided into two groups – one party (Group A) consisting of 31 outdoor listeners and another party (Group B) consisting of 30 indoor listeners during the morning session, with vice versa after lunch. The outdoor party was situated in a relatively unobstructed position on the airfield at Upwood. The indoor party occupied a room on the first floor of a barrack block adjoining that used for the afternoon demonstration of Exercise Westminster.

A wide-band white noise signal was chosen as an acoustic calibrating signal for the subjective judgements and, in order to have the level under close control, it was reproduced through loudspeakers. At the indoor location, in the barrack block, four loudspeakers were disposed at the corners of the room – at the outdoor location a ring of loudspeakers was arranged to surround the jury who were in a tightly packed group. As described in reference

9.85 (p. 243), the tests were conducted in the following way:

The first sound heard by the juries was a white noise event, presented at a level expected to lie within the range of annoyance of the other events. Subjects were instructed to consider the annoyance of this sound to be worth 10 units, and then to award every succeeding noise in the sequence, a numerical score indicating how annoying it appeared to be, in relation to this initial sound.

Following the subjective tests using white noise, the authors (ref. 9.85, p. 242) went on to describe the testing as follows:

The flying programme consisted of a series of four sonic bangs with nominal peak over-pressures ranging from 0.75 mb to 1.12 mb (1.6 lbs/ft² to 2.33 lb/ft²) and two low altitude full-power runs by a Comet jet aircraft planned to give a peak level of around 110 PNdB, the latter being included to provide a more familiar type of noise for purposes of comparison. These events followed one another about every five minutes and during the intervals a series of high explosive charges was detonated. The explosions were fired in pairs with a time delay between the detonations of about 100 msec, corresponding to the bow and stern shocks of the sonic bangs. The ground zero for the explosions was located so that the wave fronts arrived from the same direction as the sonic bangs.

Typical oscillograms of the pressure signatures measured outdoors at 1.2 m above the ground and indoors of the sonic bang and double explosion are presented in figure 9.141 (ref. 9.85). The outdoor boom signature overpressures varied from about 0.5 mb to 0.65 mb (1.04 lbs/ft² to 1.36 lbs/ft²) and the duration are the order of 100 msec with the double explosive signatures having overpressures of about 0.9 mb – 1.2 mb and a period of 82 msec.

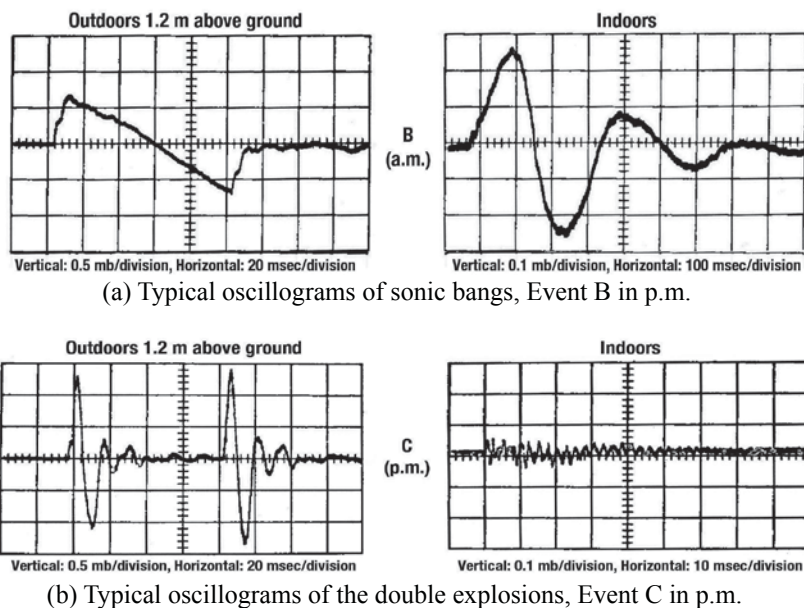


Figure 9.141. The waveforms of typical sonic bangs and explosions as measured outdoors and indoors (adapted from ref. 9.85).

While outdoors, the observers would experience a double bang from the passage of the sonic boom signature since the ear would respond to the rapid change in pressure at the bow and tail shock and would not respond to the slowly changing pressure associated with the expansion portion of the signature. Likewise, for the double explosive, the ear again would hear the bangs from both charges. The influence of the low-frequency portion of the boom signature associated with the expansion portion of the waveform is quite apparent in the indoor situation as compared to the double explosive signature. Results of the test are summarized in figure 9.142, which displays the relative annoyance as a function of loudness level in phons for both outdoor and indoor subjects for all four stimuli.

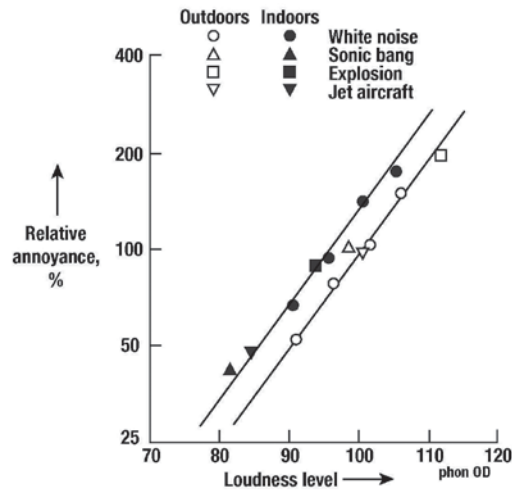


Figure 9.142. Summary of results of outdoor-indoor tests (ref. 9.85).

It is apparent that as loudness increases, so too does annoyance. Another feature is that when the loudness level is equal both outdoors and indoors, the annoyance level indoors is greater than that of outdoor exposure. In reference 9.85 (p. 257), the authors state:

For this experiment we did not adopt either the criterion of “loudness” or “noisiness”, but rather “annoyance” in order to preserve continuity with the previous laboratory experiment. No recognized evaluation procedure exists for deriving “annoyance” from physical measurements, but our results accord well with loudness and perceived noisiness calculated by the recognized methods. This suggests that the annoyance scores given by our subjects were a measure of subjective magnitude largely related to the element of intensity. In the case of bangs, it is reasonable to assume that other factors such as the degree of startle would in general contribute to the annoyance, unless they were completely dominated by the intensive element. Whether startle was absent because of the voluntary nature of our test, or whether it is a secondary effect at realistic levels cannot be inferred from our results.

A summary of the group scores relative to the annoyance of the jet aircraft outdoors is given in table 9.9 (ref. 9.85).

Table 9.9. Group Scores Relative to the Annoyance of the Jet Aircraft Outdoors (ref. 9.85)

Source	Outdoors			Indoors			Outdoor/Indoor Difference	
	Relative Annoyance	Loudness Level	Perceived Noise Level	Relative Annoyance	Loudness Level	Perceived Noise Level	Physical Reduction	Subjective* Reduction
	R_0 %	Phon OD	PNdB	R_i %	Phon OD	PNdB	Phon OD	
Jet Aircraft (Comet)	100	100.5	103.0	49	84.6	86.7	15.9	10.3
Sonic Bangs	102	98.2	99.2	41	81.6	83.0	16.6	13.2
Explosive Bangs	199	111.3	111.9	91	93.7	94.9	17.6	11.3
Door Slams	-	-	-	53	-	-	-	-

* Derived from the relative annoyance values by the formula $10 \log_2 (R_0/R_i)$.

The results are presented in the form of percentages relative to the annoyance of the jet flyover noise as heard outdoors. This comparison stems from previous efforts to relate sonic booms to the airport noise role or landing approach noise limit of 110 PNdB. Thus, from the table, it is seen that the outdoor sonic bangs were judged to be 1.02 times more annoying than the Comet aircraft at an average level of 103 PNdB. The authors translated that a N-wave type sonic bang of peak overpressure 1.4 mb would be equal in annoyance to a jet aircraft flyover noise of 110 PNdB.

U.S. Army/Construction Engineering Research Laboratories (USA/CERL) Tests

Schomer, Sias, and Maglieri (ref. 9.86) documented the results of a substantial study to validate a new method for the assessment of high-energy impulsive sounds based primarily on blast noise research (ref. 9.87, p. 169):

A key factor in the design of this study was the presentation of real blasts and booms to subjects situated in real structures in the field. The study was performed as a paired-comparison test with the same control sound being used in this study as had been used in all the previous blast research that formed the basis for the assessment method. In this new study, 232 subjects each judged 20 booms and 30 blast sounds.

Additional data concerning the subjects is provided in reference 9.86 (p. 170):

The study was performed during August 1995 at the Naval Air Station (NAS) Fallon, Nevada. The study site was located in the Nevada desert almost centrally within a 15,000-sq. km supersonic flying area. Three differing test structures were located at the test site. One structure was a rehabilitated heavy brick house with a large flat timber-beam, wooden-decked roof covered with about 350 mm of small gravel stones. The main room in this house was approximately 5.5- by 7-m living room. The second structure was a rather small, single-room, 3- by 6-m wood frame building. The third structure was a large mobile office trailer that was divided into two 3.5- by 8.5-m living rooms. Each test room was furnished as a normal living room, including couches and chairs, carpets or rugs, coffee and end tables, window treatments, etc. The booms and blasts came from about the same direction and each room had windows that faced the blast site and the direction of arrival of the sonic booms. All windows in each test room were closed.

A schematic of the test site is shown in figure 9.143. Further details of the arrangement can be obtained from reference 9.86.

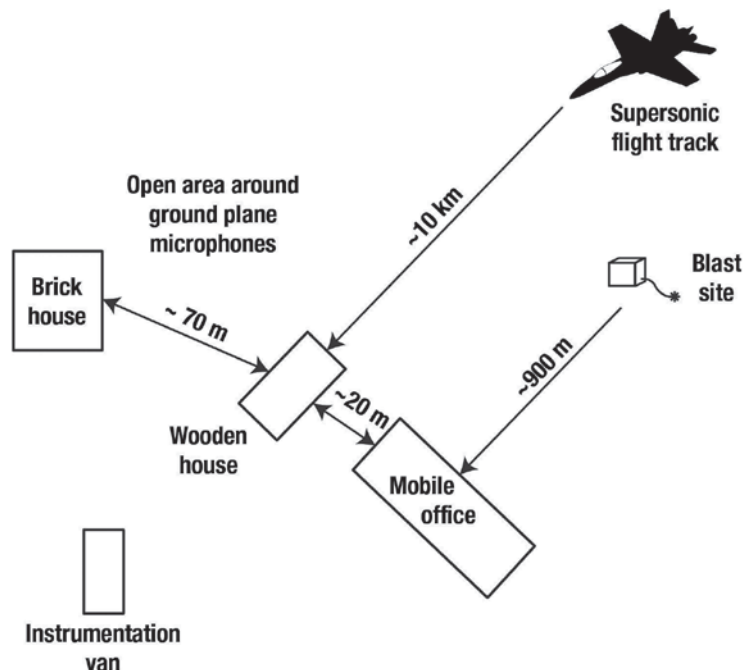


Figure 9.143. This figure, not to scale, shows the layout of the immediate test site, including the test structures and instrumentation (ref. 9.86).

The sonic booms were produced by a Navy F-5 jet fighter flying at approximately Mach 1.2 and at altitudes ranging from 6400 to 9800 m (21,000 to 32,000 ft). Flight tracks were aimed directly at the test site or offset laterally to produce lower boom levels. Blasts were generated by C-4 explosives set off at a height of ~ 0.9 m (3 ft) and at a distance of 900 m from the test houses. Three sizes of the charges were used – 2.26 Kg of C-4 explosives for the large blast, 0.55 Kg for the small blast, and the double blast was two 1.13 Kg charges set off simultaneously but were separated by about 30 feet to achieve the 100 msec delay at the test houses. The double blast was created to mimic a sonic boom as revealed in reference 9.86 (p. 174):

The metrics used were the test sound C-weighted sound exposure level (CSEL) and the control sound A-weighted sound exposure level (ASEL). The control sound was adjusted such that at low sound levels nearly all of the subjects would find the test sound more annoying and at high control sound levels nearly all of the subjects would find the test sound less annoying. In between the point where 50 percent of the subjects found the test sound to be more annoying and 50 percent found the control sound to be more annoying was the equivalency point, the point where the annoyance generated by the test sound (blast or boom) was equivalent to the annoyance generated by the control sound.

The actual determination of the equivalency point is quite complex and is described in reference 9.86.

Equivalency point data is plotted in figures 9.144 and 9.145. Figure 9.144 shows the data where the blast and booms were measured indoors, as was the control sound. Data obtained during this study as well as previous blast data are plotted. A regression line fit is shown for the older blast data. The figure shows that the previous blast noise data and the new Fallon data are generally similar but there is quite a bit of scatter. Figure 9.145 is similar to figure 9.144 except that outdoor CSEL measurements are plotted as a function of indoor measured, equivalently annoying white noise control sound ASELs.

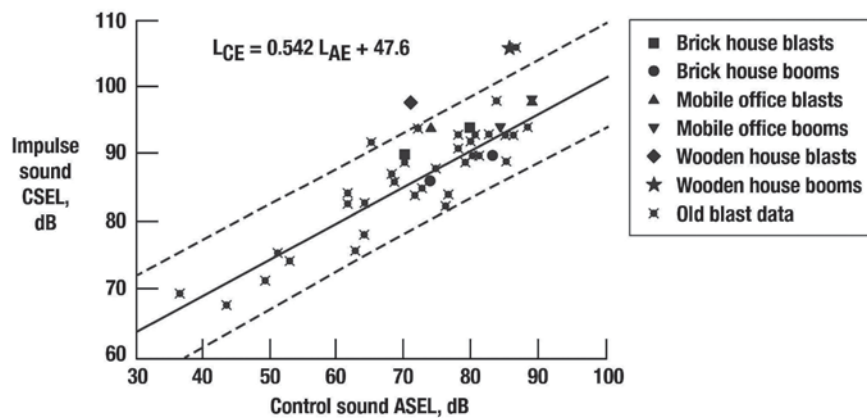


Figure 9.144. CSEL of blast or boom sounds versus ASEL of equivalently annoying control sound. Blast and booms measured indoors (ref. 9.86).

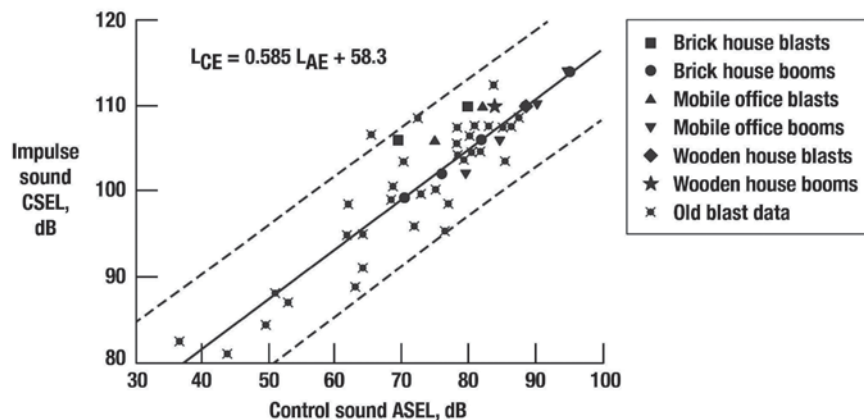


Figure 9.145. CSEL of blast or boom sounds versus ASEL of equivalently annoying control sound. Blast and booms measured outdoors (ref. 9.86).

Like figure 9.144, figure 9.145 includes the previous blast data and a regression line that has been fit to these data. Figure 9.145 also includes the outdoor measured NAS Fallon data. One can compare the fit of the Fallon data to the respective regression lines in figures 9.144 and 9.145. From observation, it is clear that the new data in figure 9.145 better fit the regression line than is the case for the data represented by figure 9.144. To quantitatively aid in this comparison, the 95 percent prediction intervals for the previous blast data are shown in figures 9.144 and 9.145. In figure 9.144, three of the new data points (25 percent) lie outside the 95 percent prediction interval for the previous blast data, while in figure 9.145 none of the new data points lie outside the indicated prediction interval. This result, that the outdoor-measured data form a better prediction of response, tends to reinforce the concept that C-weighting is a useful outdoor measure for assessing the indoor community response to high-energy impulsive sounds. It should only be used outdoors – not indoors since one reason for choosing C-weighting was to include those acoustical energies that induce building vibration and rattles.

In summary, a multitude of sonic boom simulators, designed to investigate indoor-outdoor subjective response to sonic booms, have been built. They include the use of headphones, loudspeaker enclosures, piston-driven systems, and use of explosive charges. Details of some of the facilities are given, along with some examples of the results of the research. Many of the facilities no longer exist (ref. 9.2), so the referenced papers are the only places where additional information can be obtained.

Building Response Simulations

The simulation of sonic booms on buildings and their components gained traction in the 1960s when it became increasingly clear that the use of an airplane and a single dwelling did not produce the kind of generalized or parametric results needed for different dwellings and locations subjected to different boom signatures. In any case, the expense associated with experiments requiring several airplane flights and a variety of buildings was too expensive. As noted by Hawkins and Hicks in their 1966 paper (ref. 9.88, p. 1244), “A simulation technique has the advantages of cheapness, localization of effects, and the potential ability to produce bangs characteristic of future aircraft types, for example Concorde.”

In this section, several simulation techniques and devices used to generate sonic boom signatures in the study of building and human responses, especially those indoors of structures will be discussed. Included in this review are the use of linear charges, air modulation devices, piston-driven generators, and loud speakers.

Linear Charges

The explosive line charge technique was explored in reference 9.88. A single line charge produces a pressure waveform like that shown in figure 9.146 along an extension of its line of sight. The superposition of several line charges of different strengths, as shown in figure 9.147, can be used to simulate N-waves, or tailored boom shaping of varying strength. Figure 9.148 shows the simulation of an N-wave of 200 msec duration. It was noted in reference 9.88 (p. 1245) that the straightforward application of the line-charge technique yielded frequency



Figure 9.146. Experimental pressure waveform from straight linear charge of uniform explosive linear density, length 60 in. (ref. 9.88).

contents suitable for structural studies but “in the higher frequency range divergencies appear between the spectra owing partly to the higher inherent noise level of the simulant and partly to the different pressure rise rates in its shock fronts.”

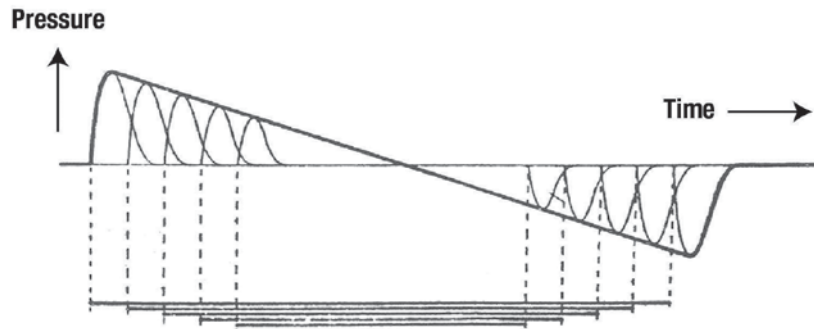


Figure 9.147. Principle of N-wave synthesis from uniform linear charges (ref. 9.88).

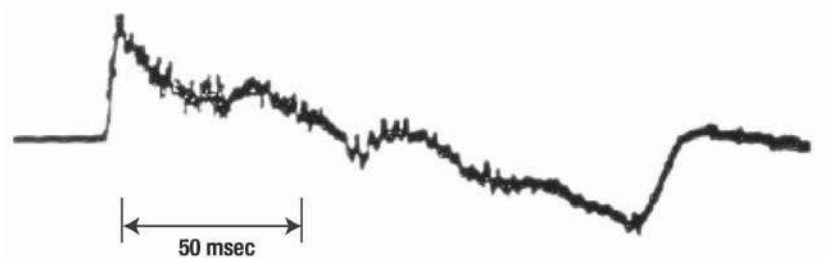


Figure 9.148. Experimental pressure waveform from 200 msec N-wave simulant (Mark I) (ref. 9.88).

With the critical roles that rise time and peak pressure play in the noise spectra and magnitude, the authors of reference 9.88 (p. 1245) were led to develop a second type of line charge distribution:

This type of simulant is composed of two identical linear charges arranged side by side and detonated consecutively with an appropriate time delay. It is designed to reproduce in amplitude and rise rate the bow and stern shocks of the sonic bang waveform--the acoustically insignificant slow linear fall in the middle of the wave is replaced in the simulant by an equally acoustically insignificant slow asymptotic return to ambient pressure; this is not possible with point source explosive charges.

Figure 9.149, from reference 9.88, shows the signature generated by the new technique where the emphasis appears to have been on rise time.

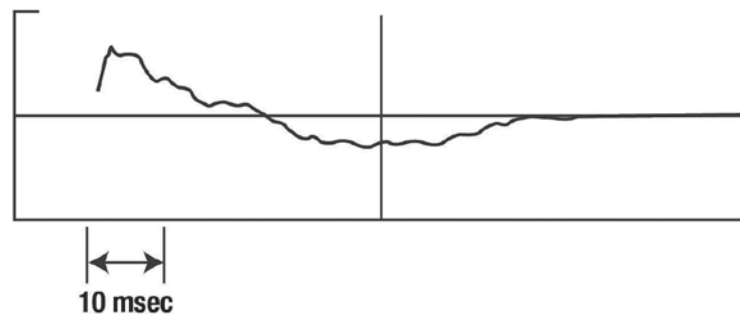


Figure 9.149. Experimental pressure waveform from one-half of Mark II sonic bang simulant (ref. 9.88).

Another explosive device invented in the late 1960s and documented in a publication in 1971 (ref. 9.89) is the gas-filled balloon with a line charge through the center. The line charge was ignited by a conventional detonator at the end of the balloon nearest to the observation point such that the detonation propagated away from the observation point. The resulting N-type signatures have less fine-structure distortion than those from the multiple line charges, probably because of the more uniform ignition characteristics of the gas.

Experiments were carried out, documented in reference 9.89, to determine the effects of shapes, length, diameter, and ignition placement. Empirical relationships were derived that permit the design of a balloon similar to that in figure 9.150. Figure 9.150 shows the shape and dimensions of a balloon used in this reference to obtain an N-wave pressure signature. The balloon is tapered on either end with a cylindrical section in the middle. An illustration of type N-wave obtained using the balloon configuration and how the boom signature develops with distance along the ground is given in figure 9.151 (ref. 9.89).

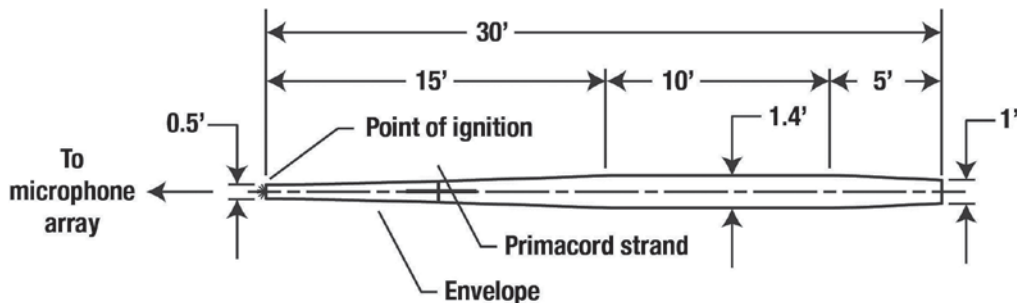


Figure 9.150. Balloon configuration to obtain N-wave (ref. 9.89).

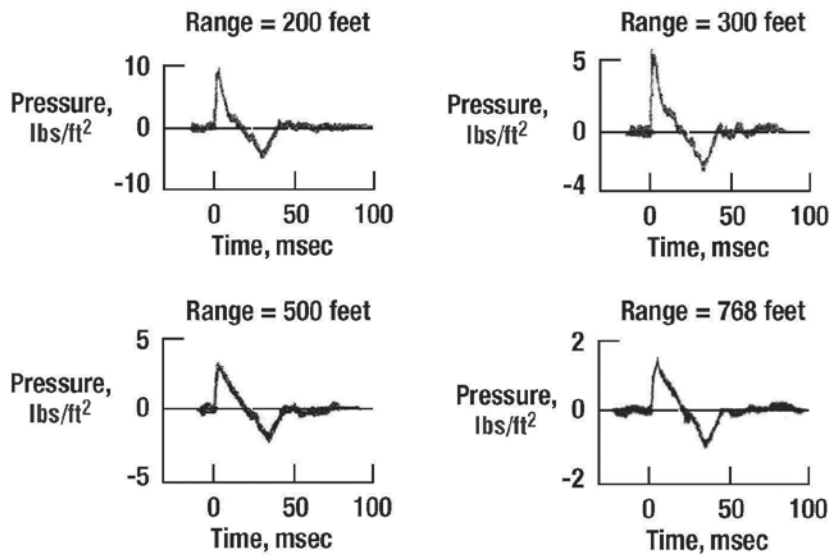


Figure 9.151. Pressure time histories at various ranges for N-wave balloon, SBS 102. Illustrating development of N-wave (adapted from ref. 9.89).

Signature overpressures vary from about 10 lbs/ft² at 200 feet from the explosion sources to about 1.5 lbs/ft² at a range of 728 feet and the signatures become more N-wave in shape with a period of about 35 msec. For the 30-foot long balloon considered here, this ultimate shape is obtained at a range of less than 800 feet. Pressure profiles for the other three N-wave balloons tested show similar profiles. The duration of the pulses, i.e., peak-to-peak, is approximately proportional to the length of the balloon.

Figure 9.152 from reference 9.89 gives results obtained from tests that employed a range of balloon sizes. Peak overpressure is plotted on a logarithmic scale versus range showing that the peak overpressure decays as

$$P = 6970(R/D_1)^{-1.11} \text{ lbs/ft}^2$$

The negative peak overpressure, P_n , is described by

$$P_n = (-2330)\left(\frac{R+L}{D_2}\right)^{-1.15} \text{ lbs/ft}^2$$

R , L , D_1 and D_2 denote the range from the end of the balloon, the length of the balloon, the diameter of the balloon at the microphone end, and the diameter of the balloon at the other end. The end product of the research, described in reference 9.89, was the design chart (see fig. 9.153) that enables one to pick the length of a balloon that will yield a required Δp and duration of pulse. Since 60 feet was the maximum balloon length tested, much of the plot is based on a reasonable extrapolation. Clearly by proper design of the balloon and controlling the constituents of the detonable gas mixture, or the relative proportion of each gas in the mixture, almost any wave shape can be generated. The equipment can be moved to almost any location, it appears to be safe to operate, and is cheap.

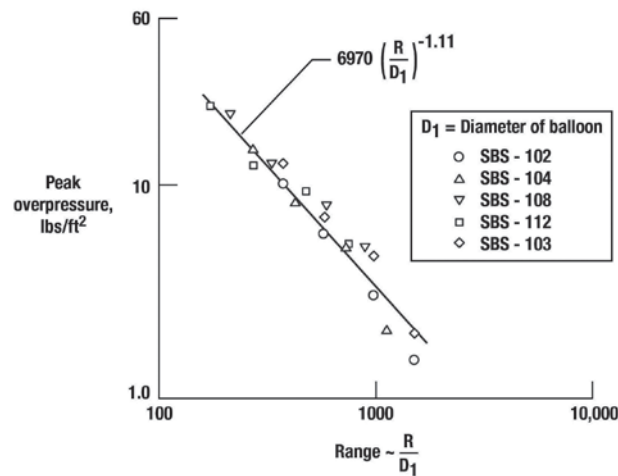


Figure 9.152. Peak overpressure versus reduced range N -wave envelopes – Series IV (ref. 9.89).

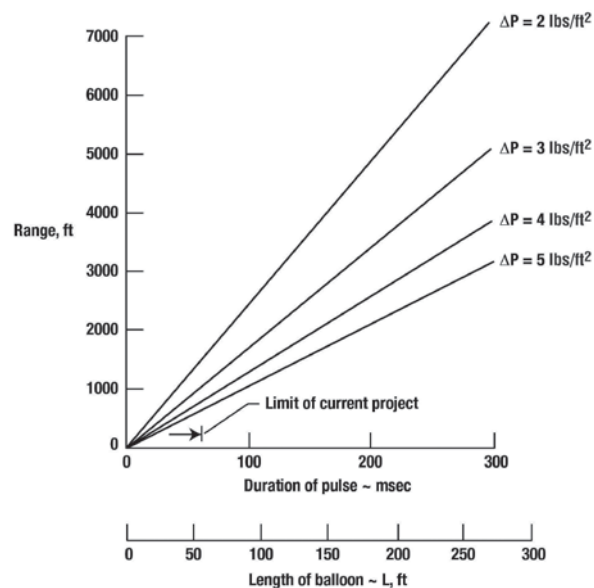


Figure 9.153. Required range for sonic boom simulations, given required peak-pressure and duration (extrapolated, ref. 9.89).

A paper by Haac et al. in 2009 (ref. 9.90) documented the initial phases of a study aimed at developing a computer-code package capable of predicting the vibro-acoustic response of residential buildings exposed to sonic booms. The booms were produced using linear explosion charges consisting of multiple detonating chord strands. The predictions from this code will eventually be used in the study of indoor subjective human response to sonic booms. In carrying out this study, a small building was fabricated using standard construction materials and techniques. It has dimensions of 4.86 x 2.82 x 3.05 m (16 x 9.25 x 10 ft) and a photograph is given as figure 9.154. Two double-panel glass windows (0.7 m x 0.90 m) were installed on the front wall of the test structure shown in the figure. A hollow core masonite door, 0.69 m x 2.01 m, was installed on one of the walls adjacent to that with the windows, as shown in figure 9.154.



Figure 9.154. Assembled test structure (ref. 9.90).

The sonic boom was generated by an explosive technique, following the work reported by Hawkins and Hicks (ref. 9.88). The test site was at the rural Kentland Farm setting of Virginia Tech. A schematic of the test setup along with the exterior microphone locations is provided in figure 9.155.

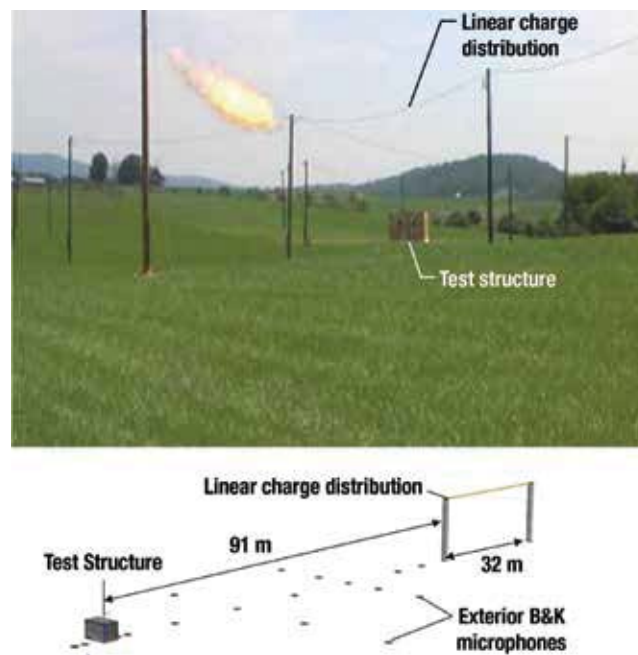


Figure 9.155. Schematic showing structure, linear charge distributions, and placement of microphones along the boom propagation path (ref. 9.90).

The charge consisted of multiple detonating chord strands positioned to create a linear charge distribution as shown in figure 9.156. This charge distribution was located at the height of 10.7 m (35 ft), parallel to the ground, and aimed at the basic structure so that the surface of the wall with windows was perpendicular to the axial propagation direction of the blast.

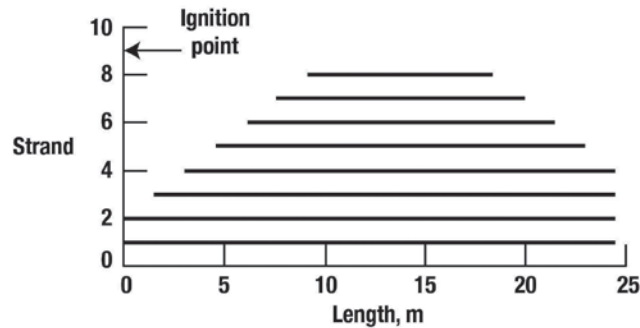


Figure 9.156. Linear charge distribution used to produce a typical sonic boom (ref. 9.90).

The pressure loading on the structure was recorded by a total of 84 microphones mounted to the outside surface of the structure and inside the room. To monitor the boom propagation generated by the linear charge, an array of microphones was also used. These microphones, which have a flat frequency response function down to 0.07 Hz, were placed on plywood on the ground and distributed over the test site. To measure the structural response, an array of accelerometers was mounted to the interior and exterior of the structure. The frequency responses of a sample of representative accelerometers were measured flat over a range from 5 to 2200 Hz.

In support of the structural and acoustical response to sonic booms, an extensive modal characterization of the structure was performed. These data were useful in the interpretation of the sonic boom measurements and in the numerical modeling of the structure. Modal testing of the structure used impulse hammers to excite the accelerometers placed on various structural components and the windows. Frequency response functions (FRFs) were then computed and selected for each structural component with a combination of sufficient levels and well-separated peaks. These were then analyzed to obtain the resonances. To this end, a mode indicator function was obtained by adding each of the FRFs together (ref. 9.91). The first 10 modes of the resonant frequencies associated with the entire test structure, the windows and the doors, are presented in tables 9.10 and 9.11.

Table 9.10. Building or Global Resonances Determined from a Simple Mode Indicator Function (Adapted from ref. 9.91)

Mode	Resonant Frequencies (Hz)
1	9.2
2	12.6
3	14.9
4	17.4
5	20.6
6	26.5
7	30.9
8	34.8
9	42.0
10	46.7

Table 9.11. Window and Door Resonances from a Simple Mode Indicator Function (Adapted from ref. 9.91)

Mode	Resonant Frequencies (Hz)	
	Window 1	Door
1	9.3	9.7
2	15.2	12.5
3	17.9	15.2
4	21.0	19.1
5	25.7	22.6
6	34.3	32.0
7	42.9	48.0
8	47.6	67.1
9	62.5	85.1
10	73.4	---

An acoustic characterization of the room was also performed using a speaker placed in a corner of the room on the floor. Acoustic data with an array of microphones were recorded in time blocks of 32 sec at a sampling frequency of 12.8 kHz. The input disturbance was white noise low-pass filtered at 400 Hz. The Natural Excitation Technique (NEXT) was used to calculate modal parameters (ref. 9.92). The modal results (first 10) are presented in table 9.12. As reference 9.90 points out, it is evident that some of the measured natural frequencies are related to the structural components, e.g., the window fundamental frequency at 15.1 Hz. Due to the simplicity of the room geometry, it was possible to calculate the room's natural frequencies tabulated in table 9.12.

Table 9.12. Room Cavity Natural Frequencies Measured Using the Natural Excitation Technique (NEXT) Compared to Theoretical Natural Frequencies (Adapted from ref. 9.90)

Mode	Experimental		Theoretical Natural Frequency (Hz)
	Natural Frequency (Hz)	Damping Ratio %	
1	15.1	3.7	-
2	22.3	0.1	-
3	29.5	8.4	-
4	37.4	2.7	37.0
5	41.7	3.2	-
6	44.7	4.7	-
7	50.1	4.7	-
8	55.2	5.4	-
9	59.4	6.3	-
10	63.1	6.6	61.1

Measurements were made of the structural response of the various building components and the acoustic response in the room to the sonic boom simulated by the linear live charge. Figure 9.157(a) shows the actual time history of the sonic boom, which has a duration of approximately 100 msec and a maximum overpressure of close to 100 Pa (2 lbs/ft²). There is considerable high frequency content, as seen in the spectrum in figure 9.157(b), particularly beyond 100 Hz.

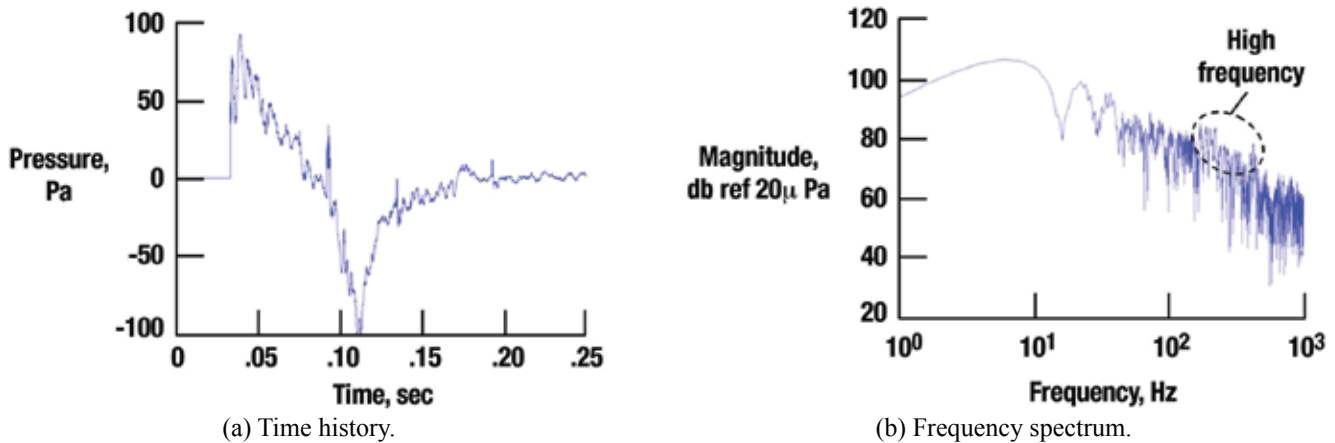


Figure 9.157. The sonic boom exciting the structure time history and frequency spectrum (ref. 9.90).

Figure 9.158 shows four acceleration time histories that were measured near the center of the interior surfaces of the structure at the locations given in the figure. As expected, the largest accelerations were experienced by the front wall and the least by the sidewall without a door. The acceleration spectra for the same components are given in figure 9.159. Similar acceleration and spectra plots for a window and the door are given in the paper.

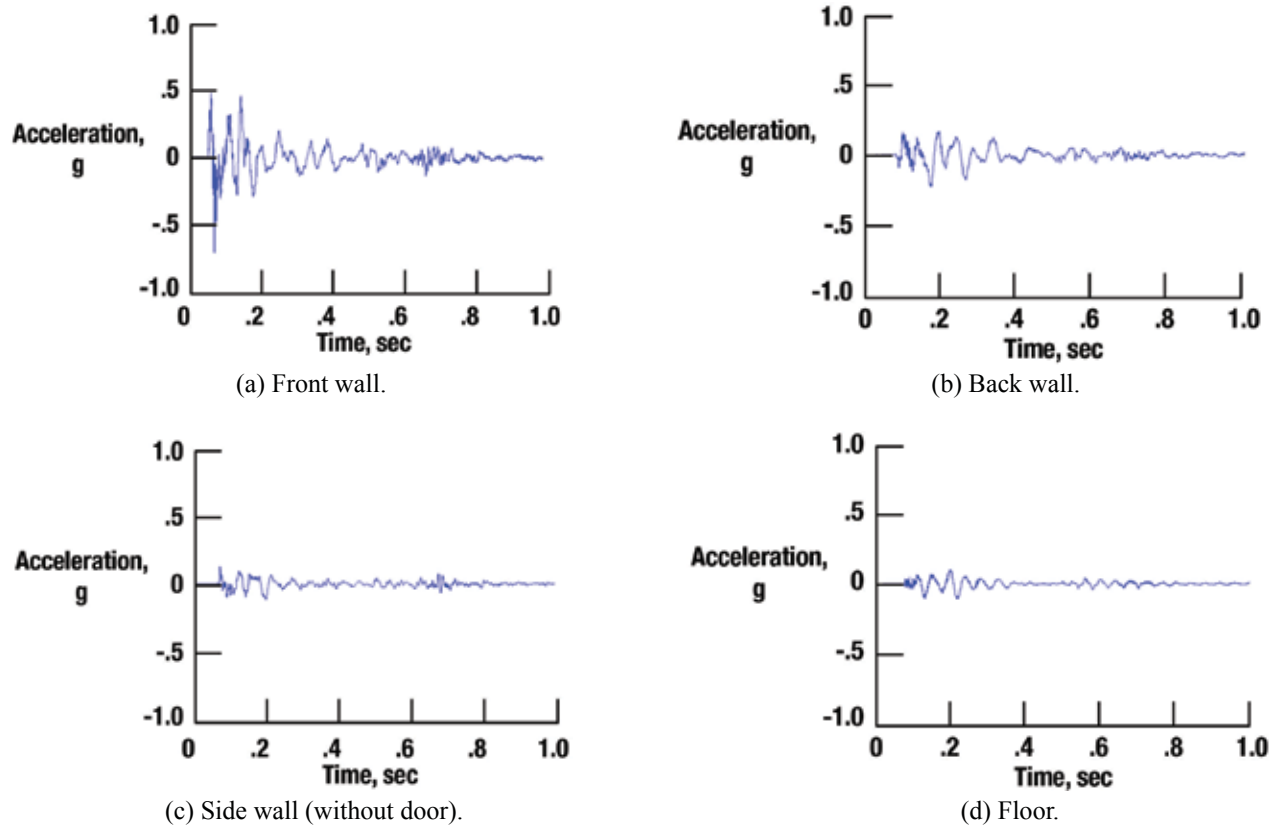


Figure 9.158. Acceleration time histories near the center of the interior surfaces of the structure (adapted from ref. 9.90).

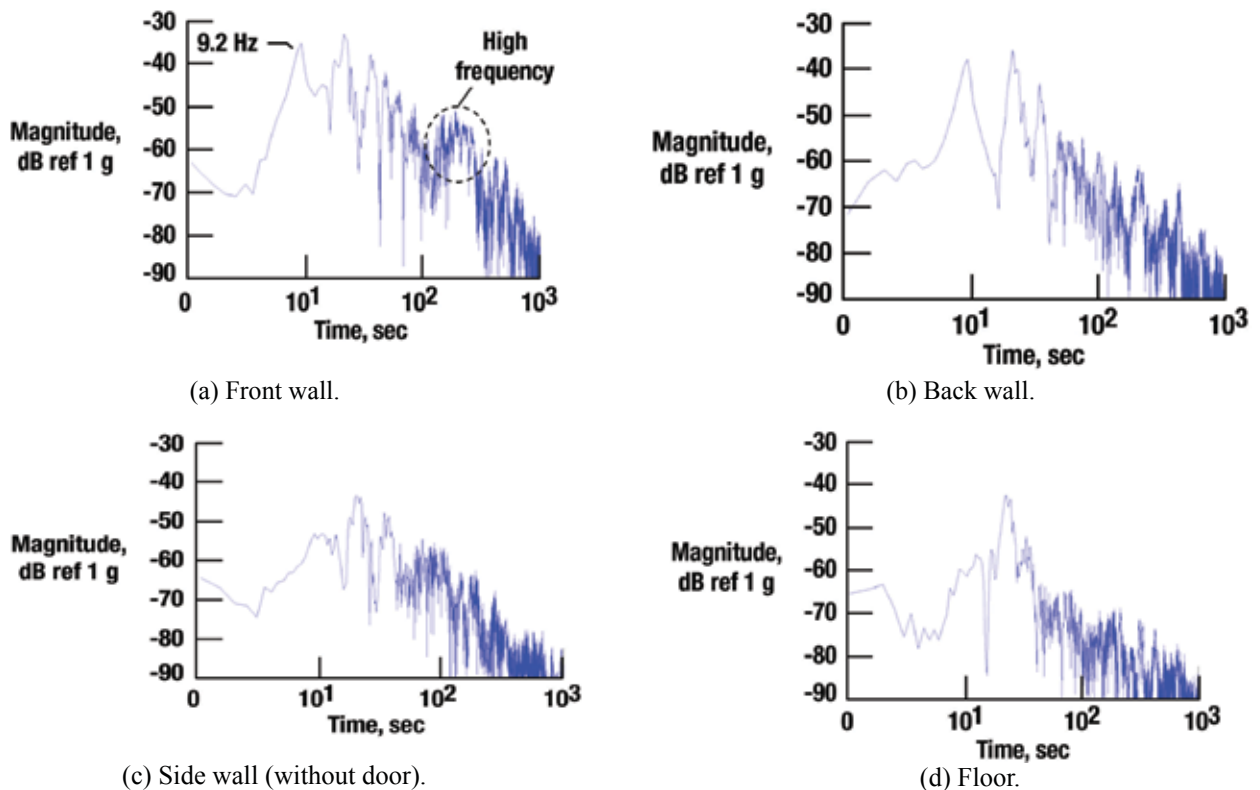


Figure 9.159. Acceleration spectra of the interior surfaces of the structure (adapted from ref. 9.90).

The interior acoustic response is depicted by the microphone measurements made near the middle of the room. The pressure time history and frequency spectrum at this location are provided in figures 9.160(a) and 9.160(b), and show that the basic character of the sonic boom is maintained, but with the maximum pressure level reduced by about a third. As noted in reference 9.90 (p. 15), “The reason the boom shape is relatively preserved while transmitted inside the room is that (i) the boom is tuned to the fundamental frequency of the structure and (ii) that the interior acoustic response is due to the bulk compressibility of the cavity...” Spectral data of figure 9.160(b) shows that the main free responder is the window (see table 9.10). Similar data is observed for a microphone near the window (see table 9.10).

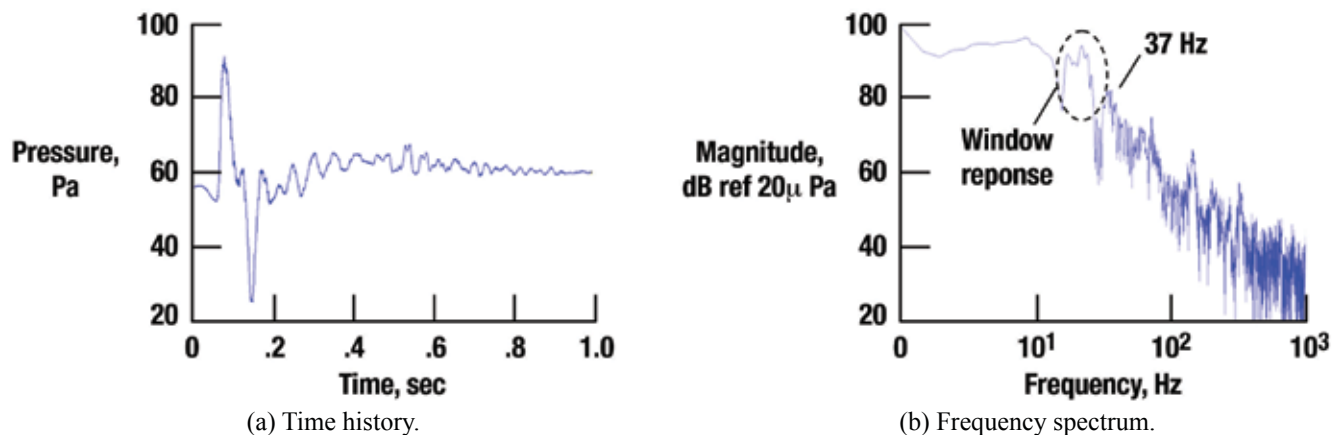


Figure 9.160. Interior microphone response positioned near middle of room (ref. 9.90).

In summary, reference 9.90 contains the results of detailed structural and acoustic modal testing of the test building that enables a better understanding of the response of the building to a sonic boom disturbance. The latter was provided by a line charge that had an overpressure of about 100 Pa (2 lbs/ft²) and duration of 100 msec. While the test building is a single-room building with two windows and a door, it is instrumented to give the most detailed measurements of all of the other known simulators. This highly detailed data set, both in terms of detail and vibroacoustic response, is intended to enable the assessment of prediction models that can be applied to a wide range of building structures.

Air Modulation Devices

There are several air modulators or horn-type simulators that differ in the way the pressure pulse is generated and in the way test specimens are exposed to the sonic booms generated.

Royal Aircraft Establishment (RAE) Blunderbuss

The Blunderbuss, developed at the British RAE, was one of the first air modulation devices conceived. The Blunderbuss was a conical cannon that fired a slug of air, the pressure distribution of which was N-wave shaped (see fig. 9.161). The horn was terminated by an acoustic absorber. As noted by Edge and Hubbard in reference 9.1 (p. 726):

Such devices can generate N-type signatures for a range of overpressures up to at least 20 lbs/ft² by varying the stagnation pressure in the driver section and by changing the rupture diaphragm configuration. The duration of the signatures can be varied over a range by changing the length dimension of the driver section (a 5-ft dimension corresponds to a 40 msec duration).

Test specimens were located near the downstream end of the horn or exposed at the surface of the horn.

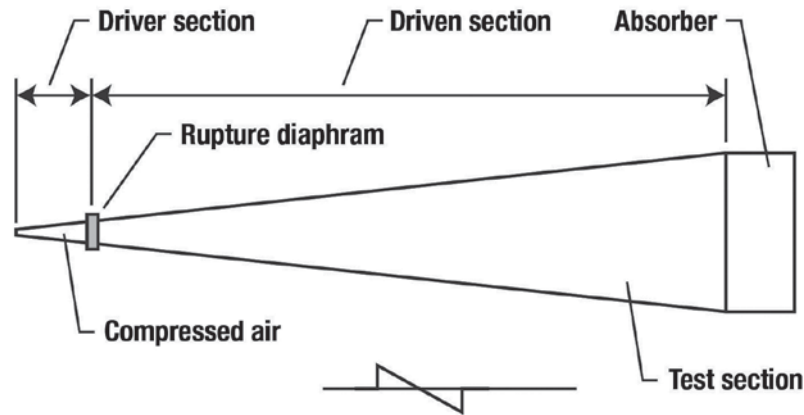


Figure 9.161. Sketch of the Blunderbuss shock-tube simulator (adapted from ref. 9.1).

LTV Twin Shock Tube

A device similar to that of reference 9.93 was the acoustic horn of LTV (ref. 9.94). It employed a twin-driver section and two diaphragms and was intended for testing of structures outside the horn. As seen in figure 9.162, the simulator was 26-feet long with a horn exit of 13-feet in diameter. An electronic time-delay circuit provided a controllable period between the rupture of the two diaphragms, thus providing a wide range of time intervals between the two-shock-wave pressure pulses. The pressure time history diagram on the right side of figure 9.162 illustrates that the device does not produce an N-wave signature due to lack of low frequencies. Two short duration pressure pulses occur at predetermined time intervals to represent any given value of duration. Because of its dimensions, there was very little radiation at frequencies below 50 Hz. This simulator was used

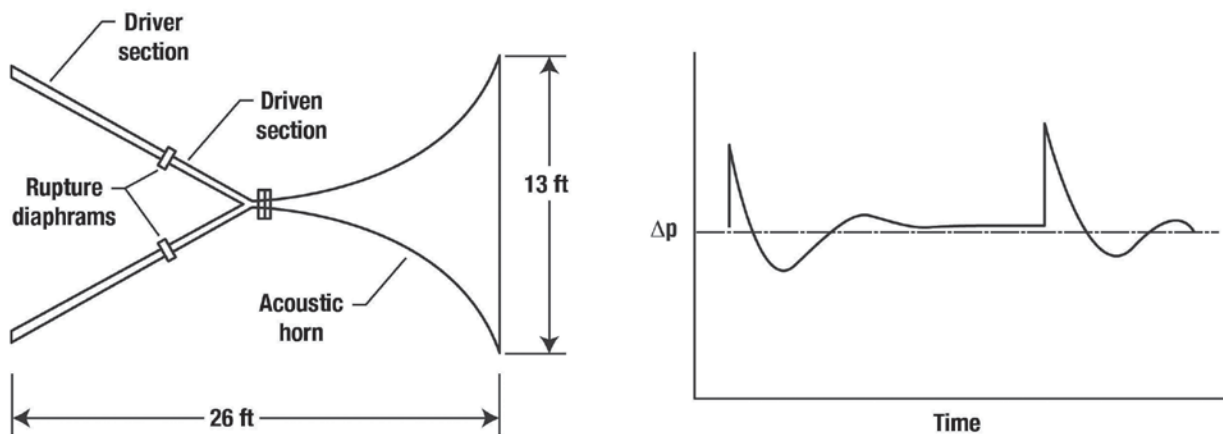


Figure 9.162. Plan view sketch of the LTV twin shock-tube simulator (adapted from ref. 9.1).

in outdoor studies of the effects of sonic booms on small animals. The acoustic horn (4 m) presently resides at NASA Goddard and all other components no longer exist.

General Applied Science Laboratories (GASL)

GASL produced another air modulation device (refs. 9.95 and 9.96) schematically depicted in figure 9.163. As with other air modulation or horn simulators, the primary control and innovative component was the driver section and the valves or diaphragms used to modulate the flow into the horn.

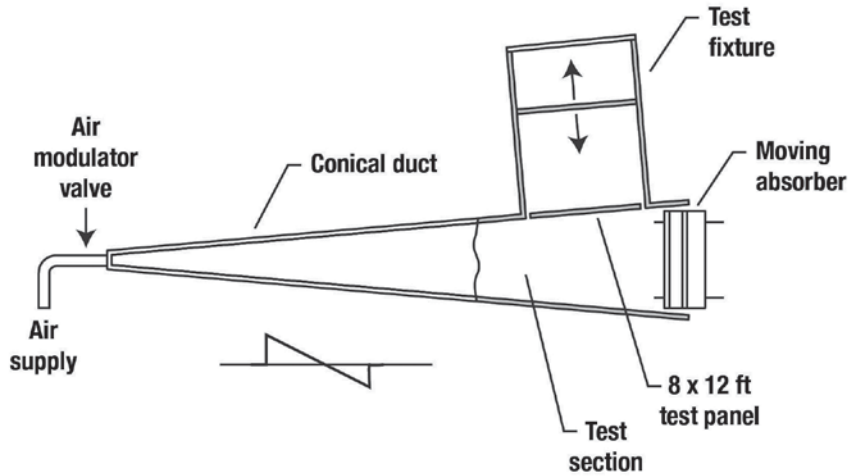


Figure 9.163. Plan view sketch of the GASL air modulator simulator, as used in panel response tests (ref. 9.1).

In the GASL facility, a plug valve similar to that of figure 9.164 (ref. 9.95) was used to control the mass flow. The shape of this plug, on the end of the driving piston, controlled the rate of change of mass flow. Reflections back into the conical duct were reduced substantially by means of a unique porous-piston absorber. This absorber consisted of a fiberglass blanket held in a frame mounted on rollers that rode on a pair of rails. The overall length of the conical duct was 100 feet. The GASL facility was capable of testing a variety of articles and recording a broad array of measurements. Figure 9.165 shows the installation of a test panel (e.g. a window) and window exposed to the passing shock for use in a psychoacoustic study.

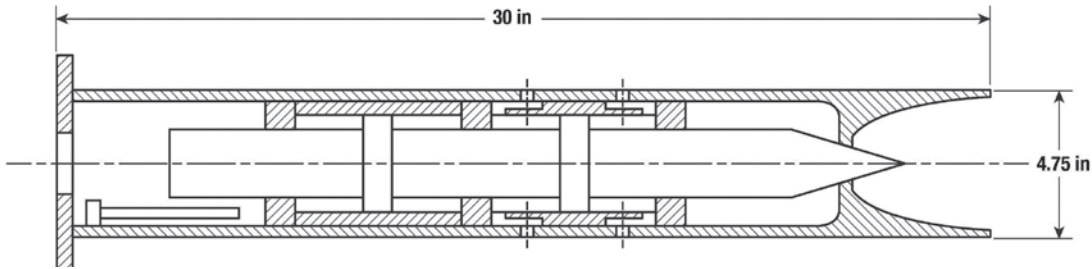


Figure 9.164. Schematic of plug valve (adapted from ref. 9.95).

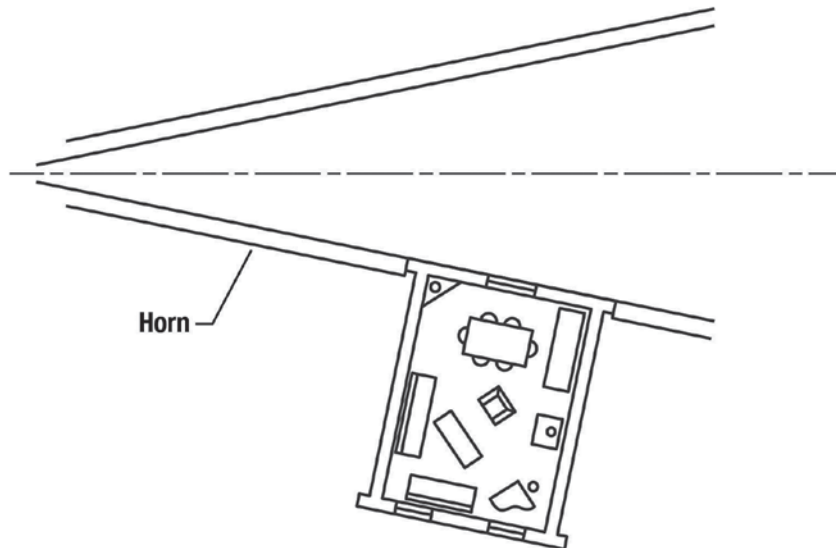


Figure 9.165. Psychoacoustic studies (ref. 9.95).

Another application of the facility was for measuring the dynamic response of large structural models, as shown in figure 9.166 (ref. 9.95). A major advantage of the air-modulation facility, as with other similar devices, was that it could be operated with only a short interval between runs, thus repeated load testing could be performed, such as required for fatigue and crack growth investigations. The GASL facility is no longer in existence.

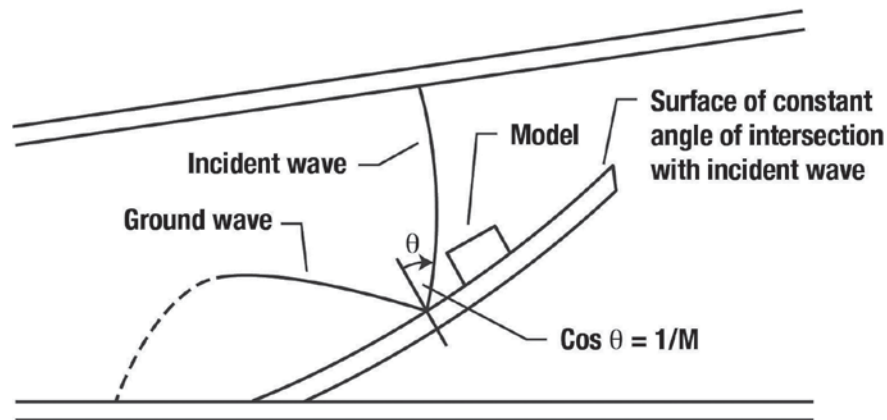


Figure 9.166. Measurement of dynamic response of large structural models (ref. 9.95).

Wyle Laboratories

An air modulator device that does not use a horn but a specialized test chamber (see fig. 9.167) is described in reference 9.97. It is 7-feet in diameter and 9-feet long, and divided into two separate compartments by glass or window test specimens. As with the horn device, compressed air was admitted at one end through an air-modulator valve. Unlike the horn devices, the compressed air was exhausted at the other end through a second air modulator valve. The valves were customized by Wyle Laboratories and controlled electrically to provide the desired operational sequences.

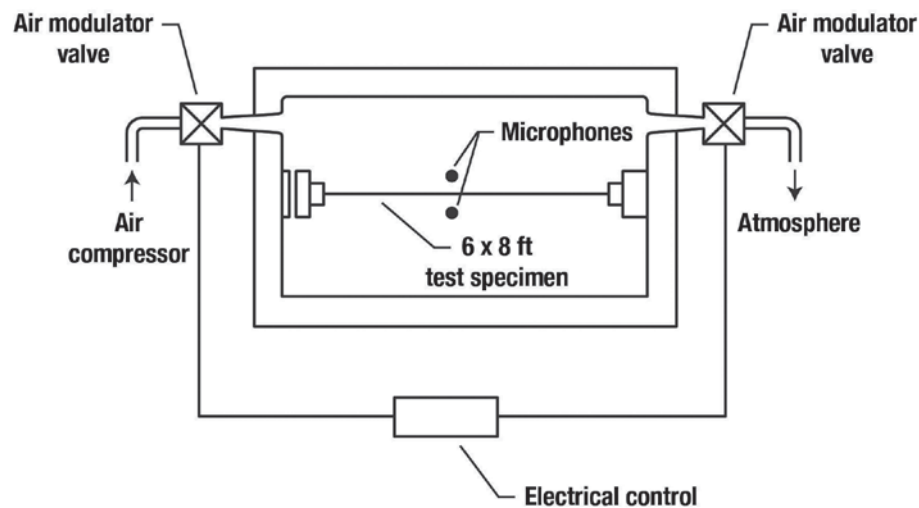


Figure 9.167. Schematic diagram of the Wyle Laboratories air modulator device used in studies of glass breakage (ref. 9.97).

Piston-Driven Devices

Piston-driven sonic boom generators have been built by several organizations, each having a different purpose. The Aeromedical Research Laboratory Dynamic Pressure Chamber at Wright Patterson Air Force Base was designed for testing humans and was discussed earlier (see fig. 9.134). The Stanford Research Institute device was designed to conduct sleep awakening and startle response studies on humans and was also discussed earlier (see fig. 9.135). However, the device built at NASA LaRC in the mid-1960s was designed to test structural models. The Langley piston-driven simulator is shown in figure 9.168 (ref. 9.1).

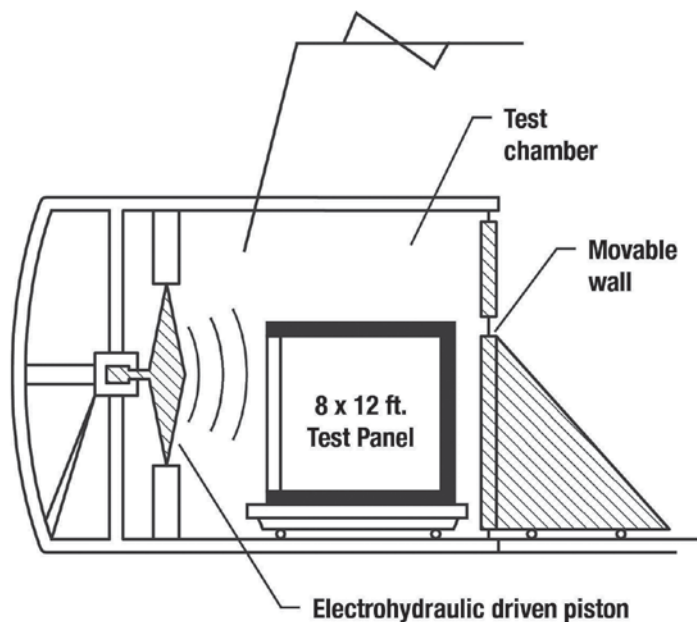


Figure 9.168. Sectional view sketch of the Langley low-frequency noise facility as used in studies of building component responses to simulated sonic booms (ref. 9.1).

As noted in reference 9.1 (p. 725):

The main features of this facility are a cylindrical test chamber, a 14-foot diameter piston, and a movable wall that can be positioned to close the opposite end of the test chamber. The facility is of sufficient size (24 feet in diameter by 21-feet long) to accommodate a small building structure or a building component for environmental testing. By means of proper control of the piston motions, N-wave type pressure transient can be generated in the range of overpressures from 0.5 to 20 lbs/ft², and for durations of 100 to 500 msec.

This facility is no longer in existence.

Loudspeakers

It has been demonstrated that loudspeakers can be used in rooms or booths to simulate outdoor and indoor sonic booms to determine their effect on humans. However, the use of a loudspeaker in the design of a simulator for use in determining the response of buildings and building components to sonic booms becomes a more difficult task due to size, intensity, and low-frequency requirements. In this section, descriptions and results will be presented on two devices – the Wyle Laboratories Acoustic Drivers used in the study of window rattle and the Acta Simulator used in the study of plaster damage.

Wyle Laboratories Acoustic Drivers

A study focusing primarily on window rattle was documented in reference 9.98 and was similar to the study described in reference 9.77, but was more restricted in nature. Instead of exposing a house with its outside wall and interior rooms to a simulated sonic boom, only a window was exposed. Window rattle is a common indoor noise in houses exposed to low-frequency noise from such sources as railroads, blast noise, and sonic boom. Human response to rattle can be a negative in the tolerance of the aforementioned noise and thus a barrier to its acceptance. The dimensions of the simulator used in the study were 1.4 m x 1.2 m x 0.5 m and the simulator had two 15-inch full range speakers (fig. 9.169, ref. 9.98). The inner part of the simulator containing the speakers had dimensions of 0.9 x 0.3 x 0.6 m. The simulator was placed outside of the house (covering the tested window) and was pressed firmly against the wall. When in position, it formed an enclosed acoustic cavity between the speakers and the exterior surface of the window. It was lined with poly-foam to dampen the acoustic resonances of the air cavity and increase the spatial uniformity of the sound field acting on the window. The simulator was capable of

generating a sound level above 140 dB (4 lbs/ft²). Transient and steady state excitation were studied and results for sinusoidal excitations were presented in the paper. Displacement and vibration were sensed using several accelerometers attached to the window and window frame, as depicted in figure 9.170. This picture is for window W6 in the house designated as house #226.

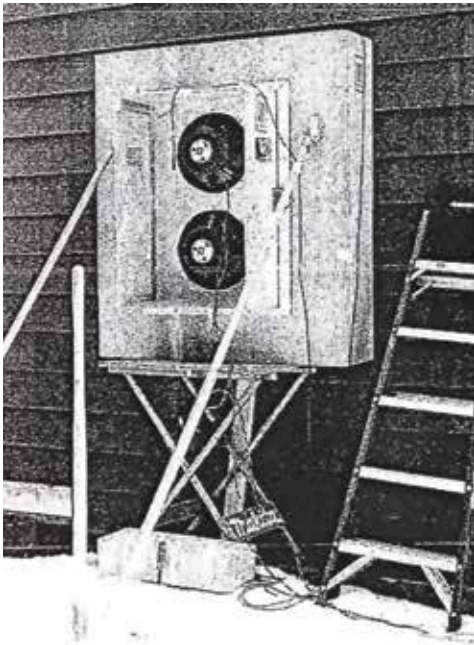


Figure 9.169. Sonic boom simulator (ref. 9.98).

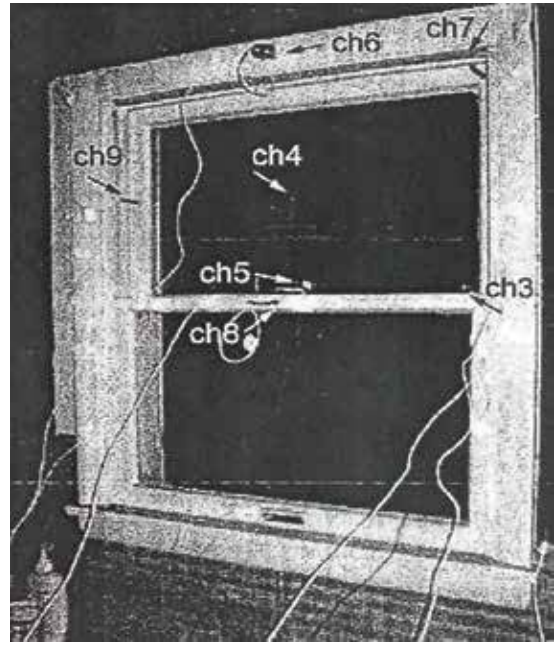


Figure 9.170. Accelerometer position inside the house (house 226, window W6) (ref. 9.98).

A database of responses from more than 40 windows was collected. Some windows had storm windows and some had screens. The presence of those components affected the measured vibration response. It was found that when a window has a storm window or screen its rattle threshold is higher. The rattle threshold of the windows was determined by exciting them acoustically using amplitude swept sinusoidal signals at discrete frequencies ranging from 10 to 500 Hz. The excitation was produced using a signal generator, the output of which was passed through an amplifier to drive the speakers of the simulator. To create the amplitude sweep, the signal generator's output voltage was gradually increased. Figure 9.171 shows the envelope of the sound pressure measured inside the simulator for a manual amplitude sweep of 50 Hz tone. As the test was performed, the sound pressure level measured by a microphone placed inside the simulator varied from low level to a maximum level of 189 Pa (140 dB, or 4 lbs/ft²), then back to a low level.

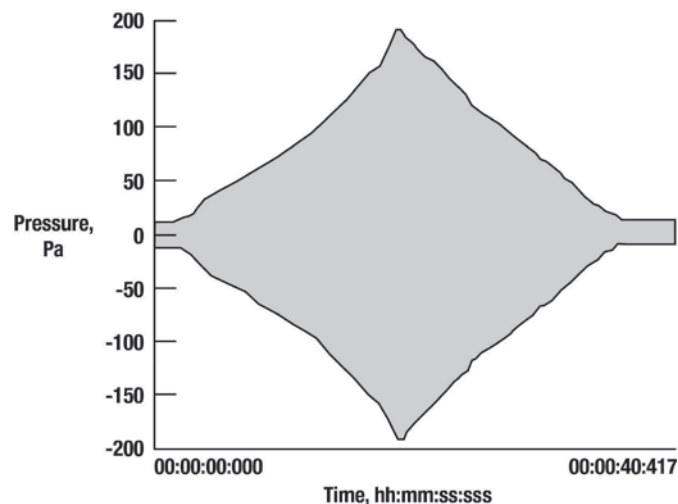


Figure 9.171. Outside pressure amplitude (50 Hz, channel 10, house #226, window W6) (ref. 9.98).

The total elapsed time of the test shown in figure 9.171 was 40.4 sec. The data was for the same window pictured in figure 9.170. Accelerometer data for the same window and 50 Hz sweep, as in figure 9.171, is shown in figures 9.172, 9.173, and 9.174. The data was for channel 8, which was located at the center of the upper horizontal sash of the lower windowpane. Rattle onset occurred at 3.4 seconds, at an acceleration level of $\sim 1.5 \text{ m/sec}^2$, and pointed out by the arrows in figure 9.172. Figure 9.173 shows the acceleration time history for the maximum acceleration experienced and figure 9.174 the acceleration variation at the time where rattle ceased.

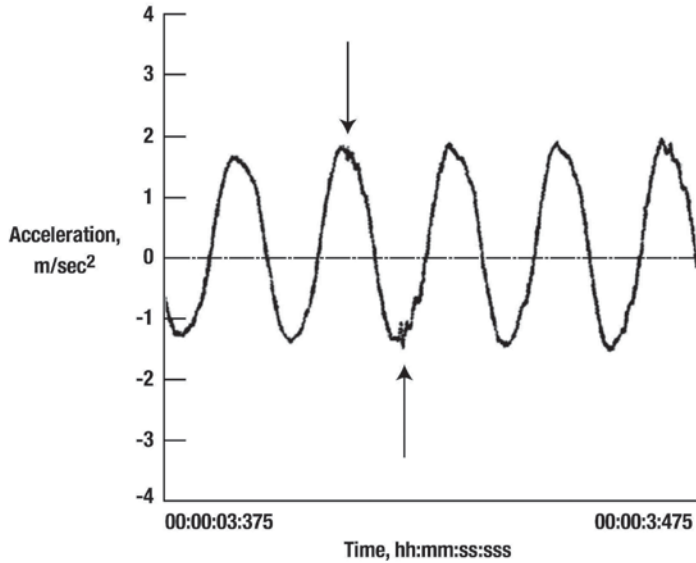


Figure 9.172. Time history of acceleration, rattle (50 Hz, channel 8 house #226, window W6) (adapted from ref. 9.99).

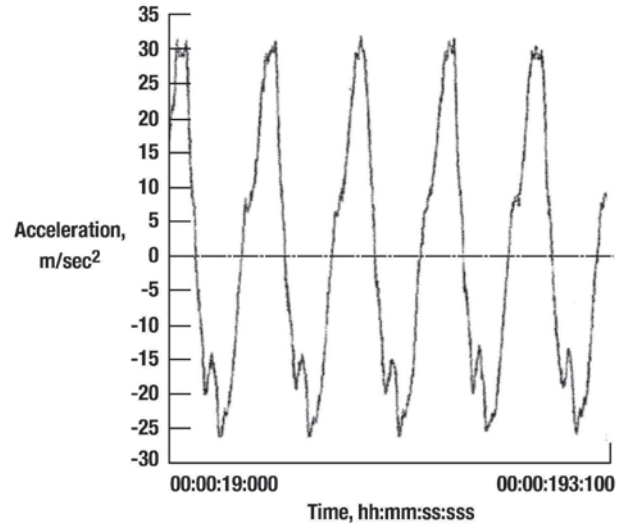


Figure 9.173. Acceleration time history at a maximum excitation (50 Hz, channel 8 house #226, window W6) (adapted from ref. 9.99).

These three figures show that there is a great variability in the response at the various locations around the window and for various window types as well. Some data are provided in reference 9.98 for the rattle threshold for various locations in W6 of house #226. Window screens and storm windows also had a big effect on window response to rattle. No sonic booms were simulated in this program, however, window responses similar to those measured in this program could be simulated. The authors noted in reference 9.98 (p. D-685) that “Results of this study will be used in further investigation of rattle mechanisms and the development of tools for predicting rattle response of windows exposed to sonic booms.”

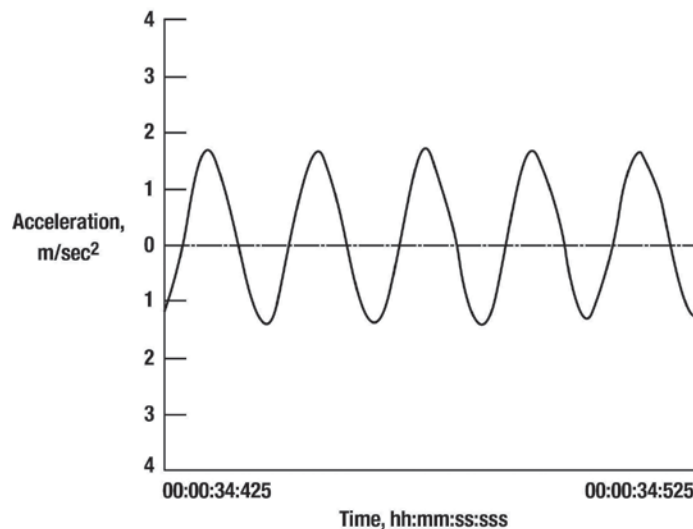


Figure 9.174. Time history of acceleration, rattle cessation (50 Hz, channel 8, house #226, window W6) (ref. 9.98).

References 9.77 and 9.98 describe simulations that are positioned outside of real houses and simulate boom or noise inputs to their walls and windows or, in the case of reference 9.98, just windows.

Acta Simulator Experiment

In 1993, Haber (ref. 9.99) investigated the potential for cumulative damage to plaster walls from sonic booms, including fixtures by simulating the plaster ceiling and room sidewalls, and exposed them to some 10,000 simulated sonic booms at overpressures that varied from about 1.8 lbs/ft² to 20 lbs/ft². A view of the Acta (BBN Systems and Technologies) Sonic Boom Simulator is shown in figure 9.175 (ref. 9.99). It was designed to expose a test article surface, ceiling, or walls measuring 8 feet by 10 feet.

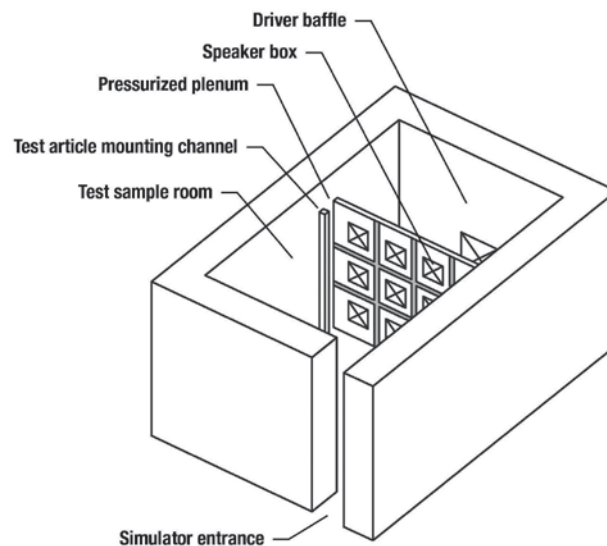


Figure 9.175. Sonic boom simulator (ref. 9.99).

Simulated booms were generated by a three-by-four array of specially designed speaker modules, each containing a pair of loudspeakers (not visible) as shown in figure 9.175. Signatures produced are shown in the upper part of figure 9.176 (ref. 9.99). An algorithm was written to compensate for the distortions in the signatures resulting from the speaker-driven motors and deformation of the test article. The compensated signature closely approximated the target N-wave. Overpressures of up to 20 lbs/ft² were obtained and signature periods were not identified.

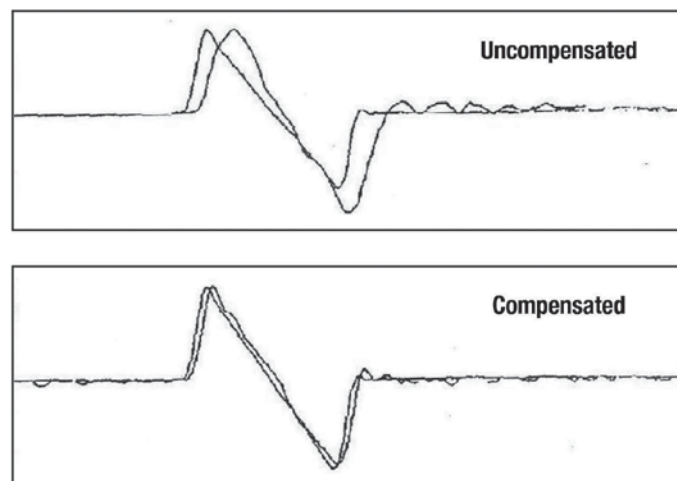


Figure 9.176. Effect of compensation on N-wave (ref. 9.99).

The test articles were full-scale walls and included window framing, exterior plywood, and interior plaster. Particular care was taken to design and install those test articles to respond like walls of residential structures having resonance frequencies in the range of 11 Hz to 25 Hz. The measured resonance of the test walls was 14 Hz. As described in reference 9.99 (p. 2), "A test sequence involved three types of activities: (1) recording the surface

plaster cracks, (2) subjecting the test article to a sequence of simulated booms at a specified overpressure, and (3) recording the number of cracks on the specimen following the sequence of booms.” A view of a test article and test fixture is shown in figure 9.177 (ref. 9.99).

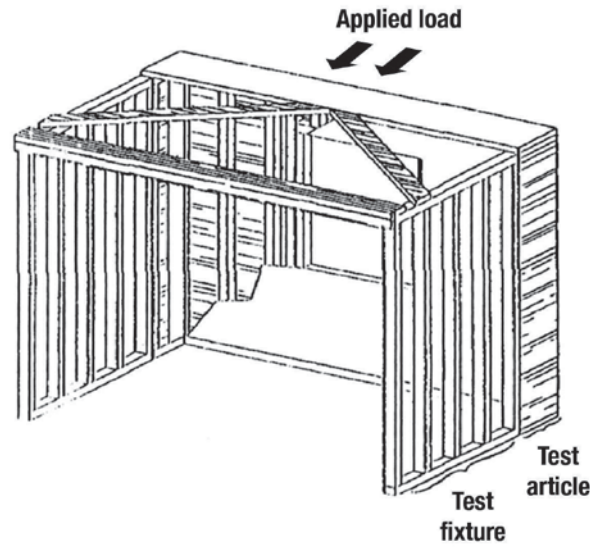


Figure 9.177. Test article and test fixture (ref. 9.99).

Framing of the test articles used two-by-three studs instead of two-by-four studs to obtain more realistic response characteristics. The base of the test article was bolted to the floor of the sonic boom simulator and the top and edges were free to move under the boom loads. The interior finish of the wall consisted of a 3/8-inch thick rock lath (board with a 1/2-inch thick base coat of plaster and a 1/8-inch thick plaster finish coat). Simulated sonic booms were imposed on three types of walls – two walls were strong plaster (i.e., tensile strength of 160 lbs/in²) and the third a weak plaster (i.e., a base coat of 80 lbs/in²). The strong plaster article was subjected to 5000 simulated booms of 20 lbs/ft² followed by 5000 more at 1.8 lbs/ft². The weak plaster article experienced three sequences of 5000 booms at 20 lbs/ft². It was stated that damage to all three walls was remarkably similar.

Figure 9.178 (ref. 9.99) presents the results of the strong plaster wall to simulated sonic booms in terms of the total crack length. This figure was also used earlier (fig. 8.12) in discussing the factors involved in structural response. Recall that this strong plaster article was subjected to two sequences of simulated booms, 5000 at 20 lbs/ft² and 5000 at 1.8 lbs/ft². A few observations can be made – (1) on the curve representing major cracks above window (solid points), a breakpoint occurs at 1000 booms – from then on, as boom exposures increase, the curve shows a constant damage rate and (2) the damage rate at this point is less than for the balance of the wall (open points).

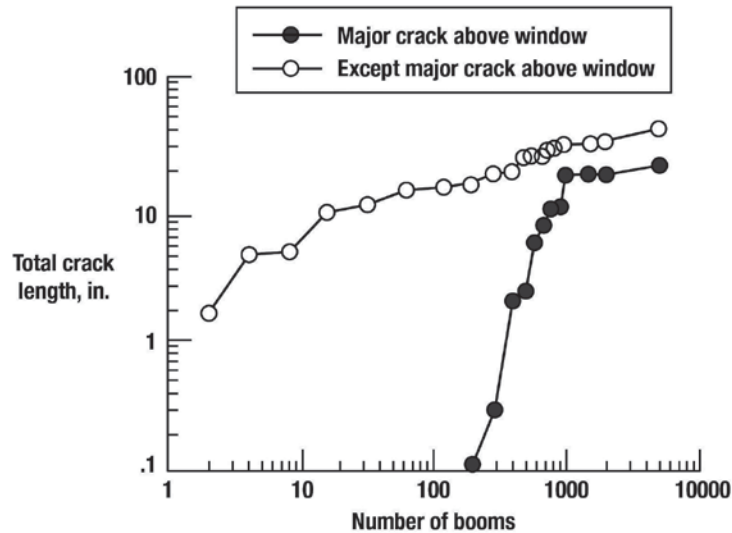


Figure 9.178. Strong plaster wall – total crack length versus number of booms (ref. 9.99, also shown as fig. 8.12).

This particular laboratory simulation was aimed at better defining how sonic booms contribute to plaster damage is an excellent example of the gathering of a substantial database under more controlled conditions at lower cost and in a relatively short time period compared to flight tests. This BBN simulator facility no longer exists.

Several simulation techniques and the many devices used to generate sonic boom signatures in the study of buildings and human response have been discussed in this section. Included are the use of linear charges, air modulation devices, piston-driven generators, and loudspeakers. Most no longer are in use or no longer exist.

Chapter 9 Summary Remarks

Sonic boom simulation devices have fulfilled a wide variety of sonic boom research needs that have led to a more complete understanding of sonic boom generation, propagation, prediction and responses.

Sonic boom simulation devices and test techniques are a necessary alternative to full-scale flight testing. In addition to providing insight and guidance, simulation devices can provide an early assessment of the viability of low-boom shaped signatures.

Sonic boom simulation experiments are shown to be less expensive and complex than flight tests and allow for more control of the physical environment and test parameters.

Issues addressed via simulators include validation of sonic boom design and prediction codes, the influence of atmospheric variability on boom signature distortions, quantifying focus boom intensities, boom penetration into water, boom reflection/refraction by building and topography, indoor-outdoor subjective response, and building response.

Controlled sonic boom disturbances can be generated using models in supersonic wind tunnels, projectiles in ballistic ranges, spark discharges, shock tubes, explosive and linear charges, piston systems, air modulator valves, and loudspeaker systems.

Chapter 9 References

- 9.1 Edge, Phillip M., Jr. and Hubbard, Harvey H.: Review of Sonic-Boom Simulation Devices and Techniques. *J. Acoust. Soc. Am.* 51, 722–728 (1972).
- 9.2 Shepherd, Kevin P. and Powell, Clemans A.: Status and Capabilities of Sonic Boom Simulators. NASA TM 87664, Jan. 1986.
- 9.3 Carlson, Harry W.: An Investigation of Some Aspects of the Sonic Boom by Means of Wind-Tunnel Measurements of Pressures About Several Bodies of Revolution at a Mach Number of 2.01, NASA TN D-161, Dec. 1959.
- 9.4 Carlson, Harry W. and Morris, Odell A.: Wind-Tunnel Sonic-Boom Testing Techniques. *AIAA J. Aircraft* 4, 245, pp. 245–249, 1967.
- 9.5 Jackson, Charlie M., Jr.; Corlett, William A.; and Monta, William J.: Description and Calibration of the Langley Unitary Plan Wind Tunnel. NASA TP 1905, Nov. 1981.
- 9.6 Mack, Robert J. and Kuhn, Neil S.: Determination of an Extrapolation Distance with Pressure Signatures Measured at Two to Twenty Span Lengths from Two Low-Boom Models. NASA TM-2006-214524, Nov. 2006.
- 9.7 Graham, David H.; Dahlin, John A.; Page, Juliet A.; Plotkin, Kenneth J.; and Coen, Peter G.: Wind-Tunnel Validation of Shaped Sonic Boom Demonstration Aircraft Design. AIAA Paper 2005-0007, Jan. 2005.

- 9.8 Carlson, Harry W.: An Investigation of the Influence of Lift on Sonic Boom Intensity by Means of Wind-Tunnel Measurements of the Pressure Fields of Several Wing-Body Combinations at a Mach Number of 2.01. NASA TN D-881, July 1961.
- 9.9 Bobbitt, Percy J. and Darden, Christine M.: A Wedge-Shaped Supersonic Flow Field Probe. NASA CP-10133, Vol. II, May 1993, pp. 379–398.
- 9.10 Carlson, Harry W.; Mack, Robert J.; and Morris, Odell A.: A Wind-Tunnel Investigation of the Effect of Body Shape on Sonic-Boom Pressure Distributions. NASA TN D-3106, Nov. 1965.
- 9.11 Shrout, Barrett L.; Mack, Robert J.; and Dollyhigh, Samuel M.: A Wind-Tunnel Investigation of Sonic Boom Pressure Distributions of Bodies of Revolution at Mach 2.96, 3.83, and 4.63. NASA TN D-6195, April 1971.
- 9.12 Carlson, Harry W.: Measurements of the Flow Properties in the Vicinity of Three Wing-Fuselage Combinations at Mach Numbers of 1.61 and 2.01. NASA TM X-64, Oct. 1959.
- 9.13 Putnam, Lawrence E. and Capone, Francis J.: Experimental Determination of Equivalent Solid Bodies to Represent Jets Exhausting into a Mach 2.24 External Stream. NASA TN D-5553, Dec. 1969.
- 9.14 Bobbitt, Percy J.; Maglieri, Domenic J.; Banks, Daniel W.; Frederick, Michael A.; and Fuchs, Aaron W.: Wind-Tunnel and Flight-Test Results for the Measurements of Flow Variables at Supersonic Speeds Using Improved Wedge and Conical Probes. NASA TM-2012-216004, December 2012.
- 9.15 Durston, Donald A.; Cliff, Susan E.; Wayman, Thomas R.; Merret, Jason M.; Elmiligui, Alaa A.; and Bangert, Linda S.: Near Field Sonic Boom Test on Two Low-Boom Configurations Using Multiple Measurement Techniques at NASA Ames. AIAA-2011-3333, June 2011.
- 9.16 Cliff, Susan E.; Elmiligui, Alaa A.; Campbell, Richard L.; and Thomas, Scott D.: Evaluation of Refined Tetrahedral Mesh with Projected, Stretched, and Sheared Prism Layers for Sonic Boom Analysis. AIAA-2011-3338, June 2011.
- 9.17 Ferri, Antonio and Wang, Huai-Chu: Observations of Problems Related to Experimental Determination of Sonic Boom. NASA SP-255, Oct. 29–30, 1970, pp. 272–284.
- 9.18 Hicks, Raymond M.; Mendoza, Joel P.; and Thomas, Charles L.: Pressure Signatures for the Apollo Command Module and the Saturn V Launch Vehicle with a Discussion of the Strong Shock Extrapolation Procedures. NASA TM X-62, 117, April 6, 1972.
- 9.19 Hicks, Raymond M. and Mendoza, Joel P.: A Brief Study of the Space Shuttle Sonic Boom during Ascent. NASA TM X-62,050, July 23, 1971.
- 9.20 Wayman, Thomas R.; Waithe, Kenrick A.; Howe, Donald C.; Bangert, Linda S.; and Wilcox, Floyd J.: Near Field Acoustic Test on a Low Boom Configuration in Langley's 4x4 Wind Tunnel. AIAA-2011-3331, June 2011.
- 9.21 Callaghan, J. G.: A Feasibility Investigation Concerning the Simulation of Sonic Boom by Ballistic Models. NASA CR-603, 1966.
- 9.22 Bauer, A. B. and Bagley, C. J.: Sonic Boom Modeling Investigation of Topographical and Atmospheric Effects. Report No. FAA NO-70-10, July 1970.
- 9.23 Downing, Micah; Zamot, Noel; Moss, Chris; Morin, Daniel; Wolski, Ed; Chung, Sukhwan; Plotkin, Kenneth; and Maglieri, Domenic: Controlled Focus Booms from Maneuvering Aircraft. *J. Acoust. Soc. Am.* 104(1), July 1998, pp. 112–121.

- 9.24 Crow, S. C.: Distortion of Sonic Bangs by Atmospheric Turbulence. *J. Fluid Mech.* (1969), Vol. 37, Part 3, pp. 529–563.
- 9.25 Hague, D. W. and Jones, R. T.: Application of Multivariate Search Techniques to a Design of Low Sonic Boom Overpressure Body Shapes. NASA SP-255, Oct. 1970, pp. 307–323.
- 9.26 Davy, Bruce A. and Blackstock, David T.: Measurements of the Refraction and Diffraction of a Short N-Wave by a Gas-Filled Soap Bubble. *J. Acoust. Soc. Am.*, Vol. 49, No. 3 (Pt. 2), March 1971, pp. 732–737.
- 9.27 Pierce, A. D.: Spikes on Sonic Boom Pressure Waveforms. *J. Acoust. Soc. Am.*, 44, 1052–1061 (1968).
- 9.28 Ribner, H. S.; Morris, P. J.; and Chu, W. H.: Laboratory Simulation of Development of Superbooms by Atmospheric Turbulence. *J. Acoust. Soc. Am.*, Vol. 53, No. 3, 1973, pp. 926–928.
- 9.29 Tubbs, P. E.: Measured Effects of Turbulence on the Rise Time of a Weak Shock. AIAA Paper 75-453 (1975).
- 9.30 Bass, H. E.; Layton, B. A.; Bolen, L. N.; and Raspet, R.: Propagation of Medium Strength Shock Waves through the Atmosphere. *J. Acoust. Soc. Am.*, 82, 306–310 (1987).
- 9.31 Lipkens, Bart and Blackstock, David T.: Model Experiment to Study Sonic Boom Propagation through Turbulence, Part 1: General Results. *J. Acoust. Soc. Am.*, 103(1), June 1998, pp. 148–158.
- 9.32 Auger, T. and Coulouvrat, F.: Numerical Simulation of Sonic Boom Focusing. *AIAA Jour.*, Vol. 40, No. 9, Sept. 2002, pp. 1726–1734.
- 9.33 Maglieri, D. J.; Bobbitt, P. J.; Massey, S. J.; Plotkin, K. J.; Kandil, O. A.; and Zheng, X.: Focused and Steady-State Characteristics of Shaped Sonic Boom Signatures: Prediction and Analysis. NASA CR-2011-217156, June 2011.
- 9.34 Peter, A.; Pfister, N.; Stimpfling, A.; and Devaud, M.: Edute Experimentale de la Refraction d'une Detonation Balistique Dans Une Atmosphere Stratifiée. Institut Franco - Allemand de Recherches de Saint-Louis, France, Rep. No. 17/71 (1971).
- 9.35 Wanner, F. C.; Vallee, J.; Viver, C.; and Thery, C.: Theoretical and Experimental Studies of Focus of Sonic Booms. *J. Acoust. Soc. Am.* 52, pp. 13–32 (1972).
- 9.36 Maglieri, D. J.; Hilton, D. A.; Huckel, V.; Henderson, H. R.; and McLeod, N. J.: Measurements of Sonic Boom Signatures from Flights at Cutoff Mach Number. NASA SP-255, Oct. 1970, pp. 243–254.
- 9.37 Haglund, George T. and Kane, Edward J.: Flight Test Measurements and Analysis of Sonic Boom Phenomena Near Shock Wave Extremity. NASA CR-2167, Feb. 1973.
- 9.38 Sanai, M.; Toong, T. Y.; and Pierce, A. D.: Ballistic Range Experiments on Superbooms Generated by Refraction. *J. Acoust. Soc. Am.*, Vol. 59, No.3, March 1976, pp. 512–519.
- 9.39 Reed, J. W.: Sonic Boom Measurements from Accelerating Supersonic Tracked Sleds. NASA CR-132388, Jan. 1974.
- 9.40 Beasley, W. D.; Brooks, J. D.; and Barger, R. L.: A Laboratory Investigation of N-Wave Focusing. NASA TN D-5306, July 1969.
- 9.41 Cornet, E. P.: Focusing of an N-wave by a Spherical Mirror. Tech. Rept. ARL-TR-72-40, Applied Research Laboratories. The Univ. of Texas at Austin, Sept. 1972.

- 9.42 Wright, Wayne M. and Blackstock, David T.: Focusing of N-Waves in Air by an Ellipsoidal Reflector. *J. Acoust. Soc. Am.*, 102(2), Pt. 1, Aug. 1997, pp. 741–746.
- 9.43 Whitham, G. B.: A New Approach to Problems of Shock Dynamics, Part 1, Two-Dimensional Problems. *J. Flid. Mech.* 2, 1957, pp. 145–171.
- 9.44 Sturtevant, Bradford: Studies of Shock Focusing and Nonlinear Resonance in Shock Tubes, “Recent Developments in Shock Tube Research,” Eds. D. Bershader and W. Griffith, Stanford Univ. Press, Stanford, CA, 1973, pp. 23–34.
- 9.45 Sanai, M.; Toong, T. Y.; and Pierce, A. D.: Ballistic Range Experiments on the Superboom Generated at Increasing Flight Mach Numbers. *J. Acoust. Soc. Am.*, Vol. 59, No. 3, March 1976, pp. 520–524.
- 9.46 Waters, J. and Glass, R. E.: Penetration of Sonic Boom Energy Into the Ocean. An Experimental Simulation. Hydrospace Research Corp., Final Report. on Contract FA-70-WAI-185 HRC TR 288, June 1970, available from NTIS-/DTIC as AD 711 963.
- 9.47 Intrieri, P. and Malcolm, G.: Ballistic Range Investigation of Sonic-Boom Overpressures in Water. *AIAA Jour.*, Vol. II, No. 4, 510-516, April 1973 (also AIAA paper 72-654, 1972).
- 9.48 Sawyers, K. N.: Underwater Sound Pressure from Sonic Booms. *J. Acoust. Soc. Am.*, 523-24, 1968.
- 9.49 Dini, Dino and Lazzeretti, Renzo: Ground Configuration Effects on Sonic Boom. Aircraft Engine Noise and Sonic Boom. FDP-PEP, CP12, AGARD, 1969, pp. 25–1 to 25–29.
- 9.50 National Sonic Boom Evaluation Office: Sonic Boom Experiments at Edwards Air Force Base. NSBEO 1-67 (Contract AF 49(638) – 1758), Stanford Res. Inst., July 28, 1967.
- 9.51 Blume, John A. and Associates: Structural Reaction Program. National Sonic Boom Study Project, FAA Rept. SST-65-15, Vol. I, Apr. 1965.
- 9.52 Klos, J.: Vibro-Acoustic Response of Buildings Due to Sonic Boom Exposure: July 2007 Field Test. NASA TM-2008-215349, Sept. 2008.
- 9.53 Cho, Sang I. and Sparrow, Victor W.: Sonic Boom Diffraction around Buildings using a Finite Difference Time Domain Approach. Noise-Con 2008, July 2008, pp. 650–657.
- 9.54 Ting, L. and Pan, Y. S.: Part II - Incidence of N-Waves on Structures. NASA SP-180, May 1968, pp. 89–98, May 1968.
- 9.55 Ting, Lu and Kung, Fanny: Studies in the Diffraction of a Pulse by a Three-Dimensional Corner. NASA SP-255, Oct. 1970, pp. 161–180.
- 9.56 Ting, L.: On the Diffraction of an Arbitrary Pulse by a Wedge on a Cone. *Quart. Appl. Math.*, Vol. 18, No. 1, April 1960, pp. 89–92.
- 9.57 Brooks, J. D.; Beasley, W. D.; and Barger, R. L.: Laboratory Investigation of Diffraction and Reflection of Sonic Boom by Buildings. NASA TN-D-5830, June 1970.
- 9.58 Turner, M.: A Sonic Boom Simulator for Subjective Testing. Master’s Thesis, Univ. Southampton. 1963.
- 9.59 Ellis, R. M.: Subjective Reaction to Simulated N Waves. Master’s Thesis, Univ. South Hampton, March 1964.
- 9.60 Zepler, E. E. and Harel, J. R. P.: The Loudness of Sonic Booms and Other Impulsive Sounds. *J. Sound Vibration* 1965 2(3), 249–256.
- 9.61 Pearsons, K. S. and Kryter, K. D.: Laboratory Tests of Subjective Reactions to Sonic Boom. NASA CR 187, Mar. 1965.

- 9.62 Shepherd, L. J. and Sutherland, W. W.: Relative Annoyance and Loudness Judgments of Various Simulated Sonic Boom Wave Forms. NASA CR-1192, Sept. 1968.
- 9.63 Falkiewicz, A.: Development of Loudspeaker-Drive Simulator for Sonic Booms and Other Transient Sounds. M.A. Sc. Thesis. Inst. for Aerospace Studies. U. of Toronto, 1972.
- 9.64 Glass, I. I.; Ribner, H. S.; and Gottlieb, J. J.: Canadian Sonic Boom Simulation Facilities. *Can. Aeronau. Space J.* 18(8), 1972, pp. 235–246. Also AIAA paper No. 72-26, Sept. 1972.
- 9.65 Niedzwiecki, A. and Ribner, H. S.: Subjective Loudness of N-wave Sonic Booms. *J. Acoust. Soc. Am.*, 64(6), Dec. 1978, pp. 1617–1621.
- 9.66 Leatherwood, Jack D.; Shepherd, K. P.; and Sullivan, Brenda M.: A New Simulator for Assessing Subjective Effects of Sonic Booms. NASA TM 104150, Sept. 1991.
- 9.67 Sullivan, Brenda M.; Davies, Patricia; Hodgdon, Kathleen K.; Salamone, Joseph A.; and Pilon, Anthony: Realism Assessment of Sonic Boom Simulators. *Noise Control Eng.* J56(2), Mar.–Apr. 2008, pp. 141–157.
- 9.68 Salamone, Joe: Portable Sonic Boom Simulation. CP838, *Innovations in Nonlinear Acoustics: 17th Int. Symp. on Nonlinear Acous.* Edited by A. A. Atchley, V. W. Sparrow and R. M.; Keolian. Melville, NY, 2006, pp. 667–670.
- 9.69 Epain, N.; Herzog, P.; Rabau, G.; and Friot, E.: Preliminary Work about the Reproduction of Sonic Boom Signals for Perception Studies. CP838, *Innov. in Nonlinear Acous. 17th Int. Symp. on Nonlinear Acous.* Edited by A. A. Atchley, V. W. Sparrow and R. M. Keolian, Melville, N. Y. 2006, pp. 663–665.
- 9.70 Niedzwiecki, A. and Ribner, H. S.: Subjective Loudness and Annoyance of Filtered N-Wave Sonic Booms. *J. Acoust. Soc. Am.* 65(3), March 1979, pp. 705–707.
- 9.71 Niedzwiecki, A. and Ribner, H. S.: Subjective Loudness of “Minimized” Sonic Boom Waveforms. *J. Acoust. Soc. Am.*, 64, 1978, pp. 1622–1626.
- 9.72 Brown, D. E. and Sullivan, B. M.: Adaptive Equalization of the Acoustic Response in the NASA Langley Sonic Boom Chamber. *Proc. of Conf. on Recent Adv. in Active Control of Sound and Vibration*, VPI&SU, Blacksburg, VA, April 15–17, 1991.
- 9.73 Rabau, G. and Herzog, P.: A Specific Cabin for Restitution of Sonic Boom; Application for Perceptive Tests. *Proc. of Joint Cong. CFA/DAGA '04(2004)* on CD ROM (2 pages).
- 9.74 Takane, S.; Suzuki, Y.; and Sone, T.: A New Method for Global Sound Field Reproduction Based on Kirchoff's Integral Equation. *ACUSTICA - Acta Acustica* 85 (1999), pp. 250–257.
- 9.75 Shepherd, Kevin P. and Sullivan, Brenda M.: A Loudness Calculation Procedure Applied to Shaped Sonic Booms. NASA TP 3134, Nov. 1991.
- 9.76 McCurdy, David A.; Brown, Sherilyn A.; and Hilliard, R. David.: Subjective Response of People to Simulated Sonic Booms in Their Homes. *J. Acoust. Soc. Am.*, 116(3), Sept. 2004, pp. 1573–1584.
- 9.77 Ahuja, K. K.; Stevens, J. D.; and Walterick, R. E.: A Giant Simulator of Sonic Boom and Aircraft Noise. AIAA Paper 93-4430, Oct. 1993.
- 9.78 Pearsons, K. S.; Tabachnick, B.; Howe, R.; Ahuja, K. K.; and Stevens, J. C.: A Study of the Effects of Sonic Boom Waveform Modification on Annoyance. NASA LaRC Contract No. NAS1-19061, Final Report, March 1993.

- 9.79 Klos, Jacob; Sullivan, Brenda M.; and Shepherd, Kevin P.: Design of an Indoor Simulator at NASA Langley Research Center. Noise-Conf. 2008, July 28–30, 2008, pp. D-638-649.
- 9.80 Johnson, Daniel J.: Auditory and Physiological Effects of Infra-sound. *Inter-Noise 75*, Aug. 27–29, pp. 475–482.
- 9.81 Lukas, J. S. and Kryter, K. D.: A Preliminary Study of the Awakening and Startle Effects of Simulated Sonic Booms. NASA CR-1193, Sept. 1968.
- 9.82 Lukas, J. S. and Kryter, K. D.: Awakening Effects of Simulated Sonic Booms and Subsonic Aircraft Noise on Six Subjects to 72 Years of Age. NASA CR-1599, May 1970.
- 9.83 Warren, C. H. E.: A Preliminary Analysis of the Results of Exercise Crackerjack and Their Relevance to Supersonic Transport Noise. RAE, TN No. Aero. 2789, Sept. 1961.
- 9.84 Webb, D. R. B. and Warren, C. H. E.: Physical Characteristics of the Sonic Bangs and Other Events at Exercise Westminster. RAE TR NO. 65248, Nov. 1965.
- 9.85 Johnson, D. R. and Robinson, D. W.: The Subjective Evaluation of Sonic Bangs, *ACUSTICA*, Vol. 18, No. 5, 1967, pp. 241–258.
- 9.86 Schomer, P. D.; Sias, J. W.; and Maglieri, D. J.: A Comparative Study of Human Response Indoors to Blast Noise and Sonic Booms, *Noise Control Eng. J.* 45(4), 1997, July–Aug. 1997, pp. 169–182.
- 9.87 Schomer, Paul D.: New Descriptor for High-Energy Impulsive Sounds. *Noise Control. Eng. J.* 42(5), 1994, pp. 179–191.
- 9.88 Hawkins, S. J. and Hicks, J. A.: Sonic Bang Simulation by a New Explosives Technique, *Nature* 211, No. 5055, 1966, pp. 1244–1245.
- 9.89 Strugielski, R. T.; Fugelso, L. E.; and Byrne, W. J.: Sonic Boom Simulation with Detonable Gasses. AIAA paper No. 71-186, January 1971.
- 9.90 Haac, T. Ryan; Corcoran, Joe M.; Ramillieux, Marcel C.; Reichard, Georg; and Burdisso, Ricardo A.: Experimental Characterization of the Vibro-Acoustic response of a Simple Residential Structure to a Simulated Sonic Boom. AIAA Paper 2009-3386, May 2009.
- 9.91 Ewins, D. J.: *Modal Testing: Practice and Application*, Philadelphia Research Studies Press, Ltd. 2000.
- 9.92 James, G. H., III; Carne, T. G.; and Lauffer, J. P.: The Natural Excitation Technique (NExT) for Modal Parameter from Operating Wind Turbines. Albuquerque, NM, Sandia Nat. Labs., 1993.
- 9.93 Webb, D. R. B. and Pallant, R. J.: A Device for Simulating the Sonic Bang. Presented at the Symp. on Aero. Acoust., Toulouse, France, March 1968.
- 9.94 Bablke, H. E.; Kantarges, G. T.; Siddon, T. E.; and Van Houten, J. J.: The Shock Expansion Tube and Its Application as a Sonic Boom Simulator. NASA CR-1053, June 1968.
- 9.95 Tombouliau, R.: Research and Development of a Sonic Boom Simulation Device. NASA CR-1378, July 1969.
- 9.96 Tombouliau, R. and Peschke, W.: Description and Capabilities of a Traveling Wave Sonic Boom Simulator. NASA CR-1696, 1970.
- 9.97 Kao, G. C.: An Experimental Study to Determine the Effects of Repetitive Sonic Booms on Glass Breakage. FAA-70-13, June, 1970.

- 9.98 Sizov, Natalia; Schultz, Troy; Hobbs, Christopher; and Klos, Jacob: Measured Rattle Threshold of Residential House Windows. Noise Con. 2008, pp. D-677-685, July 2008.
- 9.99 Haber, J.: Cumulative Sonic Boom Damage to Plaster. AIAA 93-4446, Oct. 1993.

CHAPTER 10 OUTLOOK FOR CIVILIAN SUPERSONIC OVERLAND FLIGHT

This concluding chapter presents the authors' outlook for civilian supersonic overland flight based upon their assessment of the nearly 6 decades of sonic boom research developments described in this publication. The authors are of the opinion that the technical community is currently capable of designing a SSBJ-sized aircraft similar to the supersonic airliner concepts (refs. 10.1 and 10.2) shown in figure 10.1. These aircraft would have a low-boom shaped cruise signature of maximum overpressure in the 0.3 lb/ft² to 0.5 lb/ft² range combined with signature rise times greater than 5 msec. Acceptable performance, economic feasibility, and operational safety would also be required. To enable these class of civilian supersonic aircraft and enable regulatory change, the technical community is also prepared to design a low-boom demonstration vehicle similar to the vehicle depicted in figure 10.2.



(Courtesy of Lockheed Martin, ref. 10.1)



(Courtesy of The Boeing Company)

Figure 10.1. Potential supersonic airliner concepts.



(Courtesy of NASA)

Figure 10.2. NASA low-boom demonstration vehicle concept.

The desire to fly supersonically overland has presented the technical community with a plethora of complex technical challenges with regard to research efforts aimed at mitigating the sonic boom phenomenon over the past

six decades. Most of these technical challenges have been overcome. However, four significant questions require more comprehensive resolution before civilian supersonic overland flight operations can be realized:

- (1) Will overflowed communities find the magnitude of low-boom shaped cruise signatures acceptable?
- (2) Can the magnitude and extent of the transition focus boom footprint be minimized to allow supersonic overland operations?
- (3) Are low-boom shaped signatures less influenced by the atmosphere?
- (4) Can low-boom shaped cruise signatures possibly damage ground structures or create undesired building vibration or rattle?

Each of these four questions will be addressed in this chapter, which concludes with a citing of continuing research needs. Although considerable insight is gained through the use of simulation devices and techniques, the final answer to the four questions must be acquired via flight validation of a low-boom demonstration vehicle and associated ground measurements and community response surveys.

In 1988, approximately 60 representatives of industry, academia, government, and the military gathered at NASA LaRC for a 2-day Sonic Boom Workshop on the state of the art of sonic boom physics, methodology, and understanding (ref. 10.3). Attendees included many internationally recognized sonic boom experts who were very active in the Supersonic Transport (SST) and Supersonic Cruise Aircraft Research (SCAR) programs of the 1960s and 1970s. The purpose of the workshop was to assess the state of the art in sonic boom knowledge and prediction capability and to prioritize research efforts needed in the immediate future.

Participants in the workshop agreed that efforts should begin immediately on the three primary challenges shown in figure 10.3 in order to achieve civilian supersonic overland flight operations. The 1988 workshop participants (ref. 10.3, p. 21) concluded that “Answers to whether an acceptable waveform exists, whether an aircraft can be designed to that waveform, and whether the atmosphere will destroy the benefits of that waveform will be needed very early in any studies to develop overland high-speed civil transports.” During this time period, the question arose as to whether a shaped boom signature from a full-scale aircraft would persist through a real atmosphere to the ground. Theory and wind-tunnel tests had established that would be the case. The necessity to demonstrate that this persistence would be realized was identified by Maglieri, Sothcott, and Keefer (ref. 10.4). This flight demonstration was eventually accomplished by the Shaped Sonic Boom Demonstrator (SSBD) flight-test program on August 22, 2003 (ref. 10.5). The shaped signature was produced by modifying the Northrop Grumman F-5E aircraft (see Chapter 5, figs. 5.17 and 5.18) using existing analytical design codes to alter its nominal N-wave signature into a flat-top boom signature for the forward section of the aircraft.



Figure 10.3. Primary challenges to civilian supersonic overland flight operations.

The 1988 workshop was also the waypoint leading to the NASA High Speed Research (HSR) program of the 1990s, in which minimization of the sonic boom, airport noise, and vehicle emissions were the primary challenges for the civilian supersonic transports under consideration. In early 2000, the Defense Advanced Research Projects Agency (DARPA) funded the Quiet Supersonic Platform (QSP) program that focused on a smaller supersonic vehicle. The single goal set forth was that the vehicle shall have an initial sonic boom overpressure of 0.3 lb/ft² (ref. 10.6). The same year, NASA commissioned the National Research Council (NRC) to identify breakthrough technologies for overcoming key barriers to the development of environmentally acceptable and economically viable commercial supersonic aircraft (ref. 10.7). Low-boom shaped signatures with overpressures less than 1.0 lb/ft² were cited along with the need to ascertain the limits on overpressure and rise time that would find public acceptance of overland sonic booms.

The desire and need for establishing supersonic overland operations was recognized as a necessity by the 2003 Partnership for Air Transportation Noise and Emissions Reduction (PARTNER), established between the FAA/NASA/Transport Canada Center of Excellence (CoE) (ref. 10.8) consortium. The Center sponsored several projects aimed at determining the acceptability of low-boom signatures to the general population (i.e., what signatures will be acceptable to the public for overland supersonic flight). There were three tasks that were initially funded: (1) analytical incorporation of atmospheric turbulence onto shaped waveforms, (2) determining the annoyance of low-boom shaped waveforms, and (3) the development of the proper noise metrics. In 2004, a consortium of 10 companies was formed to pursue a supersonic cruise technology demonstrator that included Boeing, Lockheed, Northrop Grumman, Gulfstream, Cessna, Raytheon, Rolls-Royce Allison, General Electric, Pratt and Whitney, and NetJets. In July 2004, the Supersonic Cruise Industry Alliance (SCIA) charter was formed with the stated objective of conducting a flight-test program to “obtain scientific data necessary to document and establish a publicly acceptable supersonic cruise acoustic signature, thereby allowing unrestricted supersonic flight overland.” Note that the objective states an acoustic signature and did not specify a particular vehicle. The low-boom demonstration vehicle would, in fact, be a “low-boom simulator” and not be associated with any specific type of civil supersonic vehicle. It is also of interest to note that the SCIA objective was essentially the same as the first of the three research priorities identified by the 2003 PARTNER (ref. 10.8) and sonic boom experts who gathered at NASA LaRC in 1988 (ref. 10.3).

Given the recommendations of the 1988 workshop members, along with the positions taken by the NRC, PARTNER and SCIA consortiums, continued advancement and of low-boom design tools, and improved understanding of community response metrics, the authors of this publication now feel that the supersonics community has reached an appropriate juncture to provide an optimistic outlook for civil overland supersonic flight.

Predicted Annoyance to Cruise Boom Levels

An enormous amount of effort has been directed toward the establishment of acceptable low-boom shaped signatures using simulator chambers (see Chapter 8) resulting in a large creditable database. In addition, recent NASA low-boom flights (see Chapter 8, figs. 8.23-8.25), where subjects outdoors and inside instrumented houses were exposed to low overpressure N-waves of less than 0.6 lb/ft² and with increased rise times, have added to the existing human response database to booms of less than 1.0 lb/ft².

Revisiting the data previously shown in Chapter 8, figure 8.36, the percentage of the population highly annoyed by N-wave type sonic booms of various levels is presented using two metrics: (1) the overpressure (Δp) in lbs/ft² together with number of booms per day and (2) day-night average C-weighted Sound Exposure Level (CSEL). The day-night average was an aggregation based on the equal energy hypothesis, accounting for the number of events as well as their level. Also plotted on the figure was the Committee on Hearing, Bioacoustics, and Biomechanics (CHABA) curve (ref. 10.9) adopted by the American National Standards Institute (ANSI) (ref. 10.10) that provided an assessment of high-energy impulsive sounds, with respect to residential communities. Examination of the data showed that the early US-SST cruise boom level design target of 1.5 lbs/ft² was predicted

to result in 10 to 35 percent of the population being highly annoyed by 1 to 8 booms/day, respectively. However, at boom levels of 0.3 lb/ft² to 0.5 lb/ft², the annoyance numbers are reduced to about 1 to 5 percent for the one to eight booms/day.

The impulsive sounds previously mentioned included explosions, quarry blasts, artillery and gunfire, as well as sonic booms. The CSEL metric is quite insensitive to rise time and is mostly controlled by overpressure and signature duration. As a result, the CSEL does not recognize the reduced loudness of a shaped signature of the same overpressure and period but with a larger shock rise time (see Chapter 8, fig. 8.37).

A shaped signature with longer rise times (e.g., $\tau > 5$ msec) will always be more acceptable than an N-wave signature of zero rise time with the same overpressure and duration. Studies using sonic boom simulators have shown that Perceived Level (PL(dB), or also referred to as PLdB), is a better metric for assessing the loudness of N-wave and shaped signature booms. Sonic boom simulator studies indicate that a civilian supersonic business jet design with a low-boom shaped cruise signature (with a rise time greater than 5 msec) of less than 80 PLdB would find outdoor and indoor community acceptance since its shaped signature has been shown to be more acceptable than an N-wave signature of the same overpressure and duration.

Transition Focus Boom

In Chapter 3, it was shown that a credible database has been acquired regarding the nature, measurement, and generation of transition focus booms for N-wave design aircraft. These focus booms from transition flight, which can be anywhere from two to five times as intense as the steady level carpet booms, can not be avoided and only minimized. However, they impact relatively small regions on the ground, are a singular occurrence, and are not dragged along with the aircraft as is the case of carpet booms.

The beginning of every supersonic flight must contend with this challenging phase of supersonic flight. Transition focus booms were not of concern during Concorde operations since they took place over the ocean. However, for civilian overland supersonic operations, transition flight will be the most critical phase of the entire overland flight profile.

Recent analytical studies (see Chapter 3, fig. 3.18) have shown that aircraft designed to generate certain shaped sonic boom signatures will result in lower transition focus booms as compared to aircraft that generate N-wave signatures. A comparison of the focus boom overpressures along the ground track for an N-wave design aircraft, such as the 105-foot long SR-71, and a similar sized low-boom shaped vehicle such as a SSBJ during transition flight from Mach 0.9 to 1.2 at a constant altitude of 30,000 feet is given in figure 10.4.

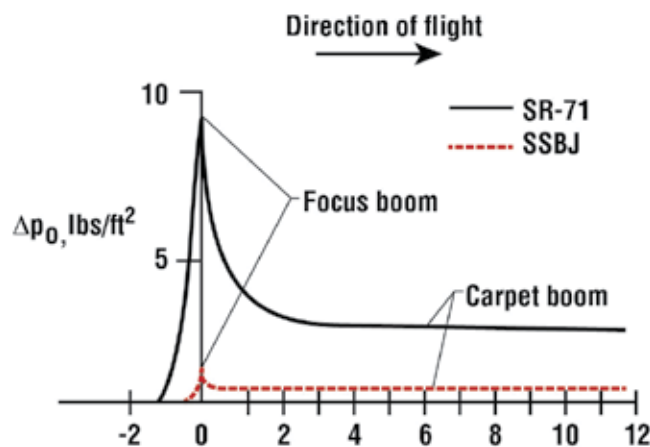


Figure 10.4. Predicted focus boom overpressures along the ground track during transition flight.

In the case of the SR-71, it can be seen that a focus overpressure of about 8.0 lbs/ft² is predicted, which is about three times as intense as the 2.5 lbs/ft² carpet boom that follows. For a low-boom shaped signature from a SSBJ, using the focus factor based on figure 3.19, the focus level is predicted to be the order of 1.0 lb/ft² or less, which is about two times the assumed 0.45 lb/ft² carpet boom at 30,000 feet. Based on the findings from references 10.11 and 10.12, one can assume that the low-boom shaped signature at cruise also retains its character during the transition phase of flight at a lower altitude and Mach number. Performing this transition at higher altitudes and incorporating an optimum climb-acceleration schedule with a robust low-boom design would likely minimize the focus boom level and footprint to the point of community acceptance.

Atmospheric Distortion of Sonic Boom Signatures

In Chapter 2, it was shown that N-wave boom signatures can become significantly distorted by turbulent activity, especially in the lower layers of the atmosphere, which cause them to become peaked or rounded. This peaking and rounding of sonic boom signatures is statistical in nature and occurs as a function of time and distance. An indication of what these statistics are for N-wave design aircraft and what they are projected to be for low-boom shaped signatures is provided in figure 10.5. A summary of the variations of the on-track N-wave signature overpressures resulting from atmospheric distortion for steady level flight (see Chapter 2, fig. 2.38) is shown again by the solid line in figure 10.5. This statistical analysis comprises most of the sonic boom experiments that have been conducted in the United States over the past 50 years. Data are included from a wide range of N-wave designed aircraft for the Mach number range of 1.2 to 3.0 and altitude range of about 10,000 to 80,000 feet. A total of 12,406 data samples have resulted from 1,625 supersonic flights.

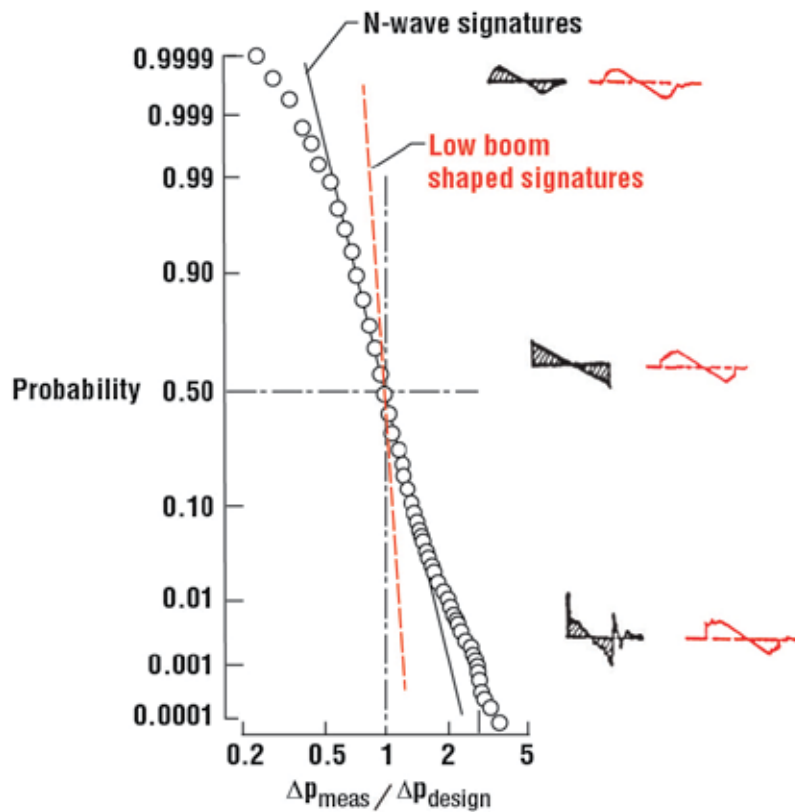


Figure 10.5. Measured and predicted statistical variation of sonic boom signatures resulting from atmospheric distortion.

The relative cumulative frequency distribution for on-track measurements showing the probability of equaling or exceeding the ratio of the measured N-wave overpressure to the design value for an N-wave designed aircraft in steady level flights, in standard atmosphere with no winds, is plotted in figure 10.5. Rounded signatures of the waveform sketched in the chart are usually associated with overpressure ratios less than 1.0. Nominal N-wave signatures are observed on the average and peaked signatures of overpressures are observed at ratios greater than 1.0. The data indicate the variations in the sonic boom signatures, resulting from the effects of the atmosphere, can be expected during routine operations. For example, one N-wave boom in a thousand is expected to exceed the design value by a factor of about 3.0. Signature variability is also known to increase with increasing distance laterally from the aircraft ground track (See Chapter 2, fig. 2.40).

Whether or not these exact statistics for N-wave booms apply to shaped signatures remains to be demonstrated. There is a reasonable expectation that the probability distribution for a low-boom shaped signature, which has low initial shock overpressure and increased shock rise time, will show less variation and thus a lesser slope, as illustrated by the dashed red line shown in figure 10.5. Since it is known that the atmospheric distortions of boom signatures take place at the bow and tail shocks, which are made up of the high frequencies, it is reasonable to expect that shaped signatures, which have less energy at high frequencies due to the increased rise times (see Chapter 8, fig. 8.7), will be less influenced by the atmosphere. As a result, the boom signatures observed at the ground during routine supersonic cruise flight operations are expected to be more closely associated with the design cruise boom signatures.

Another benefit of low-boom shaped signatures is the additional increase in shock rise time with decreasing overpressure. This increase in signature rise time is a result of atmospheric absorption due to molecular relaxation (see Chapter 2, fig. 2.45) and further reduces the influence of the atmosphere in bringing about signature distortions. The establishment of a statistical database on the variability of low-boom shaped signatures due to atmospheric variability and turbulence can be best achieved with a low-boom demonstration vehicle combined with flight and ground research instrumentation.

Sonic Boom Induced Structural Damage, Vibration, and Rattle

To appreciate the substantial, cumulative benefits that result from designing a vehicle to have a low-boom shaped signature during cruise flight, it is necessary to look back upon previous community observations to sonic boom overflights conducted during the mid-1960s, where N-wave signatures on the order of 1.0 lb/ft² to 3.0 lbs/ft² were experienced. In each of these community overflight experiments, three aspects of sonic booms were found to be most disturbing – (1) people being startled, (2) structural component vibrations and rattles, and (3) rising concerns over the possibility of sonic boom induced structural damage (see Chapter 8, figs. 8.34 and 8.35).

The nature of the sonic boom-induced damage problem as it relates to the current N-wave database wherein nominal cruise boom design levels of about $\Delta p \sim 1.5$ lbs/ft² are experienced during routine steady-level supersonic flight operations was discussed in Chapter 8 (fig. 8.22). The nature of the problem is revisited here in order to make a comparison of a likely scenario for aircraft designed with low-boom shaped signatures during cruise on the order of 0.3 lb/ft². This comparison is further illustrated in figure 10.6.

The number of damage incidents (shown by the dashed curve) for a given type of structural component increases as the overpressure increases. This is particularly evident at the higher overpressure values. Also shown is a schematic illustration of the amplitude distribution of sonic boom overpressures from current and future low-boom supersonic vehicles (the two solid line bell-shaped curves). The current N-wave database as it related to sonic boom induced damage is addressed in the figure as well. At a designed cruise overpressure of about 1.5 lbs/ft², illustrated by the vertical short-dashed line, the design boom level of 1.5 lbs/ft² is generally lower than that at which building damage might be expected for structures in good repair. However, as previously noted in figure 10.5, there is a distribution of boom overpressure amplitudes such that a small percentage of the total amplitude values occur in the relatively high overpressure range.

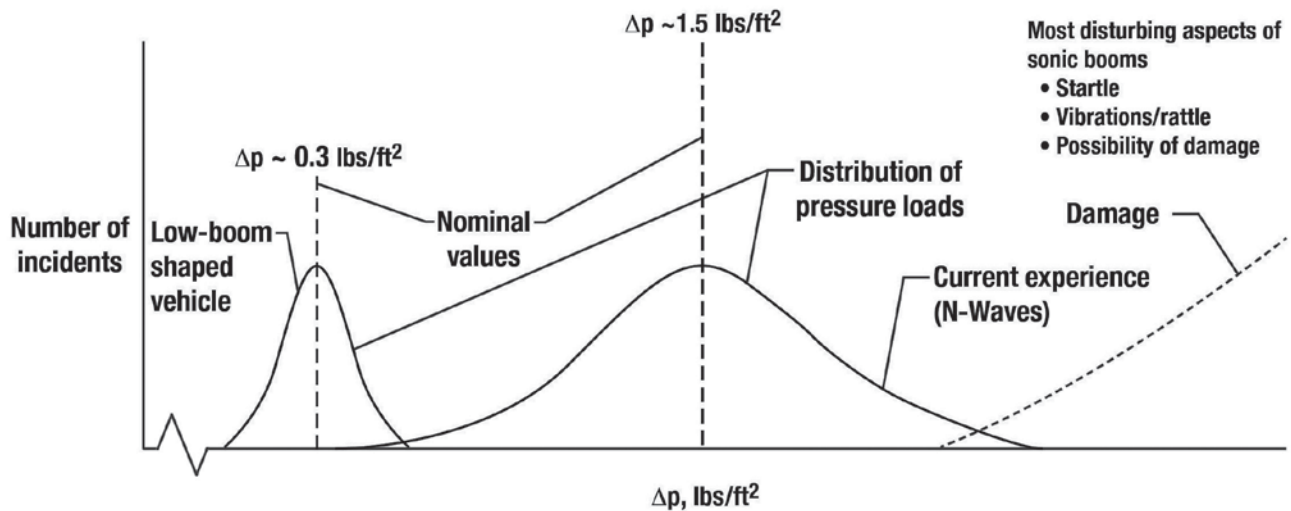


Figure 10.6. Nature of sonic boom induced damage.

These high values, which occur occasionally because of either atmospheric effects or focus booms due to maneuvers, may be sufficient to trigger incipient damage in existing structures. In order to reduce the probability of building damage, future supersonic vehicles must have much lower design cruise overpressures, as shown in figure 10.6, and shaped signatures that are less likely to be altered by the atmosphere.

The distribution of sonic boom pressure loads associated with the design of future aircraft having a low-boom shaped cruise signature of about 0.3 lb/ft² is shown in the lower left-hand side of figure 10.6. The Δp distribution of pressure loads curve shows considerably less variability (narrower bell shape distribution) because of the low-boom shaped signature experiencing less distortion by the atmosphere. It has also been noted that boom signatures with low overpressures realize increased rise times resulting from molecular relaxation and absorption. These features, along with the shaping (e.g., ramp-type signature) aspects provide a signature spectrum with even less high frequency energy and further assure that the boom signature experienced at the ground during supersonic overland flight will experience less variability and thus be much nearer the design cruise low-boom signature. Thus, a low-boom shaped cruise signature will be unlikely to damage ground structures or create undesired building vibration or rattle.

Research Needs

At the end of each of the chapters of this publication, summary remarks have been provided that capture the key concepts discussed in each Chapter. Therefore, it is appropriate to conclude with a similar, but expanded summary that also includes future research needs and the rationale for a low-boom flight demonstration. Below is a listing of research needs that should be met prior to gaining official approval for routine civil supersonic overland flight operations:

- Continue laboratory and flight activities to support the development of appropriate low-boom signatures and metrics for community acceptability.
- Continue to refine integrated aircraft design and optimization tools to achieve viable aircraft designs with optimum low-boom signatures.
- Understand and minimize the transition focus boom magnitude and footprint.
- Continue to improve our understanding of turbulence and other atmospheric effects on low-boom shaped signatures.
- Develop a low-boom demonstration vehicle that enables flight validation of low-boom technologies and the study of atmospheric effects on and community acceptability of low-boom shaped signatures.

Low-Boom Flight Demonstration

The completion of research efforts cited above combined with the nearly 60 years of fundamental research on all aspects of sonic boom will significantly advance our knowledge and understanding of this highly fascinating and complex phenomenon of the science of supersonic flight. Moreover, this level of knowledge and understanding will be advanced to the point where transition to systems level research is necessary. Further progress can be best achieved through a low-boom flight demonstration.

The need for such a vehicle was highlighted in early 2000 with the DARPA Quiet Supersonic Program (QSP) (ref. 10.6) along with the National Research Council (ref. 10.7). In 2005, NASA announced that the Vehicle Systems Program (VSP) was working on developing a low-boom flight demonstrator with the goal of providing a flight demonstration of sonic boom signatures that delineate acceptable human response. In addition to the specific vehicle designs (~100 feet in length, ~ 30,000 pounds in takeoff gross weight, Mach range 1.4-1.8 at $\leq 55,000$ feet), considerable effort was directed towards assuring that the low-boom shaped signatures of less than 0.5 lb/ft² was relevant to future larger SSBJs. During the low-boom demonstrator planning, the NASA Aeronautics Program was restructured and the project did not proceed beyond the planning phase.

In recent years, NASA's Aeronautics Program has continued research to overcome the sonic boom barrier and has produced key breakthroughs in sonic boom noise reduction through the advancement of design tools, sonic boom simulators and field studies, and advanced concept studies of civilian supersonic aircraft. In 2012, NASA began concept formulation and design studies of a new low-boom flight demonstrator taking advantage of these key breakthroughs.

A low-boom flight demonstration would enable the validation of the design tools and methods for achieving a low-boom shaped signature, enable the establishment of a database on the influence of the atmosphere on low-boom shaped signatures, and demonstrate that transition focus boom footprints can be minimized to the point of community acceptance. Such a vehicle will allow for the type of broad community experiments that will be required to fully demonstrate and garner the acceptability of low booms, generate vast sets of data that will be critical to supporting changes to the present rules that limit civil supersonic overland flight (ref. 10.8) and ultimately play a key role in the development of sonic boom standards for civilian supersonic overland flight.

Chapter 10 Summary Remarks

The authors have presented their assessment of the potential for civilian supersonic overland flight of a SSBJ type and eventually larger transport aircraft having a low-boom shaped signature during cruise flight. However, before civilian supersonic overland flight can be realized, the issues of community acceptance, transition focus minimization, impact of atmospheric distortion, and the possibility of vibration or rattle of ground structures remain for more comprehensive resolution.

This assessment shows that supersonic vehicles having low-boom shaped signatures of less than 0.5 lb/ft² would find community acceptance. Transition focus booms are shown to be on the order of 1.0 lb/ft² or less and the atmosphere is expected to have much less influence on bringing about boom signature distortions as compared to N-wave signatures. A low-boom shaped signature would significantly reduce the sonic boom startle factor, building vibrations, and thus minimize the rattle factor and greatly reduce the probability of sonic boom induced damage.

Sonic boom simulator studies indicate that a civilian SSBJ design with a low-boom shaped cruise signature (with a rise time greater than 5 msec) of less than 80 PLdB should find outdoor and indoor community acceptance since its shaped signature has been shown to be more acceptable than an N-wave signature of the same overpressure and duration.

Although considerable insight into designing an acceptable low-boom shaped signature is gained through the use of ground-based simulator signatures, conclusive data showing that civilian supersonic overland flight operations

will be acceptable can only come from the flight validation of a low-boom demonstration vehicle and associated ground measurements and community response surveys that will enable the determination of future low-boom design and community response metrics.

Chapter 10 References

- 10.1 Morgenstern, John; Norstrud, Nicole; Sokhey, Jack; Martens, Steve; and Alonso, Juan J.: Advanced Concept Studies for Supersonic Commercial Transports Entering Service in the 2018 to 2020 Period – Phase I Final Report, NASA CR-2013-217820, Feb. 2013.
- 10.2 Magee, Todd E.; Wilcox, Peter A.; Fugal, Spencer R.; Acheson, Kurt E.; Adamson, Eric E.; Bidwell, Alicia L.; and Shaw, Stephen G.: System-Level Experimental Validations for Supersonic Commercial Transport Aircraft Entering Service in the 2018-2020 Time Period – Phase I Final Report, NASA/CR-2013-217797, Feb. 2013.
- 10.3 Darden, Christine M.; Powell, Clemans A.; Hayes, Wallace D.; George, Albert R.; and Pierce, Allan D.: Status of the Sonic Boom Methodology and Understanding. NASA CP 3027, Jan. 19–20, 1988.
- 10.4 Maglieri, D. J.; Sothcott, V. E.; and Keefer, T. N., Jr.: Feasibility Study in Conducting Overflight Measurements of Shaped Sonic Boom Signatures Using the Firebee BQM 34E, RPV. NASA CR-189715, Feb. 1992.
- 10.5 Pawlowski, J. W.; Graham, D. H.; Boccadoro, C. F.; Coen, P. G.; and Maglieri, D. J.: Origins and Overview of the Shaped Sonic Boom Demonstration Program. AIAA 2005-0005, Jan. 2005.
- 10.6 Wlezien, R. and Veitch, L.: Quiet Supersonic Platform. AIAA Paper 2002-0143, Jan. 2002.
- 10.7 National Research Council, “Commercial Supersonic Technology: The Way Ahead”, National Academy Press, Washington, D.C., 2001.
- 10.8 Sparrow, Victor W.: Lowering the Boom, *Acoustics Today*, Vol. 2, Issue 1, Jan. 2006, pp. 20–28.
- 10.9 Anonymous: “Community Response to High-Energy Impulsive Sounds: An Assessment of the Field since 1981”, Committee on Hearing, Bioacoustics, and Biomechanics (CHABA). National Research Council, National Academy of Science, Washington, D.C., 1996 (NTISPB97-124044).
- 10.10 Anonymous: American Standard Method for Assessment of High Energy Impulsive Sounds with Respect to Residential Communities. ANSI S12.9, part 4, 2005.
- 10.11 Maglieri, Domenic J.; Bobbitt, Percy J.; Massey, Steven J.; Plotkin, Kenneth J.; Kandil, Osama A.; and Zheng, Xudong: Focused and Steady-State Characteristics of Shaped Sonic Boom Signatures: Prediction and Analysis, NASA/CR-2011-217156, June 2011.
- 10.12 Elmer, K.; Welge, H.; Salamone, J.; and Cowart, R.: SCAMP: Supersonic Passenger Transport Transonic Acceleration Flight Profiles with Consideration of Focused Boom, AIAA-2013-1065, Jan. 2013.

